europhysics
conference
abstracts

1992 International Conference on Plasma Physics

Joint Conference of the

9th Kiev International Conference on PLasma Theory
and the
9th International Conference on Waves and Instabilities in Plasmas
combined with the
19th EPS Conference on Controlled Fusion and Plasma Physics

Innsbruck, 29 June - 3 July 1992
Editors: W. Freysinger, K. Lackner, R. Schrittwieser, W. Lindinger

Contributed Papers, Part II

ned by: The European Physical Society
Editor: Prof. K. Bethge, Frankfurt/M
ging Editor: G. Thomas, Geneva

VOLUME 16C Part II

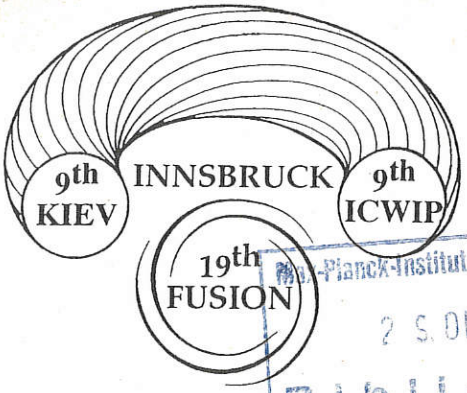

Max-Planck-Institut für Plasmaphysik
2 5. OKT. 1992
Bibliothek

Topics 4-8

1992 International Conference on Plasma Physics

Joint Conference of the

9th Kiev Interational Conference on Plasma Theory

and the

9th International Conference on Waves and Instabilities in Plasmas

combined with the

19th EPS Conference on Controlled Fusion and Plasma Physics

Innsbruck, 29 June - 3 July 1992
Editors: W. Freysinger, K. Lackner, R. Schrittwieser, W. Lindinger

Contributed Papers, Part II

0784-92

EUROPHYSICS CONFERENCE ABSTRACTS is published by the European Physical Society, © 1992

Reproduction rights reserved.

This volume is published under copyright of the European Physical Society. We wish to inform the authors that the transfer of the copyright to the EPS should not prevent an author from publishing an article in a journal quoting the original first publication or to use the same abstract for another conference. This copyright is just to protect EPS against using the same material in similar publications.

The Proceedings may be purchased from the Institute for Ion Physics, University of Innsbruck, Technikerstr. 25, A-6020 Innsbruck, Austria

PREFACE

The 1992 International Conference on Plasma Physics is held as a joint conference of the 9th Kiev International Conference on Plasma Theory and the 9th International Congress on Waves and Instabilities in Plasmas with the 19th EPS Conference on Controlled Fusion and Plasma Physics in Innsbruck, Austria, from 29 June to 3 July 1992. The conference is organized by the Institute of Ion Physics of the University of Innsbruck.

The programme, format and schedule of the Conference were determined by the International Programme Committee, which also selected the plenary and topical invited lectures based on suggestions from the International Advisory Committee of the ICPP and from other members of the scientific community. Some topical invited lectures were selected from among the contributed papers. The programme included 12 plenary, 35 topical invited lectures presented orally, and 532 poster contributions.

Innsbruck, May 1992 — The Editors

Acknowledgement:

The conference organizers acknowledge the financial support of the following agencies and institutions:

The Austrian Federal Ministry of Science and Research
The State Government ofyrol
The City of Innsbruck
The International Union of Pure and Applied Physics (IUPAP)
The Kongresshaus Innsbruck

INTERNATIONAL ADVISORY COMMITTEE

K. Appert . . . . . Switzerland
D.E. Baldwin . . . . . USA
H.A.B. Bodin . . . . . UK
T.J.M. Boyd . . . . . UK
F.F. Cap . . . . . Austria
F.F. Chen . . . . . USA
B. Chirikov . . . . . Russia
A. Dalgarno . . . . . USA
J.M. Dawson . . . . . USA
F. De Marco . . . . . Italy
S. Denus . . . . . Poland
F. Engelmann . . . . . Germany
E. Fabre . . . . . France
B.D. Fried . . . . . USA
A. Gibson . . . . . UK
D. Grésillon . . . . . France
M. Haines . . . . . UK
S. Hamberger . . . . . Australia
A. Hasegawa . . . . . USA
M.A. Hellberg . . . . . South Africa
Y.H. Ichikawa . . . . . Japan
R. Janev . . . . . Yugoslavia
A.N. Kaufman . . . . . USA
P.K. Kaw . . . . . India
T. Kawabe . . . . . Japan
L.M. Kovrizhnykh . . . . . Russia
H.J. Kunze . . . . . Germany
S. Lee . . . . . Malaysia
Zhengwu Li . . . . . China
W. Lindinger (Chairman) . . . . . Austria
J. Lingertat . . . . . Germany
P. Michelsen . . . . . Denmark
G. Murtaza . . . . . Pakistan
K. Nishikawa . . . . . Japan
T.M. O'Neil . . . . . USA
A.P. Rodrigo . . . . . Argentinia
P.H. Rutherford . . . . . USA
D.D. Ryutov . . . . . Russia
P.H. Sakanaka . . . . . Brasil
K. Sauer . . . . . Germany
F.C. Schüller . . . . . Netherlands
A.G. Sitenko . . . . . Ukrainia
H.M. Skarsgard . . . . . Canada
F.W. Sluijter . . . . . Netherlands
M.P. Srivastava . . . . . India
P. Šunka . . . . . CSFR
S. Tanaka . . . . . Japan
J.B. Taylor . . . . . UK
F. Troyon . . . . . Switzerland
P. Vandenplas . . . . . Belgium
R.R. Weynants . . . . . Belgium
H.P. Winter . . . . . Austria

PROGRAMME COMMITTEE

K. Lackner (Chairman) . . . . . Germany
W. Lindinger (Vice-chairman) . . . . Austria
F. Engelmann . . . . . Germany
V.E. Golant . . . . . Russia
G. Haerendel . . . . . Germany
M.G. Haines . . . . . UK
R. Janev . . . . . Yugoslavia
G. Laval . . . . . France
T.D. Märk . . . . . Austria
D. Robinson . . . . . UK
D.D. Ryutov . . . . . Russia
K. Sauer . . . . . Germany
F.W. Sluijter . . . . . Netherlands
R.R. Weynants . . . . . Belgium

LOCAL ORGANIZING COMMITTEE

F.F. Cap (Honorary Chairman), Institute for Theoretical Physics, University of Innsbruck;
W. Lindinger (Chairman), W. Freysinger (Scientific Secretary), M. Heigl, T.D. Märk, and R. Schrittwieser, Institute for Ion Physics, University of Innsbruck;
S. Kuhn (Minutes Secretary), Institute for Theoretical Physics, University of Innsbruck.

CONTENTS

PART I	Topic 1:	Tokamaks	I-1
	Topic 2:	Stellarators	I-487
	Topic 3:	Alternative Magnetic Confinement Schemes	I-593
PART II	Topic 4:	Plasma Edge Physics	II-721
	Topic 5:	Heating and Current Drive	II-879
	Topic 6:	Diagnostics	II-1029
	Topic 7:	Inertial Confinement Fusion	II-1223
	Topic 8:	General Plasma Theory	II-1269
PART III	Topic 9:	Space and Astrophysical Plasmas	III-1565
	Topic 10:	Basic Collisionless Plasmas	III-1675
	Topic 11:	Partially Ionized Plasmas	III-1955
	Topic 12:	Elementary Processes in Plasmas	III-2053
	Topic 13:	Plasma Applications	III-2107

LIST OF TITLES

P A R T I

Topic 1: Tokamaks

Poster-No. Volume/Page
Title,
Author(s)

1-1 I-3
High current, high power H-modes in JET,
Jones T.T.C., Balet B., Brusati M., Bures M., Hugon M., Lawson K.D., Lomas P.J., Morgan P.D., Morsi H., Nielsen P., Sadler G., Sartori R., Start D.F.H., Summers D.D.R., Tanga A., Taroni A., Thomsen K., Ward D.J.

1-2 I-7
Influence of divertor geometry and boronization on the ELM-free H-mode confinement in ASDEX,
Ryter F., Kardaun O.J.W.F., Kus A., Vollmer O., Stroth U., Wagner F., ASDEX-, NI-Teams

1-3 I-11
VH-mode discharges in the DIII-D tokamak,
Greenfield C.M., Jackson G.L., Burrell K.H., DeBoo J.C., Lao L.L., Osborne T.H., Rettig C., Schissel D.P., Taylor T.S., Winter J.

1-4 I-15
Current scaling of plasma confinement,
Christiansen J.P., Challis C., Cordey J.G., Gormezzano C., Gowers C., Kramer G.J., O'Rourke J., Taroni A., Tibone F., Tubbing B., Stubberfield P.M.

1-5 I-19
Dependence of confinement on plasma ion species in JET,
Tibone F., Balet B., Bures M., Cordey J.G., Jones T.C.C., Lomas P.J., Lawson K., Morsi H.W., Nielsen P., Start D.F., Tanga A., Taroni A., Thomsen K., Ward D.J.

1-6 I-23
Energy confinement of FTU ohmic plasma,
Alladio F., Berton F., Bracco G., Buratti P., Tudisco O., FTU Team, Bruschi A., De Luca F., Jacchia A., Mantica P.

1-7 I-27
Global energy confinement in TORE SUPRA,
Hoang G.T., Bizarro J.P., De Gentile B., Hutter Th., Laurent L., Litaudon X., Moreau D., Peysson Y., Tonon G., Van Houtte D.

1-8 I-31
Energy confinement in the tight aspect ratio tokamak, START,
Appel L.C., Duck R., Fielding S.J., Gibson K.J., Hugill J., Li J., Manhood S.J., Morris A.W., Robinson D.C., Sykes A., Turner M.F., Valovic M., Walsh M.J.

1-9 I-35
Confinement scaling for the ASDEX L-mode in different divertor configurations,
Stroth U., Kardaun O.J.W.F., Kus A., the ASDEX-, the NI-Teams

1-11 I-39
Recycling perturbations of supershot plasmas,
Scott S.D., McCune D.C., Bell M.G., Bell R., Budny R.V., Fredrickson E., Grek B., Hill K.W., Jassby D., Jobes F., Johnson D.W., Johnson L.C., Mansfield D.K., Park H.K., Ramsey A.T., Snipes J.A., Stratton B.E., Synakowski E.J., Taylor G., Towner H.H., Zarnstorff M.C.

1-12 I-43
Simulations of beam-fueled supershot-like plasmas near ignition,
Budny R.V., Grisham L., Jassby D.L., Manickam J., McCune D., McGuire K.M., Sabbagh S.A., Scott S.D., Stotler D., Wieland R., Zarnstorff M.C., Zweben S.J.

Poster-No. Volume/Page
Title,
Author(s)

1-13 I-47
The investigation of properties of ohmic, ion-cyclotron plasma heating in the condition of boronized tokamak first wall,
Azizov E.A., Buzhinskij O.I., Chernobaj A.P., Dmitriev V.I., Jakovenko V.P., Kanaev A.I., Kovan I.A., Krasilnikov A.V., Mirnov S.V., Monakhov I.A., Petrov A.A., Petrov V.G., Portnov D.V., Romannikov A.N., Semenov I.B., Sharapov V.M., Sotnikov S.M., Tugarinov S.N., Sharapov V.M., Zakharov A.P.

1-15 I-51
Confinement scaling for kinetic energy in tokamak L-mode plasmas,
Takizuka T.

1-16 I-55
The effect of current profile changes on confinement in the DIII-D tokamak,
Ferron J.R., Lao L.L., Taylor T.S.

1-17 I-59
Heat transport with strong on/off axis heating,
Balet B., Boucher D., Cordey J.G., Muir D., Neudatchin S.V., Schmidt G.

1-18 I-63
Energy confinement in high performance JET D-T plasmas,
Stubberfield P.M., Balet B., Cordey J.G., O'Brien D.P., Thomsen K., Von Hellermann M.

1-19 I-67
Determination of the ion thermal diffusivity from neutron emission profiles in decay,
Sasao M., Adams J.M., Conroy S., Jarvis O.N., Marcus F.B., Sadler G., Van Belle P.

1-21 I-71
Local power balance analysis in ohmic, ECR heated plasmas in RTP,
Konings J.A., Hogeweij G.M.D., Lopes Cardozo N.J., Oomens A.A.M., Schüller F.C., RTP Team

1-22 I-75
Perturbative transport analysis in RTP,
Hogeweij G.M.D., Lopes Cardozo N.J., Peters M., RTP Team, De Luca F., Gorini G., Jacchia A., Mantica P.

1-23 I-79
Experiments on heat pulse propagation generated by localized electron cyclotron heating on the WT-3 tokamak,
Tanaka S., Hanada K., Minami T., Maehara T., Makino K., Kisigami Y., Kishino T., Nakamura M., Maekawa T., Terumichi Y.

1-24 I-83
Characteristics of heat pulse propagation at JT-60U,
De Haas J.C.M., Nagashima K., Shirai H.

1-25 I-87
Gas puff modulation experiment on JT-60U,
Nagashima K., Sakasai A., De Haas J.C.M., Fukuda T.

1-27 I-91
Modeling simultaneous sawtooth measurements of the thermal and energetic electron diffusivities from the TEXT tokamak,
Catto Peter J., Myra J.R., Bengtson Roger D., Wootton A.J.

1-28 I-95
Asymmetry of radial heat pulse propagation at TEXTOR,
Krämer-Flecken A., Tokar M.Z., Waidmann G., Wolf G.H.

1-29 I-99
Transport studies in TJ-1 tokamak from steady and perturbative methods,
Pardo C., Rodriguez-Yunta A., Vega J., Branas B., Estrada T., Ochando M.A., Tabares F.L., Zurro B.

1-30 I-103
Magnetic turbulence measurement from pellet striations: first comparison with energy transport,
Dubois M.A., Pégourié B., Sabot R., Hoang G.T.

Poster-No. Title, *Author(s)*	Volume/Page
1-31 Transport and turbulence in TORE SUPRA ohmic discharges, *Garbet X., Payan J., Laviron C., Devynck P., Saha S.K., Capes H., Chen X.P., Coulon J.P., Gil C., Harris G., Hutter T., Pecquet A.L., Truc A., Hennequin P., Gervais F., Quéméneur A.*	I-107
1-32 Study of the plasma turbulence by means of reflectometry methods in the TUMAN-3, FT-2 tokamaks, *Aleksandrov V.O., Bulanin V.V., Korneev D.O.,Sergeyev A.A.*	I-111
1-33 Particle flux in a tokamak: fundamental experimental constraints on the form and relation to fluctuations, *Gentle K.W., Richards B., Austin M.E., Bravanec R.V., Brower D.L., Gandy R., Li W.L., Phillips P.E., Ross D.W., Rowan W.L., Schoch P.M., Sing D.C., Valanju P.M., Wootton A.J.*	I-115
1-34 Diffusion of fast electrons after a monster sawtooth crash, *Hugon M., Bartlett D., Brusati M., Froissard P., Gormezano C., Morgan P., Porte L., Rimini F., Stamp M.*	I-119
1-35 Electron temperature and density gradients across magnetic m=2 structures in RTP, *Van Milligen B.Ph., Van Lammeren A.C.A.P., Lopes-Cardozo N.J., Schüller F.C., Verreck M.*	I-123
1-37 Profile consistency on FTU, *Buratti P., Zerbini M., Bracco G., Segre S.E., Zanza V.*	I-127
1-38 Theory-based transport simulation of tokamaks: density scaling, *Ghanem E.-S., Kinsey J., Singer C.*	I-131
1-40 Role of Alfvén-Wave filaments in tokamak transport, *Morales G.J., Ramachandran H.*	I-135
1-41 Energy and current transport: symmetry breaking and degradation, *Coppi B., Pegoraro F.*	I-139
1-42 On relaxation of tokamak discharges with toroidal plasma rotation, *Throumoulopoulos G.N., Pantis G.*	I-143
1-45 Perturbative measurement of suprathermal electron diffusion in JET, Gonhhalekar A., Bartlett D., Lomas P., Martin-Solis R., O'Brien M.	I-147
1-46 Measurements of MeV energy ICRF driven minority ions in JET, *Khudoleev A.V., Afanasyev V.I., Corti S., Gondhalekar A., Maas A.C., Petrov M.P.*	I-151
1-47 Observation of relativistic runaway electrons by synchrotron radiation in TEXTOR, *Jaspers R., Finken K.H., Mank G., Rusbüldt D., Lopes-Cardozo N.J., Schüller F.C., Boedo J., Hoenen F.*	I-155
1-48 Combined repetitive pellet injection and lower hybrid current drive experiments in TORE SUPRA, *Géraud A., Foster C.A., Pégourié B., Peysson Y., Bibet P., Chatelier M., Drawin H.W., Moreau D.*	I-159
1-49 Observations of suprathermal electrons in the edge region on JET H-mode plasmas, *Bartlett D.V., Porte L., Costley A.E., Jones S.E., Smith R., Zolfaghari A.*	I-163

Poster-No. Volume/Page
Title,
Author(s)

1-50 I-167
Effects of enhanced toroidal field ripple on JET plasmas,
Sadler G., Barabaschi P., Bertolini E., Conroy S., Deksnis E., Dietz J., De Esch B., Green B., Huguet M., Huart M., Jacquinot J., Jarvis O.N., Khudoleev A., Loughlin M.J., König R., Last J., Maas A., Petrov M., Putvinskii S., Sborchia C., Stork D., Tubbing B., Van Belle P.

1-51 I-171
Two-dimensional measurement of heat load on the first wall due to fast ion ripple loss in JT-60U with near-perpendicular NBI,
Tobita K., Tani K., Neyatani Y., Takeuchi H., Miura S., Nishitani T., Matsuoka M.

1-52 I-175
Profile measurements of localized fast electrons and ions in TORE SUPRA,
Basiuk V., Roubin J.-P., Becoulet A., Carrasco J., Martin G., Moreau D., Saoutic B.

1-53 I-179
Investigation of microturbulence drive and damping mechanism in DIII-D,
Rettig C.L., Peebles W.A., Burrell K.H., Doyle E.J., Groebner R.J., La Haye R.J., Luhmann Jr. N.C., Philipona R., Rhodes T.L.

1-54 I-183
Edge ion dynamics in H-mode discharges in DIII-D,
Groebner R.J., Burrell K.H., Gohil P., Kim J., Seraydarian R.P.

1-55 I-187
Investigation of the effect of large core changes in toroidal plasma rotation and radial electric field on confinement in H-mode discharges in the DIII-D tokamak,
La Haye R.J., Groebner R.J., Hyatt A.W., Scoville J.T.

1-56 I-191
Characteristic features of density fluctuations associated with the L-H-transition in the ASDEX tokamak,
Dodel G., Holzhauer E.and the ASDEX-Team

1-57 I-195
H-mode power threshold in ASDEX,
Ryter F., Stroth U., Wagner F., ASDEX-Group, NI-Group

1-58 I-199
Measurement of the toroidal motion of fine-scale density structures in JET plasmas,
Costley A.E., Cripwell P., Fukuda T.

1-60 I-203
Plasma flows and fluctuations during H-modes in TFTR,
Bush C.E., Stratton B.C., Synakowski E., Bretz N., Budny R., Darrow D.S., Durst R., Fonck R., Fredrickson E.D., Mazzucato E., McGuire K.M., Medley S.S., Nazikian R., Paul S., Ramsey A.T., Schivell J., Scott S.D., Taylor G., Wieland R.M., Zweben S.

1-61 I-207
Autooscillating L-H transitions under ECCD in T-10,
Voitsekhovich I.A., Kislov D.A., Parail V.V., Razumova K.A.

1-62 I-211
Rotation in ohmically heated tokamaks: a detailed comparison of experiment with theory,
Rowan W., Calvin M., Hazeltine R., Meigs A., Solano E., Valanju P.

1-63 I-215
Divertor plate biasing and current injection on TdeV,
Lachambre J.-L., Couture P., Boileau A., Boucher C., Decoste R., Gregory B., Janicki C., Lafrance D., Le Clair G., Liu-Hinz C., MacLatchy C., Martin F., Michaud D., Ross G.G., Stansfield B., St.-Onge M., Terreault B., Wang Z.

1-64 I-219
Edge fluctuations at regimes with improved confinement on CASTOR tokamak,
Stöckel J., Kryska L., Zacek F., Badalec J., Jakubka K., Mlynar J., Magula P., Kletecka P.

Poster-No. Volume/Page
Title,
Author(s)

1-66 I-223
H mode induced by the biased electrode and transition of low density to high density with optimized gas puffing in HL-1,
Ran L.B., Yang H.R., Yang S.K., Zhang S.X., Zheng Y.Z., Wang E.Y., Wang Z.H., Yao L.H., Sun S.Q., Qin Y.W., Dong J.F., Deng Z.C., Deng H.C., Guo G.C., Jiang Y.X., Li H.Z., Li K.H., Zuo H.N., Yang J.W., Yang Q.W., Huang K.Q., Yuan C.J., HL-1 Team

1-67 I-227
ELM precursors in JET,
Ali-Arshad S., Campbell D., Colton A., Cripwell P., De Kock L., Kramer G.J., Nave M.F.F., Neill G.F.

1-68 I-231
Reflectometry measurements of the m=1 satellite mode in L-, H-mode plasmas in ASDEX,
Serra F., Manso M.E., Silva A., Matias J., Wagner F., Zohm H., Kallenbach A., Varela P.

1-69 I-235
A quantitative analysis of the effect of ELMS on H-mode thermal energy confinement in DIII-D,
Schissel D.P., Osborne T.H., Carlstrom T.N., Zohm H.

1-70 I-239
Steady state H-modes in JET,
Thomas P.R., Campbell D.J., Gondhalekar A., Lowry C.J.

1-71 I-243
ELM studies on DIII-D and a comparision to ASDEX results,
Zohm H., Osborne T.O., Burrell K.H., Chu M.S., Doyle E.J., Gohil P., Hill D.N., Lao L.L., Taylor T.S., Turnbull A.D.

1-72 I-247
MHD stability models of edge localized modes in JET discharges,
Huysmans G.T.A., De Blank H.J., Kerner W., Goedbloed J.P., Nave M.F.F.

1-73 I-251
Neutron profile measurements during the tritium experiments in JET,
Marcus F.B., Adams J.M., Bond D.S., Conroy S. Howarth P.J.A., Jarvis O.N., Loughlin M.J., Sadler G., Smeulders P., Van Belle P., Watkins N.

1-74 I-255
Fuelling of JET limiter, x-point plasma by deuterium pellet injection,
Schmidt G.L., Bartlett D., Baylor L., Bures M., Edwards A., Gadeberg M., Gottardi N., Jones T., Kupschus P., Lomas P., Morgan P., Morsi H., Nielsen P., O'Rourke J., Sadler G., Start D.F.H., Stubberfield P., Tanga A., Ward D.

1-75 I-259
Measurements of the electron source distribution and implications for particle transport,
O'Rourke J., Kramer G.J., Simonini R., Sips A.C.C.

1-76 I-263
Particle transport during the tritium experiments in JET,
Balet B., Cordey J.G., Jones T.T.C., König R., Marcus F., Sadler G., Stubberfield P.M., Von Hellermann M.

1-79 I-267
First results of pellet injection in ECR and ohmic heated discharges in RTP,
Oomens A.A.M., da Cruz Jr. D.F., Van Dijk G., Van Gelder J.F.M., Lok J., Rommers J.H., Tielemans A.J.H., RTP-Team

1-80 I-271
On the bootstrap current calculations based on values of the radial electron transport,
Petrzilka V.

1-81 I-275
Helium transport studies on DIII-D,
Finkenthal D., Hillis D.L., Wade M.R., West W.P., Hogan J.T., Burrell K.H., Seraydarian R., Groebner R.J., Gohil P., Klepper C.C., Mioduszewski P.K.

Poster-No. Volume/Page
Title,
Author(s)

1-83 I-279
Poloidal asymmetry of impurity in co-, counter-injection experiment at JET,
Giannella R., Christensen M., De Angelis R., Gottardi N., Lauro-Taroni L., Mattioli M., Pasini D.

1-84 I-283
Scaling of impurity transport in JET,
Pasini D., Giannella R., Lauro-Taroni L., Magyar G., Mattioli M.

1-85 I-287
Particle and impurity transport in JET versus neoclassical theory,
Lauro-Taroni L., Giannella R.

1-86 I-291
Components of P_{rad} and Z_{eff} derived from X-ray spectroscopy of the main inpurities in JET,
Barnsley R., Brzozowski J., Coffey I.H., Lawson K.D., Melnick I.M., Patel A., Patel T.K., Peacock N.J.

1-87 I-295
Effective ion charge and impurity behavior in the Frascati tokamak upgrade,
McNeill D.H., Zanza V., Mazzitelli G., Bracco G., Condrea I., De Angelis R., Orsitto F., Panaccione L., Segre S.

1-88 I-299
Studies of impurity confinement injected by laser blow-off in the TJ-1 tokamak,
Zurro B., Vega J., Aragon F., Burgos C., Pacios L., Pardo C.

1-89 I-303
Toroidal diffusion of injected impurities in the MT-1M tokamak,
Zoletnik S., Veres G., Bakos J.S., Bürger G., Ignacz P.N., Kardon B., Kalvin S., Kocsis G., Szigeti J.

1-94 I-307
Long pulse operation in JET,
Brusati M., Bures M., Clements S., Ehrenberg J., Horton L., Jones T.T.C., Lawson K., Lomas P., Morgan P., Nielsen P., Sartori R., Schmidt G., Stamp M., Summers D.

1-95 I-311
Evolution of the current profile in JET high bootstrap current plasmas,
O'Rourke J., Challis C.D., Jacquinot J., O'Brien D., Stamp M.F., Stork D., Stubberfield P., Tibone F., Tubbing B.J., Zwingmann W.

1-96 I-315
Bootstrap current driven by alpha particles in a fusion reacting tokamak,
Chang C.S.

1-97 I-319
Fast wave spectral properties in ITER tokamak,
Elfimov A.G., Medvedev S.Yu., Pestryakova G.A.

1-99 I-323
Expansion of the ablated pellet substance along the magnetic field lines,
Spathis P.N., Lengyel L.L.

1-100 I-327
Identification of ion cyclotron emission from fusion alpha particles during JET deuterium-tritium experiments,
Cottrell G.A., Bhatnagar V.P., da Costa O., Dendy R.O., Edwards A., Jacquinot J., Nave M.F.F., Schmid M., Sibley A., Smeulders P., Start D.F.H.

1-102 I-331
MHD limiting phenomena in high performance JET plasmas,
Alper B., Edwards A.W., Gill R.D., Pasini D., Smeulders P.

1-103 I-335
High-β_p MHD activity in JET,
Hender T.C., Alper B., Ali-Arshad S., DeBlank H.J., Challis D.C., Gimblett C., Han J., Jacquinot J., Kramer G.J., Kerner W., Nave M.F., O'Brien D.P., O'Rourke J., Smeulders P., Stamp M., Summers D., Tibone F., Tubbing B., Zolfaghari A., Zwingmann P.W.

Poster-No. Volume/Page
Title,
Author(s)

1-104 I-339
High β studies in the H-mode and hot ion H-mode in JET,
Stork D., Alper B., Ali-Arshad S., De Blank H.J., De Esch H.P.L., Edwards A., Hender T.C., König R., Kramer G., Marcus F.B., Nave M.F., O'Brien D.P., O'Rourke J., Smeulders P., Stamp M., Tibone F., Tubbing B.J.D., Zolfaghari A., Zwingmann P.W.

1-105 I-343
Ideal-MHD operational limits for highly elongated tokamaks,
Eriksson G., Bondeson A., Ward D.J., Hofmann F., Villard L.

1-107 I-347
Fine structure in tokamak operating region,
Li L.H., Deng C.B., Li G.X., Guo D.Q., Xie J.K., Huang R.

1-108 I-351
The high density and high β_{pol} disruption mechanism on TFTR,
Fredrickson E., Manickam J., McGuire K.M., Monticello D., Nagayama Y., Park W., Taylor G., Drake J.F., Kleva R.G.

1-109 I-355
Generation and loss mechanisms of runaway electrons following disruptions in JET,
Gill R.D., Edwards A.W.

1-110 I-359
Density turbulence and disruptive phenomena in TEXTOR,
Waidmann G., Jadoul M., Kuang G.

1-111 I-363
Electron density profile and microturbulence modification by MHD instabilities,
Brower D.L., Yu C.X., Jiang Y., Chen J.Y., Lin H., Luhmann Jr. N.C., Peebles W.A., Yang X.Z., Zhao S.J.

1-112 I-367
Investigation of tearing modes with toroidal coupling in a tokamak with arbitrary cross-section and aspect ratio,
Atanasiu C.V., Zakharov L.E., Subbotin A.A., Chudin N.V.

1-115 I-371
Internal MHD perturbations in T-10 tokamak,
Savrukhin P., Kislov D., Lyadina E., Razumova K., Bagdasarov A., Volkov V.

1-117 I-375
The sawtooth collapse in rotating JET plasmas,
Büchse R., Campbell D.J., Edwards A.W., Gill R.D.

1-118 I-379
A comparison of JET sawtooth behaviour in plasmas with co- and counter-neutral beam injection,
Edwards A.W., Bickley A., Büchse R., Challis C.D., König R., Marcus F.B., O'Rourke J., Stork D.

1-119 I-383
Investigation of the sawtooth precursor oscillations of electron density and electron temperature in ohmic tokamak discharges on TEXTOR,
Koslowski H.R., Krämer-Flecken A.

1-120 I-387
The influence of mode locking by resonant helical fields on fluctuations induced particle transport in Tokoloshe Tokamak,
Van Vurren G.W., Roberts D.E., Fletcher J.D., Hellberg M.A., De Villiers J.A.M.

1-122 I-391
Sawtooth oscillations with q_o, the safety factor on axis, below unity,
Anderson D., Kolesnichenko Ya.I., Lisak M., Wising F., Yakovenko Y.V.

1-123 I-395
Sawtooth activity and photoneutron production,
Guo G.C., Zhong Y.Z., Dong J.F., Fu B.Z., Yang J.W., Zhang G.Y., Liang W.X., Gong D.F., Shi M.L.

Poster-No. Volume/Page
Title,
Author(s)

1-124 I-399
MHD properties of low-aspect-ratio tokamak plasmas,
Gryaznevich M., Bondeson A., Duck R., Hender T., Robinson D.C., Sykes A.

1-125 I-403
Excitation of fast density oscillations by pellet injection and its relation with sawtooth activity in TEXTOR plasmas,
Sato K.N., Akiyama H., Kogoshi S., Noda N., Sakamoto M., Dippel K.H., Finken K.H., Fuchs G., Koslovski H.R., Soltwisch H., KFA TEXTOR Team

1-126 I-407
First measurements of fast MHD fluctuations in JET by ECE correlation radiometry,
Zolfaghari A., Bartlett D.V., Costley A.E., Cripwell P., Jones S.E., Kesner J., Luckhardt S.C., Porte L., Ramos J.J., Smith R.J., Woskov P.P.

1-128 I-411
Fluid rotation and resonant magnetic perturbations in COMPASS-C,
Carolan P.G., Fitzpatrick R., Hender T.C., Morris A.W.

1-129 I-415
A study of the difference in confinement properties between large rotating and large locked modes on Tokoloshe tokamak,
Fletcher J.D., Roberts D.E., Nothnagel G., Van Vuuren G.W., De Villiers J.A.M.

1-130 I-419
Activation/inibition of plasma instabilities caused by resonant magnetic fields,
Araujo M.S.T., Vannucci A., Caldas I.L.

1-131 I-423
Feedback stabilisation of resistive tearing modes in tokamaks,
Morris A.W., Fitzpatrick R., Hender T.C., O'Brien M.R.

1-132 I-427
Nonlinear mechanism for the suppression of error field magnetic islands by plasma flow,
Parker R.D.

1-133 I-431
Observations of beam ion losses in TFTR during TAE modes and other MHD activity,
Darrow D.S., Fredrickson E.D., Mynick H.E., Nazikian R., White R.B., Wong K.-L., Zweben S.J., Tuszewski M.

1-135 I-435
Global Alfvén Eigenmodes in DIII-D,
Turnbull A.D., Chu M.S., Strait E.J., Heidbrink W.W., Duong H., Lao L.L., Greene J.M., Chance M.S., Taylor T.S.

1-136 I-439
Energetic particle driven instabilities at JET,
Nave M.F.F., Borba D., Cripwell P., Von Hellermann M., Kerner W., Porcelli F., Sadler G., Smeulders P.

1-137 I-443
Plasma characteristics during soft disruptions,
Lazzaro E., Simonetto A., Tanga A.

1-138 I-447
Disruption behavior of plasma and vacuum vessel in JT-60U,
Neyatani Y., Ushigusa K., Matsukawa M., Ninomiya H.

1-140 I-451
Discharge scenarios for the first operational phase of ASDEX-Upgrade,
Seidel U., Gruber O., McCarthy P., Cha S.S., Köppendörfer W., Krause A., Mertens V., Woyke W. and ASDEX-Upgrade Team

1-141 I-455
Performance of the equilibrium control system for ASDEX upgrade,
Woyke W., Gernhardt J., Gruber O., Jülich A., Lackner K., McCarthy P.J., Seidel U., ASDEX-Upgrade Team

Poster-No. Volume/Page
Title,
Author(s)

1-142 I-459
MHD equilibrium identification on ASDEX-upgrade,
Mc Carthy P.J., Schneider W., Lackner K., Zehrfeld H.P., Büchl K., Gernhardt J., Gruber O., Kallenbach A., Lieder G., Wunderlich R., ASDEX-Upgrade Team

1-143 I-463
Volt-second consumption and current ramp experiments on FTU,
Apruzzese G., Crisanti F., Frigione D., Kroegler H., Lovisetto L., Mazzitelli G., Podda S., Buratti P., Zerbini M., Romanelli F., Tudisco O.

1-144 I-467
Stabilization of axisymmetric modes and the effects of plasma deformability in elongated tokamak plasmas using active feedback coils inside and outside the vacuum vessel,
Ward D.J., Hofmann F.

1-145 I-471
Plasma performance, equilibrium and stability in spherical tokamak GLOBUS,
Belyakov V.A., Bender S.E., KavinA.A., Kostsov Yu.A., Minyaev O.A., Vasiliev V.I., Golant V.E., Levitsky A.N., Sakharov N.V., Fedorov O.V., Shakhovets K.G.

1-146 I-475
Rapid controlled shutdown of a burning plasma,
Pacher G.W., Pacher H.D.

1-147 I-479
Neutral beam heating in Alvand IIC tokamak,
Ghorannevisse M., Moradshahi M., Avakian M.

1-149 I-483
Operational start-up and vessel conditioning of the Novillo tokamak,
Melendez-Lugo L., Lopez-Callejas R., Valencia-Alvarado R., Chavez-Alarcon E., Colunga-Sanchez S., Jimenez-Dominguez H., Gaytan-Gallardo E.

Topic 2: Stellarators

Poster-No. Volume/Page
Title,
Author(s)

2-1 I-489
Confinement studies in recent NBI experiments of Heliotron E,
Sano F., Kondo K., Zushi ., Sudo S., Sato M., Mizuuchi T., Matsuura H., Hanatani K., Nakasuga M., OKada H., Besshou S., Nakamura Y., Nagasaki K., Ijiri Y., Iima M., Senju T., Yaguchi K., Baba T., Kobayashi S., Toshi K., Sakamoto K., Wakatani M., Obiki T.

2-2 I-493
Electron heat transport in the LMFP-regime for the stellarators W7-A, W7-AS and L2,
Dyabilin K.S., Gasparino U., Maaßberg H., Renner H., Ringler H., W7-AS Team, ECRH Group

2-3 I-497
Diffusive and convective transport modelling from analysis of ECRH-stimulated electron heat wave propagation,
Erckmann V., Gasparino U., Giannone L., Hartfuß H.J., Maaßberg H., Tutter M., W7-AS Team, IPF-ECRH Group, KFK-Gyrotron Group

2-4 I-501
Towards higher β in the stellarator Wendelstein W7-AS,
Renner H., Ringler H., Kißlinger J., Kühner G.and the W 7AS-Team, NBI-Group

2-5 I-505
The optimum ion confinement mode in W7-A stellarator induced by fast orbit losses of the nearly perpendicular NBI,
Gasparino U., Kick M., Maaßberg H., Renner H., Ringler H., Sardei F., W7-AS Team

Poster-No. Volume/Page
Title,
Author(s)

2-6 I-509
Local neutral particle density in the W7-AS stellarator,
Junker J., Kick M., Maaßberg H., Sardei F., Stroth U., Zöpfel S., WVII AS-Team, NBI-Team

2-7 I-513
ECH power deposition control in CHS,
Kubo S., Idei H., Hosokawa M., Takita Y., Iguchi H., Yamada I., Arimoto H., Ueda M., Ida K., Matsuoka K., Morita S., Nishimura K., Okamura S., Takahashi C., Yamada H., Fujiwara M., Noda N., Sagara A., Sanuki H., Todoroki J., Toi K.

2-8 I-517
Density profile and particle transport of NBI-heated plasmas in the low-aspect-ratio Heliotron/torsatron CHS,
Iguchi H., Ida K., Morita S., Yamada H., Okamura S., Matsuoka *K., Akiyama R., Arimoto H., Hosokawa M., Idei H., Kaneko O., Kohmoto T., Kubo S., Nishimura K., Noda N., Ozaki T., Sagara A., Sakakibara S., Sanuki H., Takeiri Y., Takita Y., Takahashi C., Ueda M., Yamada I., Uchino K., Takenaga H., Muraoka K., Maeda M.*

2-9 I-521
Transport studies using modulation of dimensionless parameters in the advanced toroidal facility,
Murakami M., Bigelow T.S., Carreras B.A., Dory R.A., Wilgen J.B., Baylor L.R., Dyer G.R., England A.C., Hutchinson D.P., Isler R.C., Jernigan T.C., Ji H., Ma C.H., Morimoto S., Motojima O., Rasmussen D.A., Sato M., Wing W.R., Yamada H., the ATF Group

2-10 I-525
Fluctuation studies of ECH plasmas in the ATF torsatron,
Harris J.H., Hanson G.R., Wilgen J.B., Bell J.D., Murakami M., Carreras B.A., Baylor L.R., Aceto S., Bigelow T.S., Colchin R.J., Dunlap J.L., Dominguez N., Dyer G.R., England A.C., Isler R.C., Jernigan T.C., Leboeuf J.N., Lee D.K., Lyon J.F., Ma C.H., Quallis A.L., Rasmussen D.A., Thomas C.E., Uckan T., Zielinski J., Shats M.G., Likin K.M., Sarksyan K.A., Kovrizhnykh L.M.

2-11 I-529
Results of the heavy ion beam probe measurements on the advanced toroidal facility,
Aceto S.C., Schwelberger J.G., Connor K.A., Zielinski J.J., Glowienka J.C., Isler R.C., Murakami M., Bell J.D., Uckan T.

2-13 I-533
A general solution of the ripple-averaged kinetic equation (GSRAKE),
Beidler C.D., W.D. D'haeseleer

2-14 I-537
Influence of electric fields on the heating efficiency in the W7-AS stellarator,
Teubel A., Penningsfeld F.-P.

2-15 I-541
Change of adiabatic invariant in trap-detraping processes in stellarator,
Bulanov S.V., Shasharina S.G.

2-16 I-545
-particle behaviour outside the last closed magnetic surface in divertor stellarators,
Alladio F., Batistoni P., Mancuso A.

2-17 I-549
Mode activity at high plasma pressure in the stellarator Wendelstein W7-AS,
Weller A., Jaenicke R., Kißlinger J., Lazaros A., Maaßberg H., Sardei F., Schwab C., W7-AS Team, ECRH Group, NI Group

2-18 I-553
Finite ion gyro radius stabilization of ideal MHD ballooning modes in optimized stellarators,
Nührenberg J., Zheng L.-J.

2-19 I-557
Linear MHD stability computations in 3D plasmas,
Cooper W.A., Nakamura Y., Wakatani M., Gruber R., Merazzi S., Anderson D.V., Schwenn U.

2-20 I-561
Interchange modes in torsatrons, heliacs,
Jimenez J.A., Varias A., Dominguez N.

Poster-No. Title, *Author(s)*	Volume/Page
2-21 Ideal MHD studies of the TJ-IU Torsatron, *Alejaldre C., Ascasibar E., Garcia L., Lopez-Fraguas A., Varias A., Carreras B., Dominguez N.*	I-565
2-22 Progress in the studies of URAGAN-2M stability and transport properties, *Besedin N.T., Grekov D.L., Pavlichenko O.S., Shishkin A.A., Zolotukhin A.V., Beidler C.D., Kißlinger J., Maaßberg H., Rau F., Wobig H., Carreras B.A., Dominguez N., Lynch V.E.*	I-569
2-23 Destruction of Alfvén modes on a torus due to large nonaxisymmetry, *Salat A.*	I-573
2-24 Study of magnetic surfaces with islands using the PIES code, *Lopez-Fraguas A., Salas A., Reiman A.H., Monticello D.A., Johnson J.L.*	I-577
2-25 Modifies vacuum fields and compensation of islands in the stellarator W7-AS, *Beidler C., Harmeyer E., Gasparino U., Kißlinger J., Kühner G., Maaßberg H., Rau F., Ringler H., Wobig H., W 7-AS Team, ECRH-Group, W7-X Team*	I-581
2-26 Optimization of coils and a sweep coil system for W7-X, *Merkel P., Kißlinger J.*	I-585
2-27 Anisotropic pressure numerical 3D MHD equilibria, *Hirshman S.P., Cooper W.A., Merazzi S., Gruber R.*	I-589

Topic 3: Alternative Magnetic Confinement Schemes

Poster-No. Title, *Author(s)*	Volume/Page
3-1 Confinement studies of a high current density RFP in the extrap T1 upgrade device, *Drake J.R., Brzozowski, Brunsell P., Hellblom G., Karlsson P., Mazur S., Nordlund P., Welander A., Zastrow K.-D.*	I-595
3-2 Reversed field pinch equilibria and profile dynamics in a high aspect ratio geometry, *Nordlund P., Mazur S., Drake J.R.*	I-599
3-3 Stability of kink modes in a noncircular z pinch surrounded by a resistive and a conducting wall, *Jiang Z.X., Wahlberg C.*	I-603
3-4 Studies of edge plasma and impurities in extrap T1 using surface probes, *Bergsåker H., Gudowska I., Emmoth B., Tennfors E.*	I-607
3-5 Plasma spectroscopy at the extrap T1 RFP experiment, *Zastrow K.-D., Hörling P., Brzozowski J., Källne E.*	I-611
3-6 RFP set-up and confinement in SWIP-RFP device, *Zhang P., Fang S., Li J., Luo C., Li Q., Zhang S., Yi P., Xu Y.*	I-615

Poster-No. Title, *Author(s)*	Volume/Page
3-7 Ion temperature measurements in the reversed field pinch plasmas, *Schiavi A., Buffa A., Costa S.*	I-619
3-8 Generation of fast electrons by magnetic reconnection processes in RFP plasmas, *Erba M., Martin P., Ortolani S., Rossi A.*	I-623
3-9 Relaxed states for a driven reverse field pinch, *Paccagnella R.*	I-627
3-10 Electron diffusion and energy loss in a reversed field pinch plasma, *Antoni V., Bagatin M., Martines E.*	I-631
3-11 Self-similar solutions for trapping and diffusion of magnetic flux during formation of field-reversed configuration, *Bud'ko A., Karlson E.T., Liberman M.A.*	I-635
3-12 Study of current drive and particle flux in the SPEX spheromak, *Browning P.K., Cunningham G., Gee S.J., Al-Karkhy A., Martin R., Roe G., Rusbridge M.G.*	I-639
3-13 Toroidal current enhancement with strong poloidal plasma current drive in FBX-II spherical torus, *Irie M.*	I-643
3-14 Parametric investigation of the rotamak discharge in a 10-litre spherical vessel, *Donaldson N., Hahnheuser R., Jones I.R., Staines G.W., Xu S.*	I-647
3-17 An alternative configuration of axially pinched spherical torus, *Sinman S., Sinman A.*	I-651
3-18 Centrally peaked temperature profiles due to the Ettinghausen effect, *Haines M.G., Chittenden J.P.*	I-655
3-19 Viscous effects on equilibrium states of isolated z-pinches, *Miyamoto T.*	I-659
3-21 FIGARO: A large larmor radius stability code, *Coppins M., Scheffel J.*	I-663
3-22 The interrupted z-pinch dynamics modeling, *Kubes P., Kravarik J., Hakr J., Kulhanek P., Pichal J.*	I-667
3-23 Stabilization of the long wavelength sausage and kink modes of a Z-pinch by nonlinear radial oscillations, *Bud'ko A., Karlson E., Liberman M.A.*	I-671
3-25 Ideal and resistive MHD analysis of rotational instabilities in FRC, *Sakanaka P.H., Machida M., Honda R.Y., Aramaki E.A., Berni L.A., Santiago M.A.A., Tsui K.-H., Tavares-Azevedo M.*	I-675
3-26 Discrete Alfvén waves in reversed field pinches, *Sakanaka P.H., Shigueoka H., Azevedo C.A., Assis A.S.*	I-679

Poster-No. Title, *Author(s)*	Volume/Page
3-27 Hot spot X-ray and microwave emission of the DPF-78 plasma focus, *Antsiferov P., Franz D., Pfau R., Rupasov A., Schmidt H., Schulz D.*	I-683
3-28 The relative role of the macroscopic and microscopic phenomena in the plasma focus performance, *Zambreanu V., Zoita V.*	I-687
3-29 Investigation of charged-particle and X-ray pulses emitted from PF-type discharges, *Sadowski M., Szydlowski A., Zebrowski J., Al-Mashhadany E.M.*	I-691
3-30 Fusion reaction yield in focused discharges with variable energy and plasma fine structure, *Bortolotti A., Brzosko J.S., DeChiara P., Kilic H., Mezzetti F., Nardi V., Powell C., Wang J.*	I-695
3-35 Parametric study of mirror plasma based neutron source FEF-II, *Mizuno N., Yamaguchi H., Kawabe T., Hirayama S.*	I-699
3-37 Direct conversion of a fusion energy into an electric one in the DRACON-trap, *Glagolev V.M., Kuvshinov B.N., Proshin M.A., Timofeev A.V.*	I-703
3-39 Electrodynamics of plasma-molecular systems with drift motion of charged and neutral particles, *Moiseev S.S., Suyazov N.V., Yakimenko I.P.*	I-707
3-41 D-^{3}He fusion reactor based on a dipole magnetic field, *Hasegawa A., Fowler T.K., Mauel M.E.*	I-711
3-42 Proposed experiment with injection of a small angular spread beam in the oscillated REB regime, *Piffl V., Sunka P., Clupek M., Raus J.*	I-713
3-43 Confinement of laser-produced plasma by a strong external magnetic field, *Miklaszewski R., Farynski A., Fiedorowicz H., Mroczkowski M., Parys P., Pisarczyk T., Szczurek M.*	I-717

PART II

Topic 4: Plasma Edge Physics

Poster-No. Title, *Author(s)*	Volume/Page
4-1 Edge measurements in the divertor region in high density discharges at JET, *Clement S., Erents S.K., Gottardi N., Harbour P.J., Jaeckel H., Janeschitz G. De Kock L., Loarte A., Lowry C., Saibene G., Summers D., Tagle J.A., Vlases G.*	II-723
4-2 High power operation with a radiative divertor in JET, *Janeschitz G., Clement S., Gottardi N., Lesourd M., Lingertat J., Lowry C., Radford G., Saibene G., Stamp M., Summers D., Taroni A., Thomas P.R., Vlases G.*	II-727
4-3 Energy exhaust through neutrals in a tokamak divertor, *Watkins M.L., Rebut P.-H.*	II-731

Poster-No. Volume/Page
Title,
Author(s)

4-4 II-735
Modelling of the density limit in JET beryllated limiter discharges,
Borrass K., Campbell D., Clement S., Vlases G.

4-5 II-739
Modelling of neutral and charged helium transport in scoop of a pump limiter,
Tokar M.Z., Reiter D.

4-6 II-743
Marfe detection by radiation monitoring and control of density limit disruptions,
Steuer K.-H., Junker W., Röhr H., Büchl K., Engelhardt W., Gruber O., Kaufmann M., Mertens V., Neuhauser J., Stäbler A., Zohm H., ASDEX-, ASDEX-Upgrade Teams

4-7 II-747
Modelling of the ASDEX-Upgrade scrape-off layer plasma,
Bosch H.-S., Neuhauser J., Bachmann P., Schneider R., Kaufmann M., Reiter D., Baelmans T., Braams B.

4-8 II-751
Modeling the DIII-D plasma boundary with the LEDGE code,
Porter G.D., Rensink M.E., Rognlien T.D., Jong R.A., Hill D.N.

4-9 II-755
2-D edge modelling: convergence and results for next step devices in the high recycling regime,
Pacher H.D., D'haeseleer W.D., Pacher G.W.

4-10 II-759
Modelling of TEXTOR edge plasma in discharges with auxiliary heating, neon puffing,
Tokar M.Z., Samm U.

4-12 II-763
A study of the SOL density profile behaviour in ASDEX,
McCormick K., Schweinzer J., Pietrzyk Z.A.

4-13 II-767
Power flux widths in the ASDEX divertor,
Kyriakakis G., Kakoulidis E., Tsois N., McCormick K., Neuhauser J.

4-14 II-771
Spatial distribution of carbon ions and ion temperature measurements in the plasma edge of TEXTOR using emission spectroscopy,
Telesca G., Claaßen H.A., Graffmann E., Van Oost G.

4-15 II-775
Poloidal rotation in the limb of the TEXTOR plasma measured by the Doppler shift of a BII-line,
Conrads H., Euringer H., Rusbüldt D.

4-16 II-779
The effect of radial electric field on fast ion losses in divertor tokamaks,
Chankin A.V., Summers D.D.R., McCracken G.M.

4-17 II-783
Density, potential and temperature fluctuations in Wendelstein 7-AS, ASDEX,
Balbin R., Carlson A., Endler M., Giannone L., Hidalgo C., Niedermeyer H., Rudyj A., Theimer G., W7-AS Team, ASDEX Team

4-18 II-787
Attempt to model the edge turbulence of a tokamak as a random superposition of eddies,
Endler M., Theimer G., Weinlich M., Carlson A., Giannone L., Niedermeyer H., Rudyj A., the ASDEX-Team

4-19 II-791
Mechanisms inducing changes on the edge turbulence in the TJ-I tokamak,
Pedrosa M.A., Garcia-Cortes I., Balbin R., Hidalgo C., Ochando M.A., Liniers M.

4-20 II-795
m=1 activity prior to the onset of sawtoothing on Tokoloshe tokamak,
Nothnagel G., Sherwell D., Roberts D.E., Fletcher J.D., De Villiers J.A.M., Walters P.E.

Poster-No. Title, *Author(s)*	Volume/Page
4-21 Role of edge plasma in a high ß very low q tokamak regime, *Kiyama H., Kiyama S.*	II-799
4-22 Fluctuations and transport in a tokamak with high MHD activity, *Heller M.V.A.P., Castro R.M., Caldas I.L., da Silva R.P., Brasilio Z.A., TBR-1 Team*	II-803
4-23 Kinetic instabilities in a plasma in E x B fields, *Shoucri M., Bertrand P., Ghizzo A., Knorr G.*	II-807
4-24 Coherent vortical structures in two-dimensional plasma turbulence, *Lynov J.P., Nielsen A.H., Pécseli H.L., Rasmussen J.J.*	II-811
4-25 Guided Alfvén beams in the Tortus tokamak, *Cross R.C., Miljak D.G.*	II-815
4-26 Measurement of sputtering yields at the JET beryllium and carbon x-point tiles, *Stamp M.F., Thomas P.R.*	II-819
4-27 Radial carbon flux profiles in the upper divertor in JET at high target load, *Jäckel H.J., Clement S., Lesourd M., Lingertat J., Maggi C.F., Matthews G.F., Summers D.D.R., Summers H.P.*	II-823
4-28 Chemical impurity production under boronized wall conditions in TEXTOR, *Philipps V., Vietzke E., Erdweg M.*	II-827
4-29 Divertor retention for recycling impurities, *Krieger K., Roth J., Fussmann G.*	II-831
4-30 Particle influx and impurity behaviour in the ASDEX-Upgrade tokamak, *Kallenbach A., Fuchs C., Fussmann G., Jenichen F., Mast K.F., H.-M.Mayer, Schumacher U., the ASDEX-Upgrade Team*	II-835
4-31 Reduction in SOL Φ_p increases and impurity generation caused by RF near ω_{ci} by the use of insulating Faraday shield limiters in the Phaedrus-T tokamak, by elimination of Faraday shields, *Hershkowitz N., Majeski R., Diebold D., Tanaka T., Sørensen J., Breun R., Brouchous D., Fonck R., Intrator T., McKee G., Probert P.*	II-839
4-32 Plasma induced material transport on limiter probes in the boundary plasma of fusion experiments, *Naujoks D., Behrisch R.*	II-843
4-33 Production and control of an edge radiating layer with the ergodic divertor on TORE SUPRA, *Poutchy L., Vallet J.C., DeMichelis C., Grosman A., Hess W., Mattioli M., Monier-Garbet P.*	II-847
4-34 Edge transport induced by the interaction of a stochastic layer with the wall, *Nguyen F., Ghendrih Ph., Samain A., Grosman A.*	II-851
4-35 Control of the MHD activity with the ergodic divertor on TORE SUPRA, *Vallet J.C., Edery D., Van Houtte D., Mohamed-Benkadda M.S., Joffrin E., Lecoustey P., Pecquet A.L., Samain A., Talvard M.*	II-855

Poster-No. Title, *Author(s)*	Volume/Page
4-36 Plasma edge structure of a tokamak with ergodic magnetic limiter, *Takamura S., Oda Y., Sakurai S.*	II-859
4-37 Stochastic broadening in the scrape-off layer of a single-null divertor tokamak, *Punjabi A., Verma A., Boozer A.*	II-863
4-38 On stationary flow in the boundary region of toroidal systems, *Wobig H.*	II-867
4-39 Sheath potential at a target with almost parallel magnetic field, *Chodura R.*	II-871
4-41 Boundary conditions for the momentum and energy flux of ions at the plasma-sheath interface, *Günther K.*	II-875

Topic 5: Heating and Current Drive

Poster-No. Title, *Author(s)*	Volume/Page
5-1 Enhanced performance of neutral beam heated hot-ion H-modes on JET by central ICRF heating, *Bures M., Balet B., Campbell D., Cottrell G.A., Elevant T., Eriksson L-G., Jacquinot J., Jarvis N., Jones T., König R., Lomas P., Marcus F., Righi E., Sadler G., Start D.F.H., Tanga A., Van Belle P., Von Hellerman*	II-881
5-2 RF heating and current drive experiments in TORE SUPRA, *Hoang G.T., Agarici G., Beaumont B., Becoulet A., Berger G.By, Bibet P., Bizarro J.P., Capitain J.J., Carrasco J., Goniche M., Joffrin E., Kupfer K., Kuus H., Litaudon X., Moreau D., Parlange F., Peysson Y., Rey G., Saoutic B., Tonon G., Van Houtte D.*	II-885
5-3 ICRF power limitation relation to density limit in ASDEX, *Ryter F., ICRH-Group, ASDEX-Group*	II-889
5-4 Fast wave current drive experiments on the DIII-D tokamak, *Petty C.C., Pinsker R.I., Porkolab M., Baity F.W., Chiu S.C., Goulding R.H., DeGrassie J.S., Harvey R.W., Hoffman D.J., James R.A., Kawashima H., Lohr John, Luce T.C., Mayberry M.J., Prater R.*	II-893
5-5 Observation of fast wave ion current drive effects on sawteeth in JET, *Start D., Bhatnagar V., Bosia G., Brusati M., Bures M., Campbell D., Cottrell G., Cox M., DeEsch H., Edwards A., Eriksson L-G., Gormezano C., Jacquinot J., Lomas P., Marcus F., O'Brien M.R., Porcelli F., Rimini F., Stork D., Tanga A., Tubbing B., Warrick C.D., Wesson J.*	II-897
5-6 Resistive internal kinks and ICRF phasing current drive, *Porcelli F., Bhatnagar V.P., Bosia P., Cherubini A., Jacquinot J., Start D., Taroni A.*	II-901
5-7 Kinetic effects in fast wave current drive, *Becoulet A., Giruzzi G., Kupfer K., Moreau D., Saoutic B.*	II-905
5-8 Theoretical studies of fast wave plasma heating and current drive in tokamaks, *Moroz P.E., Hershkowitz N., Tataronis J.A.*	II-909

Poster-No. Title, *Author(s)*	Volume/Page
5-9 Influence of various physics phenomena on fast-wave current drive in advanced tokamaks, *Batchelor D.B., Jaeger E.F., Carter M.D., Goldfinger R.C., Stallings D.C.*	II-913
5-11 Current density profile control in reversed field pinch plasma by RF current drive, *Shiina S., Saito K., Kondoh Y., Ishii H., Shimada T., Hirano Y.*	II-917
5-15 A method of increasing the ion Bernstein wave excitation efficiency in plasmas, *Longinov A.V., Lukinov V.A., Pavlov S.S.*	II-921
5-16 The local power dissipation of ion Bernstein waves in a weakly inhomogeneous plasma, *Werthmann H., Brambilla M.*	II-925
5-17 The slot-in-recess antenna system for ion Bernstein wave excitation in plasmas, *Gribok V.A., Longinov A.V., Lukinov V.A.*	II-929
5-18 RF system for plasma production, heating in TJ-IU torsatron, *Ascasibar E., Castejon F., Rodriguez L., Navarro A.P., Dyakov V.E., Longinov A.V., Pavlichenko O.S., Pavlov S.S., Stepanov K.N.*	II-933
5-20 The separation of ion Bernstein waves and incoherent ion gyroresonant ballistic waves in a dispersive, spatially varying medium, *Flå T., Cook D., Tracy E., Kaufmann A.N.*	II-937
5-21 Plasma heating and generation current drive study in the torsatron U-2M using ion Bernstein wave, *Dyakov V.E., Longinov A.V.*	II-941
5-22 Resistive flux saving, current profile control during lower hybrid waves assisted current rise in TORE SUPRA, *Van Houtte D., Hoang G.T., Joffrin E., Lecoustey P., Moreau D., Parlange F., Tonon G., Vallet J.C.*	II-945
5-23 Initial lower hybrid current drive results and first two-dimensional images of hard X-ray emission in PBX-M, *Von Goeler S., Asakura N., Bell R., Bernabei S., Chance M., Chu T.K., Dunlap J., England A., Fishman H., Gettelfinger G., Greenough N., Harris J., Hatcher R., Herrmann H., Ignat D., IslerR., Jardin S., Jones S., Kaita R., Kaye S., Kesner J., Kugel H., LeBlanc B., Luckhardt S., Levinton F., Manickam J., Okabayashi M., Ono M., Paul S., Preische S., Roney P., Sauthoff N., Seki S., Sesnic S., Stevens J., Takahashi H., Valeo E., Voss K.*	II-949
5-24 Performance of the LHCD in high current regime in JT-60U, *Imai T., Ushigusa K., Ikeda Y., Ide S., Naito O., Seki M., Kondoh T., Nemoto M., Wolfe S., Sato M., Takeuchi H.*	II-953
5-25 Change of internal inductance and anisotropy during lower hybrid current drive in ASDEX, *Leuterer F., Söldner F.X., Bartiromo R., Bernabei S.*	II-957
5-26 Electron and ion heat transport with LH, NBI heating in ASDEX, *Söldner F.X., Pereverzev G.V., Bartiromo R., Fahrbach H.U., Leuterer F., Murmann H.D., Steuer K.-H., LH-Team, NBI-Team, ASDEX-Team*	II-961
5-27 Experimental studies of high energy X-ray emission and bootstrap current generation in high β_p lower hybrid driven plasmas, *Squire J.P., Porkolab M., Bonoli P.T., Colborn J.A., Villasenor J.*	II-965

Poster-No. Volume/Page
Title,
Author(s)

5-28 II-969
Investigation of high energy electrons produced by lower hybrid waves with measurement of the hard X-ray in JT-60U,
Kondoh T., Ide S., Imai T., Ushigusa K., Ikeda Y., Seki M., Takeuchi H.

5-29 II-973
Characterization of LH induced current carrying fast electrons in JET,
Ramponi G., Airoldi A., Bartlett D., Brusati M., Froissard P., Gormezano C., Rimini F., da Silva R.P., Tanzi C.

5-30 II-977
A phenomenological description of fast electrons induced by LH waves in tokamaks,
Conceicao P., Brusati M., Froissard P., Varandas C.A.F.

5-31 II-981
Impurity transport during RF current drive in WT-3 tokamak,
Nakamura M., Sawada K., Kawachi T., Suemitu H., Maekawa T., Terumichi Y., Tanaka S.

5-32 II-985
The distant coupling of LHCD launcher in the JT-60U,
Seki M., Ikeda Y., Imai T., Ushigusa K., Naitou O., Ide S., Kondoh T., Nemoto M., Takeuchi H., Suganuma K., Sawahata M., Takasa A., Takahashi S., Yamamoto T.

5-33 II-989
Coupling analysis and experiment of the multijunctional grill near the lower hybrid frequency,
Ohkubo K., Matsumoto K.

5-36 II-993
Modulational instability development and current drive,
Popel S.I., Vladimirov S.V., Tsytovich V.N.

5-39 II-997
Fast ion generation during RF discharge on the FT-2 tokamak and parametric decay instabilities,
Budnikov V.N., Dyachenko V.V., Esipov L.A., Its E.R., Lashkul S.I., Novik K.M., Stepanov A.Yu., Shcherbinin O.N., Alexandrov V.O., Sakharov I.E., Shatalin S.V.

5-43 II-1001
Measurements of electron cyclotron emission during high power ECRH in the W7-AS stellarator,
Gasparino U., Hartfuß H.J., Tribaldos V., Tutter M., W7-AS Team, ECRH Group

5-44 II-1005
Simulations of fast electron generation by stimulated Raman forward scattering in a magnetized plasma,
Bertrand P., Ghizzo A., Karttunen S.J., Pättikangas T.J.H., Salomaa R.R.E., Shoucri M.

5-45 II-1009
Effects of fluctuations on magnetohydrodynamic wave heating and current drive,
Tataronis J.A., Antani S.N.

5-46 II-1013
Radial diffusion of toroidally trapped particles induced by lower hybrid and fast waves,
Krlin L.

5-47 II-1017
ICRF Minority plasma heating in realistic geometries,
Friedland L., Cohen D.

5-48 II-1021
Simulation of runaway electrons in a toroidal geometry,
Sipilö S.K., Heikkinen J.A., Pättikangas T.J.H.

5-49 II-1025
Modelling of the FMS wave propagation and transformation in the ion-cyclotron frequency domain for the TUMAN-3 tokamak plasma,
Irzak M.A., Pavlov I.P., Shcherbinin O.N.

Topic 6: Diagnostics

Poster-No. Volume/Page
Title,
Author(s)

6-2 II-1031
Neutral particle analysis in the MeV range in JET,
Petrov M.P., Afanasyev V.I., Corti S., Gondhalekar A., Khudoleev A.V., Korotkov A.A., Maas A.C.

6-3 II-1035
Investigation of alpha particle slowing-down features in helium neutral beam fuelling experiments at JET,
Von Hellermann M., Core W.G.F., Frieling J., Horton L.D., König R., Mandl W., Summers H.P., Wolle B.

6-5 II-1039
Prospects for investigation of alpha particles velocity distribution by charge exchange spectroscopy in ITER,
Korotkov A.A., Belik V.P., Shmaenok L.A., Platonov Yu.Ya., Salashchenko N.N.

6-6 II-1043
Helium stopping cross-section in fusion plasma taking into account the multistep collision processes,
Korotkov A.A.

6-7 II-1047
Neutron spectrometry concepts for diagnosing DT plasmas of Q ~ 1,
Källne J., Gorini G., Condé H., Renberg P.U.

6-8 II-1051
Effects of neutron on the JET soft X-ray detectors,
Gill R.D., Alper B., Edwards A.

6-9 II-1055
The application of x-mode reflectometry to the study of large scale density fluctuations in TFTR,
Mazzucato E., Nazikian R., the TFTR-Group

6-11 II-1059
A multi-channel reflectometer for the RTP tokamak,
Heijnen S.H., Hugenholtz C.A.J., Van de Pol M.J.

6-12 II-1063
A microwave reflectometric system for tokamak ASDEX upgrade,
Silva A., Manso M.E., Serra F., Söldner F.X., Cupido L., Pereira J., Neves J., Nunes F., Varela P., Moreira A., Fernandes C., Loureiro C., Correia C., Santos J., Zilker F.

6-13 II-1067
Simulation of correlation reflectometry,
Michelsen P., Pécseli H.L.

6-14 II-1071
Microwave reflectometry as a density fluctuation diagnostic: a comparison between a controlled laboratory experiment and a one dimensional numerical model,
Rhodes T.L., Baang S., Chou A.E., Domier C.W., Luhmann Jr. N.C., Peebles W.A.

6-15 II-1075
Amplitude modelation reflectometry for large fusion devices,
Sanchez J., Zhuravlev V., De la Luna E., Estrada T., Branas B.

6-17 II-1079
Fluctuations spectra in TORE SUPRA from scattering experiment,
Gervais F., Grésillon D., Hennequin P., Quéméneur A., Truc A., Devynck P., Garbet X., Payan J., Laviron C., Saha S.K.

6-18 II-1083
From incoherent to collective scattering,
Maafa N., Grésillon D., Cabrit B.

Poster-No. Title, *Author(s)*	Volume/Page
6-19 Effects of the ohmic plasma current on collective scattering spectra, *Tartari U., Castiglioni S., Lontano M.*	II-1087
6-20 Ion temperature measurements by Rutherford scattering at TEXTOR, *Tammen H.F., Van Blokland A.A.E., Oyevaar Th., Schüller F.C., Donné A.J.H.*	II-1091
6-21 CO_2-scattering and RF probe measurements of lower-hybrid wave spectra in the presence of low-frequency fluctuations, *Fischer B., Krämer M.*	II-1095
6-22 Measurement of coherent temperature fluctuations on the stellarator Wendelstein 7-AS, *Hartfuß H.J., Sattler S., W7-AS Team, NBI-Team, ECRH-Group*	II-1099
6-23 Electron cyclotron non thermal spectra during ohmic and RF assisted discharges on TORE SUPRA, *Talvard M., Giruzzi G., Liu W.D.*	II-1103
6-24 First electron cyclotron emission and electron temperature profile measurements on ASDEX-upgrade, *Salmon N.A., Eberhagen A.*	II-1107
6-26 The heavy ion beam diagnostic for the tokamak ISTTOK, *Cabral J.A.C., Malaquias A., Praxedes A., Van Toledo W., Varandas C.A.F., Dias J.M.*	II-1111
6-27 Development of Boxcar imaging system for visualizing magnetic field structure in tokamak plasma, *Sakurai S., Ohno N., Takamura S.*	II-1115
6-29 Statistical analysis of luminescence signals observed during pellet injection, *Baldzuhn J., W7-AS Team*	II-1119
6-31 Dispersion interferometer for controlled fusion devices, *Drachev V.P., Krasnikov Yu.I., Bagryansky P.A.*	II-1123
6-32 Visible spectroscopic measurements on FTU, *Condrea I., Bartiromo R., Mazzitelli G., McNeill D.H.*	II-1127
6-33 Determination of O^{8+} to electron density ratio by the intensity ratio of the charge exchange recombination and the Doppler-shifted H_α emissions of the injected neutral beam, *Kondo K., Sano F., Sudo S., Zushi H., Mizuuchi T., Okada H., Besshou S., Nagasaki K., Higashijma S., Hanatani K., Nakasuga M., Wakatani M., Obiki T.*	II-1131
6-34 Spatial structure of nonthermal fluctuating electric fields in the TJ-I tokamak, *Zurro B., Castejon F., Burgos C.*	II-1135
6-37 Fast analysis of spectral data using neural networks, *Roach C.M.*	II-1139
6-38 Tomography algorithms for visible light tomography on RTP, *Pickalov V.V., Ingesson L.C., Donne A.J.H., Schram D.C.*	II-1143
6-39 Investigation of the sensitivity of visible continuum $Z_{eff}(0)$ to edge radiation, *Telesca G., Van Oost G., Ongena J., Leys C., Schoon N.*	II-1147

Poster-No. Volume/Page
Title,
Author(s)

6-40 II-1151
Spatially resolved diagnostics of inhomogeneous low temperature plasmas: new techniques,
Neger T., Jäger H.

6-41 II-1155
Localized impurity flux measurements on Wendelstein 7-AS,
Hofmann J.V., W7-AS Team, ECRH Group, NI Group

6-42 II-1159
Diagnostic for hydrogen behaviour at edge regions of high temperature plasmas,
Muraoka K., Maeda M., Honda C., Okada T., Uchino K., Kajiwara T., Takenaga H.

6-43 II-1163
Determination of plasma edge parameters with fast lithium beams,
Schweinzer J., McCormick K., Fiedler S., Aumayr F., Pöckl M., Winter H.

6-44 II-1167
Sniffer probe measurements in W7-AS,
Wolff H., Grigull P., Poschenrieder W., Roth J., Pech P., the W7-AS Team

6-47 II-1171
Electric current collection by Langmuir probe in strong magnetic fields,
Stanojevic M., Cercek M., Jelic N., Gyergyek T.

6-48 II-1175
A double probe for electron flux measurements in inhomogeneous and time-varying plasmas,
Axnäs I., Torvén S.

6-49 II-1179
A processing method of the probe characteristic in a two electron temperature plasma,
Ruscanu D., Popa G., Stamate E.

6-50 II-1183
Comparison of the wavenumber sensitivity and spatial resolution between Langmuir probes and reflectometry in a longitudinally magnetized RF plasma waveguide,
Anabitarte E., Senties J.M., Bustamante E.G., Calderon M.A.G., San Jose M.A.G., Monterde P., Vila J.

6-51 II-1187
RF pulse interaction with low density plasma diagnosed by gated Langmuir probe,
Cicconi G., Paris P.J., Rosatelli C., Tarditi A.

6-57 II-1191
Development of a diagnostic system for high power microwave (FEL) electric fields in the microwave tokamak experiment,
Oda T., Odajima K., Takiyama K., Foote J.H., Mizuno K., Ogawa T., Sato K., Ohasa K., Hoshino K., Maeda H., Nilson D.G.

6-59 II-1195
Laser shadowgraphic study of plasma sheath in dense plasma focus in the presence of external axial magnetic field,
Rawat R.S., Srivastava M.P., Mohanty S.R.

6-61 II-1199
Measurement of plasma drifts in space and laboratory plasmas by the resonance cone technique,
Rohde V., Piel A.

6-62 II-1203
The time-delay of a microwave signal, backscattered at the hybrid resonance and new possibilities for the diagnostics of small-scale plasma fluctuations,
Arhipenko V.I., Simonchik L.V., Budnikov V.N., Gusakov E.Z., Piliya A.D., Selenin V.L.

6-65 II-1207
Excimer laser driven soft X-ray plasma source: preliminary results,
Palladino L., Reale A., Taglieri G., Batani D., Bollanti S., Di Lazzaro P., Flora F., Letardi T., Schina G., Belli M., Scafati A.

Poster-No. Title, *Author(s)*	Volume/Page
10-45 Effect of second ion species on ion-acoustic rarefactive soliton in two-electron temperature plasma, *Sayal V.K., Yadav L.L., Sharma S.R.*	III-1823
10-46 Transport of time-varying currents by whistler waves, *Urrutia J.M., Stenzel R.L., Rousculp C.*	III-1827
10-47 Excitation of low-frequency whistlers by magnetic loops, *Stenzel R.L., Urrutia J.M., Rousculp C., Golubyatnikov G.Yu.*	III-1831
10-49 Non-stationary propagation of nonlinear ion acoustic waves in a plasma with negative ions, *Uehara M., Maciel H.S.*	III-1835
10-52 Relaxation and self-organization of a nonneutral plasma, *Ramachandran H., Morales G.J., Decyk V.K.*	III-1839
10-53 Low-dimensional attractors arising from the interaction of drift waves with low frequency instabilities, *Klinger T., Piel A.*	III-1843
10-54 Ion-holes associated with rarefactive ion acoustic pulse, *Singh A.K., Saxena Y.C.*	III-1847
10-55 Cascading bifurcations to chaos in a current carrying ion sheath, *Kono M., Komori A.*	III-1851
10-56 Experimental measurements of cascading bifurcations to chaos in an ion sheath, *Komori A., Kono M., Norimine T., Tanaka M., Kawai Y.*	III-1855
10-57 Nonlinear evolution and localized structure of unstable waves in an electron-beam plasma, *Yamagiwa K., Mieno T., Tanaka M.*	III-1859
10-58 Observation of two wave induced chaos in a magnetized plasma, *Fasoli A., Paris P.J., Tran M.Q., Skiff F.*	III-1863
10-59 Observations of intermittent structures in association with low frequency turbulence in toroidal magnetized plasma, *Singh A.K., Saxena Y.C.*	III-1867
10-60 Lower hybrid turbulence excited by electron diamagnetic drifts, *Stenzel R.L.*	III-1871
10-61 Experimental studies of anomalous potential drops due to ion density inhomogeneities, *Axnäs I., Bohm M., Torvén S.*	III-1875
10-62 Ion resonance cones and intrinsic diffraction, *Pierre T., Bonhomme G.*	III-1879
10-63 Reflection of a divergent resonance cone near the plasma layer in a magnetized inhomogeneous plasma, *Boucher I., Pierre T., Leclert G.*	III-1883

Poster-No. Title, *Author(s)*	Volume/Page
7-17 Fusion-fission triggers for advanced fuels, *Linhart J.G.*	II-1265

Topic 8: General Plasma Theory

Poster-No. Title, *Author(s)*	Volume/Page
8-1 Wave collapse of strong lower-hybrid turbulence, *Bingham R., Su J.J., Dawson J.M., Shapiro V.D., Shevchenko V., Tsytovich V.N.*	II-1271
8-2 Empirical spectral codes for tokamak turbulence, *Smith G.R., Cohen R.H., Boerner E.D., Dimits A.M.*	II-1275
8-5 Frequency and heater power dependency of RF generated Langmuir turbulence, *Hanssen A., Mjølhus E.*	II-1279
8-7 Nonlinear modulational instability of whistler waves, *Karpman V.I., Lynov J.-P., Michelsen P., Rasmussen J.J.*	II-1283
8-8 Low-frequency kinetic structures in plasma quasiparticle concept, *Sitenko A.G., Sosenko P.P.*	II-1287
8-15 A novel approach to the interaction between the plasma wake field and the driving relativistic electron beam, *Fedele R., Shukla P.K.*	II-1293
8-18 Simultaneous emissions at harmonics and half harmonics of the electron gyrofrequency, *Krafft C., Matthieussent G., Belmont G.*	II-1297
8-20 Intense laser pulse propagation in a plasma, *Kaw P.K., Sen A., Katsouleas T.*	II-1301
8-21 Nonlinear depletion of short, relativistically strong laser pulses in an underdense plasma, *Bulanov S.V., Inovenkov N., Kirsanov V.I., Naumova N.M., Sakharov A.S.*	II-1305
8-25 Nonlinear modulated waves near marginal state of instability, *Flå T., Wyller J.*	II-1309
8-27 Plasma oscillations wave breaking in inhomogeneous collisional plasmas, *De Nicola S., Nappi C.*	II-1313
8-30 Nonlinear absorption on the front of relativistically strong electromagnetic pulse in an underdense plasma, *Bulanov S.V., Inovenkov I.N., Kirsanov V.I., Naumova N.M., Sakharov A.S., Shah H.A.*	II-1317
8-31 "Plasma maser" effect in turbulent plasma with regular and random magnetic fields, *Pryadko J.M., Tsytovich V.N.*	II-1321

Poster-No. Title, *Author(s)*	Volume/Page
8-32 Nonlinear evolution of the modulational instability and chaos by using ID-Zakharov equations, *Sharma R.P., Verga A.D.*	II-1325
8-33 Energy of linear quasi-neutral electrostatic drift waves, *Pfirsch D., Correa-Restrepo D.*	II-1329
8-34 General theory of modulational interactions of two modes, *Vladimirov S.V., Tsytovich V.N.*	II-1333
8-35 Nonlinear evolution of solitons with oscillations under the influence of resonant ions, *Honzawa T., Arakawa M., Singh S.*	II-1337
8-36 3D non-linear kinetic equation for the calculation of neoclassical effects in tokamak plasmas, *Zaitsev F.S., O'Brien M.R., Cox M.*	II-1341
8-37 Nonlinear Langmuir pulses in the active plasma, *Bachin I.V., Prudsky V.V.*	II-1345
8-39 Soliton formation in quasiparallel MHD waves, *Hamilton R.L., Kennel C.F., Mjølhus E.*	II-1349
8-41 Nonlinear wave behaviour determined by high-frequency plasma response, *Georgieva M., Khristova D., Shivarova A.*	II-1353
8-42 Evolution of electron two-stream instability and generation of nonlinear structure, *Tanaka M.*	II-1357
8-44 Gyroinvariant second order drifts in electric fields of the same order of the magnetic field, *Martin P.*	II-1361
8-45 Charge shielding by trapped ion orbits in a dusty plasmas, *Goree J.*	II-1365
8-48 Vlasov solution describing nonabdiabatic plasma heating by magnetic compression, *Persson H., Ågren O.*	II-1369
8-50 The Pade approximate method for solving problems in plasma kinetic theory, *Jasperse J.R., Basu B.*	II-1373
8-51 Correlation theory of particle distribution near the plasma boundary in the presence of strong electric field, *Korchinsky G.M., Yakimenko I.P., Zagorodny A.G.*	II-1377
8-54 Possible changes of temperature and density power law exponents in expressions for plasma transport quantities under many particle interaction conditions, *Larenz R.W.*	II-1381
8-56 Dynamical screening in the Coulomb relaxation of anisotropic plasmas, *Wolf U., Schamel H.*	II-1385

Poster-No. Title, *Author(s)*	Volume/Page
8-57 Wiedemann-Franz-Law for magnetized plasmas, *Hensler E.*	II-1389
8-58 The influence of toroidicity, pressure and local profile changes on tearing mode stability, *Connor J.W., Cowley S.C., Hastie R.J., Martin T.J.*	II-1393
8-60 Linear and non-linear modelling of island control in tokamaks, *Hansen B.M.S., Hellberg M.A., Sherwell D., Roberts D.E., McLoud W.S.*	II-1397
8-61 Resistive wall instabilities for axisymmetric systems, *Berge G., Freidberg J.P.*	II-1401
8-62 Stability of force-free axisymmetric spherical plasma with flow, *Sugimoto H., Ashida H., Kurasawa T.*	II-1405
8-64 Internal disruption = catastrophic ergodisation, *Dubois M.A., Hennequin P., Nakach R., Sabot R.*	II-1409
8-65 Stability of ideal ballooning modes near a magnetic island, *Hegna C.C., Callen J.D.*	II-1413
8-66 Sheared flow effects on resistive pressure-gradient-driven turbulence, *Garcia L., Carreras B.A., Lynch V.E., Diamond P.H.*	II-1417
8-67 Mechanism of MHD modes stabilization by the ergodic divertor, *Edery D., Samain A., Vallet J.C., Morera J.P., Joffrin E., Lecoustey P., Pecquet A.L., Talvard M.*	II-1421
8-68 Nonlinear island dynamics, *Schep T.J., Pegoraro F., Rem J.*	II-1425
8-69 Magnetic reconnection in electron-magnetohydrodynamics, *Bulanov S.V., Pegoraro F., Sakharov A.S.*	II-1429
8-70 Radial propagation of microturbulence in tokamaks, *Garbet X., Laurent L., Roubin J.P., Samain A.*	II-1433
8-71 On the threshold of the ion temperature gradient driven mode, *Guo S.C., Romanelli F., Rewoldt G., Tang W.M.*	II-1437
8-72 Stability and transport due to ITG modes in a toroidal plasma with impurities, trapped electrons and vortex formation effects, *Jarmen A., Fröjdh M., Pavlenko V., Weiland J.*	II-1441
8-74 Dissipative-drift wave instability in the presence of impurity radiation, *Bharuthram R., Shukla P.K.*	II-1445
8-75 Nonadiabaticity and toroidal mode coupling in collisional drift waves, *Schlüter M., Scott B.D.*	II-1449

Poster-No. Title, *Author(s)*	Volume/Page
8-76 On the "captured" energy in freely decaying two-dimensional hydrodynamic and drift-wave plasma turbulence, *Bazdenkov S.V., Kukharkin N.N.*	II-1453
8-77 Effect of parallel heat flows on electron heat conduction losses due to electrostatic turbulence, *Becker G.*	II-1457
8-79 An energy balance approach to L-H transition at the edge, *Martinell J.J., Ramos G.*	II-1461
8-80 Pedestal sustenance, heat transport at the edge in the H-transition, *Minardi E.*	II-1465
8-81 Non-standard high energy ion orbits, *Eriksson L.-G., Berk H., Porcelli F., Stankiewicz R.*	II-1469
8-83 Plasma transport as a dissipative structure, *Uehara K.*	II-1473
8-84 Ambipolar transport in a magnetically perturbed tokamak edge-region, *Wittenberg R.W., Hellberg M.A., Feneberg W.*	II-1477
8-85 Neoclassical transport with surface variation of the macroscopic quantities, *Feneberg W.*	II-1481
8-87 Time-dependent neutron rate interpretation for deuterium injection into deuterium plasmas, *Wolle B., Eriksson L.-G., Hübner K., Morgan P.D., Sadler G., Tsintsadze L.N., Von Hellermann M.G.*	II-1485
8-88 Multidimensional WKB solution of a wave equation, *Pereverzev G.V.*	II-1489
8-89 Electron cyclotron emission and absorption in two dimensional momentum distribution, *Bornatici M.*	II-1493
8-90 Oblique propagation of electron-cyclotron-waves in non-maxwellian, weakly relativistic Vlasov-plasmas, *Moser F.*	II-1497
8-92 Partially transient plasma response near an attainable harmonic state, *Lim C.S., Suchy K.*	II-1501
8-94 Mode coupling of the ordinary and extraordinary waves in a cylindrical plasma, *Ramsay D., Laing E.W.*	II-1505
8-97 High frequency electrostatic plasma instabilities and turbulence in the lower ionosphere, *Basu B., Jasperse J.R., Retterer J.M., Decker D.T., Chang T.*	II-1509
8-99 Numerical calculation based on multipole expansions was used to study the linear instability in a DP-Machine, *Cereceda C., Ruiz J., Puerta J.*	II-1513

Poster-No. Volume/Page
Title,
Author(s)

8-100 II-1517
Dispersion characteristics of electromagnetic waves in dipolar (m=+/-1) modes travelling along a magnetized plasma column,
Benova E., Ghanashev I., Zhelyazkov I.

8-102 II-1521
Cyclotron autoresonance current drive in tokamaks,
Kuyanov A.Yu., Skovoroda A.A., Timofeev A.V., Zvonkov A.V.

8-103 II-1525
Application of a reconstructive MHD code based on the formalism of the toroidal multipoles to the ITER tokamak,
Alladio F., Lalousis P., Micozzi P.

8-105 II-1529
MHD theory with induced surface current effects,
Lehnert B.

8-107 II-1533
Exact surface waves on spheres, cylinders,
Yu M.Y., Stenflo L.

8-109 II-1537
1st and 2nd elliptic solutions to the extended Grad-Shafranov-Schlüter equation for asymmetric tokamak plasma with stationary flows,
Zelazny R., Stankiewicz R., Galkowski A., Potempski S.

8-110 II-1541
A new fast 2-d MHD-equilibrium solver,
Hübner G.

8-111 II-1545
A civil engineering approach to ideal MHD,
Jensen V.O.

8-112 II-1549
A general formulation of the nonlinear plasma theories,
Kuhn S., Assis A.S.

8-113 II-1553
Uniqueness of solution to a stationary boundary kinetic problem,
Zhykharsky A.

8-114 II-1557
Solution to the boundary kinetic problem presenting the interaction of plasma flows with a solid,
Zhykharsky A., Shmykov V.

8-115 II-1561
A theoretical model for transient cataphoretic segregation,
Dumitrascu N., Berbece D., Popa Gh.

PART III

Topic 9: Space and Astrophysical Plasmas

Poster-No. Volume/Page
Title,
Author(s)

9-1 III-1567
Modulational instability of lower hybrid wave in a cylindrical plasma,
Sharma S.K., Sudarshan A.

Poster-No. Title, *Author(s)*	Volume/Page
9-5 Interaction of a magnetized plasma stream with an immobile ion cloud, *Baumgärtel K., Sauer K.*	III-1571
9-7 Rayleigh-Taylor instability favoured drift turbulence in a spread F simulation experiment, *Prasad G., Bora D., Saxena Y.C.*	III-1575
9-9 Simulation of electron beam-driven instabilities by a 3-D electromagnetic particle code, *Nishikawa K.-I., Buneman O., Neubert T.*	III-1579
9-13 Night time equatorial spread F simulation in a laboratory plasma, *Prasad G., Bora D., Saxena Y.C.*	III-1583
9-14 Stimulated attachment instability of electromagnetic waves in the ionosphere, *Shukla P.K., Stenflo L., Borisov N.D.*	III-1587
9-17 Radar collective backscattering and the high latitude plasma turbulence, *Grésillon D., Cabrit B., Hanuise C., Villain J.P., Greenwald R.A., Baker K.B.*	III-1591
9-19 Stimulated scattering of EM wave by ICW in a two electron temperature plasma, *Sudarshan A., Sharma S.K.*	III-1595
9-20 Binding energy and triplet-splitting of the hydrogen molecule in ultrahigh magnetic fields, *Korolev A., Liberman M.A.*	III-1599
9-21 Behaviour of two-dimensional ion-acoustic soliton in relativistic plasmas of radiation belts, *Singh S., Honzawa T.*	III-1603
9-23 The Rayleigh-Taylor instability in a super-dense igniting plasma, *Garcia D., Serichol N., Bravo E., Diaz-Pinto A.*	III-1607
9-26 New electrostatic instabilities in nonuniform partially ionized magnetoplasmas, *Shukla P.K., Dwivedi C.B., Das A.C.*	III-1611
9-27 Spontaneous formation of intermediate shocks, *Chao J.K., Chiu C.Y., Chiueh T.H.*	III-1615
9-33 Spectrum of MHD waves in cometary tails, *Matsuura O.T., Azevedo C.A., Assis A.S., Shigueoka H., Sakanaka P.H.*	III-1619
9-34 Low-frequency resonant ion-beam turbulence in cometary plasmas, *Verheest F., Lakhina G.S.*	III-1623
9-35 Lower hybrid resonance acceleration of electrons and ions in the aurora and solar flares, *Bingham R., Bryant D.A., Hall D.S., Su J.J., Dawson J.M.*	III-1627
9-38 Solar flare mechanism based on MHD relaxation model, *Kusano K., Kubo H., Tamano T., Sato T.*	III-1631

Poster-No. Title, *Author(s)*	Volume/Page
9-39 Nonlinear MHD surface waves on plasma interfaces and their evolution equation in solar and magnetospheric conditions, *Nenovski P., Zhelyazkov I., Murawski K.*	III-1635
9-42 Generation of large amplitude plasma waves in space phenomena, *Dudnikova G.I., Vshivkov V.A.*	III-1639
9-43 Parametric instabilities of Langmuir waves in dusty plasmas, *Shukla P.K., Feix G., Rao N.N.*	III-1643
9-44 Magnetic reconnection in the plasma within clusters of galaxies, *Jafelice L.C., Friaca A.C.S.*	III-1647
9-46 Quantitative analysis of cosmic noise coming from plasma jets of quasar, *Tanizuka N., Kawaguchi N., Mikoshiba H., Inoue M.*	III-1651
9-47 A theory on the evolution process of the fine structure in space, *Nejoh Y.*	III-1655
9-48 The effects of slightly oblique propagation on nonlinear Alfvén waves, *Spangler S.R., Plapp B.B.*	III-1659
9-50 Mathematicl theories of resonant absorption of Alfvén waves in space plasmas: time dependent solution, *Uberoi C.*	III-1663
9-51 Runaway electrons in the presence of kinetic Alfvén waves, *Assis A.S., Leubner C.*	III-1667
9-52 Polarization changes through stimulated Raman scattering, Krishan V., Gangadhara R.T.	III-1671

Topic 10: Basic Collisionless Plasma Physics

Poster-No. Title, *Author(s)*	Volume/Page
10-1 Transition to chaos in periodically driven thermionic diodes at low pressure, *Klinger T., Timm R., Piel A.*	III-1677
10-3 Equilibrium double layers in extended Pierce diodes, *Ciubotariu-Jassy C.I.*	III-1681
10-4 New results on weakly nonlinear driven oscillations in the Pierce diode, *Hörhager M., Kuhn S.*	III-1685
10-7 Laboratory study of collisionless interaction processes between supernova-like ejectas and magnetized background under conditions of a laser-produced-plasma experiments, *Zakharov Yu.P., Orishich A.M., Ponomarenko A.G., Snytnikov V.N.*	III-1689

Poster-No. Title, *Author(s)*	Volume/Page
10-8 Total energy conservation, Manley-Rowe relations for plasma-maser interaction, *Nambu M.*	III-1693
10-9 Phase-space topology in the dynamics of cyclotron-masers, *Pakter R., Schneider R.S., Rizzato F.B.*	III-1697
10-10 RF production of long, dense plasma columns, *Chen F.F., Chevlaier G.*	III-1701
10-11 Plasma potential formation in the presence of localized radio-frequency electric fields, *Sato N.Y., Hatakeyama R., Sato N.*	III-1705
10-12 Inward and outward plasma motion induced by axisymmetric electromagnetic fields around the ion cyclotron frequency, *Hatakeyama R., Miyakuni S., Sato N.Y., Sato N.*	III-1709
10-13 The exact and drift Hamiltonian, *Yao Q., Boozer A.H.*	III-1713
10-14 Collisionsless driftwaves in anisotropic cylindrical plasmas, *Korn J., Schamel H.*	III-1717
10-15 Instabilities of gyro-kinetic plasmas with a guiding center density gradient, finite Larmor radius and polarization drift, *Knorr G., Shoucri M.*	III-1721
10-16 The launching and propagation of drift waves in a steady-state plasma, *Sandeman J., Elliott J.A., Sutcliffe M., Rusbridge M.G.*	III-1725
10-17 Studies of non-linear interactions of drift waves in the UMIST quadrupole "GOLUX", *Duncan P.J., Chekroud D., Rusbridge M.G.*	III-1729
10-18 Excitation of electron cyclotron waves and related physics experiments, *Tanaka M., Tamaoki M., Shoyama H., Nagao K., Komori A., Kawai Y.*	III-1733
10-19 An Eulerian Vlasov plasma simulation code for ion phase space phenonema, *Cherkhani R., Bonhomme G., Ghizzo A., Bertrand P.*	III-1737
10-20 An Eulerian code for the study of the gyro-averaged kinetic Vlasov equation, *Ghizzo A., Bertrand P., Shoucri M., Fijalkow E., Feïx M.*	III-1741
10-21 Relativistic Vlasov-Maxwell equilibria of anisotropic charge-separation-free plasmas, *Kamp L.P.J., Van Bruggen-Kerkhof M.J., Sluijter F.W.*	III-1745
10-22 A new action principle for the Vlasov-Maxwell system, *Larsson J.*	III-1749
10-23 Negative-energy waves in an inhomogeneous force-free Vlasov plasma with sheared magnetic field, *Correa-Restrepo D., Pfirsch D.*	III-1753

Poster-No. Title, *Author(s)*	Volume/Page
10-24 Electrons passing through a negatively biased grid due to collective trapping, *Popa G., Schrittwieser R.*	III-1757
10-26 Experimental analysis of a low frequency instability in a magnetized discharge plasma, *Gyergyek T., Cercek M., Jelic N., Stanojevic M.*	III-1761
10-27 Ion cyclotron oscillations induced by an emissive electrode floating in a magnetized collisionless plasma column, *Sato N., Hatakeyama R., Aoyama K., Ding W.X.*	III-1765
10-28 On the double layer phenomenology, *Sandulovicіu M., Lozneanu E.*	III-1769
10-29 A probe sheath instability in a double plasma device, *Dempers C.A., Krumm P., Schrittwieser R.*	III-1773
10-30 Progress in the kinetic modeling of collisionless two-dimensional bounded plasma systems, *Pedit H., Kuhn S.*	III-1777
10-31 Anisotropic conductivity of the collisionsless magnetized plasma, its application to the cylindrical plasma column, *Kiyama S.*	III-1781
10-32 Analytic solution to longitudinal eigenmodes in a collisionless bounded plasma, *Kuhn S., Schupfer N., Assis A.S., Santiago M.A.M.*	III-1785
10-36 A collisionless **ExB** instability with large ion orbits, *Chen F.F.*	III-1789
10-37 Influence of the thermoionic emission on the current-driven ion-acoustic instability, *Donoso G., Martin P.*	III-1795
10-38 Modulational instability of relativistic ion acoustic waves in a plasma with trapped electrons, *Nejoh Y.*	III-1799
10-39 Cross-field ion acoustic instability and turbulence in a weakly magnetized plasma, *Barrett P.J., Popov G.H.*	III-1803
10-40 Numerical study of potential formation and negative resistance in a current-carrying ion sheath, *Ohno N., Komori A., Takamura S., Kawai Y.*	III-1807
10-41 Asymmetric **ExB** equilibria and diocotron adiabatic invariants, *Chu R., Wurtele J.S., Notte J., Fajans J.*	III-1811
10-43 Compression of multiple ion acoustic solitons at the plasma sheath edge, *Nagasawa T., Nishida Y.*	III-1815
10-44 The effects of finite electron mass on ion-acoustic solitons, *Rice W.K.M., Hellberg M.A., Mace R.L., Baboolal S.*	III-1819

Poster-No. / Title, / *Author(s)*	Volume/Page
10-45 Effect of second ion species on ion-acoustic rarefactive soliton in two-electron temperature plasma, *Sayal V.K., Yadav L.L., Sharma S.R.*	III-1823
10-46 Transport of time-varying currents by whistler waves, *Urrutia J.M., Stenzel R.L., Rousculp C.*	III-1827
10-47 Excitation of low-frequency whistlers by magnetic loops, *Stenzel R.L., Urrutia J.M., Rousculp C., Golubyatnikov G.Yu.*	III-1831
10-49 Non-stationary propagation of nonlinear ion acoustic waves in a plasma with negative ions, *Uehara M., Maciel H.S.*	III-1835
10-52 Relaxation and self-organization of a nonneutral plasma, *Ramachandran H., Morales G.J., Decyk V.K.*	III-1839
10-53 Low-dimensional attractors arising from the interaction of drift waves with low frequency instabilities, *Klinger T., Piel A.*	III-1843
10-54 Ion-holes associated with rarefactive ion acoustic pulse, *Singh A.K., Saxena Y.C.*	III-1847
10-55 Cascading bifurcations to chaos in a current carrying ion sheath, *Kono M., Komori A.*	III-1851
10-56 Experimental measurements of cascading bifurcations to chaos in an ion sheath, *Komori A., Kono M., Norimine T., Tanaka M., Kawai Y.*	III-1855
10-57 Nonlinear evolution and localized structure of unstable waves in an electron-beam plasma, *Yamagiwa K., Mieno T., Tanaka M.*	III-1859
10-58 Observation of two wave induced chaos in a magnetized plasma, *Fasoli A., Paris P.J., Tran M.Q., Skiff F.*	III-1863
10-59 Observations of intermittent structures in association with low frequency turbulence in toroidal magnetized plasma, *Singh A.K., Saxena Y.C.*	III-1867
10-60 Lower hybrid turbulence excited by electron diamagnetic drifts, *Stenzel R.L.*	III-1871
10-61 Experimental studies of anomalous potential drops due to ion density inhomogeneities, *Axnäs I., Bohm M., Torvén S.*	III-1875
10-62 Ion resonance cones and intrinsic diffraction, *Pierre T., Bonhomme G.*	III-1879
10-63 Reflection of a divergent resonance cone near the plasma layer in a magnetized inhomogeneous plasma, *Boucher I., Pierre T., Leclert G.*	III-1883

Poster-No. Title, *Author(s)*	Volume/Page
10-64 Production of a high density plasma by helicon waves, *Komori A., Sugimoto M., Kono M., Tanaka M., Kawai Y.*	III-1887
10-65 Development of spiral structures on a rotating plasma column with large ion-gyroradius, *Ikehata T., Mase H.*	III-1891
10-66 Waves driven by strong transverse potential structures, *Koepke M.E., Alport M.J., Sheridan T.E., Amatucci W.E., Carroll III J.J.*	III-1895
10-67 Experimental dynamics of 2-D vorticity rings, *Peurrung A.J., Fajans J.*	III-1899
10-68 Dynamics of non-stationary dipole vortices in the Hasegawa-Mima equation, *Hesthaven J.S., Lynov J.-P., Nycander J.*	III-1903
10-69 Localized vortices in η_i-modes, *Nycander J., Lynov J.-P., Rasmussen J.J.*	III-1907
10-72 Breaking of waves into wave packets observed in a beam-plasma system, *Honzawa T., Singh S.*	III-1911
10-74 Experimental measurement of the deflection of an electron beam due to the ponderomotive force of a HF wave in a waveguide, Hadjoudj Y., Heuraux S., Pierre T., Leclert G.	III-1915
10-76 Generation of ion cyclotron wave in an ion beam by a periodic magnetic field, *Mieno T., Hatakeyama R., Sato N.*	III-1919
10-77 Non-linear ion acceleration in electrostatic wave fields, *Alava M.J., Heikkinen J.A.*	III-1923
10-78 Electron acceleration by $\mathbf{v}_p \times \mathbf{B}$ mechanism in vacuum, *Yugami N., Nishida Y.*	III-1927
10-79 Plasma wave wake field excited by short pulse microwave, *Nishida Y., Kusaka S., Yugami N.*	III-1931
10-82 Direct measurements of velocity space transport in a fully ionized plasma, *Rynn N., Bowles J., McWilliams R.*	III-1935
10-83 Phase conjugation via Brillouin enhanced four-wave mixing in a plasma, *Domier D.W., Luhmann Jr. N.C., Peebles W.A.*	III-1939
10-84 High frequency modes of a plasma column loaded in a sheath helix, *Ganguli A., Appala N.P., Umesh G.*	III-1943
10-85 Estimation of electron temperature and density by deconvolving the absorption part of the plasma dispersion function, *Jimenez-Dominguez H., Cabral-Prieto A., Melendez-Lugo L., Lopez-Callejas R., Colunga-Sanchez S., Valencia-Alvarado R., Cruz-Jimenez S., Gaytan-Gallardo E., Chavez-Alarcon E.*	III-1947

Poster-No. Title, *Author(s)*	Volume/Page
10-86 Kinetic description of modulated electromagnetic wave in relativistic plasma, *Ekiel-Jezewska M., Flå T., Kaufman A.N.*	III-1951

Topic 11: Partially Ionized Plasmas

Poster-No. Title, *Author(s)*	Volume/Page
11-2 Experimental evidence of self-organization and chaos in some plasma devices, *Sanduloviciu M., Alexandroaei D., Talasman S.J. and Ianopol B.*	III-1957
11-5 Tomographic time-resolved reconstruction of the three dimensional electron velocity distribution in a partially ionized RF plasma, *Matsumoto K., Iwama N., Ishii S.*	III-1961
11-6 Large amplitude striations in an RF discharge, *Sato T., Shoji T., Sakawa Y., Hori M.*	III-1965
11-9 Ionization front structure in the lateral spreading of a DC discharge along cylindrical coaxial electrodes, *Gavrilescu C., Popa G.*	III-1969
11-10 Plasma heating in low pressure RF discharges, *Skorik M.A., Braithwaite N.St.J., Allen J.E.*	III-1973
11-11 Ion energy distribution in an RF Argon plasma, *Annaratone B.M., Skorik M.A., Goruppa A.A., Allen J.E.*	III-1977
11-12 Observation of coherent drift structures in the turbulence of a DC discharge, *Kauschke U., Schlüter H.*	III-1981
11-13 Effects of magnetic field on a magnetron discharge, *Mase H., Tanabe T., Ikehata T., Sato N.Y.*	III-1985
11-17 The Langmuir probe study of the electron energy distribution function in the flowing afterglow plasma, *Glosik J., Cermak I., Sicha M., Tichy M., Zakouril P.*	III-1989
11-18 Computer simulation of RF discharges and comparison with laboratory results, *Vahedi V., Surendra M., DiPeso G., Mirrashidi P., Birdsall C.K.*	III-1993
11-19 On modelling of steady states in toroidal machines for basic plasma physics, *Øien A.H.*	III-1997
11-23 A one-dimensional q-machine model taking into account charge-exchange collisions, *Maier H., Kuhn S.*	III-2001
11-24 Determination of composition and physical properties of partially ionized plasmas in the function of temperature, *Zaporowski B.*	III-2005

Poster-No. Title, *Author(s)*	Volume/Page
11-25 Thermodynamic functions for partially ionized plasmas in the mean spherical approximation, *Kahlbaum T., Schneidenbach H.*	III-2009
11-26 Dielectric constant of weakly-ionized magnetized plasmas, *Kiss'ovski Zh., Pironkova A., Shivarova A.*	III-2013
11-28 Ion Bernstein waves in a toroidal steady-state device, *Batani D., Fontanesi M., Galassi A., Riccardi C., Sindoni E.*	III-2017
11-33 Study of low frequency flute type oscillations, their nonlinear interaction in toroidal plasma, *Prasad G., Bora D., Saxena Y.C., Sethia G.C.*	III-2021
11-39 Behaviour of charged particle motion along an inhomogeneous magnetic field and a retarding electric field - evidence for the existence of discrete energy states, *Varma R.K., Punithavelu A.M.*	III-2025
11-40 Unstable behaviour of globular anode structures, *Biborosch L., Toma M., Sanduloviciu M.*	III-2029
11-41 On the electrodynamic explanation of the retrograde motion of the electric arc, *Hong J.S., Allen J.E.*	III-2033
11-42 Nonequilibrium transport phenomena of a plasma in a nonuniform electric field, *Cicconi G., Molinari V., Sumini M.*	III-2037
11-43 Experimental study of the axial structure of an argon plasma column sustained by an electromagnetic wave in the presence of an external magnetic field, *Staikov P., Grozev D., Zhelyazkov I., Benova E.*	III-2041
11-46 Electromagnetic surface waves for large-area RF plasma productions between large-area planar electrodes, *Nonaka S.*	III-2045
11-49 CO_2-TE laser-produced cadmium plasma in vacuum experiment, kinetics, *Apostol I., Bahrim B., Bahrim C., Vasilescu C.*	III-2049

Topic 12: Elementary Processes in Plasmas

Poster-No. Title, *Author(s)*	Volume/Page
12-1 Measured and calculated charge density in Ce, Cu vapor produced by an electron gun, *Blumenfeld L., Gonella C., Morin M.*	III-2055
12-5 Stokes parameters for Compton scattering in a strong magnetic field, *Chou C.K., Chen H.H.*	III-2059

Poster-No. Volume/Page
Title,
Author(s)

12-6 III-2063
CTMC study of collisions of Carbon ions with H and He, relevant to magnetically confined fusion plasmas,
Katsonis K., Maynard G.

12-8 III-2067
Investigation on the metastable fragmentation of mixed argon-oxygen, argon-krypton cluster ions: the observation of two new fragmentation decay channels - evidence for the existence of metastable excited dimer ions ArO^{+*}, $ArKr^{+*}$,
Foltin M., Lukac P., Märk T.D.

12-12 III-2071
Ion attachment to van der Waals clusters: reactions of NO^+ with Ar_m,
Lezius M., Scheier P., Märk T.D.

12-13 III-2075
On the interation of low energy electrons with vdW-Clusters: electron attachment reactions, auto-scavenging,
Rauth T., Lezius M., Foltin M., Grill V., Märk T.D.

12-16 III-2079
Particle exchange reactions at low kinetic energies,
Praxmarer C., Freysinger W., Hansel A., Lindinger W.

12-17 III-2083
Collisional induced dissociation of Kr_2^+, $(CO)_2^+$, N_4^+, N_2Ar^+,
Praxmarer C., Glosik J., Smith D., Freysinger W., Lindinger W.

12-18 III-2087
Theoretical studies of the vibrational relaxation of $N_2^+(v=1)$ in collisions with He using the semiclassical method,
Zenevich V.A., Freysinger W., Lindinger W.

12-20 III-2091
Ionization, recombination processes in dense nonideal plasmas,
Bornath Th., Schlanges M., Kremp D., Bonitz M.

12-23 III-2095
Experimental, theoretical determination of electron impact ionization cross sections of atoms and molecules,
Grill V., Margreiter D., Walder G., Scheier P., Winkler C., Kurdel M., Poll H.U., Deutsch H., Stephan K., Märk T.D.

12-26 III-2099
Microwave determination of the coefficient of dissociative recombination of molecular ions of argon,
Okada T., Sugawara M.

12-27 III-2103
On the laser cooling of ions in oscillating traps,
Reyna L.G., Sobehart J.

Topic 13: Plasma Applications

Poster-No. Volume/Page
Title,
Author(s)

13-2 III-2109
One-dimensional modeling for magneto-microwave plasma using the Monte Carlo method,
Ikegawa M., Kakehi Y., Kobayashi J.

13-3 III-2113
ECR plasma source in ICR separation device,
Meis C., Compant La Fontaine A., Louvet P., Meyer R.L.

Poster-No. Title, *Author(s)*	Volume/Page
13-6 Current and geometry dependence of mass and energy fluxes in capillary, ablative critical flows, *Cuperman S., Zoler D., Ashkenazy J., Caner M., Kaplan Z.*	III-2117
13-7 New method of ion extraction from plasma by using radio-frequency electric field, *Matsui T., Tuchida K., Nishio R., Suzuki K., Shoji T.*	III-2121
13-8 Density and temperature measurements by laser absorption diagnostic on a magnetized plasma, *Compant La Fontaine A., Le Gourrierec P., Louvet P.*	III-2125
13-9 The plasmachemical reactions in negative corona discharges, *Skalny J.D., Lukac P., Gabris R.*	III-2129
13-12 Plasma parameter profiles and fluctuation properties of an ECR process plasma source for Si etching at LN_2 temperatures, *Kim S.K., Park C.W., Cho S., Choi E.H., Kwak J.K., Park J.K., Rhee C.*	III-2133
13-14 Magnet plasma dynamic accelerator with ultra high frequency resonator, *Kubarev Y.V., Tashaev Y.N., Safronov V.P., Kholin N.N.*	III-2137
13-16 Ion irradition studies from dense plasma focus for change of phase for thin film of CdS, *Sagar R., Srivastava M.P., Rawat R.S.*	III-2141
13-17 Influence of metastable atoms on the characteristics of surface wave produced plasmas, *Kortshagen U., Schlüter H.*	III-2145
13-19 Use of cold plasmas in film deposition and structuring, *Edlinger J., Pulker H.K., Rille E., Vogl G.*	III-2149
13-22 Experimental study of plasma effect on oxidation of solid surface, *Kitajima M., Kuroki H., Shinno H., Kawabe T.*	III-2155

Topic 8: General Plasma Theory
(Contribution added in print)

8-116 Langevin-equation for charged particles in microturbulent plasma, *Meister C.-V.*	III-2159

Topic 4:

Plasma Edge Physics

EDGE MEASUREMENTS IN THE DIVERTOR REGION IN HIGH DENSITY DISCHARGES AT JET

S Clement, S K Erents*, N Gottardi, P J Harbour, H Jaeckel, G Janeschitz, L de Kock, A Loarte, C Lowry, G Saibene, D Summers, J A Tagle, G Vlases
JET Joint Undertaking, Abingdon, OXON, OX14 3EA, UK.
**AEA Technology, Culham, Abingdon, OXON, OX14 3EA, UK.*

Introduction During the 1991-1992 experimental campaign JET has operated routinely in single null magnetic divertor configurations, using either the upper C target plates (single null upper, SNU), or the lower Be target plates (SNL). The edge parameters have been measured in high density discharges in a variety of operating conditions. This paper studies the behaviour of the scrape-off layer (SOL) parameters in the divertor region, for a series of operating scenarios in which a high density and/or a highly radiative divertor was pursued. These conditions in which a density limit can occur, are important for the future pumped divertor of JET. Differences are observed between the operation in the two targets. On the C target, strong gas fuelling during ohmic or low power additional heating discharges results in non-disruptive density limits of the same nature as those observed in limiter configuration [1,2], with the appearance of a MARFE and a pulsating behaviour of the edge density; with higher power additional heating, strong gas puffing during the high confinement mode phase (H mode) causes the appearance of ELMs and, at higher rates, the loss of the improved confinement regime [3]. On the Be target, with ohmic and low additional heating, strong gas fuelling causes in some cases the complete detachment of the inner strike zone, with the outer strike zone parameters remaining unaffected. With higher input power and strong gas fuelling, a gas divertor is obtained, where all the power in the SOL is radiated close to the X-point and the plasma completely detaches from the two sides of the target. This configuration can be maintained in a stable way as long as there is additional heating, but, in this situation, the transition to the H mode does not occur.

Experimental Two poloidal arrays of single Langmuir probes mounted in the upper and lower protection tiles are used to obtain the electron temperature and density profiles in the divertor region, and a fast reciprocating probe has been used in the main SOL region [4]. The profiles obtained in the divertor region are fitted with Gaussians, which have been shown to correspond to exponential profiles in the main SOL [5]. Bolometry and VUV spectroscopy measurements are also used, and CCD cameras have been used to identify the MARFE events.

Results Density limits are often obtained when the additional heating is stepped down while densities are high (and these are often disruptive), but we will limit the study to the cases where the density limit is reached by increasing the density at constant input power.

-Operation on the C target (SNU)

On the C target, in a series of ohmic discharges, a non disruptive density limit is observed when the total radiated power exeeds about 65% of the input power (about 55% is radiated in the

divertor region), where MARFEs appear [figs.1 and 2]. In general, the power deposition between the inner and outer strike zones is asymmetric, and the density limit is determined by the density of the inner scrape-off layer, where the breakdown of the local power balance happens first. As the density builds up in the divertor region, the electron temperature observed at the magnetic separatrixes decreases to values below 10eV, with and inverted profile; a collapse of the divertor density is then observed in the inner strike zone, and simultaneously in the outer strike zone, but to a lesser extent [fig 3]; the radiated power increases then in the inner wall region. In this case carbon is the main radiating impurity; a slow movement of the CII peak is observed along the inner wall during the pulsation. After a while the edge parameters recover their initial values, and the whole process can be repeated.

With additional heating, a transition into H mode takes place at low or medium central densities. With gas fuelling after the transition, the discharge develops elms and can maintain a "steady" H mode; if the fuelling increases, a flattening of the density profiles is observed which brings back the scrape-off lengths to L mode values [4], and the discharge eventually loses the high confinement regime [3]. Neither a highly radiating divertor nor a full gas target plasma have been attempted in SNU with strong D gas fuelling, but in double null operation long elmy H modes and no gas target have been obtained with this procedure. In a series of experiments performed in SNU with ^{4}He with typically 10MW of additional heating, a Ne gas puff together with continuous ^{4}He gas fuelling has been succesful in increasing the radiation up to 100% of the input power. The plasma then disrupts, and no H modes have been obtained in this case. Langmuir probe measurements are only available in the inner strike region, and show that detachment occurs when the radiated power reaches a value around 70% of the input power.

-Operation on the Be target

In addition to the flattening of the density and temperature profiles with increasing gas fuelling observed in both SNU and SNL [4], the response of the SOL parameters to high gas fuelling on the Be plates shows some differences with that observed on the C target, mainly in the fact that on the Be target, a situation of detachment of one or both strike zones can be maintained in a stable way. In a series of discharges with fuelling from the X-point (with 7 10^{21} D atoms s^{-1} for 4 s approx), the Langmuir probes show that the plasma completely detaches from the inner strike zone during the ohmic phase whereas in the outer strike zone the high density is maintained unchanged; the further addition of beam heating does not cause the reconnection of the inner strike zone, all the power going to the outer one [fig.4]. This experiment was performed when the Be targets were new and a strong pumping was observed.

High power discharges (up to 20 MW additional heating) have been performed with very strong gas fuelling to protect the Be target plates from melting. With 10 MW of input power, a gas target has been sustained for 4s in steady state [6], with a fuelling rate around 10^{22} atoms s^{-1} for 7 s, and a total maximum radiated power around 70% of the input power according to the bolometers.

In this case, the target probes show a detachment in both strike zones, starting in the inner side when the radiated power fraction reaches 50-60%. Temperatures below 5eV are measured close to the magnetic separatrix before the plama detaches and virtually no power reaches the target plates. A stable MARFE is formed in the X point region, which deteriorates the purity of the plasma [6]. The discrepancy in the power balance between bolometric and Langmuir probe measuments can be due to radiation losses not seen by the bolometers (recycling , and Be in low charge states), as it has been observed in limiter configuration [7].

In a further experiment, an attempt has been made to combine a highly radiating divertor with an H mode by allowing the transition to occur at medium densities, and then fuelling the discharge. Only very short H-mode phases have been obtained, when at all, before the plasma reverts to the L mode and detaches at least in the inner stike zone. The Langmuir probe data show that the transition to H mode has occurred only when the additional heating succeeds in increasing the electron temperature in the inner strike zone above 10eV, the H mode thus being incompatible with a semi-detached configuration.

Conclusions

-Detached plasmas can be sustained on the Be target but not on the C target; this difference is not related to the position and shape of the plasma (many magnetic configurations have been used on each target) but to differences in the main radiating species and in the recycling.

-On the C target, the results are consistent with a SOL model of the density limit, as it has been also found for JET limiter discharges [8]. The onset of the MARFE coincides with the maximum in the electron density, and the density exibits the pulsating behaviour that the model predicts when the gas throughput remains approximately constant during that period. This is also the case on the Be target, if the plasma does not detach completely.

-The observed broadening of the profiles of density, temperature and radiation near the density limit could affect the formation of the pedestal and impede the transition to H-mode.

-The apparent incompatibility between an H mode and a gas target has implications for the design of divertors.

References

[1] C G Lowry et al, Europhysics Conference Abstracts 14B Vol. I (1990) 339.

[2] S Clement et al, Europhysics Conference Abstracts 14B Vol III (1990) 1373.

[3] C G Lowry et al, to be published in J. Nucl. Mater..

[4] J A Tagle et al, to be published in J Nucl. Mater..

[5] A Loarte et al, to be published in Nucl. Fusion.

[6 G Janeschitz et al, these proceedings.

[7] A Loarte et al, JET-P(91)22

[8] K Borrass, Nuclear Fusion 31 (1991) 1035.

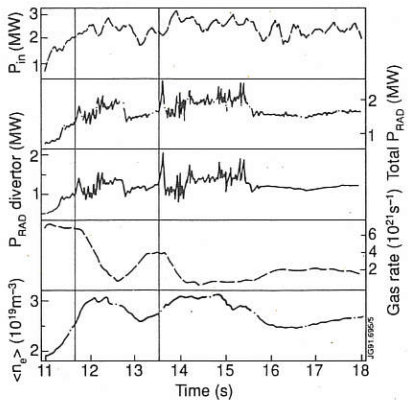

Fig.1. Total input power, total radiated power, radiated power in the X point region, gas introduction rate and volume averaged density versus time in a density limit SNU discharge. The first MARFE occurs at 11.6s, the second at 13.5s.

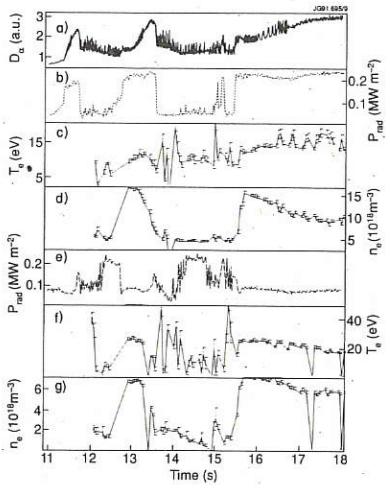

Fig.2. Edge parameters (D , radiated power density, electron temperature and density) in the outer (a,b,c,d) and inner (e,f,g) strike zones for the same discharge than fig.1.

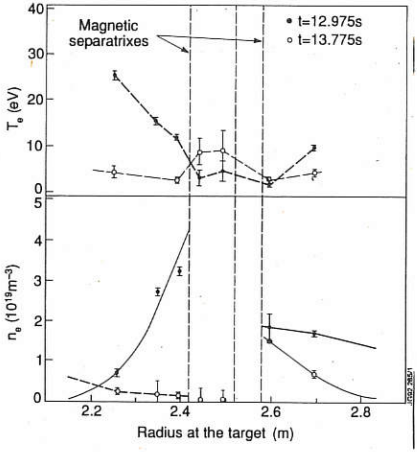

Fig.3. Electron temperature and density profiles in the upper divertor before and after the second MARFE (see fig. 1). The full lines are gaussian fittings, the dashed lines are only to guide the eye.

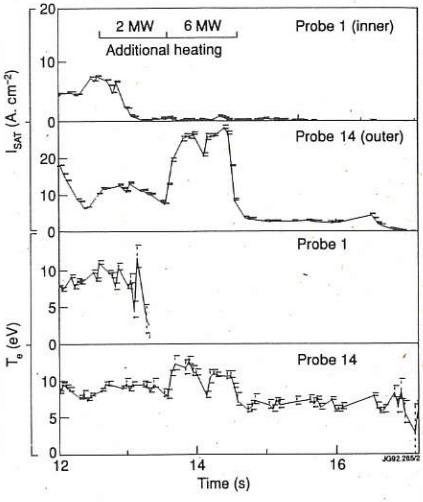

Fig.4. Ion fluxes and electron temperatures at two Langmuir probes situated at similar distances of the inner and outer separatrixes in a SNL discharge.

High Power Operation with a Radiative Divertor in JET

G. Janeschitz, S. Clement, N. Gottardi, M. Lesourd, J. Lingertat, C. Lowry,
G. Radford, G. Saibene, M. Stamp, D. Summers, A. Taroni, P.R. Thomas, G. Vlases
JET Joint Undertaking, Abingdon, Oxon, OX14 3EA, U.K.

Introduction:

The control of the power flow conducted to the divertor target tiles is one of the major problems to be solved in present day divertor designs. This concern assumes still greater importance for the pumped divertor phase of JET or for ITER, where the power conducted to the divertor has to be distributed onto a large surface area in order to prevent excessive heat loads onto the target tiles. A possible solution, which is also being pursued in recent concepts for ITER, is a radiative divertor (divertor marfe, gas target divertor).

Experiments to investigate such radiative divertor concepts have been performed at JET as well as on DIII-D [1]. In this paper we report on steady state radiative divertor experiments at JET during the 1991/92 campaign.

Experiments:

All radiative divertor experiments were performed in 3 MA SN X-point discharges using the Be tiles with the ion grad B drift pointing away from the target. The reversed ion grad B drift provides a more even distribution of the conducted power between inner and outer strike zone and so enables stable operation with a gas target divertor. The discharges were heated by a combination of ICRH (10 MW) and NBI (2 to 12 MW). The Be target was designed such [2] that the maximum heat load occurs on sloped areas of the target tiles which hide exposed edges due to tile misalignment. The most important diagnostic used to assess the quality of a gas target (protection of the Be tiles from excessive heat loads) is a CCD camera monitoring the sloped areas of the Be target through a O I filter (844.5 nm). Since very little oxygen is present in Beryllated JET discharges the signal so obtained represents the thermal radiation emitted from the target and thus is a measure of the tile temperature. In some early gas target discharges the CCD camera was equipped with a 1 mm filter, again aimed at measuring the tile temperature. However, a break through of light from the wings of a Paschen hydrogen line (1004.6 nm) made reliable tile temperature measurements impossible. These measurements were nevertheless quite important because they revealed the geometric structure of the divertor marfe, which is shown in Fig. 1.

Gas target experiments with a pre-programmed gas puff:

In an initial set of experiments, the pre-programmed gas puff, which is required to produce a radiative divertor, was applied at the beginning of the additional heating pulse and was stepped up with increasing power. The consequent detachment of the plasma from the divertor target always starts at the inner strike zone [3,4] and a marfe like structure (cold radiating plasma cloud) very quickly fills the inner scrape off layer from the target up to the X-point (Fig. 1).

When increasing the gas puff even further at this stage the growth of the inner divertor marfe stops and a marfe starts to develop at the edge of the outer strike zone (Fig. 1b). This outer divertor marfe grows slowly towards the separatrix when increasing the gas puffing rate until it fills the outer divertor scrape off layer (Fig. 1a). Once this situation is established, the power conducted to the target (calculated from the tile temperature rise) drops below one MW regardless of the additional heating power applied. At this stage a stable divertor marfe can be maintained practically indefinitely by reducing the gas puff rate slowly to a level where it just replaces the particle losses due to wall pumping. Steady state operation (up to 3.5 sec) with these gas target divertors was demonstrated for various power levels of up to 22 MW of combined ICRH + NBI heating (Fig. 2). The operational window for a radiative divertor when applying a particular heating power is limited at the lower end by the gas puffing rate necessary to fully develop the divertor marfe at both strike zones and at the upper end by the gas puffing rate at which the inner divertor marfe becomes unstable. In the latter case, the marfe at the inner strike zone leaves the divertor area, moves up and down along the inner wall (main plasma marfe) and eventually results in a normal density limit disruption.

The amount of gas puffing rate necessary to establish a gas target divertor increases roughly proportional to the heating power. In our experiments, fully developed gas targets at 12 MW and 22 MW of additional heating required puffing rates of 1.10^{22} at/sec and 2.10^{22} at/sec, respectively (Fig. 2, Fig. 3). The width of the above mentioned operational window in terms of gas puffing rate is in the order of several 10^{21} at/sec.

Fig. 2 shows the radiative divertor discharge with the highest heating power applied (22 MW). The three curves in the top section represent the power balance by comparing the total input power (full line) with the total radiated power (dotted line) and with the power conducted to the target (dashed line), which is only in the order of 0.5 MW. The total radiated power is the sum of bulk radiation (8 MW) and divertor radiation (8 MW). Thus up to 6 MW of power is not accounted for in the 2 sec period with 22 MW additional heating. Calculations (EDGE1D) indicate that approximately 1.5 MW of power loss can be attributed to neutral particles in the divertor which would not be detected by the bolometer. Another possible effect reducing the amount of divertor radiation seen by the bolometers is the optical thickness of such a divertor marfe to the hydrogen Lyman series radiation (121.5 nm etc.). This effect would shift the hydrogen radiation to the longer wavelength (above 400 nm) Balmer or higher series, where the bolometers are insensitive. The magnitude of power missed by the bolometer due to optical thickness is very difficult to estimate with the information available. An effort to calculate this effect, which should be present in partly ionised plasmas such as marfes is under way (modifying EDGE1D, -2D).

It can be seen from Fig. 2 that all important plasma parameters such as Zeff, the central line integrated electron density and the energy content in the plasma as well as the target tile temperature, attain steady state shortly after the start of the high power phase. However, the

Be-II intensity (not shown in Fig. 2) originating from the divertor marfe displays a continues rise during the high power phase suggesting a slow accumulation of Be in the marfe. The slight increase in the total radiation (Fig. 2) during this phase can be probably attributed to this rising Be radiation. An important disadvantage of all these discharges is that they do not display H-mode confinement. This can be seen from the relatively low plasma energy content (bottom section of Fig. 2), which is comparable to the energy content of a limiter discharge with similar heating power and plasma parameters [2].

Gas target experiments with a tile temperature feedback system:

In order to get better operational control of the gas puffing rate, when producing radiative divertors, a simple tile temperature feedback system was introduced. It consists of a fiberscope aimed at one of the sloped areas at the outer strike zone of the Be target, which usually sees the highest power deposition. The fiber was coupled through an O I filter, identical to the one used for the CCD camera, to a photomultiplier. The temperature signal so obtained was then transformed by a simple algorithm into a pseudo density signal and fed into the standard density feedback system.

Npseudo = G (T0 - Tmeasured) + Offset

(G... gain, T0... requested temperature, Tmeasured... measured temperature)

The aim of this second set of radiative divertor experiments was to achieve H-mode together with a gas target and to test the simple tile temperature feedback system. H-modes could be achieved when the feed forward gas puff was delayed by about 0.5 sec. This allowed the H-mode transition to occur before the gas target was established. It turned out that the tile temperature feedback system, when given full control over the gas modules, did exactly the same (T0 = 1000 ^{0}C). These discharges (Fig. 3) displayed an initial ELM free H-mode phase and made a transition into an ELMy H-mode once the gas target was established. The relatively high ELM frequency deteriorated the energy confinement considerably, resulting in only 1.4 times L-mode confinement. As can be seen from Fig. 3, all plasma parameters are in steady state for several seconds after the onset of the ELM's as also observed in long pulse H-mode experiments [5] where similar gas puffing techniques were used.

Conclusions:

- Stable radiative divertor discharges were produced at various power levels.
- The energy confinement is either L-mode or ELMy H-mode (1.4 time L-mode).
- Divertor physics experiments at JET [4] as well as results from the PISCES device [6] suggest that the impurity retention of the divertor is strongly deteriorated when a divertor marfe extends close to the main plasma (X-point).
- Many of the above disadvantages will disappear when introducing effective baffling for neutrals in the divertor together with a long connection length. In this case the divertor marfe would be achieved at lower main plasma density and could be kept further away from the closed flux surfaces.

Literature:

[1] T.W. Petrie, et. al., Proceedings of 10th PSI Conference, Monterey 1992
[2] C. Lowry, et. al., Proceedings of 10th PSI Conference, Monterey 1992
[3] S. Clement, et. al., Proceedings of this Conference
[4] G. Janeschitz, et. al., Proceedings of 10th PSI Conference, Monterey 1992
[5] P.R. Thomas, et. al., Proceedings of this Conference
[6] R. W. Conn, et. al., Proceedings of 10th PSI Conference, Monterey 1992

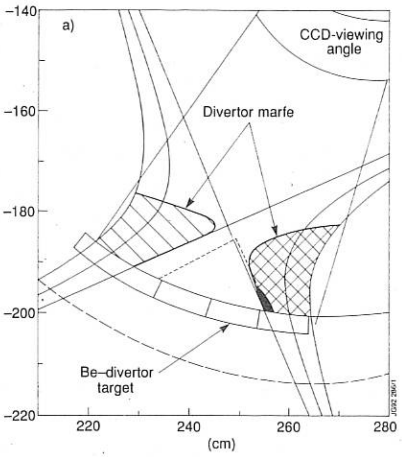

Fig. 1a: Shows a sketch of the structure of the divertor marfe based on video recordings of Deuterium radiation. Dark shadings or black regions represent stronger radiation than light shaded areas.

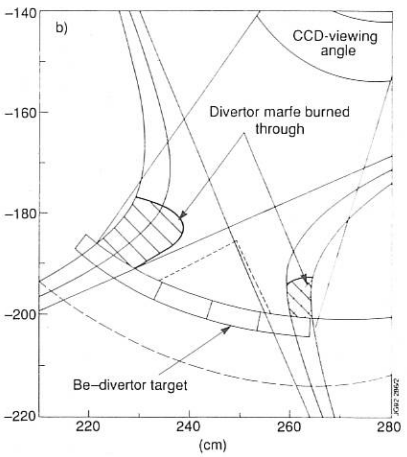

Fig. 1b: Displays a sketch of the structure of a divertor marfe which is not sustained at the outer strike zone. The radiating cloud is burned through at the inner part of the outer scrape off layer.

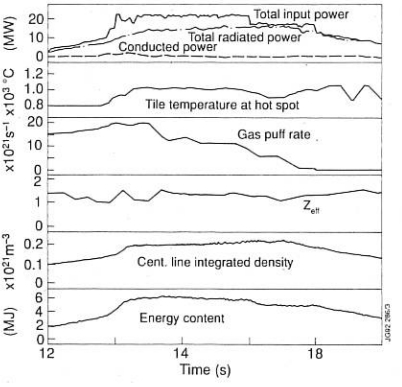

Fig. 2: Radiative divertor discharge with 22 MW input power and 0.5 MW conducted power onto the target tiles. The quasi steady state operation of such discharges is demonstrated.

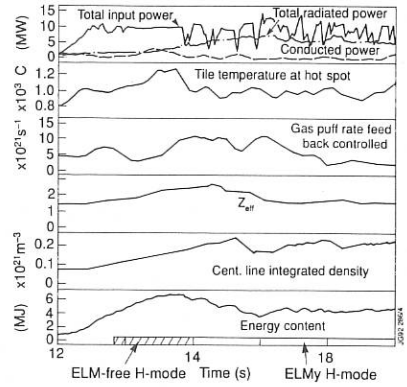

Fig. 3: Radiative divertor discharge with 10 MW input power. A simple feedback system was used to keep the tile temperature constant at 1000 degrees Celsius by gas puffing.

ENERGY EXHAUST THROUGH NEUTRALS IN A TOKAMAK DIVERTOR

M. L. Watkins and P-H. Rebut
JET Joint Undertaking, Abingdon, Oxon, OX14 3EA, UK.

Introduction

The interaction of neutrals and plasma in the scrape-off layer (SOL) and divertor region of a tokamak is essentially two-dimensional and requires, in general, a full 2-D plasma-neutral transport code [1,2] to study, for example, the complex plasma flow generated by ionisation and energy losses by charge-exchange. For the JET pumped divertor, these effects are expected to lead to a more even heat load distribution on the divertor target plates and the retention of target-produced impurities in the divertor region with friction overcoming thermoelectric forces [3,4]. However, in the interesting regime of high density and low temperature, the application of such a 2-D model becomes increasingly difficult. A new formulation of the 2-D plasma-neutral interaction is presented for an idealised SOL/divertor geometry. It contains the essential elements of plasma transport along the magnetic field and neutral transport orthogonal to the magnetic field and is reduced to a 1-D problem by a suitable transformation of coordinates. Solutions at the target of the JET pumped divertor are obtained and the condition to extinguish the SOL plasma before reaching the target is derived.

Formulation of the model

The SOL is represented by an infinite two-dimensional plasma comprising ions, hot neutrals and cold neutrals of mass, m. The ion/hot neutral mixture is assumed to be in collisional equilibrium (due to ion-neutral collisions, such as charge-exchange) at a temperature, T density, n and speed, V. The cold neutrals with density, n_0 and speed, V_0 have little effect on the momentum or energy balance equations. Electrons maintain charge neutrality, contribute to the plasma pressure, p, the conductive heat flux, q, the electron thermal energy, ε and the radiated power loss, P_r. The conservation laws for particles, momentum and energy are:

Ions/hot neutrals

$$\nabla \cdot nV = S - R + C$$

Cold neutrals

$$\nabla \cdot n_0 V_0 = -S + R - C$$

Momentum

$$nmV \cdot \nabla V + \nabla p = 0$$

Energy

$$\nabla \cdot \left(q + \left(\tfrac{5}{2}T + \tfrac{1}{2}mV^2 + \varepsilon \right) nV \right) = -P_r$$

S, R and C are sources/sinks due to ionisation, recombination and ion-neutral collisions.

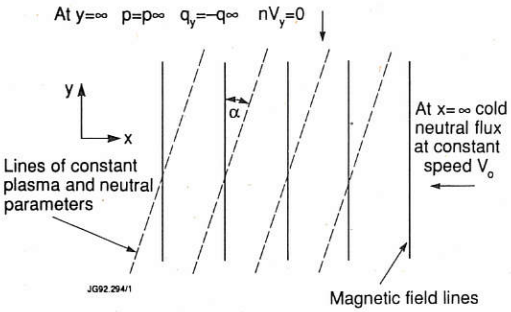

Fig.1 Geometry of the magnetic field and lines of constant parameters in the SOL

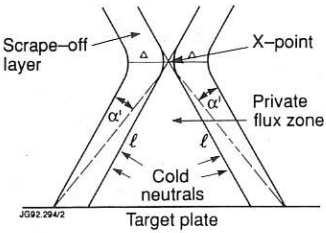

Fig.2 Poloidal projection of the SOL

Consider the flow, nV_y, of ions/hot neutrals along the open magnetic field lines which define the y-direction (Fig. 1). At y=∞, the plasma pressure is p_∞, there is a heat source, q_y=-q_∞ but no particle flux ($(nV_y)_\infty$=0). At y=-∞, ions/hot neutrals leave the SOL to be returned in the x-direction, orthogonal to y, as cold neutrals with constant speed, V_0. We consider the interaction of the plasma and neutral flows and look for solutions with q_y=0. We make the transformation to the coordinate Y=y-x/Tanα, where α is the inclination to the y-axis of lines of constant plasma and neutral parameters. With this coordinate, the plasma and neutral transport equations in conservative form are:

Ions/hot neutrals

$$\frac{\partial nV_y}{\partial Y} = S - R + C$$

Momentum

$$\frac{\partial}{\partial Y}\left(nmV_y^2 + p\right) = 0$$

Energy

$$\frac{\partial}{\partial Y}\left(q_y + \left(\tfrac{5}{2}T + \tfrac{1}{2}mV_y^2 + \varepsilon\right)nV_y\right) = -P_r$$

Cold Neutrals

$$\frac{1}{Tan\alpha}\frac{\partial n_0 V_0}{\partial Y} = S - R + C$$

The first three of these equations are identical to those normally used to study 1-D transport along the magnetic field in the SOL [5]. On the other hand, the penetration of cold neutrals into the plasma is enhanced by the factor 1/Tanα, and hence the ion-neutral losses are increased and the range of impurity retention by plasma flows is extended.

Solutions to the equations

Given the boundary conditions at y=∞, the above equations can be integrated to give:

$$nV_y - \frac{n_0 V_0}{Tan\alpha} = 0$$

$$(\beta+1)nmV_y^2 = p_\infty$$

$$(5\beta+1)\tfrac{1}{2}nmV_y^2 V_y = -\left(q_\infty - \int_Y^\infty P_r dY\right) \equiv -(q_\infty - \Re)$$

where $\beta = p / nmV_y^2 = 1/M^2$ (M is the Mach number of the flow) and q_y and ε are assumed small in comparison with the other terms in the energy balance. The solutions then become:

$$V_y = -\left(\frac{q_\infty - \Re}{p_\infty}\right)\cdot\left(\frac{2(\beta+1)}{5\beta+1}\right)$$

$$n = \left(\frac{P_\infty^3}{(q_\infty - \Re)^2}\right)\cdot\left(\frac{(5\beta+1)^2}{4(\beta+1)^3}\right)\cdot\frac{1}{m}$$

$$\frac{n_0 V_0}{Tan\alpha} = -\left(\frac{P_\infty^2}{(q_\infty - \Re)}\right)\cdot\left(\frac{5\beta+1}{2m(\beta+1)^2}\right)$$

Application of the model to the JET pumped divertor

We calculate the conditions at the target of the JET pumped divertor for a plasma pressure, p_∞=6x10^{3}P (corresponding to T_i=500eV, T_e=250eV and n=5x10^{19}m^{-3} at the mid-plane of the SOL) and q_∞=530MWm^{-2} (corresponding to a total input power, P_{in}=40MW, a major radius, R=3m, a SOL thickness, Δ=0.01m and a ratio of toroidal to poloidal magnetic field, B_T/B_P=5). Assuming β=0 and total radiated power, P_{rad}=0, the above solutions give:

V_y = - 1.77x10^{5}ms^{-1}; n = 5.8x10^{19}m^{-3}; $n_0V_0/Tan\alpha$ = - 1.02x10^{25}m^{-2}s^{-1};

It should be noted that compatibility between momentum and energy balance is ensured provided that ions/hot neutrals leave the SOL with a minimum speed, corresponding to an energy, $E_{min} = \tfrac{1}{2}mV_y^2$, which, in this case for a deuterium plasma, is 326eV. For a given input power and a limit on the plasma pressure at the mid-plane of the SOL (inorder to allow reasonable plasma conditions in the centre of the tokamak), E_{min} can be reduced only by radiation and rapid equipartition between electrons and ions. Furthermore, if ions leave the SOL with E_{min}, the energy will be concentrated in a SOL thickness. If, however, charge exchange first occurs, the hot neutrals could spread E_{min} over a larger target area.

Condition to extinguish the SOL plasma

The condition to extinguish the SOL plasma before the target plates are reached is most readily seen as a geometrical condition on the angle, α' in the poloidal projection (Fig. 2). If ℓ is the projected length of the magnetic field onto the poloidal plane and Δ is the SOL thickness (or $\Delta/2$ if cold neutrals are incident from outside the SOL as well as from the private flux zone), the SOL plasma is extinguished before the target plates are reached if:

$$\mathrm{Tan}\alpha' > \Delta/\ell$$

Using the solutions for V_y and $n_o V_o/\mathrm{Tan}\alpha$ derived above, and noting that with the transformations: $\alpha'=\alpha B_T/B_P$; $Y'=YB_P/B_T$; $(nV_y)'=(nV_y)B_P/B_T$; $q_y'=q_y B_P/B_T$; etc. the equations and solutions in the poloidal projection are identical to those along the magnetic field, the condition to extinguish the SOL plasma can also be written:

$$2 \times 2\pi R \ell n_o V_o E_{min} > (P_{in} - P_{rad})$$

That is, the power transmitted by a particle flux, $n_o V_o$ at an energy, E_{min} across two surfaces, each of area $2\pi R\ell$, must exceed the net input power. It is assumed that the layer is opaque to the incident cold neutrals and that $\beta=0$. For the JET pumped divertor conditions above (P_{in}=40MW, E_{min}=326eV) and ℓ=0.5m the SOL plasma can be extinguished with:

$$\alpha = 4\times10^{-3} \quad \Rightarrow \quad n_o = 1.35\times10^{19}\mathrm{m}^{-3} \quad \text{for} \quad V_o = 3\mathrm{kms}^{-1}$$

Conclusions

We have derived the condition to extinguish the SOL plasma before the divertor target plates are reached and have shown that this condition is satisfied for 40MW into the SOL of the JET pumped divertor at the relatively high density of $5\times10^{19}\mathrm{m}^{-3}$. Even then, the minimum energy of the hot neutral exhaust at the targets, set by ensuring compatibility between momentum and energy balance, is 326eV. This energy could be reduced by radiation and rapid equipartition between electrons and ions, although radiative losses could be low if impurity control was highly effective. Of course, more precise estimates should be obtained by solving the above equations with a full 1-D code (such as that described in [5]) and including impurity retention and radiation, ion-neutral and electron-ion collisions and re-ionisation outside the SOL.

References

[1] BRAAMS, B. J., in Controlled Fusion and Plasma Physics (Proc. 11th Eur. Conf. Aachen, 1983) **7D(II)** European Physical Society (1983) 431.

[2] SIMONINI, R., et al., in Controlled Fusion and Plasma Physics (Proc. 12th Eur. Conf. Budapest, 1985) **9F(II)** European Physical Society (1985) 484.

[3] SIMONINI, R., et al., 10th PSI, Monterey. To be published in J. Nucl. Mater. (1992)

[4] KEILHACKER, M., et al., in Plasma Physics and Controlled Nuclear Fusion Research 1990 (Proc. 13th Int. Conf. Washington, 1990), **1** IAEA, Vienna (1991) 345.

[5] KEILHACKER, M., et al., Nucl. Fusion **31** (1991) 535.

MODELLING OF THE DENSITY LIMIT IN JET BERYLLATED LIMITER DISCHARGES

K. Borrass†, D. Campbell‡, S. Clement‡, G. Vlases‡
† NET Team, Max-Planck-Institut für Plasmaphysik, Garching bei München, Federal Republic of Germany
‡ JET Joint Undertaking, Abingdon, Oxfordshire, United Kingdom

ABSTRACT. A scrape-off layer based interpretation of the density limit in beryllated JET limiter discharges is given. In these discharges JET edge parameters show a complicated time evolution as the density limit is approached, and the limit is manifested as a non-disruptive density maximum which cannot be exceeded by enhanced gas puffing. The occurrence of marfes, the manner of density control and details of recycling are essential elements of the interpretation. Scalings for the maximum density are derived and compared with the JET database.

1. INTRODUCTION

A series of density limit (DL) discharges run on the beryllium belt limiter with a beryllium evaporation coating on the walls showed the occurrance of a DL, manifested as a resistance to further density increase, irrespective of the strength of gas-puffing (refuelling limit). The limit always coincided with the appearance of a marfe [1]. A distinguishing feature of these discharges was that they were almost never disruptive, and in many cases the marfe would extinguish, after which the density would recover to its pre-marfe value, and the entire cycle would be repeated one or more times. It was further shown that the DL was associated with the edge density rather than the line averaged density [1]. In the present paper a SOL based analysis is applied to this limit. The study is based on a series of forty JET pulses which form a database for density limit studies carried out using the solid beryllium belt limiter and beryllium evaporation [1]. Extensive use is made of data from Langmuir probes located in the belt limiter facing towards the inboard SOL.

2. DESCRIPTION OF SOL MODEL

The two-point analytical SOL model of Ref. [2], originally formulated for ASDEX-type divertor configurations, has been extended to limiter cases by (1) assuming $L = L_s$ (L: total connection length, L_s: connection length to the X-point), (2) extending the model to allow for arbitrary poloidal distributions of the power flux across the separatrix and (3) appropriately modifying the recycling model. The model basically relies on the momentum and energy balance equations in the SOL, which, within the framework of a 1-D treatment, can be integrated to give a set of four algebraic equations for the six variables n_S, T_S (density, temperature at the stagnation point), n_D, T_D (density, temperature at the sheath), Δ (temperature decay length) and $q_\perp$ (mean power flux across the separatrix), which can be supplemented by the definition equations of derived quantities. Generally, fixing of two variables determines a solution.

An important derived parameter is the gas throughput as given by

$$\dot{N} = 2\pi R_D \Gamma_D \Delta P_{exh} \qquad (1)$$

where R_D is the plate/limiter radius, Γ_D is the particle flux into the sheath and P_{exh} is the exhaust probability of a recycling neutral.

In the present SOL model recycling is completely described by P_{exh}. A slab model for fast and slow neutrals which includes pumping by the wall (characterized by the wall sticking probability s_w) and diffusion of neutrals into the bulk plasma provides an explicit expression for P_{exh}

$$P_{exh} = \left[1 + \frac{1}{s_w}\left(\frac{1+\rho}{1+2\rho}\sqrt{\frac{S_i}{3S_{cx}}} + \frac{4+6\rho V_0^s/V_0^f}{1+2\rho}\frac{S_i \Delta n_D}{V_0^s}\right)\right]^{-1} \quad (2)$$

where S_i and S_{cx} are the ionization and charge exchange rates, respectively; V_0^s and V_0^f are the mean velocities of slow and fast neutrals; $\rho = 1 + \Delta S_i n_D / V_0^s$.

The present analysis refers to the inboard SOL, which determines the DL [2]. Assumptions have to be made on the relation between global quantities P_{in} (net power to the total SOL) and $\dot{N}_{tot}$ (total gas rate) and the corresponding quantities $q_{\perp,in}$ and $\dot{N}_{in}$, referring to the SOL channel considered. With these assumptions P_{in} and $\dot{N}_{tot}$ are conveniently used instead of $q_{\perp,in}$ and $\dot{N}_{in}$.

3. BULK RADIATION

Within the SOL model n_S and P_{in} are independent parameters. Actually $P_{in} = P_{heat} - P_{rad}$, the time evolution of P_{heat} being explicitly prescribed, while P_{rad} evolves self-consistently. Under quasi-steady-state conditions P_{rad} is mainly a function of density. This relation between density and P_{in} provides an additional constraint for the SOL solution space. A widely used model assumption for the power radiated under quasi-steady-state conditions from the bulk plasma layer is $P_{rad} \propto (Z_{eff} - 1) n_S^2$. It is also frequently observed that $(Z_{eff} - 1) \propto 1/n_s$, corresponding to an approximately constant impurity content. In that case

$$P_{rad} \simeq \tilde{C}_{rad} n_S \quad (3)$$

where $\tilde{C}_{rad}$ is in general discharge dependent. Equation (3) is a relatively crude approximation which is used for illustrative purpose.

4. EMPIRICAL DATABASE AND MODEL VALIDATION

Figure 1 shows the time evolution of edge and related parameters for a typical JET limiter discharge in the vicinity of the DL. In the interval ($t = 8$ s to $t = 9.5$ s), where the edge density reaches its first maximum, the following observations can be made:

(1) The radiated power increases monotonically at nearly constant heating power. Hence the net input power P_{in} into the SOL decreases monotonically.
(2) After the onset of marfing (at $t = 48.8$ s) the gas throughput stays approximately constant.
(3) The plasma temperature at the limiter decreases continuously.
(4) The plasma density at the limiter runs through a maximum (at $t = 48.8$ s).

Figure 1 also includes a comparison with modelling results. Probe data for T_D and n_D ($\triangle$ in Figs 1 (a) and (b)) were used to calculate P_{rad} (using the measured P_{heat}) and the gas rate $\dot{N}_{tot}$ (+ in Figs 1 (c) and (d)). There is good agreement between experiment and modelling.

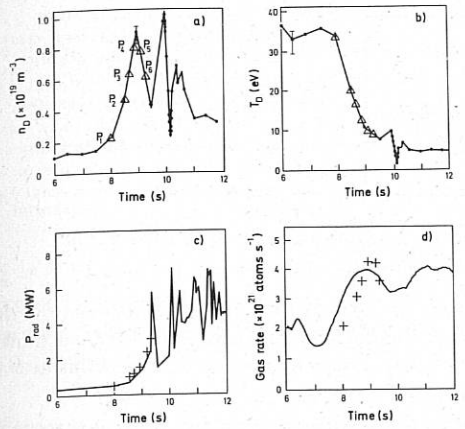

FIG. 1. *Time evolution of relevant parameters close to the density limit of shot 20845. Discharge parameters are: NBI power 4.7 MW, $q_c = 2.22$ and $B_t = 2.59$ T. + denotes values of P_{rad} and $\dot{N}$ calculated with measured values ($\triangle$) of n_D and T_D.*

(a) Limiter density (probe data) *(b) Limiter temperature (probe data)*

(c) Total radiation (bolometric measurement) *(d) Total gas consumption*

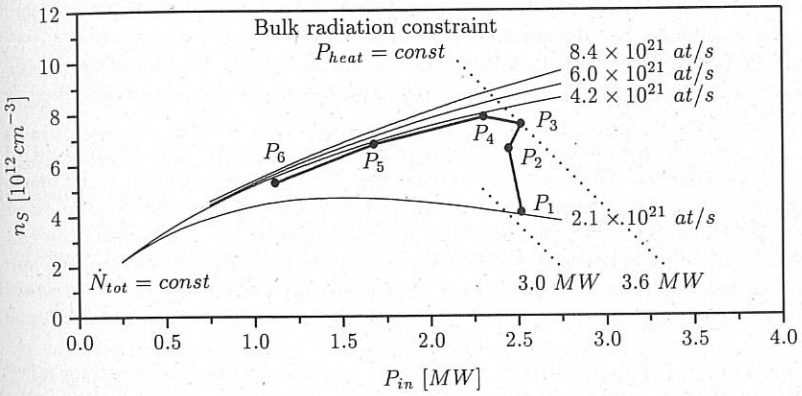

FIG. 2. *Illustration of the mechanism leading to a maximum density (shot 20845). Thin solid curves: curves of constant gas throughput $\dot{N}_{tot}$. Dotted curves: bulk radiation constraint according to Eq. (3) for constant heating powers $P_{heat} = 3.0$ MW (heating power in P_1) and $P_{heat} = 3.6$ MW (heating power in P_3). Thick solid curve: trajectory of shot 20845. • are the points considered in Fig. 1.*

5. DISCUSSION

In Fig. 2 we consider n_S as a function of P_{in} and $\dot{N}_{tot}$ ($n_S = n_S(P_{in}, \dot{N}_{tot})$). Various calculated $\dot{N}_{tot} = const$ curves, the bulk radiation constraint according to Eq. (3) and the trajectory of shot 20845 are plotted in the n_S-P_{in} plane.

During the density ramp-up phase, when quasi-steady-state conditions prevail, one moves along the bulk radiation constraint. In Fig. 2 the radiation constraint is given for fixed values of P_{heat}. Actually it differs from this simple straight line form, since P_{heat} increases somewhat during the discharge.

When marfing starts ($t = 49$ s), P_{rad} continues to increase and hence P_{in} continues

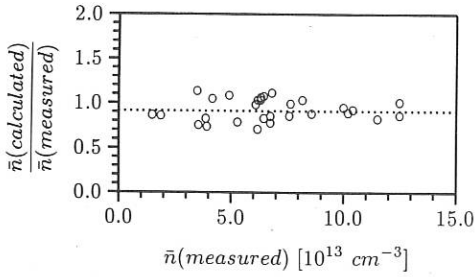

FIG. 3. *Calculated/measured maximum line average densities versus measured maximum line average density for beryllated JET density limit discharges. Range of parameter variation:* P_{in}*:* $0.9-21\ MW$*;* B_t*:* $1.5-2.6\ T$*;* q_c*:* $1.7-6.2$*.* $\bar{n}/n_S = const$ *has been assumed and the actual value of 5.5 for this constant has been determined from point* P_3 *in Fig. 1*

to decrease, as is known from experiment. At the same time $\dot{N} \simeq const$ follows from the way in which density control is operated. Hence, after the onset of marfing one moves along the $\dot{N} = const$ curve in Fig. 2, which is defined by the $\dot{N}$ value prevailing at this moment, and n_S decreases.

Thus the density maximum should coincide with the onset of marfes, as is actually seen in experiment. This typically occurs for values of T_D in the $10\ eV$ range.

For $\dot{N}$ values above the actual value of $\dot{N}_{tot} = 4.4 \times 10^{21}$ the $\dot{N}_{tot} = const$ curves become very narrowly spaced. Hence even a slight increase of n_S requires a drastic increase of the fuelling rate. This is experimentally observed and has been described as refuelling limit [3].

The above picture also offers a qualitative explanation of the cyclic behaviour of the edge parameters. The rapid decay of the edge density after the onset of the marfe ultimately reduces the density at the marfe radius below the threshold for the onset of marfes. Once the extra radiation of the marfe disappears, P_{in} increases and n_S can recover. It is indeed confirmed by experiment that marfes periodically disappear and that the onset continues to coincide with the edge density maxima [1].

6. SCALINGS

For practical applications there is a need for simple scaling-type relations for n_S^{max} in terms of global discharge parameters (a, R, κ, B_t, q) and the net input power P_{in}. With the empirical information that $T_D \simeq 10\ eV$, the SOL model provides n_S^{max} in terms of these variables. The numerical results are well described by the scaling

$$n_S^{max} = 12.3 \frac{Q_\perp^{0.66} B_t^{0.33}}{(qR)^{0.06}} \qquad (4)$$

where n_S^{max} is in $10^{19}\ cm^{-3}$, $Q_\perp = \frac{P_{in}}{4\pi R a \sqrt{\kappa}}$ in MW/m^2, B_t in T and R in m. Of course, the coefficient in Eq. (4) depends on the configuration. Figure 3 compares JET results with model predictions.

REFERENCES

[1] LOWRY, C. G., CAMPBELL, D. J., GOTTARDI, N., LAWSON, K., VLASES, G., et al., in Controlled Fusion and Plasma Heating (Proc. 17th Europ. Conf. Amsterdam, 1990), Vol. 14B, Part I, European Physical Society (1990) 339.

[2] BORRASS, K., Nucl. Fusion **6** (1991) 1035.

[3] DIETZ, K. J., and the JET TEAM, Plasma Phys. Controll. Fusion **32** (1990) 837.

MODELLING OF NEUTRAL AND CHARGED HELIUM TRANSPORT IN SCOOP OF A PUMP LIMITER

M.Z.Tokar', D.Reiter

Institut für Plasmaphysik, Forschungszentrum Jülich, Ass. EURATOM-KFA, Germany

1. Introduction.

The recent TEXTOR experiments[1] have shown a high efficiency of the exhaust of injected helium by the ALT-II pump limiter from discharges with auxiliary heated plasmas of high densities and with strong edge cooling by neon radiation. A minimum value of the effective α-particle confinement time τ_α^* of 350 ms was obtained with an energy confinement time τ_E of 35-40 ms. According to Ref.[2], in order to sustain steady thermonuclear burning in a reactor, the ratio of τ_α^* to τ_E must be smaller than 15.

Various processes in the limiter scoop channel, i.e. interactions of charged and neutral particles during ionization, dissociation, excitation, charge-exchange, nonlocality of the energy transport due to large mean free path lengths between Coulomb collisions essentially determine the efficiency of the pump limiter operation.

In the present paper we extend the model of Ref.[3] for the hydrogen neutrals and ions in the limiter scoop to include a more realistic spectrum of neutral particles, take into account the energy transfer and the transport of helium atoms and ions. As the most decisive parameter the "transformation factor" - the ratio of the neutral density in the limiter chamber to the ion density at the scoop entrance - is computed. The results are compared with calculations by the EIRINE Monte-Carlo code[4] and with recent TEXTOR data.

2. Neutral transport.

Deuterium and helium atoms arise during the charged particle recombination on the neutralizing plate and enter the limiter chamber - Fig.1. They acquire the wall temperature T_w, and deuterium atoms recombine into molecules. Usually the probability for neutrals to be pumped out is smaller than 1 and so they return partly back into the plasma layer, where they are dissociated and ionized by electron collisions and charge-exchange with ions. For helium atoms, ionization is the most important process.

In a narrow scoop channel ($\delta \ll L$) neutrals collide with the walls many times before they are ionized or escape into the scrape-off layer(SOL) of the limiter. As a result, their distribution functions are randomized and the flow velocity U_x along the channel is much smaller than the sound speed $U_s=(T_n/m_n)^{1/2}$ (T_n and m_n are the temperature and mass of the neutrals). In such a case a hydrodynamic approximation is appropriate to describe the neutral transport. The continuity equation and the x-component of the equation of motion, averaged over the scoop width, are the following:

$$\frac{d(N_n U_x)}{dx} = S_n - S_w, \quad \frac{d(N_n T_n)}{dx} = F_n - F_w \tag{1}$$

where N_n is the density of neutrals; the terms $S_{n,w}$ and $F_{n,w}$ describe respectively the change of neutral particle density and momentum during collisions with electrons and ions (subscript n) and with the scoop walls (subscript w); in the case of helium atoms

$$S_n = -k_i^{He} N_{He} n\,; \; S_w = 0\,, \; F_n = S_n m_{He} U_x\,, \; F_w = \frac{N_n U_x (1-R_f) m_{He} v_T}{4\delta} \tag{2}$$

where k_i^{He} is the constant of ionization, n is the plasma density, $v_T=(8T_{He}/\pi m_{He})^{1/2}$ is the thermal velocity

and $U_x R_I$ is the mean velocity after a collision with the wall. For diffusive reflections one has $R_I=0$.

From Eqs.(1)-(2) we obtain the diffusion equation for N_{He}:

$$\frac{d}{dx}\left(-D_{He}\frac{dN_{He}}{dx}\right) = -k_i^{He} n N_{He} \tag{3}$$

where

$$D_{He} = \frac{\pi}{2}\nu_T\delta\left(1-R_I+\frac{k_i^{He} n\delta}{\nu_T}\right)^{-1}$$

As a boundary condition of Eq.(3) at $x=0$ we equate the atom flux, $-S_{Sl}D_{He}dN_{He}/dx$, to the difference of the He ion flux to the neutralizing plate and the number of pumped atoms, $N_{He}S_{eff}$, where S_{Sl} and S_{eff} are the scoop cross-section and the effective pumping speed. At $x=L$ the particles escape into the SOL with the sound velocity so that $-D_{He}dN_{He}/dx = N_{He}U_s$.

3. Transport of charged particles and energy.

For the experimental conditions in question the mean free path λ_c of charged particles between Coulomb collisions is smaller than the scoop length L. Hence we treat the transfer of the main ions - deuterons - and their momentum along x-axis in a hydrodynamic approximation[3]. The behaviour of helium ions, arising in the scoop during the atom ionization, is modelled by the equation of motion for a test particle in the background plasma

$$m_{He}\frac{dV_\parallel^{He^+}}{dt} = m_{He}\frac{V_\parallel - V_\parallel^{He^+}}{\tau_{He^+d}} + ZeE_\parallel + F_T \tag{4}$$

where $V_\parallel$ is the flow velocity of deuterons and $V_\parallel^{He+}$ is the speed of the test helium ion, $\tau_{He+d}=3/16[(m_{He}+m_d)m_{He}/\pi/m_d]^{1/2}T^{3/2}/\Lambda/Z^2/e^4/n$ is the time between coulomb collisions of ions, Z is the He ion charge, $E_\parallel=-1/(en)\cdot d(T_e n)/dx-0.71dT_e/dx$ is the electric field, $F_T=0.71Z^2dT_e/dx+(1.22Z^2-0.27)dT_i/dx$ is the thermal force, $T_{e,i}$ are the electron and ion temperatures.

Calculations have shown that a helium ion is carried by the friction force with deuterons (the first term in r.h.s. of Eq.(4)) at a distance from its origin point much smaller than L. Hence $V_\parallel^{He+}\approx V_\parallel$ is a good approximation.

In the present paper the plasma components have the same temperature $T\equiv T_e=T_i$ and its change along the scoop is computed from the energy balance equation:

$$\frac{dq_\parallel}{dx} = Q \tag{5}$$

Here the heat flux density $q_\parallel$ is the sum of a convective, $5nV_\parallel T$, and a conductive, q_{cond}, part.

According to Ref.[6] $q_{cond}=q_\kappa\equiv-\kappa_e dT/dx$ with the Spitzer heat conductivity $\kappa_e\approx10^{20}T^{5/2}(cm^{-1}s^{-1}, eV)$ when λ_c is smaller then $\sim1/40\cdot dx/d(lnT)$; in the opposite case q_{cond} is limited by the value $q_{max}=\alpha n v_e T$, where $v_e=(T/m_e)^{1/2}$ and $\alpha\approx0.09$ in the case of hydrogen plasma. To take this into account we use the formula:

$$q_{cond} = \frac{q_\kappa q_{max}}{q_\kappa + q_{max}}$$

The boundary conditions of the plasma transport equations at the neutralizing plate are: $V_\parallel=V_s\equiv(2T/m_i)^{1/2}$ - i.e.the ion sound velocity - and $q_\parallel=\gamma nV_s T$ with $\gamma=7.5$. At the scoop entrance, the plasma density n_{sc} and

temperature T_{sc} are given; they are determined by transport processes in the SOL.

4. Numerical results and comparison with experiment.

The calculations have been performed for the conditions of TEXTOR SOL plasmas in discharges high averaged densities of 5.5 $10^{13}cm^{-3}$ and auxiliary heating by neutral injection with a total power of 2MW. The limiter characteristics correspond to the ALT-II: L=30 cm, δ=2.7 cm, S_{Sl}=600 cm, S_{eff}=5200 l/s.

With edge cooling by neon puffing the radiated part of the power increases from 20% up to 90% and the SOL plasma parameters are changed substantially: T_{sc} from 8-10 to 4-5 eV, n_{sc} from 7 to $5\cdot10^{12}cm^{-3}$. This affects on the transport of neutrals and ions in the scoop. Fig.2 demonstrates for two magnitudes of n_{sc} the T_{sc}-dependences of the probabilities ω_D and ω_{He} for D and He neutrals to escape from the scoop into the SOL plasma. Evidently an increase of ω_{He} when T_{sc} decreases results in a reduction of the pumping probability. On the other hand, a simultaneous decrease of ω_D implies that the deuteron flux changes more weakly along the scoop. With constant n_{sc} this means an increase in the mass velocity - see Fig.3 where the calculated profiles of the Mach number $M=V_{\parallel}/V_s$ are shown for two sets of parameters. An increase of $V_{\parallel}$ results in an increase of the He ion flux to the neutralizing plate, which compensates partly the reduction of ω_{He}.

Globally the efficiency of the pump limiter operation can be characterized by the "transformation factor" g, which is equal to the ratio of the atomic density in the limiter chamber to the ion density at the scoop entrance. The calculated dependences of g on T_{sc} are presented for different n_{sc} in Fig.4. An experimental estimate of g can be made by using the information on the effective and usual confinement times of α-particles τ_α^* and τ_p^α. Assuming an exponential decay of the density in the SOL with the distance from the last closed magnetic surface (LCMS) one obtains

$$\tau_\alpha^* = \tau_p^\alpha \frac{\xi}{\varepsilon_{coll}\, g_{He}} \frac{V_s^0 \delta\, S_p}{L_s\, S_{eff}} \qquad (6)$$

where S_p is the LCMS area, $\varepsilon_{coll}=[\exp(-h/\delta_n)-\exp(-(h+\delta)/\delta_n)]$ is the collection efficiency, δ_n, L_s are the decay connection lengths, V_s^0 is the ion sound velocity calculated for a plasma temperature T_s at the LCMS, $\xi\approx0.56$.

According to the measurements[1] $\tau_\alpha^*\approx300$ ms, $\varepsilon_{coll}\approx0.35$ in discharges without neon and $\tau_\alpha^*\approx360$ ms, $\varepsilon_{coll}\approx0.38$ with a radiation level of 90%. Calculations[7] give T_s and τ_p^α magnitudes of 40 eV, 15ms and 10 eV, 22 ms, respectively. For the TEXTOR geometry - S_p=32 m^2, L_S=22 m - we obtain from Eq.(6) g_{He} magnitudes of 45 and 25, respectively, which are in good agreement with the results of our calculation - Fig.4.

Acknowledgement.

The authors would like to thank Dr.U.Samm for fruitful discussions, the work of M.Z.Tokar' has been done under financial support of the A.von Humboldt Foundation.

References.

1. Samm,U., Dippel,K.H., Bertschinger G., et.al. "Helium Exhaust in Plasmas with Strong Radiative Edge Cooling", Rep. on 10th PSI Conf., Monterey, 30.03-03.04.92.

2. Reiter,D., Wolf,G.H., Kever,H., Nucl. Fusion 30(1990)2141.

3. Tokar',M.Z., in Controlled Fusion and Plasma Heating (Proc. 17th European Conf., Amsterdam), Pt.III, EPS(1990)H29.

4. Reiter,D., "Development and Application of Stochastic Models for the Description of Neutral Gas

Transport", Rep. Jül-1947, IPP, Ass. EURATOM-KFA(1984).

5. Braginskii,S.I., in Reviews of Plasma Physics (M.A.Leontovich, Ed.), N.Y., Cons. Bureau, V.1(1965).

6. Luciani,J.F., Mora,P., Virmont,J., Phys. Rev. Lett. 51(1983)1664.

7. Tokar',M.Z., Samm,U., "Modelling of TEXTOR Edge Plasma in Discharges with Auxiliary Heating and Neon Puffing", this conference.

Figure captions.

Fig.1. A schematic view of a pump limiter.

Fig.2. The escape probabilities for D an He neutrals: 1. $n_{sc}=5\ 10^{12}cm^{-3}$, 2. $n_{sc}=7\ 10^{12}cm^{-3}$.

Fig.3. The profiles of the Mach number: 1. $n_{sc}=7\ 10^{12}cm^{-3}$, $T_{sc}=10$ eV; 2. $n_{sc}=5\ 10^{12}cm^{-3}$, $T_{sc}=4$ eV.

Fig.4. The "transformation factor" g for D and He particles: ×, □ - $n_{sc}=5\ 10^{12}cm^{-3}$; +, △ - $n_{sc}=7\ 10^{12}cm^{-3}$.

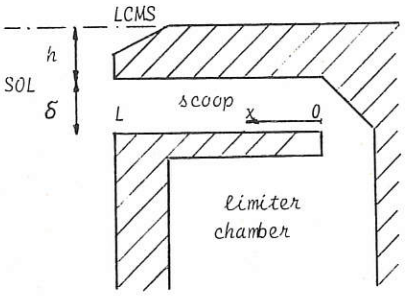

Fig.1

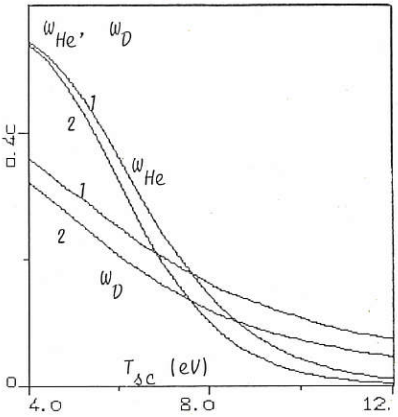

Fig.2

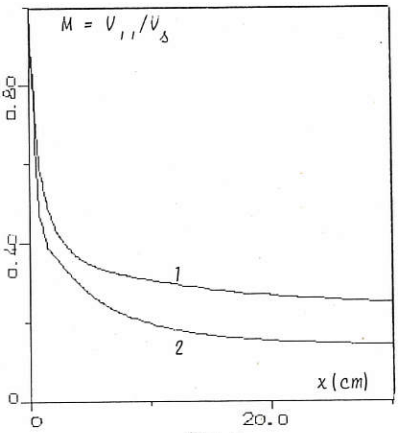

Fig.3

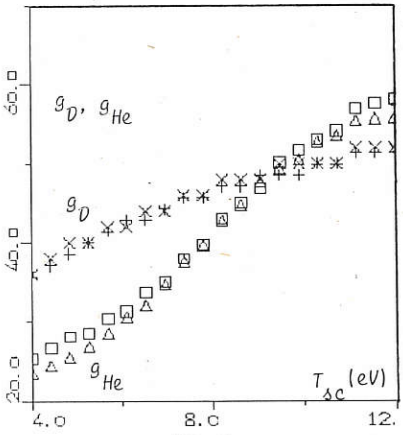

Fig. 4

MARFE DETECTION BY RADIATION MONITORING AND CONTROL OF DENSITY LIMIT DISRUPTIONS

K.-H. Steuer, W. Junker, H. Röhr, K. Büchl, W. Engelhardt, O. Gruber, M. Kaufmann, V. Mertens, J. Neuhauser, A. Stäbler, H. Zohm, ASDEX, ASDEX Upgrade teams
(Max-Planck-Institut für Plasmaphysik - EURATOM Ass., 8046 Garching, Germany)

Introduction

In future reactor size fusion devices like ITER it is necessary to keep the temperature in front of the divertor plates sufficiently low to avoid excessive erosion of wall material. This requires operation at high plasma densities, in the so called high recycling mode. This regime, however, is constrained by the occurrence of density limit disruptions. In principle, disruptions can be avoided by applying certain measures like reduction of gas puffing or increase of additional heating power. It is therefore desirable 1) to have an early warning system indicating imminent disruptions and 2) to develop suitable control scenarii to prevent disruptions. In ASDEX (and other tokamaks) so-called Marfes are precursors to density limit disruptions except for the lowest q_a-values [1,2]. Marfes show up as a poloidally asymmetric radiating zone at the high field side of the torus. They are produced as a consequence of a radiation driven instability at the inboard edge of the plasma leading to a low temperature and, because of $p = const.$ along field lines, high density plasma region [3]. The poloidally asymmetric increase of plasma resistivity due to the Marfe cooling leads to a global contraction of the current profile. The gradient of $j(r)$ will be steepened and destabilization of the $m = 2$ mode ocurring at the $q = 2$ surface triggers the disruption. Marfe detection should therefore be a powerful tool to monitor arising disruptions.

Marfe Detection

A particular sensitive diagnostic for Marfes is the measurement of bremsstrahlung continuum profiles in the near infrared. This signal is proportional to $n_e^2 Z_{eff}/\sqrt{T_e}$ and is therefore especially high in regions of cold dense plasmas like in Marfes. Fig. 1 shows the experimental setup of the bremsstrahlung measurement at ASDEX-Upgrade which is similar to the ASDEX system [4]. The viewing optics and the detection system of the Nd:YAG scattering device are used to detect the bremsstrahlung along 16 chords in 4 different wavelength bands between 800 - 1000 nm with a time resolution of up to 50μs. To identify linefree spectral regions for the continuum measurements (primarily used for Z_{eff} determination), the emission spectrum in the near infrared has independently been measured. Fig. 2 shows a typical spectrum observed in AUG helium discharges. The indicated linefree regions are used for the continuum measurements, a set of spectral channels containing the dominant $HeII$-line ($\lambda = 1012.3\ nm$) can simultaneously be used as a spectrometer for $HeII$-radiation. Additionally a wide angle CCD camera looking radially in the midplane of the torus is used to image the whole plasma ring contour in the visible part of the spectrum. The exposure time is 20 ms, the spatial resolution is about 0.5 cm.

Marfe Observation in ASDEX-Upgrade

A typical Marfe as observed in ASDEX-Upgrade is shown in Fig. 3 (continuum radiation) and Fig. 4 (CCD camera). It is a Single Null He discharge with $\bar{n}_e = 2.9 \times 10^{19}\ m^{-3}$ and $q_a = 8$. A bright zone of continuum light develops in the lower X-point region just after the establishment of the Single Null configuration. The continuum signals which are sampled with 10 kHz show that the Marfe is moving upwards with a velocity of $100 m/s$. The position of the bright moving zone is marked in Fig.1 on the last closed flux surface in intervals of 2 ms. The CCD camera pictures clearly show that the marfe is toroidally symmetric. Shortly after the occurence of the Marfe the plasma tends to detach as the current density is not high enough to sustain heating in the outer region of the plasma. The radiated power as measured by bolometers is dominated by poloidally symmetric edge radiation which, at that time, is nearly equal to the ohmic power. The CCD camera shows that due to the detachment the plasma is disconnected from the divertor ($t = 0.8\ s$).
At lower densities ($\bar{n}_e \approx 1.5 \times 10^{19}\ m^{-3}$) Marfes are much less pronounced and there is no indication for detachment. In these cases the radiated power is equal to about 60% of the ohmic input.

ASDEX results

A more detailed study of marfe behaviour in density limit shots has been performed on ASDEX using a similar continuum measurement system [4]. In deuterium plasmas with high q values ($q > 3$) strong Marfes are observed already 100 ms before the discharge disrupts. The starting point of these Marfes is preferentially close to the active X-point. The time from the onset of the Marfe to the disruption increases with increasing q_a. This might be due to the increasing distance of the $q = 2$ surface from the plasma edge: in order to trigger the disruption, the current profile contraction introduced by the Marfe has to propagate to the $q = 2$ surface.
With decreasing q ($3 > q_a > 2.4$) the period during which Marfes are observed shortens to about 10 ms, the radiation enhancement is lower and continuum radiation is the only signal indicating that marfes are present.
In clean helium discharges on ASDEX no clear Marfes have been seen in contrast to the findings on ASDEX-Upgrade, even at the highest q_a values. Continuum radiation signals as well as bolometer channels indicate just before reaching the density limit an up/down symmetric increase in radiation from an area of a few centimeters inside the separatrix. These observations can be explained with the development of a strongly radiating shell. The analysis of the spectral channels of the continuum radiation system which contain the $HeII$ - line (c.f. Fig. 1) shows that the increase in radiation is mainly due to helium line radiation.

Prevention of Density Limit Disruptions

Fig. 5 presents two ASDEX ohmic density limit shots ($I_p = 320\ kA$, $B_t = 2.17\ T$, $q_a = 3.3$). Fig. 5a shows the sequence as described above: At $t = 1.5\ s$, a Marfe develops, leading to a disruption at $t = 1.52\ s$. Fig. 5b shows a shot in which, after the occurrence of the Marfe, NI (1.9 MW) was applied. Here the start of the NI was triggered on-line by a combination of saddle loops detecting the locked mode occurring together with the

Marfe [5]. For future applications this trigger will be given by the onset of the Marfe (e.g. from bremsstrahlung). In this case, the additional heating stabilizes the thermal instability of the edge plasma and no disruption occurs. In addition, the density drops during this sequence and the shot recovers. The second Marfe in Fig. 5b occurs during the current ramp down (there is no control of density during ramp down). This scenario might provide a possibility to avoid density limit disruptions.

Conclusions

Investigations on ASDEX and ASDEX-Upgrade show that Marfes are a reliable indicator of imminent high density disruptions. Monitoring of bremsstrahlung in the near infrared is particulary suited to detect even weak Marfes. This provides, therefore, an efficient early warning system giving enough time to apply control measures to avoid high density disruptions. It has been shown that an increase in additional heating power can successfully suppress disruptions in ASDEX.

References

[1] B.Lipschultz, Journal of Nucl. Materials 145-147 (1987) 15-25
[2] A. Stäbler et al. Density Limit investigations on ASDEX, submitted for publication in Nuclear Fusion
[3] Neuhauser,J., Schneider,W., Wunderlich,R. Nucl.Fusion 26 (1986) 1679
[4] K.-H. Steuer, H. Röhr, B. Kurzan, Rev.Sci.Instrum. 61(10),3084 (1990)
[5] H. Zohm et al. Plasma Physics and Controlled Fusion, Vol.33, No.12, pp.1423-1434 (1991)

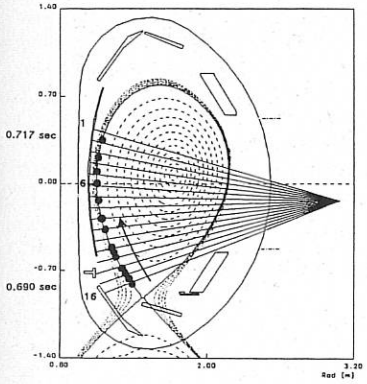

Fig. 1. Cross section of the ASDEX-Upgrade vessel with the 16 sightlines of the spatial channels of the bremsstrahlung system. The full points mark the position of the upward moving Marfe of Fig. 3 in intervals of 2 *ms* starting at 0.690 *s*.

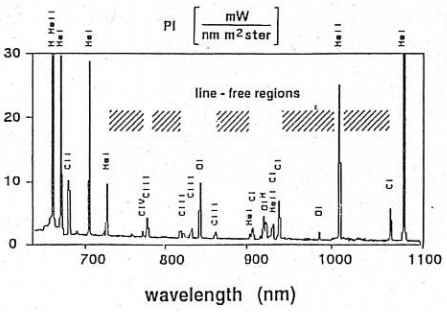

Fig. 2. Plasma emission spectrum in the near infared and the identification of linefree regions for bremsstrahlung measurements.

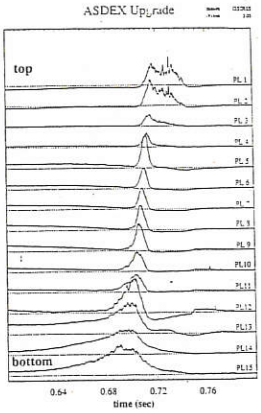

Fig. 3. Bremsstrahlung signals (c.f. Fig. 1) showing the Marfe in a high q SN divertor discharge ($No.1233$) moving from the lower X-point upwards.

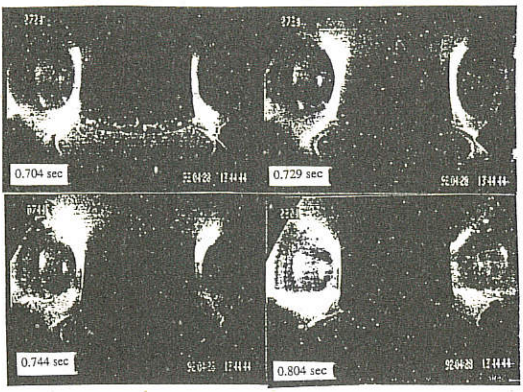

Fig. 4. CCD camera pictures from the Marfe for different times (No.1233). The Marfe is toroidally symmetric and moves (c.f. Fig. 3) from the lower X-point to the upperside of the plasma. At 0.8 s the plasma is detached.

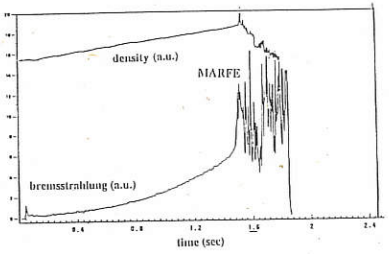

Fig. 5a. Density limit shot at ASDEX (No.33255, $q_a = 3.3$); at $t = 1.5$ s a Marfe develops leading to a disruption.

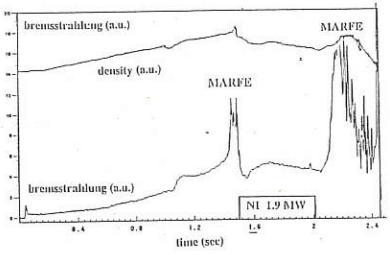

Fig. 5b. Density limit shot (No.33558, $q_a = 3.3$); a Marfe develops and is stabilized by NI, no disruption occurs.

MODELLING OF THE ASDEX-UPGRADE SCRAPE-OFF LAYER PLASMA

H.-S. Bosch, J. Neuhauser, P. Bachmann, R. Schneider,
M. Kaufmann, D. Reiter[1], T. Baelmans[2], B. Braams[3]

Max-Planck-Institut für Plasmaphysik, EURATOM Association, D-8046 Garching
1) IPP, Forschungszentrum Jülich GmbH, EURATOM Association, D-5170 Jülich
2) Katholieke Universiteit Leuven, 3001 Heverlee, Belgium
3) Courant Institute, New York University, New York, NY 10012

Introduction

For future fusion experiments like ITER the plasma edge and divertor region is of crucial importance with regards to power and particle control, impurity transport and helium removal. To understand the underlying physics appropriate models have to be developed and must be validated using experiments in tokamaks like ASDEX-Upgrade. These models then can also be used to predict the behaviour of future fusion devices or to optimize their design, but also to simulate different installations in present machines, in order to optimize them before installation in the machine. In this paper we present first calculations with the B2-EIRENE code package for the design of a divertor baffle for the ASDEX-Upgrade tokamak. This baffle will be installed to enhance the neutral gas pressure in the pumping duct for increased pumping capability.

B2-EIRENE code package

For modelling calculations of the edge plasma and divertor region we use version B2-88 of the two-dimensional multi-species fluid code of B. Braams[1]. For a kinetic description of neutral atoms and molecules the three-dimensional linear Monte-Carlo code EIRENE of D. Reiter[2] is chosen (It is used, however, only in a two-dimensional manner). These two codes are coupled such that in each iteration EIRENE calculates the source terms for the fluid equations and gives them back to B2. Iterating this procedure in a fully automatic manner results in a self-consistent description of mutual effects of charged particles and neutrals in the whole edge and divertor region.

The correct simulation of the plasma edge requires a numerical grid that is based on the correct equilibrium flux surfaces. With a newly developed grid generator results from the DIVA equilibrium code can be implemented easily into the B2-EIRENE code package[3].

For the treatment of oblique target plates or baffles penetrating into the computational region, the numerical grid has to be distorted, i.e. it is not orthogonal close to these structures. This introduces a small error in the cross-field transport[3]. However, near targets the radial transport is dominated by neutrals which are treated correctly anyway. The B2 code has also been modified to avoid the artificial isolating barrier in the X-point region which resulted previously from the mapping procedure.

Modelling results

First we discuss a specific run for the existing geometry as it is shown in figure 1a. The divertor chamber is open, only a vertical plate partially prevents backstreaming of neutrals into the main chamber. Optimized plasmas, however, are larger (mainly wider in radial direction) than this theoretical plasma equilibrium and therefore they are closer to this plate and to the ICRH antena visible between the two passive stabilising coils.

We assume a saturated wall that does not pump, and only the pumping port pumps with a sticking coefficient of 1 % which matches roughly the total external pumping speed of about

2×10^4 l/s. A total input power of 4 MW into the scrape-off layer is imposed, and the density is close to the density limit[3]. Contour plots of particle densities and of the temperatures are shown in Figure 3.

A vertical baffle has been added in this configuration to increase the pressure in the divertor chamber in order to increase the pumped flux for a given pumping speed, and we discuss two different versions of it. As mentioned before, optimized plasmas are closer to the divertor chamber, and therefore for version A the horizontal plate was extended, and a detailed view of this baffle is shown in figure 1b. For comparison, version B of the baffle is a vertical plate which is much further away from the plasma, at the position indicated by an arrow in figure 1a. For both of the baffle versions a converged solution with the coupled codes was calculated for a baffle reaching about half way into the divertor.

Then for both of the versions the length of the baffle was varied in EIRENE standalone runs, and in figure 2 the gross fluxes into the divertor chamber and the net fluxes (which are identical to the net pumping fluxes) are shown as a function of the baffle length. As the height of the divertor opening is different at the two positions, the baffle lengths have been normalized to this height.

Figure 2 can be explained with a simple model. The source of neutrals extends over a small region on the target plate and for these parameters this area has a radial width of about 5 cm. The emission, however is not isotropic, but it is larger at small angles because here transparency of the edge plasma is higher, and decreases toward the plama resulting in a club like distribution directed outward, towards the divertor chamber. For a baffle that is radially close to this source, the neutrals entering the divertor chamber are hardly affected by a short baffle, but the retention of backstreaming neutrals (which fill the divertor chamber homogenuously) is proportional to the baffle length.

Therefore the neutral density in the divertor chamber and the pumping flux (which is proportional to it) increase with baffle length. As soon as the baffle starts to reach into the main stream of neutrals, the flux into the chamber decreases so rapidly that the pump flux (as the density) decreases.

The situation is different for the baffle B which is far away from the source of neutrals. There is already a region of homogenuous particle density in front of the baffle, and therefore for short baffles the flux into the divertor chamber is about proportional to the open width. As this is a staionary system, the particle density in the chamber is identical with the density in front of the baffle, and therefore independent of the baffle length, as can be seen in the figure 2. Only for very long baffles, when the opening becomes small and the conductance of the divertor opening plays a role, the flux is so strongly decreased that the density in the chamber decreases resulting in a decreasing pump flux.

Conclusion

First modelling calculations using the improved B2-EIRENE code package and real equilibrium surfaces for ASDEX-Upgrade show an improvement in pumping efficiency as result of a divertor baffle. The influence of this baffle can be understood with a very simple model, but more detailed calculations will have to be done for optimization of the baffle.

[1] B. J. Braams. A multi-fluid code for simulation of the edge plasma in tokamaks. NET Report No. 68, January 1987 (EUR-FU/XII-80/87/68).

[2] D. Reiter. Randschicht Konfiguration von Tokamaks, Entwicklung und Anwendung stochastischer Modelle zur Beschreibung des Neutralgastransports. Technical Report Jül-1947, KFA Jülich, Germany, 1984.

[3] R. Schneider, D. Reiter, H. P. Zehrfeld, B. Braams, M. Baelmans, J. Geiger, H. Kastelewicz, J. Neuhauser, and R. Wunderlich. B2-EIRENE simulation of ASDEX and ASDEX-Upgrade scrape-off layer plasmas. to be published in Journal of Nuclear Materials.

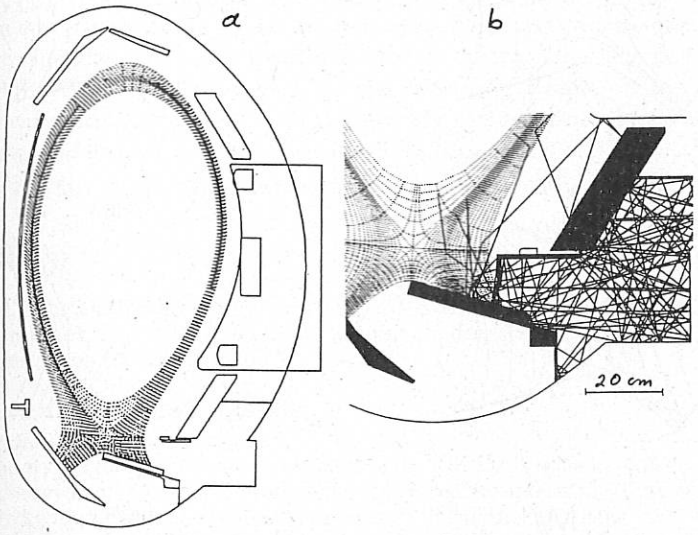

Figure 1a) View of the ASDEX-Upgrade model with the numerical grid and installations in the vessel. 1b) shows the divertor region with baffle version A in detail, with some neutral particle histories.

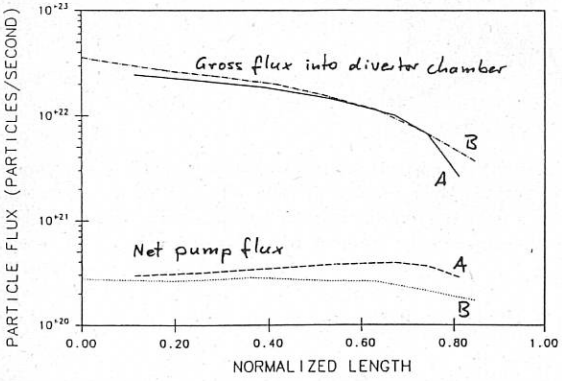

Figure 2) Gross fluxes into the divertor opening (upper curves) and net pump fluxes (lower curves) for baffle versions A and B as a function of the normalized baffle length.

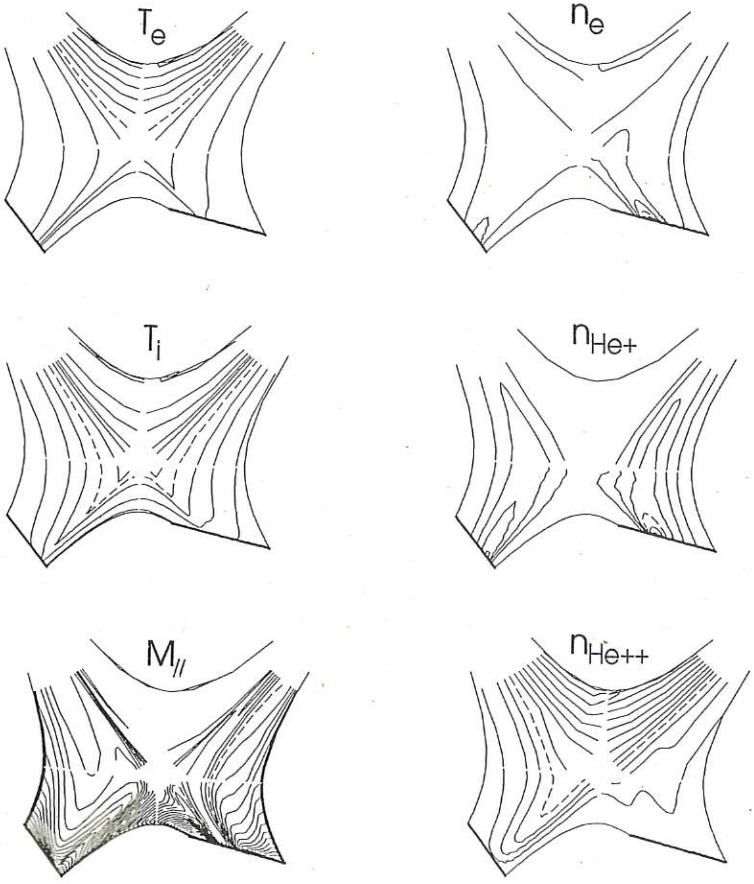

Figure 3) Comparison of the plasma solution without any baffle. In the temperature plots the increment is 10 eV, for the Mach number it is 0.05. The electron density increment is 1×10^{19} m^{-3}, but helium is a trace element and only the spatial distributions of the helium species are of interest. Dashed contour lines correspond to a value of four times the increment.

Modeling the DIII-D Plasma Boundary With the LEDGE Code*

G. D. Porter, M. E. Rensink, T. D. Rognlien, R. A. Jong, D. N. Hill
Lawrence Livermore National Laboratory

1. Introduction

We report here the results of a determination of the radial transport coefficients in the boundary plasma of the DIII-D tokamak. We define the boundary plasma to be the plasma in the region immediately outside the last closed flux surface of a diverted plasma configuration. We obtain values of the electron thermal diffusivity, χ_e, the particle diffusivity, $D_\perp$, and the radial convective velocity, $v_\perp$, by comparison between experimental data and a 2-D fluid model. The data are obtained from neutral beam heated ELMing H-mode discharges with $5.0 \le P_{beam} \le 11.0$ MW, and $1.0 \le I_p \le 1.75$ MA. We find the diffusion coefficients lie in the range $0.03 \le D_\perp \le 0.25$ m^2/s, and $0.2 \le \chi_e \le 0.5$ m^2/s. We find the convective velocity to be zero for all data discussed in this report.

We describe the 2-D fluid code and the data used for determination of the transport coefficients in Section 2. The results of our analysis are described in Section 3, and conclusions are presented in Section 4.

2. Description of Modeling Technique

2.1 Boundary Plasma Diagnostics

The boundary diagnostics which are available in the DIII-D tokamak have been described elsewhere[1]. The radial profiles of electron density and temperature are determined with a Thomson scattering system near the plasma midplane, an insertable Langmuir probe near the midplane, and an array of Langmuir probes on the divertor floor. The radial profile of the power deposited on the divertor floor is determined with an absolutely calibrated infrared TV system which views the divertor floor from the top of the device. Additional diagnostics for the boundary plasma are available, but we have not used the data in the study reported here.

In addition to diagnosis of the boundary plasma, we require information about the magnetic geometry and the power input to the boundary. The magnetic geometry is obtained from equilibrium analysis of the data obtained from magnetic probes around the plasma periphery, using the code EFIT. We allow finite plasma current at the last closed flux surface. The power input to the boundary plasma is determined by measurements of the input neutral beam power, and bolometric measurements of the power radiated from the plasma.

2.2 Code Description

We determine the anomalous radial transport coefficients in the boundary plasma by simulating the plasma with the 2-D fluid code LEDGE. This fully implicit code solves

---

* Work performed under auspices of USDOE by LLNL under Contract W-7405-ENG-48.

[1] Hill, D. N., et.al., Plasma Diagnostics for the DIII-D Divertor Upgrade, Rev. Sci. Instrum. 61 (11), November, 1990.

the continuity equations for heat, particles, and momentum given the anomalous radial transport coefficients $\chi_{i;e}$, $D_\perp$, and $v_\perp$[2]. We assume transport along the magnetic field lines outside the last closed flux surface is determined by classical processes in a collisional plasma. A single group diffusion model for neutral transport in the divertor region is included to better simulate the target plate recycling which dominates the behavior of the boundary plasma.

2.3 Technique Used

We apply the LEDGE code to simulate the radial profiles of the boundary plasma measured in a series of experiments in which the beam power and plasma current on DIII-D were varied. The code is run with fixed density and temperature at the 99% flux surface, i.e. just inside the last closed flux surface. In addition, we assume a fixed electron temperature (2 eV) and a zero density gradient at the outer flux surface in the boundary. Typically, the outer surface is chosen to correspond to the surface which intersects a radial limiter in DIII-D. Finally, we assume the recycling coefficient at the divertor floor is 95%. This means that 95% of the ion flux which strikes the divertor floor is recycled as neutrals with a mean energy of 5 eV.

Specifically, we vary the thermal diffusivity, χ_e, and particle diffusivity, $D_\perp$, until the simulated midplane profiles of the electron density and temperature are consistent with that determined experimentally, using the Thomson scattering diagnostic. In all cases we are able to fit the measured profiles without invoking an anomalous convective velocity. We have not completed analysis of existing ion temperature data in the boundary plasma. Hence we do not have the information required to determine χ_i. We assume $\chi_i = \chi_e$ for simplicity here.

3. Results

3.1 Profile Fits

We compare a typical simulated radial profile of electron density and temperature with that measured with the Thomson diagnostic in Figure 1. These data are taken for a shot with 6.2 MW neutral beam power, and 1.3 MA of plasma current. We use the normalized poloidal flux, Ψ_N for the abscissa of this figure. This parameter is proportional to the total poloidal flux, and is defined to be zero on the magnetic axis, and unity at the separatrix. The parameters $D_\perp = 0.06\ m^2/s$, and $\chi_e = 0.3\ m^2/s$ provide good agreement between the calculated and measured profiles for this shot.

Having obtained the boundary transport coefficients by matching to the density and temperature profiles, we determine consistency by comparing the calculated and measured radial profiles of power density at the divertor floor. We use the power per unit area normal to the magnetic field lines to simplify comparison between calculation and measurement, i.e. $P_\perp = P_{irtv} / |\hat{n} \cdot B/B|$. The power density profile for the shot shown in Figure 1 is shown in Figure 2.

---

[2]Rognlien, T. D., et.al., presented at 1992 PSI Conference.

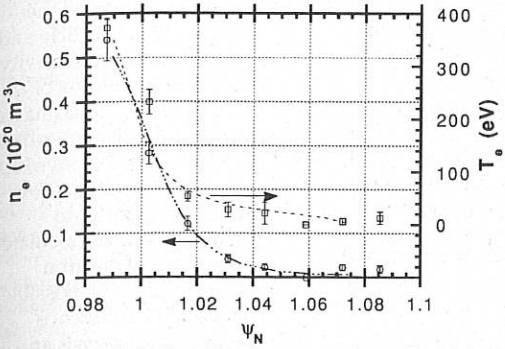

Figure 1 Calculated and measured profile of the electron density and temperature for a low power ELMing H-mode plasma in DIII-D (shot 73584).

We see there is reasonable agreement between the calculated and measured profiles at the outer strike point, but poor agreement at the inner strike point. In addition, there is poor agreement for the total power. We note, however, that the measured divertor power only accounts for approximately 20% of the power across the separatrix. Hence we have poor power accountability on the experiment for this operation. We are exploring the origins of this discrepancy.

3.2 Scaling of Transport Coefficients

The consistency between the measured and calculated profiles is shown in Figures 1 and 2. We have obtained these fits over a range of beam power and plasma current. The scaling of the diffusion coefficients in the boundary layer with these plasma parameters is shown in Figure 3.

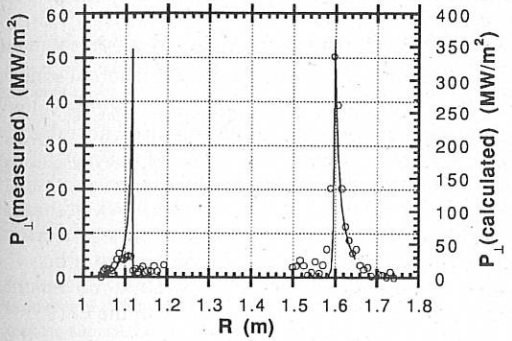

Figure 2 Calculated (solid line) and measured (open circles) power density, normal to the magnetic field, versus major radius at the divertor floor.

We see the particle diffusivity decreases with increasing plasma current, and increases by approximately a factor of four when the heating power is doubled. The electron thermal conductivity, on the other hand behaves less systematically. It increases with increasing plasma current, up to 1.5 MA, but decreases beyond that. The thermal conductivity approximately doubles when the heating power is doubled.

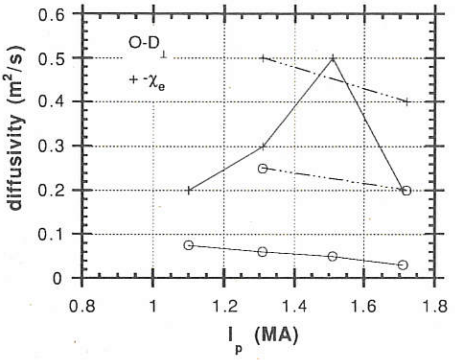

Figure 3 Scaling of particle diffusivity (O), and electron thermal conductivity (+) with plasma current for 5 MW (solid line) and 10 MW (chain dash line) neutral beam heating.

4. Summary and Conclusions

We have determined the behavior of the particle and electron thermal diffusivity in the boundary plasma of an ELMing H-mode plasma. In contrast to previous studies[3], we find no need to invoke an anomalous particle convective velocity to adequately match calculated and measured electron density profiles. A possible source of the difference between this analysis and previous result is the variation in the neutral gas model used in the 2-D fluid code. We use a single group diffusion model which yields a gas density profile which is much more tightly peaked near the divertor floor than the earlier neutral model used in the B2 code. In addition to the different neutral model used, the previous determination of the thermal diffusivity was obtained during an ELM-free H-mode plasma, and the simulation was fit to only the power profile data since there was no Thomson measurement in the boundary plasma.

Earlier studies of the electron thermal diffusivity during ELM-free H-mode obtained values of $\chi_e \approx 1.0\ m^2/s$. The values we report here are significantly smaller. In some cases, the value reported here is a lower limit. In particular, we have used the value which provides the best fit to the electron temperature profile measured near the plasma midplane with the Thomson scattering system. This choice of thermal diffusivity sometimes produces a calculated power profile which is narrower than that measured with the IRTV system (most notably at 1.7 MA, and 5 MW). In these cases, we are unable to simulate the electron temperature profiles and the power profile at the divertor floor simultaneously. We believe this discrepancy may be attributed, in part, to uncertainties in the exact location of the separatrix. Movement of the separatrix location by as little as 1 cm, the estimated uncertainty in the EFIT determined location, can be significant.

We have obtained initial estimates of the scaling of the radial diffusion coefficients in the boundary plasma of an ELMing H-mode plasma. We find the diffusivity increases with increasing auxiliary heating power. The measured diffusivity reported here is smaller than previously calculated. This raises concern about the already difficult task of designing a divertor for ITER.

---

[3]Rensink, M. E., et.al, Fluid Model Simulation of the Scrape-Off-Layer in DIII-D Single-Null Divertor Plasma, Bull. APS, Division Plasma Physics, 1990.

2-D EDGE MODELLING: CONVERGENCE AND RESULTS FOR NEXT STEP DEVICES IN THE HIGH RECYCLING REGIME

H. D. Pacher, W. D. D'haeseleer and G. W. Pacher
The NET Team, c/o Max-Planck-Institut für Plasmaphysik, D-8046 Garching, Germany

Introduction

In the present work, we apply the Braams B-2 code [1] to a next step device, with particular emphasis on convergence of the solutions and on the scaling of the peak power load per unit area on the divertor plate, f_p, on the electron temperature $T_{e,p}$ at the point of peak power load, complementing scaling results given in [2,3]. A double null geometry is chosen (ITER as defined in [4], 22 MA, 6 m). The input power P to one outer divertor is 0.4 of the total power to the SOL and 0.05 of the fusion power, and f_p is given without safety and peaking factors. Recycling is treated by an analytical model [5] including atoms and molecules. The model is appropriate for the high recycling regime down to $T_{e,p}$~5-10 eV as long as impurity radiation can be neglected, but not beyond since sideways neutral motion is not included. DT ionization and radiation losses are included. Only D-T ions are treated, but collision frequencies are corrected for impurities. Radial transport coefficients are uniform in space, with χ_e=2 m^2/s and D=χ_i=χ_e/3=const, for most of the cases but Bohm-like scaling is also investigated.

Convergence characteristics of the B2 code

In the course of iteration of the B-2 code [1], the residuals, R, at the end of a time step are the input for the correction equation $\mathbf{M}\xi=\mathbf{R}$, from which the updated variable ϕ_{new} (e.g., n or T) is obtained as $\phi_{old} + r\xi^*$, where ξ^* is an approximation to ξ. $r \leq 1$ is the relaxation factor, and $\mathbf{M}$ is the (plasma-state dependent) coefficient matrix. ξ^* is found via an incomplete $\mathbf{LU}$ decomposition of $\mathbf{M}$ [1]. The error in the correction $\Delta\xi \equiv \xi - r\xi^*$ is then $(1 - rU^{-1}L^{-1}M)\,\xi$. When the plasma approaches a final state, the expression in brackets becomes constant and independent of ξ. Therefore an exponential behaviour is expected. The time constant in the course of the iteration depends on r and on the plasma state via the difference between $\mathbf{M}$ and $\mathbf{LU}$, and is insensitive to the time step used. The same exponential behavior is expected in the particle and power balances, since their change near the final state is a linear combination of the corrections. Especially the *power balance* is a reliable convergence diagnostic.

Therefore, convergence to a final state is only accepted if, *after an initial transient, the corrections decrease rigorously exponentially.* In particular, when oscillations of critical plasma parameters (such as $T_{e,p}$ or Γ at the plate) occur, we have found that the apparently final, but incorrect, state can be macroscopically different from the correct final state obtained after adjustment of the time step and exponential convergence. Higher recycling generally requires a smaller time step.

In Figs. 1 and 2, the evolution towards convergence with 10^4 steps of 40 μs is shown for the standard case; $T_{e,p}$ remains basically unchanged (Fig.1) from the start of the rigorous exponential decrease of the power balance (Fig.2). While the additional run time beyond 0.2 s appears superfluous to determine the *final plasma state*, it is mandatory to establish *convergence*, as is strikingly demonstrated by the transition case also shown in Figs. 1 and 2. Here, the solution hesitates around $T_{e,p}$≈20 eV, and the power balance initially decays, but not quite exponentially. Although the power balance reaches $2x10^{-5}$, the solution subsequently readjusts to $T_{e,p}$ close to 10 eV with exponential convergence. Using these diagnostic tools to evaluate convergence and adjust the time step, we have reached convergence over a wide input parameter range.

Scaling as a function of electron temperature at the divertor plate

Modelling of the plasma edge of ITER [4] showed three classes of operation: a) high $T_{e,p}$

resulting from high power, low density operation and leading to high and probably unacceptable erosion and contamination, b) medium $T_{e,p}$ ($\approx$ 15 eV, standard physics ignition scenario) leading to high but probably tolerable power loads and erosion levels and c) low $T_{e,p}$ scenarios. The latter were not chosen as the standard scenarios because analysis of experiments at the time showed [6] a strong correlation between low-temperature divertor operation and density limit disruptions. More recent experiments [7,8] now indicate that operational scenarios can be found at low $T_{e,p}$ which do not result in a disruption. We therefore examine the modelling results as a function of $T_{e,p}$, the temperature at the point y_{peak} of peak power load on the divertor plate.

Extensive scaling studies for the high recycling regime have been performed, varying both plasma input parameters (power, upstream density n_s at the intersection of separatrix and midplane, transport coefficients) as well as geometry (size, pitch, divertor depth). In these studies [2,3], two regimes of operation are identified. They exhibit different power law scalings and are classified according to $T_{e,p}$ into a high-temperature regime ($T_{e,p}$>30 eV), and a low-temperature regime having even higher recycling. These two regimes are clearly distinguished in Fig. 3 (χ_{const} curves), where both n_s and input power P are varied. From Fig. 3, it is clear that, for the density regime examined and for the standard distance d from X-point to divertor strike point, d=1.38 m, for ITER [4], converged solutions are obtained for $T_{e,p}$ as low as 5 eV. The peak power per unit area f_p (Fig. 4, χ_{const} curves) varies strongly with P and n_s. However, when the normalized peak power per unit area, f_p/P, is plotted as a function of $T_{e,p}$ in Fig. 5 (lower curves marked χ_{const} ; curves marked χ_{Bohm} are discussed later), a universal curve independent of P results, for which $f_p/P \sim T_{e,p}^{1/3}$ below $T_{e,p}$=30 eV. (Note that DT radiation is not very important, varying from 2 MW at the lowest n_s to 5 MW at the highest n_s).

Therefore, it is seen from these 2-D modelling results that the effective power scrapeoff width, characterized by the inverse of f_p/P, does not depend separately on n_s and P, but only on the resulting $T_{e,p}$ at the divertor plate, i.e. the problem is dominated by the strong temperature dependence of the parallel heat conduction. Since this broadening of the profile leads to a significant improvement in f_p as $T_{e,p}$ is reduced (Fig. 5), low temperature operation is desirable from the point of view of both peak power load and erosion.

Divertor depth variation

The improvement of f_p with reduction of $T_{e,p}$ observed above is maintained when the X-point-to-strike-point distance d is changed. The poloidal angle is varied simultaneously to keep the angle between B_{tot} and the plate constant. As d is increased from 0.9 m to 1.38 m, f_p decreases by 30% at constant n_s (circled points in Fig. 6). However, f_p decreases by only 13% at constant $T_{e,p}$ if n_s is adjusted to a higher value (Fig. 6, see also [3]) during this depth change.

For the shortest divertor examined here, d=0.66 m, a low-temperature and a high-temperature branch is found as n_s is varied, linked by an unstable intermediate region (Fig. 7). All these cases are well-converged; in fact, the transition case of Figs. 1 and 2 transits from the high-temperature to the low-temperature branch during its iteration procedure. Despite the existence of the intermediate region, the set of results for the shortest divertor follows the same pattern as the other three sets, i.e. similar functional dependence of f_p on $T_{e,p}$ (Fig. 6), with a somewhat narrower profile and higher f_p at constant $T_{e,p}$.

Bohm-like scaling

All of the parameter variations discussed to this point were performed for uniform radial transport coefficients. This value and dependence, chosen in [4] as representative of results then available from experiments, probably still represents the best compromise. However, since some experimental evidence now exists that the transport coefficients may vary with edge temperature (indicative in [9], dependence proportional to T_{edge} but independent of 1/B in [10]), we have investigated the effect that the spatial variation of Bohm-like transport would have on the modelling predictions. We use a scaling of D, χ_i, and χ_e with T_e/B locally (the B variation is

relatively unimportant), but keep the same values at the intersection of separatrix and midplane as quoted in the introduction.

Despite the fact that the spatially varying transport coefficients lead to a different form of the profiles both radially and along the field than the uniform ones, the functional variation of $T_{e,p}$ with n_s (Fig. 3) and of the peak power per unit area f_p with n_s (Fig. 4) is very similar to the χ_{const} cases. In particular, f_p/P (Fig. 5) again follows a universal curve with P, but the χ_{Bohm} cases lie 35% higher at the same $T_{e,p}$ (effective profile width 73% of the χ_{const} cases). From this result and by comparing the values of P for almost identical curves for the Bohm and constant cases in Figs. 3 and 4, it is seen that the power-handling capacity is significantly reduced if χ_{Bohm} is assumed rather than χ_{const}. To obtain the same f_p : at constant $T_{e,p}$, P must be reduced to 73%; and at constant n_s , P must be reduced to 67%. To obtain the same $T_{e,p}$: at given n_s, P must be reduced to 62%.

Conclusions

The present results, applicable to the high recycling regime of next step devices, show clearly that, in the absence of impurity radiation, the power load on the divertor plates can be reduced by operating at lower electron temperature at the divertor plate, provided that density limit disruptions can be avoided and the resulting density profiles are compatible with those required for the main plasma. Convergence of the 2-D results from the B2 code is demonstrated and a prescription to determine convergence is given. Bohm-like transport scaling would reduce the power handling capability for the same conditions to 60% - 70% of the value for constant transport coefficients, when the values at the midplane are kept the same.

References

1. B.J.Braams, NET Report EUR-FU/XII-80/87/68, Jan. 1987
2. H.D.Pacher, W.D.D'haeseleer, G.W.Pacher, submitted to Nucl. Fusion
3. H.D.Pacher, W.D.D'haeseleer, G.W.Pacher, Proc. 10th PSI Conf, Monterey, 1992 (J. Nucl. Mat.)
4. D.E.Post et al, ITER Physics, ITER Documentation Series No. 21, IAEA Vienna, 1991
5. M.F.A.Harrison, E.S.Hotston et al, NET Report EUR-FU/XII-80/91/100 Feb. 1991.
6. K.Borrass, Nucl. Fusion Vol.31, No.6 (1991) 1035 and references therein.
7. T.Petrie et al, Proc. 10th PSI Conf., Monterey, 1992 (J.Nucl.Mat.)
8. G.Janeschitz, contribution to panel at 10th PSI, 1992 (private comm.)
9. J.A.Tagle et al., Proc. 18th EPS Conf. Contr. Fusion and Plasma Physics, III-149, Berlin, 1991
10. K.McCormick et al., Proc. 10th PSI Conf., Monterey, 1992, (J. Nucl. Mat.)

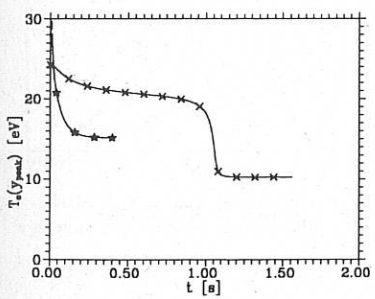

Fig. 1 T_s near plate at y_{peak} vs. time timestep 40 μs

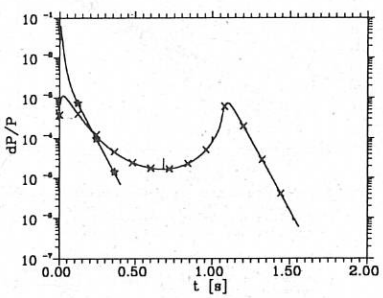

Fig. 2 Fractional power balance dP/P vs. time timestep 40 μs

xxxxx Transition case
***** Standard convergence

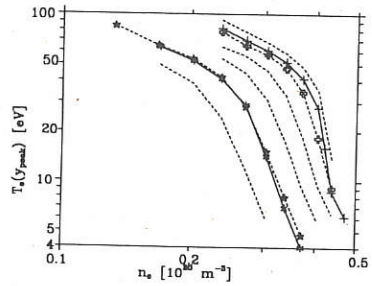

Fig. 3 T_e at plate (at y_{peak}) vs. n_e at constant total power

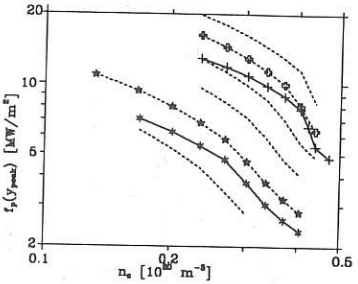

Fig. 4 Peak Power per unit area to plate f_p vs. upstream density n_e at const. total power

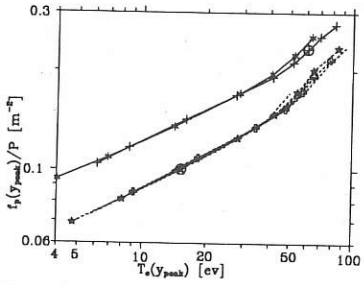

Fig. 5 Peak Power per unit area to plate norm. to total power, f_p/P, vs. $T_{e,p}$ at y_{peak} for various P and for χ_{Bohm} and χ_{const}

Legend for Figures 3, 4, and 5:
Bohm-like transport χ_{Bohm}
28 MW
46 MW

Constant transport χ_{const}
37 MW
46 MW
56 MW
65 MW
74 MW
84 MW
Circles in Fig.5: n_e=0,3x10^{20} m^{-3}

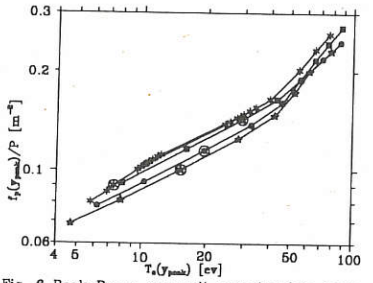

Fig. 6 Peak Power per unit area to plate norm. to total power, f_p/P, vs. $T_{e,p}$ at y_{peak} for various divertor depths d; pol. angle adjusted for same angle B_{tot}-plate

Circles: cases for n_e=0.3*10^{20} m^{-3}

d=1.38m, 15.0°
d=1.14m, 17.7°
d=0.90m, 21.9°
d=0.66m, 29.2°

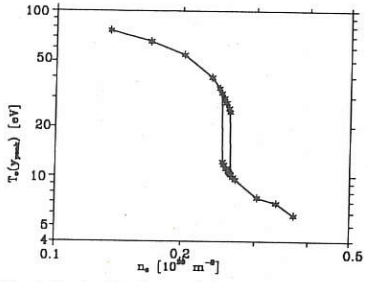

Fig. 7 T_e at plate (at y_{peak}) vs. n_e at const. total power for short divertor poloidal depth d=0.66 m, pol. angle 29.2°

MODELLING OF TEXTOR EDGE PLASMA IN DISCHARGES WITH AUXILIARY HEATING AND NEON PUFFING

M.Z.Tokar', U.Samm

Institut für Plasmaphysik, Forschungszentrum Jülich, Ass. EURATOM-KFA, Germany.

1. INTRODUCTION

The problem of hot plasma interaction with the material walls is one of the burning questions, the solution of which is essential for the creation of a viable thermonuclear reactor. One of the ways to reduce the temperature of the plasma in contact with the wall elements and the heat loads on them is an increase of impurity radiation from the discharge. However, the source of radiation should be localized in the peripheral region and impurities should not contribute significantly to the energy balance of the central plasma and hinder its heating up to thermonuclear temperatures. The light impurities - from boron to neon - satisfy these requirements since they are ionized up to the helium-like states in a relatively thin layer at the discharge edge. The TEXTOR experiments[1] have shown, that in discharges with auxiliary heating more than 95% of the power can be radiated by neon puffing without the onset of Marfe or detachment and with the source of radiation staying in the vicinity of the last closed magnetic surface (LCMS), touching the limiter. It is remarkable that this state is compatible with a good exhaust of injected helium by the pump limiter ALT-II.

In the present paper we elaborate the model proposed in Ref.[2] of the edge plasma particle and energy balances for the case of discharges with auxiliary heating and neon puffing and compare the results of calculations with experimental data from TEXTOR.

2. THE EQUATIONS OF PARTICLE AND HEAT BALANCES.

The transport equations for neutral and charged particles and energy in the peripheral plasma, averaged over the magnetic surfaces, have the following form:

the continuity equations

deuterium atoms

$$\frac{d}{dx}\left(v_a^{1,2}\, n_a^{1,2} \right) = -\left(k_i^a + k_c \right) n\, n_a^{1,2} \tag{1a}$$

$$\frac{d}{dx}\left(-D_a \frac{dn_a^*}{dx} \right) = -k_i^a\, n\, n_a^* + k_c\, n\, \left(n_a^1 + n_a^2 \right) \tag{1b}$$

impurity atoms

$$\frac{d}{dx}\left(v_0\, n_0 \right) = -k_i^0\, n\, n_0 \tag{2}$$

deuterons

$$-\frac{d\Gamma_\perp}{dx} = k_i^a\, n\, \left(n_a^* + n_a^1 + n_a^2 \right) \tag{3}$$

impurity ions

$$-\frac{d\Gamma_{\perp}^{z}}{dx} = k_i^{z-1}\, n\, n_{z-1} - k_i^{z}\, n\, n_z \qquad (4)$$

the plasma heat balance

$$-\frac{dq_{\perp}}{dx} = -k_i^{a}\, n\, (n_a^{*} + n_a^{1} + n_a^{2})\, E_a - \sum_{1\le z\le z_{Li}} n\, n_z\, L_z \qquad (5)$$

Here x is the distance from the LCMS in the direction to the discharge centre, $n_a^{1,2,*}$ are the densities of Franck-Condon, reflected and charge-exchanged deuterium atoms, n_0 is the density of impurity atoms, $v_a^{1,2}$, v_0 are the velocities of neutral particles; n, T are the plasma density and temperature, n_z is the density of the impurity ions with the charge z, z_{Li} is the charge of the lithium-like ions; $\Gamma_{\perp} = D_{\perp} dn/dx$, $\Gamma_{\perp}^{z} = D_{\perp} dn_z/dx$, $q_{\perp} = \kappa_{\perp} dT/dx + a\Gamma_{\perp} T$ are the densities of the particle and heat fluxes in the direction from the discharge centre to the LCMS, E_a is the energy loss by electrons on the ionization and excitation of deuterium atoms; the diffusivity of deuterium atoms in the plasma due to their charge-exchange is given by the formula[3]

$$D_a = \frac{2\,T}{m_i\,(k_i^{a} + k_c)\,n}$$

where k_c is the constant of charge-exchange.

The charged particle diffusivity and the plasma heat conductivity are assumed in the form:

$$D_{\perp} = \frac{A_D}{n} + \Delta D\,,\quad \kappa_{\perp} = \frac{A_D}{\varepsilon_{\kappa}} + \Delta\kappa$$

The fist terms in $D_{\perp}$, $\kappa_{\perp}$ correspond to the Alcator scaling, which describes well enough TEXTOR ohmic discharges by $A_D = 10^{17}\,cm^{-1}s^{-1}$ and $\varepsilon_{\kappa} = 0.4$; the second terms describe the transport change by auxiliary heating. For $\Delta\kappa$ we use the formula obtained in Ref.[4]:

$$\Delta\kappa = \alpha_{\Delta}\frac{n c_s^3}{\omega_i^2}\frac{d}{dx}\ln\frac{n}{\sqrt{T}}$$

where α_{Δ} is a numerical factor, $c_s = (T_e/m_i)^{1/2}$ is the ion sound velocity, $\omega_i = eB/(m_i c)$ is the ion Larmor frequency.

A preliminary analysis has shown that for the TEXTOR discharges in question ΔD can be modelled by the Bohm diffusivity $D_B = cT/(16eB)$. In order to avoid an unrealistically strong increase of $D_{\perp}$ to the discharge centre the magnitude of ΔD is restricted by the D_B value at T = 100 eV.

The cooling rates L_z of impurity ions are computed according to the approximative formulas, derived in Ref.[2].

The boundary conditions of the system (1)-(5) are posed at the LCMS ($x = 0$) and at the conventional border between the peripheral region and the central part of the discharge($x = x_0$). The latter is determined such that with $x \ge x_0$ the atoms of deuterium and impurity and the impurity ions with $z \le z_{Li}$ are practically absent. At the LCMS we

assume the total recycling of deuterium particles and the continuity of particle and heat fluxes; at $x = x_0$ the electron density n_b, the neon concentration c_{Ne} and the density of the heat flux q_0 are given.

3.THE RESULTS OF CALCULATIONS AND COMPARISON WITH TEXTOR DATA.

The calculation has been done with $q_0 = 5.5 W/cm^2$, which corresponds to the total heat flux to the peripheral region of 1.8 MW; besides neon, carbon atoms are released into the plasma with an erosion coefficient of 0.03 and a velocity of $5 \cdot 10^5 cm/s$; in the formula (22) $\sigma_\Delta = 2.5$.

Fig.1 shows how the radiation level p_r - the radiated part of the total power - depends on neon concentration c_{Ne}. The different curves correspond to different magnitudes of n_b. The heat flux into the SOL decreases with increase in c_{Ne} owing to diminution both of the plasma temperature at the LCMS T_s and of the charged particle flux into the SOL. This is demonstrated in Fig. 2 and 3, where the dependences of T_s and of the deuterium particle confinement time τ_p on p_r are presented for different n_b.

In order to interpret the results of experiments on the helium pumping from the discharges with strong radiative edge cooling we have calculated also the confinement time of α-particles τ_p^α. The results are shown in Fig.4. One can see with increase of the radiation level up to 80% τ_p^α grows not more than by 1.4. Consequently the flux of α-particles also does not change essentially. This may be a one of the reasons, why the pumping efficiency of ALT-II does not deteriorate with increase of the edge radiation.

In TEXTOR radiation of 90% of the net power is attainable with a neon concentration in the discharge of 0,5%. According to Fig.1(curve 3) the calculations give a similar value of 0.75%. A magnitude of τ_p, estimated from the spectroscopic measurements, is of 13 ms for a mean plasma density of $5.5\ 10^{13} cm^{-3}$ and without neon. With increase of p_r up to 90% τ_p grows by 1.8-2 times in agreement with Fig.3. The absolute value of τ_p^α has not yet been determined experimentally. Relative measurements show in agreement with calculations a weaker dependence of τ_p^α on p_r, than for τ_p: with the increase of p_r from 0.2 up to 0.9 τ_p^α changes less than by 1.5 times.

Acknowledgments

The work of M.Z.Tokar' has been done under the financial support of the A. von Humboldt Foundation.

REFERENCES

[1] SAMM,U., DIPPEL,K.H., BERTSCHINGER, G., et al., Helium exhaust in plasmas with strong radiative edge cooling, Rep. on 10th PSI Conf., Monterey(1992).

[2] TOKAR',M.Z., in Controlled Fusion and Plasma Heating (Proc. 18th Eur. Conf. Berlin, 1991), Vol. 15C, Part III, European Physical Society (1991)1.

[3] LEHNERT,B., Nucl. Fusion 8(1968)173.

[4] KADOMTSEV,B.B., Nucl. Fusion 31(1991)1301; DNESTROVSKII,A.YU., IVANOV,V.V., PARAIL,V.V., Sov.J.Plasma Phys.14(1988)529.

FIGURE CAPTIONS.

Fig.1 - Radiation level p_r in TEXTOR auxiliary heated discharges as a function of neon concentration c_{Ne}: 1 - $n_b = 4.4 \cdot 10^{13} cm^{-3}$, 2 - $n_b = 5 \cdot 10^{13} cm^{-3}$, 3 - $n_b = 5.6 \cdot 10^{13} cm^{-3}$.

Fig.2 - Dependences of the plasma temperature at the LCMS on the radiation level: 1 - $n_b = 4.4 \cdot 10^{13} cm^{-3}$, 2 - $n_b = 5 \cdot 10^{13} cm^{-3}$, 3 - $n_b = 5.6 \cdot 10^{13} cm^{-3}$.

Fig.3 - Dependences of the deuterium ion confinement time on the radiation level: 1 - $n_b = 4.4 \cdot 10^{13} cm^{-3}$, 2 - $n_b = 5 \cdot 10^{13} cm^{-3}$, 3 - $n_b = 5.6 \cdot 10^{13} cm^{-3}$.

Fig.4 - Dependences of the α-particle confinement time on the radiation level: 1 - $n_b = 4.4 \cdot 10^{13} cm^{-3}$, 2 - $n_b = 5 \cdot 10^{13} cm^{-3}$, 3 - $n_b = 5.6 \cdot 10^{13} cm^{-3}$.

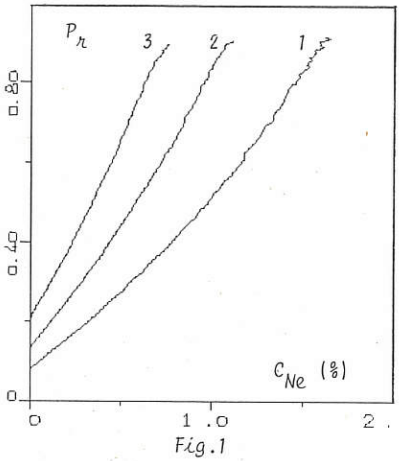

Fig.1

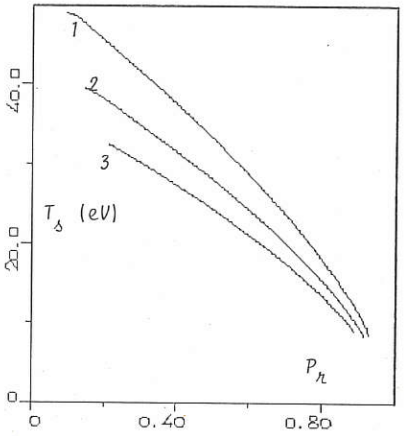

Fig.2

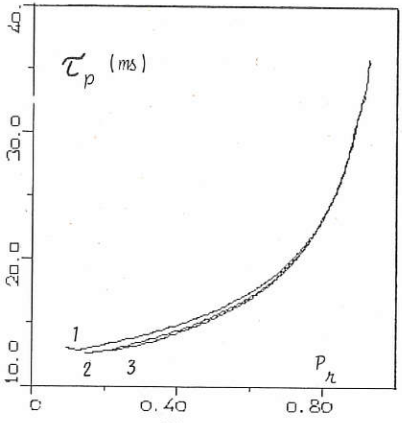

Fig.3

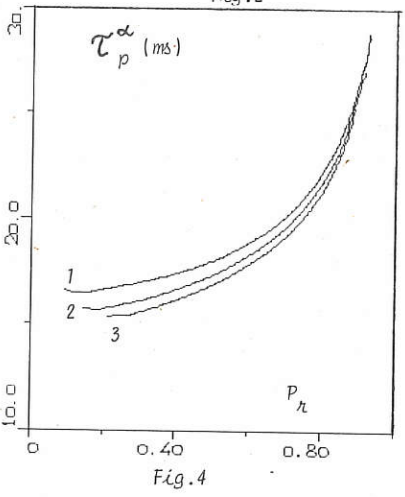

Fig.4

A Study of the SOL Density Profile Behavior in ASDEX

K. McCormick, J. Schweinzer, and Z.A. Pietrzyk*
Max-Planck-Institut für Plasmaphysik, 8046 Garching, Germany
*CRPP, Lausanne, Switzerland

Introduction: Scrape-off layer (SOL) density profiles measured in the outer midplane of ASDEX by the lithium beam probe diagnostic have been presented in the past /1-8/. This work places these results on a common basis for OH and NI-heated discharges (L-mode), and suggests a scaling for the particle diffusion coefficient D_p which is derived using λ_n, the exponential fall-off length in the SOL near the separatrix. Density profiles for the H-mode have now also been extended to inside the separatrix.

Characterization of the SOL Density Profile: Only data from the steady-state phase of double-null (DN), diverted discharges fueled by gas puffing are discussed in detail. While no systematic evaluation of the single-null (SN) configuration has been carried out to date, the indications are there is little difference between DN and SN. Pellet-fueled discharges, as well as discharges exhibiting Improved Ohmic Confinement (IOC) /6,7/ influence the separatrix density n_{es}, but λ_n is essentially not affected.

Fig. 1 depicts λ_n values vs. electron temperature slightly inside the separatrix T_s /8/ for dataset **A** (divertor configuration DV II /7/, both divertor bypasses open /7/, carbonized walls; H^+, D^+; OH; $\bar{n}_{e13}$= 0.8-5.5×10^{13}cm^{-3}, I_p=150-420kA, B_t=1.9-2.55T /6/. For T_s>40eV, the points scatter about a line roughly given by λ_n~1.9cm, but for T_s<40eV there is a dramatic increase in λ_n with decreasing T_s. This is in the regime (low T_s, $q_a \geq 5$) favorable to the formation of MARFES. Early λ_n-scalings for ASDEX indicated a q_a-dependence /4/, but for dataset **A** as an entity this approach was not appropriate /6/ due to the presence of the two different regimes. The behavior of λ_n as a function of q_a for a small density window, $\bar{n}_{e13}$=1.5-1.75, is illustrated in fig. 2: As q_a is increased through variation of I_p and B_t, the power flow P_{sol} into the SOL falls with I_p, as does the edge temperature T_s and density n_{es} /7/. (Note, the high colinearity of T_s with I_p, and thus q_a, makes it impossible to derive any scaling involving both T_s and q_a for this subset - in marked contrast to the entire dataset.) Of interest is that D_p (discussed below) initially falls with q_a and then increases for $q_a \geq 5$, directly mirroring the behavior of T_s and q_a.

The dynamic evolution of λ_n, T_s and n_{es} as a MARFE is provoked by ramping $\bar{n}_e$ until disruption occurs (at t~2.45 s) is displayed in fig. 3: n_{es} drops by 30% and then stabilizes on a time scale correlated with the establishment of the MARFE - while $\bar{n}_e$ continues to climb. (Here, $P_{RAD,div}$ is the best indicator of the reduced power flow to the outer divertor, signaling the presence of a MARFE) The pronounced temporal increase in λ_n from 3→5cm follows the development of T_s. Note, the MARFE influence on the outer SOL is indirect: the MARFE-related, reduced power flow to the SOL leads to lower temperatures, causing in turn larger λ_n and lower n_{es}.

λ_n scaling laws for datasets **A** and **B** [/3,6/: DV I /7/, stainless steel walls: D^+, He^{2+}; OH, NI (H^o→D^+, He^{2+}) P_{NI}=0.4-1.7MW; $\bar{n}_e$=1-5×10^{13}cm^{-3}, I_p=270-420kA (for He, only 420 kA), B_t=2.17T] are presented in fig. 4, and summarized in table 1. For **A**, $\lambda_n(H) \sim \lambda_n(D)$ /8/. Regressions are given in terms of the quantities A, T_s and q_a - which lead to a more unifying description of λ_n - and in terms of the machine parameters $\bar{n}_e$, I_p, B_t and P_{sol}. In both cases **A** and **B**, the exponents of T_s and q_a are at least similar. If **B** is restricted to OH points, the scaling becomes $\lambda_n(D,He) \sim A^{0.21} T_s^{0.18} q_a^{0.6}$, i.e. almost identical to that of **A.** On the other hand, the global scalings do not reveal a common basis. The accompanying regression for T_s makes it clear that the global expression represents a hidden fit to the relevant parameter T_s. In the regime T_s<40eV of **A**, λ_n may be described as $q_a^{1.96\pm0.16}\, \bar{n}_e^{0.66\pm0.09}$ (R=0.93), where the $\bar{n}_e$-dependence is probably a hidden T_e-dependence in the sense $T_e \sim n_e^{-1}$ /7/; T_s itself is not well determined for T_e<40eV.

Noteworthy is that for both datasets λ_n varies only over the range 1.6-2.7cm, for T_s>40eV. The experimental systematic uncertainty associated with λ_n is about ±1mm, corresponding closely to the vertical spread of points in fig. 4.

Diffusion Coefficients: An estimate of the diffusion coefficient may be attained from $D_p = \lambda_n^2 \nu_{\parallel}/L_c = \lambda_n^2 f_{\parallel} C_s/L_c = \lambda_n^2 f_{\parallel}(eT_s(\gamma_i+Z_i\gamma_e)/m_i)^{0.5}/L_c$, predicating a source-free SOL, no inward drift, no influence of electric fields, $T_e=T_i$, only one ion species with charge Z_i, and a global streaming velocity $v_{\parallel}=f_{\parallel}C_s$ (averaged over the midplane/divertor plate distance of $L_c=q_aL_o$; L_o=3.33m) where C_s is the sound speed. Below, $\gamma_i=\gamma_e=1$ is taken.

From the approximate relationship $\lambda_n \sim q_a^{0.5} T_s^{0.25}$ of table 1, D_p would be expected to scale as T_s. This is confirmed in fig. 5, where $D_p/f_{\parallel}$ is plotted vs. T_s, showing a uniformly linear increase of $D_p/f_{\parallel}$ for both datasets. ($D_p/f_{\parallel}$ is taken, since $f_{\parallel}$ may contain dependencies, intermingling with those of D_p, to give the regressions in table 1.) In **A** the scaling is $D_p/f_{\parallel} \sim q_a^{-0.18} T_s^{1.00}$, and for **B** we have $D_p/f_{\parallel} \sim A^{0.19} T_s^{1.02} q_a^{0.68} P_{sol}^{0.22}$. In both cases, T_s is the predominant factor as expected from fig. 5, but the q_a exponents are substantially different. One might speculate that this represents different $f_{\parallel}$-regressions coming about as a result of NI, or simply that some aspect of the model is not being fulfilled.

The T_e-dependence of $D_p/f_{\parallel}$ is reminiscent of Bohm diffusion since $D_{Bohm}=T_e/16B_t$. Code calculations carried out over a wide range of ASDEX conditions (not q_a) and calibrated against experimentally observable quantities gave $f_{\parallel}$=0.3 as a good description /9/. Assuming $f_{\parallel}$=0.3 for these datasets yields $D_p \sim 1/3 - 1/2\ D_{Bohm}$ for the range T_s>40eV.

H-Mode Density Profiles: The behavior of the SOL $n_e(r)$ profile during the H-mode has been addressed previously /1,5/, but now the data have been extended to inside the separatrix by virtue of an improved algorithm for reconstructing the density profile from the lithium beam probe data /10,11/. Fig. 6(a) illustrates that the steep density gradient typical of the H-phase continues for a few mm inside the magnetically-determined separatrix, and only then makes the transition into a much flatter shoulder. Fig. 6b depicts the relaxation of the density profile after an ELM. Important is that the density gradient transition region is again within the separatrix, and has fully restablished itself while the SOL density perturbation associated with the ELM is still relaxing. More on the temporal processes during the L-H transition is contained in /12/.

Discussion and Conclusions: λ_n has been shown to vary about as $T_s^{0.25} q_a^{0.5}$ for OH discharges, when T_s>40eV. This is in accordance with that expected from connection length arguments within the framework of a simple 1-D SOL model where D_p scales as T_s. The emergence of a stronger q_a-scaling, along with a weak P_{sol}-scaling for the NI-heated dataset **B** might be a direct consequence of variations of $f_{\parallel}$ with these parameters. Presently, there is no indication that D_p exhibits a toroidal field component, and hence is not Bohm-like even though $D_p \sim D_{Bohm}$. Nevertheless, the possibility cannot be excluded, until further code work has been performed, that $f_{\parallel}$ scales such as to nullify an explicit B_t dependence of $D_p/f_{\parallel}$. Then again, the fact that $D_p(D^+)$ varies in a more-or-less continuous fashion from one dataset to another, where the divertor configuration and wall conditioning techniques were changed, indirectly supports the code result /9/ that $f_{\parallel}$ does not underlie strong modifications.

The implied scaling of D_p with T_s is not meant to be taken locally; rather, T_s is to be regarded as a temperature which characterizes the entire SOL. A local variation of D_p with T_e would lead to profile forms inconsistent with those observed. In particular, for R-R_s>2cm a shoulder in the $n_e(r)$ profile often appears /5,6,8/, suggesting an augmentation of D_p (if $f_{\parallel}$=const.) instead of a reduction as would be predicted by a $D_p \sim T_e(r)$ scaling (since T_e decreases strongly with r). Phenomenologically, the density profile behavior for R-R_s>2cm bears resemblence to the region T_s<40ev of fig.1, leading one to speculate if the underlying physics is of the same nature.

For the H-mode the transition region from a steep to a flat gradient is found to be slightly within the separatrix for a very early divertor configuration of ASDEX. Analysis of discharges taken in the last month of ASDEX operation (not shown here) actually determines the break point to lie a few mm to the outside. Considering that experiments to localize the separatrix position (albeit at a toroidal position different from that of the Li-beam) consistently show the true separatrix to lie about one cm outside the separatrix derived by magnetics, it is probable that the density gradient transition point occurs within the separatrix in all cases.

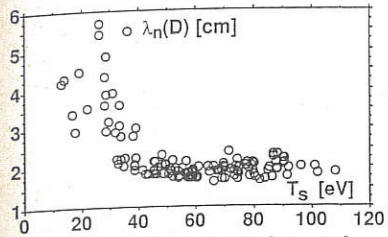

Fig.1 SOL density falloff lengths for case **A**. Only D^+ is shown, but $\lambda_n(D) \sim \lambda_n(H)$.

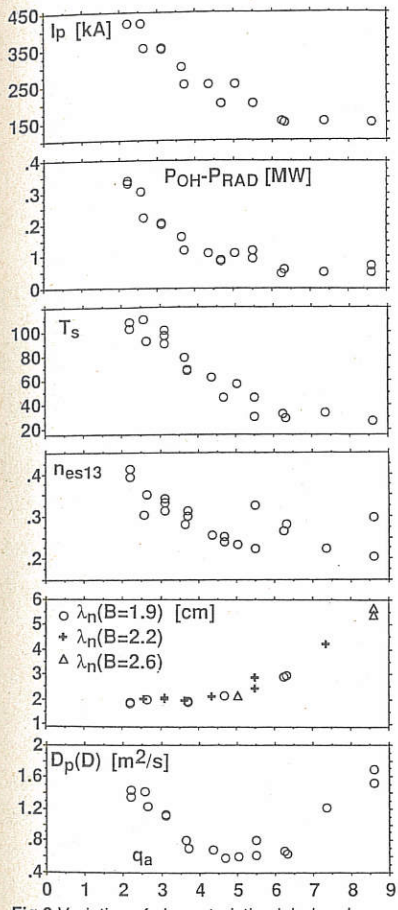

Fig.2 Variation of characteristic global and edge parameters vs. q_a for $\bar{n}_{e13}$=1.5-1.75, D^+.

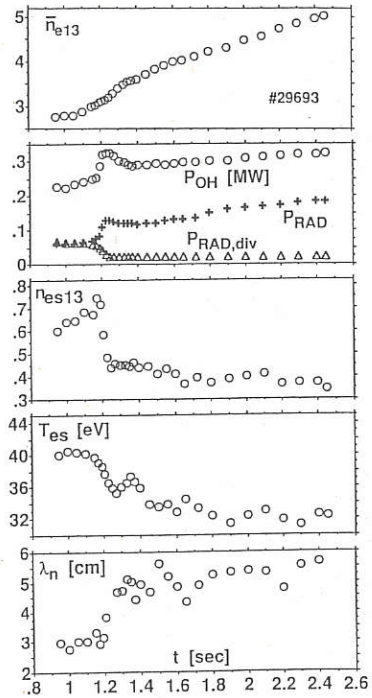

Fig.3 Time behavior of global and edge parameters during an $\bar{n}_e$-ramp, which triggers a MARFE at t~1.17 s. q_a=5.9

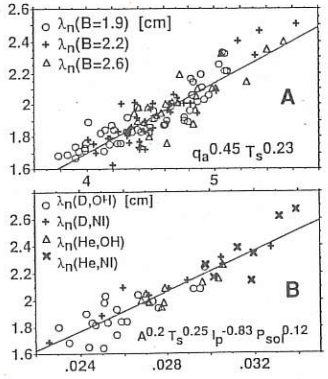

Fig.4 λ_n regression fits for cases **A** and **B**. In **B**, NI-points for $\bar{n}_{e13}$<1, $P_{sol} \geq 1$MW (P_{tot}>1.4MW) are excluded, as they lie noticably above the others, possibly indicating another physics regime.

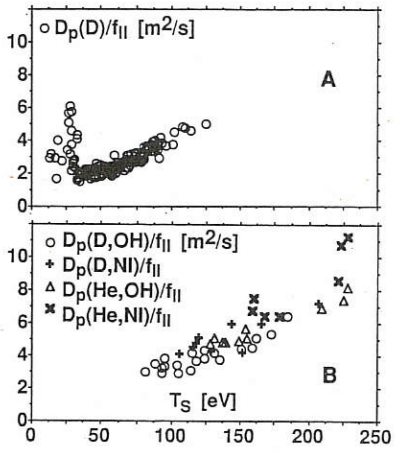

Fig.5 D_p/f_{II} for **A** and **B**. The (He,NI) points lying above the major grouping are for the lowest density ($\bar{n}_e$=2) and higher power (P_{sol}~0.9MW) of this subset.

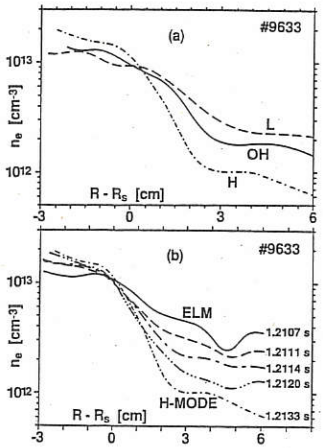

Fig.6 Edge/SOL n_e-profiles: B_t=2.17T, $\bar{n}_e$13~4, I_p=315kA, $P_{NI}(H^0 \rightarrow D^+)$2.8MW. (a): steady-state OH-, L-, H-phases, (b): during decay phase of ELM. sample freq.=10kHz, cutoff freq.=4kHz.

	case	const.	A		ne13		Ip		Bt		Psol		qa		Ts		R
lam	A	7.32					-0.45	0.03	0.44	0.04					0.23	0.02	0.88
lam	A	3.91			-0.15	0.01	-0.15	0.02	0.42	0.04							0.9
Ts	A	0.105			-0.58	0.02	1.2	0.04	0	0							0.96
Dp/fII	A	0.048											-0.18	0.04	1.01	0.04	0.95
lam	B	74.7	0.2	0.03			-0.83	0.08			0.12	0.02			0.25	0.04	0.91
lam	B	50.1	0.26	0.03	-0.13	0.02	-0.54	0.07			0.14	0.02					0.91
Ts	B	0.2	0.24	0.04	-0.51	0.03	1.17	0.1			0.1	0.03					0.97
Dp/fII	B	0.018	0.19	0.06							0.22	0.05	0.68	0.15	1.02	0.08	0.97

Table 1 Exponents for regression fits of the form: const.x $A^{\alpha}n_e^{\beta}$... λ_n[cm], D_p/f_{II}[m^2/s], A[ion mass], n_e[10^{13} cm^{-3}], I_p[kA], B_t[T], P_{sol}[MW], T_s[eV]. Standard error is in the adjacent column. R is the regression coefficient. Blank spaces indicate that the parameter was not included in the regression.

References

/1/ K. McCormick, H. Murmann, M. El Shaer, J. Nucl. Mater. **121** (1984) 48
/2/ K. McCormick, et al., Rev. Sci. Instrum. **56** (1985) 1063
/3/ K. McCormick, Z.A. Pietrzyk, et al., Proc. 14th EPS Conf. Madrid **11d** (1987) 666
/4/ K. McCormick, Z.A. Pietrzyk, et al., J. Nucl. Mater. **145-147** (1987) 215
/5/ G.K. McCormick, Z.A. Pietrzyk, et al., J. Nucl. Mater. **162-164** (1989) 264
/6/ K. McCormick, Z.A. Pietrzyk, et al., Proc. 16th EPS Conf. Venice **13B** (1989) 895
/7/ K. McCormick, et al., J. Nucl. Mater. **176&177** (1990) 89
/8/ K. McCormick, G. Kyriakakis, et al., 10th PSI Conf., to be pub. in J. of Nucl. Mater.
/9/ W. Schneider, J. Neuhauser, et al., Contrib. Plasma Phys. **28** (1988) 387
/10/J. Schweinzer, E. Wolfrum, F. Aumayr, et al., Plasma Phys. Contr. Fusion (1992) in print
/11/ J. Schweinzer, K. McCormick, S. Fiedler, et al., this conference
/12/ D. Dodel, H. Holzhauer, et al., "Characteristic Features of Density Fluc..", this conf.

POWER FLUX WIDTHS IN THE ASDEX DIVERTOR

G.Kyriakakis*,E.Kakoulidis*,N.Tsois*,K.McCormick,J.Neuhauser
Max Planck Institut für Plasmaphysik,Euratom Association,
D-8046 Garching,BRD.

I.Introduction

The reciprocating Langmuir probe on ASDEX is located in the upper outer divertor (Fig.1) and is capable of delivering a maximum of four radial profiles of plasma parameters during a discharge.The power flux profiles allow a direct evaluation of t he effective power channel width which apart from offering a direct estimate of target plate power loading, it is also fundamental in understanding SOL transport processes. The evolution of power flux profiles and systematic trends of the corresponding widths for ohmically and NI heated discharges are presented for parametric scans in n_e, I_p, B_t and injected neutral power.Langmuir probe data are compared and correlated with data from the Lithium beam probe which delivers density profiles in the outer midplane and the YAG Thomson scattering system which yields density and temperature near the separatrix at the lower plasma.

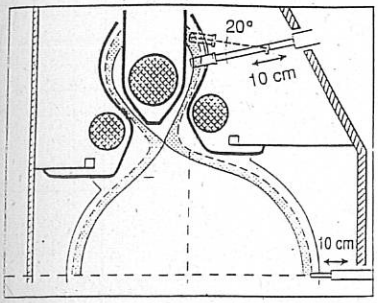

Fig.1: Langmuir probe location in ASDEX divertor.

II.Experimental Results

Power flux profiles in the ASDEX divertor evaluated with the triple probe technique,are described in terms of a peak value and their width.Normally widths are conveniently documented in terms of radial decay lengths or FWHM values. On ASDEX attempts to produce meaningful scalings with the above quantities have in general failed due to irregularities in the profile shapes. In particular it is observed that the profiles change their form in a two-dimensional fashion whereby the steep slopes on either side of the peak

change only marginally,with the appearance of a shoulder dominating profile variation. Fig 2.a demonstrates a typical power flux profile evolution of a density limit series in H_e where qa was scanned by varying I_p and B_t. A parallel development is also evidenced in density profiles in the midplane with the Li-beam /1/.

Use of an equivalent width defined as the ratio of the area under the profile to its peak value considerably reduces scatter and permits identification of systematic trends.The inadequacies of FWHM values due to profile shape changes are also reported elsewhere /2/.

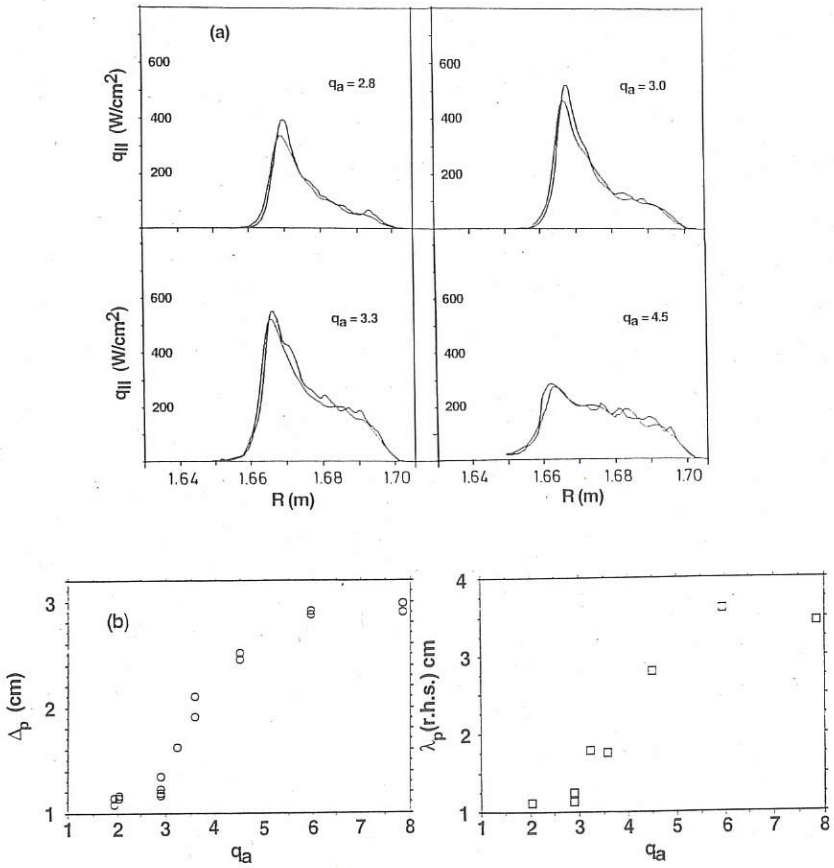

Fig.2 : (a) Power flux development from an ohmically heated density limit shot series in He. (b) Power flux widths (left) and e-folding lengths (right) vs q_a (n_e = 5-6x10^{19}m^{-3}).

Fig.2.b shows the resulting variation of Δ_p with q_a which is also found to be in agreement with the q_a dependence of λ_p (exponential decay length) if the latter is evaluated over the entire width of the profile (Fig.2.b right).

Figure 3.a illustrates how typical power flux profiles develop during a discharge series of ohmically heated plasmas with different current levels (I_p = 280,320,420 kA). Both sets of data demonstrate that the power widths exhibit a significant change with q_a which is at least linear in the range q_a = 2 - 6. Based on evidence from a NI power scan series in D_2 (Psol ≤ 1.8 MW) that the power widths exhibit essentially no dependence on P_{sol} (Fig.3.b) the decrease of Δ_p with I_p may be interpreted as a q_a or T_e dependence (Figs 4.a,4.b) since lower I_p decreases power input to the SOL and hence T_e. A comparison of Figs 4.a and

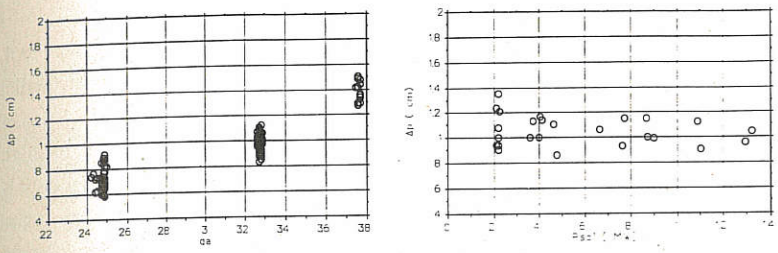

Fig.3: (a) Δ_p vs q_a from an OH current scan series in D_2 (I_p=280,320 and 420kA),
(b) Δ_p vs P_{sol} from a NI power scan series in D_2 (n_e=2-3.5x$10^{19}m^{-3}$)

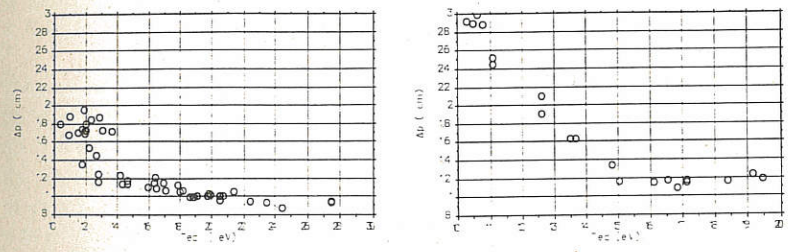

Fig.4: Power flux widths vs divertor temperature. T_{ed} is varied via a n_e,P_{NI} scan in D_2-(a) and an OH, q_a scan in He - (b).

4.b shows that despite the similar relative variations of Δ_p with T_{ed} absolute differences in Δ_p at a given T_{ed} exist which are attributed to an inherent q_a-dependence. No isotope dependence of Δ_p (or λ_n ,the e-folding length evaluated from midplane density profiles /1/) is found in any of the data sets considered.

A regression on the combined sets of Fig.4 yields the scaling $\Delta_p \sim q_a^{\alpha} T_{ed}^{\beta}$ where $\alpha = 0.45$, $\beta = -0.86$ with a regression coefficient $R = 0.93$.A similar behaviour of Δ_p with T_s,the electron temperature near the separatrix in the outer midplane is also observed and agrees well with trends of λ_n vs T_s .

III.Discussion

The observed Psol - independence of Δ_p /3/ allows a classical heat-conductivity SOL model which adequately describes ASDEX SOL behaviour up to the density limit to predict the experimental scalings of edge density with P_{sol} in the NI-heated power scan series of Fig.3b /1/. So far as the scalings of the density limit in this model are concerned, the high colinearity of q_a and T_{ed} yield an effective linear q_a dependence of Δ_p ,which enables this simple model to describe the density limit in ASDEX. The derived scaling exponents α and β of Δ_p are found very close to those predicted for the power channel width by an analytical heat-flow model by Harrison /5/.The emerging T_{ed} dependence of Δ_p is significant in interpretations of transport coefficients and 2D SOL model validation studies /6/, a subject of ongoing study.

* NCSR - "Demokritos", Athens, Greece.

/1/ K.McCormick et.al. ,"Particle and Energy Transport Scalings in the ASDEX Scrape-Off Layer,10th PSI,Monterey,USA,1992.

/2/ K.Itami et.al., J.Nucl.Mater. 176&177 (1990) 504.

/3/ K.McCormick et.al., J.Nucl.Mater. 176&177 (1990) 89

/4/ A.Staebler et.al.,"Density Limit Investigations on ASDEX",1991,submitted to Nuclear Fusion.

/5/ M.Harrison "Analytical Modeling of Divertor and Scrape-Off Layer" ,1989 ITER-IL-PH-13-9-E12 (to be published).

/6/ R.Schneider et.al.,"B2-Eirene Simulation of ASDEX and ASDEX-U SOL Plasmas ,10th PSI,Monterey,USA,1992.

SPATIAL DISTRIBUTION OF CARBON IONS AND ION TEMPERATURE MEASUREMENTS IN THE PLASMA EDGE OF TEXTOR USING EMISSION SPECTROSCOPY

G. Telesca, H.A. Claaßen, E. Graffmann, G. Van Oost[1]

Institut für Plasmaphysik, Forschungszentrum Jülich,
Association EURATOM-KFA, Germany
[1]Laboratoire de Physique des Plasmas - Laboratorium voor Plasmafysica - Association "Euratom-État belge" - Associatie "Euratom-Belgische Staat" École Royale Militaire - B-1040 Brussels - Koninklijke Militaire School

1. Introduction

In this paper we present experimental data of the plasma edge ion temperature on TEXTOR [1]. The spontaneous radiation emitted in the UV range by three carbon ions allows the determination of their radial position and temperature.
The toroidal belt limiter ALT-II strongly affects the poloidal distribution of the impurity concentration of the lower ionization states. This is illustrated and discussed in section 2 together with the problem of thermalization between impurities and deuterons. In section 3 the edge T_i is given for ohmic and NBI-heated plasmas and compared with the central T_i and with the electron temperature profile. Section 4 contains a comment on the analogies between Z_{eff} and the edge temperatures.

2. Radial position and temperature of carbon ions

The maximum of the emissivity of three spectral lines of carbon (CIII at 2296 A, CIV at 2530 A, CV at 2271 A) is determined by Abel inversion of line integrated signals. In fig. 1 is shown the poloidal cross section of the plasma and the experimental set-up for the plasma scanning and for the Doppler broadening measurements. By tilting mirror M1 the whole plasma cross section is scanned from the low field side (LFS) to the high field side (HFS) and vice versa resulting in the line integrated signals as illustrated in fig.2. The most striking feature of these signals is the difference between CIII and CIV on the one hand and CV on the other hand. The strong poloidal asymmetry of the CIII and CIV signals indicate their higher concentration in the neighborhood of the limiter. Indeed, the time for double and triple ionization of carbon flowing from the limiter into the plasma is shorter than the time for the carbon ions to be poloidally homogeneously distributed. On TEXTOR $T_e(a)$ is, in fact, of the same order as the ionization potential of CIII and

CIV. The situation changes drastically for CV ions, whose ionization potential (~ 400 eV) is much higher than $T_e(a)$. Therefore, the maximum of the emission of the CV line is more inside in the plasma and the distribution is poloidally uniform. Neglecting the signals from LFS the Abel inversion of the CIII and CIV is still meaningful, if sufficiently far from the limiter the ions are homogeneously poloidally distributed. Considering the parallel flow as the main transport mechanism and using the results given in ref. [2] the CIII and CIV density distribution can be assumed to be poloidally homogeneous in the HFS.

In fig.3 an example of the Abel inverted emissivities is shown for the three carbon ions. Details of the inversion procedure can be found in ref. [3] and [4]. The radial position of the maximum of the emissivity is a function of electron temperature and density profiles and consequently depends on the plasma conditions. For the discharges examined the CV emissivity maximum is located between 37 and 40 cm, CIV between 44 and 45.5 cm and CIII between 46.5 and 48 cm compared to the limiter position of 46 cm. The radial position of the maximum emissivity of CV has been compared to the position of the maximum of the C^{4+} ion density as derived from the Lithium Charge Exchange Spectroscopy (Li-CXS) [5]. The emissivity maximum is shifted 2-3 cm towards the plasma center with respect to the ion density maximum due to the electron temperature and density gradients.

The Doppler broadening measurement is performed by keeping the mirror M1 in such a position that the line of sight crosses the plasma center. In the UV range the Zeemann splitting is very small and can be included in the instrumental function.

The impurity ions are in thermal equilibrium with deuterons (hence the edge T_i can be constructed) if the energy equipartition time between impurities and deuterons is smaller than the impurity ion confinement time. The equipartition time for C^{2+} ions is the longest one out of the three charges under consideration and amounts to 0.2-0.3 ms. The calculated edge impurity confinement time of 1-2 ms guarantees thermalization of the impurities [6].

3. Results for ohmic and NBI-heated discharges

The edge ion temperature profile derived by using the procedure outlined in the preceding section has been compared with the edge T_i from Li-CXS [6], showing very good agreement (fig.5). In fig. 4 temperatures for CIII, CIV and CV are shown in a density scan for OH, co-NBI and cnt-NBI. The data refer to many series of similar discharges (I_p = 350 kA, B_T = 2.25 T, boronized walls, $H^o \rightarrow D^+$) at NBI power level of 1.6 MW both for co and counter injection. The relative increase of the edge ion temperature for co-NBI is lower than the relative increase of the central T_i, which reaches a factor of 2 [7]. The limited cnt-NBI data base shows a stronger increase of the edge T_i, especially at low density. The diamagnetic and equilibrium energies and TRANSP simulations [7] indicate, that the central T_i is lower for counter Injection than

for co injection, resulting in a flattening of the T_i profile. The Thomson scattering T_e-profile is similar for co and counter injection at the edge, but slightly higher in the center for co injection. Both for OH and NBI the edge T_e is lower than the edge T_i approaching $T_e(a) = 1/2\ T_i(a)$.
All these experimental results clearly indicate a difference in the power deposition profile, which is centrally peaked for co injection and broader for counter injection with a possible modification of the viscous edge heating for the two heating methods.

4. Z_{eff} and edge temperature

In fig.6 the line integrated visible continuum Z_{eff} is plotted versus density for OH, co and counter injection at 1.6 MW. The strong similarities with the edge ion temperatures (fig.4)
suggest the existence of a tight relationship between impurity production and the plasma temperature at the limiter.This relationship appears not to be affected by the heating method, so that the interaction of the thermal plasma with the limiter seems to be the main impurity source.

5. Acknowledgement

The measurements presented in this paper were only possible thanks to the excellent technical cooperation of J.Schwarz.

References

[1] U. Samm et al., Plasma Phys. Contr. Fus. 29 (10A), 1321 (1987)
[2] H.A. Claaßen, H. Gerhauser, D. Reiter, Contribution to Plasma Physics 30 (1), 83 (1990)
[3] N. Schoon et al., Report LPP-ERM/KMS Brussels N 92 (1990)
[4] G. Telesca et al., Report LPP-ERM/KMS Brussels N 91 (1990)
[5] H.A. Claaßen, R.P. Schorn et al., J. Nucl. Mat. 176 & 177, 398 (1990)
[6] R.P. Schorn, E. Wolfrum et al., Nucl. Fus. 32 (3), 351 (1992)
[7] A.M. Messiaen et al., Plasma Phys. Contr. Fus. 32 (11), 889 (1990)

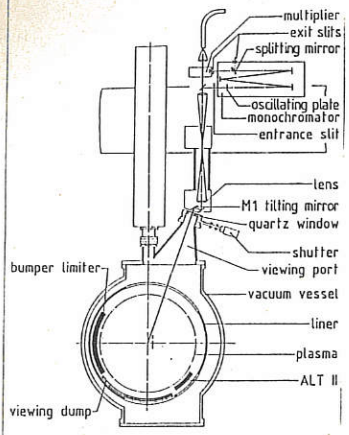

Fig.1 Experimental set-up

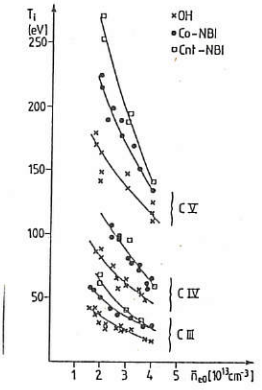

Fig.4 Temperatures from Doppler broadening of CIII, CIV, CV lines

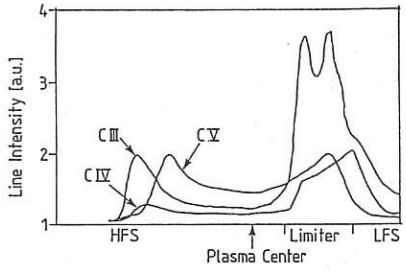

Fig.2 Radial scan of CIII, CIV, CV line emission

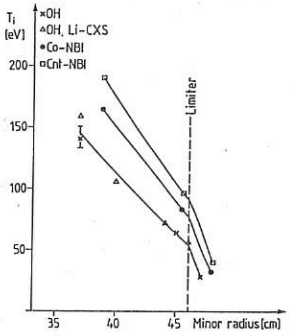

Fig.5 T_i profile from fig.4 comparison with Li-CXS T_i profile

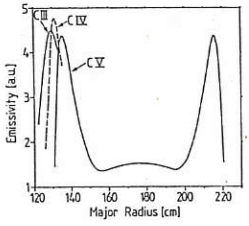

Fig.3 Emissivity profile for CIII, CIV, CV (Abel inverted data from fig.2)

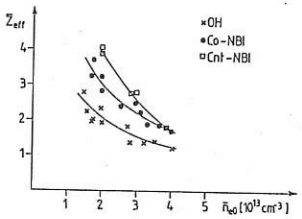

Fig.6 Visible continuum Z_{eff}, density scan

POLOIDAL ROTATION IN THE LIMB OF THE TEXTOR PLASMA MEASURED BY THE DOPPLER SHIFT OF A BII-LINE

H. Conrads, H. Euringer, D. Rusbüldt

Institut für Plasmaphysik, Forschungszentrum Jülich GmbH,
Association EURATOM-KFA, P.O.B. 1913, D-5170 Jülich

1. Introduction

Local measurements of the poloidal rotation of the plasma near the boundary layer of a tokamak gain more and more interest because the poloidal shear, produced by a differential rotation in the plasma boundary can decorrelate radial turbulence /1/. The analysis of this problem showed a bifurcation like behavior of the plasma boundary pointing to an impact of the boundary condition on the capability of energy confinement in the bulk of a tokamak plasma. Establishing a radial electric field in the boundary artificially by introducing an electrode into the plasma enforced a poloidal rotation /2/ and allowed a successful study of the interdependence of L- and H-mode energy confinement and local poloidal rotation.

In several divertor experiments /3,4/ a natural radial electrical field and an associated poloidal plasma rotation has been observed, which was in its magnitude related to the occurrence of L- or H-mode energy-confinement. From Alcator-C quite large poloidal velocities of 5 km/s in the region of the emission of highly ionized oxygen during ohmic heating have been reported /5/.

TEXTOR is the largest experiment in which the influence of artificially introduced radial electric fields on a plasma heated by neutral beams and by ICRH is studied. A first evidence of the poloidal plasma rotation in TEXTOR has been reported in /6,7,8/. A more direct access to the rotation velocity offers the Doppler effect, which causes a wavelength shift of the spectral lines emitted by atoms and ions in the rotating layer. Spatial resolution, often a problem in spectroscopy, can be achieved by choosing a stage of ionization existing in a thin layer only. Near the plasma boundary this is the case if the ionization energy increases weakly for subsequent stages only. A B II line at 494.0 nm proved to be particularly suitable. The ionization energies for boron are: 8.3 eV, 25.1 eV, 37.9 eV, etc. Boron is present in the plasma boundary of TEXTOR due to the boronization of the plasma facing components. Initially only changes of the rotation velocity have been measured /9/. Due to the lack of an unshifted reference line a measurement of the absolute value of the poloidal rotation velocity was not possible. However, a reference line is not necessary if the radiation of the moving atoms or ions is observed from opposite directions, resulting in both a blue and a red shifted spectral line. By recording both spectra with the same instrument one has the advantageous side effect that the line shift is doubled. The realization of this concept is described in reference /10/.

2. Experimental Conditions

All plasma facing components have been boronized by diborane dissociated in a glow discharge /11/ prior to an experimental campaign.

Usually, the plasma current was 350 kA and the toroidal magnetic field amounted to 2.25 T. In some cases B_T was varied between 1.7 T and 2.25 T, in order to study its influence on the plasma rotation. The plasma was heated by balanced injection of 2 neutral beams each of 1.5 MW power and 52 keV energy turned on sequentially: first the co-injector fired 0.8 s after the start up and 0.4 s later the counter-injector. The balanced injection lasted 1.0 s typically.

During this time electron density and temperature in the plasma core remained constant, i.e. without saw teeth oscillations and had values of $2 - 3 \times 10^{19}$ m^{-3} and 1.5 - 1.2 keV respectively. Concerning confinement the plasma was in the i-mode /12/ i.e. energy confinement was equal or better than the one of a tokamak plasma in the elmy-H-mode according to the ITER scaling.

During the whole discharge the plasma limb rested on the 8 pumped blades of ALT-II, one of the toroidal belt limiters of TEXTOR, which is positioned at a = 46 but 45° underneath the mid plane. The rotation was measured in the mid plane at 45 cm $\leq r \leq$ 46 cm. Here the electron temperature exceeded 80 eV always, and the electron density had values of 8×10^{18} m^{-3}. Measurements of T_i and dT_i/dr by the Doppler broadening of C VI lines, generated by charge exchange with a 20 keV - Lithium beam, delivered values of up to 70 eV and 2.5 keV/m respectively.

Details of these measurements togehter with a description of the spectrometer are given in reference /10/. The spectrometer has been developed especially for these measurements. Blue- and red-shifted lines out of the same volume outboard in the midplane of the plasma are recorded simultaneously. Because of the outstanding resolution of the spectrometer even minute changes in the rotation velocity can be measured with an absolute accuracy of $\pm$ 75 m/s.

3. Range of Confidence to attribute the measured Doppler-Shift to radial electric Fields in the Limb

First it has to be checked, whether the observed Doppler-shift might be caused by the gyromotion of the B II - ions, since the gradients of electron temperature and density are steep. However, the product of the life time of the upper level for the said transition times the cyclotron frequency of B^+ is much smaller than unity, i.e. the shifts due to gyromotions are symmetric and produce no net shift of the line.

The next problem is the locus of emission and the space resolution, which addresses the question of rate coefficients and momentum transfer. Neither Saha nor Corona equilibria are relevant. The picture is that Boron is liberated from the limiter by sputtering and that the momentum distribution of the sputtered Boron in space is highly anisotropic: No momenta are directed outboard and the vector sum of all momenta is directed inboard and determined by the grazing incidence of deuterons striking the ALT-II blades. A calculation of the rate coefficient for ionization delivers a radial mean free path

of 1 cm. Since the velocity vector of the Boron is not changed significantly during the impact the movement of B II is determined by its velocity prior to ionization and by the magnetic field. The same holds for further ionization which occurs within another centimeter inward. All these amounts to an emission of the BII line in a thin skin of 1-2 centimeters. The center of gravity for the emission is within the last closed flux surface. There is little integration of B II - emission along the line of sight, i.e. a defolding of the signals is not necessary.

The plasma drift due to pressure gradients, the diamagnetic drift, has to be addressed as well. With the measured values of temperature, density and their gradients in 45 cm $\leq r \leq$ 46 cm i.e. in the range of B II - emission, the diamagnetic drift is about 1 km/s. All values much higher e.g. 5-10 km/s could be attributed to the existence of radial electric fields.

4. Results

a) Enforcing a positive potential across the plasma limb by an electrode /7/ delivered a poloidal plasma velocity of 12 km/s. Here the plasma current was reduced to 200 kA and the heating power (co-injection only) to 150 kW.

b) Adding in normal discharges counter-injection to the co-injection dropped the toroidal velocity from 100 km/s to a few km/s and increased the poloidal velocity from 5 km/s to 7 km/s into the ion direction, i.e. the observed poloidal velocity is not the poloidal fraction of a toroidal bulk motion of the plasma but a result of a radial electric field. The plasma potential is positive.

c) For all cases investigated the density peaking factor is proportional to the observed poloidal rotation, i.e. $\frac{N_e(o)}{\langle N_e \rangle} = A \cdot V_{pol} + C$. The slope A depends on the central density and on the potential across the limb. The slope is small for large central densities and largest for an external potential enforced across the plasma limb by an electrode.

d) The radial gradient of the poloidal velocity is steep and at least 100 km/s · m as obtained from an enforced shift of the limb across the locus of observation.

e) The poloidal velocity seems to increase, when a rational magnetic surface touches the limiter. For the q = 3 - surface the increase was 2 km/s. But this issue is subjected of further investigations.

5. Conclusions

a) In the vicinity of the last closed surface determined by the limiter position, the plasma boundary looses electrons and becomes electro positive, a common situation for a plasma in contact with surfaces. However, this radial potential

extends poloidally and forces the skin of the plasma to rotate poloidally into the ion direction. Most likely, enhanced losses at the magnetic islands in the vicinity of the rational surfaces increase this potential as seen by the enhanced poloidal rotation.

b) The potential is changing rapidly in the radial direction as deduced from the observed steep gradients in velocity.

c) The increase of the enhancement factor of the electron density points to on improvement in local confinement. The fact, that this factor is direct proportional to the poloidal velocity suggest the conclusion, that radial transport is reduced by poloidal shear, which is proportional to the gradient of the poloidal velocity at 45 cm $\leq r \leq$ 46 cm. And this gradient itself is proportional to the poloidal velocity, since the latter must be zero at r = 46, the position of the limiter. If this conclusion is valid, shear perpendicular to the magnetic field becomes significant as well. In the literature parallel shear has been taken into account to explain decorrelation of radial turbulence of divertor-H-mode-discharges, having a free boundary at the last closed flux surface. In a tokamak with a full toroidal limiter perpendicular shear is generated at small poloidal velocities already. This could explain the lack of any threshold power in obtaining the i-mode, the good mode of energy confinement of limiter tokamaks obtained with balanced injection of neutral beams or by a combination of neutral beams with ICRH /13/.

References

/1/ Biglari, H., Diamond, P.H., Terry, P.W.: Phys. Fluids B, Vol 2, No 1 (1990),
/2/ Weynants, R.R., Taylor, R.W.: Nucl. Fusion Vol 30, No 5 (1990), 954
/3/ Groebner, R.J., Burell, K.H., Seraydarin, R.P.: Phys. Rev. Lett. Vol. 63 (1989) 2369
/4/ Field, A.R., Fussmann, G., Hofmann, J.V.: IPP.III/165, 1990
/5/ Benjamin, R.D. et al.: Phys. Rev. A , Vol.41, No2 (1990), 1034
/6/ Weynants, R.R. et al.: IAEA-CN-53/A-VI-6 Washington (1990) 473
/7/ Weynants, R.R., van Oost, G. et al.: Nucl. Fusion accepted for publication in 1992
/8/ R. van Nieuwenhove et al., Fusion Engineering and Design 12 (1990), 231-235
/9/ Moyer, R.A. et al.: J. Nucl. Materials 293 (1991) 176
/10/ Conrads, H., Euringer, H., Rusbüldt, D.: submitted for publication in Rev. of Sc. Instr.
/11/ Winter, J. et al.: J. Nucl. Materials, 162-164 (1989), 713
/12/ Gaigneaux, M. et al.: Proc. 18th EPS Conf. on Contr. Fusion and Plasma Heating Berlin (1991) EUROPHYS Conf. Abstract Vol 15c, Part I, 409
/13/ Ongena, J., Conrads, H. et al.: submitted to Nuclear Fusion for publication

The effect of radial electric field on fast ion losses in divertor tokamaks

A V Chankin[1], D D R Summers and G M McCracken[2]
JET Joint Undertaking, Abingdon, Oxfordshire, OX14 3EA, U.K.
[1]I V Kurchatov Institute of Atomic Energy, Moscow, Russia
[2]AEA Fusion, (Euratom/UKAEA Fusion Association), Abingdon, OX14 3DB, U.K.

Introduction Direct ion losses to the target plate in divertor plasmas may occur from a region up to a distance about twice the ion poloidal larmor radius, $\varrho_{i\vartheta}$, inside the Last Closed Flux Surface (LCFS). Since during intense additional heating the ion temperature near the edge may reach a magnitude of a few kV [1], strong collisionless ion losses can induce electric fields. These fields may play a role in reducing turbulence in the boundary [2,3] and in the L-H transition [2]. However, the response of fast ion losses to the magnitude of the electric field has not yet been analysed in detail.

In the present work a particle following code has been developed to assess the loss region of escaping ions in velocity space and its transformation in the presence of a radial electric field. The code uses the guiding centre approximation to calculate ion orbits and the electric potential is included as a quadratic polynomial function of the poloidal magnetic flux. Orbits of deuterium ions launched from a region corresponding to a few poloidal Larmor radii inside the midplane plasma edge in the magnetic configuration of JET single-null diverted discharges, have been studied.

Orbits in the absence of electric field Taking a given radius inside the LCFS at the midplane it is possible to show that there is a minimum energy at which ions may be lost. For the specific case of Δr = 1cm and a JET discharge with B_T = 2.3 T, I_p = 3.1MA, the threshold energy for zero electric field $\varepsilon_0 \simeq$ 600eV. At this energy there is a unique angle of attack $\Theta = 44°$ (defined as arctg $v_\parallel/v$) at which an ion may be lost. The orbit of such an ion is shown in Fig. 1 a, curve 1, (ion grad-B drift is directed upwards).

As the ion energy is increased the range of angles over which losses can occur increases. For the above example the loss region is shown in fig. 2a. It consists of a long "nose" with $\Delta\Theta \approx 10°$ and broad region $\Delta\Theta \approx 55°$ for $\varepsilon_i > 4.5$ keV. The threshold energy ε_o was found to be proportional to Δr^2, so the x-axis in fig. 2a is $\varepsilon_i/[\Delta r(cm)]^2$. Using the integrals of motion our numerical results can be extrapolated to other discharge/machine parameters, with the only restriction that the ratio of major radii of midplane LCFS position to x-point position is kept the same as in our calculations, (equal to 1.6.) We

obtain:

$$\varepsilon_o(keV) = 2.13\,[\Delta r(cm) B_p(T)]^2 \qquad (1)$$

While most of the orbits inside the "nose" terminate at the inner (ion) side of target plate (curve 1 in fig. 1 a), all orbits at high energies strike the outer (electron) side of the plate (curve 2 in fig. 1 a). With the grad-B drift directed away from the x-point the orbit from the "tip" of the "nose" is shown in fig. 1b (curve 1). It terminates at the outer strike zone, which is now the ion side, with the orbits of high energy ions again striking the electron side, which is now the inner side (curve 2).

Modest collisionality will prevent the loss of ions from the "nose" because of the very narrow loss-cone angle. We can arbitrarily define the effective energy ε_F at which significant losses occur as that at which the loss cone width is 20°, since it represents fairly well the position of a sharp transition in $\Delta\Theta$ between the "nose" and broad loss region. Most of the power deposited on the target is associated with orbits from the broad loss region, ($\varepsilon_i > \varepsilon_F$), and orbits terminating at the electron side. As the edge ion temperature goes up during additional heating, losses from the "nose" at positions deeper in the plasma, where it is collisionless, are able to create localized hot spots on the ion strike zone of the target plate, close to separatrix position. Hot spots have been observed experimentally at JET [5] and modelled by orbit [6] and Monte Carlo calculations [7].

<u>The effect of electric field</u> The effect of increasing the negative electric potential at the launching point of the ions is shown in figures 2a-d. With the increase of the potential the "nose" tends to become narrower and finally disappears. The effective loss energy ε_F goes down and reaches a minimum at $\Delta\Phi/\varepsilon_o \approx 1.7$, and then goes up because of the strong energy barrier, imposed by the potential. The surprising effect of decreasing ε_F at modest $\Delta\Phi$ is attributed to the resonant interaction of poloidal ion velocity $v_\parallel B_p/B_t$ with the cE_r/B_T drift. Because of this interaction the ion spends more time around the x-point where the ΔB-drift direction is favourable for it to escape to the target. The dependence of ε_F on $\Delta\Phi$ is shown in fig. 3, for both parabolic profiles $\Phi(\psi)$ with $E_r = 0$ at LCFS (curve 1) and linear potential profiles, at $d\ell/d\psi = \text{const}$ (curve 2). As the general features of both curves are the same, the effect of radial electric field on fast ion losses is basically independent of the exact profile of the potential.

To identify the region inside the LCFS, from which we expect high fast-ion losses, we have to assume a specific ion temperature profile at the edge. Fig. 4 represents the simplest case of constant $T_i(r)$ at the edge. The intersection of $\frac{3}{2}T_i(r)$ and $\varepsilon_O(r)$ defines the radial zone inside the LCFS from which we would expect high fast-ion losses, if there

are no collisions. Substituting $\varepsilon_o = \frac{3}{2}T_i$ in equation (1) we can find the radial width of this zone. It is more convenient to calculate the poloidal larmor radius and represent Δr loss in terms of $\varrho_{i\theta}$. We find: $\Delta r_{thr} \approx 1.8\varrho_{i\theta}$, where $\varrho_{i\theta} = \sqrt{T_i/m_i}/w_{i\theta}$.

Due to the effect of collisions the effective zone of fast-ion losses shrinks to the region 'a' indicated in fig. 4, provided the effective collisionality $\nu^*_{i\,eff}$ in this zone is below 1. The effect of E_r is shown as an extension of the loss-orbit zone due to the reduction in ε_O. So we get the loss zone (a + b). It is noted that the b-zone is widest for $\Delta\Phi/\varepsilon_O$ = 1.7 when a parabolic potential profile is assumed.

The rate of build up of potential in the Δr layer is readily calculated by taking the dielectric constant of the plasma (about 1000 in the above example). Taking typical parameters $n_i = 10^{19}m^{-3}$, $T_e = 0.5$keV and $\Delta r = 0.01$m we find that a potential of 1 keV is reached after the loss of a few percent of the ions in the layer. Estimates of the loss rate indicate a typical time for this potential to build up of $\sim$ ms.

Summary and Conclusions

Edge heating results in an increase in fast-ion losses and in turn causes the plasma potential to become more negative. The numerical calculations described show that the decrease in plasma potential rather surprisingly causes the collisionless ion loss rate to increase. This effect is ascribed to increased vertical drift near the X point. The effect continues until the plasma potential reaches a critical value $\Delta\Phi \approx 1.7\varepsilon_o$, above which the electrostatic potential makes it more difficult for the ions to escape. The non-monotonic dependence of collisionless fast-ion losses on the magnitude of negative potential provides a new possibility of modelling the L-H transition. Since the initial increase in the fast ion losses is caused by the radial extension of the loss zone inside the LCFS, the L-H transition is likely to be related to the fast increase in ion losses due to newly formed loss orbits, as the potential "wave" propagates inside the plasma.

References 1. H Weisen et al, Boundary ion temperatures in JET, Nuclear Fusion 31 (1991) 2247. 2. K C Shaing et al, Phys. Fluids B, 2 (1990), 1492. 3. H Biglari and P H Diamond, Phys. Fluids B, 2 (1990), 1. 4. F L Hinton and R D Hazeltine, Rev. Mod. Phys., 48 (1976), 239. 5. R Reichle et al, J. Nucl. Mat., 176-177 (1990) 375. 6. D D R Summers et al, in Proc. of 18th EPS Conf. on Contr. Fus. and Plasma Phys. (Berlin 1991), part 1, p.5. 7. M A Kovanen et al, Modelling of the Observed Particle and Heat Fluxes in the X-point region at JET, JET Report, JET-P(91)06 (March 1991). 8. R D Hazeltine, Phys. Fluids B, 1 (1989) 2031.

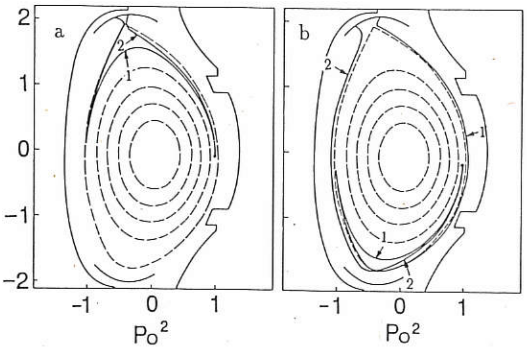

Fig. 1 a,b. Loss orbits with ion grad-B drift directed towards (a) and away (b) from the x-point. Curves 1 correspond to orbits from the "tip" of the "nose", curves 2 - to higher energy ions with $\varepsilon_i > \varepsilon_F$

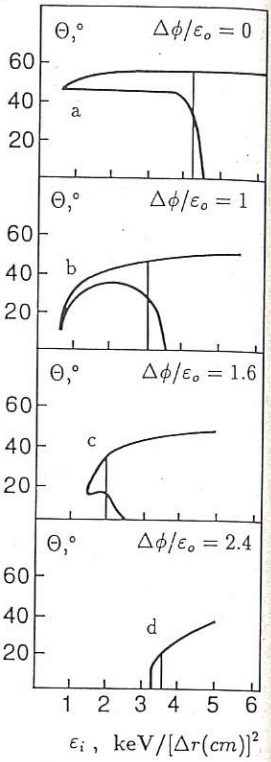

Fig. 2. Loss orbit regions for different negative potentials. Ion energy ε_i is measured in keV/$[\Delta r(cm)]^2$, Θ is angle of attack of launched ion (e.g.$\Theta = (v_{\|}/v)$, energy ε_F is indicated by vertical lines.

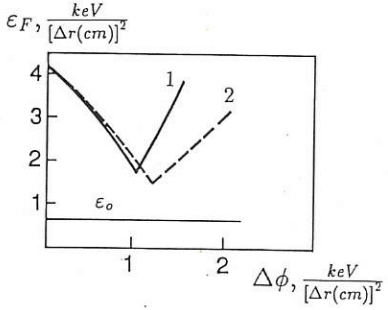

Fig. 3. Dependence of effective threshold energy of escaped ions ε_F on $\Delta\phi$ for parabolic (solid line) and linear (dashed line) profiles of potential.

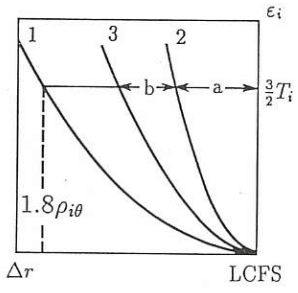

Fig. 4. Curves of $\varepsilon_O(1), \varepsilon_F$ ($E_r = 0$)(2), $\varepsilon_F(\Delta\phi/\varepsilon_O = 1.7)(3)$ and zones of lost orbits for the case of constant T_i at the edge.

DENSITY, POTENTIAL AND TEMPERATURE FLUCTUATIONS IN WENDELSTEIN 7-AS AND ASDEX

R.Balbin[1], A.Carlson, M.Endler, L.Giannone,
C. Hidalgo[1], H.Niedermeyer, A.Rudyj, G.Theimer,
W7-AS Team and ASDEX Team

Max-Planck-Institut für Plasmaphysik,
EURATOM-IPP Association, D-8046 Garching, F.R.G.
[1]CIEMAT , 28040, Madrid, Spain.

1. INTRODUCTION

Measurements of density, potential and temperature fluctuations in Wendelstein 7-AS stellarator (W7-AS) and ASDEX tokamak have been carried out. The properties of plasma fluctuations in a tokamak and stellarator can then be compared.

A reciprocating Langmuir probe with an array of 19 graphite tips has been used to measure the radial profiles of fluctuations in the ion saturation current and floating potential in W7-AS and ASDEX. In both devices, a reversal in radial electric field and an associated velocity shear layer at the plasma boundary have been observed and in both cases the normalised ion saturation current fluctuation level decreases monotonically moving towards the plasma centre and through the shear layer. At the radial position where the phase velocity in the poloidal direction of the fluctuations goes to zero, the normalised ion saturation current fluctuation level of 0.25 are similar for edge plasma parameters of similar temperatures and densities. A spatial crosscorrelation between fluctuations in floating potential and ion saturation current has been observed in both machines.

2. RADIAL PROFILES

A radial scan of the reciprocating Langmuir probe through 10cm in 150ms provides the radial profiles of the mean and RMS values of the floating potential and ion saturation current. In W7-AS, discharges with 200kW ECRH power with B_o=1.28T and n_e=1x10^{19} and n_e=2x10^{19} and in ASDEX , Ohmic discharges with B_o=2.17T and n_e=1x10^{19} and n_e=2.9x10^{19} were studied.

The radial profiles of electron temperature and density for the discharges at the higher density are shown in Fig. 1. The radial profile of the floating potential with reference to the limiter or separatrix radius is shown in Fig. 2. In both machines the sharp dip in the floating potential at the limiter or separatrix position and the decrease in plasma temperature with minor radius leads to a plasma potential profile with a maximum in the vicinity of r/a=1. In the experiments on W7-AS one of the two limiters was stepped inwards to clearly demonstrate that the limiter determines the spatial location of this dip in floating potential.

The normalised value of the ion saturation current fluctuation, $\tilde{i}_{sat}/i_{sat}$ decreases with decreasing normalised radius in both machines, with a typical value of 0.25 at r/a=1. The normalised value of the floating potential fluctuation, $\tilde{\varphi}_{fl}/T_e$, also decreases with decreasing minor radius also with a typical value of 0.25 at r/a=1 in both machines.

3. SHEAR LAYER

The peaking of the plasma potential in the vicinity of r/a=1 leads to a reversal in the radial electric field at this position and an inversion of the poloidal propagation direction of the fluctuations (1). Shown in Fig. 3 is the radial profile of the poloidal phase velocity of the floating potential fluctuations in W7-AS and ASDEX.

The poloidal phase velocity of fluctuations in ASDEX was found to be strongly dependent on the plasma density. The poloidal phase velocity of H_α fluctuations, with emission from a region ~2cm outside the separatrix, decreased from 300m/s at a density of $2.0 \times 10^{19}\ m^{-3}$ to zero at the density limit of $5.0 \times 10^{19}\ m^{-3}$. Preliminary studies in W7-AS from H_α fluctuations suggest that the density dependence is much weaker, while at 2.56T the poloidal velocity is typically a factor of 5 slower. Phase velocities of the fluctuations measured with the Langmuir probe in W7-AS are therefore significantly greater than those in ASDEX in this case as they have been taken at the lower magnetic field.

These experiments are relevant to the investigations of velocity shear suppression of edge turbulence (2). As in previous experiments a decrease in coherency and an increase in the autocorrelation function of the fluctuations in the laboratory frame are found. The Langmuir probe array allows such calculations to be made in the rotating plasma frame (3) and a comparison of results from both machines will be presented. Moving towards the plasma centre, the normalised ion saturation current fluctuation level decreases monotonically as the velocity shear layer is crossed. With the low coherence of the fluctuations in the shear layer it is not possible to show that particle transport is reduced in the shear layer.

4. SPATIAL CORRELATION

In Fig. 4 the cross correlation found between floating potential and ion saturation current as a function of poloidal separation in both machines can be explained in terms of a turbulent eddy model. A local potential hill induces an ExB drift that pushes plasma of higher (lower) density onto tips in front (behind) of the potential maximum. The crosscorrelation maximum (minimum) is then found on the dominant spatial scale of the turbulent eddies. In Fig. 4 the poloidal propagation of the fluctuations is superimposed on this simple picture and causes the correlation maxima to be skewed. The details of this process are discussed in more detail in an accompanying paper.

5. TEMPERATURE FLUCTUATIONS

The need to measure temperature fluctuation levels to quantify their role in edge plasma transport is the motivation for the development of techniques to obtain reliable estimates of this parameter. Estimates of the temperature fluctuation level from one triple probe suffer from the justification of the assumption that spatial gradients of the fluctuating quantities are negligible. Using two or more triple probes can remove this problem (4). This technique was employed on ASDEX and a normalised temperature fluctuation of 0.48, significantly greater than the normalised density fluctuation of 0.27, was found. A double probe swept at 10 kHz also provides a measurement of the magnitude of the temperature fluctuation (5). In this experiment a normalised temperature fluctuation level of 0.1, significantly less than the normalised density fluctuation level of 0.3, was found.

Both techniques cannot be readily used in W7-AS as the array of probe tips are not exactly on the same flux surface, and hence are at slightly different plasma potential. This difficulty can be removed by monitoring the I-V characterisic of a single tip on a fast time scale (6). The Langmuir probe characteristic in W7-AS was obtained by sweeping the applied voltage at 400 kHz and digitising at 10 MHz. Transformer coupling of the amplifier and balancing the cable capacitance allowed capacitve currents to be reduced to 2 mA. The limiting factor in these measurements is the necessity of the temperature fluctuation level to be greater than the level set by the fitting procedure on a finite number of points in the characteristic. A normalised temperature fluctuation level of 0.2 at the limiter radius was determined, while the mean in the relative temperature fit error was below 0.1. This temperature fluctuation value is then comparable to the normalised ion saturation current fluctuation level in this discharge, while the normalised density fluctuation level from the swept probe technique yields a value of 0.2. The Langmuir probe characteristics taken at lower sweep frequencies show however that the mean temperature increases with decreasing sweep frequency. This feature is consistent with local plasma heating by the probe since electron saturation currents up to 0.5A are drawn. At a sweep frequency of 100kHz the temperature decreases from 40eV to 33eV and at a sweep frequency of 400kHz the temperature decreases from 29eV to 25eV, as the sweep amplitude is reduced from 150V to 80V. A high sweep frequency and the smallest time available for plasma heating is necessary to achieve an unperturbed measurement.

(1) Ch.P.Ritz, R.D.Bengston, S.J.Levinson and E.J.Powers, Phys. Fluids, 27, 2956, 1984.

(2) Ch.P.Ritz, H.Lin, T.L.Rhodes and A.J.Wooton, Phys. Rev. Lett, 65, 2543, 1990.

(3) H.Niedermeyer et. al,
18th EPS Conference on Controlled Fusion and Plasma Physics (Berlin), IV 301, 1991.

(4) A. Carlson, L. Giannone and the ASDEX team,
18th EPS Conference on Controlled Fusion and Plasma Physics (Berlin), IV 305, 1991.

(5) H.Lin, R.D.Bengston and Ch.P.Ritz, Phys. Fluids B 1, 2027, 1989.

(6) C. Hidalgo et. al,
18th EPS Conference on Controlled Fusion and Plasma Physics (Berlin), III 85, 1991.

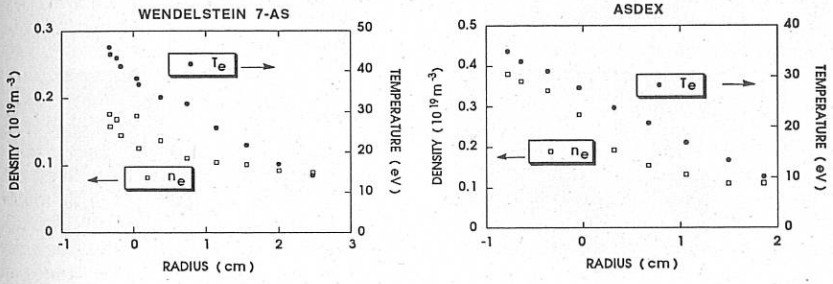

Fig. 1 Electron density and temperature profiles with reference to the separatrix radius in ASDEX (40cm) or the effective limiter radius in Wendelstein 7-AS (18cm).

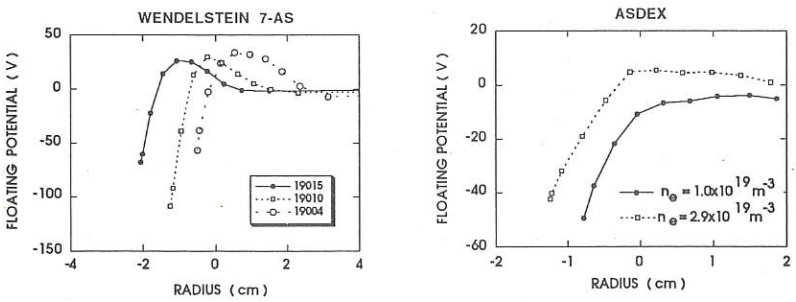

Fig. 2 Radial profiles of the floating potential showing the dip at the effective limiter radius in Wendelstein 7-AS and at the separatrix in ASDEX.

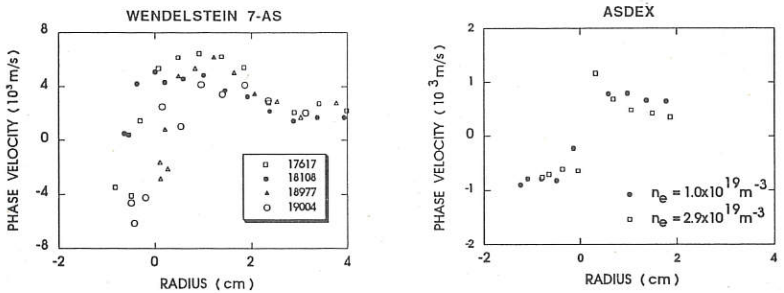

Fig. 3 Reversal of the poloidal phase velocity from the ion diagmanetic drift direction to the electron diamagnetic drift direction.

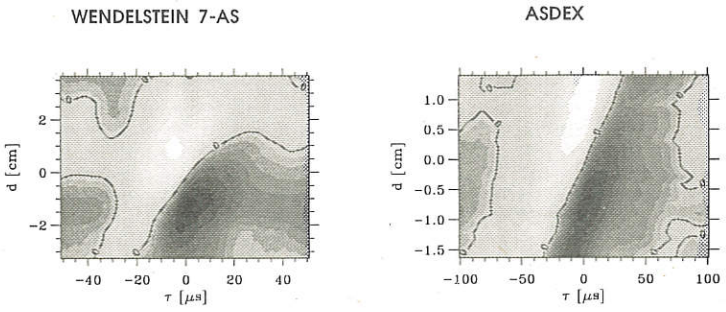

Fig. 4 Crosscorrelation of ion saturation current and floating potential fluctuations showing the maxima (light) and minima (dark) at a distance of 1cm. The distance between probe tips is 2mm and the poloidal extent of the array is 3.6cm.

ATTEMPT TO MODEL THE EDGE TURBULENCE OF A TOKAMAK AS A RANDOM SUPERPOSITION OF EDDIES

M. Endler, G. Theimer, M. Weinlich, A. Carlson, L. Giannone, H. Niedermeyer, A. Rudyj
and the ASDEX-Team

Max-Planck-Institut für Plasmaphysik, EURATOM Association,
D-8046 Garching, Germany

Introduction

Turbulence is considered to be the most likely origin of the anomalous transport in tokamaks. Although the main interest is focussed on the bulk plasma, transport in the scrape-off layer is very important for reactor design. For this reason extensive experimental investigations of the edge turbulence were performed on the ASDEX divertor tokamak.

Langmuir probe arrays were used in the floating potential mode and in the ion saturation mode to measure the poloidal distribution of density and plasma potential fluctuations neglecting temperature fluctutions. Density fluctuations integrated radially over the boundary layer were derived from H_α-measurements. Data from up to 16 channels were sampled with a frequency of 1 MHz during time windows of 1 s. Often one parameter like the plasma density or the radial probe position were scanned during this interval.

The well known statistical functions like probability distributions of amplitudes, correlation functions and spectra were computed from blocks of typically 20000 data points per channel. Recently a bi-spectral frequency analysis of single channels was performed. The bi-spectrum is defined as $\langle F(\omega_1)\cdot F(\omega_2)\cdot F^*(\omega_1+\omega_2)\rangle$ where F is the Fourier transform of the signal. It is a measure of the coherence and the average phase shift between the component measured at a frequency $\omega_1+\omega_2$ and the result of a fictive quadratic mixing of the two components at frequencies ω_1 and ω_2.

It is impossible to derive physical mechanisms directly from these statistical observations. We draw general conclusions about the physics involved from the entity of observations and propose a set of basic effects to include in a theoretical model. Being still unable to solve the complex nonlinear problem of the fully developed turbulence exactly we attempt to describe the turbulence with a simple non-self-consistent statistical model. This allows to derive plausible physical interpretations of several features of the statistical functions and may be used as a guide-line for the development of a manageable theoretical model.

Experimental description of the edge turbulence

From the fluctuations of the ion saturation current and the floating potential measured with probes one derives density fluctuations with a relative level $\tilde{n}/n$ up to 50 % and potential fluctuations with rms values of typically 5 V, respectively. Reliable measurements of temperature fluctuations are not available. There are, however, indications that the relative level of temperature fluctuations is in the same order of magnitude as that of density fluctuations. Mainly potential fluctuation measurements may therefore be disturbed by temperature fluctuations.

The fluctuations show a flute-like (2-d $\perp\vec{B}$) structure. Correlation lengths are typically 1 cm $\perp\vec{B}$ and several 10 m along field lines. Poloidal propagation velocities outside the separatrix are a few 100 m/s in the ion diamagnetic drift direction during ohmic medium density discharges. With beam injection the velocity is higher and is influenced by Doppler-shift due to the toroidal plasma rotation. In ohmic high density discharges the velocity goes to zero or even changes sign. Inside the separatrix the

fluctuations always propagate in the electron diamagnetic drift direction. In the so-called shear layer at the separatrix (typical width 1 cm) there is a steep velocity gradient. In double-null discharges the scrape-off layer is divided in two parts by the two stagnation points. Fluctuations appear only in the low-field part.

Details about experimental statistical functions can be found in earlier papers [1-4]. We present here a few examples. Fig. 1a shows a time-space correlation function of the plasma potential measured during a high density discharge where the fluctuations did not propagate. The time-space cross-correlation between density and potential from the same shot is shown in fig. 2a. Eddies around potential maxima or minima due to E×B-drift explain the structure of this correlation function. A time-averaged k-spectrum of the potential fluctuations from another shot is shown in fig. 3a. The only scale length which can be derived from this spectrum is the inverse of the k at the transition from the flat part to the decay. It corresponds to the width of the scrape-off layer.

When the fluctuations propagate (i. e. in the normal case), space-time correlation functions and frequency-wavenumber spectra both show a skewed structure. In the model described in the following section this trivial effect is not included. For easier comparison we present here examples from special discharges with $v = 0$. Generally one should compare only invariant parameters and properties.

Density correlation functions show a typical undershoot to negative correlations up to 20% . The half width or the zero-correlation point allow to define an invariant correlation length. To define a correlation time one has to trace the spatial maximum of the correlation for each time point. This invariant temporal correlation function can be approximated by an exponential defining an invariant correlation time. k-ω-spectra at different radii and the variation of correlation parameters and of the propagation velocity with the plasma current and density can be found in [4].

The frequency bi-spectrum is a function of two variables, the wavenumber-frequency bi-spectrum would be a function of four variables. With reasonable CPU time it was only possible to compute frequency bi-spectra, which also contain spatial information due to the Doppler-shift. Bi-coherence values are above noise level only at low frequencies up to about 100 kHz. The most prominent observation are the different bi-phases from potential and density fluctuations. Bi-phases are rather constant in the range of significant bi-coherence. For potential fluctuations they are always around π, for density fluctuations around $-\pi/3$. This means that the "typical waveform" of potential signals is symmetric, that of density signals tends to a sawtooth with steep leading edge.

Components of a physical model

In the scrape-off-layer all field lines intersect the target plates. The physics of the sheath and of the pre-sheath determine the average electrostatic potential along $\vec{B}$ and the energy balance on flux bundles. The correlation length along the magnetic field is much longer than the connection length between the target plates. There will be a relatively short gradient zone in front of the target plates. For this reason a 2-d model should be adequate. Similar considerations can be found in [5,6]. Algebraic equations are good approximations to describe the physics at the target plate, i. e. the relation of variables like T_e, n_e, Φ between the target plates and the plateau zone. 2-d differential equations neglecting inertia seem to be adequate to describe the rather slow drift motion of the plasma perpendicular to the magnetic field. An electrostatic fluid model should be sufficient. There is no indication that kinetic effects are important in this collision-dominated plasma nor that electromagnetic effects are significant.

Φ is determined by the sheath potential (including a resistive part), the thermoelectric force, the parallel electron pressure gradient and a resistive voltage drop due to the parallel current density. In a non-uniform plasma currents $\parallel \vec{B}$ are generally necessary to compensate the divergence of the diamagnetic current density. In the turbulent state the plasma parameters vary in space on a short scale length. Consequently the electrostatic potential varies $\perp \vec{B}$ causing a random E×B-drift motion with a

non-zero average poloidal component in the ion diamagnetic drift direction (due to the strong average inward T_e gradient).

Neglecting classical transport $\perp \vec{B}$ energy and particles on flux bundles are lost to the region near the target plate. Atomic physics processes are important for the particle balance and energy loss. For the energy loss also the finite parallel heat conductivity and the energy transfer to the target plate, which depends on plasma parameters and on the parallel current density, are important.

The curvature of the magnetic field could be an explanation for the in-out asymmetry of fluctuations. Individual terms may be negligible at least in parts of the full parameter range. For example the electrical resistivity of the sheath may be negligible in the high-density low-temperature range where the resistivity of the plasma is large and vice-versa.

Ad -hoc model as a zero-order description of the turbulence

As an aid for the interpretation of statistical functions and as a guide-line to the development of the self-consistent nonlinear model as outlined above we try to model zero-order effects of the turbulence by a simple random superposition of eddies in a 2-d space with a given non-uniform density distribution. The eddies are generated by spontaneous rotationally symmetric "potential events" with given radial profile and temporal waveform (cosine-bell and 1/cosh, respectively). The diameter of the events is random with a given probability distribution, their life time is statistically coupled to the diameter, the spatial and temporal distributions are uniform.. Density fluctuations evolve due to the E×B-rotation of the non-uniform initial density. The density perturbation is assumed to be damped with a time constant proportional to the life-time of the potential perturbation. For the figures shown (1b, 2b, 3b) the radius of the eddies varies between 2 mm and 2 cm. Zero time shift of the maximum correlation between density and potential perturbations as measured (see fig 2a) is only obtained if the potential amplitude is chosen such that the eddies perform a half-turn in the average. An inverse pendulum with strong viscous damping would perform a motion of this kind. In the plasma damping of the rotation could be caused by interaction with smaller eddies. The density decay is a crude model for a diffusive decay (also due to the interaction with smaller eddies) and losses to the target plate. It was found that the shape of contours of the statistical functions and other features are better modeled if we assume double eddies, i. e. two equal potential "events" with opposite sign at a distance of the radius of one event. Time constants and diameters were chosen to give reasonable agreement with measurements, but a full optimization was not performed. The best choice for the time constant is proportional to the square of the size, i. e. a diffusive time constant. In order to obtain a size-independent density in time and space the probability distribution has to be inversely proportional to the fourth power of the size.

Conclusions

Rather sophisticated measurements and evaluations were performed on the edge turbulence of ASDEX. Many features of the measured statistical functions may have a rather simple interpretation. The steep probability distribution of the size of eddies necessary in this model indicates some problems to be expected when attempting to obtain a relevant numerical solution of the physical model.

References

/1/ A. Rudyj, IPP III/160, July 1990.

/2/ G. Theimer, IPP III/169, Dec. 1990.

/3/ A. Rudyj et al., 17th EPS Conference on Controlled Fusion and Plasma Heating, Amsterdam 1990. Europhysics Conference Abstracts Vol. 14B, part III, p. 1464 - 1467.

/4/ H. Niedermeyeret al., 18th EPS Conference on Controlled Fusion and Plasma Physics, Berlin 1991. Europhysics Conference Abstracts Vol. 15C, part I, p. I-301–I-304.

/5/ A. V. Nedospasov, Sov. J. Plasma Phys. **15** (10), 1989, p. 659.

/6/ X. Garbet et al., Nuclear Fusion, Vol 31, No. 5 (1991), p. 967.

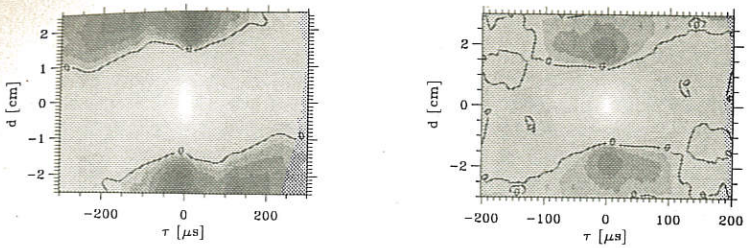

Figs. 1a (left) and 1b (right). Time-space correlation function of plasma potential fluctuations computed from measured (left) and simulated data. For easier comparison with the simulation a discharge with zero propagation velocity was chosen. Dark means negative correlation, light means positive correlation. The zero contour is indicated by a solid line.

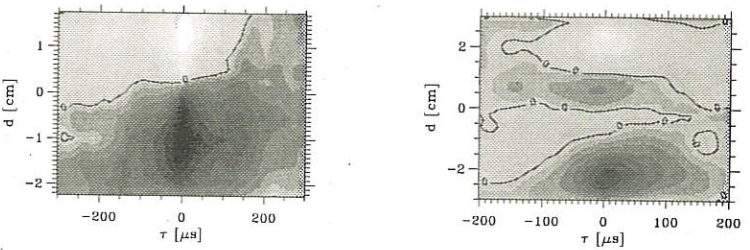

Figs. 2a (left) and 2b (right). Time-space cross-correlation function of density and potential fluctuations from measured (left) and simulated data. Same discharge and simulation, respectively as for fig. 1. These plots show that a positive potential is correlated with high density on one side and low density on the other side consistent with an E×B-motion causing influx of thin plasma on one side and outflux of dense plasma on the other side of the potential "event".

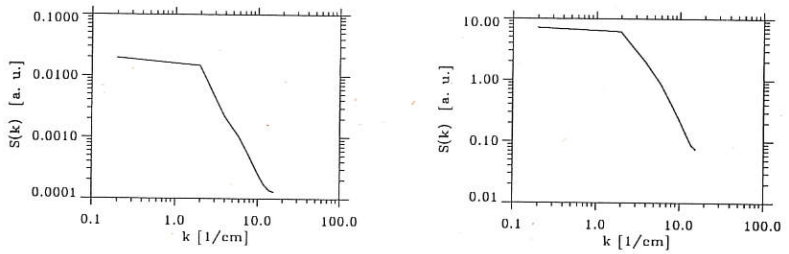

Figs. 3a (left) and 3b (right). Time-averaged wavenumber-spectra of potential fluctuations from measured (left) and simulated data. Different discharge but same simulation as for figs. 1 and 2. The spectra decay $\propto k^{-2.5}$ and $k^{-2.2}$, respectively. Leveling-off at high k due to aliasing.

MECHANISMS INDUCING CHANGES ON THE EDGE TURBULENCE IN THE TJ-I TOKAMAK

M.A. Pedrosa, I. García-Cortés, R. Balbín, C. Hidalgo, M.A. Ochando, M. Liniers
Asociación **EURATOM-CIEMAT**, 28040 Madrid, **SPAIN**

I.- Introduction

In spite of the theoretical and experimental efforts made during the last two decades, transport mechanisms in tokamaks and stellarators are still not well understood. Electrostatic fluctuations are probably the major cause of the edge anomalous transport. Many mechanisms have been proposed to explain edge turbulence in magnetically confined plasmas. Atomic physics processes, such as radiation, ionization and charge-exchange, should be considered as candidates to explain fluctuations levels in the plasma edge [1]. In order to determine the role of radiative instabilities on edge turbulence, a comparative study of density and temperature fluctuations has been performed in the plasma edge region of the TJ-I tokamak.

The problem of the influence of electric fields on turbulence and confinement has become prominent during the last few years. Two different approaches are being used to understand the influence of electric fields on plasma properties in the TJ-I tokamak. First, the role of the naturally occurring radial electric fields on edge turbulence has been investigated. Second, in order to study the possibility of externally controlling edge turbulence and plasma edge properties, experiments using biased electrodes are being performed in TJ-I.

II.- Experimental

A square array of four Langmuir probes was inserted at the outer side of the equatorial plane of the TJ-I tokamak (R = 30 cm, $\bar{a}$ = 9.5 cm) to measure the ion saturation current, floating potential, their fluctuations and temperature. Additionally, probe-current and temperature fluctuations have been determined using a fast swept Langmuir probe technique [2]. A broad-band (1 MHz) 75 watts amplifier was used to supply the swept voltage (≈ 150 V) to a single Langmuir probe at 300 kHz. The current-voltage characteristic has been fitted by the expression,

$$I=I_S\{1-\exp[e(V-V_f)/kT_e]\}$$

where I_S is the ion saturation current, T_e is the electron temperature and V_f is the floating potential. Using a nonlinear least-squares fitting routine, we have determined T_e, V_f and I_S in a time scale (≈ 2 μs) which is smaller than the relevant times of the turbulence (≈ 10 μs). Capacitance to ground has been minimized to reduce parasitic capacitive currents to less than 3 mA (rms). Radiation profiles have been characterized by means of a bolometer array.

Radial electric fields were externally applied by means of a biased electrode located at the

top of the vacuum chamber and in a poloidal section 120º away from the Langmuir probes system. The electrode used was a stainless steel cylinder (0.5 cm radius and 1 cm length).

Measurements were carried out in plasmas with chord average density $\bar{n}_e \approx (1\text{-}2)10^{13}$ cm^{-3}, plasma current $I_p \approx$ (20 - 40) kA, and toroidal magnetic field B_t = (0.8 - 1.4)T. Data were digitized at 5 MHz, using a 12 bit CAMAC digitizer.

III.- Density and Temperature Fluctuations near the Shear Layer Location

In TJ-I, as in other devices the poloidal phase velocity of the fluctuations computed from the S(k,ω) function using two floating potential signals, $v_{ph} \approx \Sigma_{\omega,k}(\omega/k)S(k,\omega)/\Sigma S(k,\omega)$, has been observed to change sign (velocity shear) in the vicinity of the limiter radius (a_s); for $r<a_s$ fluctuations propagate in the electron diamagnetic drift direction ($v_{ph} \approx 2\ 10^5$ cm s^{-1}) and for $r>a_s$, the fluctuations propagate in the ion diamagnetic direction .

Density ($n_e \approx I_s T_e^{-1/2}$) and temperature profiles are rather flat in the scrape-off layer region whereas they are much steeper in the bulk plasma side of the velocity shear location (Fig.1), suggesting that the shear layer acts as a demarcation line of the plasma edge of TJ-I tokamak. Fluctuation levels of the ion saturation current ($\tilde{I}_s/I_s$) are about 30% at the shear layer location and decrease when moving radially inwards.

There was good agreement between the measured ion saturation currents obtained from the fast swept probe method and from the fixed bias probe.

The fitting errors of the I-V characteristic, obtained by means of the fast swept probe, are in the range of 10% for the ion saturation current and about 15% for the electron temperature. However, the measured current and temperature fluctuation levels are well above the maximum uncertainties. Figure 2 shows the ion saturation current, density and temperature fluctuations in the plasma bulk side of the velocity shear location ($r/a_{shear} < 1$) plotted versus the local electron density (that can be considered as a monitor of the probe position). Fluctuations in the ion saturation current decrease when the probe moves radially inwards. However, whereas $\tilde{I}_s/I_s$, $\tilde{T}_e/T_e$ and $\tilde{n}_e/n_e$ are comparable near the shear location, $\tilde{I}_s/I_s$ is smaller than both $\tilde{n}_e/n_e$ and $\tilde{T}_e/T_e$ in the plasma bulk region. Taking into account that the ion saturation current is proportional to the local electron density and to the square root of the electron temperature ($I_s \approx n_e T_e^{1/2}$), the present results imply that density and temperature are fluctuating in phase close to opposition. These results suggest the possible role of radiation in driving edge fluctuations.

The relevant parameter for the impurity condensation drive is $n_z I_z$, where n_z is the impurity concentration. Thus, the existence of radiation (present in all devices) and some kind of coupling mechanism between density and temperature fluctuations are the only required conditions for the condensation drive. The condensation drive could partially explain edge turbulence features in TJ-I. A systematic study of the correlation between edge fluctuation levels and radiation levels is in progress.

IV.- Influence of Electric Fields on Turbulence

The question of the influence of electric field on turbulence has raised during the latest years [3]. In the plasma region where dE_r/dr is high (the velocity shear layer) any fluid element is strained by the differential velocity, resulting in a decorrelation time $\tau_{shear} \approx (dv/dr)^{-1}$. This mechanism could account for the reduction (in the plasma frame) of the auto-correlation times at the shear location in TJ-I [4] and in TEXT [5].

In TJ-I, the strength of the shear layer (dv/dr) appears to be sensitive to the plasma conditions. Typically the strength of the shear increases with increasing the magnetic field. However, no causal relationship between dv/dr and B_t has been established. So far, and within our experimental error, the fluctuation levels in the ion saturation current near the shear location are not related with the strength of the shear (dv/dr). Modifications in dv/dr by changing the plasma conditions have also been observed in ATF.

Positive and negative radial electric fields have been induced in the plasma edge ($0.8<r/a<1.0$) of TJ-I by means of a biased electrode. Potentials applied to the electrode were typically in the range ±700 V. Preliminary results show a modification in the global plasma behaviour when biasing is applied to the electrode. Fig.3.a shows the increase in the chord average density and the simultaneous decrease of the edge density with increasing biasing; thus density profiles are modified by the externally applied radial electric field. The influence of biasing on the poloidal phase velocity of the fluctuations (v_{ph}), measured in the plasma bulk side of the shear location, is shown in Fig.3.b.

When positive biasing is applied to the electrode in low density shots, fluctuations of high frequency (200-300 kHz) with low edge poloidal wave number and of possibly magnetic origin have been observed in different diagnostic signals (H_α, Mirnov coils and pyroelectric) as well as in the probe-current measured by Langmuir probes (Fig. 4). As shown in Fig.5 the spectra of probe-current fluctuations show an increase in the power for frequencies above 200 kHz with increasing positive biasing. Further experiments, including the study of the correlation between electrostatic and magnetic fluctuations need to be done to clarify the origin of this high frequency fluctuations.

Acknowledgements

This work was supported in part by the Dirección General de Investigaciones Científicas y Técnicas of Spain, under project number PB90-0639-C02-02.

References

[1] Ch.P. Ritz, T.L. Rhodes, H. Lin, et al., Proc. 13th Int. Conf. on Plasma Phys. and Cont. Nucl. Fusion, Washington, 1990 (IAEA, Vienna, 1991), IAEA-CN-53/C-3-4, vol 2, 589.
[2] R. Balbín, C. Hidalgo, M.A. Pedrosa, I. García-Cortés, *Rev. Sci. Instrum.* (1992) in press.
[3] H. Biglari, P.H. Diamond, P. Terry, *Phys. Fluids B* **2**, 1 (1990).
[4] I. García-Cortés, M.A. Pedrosa, C. Hidalgo et al., submitted to *Phys. Fluids B*.
[5] Ch.P. Ritz, H. Lin, T.L. Rhodes and A.J. Wootton, *Phys. Rev. Letters* **65**, 2543 (1990).

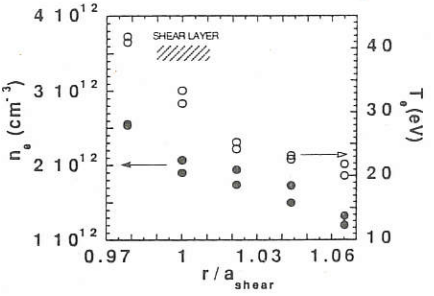

Fig.1.- Radial profile of electron density and temperature.

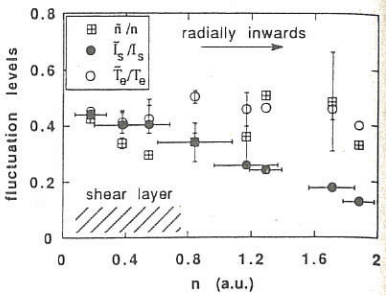

Fig.2.- Fluctuations in the ion saturation current, electron temperature and density versus the local electron density.

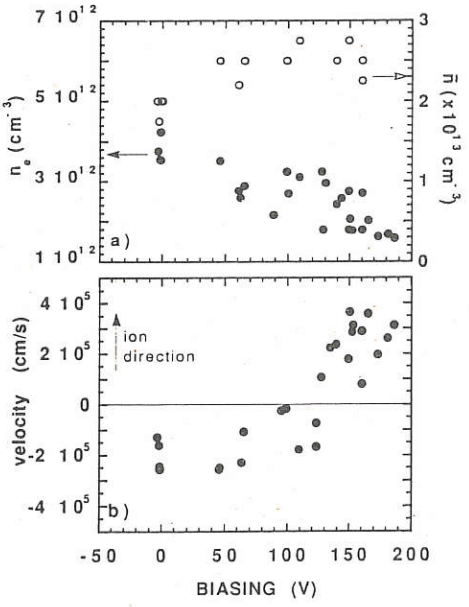

Fig.3.-a) Chord average density and edge density versus biasing. b) Poloidal phase velocity versus biasing.

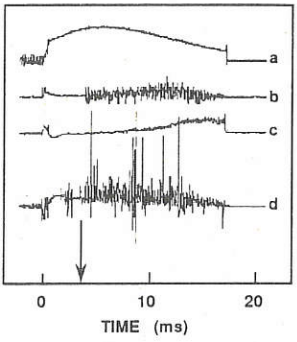

Fig.4.- Traces of a) Plasma current b) H_α c) X-rays and d) pyroelectric for a biasing of 600 V (the arrow shows the time for the beginning of biasing).

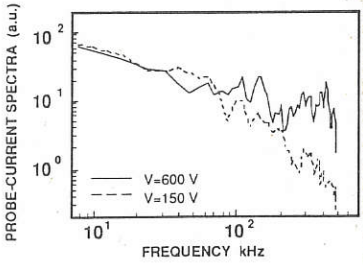

Fig.5.- Ion saturation current spectra.

m = 1 Activity Prior to the Onset of Sawtoothing on Tokoloshe Tokamak.

G. Nothnagel, D. Sherwell*, D.E. Roberts, J.D. Fletcher, J.A.M. de Villiers, P. E. Walters**
Atomic Energy Corp. of South Africa, PO Box 582, Pretoria 0001, R.S.A.
** Centre for Non-linear Studies, University of the Witwatersrand, R.S.A.*
*** Department of Physics, University of Stellenbosch, R.S.A.*

1. Introduction: In this paper we present experimental results that show a unique high amplitude burst of oscillations which occur prior to the onset of sawtoothing on Tokoloshe. The data show that the burst of oscillations is due to a large $m = 1, n = 1$ mode which is present early during the discharge at a time when the soft X-ray intensity profile is peaking and the radius of inversion is increasing. Despite its large size the mode does not seem to play a direct role in causing the sawtooth crash and this fact may have interesting implications for sawtooth theory.

2. Observations: The observations were made on ohmically heated Tokoloshe discharges ($R/a = 0.52m/0.24m\,; I_p = 140kA\,; B_\phi = 0.6T$). The minor cross-section is viewed by two single scanning soft X-ray diodes and an eight diode array separated by 180° in toroidal angle. On many shots the sawtooth oscillations rise smoothly from the background (initial relative amplitude $\Delta A/A \simeq 0$). For these shots we observe (on a diode viewing the plasma at $r \simeq 4$ cm) that the first small amplitude sawtooth oscillation starts off inverted and evolves into normal sawtooth oscillations, showing that the radius of inversion originates close to the plasma centre and then moves out rapidly (on a timescale of 1 to 2 ms) to $r = 7.5$ cm where it remains for the duration of the discharge . The sawtooth crash time is $\simeq 60\ \mu s$ which is $\simeq 6\times$ faster than the Kadomtsev time [1] for Tokoloshe parameters when the normal radius of inversion is 7.5 cm. An $m = 1$ is present on all sawteeth before and after the crash.

For some shots a single burst of $m = 1$ oscillations is observed immediately prior to the onset of normal sawtooth oscillations. In Fig. 1 traces (a) and (b) show the X-ray intensities on two diodes during the burst phase. Radii indicated are measured from the centre of the normal radius of inversion. A growing large amplitude $m = 1, n = 1$ mode is seen with a resulting centre diode signal that resembles a slow sawtooth crash with the $m = 1, n = 1$ oscillation superimposed on it. The amplitude of the $m = 1$ mode and the magnitude of the apparent slow "crash" varies from shot to shot.

Intensity profile data show that the profile is monotonically peaking during the pre-burst phase ($t_1 \rightarrow t_2$ in Fig. 1). During this phase a small constant amplitude oscillation

is seen on the centre diode signal only. This mode grows without discontinuities in amplitude or phase. At time t_2 an $m = 1$ oscillation starts to grow in amplitude on both diode signals. On the centre signal, frequency doubling is seen as can be expected for the case of precise central alignment of the observation chord and a rotating $m = 1$ structure.

During the time interval $(t_3 - t_4)$ the $m = 1$ mode amplitude decreases slowly until the first sawtooth crash occurs at $\simeq t_4$. Hard X-ray spikes accompany the first few sawtooth crashes (Fig.1 (c)), decreasing with each crash, probably due to a net loss of runaway electrons to the limiter at each crash. During the burst phase no hard X-ray spikes are observed. After time t_3, when the $m = 1$ is still present at relatively large amplitude the first characteristic hard X-ray spike signals the onset of the first sawtooth crash apparently independent of the $m = 1$ amplitude. The mode amplitude remains relatively unchanged after the first fast crash.

Fig. 2 shows the soft X-ray profile development for 4 different times during the $m = 1$ burst, immediately after the first sawtooth crash and directly prior to the second sawtooth crash. All the profiles were taken for the same phase of the $m = 1$ oscillations. The results show that the hot spot (maximum intensity) of the $m = 1$ mode moves out from the centre during the burst phase. This results in a decrease in average intensity on a centre diode. When the hot spot is approximately at the normal radius of inversion ($r = 7.5$ cm) the first sawtooth crash occurs as indicated by the hard X-ray spike. As a result of the crash the hot spot moves back in towards the centre. During the heating phase of the next sawtooth the hot spot shifts out towards the radius of inversion again. The effect on the $m = 1$ signal at $r = 7.4$ cm, seen directly after the crash in Fig. 2, is due to the change in position of the hot spot and is not due to a change in $m = 1$ amplitude.

Discussion: The results show interesting behaviour of sawtooth activity, during a time when a large saturated $m = 1$ mode is present, and may have implications for sawtooth theory. If the observed $m = 1$ mode is a tearing mode, thereby implying $q_0 < 1$, the results indicate that such a mode can saturate (Fig. 1). The results of Fig. 1 further imply that this mode is not the direct cause of the sawtooth crash unlike the predictions of the Kadomtsev [1] model. On the other hand, if q_0 is greater than 1 the observed $m = 1$ mode can be attributed to a saturated kink mode. However, then the sawtooth crash occurs during a time when a large saturated $m = 1$ kink mode is present, implying that conditions are not favourable for the onset of the quasi-interchange mode suggested by Wesson [2].

References

1. B B Kadomtsev, *Sov. J. Plasma Phys.*, **1**, 389 (1975)

2. J A Wesson, *Plasma Phys. and Contr. Fus.*, **28**, 243 (1986)

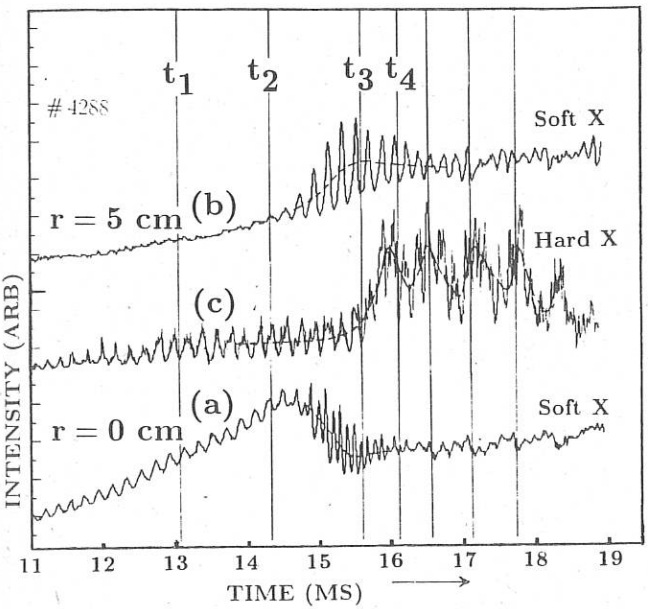

Figure 1: *Soft X-ray ((a),(b)) and hard X-ray (c) traces during the time of the* $m = 1$ *burst.*

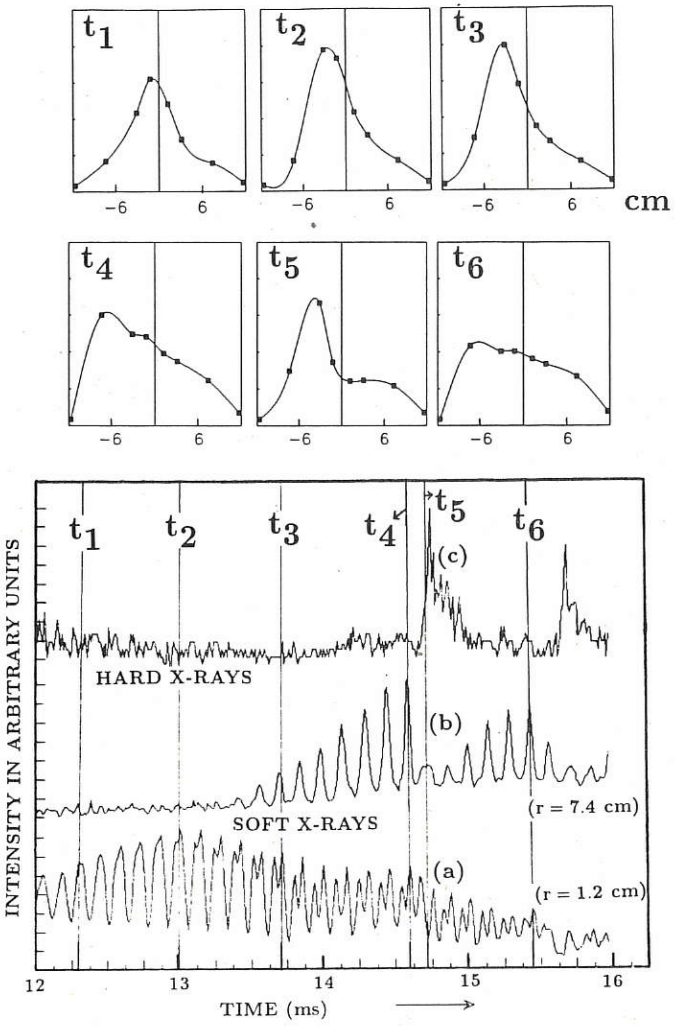

Figure 2: *The burst as seen on two soft X-ray signals at 1.2 ((a)) and 7.4 cm ((b)) respectively and by a hard X-ray detector viewing the limiter ((c)). Soft X-ray profiles at six indicated times are shown above the main figure.*

ROLE OF EDGE PLASMA IN A HIGH β VERY LOW q TOKAMAK REGIME

H. KIYAMA and S. KIYAMA
Electrotechnical Laboratory, Tsukuba-shi, Ibaraki-ken, Japan

1. Introduction

In this paper, the role of edge plasma related to dynamic motion of the plasma and to three kinds of edge fluctuations (10~400kHz) in a high β very low q tokamak plasma ($\beta_p \geq 1, q_l < 2$) is investigated. The edge plasma has a sharp density profile and stops the dynamic motion. The local edge fluctuations do not cause large energy loss. These experimental phenomena are investigated in the dynamic process in the TPE-2 experiment.

2. Features of the experimental conditions

TPE-2 is a toroidal screw pinch device with an elongated cross section and a conducting shell/1,2,3/. High β very low q tokamak plasmas ($\beta_p \geq 1, 1.2 < q_l < 3$) are produced by fast and/or slow pulsed discharges, and by ramping up of the toroidal and poloidal fields simultaneously with sustaining q_l constant, and then, they are stable confined ($\tau_E \geq$ 1msec). The duration of the toroidal magnetic field is about 1msec. The initial implosion heated plasma ($\beta_p \geq 1$) has peaked density and pressure profiles, which relax to broad profiles in 5~50μsec. At the transition, the density decreases by 30~50% in the case of He conditioning surface (Recycling rate; R~0.3), while by 10~20% in the case of D_2, H_2 conditioning surface (R~0.7)/4/. As gas puff is not used, the recycling rate sustains in the low level. The global density decay time is 1msec in low q ($q_l < 2$) plasma and 1.5msec in high q ($2 < q_l < 4$) plasma in the case of R~0.3. The specific lengths of edge density and temperature are λ_n~5mm, λ_{Te}~15mm. The particle confinement time is shorter as the core plasma density increases and q_l decreases. Helium discharge cleaning just before every screw pinch discharge was effective to produce low q, high density and reproducible plasmas and to improve the energy confinement. Helium cleaning dissociates D, H particles from the alumina ceramic surface precoated with titanium and provides the active surface. Therefore, in this short discharge duration, the particles which diffuse to the wall are absorbed on it and are not reflected. So, it is effective to observe the dynamic motion.

3. Three kinds of fluctuations

The fluctuations of the saturation current of the edge static double-probe are observed, whose frequencies are shown against q_l in **Fig.1**. The frequencies increase with decreasing of q_l. There are three kinds of the fluctuations, which are marked by ○, ▲, ●, respectively. **(1)** The relaxation oscillation, which has the lowest frequency and the period is about a half of the relaxation. This may be small sawteeth, and has a pulsed change of q profile, but $q(0)$ is more than 1. **(2)** The magnetic edge deformation, whose frequency is in the middle range, 30~100kHz. This is localized near outside of the torus. **(3)** The electrostatic edge density fluctuation, whose

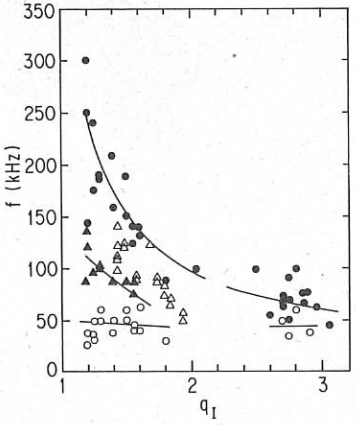

Fig.1 Frequencies of the edge density fluctuations measured by electrostatic double probe against q_l.

frequency is in the highest range, 40~300kHz, and inversely proportional to q_l, consequently, to the density gradient. The intensity is large at the edge. When $k_\theta \sim 2\pi/\lambda_n$ is assumed, the frequency is roughly f^* ; $2\pi f^* \sim \frac{kT_e}{eB} k_\theta \cdot \frac{dn}{ndr}$. Therefore, this fluctuation may be estimated to be a kind of drift waves from the frequency.

4. Dynamic motion of the plasma

The energy minimum state of high β very low q tokamak plasma has the broad current and pressure profiles/5,6/. The q and density profiles in the TPE-2 relax in 5~50μsec simultaneously to a specific q profile that has a uniform current density, and to a broad electron density profile, respectively. The density profile broadens with decreasing of q_l. When q_l increases by ramping down the plasma current, the density profile becomes steep. The shape of the electron temperature profile does not depend on q_l, which suggests the profile consistency. Consequently, the pressure of the high β very low q plasma has steep boundary near the wall (5~10mm), and then, provides the global neo-classical like energy confinement when the fluctuations are reduced. That is similar to the H mode structure. These relaxation phenomena mean that when the profile deviates from the specific q profile, whose deviation originates in energy loss or excess energy input, it relaxes to the profile always. The period of it is 50~200μsec in low q plasma or more than 1msec in high q plasma. We denote it as relaxation oscillation. The density profile, q profile and the edge density profile, near the relaxation transition are shown in **Fig.2(a),(b),(c)**, respectively. The q profile changes quickly and returns to the specific one, and one turn voltage, V_s, and soft Xray have large spikes. Usually, the change is toroidal axi-symmetric. The rapid macroscopic plasma motion or the density profile change is observed in the relaxation. The

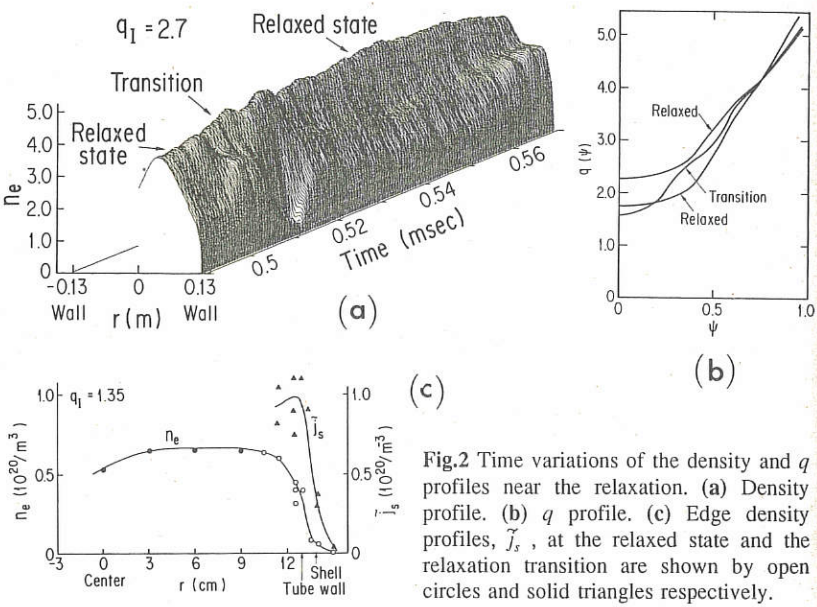

Fig.2 Time variations of the density and q profiles near the relaxation. **(a)** Density profile. **(b)** q profile. **(c)** Edge density profiles, $\tilde{j}_s$, at the relaxed state and the relaxation transition are shown by open circles and solid triangles respectively.

peaked profile becomes broad rapidly and it changes into peaked one in a few μsec, sometimes without particle loss. The particle motion is stopped at the sharp boundary near the wall surface. The energy and the particles are lost from the outward edge of the torus. These graphs show the structure is formed dynamically. The quick dynamic motion needs an inward drift force. The conducting shell may have a role to balance the motion, that is, the ion diamagnetic drift may cause the inward drift and may balance the motion.

5. Rotation of the magnetic deformation

The edge poloidal magnetic fluctuations $\tilde{B}_p$ are measured at 42 poloidal and toroidal positions, which are shown in **Fig.3(a)**. The edge magnetic flux surface deforms. The deformation rotates in the toroidal direction. It is a wave packet with 3-4 damping waves. The frequency of the damping wave is shown in Fig.1 by △. This magnetic deformation affects on the edge density slightly. The rotating speed of the mode decreases with increasing of q_I, as show in **Fig.3(b)**. It also decreases with increasing of the core density. Therefore, the deformation disappears during discharge in high density plasma. The speed of the rotation is 10~25 km/sec, and becomes fast, when the sharp edge density gradient is produced. This deformation is caused by the relaxation process. The initial plasma is sometimes not in the complete relaxed state and has not a toroidal symmetry. Then it relaxes so as to be a toroidal symmetric plasma in 5~50μsec. The toroidal rotating direction is the ion diamagnetic drift. The mode seems to be a kind of ballooning mode because the deviation occurs at the magnetic bad curvature and it is very small at the good curvature. The toroidal mode number is about 7. Usually only 3-4 wave trains are seen. The intensity of the mode is very small inside of the torus, that is, at the 2/3 parts of the poloidal circumference. The low energy soft Xray and CV radiations at the edge plasma apparently increase when the deformation is passing near the observation point. However, this edge

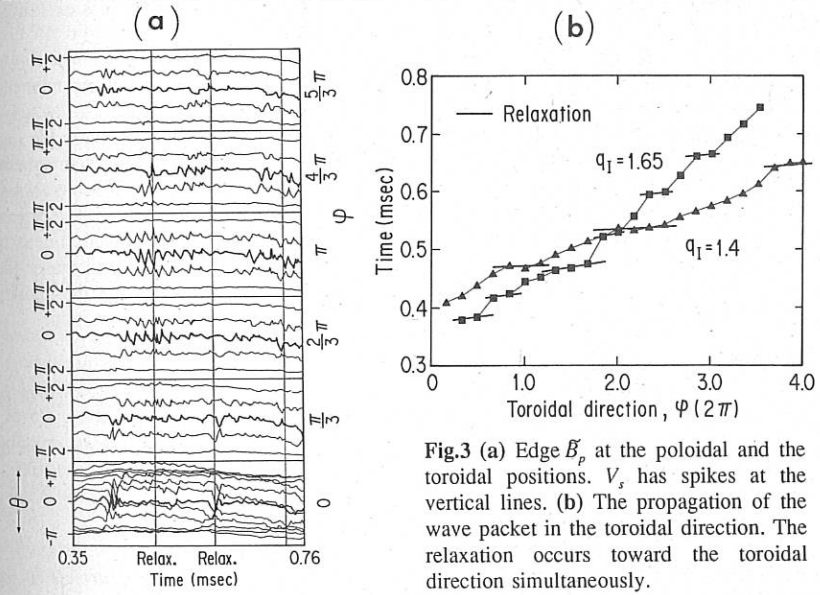

Fig.3 (a) Edge $\tilde{B}_p$ at the poloidal and the toroidal positions. V_s has spikes at the vertical lines. (b) The propagation of the wave packet in the toroidal direction. The relaxation occurs toward the toroidal direction simultaneously.

deformation affects slightly on q profile or one turn voltage and then the radiation flux or thermal flow does not increase by the deformation. One of causes of the edge deformation is the nonuniformity of the magnetic surface against the tube wall. The mode of n=6,7 may be caused by shell cut of 6 sections. When button limiters were fixed on the wall surface, the period was short and continuous. The confinement was 2-3 times improved by taking off the button limiters and smoothing the tube surface.

6. Relaxation oscillation

The relaxation oscillation with the q profile change is observed with the toroidal rotating deformations. It can be distinguished from the magnetic deformations by the difference of the propagating speed. V_s has the large spikes at the relaxation transition, which is shown in Fig.3(a) by the vertical lines. It occurs every 1~3 turn, as shown in Fig.3(b). The relaxation occurs simultaneously over the 1/3 of full torus. At first, the q relaxation, that is, the magnetic flux reconnection, occurs at a certain point of the toroidal direction and the flux change propagates along the magnetic field line by Alfven time (~1μsec). When the deviation is not so large, the magnetic flux change may not be necessary to occur over the full torus. When q_l decreases, the period of the relaxation becomes shorter, but the energy loss power at each relaxation is almost the same, and then the global energy confinement deteriorates. Near the low q limit, the period becomes one rotating time of the toroidal direction, the edge magnetic deformation is from the wave packet to small continuous pulses. As the exhaust energy is roughly same in every pulse, the threshold energy of the relaxation may be the same and the plasma may be in the high β limit. These phenomena may be recognized to be a kind of ELMs. In the case that q profile is carefully controlled to be the relaxed state, the relaxation oscillation disappears, and consequently, the plasma without particle loss and with a slight energy loss is obtained and then good confinement is established, in spite of that the magnetic edge deformation still exists and is rotating and the density fluctuations exist near the edge region.

7. Conclusion

The edge density profile of the high β very low q plasma has a sharp boundary near the edge when q_l decreases. The frequencies of the edge fluctuations are related to the edge density gradient. The edge magnetic deformation, which resembles a ballooning mode and is a wave pocket caused by a relaxation process, propagates in the toroidal ion diamagnetic direction. The magnetic deformation does not cause so large energy and particle losses, because one turn voltage or thermal flux does not increase. However, the high β very low q plasma has a specific q and density profiles whose current density and the electron density profile are broad. The plasma relaxes to the state always. The relaxation process causes the energy and particle losses. At the process, the q profile changes quickly and the density profile changes dynamically. The conducting shell may balance the dynamic motion.

REFERENCE

/1/ KIYAMA, S., et al., *in Plasma Physics and Controlled Nuclear Fusion Research (Proc.of 10th Int.Conference London, 1984)* Vol.1, IAEA, Vienna (1984) p.393.
/2/ HAYASE, K., et al., *in Plasma Physics and Controlled Nuclear Fusion Research (Proc.of 11th Int.Conference Kyoto, 1986)* Vol.2, IAEA, Vienna (1986) p.563.
/3/ KIYAMA, S., et al., Bull. Electrotech. Laboratory **50** (1986) 95.
/4/ KIYAMA, H., et al.,Bull. Electrotech. Laboratory **55** (1991) .
/5/ TAYLOR, J.B., Plasma Physics and Controlled Fusion **27** (1985) 1439.
/6/ KIYAMA, H., et al., *in Plasma Physics and Controlled Nuclear Fusion Research (Proc.of 12th Int.Conference Nice, 1988)* Vol.1, IAEA, Vienna (1989) p.437.

FLUCTUATIONS AND TRANSPORT IN A TOKAMAK WITH HIGH MHD ACTIVITY

Maria Vittoria A.P. Heller, Raul M. Castro, Iberê L. Caldas,
Ruy P. da Silva, Zoezer A. Brasilio, TBR-1 Team
Institute of Physics, University of São Paulo
C.P. 20516, 01498 São Paulo, S.P., Brazil

The purpose of our investigation is to characterize the local statistical space/time properties of the turbulence, observed in the plasma edge of TBR-1, a small tokamak with high MHD activity and turbulence, and to estimate directly the effect of turbulence on particle transport. The edge potential and density fluctuations were measured with Langmuir probes and the edge magnetic fluctuations with magnetic probes. Radial profiles of temperature and density were measured with a triple probe [1]. The particle flux is outward and occurs mainly in the frequencies typical of macroscopic MHD oscillations. Thus, there is an unusual superposition between the Mirnov and turbulent fluctuation spectra, that may contribute to elucidate any possible influence of magnetic oscillations on the electrostatic transport observed at plasma edge.

TBR-1 is an ohmically heated tokamak (minor radius $a = 8$ cm, $R = 30$ cm). For the reported experiments, the machine was operated with a central electron temperature $Te(0) \cong 200$ eV , central density $n(0) \cong 6.10^{12}$ cm^{-3}, plasma current $I_p \cong 8.5$ kA, toroidal field $B_\phi \cong 0.4$ T (corresponding to a safety factor $q(a) \cong 5$).

A square array of four single Langmuir probes, separated both toroidally and poloidally by 2 mm, was located at the top of the tokamak, along the plasma centerline and was used to measure density and potential fluctuations [2]. The effect of temperature fluctuations is neglected. The poloidal and radial components of magnetic oscillations were measured, near the Langmuir probes, by a set of four coils radially separated (two for poloidal components and the others for radial components [3]). The signals were digitized at 1 MHz. The data presented (averaged over four consecutive shots) were obtained for driving intervals of approximately 2.0 ms ; digital spectral analysis, based on a correlation technique developed by Powers and collaborators, was used to reduce the information contained in the time series of $\tilde{n}(t)$, $\tilde{\varphi}(t)$, $\dot{\tilde{B}}_\theta(t)$ and $\dot{\tilde{B}}_\phi(t)$.

The edge density and temperature are in the range $n \cong 0.5 - 5.0 \times 10^{11}$ cm^{-3}, $Te \cong 5 - 40$ eV and $Ti \cong 2Te$. In the interval $0.87 < r/a < 1.1$ the density scale lenght is $L_n \cong 1.1$ cm, whereas the temperature scale lenght is $L_{Te} \simeq 1.0$ cm. Fluctuation profiles were estimated from probe measurements of $\tilde{n}/\langle n \rangle$ and $e\tilde{\varphi}/kTe$ (space potential was computed from floating potential) their root-mean-square fluctuations levels are higher than those observed in other tokamaks, Fig. 1. The different radial dependence of these variables indicates that the linearized Boltzmann relation is not satisfied.

The radial induced particle flux Γ was estimated from the correlation between $\tilde{n}$ and $\tilde{\varphi}$ [2]. A particle flux Γ results from $\langle \tilde{n}\tilde{v}_r \rangle$, where $\tilde{v}_r$ is the fluctuating radial velocity given by $\tilde{E}_\theta/B_\phi \rightarrow ik_\theta\tilde{\varphi}/B_\phi$. Fig. 2 shows the radial profile of fluctuations induced particle flux with a maximum at the location where $\tilde{n}$ and $\tilde{\varphi}$ are maximum.

From the $S(k,\omega)$ function computed with the two point correlation technique using two floating potential signals [2,4], we determine the poloidal velocity of the fluctuations. Fig. 3 shows the measured radial profile of poloidal velocity for $\tilde{\varphi}$ fluctuations. As it has been reported [5] the values of v_{ph} are of the same order of magnitude than the diamagnetic drift velocity and the same direction of the ion diamagnetic drift velocity in the edge plasma.

The poloidal $S(k,\omega)$ spectra are broad and asymmetric about the $k_\theta = 0$ axis [2]. The fluctuation power is confined to frequencies $\omega/2\pi < 150$ KHz and wave-numbers $0 < k_\theta < 3.5$ cm^{-1}. As usually reported, also the poloidal spectra are broader than the toroidal ones. Fig. 4 shows typical frequency spectra for $\tilde{B}_\theta$ and $\tilde{B}_r$ at $r/a = 1.16$. The spectra of $\dot{\tilde{B}}_\theta$ and $\dot{\tilde{B}}_r$ observed in the scrape-off layer are similar for different radial positions except for the lower relative level of high frequency components nearer the wall.

The relationship between Langmuir and magnetic probes measurements was investigated by computing the cross-correlation and coherence between signals measured by two probes radially separated by 2.3 cm . In fig. 5 we see the coherence between $\dot{\tilde{B}}_\theta$ and $\tilde{n}$ at various positions of the electrostatic probe, together with the correspondent resolved particle fluxes for the same positions. In these figures the coherence is not high, but seems to be better for values that correspond to typical Mirnov oscillation frequencies (values around 50 KHz) observed in TBR-1 [6]; this is observed even with the Langmuir probe beyond the limiter.

In conclusion, measurements of broadband density, potential, and magnetic fluctuations at the plasma edge presented in this paper illustrate some distinguishing features under ohmic conditions and high MHD activity, typical of TBR-1 tokamak discharges. The strenght of the turbulence in TBR-1 is higher than in other tokamaks. The $\dot{\tilde{B}}_\theta$ and $\dot{\tilde{B}}_r$ spectra are similar but the radial profiles of their amplitudes are different and seem to be determined by Mirnov oscillations. The particle flux resulting from $\tilde{n}$ and $\tilde{\varphi}$ is outward, limited to frequency lower than 100 KHz. In our results there is a partial superposition of the $\dot{\tilde{B}}_\theta$ and $\tilde{n}$ spectra at the Mirnov frequencies and this could influence the $\tilde{n}\tilde{\varphi}$ phase difference at these frequencies and, consequently, increase the transport in these frequency range. The high MHD activity in our discharges creates a stochastic magnetic field in the plasma edge and propagation along this stochastic field could contribute to particle field line transport.

References

1. Chen S.L., Sekiguchi T., *J. Appl. Phys.* **36**, 2363 (1965).
2. Levinson S.J., Beall J.M., Powers E.J., Bengtson R.D., *Nuclear Fus.* **24**, 527 (1984).
3. Kim Y.J., Gentle K.W., Ritz Ch.P., Rhodes T.L., Bengtson R.D., *Phys. Fluids* **B3**, 674 (1991).
4. Hidalgo C., Hanis J.H., Uckan T., Bell J.D., Carreras B.A., Dunlop J.L., Dyer G.R., Ritz Ch.P., Wootton A.J., Meier M.A., Rhodis T.L., Carter K., *Nuclear Fus.* **31**, 1471 (1991).
5. Lin H., Ph. D. Dissertation, Report FRCR#401 (1991).
6. Vannucci A., Nascimento I.C., Caldas I.L., *Plasma Phys. Contr. Fus.* **31**, 147 (1989).

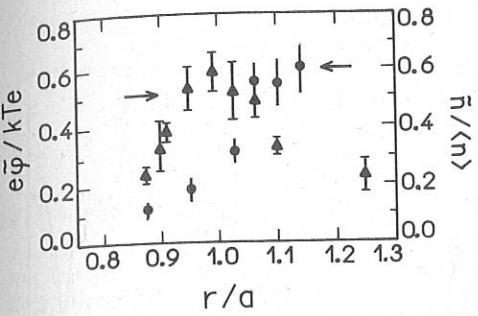

Fig. 1. Radial dependences of the normalized rms fluctuating amplitudes of potential $e\tilde{\varphi}/kTe$ and density $\tilde{n}/\langle n \rangle$.

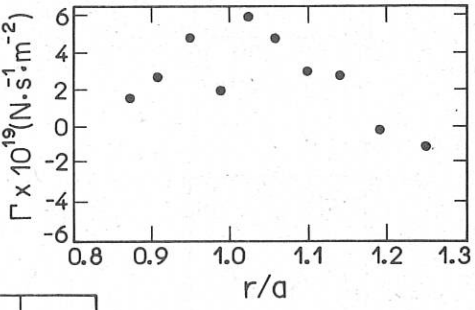

Fig. 2. Radial profile of fluctuation induced particle flux Γ.

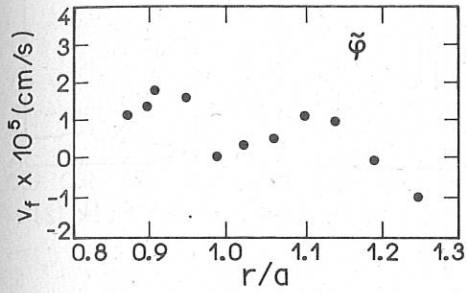

Fig. 3. Radial dependence of the fluctuation phase velocities for $\tilde{\varphi}$.

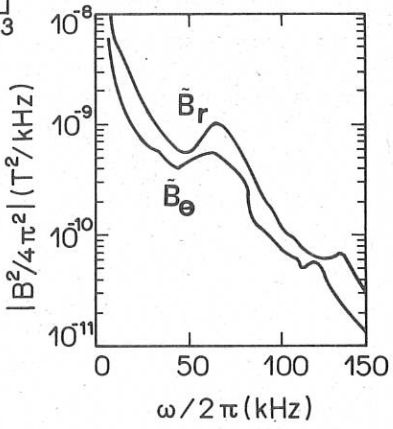

Fig. 4. Typical frequency spectra for magnetic fluctuations of $\tilde{B}_\theta$ and $\tilde{B}_r$ at $r = 9.3$ cm.

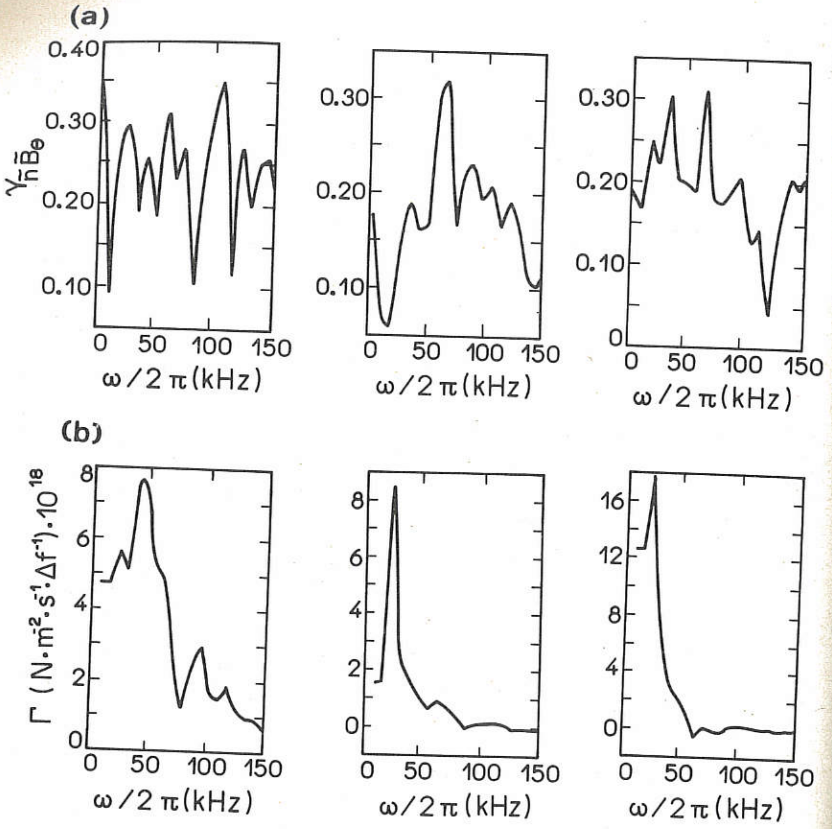

Fig. 5. Coherency between density fluctuations and magnetic fluctuations, distance between the probes 2.3 cm, at various positions of the electrostatic probe (r/a = 0.95, 0.99, 1.02, from left to right) (a). Particle transport spectrum at the same positions (b).

Kinetic Instabilities in a Plasma in $\vec{E} \times \vec{B}$ Fields

M. Shoucri, P. Bertrand[1], A. Ghizzo[1], G. Knorr[2]

Centre Canadien de Fusion Magnétique
Varennes, Québec, Canada, J3X 1S1

1 Introduction

Anomalous particle and energy transport at the plasma edge of a tokamak is caused by turbulent fluctuations. The physical nature of these low frequency fluctuations need to be identified for a self-consistent transport theory to be developed. These low frequency fluctuations are thought to be generated by instabilities due to $\vec{E} \times \vec{B}$ drift. In this work, we study surface waves at the plasma edge in $\vec{E} \times \vec{B}$ fields, and the problem of the ion-temperature-gradient instability (ITG) in a quasi-neutral plasma.

2 Unstable Surface Waves

Surface waves [1] exist at a plasma edge. We use the gyro-averaged Vlasov equation to study the problem of the linear stability of surface waves at the edge of plasmas in $\vec{E} \times \vec{B}$ fields. A similar problem has been previously studied using fluid equations, [2]. The gyro-averaged Vlasov equation is written as follows [3]:

$$\frac{\partial F}{\partial t} + \nabla . \left(v_{\|} \hat{b} + + J_o \bar{v}_{E \times B} \right) F - \frac{e}{m} \frac{\partial}{\partial v_{\|}} F \hat{b} . \nabla J_o \varphi = 0 \qquad (1)$$

F $(\vec{R}, v_{\|}, v_{\perp}, t)$ is the gyrophase-independent part of the distribution function, $\vec{v}_{E \times B} = c (\hat{b} \times \nabla \varphi)/B$, $\hat{b}$ is the unit vector in the direction of the magnetic field. J_o is a linear operator which carries out the gyro-averaging of the field:

$$J_o \left(k_{\perp} \frac{v_{\perp}}{\omega_{ci}} \right) = \frac{1}{2\pi} \int_o^{2\pi} d\theta \, e^{i k_{\perp} \frac{v_{\perp}}{\omega_{ci}} \cos \theta} \qquad (2)$$

$$\nabla^2 \varphi = -4\pi e (\bar{n}_i - n_e) \; ; \; \bar{n}_i = \int d\vec{v} \, J_o F \qquad (3)$$

Similar equations hold for the electrons with the finite gyro-radius being neglected. Subscripts $(\|)$ and $(\perp)$ denote the direction parallel and perpendicular to the magnetic field. We consider the case where the magnetic field is in the z-direction and is uniform, with a uniform neutral plasma filling the half-space $x < 0$, vacuum in the region $x > 0$ and an interface at $x = 0$. (See Ref. [4] for the case with a linear variation in density). The equilibrium solution for Eq.(1) for $x < 0$ has $\varphi = 0$, with the distribution function F given by a Maxwellian:

$$F = f_o(x, v_z) \frac{m}{2\pi T} e^{-m \, v_{\perp}^2 / 2T} \qquad (4)$$

The linearization of Eq. (1) with a perturbation $e^{-i\omega t + i k_z z + i k_y y}$ leads for the perturbed distribution functions of the ions:

[1] Physique théorique, Université de Nancy, France
[2] Dept. of Physics, University of Iowa, Iowa City, Iowa, U.S.A.

$$\delta f_i = \frac{i}{-\omega + k_z v_z}\left[-ik_y e^{-k_y^2\rho_i^2/2}\frac{c}{B}\delta\varphi_k\frac{\partial f_{oi}}{\partial x} - ik_z\frac{e}{m_i}\delta\varphi_k e^{-k_y^2\rho_i^2/2}\frac{\partial f_{oi}}{\partial v_z}\right] \quad (5)$$

ρ_i is the ions gyro-radius. We have a similar equation for the electrons, where the index i is replaced by e, $\rho_e = 0$, and the last term on the right of Eq. (5) has a + sign in front of it.

Poisson equation for the perturbed potential $\delta\varphi_k$ is written after substitution for $\delta\bar{n}_i$ and δn_e, and neglecting terms of order $\rho_i^2\frac{\partial^2}{\partial x^2}$:

$$\begin{aligned}\frac{\partial^2\delta\varphi_k}{\partial x^2} - k_z^2\delta\varphi_k - k_y^2\delta\varphi_k = -\delta\varphi_k\Bigg\{&4\pi e\frac{ck_y}{B}\,e^{-k_y^2\rho_i^2}\int\frac{dv_z}{-\omega+k_zv_z}\frac{\partial f_{oi}}{\partial x}\\ -\ &4\pi e\frac{ck_y}{B}\int\frac{dv_z}{-\omega+k_zv_z}\frac{\partial f_{oe}}{\partial x}\Bigg\}\\ -\ \delta\varphi_k\Bigg\{&\frac{4\pi e^2k_z}{m_i}e^{-k_y^2\rho_i^2}\int\frac{dv_z}{-\omega+k_zv_z}\frac{\partial f_{oi}}{\partial v_z}\\ +\ &\frac{4\pi e^e k_z}{m_e}\int\frac{dv_z}{-\omega+k_zv_z}\frac{\partial f_{oe}}{\partial v_z}\Bigg\}\end{aligned} \quad (6)$$

For the uniform plasma in the region $x < 0$, we assume a Maxwellian distribution in a uniform plasma:

$$f_{oi,e} = n_{oi,e}\left(\frac{m_{i,e}}{2\pi T_{i,e}}\right)^{1/2} e^{-m_{i,e}v_z^2/2T_{i,e}} \quad (7)$$

A solution of Eq. (6) for $x < 0$ is given by:

$$\delta\varphi_k = Ae^{+Kx} \qquad x < 0 \quad (8)$$

$$\text{with} \quad K^2 = k_z^2 + k_y^2 + \frac{\omega_{pi}^2}{v_i^2}e^{-k_y^2\rho_i^2}\left(1+\zeta_i Z(\zeta_i)\right) + \frac{\omega_{pe}^2}{v_e^2}\left(1+\zeta_e Z(\zeta_e)\right) \quad (9)$$

$v_{i,e} = T_{ie}/m_{i,e}$ and $\omega_{pi,e}$ is the plasma frequency and $\zeta_{i,e} = \omega/\sqrt{2}k_z v_{i,e}$
For $x > 0$, the solution is given by:

$$\delta\varphi_k = Be^{-\sqrt{k_y^2+k_y^2}x} \quad (10)$$

The boundary conditions at $x = 0$ consist in the continuity of the potential $\delta\varphi_k$, and the discontinuity in the derivative of $\delta\varphi_k$ at $x = 0$ is calculated from Eq. (6) and is given by:

$$\left[\frac{\partial\delta\varphi_k}{\partial x}\right]_{x=0-}^{x=0+} = -\delta\varphi_k\left\{4\frac{\pi eck_y}{B\sqrt{2}}\frac{n_{oi}}{v_i}\frac{\sqrt{\pi}}{k_z}\,e^{-k_y^2\rho_i^2}\,Z(\zeta_i) - 4\pi e\frac{ck_y}{B\sqrt{2}}\frac{n_{oe}}{v_e}\frac{\sqrt{\pi}}{k_z}Z(\zeta_e)\right\}_{x=0} \quad (11)$$

Equations (10) and (11) leads to the dispersion relation

$$-\sqrt{k_z^2+k_y^2} - K = -4\pi\frac{eck_y}{B\sqrt{2}}\frac{n_{oi}}{v_i}\frac{\sqrt{\pi}}{k_z}\,e^{-k_y^2\rho_i^2}\,Z(\zeta_i) + 4\pi\frac{eck_y}{B\sqrt{2}}\frac{n_{oe}}{v_e}\frac{\sqrt{\pi}}{k_z}Z(\zeta_e) \quad (12)$$

We assume $k_y >> k_z$. Also with $T_i \approx T_e$, we have $v_e >> v_i$. We can find the approximate solution for the real part ω_r and imaginary part ω_i of the frequency ω, under the condition $\zeta_e << 1$ and $\zeta_i >> 1$. We consider the case when $\omega_{pi}/\omega_{ci} \sim 1$. Then $\omega_{pe}/\omega_{ce} \sim \sqrt{m_e/m_i}$. This, together with $k_y >> k_z$ and $\frac{\omega_{pi}}{k_y v_i} > 1$ leads to a root of Eq. (12):

$$\omega_r \approx 0 \; ; \; \frac{\omega_i}{\sqrt{2} k_z v_e} \approx \frac{1}{\sqrt{\pi}} \, e^{-k_y^2 \rho_i^2} \tag{13}$$

We have also assumed $k_z/k_y \ll \omega_{pe}/\omega_{ce}$. The condition $\zeta_e << 1$ and $\zeta_i >> 1$ satisfied by the solution in Eq. (13), provided the finite ion gyro-radius effect with $k_y \rho_i \sim 1$ is included. Thus the inclusion of the ion gyro-radius ρ_i allows unstable surface modes to exist when the wavenumber k_z along the external magnetic field is different from zero.

3 ITG Instability in Inhomogeneous Quasi-Neutral Plasmas

This instability is usually calculated solving the local dispersion relation of the drift-kinetic Vlasov equation in an inhomogeneous neutral plasma. However, experimental results indicate the presence of inhomogeneous equilibrium electric fields at the plasma edge. It is the purpose of the present work to derive the local dispersion relation of these ion-temperature-gradient modes in a quasi-neutral plasmas in the presence of equilibrium electric fields [5].

Equation (1) admits equilibrium solutions function of one space variable; as indicated in Eq.(4). The electric field associated with this equilibrium is given by

$$\frac{\partial E_{ox}{}^{(x)}}{\partial x} = 4\pi e \left(n_i(x) - n_e(x) \right) \; ; \; n_{i,e}(x) = \int_{-\infty}^{\infty} f_{i,e}(x, v_z) \, dv_z \tag{14}$$

We neglect the ion gyro-radius. It is easy to verify that Eq. (14) gives a self-consistent equilibrium solution for Eq. (1). We assume $f_{oi,e}$ to be given by a local Maxwellian:

$$f_{oi,e}(x, v_z) = n_{i,e}(x) \left(\frac{m_{i,e}}{2\pi T_{i,e}(x)} \right)^{1/2} e^{-m_{i,e} v_z^2 / 2 T_{i,e}(x)} \tag{15}$$

The electron distribution function perturbations $\delta f_{i,e}$ are given by:

$$\delta f_{i,e} = \frac{i}{-\omega + k_z v_z - k_y c E_{ox}/B} \left[\frac{cE_y}{B} \frac{\partial f_{oi,e}}{\partial x} \pm \frac{eE_z}{m_{i,e}} \frac{\partial f_{oi,e}}{\partial v_z} \right] \tag{16}$$

The local dispersion relation is derived by imposing the quasi-neutrality condition:

$$\delta n_e = \delta n_i \; , \text{ i.e. } \int \delta f_i dv_z = \int \delta f_e dv_z \tag{17}$$

We get the following local dispersion relation:

$$1 + \left[\zeta_i - \zeta_{*i} \left(1 - \frac{\eta_i}{2} + \eta_i \zeta_i^2 \right) \right] Z(\zeta_i) - \eta_i \zeta_{*i} \zeta_i$$

$$= \frac{T_i}{T_e} \frac{n_e}{n_i} \left\{ -1 + \left[-\zeta_e - \zeta_{*e} \left(1 - \frac{\eta_e}{2} + \eta_e \zeta_e^2 \right) \right] Z(\zeta_e) - \eta_e \zeta_{*e} \zeta_e \right\} \tag{18}$$

$$\text{where} \quad \zeta_{i,e} = \frac{\omega + k_y\, c\, E_{ox}/B}{\sqrt{2} k_z v_{i,e}} \; ; \; \zeta_{*i,e} = \frac{\omega_{*i,e}}{\sqrt{2} k_z v_{i,e}} \; ; \; \eta_{i,e} = L_{ni,e}/L_{Ti,e} \tag{19}$$

$$\omega_{*i,e} = \left(\frac{c\, T_{i,e}}{e\, B_o} k_y / L_{ni,e}\right) \; ; \; \frac{1}{L_{ni,e}} = \frac{1}{n_{i,e}} \frac{\partial n_{i,e}}{\partial x} \; ; \; \frac{1}{L_{Ti,e}} = \frac{1}{T_{i,e}} \frac{\partial T_{i,e}}{\partial x} \tag{20}$$

Eq. (18) is the local dispersion relation usually derived for inhomogeneous neutral plasma ($E_{ox} = 0$) [6]. It is also valid for a nonneutral plasma ($E_{ox} \neq 0$), provided $\zeta_{i,e}$ contains the term $ck_y\, E_{ox}{}^{(x)}/B$. For $T_i \sim T_e$, we have $v_e >> v_i$. We restrict ourselves to the case when $\zeta_e << 1$. There is a marginal stability limit $\eta_i \geq 2$ for the solution of Eq. (18). If we denote by ω_i and ω_r the imaginary and real part of the frequency ω, we get for $\zeta_i << 1$:

$$\frac{\omega_i}{\sqrt{2} k_z v_i} \approx \frac{\sqrt{\pi}}{4} (\eta_i - 2) \; ; \; \omega_r \approx -cky\, E_{ox}/B \tag{21}$$

the unstable mode has a phase velocity equal to the local $\vec{E} \times \vec{B}$ drift. For $\zeta_i >> 1$, we have:

$$\omega_r + k_y\, c\, E_{ox}{}^{(x)}/B \approx \omega_{*i} \left(\frac{\eta_i}{2} - 1\right) \frac{T_e n_e}{T_i n_i} \tag{22}$$

$$\frac{\omega_i}{\sqrt{2} k_z v_i} \approx -\pi\, \zeta_i^2\, e^{-\zeta_i^2} \left[1 - \zeta_{*i}\, \eta_i\, \zeta_i\right] \frac{T_e n_e}{T_i n_i} \tag{23}$$

The imaginary part in Eq. (23) is exponentially small. One can substitute for ζ_i in Eq. (23) as a first approximation from the solution in Eq. (22). An unstable solution exists for

$$1 - \zeta_{*i}\, \eta_i\, \zeta_i = 1 - \zeta_{*i}^2\, \eta_i \left(\frac{\eta_i}{2} - 1\right) \frac{T_e n_e}{T_i n_i} < 1 \tag{24}$$

which can be easily satisfied since usually $T_e > T_i$, $n_e > n_i$, provided $\eta_i > 2$. In this case:

$$\frac{\omega_i}{\sqrt{2} k_z v_i} \approx \pi \zeta_{*i}^2 \left(\frac{\eta_i}{2} - 1\right)^2 \left(\frac{T_e n_e}{T_i n_i}\right)^2 \left[\zeta_{*i}^2\, \eta_i \left(\frac{\eta_i}{2} - 1\right) \frac{T_e n_e}{T_i n_i} - 1\right] \exp\left[-\zeta_{*i}^2 \left(\frac{\eta_i}{2} - 1\right)^2 \frac{T_e^2 n_e^2}{T_i^2 n_i^2}\right]$$

The above equation is exponentially small. However, for those parameters for which:

$$\zeta_{*i} \left(\frac{\eta_i}{2} - 1\right) \frac{T_e n_e}{T_i n_i} \sim 2 \text{ to } 3 \tag{25}$$

the growth rate can be made finite.

References

1 Shoucri M. and Kitsenko A.B., (1968) Plasma Phys. 10, 633.
2 M. Shoucri, J.Appl.Phys. 47, 518 (1976); G. Knorr, Phys. Fluids 18, 1546 (1975).
3 W.W. Lee, Phys. Fluids 26, 556 (1983).
4 M. Shoucri, Plasma Phys. 19, 294 (1977).
5 S. Migliuolo and A.K. Sen, Phys. Fluids B2, 3047 (1990).
6 G.W. Hammett and F.W. Perkins, Phys. Rev. Lett. 64, 3019 (1990).

Coherent Vortical Structures in Two-Dimensional Plasma Turbulence

J.P. Lynov, A.H. Nielsen, H.L. Pécseli[1] and J. Juul Rasmussen
Association EURATOM-Risø National Laboratory,
Optics and Fluid Dynamics Dept., Risø, DK-4000 Roskilde, Denmark

Low-frequency, flute-type electrostatic plasma fluctuations propagating across a strong, homogeneous magnetic field are studied experimentally and numerically. In particular the formation and dynamics of coherent vortex-like structures appearing in the background of wide-band turbulent fluctuations are investigated.

The experimental investigations were performed in the Risø Q-machine. The fluctuations were generated by the Kelvin-Helmholtz instability due to a strongly sheared azimuthal flow in the residual plasma (the scrape-off layer) surrounding the main plasma column /1-3/. The radially varying dc-electric field $\mathbf{E}_0(r)$ was controlled by the bias on a limmiting aperture inserted perpendicularly to the plasma column near the plasma source (i.e. the hot plate). The fluctuations in the floating potential and density were measured by small 1 mm diam. platinum probes. Fluctuating electric field components were measured by taking the potential difference between two closely spaced probes. The fluctuations were characterized by a broad frequency spectrum for a weak radial electric field $\mathbf{E}_0$, whereas narrow peaks appeared for strong, localized radial electric fields /2,3/.

We demonstrated the presence of relatively long-lived coherent vortical structures by employing a conditional sampling technique /3/. The basic idea of this technique, which can reveal the averaged properties of large structures appearing in the turbulence, is described in Ref. 4. For the present investigations we recorded simultaneously two time series of 200 ms duration obtained with a sampling rate of 125 kHz and an 8-bit resolution. One of the series, the reference, came from the azimuthal electric field component, E, the other from the potential fluctuations, ϕ, measured by a movable probe. Such pair of time series were obtained for positions in a grid of 9×13 points with a 3 mm spatial resolution in the plane perpendicular to the magnetic field. The conditional averaging was subsequently performed numerically for each probe position. The space-time evolution of the conditional averaged potential is shown in Fig. 1 for typical plasma parameters with a relatively strong radial electric field. The formation, propagation and beginning decay of a large monopole-like structure is clearly noticable. The propagation velocity is approximately 250 m/s, which is compatible with the averaged plasma $\mathbf{E}_0 \times \mathbf{B}_0/B_0^2$-velocity in the scrape-off layer. Coherent vortical structures have been observed for varying plasma parameters /3/. Depending on the parameters the dominant structures can appear as monopole or dipole vortices. Monopoles with negative potential, i.e. they have a rotation in the same direction as the bulk plasma rotation in the scrape-off layer, tend to dominate in the cases with strong radial electric fields.

The properties (such as growth or damping) of the averaged vortical structures obtained by the conditional sampling method need not reflect the properties of the vortices in individual realizations. Thus, an apparent damping of the averaged structures may simply be caused by a "smearing-out" due to a spread in the velocities of the individual structures. This problem was resolved by performing a coincidence counting of the occurrence of local extrema in the fluctuating potential signals at two points in space separated by a distance, L, in the direction of propagation. In Fig. 2 we show the distribution of time delays Δt between local minima occurring at two probes (with L=14.6 mm), subject to the condition that the minimum at

[1]Permanent address: Institute of Physics, University of Oslo, Blindern, N-0316 Oslo 3, Norway

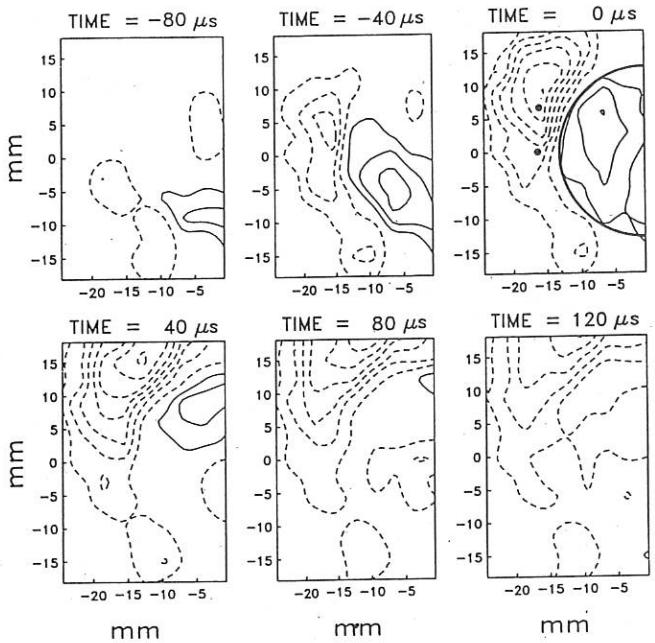

Figure 1: Space-time evolution of the conditional averaged potential. The imposed condition was that E should exceed the value $E_* = 1.5\sigma$ and that $\partial_t E > 0$. Positive potentials are given with full lines, negative ones with dashes lines. The contour inteval is 0.025 V. The heavy semi-circle in the panel for $t = 0\,\mu$s indicates the projection of the aperture opening. Plasma conditions were $n_0(r = 0) = 2 \cdot 10^{15}\,\mathrm{m}^{-3}$ and $B_0 = 0.35$ T.

the first probe is smaller than $\phi_* = -\sigma, -1.5\sigma$ or -2σ , respectively. Here σ denotes the RMS value of the fluctuations. Subsequently the signal from the other probe is searched in a suitably chosen time interval for the deepest minimum, which defines Δt. The distributions obtained for the three values of ϕ_* are essentially identical giving an averaged value of the velocity corresponding to 300 m/s. From results as those shown in Fig. 2 we have derived velocity distributions, and we observed that the potential wells, corresponding to the vortical structures, propagate with a moderate spread in velocity (for the case in Fig. 2 $\Delta V \approx 30$ m/s). Thus, it may be argued that the evolution of the conditionally averaged structures of negative potential reflect the properties of individual structures, and is not just a consequence of a spread in their velocities. For these plasma parameters, where monopolar vortices with negative potential were found to dominate, a similar analysis of the occurrences of local maxima gave a different result. Although a peak in the distribution of time delays could be discriminated, it was not significantly above the background level, and it was not possible to assign a velocity distribution for potential humps.

The formation of the large scale vortical structures is believed to be accomplished by an inverse spectral cascade, which is characteristic for two-dimensional turbulence and was studied previously for our experimental conditions/2/. The saturated turbulent spectrum

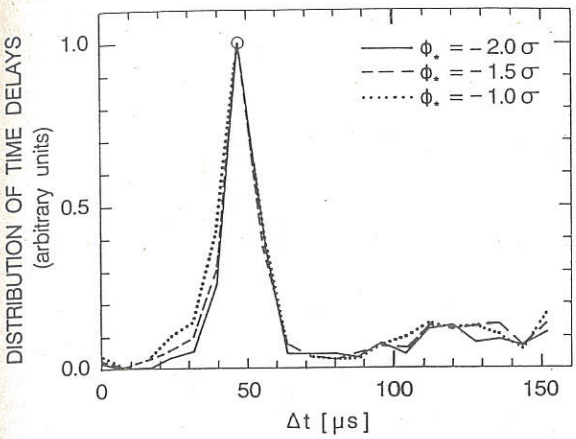

Figure 2: Distribution of time delays Δt between occurence of local potential minima at two probes seperated azimuthally by L = 14 mm. The curves are normalized by the peak value, indicated by a circle. Plasma conditions were $n_0(r=0) = 7 \cdot 10^{14}\,\mathrm{m}^{-3}$, $B_0 = 0.285$ T.

will thus be dominated by the large scale structures, and it contain little information about the linear instability, which is driving the fluctuations. The observations of the formation of large scale structures is supported by a numerical study of the nonlinear evolution of the Kelvin-Helmholtz instability on an annulus, modelling the edge rigion of the Q-machine plasma.

These investigations are based on the flute-mode equations for low-frequency electrostatic fluctuations (i.e. the frequencies are much smaller than the ion cyclotron frequency), which is equivalent to the Navier-Stokes equations for two-dimensional incompressible flows:

$$\omega_t + (\hat{z} \times \nabla\phi) \cdot \nabla\omega = \nu\nabla^2\omega, \qquad (1)$$

where the normalized potential, ϕ, takes the role of the streamfunction with the velocity given as $\mathbf{V} = \hat{z} \times \nabla\phi$, $\hat{z}$ is the unit vector in the direction of $\mathbf{B}_0$, and the vorticity, $\omega = \nabla^2\phi$, is equivalent to the charge density. Equation 1 is solved numerically in an annular geometry employing a fully de-aliased, spectral scheme /5/. The viscosity on the rigth hand side is introduced to suppress, in a controlled manner, the short wavelength ringing that is otherwise produced due to the finite spatial resolution. This viscosity may be thought of as representing damping due to finite Lamor radius effects. As initial condition we have set up a vorticity (charge) distribution corresponding to the averaged distribution in the experiments. This distribution corresponds to an azimuthal velocity with a jet-like radial profile, and a radial potential profile increasing from the inner boundary. The potential was kept at a constant, prescribed, value on the boundaries resulting in free slip boundary conditions, i.e. the radial velocity component vanished on the boundaries. The vorticity was set equal to zero on the boundaries. In Fig. 3 we show an example of the evolution of the potential. The flow quikly develops a growing short wave instability in correspondence with predictions from a linear stability analysis. However, this high mode-number instability evolves nonlinearly, demonstrating the inverse cascade behavior. This cascade is mediated by coalescence of like-signed vortices and the instability saturates when the energy is collected in large scale

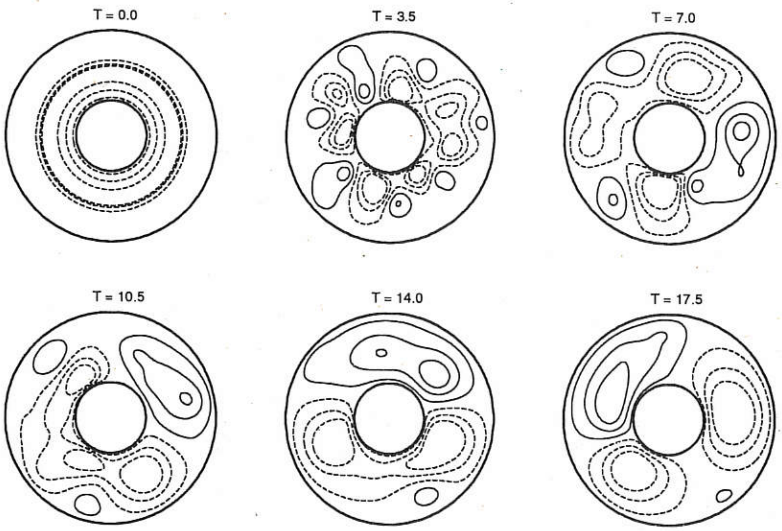

Figure 3: Space-time evolution of the perturbed potential, ϕ, for an initial unstable potential profile. The equilibrium profile $\phi_0 \sim lnr$ has been subtracted. Positive ϕ-values are shown with full lines, negative ϕ-values with dashed lines

structures. Note that for the present profile the $m = 1$ mode is *linearly* stable, while the $m = 2$ mode is only weakly unstable. Thus the saturated state is far from what would have been predicted by a quasi-linear analysis. This behavior agree qualitatively with our experimental observations, noting the obvious differences between the experiments and the simulations. In the experiments the fluctuations can be considered as constantly pumped by the instability at the high mode-numbers. In the simulations, on the other hand, we considered an initial value problem and the fluctuation level was slowly decaying due to the viscosity, while the potential profile relaxed toward the equilibrium profile with $\phi_0 \sim lnr$ resulting in a stable velocity profile $V \sim \frac{1}{r}$.

References

/1/ Kent, G.I., Jen,N.C. and Chen, F.F., Phys. Fluids **12**, 2140 (1969).

/2/ Huld, T., Iizuka, S., Pécseli, H.L. and Rasmussen, J.J., Plasma Phys. Contr. Fusion **30**, 1297 (1988).

/3/ Huld, T., Nielsen, A.H., Pécseli, H.L. and Rasmussen, J.J., Phys. Fluids **B3**, 1609 (1991).

/4/ Johnson, H., Pécseli, H.L. and Trulsen, J., Phys. Fluids **30**, 2239 (1987); Kofoed-Hansen, O., Pécseli, H.L. and Trulsen, J., Physica Scripta **40**, 280, (1989).

/5/ Coutsias, E.A., Hansen, F.R., Huld, T. Knorr, G. Lynov, J.P., Physica Scripta **40**, 270 (1989).

GUIDED ALFVEN BEAMS IN THE TORTUS TOKAMAK

R.C. Cross and D.G. Miljak

Plasma Physics Department, University of Sydney, Sydney. NSW 2006, Australia.

1. Introduction

The main function of an ICRF heating antenna is to launch a fast wave which propagates into and heats the plasma interior. However, the antenna may also generate wave modes which propagate only in the plasma edge region. In this paper, we describe observations of Alfven wave modes which propagate, in the form of a narrow beam, along magnetic field lines in the plasma edge. Several types of beam were observed, including beams composed of (a) fast Alfven surface modes, (b) propagating shear waves, (c) evanescent shear waves and (d) ion–ion hybrid modes. For all of these modes, the group velocity vector is essentially parallel to the steady **B** field.

2. Experimental arrangement

The experimental arrangement is shown in Fig.1. A very small antenna was used to deliberately excite a broad spectrum of modes, and the edge wave fields were measured with a poloidal array of 8 magnetic probes enclosed in a quartz tube surrounding the plasma at $r = 11$cm, just outside the limiter radius (10.5cm). A complete 360° poloidal profile of the b_θ wave magnetic field component was obtained by moving the probe array between successive discharges.

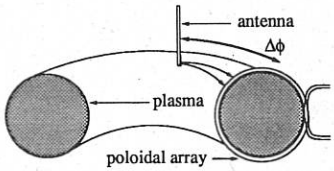

Figure 1: Schematic experimental arrangement showing beam paths from the antenna to the poloidal array

The wave frequency was varied from 11MHz to 19MHz to span a range of frequencies $0.8 < \Omega < 3.5$, where $\Omega = \omega/\omega_{ci}$ and ω_{ci} is the ion cyclotron frequency. The antenna consisted of an 8mm diameter, 4–turn coil located in a 10mm OD quartz tube inserted vertically into the plasma to $r = 11$cm. The axis of the coil was aligned parallel to **B** (b_z antenna) or perpendicular to **B** (b_θ antenna). Several such tubes were inserted to the plasma edge at different toroidal locations so that the wave phase and amplitude could be measured at different distances from the poloidal probe array. The antenna was driven at low power, about 2kW, with an antenna current of about 30A. The probes were fed to hybrid combiners to eliminate electric field pickup and then to balanced mixers to monitor the wave field amplitude and phase.

All results below were obtained in pure hydrogen plasmas or in hydrogen/deuterium gas mixtures with typical discharge conditions $B_\phi \approx 0.8$T, $I_p \approx 25$kA, $n_e \approx 2 \times 10^{19}$m^{-3} and $T_e \approx 150$eV. Since the wave field amplitude near the plasma edge is sensitive to the in–out plasma position, special efforts were made to keep the position constant during each discharge and from one discharge to the next.

3. Results at $\Omega \approx 1$ in Hydrogen

In order to assist the interpretation of results obtained in H/D mixtures, experiments were conducted in pure hydrogen plasmas near $\Omega = 1$, where the shear wave is propagating if $\Omega < 1$ and evanescent if $\Omega > 1$. The shear wave propagates as a narrow, guided beam if it is generated by a small, poloidally localised antenna [1], and is essentially transverse magnetic when $\Omega \ll 1$. Results at 13MHz are shown in Fig. 2. The toroidal field decreases by about 20% during the discharge, with the result that $\Omega < 1$ early in the discharge and $\Omega > 1$ late in the discharge. The amplitude of the b_θ component in the beam does not change significantly during the discharge for a b_θ antenna. However, for a b_z antenna, the amplitude of the b_θ component decreases significantly when $\Omega > 1$, as shown in Fig.2.

There is no phase variation of b_θ in the poloidal or toroidal directions, or with time, when $\Omega > 1$, but the beam amplitude decreases with distance from the antenna as shown in Fig 3. Consequently, the beam at $\Omega > 1$ is a transverse magnetic, evanescent shear wave beam, as observed previously [2] under conditions where $\Omega > 2$. The beam at $\Omega < 1$, observed early in the discharge, is most likely to be a propagating shear wave beam, but it is not transverse magnetic. There is a small variation of phase with time and position in the beam when $\Omega < 1$, but not as much as one would expect for a wave near resonance. The results at $\Omega < 1$ are therefore surprising, and we can offer no simple explanation, but significant phase mixing of the many modes which comprise the beam is to be expected.

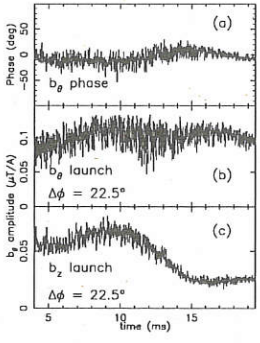

Figure 2: Beam behaviour at $\Omega \approx 1$. (a) b_θ phase. (b) b_θ antenna launch. (c) b_z antenna launch.

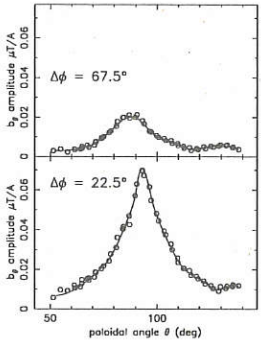

Figure 3: Evanescent beam profile at two toroidal locations. $\Omega = 1.3, H_2$ plasma

4. Results at $\Omega > 1$ in Hydrogen

Results obtained at a wave frequency of 19MHz ($\Omega = 1.8$) in a pure hydrogen plasma are shown in Figs. 4 and 5. For these results, the antenna was located at $r = 11$cm, $\theta = 135°$, where the θ coordinate is defined to be 0° on the high field side, 90° at the top of the plasma, and 180° on the low field side. A b_θ antenna was used to generate a strong beam signal, the beam being essentially transverse magnetic. The antenna was located 45° toroidally from the probe array.

Small, relatively broad peaks in the b_θ waveforms correspond to $m = +1$ fast wave eigenmodes, where m is the poloidal mode number. As described previously [2], $m > +1$ modes are predicted theoretically but are not observed experimentally, presumably because these modes are heavily damped. In addition to eigenmodes, which are observed at all locations in the plasma edge, we also observe a narrow beam which is observed only on steady magnetic field lines passing through the antenna.

Under some conditions, we also observe a second beam, as shown in Fig. 4, which emerges from the antenna at a slight angle to the first beam. The amplitude of the second beam is largest when the two beams are guided towards the outer or inner vertical walls of the vacuum vessel. The amplitude of the second beam is very sensitive to density fluctuations in the plasma edge, with the result that the b_θ waveform is noisy, containing many large amplitude spikes, as shown in Fig 5. Each spike is directly correlated with a local increase in electron density near the antenna, as measured with a Langmuir probe near the antenna. The poloidal profile of the b_θ amplitude in Fig. 4 was therefore obtained by taking a time average amplitude over a 0.2ms period. The wave phase, with respect to the antenna current, is plotted as a function of poloidal angle in Fig. 4a, for conditions where the amplitude of the second beam is large and there is no interference from eigenmodes. There is essentially no phase variation across the first beam, the phase does not vary with time, and the phase does not vary along the beam (in the toroidal direction). The amplitude of the first beam decreases with distance from the antenna. Consequently, the first beam is toroidally evanescent, with $k_\parallel^2 < 0$, and is therefore Alfven resonant. The polarisation of the beam is consistent with that expected for an evanescent shear wave beam.

The phase of the second beam varies with poloidal angle, with a slope equivalent to that of an $m = +6$ mode. Since the beam is quite narrow in the poloidal direction, it must contain a broad spectrum of integer m components, and not just an $m = +6$ component. Indeed, it is possible to synthesise the phase and amplitude structure of the beam by summing a large number of integer $m > 0$ modes, up to say $m = 20$, with an appropriate amplitude weighting factor for each mode. If a finite k_z is assumed for each mode, then the position of the peak in the beam profile shifts in the positive θ direction as z increases, as observed experimentally. Consequently, the second beam can be interpreted as a superposition of $m > 0$, finite k_z modes. These modes propagate as surface waves, and are therefore sensitive to density fluctuations in the plasma edge. The second beam is strongly attenuated, and is not observed at relatively large distances from the antenna, nor is it observed at the top or bottom of the plasma. The plasma is well separated from the top and bottom walls, whereas the wave fields in the region between the plasma edge and the vertical walls are enhanced by flux compression.

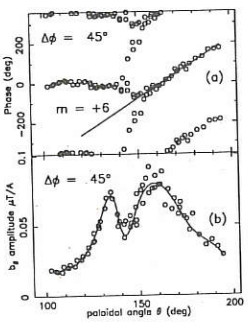

Figure 4: (a) Phase and (b) b_θ amplitude profile for conditions where a second beam appears.

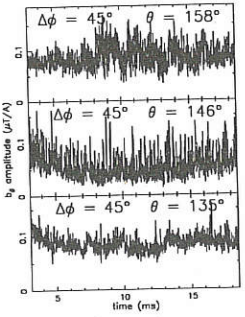

Figure 5: b_θ amplitude variation with time at three poloidal positions in the beams shown in fig 4.

5. Results at $\Omega > 1$ in H/D plasmas

Results obtained in deuterium, with hydrogen as a minority species, were very similar to those obtained in pure hydrogen plasmas. We were unable to reproduce the result obtained in Ref.[2] where it was observed that the evanescent shear wave beam is strongly attenuated at $\Omega = 2$ in a pure deuterium plasma. The minimum hydrogen concentration could not be reduced below 10% in the current series of experiments. As a result, there is a third type of beam which can propagate toroidally, at frequencies near $\Omega = 2$, due to the ion–ion hybrid wave [1], and which is easily identified by its strong phase variation with time and position. Typical b_θ amplitude and phase waveforms at $\Omega \approx 2$ are shown in Fig. 6.

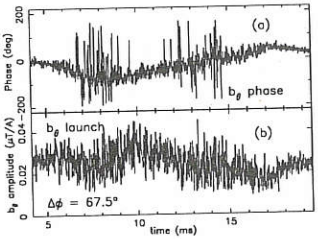

Figure 6: (a) Phase and (b) b_θ amplitude variation with time for a H/D mixture at $\Omega \approx 2, f = 13MHz$, 10% H_2

References

[1] BORG G.G. and CROSS R.C. (1987) *Plasma Phys. Contr. Fusion* **29**, 681.

[2] BALLICO M.J. and CROSS R.C. (1991) *Plasma Phys. Contr. Fusion* **33**, 1841.

MEASUREMENT OF SPUTTERING YIELDS AT THE JET BERYLLIUM AND CARBON X-POINT TILES

M F Stamp and P R Thomas

JET Joint Undertaking, Abingdon, Oxon., UK

1. Introduction

Visible spectroscopy of the X-Point tiles in JET has been used to measure the effective impurity sputtering yields from the tiles. An understanding of these yields is essential for a realistic description of impurity effects in edge modelling codes [e.g. 1,2].

An analytic model has been developed in order to gain insight into the physical processes that are important in determining the sputtering yields. The model tracks ion orbits through the sheath calculating the angles at which they strike the surface, and the consequent sputtering yields. The model illustrates that the ion temperature has a significant effect on the angle of incidence at the surface, and on the sputtering yield.

2. Experimental

Spectral lines of deuterium (D_α, D_γ), carbon (CII 6578, 6582Å) and beryllium (Be I 4407Å and Be II 4361 Å) are routinely monitored with a 1-m Czerny Turner spectrometer equipped with a linear diode array detector [3]. Plasma light emitted from in front of the upper (carbon) and lower (beryllium) outer X-point strike zones is collected by achromatic lenses and fed into the spectrometer via a quartz optic fibre. The spectrally resolved data is analysed with a multigaussian line fitting routine, to give spectral line intensities, positions and widths [4].

When the edge plasma is strongly ionising, the influx of impurity i, Γ_i, is related to the impurity spectral line intensity I_i, by $\Gamma_i = 4\pi\ (S/XB)\ I_i$, where (S/XB) is the photon efficiency for the spectral line measured. The photon efficiencies are electron temperature (T_e) dependent, and values of T_e have been taken from the JET edge database of Tagle [5].
The effective sputtering yield, Y^i_{eff}, is given by $Y^i_{eff} = \Gamma_i/\Gamma_D$ where Γ_D is the measured deuterium influx.

3. Experimental Results

Figs. 1 and 2 show the measured carbon and beryllium effective sputtering yields as a function of the edge electron temperature, T_{ed}, for a series of 3MA X-point discharges with different

volume average electron density, $<n_e>$. Data were taken only during the ohmic phases of discharges with less than about 20% carbon contamination of beryllium X-point tiles or less than 20% beryllium contamination of carbon tiles.

The carbon yield varies from 2-10% for T_{ed}= 30-100eV, and the beryllium yield from 0.4 - 15% for T_{ed} = 20-80eV. These yields show a steadily increasing trend with increasing edge temperature, which is not expected from simple sputtering models because normal incidence sputtering yields decrease at high energies.

In these discharges, the edge ion temperature was measured from the Doppler width of the "warm" D_α component [4]. The beryllium X-Point shots showed $T_{id} \sim 2 \times T_{ed}$, whilst for carbon X-points, $T_{id} \sim 1.5 \times T_{ed}$. Within the error bars ($\pm$ 25%) there was no discernable variation of T_{id}/T_{ed} with $<n_e>$. Section 5 discusses these results in conjunction with the analytic model presented in the next section.

4. Sputtering Model

The motion of ions in the plasma edge through the sheath onto a surface has been simulated by solving the equations of motion subject to a few simplifying assumptions. We firstly note that, at least for JET edge plasmas, the ion Larmor radius is always larger than the sheath thickness and that the drift speed is always greater than the thermal speed (See table 1). Therefore ions do not make complete gyrations about their guiding centre motion when they are in the sheath. The model also assumes that ions come in at glancing angles to the sheath, and that the sheath electric field only increases the ion velocity perpendicular to the surface.

T_e (eV)	T_i (eV)	N_e (m^{-3})	d (m)	ρ_i (m)	E/B (m/s)	v_i (m/s)
50	50	10^{18}	2.0×10^{-4}	4.2×10^{-4}	1.6×10^{5}	0.7×10^{5}
50	50	10^{19}	0.6×10^{-4}	4.2×10^{-4}	5.1×10^{5}	0.7×10^{5}
50	250	10^{18}	1.2×10^{-4}	9.4×10^{-4}	2.0×10^{5}	1.5×10^{5}
20	20	10^{19}	3.9×10^{-5}	2.7×10^{-4}	3.2×10^{5}	0.4×10^{5}

Table 1. Values of the sheath thickness (d), ion Larmor radius (ρ), drift velocity in the average sheath electric field (E/B) and the ion thermal velocity (v_i) for values of edge temperature and density corresponding to the extremes found in JET.

The gyratory motion of ions along glancing field lines means that the range of angles onto the sheath is constrained between two values determined by the angle of the field line, and the parallel and perpendicular ion velocities. Since T_i determines the size of the parallel velocity

and T_e determines the sheath acceleration (the sheath potential is approximately $3T_e$), it is clear that the ratio T_i/T_e is important in determining the impact angle of the ion on the surface.

This impact angle is used with the sputtering yields of Roth [6] and the angular dependency of Bohdansky [7], to calculate the distribution average sputtering yield <Y>. The effective sputtering yield is then given by

$$<Y_{eff}> = (1-\eta)\ <Y_{DI}> / (1 - \eta<Y_{II}'> - (1-\eta) <Y_{II}>)$$

where η is the fraction of impurity that returnes promptly to the surface with a reduced self-sputtering yield of $<Y_{II}'>$, and the fraction $(1-\eta)$ reaches the plasma core and returns to the surface with yield $<Y_{II}>$.

5. Model Results and Discussion

Figures 1 and 2 show the results from the model calculations for four cases:

a) $T_{id}=T_{ed}$, $\eta=0.5$.

b) $\eta = 0.5$, with experimental values of T_{id}/T_{ed}; 2 for beryllium, 1.5 for carbon.

c) Same as (b), but with doubled ion temperatures.

d) Same as (b), but with $\eta = 0.2$ for carbon, $\eta = 0.9$ for beryllium.

The figures show that increasing T_{id}/T_{ed} increases the sputtering yield at all T_{ed}, and that increasing η reduces the yield. It can also be seen that changes in η have a larger effect than changes in T_{id}/T_{ed}.

The curves (a) - (d) are too flat to be a good fit to the experimental data, but with a screened fraction $\eta = 0.2$ to 0.4, the model is a good fit to the measured experimental sputtering yields of carbon and beryllium on the JET belt limiters [8]. In the X-Point configuration screening is expected to be higher, especially at high edge densities and low edge temperatures [1,2]. The difference between the experimental data and modelled curves could therefore be explained by a density and temperature dependent η, with η varying from about 0.3 to 0.6 for carbon, and from about 0.5 to 0.98 for beryllium.

6. References

[1] M Keilhacker et al., Nucl. Fus. 31 (1991) 535

[2] G Vlases, R Simonini, 18th EPS Berlin, 1991, Vol. 3, p221.

[3] M F Stamp et al., J Nucl. Mat. 162-164 (1989) 404.

[4] M F Stamp and H P Summers, 17th EPS Amsterdam, 1990, Vol 14B p.1377.

[5] J A Tagle et al., Proceedings of the 10th PSI Conference, Monterey, April 1992.

[6] J Roth et al., J Nucl. Mat. 176-177 (1990) 132, and references therein.

[7] J Bohdansky, Nucl. Instr. Meth. B2 (1984) 587.

[8] A Hwang et al., J. Nucl. Mat. 176-177 (1990) 588.

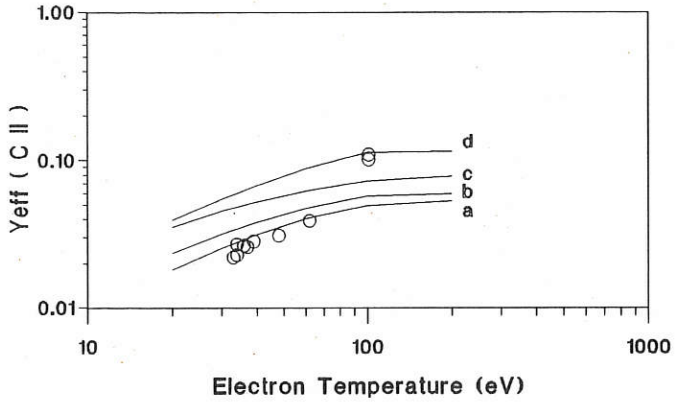

Fig. 1 The effective sputtering yield for carbon as a function of the edge electron temperature.
o - experimental data, — model predictions, see text for details.

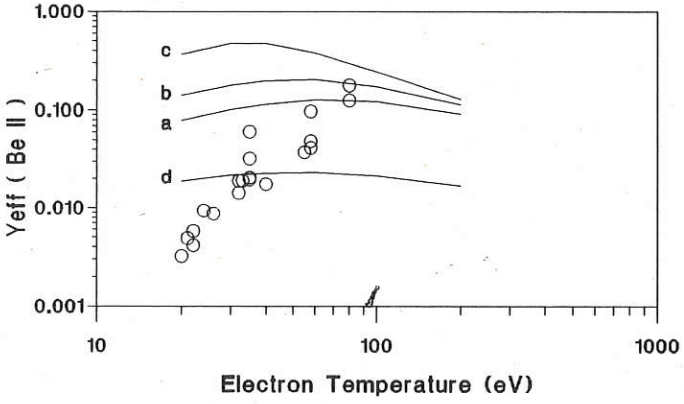

Fig. 2 The effective sputtering yield for beryllium as a function of the edge electron temperature.
o - experimental data, — model predictions, see text for details.

Radial Carbon Flux Profiles in the upper Divertor in JET at high Target Load.

H.J. Jäckel, S. Clement, M. Lesourd, J. Lingertat [1],
C.F. Maggi, G.F. Matthews, D.D.R. Summers, H.P. Summers
JET Joint Undertaking, Abingdon, Oxon OX14 3EA, U.K.
[1]*Max Planck Institut für Plasmaphysik, Garching, Germany*

Introduction: High performance plasma parameters have been achieved in JET/1/ in discharges with a closed magnetic separatrix inside the vacuum vessel, operating with one or two open divertors on top and/or bottom of the plasma cross-section. The upper divertor target material is graphite, the lower is beryllium. For the preliminary tritium experiments (PTE)/2/, carried out in november 1991, a magnetic single null (SN) configuration with an upper X-point was chosen. In preparation of the PTEs a series of hot ion mode discharges were carried out, which achieved high ion temperatures and good confinement, but were terminated in many cases by high carbon influxes from the divertor, due to high power load onto the target tiles and/or the breakdown of the retention properties of the divertor. A strong correlation can be observed between the total heating power P_{heat}, or respectively, the power conducted to the divertor target, $P_{target} = P_{heat} - P_{rad} - \dot{W}_p$, and the intensity of the carbon fluxes. Figure 1 shows the development of the total divertor carbon flux versus $\hat{E}_{target}$ for six discharges in the time window from about one second before the carbon bloom (=high avalanche-like carbon influx) till 0.2 seconds into the bloom. $\hat{E}_{target}(t_o)$ is the integrated power into the scrape-off-layer (SOL) from the time of the onset of the X-point configuration, t_{xp}, to the current time t_o, multiplied by an exponential decay function, which roughly takes into account the conductive and radiative heat losses of the target:

$$\hat{E}_{target}(t_o) = \int_{t_{xp}}^{t_o} P_{target}(t) \cdot \exp\left(\frac{t - t_o}{\tau}\right) dt$$

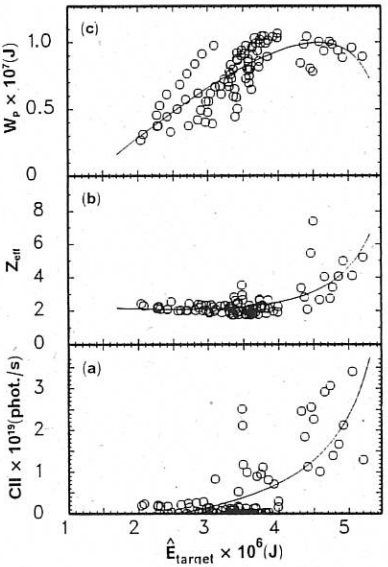

Fig. 1: *Development of $\Gamma_{C,div}$ (a), Z_{eff} (b) and W_p (c) at increasing $\hat{E}_{target}$ (see text) for a series of discharges before and during the carbon bloom.*

In figure 1 $\tau = 0.5\ s$ is assumed. At $P_{heat} \simeq 15\ MW$, as used in the PTEs, the take-off (fig.1a) of the carbon flux corresponds to a power into the scrape-off-layer $P_{SOL} \simeq 8\ MW$, causing a subsequent rise of Z_{eff} (fig.1b) and a stagnation and eventually a decay of the stored energy, W_p (fig.1c).

Experimental: The temporal evolution of the carbon fluxes and their spatial distribution can be assessed by two spectrocopic diagnostics: two duo chrome scanning VUV spectrometers and three CCD cameras, equipped with different interference filters. An array of 12 Langmuir probes in the divertor target plates provide local electron temperature and density. The VUV spectrometers scan across the divertor region using rotating mirrors at a minimum repetition time of 0.1 s and a sweep time of $\simeq$2 ms. Each spectrometer measures two spectral lines at a time. The spectral wavelength range is $100 \lesssim \lambda(\text{Å}) \lesssim 2000$. The instruments are not absolutely calibrated. Relative intensities of the carbon fluxes are mainly deduced from CII-emission (687.4 Å), deuterium fluxes from DI (1025.4 Å). The CCD-cameras use mainly CII-filters (5145 Å) for the estimate of carbon fluxes and D_α-filters for the deuterium fluxes. A time frame can be acquired every 20 ms. The cameras are calibrated and supply absolute photon fluxes. In normal divertor-plasma conditions (ie plasma not "detached") the local electron temperature, $T_{e,div}$, and density, $n_{e,div}$, derived from the Langmuir probes are taken to calculate the particle fluxes, using the respective excitation and ionisation rate coefficients/3/. In cases where $T_{e,div}$ and $n_{e,div}$ are not available, the photon fluxes are used to get a qualitative picture of the divertor particle fluxes. At low to moderate target load the CCD and VUV-spectrometer measurements agree qualitatively. At high target load the CCD images are often blurred by thermal radiation due to a thermal break-through of the interference filters.

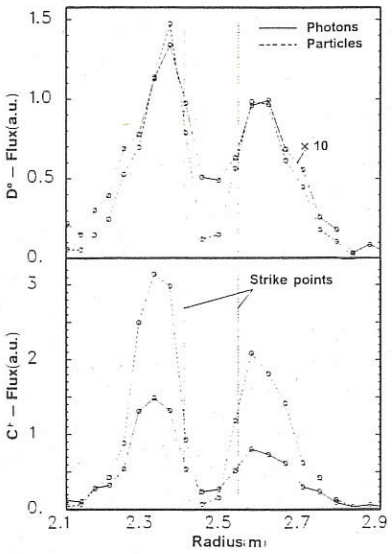

Fig. 2: *Relative intensities of CII and DI emission and of particle fluxes across the divertor region (pulse 25977). The vertical dotted lines mark the two strike points of the seperatrix on the target.*

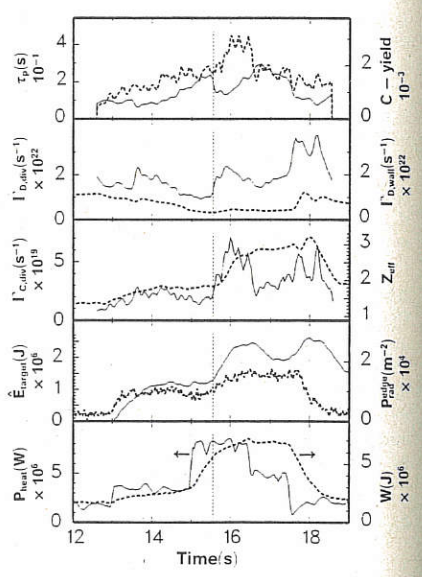

Fig. 3: *Divertor related parameters for a moderately heated H-mode discharge (pulse 25977). The dotted vertical line mark the change in the bulk plasma confinement.*

Results: The carbon and deuterium fluxes typically show two prominent maxima in the divertor on either side of the private region near the seperatrix strike points/4/. The positions of the maxima are about where, on the basis of measured midplane SOL-profiles and the actual magnetic divertor topology, calculated perpendicular particle fluxes have their maxima/5/. At normal discharge conditions, when the target load is low to moderate, the carbon and deuterium maxima almost coincide (fig.2), indicating, that deuterium sputtering and self-sputtering is the dominant mechanism for carbon release from the graphite target.

Figure 3 shows the positive feedback between the bulk plasma confinement and the divertor fluxes for a moderately heated discharge with an H-mode regime from 15 to 17.5 s. The change in the confinement properties during the H-mode, marked by the dotted vertical lines, cause a strong increase of $\hat{E}_{target}$, mainly through the change of $\dot{W}_p$, and an increase of the deuterium divertor flux, $\Gamma_{D,div}$, The growing $\hat{E}_{target}$ and $\Gamma_{D,div}$ cause a significant rise in the carbon divertor flux, $\Gamma_{C,div}$. The total divertor carbon yield, $Y_{C,div} = \Gamma_{C,div}/\Gamma_{D,div}$, is enhanced due to self-sputtering. Eventually the increase in Z_{eff} and the corresponding growth of the radiation losses limits $\hat{E}_{target}$. At higher heating power this scenario would very likely have led to a carbon bloom. The process seems to be initiated by a gradually rising influx of impurities: the edge radiation, P_{rad}^{edge} as well as $\hat{E}_{target}$ start rising before the marked time.

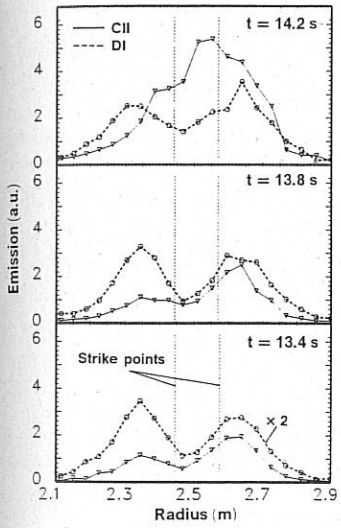

Fig. 4: *The CII and DI emission shows typically two pronounced maxima on either side of the private region (lower two pictures). During a bloom a strong third maxima shows up between the original ones (pulse 26026).*

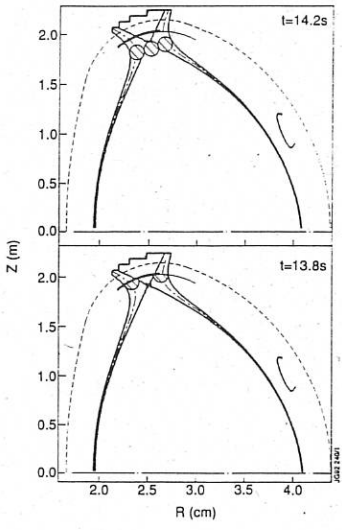

Fig. 5: *The maxima of the CII- and DI-emission (hatched areas) are observed close to the divertor target (bottom). During the bloom the radiation maxima move down and a third one can be identified close to the boundary of the bulk plasma (top).*

In high performance discharges avalanche-like carbon (or beryllium) influxes (bloom) can occur, if the target load exceeds a certain threshold (fig. 1). The bloom is often preceeded by a gradual increase of the divertor deuterium and carbon fluxes, but is observed also without a distinct precursor, coinciding e.g. with a giant ELM. The onset of a bloom is marked not only by a significant increase of carbon line radiation in the divertor, also the local radiative power dissipation, measured by bolometers, increases strongly and reaches values of about 10 MW and above. The two distinct maxima in the CII- and DI-emission which generally are observed, are often blurred by a third one, when a bloom occurrs (fig.4). With the two VUV spectrometers the radiation maxima can be localised in the immediate vicinity of the target (fig.5, bottom). In the case of a bloom, the two radiation peaks move away from the target along the SOL. A third maxima can be identified at about the tip of the confined plasma (fig.5, top). As reliable Langmuir data are not available during the bloom, one can only conclude from the positions of the CII-maxima that, due to the intense radiative power loss in the divertor, its retention properties break down: $T_{e\,div}$ becomes so low, that the ionization length λ_i increases to the distance of the X-point to the target and high neutral particle fluxes can cross the seperatrix.

Conclusions:

- Carbon and deuterium emission show distinct maxima on either side of the private region which are observed with CCD-cameras as well as with spatially scanning VUV-spectrometers.
- The CCD-cameras are absolutely calibrated and divertor particle fluxes can be estimated by using local electron density and temperature provided by Langmuir probes in the divertor target. In H-mode discharges, at moderate P_{heat}, the divertor fluxes are typically 2 to 4 times above the wall fluxes.
- CCD- and VUV-measurements agree with each other qualitatively, as long as the target load is not to high.
- A threshold for the power conducted to the target can experimentally be identified, above which a carbon bloom can occur. In many cases the bloom is preceeded by increasing divertor fluxes of deuterium and carbon, but it can be triggered also e.g. by giant ELM's. When P_{target} is above a certain threshold value, which depends on P_{heat}, a small additional incremental target load provided e.g. by $\dot{W}_p$, can obviously initiate the bloom due to a strong positive feedback via $\dot{W}_p$.
- Strong influxes of carbon into the bulk plasma during the bloom are very likely caused by a breakdown of the retention properties of the divertor, due to intense radiative cooling and recycling losses and hence an increase of the respective ionisation lengths to the amount of the divertor-target distance.

References:

[1] M.Keilhacker and JET Team, Phys. Fluids B, 2(1990) 1291.
[2] JET Team, Nucl. Fus., 32(1992) 187
[3] H.P.Summers, to be published
[4] H.J.Jaeckel et al., 33rd APS Conf., Tampa 1991
[5] P.J.Harbour, A.Loarte et al., PSI-conference 1992

CHEMICAL IMPURITY PRODUCTION UNDER BORONIZED WALL CONDITIONS IN TEXTOR

V.Philipps, E.Vietzke, M.Erdweg

Institut für Plasmaphysik,Forschungszentrum Jülich,Association Euratom-KFA,5170 Jülich,FRG

ABSTRACT: The TEXTOR SNIFFER probe has been used to analyse the chemical impurity production under various plasma and boronized wall conditions. Methane formation has been observed to 0.6-1 x 10^{-2} CH_4/H at room temperature,increasing slightly with increasing density in the SOL. The hydrocarbon formation yields increase from R.T. to the maximum at about 500°C by a factor of 1.5-2.5. Increasing the impact energy by biasing the graphite plate lead to a decrease of the hydrocarbon yield at room temperature but to an increase at 500°C. Chemical CO formation due interaction of oxygen impurities with the graphite reaches ratios between 0.5 and 3 x 10^{-2} CO/H,D increasing with increasing distance to the limiter edge.

1. INTRODUCTION: Carbon walls together with boronisation are now widely used as plasma facing materials. The main benefit of the use of boron is a significant reduction of the oxygen impurities in the plasma. Under fully carbon wall conditions the ratio of chemical CO formation to the incoming hydrogen flux in the SOL of TEXTOR has been measured with the SNIFFER probe to 4-12x10^{-2},depending on the actual oxygen impurity situation and the radial position in the SOL /1/. Similar values have been observed spectroscopically for the carbon to hydrogen flux-ratio emitted from the limiters and walls /2/. The carbon release from the walls in tokamaks under fully carbon wall conditions (and no additional gettering by boron or beryllium) is largely determined by chemical CO formation of the oxygen impurities with the walls,in particular at low plasma edge temperatures /3,4/.

The hydrocarbon formation at pure graphite measured either in low energy beam /5 /,in plasma simulation experiments /6/ and in TEXTOR with the SNIFFER probe, show a consistent behaviour: the characteristic temperature dependence of the yields observed at higher impact energies (>1keV) and lower flux (10^{15} H/cm^{2}s) levels off with no energy treshold at low energies. From RT to the maximum at about 500°C the yields increase only by a factor of about 2-3. With decreasing impact energy the C_2- hydrocarbon formation become increasingly important.
Within this work CO and hydrocarbon formation has been observed during the interaction of the TEXTOR scrape-off plasma with a carbon target under boronized wall conditions. The conditions are characterized by incoming hydrogen flux densities between 10^{16}-10^{18} H,D/cm^{2}s, hydrogen(deuterium) impact energies between 20 and 250eV and simultaneous impact of carbon, boron and oxygen impurities. The boron to carbon impurity flux ratio in the SOL of TEXTOR depends on the history of the boronisation procedures and extends to values typically between about 0.05 and 0.25 /7 /. The interaction of these particle fluxes with the target leads under most of the conditions to the formation of a redeposited carbon/boron layer. Thus,the formation of volatile reaction products has been observed here under the condition of the formation of a fresh redeposited hydrogen containing carbon/boron layer.

2. EXPERIMENTAL: The SNIFFER probe acts in principal as a small pump limiter. Ions flowing along the magnetic field lines pass the aperture (4mm broad and 10mm high) of the SNIFFER tube and interact with a graphite plate in the middle of the tube which can be heated by direct current

up to about 2000°C. Recycled hydrogen and any volatile reaction products are detected at the end of the tube by a quadrupole mass spectrometer. The vacuum conductance of the tube is about ten times that of the aperture. The vacuum time constant is about 350ms for D_2 molecules.

3. RESULTS AND DISCUSSION:

3.1. HYDROCARBON FORMATION:Fig 1 shows as an example the evolution of the recycled particle fluxes of deuterium and the formed methane (CD_4) 2cm in the limiter shadow (R_S=48cm,R_{Lim}=46cm) for two subsequent ohmic heated discharges (ne=$3x10^{13}cm^{-3}$) where the temperature of the graphite plate was changed from 50°C to 500°C. The signals correspond directly to the measured pressure rises at the QMS and include thus the vacuum time delay. To evaluate absolute methan formation yields the contribution of the hydrogen minority fluxes in the SOL must be included. Hydrogen minority fluxes (evaluated from the HD flux) under deuterium fueled discharges extend typically to ratios of 0.08-0.2 of the deuterium flux. This leads to significant formation of CD_3H (mass19) and some $C_2D_2H_2$ (mass18). It has been observed that the isotope mixing of the C_1-type hydrocarbons(CD_4,CD_3H ,CD_2H_2) is governed by the deuterium and hydrogen flux ratios,c_D and c_H, according to a process of 4th order as $(c_D+c_H)^4$. A hydrogen minority flux ratio of 0.2 leads thus to the formation of about equal amounts of CD_3H and CD_4. In the following the methan formation will be referred to as CD_4 and CH_4 but contain all C_1-hydrocarbons.

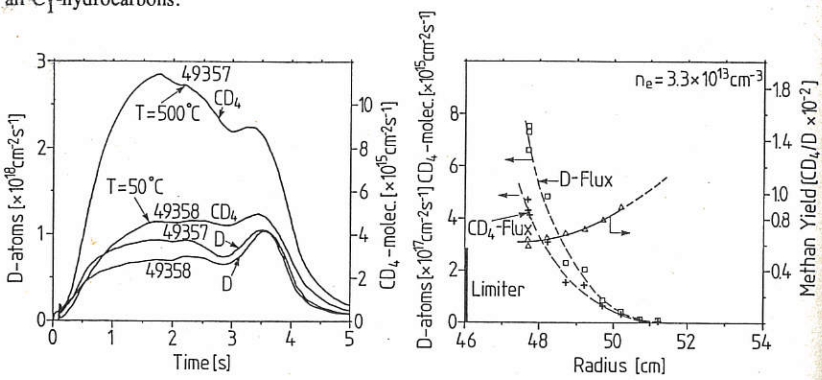

Fig 1: Evolution of the deuterium flux and the formed methane for to subsequent shots where the graphite temperature was changed from 50°C to 500°C.

Fig 2:Radial dependence of the deuterium flux,the formed methane and the methane formation yield for ohmic discharges with constant central density.

Fig 2 shows a radial scan of the deuterium flux (H+D), the formed methane and the methane formation yield for RT target temperature for a serie of ohmic discharges with $n_e=3x10^{13}cm^{-3}$. The hydrogenic flux extends from $2x10^{16}$ to $1x10^{18}$ H+D/cm^2s. The methane formation yield is 0.7-$1x10^{-2}$ CD_4/D,with a slight tendency to increase at lower fluxes at increasing radius.
Fig 3 shows the methane formation yields at RT and 500°C target temperature as a function of the negative bias voltage on the target for ohmic discharges at a central density of $n_e=3.3x10^{13}cm^{-3}$. The yields decrease at RT from $0.9x10^{-2}$ to $0.5x10^{-2}$ CD_4/D but increase at 500°C from 1.4 to 1.9 $x10^{-2}$ CD_4/D. At this central density the hydrogenic impact energy on the target under floating conditions at R=48cm (measured by a calorimetric technique within the SNIFFER probe /8/) is about 20-30 eV. Thus,the methane formation yield changes mainly in the energy range from zero to about 100eV. The figure demonstrate again the general behaviour: at

floating potential (impact energy about 20-30eV) the yields increase only from 0.9 to 1.4 x10^{-2} CD_4/D from RT to 500°C, which is only a factor of about 1.5 but at 200 eV bias (impact energy 225eV) the yields increase from 0.5 to 1.9x10^{-2} CD_4/D which is a factor of about 4. Fig 4 shows an example of the temperature dependence of the methane formation (in this case for hydrogen as majority at floating potential)) measured at R=48cm for ohmic discharges at n_e=3x10^{13}cm^{-3}.

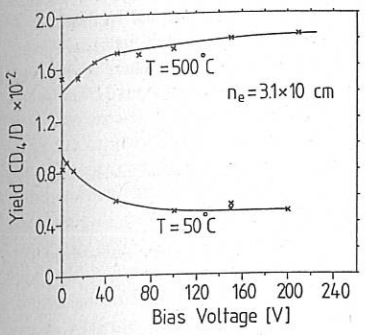

Fig 3: Methane formation yields at T=50°C and at T=500°C as a function of the negat. bias voltage for ohmic discharges. with n_e=3.1x10^{13}/cm^3(R=48cm)

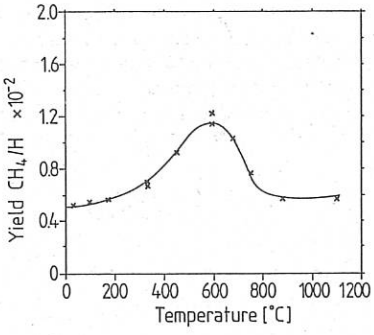

Fig 4:Methane formation yield as a function of the graphite temperature for ohmic discharges with n_e= 2.5x10^{13}/cm^3 (R=48cm).

Formation of higher hydrocarbons shows a similar behaviour with respect to the energy and temperature dependence. The dominant C_2-type hydrocarbon is C_2H_2 followed by C_2H_4 and a minor contribution of C_2H_6. C_2H_4 formation is roughly 0.3 of the methane formation and C_2H_2 between 0.5 and 1 of the methane yield. To evaluate the total carbon atom emission in form of hydrocarbons the contribution of the C_2-hydrocarbons is at least as strong as the methane formation but exceeds it in most of the cases. Thus, the total carbon release by hydrocarbon formation is about 1.0-2 x10^{-2} at RT target temperature and increases by a factor of 1.5-2.5 (depending on the hydrogen impact energy and thus on the plasma edge temperature) at 500°C . Details of the higher hydrocarbon formation will be published in a forthcoming contribution. The results show that the hydrocarbon formation observed here is very similar as observed in TEXTOR under fully carbon wall conditions/1 /. However,we have to note that no direct experimental comparison is possible presently in TEXTOR with and without the boronized wall and we have to compare the present data with mass-spectroscopic data from 1988. However,the hydrocarbon formation yields do not change after fresh boronization of TEXTOR which change the boron to carbon flux ratio in the SOL of TEXTOR typically by factors up to 3 (from 0.15 to 0.5). We can state that the decrease of the hydrocarbon formation by boronization under the flux amd energy conditions in the plasma edge is weak (<50%). This is in contrast to beam experiments which show a significant decrease of the hydrocarbon formation of boron-doped carbon materials /9/ but is in line with plasma simulation experiments which show also only a minor reduction of hydrocarbon formation of boron-doped carbon materials /7 /.

3.2. CO FORMATION: CO formation has been evaluated from the mass 28 signal and a simultaneous measurement of a sourrounding hydrocarbon. In deuterium plasmas about 1/3 of the mass 28 signal originates from hydrocarbons. However,a detailed correction of the signal with respect to hydrocarbons remains often difficult due to the complex structure of the C_2-hydrocarbon spectrum in particular if significant hydrogen/deuterium minority fluxes are present. Fig5 shows the radial dependence of the CO formation ,the deuterium flux and the ratio of CO to the impinging deuterium flux for the same serie of discharges as shown in fig 1. The ratio is about $1x10^{-2}$ near the limiter edge increasing to $3x10^{-2}$ deeper in the SOL. Fig 6 shows the evolution of the CO/D ratio at r=48 cm for two subsequent operation days including ohmic and NI heated discharges at different densities where a fresh boronization has been performed in between. As can be seen,the CO ratio has decreased by roughly a factor of two. A similar tendency is observed spectroscopically /10/. CO formation ratios have been decreased by a factor of about 3-5 under boronized wall compared to fully carbon wall conditions in TEXTOR.

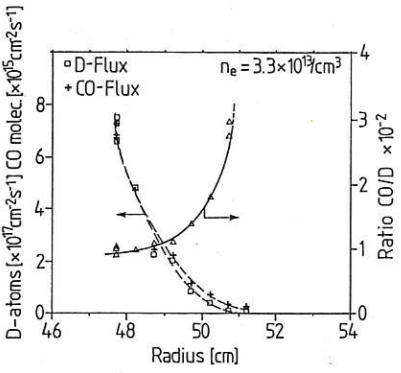

Fig 5: Radial dependence of the deuterium flux,the formed CO and the ratio CO/H for ohmic discharges with constant density.

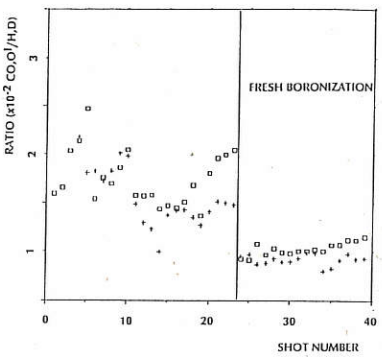

Fig 6: Evolution of the ratio of CO/D (+) measured with the SNIFFER probe and the ratio of O^I/H ([]) measured spectroscopically at the limiter during transition from an old to a new boronization.

References:

/1/ V.Philipps,E.Vietzke,M.Erdweg, J.Nucl.Mat. 162-164 (1989) 550
/2/ A.Pospieszczyk et al, J.Nucl.Mat. 145-147 (1987) 574
/3/ G.M.McCracken, S.J.Fielding, G.F.Matthews, J.Nucl.Mat. 162-164(1989) 392
/4/ P.R.Thomas,J.Nucl.Mat 176-177 (1990) 3
/5/ J.Roth,J.Bohdansky, Nucl. Instr. and Meth. B23 (1987) 549
/6/ Y.Hirooka,R.W.Conn et al, Fus. Techn. Vol 19 (1991) 2059
/7/ P.Wienhold et al, 10 th Conference on Plasma Surface Interactions,Monterey, USA,30.3-4.4.,1992
/8/ V.Philipps et al, to be published
/9/ J.Roth, J.Nucl.Mat. 145-147 (1987) 87
/10/ A.Pospieszczyk, private communication

DIVERTOR RETENTION FOR RECYCLING IMPURITIES

K. Krieger, J. Roth, G. Fussmann

Max-Planck-Institut für Plasmaphysik, EURATOM Association,
8046 Garching, Germany

INTRODUCTION

As an important issue for fusion devices with divertor configurations the retention capability for both recycling and non-recycling impurities receives increasing interest. In the case of recycling, gaseous, impurities the retention capability is usually investigated by means of short impurity gas puffs into the plasma vessel and the analysis of the time dependence of the observed line radiation[1-5]. The detailed understanding of the impurity transport processes related to the retention capability of a certain divertor structure will require modelling of the experimental results with 2D or 3D transport code simulations. However, for the comparison of the global behavior of different configurations a much simpler description of the divertor retention in terms of global time constants may be sufficient.

We will give a summary of experimental results from ASDEX for the dependence of the retention capability on parameters like divertor plasma density and temperature and the distance along field lines between main plasma and divertor. In addition we will compare some of these results with similar experiments on DIIID [5].

TWO CHAMBER MODEL

The results from experiments with short impurity gas puffs show a time behavior which is clearly characterized by two different time constants (Fig. 1). This can be explained by a global model of the particle balance between the confined plasma in the main chamber and the plasma in the divertor region [1, 5].

The confined plasma with a total number of impurity ions N_+ looses a flux of ions into the divertor chamber with a rate $-N_+/\tau_p$. Although the loss rate is actually obtained by integrating the outgoing flux density over the plasma surface (separatrix), it appears in this global treatment as a volume averaged sink term with τ_p being the mean confinement time for an impurity density distribution as obtained under steady state conditions. The outflowing ions are neutralized at the divertor plates and set up a neutral density in the divertor chamber with a total particle number N_0. These particles produce a refuelling flux out of the divertor back into the main plasma chamber providing there a particle source N_0/τ_D in the edge region. τ_D can be understood as the mean residence time of a particle in the divertor without external pumping. However, in order to be consistent with the sink term this edge source is to be multiplied by a factor $\gamma < 1$ to convert it into an equivalent core source (i.e. postulating the same radial particle distribution for the sink and the source term). In smaller devices like ASDEX, where external pumping takes place on a time scale comparable to the discharge times, we have to take into account an additional flux of neutral particles out of the divertor region with a corresponding loss rate $-N_0/\tau_{\mathrm{pump}}$. This term has been omitted in earlier analytical evaluations of Ar and Ne pulse experiments [1, 2] but proves to be important as τ_{pump} is, at least for ASDEX and DIII-D, of the same order of magnitude as τ_D/γ.

Taking all terms into account one obtains two coupled differential equations

$$\frac{dN_+}{dt} = -\frac{N_+}{\tau_p} + \gamma\frac{N_0}{\tau_D} \quad \text{and} \quad \frac{\mathrm{dN_0}}{\mathrm{dt}} = \frac{\mathrm{N_+}}{\tau_\mathrm{p}} - \gamma\frac{\mathrm{N_0}}{\tau_\mathrm{D}} - \frac{\mathrm{N_0}}{\tau_{\mathrm{pump}}}. \qquad (1)$$

The solution is a sum of two decaying exponentials with characteristic time constants τ_{short}, τ_{long} corresponding to the experimental observations. τ_{short} and τ_{long} are connected to the model

parameters by

$$\tau_{\text{pump}} = \frac{\tau_{\text{short}}\tau_{\text{long}}}{\tau_p} \tag{2}$$

$$\frac{\tau_D}{\gamma} = \frac{\tau_{\text{short}}\tau_{\text{long}}\tau_{\text{pump}}}{(\tau_{\text{pump}} - \tau_{\text{short}})(\tau_{\text{long}} - \tau_{\text{pump}})}. \tag{3}$$

τ_p is, within certain limits, known from other experiments, while γ can be determined approximately by transport code simulations. From that it should be possible to determine τ_D and τ_{pump} directly from the measured time constants. However, τ_p is often not precisely known and close to τ_{short}. In this case τ_{pump} will be close to τ_{long} because of eq. (2) and the extraction of τ_D will be highly uncertain due to the factor $\tau_{\text{long}} - \tau_{\text{pump}}$ in the denominator of (3).

To avoid this problem, τ_D was determined by simulations of the measured impurity line intensities in the main plasma using the fully time dependent 1D impurity transport code ZEDIFF. Input parameters into the code are the experimentally determined $n_e(r)$ and $T_e(r)$ profiles, the cross field diffusion coefficient, $D_\perp$, the inward drift velocity, v_{in}, the mean energy of the neutral source atoms, E_0, and the time constant $\tau_{||}$ for losses parallel to the magnetic field lines outside the separatrix. Main output parameters are the traces of selected line intensities and the impurity density in the main plasma. Fitting parameters to experimental data are the divertor retention time constant, τ_D, and the pumping time constant, τ_{pump}.

SCALING LAWS FOR τ_D

For the dependence of τ_D on divertor plasma parameters (n_e, T_e) as well as on the impurity species some qualitative predictions can be made. If neutral gas flow from the divertor to the main plasma is the dominant recycling path, the time constant τ_D/γ will depend on the ionization length $\lambda_{\text{ion}} = v_0/n_e S_{\text{ion}}(T_e)$ of recycling impurities in relation to the dimensions of the divertor plasma, where v_0 is the thermal velocity of the recycling gas, and S_{ion} is the ionization rate coefficient for impurity atoms. Evidently, recycling by neutral backflow will get less probable, i.e. τ_D will get longer, as electron density and temperature in the divertor increase and as the impurity mass, which determines v_0, increases. For low divertor temperatures and long ionization lengths the divertor retention time constant is ultimately equal to the vacuum time constant of the divertor entrance slits[1].

For high divertor temperatures, where the ionization length gets so small that neutral backflow is no longer of importance, the retention of impurity ions has to be considered. The characteristic decay length, $\lambda_{||}$, of the impurity density along fieldlines is given by the ratio of the diffusion coefficient along field lines, $D_{||}$, to the velocity of the background plasma, $v_{||}$, which streams towards the divertor plates [6]

$$\lambda_{||}(\text{m}) = \frac{D_{||}}{v_{||}} \simeq \frac{8.84 \cdot 10^{16}\, T_i^2(\text{eV})}{\left(1 + \frac{m_i}{m_z}\right) \ln\Lambda\, M\, Z^2(\text{e})\, n_i(\text{m}^{-3})}. \tag{4}$$

This characteristic length has to be compared to the connection length, $L_{||}$, of the field lines from the divertor plates to the X-point resulting in a residence probability

$$P \propto \epsilon^{-L_{||}/\lambda_{||}}. \tag{5}$$

for impurities in the main plasma. In reality, further parameters e.g. thermal drag forces which depend on the gradient of T_i, have to be taken into account. This simplified consideration may, however, help to understand the importance of divertor ion temperature and density. The

dependence of $\lambda_{||}$ on T_i and n_i shows that for high ion temperature and consequently low density, the retention for ionized impurities may break down. Thus, a minimum divertor temperature is required for the retention of neutral atoms whereas a maximum divertor temperature exists for the retention of ions. Additionally, the retention of ions depends critically on the ion charge state Z.

In the following, we will compare some of these predictions with experimental observations mainly from ASDEX.

DEPENDENCE ON SAFETY FACTOR q

In ASDEX the divertor retention has been investigated extensively for inert gases like Argon. Fig. 1 shows the temporal decay of an Ar XVI line after Ar injection into the ohmic phase of discharges with various safety factors q (I_p = const.). Clearly, two exponential decay times are seen as predicted by the two-chamber model. The fast decay shows the outflux from the plasma into the divertor until equilibrium is established. The slow decay shows mainly the effect of Ar pumping through the divertor chambers by external pumps. The pumping time constant was obtained to $\tau_{\text{pump}} \simeq 1\,\text{s}$ from fits of the data to the analytical model.

For the determination of τ_D the data have been fitted using the impurity transport code ZEDIFF. The results are given in table 1 together with the values of τ_p. These parameters were used to calculate the respective time dependence from the analytical model as shown in fig. 1 (dashed lines). As can be seen the calculated traces are in very good agreement to the experimental data. The values given in table 1 show an increase of τ_p and decrease of τ_D with decreasing q. The increase of τ_p is in accordance to earlier investigations of impurity transport on ASDEX [7, 8]. The decrease of τ_D with decreasing q can be understood by the increase of the connection length, $L_{||}$, along field lines from the divertor plates to the X-point, indicating that ionic impurity transport dominates in this operational regime. $L_{||}$ increases from 1.3 m at $q = 2.2$ to 2.8 m at $q = 4.2$. However, taking the typical divertor parameters, i.e. $T_e = 13\,\text{eV}$ and $n_e = 1 \cdot 10^{19}\text{m}^{-3}$ independent of q, $T_e = T_i$ and $M = 0.1$, a much stronger dependence on q would be expected from eq. (5). Assuming lower Mach numbers ($M = 0.02$) a weaker dependence on q i.e. a better agreement with the experimental data is obtained.

DEPENDENCE ON AUXILIARY HEATING POWER (NBI)

For additional heating, a decrease of the divertor retention has been observed in ASDEX [2], DIII-D [5] and JET [4]. The dependence of τ_D on NBI-power is given in table 2 together with the divertor plasma parameters n_e and T_e. Fig. 2 shows the data from table 2 as a function of NBI-power together with similar data from DIII-D. Also introduced are normalized values for τ_D as expected from eq. (4) and (5) taking a connection length of L of 2 m, an ion charge state $Z = 2$, a Mach-number of 0.1 and assuming $n_i = n_e$ and $T_i = T_e$. It is evident that with these assumptions a much stronger decrease of τ_D would be expected. If, however, a Mach number of only 0.015 is used, a reasonable good scaling can be obtained. This low Mach number agrees very well to the value obtained for the q-dependence. Fig. 2 shows clearly that for OH or moderate NBI the divertor temperatures are low and friction with the streaming background plasma retains the impurity ions to the divertor. τ_D-values considerably higher than the vacuum time constant for neutral gas [1] are obtained. As the temperature increases $\lambda_{||}$ gets larger with T_i^2 and eventually the plasma pumps ionized impurities more efficiently along field lines than neutral gas streams through the divertor throat. Therefore, the high temperature limit of τ_D is only a fraction of the vacuum time constant.

REFERENCES

[1] G. Fussmann et al., J. Nucl. Mater. **121**, 164 (1984).
[2] G. Janeschitz et al., Nucl. Fusion **26**, 1725 (1986).
[3] D. L. Hillis et al., Phys. Rev. Lett. **65**, 2382 (1990).

[4] G. Janeschitz et al., Europhysics Conference Abstracts **15C** Part III, page 97, 1991.
[5] S. Lippmann et al., Europhysics Conference Abstracts **15C** Part III, page 201, 1991.
[6] G. Fussmann, Divertor retention for noble gases, European Tokamak Workshop, Ising, 1989.
[7] C. Setzensack, Laser-blow-off-Experimente am ASDEX, IPP Report IPP-III/119, Max-Planck-Institut für Plasmaphysik, 1987.
[8] K. Krieger and G. Fussmann, Nucl. Fusion **30**, 2392 (1990).

Table 1 Values of τ_p (ms) and τ_D (ms) in ohmic ASDEX divertor discharges for different safety factors q with $\tau_{\text{pump}} = 1\,\text{s}$.

q_a	τ_p	τ_D
4.2	65	700
3.3	95	650
2.5	130	550
2.16	150	300

Table 2 Values of τ_D (ms) vs. NBI-power for ASDEX divertor discharges (n_e in 10^{19}m^{-3}, T_e in eV, P_{NI} in MW). The value for $P_{\text{NI}} = 3.4$ MW is from [2] with $\tau_{\text{pump}} = \infty$.

P_{NI}	n_e	T_e	τ_D
0.			320
0.3	1.3	11	320
0.6	1.65	16	220
1.2	1.65	19	130
1.8	1.7	21.5	90
3.4	1.5	20	20

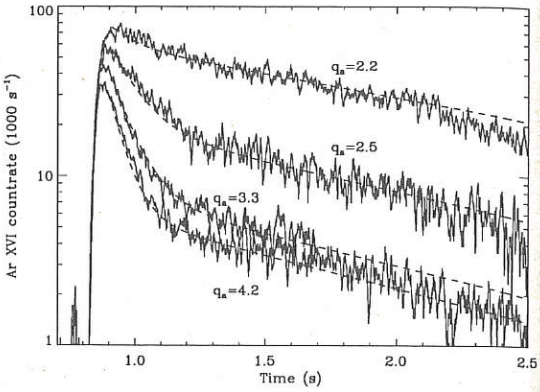

Figure 1 Temporal decay of the Ar XVI line after Ar injection in ohmic discharges.

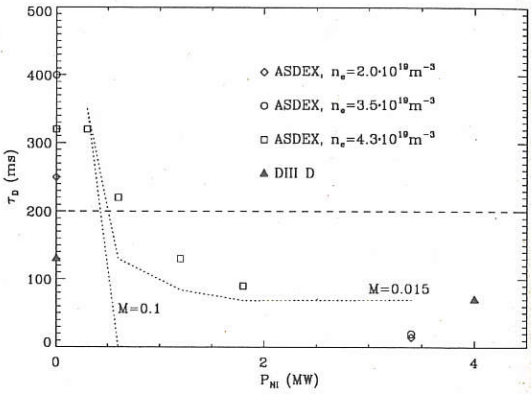

Figure 2 Dependence of τ_D on the NBI-power. The dotted lines are calculated from eqns. (4) and (5) for different Mach numbers M. The dashed line indicates the vacuum time constant of the divertor throat for Ar.

PARTICLE INFLUX AND IMPURITY BEHAVIOUR IN THE ASDEX UPGRADE TOKAMAK

A. Kallenbach, C. Fuchs, G. Fussmann, F. Jenichen, K.F. Mast, H.M. Mayer, U. Schumacher and the ASDEX Upgrade Team

Max-Planck-Institut für Plasmaphysik, EURATOM Association, D-8046 Garching, Fed. Rep. of Germany

1 Introduction

We have investigated the impurity behaviour in the ASDEX Upgrade tokamak using a 40-channel bolometer array, a fixed-frequency Bragg spectrometer (C+O monitor), a VUV-survey spectrometer (SPRED) and a multichordal visible spectrometer. Fig. 1 shows the arrangement of the diagnostics. All discharges discussed in the following were ohmically heated and helium was used as working gas. No special wall conditioning has been applied to ASDEX Upgrade so far.

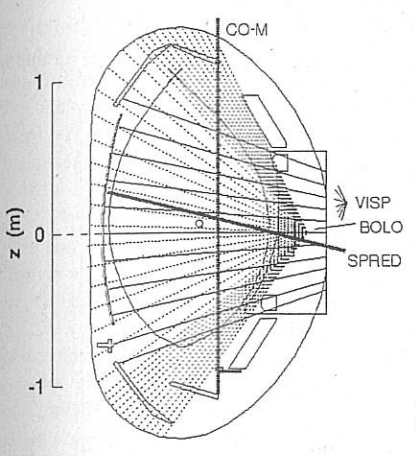

The main emphasis in this paper is placed on the measurement of impurity fluxes from the inner wall (limiter). The flux contributions of all major species occurring in the plasma (He, H, C, O) were obtained. Owing to the so far low current density (I_p= 350 kA), the radiative losses are high and amount to about 60 % of the heating power. As soon as temperature and density profiles are available, Z_{eff} and the plasma composition will be determined.

Figure 1 Viewing lines of various diagnostics projected into one poloidal plane.

2 Experimental results

The SPRED spectrometer gives an overview on the impurity influxes ($Z \leq 3$) and contents ($Z \geq 6$). It is equipped with two detectors based on linear Reticon arrays (2048 pixel) intensified by microchannel plates. A typical spectrum obtained during a divertor phase is shown in Fig. 2. The absence of metallic lines indicates the dominance of low-Z impurities.

The temporal developments of the O^{II} influx, O^{VIII} density and total radiated power versus the plasma current and heating power are shown in Fig. 3 for a typical inner-limiter

discharge. The radiated power ($\approx$ 60 % P_{OH}) is evaluated from the 40 line-integrating bolometer chords on the assumption of constant emission on elliptical, unshifted flux surfaces. During the flat-top phase, a gradual reduction of the oxygen influx occurs, accompanied by a reduction of the oxygen content and, consequently, of the loop voltage and the radiated power.

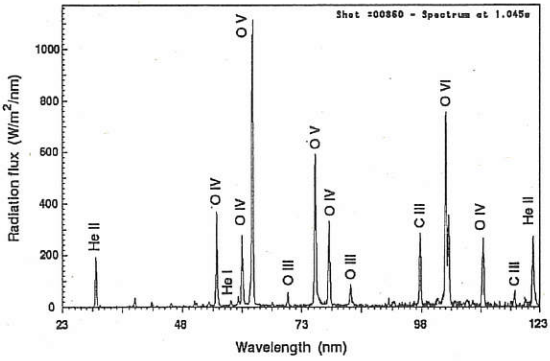

Figure 2 *VUV overview spectrum taken by the SPRED spectrometer during an upper single null divertor phase.*

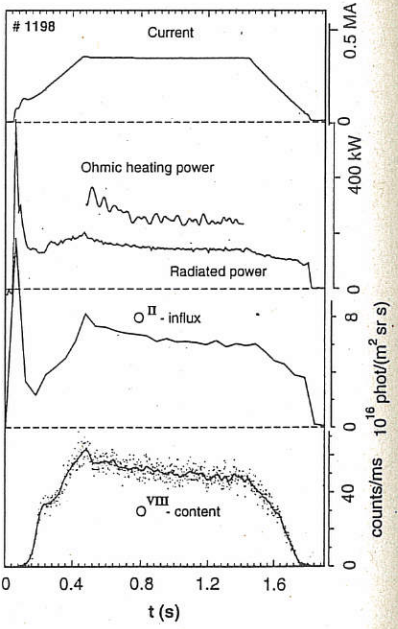

Figure 3 *Temporal developments of plasma current, heating power, radiated power, O^{II} influx near the horizontal plane and O^{VIII} density for a typical inner-limiter discharge (I_p = 0.35 MA, $\overline{n}_e$ = $2 \cdot 10^{19}$ m^{-3}). The signal of the C+O monitor, which is fixed to the O^{VIII} L_α transition at λ= 1.897 nm by using a KAP(001) crystal, is taken with 1 kHz sampling frequency (dots) and smoothed over 10 ms (solid line). For low I_p at the beginning and end of the discharge, the plasma temperature is not high enough to ionize oxygen atoms to O^{7+}.*

species	wavelength	ground / metastable state	$\frac{S}{XB}$ [2,3]	partial flux $[10^{20}\ m^{-2} \cdot s^{-1}]$	est. total flux $[10^{20}\ s^{-1}]$
He^0	667.82 nm	$1s^2\ ^1S$ (g)	200	4.5	
He^0	587.56 nm	$1s2s\ ^3S$	(0.5)	(0.08)	32
He^+	468.57 nm	$1s\ ^2S$ (g)	75	5	35
H^0	656.28 nm	$1s\ ^2S$ (g)	15	0.5	3.5
C^{2+}	464.74 nm	$2s2p\ ^3P$	3	0.2	
C^{2+}	569.59 nm	$2s^2\ ^1S$ (g)	200	~0.1	2.1
O^+	374.95 nm	$2s^22p^3\ ^4S$ (g)	40	0.09	
O^+	397.33 nm	$2s^2sp^3\ ^2P$	33	0.075	
O^+	441.49 nm	$2s^2sp^3\ ^2D$	24	0.095	1.8

Table 1: *Particle fluxes from the inner heat shield (limiter) obtained spectroscopically for typical experimental conditions ($I_p = 0.35\ MA$, $\overline{n}_e = 2 \cdot 10^{19}\ m^{-3}$). The effective limiter surface is about 7 m^2, the partial flux densities given are average values over the full height of the heat shield. The flux calculation of the two metastable levels of O^+ includes corrections for overlapping excitation pathways[2]. The uncertainty of the absolute calibration is 25 %. The S/XB values are subject to uncertainties in the rate coefficients (≈ a factor of two for oxygen and carbon[2]) as well as to an unknown energy distribution of the neutral particles, which affects the penetration depth.*

The good optical access of the multichordal visible spectrometer system[1] to the inner limiter allows one to determine the total influx of different particle species simply by multiplying the measured photon fluxes by the number of ionizations per emitted photon, S/XB. The fluxes shown in Table 1 are obtained from poloidal profiles on the assumption of toroidal symmetry. It was found to be necessary to take into account full poloidal profiles, since even near the midplane spatial variations of the local flux within a factor of three are observed owing to slight changes in the plasma shape and position.
After transition to the divertor or outer-limiter configuration, the fluxes on the observed transitions decrease by a factor of 3 (see Ref. 5).

3 Discussion

Physical sputtering by helium atoms is expected to be the production mechanism of the observed carbon flux[4]. The fluxes shown in Table 1 give a sputtering yield of 10 %, in agreement with results obtained on JET[3]. The ratio Γ_H/Γ_O is about 2. The oxygen and hydrogen influx is assumed to originate from H_2O.

The atomic database for the calculation of the S/XB values suffers from considerable uncertainties in the excitation and ionization rate coefficients. Furthermore, the mechanism which produces the neutral particles at the wall, and consequently their energy

distribution, is not well-known. The resulting lack of information concerning the energy of the neutrals leads to uncertainties in the penetration depth and thus to the local temperature for which S/XB has to be evaluated.

To reduce these impairments of the particle flux measurements, additional information can be taken from highly resolved spectral line profiles. The spatial positions of emission can be calculated from the resolved Zeeman splitting of line profiles. The width of the line profile of the neutrals yields information about their energy distribution.

The influx of helium in the metastable triplet state is shown in Fig. 4. The corresponding photon flux is emitted directly at the limiter surface, with the emission maxima lying near the upper and lower edges of the limiter. From the narrow line profile an upper limit of the 'temperature' of the neutrals, $T_0 < 0.5$ eV, for the main fraction of particles is obtained. The mechanism which leads to emission at the limiter surface instead of at the plasma boundary, where an appropriate electron temperature for excitation exists, is not yet understood. Therefore, the validity of the corona approximation used for the conversion of the photon to the particle flux is also questionable in this particular case.

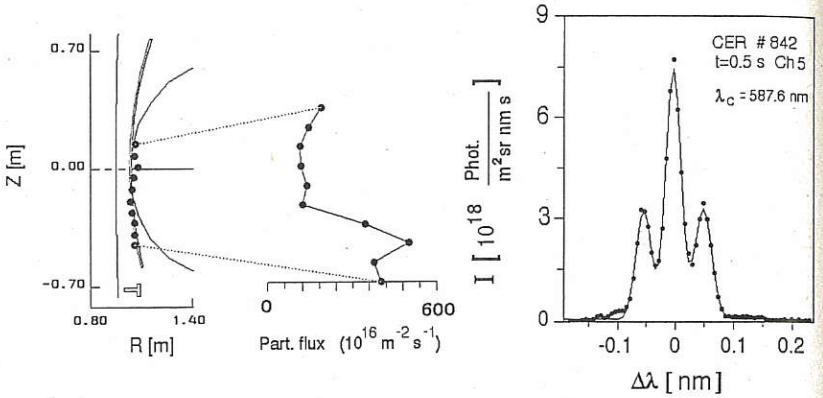

Figure 4 Spatial positions of spectral line emission and intensity distribution of He^0 ($1s2s\ ^3S$) flux from the inner heat shield for a viewing line arrangement alternative to that shown in Fig. 1. Positions are determined from the Zeeman splitting and the known radial dependence of the magnetic field. The line width is essentially determined by the apparatus broadening ($\approx$ 0.03 nm), except a small feature systematically occuring on the blue wing (see arrow) which is attributed to the Doppler shifted σ−light of neutrals leaving the wall with $T_0 \approx 10$ eV ($I_p = 0.35MA$, $\overline{n}_e = 8 \cdot 10^{18}\ m^{-3}$, $B_{t0} = 2.0\ T$).

References

/1/ A. Kallenbach et al., Report IPP 1/265 (1992).
/2/ K. Behringer et al., Plasma Phys. and Contr. Fusion **31** (1989), 2059.
/3/ M. F. Stamp et al., J. Nucl. Mater. **162-164** (1989), 404.
/4/ A. Pospieszczyk et al., J. Nucl. Mater. **145-147** (1987), 574.
/5/ P.J. McCarthy et al., this conference.

REDUCTION IN SOL ϕ_p INCREASES AND IMPURITY GENERATION CAUSED BY RF NEAR ω_{ci} BY THE USE OF INSULATING FARADAY SHIELD LIMITERS IN THE PHAEDRUS-T TOKAMAK AND BY ELIMINATION OF FARADAY SHIELDS

N. Hershkowitz, R. Majeski, D. Diebold, T. Tanaka, J. Sorensen, R. Breun,
D. Brouchous, R. Fonck, T. Intrator, G. McKee and P. Probert
University of Wisconsin-Madison
Department of Nuclear Engineering & Engineering Physics
1500 Johnson Drive, Madison, WI 53706-1687 USA

Introduction

Many past tokamak rf experiments have been plagued by uncontrolled increases in impurity generation during rf. One solution, which worked in the JET tokamak rf heating experiments /1/, is to employ 180° antenna phasing, align the Faraday shield bars with the local magnetic field, and coat both Faraday shield and walls with Be. Other experiments have found that B wall coatings were effective /2/. Coating with Be or B reduces impurity generation by lowering sputtering rates, by providing some gettering and also by providing a low Z wall material.

It is now thought that much rf impurity generation is due to the antenna near field $\partial B/\partial t$ which, via Faraday's law, generates rf sheath voltages at the Faraday shield and nearby grounded, conducting limiters /3/. As a consequence, the time-average plasma potential ϕ_p increases (self-biases) in the scrape-off layer (SOL) to limit electron losses. Ions are accelerated in the resulting large sheath potentials at the Faraday shield and limiters, with an attendant increase in sputtering. Operation with 180° phasing of adjacent current straps approximately cancels out the net near field $\partial B/\partial t$ /4/ and thus reduces the rf-induced SOL potential increase. However, phasing at other than 180° is often required. Tokamak current drive experiments require smaller antenna phase intervals (90° or less) to obtain a directional wave launch. These phasings produce a net $\partial B/\partial t$ and potential increases in the SOL. This effect is emphasized in medium-size tokamaks where the plasma loading resistance is often lower in comparison to large machines, necessitating higher antenna currents (and higher $\partial B/\partial t$) for a given coupled power.

Experiments on the Phaedrus-T tokamak have demonstrated that the problem of uncontrolled increases in impurity flux during rf can be solved by employing "thick" insulating Faraday shield limiters in place of the usual grounded conducting limiters. With insulating limiters, the potential drop induced by the changing magnetic flux can take place in the limiter rather than the SOL. Here we present experimental results which show that the

presence of insulating limiters can result in satisfactory operation without SOL ϕ_p increases and without significant increases in impurity flux, even when no Faraday shield is present.

Phaedrus-T Tokamak

Phaedrus-T is a medium-sized tokamak with a circular plasma (R = 0.92 m, a = 0.26 m, B ≤ 1 T, n ~2 x 10^{19} m^{-3}, T_i, T_e ~ 500 - 800 eV, I_p ≤ 120 kA, 0.2 s discharge). The goal of present experiments is to study ICRF current drive. The vacuum chamber is stainless steel and a full poloidal carbon limiter is employed. All experiments now take advantage of boronization with trimethyl boron (approximately once each week). Helium glow discharges are employed between each plasma discharge. The ICRF is exited by two parallel poloidal current straps, 60° in extent, 4 cm wide, separated by 17 cm. Satisfactory operation with arbitrary current phasing has been achieved by employing a novel approach /5/ to cancel out the strap mutual inductance. Initial ICRF experiments have been at $1.5\Omega_{ci}$ (with H), $2\Omega_{ci}$ (with D) and $0.7\Omega_{ci}$ (with H). Powers of up to 250 kW have been coupled. SOL data presented here were taken with triple probes while impurity radiation was monitored with a VUV spectrometer (SPRED).

Experimental Results

Our initial experiments were carried out with an open stainless steel Faraday shield with no Faraday shield limiters. Both uncontrolled impurity flux and increased SOL plasma potential ϕ_p were identified as problems. The impurity flux was improved by weekly boronization and He glow discharge cleaning. The installation of insulating (boron nitride) Faraday shield side limiters further reduced the impurity flux and also reduced the SOL increases. Only a small iron influx from the Faraday shield remained. Last, the Faraday shield was removed, the current straps were covered with boron nitride tiles and the insulating side limiters were left in place. The residual iron influx was further reduced and the dependence of iron influx on rf power became weak or nonexistent. Bare strap experiments differ from those on TEXTOR /6/ in that the straps are protected by boron nitride (insulting) surrounds.

Data for iron impurity influx vs input power for 0°, 90° and 180° phasing are given in Fig.1. Data labelled S.S. were taken without insulating edge limiters. They show that 0° and 90° have similar effects and that impurity emission associated with 180° phasing is significantly reduced. Data labelled in the presence of insulating limiters at 0° fall slightly below the best 180° data. Measurements made with the unshielded, insulated antenna phased at 90° are seen to be well below those obtained in the presence of the Faraday shield.

It is apparent that the impurity influx is reduced as we go from 0° to 180° phasing and that 0° and 90° phasing are comparable. Data are given for boronized Faraday shields, for boronized Faraday shields with insulating limiters and for unshielded antenna with insulating surround. Note that the impurity generation for the worst case with insulating Faraday shield

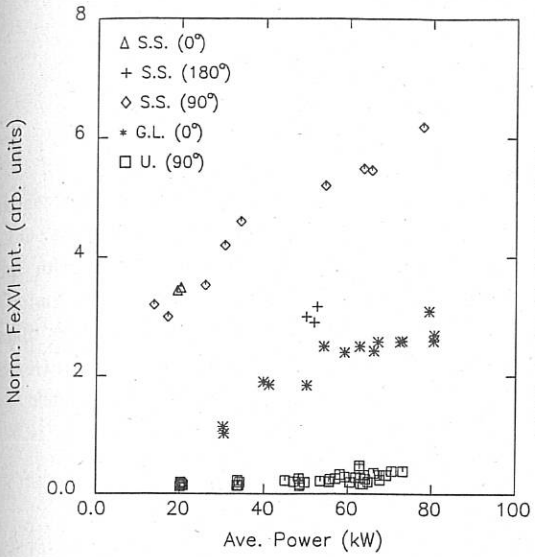

Fig 1:- Intensity of the FE XVI line at 335 Å, normalized to the plasma line density, as a function of rf power for various phasings. Data were taken with the unprotected Faraday shield (S.S.), with the insulating guard limiters (G.L.), and with the unshielded antenna (U.).

limiters (i.e. 0°) is better than the best case for conducting Faraday shields with no limiters (i.e. 180°).

Triple probe data provided the SOL electron temperature T_e and floating potential ϕ_f. SOL plasma potential ϕ_p was calculated using $\phi_p = \phi_f + [3.3 + \frac{1}{2}\ln(m_i/m_H)]\, T_e$, where m_i and m_H are the ion mass and proton mass respectively. Plasma potential increases were generally confined to those regions of the SOL which map to the Faraday shield with largest increases seen by probes which map to the strap current feeder locations. Plasma potential increases were approximately linear with strap current.

The measured SOL plasma potential (measured at the same position) with and without the insulating Faraday shield limiters for 0° phasing are compared in Fig.2. In the absence of the insulating limiters, ϕ_p increases by more than 100 V for an increase in antenna current of 50 A. In the presence of the insulating limiters, ϕ_p does not appear to increase at all.

An additional feature was that the antenna loading dropped by approximately a factor of two when the insulating limiters were installed and toroidal eigenmodes became apparent in the loading data. Bare strap experiments have found that the loading was virtually unchanged when the shield was removed and that the loading was not power dependent. The highest operating voltages (25 kV) were sustained without a shield.

Discussion and Conclusions

Experimental measurements of plasma potential ϕ_p in the SOL and impurity generation demonstrate that ϕ_p and impurities are reduced to below the level previously achieved with

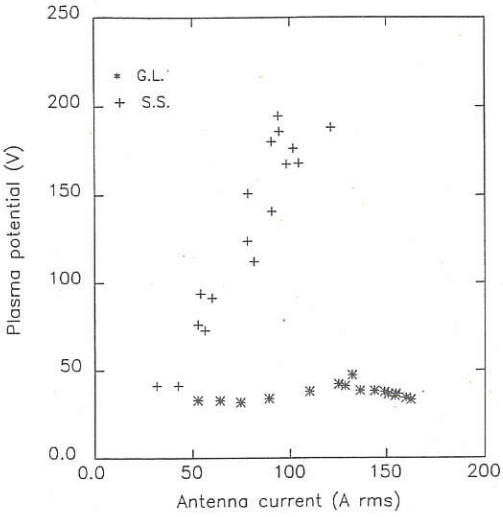

Fig. 2: Plasma space potential vs. antenna strap current. G.L. denotes data taken with the boron nitride guard limiters installed, S.S. denotes data taken with the unprotected stainless steel Faraday shield.

180° operation with grounded limiters through the use of insulating guard limiters. Best power handling and least impurity influx has been achieved by removing the Faraday shield, employing insulating antenna limiters, and covering the antenna straps with insulating tiles.

Acknowledgement

This work is supported by U.S. DOE Grant DE-FG02-88ER53264.

References

/1/ D.A. D'Ippolito, J.R. Myra, M. Bures, J. Jacquinot, "Impurity Release by ICRF Antennas in JET," Fusion Eng. and Design 12, 209 (1990).

/2/ A. Messiaen, R.R. Weynants, J.M. Beuken, L.D. Keyser, et al., "Effect of Antenna Phasing and Wall Conditioning on ICRH in TEXTOR," Plasma Phys. Contr. Fusion 31, 921 (1989).

/3/ D.A. D'Ippolito, J.R. Myra, M. Bures, J. Jacquinot, "A Model of Sheath-Driven Impurity Production by ICRF Antennas," Plasma Phys. Contr. Fusion 33, 607 (1991).

/4/ M. Bures, H. Brinkschulte, J. Jacquinot, et al., "The Modification of the Plasma Edge and Impurity Production by Antenna Phasing During ICRF Experiments on JET," Plasma Phys. Contr. Fusion 30, 149 (1988).

/5/ R. Majeski, P. Probert, T. Tanaka, D. Diebold, et al., "The Phaedrus-T Antenna System," submitted to Fusion Eng. and Design.

/6/ R. Van Nieuwenhove, R. Koch, G. Van Oost, et al., "Ion Cyclotron Resonance Heating of a Tokamak Plasma Using an Antenna Without a Faraday Shield," Nucl. Fusion 31, 1770 (1991).

PLASMA INDUCED MATERIAL TRANSPORT ON LIMITER PROBES IN THE BOUNDARY PLASMA OF FUSION EXPERIMENTS

D.Naujoks, R. Behrisch
Max-Planck-Institut für Plasmaphysik
D 8046 Garching bei München, Germany

The limited magnetic confinement of a hot plasma such as investigated in controlled thermonuclear fusion research causes large fluxes of energetic ions to impinge on the walls of the vacuum vessel, predominantly on the limiters and divertor plates. The atoms eroded at these areas by sputtering enter the SOL plasma and partly the central plasma. A major fraction diffuses back to the limiters, divertor plates and the vessel wall and may cause further sputtering and/or will be redeposited. This material transport along the vessel walls by erosion and redeposition is investigated with the computer simulation program ERO for a limiter probe exposed in the SOL plasma of JET during single discharges.

MODEL

The idea of the investigations is to expose a carbon limiter probe in the SOL with the surface at an angle α relativ to the magnetic flux surfaces (Fig.1). The probe is implanted with a depth marker and evaporated with a well defined surface deposit of Si which has a differt sputtering yield and ionization probability in the SOL plasma.

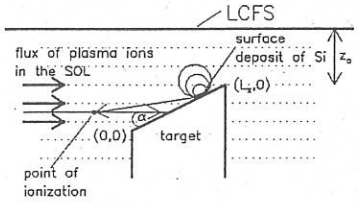

Fig 1: Schematic of the probe

Most of the atoms sputtered by plasma and impurity ions leave the probe surface as neutrals and travel on approximately straight trajectories until they become ionized. Subsequently they gyrate around the magnetic field lines where they have been ionized according to their velocity component $v_\perp^\circ$ and they move along the magnetic field lines with their initial velocity component $v_\parallel^\circ$. They may be additionally accelerated by the hydrogen plasma flow toward the probe limiter. Before reaching the surface of the probe

limiter they will further be accelerated in the sheath potential and they will impinge on the surface with an energy $E=m_I v_\parallel^2/2+3T_e q$. They may be implanted or reflected and cause sputtering.

For a limiter probe with surface area $L_x * L_y$, exposed in the SOL plasma, the change of surface concentration of atomic species I, $\partial n_s^I(x,y,t)/\partial t$ [$cm^{-2}s^{-1}$], with time t at the point (x,y) is given by

$$\frac{\partial n_s^I(x,y,t)}{\partial t} = \Gamma^I(x,y,t)*(1-R_n^I) - \sum_i \Gamma^i(x,y,t)*Y_{i,I}(E,\Omega,n_s^I) + \int_0^{L_x}\int_0^{L_y}\frac{dx'dy'}{\Delta S}\sum_i \int_{E'}\int_{\Omega'} \Gamma^i(x',y',t)*\frac{\partial^2 Y_{i,I}}{\partial\Omega'\partial E'}(E,\Omega,E',\Omega',n_s^I))*\xi\, dE'd\Omega' \quad (1)$$

Here $\Gamma^i(x,y,t)$ is the plasma ion flux of species (i) to the probe; $Y_{i,I}(E,\Omega,n_s^I)$ are the sputtering yields of probe species (I) at bombardment with ion species (i); $\partial^2 Y_{i,I}/\partial\Omega'\partial E'$ represents the energy and angular distributions of sputtered particles (I), which depend on the incident energy E and the angle of incidence $\Omega=(\theta,\phi)$ of the ions, R_n^i is the particle reflection coefficient and $\Delta S=dxdy$ denotes the irradiated surface area.

The coefficient ξ is a geometry factor which is determined by the mean ionization length $\lambda_{iz}^I = (2E'/m_I)^{1/2}/(n_e*\langle\sigma v\rangle)$ (with m_I being the mass of ions (I)), the angle θ', the azimuthal angle ϕ and by the angle α between the surface of the probe and the magnetic field lines with:

$\xi=1$ for $(x'-x)^2+(y'-y)^2=\lambda_{iz}^2(E,r_{LCFS})*(a^2+b^2-2ab\cos(180°-\phi'))$

(with $a=\sin(\theta')$ and $b=\cos(\theta')/\tan(\alpha)$) and $\xi=0$ else.

The rate coefficient for electron impact ionization $\langle\sigma v\rangle$ as a function of the local plasma temperature T_e was taken from /1/. The fluxes of plasma ions and impurity ions to the probe limiter and the plasma temperature profile are assumed to be given by /2/

$$\Gamma^i(x,y,t) = 0.5*f_i*n_e^{LCFS}(t)*c_s*\exp(-r_{LCFS}(x,y)/\lambda_\Gamma)*\sin(\alpha), \quad (2)$$

$$T_e(x,y,t) = T_e^{LCFS}(t)*\exp(-r_{LCFS}(x,y)/\lambda_T), \quad (3)$$

where $c_s=((T_i+T_e)/m_p)^{1/2}$ is the ion acoustic speed at the

LCFS and m_p is the mass of plasma ions; n_e^{LCFS}, T_e^{LCFS} are the plasma density and the electron temperature at the LCFS; λ_Γ and λ_T denote the density and temperature e-folding lengths; r_{LCFS} is the distance to the LCFS. The use of the "concentrations" f_i in equ. (2) assumes that the impurities in the SOL move with the plasma ion velocity /3/.

The motion of atoms which are sputtered at the probe limiter and subsequently ionized is determined by the initial velocity components $v_\perp^\circ$ and $v_\parallel^\circ$ and the acceleration by the friction force with the plasma ions. This can be described by the following differential equation

$$dv_\parallel/dt = \nu_{coll} * (v_{pl} - v_\parallel), \qquad (4)$$

where $v_\parallel$ is the velocity of impurity ions and v_{pl} the velocity of plasma ions parallel to the field lines; ν_{coll} denotes the collision frequency /4/. By using (4) we can also calculate the time of flight until the sputtered atoms reach the surface and thus their ionization stage q.

RESULTS AND DISCUSSION

Using the densities, the temperatures and e-folding lengths as measured for the JET scrape-off layer (λ_Γ=15 mm, λ_T=40 mm /5/), eq. (1) has been solved with a computer program to calculate erosion and redeposition on the probe surface for a D-plasma with impurity concentrations f_{Oxygen}=0.01 and f_{Carbon}=0.1 in the SOL. Only physical sputtering was considered and the distributions of the sputtered particles were calculated by the TRIM type Monte Carlo program IIAM /6/ with the average angles of incidence taken from /7/.

For Carbon the calculated thickness $d = n_s/(n_o * t)$ of deposition/erosion per second along the middle line of the probe y=10 mm (L_x=L_y=20 mm, z_o=5 mm, α=45°, n_o=1.13*10^{22} cm^{-3}) are shown in Fig.2 for a range of edge temperatures and densities and a constant power flux $\Gamma_p \approx T_e^{3/2} * n_e^{LCFS}$ of 2.2 kW/cm^2. For plasma densities below 10^{13} cm^{-3} the deposition behavior is determined by the incoming fluxes of carbon

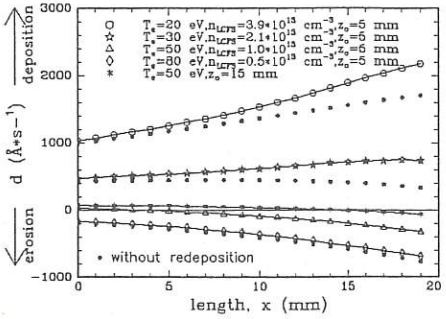

Fig 2: Erosion/redeposition of C along the C probe

ions present in the SOL; erosion dominates closest to the LCFS and deposition dominates further away. For carbon atoms which are sputtered from the target the ionization lengths become short enough only for higher plasma densities so that they can be redeposited on the probe.

Assuming a deposition of $4*10^{16}$ Si atoms/cm^2 at an erosion dominated position x=16, y=10 (Fig.2) on a area of 4 mm^2 prior to the exposure to the JET plasma the calculated distribution of Silicon redeposited on the target after 1 s is shown in Fig.3 (T_e=50 eV, n_e^{LCFS}=1.*10^{13}cm^{-3}, z_o=15 mm, α= 45°). Because of the short redeposition times which are of the order of 10^{-6}s, i.e. because of the very fast multistep transport along the target, redeposited Si can only be found on a deposition dominated area where it is co-deposited with C atoms. Only a small fraction of Si which was sputtered in a direction away from the LCFS (Fig.1) is found to be redeposited. First experiments with a limiter probe exposed in the SOL of JET confirm these results.

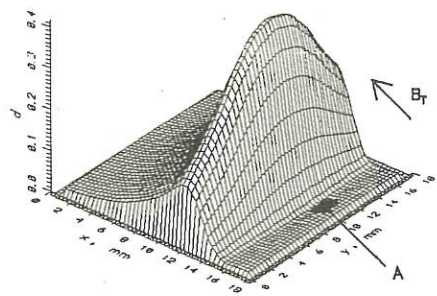

Fig 3: Spatial distribution of a Si deposit at A after 1 s JET discharge

REFERENCES:
/1/ M.A. Lennon et. al., Culham Laboratory, CLM-R270 (1986)
/2/ G.M.McCracken et.al., J. Nucl. Mater. 145-147,621(1987)
/3/ P.C. Stangeby et. al, Nucl. Fusion 30, 1225 (1990)
/4/ S.I. Braginski, Sov. Phys. JETP 6(33), No.2, 358 (1958)
/5/ S.K.Erents et. al, J. Nucl. Mater. 162-164, 226 (1989)
/6/ D. Naujoks, Ph.D. Thesis, Moscow State University 1991
/7/ A.B. DeWald et. al., Phys. Fluids 30(1), 267 (1987)

PRODUCTION AND CONTROL OF AN EDGE RADIATING LAYER WITH THE ERGODIC DIVERTOR ON TORE SUPRA

L.Poutchy, J.C.Vallet,
C.DeMichelis, A.Grosman, W.Hess, M.Mattioli, P.Monier-Garbet.
Association EURATOM-CEA sur la fusion C.E.N. CADARACHE F13108
Saint-Paul-lez-Durance

Abstract

We have recently defined on TORE SUPRA a discharge piloting strategy to prevent disruptions at the density limit, based on the property of the Ergodic Divertor to stabilize MHD activity. This strategy allows plasma studies close to the density limit without disruptions, and has been successfully used on TORE SUPRA ohmicly heated plasmas. The Ergodic Divertor allows also the stabilization of detached plasmas which appear spontaneously near the density limit. Edge impurities are shown to play a fundamental role in this stabilization. Detached plasmas have been thereby controlled during 10 seconds.

I) Introduction

The control of a stable edge radiating layer is a possible alternative to solve the open problem of the divertor plates design for a machine like ITER. Those divertor plates will have to withstand a continous peak heat flux in the range of 15-30 MW/m^2, assuming that 50% of the thermal exhaust power (200MW) is radiated. These design values address three questions: first what are the conditions needed to radiate 50% of the plasma output power on ITER, second is 50% of radiated power enough compared to the technical possibilities and third, if not, will it be possible to radiate more power?

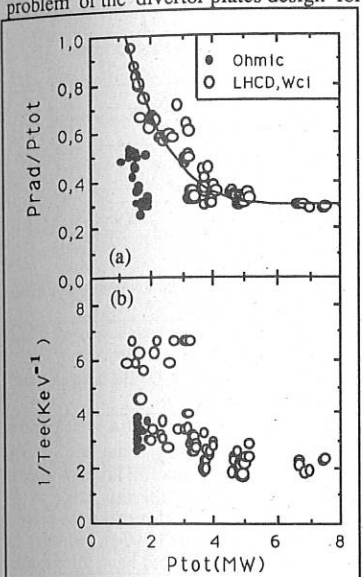

fig.1. Relative radiated power and edge inversed electron temperature $1/T_{ee}$ (measured at ρ=0.95) for D2 discharges with additional power. In the range $1<P_{tot}<2$MW T_{ee} decreases since a part of the R.F. power is used for the current drive.

We find on TORE SUPRA that the ratio of the radiated power P_{rad} (measured by an array of 16 bolometer located in a poloidal section) to the total input power P_{tot} (where $P_{tot}=P_{ohm}+P_{LHCD}+P_{wci}$) decreases with the total input power (fig.1.a) according to the large increase of the edge temperature (fig.1.b). So, for a perpendicular heat flux in the range of 0.05 to 0.1MW/m^2 at the plasma periphery and an edge density of about 1.5 10^{18}m^{-3} (shots with P_{tot}=7-8MW) the power ratio $P_{rad}/P_{input}\approx$30% is obtained. In this case, the edge electron temperature measured at (r/a)$\approx$0.95 is 500eV. This high edge temperature does not allow high radiation rates. We find also that the ratio P_{rad}/P_{input} increases with the density. This is a reason why high edge densities close to the density limit are attractive.

Recently we found in ohmic heated plasmas that the Ergodic Divertor (ED) can be an interesting tool to control the plasma edge temperature[1,2].

II) Experiments near the density limit with the Ergodic Divertor

Two effects of the ED have been used on TORE SUPRA to elaborate a discharge

piloting strategy to prevent density limit disruptions [3]: first, the ED stabilizes the m=2 n=1 tearing mode[4] and second in deuterium discharges it induces a large pump out of plasma particles. The tearing mode stabilization is not a consequence of the density decrease. It is also observed in helium discharges in which gas puffing compensate for the density decrease induced by the ED.

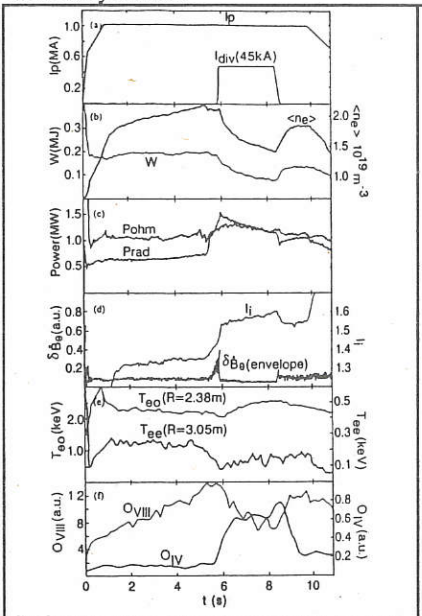

fig.2.a Shot 6081. Disruption avoidance in a dirty D2 discharge at q=3.8

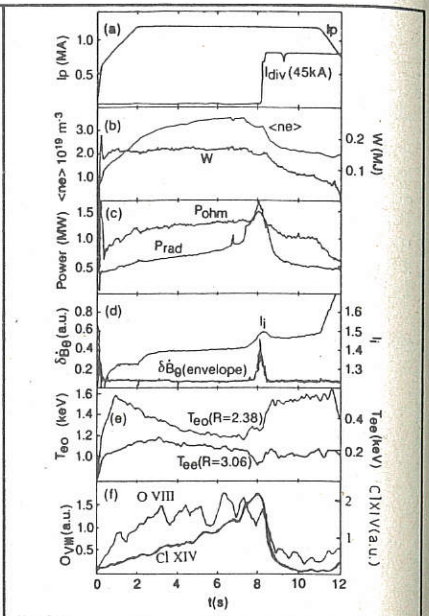

fig.2.b Shot 6869. Disruption avoidance in a clean D2 discharge at q=3.6

fig 2.a and fig 2.b show the plasma current I_p; the divertor current I_{div}; the average electron density $<n_e>$; the stored kinetic energy W; the ohmic power P_{ohm} and the radiated power P_{rad}; the internal inductance l_i; the MHD monitor $\delta \dot{B}_\theta$; central (Teo) and edge (Tee) electron temperature, "central" OVIII(λ=1,9nm) and "peripheral" OIV(λ=23,8nm) oxygen lines and "central" ClXIV(λ=23,7nm) chlorine line.

Our strategy is to trigger the ED and to switch off the gas puff at a well defined threshold of the m=2 n=1 mode amplitude ($\delta B_\theta/B_\theta \approx 3.10^{-3}$) when the plasma has already detached (the plasma is detached when a toroidally and poloidally symmetric layer of intense radiation is observed at the edge). We have checked the efficiency of this strategy on discharges where the density was ramped up close to the density limit, for different plasma conditions as wall conditionning and plasma purity. These experiments have shown that the ED is able to stabilize both the MHD activity and the detached plasma, and have allowed the determination of the conditions necessary for the stabilization of the detached plasma.

The data reported in this section concern two series of shots on which the strategy has been applied. Each series is characterized by a highest value obtained of Mq (M=<ne>R/Bt being the Murakami parameter and q the safety factor at the edge)which depends on the impurity contamination of the plasma. In the first series the density limit is encountered at $Mq=7.10^{19}m^{-2}T^{-1}$. This rather low value corresponds to "dirty" discharges (carbonized vessel), highly contaminated by oxygen due to a small air leak ($n_O/n_e \approx 1.4\%$, $n_C/n_e \approx 0.8\%$). In the second series the density limit is reached at $Mq=10.10^{19}m^{-2}T^{-1}$ and correspond to "clean" discharges after boronization, with a very low oxygen rate ($n_O/n_e \approx 0.13\%$, $n_C/n_e \approx$

0.41%). In these two series the behavior of the discharges after the application of the ED is quite different.

In the "dirty" series ($Z_{eff}\approx 2$) it is observed that the ED stabilizes both the MHD activity (fig.2.a(d)) and the detached plasma: in spite of the density decrease the radiated power is maintained very close to Pohm (in fact, Pohm-dW/dt, W being the stored kinetic energy) during the application of the ED(2.5s), and even afterwards (fig.2.a(c)). The edge electron temperature T_{ee} measured at r=r/a≈.9 (with a≈.77m) drops from 300eV to below 200eV in the "predisruptive phase" of the discharge preceeding the application of the ED (fig.2.a(e)). With the ED the edge electron temperature is maintained at this low level (fig.3.b). It is observed that the peripheral lines located in the ergodic layer (like oxygen line OIV) increase while the more central lines located in the plasma bulk (like OVIII line) decrease with the density (fig.2.a(f)) [5]. The carbon line CVI(Lyα) and the oxygen line OVIII(Lyα) show the same dependence. The shrinking of the radiating layer observed during the "predisruptive phase" is stopped and reversed when the ED is turned on (fig.3.a.). The expansion of the radiating layer radius is quite slow (5cm/s).

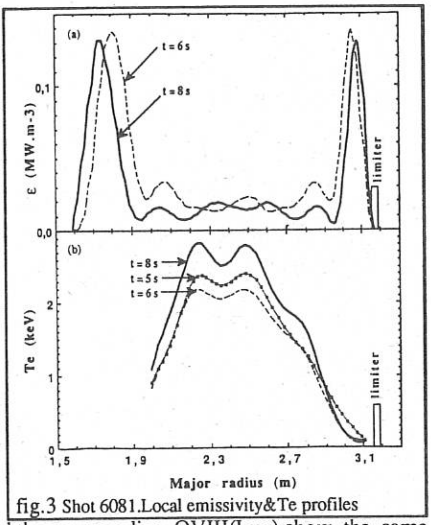

fig.3 Shot 6081.Local emissivity&Te profiles

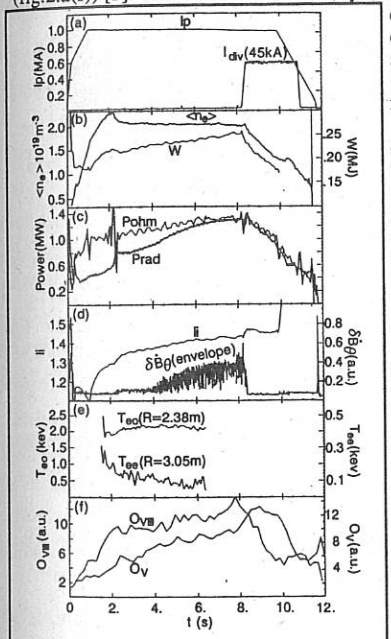

fig.4. Shot 5568 .Disruption avoidance in a dirty D2 discharge at q=3.9

Using the strategy we could produce a detached plasma during 10s (fig.4.c). The detachement (t=2.4s) is induced by a strong gas puff. The electron density is then stabilized 15% below the density limit(fig.4.b) and we observe that the plasma does not reattach(fig5). The cooling of the plasma boundary, the shrinking of the plasma profiles and the whole set of predisruptive phenomena (growth of MHD activity, increase of l_i, increase of P_{rad}/P_{ohm}) are quite slow: the ratio P_{rad}/P_{ohm} which is about .8 when the plasma detaches takes more than 6s to reach 1 (fig.4.c). The radius of the radiating layer has then decreased by ≈15cm. At that time, the mode amplitude reaches the critical level and the ED is triggered. In this case too, the inward motion of the radiating layer is reversed and the ratio P_{rad}/P_{ohm} stays close to 1. In this discharge we observed that the ohmic power decreases with the ED by about 20%, corresponding to the impurity decrease in the confined plasma.

In the "clean" series (Zeff≈1.2) it is observed that after the triggering of the ED, the ratio P_{rad}/P_{ohm} drops from 1 to .5 corresponding to the plasma reattachement (fig2.b(c)). Correlatively the edge electron temperature T_{ee}

after the "predisruptive phase" recovers a level close to 200eV (fig2.b(e)). At this high edge temperature, the OIV emission is below the detection limit. On the other hand, as in every high density shot, chlorine emission is recorded. With the ED, the peripheral lines brightness do not increase and a drastic decrease of chlorine emission is observed (n_{Cl}/n_e drops from $n_{Cl}/n_e \approx 0.065\%$ to $n_{Cl}/n_e \approx 0.008\%$) (fig.2.b(f)). The plasma reattachment is attributed to the fact that there are not enough impurities in the plasma to sustain a high radiation rate and a low edge temperature when the density decreases. In this case the expansion of the radiating layer is faster than in the dirty series (typically 30-50cm/s).

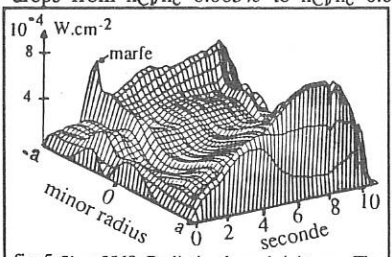

fig.5 Shot 5568. Radiative layer brightness. The ED is applied at t=8.3s

This reattachment allows an additional observation during the shrinking phase of the plasma: the very cold region between the wall and the radiating layer is filled with neutral particles corresponding to a partially ionized plasma. With the ED the plasma reattaches and this cold region is heated up. The visible light recorded on a CCD camera looking tangentially at the plasma boundary on the high field side reveals for the first time structures of magnetic flux tubes in the ergodic layer (fig.6). Although magnetic surfaces are fully destroyed, modulation of field line connection lengths reminds the topology of the magnetic islands induced by the resonant perturbation created by the ED [6,7]. The poloidal and radial extension of the structures corresponds to the expected size of the magnetic perturbation m=18±3 n=6. The visible light intensity modulation may represent the density modulation associated with the modulation of the field lines connection. When the edge temperature increases neutral particles are ionized and the structures are no longer visible.

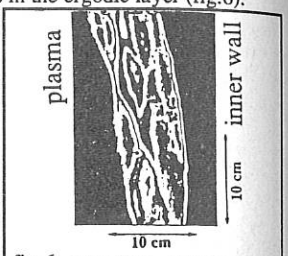

fig.6 Shot 6877. Ergodic layer during the shrinking phase of the plasma

III) Conclusion

The discharge piloting strategy which allows the stabilization of the MHD activity is a powerful tool for the study of radiating layers stability. Indeed, if the impurity concentration is sufficient, this strategy allows the stabilization of an edge radiating layer which dissipates 100% of the input power. ED experiments are planned on Tore Supra to succeed in stabilizing a radiative layer in a clean discharge, with the help of an extrinsic impurity injection (N or Ne) at the edge. Experiments with a stable and high density (10 or 15% below the density limit) would also be quite interesting and would allow the stabilization of an edge radiating layer, without any impurity injection. The ability of the radiating layer to dissipate a large amount of additional power will also be studied soon.

Acknowledgements

The authors are grateful to Ph.Ghendrih, F.NGuyen, A.Samain for fruitful discussions, P.Chappuis, D.Guilhem, R.Guirlet, P.Lecoustey, A.L.Pecquet for providing data and to C.Balorin for her help in the data analysis.

References

[1] A.SAMAIN, T.BLENSKI &al. Contribution to Plasma Physic. 30,157(1990)
[2] A.GROSMAN &al. Pl. Phys. and Contr. Fus. 32 (1990)1011
[3] J.C.VALLET, L.POUTCHY &al. Phys. Rev. Letters 67 (1991)2662
[4] J.C.VALLET, D.EDERY &al."Control of the MHD activity with the Ergodic Divertor on Tore Supra". (This conference paper n°4-1-131)
[5] C.BRETON, C.DE MICHELIS &al. Nucl. Fus. 31(1991)1774
[6] G.FUCHS, K.H. DIPPEL &al. Proc. 14th Eur. Conf. Madrid vol.1(1987)253
[7] P.GHENDRIH, F. NGUYEN "Edge transport induced by the interaction of a stochastic layer with the wall" (This conference paper n°4-1-26)

EDGE TRANSPORT INDUCED BY THE INTERACTION OF A STOCHATIC LAYER WITH THE WALL.

F. Nguyen, Ph. Ghendrih, A. Samain, A. Grosman
Association Euratom-CEA, CE Cadarache, 13108 St Paul lez Durance, Cédex, France.

The Ergodic Divertor (ED) implemented in Tore Supra is designed to organize the plasma wall interaction by creating a soft separatrix between the core plasma ($q < 2$) and the wall ($q > 3$). This soft separatrix is in fact a layer where the flux lines are stochastic and ergodic. This allows in principle to control the transport through the layer and hence the basic parameters of the edge plasma [1]. However, between the ergodic layer and the wall the flux lines have a relatively simple behaviour [2], thus leading to a laminar domain of transport. The experiments on Tore Supra [3] have demonstrated that both the ergodization and the wall connection pattern are important, the latter prevailing in the deposition of heat and particles. In the present paper, we further investigate the heat transport in the laminar boundary and the implications on the heat deposition. We consider the case where the ED coils are the limiters, so that the wall to wall connection takes place between the different ED coils. Experimental H_α signals are also analysed in terms of heat flux inhomogeneity which may occur in the laminar domain.

Magnetic topology induced by the Ergodic Divertor

The Ergodic Divertor of Tore Supra [4] consists of 6 octopolar coils over $\Delta\varphi = \pi / 14$ (equally spaced toroidally). The 8 current bars of each coil are localized on the low field side of the torus over $\Delta\theta = \pi / 3$ (as sketched on Fig.2). The spectrum of the magnetic perturbation is such that the magnetic surfaces are destroyed for q values ranging between 3.5 and 2.5. The ergodicity of the field lines is characterized by the diffusion of the field lines D_{FL} ($\sim 10^{-4}$ m^2/m) and the stochasticity by the length L_K ($\sim \pi qR$) which governs the exponential divergence of neighbouring flux lines. However this picture is modified if one introduces a wall in this layer. The field lines are then connected to the wall and thus exhibit a finite wall to wall connection length. One can readily expect the basic properties of the stochasticity to hold provided the distance along the field line to the wall, the connection length L_{wall}, is larger than L_K. When L_{wall} is smaller than L_K, the distance to the wall is too short to allow a stochastic behaviour, this defines the laminar domain. The width of this domain, $\Delta r_{laminar}$, can be computed from the diffusion in the ergodic domain over the length L_K, $\Delta r_{laminar} \approx (D_{FL} L_K)^{1/2} \approx 5.10^{-2}$ m. This defines the statistical boundary between the laminar and ergodic regions.

Let us first consider the statistical properties of the field lines starting from an Ergodic Divertor coil. The dependence of the radial penetration on the connection length is computed precisely by the code MASTOC [2]. As the parallel distance is increased, the field lines form

different classes of flux tubes which either reconnect to the wall or penetrate further towards the plasma core. The flux tubes only reconnect onto other Ergodic Divertor coils, on inwards (outwards) perturbation domains if one follows field lines in the co (counter) direction. One thus finds that the wall to wall connection length is quantizied by two typical scales : a small scale $2\pi R/6$ which is the parallel distance between two coils and a large scale $2\pi qR$ for a complete poloidal rotation (including the transit on the high field side). The statistics indicate that 40 % of the field lines have significant connection lengths, larger or equal to $4\pi qR$ (2 poloidal turns), fig. 1. As can be expected the short connection lengths are associated to limited radial excursion in the edge layer while the largest radial excursion are found for long connection lengths.

Heat deposition on the Ergodic Divertor coils.

Owing to the magnetic topology, one expects the heat deposition to be localised on the set of ED coils and especially between the current bars where actively cooled neutralizer plates have been implemented. One can readily assume that the outward heat flow is homogeneous in the ergodic domain ($r < a-\Delta r_{laminar}$). The structure of the heat deposition on the ED coil will then depend on the heat transport in the laminar domain. For each flux tube impinging the ED coil a convenient description of the deposited power can be obtained by a combination of the radial excursion and the associated parallel scale. The relevent parallel scale for the heat transport is L_T, $L_T \sim L_K \, \mathrm{Log}(\chi_{//} D_{FL} / (\chi_{\perp} L_K))$ [4], such that the heat flux is transported along a single flux tube. For Tore Supra one finds that $L_T \approx 2 L_K$, which corresponds to a complete poloidal rotation. One then relates the capability of heat deposition of a given field line to the maximum radial excursion Δr_{max} achieved over the parallel displacement L_{max} bounded by L_T. The three figures of merit Δr_{max}, $\Delta r_{max} L_{max}^{1/2}$ and $\Delta r_{max} L_{max}$ have been tested and yield similar results. The values of the figure of merit Δr_{max} are displayed on Fig. 2 for a given ED coil mapped on the θ, φ plane. One finds that the heat deposition pattern is smooth and does not exhibit hot spots but rather a localized deposition between the current bars. The figure of merit indicates that 40 % of the heat flux flows between the current bars while the remaining 60 % are spread on the ED graphite protection tiles, Fig.3. The average radial excursion of the field lines which channel the heat flux to the wall, $\Delta r_{channel} \approx 0.08$ m, is large compared to the e-folding length of the heat flux in the SoL for limiter plasmas, $\lambda_q \approx 0.01$ m. This indicates that the heat deposition pattern is robust with respect to magnetic misalignements in the poloidal plane which is usually estimated as a significant fraction of λ_q. The robustness with respect to a misalignement of the main magnetic axis in the equatorial plane is further ensured by the radial spreading between the current bars on the neutralizer plates, $\Delta r_{spread} \approx 0.03$ m [2]. The effective "λ_q" for the ED which accounts for the robustness of the heat deposition with respect to misalignements is thus larger than the values achieved in limiter plasmas.

Poloidal modulation in the stochastic Scrape Off Layer.

On a given set of experiments, the ergodic divertor was applied on a detached plasma [5]. The plasma then reattaches and over a transient time one observes a structure in the emitted H_α light seen with a tangential view of the inner wall. One considers, in a very crude model for the scenario, that the complex physics involved in this experimental result is governed by the heat transport along the perturbed flux tubes through the cold detached plasma. The H_α map then delineates the "hot" flux tubes where the neutrals are ionized. In the present model, the points in the r, θ plane are labelled as hot provided they belong to flux tubes which exhibit inward radial excursions beyond the radiating layer, r = 0.73 m, over a finite length bounded by L_T. The trace of these hot flux tubes in the poloidal plane (r, θ) is displayed on Fig.4. The crosses (circles) form a series of bands which are associated to flux lines connected to the core in the co (counter) direction. The structure given by these crosses has a poloidal period of $2\pi / 16$ and a slope $dr / d\theta$ governed by the shear which ensures that neighbouring crosses experience a similar radial excursion. This slope changes sign for the structure in the counter direction so that the global structure (crosses + circles) has an island like shape with a poloidal wave number of 0.19 m in close agreement with the measured value of 0.17 m.

Conclusion

The deposition of heat and particle on the wall is governed by a laminar regime of transport, between the truly stochastic and ergodic layer and the coils, over flux tubes with a parallel length $L_T \leq 2\pi qR$ experiencing a radial excursion up to 0.08 m. The heat deposition is smooth with a marked localisation between the current bars. Moreover, this heat deposition pattern is robust to magnetic misalignement since the energy is collected over 0.08m radially inside the plasma (and spred further 0.03m between the current bars). The periodicity observed in H_α light in some experiments is understood as the signature of hot flux tubes conducting the heat through the cold detached plasma. The structure then results from superimposed series of bands with opposit slopes governed by the magnetic shear. The tangential view of such structures has an island like shape even though no such magnetic structure exists. This interpretation should be considered in experiments where similar patterns have been reported, in other experiments using helicoidal coils [6] but also and in pellet injection experiments [7].

References

[1] A. Samain *et al.*, Contr. Plasma Phys. 30(1990)1,157-165.

[2] F. Nguyen *et al*, J. Nucl. Mat., 176&177(1990)499

[3] A. Grosman *et al.*, Plasma Physics and Contr. Nuc. Fusion, 32(1990)1011

[4] A.B. Rechester, M.N. Rosenbluth, PRL 40(1978)38.

[5] L. Poutchy *et al.*, IV-27, this conference

[6] K.H. Dippel, J. Nucl. Mat., 145&147(1987)3

[7] H.-W. Drawin and M.A. Dubois, submitted to Nucl. Fus.

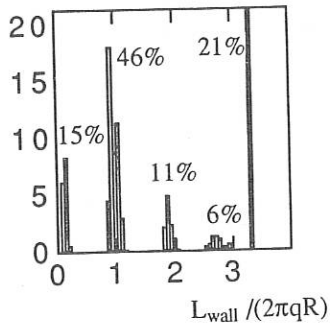

fig. 1 : statistics of the connexion length L_{wall} where 2πqR is a poloidal turn

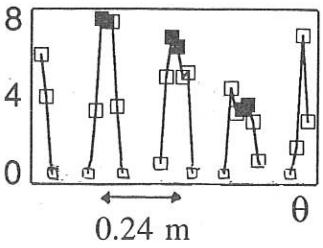

fig. 3 : poloidal dependence in percent of the heat deposition (counter direction) on one ED coil

■ neutralizer plate ▯ coil protection

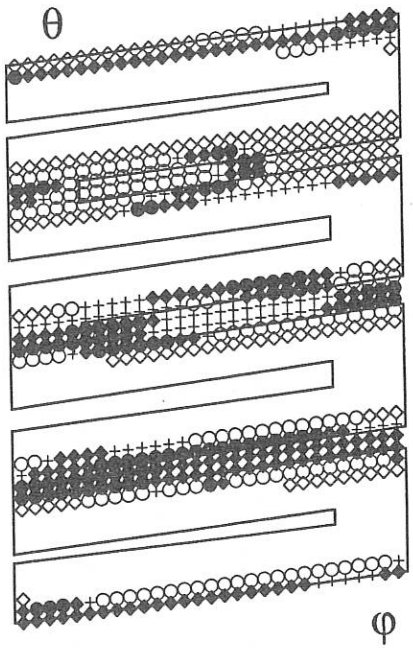

fig. 2 : connexion (in the counter direction) of the field lines on an ED coil depending of the maximal radial excursion (m)
◇[0, 0.02] ○[0.02, 0.04] +[0.04, 0.06]
◆[0.06, 0.08] ●[0.08, 0.1]

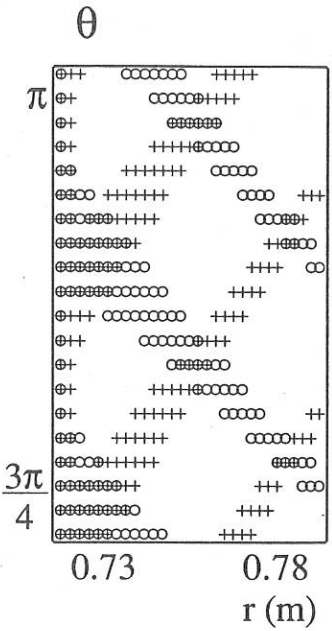

fig. 4 : poloidal structure of the hot flux tubes

CONTROL OF THE MHD ACTIVITY WITH THE ERGODIC DIVERTOR ON TORE SUPRA

VALLET, J.C., EDERY, D., VAN HOUTTE,D., MOHAMED-BENKADDA, M.S., JOFFRIN, E., LECOUSTEY, P., PECQUET, A.L.,SAMAIN, A., TALVARD, M.

Association EURATOM-CEA sur la fusion
C.E.N. CADARACHE F13108 Saint-Paul-lez-Durance

Abstract

On TORE SUPRA it has been experimentally found that the ergodization of magnetic field lines on a thin layer (0.1-0.2m) at the plasma boundary has a strong stabilizing effect on the m=2 n=1 tearing mode. This is observed on a wide range of edge safety factor($2.5<q\psi(a)<4.5$) and of internal inductance ($0.8<li<1.6$). This stabilizing effect have been successfully used to prevent both density limit disruptions and the disruptions triggered by mode locking in fast plasma current rises. A set of experimental data is reported in this paper.

1) Introduction

The aim of an Ergodic Divertor (ED) is to destroy the magnetic surfaces in a thin layer (the Ergodic Layer) at the plasma boundary. This is achieved by creating a radial magnetic field perturbation δB_r^{ED} which is the sum of resonant components along magnetic field lines. The TORE SUPRA ED is composed of 6 octopolar coils (equally spaced in the toroidal direction) which ensure magnetic perturbations $15 \leq m \leq 22$ and n=6 resonant for $q\psi = m/n$ localized in the first twenty centimeters inside the plasma [1]. For a perturbation amplitude of the order of $(\delta B_r^{ED}/B\theta) \approx 10^{-2}$ (corresponding to a total current intensity flowing into the divertor coils of Idivertor=45kA) the magnetic islands created on resonant surfaces strongly overlap leading to a stochastic behavior of the magnetic field lines.

The expected benefits of an ergodic layer at the plasma boundary in which both particles and energy transport are hugely increased, mainly concerned the control of the plasma wall interactions: control of impurity production, screening of the impurities, production of a cold mantle surrounding the plasma...[2]. In addition a strong stabilizing effect on the m=2 n=1 tearing mode has been identified. A full stabilization or at least a noticeable amplitude reduction of the MHD activity (when it exists) has been recorded in all standard TORE SUPRA experiments with $2.5<q\psi(a)<4.5$ and with a minor radius a >.75m in which the ED was applied.

2)Stabilisation of the m=2 n=1 mode by the ED on standard steady state TORE SUPRA experiments.

The fig1 shows a typical example of m=2 n=1 mode stabilization in the helium discharge n°5179 at $q\psi(a) \approx 2.5$. TORE SUPRA ohmic discharges with $q\psi(a)<3$. always shows a saturated m=2 n=1 tearing mode activity. The MHD activity amplitude monitored by the positive envelope of a Mirnov coil signal reaches the noise level when the ED is turned on (Fig.1.c). The signal recorded on the locked mode detector

(composed of four saddle loops measuring the n=1 radial field perturbation near the wall inside of the vacuum vessel) remains at the noise fluctuation level which corresponds to $\delta B_r/B_\theta \approx 10^{-4}$ (Fig1.c). The analysis of the Mirnov signals recorded on an array of 16 poloidal field pick up coils shows that the δB_θ amplitude of the m=2 n=1 tearing mode vanishes and that as usually observed the decrease of the mode amplitude is accompanied by a slight increase of the mode frequency as long as the m=2 mode is detectable i.e. $\delta B_\theta/B_\theta \approx 10^{-5}$ (Fig 2.b&2.c). A limited scan in divertor current intensity Idiv made on shots similar to n°5179, has shown that the full mode stabilization requires Idiv≥18kA; at Idiv=13kA a mode amplitude reduction of the order of 50% is obtained. To explain the stabilization one may first envisage thermal effects around the q=2 surface [3]. The large variation of the radiated power behaviour observed in stabilization experiments leads to consider rather direct effects on the current density profile. Following the Δ' theory, the stabilization is interpreted as a modification of the edge current density gradients.

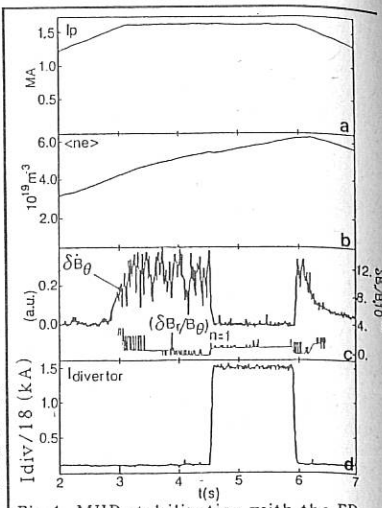

Fig 1 MHD stabilization with the ED shot 5179 helium discharge at q=2,5

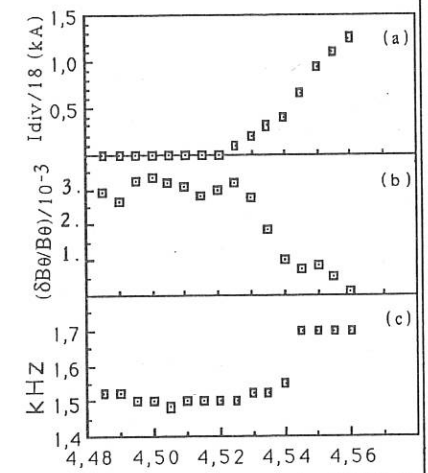

FIG.2 SHOT 5179
(a)divertor current; (b) m=2 mode amplitude $\delta B_\theta/B_\theta$; (c) m=2 frequency

A part of the initial current flowing at the plasma edge is forced to flow deeper in the confined plasma: the resistivity is indeed enhanced inside the ergodic layer because of the finite connection lengths of the ergodic magnetic field lines with the wall [4]. This interpretation is supported by a systematic increase of the internal inductance observed when the ED is turned on. An analytical Δ' analysis demonstrates that the shrinking of the current density profile imposed by the ED could explain the mode stabilization [4].

The stabilizing effect associated with the density decrease produced by the ED in deuterium discharges has been used to define a strategy for preventing density limit disruptions [5]. The strategy consists of both in stopping the gaz puff and triggering the ED at a given MHD activity threshold: $\delta B_\theta/B_\theta \approx 3.10^{-3}$. So far the efficiency of this strategy is 100% on a database of 20 D2 shots in which the density is increased up to the limit.

An analysis of the discharge behaviours following the turning on of the ED is given in [6].

3)Locked modes and ergodic divertor in current rise experiments

The success obtained on density limit disruption avoidance by the control of the m=2 n=1 tearing mode address the question of the effect of the ED on the other disruptive limits for which low m MHD modes are involved. A new series of experiments has been devoted to locked mode disruptions triggered by fast plasma current rise.

It is observed on TORE SUPRA as on other Tokamaks that the Mirnov activity produced when rational surfaces are expelled from the plasma, increases with the current rate dIp/dt. On many devices for .5≤dIp/dt≤1MA/s the amplitude of the MHD activity at $q\psi(a)\approx 4$. is so large that the modes lock, leading either to disruption or to poor discharge performances [7]. The experimental results are summarized on fig.3. Two current rises without ED are shown :first a fully stable current rise at dIp/dt=0.4MA/s, which is the standard current rise used on TORE SUPRA, and secondly a current rise at dIp/dt=0.8MA/s which disrupts. On this discharge we observed the Mirnov activity and the mode locking at $q\psi(a)\approx 4$. The locked mode induces a strong perturbation on the plasma current such as the determination of the poloidal mode number is quite difficult.

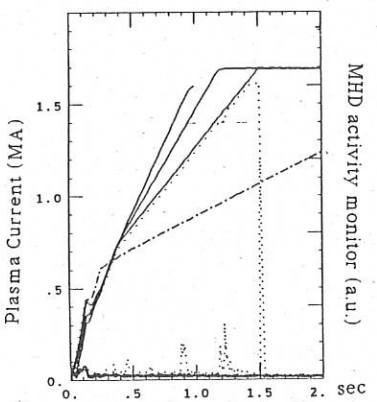

Fig.3 current rises and Mirnov activity.(solid lines with ED brokenlines without).
$q\psi(a)\approx 4$ corresponds to Ip≈1.3MA

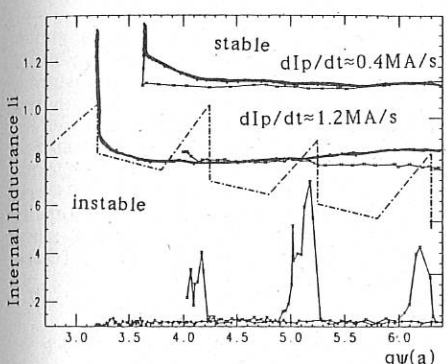

Fig.4 trajectories in the li(a),qψ(a) diagram & Mirnov activity with and without ED(thick and thin lines respectively) at dIp/dt=.4 &1.2MA/s

On the sameFig.3 current rises, with the ED, at dIp/dt≈0.8, 1.2&1.5MA/s are shown. With the ED neither Mirnov activity nor mode locking are detected. The dIp/dt≈1.5MA/s shot disrupts because the ED is too early switched off, nevertheless $q\psi(a)\approx 4$ is crossed without producing a locked mode. One may admit that the stability of the current rise is governed by the trajectory of the discharge in the li(a),qψ(a) diagram, in which at low li a semi-empirical stability limit corresponding theoritically to surface kink modes can be defined [8]. The limit applicable to TORE SUPRA is shown on fig.4 (broken line). Examples of trajectory and Mirnov activity are also shown on fig4 for dIp/dt≈0.4MA/s and 1.2MA/s respectively with and without ED.

Two behaviours corresponding to favourable actions of the ED on the plasma stability can be observed on fig.4: first at low dIp/dt≈0.4MA/s the trajectory of the discharge with ED exhibits a positive drift compared to the

8046 Garching bei München

trajectory without ED. The drift starts at about $q\psi(a)\approx 5$ and increases as $q\psi(a)$ approaches the ED resonant value i.e.$q\psi(a)\approx 3.2$; secondly at high $dIp/dt\approx 1.2MA/s$ the two trajectories with and without ED cross the instable domain. At $q\psi(a)\approx 4$ without ED, Mirnov activity is produced and a disruption occurs while, with the ED, the discharge is fully stable. It appears that with the ED the stability at $q\psi(a)\approx 4$ remains at $li\approx .8$ while it requires $li\geq 1$. without. The first effect observed at $dIp/dt\approx 0.4MA/s$ reflects the statement given above that the ED increases the plasma boundary resistivity and thus the plasma current diffusion and the value of li. Even when this effect is attenuated by a larger current rise rate $dIp/dt\approx 1.2MA/s$ a stabilizing effect remains. It is plausible in such a case that current density gradients are canceled at the very plasma edge and that this is sufficient to insure the stability of the surface kink mode occuring when $q\psi(a)$ cross the value 4. The stability limit shown in fig.4 corresponding to the standard shape of current density profile is lowered with the ED. However it has been found that for lower li value i.e. $li\leq .7$ disruptions with the ED on are also triggered. Independently of the achieved performances these new experiments have demonstrated the capability of an ED to control the Mirnov activity and to prevent mode locking.

4) Disruptions induced by the ED.

In the current rise experiments described above it appears interesting to increase the ED perturbation level to control discharge at very low li. In contrast with TEXTOR [9] the available maximum perturbation level on TORE SUPRA is well below the disrupting limit: for standard steady state TORE SUPRA experiments performed at $a\geq 2.75m$ the ED does not produce disruptions even at the maximum perturbation level. The only way on TS to reach the disrupting level -by increasing the relative penetration depth of the perturbation- is to reduce the plasma minor radius, because of the strong localization of the ED perturbation the actual δB_r on the q=2 surface can be largely increased by a small variation of its position toward the ED coils. It is found that there exists a very sharp transition: for plasma minor radius $a\leq .74m$, disruptions are produced at half the maximum perturbation level. In this case the disruption is interpreted as resulting from an enhancement of the current density gradient inside the q=2 surface.

5) Conclusion: Experiments made on TORE SUPRA have demonstrated that the Ergodic Divertor is a powerfull tool to stabilize the MHD activity. The stabilizing effect is attributed to a modification of edge current density gradients resulting from the finite connection lenght of the ergodic magnetic field lines with the wall. Analytical studies of current density profile showing the stabilization effect is reported in the paper given in reference[4]. In previous experiments the ED has been successfully used to prevent density limit disruptions[5,6]. In a new series of preliminary experiments the ED has been used both to stabilize Mirnov activity and to prevent mode locking during the fast plasma current rises. These new results reinforced the assumption of the direct effect of the ED on the current density profile as being the origin of the stabilization mechanism. It is envisaged in future experiments to study the influence of the ED on the q=2 limit.

references

[1]A. SAMAIN, T. BLENSKI &al. Contribution to. Plasma Physics.30, 157 (1990).
[2]A. GROSMAN, T. EVANS &al. Plasma Physics and control led fusion 32,157 (1990)
[3]P.H. REBUT & M.HUGON Plasma and Controlled Fusion Research 2,197 (1984)
[4]D. EDERY, A. SAMAIN &al.. Mechanism for MHD modes stabilization by the Ergodic Divertor. (this conference paper n°8-18)
[5]J.C.VALLET, L.POUTCHY &al. Physical Review Letters, Vol 67, 1991, p2662
[6]L.POUTCHY, J.C VALLET &al. Production and control of an edge radiating layer with the ergodic divertor on TORE SUPRA (this conference paper n°4- 27).
[7]M. HUGON , B. BALET &al. 18th Eur. Conf. on Cont. Fus.& Plas. Phys.,'Berlin, 1991,Vol.I, p.41
[8] D.VanHOUTTE, M. TALVARD&al. 18th Eur. Conf. on Cont. Fus. & Plas.Phys.,Berlin, 1991,Vol.I, p. 61
[9]G.FUCKS, K.H DIPPEL &al. 14th Eur.Conf. on Contr Fus.& Plas.Phys.,Madrid,1987, VolI, p253

PLASMA EDGE STRUCTURE OF A TOKAMAK WITH ERGODIC MAGNETIC LIMITER

S. Takamura, Y. Oda and S. Sakurai
Department of Electrical Engineering, Faculty of Engineering
Nagoya University, Nagoya 464-01, Japan

INTRODUCTION: Stochastic Magnetic Fields have been found to have potential effects on the plasma transport at the edge of toroidal confinement devices. We have been studying on the modification of plasma density and temperature, electric field, and impurity transport at the tokamak edge by the ergodic magnetic limiter (EML) [1～4].

Here we would like to report on the structure of tokamak edge observed by five-channels computed tomography on a poloidal plane, which gives images of visible light emission and has shown an enhancement of Fourier-components with some poloidal mode numbers corresponding to supposed chain of magnetic islands. The relation between the magnetic field structure and the impurity transport is discussed.

EXPERIMENTS: The EML experiments have been carried out on a small research tokamak, HYBTOK-Ⅱ. The major radius is 0.4m, and the minor radii of the wall and the limiter are 12.8cm and 11cm, respectively. The discharge conditions are as follows: The plasma current $I_p \leq 15$kA, the line-averaged electron density $n_e \leq 1.5 \times 10^{19} m^{-3}$, the toroidal magnetic field $B_t \leq 0.4$T, and the discharge duration $\tau \leq 10$ms. An array of eight local helical coils with m/n=6/2 for EML magnetic configuration is installed [1].

The CT system with an array of five CCD detectors is installed on a poloidal plane of the tokamak machine [5]. The present system with a slit-hole imaging arrangements improves the sensitivity as well as the spatial resolution in a great deal compared with the old three-port version with a pin-hole [4,6]. The CCD has a sensitivity over the wavelength range from 420 through 870nm, in which the Fe, Ti, C and O atomic and ionic spectral lines together with hydrogen Balmer series

are contained. The contribution of H_α line to the total light is less than 10% so that the emission detected with the present CCD sensors may come from impurities in tokamak plasma.

Figure 1 is a typical example of modification of emission profile reconstructed by ART algorithm under the resonance condition, $q(a) \sim 4$. Relative changes with respect to the unperturbed profile are shown in the insert of Fig.2 for both polarity of local helical coil current. We can distinguish some undulation of light intensity in the poloidal direction, especially in the outer side of the torus. Such an periodic island-like chain changes its phase by π if the direction of current flow of helical coils is reversed. The light increment integrated in a radial width is Fourier-decomposed over the poloidal mode numbers up to about 10, and shown in Fig.2. The ratio of Fourier components with high poloidal mode numbers ($m=4 \sim 7$) to those with low mode numbers ($m=0 \sim 3$) is plotted in Fig.3 under the various conditions Open marks show the data integrated in the edge region ($r=8 \sim 11$cm), while the solid ones are those in the inner region ($r=5 \sim 8$cm). The helical magnetic field in (b) is relatively stronger than that in (a). Therefore, it seems that the modification with high poloidal mode numbers reaches the inner region. In the non-resonant condition shown in Fig.3(c) all Fourier components are insensitive to the presence of helical perturbation.

DISCUSSIONS: The precise correspondence between the total light intensity and the magnetic field structure will be difficult. However, it is thought that the impurity ions stay longer around the "O" point of magnetic island than near "X" point or in the fully stochastic region [7]. Poincaré mapping of magnetic field line on the poloidal plane of CT observation under the experimental condition for Ih=+500A is shown in Fig.4. It seems that the magnetic islands of mode number of 5 is responsible to the change of emission profile. But more detailed analysis is needed to determine the relation.

CONCLUSION: A poloidal modulation of light intensity with the mode numbers of 5 through 7 is observed with CT technique

by the application of external helical perturbation (m/n=6/2). It gives the information on the impurity transport in the EML configuration in which the magnetic islands with the mode numbers of 5 and 6 are distinguished inside the stochastic layer.

ACKNOWLEDGEMENT: The authors would like to thank Y.Uesugi, N.Ohno and S.Sasaki for their valuable discussions.

[1]Y.Shen, M.Miyake, S.Takamura et al.:J. Nucl. Mater. 168(1989)295.
[2]M.Miyake, Y.Shen and S.Takamura:in Controlled Fusion and Plasma Physics (Proc. 16th Eur. Conf. Venice, 1989), vol.13B, PartⅢ, European Physical Society (1989)p.1047.
[3]S.Takamura:Phys. Fluids B2(1990)1947.
[4]S.Takamura et al.:in Plasma Physics and Controlled Nuclear Fusion Research (Proc. 13th Int. Conf. Washington D.C., 1990), vol.1, p.549 (IAEA, Vienna, 1991).
[5]Y.Oda, S.Takamura et al.: to be submitted to Kakuyugo Kenkyu.
[6]H.Hodo and S.Takamura: Trans. IEE Japan, 111(1991)64.
[7]W.L.Rowan et al.:in Controlled Fusion and Plasma Physics (Proc. 14th Eur. Conf., Madrid, 1987), vol.11D, European Physical Society (1987), p.117.

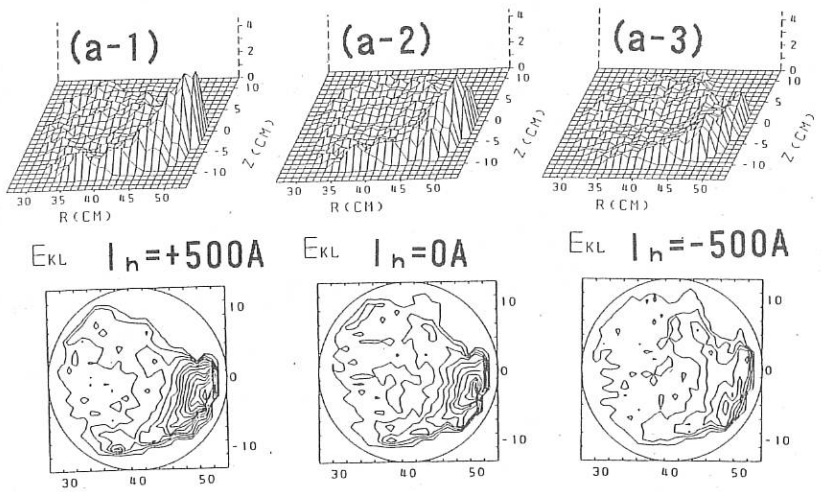

Fig.1 Modification of visible light emissionprofile on the poloidal plane. Ip=15kA and Bt=0.4T.

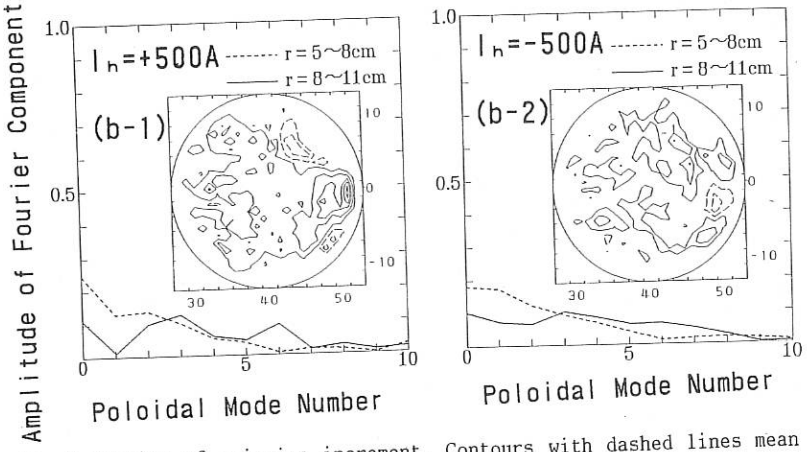

Fig.2 Profile of emission increment. Contours with dashed lines mean decrement. (b-1)=(a-1)-(a-2), (b-2)=(a-3)-(a-2). Fourier components.

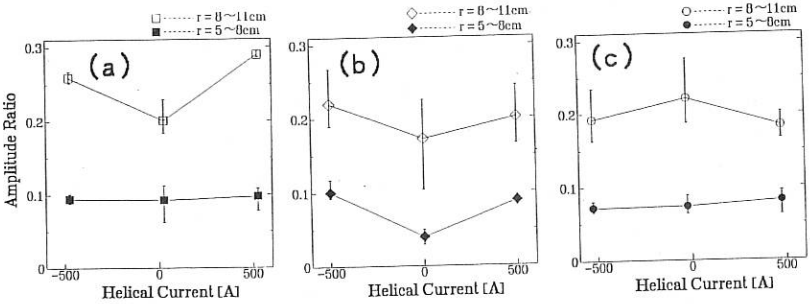

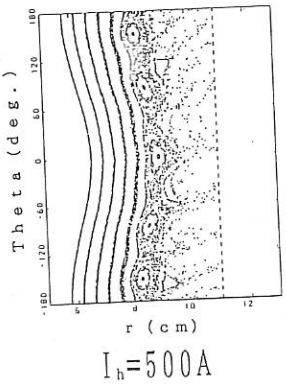

Fig.3 Ratio of Fourier components with high poloidal mode numbers to those with low ones. (a) Ip=15kA, Bt=0.4T, q(a)~4; (b) Ip=9.5kA, Bt=0.25T, q(a)~4; (c) Ip=12kA, Bt=0.4T, q(a)~5.

Fig.4 Poincaré mapping of magnetic field lines on the poloidal plane of CT observation. Ip=15kA, Bt=0.4T, m/n=6/2, Λ=0.36. Parabolic distribution for current density is assumed.

Stochastic Broadening of the Scrapeoff Layer of a Single-Null Divertor Tokamak

A. Punjabi and A. Verma
Hampton University, Hampton, VA 23668, USA
and
A. Boozer
College of William and Mary, Williamsburg, VA 23185, USA and
Max-Planck-Institut für Plasmaphysik, D8046 Garching, GERMANY

Abstract

Magnetic perturbations cause the region near the separatrix of a magnetic divertor to become stochastic. The last magnetic surface to provide magnetic confinement passes inside the X-point a distance that is proportional to the square root of the applied perturbation. Particles that diffuse across the last confining surface can follow open magnetic lines to the divertor plates. The strike points of these field lines on the divertor plates lie in helical discrete stripes. The properties of these stripes is important for determining if one can control the heat loads on divertor plates as well as assessing the effects of natural perturbations, such as MHD activity, on divertor designs.

Introduction

The prediction and preferably the control of the width of the scrapeoff layer of a divertor is a central issue in the design of ignition tokamaks such as ITER. Divertor simulations generally assume that the plasma is bounded by a sharp separatrix, which is correct only if the toroidal symmetry is perfect. Toroidal asymmetries in the magnetic field cause the last confining magnetic surface to lie inside the ideal separatrix and create a layer of open magnetic field lines that lies between the last confining magnetic surface and the ideal separatrix. The width of this layer, which we call stochastic layer, is approximately proportional to the square root of the toroidally asymmetric perturbation near the X-point.[1] It is important to know the effects of naturally occurring perturbations, such as toroidal ripple or MHD modes, on the design of divertors. The introduction of magnetic perturbations may allow an optimization of the width of the divertor scrapeoff layer and control of the heat deposition on the divertor plates.

In the simulations that assume a sharp separatrix, the width of the scrapeoff layer is determined by the assumed diffusion coefficient, which is usually of order 1 m^2/s. The field lines of scrapeoff layer strike the divertor plates in a stripe with a width that is simply determined by axisymmetric magnetics.

If the magnetic perturbations are sufficiently large, the scrapeoff layer will be dominated by the stochastic layer. The field lines of the stochastic layer strike the divertor plate in a stripe that is in proportion much narrower (about a factor of 6) than is the divertor stripe filled by the field lines of an axisymmetric scrapeoff layer. The greater width of the scrapeoff layer in comparison to the divertor stripe has important implications for the design of divertors.

Methodology

The basic features of magnetic field line motion near a separatrix are generic and can be efficiently investigated using an area preserving map. Pomphrey and Reiman have made related calculations[2] using wires to model a divertor configuration instead of a map. The simplest divertor map has a single positive parameter k,

$$x_{n+1} = x_n - k\, y_n\, (1-y_n)$$
$$y_{n+1} = y_n + k\, x_{n+1},$$

an O-point at x=0, y=0, and an X-point at x=0, y=1. The map provides a good representation of the magnetic field lines of a single-null tokamak divertor. Toroidal asymmetries can be simulated using k or by additional terms.[3] Here, toroidal asymmetries will be simulated using k, but the results are not qualitatively changed by other representations. The smaller k, the closer the last confining magnetic surface passes to the X-point. For k=0.6, the closest approach is x=0, y=0.997, Fig. (1a,b); for k=0.9, the closest approach is x=0, y=0.854. Each iteration of the map corresponds to a toroidal angular advance ζ_0. Near the O-point the rotational transform of the field lines per iteration $1/q_1$ is

$$\sin(2\pi/q_1) = k\,(1-k^2/4)^{1/2}.$$

One obtains a transform of roughly unity near the axis if 10 iterations of the map constitute a single toroidal circuit, $\zeta_0=2\pi/10$.

The width of the stripe on the divertor plates is uniquely determined by the stripe formed by field lines as they cross the plane y=1, which passes through the X-point. The toroidal location ζ at which field lines cross x-ζ plane is determined using a continuous analogue to the discrete map. Letting $\phi=\zeta/\zeta_0$, $0\le\phi\le1$, the (area preserving) continuous analogue is

$$x(\phi) = x_n - k\, y_n\, (1-y_n)\, \phi$$
$$y(\phi) = y_n + k\, x(\phi)\, \phi.$$

The behavior of field line trajectories that cross the last confining surface at a random point can be assessed by adding a small area-expanding step to each iteration of the discrete map, $x_{new}=(1+R\delta)x_{old}$, with R a random number between 0 and 1 and δ the expansion coefficient. For k=0.6, we find that for $\delta<<10^{-13}$ the strike points form helical stripes that are independent of δ, Figs. (2a,b). For larger values of δ the strike points form a single stripe, Fig. (3-4), which has a width that scales as $\delta^{1/4}$.

Discussion of Results

Particles that diffuse across the last confining surface of a tokamak with a divertor can follow open magnetic field lines to the divertor plates. The strike points of these field lines on the divertor plates lie in discrete stripes. The region between the last confining magnetic surface and the separatrix of the ideal divertor is called the stochastic layer. The open magnetic field lines of the stochastic layer enter the region from one divertor plate and leave striking another divertor plate after an integer number of complete poloidal circuits N_p. The discrete stripes on the divertor plates correspond to the number of poloidal circuits made by open field lines. The area of the stripes scales as $1/N_p^2$. The open field lines that approach the last confining surface make many poloidal circuits before striking a divertor plate in a stripe that is much narrower than the stochastic layer (≈15%) but nonetheless of non-zero width. An open field line that makes many poloidal circuits in going from one divertor plate to another in essence densely fills the stochastic layer except for the regions in the stochastic layer that are occupied by magnetic islands.

The complicated filling of the stochastic region by the open field lines gives an associated complexity to the ambipolar electric potential that exists along any open magnetic field line that is embedded in a plasma. Although we have not calculated the particle transport from the EXB drifts associated with the ambipolar potential, we expect a diffusive effect that would smear the stripe structures.

Acknowledgement

This work was supported in part by US DoE grants DE-FG05-88ER53265 and DE-FG05-90ER54106.

References

1. A. Boozer and A. Rechester, Phys. Fluids, 21, 682 (1978)

2. N. Pomphrey and A. Reiman, PPPL Rpt. 2801 (1992)

3. T. J. Martin and J. B. Taylor, Plasma Phys. Contr. Fus., 28, 321 (1984)

FIGURES

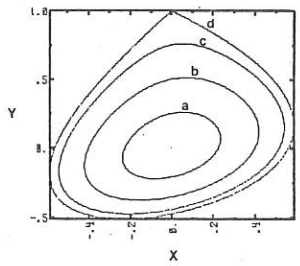

Fig. 1a Phase portrait for the simple single-null tokamak divertor map when map parameter k=0.6. Initial conditions are x_0=0, a:y_0=.25, b:y_0=.5, c:y_0=.75, d:y_0=.997.

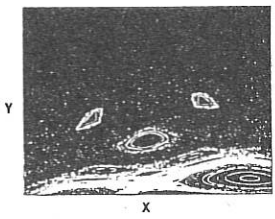

Fig. 1b Reverse video of the phase portrait near X-point. Abscissa goes from -0.001 to 0.001, and ordinate goes from 0.997 to 1.

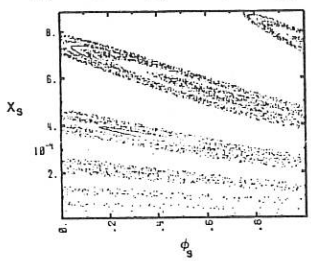

Fig. 2a Foot-print of the strike points on the divertor plate when the expansion coefficient δ=0. Trajectories start in the stochastic scrapeoff layer at x_0=0 and $0.997<y_0<1$.

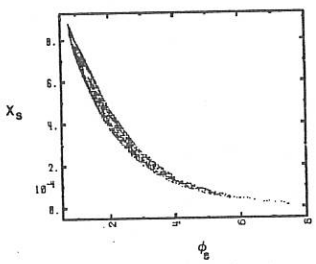

Fig. 2b When the foot-print for δ=o is unfolded in the ϕ direction, we get a sharply defined, narrow, helical stripe.

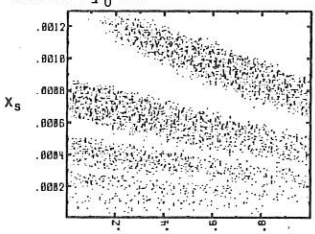

Fig. 3 Foot-print of the strike points when $\delta=10^{-13}$.

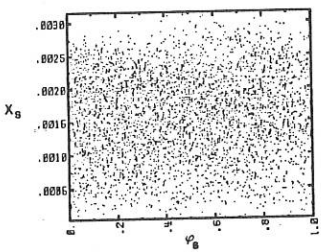

Fig. 4 Foot-print when $\delta=10^{-11}$. Now the foot-print is a continuum, whose width scales as $\delta^{1/4}$.

ON STATIONARY FLOW IN THE BOUNDARY REGION OF TOROIDAL SYSTEMS

Horst Wobig
Max-Planck-Institut für Plasmaphysik, IPP-EURATOM Association
W-8046 Garching bei München, Germany

Abstract-A one-fluid model with ion-neutral interaction is presented which is appropriate to describe a collision-dominated plasma in the region between wall and last magnetic surface. The model yields a nonlinear elliptic system for temperature, pressure and electric potential. Boundary conditions at the material walls can be imposed. An essential feature is the non-uniqueness of the solutions, therefore bifurcation phenomena and convective solutions have to be expected. Only in the case of large dissipative effects and small source terms can uniqueness be proved. Some applications of the model to the scrape-off layer of tokamaks and stellarators are discussed.

Introduction. The boundary region of stellarators and tokamaks is characterized by a last closed magnetic surface surrounded by a domain of open surfaces, stochastic regions and magnetic islands. The plasma in this region is collision dominated and interacts with material walls. The recycling neutral gas is ionized and provides a sink for energy and momentum of the plasma. The effect of neutrals on the plasma has already been studied by S. Yoshikawa [1]; further investigations were made by Wobig [2, 3]. Friction between the plasma and neutrals via charge exchange is a stabilizing factor and it fully determines the stationary flow if its effect is strong enough. Typical values of the charge exchange rate are $< \sigma v >_{cx} = 2-4 \cdot 10^{-8}$ cm^3/s and the frequency of momentum transfer becomes $\nu_{in} \approx 2-4$ kHz (density of neutrals $n_o = 10^{11}$ cm^{-3}). This must be compared with viscous dissipation. Of the 5 terms of the Braginskii viscosity only the bulk viscosity is large enough to compete with plasma neutral interaction. In the following, however, we neglect viscous terms and inertial forces and consider the one-fluid model with friction between ions and neutrals. The friction introduces a feedback of the plasma flow on the momentum balance and therefore Ohm's law, the equation of continuity, and the energy and momentum balance have to be solved together. An iteration scheme is discussed and some applications to the boundary regions of tokamaks and stellarators are presented.

The model. Let us consider a domain Ω, which is bounded by the last closed magnetic surface $\partial\Omega_1$ and by the wall of the vacuum tube, limiters or divertor target plates $\partial\Omega_2$. The basic equations of the one - fluid model are

$$0 = -\nabla p + \mathbf{j} \times \mathbf{B} - \alpha \mathbf{v} \tag{1}$$

$$-\nabla \Phi + \mathbf{v} \times \mathbf{B} = \eta \mathbf{j} \tag{2}$$

$$\nabla \cdot \mathbf{j} = 0 \quad , \quad \nabla \cdot n\mathbf{v} = S \quad , \quad p = 2n\,kT \tag{3}$$

$$\nabla \cdot (\mathbf{q} + \frac{5}{2} p\mathbf{v}) = \nabla \Phi \cdot \mathbf{j} + Q \tag{4}$$

$$\mathbf{q} = \mathbf{q}_e + \mathbf{q}_i - \frac{5}{4}p\frac{\mathbf{j}}{en} \quad ; \quad \mathbf{q}_e + \mathbf{q}_i = -\chi_\perp \nabla T - \chi_\parallel \nabla_\parallel T \tag{5}$$

Here, electron and ion temperature are equal and $\alpha = m_i n n_0 < \sigma v >_{cx}$ is the ion - neutral friction coefficient. S and Q are the source terms of density and energy, in this context they are given terms. The macroscopic velocity of the neutrals has been set to zero, in principle, an equation could be added which calculates the data of the neutrals. Here, we consider the neutrals as given. $\chi_\perp$ and $\chi_\parallel$ are the sum of ion and electron thermal conductivities.

The advantage of this approximation is that the velocity and the current ($\mathbf{v}$ and $\mathbf{j}$) can be eliminated from eqs. (1) and (2).

$$\mathbf{j} = -\frac{\alpha}{B^2+\alpha\eta}\nabla_\perp\Phi - \frac{1}{\eta}\nabla_\parallel\Phi - \frac{1}{B^2+\alpha\eta}\nabla p \times \mathbf{B} \tag{6}$$

$$\mathbf{v} = -\frac{\eta}{B^2+\alpha\eta}\nabla_\perp p - \frac{1}{\alpha}\nabla_\parallel p - \frac{1}{B^2+\alpha\eta}\nabla\Phi \times \mathbf{B} \tag{7}$$

The first two terms of the plasma velocity $\mathbf{v}$ are the classical perpendicular diffusion and a parallel diffusion resulting from the interaction with neutrals. The last term is the convective velocity. Inserting these results into eqs. (3) and (4) yields 3 equations for the unknowns p, Φ and T:

$$-\nabla\cdot\{\frac{\alpha}{B^2+\alpha\eta}\nabla_\perp\Phi + \frac{1}{\eta}\nabla_\parallel\Phi\} = \nabla\cdot\{\frac{1}{B^2+\alpha\eta}\nabla p\times\mathbf{B}\} \tag{8}$$

$$-\nabla\cdot\{\frac{p}{2nkT}\frac{\eta}{B^2+\alpha\eta}\nabla_\perp p + \frac{n}{\alpha}\nabla_\parallel p\} = \nabla\cdot\{\frac{p}{2nkT}\frac{1}{B^2+\alpha\eta}\nabla\Phi\times\mathbf{B}\} + S \tag{9}$$

Eqs. (4),(8) and (9) are quasilinear elliptic equations for T, Φ and p. Solving these equations requires boundary conditions of the Dirichlet type, Neumann type or mixed type.

Boundary conditions. On the last magnetic surface we may assume Dirichlet boundary conditions for T, p and Φ. T, p are constant on $\partial\Omega_2$; the potential Φ varies on the last magnetic surface and has to continuous across $\partial\Omega_1$. The choice of the boundary conditions on $\partial\Omega_2$ depends on the physics in front of the material walls. In case of a conducting wall the potential is given by the potential drop $\delta\Phi(n,T)$ across the Langmuir sheath. In general this value is not constant and has to be calculated self-consistently. If the wall is an insulator the condition of zero current $j_n = 0$ yields a Neumann-type boundary condition for Φ. The Bohm criterion $v_\parallel \propto v_S(T)$ provides another boundary condition for the pressure gradient: $(1/\alpha)\nabla_\parallel p = v_S(T)$. Furthermore, the parallel heat flux $q_\parallel$ into the Langmuir sheath is correlated to the density and temperature in the sheath: $q_\parallel = (\delta_t\, kT + \epsilon_{ion})n\sqrt{kt/M_i(\gamma_e+\gamma_i)}$ [4]. In summary, we are faced with a set of nonlinear boundary conditions of mixed type.

Existence and uniqueness of solutions. The problem contains several iterative loops which only converge if some additional conditions are met. Eqs. (4), (8) and (9) can be

solved with a given magnetic field $\mathbf{B} \in H$, where H is an appropriately defined Banach space. The solution yields the plasma current $\mathbf{j}$ and from $\mathbf{j} = \nabla \times \mathbf{B}, \nabla \cdot \mathbf{B} = 0$ a new magnetic field is calculated. The fixed point of the map $\mathbf{B} \longrightarrow \mathbf{B}$ is the desired self-consistent magnetic field. The pressure is another quantity which has to be calculated iteratively. We consider the temperature in eqs. (8) and (9) as given and solve these equations for p and Φ. In ref.[3]this problem has been studied assuming constant temperature; an existence theorem has been established. Here, also the temperature equation must be solved iteratively. It is not yet known under what conditions the iteration converges.

Another important issue is the uniqueness of the solutions. As it is well-known from the theory of Rayleigh-Bénard convection, convective solutions may exist besides the solution of the stratified layer. The uniqueness of the solutions is destroyed by the convective terms $p\mathbf{v}$ in eq. (4) and the $\nabla\Phi \times \mathbf{B}$ term in eq. (9). However, if these terms are sufficiently small, only one solution of eqs. (4) and (9) exists. Therefore, the main problem is to find an a priori estimate of the solution $\mathbf{v}$ and $\mathbf{j}$. Such estimates can be found from the entropy equation which is written in the form

$$\nabla \cdot \{sn\mathbf{v} - \frac{5}{2}\frac{\ln T}{e}\mathbf{j} + \frac{\mathbf{q}_e + \mathbf{q}_i}{T}\} = \frac{1}{T^2}\{\chi_\perp(\nabla_\perp T)^2 + \chi_\parallel(\nabla_\parallel T)^2\} + \frac{\eta}{T}\mathbf{j}^2 + \frac{\alpha}{T}\mathbf{v}^2 + \frac{Q}{T} - S(s - \frac{5}{2}) \tag{10}$$

$s = \ln T^{3/2}/n$ is the entropy density. Using constant boundary conditions $T, n, p, \Phi =$ const., it can be shown that the entropy production

$$\int_\Omega \{\frac{1}{T^2}\{\chi_\perp(\nabla_\perp T)^2 + \chi_\parallel(\nabla_\parallel T)^2\} + \frac{\alpha}{T}\mathbf{v}^2 + \frac{\eta}{T}\mathbf{j}^2\}\, d^3x \longrightarrow 0 \tag{11}$$

if the source terms $Q, S \longrightarrow 0$. In other words, this relation says that $\nabla T, \nabla p, \mathbf{v}$ and $\mathbf{j}$ are uniformly bounded by constants depending only on the source terms, the dissipative coefficients η, α, χ and the domain Ω. Therefore, uniqueness of the nonlinear boundary value problem (4),(8) and (9) can only be expected if dissipation is sufficiently large and source terms are sufficiently small.

Tokamak scrape-off layer. As an example we consider the boundary region of a divertor tokamak outside the separatrix. The magnetic field $\mathbf{B} = \mathbf{B}_t + \mathbf{B}_p = J(\psi)\nabla\varphi + \nabla\psi \times \nabla\varphi$ is axisymmetric. The field lines in this regions are bounded by the divertor plates. To calculate an axisymmetric solution of eqs. (4),(8) and (9) would be straightforward and would yield a scrape-off layer with very small radial decay lengths, since perpendicular to the magnetic field only classical transport processes are involved. Of more interest are non-axisymmetric solutions where Φ, p and T are periodic functions of the toroidal angle φ. Such solutions with large convective velocity $\mathbf{v}_c \propto \nabla\Phi \times \mathbf{B}$ lead to much larger radial transport and therefore to a broadening of the scrape-off layer. The key to understanding these solutions is the feedback of the pressure gradient $p'(\varphi)$ in eq. (8) on the electric potential. In a tokamak this equation is

$$-\nabla \cdot \{\frac{\alpha}{B^2 + \alpha\eta}\nabla_\perp\Phi + \frac{1}{\eta}\nabla_\parallel\Phi\} = (\nabla\frac{1}{B^2} \times \nabla p) \cdot \mathbf{B}_t + B_p^2\, p'(\varphi)\frac{\partial}{\partial\psi}(\frac{1}{B^2}) \tag{12}$$

In case of non-axisymmetry the last term on the right hand side is the important one: any $p' \neq 0$ will lead to $\Phi' \neq 0$ and a radial convective velocity $\nabla\Phi \times \mathbf{B}$ will arise. This convective velocity feeds back on the temperature and pressure in eqs. (4) and (9) and thus enhances the toroidal variation of T and p. The dissipative processes saturate the amplitude of the convection in a similar way as viscosity and thermal conductivity saturate the Rayleigh-Bénard convection. The role of the gravity is played by the gradient of the magnetic field $\frac{\partial}{\partial\psi}\frac{1}{B^2}$; its sign determines whether convection arises or not. In the outer boundary layer of a divertor tokamak the sign of this term is mainly positive, which favours convective solutions. The mechanism is the same which excites interchange instabilities in regions of unfavourable field line curvature.

Boundary region in stellarators. In a stellarator there is no ignorable coordinate and therefore all solutions will depend on the toroidal coordinate φ. Since magnetic coordinates do not exist outside the last magnetic surface we will utilize the Clebsch representation $\mathbf{B} = \nabla\psi \times \nabla\chi$ to define a coordinate system $\{\psi, \chi, l\}$, where l is the length along the field line. Locally this coordinate system always exists. To simplify the analysis we approximate the magnetic field in the boundary region by the vacuum field and retain only the convective velocity $\mathbf{v}_c \propto \nabla\Phi \times \mathbf{B}$ in the energy balance equations. After these approximations the equations are

$$-\nabla\cdot\Big\{\frac{\alpha}{B^2+\alpha\eta}\nabla_\perp\Phi + \frac{1}{\eta}\nabla_\parallel\Phi\Big\} = B^2\Big\{\frac{\partial p}{\partial\chi}\frac{\partial}{\partial\psi}\Big(\frac{1}{B^2}\Big) - \frac{\partial p}{\partial\psi}\frac{\partial}{\partial\chi}\Big(\frac{1}{B^2}\Big)\Big\} \tag{13}$$

$$-\nabla\cdot\Big\{\frac{n\eta}{B^2+\alpha\eta}\nabla_\perp p + \frac{n}{\alpha}\nabla_\parallel p\Big\} = B^2\Big\{\frac{\partial\Phi}{\partial\chi}\frac{\partial}{\partial\psi}\Big(\frac{n}{B^2}\Big) - \frac{\partial\Phi}{\partial\psi}\frac{\partial}{\partial\chi}\Big(\frac{n}{B^2}\Big)\Big\} + S \tag{14}$$

$$-\nabla\cdot\{\chi_\perp\nabla_\perp T + \chi_\parallel\nabla_\parallel T\} = \frac{5}{2}B^2\Big\{\frac{\partial\Phi}{\partial\chi}\frac{\partial}{\partial\psi}\Big(\frac{p}{B^2}\Big) - \frac{\partial\Phi}{\partial\psi}\frac{\partial}{\partial\chi}\Big(\frac{p}{B^2}\Big)\Big\} + \nabla\Phi\cdot\mathbf{j} + Q \tag{15}$$

Conclusions. The frictional model of the boundary region allows one to calculate plasma parameters in any magnetic field, the existence of magnetic surfaces is not required. Furthermore, boundary conditions on T, p and Φ can be imposed. The physics of the Langmuir sheath in front of material walls indicates that boundary conditions in general are inhomogeneous and nonlinear. Since in realistic situations dissipative effects are small, we have to expect that multiple solutions exist. Solutions with large convective velocities will lead to enhanced radial transport and to a broadening of the scrape-off layer.

References:

[1] S. Yoshikawa, *Phys. Fluids* **13**, 2300 (1970)

[2] H. Wobig, *Plasma Physiscs* **15** 1101 (1986)

[2] H. Wobig, *Z. f. Naturforsch.* **41a** 1101 (1986)

[4] K. Lackner et al., *Plasma Physics and Contr. Fusion*, **26**, 105 (1984)

Sheath Potential at a Target with Almost Parallel Magnetic Field

R. Chodura
Max-Planck-Institut für Plasmaphysik, EURATOM Association,
D-8046 Garching, Fed. Rep. Germany

Abstract

The sheath of a plasma in contact along magnetic field lines with an absorbing target exhibits a double structure on two length scales, the ion gyroradius and the Debye length [1]. For moderate incidence angles of the magnetic field on the target plate the potential in the sheath falls monotonically on both length scales. For grazing incidence of the magnetic field on the other hand the potential profile in the sheath becomes non monotonically: it falls to a minimum of the order of T_e/e on the ion gyro scale and rises again on the Debye length scale. The critical angle for the occurrence of this double sheath structure is of the order of the square root of the mass ratio of electrons and ions, i.e. about 1° for hydrogen ions.
The reason for the potential rise at the target is the larger mobility perpendicular to the magnetic field of ions as compared to electrons for grazing incidence. The potential rise is enhanced with increasing ion temperatures. The overall potential difference between plasma and target for grazing incidence of the magnetic field is smaller than the usual $\sim 3T_e/e$.

Introduction

In most plasma arrangements parts of the plasma are connected along magnetic field lines with material walls or targets, e.g. the scrape-off layer of confinement devices like tokamaks or stellerators. A very simplified version of this situation is indicated in Fig. 1: A plasma slab of extension 2L interspersed with an oblique magnetic field B is confined by two particle absorbing walls. Since the walls are plasma absorbing sinks one has to assume some kind of plasma source in order to achieve a steady state situation. Thus a plasma flow from the source region to the walls arises. This flow is driven by the pressure gradient of the plasma, which is directed along x. But the magnetic field forces the plasma to flow mainly parallel to its lines of force, i.e. at an angle ψ oblique to x. Only in a small sheath in the vicinity of the walls the flow of plasma ions deviates appreciably from the direction of the magnetic field.
The main function of the sheath is to reflect most of the incoming electrons in order to maintain quasineutrality of ions and electrons in the plasma upstream of the sheath. This is achieved by a potential drop in the sheath of the order of the electron temperature nearly independent of the magnetic field T_{es} at the sheath edge. The electric field connected with this potential drop is directed perpendicularly to the wall and thus, in general, obliquely to the magnetic field. It bends the ion flow direction toward the wall on a length scale $\lambda_m = C_s sin\psi/\omega_{ci}$ along x, with $C_s = (ZT_{es}/m_i)^{1/2}$ the ion acoustic speed and ω_{ci} the ion gyro frequency [1]. Electrons, due to their larger Lorentz force, continue to follow the magnetic field lines. In general λ_m is much larger than the Debye length $\lambda_D, \lambda_m > \lambda_D$. Therefore, this part of the total sheath ("magnetic sheath") is quasineutral. Closer to the wall, within a distance of the order of some Debye lengths, the restriction of quasineutrality does no longer hold and electron and ions can move more independently ("Debye sheath"). In a strong magnetic field such that $\omega_{ce} \gg \omega_{Pe}$

electrons follow magnetic field lines also in the Debye sheath. Ion orbits are bent still more to the wall.

2. Sheath Structure for $\psi \to 90^o$

For moderate angles ψ the electric field in the whole sheath is directed to the wall and the potential falls monotonically towards the wall. This is due to the fact that without the electric sheath field electrons would flow faster to the wall than ions. But the electron flow velocity along the magnetic field is limited. It cannot exceed their thermal speed $V \lesssim v_{te} = (T_{es}/m_e)^{1/2}$. Thus the electron flow velocity component to the wall is limited to

$$V_{ex} \lesssim v_{te} cos\psi$$

and approaches zero as $\psi \to 90^o$. On the other hand, the x-component of the ion flow velocity in the Debye sheath is at least of the order of their thermal velocity v_{ti},

$$V_{ix} \gtrsim v_{ti}.$$

Thus for angles ψ above a critical value ψ_{cr} with

$$cos\psi_{cr} = v_{ti}/v_{te}$$

ions in the Debye sheath flow faster to the wall than electrons and the potential rises. Above the critical angle ψ_{cr} the total sheath develops a double sheath structure. It is charged positive (but quasineutral) in the magnetic sheath and negative in the Debye sheath part.
The case $\psi = 90^o$ is singular in the sense that no connection along field lines exist anymore between the upstream plasma and the wall. There is, therefore, no need anymore for a negative sheath potential to confine electrons electrostatically. The sheath becomes negatively charged due to ion losses to the wall and the potential rises monotonically on the Debye scale length.

3. Simulation

A 1d particle code was used to study the electric field structure of the sheath under coditions of grazing incidence of the magnetic field. Ions and electrons are fed into the system at equal rates at $0 \leq x < 5\lambda_D$ and absorbed at the right boundary at $L = 480\lambda_D$. The symmetry plane at $x = 0$ is particle reflecting. Ions have hydrogen mass. Collisions are neglected and $\omega_{ce} \gg \omega_{pe}$.
Fig. 2 shows the electric field E_T and the potential Φ_T at the target (at x=L) for different angles of the magnetic field ψ. For increasing ψ the electric field E_T decreases. It goes through zero at a critical angle $\psi_{cr} \sim 89^o$ which is different from 90° by an angle according to the square root of the mass ratio $(m_e/m_i)^{1/2} \hat{=} 1.3^o$. Potential profiles at a subcritical angle $\psi = 80^o$ and a supercritical angle $\psi = 89.8^o$ for two ion temperatures T_{is}/T_{es} about 1 and 2.5 are shown in Fig. 3 and 4. It can be seen that the depth of the potential well at the wall depends on the ion temperature as is to be expected from the considerations mentioned above.

Conclusions

For grazing incidence angles of the magnetic field the sheath potential develops a double structure with a minimum of $\sim -3T_e$. Ions traversing the sheath experience a smaller potential difference between plasma and target and will gain less energy than the usual $\sim 3T_e$ for steeper incidence angles. This may reduce the ion sputtering yield at the target.

References

[1] R. Chodura, Phys. Fluids 25 (1982), 1628

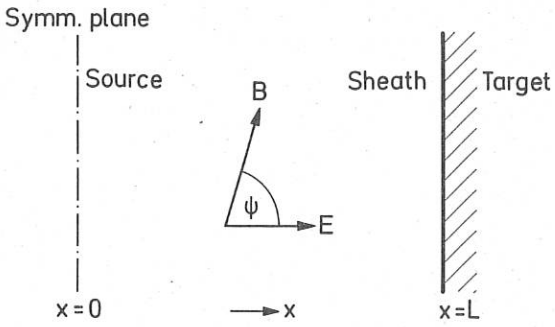

Fig. 1 Shematic view of plasma in contact with a target

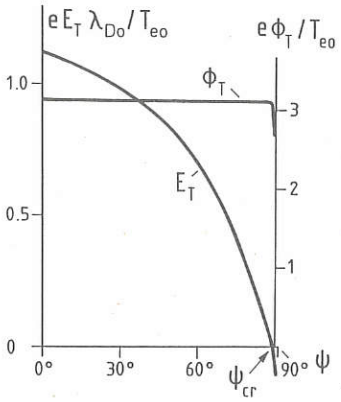

Fig. 2 Electric field E_T and potential ϕ_T at the target for different incidence angles ψ of the magnetic field

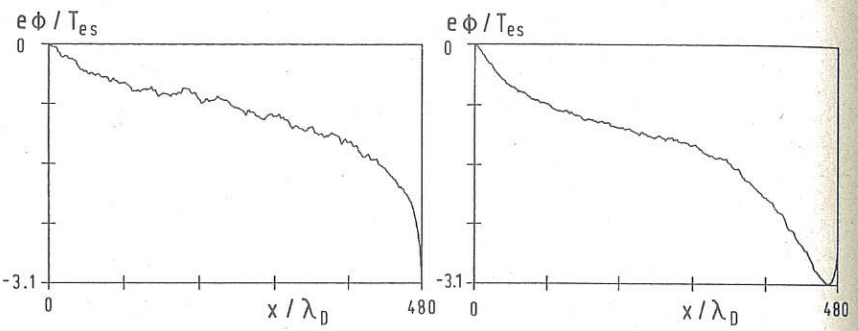

Fig. 3 Potential distribution $\phi(x)$ for $T_{is} = T_{es}$ at subcritical and supercritical angles ψ a.) $\psi = 80^o$ b.) $\psi = 89.8^o$

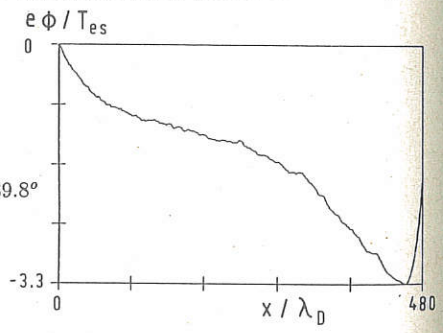

Fig. 4 Potential distribution $\phi(x)$ for $\psi = 89.8^o$ and $T_{is} = 2.5T_{es}$

BOUNDARY CONDITIONS FOR THE MOMENTUM AND ENERGY FLUX OF IONS AT THE PLASMA-SHEATH INTERFACE

K. Günther

Max-Planck-Institut für Plasmaphysik, Bereich Berlin, Hausvogteiplatz 5–7, O-1086 Berlin, Germany

Introduction: For the fluid-theory description of the parallel flow of particles, momentum, and energy towards a target plate in a scrape-off plasma to yield unambiguous solutions, boundary conditions at the sheath edge are needed. Particularly problematic are the boundary fluxes associated with the ion component: Rather arbitrary transmission coefficients are in use regarding the ion energy flux, while in place of a momentum flux condition the so-called Bohm condition $V = c_s = \sqrt{(T_e + T_i)/m_i}$ for the hydrodynamic flow velocity V at the sheath edge is widely used in fluid theory calculations. However, unless $T_i = 0$, neither sheath theory (*generalized* Bohm criterion) nor the character of the fluid equations (singularity at $V = c_s$ hinges upon *neglecting* viscosity) warrants this Mach-one condition.

The approach proposed in the present paper rests on modelling ("guessing") the parallel velocity distribution function, $f_{i\|}(v) = \iint d\vec{v}_\perp\, f_i(\vec{v})$, for the ions at the sheath edge, taking into account several conditions and restrictions.

Fundamentals: An absorbing wall implies that $f_{i\|}(v) \equiv 0$ for $v < 0$, while sufficiently far away from the wall the ions can approximately be described longitudinally by a shifted Maxwellian:

$$f^*_{i\|}(v) = \sqrt{\frac{m_i}{2\pi T^*_{i\|}}}\, n^* \exp\left[-\frac{m_i}{2T^*_{i\|}}(v - V^*)^2\right]. \qquad (1)$$

Hence, there exists a *transition region* (TR) before the sheath [1] where the distribution is of intermediate character and where collisions produce the negative-v particles occurring in the distribution function (1) which virtually defines the edge of the TR designated by an asterisk.

Most important for the construction of an ansatz for $f_{i\|}(v)$ is the argument that very fast ions will not collide within the TR, i.e. asymptotically ($v \to \infty$)

$$f_{i\|}(v)\, v\, dv = f^*_{i\|}(v^*)\, v^*\, dv^* \qquad \frac{m_i}{2}v^{*2} = \frac{m_i}{2}v^2 - e\,\Delta\Phi \qquad (2)$$

must be true, where $\Delta\Phi$ is the potential drop in the TR. By inserting Eq. (1) and series expansion for large v in the exponent one finds that $f_{i\|}(v)$ is asymptotically identical to $f^*_{i\|}(v)$ apart from an *additional pre-factor*: $\exp(e\,\Delta\Phi/T^*_{i\|})$. Therefore, modelling $f_{i\|}(v)$ should start from

$$f_{i\|}(v) = C\sqrt{\frac{m_i}{2\pi T^*_{i\|}}}\, n\, r\left(\frac{s}{S^*}\right)\, e^{-(s-S^*)^2}, \qquad s = \sqrt{\frac{m_i}{2T^*_{i\|}}}\, v, \qquad S^* = \sqrt{\frac{m_i}{2T^*_{i\|}}}\, V^*, \qquad (3)$$

where the intrinsic *model function* $r(\sigma)$ is subject to both the restrictions

$$r(\sigma) \geq 0, \qquad r(\infty) = 1, \qquad r(0) = 0, \qquad r'(0) = 0, \qquad (4)$$

and the *very important* integral condition ("asymptotic condition")

$$C = \left[\frac{S^*}{\sqrt{\pi}} \int_0^\infty d\sigma\, r(\sigma)\, e^{-S^{*2}(\sigma-1)^2}\right]^{-1} = \left(\frac{n^*}{n}\right)^{1+T_e/T^*_{i\|}} \qquad (5)$$

obtained by assuming constancy of T_e in the TR: $e\Delta\Phi = T_e \ln(n^*/n)$. Another condition, which involves (4c, d), is the generalized Bohm criterion following from sheath theory [2,3]:

$$B = \frac{T_e}{m_i n}\int_0^\infty dv\,\frac{1}{v^2}\,f_{i\|}(v) = \frac{T_e}{T_{i\|}^*}\,\frac{1}{2S^{*2}}\,\frac{\int_0^\infty d\sigma\,\sigma^{-2}\,r(\sigma)\,e^{-S^{*2}(\sigma-1)^2}}{\int_0^\infty d\sigma\,r(\sigma)\,e^{-S^{*2}(\sigma-1)^2}} \le 1\,. \tag{6}$$

The asterisked parameters (TR edge) can be eliminated in the end by making use of the particle and momentum continuity relations if any sources within the TR are neglected (and $T_e^* = T_e$):

$$n^*V^* = n\,V \qquad\qquad n^*(m_iV^{*2} + T_{i\|}^* + T_e) = n\,(m_iV^2 + T_{i\|} + T_e)\,, \tag{7}$$

where the sheath edge parameters V and $T_{i\|}$ are given by the moments

$$V = \frac{1}{n}\int_0^\infty dv\,v\,f_{i\|}(v) \qquad \text{and} \qquad T_{i\|} = \frac{m_i}{n}\int_0^\infty dv\,(v-V)^2 f_{i\|}(v)\,. \tag{8}$$

General Evaluation: Using the distribution function (3) the moments (8) read

$$V = \sqrt{\frac{2T_{i\|}^*}{m_i}}\,S\,, \qquad\qquad S = S^*\,C\,\frac{S^*}{\sqrt{\pi}}\int_0^\infty d\sigma\,\sigma\,r(\sigma)\,e^{-S^{*2}(\sigma-1)^2}\,, \tag{9}$$

$$T_{i\|} = 2\,T_{i\|}^*\,C\,\frac{S^*}{\sqrt{\pi}}\int_0^\infty d\sigma\,(S^*\sigma - S)^2\,r(\sigma)\,e^{-S^{*2}(\sigma-1)^2}\,, \tag{10}$$

and partial integration leads to

$$S = S^*\left(1 + \frac{\eta}{2S^{*2}}\right) \qquad\qquad \eta = \frac{\int_0^\infty d\sigma\,r'(\sigma)\,e^{-S^{*2}(\sigma-1)^2}}{\int_0^\infty d\sigma\,r(\sigma)\,e^{-S^{*2}(\sigma-1)^2}} \tag{11}$$

$$T_{i\|} = T_{i\|}^*\left[1 - (\eta-\chi)\frac{\eta}{2S^{*2}}\right] \qquad\qquad \chi = \frac{\int_0^\infty d\sigma\,r''(\sigma)\,e^{-S^{*2}(\sigma-1)^2}}{\int_0^\infty d\sigma\,r'(\sigma)\,e^{-S^{*2}(\sigma-1)^2}}\,. \tag{12}$$

These expressions together with (3c) allow the evaluation of Eqs. (7): $T_e/T_{i\|}^* = 2S^{*2} + \chi - 1$, so that all quantities including $f_{i\|}(v)$ itself can now be expressed in terms of T_e and S^* alone:

$$V/\sqrt{T_e/m_i} = U = \sqrt{2}\,S^*\,[1 + \eta/(2S^{*2})]/\sqrt{2S^{*2} + \chi - 1} \tag{13}$$

$$T_{i\|}/T_e = \tau = [1 - (\eta-\chi)\,\eta/(2S^{*2})]/(2S^{*2} + \chi - 1)\,. \tag{14}$$

In place of S^* the mean velocity U may be looked upon as the variable parameter that determines the rest, which implies the astonishing result that in the framework of a given model, i.e. $r(\sigma)$, the longitudinal ion velocity distribution function at the sheath edge depends on nothing but the sheath edge values of electron temperature T_e and hydrodynamic velocity V. However, varying U requires that the model function $r(\sigma)$ contain at least one adjustable parameter because the asymptotic condition (5), i.e.

$$(2S^{*2} + \chi)\,\ln[1 + \eta/(2S^{*2})] = \ln C\,, \tag{15}$$

must always be satisfied.

According to Eqs. (13), (14), the limiting case $S^* \to \infty$ yields longitudinally cold ions, $\tau = 0$, just for $V = \sqrt{T_e/m_i}$, which means that the Bohm criterion is marginally fulfilled ($B = 1$).

Models: As $r(\sigma)$ in the ansatz (3) describes the depletion of low-velocity particles near the wall (compared to a pure Maxwellian), it seems to be justified if we confine ourselves to monotonically increasing functions $r(\sigma)$ in addition to the conditions (4). A broad variety of such models have been studied, distinguishing two types,

$$\text{Type I:}\quad r(\sigma) = [\varrho(\kappa)]^\alpha, \qquad \text{Type II:}\quad r(\sigma) = \varrho(\kappa^\alpha), \qquad \kappa = \sigma/\gamma, \qquad \alpha > 1, \tag{16}$$

where $\varrho(\kappa)$ increases from $\varrho = \kappa$ (as $\kappa \to 0$) to $\varrho(\infty) = 1$, and using two different ϱ-models:

$$\text{Model A:}\quad \varrho(\kappa) = \frac{\kappa(1+\beta\kappa)}{1+2\kappa+\beta\kappa^2}, \qquad \text{Model B:}\quad \varrho(\kappa) = \frac{1-e^{-\beta\kappa}}{1+(\beta-1)\,e^{-\beta\kappa}}. \tag{17}$$

With the four combinations possible the integrals (5),(6),(11),(12) have been calculated numerically in dependence on S^*, varying the parameters α, β and obtaining the parameter γ (the scaling factor) in each case as the solution to Eq. (15). It is not self-evident that a solution exists and is unique; however, this proves to be generally the case except for Type I, Model A, which yields solutions only for $\beta > 1.5$ and a restricted range of U.

Results: Fig. 1 demonstrates that the most important result, $T_{i\|}/T_e$ as a function of U, is rather insensitive to the entire modelling if the dotted line is disregarded because a step model for $\varrho(\sigma)$ is irrelevant from the physical point of view. (A two-step model with the second step at $\sigma \to \infty$ can even produce $T_{i\|} \equiv 0$.) The upper curve, which is closely fitted by the expression

$$\tau(U) = [0.5255 + 0.1595\,e^{-8.5(U-1)}](U-1) + 0.1703\,(U-1)^2 - 0.0006613\,(U-1)^{3.5}, \tag{18}$$

has been obtained from several models/types with varying β values, both chosen to maximize τ as long as $B \le 1$. $B = 1$ was reached for $U < 2.3$. This curve is likely to best approach reality if the speculation that both the Bohm condition has to be fulfilled marginally ($B = 1$) [4,5,6] and $f_{i\|}(v)$ can be expanded in powers of v (i.e. $\alpha =$ integer $= 2$) should be correct.

Fig. 2 shows some examples of the modelled velocity distribution functions characterized by their mean values (thin vertical lines). Remarkable is the apparently high degree of symmetry.

Fig. 3 and Fig. 4 are devoted to the intrinsic objective of the approach – the boundary conditions. The viscous stress $-\pi_{i\|} = n(T_i - T_{i\|})$ can be expressed by $T_{i\|}/T_e$ according to

$$-\frac{\pi_{i\|}}{nT_i} = 1 - \frac{T_e}{T_i}\frac{T_{i\|}}{T_e} = 1 - \frac{T_e}{T_i}\,\tau\!\left(\sqrt{1+T_i/T_e}\,M\right), \tag{19}$$

where the Mach number $M = V/\sqrt{(T_e+T_i)/m_i}$ has been introduced to demonstrate that this bondary condition allows both $M < 1$ and $M \ge 1$ in dependence on the particular situation the fluid model is applied to (sources etc.). However, if $T_i/T_e \ll 1$ (cold ions) nothing but $M \approx 1$ can result in any case. The conducted ion heat flux $q_{i\|}$ is given by

$$\varepsilon_i = \frac{q_{i\|}}{nVT_e} = \frac{m_i/2}{nVT_e}\int_0^\infty dv\,(v-V)^3 f_{i\|}(v) = \frac{T^*_{i\|}}{T_e}\,\frac{1}{S}\,C\,\frac{S^*}{\sqrt{\pi}}\int_0^\infty d\sigma\,(S^*\sigma - S)^3\,r(\sigma)\,e^{-S^{*2}(\sigma-1)^2}$$

$$\varepsilon_i = \frac{\eta}{2S^*S(2S^{*2}+\chi-1)}\left[\left(\eta-\frac{3}{2}\chi\right)\frac{\eta}{2S^{*2}} + \frac{1}{2}\,\frac{\int_0^\infty d\sigma\,(\sigma-1)\,r''(\sigma)\,e^{-S^{*2}(\sigma-1)^2}}{\int_0^\infty d\sigma\,r'(\sigma)\,e^{-S^{*2}(\sigma-1)^2}}\right]. \tag{20}$$

This relation is shown in Fig. 4. For practical puposes one may use the fit

$$\varepsilon_i(U) = 0.08\,[1 - e^{-1.3(U-1)}]\,\tau(U). \tag{21}$$

Finally, the boundary conditions for the *total fluxes* of momentum and energy in terms of transmission coefficients can be written down ($U = V/\sqrt{T_e/m_i}$):

$$\Pi_{\|} = nT_e\,\delta \qquad Q_{i\|} = nVT_e\,\delta_i \qquad Q_{e\|} = nVT_e\,\delta_e$$

$$\delta = U^2 + \tau(U) + 1 \qquad \delta_i = 1.5\,(T_i/T_e) + 0.5\,U^2 + \tau(U) + \varepsilon_i(U) \qquad \delta_e = 2 - \ln(U\sqrt{2\pi\,m_e/m_i}).$$

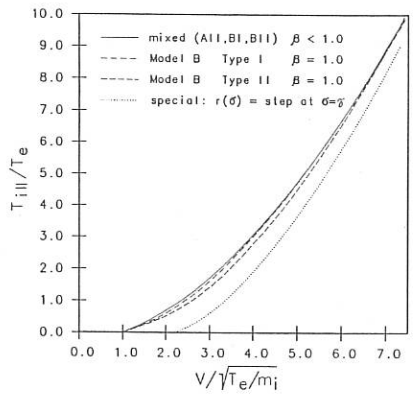

Fig. 1. Longitudinal ion temperature versus mean ion velocity at the sheath edge. Different models with $\alpha = 2$.

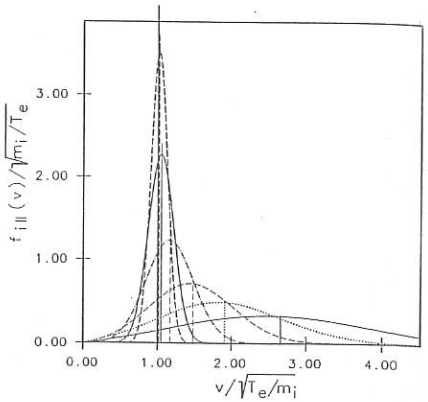

Fig. 2. Ion velocity distribution functions at the sheath edge. Modelling corresponding to the upper curve in Fig. 1.

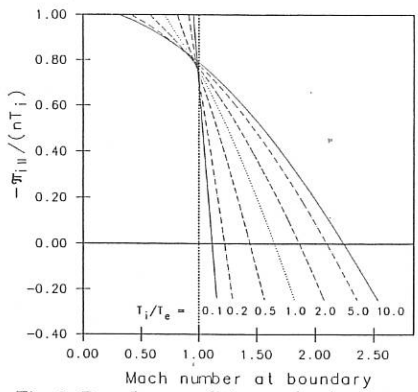

Fig. 3. Boundary condition at the sheath edge for the dissipative part of ion momentum flux (i.e. non-convective part or "viscous stress" $-\pi_{i\|}$), based on the fit (18).

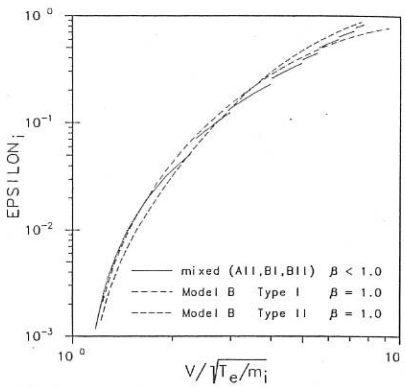

Fig. 4. Boundary condition at the sheath edge for the dissipative part of ion energy flux $q_{i\|} = nVT_e\,\epsilon_i$ (conducted ion heat flux). Different models with $\alpha = 2$.

[1] Yu.L. Igitkhanov, V.I. Pistunovich, V.A. Posharov, "Description of the Near-Wall Plasma ..." (in Russian), Report IAE-4217/8, I.V. Kurchatov Institute of Atomic Energy, Moscow (1985).

[2] E.R. Harrison, W.B. Thompson, Proc. Phys. Soc. **72** (1959) 2145.

[3] H. Gerhauser, H.A. Claaßen, "Calculation of Poloidal Rotation in the Edge Plasma of Limiter Tokamaks", Report JUEL-2125, Kernforschungsanlage Jülich (1987) 68 pp.

[4] K.U. Riemann, Phys. Fluids **24** (1981) 2163.

[5] R.C. Bissell, Phys. Fluids **30** (1987) 2264.

[6] J.T. Scheuer, G.A. Emmert, Phys. Fluids **31** (1988) 3645.

Topic 5:

Heating and Current Drive

ENHANCED PERFORMANCE OF NEUTRAL BEAM HEATED HOT-ION H-MODES ON JET BY CENTRAL ICRF HEATING

M Bureš, B Balet, D Campbell, G A Cottrell, T Elevant, L-G Eriksson, J Jacquinot, N Jarvis, T Jones, R Konig, P Lomas, F Marcus, E Righi, G Sadler, D F H Start, A Tanga, P Van Belle and M von-Hellerman

JET Joint Undertaking, Abingdon, Oxon, OX14 3EA, UK

Introduction. Hot-ion H-mode discharges on JET are produced by high power Neutral Beam Injection (NBI) into a low density plasma, $< n_e > \approx 1 \times 10^{19}$ m^{-3}, in either Double (DNX) or Single (SNX) Null X-point configuration. The central particle fuelling combined with mainly ion heating by the NBI results in a discharge which, in addition to the H-mode enhancement, is found to benefit from improved central confinement. The hot-ion mode discharges can be optimised by combining, NBI with ICRF heating, depositing the RF power in the central region where the confinement is enhanced. In this paper, we report on two sets of experiments.

DNX Configuration. A modest amount of RF power P_{RF} = 1.5 - 3 MW was coupled into the 3 MA 2.8 T DNX discharges with P_{NBI} = 14 - 16.5 MW. The configuration is up-down symmetrical and the plasma boundary can be kept close to the antenna without adversely affecting the H-mode conditions. The coupling resistance $R_c \approx 2\ \Omega$ allowed the coupling of RF power without using the R_c-plasma position feedback. High values of neutron yield R_{NT} in the range 3.5×10^{16} s^{-1} were achieved reliably and reproducibly and the performance was ultimately limited by the influx of impurities, from the upper carbon target plates, after approximately 1 s of the high power heating. The NBI power could be exchanged for RF power at the level of few MW whilst maintaining or even increasing the reactivity. Additional RF power results in an important gain, 20 - 30 %, in the reactivity rate $d(R_{NT})/dt$. This is shown in Fig 1 where the D-D fusion yield ($R_{DD} \approx 2 \times R_{NT}$) is compared to two similar hot-ion discharges with NBI heating alone. This feature was observed in a number of discharges and can be reproduced by the TRANSP simulation of the measured neutron yield taking into account the increase in T_e, in these cases δT_{eo} = 0.5 - 2 keV. The role of the 2 ω_{CD} acceleration of the NBI particles is studied in the next section for a discharge with higher RF power.

SNX Configuration. The best performing discharge on JET (#26087) was run in the SNX configuration at 3 MA and reversed toroidal field 2.8 T, and was heated by NBI alone. In this configuration the power flow is more evenly distributed on the target plates and the impurity influx is slightly delayed. Previously, it proved to be difficult to couple the RF power into the SNX plasma. The standard configuration was unsuitable for RF heating; it is poloidally asymmetric with respect to the plasma midplane and the RF coupling resistance was close to the resistance in vacuum. A modification of the plasma position control, which allowed repositioning of the plasma, resulted in a new configuration suitable for RF heating. The modified configuration was used in a discharge with combined NBI and ICRH heating, $P_{NBI} = 14$ MW ($P_{NBI80} = 4$ MW, $P_{NBI140} = 10$ MW) and $P_{RF} = 6$ MW. The coupling resistance was 2.5 Ω. In the new configuration, a high performance hot-ion H-mode of duration 0.9 s was obtained (Fig 2) with peaked stored energy 11.7 MJ and central temperatures $T_{io} = 20$ keV and $T_{eo} = 12.7$ keV. The H-mode phase was terminated by the onset of giant ELMs as shown. The maximum neutron yield reached the value $R_{NT} = 3.7 \times 10^{16}$ s^{-1} with a rate of increase $dR_{NT}/dt \approx 4.15 \times 10^{16}$ s^{-2}. Corresponding numbers for the record yield discharge #26087 are $R_{NT} = 4.2 \times 10^{16}$ s^{-1} and $dR_{NT}/dt = 2.9 \times 10^{16}$ s^{-2}; in this discharge the giant ELM appeared 0.3 s later. The evolution of the yield in #26087 was previously reproduced[1] by TRANSP calculations where the thermal-thermal and beam-thermal contributions were roughly equal. In the RF heated discharge #26625 the similar TRANSP simulation of the thermal-thermal and beam-thermal neutrons can account for only 50 - 60 % of the total. The TRANSP and the PION[2] code calculations are presented in Fig 3. Assuming hydrogen minority concentration $n_H/n_D = 3$ % the total neutron yield 3.4×10^{16} s^{-1} is derived. Disregarding the RF heating, keeping the same background parameters, the total NBI yield becomes 1.51×10^{16}, roughly consistent with the TRANSP value. The RF power coupled to the deuterium by 2 ω_{CD} damping is 3.52 MW; 1.88 MW is coupled to the H minority and 0.6 MW is absorbed by direct electron damping. Decreasing the H-minority concentration in the PION code simulation results in a substantially enhanced neutron yield above the measured value. The calculated RF power deposition profile is peaked and the central power density is high. In Fig 4 the power deposition profile ($k_{||} = 7$ m^{-1}), for the power coupled to deuterium, is plotted together with the total power deposition from the beams. We note that the central power density for 3.52 MW of RF power exceeds that due to the 14 MW of NBI. The contribution from the H and electron damping to the central power density is ≈ 0.4 MW m^{-3}. The relative importance of the effect of T_e on the

slowing down of the fast beam ions versus $2\omega_{CD}$ damping can be estimated by calculating the neutron production by NBI alone ($P_{RF} = 0$) and by varying the background electron temperature. Changing the temperature by 15 %, eg $\delta T_{eo} \pm 2$ keV, the neutron yield changes by ±10 %. Thus it appears than an important contribution to the neutrons comes from the 2 ω_{CD} damping on the fast beam ions. The calculated deuterium energy distribution function is plotted in Fig 5.

Summary

Acceleration of deuterium beams by ICRH at 2 ω_{CD} appears to be unattractive for D-T since the deuterium ions rapidly reach too high energy to make an effective contribution to the D-T reactivity. In JET this limits the applied RF power to less than ≈ 5 MW. TRANSP and PION simulations show that a more promising use of RF in NBI-created hot-ion mode discharges is to raise the electron temperature, which, through equipartition, increases T_i and hence the reactivity. In addition, higher T_e increases the α-particle beta through the increased slowing down time.

References

[1] The JET Team, JET-P(91)66.

[2] L G Eriksson et al, Proc "Theory of Fus Plasmas", Varenna 1990, p 421.

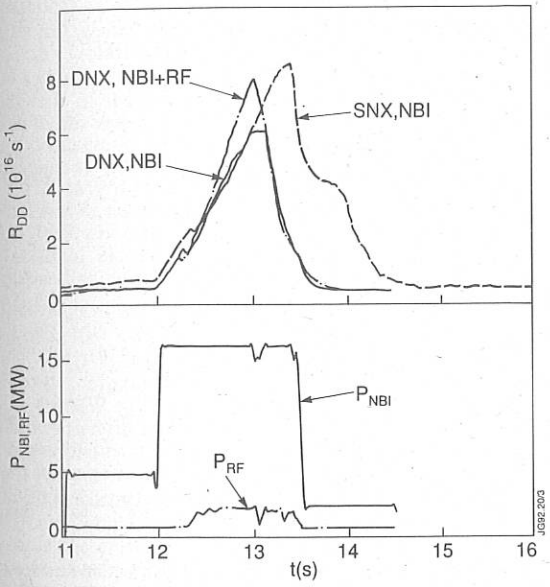

Fig 1: Total fusion yield time evolution in a 16 MW NBI hot-ion discharge in a DNX with 2 MW RF power compared to DNX and SNX with NBI only.

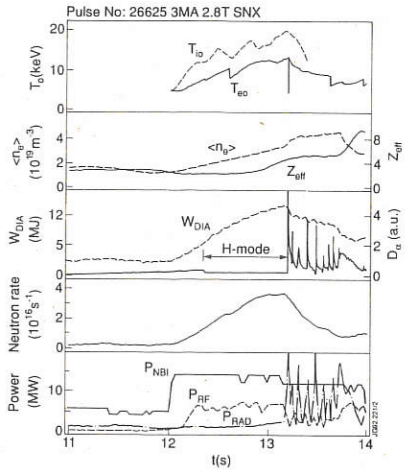

Fig 2: The time evolution of the central electron and ion temperatures, the volume-averaged electron density, the line-averaged Z_{eff}, the plasma diamagnetic energy, the Dα emission, the total neutron rate and the NBI, RF and radiated powers. Single, upper X-point configuration optimised for ICRF coupling.

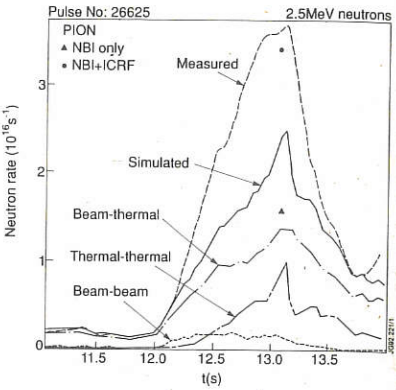

Fig 3: Measured and simulated (TRANSP) neutron rates. The single value points are derived using the PION code. The TRANSP calculation does not include the $2\omega_{CD}$ acceleration of the NBI ions.

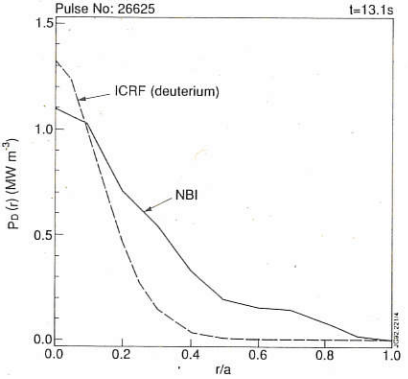

Fig 4: Total NBI power deposition profile and RF power deposition profile by 2 ω_{CD} damping which is dominated by the damping on the fast beam ions.

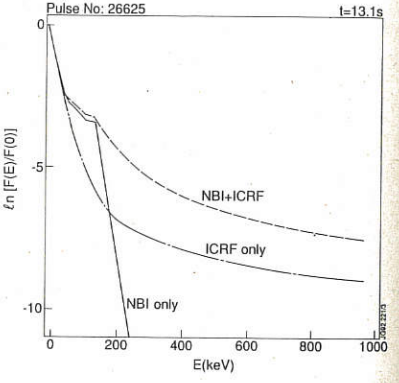

Fig 5: Deuterium energy distribution functions for 3 cases, NBI, ICRF and NBI + ICRF heating. The background parameters are identical as measured in the experiment.

RF heating and current drive experiments in TORE SUPRA

G.T. Hoang, G. Agarici, B. Beaumont, A. Bécoulet, G. Berger By, Ph. Bibet, J.P. Bizarro, J.J. Capitain, J. Carrasco,M. Goniche, E. Joffrin, K. Kupfer, H. Kuus, X. Litaudon, D. Moreau, F. Parlange, Y. Peysson, G. Rey, B. Saoutic, G. Tonon, D. van Houtte.
Département de Recherches sur la Fusion Contrôlée, Association Euratom-CEA
Centre d'Etudes de Cadarache - 13108 Saint-Paul-Lez-Durance- FRANCE.

Introduction:

Lower hybrid current drive (LHCD) experiments have been performed in TORE SUPRA by means of a quasi-continuous 3.7GHz / 8MW system using two large multijunction launchers [1]. A maximum of 6MW LH power has been coupled into the plasma during 3s. Up to central densities of $1x10^{20}m^{-3}$, the 1.6MA plasma current was still partially driven by LH waves indicating that the LHCD density threshold ($\propto f^2$) was not yet reached. LH current ramp-up assist, without MHD activity, permitted to reduce the resistive flux consumption. A 42 second / 1.3MA quasi-stationary discharge has been achieved at line-averaged density $\overline{n}_e = 2.6x10^{19}$ m^{-3} while a 3MW / 38s LH pulse was applied. Full current was driven in 0.8MA deuterium discharges with 2.9MW LH power at $\overline{n}_e = 2x10^{19}$ m^{-3}, and at lower density ($\overline{n}_e = 1.5x10^{19}$ m^{-3}) a recharge of the transformer (negative loop voltage) has been achieved with the same injected power.

Current drive and electron heating results:

LHCD experiments have been carried out in the typical 1.6MA/3.9T Tore Supra plasmas, at line-averaged densities between 1.5 - $6x10^{19}$ m^{-3} with a clear signature of suprathermal electrons from hard X-rays and electron cyclotron emission diagnostics up to the highest densities. The current drive density limit was not observed and therefore lies above $\overline{n}_e = 6x10^{19}$ m^{-3} (central density larger than $9x10^{19}$ m^{-3}), as expected at a frequency of 3.7 GHz.

At relatively high density ($\overline{n}_e \approx 4x10^{19}$ m^{-3}) in a helium plasma, about half of the plasma current was driven by the waves. In this case, taking into account the change of resistivity due to changes in electron temperature and Z_{eff}, with 4MW LH power the rf driven current was found to be about 850 kA of which 15% was estimated to be due to the residual electric field. Then the corresponding current drive efficiency, defined as $\gamma = \overline{n}_e R I_{rf} / P_{LH}$, is of the order of $2x10^{19}$ Am^{-2}/W. At densities of $\overline{n}_e = 1.5x10^{19}$ m^{-3} the loop voltage dropped close to zero for $P_{LH} \approx 4.8$ MW while the electric field and current profile reached equilibrium. For lower plasma current Ip=0.8MA, as shown in figure 1, full current drive was achieved in a deuterium discharge at $\overline{n}_e = 2x10^{19}m^{-3}$ with 2.9MW LH power. In this case the current diffusion time is about 4s instead of 1s for the pure OH case due to electron heating. The plasma surface voltage (V_s) was maintained to

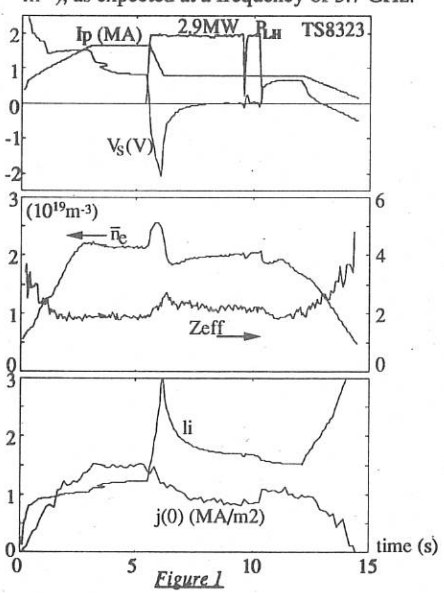

Figure 1

zero (or negative) during the LH pulse even though the plasma internal inductance (li) and the central current density (j(0)) obtained from Faraday rotation measurements reached equilibrium during the last second before LH switch off. Thus steady-state full current drive was obtained during one second. During LH, the j(0) value is less than the OH one (comparison between the values during and after LH application), whereas li increases from 1.4 to 1.8 when the LH power is applied. This could suggest that the LH current density gradient is larger than the OH one, and that the current distribution is flatter in the plasma center. Note that at lower density ($\overline{n}_e$= 1.5x10^{19}m^{-3}), 1.9MW LH power sufficed to fully drive the current, and a transformer recharge has been obtained when 2.9MW LH power was applied (Fig. 2). In figure 3, the relative drop of the plasma resistive loop voltage ($\Delta V/V$) is plotted versus injected power normalized to the line-averaged density, the plasma current and the major radius. This figure illustrates the electric field effect on suprathermal electrons by the non-linear increase of $\Delta V/V$.

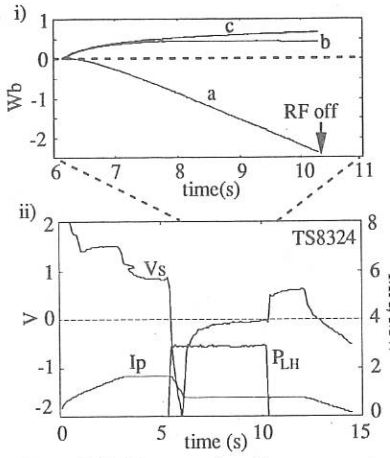

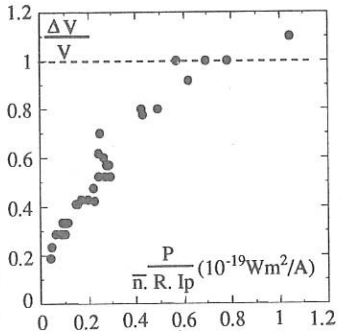

Figure 3 : Relative drop of plasma resistive loop voltage versus normalized LH power

Figure 2: i) Plasma surface flux consumption at Ip = 0.8 MA
a) OH plasma, $\overline{n_e}$= 2x10^{19}m^{-3} ; b) LH-OH plasma (2.9MW LH), $\overline{n_e}$= 2x10^{19}m^{-3}
c) LH-OH plasma (2.9MW LH), $\overline{n_e}$= 1.5x10^{19}m^{-3}
ii) Transformer recharge discharge: plasma surface voltage (Vs), plasma current (Ip), and LH power

Combined LHCD and ion cyclotron resonant frequency (2.2 MW, dipole phasing) hydrogen minority heating (ICRF) experiments have been performed in helium and deuterium plasmas with an injected power up to of 7.5 MW (0.8MW OH, 4.5MW LH, 2.2MW ICRF). In such experiments where ICRF power was applied during the LHCD phase, a weak drop of internal inductance parameter, l_i, was observed in the combined LH-ICRF phase over a time constant longer than the slowing down time of fast ions, which indicates a slight broadening of the current profile despite the peaking of the OH current component through the peaking of the electron temperature profile (Fig.4 and Fig. 5). This suggests that the LH power absorption occured in the outer part of the plasma during ICRF power application.

After the resistivity correction, the LH driven current was found to be lower in LH-ICRF phase than the one obtained with the same LH power alone.This is in agreement with the decrease of the residual loop voltage due to electron heating and the decrease of the suprathermal electron signal observed through hard X-ray measurements (reduction of the OH-LH synergy through acceleration of the fast electrons by the dc electric field).

During LHCD experiments, the bulk electrons were heated by slowing down of suprathermal electrons. At low densities ($\overline{n}_e$ = 1.5x10^{19} m^{-3}) a strong central electron heating

was observed. The electron temperature reached 8 keV on axis during the application of a 3.6 MW LH pulse which suppressed sawtooth relaxations [2]. The peaking factor $T_e(0)$ / <Te> increased from 2.2 in the ohmic phase to 3 in the LH one. At higher densities, $n_e(0) \approx 5x10^{19}$ m^{-3}, the central temperature was raised typically from 2 keV to 3 keV with the same amount of power, the central temperature increase scaled linearly with power and the peaking factor was approximately constant.

Global confinement studies with rf auxiliary heating have shown a much larger density dependence than the ITER 89-P scaling would predict, and is in fair agreement with the offset linear Rebut-Lallia scaling. A series of promising experiments have been performed in which an improved confinement has been obtained for steady-state plasmas where the confinement time was about 40% higher than the L-mode prediction while plasma current was peaked by LH waves [3].

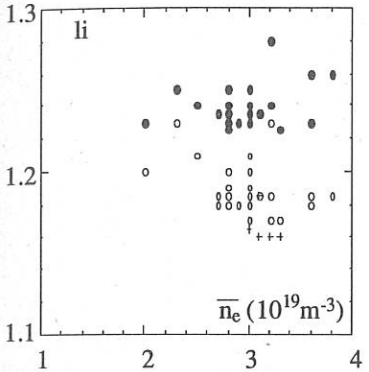

Figure 4 : Plasma internal inductance versus line-averaged density (Ip=1.6MA)
OH (l)
4.2MW LH (o)
4.2MW LH + 2.2MW ICRF (+)

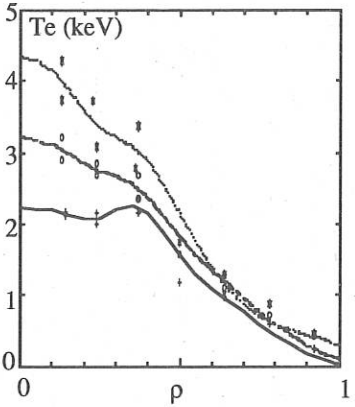

Figure 5 :Te profile from Thomson scattering
OH (+), 4.2 MW LH (o),
4.2MW LH + 2.2MW ICRF (*)

OH-LH current ramp experiments:

Current ramp-up experiments were characterized by a resistive flux saving efficiency $\xi_{res} = 0.25x10^{13}$ $Wb.m^{-1}/J$ for $P_{LH} \geq 1MW$ and $dI_p / dt = 0.4$ MA/s [4]. A MHD-stable domain exists in the (P_{LH}, dI_p / dt) diagram indicating that, in the mixed LH/OH regime, current ramp-up rates can be made larger than in the pure ohmic one by driving enough non-inductive current on axis. Recent experiments have been performed with 2 MW LH power, and the plasma current was raised from 0.6MA to 2 MA at a rate of 0.160 MA/s, while the primary voltage was maintained constant . No sign of MHD activity was observed.

During current ramp-down experiments at $\overline{n_e} = 2.3x10^{19}$ m^{-3} in which the voltage on the ohmic primary coil was held constant and the plasma current stabilized at about 500-600 kA with 2MW LH power, high β_p plasmas were obtained (≈0.6) with peaked current and temperature profiles (Te(0)/<Te> = 4-5), leading sometimes to a minor disruption in which the central temperature dropped by a factor 2. MHD modes were observed prior to this event.

Long OH-LH discharges:

Thanks to LH primary flux saving, a 42-second-long, 1.3 MA / 35s plateau, OH+LH quasi-stationary discharge has been achieved at a line-averaged density of $2.6x10^{19}$ m^{-3} with a 3MW/38s LH pulse. For such a discharge, in order to reduce the resistive flux consumption and to avoid the MHD activity the current ramp-up assisted by high LH power was operated with the safety factor, q_a, maintained constant. A typical long deuterium discharge is shown in Fig. 6, in

which a 30s plateau was obtained with 3MW LH power coupled to the plasma during 35s while global reflection coefficients were constant (≤ 3%). With a 1MW/7s ICRF pulse applied during the LH power application, the total energy injected into the plasma reached 112MJ. During RF power application, the carbon main impurity (metallic impurities were not observed) stayed at a level which is two times higher than the OH one and the radiated loss power was about 30% of the total injected power. The global confinement deduced from diamagnetic measurements was approximately constant (≈ 100ms).

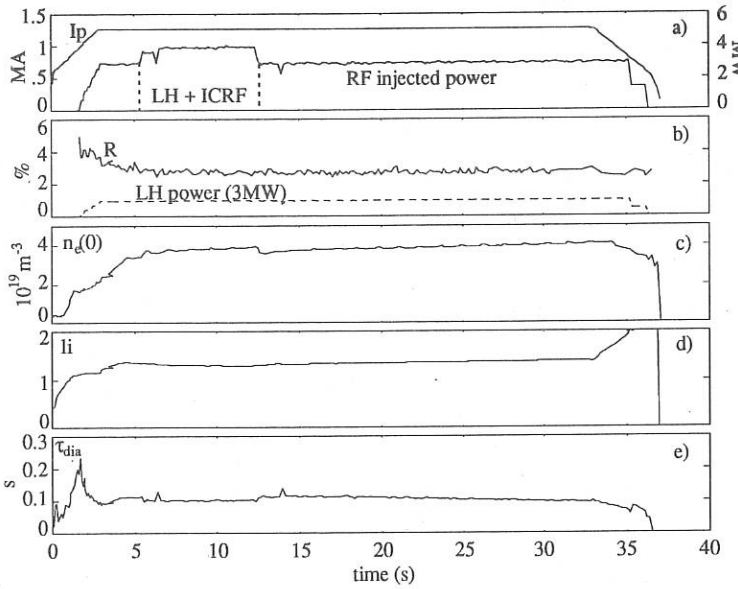

Figure 6: Long RF discharge (TS8301)
a) plasma current(Ip), total RF injected power; b) LH power and global reflection coefficients (R)
c) central density; d) plasma internal inductance; e) confinement time

Summary:

A maximum of 6 MW of lower hybrid power have been coupled in TORE SUPRA through 2 multijunction launchers, i.e. at a power density level in the waveguides which is relevant for next step fusion devices such as ITER (≈ 45MW/m^2).

Full current drive and also recharge of the transformer have been obtained during 1s in 0.8MA plasmas with 2.9MW / 5s LH pulse while steady-state was achieved. Combined LHCD and ICRF heating experiments have been performed with a total power of up to 7.5MW in which a strong electron heating occured in the center of the plasma. Stable LH current ramp-up assist was achieved with significant resistive flux saving. Thus a 42 second / 1.3MA quasi-stationary discharge has been achieved for a 3MW / 38s LH pulse.

References:

[1]: X. Litaudon et al, submitted to Nucl. Fus. (1992).

[2]: D. Moreau and Tore Supra Team, invited paper at the 33rd Annual Meeting of the APS, Tampa (1991), to be published in Phys. Fluids (1992)

[3]: G.T. Hoang et al, paper n° 1/130, this conference.

[4]: D. van Houtte et al, paper n° 5/35, this conference

ICRF power limitation relation to density limit in ASDEX

F. Ryter, ICRH-group, ASDEX-group

Max-Planck-Institut für Plasmaphysik, EURATOM-IPP Association
D-8046 Garching, FRG

1. Introduction

Launching high ICRF power into ASDEX plasmas required good antenna-plasma coupling. This could be achieved by sufficient electron density in front of the antennas i.e. small antenna-plasma distance (1-2 cm) and moderate to high line-averaged electron density compared to the density window in ASDEX. These are conditions eventually close to the density limit. ICRF heated discharges terminated by plasma disruptions caused by the RF pulse limited the maximum RF power which can be injected into the plasma. The disruptions occurring in these cases have clear phenomenological similarities with those observed in density limit discharges. We show in this paper that the ICRF-power limitation by plasma disruptions in ASDEX was due to reaching the density limit.

The density limit phenomena in OH and NBI heated discharges of ASDEX were studied in detail and summarised in [1]. The plasma evolution causing a density limit disruption can be described as follows. As the line averaged density is linearly increased by gas puffing, the edge and divertor electron density increases and the electron temperature in these regions decreases. Above a line averaged density of the order of 3-4 10^{19} m^{-3}, a poloidal asymmetry of the plasma edge radiation gradually develops. This asymmetry is seen by the bolometer camera as an up-down asymmetry and its sign depends on the plasma configuration and on the ion drift direction. When the divertor temperature reaches 7-5 eV a Marfe appears on the side of higher radiation and moves to the high field equatorial part of the machine. A plasma disruption, caused by the m=2 mode destabilization, occurs after a time delay depending on the edge q value. The density limit is interpreted as an edge density limit: the occurrence of the disruption is determined by the divertor temperature reaching very low values ($\approx$ 5 eV). Due to the relation of electron density and temperature with power balance in the separatrix and divertor regions, the density limit is determined by the edge density and by the power balance.

2. ICRF induced disruptions

The ICRF heated discharges were usually performed with density feedback programmed for constant density. In most of the discharges no disruption occurred. Under unfavourable conditions, however, the maximum ICRF power which could be launched into the plasma was limited by ICRF-induced disruptions. They can be classified into two types: "early disruptions" occurring within 100 ms after the beginning of the RF pulse and linked to the turn-on of the RF, "later disruptions" happening clearly later in the RF-pulse and related to a slow evolution of the plasma under RF conditions.

2.1. Early disruptions

Fig.1 a and b show some time traces for one discharge without disruption and one with an early disruption. The rather old boronisation still reduced the oxygen and metallic impurity concentrations by a factor of the order of 2 compared with a situation without coating at all. The common features of both discharges are the edge and divertor density increase, the divertor cooling, the quick increase of the edge radiation as well as that of its asymmetry, just after the RF turn-on. In Fig.1.a. the divertor temperature recovers after 100 ms and enters a quasi-stationary phase, in Fig.1.b a disruption occurs. Discharge #27984 was a repetition of #27983 except that #27984 was pushed closer to the antenna by 5 mm. This somewhat changed the plasma edge in such a way that the marfe (1.25s) which did not fully develop in #27983 did extend in #27984 and the disruption occurred. The universal feature of the early disruptions is

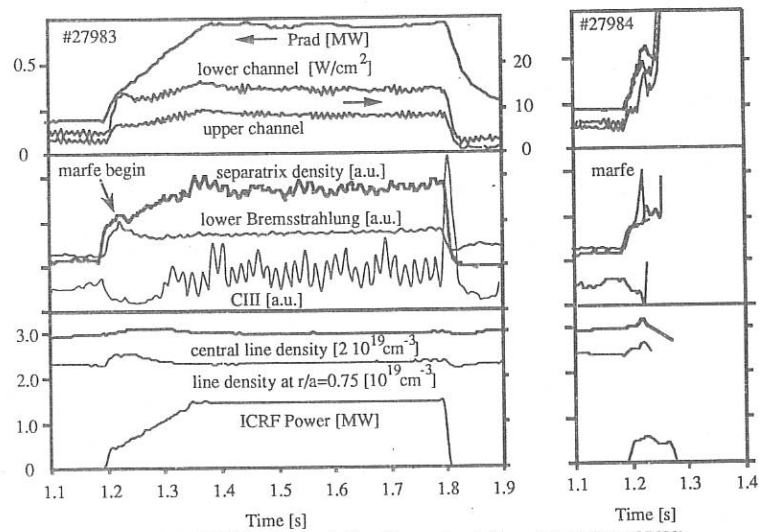

Fig. 1 a (#27983) and b (#27984). Time evolution of some signals (boronized before #27602). Prad is the volume integrated radiation power. The upper and lower channels are the line integrated radiation fluxes of two chords of the bolometer camera looking at z = +38 cm and z = -38 cm respectively. The lower bremsstrahlung is the line integrated visible bremsstrahlung intensity (~ ne2 Zeff Te-0.5) viewing at z = -38.5 cm. This signal is a clear monitor for marfes. CIII is the intensity of the CIII line in divertor and is proportional to the electron temperature in divertor. The separatrix density is given by the lithium beam diagnostic (here not calibrated) in the low field side equatorial plane.

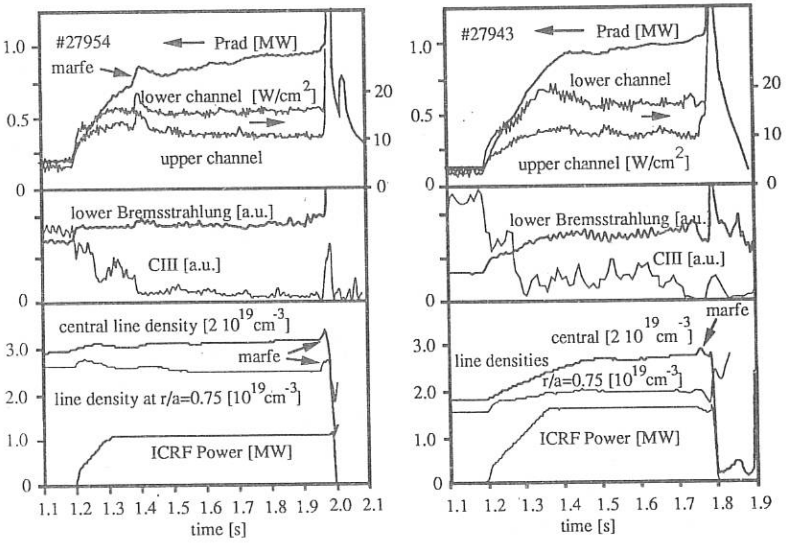

Fig. 2 a (#27954) and b (#27943). Time evolution of some traces for later disruptions. Same signals and conditions as in Fig. 1.

the divertor cooling and the occurrence of a marfe prior to the disruption. This suggests similarities with density limit disruptions [1]. An early disruption occurs when the perturbations due to the RF are too large. To reduce the effect of the RF turn on the power was generally ramped as shown in Fig.1 (the power pedestal of 0.2-0.5 MW was necessary for technical reasons). It was qualitatively observed that early disruptions occurred preferentially under high recycling conditions, for instance fresh carbonisation, that RF-conditioning (gradual shot-to-shot power increase) played an important positive role and that poor RF absorption was unfavourable. The best conditions were obtained with boronization combining both low recycling and reduced impurity production.

To interpret these observations we invoke the mechanism assumed for the impurity production in ASDEX, reviewed in [2] and summarised as follows. In the scrape-off layer where magnetic lines hit parts of the machine, ions are accelerated onto these parts by RF fields through sheath rectification effects. This mechanism is fully active as soon as the RF is turned on and causes higher recycling [3] (at least transiently) and impurity production in theses regions immediately after the RF was turned on. Thus, compared to heat diffusion from the plasma core, the edge increase of density, radiation and Z_{eff} is fast and causes the divertor temperature to quickly decrease. These early disruptions are clearly due to the density limit being reached at the beginning of the RF pulse. In good discharges, as in Fig.1.a, the density limit is only transiently approached until the ICRF central heating causes the divertor temperature to increase, after typically one energy confinement time.
Consequently, the density at the beginning of the RF-pulse must be far enough from the OH density limit to avoid early disruptions. For example, at $q_a = 3$, in the best cases, a maximum value of the Murakami parameter of $M = 4.3$ is tolerable before the RF pulse, compared to $M = 5.5$ reached at Ohmic density limit with the same parameters and wall conditions. It will be shown in the next section, however, that starting at low density leads to other difficulties. A very reliable method to avoid the early disruptions was to preheat the plasma with NBI preventing the divertor temperature reaching very low values when the RF was turned on. This scenario is discussed in section 2.3.

2.2. Later disruptions
Under certain conditions, the divertor temperature did not stabilise as in Fig.1.a, but slowly decreased on the time scale of some 100 ms eventually provoking disruptions as illustrated in Fig. 2 a and b. This evolution depended on the machine conditions and on the density prior to the RF pulse. For densities slightly under the OH density limit (Fig.2.a), the divertor temperature remained low during the RF pulse and a small perturbation or a slow increase of the radiation or density lead to a disruption. When the density prior to the RF-pulse was lower (Fig.2.b), the density during the RF could not be controlled and increased although the gas puffing was reduced. This behaviour of the density is not understood and seriously reduced the experimental density window with ICRF. Both later disruptions illustrated here are clearly due to the divertor temperature reaching a critical low value and are therefore identified as density limit phenomena. Thus, this feature is universal to both early and later disruptions. In addition to these observations in the edge and divertor regions, the cause of the disruptions being a radiation collapse is excluded by plasma core measurements. In fact, the total radiation power prior to the marfe reaches at most 70% of the total heating power, and no decrease of the central electron temperature is observed.

2.3. Limitation of the combination with NBI
The combination of ICRF with NBI allowed reliable operation due to higher divertor temperature. It also greatly improved the density control. However, in contradiction to the expectation, the divertor temperature of the discharge during the steady-state phase decreased with increasing ICRF power, as shown in Fig. 3. For comparison some points for ICRF not combined with NBI are given. The reasons for this temperature decrease are not clearly identified but are possibly linked with edge and divertor effects (recycling, impurity production and/or radiation) increasing faster with ICRF power than the heating power flux across the

separatrix. The favourable influence of shot-to-shot RF conditioning achieved by gradually increasing the power also appears in Fig. 3. This figure shows the limits of the combination with NBI: the maximum ICRF power which can be launched without causing a disruption depends on the NBI power for given machine conditions. For the example of Fig. 3 disruptions occur when the absorbed ICRF power is only around 50% of the total heating power.

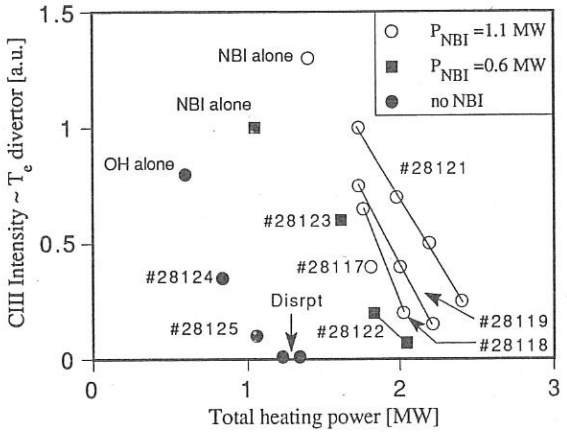

Fig. 3 CIII intensity in divertor versus total heating power (boronized before #27602). In the series (#28117 - #28123) ICRF was combined with NBI at two different powers 1.1 MW and 0.6 MW. The ICRF power was launched in steps during each discharge. For each discharge, identified by its number, a straight line links the values obtained in each of the plateaus corresponding to the power steps. For the discharges represented with circles (P_{NBI} = 1.1 MW) the improvement with RF conditioning appears clearly: for a given power, the CIII intensity (~ T_e(div)) increased from shot to shot.

3. Conclusion

Enhanced recycling and impurity production with ICRF cause disruptions due to a decrease of the divertor temperature down to a critical value, similarly to density limit discharges. Operating near the density limit with a cold divertor, as probably necessary in a future reactor, will require an improved control of the edge phenomena with ICRF.

References

[1] A. Stäbler, et al., Density limit investigations on ASDEX, to be publ. in Nucl. Fus. (1992)

[2] J.-M. Noterdaeme, et al., Fusion Engineering and Design **12** 127 (1990)

[3] J. V. Hofmann, et al., Fusion Engineering and Design **12** 179 (1990)

FAST WAVE CURRENT DRIVE EXPERIMENTS ON THE DIII-D TOKAMAK*

C.C. Petty, R.I. Pinsker, M. Porkolab,† F.W. Baity,‡ S.C. Chiu, R.H. Goulding,‡ J.S. deGrassie, R.W. Harvey, D.J. Hoffman,‡ R.A. James,♯ H. Kawashima,♭ John Lohr, T.C. Luce, M.J. Mayberry,° and R. Prater

General Atomics, San Diego, California, U.S.A.

Introduction. One method of radio-frequency heating which shows theoretical promise for both heating and current drive in tokamak plasmas is the direct absorption by electrons of the fast Alfvén wave (FW). Electrons can directly absorb fast waves via electron Landau damping and transit-time magnetic pumping when the resonance condition $\omega - k_{\parallel} v_{\parallel e} = 0$ is satisfied.[1,2] Since the FW accelerates electrons traveling in the same toroidal direction as the wave, plasma current can be generated non-inductively by launching FW which propagate in one toroidal direction. Fast wave current drive (FWCD) is considered an attractive means of sustaining the plasma current in reactor-grade tokamaks due to the potentially high current drive efficiency achievable and excellent penetration of the wave power to the high temperature plasma core.[3]

Ongoing experiments on the DIII-D tokamak are aimed at a demonstration of FWCD in the ion cyclotron range of frequencies (ICRF). Using frequencies in the ICRF avoids the possibility of mode conversion between the fast and slow wave branches which characterized early tokamak FWCD experiments in the lower hybrid range of frequencies.[4,5] Previously on DIII-D, efficient direct electron heating by FW was found using symmetric (non-current drive) antenna phasing.[6] However, high FWCD efficiencies are not expected due to the relatively low electron temperatures (compared to a reactor) in DIII-D.

Experimental Setup. The FWCD experiments use a four-element toroidally phased antenna array to launch fast waves at 60 MHz with a highly directional spectrum. The current straps are 45 cm high and 11 cm wide, and are spaced 22.5 cm apart (center-to-center). The Faraday shield consists of two staggered tiers of Inconel rods which are copper plated and have a TiC/TiN coating. The antenna is fed by a single 2 MW transmitter, thus all phase control and current amplitude balancing of the antenna array must be accomplished at high power. The coupled spectrum has a peak $|n_{\parallel}| \approx 5$ for ± 90 deg phasing, which requires $T_e \geqslant 4$ keV for efficient direct electron absorption.

The antenna phasing, power division, and impedance matching necessary for FWCD experiments has been achieved, despite the substantial mutual inductive coupling between the current straps.[7] Figure 1 shows the satisfactory antenna array phasing and voltage amplitude balance (within 20%) during a counter current-drive plasma shot. The reflected power at the transmitter was $\approx 1\%$. Verification of the antenna phasing was made using additional current and voltage probes in combination with the calibrated lengths of the tuning stubs and transmission line as well as directional coupler measurements. The antenna can be switched from co-current to counter-current phasing in one shot. Symmetric antenna phasings can also be done for comparison.

*Report of work sponsored by the U.S. Department of Energy under Contracts DE-AC03-89ER51114, DE-AC03-78ET51013, DE-AC02-76-CHO-3073, and DE-AC05-84OR21400.
†Permanent address: Massachusetts Institute of Technology, Cambridge, Massachusetts, U.S.A.
‡Permanent address: Oak Ridge National Laboratory, Oak Ridge, Tennessee, U.S.A.
♯Permanent address: Lawrence Livermore National Laboratory, Livermore, California, U.S.A.
♭Permanent address: Japan Atomic Energy Research Institute, Tokai, Japan.
°Present address: Stanford University, Stanford, California, U.S.A.

Analysis Method. To date, FWCD experiments on DIII–D have not driven all the plasma current, therefore the level of rf current drive is determined by comparing the plasma resistance determined from the loop voltage and plasma current (excluding bootstrap current) with that calculated from neoclassical resistivity. The rf current drive from this analysis method, written in terms of plasma loop voltage rather than plasma resistance, is given by

$$I_{rf} = \frac{V_L^* - V_L}{V_L^*} \; (I_p - I_b) \quad , \tag{1}$$

where V_L is the experimentally measured loop voltage, V_L^* is the calculated loop voltage using neoclassical resistivity (without rf current drive), I_p is the total plasma current, and I_b is the calculated bootstrap current. In the calculation, the measured profiles of n_e, T_e, T_i, and Z_{eff} are utilized; the plasma current profile is determined from a magnetic topology reconstruction using external magnetic measurements, the kinetic profile data, and the location of the $q = 1$ surface from soft x–ray measurements.[8] The calculation of the plasma loop voltage assumed steady-state conditions and a fully penetrated electric field. The calculation was benchmarked against ohmic, electron-cyclotron heating (ECH), and neutral beam injection (NBI) plasmas, with a typical discrepancy of ± 0.03 V between the calculated and measured loop voltage.

Experimental Results. FWCD experiments have been performed in DIII–D with co-current and counter-current phasings at coupled power levels up to 1.1 MW. The working gas was deuterium ($\approx$ 2% residual hydrogen), and the vacuum vessel was boronized to reduce the metal influx and plasma density increase during FW injection. Substantial electron heating and decreases in the plasma loop voltage were observed during FWCD at $B_T = 1.1$ T ($\omega = 4\omega_H = 8\omega_D$) and $B_T = 2.0$ T ($\omega = 2\omega_H = 4\omega_D$), with and without electron preheating by 60 GHz ECH. The largest fractions of non-inductive current drive were obtained for $B_T = 1.1$ T and $n_e = 1.0 \times 10^{13}\,cm^{-3}$, shown in Fig. 2. The calculated plasma loop voltage, including bootstrap current (but not rf current drive), is indicated in Fig. 2(b) by the dashed horizontal lines. From Eq. (1), the rf current drive during the combined ECH and FW phase was 117 ± 27 kA out of 395 kA of plasma current (30%); the bootstrap current was an additional 44 kA of non-inductive current drive (11%). The portion of the rf current drive due to electron cyclotron current drive (ECCD) was calculated to be 29 kA for this case, including the effect of the residual loop voltage. The FWCD was also measured after the ECH pulse, and thus at a lower electron temperature. For this condition, the loop voltage analysis found 81 ± 22 kA of FWCD, with an additional 41 kA of bootstrap current.

An x–ray spectrometer observed a perpendicular tail in the electron distribution function during ECH preheating which was further enhanced by FWCD. For $B_T = 1.1$ T operation, the tail temperature was $\approx$4 times greater than the central thermal temperature, and the energetic electron density was $\approx$10% of the central thermal electron density. Fast wave injection by itself did not produce a perpendicular electron tail at $B_T = 1.1$ T. Co-current phasing was found to enhance the energetic tail more than counter-current phasing for otherwise similar conditions.

The rf current drive increased with FW power and decreased with plasma density, as shown in Fig. 3. The faster-than-linear increase in I_{rf} with $P_{FW}/\bar{n}_e$ was probably due to a favorable T_e dependence in the FWCD efficiency. The rf current drive was larger for ECH combined with FW compared to FW alone; this can be explained by the higher T_e during ECH preheating plus some level of ECCD. Experimentally, the FWCD efficiency was found to increase significantly when the outer gap was increased from 1.2 to 2.5 cm, probably due to reduced wall interaction and increased spectral filtering. The calculated NBI current drive with a low-power beam is also shown in Fig. 3 for comparison. When NBI preheating of the plasma was used in combination with FWCD, no rf current drive was found outside of the error bars due to a relatively low T_e and high $\bar{n}_e$ compared to ECH preheating.

Surprisingly, the magnitude and direction of the rf current drive was found to be independent of which direction the FW was launched relative to the plasma current. As shown in

Fig. 4, I_{rf} was the same for co-current and counter-current phasing of the antenna (the ECCD was always in the co-current direction). The lack of a clear dependence of the FWCD on the relative sign of I_p and $k_\parallel$ is the topic of current theoretical investigation. However, the fact that co-current phasing enhanced the energetic electron tail more than counter-phasing suggests a synergism between the fast wave and the residual toroidal electric field. This result may also be related to poor first pass absorption of the FW. The calculated first pass absorption of the FW during the combined ECCD and FWCD phase of Fig. 2 was only 10%, and the calculated first pass current drive using a slab model was only 12 kA.[9] Since the measured rf current drive is an order of magnitude greater than this, either multiple pass current drive is occurring or the rf generates an enhanced bootstrap current.

The directivity of the coupled spectrum was evident from the FW heating results obtained at $B_T = 2.0$ T. A manifest difference in the electron heating efficiency and impurity production between the co-current and counter-current phasings was observed, with the counter-current phasing heating better and producing fewer impurities. When the plasma current was reversed, the effects of the antenna phasing reversed with it, so that the phasing counter to the new I_p direction was again superior. The reason for this difference in electron heating is not presently understood. The FWCD results for $B_T = 2.0$ T were similar to those at $B_T = 1.1$ T, with $I_{rf} \approx 100$ kA and independent of the antenna phasing. This level of rf current drive was obtained at twice the plasma density, however, indicating a higher current drive efficiency. For $B_T = 2.0$ T, an energetic electron tail with $T_{tail} \approx 8$ keV was observed during FWCD, even without ECH preheating. The co-current phasing again produced a larger tail than the counter-current phasing.

Conclusions. Experiments to demonstrate FWCD in the ICRF have been performed on DIII–D with coupled power levels up to 1.1 MW. The antenna phasing, power division, and impedance matching necessary to launch a directed spectrum with a four-strap antenna has been achieved. Electron heating and loop voltage drop was observed during FWCD at $B_T = 1.1$ and 2 T with and without ECH preheating. Although full current drive has not been achieved yet, a loop voltage analysis shows that up to 135 ± 25 kA of rf current was driven during combined ECCD and FWCD, and up to 95 ± 20 kA was driven during FWCD alone. The rf-driven current increased with FW power and decreased with plasma density. However, the rf-driven current was independent of the direction (co- or counter-) of propagation of the launched FW. A manifest difference in the electron heating efficiency and impurity production between co-current and counter-current phasing was observed in 2 T discharges, indicating that the FW launching was indeed directional. Future FWCD experiments will be performed with higher ECH power to increase the electron temperature and thus further optimize the first pass absorption and FWCD efficiency.

References

[1]T.H. Stix, Nucl. Fusion **15**, 737 (1975).
[2]M. Porkolab, in *Radiofrequency Power in Plasmas* (Proc. 9th Top. Conf., Charleston, 1991), American Institute of Physics, New York (1992), p. 197.
[3]N.J. Fisch, Rev. Mod. Phys. **59**, 175 (1987).
[4]K. Ohkubo *et al.*, Phys. Rev. Lett. **56**, 2040 (1986).
[5]R.I. Pinsker, "Fast wave current drive experiments on the Princeton Large Torus," Ph.D. dissertation, Princeton University, 1988.
[6]C.C. Petty *et al.*, in *Radiofrequency Power in Plasmas* (Proc. 9th Top. Conf., Charleston, 1991), American Institute of Physics, New York (1992), p. 96.
[7]R.H. Goulding *et al.*, in *Radiofrequency Power in Plasmas* (Proc. 9th Top. Conf., Charleston, 1991), American Institute of Physics, New York (1992), p. 287.
[8]L.L. Lao *et al.*, Nucl. Fusion **30**, 1035 (1990).
[9]S.C. Chiu, V.S. Chan, R.W. Harvey, and M. Porkolab, Nucl. Fusion **29**, 2175 (1989).

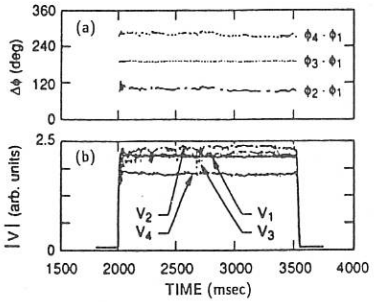

FIG.1 (a) Voltage probe phases relative to line 1, and (b) voltage probe amplitudes for a counter-current antenna phasing.

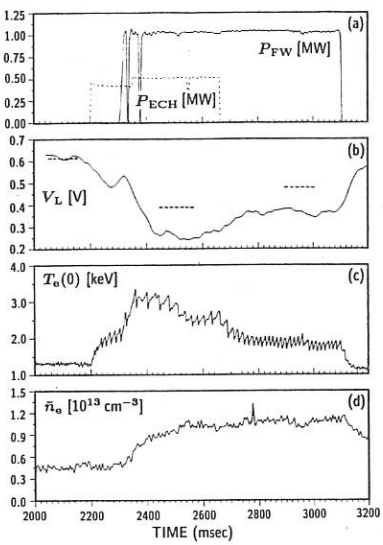

FIG. 2 FWCD discharge with co-current drive phasing: (a) coupled FW and ECH power, (b) measured (solid) and calculated (dashed) plasma loop voltage, (c) central electron temperature, and (d) line averaged density ($B_T = 1.1$ T, $I_p = 395$ kA).

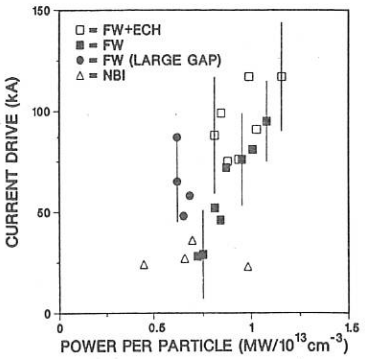

FIG. 3 RF (and NBI) current drive as a function of FW (and NBI) power per particle. The filled circles are for FWCD (without ECH) with a 2.5 cm outer gap instead of a 1.2 cm outer gap ($B_T = 1.1$ T, $I_p = 400$ kA).

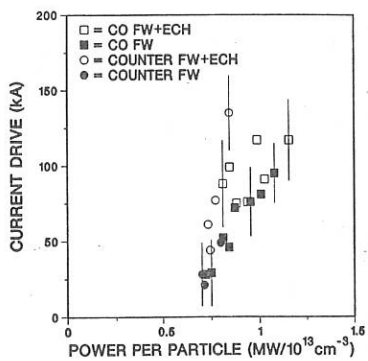

FIG. 4. RF current drive as a function of FW power per particle for co-current and counter-current phasings ($B_T = 1.1$ T, $I_p = 400$ kA).

Observation of Fast Wave Ion Current Drive Effects on Sawteeth in JET

D F H Start, V P Bhatnagar, G Bosia, M Brusati, M Bures, D Campbell, G A Cottrell, M Cox[1], H P L DeEsch A Edwards, L–G Eriksson, C Gormezano, J Jacquinot, P Lomas, F B Marcus, M R O'Brien[1], F Porcelli, F Rimini, D Stork, A Tanga, B Tubbing, C D Warrick[1] and J Wesson.

JET Joint Undertaking, Abingdon, Oxon., OX14 3EA, UK
[1]Culham Laboratory, Abingdon, Oxon, OX14 3DB,UK

Introduction Recent technical improvements[1] to the JET ICRH system have enabled the two striplines in each antenna to carry currents with equal amplitude but arbitrary phasing. As a result, travelling fast waves can be launched to perform current drive experiments. This paper describes the effects on sawteeth when such waves are absorbed at a minority ion fundamental resonance placed tangential to the q=1 surface. The aim of the experiments was to affect sawtooth stability by using minority ion current drive[2] to modify the current density and hence the magnetic shear. Such a scheme drives current in opposite directions on either side of the resonance layer to form a highly localised current density perturbation with a bipolar radial profile. This bipolar current can then be used to increase or decrease the shear locally at the q=1 surface depending on the direction of propagation of the travelling waves.

Experimental Results The experiments were carried out in 2MA limiter deuterium plasmas with H–minority ICRH at a frequency of 42.7MHz. Toroidal fields of 2.6T and 3.1T were used to place the minority resonance tangential to the q=1 surface on either the inboard or the outboard side of the magnetic axis, respectively. In a typical discharge the central electron density, $n_e(0)$, was $2.7\times10^{19}m^{-3}$ and the electron temperature,$T_e(0)$, was 5.5keV. ICRF power levels up to 14MW were applied and the H–minority density was varied from 3% to 43% of the electron density according to neutral particle analyser measurements. The behaviour of the sawteeth was monitored by both ECE and soft X–ray emission. The experiments were carried out with 90^0 phase difference between the antenna current straps which gave a parallel wavevector spectrum centred on $k_z = 3.5m^{-1}$ with a full width at half maximum of about $8m^{-1}$.

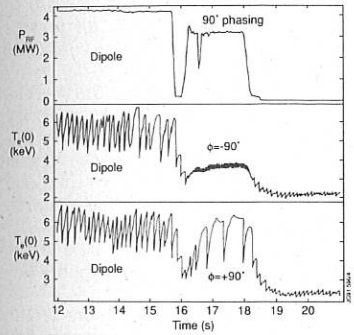

Fig.1 Effect of $\varphi=\pm90^0$ on sawteeth.

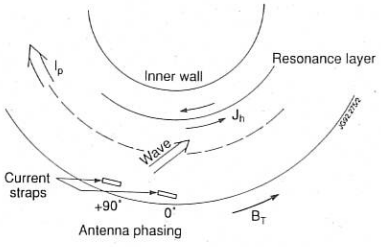

Fig.2 Direction of J_h for $\varphi=+90^0$

The directivity of this spectrum was calculated to be 66%. Most of the experiments were made with the resonance on the high field side of the magnetic axis. In this situation, applying RF power with $+90^0$ phase produced monster sawteeth in conditions where dipole phasing, for example, creates only long sawteeth. The T_e profile showed the usual central peaking characteristic of monster sawteeth despite the off–axis power deposition. In complete contrast, reversing the toroidal direction of the wave by using -90^0 phasing

produced a dramatic destabilisation, as shown in fig 1, and created sawteeth of very short period (40ms). In this case the T_e profile was flattened inside the inversion radius. With positive phase difference between antenna currents the wave propagates antiparallel to the plasma current as shown in fig 2. On the low field side of the resonance the wave damps on hydrogen ions travelling in the same direction as the wave according to the resonance condition $\omega - \Omega = k_z v_z$, where ω is the wave frequency, Ω is the ion gyrofrequency and the z axis is along the magnetic field line. On the high field side of the resonance damping takes place on ions travelling towards the wave. Thus for positive phasing and the resonance at q=1, the minority current reduces the plasma current inside the q=1 surface and increases the plasma current outside the q=1 surface. Two power scans were carried out with φ=+90^0 for minority densities of about 3% and 30%, respectively. The data for the 3% case are shown in fig 3 and plots of maximum

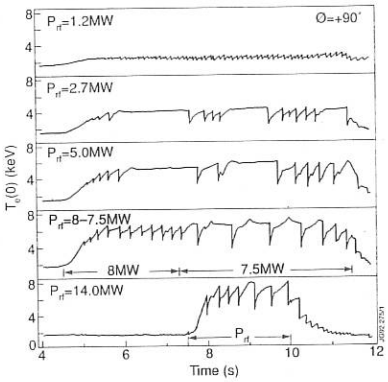

Fig.3 Sawtooth dependence on P_{rf}.

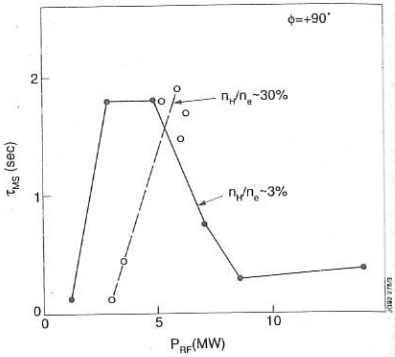

Fig.4 Sawtooth period versus P_{rf}.

sawtooth period versus RF power are shown in fig 4. For the 3% minority, monster sawteeth were created with only 2.7MW of power and are maintained for powers up to 5MW. However, above 5MW the sawtooth period decreases and is only 0.3s for powers exceeding 8MW. With 30% concentration twice the power was required to produce monster sawteeth and no decrease in period was seen up to 6.5MW.

A scan of minority concentration was also made at a constant power level of 5MW. The results are shown in fig 5. The stabilising effect with φ = +90^0 is lost as the minority concentration is raised from 16% to 43% but is regained at the highest minority density by raising the power to 6.5MW. At such high minority concentrations mode conversion tends to reduce the power absorbed by the minority ions and increase the power damped directly on the electrons. In the present experiments the direct electron heating fraction P_e/P_{rf} was measured from the change in the electron temperature rate of rise (dT_e/dt) as the RF power was switched off. For the 30% minority case, approximately 20% of the input power was found to be damped on the electrons and this represents a significant correction to any current drive calculations.

Experiments with the resonance touching the q=1 surface on the outboard side of the plasma centre were made at a toroidal field of 3.14T. At 6MW of RF power, –90^0 phasing produced a monster sawtooth, in contrast to the destabilising effect of this phasing for the inboard resonance. With +90^0 phasing, sawteeth lasting for up to 0.6s were observed. Thus for the outboard resonance position directed waves have only a minor effect on the sawtooth stability with the correlation between stability and the sign of the phase tending to be opposite to that for the inboard resonance. This sign reversal is expected since the current driven on the low field side of the resonance is inside the q=1 surface for the inboard resonance and outside the q=1 surface for the outboard resonance.

The stability of sawteeth has also been controlled using second harmonic ICRH in a 50/50 mixed H/D plasma. The magnetic field was 1.3T and the RF frequency was 42.7MHz so that the $2\omega_{ch}$ resonance touched the q = 1 surface at the inboard position. As in the minority ICRH experiments, $+90^0$ phasing was stabilising whereas -90^0 phasing was destabilising as shown in fig 6. Note that with 135^0 phase, the sawteeth are unaffected by a change of wave direction, possibly due to the lower directivity.

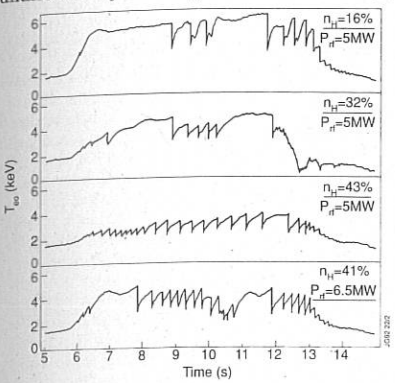

Fig.5 Scaling of τ_{ms} with n_h/n_e.

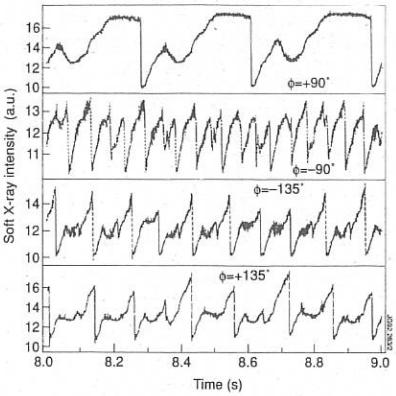

Fig.6 Phasing effect at $\omega=2\omega_{ch}$.

Discussion The original theory of minority ion current drive by Fisch[2] was relevant to plasmas in a uniform magnetic field. For the present experiments using hydrogen minority in deuterium plasmas this theory predicts zero total current since the return electron current completely cancels the ion current. Taking account of electron trapping and $Z_{eff} \neq Z_i$ the total current density is given by[3,4]

$$J_t = J_h\{1-Z_h/Z_{eff} + 1.46\sqrt{\epsilon}\,[Z_h/Z_{eff} - \lambda Z_i m_h/Z_h m_i].A(Z_{eff})\}.$$

where the subscripts h and i refer to the hot minority and majority ions, respectively. and ϵ is the inverse aspect ratio, $\epsilon=r/R$. The function $A(Z_{eff})$ has a value of 1.4 for $Z_{eff}=1.7$ which is typical of the present experiments. The parameter λ is unity if the majority ion rotation is undamped and is zero if the rotation is completely damped[3].
The minority ion current density has been calculated using the 2–D Fokker–Planck code developed by Cox et al[5]. The RF diffusion coefficient is calculated from the acceleration of each ion as it passes through a 'beam' of RF in front of each antenna. The width of this beam is determined by the width of the antenna k_z spectrum($8m^{-1}$) and its angle of incidence corresponds to the value of k_z at peak power($3.5m^{-1}$). For trapped ions which turn at the resonance layer, the usual Airy function form of the diffusion coefficient is used. The variation of $|E^+|^2$ along the beam axis is obtained from ray tracing calculations[6]. Profiles of current density and power absorption are obtained by solving the Fokker–Planck equation on each flux surface. The velocity space grid size was 300x250 in velocity and pitch angle respectively, with the maximum energy at $30T_i$. Total current density profiles, calculated for $\lambda=0$ and $\lambda=1$ and for 30% minority density are shown in fig 7 as a perturbation to the ohmic current profile. The phasing was $+90^0$ and the the resonance was at the inboard position. The RF power coupled to the minority ions was 4.8MW to simulate a monster sawtooth discharge having 6MW of input power of which 1.2MW was damped on the electrons.
From figure 7 it is clear that RF driven current can substantially modify the current density profile and even produce a positive gradient at the q=1 surface. This level of current perturbation can almost double, or cancel, the local shear produced by the ohmic

current, depending on the direction of the fast waves. Calculations by Porcelli et al[7] show that such changes in shear could account for the observed changes in sawtooth stability, on the basis of the theory of resistive kink modes.
Further current drive calculations are shown in fig 8 for 17% and 30% minority densities and for an input power level of 5MW. These examples correspond to the minority density scan at constant power (fig 5). The driven current is significantly greater inside the resonance layer for the 17% case and this might explain the loss of stabilising effect as the minority density is raised. About 1/3 of the reduction in current at 30% minority density is due to the increased direct electron damping with the remaining 2/3 due to decreased current drive efficiency. Calculations are in progress in relation to the scaling with power (fig 4) but are incomplete as yet.

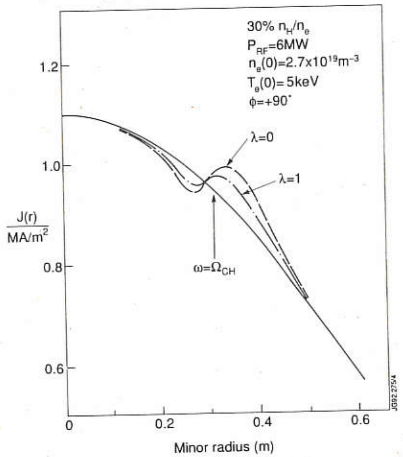

Fig.7 J_t profile for n_h/n_e=0.3.

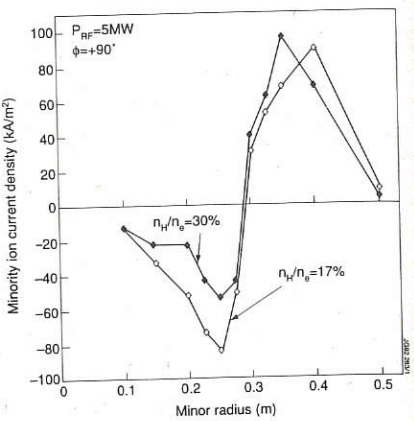

Fig.8 $J_h(r)$ for n_h/n_e=0.17 and 0.3 for P_{rf}=5MW.

Summary Phasing the ICRF antennas in current drive mode has been shown to have a strong effect on sawtooth stability when the minority ion resonance touches the q=1 surface on the inboard side of the magnetic axis. The results are consistent with modification of the current density profile by minority ion current drive and form the first evidence for this type of current drive method. So far complete stabilisation has not been achieved perhaps due to the movement of the q=1 surface as sawteeth get longer. Nevertheless, by controlling the sawtooth period, and thus the rate of ejection of fast particles from the plasma centre, this method offers potential for burn control in a reactor.

References

[1] G Bosia and J Jacquinot, IAEA Tech. Comm. Meeting on Fast Wave Current Drive in Reactor Scale Tokamaks, Arles 1991, p471
[2] N J Fisch, Nuclear Fusion 21(1981)15.
[3] S C Chiu et al., Nuclear Fusion 23(1983)499
[4] D F H Start, J G Cordey and E M Jones Plasma Physics, 22(1980)303.
[5] M Cox and D F H Start, 1978 Int.Conf. on Plasma Physics, Kiev, 1(1987)232.
[6] V P Bhatnagar, R Koch, P Geilfus et al., Nuclear Fusion 24(1984)995.
[7] F Porcelli et al., this conference.

Acknowledgements It is a pleasure to acknowledge the help of our JET colleagues who have operated the tokamak and its diagnostics during the experiments reported here.

RESISTIVE INTERNAL KINKS AND ICRF PHASING CURRENT DRIVE

F. Porcelli, V.P. Bhatnagar, P. Bosia, A. Cherubini, J. Jacquinot, D. Start and A. Taroni
JET Joint Undertaking, Abingdon, Oxon, OX14 3EA, UK.

Abstract. We present a model for the stability of resistive internal kinks which encompasses both effects of fast particle pressure and local (q = 1) magnetic shear. Sawtooth stabilization by fast particle pressure is most effective with on-axis ICRF heating. With off-axis ICRF current drive in low β_p discharges, the modification of the local of the shear near q = 1 may play the most important role.

Introduction Thanks to a recent technical improvement [1], it is now possible to phase the JET ICRF antennas in such a way as to produce a RF power spectrum which is non symmetric as a function of the parallel wavevector, $k_{||}$. When a phased ICRF waves is launched into the plasma and the wave frequency ω_{RF} is such that the minority ion cyclotron layer is nearly tangent to the q = 1 radius on the high field side, some very striking effects on sawteeth are observed. Specifically, with a +90° phase, the sawtooth period is significantly lengthened compared with the observed period in the presence of a symmetric (i.e. dipole) power spectrum, for the same RF power and plasma parameters. With a phase of -90°, the sawtooth period can be dramatically shortened (see, e.g., Fig. 1 of Ref. [2], presented at this Conference). With the cyclotron layer tangent to the q = 1 surface on the low field side, the effects of the two phases are interchanged, although these effects are now less pronounced. No significant difference in the sawtooth behavior between the two phases is observed when the cyclotron layer passes well inside the q = 1 surface. These recent experimental results contrast with our previous experience, where sawtooth stabilization was found to be most effective with on-axis ICRF heating, while no significant sawtooth suppression was observed when ICRF waves with symmetric spectra were absorbed near the q = 1 radius [3]. Thus, experiments indicate that two different mechanisms to control sawteeth while allowing q on axis to drop below unity can be exploited: (i) stabilization by fast particle pressure; (ii) a reduction of the local (q = 1) magnetic shear. The interplay between these two mechanism is the theme of the present paper.

Sawtooth stabilization mechanisms. We assume that sawtooth relaxations are triggered by resistive internal kinks [4]. In this paper we consider the "practical" stability criterion,

$$[\delta W_{MHD} + \delta W_{hot}]/\varepsilon_\eta^{1/3} > 0(1) \qquad (1)$$

for stability, where δW_{MHD} is the ideal MHD energy functional for internal kink perturbations (normalised so that the ideal MHD growth rate $\gamma_{MHD} \equiv - \omega_A \delta W_{MHD}$, with $\omega_A = V_A/R$), δW_{hot} is the fast particle perturbed energy and $\varepsilon_\eta \equiv \eta c^2 s_1^2/4\pi r_1 \omega_A^2$ is the inverse magnetic Reynolds' number, with $q(r_1) = 1$ and $s_1 = r_1 q'(r_1)$. The threshold value at the r.h.s. of (1) is model-dependent and its exact determination involves refined considerations, such as diamagnetic effects, ion Larmor radius, electron inertia, viscosity, electron thermal conductivity, neo-classical physics etc. We do not discuss these effects here, but simply state that for the JET discharges of interest, most models converge to give a threshold value close to unity. An example calculation of the threshold according to the two-fluid model is given in Ref. [5]. Note that diamagnetic effects are indeed important for JET RF phasing experiments, where typically
$\omega_*/\omega_A \varepsilon_\eta^{1/3} \sim 2 \rightarrow 5$.

The ideal MHD energy functional has the scaling [6]

$$\delta W_{MHD} \sim (r_1/R)^2 s_1^{-1}\left[\left(\beta_{p,cr}^{MHD}\right)^2 - \beta_{p1}^2\right], \qquad (2)$$

where β_{p1} is the properly defined [6] poloidal beta within the q = 1 surface and $\beta_{p,cr}^{MHD} \sim 0.1 \rightarrow 0.3$ is the ideal MHD threshold value for β_p. Let us assume, for a moment, that δW_{MHD} is positive. Then, the basic observation is that

$$\delta W_{MHD}/\varepsilon_\eta^{1/3} \propto s_1^{-5/3}. \qquad (3)$$

Hence, it is possible to achieve large positive values of the stability parameter, therefore sawtooth stabilization, by reducing the local (q = 1) magnetic shear parameter, s_1. In fact, when δW_{MHD} is positive, the instability of the m = 1 mode relies on magnetic reconnection near the q = 1 surface. For $\delta W_{MHD}/\varepsilon_\eta^{1/3}$ small, the m = 1 mode has the structure of a resistive internal kink, involving macroscopic flows across the entire $q \leq 1$ region. For $\delta W_{MHD}/\varepsilon_\eta^{1/3}$ large, the m = 1 mode structure resembles that of a tearing mode, with flows which are relatively large only in a small layer near the q = 1 surface. Thus, it becomes possible to suppress the growth of an m = 1 tearing mode by consideration of non-ideal effects which can be important near q = 1. When, on the other hand, δW_{MHD} is negative, the m = 1 instability is driven by the macroscopic

pressure and current density gradients. In this case, reducing the local magnetic shear will do no good. We conclude that reducing s_1 is not an effective means to stabilize sawteeth when $\beta_{p1} \geq \beta_{p,cr}^{MHD}$.

The fast particle perturbed energy has the scaling [3]

$$\delta W_{hot} \sim (r_1 / R) s_1^{-1} \langle 1 - q \rangle_h \beta_{ph} \tag{4}$$

where $\langle 1\text{-}q \rangle_h$ is the fast ion pressure-weighted average value of (1-q) and β_{ph} is the properly defined [3] poloidal beta of the fast particles. Eq. (4) assumes very energetic ions [$\omega_{Dh}/\omega_{*i} \sim (E_h/T_i)(r_1/R) > 1$, with ω_{Dh} the fast ion processional frequency and E_h the fast ion energy] with mostly trapped orbits, which is the relevant situation with intense ICRF heating. As explained in Ref. [3], the mechanism for sawtooth stabilization by fast particle pressure is related to the non-MHD constraint of magnetic flux conservation through the processional drift orbits of the energetic ions. It is concluded in [3] [but, also, inspect Eq. (4)] that this stabilization mechanism is most effective with on-axis RF heating. Note that β_{ph} becomes small, or even negative, when the fast ion pressure $p_{\perp h}$ is peaked near the q = 1 surface. Thus, with off-axis phased ICRF, the modification of the local magnetic shear appears to play a more important role.

Principles of ICRF current drive [7]. As consequence of the non-symmetric ICRF power spectrum, the typical resonant minority ion on a given flux surface will have a specific sign of the resonant parallel velocity, $v_{\|res} = (\omega_{RF} - \Omega_c)/k_\|$. This ion will gain energy from the wave, so that its collisionality may decrease. Thus, the minority ions drifting in one sense along the toroidal direction will collide less frequently against the background plasma than the minority ions drifting in the opposite sense. Hence, a net toroidal drifting of the minority ions may result. In order to conserve the total toroidal momentum, the majority ions acquire a toroidal drift, u_i, of the opposite sign: $m_i n_i u_i \approx -m_h n_h u_h$. A relative drift between the two ion species is thus established. This is reminiscent of the situation first discussed by Ohkawa in 1970 in connection with beam driven currents [8].

It must be pointed out that there is an optimum RF power to drive current this way. In fact, the energy gained by a minority ion is roughly proportional to the RF power, and the collisionality is a function of energy only for $E_h \leq E_{cr}$, where E_{cr} is the critical energy where electron and background ion drags are equal. For RF powers exceeding the optimum value, the minority ions become so energetic that their collisionality becomes insensitive to their energy, making the ICRF current drive mechanism ineffective.

The electrons will be dragged by the drifting ions along the toroidal direction. Therefore, there will be a return current, which, in a homogeneous magnetic field, can be obtained by setting to zero the friction force on the electrons along the parallel direction, $\sum_j \nu_{ei}(u_j - u_e)_\| = 0$, and by equasineutrality, $\sum_j Z_j n_j = n_e$. Using $\nu_{ej} \propto Z_j^2 n_j$, the total RF-driven current, $J_{RF} = e\,(\sum_j Z_j n_j u_j - n_e u_e)_\|$, can be expressed as $J_{RF} = \alpha_{ret} J_h$, where $\alpha_{ret} = (1 - Z_h/Z_{eff})(1 - u_i/u_h)$. Thus, granted a relative drift, u_h-u_i, between the two ion species, J_{RF} is nonzero provided $Z_h \neq Z_{eff}$. In an inhomogeneous field, particles with trapped orbits will exchange momentum with the magnetic field. Therefore, these particles will not contribute to the return current. This is accounted for by a correction $O[(r/R)^{1/2}]$ to α_{ret} (see e.g. Ref. 2), which ensures that J_{RF} remains finite even when $Z_h = Z_{eff}$.

From Fisch's paper [7], assuming optimum RF power density, $\wp_{RF}^{opt}$, we can estimate the magnitude of J_h as

$$J_h \approx 0.8\alpha_{tr} \frac{Te / 5KeV}{n_e / \left(3x10^{19}\,m^{-3}\right)} \frac{\wp_{RF}^{opt}}{\left(0.2\ MW/m^3\right)} \frac{MA}{m^2}, \tag{5}$$

where $\alpha_{tr} < 1$ is a numerical factor, not contained in [7], which accounts for minority ion trapping. Taking $\wp_{RF}/\wp_{RF}^{opt} \sim \alpha_{ret} \sim \alpha_{tr} \sim 0.5$, values of $J_{RF} \sim 0.1$ MA/m^2 appear reasonable for the JET discharges of interest.

We point out some important features of the ICRF driven minority current density, J_h:

i) For a given $k_\|$, the minority ion resonant velocity changes sign across the cyclotron layer. In fact, on the poloidal midplane, $v_{\|res} = \pm(\Omega_{co}/k_\|)(r - r_{RF})/R$, where r_{RF} is the distance of the layer from the magnetic axis. We have taken $B = B_0\,[1\text{-}(r/R)\cos\theta]$ and $\Omega_{co} = Z_h e B_0/mc$. The upper (lower) sign corresponds to cyclotron resonance on the low (high) field side, respectively. Consequently, J_h also changes sign across the layer, as shown in Fig. 1a, and it may well be that J_h integrated over the plasma cross-section yields a negligible total minority current. Nevertheless, a profile of J_h as shown in Fig. 1a with a peak value as estimated by Eq. (5) can be sufficient to produce a significant modification of the q profile, as shown in Fig. 1b; ii) Changing from positive to negative phasing corresponds to changing the sign of $k_\|$. Consequently, also J_h flips sign. Thus, for instance, if positive phasing and absorption on the high field side leads to a reduction of the local shear near q = 1, negative phasing leads to the opposite result of increasing shear. These considerations can account for the

observed differences in the sawtooth behavior between the two phases; iii) Minority ion trapping is more severe when the RF wave is absorbed on the low-field side. In this case, $J_{hot} \propto \alpha_{tr}$ is considerably reduced. Hence, one can expect a pronounced effect on sawteeth only for high-field-side absorption.

All these features of the minority ion current density have been investigated and confirmed by numerical integration of the relevant Fokker-Planck equation (see Fig. 7 of Ref. 2). The prediction of an optimum ICRF power is corroborated by experiments, discussed in Ref. 2, where P_{RF} has been scanned.

Simulations. A numerical scheme has been set up to investigate the effect of ICRF phasing current drive on the stability of resistive internal kinks. The scheme involves (i) a JET equilibrium code; (ii) a Fokker Planck solver for J_{RF}; (iii) a transport code which monitors the time evolution of the total current density, $J_{tot} = J_{ohm} + J_{RF}$; (iv) experimental profiles for temperature and density, interpolated in time; (v) a code to evaluate $\delta W = \delta W_{MHD} + \delta W_{hot}$, based on an aspect ratio expansion. The aim is to compute $\delta W/\varepsilon_\eta^{1/3}$ during sawtooth ramps. This procedure requires the choice of an initial q profile at the bottom of the sawtooth ramp. This is done in two steps. The first step is to run the transport code with neoclassical current penetration. This yields a q profile which is consistent with the total current and with the experimental T and n profiles. However, no sawteeth are assumed in the simulation. Therefore, the obtained q profile is credible only outside the q = 1 radius. The second step is to modify q(r) in the region $q \leq 1$. We conjecture that, after a sawtooth crash, q(r) has a low-shear (s~0.1) shoulder of width Δ around the experimental sawtooth inversion radius, r_{inv}, extending to the experimental mixing radius. Further, we assume that the new q = 1 radius $r_1 \approx r_{inv}$, while q_0 is set to a value compatible with polarimetric measurements. The sawtooth period is defined in the simulation as the time it takes for $\delta W/\varepsilon_\eta^{1/3}$ to evolve from the initial profiles after a crash, where $\delta W/\varepsilon_\eta^{1/3} >> 1$, to a value $\delta W/\varepsilon_\eta^{1/3} = 0(1)$. Clearly, this procedure makes sense provided we obtain roughly the same simulated period for several choices of q_0 and Δ varying within realistic bounds (see also Ref. 9).

Fig. 2 shows an example of the evolution of $\delta W/\varepsilon_\eta^{1/3}$ with time for a discharge with positive ICRF phasing on the high field side (discharge # 25652, I_p = 2MA, B_T = 2.6T, P_{RF} = 2.5MW). When J_{RF} is switched off in the simulation, we find a sawtooth period ~100ms. With J_{RF} on, the period is lengthened to a value ~1s. While an accurate quantitative agreement with the experimental periods before and after the launching of phased RF waves is too demanding at this stage, the qualitative trends as well as the order of magnitude of the simulated periods are in good agreement with the experimental ones. The nonmonotonic behaviour of $\delta W/\varepsilon_\eta^{1/3}$ reflects that of s_1. The latter is a consequence of the q = 1 radius being initially trapped in the low shear region maintained by J_{RF}. Eventually, r_1 drifts outside of this region and the resistive kink threshold is crossed. The evolution of s_1, r_1/a and β_{p1} in time are shown in Fig. 3.

Several examples of this type have been produced, including the shortening of the sawtooth period with negative ICRF phasing and resonance on the high field side. These examples confirm the possibility of influencing the sawtooth period by phasing of the ICRF antennas.

Predictions. The formulated model has the following consequences which may be tested experimentally: (i) Sawtooth stabilization by ICRF phasing alone (i.e. with $\delta W_{hot} = 0$) is possible only in low-β_p discharges. For $\beta_{p1} > \beta_{p,cr}^{MHD}$, δW_{MHD} becomes negative and Eq. (1) can no longer be satisfied for any value of s_1; (ii) It may be possible to prolong the sawtooth-free period by a combination of fast ion pressure on axis (monopole or dipole on-axis ICRF), which leads to positive δW_{hot}, and phased ICRF waves near the q = 1 region on the high-field side; (iii) Following a sudden switch-off of the phased ICRF power, the low-shear region decays on the local resistive diffusion time, $\tau_\eta \sim 4\pi\delta_{RF}^2/\eta_1 c^2$ with δ_{RF} the width of J_{RF}. This should set the time scale for the delay between the RF switch off time and the following sawtooth crash.

Conclusions. We have introduced in Eq. (1) a "practical" criterion for the onset of resistive internal kinks. Stability may be achieved by reducing the local (q = 1) magnetic shear, provided β_p is sufficiently low. Phased ICRF waves absorbed near the q = 1 radius may provide a means to vary s_1. Simulations of JET discharges show that positive phasing on the high field side leads to a reduction of the local shear, hence to a lengthening of the sawtooth period to ~1 sec. Negative phasing on the high field side has the opposite effect of shortening the sawtooth period.

We would like to thank E. Springmann for numerical support.

References
[1] G. Bosia and J. Jacquinot, IAEA Tech. Comm. Meeting on FWCD in Reactor Scale Tokamaks, Arles 1991, p. 471. [2] D.F.H. Start et al., this conference; [3] F. Porcelli, Plasma Phys. Cont. Fusion 33, 1601 (1991); [4] B. Coppi et al., Fiz. Plasmy 6, 961 (1976); [5] S. Migliuolo et al., Phys Fluids B3, 1938 (1991); [6] M.N. Bussac et al., Phys. Rev. Lett. 35, 1638 (1975); [7] J. Fisch, Nucl. Fusion 23, 499 (1983); [8] T. Ohkawa, Nucl. Fusion 10 185 (1970); [9] F. Porcelli et al., JET-IR (88) 16.

Figure 2

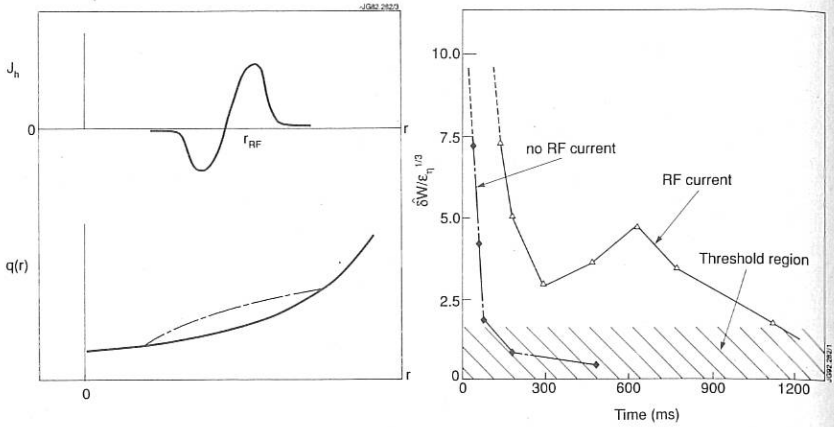

Figure 1

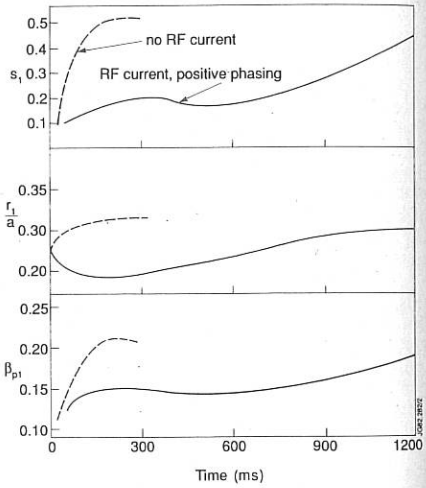

Figure 3

KINETIC EFFECTS IN FAST WAVE CURRENT DRIVE

A. Bécoulet, G. Giruzzi, K. Kupfer, D. Moreau, B. Saoutic

Association EURATOM-CEA sur la Fusion Contrôlée
C.E. Cadarache, 13108 Saint-Paul-lez-Durance (FRANCE)

In order to evaluate the relative importance of quasilinear effects in Fast Wave Current Drive (FWCD) experiments in Tokamaks, possibly leading to a tail formation in the electron distribution function, and to estimate the influence of the radial transport, either induced by the wave itself and/or by anomalous mechanisms, the full wave code ALCYON has been coupled to a 3-D Fokker-Planck code [1].

I. Description of the model

ALCYON is a variational full-wave code that computes the components of the fast wave field in axisymmetrical Tokamak geometry, including shaped (numerically calculated) equilibrium. The wave-particle interactions are analyzed through the hamiltonian formalism, using action(**J**)-angle(Φ) variables to describe particle trajectories [2]. This includes both first and second ion harmonic cyclotron damping as well as direct resonant coupling to electrons through electron Landau damping (ELD) and transit time magnetic pumping (TTMP). The formalism allows us to take into account the coupling between the wave poloidal modes in the damping terms. Under these conditions, ALCYON computes the Fourier components of the radiated field, and especially $(\delta B_{//})_{m,N}$ (resp.$(\delta E_{//})_{m,N}$), the poloidal(m)-toroidal(N) components of the parallel magnetic (resp. electric) field, on each magnetic flux surface. This complete set of field components is then used for computing the quasilinear tensor, in the action space **J**:

$$(D_{QL})_{ij} = 4\pi \sum_{N} N_i N_j \, |h_N(J)|^2 \, \delta(\omega + N_k \omega_k(J)) \qquad (1)$$

where $N=(0, m, N)$, $\omega_k = d\Phi_k/dt$, $h_N = \mu_e(\delta B_{//})_{m,N} + e(\delta U)_{m,N}$ is the Fourier component of the perturbative Hamiltonian (δU being the wave scalar potential) and $\omega + N_k\omega_k = 0$ is the resonance condition in action space, corresponding to the local Landau resonance condition $\omega + k_{//}v_{//} = 0$. This diffusion tensor is related to the Fokker-Planck equation:

$$\frac{\partial \bar{f}}{\partial t} = \frac{1}{2}\frac{\partial}{\partial J_i}\left((D_{QL})_{ij} \frac{\partial \bar{f}}{\partial J_j} \right) \qquad (2)$$

where $\bar{f} = \bar{f}(\mathbf{J},t)$ is the electron distribution function, averaged over the angles Φ_k.

Of course, equation (2) can only be considered as a diffusion equation in the phase-space domain where the phase $\omega t + N_k\Phi_k(t)$ is ergodic. This ergodicity is considered hereafter as effective on the whole phase-space, both due to extrinsic decorrelations (collisions, anomalous radial diffusion) and to intrinsic stochasticity [3]. We will see that this assumption is not very strong, with regard to the very small computed deformations of the electron distribution function. Under those conditions, the quasilinear tensor (1) becomes a diffusion tensor.

The numerical computation of this tensor then requires assumptions concerning the "resonance broadening" (i.e. the resolution of the δ-function). This broadening is performed by assuming a local conservation of the absorbed power [4], preserving, in velocity space, the local characteristics of the perturbation.

The diffusion tensor is then transformed from the action space to velocity space, using approximate expressions for the action-angle variables, assuming passing electrons. Thus, defining the normalized parallel velocity $u = v_{//}\sqrt{m/T_{e0}}$, and the normalized time $\tau = t\nu_e$, where ν_e is the collision frequency, equation (2) reads:

$$\frac{\partial \bar{f}}{\partial \tau} = \frac{\partial}{\partial u}\left(D_{uu}\frac{\partial \bar{f}}{\partial u} \right) + \frac{\partial}{\partial u}\left(D_{ur}\frac{\partial \bar{f}}{\partial r} \right) + \frac{1}{r}\frac{\partial}{\partial r}\left(r\, D_{ur}\frac{\partial \bar{f}}{\partial u} \right) + \frac{1}{r}\frac{\partial}{\partial r}\left(r\, D_{rr}\frac{\partial \bar{f}}{\partial r} \right) \qquad (3)$$

where $r/a = \sqrt{\psi}$ is the normalized minor radius. The D_{uu} coefficient is proportional to $D_{33} + 2\,D_{23}/q + D_{22}/q^2$ {q(r) being the safety factor). Following (1), this confirms that D_{uu} is linked to the mode combination N+m/q, i.e. to the parallel wave vector $k_{//}$. Moreover, D_{rr} is proportional to D_{22} and D_{ur} to $D_{23}+D_{22}/q$. Finally, one can estimate the relative ordering of the different terms in (3) (RHS): relative to D_{uu}, the second and the third terms (i.e. the cross-terms) are of the order of ξ, and the fourth term (radial diffusion) is of the order of ξ^2, where:

$$\xi = \frac{\sqrt{m_e T_{e0}} R_0}{e\Delta\psi} \approx \frac{\rho_{e0}}{a}\frac{qR_0}{a} \qquad (4)$$

$\Delta\psi$ being the variation of the poloidal flux from the plasma center to the edge, and ρ_{e0} the electron Larmor radius. In a typical ITER case (T_{e0}=35keV, $\Delta\psi\approx$20Wb), ξ is of the order of 2.10^{-4}, and in a Tore Supra case (T_{e0}=5keV, $\Delta\psi\approx$1Wb), $\xi \approx 5.10^{-4}$. This means that the radial diffusion induced by the interaction is always negligible with respect to the cross-terms. We will see hereafter that those cross-terms are also weak compared to a typical anomalous radial diffusion term, and to the collisional drag itself.

The evolution of the electron distribution function is governed by the quasilinear diffusion as well as by Coulomb collisions and radial diffusion due to anomalous transport. Several different mechanisms can be proposed to explain the observed macroscopic transport coefficients. In the following, we make the assumption that magnetic turbulence is the dominant fast electron transport mechanism. The two reasons for such a choice are: i) a strong evidence that magnetic turbulence is a very good candidate for explaining most tokamak experimental scaling laws [5,6], and ii) magnetic turbulence is expected to act more strongly on high-$v_{//}$ electrons (at least in the mildly superthermal energy range relevant for FWCD) [7]. Thus, assuming that a broad-spectrum turbulent magnetic field is present in the plasma, an electron transport term can be derived [7,8], i.e.,

$$\left(\frac{\partial \bar{f}}{\partial t}\right)_{transp} = \frac{1}{r}\hat{L}\, r\, D_T \hat{L}\, \bar{f} \quad , \quad D_T = 2\pi q R_0\, |v_{//}|\, |\tilde{b}|^2 \quad , \quad \hat{L} = \frac{\partial}{\partial r} + eE_A \frac{\partial}{\partial E} \, , \qquad (5)$$

$\tilde{b} = \tilde{B}/B$ is the ratio of the fluctuating magnetic field to the tokamak magnetic field, which in the following will be assumed vanishing at the plasma center and increasing as r^2 from the center to the edge. Since the ions are too heavy to interact with the magnetic turbulence, as the electrons diffuse radially an ambipolar electric field is created which slows them down. This effect is described by the second term of the $\hat{L}$ operator, where E is the electron kinetic energy and E_A is the ambipolar field, which can be evaluated by imposing electron density conservation on each flux surface. Such a transport term has the effect of letting energy and current diffuse radially while density is conserved. From the kinetic point of view, the distribution function will be distorted in the T_e-gradient region: hot electrons from the center diffuse to the colder region off-axis, for high enough energies the diffusion time is shorter than the collision time, and an electron tail is created. Such tails have been experimentally observed even in high density plasmas [8]. These tails are expected to interact with the RF power and their presence may affect rf current profile and thus the global efficiency.

The kinetic equation is numerically solved as a mixed initial/boundary value problem, assuming a Maxwellian distribution as the initial condition and advancing the solution in time until a kinetic steady-state (i.e., for fixed density and temperature profiles) is attained.

II FWCD simulation for ITER

A FWCD simulation has been performed for the typical ITER plasma (I_p=22MA, B_0=4.85T, R_0=6m, a=2.15m, T_{e0}=35keV, n_{e0}=1.5e20m^{-3}, D(50%)-T(50%)). The fast wave frequency is 33 MHz. In this situation the wave, launched from the plasma low field side, is reflected from a cutoff located on the high field side of the plasma core. Due to the strong single-pass absorption on electrons, the wave is rapidly damped without filling up the whole plasma and without up- and down-shifting. The current drive efficiency is optimized by varying the phasing between the 30 antenna straps. Due to the strong single-pass absorption (≈60%) and antenna directivity, the optimum efficiency is obtained when the

maximum power is absorbed in the plasma central region. Under these conditions, a linear estimation of the power deposition profile, driven current profile (fig.1a) and current drive efficiency has been made, without including deformations of the electron distribution function. The efficiency is $\gamma \approx 0.3e20$ A/W/m^2. Under the same conditions, the FWCD diffusion tensor has been computed and the Fokker-Planck calculation performed. The results can be summarized as follows:

- Without including any radial or cross-term effect, the Fokker-Planck calculation shows no noticeable deformation of the electron distribution function and thus leads to the same results as the linear simulation (fig.1b). This can be related to the diffusion coefficient in velocity space, which remains weaker than the collisional drag, except at high perpendicular velocities (TTMP) for which there are no electron.
- Including the radial and cross-term effects due to the wave-particle interaction does not significantly alter the result, as expected because of the very low value of ξ.
- The presence of anomalous radial diffusion broadens the driven current profile (fig.2). The resulting current drive efficiency increases ($b \approx 5.10^{-5}$ leads to $\gamma \approx 0.45e20$ A/W/m^2 and $b = 10^{-4}$ to $\gamma \approx 0.8e20$ A/W/m^2), because current is driven in regions of lower density.

III Combined Fast Wave - Lower Hybrid Current Drive effects

Fast parallel electrons, produced during LHCD, can interact with the fast wave resonances, indicating a possible supplementary current drive effect. The analysis of such a "synergism" however requires a 2D model in velocity space, because the fast wave diffusion coefficient D_{uu} (normalized to the collisional drag) has a strong perpendicular velocity dependence. The main characteristics of this dependence are: $D_{uu} \approx$ cst and much less than 1 for $v_\perp < v_{crit}$ (ELD region), $D_{uu} = 0$ for $v_\perp = v_{crit}$, and D_{uu} proportional to $v_\perp^4$ and of order unity for $v_\perp > v_{crit}$ (TTMP region). The critical perpendicular velocity v_{crit} is very close to the thermal velocity [9]. The combination of FWCD and LHCD effects results in a simple addition of the two diffusion coefficients. The combined situation is thus rather similar to LHCD alone, except for high perpendicular velocity electrons which experience an enhanced parallel diffusion. Such electrons are produced during LHCD by pitch-angle scattering from high parallel energies.

The simulation of such a situation has been performed with our combined full wave/FP code. The FW diffusion coefficient has been computed by ALCYON on a typical Tore Supra ohmic plasma (I_p=1.84MA, B_0=4T, T_{e0}=5keV, n_{e0}=3e19m^{-3}, Deuterium), in a situation where the direct electron coupling is the only damping mechanism present in the plasma (f=42MHz). For the chosen FW antenna phasing, 2MW of FW drive 76kA of current. The FW diffusion coefficient has then been computed on the same plasma, for which the 1.84MA current was fully sustained by 5.5 MW of LHCD. We found that the fast electron distribution function does not significantly affect the ALCYON (linear) results, avoiding additional iterations between ALCYON and the FP code. As expected, the kinetic calculation shows that the electron distribution function flattens (fig.3) in the high perpendicular velocity region. The total (FW+LH) driven current is 2.05MA, i.e. larger than the linear superposition of rf currents. However, due to the distribution function flattening (and to the fact that in this simulation the LH diffusion coefficient is kept constant), P_{LH} decreases from 5.5MW to 4.5MW. In a simulation where P_{LH} would remain constant, one should expect a LH absorption at lower parallel velocities, or non-resonant parasitic absorption at the edge. Thus, while there is a synergistic effect on FWCD, the resulting efficiency is in this case smaller than for LHCD alone.

Conclusions

Kinetic effects have been investigated concerning FWCD in Tokamaks. The FW itself does not induce significant radial transport effects. The FWCD efficiency is improved when anomalous radial diffusion is taken into account. A synergistic effect in velocity space has been numerically demonstrated, when FWCD is combined with LHCD.

References
[1] GIRUZZI, G., BECOULET, A., MOREAU, D., SAOUTIC, B., Proc. of the IAEA Tech. Comm. Meeting on FWCD in Reactor Scale Tokamaks, Arles (FRANCE) 1991, pp.77.
[2] GAMBIER, D.J., SAMAIN, A., Nucl. Fus. **25** (1985) 283.
[3] BECOULET, A., MOREAU, D., GAMBIER, D.J., RAX, J.-M., SAMAIN, A., 13th Int. Conf. on Plasma Phys. and Cont. Nucl. Fus. Research, Vol. 1, pp.811, Washington D.C. (USA), 1990.
[4] BECOULET, A., GIRUZZI, G., MOREAU, D., SAOUTIC, B., CHINARDET, J., IAEA Tech. Comm. Meeting on FWCD in Reactor Scale Tokamaks, Arles (FRANCE) 1991, pp.63.
[5] REBUT, P.H., BRUSATI, M., Plasma Phys. **28** (1986) 113.
[6] KADOMTSEV, B.B., Nucl. Fusion **31** (1991) 1301.
[7] GUREVICH, A.V., ZYBIN, K.P., ISTOMIN, Y.N., Nucl. Fusion **27** (1987) 453.
[8] RICE, J.E., MOLVIG, K., HELAVA, H.I., Phys. Rev. A **25** (1982) 1645.
[9] MOREAU, D., JACQUINOT, J., LALLIA, P., 13th Eur. Conf. on Cont. Fusion and Plasma Heating, Schliersee (FRG) 1986.

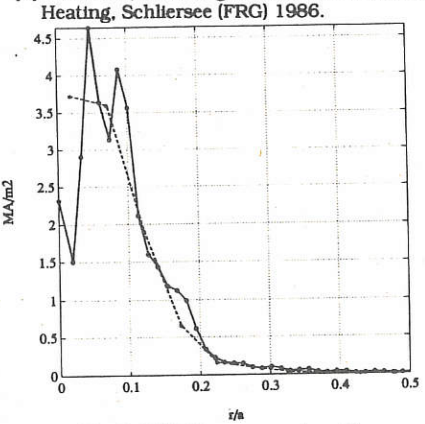

Fig.1: FW driven current profile for the optimized ITER 33MHz case; a)(solid line) computed by ALCYON, b)(dashed line) computed by the FP code.

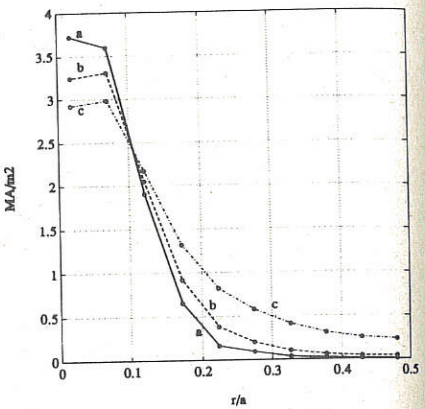

Fig.2: FW driven current profile for the optimized ITER 33MHz case; a) without magnetic turbulence, b) $b=5.10^{-5}$, c) $b=10^{-4}$.

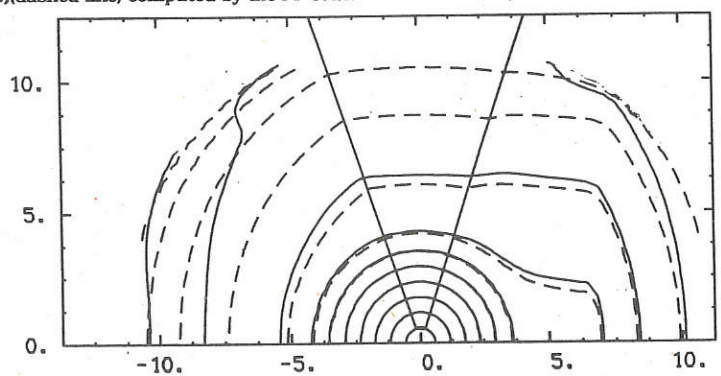

Fig.3: Electron distribution function for the Tore Supra LHCD (dashed lines) and LHCD+FWCD (solid lines) cases, in the $(v_{//}/v_{e0}, v_{\perp}/v_{e0})$-space.

THEORETICAL STUDIES OF FAST WAVE PLASMA HEATING AND CURRENT DRIVE IN TOKAMAKS

P. E. Moroz, N. Hershkowitz, J. A. Tataronis

Nuclear Engineering and Engineering Physics Department
University of Wisconsin, Madison, WI 53706, U.S.A.

I. INTRODUCTION.

Plasma heating via fast magnetosonic waves in the ion cyclotron range of frequencies (ICRF) is the one of the most promising methods of plasma heating in tokamaks and other devices, and has been a subject of intensive theoretical and experimental research for the last decade. The understanding of ICRF heating physics is coming not only from theory and experiments considered separately, but often from the comparison between them. However, most theoretical models are based on overly simplified geometries and assumptions. In this situation the development of full wave codes able to model an experiment more realistically has a growing importance. Although many properties of fast magnetosonic waves are well known for homogeneous plasmas in homogeneous magnetic fields, many problems arise when one tries to incorporate realistic properties of tokamaks such as inhomogeneity, toroidicity, or finite size. The WKB approximation that is usually used for high frequency waves is not uniformly valid in the ion cyclotron range of frequencies because the effects of diffraction and wave interference are very significant. In this report, the theoretical model for consideration of fast wave plasma heating and current drive is described. It has the following advantages: a) the hot plasma is considered without introducing any artificial collision frequency to resolve the plasma resonances, b) the parallel electric field of the fast wave, and electron absorption power through the Landau damping, TTMP, and the cross-term effect are considered, c) mode converted power is included in the analysis, and d) the resonant and nonresonant RF driven currents are considered.

The main purpose of the following RF current drive analysis is to evaluate a driven current in an axisymmetric tokamak geometry. At the same time, because an RF current appears on the background current, which is a sum of Ohmic and bootstrap current, it is necessary to include them in the analysis as well. The current, J_M , driven due to the momentum transfer from fast waves to electrons, is calculated through the published[1] expressions for the current drive efficiency and electron absorption power determined by the code. The total steady driven current, $J_{||}$, is evaluated from the electron momentum equation. The difference, current J_A , represents an additional current resulting from the influence of nonresonant effects such as plasma inhomogeneity or helicity injection. The bootstrap current is calculated consistently with the poloidal magnetic field.

II. FAST WAVE PLASMA HEATING IN TOKAMAKS.

The starting point for the derivation of wave equations for fast waves is Maxwell's equations, which in the case of non-uniform plasma include an integral operator. An important simplification of these equations results when the parameters:

$$\lambda_i = \frac{1}{2} k_\perp^2 \rho_i^2 \ , \quad \frac{\rho_i}{L} \ , \quad \frac{\omega^*}{\omega} \approx \frac{\rho_i}{L} \frac{k_\perp v_i}{\omega} \ , \quad (k_{||} l_{res})^{-1} \approx \left(\frac{\mathbf{B}_0 \cdot \nabla B_0}{\rho_i k_{||}^2 B_0^2} \right)^{0.5} \qquad (1)$$

are small in comparison with unity. Here, ρ_i is the ion Larmor radius, L is the characteristic scale length of the spatial inhomogeneity in a tokamak, ω^* is a drift frequency, and l_{res} is a characteristic length along which a gyrating ion experiences a cyclotron resonance interaction. Under these conditions, the wave equations describing fast wave penetration and absorption, in standard toroidal coordinates (r,ϑ,φ), can be written in the form[2],

$$\begin{cases} \dfrac{\partial}{\partial x}(xE_\vartheta) = i\,x\,B_\varphi + i\dfrac{\partial}{\partial \vartheta}\left(-\dfrac{\varepsilon_2^t}{\varepsilon}E_\vartheta + \dfrac{1}{\varepsilon x R}\dfrac{\partial}{\partial \vartheta}R\,B_\varphi\right) \\ \dfrac{1}{R}\dfrac{\partial}{\partial x}(RB_\varphi) = i\left(n_{\perp F}^2 E_\vartheta + \dfrac{\varepsilon_2^t}{\varepsilon x R}\dfrac{\partial}{\partial \vartheta}R\,B_\varphi\right) \end{cases} \qquad (2)$$

where dimensionless variables have been introduced, $x = k_o r$ and $R = 1 + \frac{r}{R_o}\cos\vartheta$. Here ε_1^t and ε_2^t are components of the dielectric tensor, and $\varepsilon = \varepsilon_1^t - n_\parallel^2$,

$$\varepsilon_1^t = \varepsilon_1 + n_{\perp F}^2\alpha_1 + \sum_{n=3}^{n_{max}}\delta\varepsilon_n\,, \qquad \varepsilon_2^t = \varepsilon_2 + n_{\perp F}^2\alpha_2 + \sum_{n=3}^{n_{max}}\delta\varepsilon_n \qquad (3)$$

The factors ε_1 and ε_2, describe the fundamental cyclotron absorption, and α_1 and α_2 describe the finite Larmor radius effects such as second harmonic cyclotron absorption. The corrections $\delta\varepsilon_n$ are introduced to include the effects of high order (n=3 and higher) cyclotron harmonic resonances. The number n_{max} corresponds to the maximal cyclotron harmonic included in calculations. If the frequency is much higher than the ion cyclotron, $\omega >> \Omega_i$, it may be necessary to include many harmonics and choose n_{max} be a big number. The following expression can be used for $\delta\varepsilon_n$:

$$\delta\varepsilon_n = \sum_i \frac{\omega_{pi}^2}{\omega k_\parallel v_i} n^2\, A_n(\lambda_i)\, Z(\zeta_n^i), \qquad (4)$$

where λ_i corresponds to the fast wave root and $A_n(\lambda) = \exp(-\lambda)\, I_n(\lambda)/\lambda$. Here, $I_n(\lambda)$ – is a modified Bessel function of the first kind. The value of $n_{\perp F}$ is the fast wave root of the hot plasma dispersion relation.

The parallel component of fast wave electric field $E_\parallel$ is usually small in comparison with $E_\perp$. However, it can be very important in determining the electron absorption or in fast wave current drive applications. The value of $E_\parallel$ can be found perturbatively through the calculated $E_\perp$ and $B_\parallel$ components of fast wave[2]. The direct electron absorption P_e can be divided on three parts: P_{MP} – transit time magnetic pumping, P_{LD} – Landau damping, and P_{CR} – cross-term absorption $P_e = P_{MP} + P_{LD} + P_{CR}$, where[2]

$$P_{MP} = 2\gamma G\,|B_\parallel|^2, \quad P_{LD} = \frac{1}{\gamma n_\parallel^2} G\,|E_\parallel|^2, \quad P_{CR} = \frac{2}{n_\parallel} G\,\mathrm{Im}\,(B_\parallel^* E_\parallel) \qquad (5)$$

Here $G = \dfrac{\omega_{pe}^2}{8\pi\Omega_e}\zeta_o^e\,\mathrm{Im}\,Z(\zeta_o^e)$. Power absorbed by ions at the fundamental and harmonic cyclotron resonances can be expressed as

$$P_i = \frac{\omega_{pi}^2}{8\pi k_\parallel v_i}\sum_{n=1}^{n_{max}} n^2\,\mathrm{Re}(A_n)\cdot\mathrm{Im}\,Z(\zeta_n^i)\,|E^+|^2 \qquad (6)$$

The difference between total absorbed power, and the power absorbed by ions, P_i, and electrons, P_e, gives the power, P_c, absorbed through the mode conversion process[3].

III. THEORETICAL MODEL FOR CURRENT DRIVE.

An RF current appears on the background current, which is a sum of Ohmic and bootstrap current. For the estimation of an Ohmic current profile our model uses either of two different methods. The first one uses the total Ohmic current, I_o, and electron temperature profile as given. Then, the Ohmic current profile is found through the plasma conductivity corrected for the neoclassical effects. In the other method, the total Ohmic current, I_o, and the safety factor, q_o, at the magnetic axis are input parameters. The Ohmic current profile is then chosen to correspond to the, so-called, "natural current profile", which is usually observed in tokamak experiments. In our model we use slightly modified version of this natural profile, in comparison with the one proposed in Refs.4-6, to satisfy the condition $J(\rho_p) = 0$ at the plasma edge.

An expression for the steady RF driven current, $J_{||}$, resulting from the wave-electron interaction, is obtained by averaging the electron momentum equation over the RF period of the wave and over the tokamak magnetic surface. The steady driven current, $J_{||}$, can be expressed as a sum of two components, $J_{||} = J_M + J_A$. The first component, J_M, is the current resulting from the wave momentum transfer to the electrons because of the resonant electron-wave interactions, and the second component, J_A, represents additional current resulting from the influence of nonresonant effects such as plasma inhomogeneity or helicity injection. The current J_A does not include the electron absorption and any other resonant effects. In that sense, the current J_A is similar to the Ohmic current, and is the result of the electric field action on all electrons, unlike the resonant interaction $\omega = k_{||} v_{||}$, when the wave field acts only on the resonant group of electrons. This was the reason why we incorporated the trapped electron effect[1,7-11] only for J_M current. In this case, current J_M can be written in the form

$$J_M = \frac{38.4 \cdot 10^{18}}{\ln\Lambda} \cdot \frac{T_e}{N_e} \cdot \langle \eta P_e \rangle, \qquad (7)$$

where the normalized current drive efficiency, η, includes the trapped particle effect[1]. An explicit expression for J_A can be written, which, if includes the lower order corrections in ponderomotive effects, reads[12]:

$$J_A = -\left\langle \frac{e}{2mv_e\omega} \mathrm{Im}\left[\left(\nabla \mathbf{j_e} - \mathbf{j_e}\nabla\right)\left(E_{||} - \frac{im\omega}{e} v_{e||}\right)^* \right] \right\rangle \qquad (8)$$

The nonresonant current, described by Eq.(8) is absent in two limits, for plane-wave fluctuations ($\sim e^{ikr}$), because $\nabla \mathbf{j_e} - \mathbf{j_e}\nabla = 0$, and in the cold plasma approximation, because $E_{||} - \frac{im\omega}{e} v_{e||} = 0$. However, in tokamak geometry and in the case of hot plasma, this nonresonant current can be significant and comparable with the resonant, momentum transfer current. The nonresonant current, J_A, increases with increasing of electron temperature faster than the resonant current, J_M.

The following figures illustrate our calculations via the FASTWAC code[12] for the Phaedrus-T tokamak. They show distribution of $Re(E_x)$ in the poloidal cross-section of the tokamak, and radial dependence of non-inductive current which consists of the momentum transfer current (labeled "M"), additional, nonresonant current ("A"), and bootstrap current ("B"). The unlabeled curve represents their sum. For fast magnetosonic waves (FMW) at $\omega > \Omega_i$ (Fig. 1), which have $|E^-|^2 >> |E^+|^2$ and negative helicity content, the non-resonant current in all cases considered has been in opposite direction to the momentum-transfer current. In the case of global Alfven waves (GAW) at $\omega < \Omega_i$ (Fig. 2), which have $|E^+|^2 >> |E^-|^2$ and positive helicity content, the non-resonant current has been found preferentially in the same direction as the momentum-transfer current.

ACKNOWLEDGMENT.
This work was supported by US Department of Energy Grant DE-FG02-88ER53264.

1. D. A. Ehst, C. F. F. Karney, Nuclear Fusion **31**, 1933 (1991).
2. P. E. Moroz and P. L. Colestock, Plasma Phys. & Contr. Fusion **33**, 417 (1990).
3. P. E. Moroz and N. Hershkowitz, Proc. 9th Top. Conf. on RF Power in Plasmas, Charleston, SC, 1991, AIP, New York, 1992, p. 201.
4. D. Montgomery, L. Turner, G. Vahala, J. Plasma Physics **21**, 239 (1979).
5. B. B. Kadomtsev, Sov. J. Plasma Phys. **13**, 443 (1987).
6. J. B. Taylor, The University of Texas at Austin, Report IFSR # 447 (1990).
7. K. Yoshioka, T. M. Antonsen, Jr., Nuclear Fusion **26**, 839 (1986).
8. J. G. Cordey, T. Eddlington, D. F. H. Start, Plasma Physics **24**, 73 (1982).
9. R. H. Cohen, Phys. Fluids **30**, 2442 (1987).
10. G. Giruzzi, Nuclear Fusion **27**, 1934 (1987).
11. S. C. Chiu, V. S. Chan, R. W. Harvey, M. Porkolab, Nucl. Fusion **29**, 2175 (1989).
12. P. E. Moroz, University of Wisconsin-Madison, Report PLR-91-17 (1991).

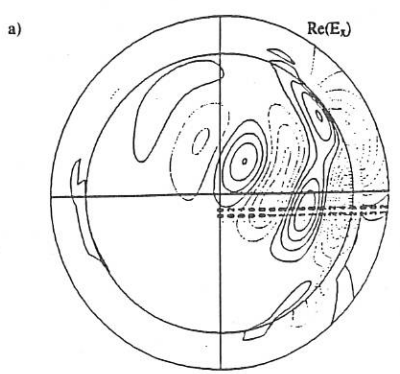

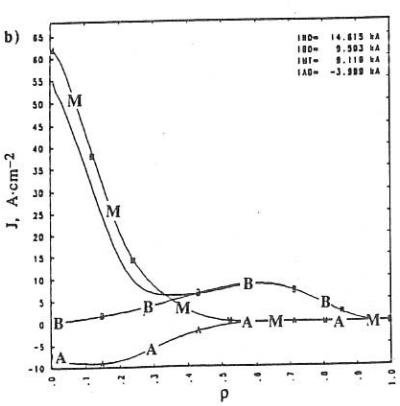

Fig.1. FMW at $\omega=3\Omega_D$ in D-plasma.

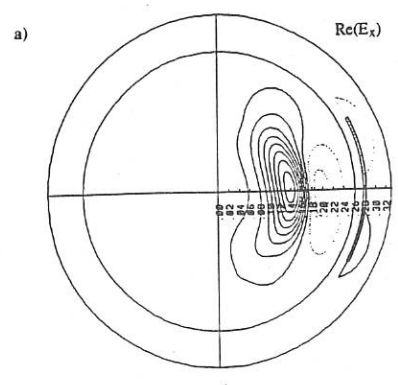

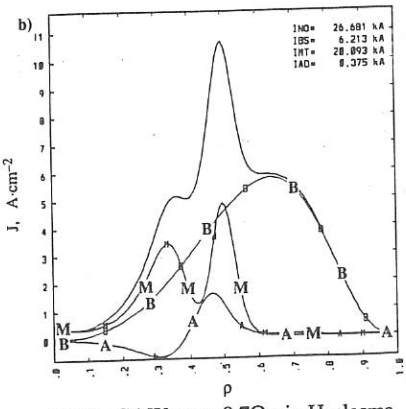

Fig.2. GAW at $\omega=0.7\Omega_H$ in H-plasma.

Influence of Various Physics Phenomena on Fast-Wave Current Drive in Advanced Tokamaks*

D. B. Batchelor, E. F. Jaeger, M. D. Carter, R. C. Goldfinger, and D. C. Stallings

Oak Ridge National Laboratory, Oak Ridge, TN 37831-8071, U.S.A.

INTRODUCTION

The need for some type of noninductive current drive in advanced tokamaks has been recognized for some time. In reactor-grade plasmas, as envisioned in the International Thermonuclear Experimental Reactor (ITER),[1] high density and temperature may limit the penetration of lower hybrid (LH) waves to only the outer layers of the plasma. Fast waves in the ion cyclotron range of frequencies (ICRF), however, can easily penetrate to the center of such high-density plasmas. With sufficient directivity in the launched wave spectrum, currents can be driven by combined damping of the fast waves on resonant electrons through electron Landau damping (ELD) and transit-time magnetic pumping (TTMP). Experiments to study the feasibility of fast-wave current drive (FWCD) have only recently begun, but theoretical predictions look promising.[2]

In this paper we analyze the influence of the relevant physics phenomena, which are not necessarily independent, on current drive performance. Such phenomena include diffraction and other nongeometrical optics processes, $k_\parallel$ modification, single-pass absorption, and antenna characteristics, such as poloidal extent and poloidal location. To do this, we apply a two-and-one-half dimensional (2 1/2-D), full-wave code (PICES) for modeling ion cyclotron resonance heating (ICRH) and current drive based on the poloidal mode expansion method and the reduced-order expansion. By 2 1/2-D, we mean that 3-D wave fields are calculated in axisymmetric geometry (2-D solution domain $-r, \theta$), while the correct toroidal dependence of the antenna source currents is obtained from a 2-D (r, ϕ) recessed antenna code. The model includes the poloidal and toroidal structure of the antennas, the modification of the $k_\parallel$ spectrum due to the poloidal magnetic field, and a nonperturbative solution for $E_\parallel$. A semianalytic model for current drive, including trapped electron effects, is employed. The code has been used extensively to model DIII-D, ITER, SSAT, and other tokamaks.

Ray tracing calculations[3,4] show that the projection of the wave number along the magnetic field ($k_\parallel$) varies greatly over a ray trajectory, causing a change in the parallel phase speed and a corresponding change in the current drive efficiency. Ray tracing calculations include the $k_\parallel$ variation naturally, but neglect large-scale coherent effects such as diffraction and wave focusing, which are equally important in determining current drive efficiency. In these cases, full-wave or global-wave solutions are needed. Finite difference full-wave codes, such as ORION[5], generally neglect the $k_\parallel$ variation

* Research sponsored by the Office of Fusion Energy, U.S. Department of Energy, under contract DE-AC05-84OR21400 with Martin Marietta Energy Systems, Inc.

because to do otherwise leads to the appearance of the differential operator $\partial/\partial\vartheta$ in the argument of the plasma dispersion function. This problem can be alleviated by expressing the electric field as a superposition of poloidal modes,[6,7] in which case $k_\parallel$ is purely algebraic:

$$k_\parallel^{n,m} = n\frac{\cos\Theta}{R} + m\frac{\sin\Theta}{N_\tau}\ , \tag{1}$$

where R is the major radius, Θ is the angle that the magnetic field $\vec{B}$ makes with the toroidal direction, and N_τ is the metric tensor element corresponding to the minor radius.

FAST-WAVE CURRENT DRIVE IN ITER

The current density $J_\parallel(\rho,\vartheta)$ driven by fast waves is directly proportional to the power absorbed by the electrons $\dot{W}_e$:

$$J_\parallel(\rho,\vartheta) = C_E\left(\rho,\vartheta,k_\parallel\right)\dot{W}_e(\rho,\vartheta). \tag{2}$$

Ehst and Karney[8] have provided an algebraic expression for $C_E\left(\rho,\vartheta,k_\parallel\right)$. In Eq. (2), $k_\parallel$ is the local value in space, $k_\parallel(\rho,\vartheta)$. For one such local value $k_\parallel(\rho,\vartheta) = k_\parallel^0$, we sum over all poloidal and toroidal harmonics m,n that give $k_\parallel^0$ when calculating $\dot{W}_e$. Then all values of $k_\parallel^0$ are summed. A useful figure of merit is the normalized current drive efficiency $\gamma = \bar{n}_e R_0 I/P_{\rm rf} \times 10^{-20}$, where $I/P_{\rm rf}$ is the ratio of driven current to power absorbed.

Consider first a proposed low-frequency FWCD scenario[9] for ITER with $f = 17$ MHz such that no ion cyclotron resonances appear in the plasma. Parameters are $R_0 = 6.0$ m, $B_0 = 4.8$ T, $a_{\rm plasma} = 2.15$ m, $K = 2.0$, $T_e(0) = T_i(0) = 33$ keV, and $n_{e0} = 1.1 \times 10^{20}$ m^{-3}, with a 50–50 mixture of D-T gas, and $Z_{\rm eff} = 2.26$. Density and temperature profiles are parabolas raised to the α_n and α_T powers respectively, with $\alpha_n = 0.5$ and $\alpha_T = 1.0$. The antenna current is Gaussian in the poloidal dimension with width corresponding to a height of $\sim$2 m and centered on the midplane. A population of fast alpha particles is modeled by a Maxwellian velocity distribution with $T_\alpha = 1$ MeV = const. The alpha density is assumed to be 1% of the electron density on the magnetic axis with a radial profile proportional to $n_e T_e^{5/2}$. A Solov'ev[10] equilibrium is used.

In Fig. 1, γ is plotted as a function of toroidal mode number n for the 17 MHz case both with and without the $k_\parallel$ variation (solid and dashed curves, respectively). The dotted curve shows the fraction of power absorbed for $m = 0$ in a single pass. This figure makes evident the adverse effect that the $k_\parallel$ variation has on current drive efficiency at low frequency. The degradation is almost entirely due to the second term in Eq. (1), which represents the effect of the poloidal field on $k_\parallel$. This is shown by the chain-dashed curve, for which the second term in Eq. (1) has been set to zero. Figure 2 shows the sensitivity of this result to the poloidal position and extent of the antenna. The highest driven currents are obtained with short antennas, between 0.5 and 1.0 m in height, which are centered at or near the equatorial plane.

An alternative high-frequency (56 MHz) scenario for ITER places the plasma in the gap between the first and second harmonic resonances of the alphas and deuterium. The

second harmonic is just behind the antenna, and the first harmonic is at the inboard edge of the plasma. Thus, the deuterium and alpha species do not absorb appreciable amounts of power. Tritium, on the other hand, has its second harmonic resonance close to the magnetic axis and is therefore a potentially significant parasitic absorber. The shorter wavelength in this case reduces the adverse effect of the $k_{\|}$ variation by reducing diffraction and increasing focusing onto the hot central region of the plasma where trapped particle losses are small. The resulting increase in efficiency is more than offset by the parasitic ion absorption at the tritium second harmonic. At 56 MHz, the wavelength is small relative to the minor radius ($\lambda/a \sim 0.058$), and an accurate determination of the fraction of power lost to tritium requires a high degree of numerical accuracy. Figure 3 shows that more than 300 radial mesh points are required before the solution converges. The resulting efficiency is only $\gamma \sim 0.20$ A/W·m^2 with 34% of the power lost to tritium. The result efficiency is reduced even further if a significant nonlinear high-energy tritium tail develops to enhance the cyclotron absorption.

Figure 4 shows a similar case for SSAT, a machine about one-third the size of ITER. Here, the parasitic absorption is at the deuterium third harmonic, and the relatively longer wavelength ($\lambda/a \sim 0.178$) allows convergence with only one-third as many points. In this case, about 24% of the power is lost to deuterium. Both Figs. 3 and 4 show convergence when the number of radial mesh points per wavelength is about 17.

SUMMARY AND CONCLUSION

We have seen that the current driven by fast waves in a tokamak can be strongly suppressed at low frequencies because of variations in the $k_{\|}$ spectrum caused by the poloidal field. One way to reduce this effect is to work at a higher frequency where diffraction is reduced and focusing increased. But in ITER, the price paid for this improvement is a significant loss of power due to parasitic ion absorption at the tritium second harmonic resonance. Adjusting the poloidal location and/or extent of the antenna array shows that the highest efficiencies are achieved with short antennas at or near the equatorial plane.

REFERENCES

1. K. Tomabechi, J. R. Gilleland, Yu. A. Sokolov, R. Toschi, and the ITER Team, *Nucl. Fusion* **31**, 1135 (1991).
2. S. C. Chiu, V. S. Chan, R. W. Harvey, and M. Porkolab, *Nucl. Fusion* **29**, 2175 (1989).
3. D. B. Batchelor, R. C. Goldfinger, E. F. Jaeger, D. Ehst, and C. F. F. Karney, in Proceedings of the Thirteenth International Conference on Plasma Physics and Controlled Nuclear Fusion Research, Washington, 1990 (IAEA, Vienna, 1991), Vol. 1, p. 817.
4. V. P. Bhatnagar, J. Jacquinot, and D. F. H. Start, "Fast Wave Current-Drive Calculations for JET A2-Antennas," Proceedings of the IAEA Technical Committee Meeting on Fast Wave Current Drive in Reactor Scale Tokamaks, Arles, France, September 23–25, 1991.
5. E. F. Jaeger, D. B. Batchelor, M. D. Carter, and H. Weitzner, *Nucl. Fusion* **30**, 505 (1990).
6. M. Brambilla and T. Krucken, *Nucl. Fusion* **28**, 1813 (1988).

7. A. Bécoulet, D. Moreau, G. Giruzzi, B. Saoutic, and J. Chinardet, "Analysis of Fast Wave Current Drive from the ALCYON Code," Proceedings of the IAEA Technical Committee Meeting on Fast Wave Current Drive in Reactor Scale Tokamaks, Arles, France, September 23–25, 1991.
8. D. A. Ehst and C. F. F. Karney, *Nucl. Fusion* **31**, 1933 (1991).
9. J. Jacquinot (private communication, March 9, 1990).
10. L. S. Solov'ev, Sov. Phys.-JETP **26**, 400 (1968).

ACKNOWLEDGEMENT

The authors are indebted to J. Jacquinot, D. Moreau, D. A. Ehst, C. F. F. Karney, and V. Bhatnagar for helpful discussions.

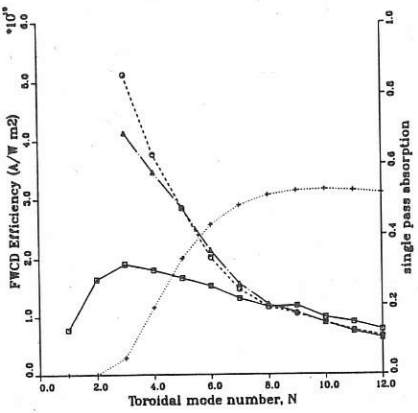

Fig. 1. FWCD efficiency in ITER at 17 MHz.

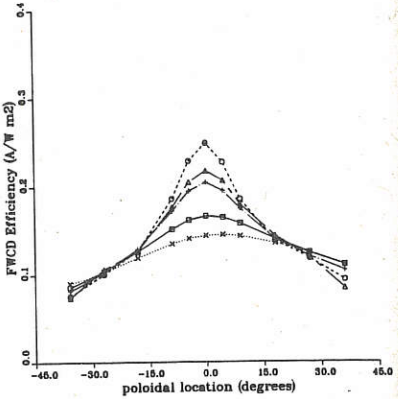

Fig. 2. FWCD efficiency vs poloidal location in ITER at 17 MHz.

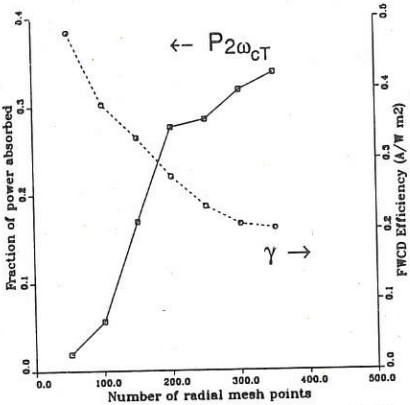

Fig. 3. Second harmonic tritium in ITER at 56 MHz.

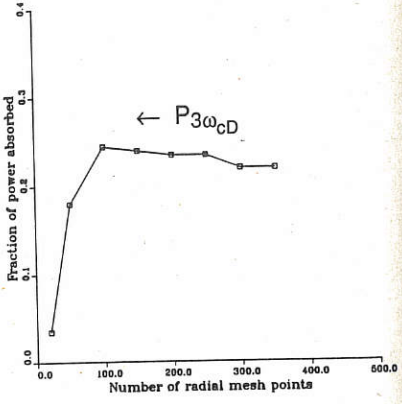

Fig. 4. Third harmonic deuterium in SSAT at 80 MHz.

CURRENT DENSITY PROFILE CONTROL IN REVERSED FIELD PINCH PLASMA BY RF CURRENT DRIVE

S. Shiina, K. Saito, Atomic Energy Research Institute, Nihon Univ.
Y. Kondoh, H. Ishii, Faculty of Technology, Gunma Univ. Japan
T. Shimada, Y. Hirano, Electro Technical Laboratory, Tsukuba, Japan

1. Introduction

This paper addresses aspects of wave current-drive(CD) in reversed field pinch(RFP)plasma. Benefits of CD are steady-state operation where could be used to provide tailored current profile such that the plasma is in, or close to, a relaxed(Taylor)state, and partial CD to drive only part of the current if this improves the energy confinement by reducing or eliminating the need for a dynamo mechanism within the plasma.

A wide variety of schemes can generate non-inductive currents in a plasma eg, Landau damping(LD) or Transit Time Magnetic Pumping(TTMP) by various waves, absorption of travelling cyclotron waves or asymmetric particle injection. Fast Magnetosonic (FM) wave has been found to be an useful candidate for CD in high beta plasma as RFP plasma /1/. In this paper, the radial profile of driven curent density parallel to magnetic line of force by FM wave is theoretically investigated as function of parallel refraction index.

2. Ray tracing and current generation

We are particularly interested in RF current drive for TPE-RX RFP device under design study; the plasma parameters are listed in Table 1. Here the plasma is modeled as cylindrical plasma and the equilibrium state is described by a partially relaxed state model(PRSM) as shown in Fig.1, where the force-free field is assumed for the poloidal component only, $j_\theta = \lambda B_\theta / \mu_0$, $\lambda = \lambda_0 \{1-(\phi/\phi_w)^5\}^2$, ϕ is the poloidal flux and ϕ_w that at the wall. The pressure gradient is given by $dp/dr = -S_0 r B_z^2 (dq/dr)^2 / 8\mu_0 q^2$ and So=0.4, taking account of the Suydam criterion ($S_0<1$) /2/. The ray path of FM wave($\omega_{LD} > \omega > \omega_{DC}$) is calculated in three dimensions. The wave is launched near the plasma edge, and the ray path and wave vector($\vec{k}$) evolution is followed. The wave frequency, the initial parallel index of refraction($n_{\parallel 0} = c\vec{k} \cdot \vec{B}/B\omega$), and the poloidal index($n_\theta = c\vec{k} \cdot \vec{\chi}/\omega$) are specified at the start, and the ray's progress is calculated thereafter from a WKB analysis of the spatial variations in the hot plasma dielectric tensor, $\overleftrightarrow{K}(\vec{r}, \omega, \vec{k})$. Along the ray trajectry the imaginary part of the k vector is determined

in order to compute wave damping and the resulting plasma heating. Since we typically choose a wave frequency above the tenth deuterium cyclotron harmonic, ion damping is usually neglegible. The wave damping becomes strong as beta value increases, indicating the dominant wave damping is due to TTMP. The wave power flux, P(r), along the ray path is calculated as follows; $P(r)=P(r_w)\exp(-2\int^r\{\mathrm{Im}\ k_r\}\,dr)$, where $P(r_w)$ is the injected wave power and Im k_r the imaginary part of k_r. To calculate the driven current, the power absorbed by electrons over an incremental radius is determined and averaged over the flux surface to obtain the local absorbed power density, $\langle p^{rf}\rangle$. We typically terminate the ray tracing once $P/P(r_w)=1\times10^{-2}$. The local driven current density parallel to the magnetic line of force, $j_\parallel$, is then given by $j_\parallel = 19.2\times10^{18}/\ln\Lambda\cdot Te/n_e\cdot\eta\cdot\langle p^{rf}\rangle$ with Te in Kev and the other variables in MKS units. Here η is the Fisch-Karney normalized current-drive efficiency/3/ and is given by $\eta = 8U^2/(5+Z) + 2 + 12(6+Z)/\{(5+Z)(3+Z)\} + 2D/ZU$ where $U = \omega/k_\parallel v_e$ (v_e is electron thermal velosity), $Z \equiv$ Zeff and D is 3.76 for LD and 8.09 for TTMP. Using TPE-RX parameters listed in Table 1 and the following density and temperature profiles: $n_e = n_e(0)\{1-(\psi/\psi_w)^5\}^{1/2}$ and $Te = Te(0)\{p/p(0)\}$, FM wave has been examined as a means to drive current within the plasma. It is useful for reactor designs to convert the local CD efficiency to a global ratio of generated toroidal current, I_o, to absorbed wave power, $P(r_w)$. In addition, the toroidal stacking effect leads to a dependence $I_o/P(r_w) \propto R_o^{-1}$, whereas the current carriers are generallyslowed by collisions such that $I_o/P(r_w) \propto n_e^{-1}$. Hence, to lowest order,the ratio of $\gamma \equiv I_o\bar{n}_eR_o/P(r_w)$ is expected to be roughly constant in plasma. This ratio, γ, is a figure of merit which must be maximized in order to minimize capital costs and circulating power for current drive.

3. Profile of driven parallel current density

Typical results are shown in Fig.2, with $n_{\parallel o} = 5.5$ and $f = 12f_c(0)$(=330 MHz). For this wave parameters, the wave power damps over the shortest distance of about single pass through the plasma. Both the deposited power density, $\langle p^{rf}\rangle$, and the driven parallel current density, $j_\parallel$, profiles have two local maxima; the first is at r=0.05 m, which approaches to the axis with decrease of $n_{\parallel o}$, and the second corresponds to the location of local beta maximum (see Fig.1). The 2nd peak value of $j_\parallel$ depends on n_e and Te profiles in the outer region since it scales as Te/n_e. The more flat Te and more sharp n_e profile enhances the 2nd peak value. This 2nd peak parallel current leads to the high shear which would stabilize internal m=1 modes, and provides poloidal current in the outer regions

to reverse the toroidal field which could eliminate or reduce the need for a dynamo mechanism within the plasma and thereby reduce fluctuations and losses. The faster waves, with $n_{\parallel o} < 5.5$, penetrate to the central region and drive the parallel current with a larger driving efficiency, although the wave damping is weaker slightly than that for $n_{\parallel o} = 5.5$. This scenario using the faster waves could be used for the steady-state operation of RFP. A global CD efficiency, $I_o/P(r_w)$, is about 0.1A/W and a figure of merit, γ, is 0.2 [10^{20} m^{-3}-MA-m/MW]. If $n_{\parallel o} < 2$ the electron damping is much weaker, so multiple passes through the plasma are required to deposite wave energy in the electrons. Thermal ions will compete strongly with electrons to absorb wave power. Such parastic absorption must be avoided to maximize the current driving efficiency.

The slower waves, with $n_{\parallel o} > 5.5$, have the more shallow penetration as shown in Fig.3(for $n_{\parallel o} = 12.5$, f=140 MHz. The higher is the frequency, the more shallow is the penetration). The damping is relatively weak and requires about 5 paths through the plasma. The radial profile of $\langle p^{rf} \rangle$ has two peaks, but $j_\parallel$ becomes maximum at r=a/3 and small at the local beta maximum since the current driving factor of Te/n_e is small there. The location of $j_\parallel$ maximum shifts toward the outer region with increase of frequency. For f=330 MHz($n_{\parallel o} = 12.5$), $j_\parallel$ becomes maximum at r= 0.6a corresponding to the local beta maximum. The current driving efficiency is relatively poor. However, this scenario may still be advantageous to drive the enough poloidal current in the outer regions to reverse the toroidal field, thereby to improve the energy confinement. If $n_{\parallel o} > 12.5$ the resonant electrons become slower than electron thermal velosity, then can be trapped in a magnetic well and consequently become incapable of carring currents. Any portion of the wave power absorbed by these trapped electrons, therefore, will not contribute to the current, resulting in a lower driving efficiency.

4. Conclusion

FM wave is an useful candidate for the current drive in high beta plasma as RFP plasma, in which the dominant wave damping is due to TTMP having high driving efficiency. The faster wave with $n_{\parallel o} < 5.5$ could be used for the steady-state operation of RFP since it would control the profile and direction of the current density everywhere in the plasma. The local beta maximum appropriate to RFP configuration enhances the driven current and the magnetic shear in the outer regions, which would stabilize m=1 internal modes and eliminate the need for a dynamo mechanism. A global current driving efficiency and a figure of merit are about 0.1A/W and 0.2 [$10^{20}m^{-3}$-MA-m/MW]. The slower waves with $n_{\parallel o} > 5.5$ is ad-

vantageuos to drive the enough poloidal current in the outer regions to reverse the toroidal field, which would reduce fluctuations and losses, thereby improve the energy confinement.

TABLE 1 TPE-RX parameters used for rf current drive calculation

Parameter	Value
Major radius, R_0(m)	1.5
Minor radius, a(m)	0.3
Toroidal plasma current, I_t(MA)	2.0
Peak toroidal field, $B_z(0)$(T)	3.3
Poloidal flux at wall, ψ(a)(Wb)	3.46
Edge density, $n_e(a)(10^{20}/m^3)$	0.18
Peak density, $n_e(0)(10^{20}/m^3)$	1.5
Edge temperature, T_e(a)(Kev)	0.48
Peak temperature, $T_e(0)$(Kev)	4.0
Suydam factor, S_0	0.4
Poloidal beta, $\beta_p(0)(2\mu_0 p(0)/B_p^2(a)$	0.22
Effective charge number, Z_{eff}	2
F/Θ	-0.2/1.7

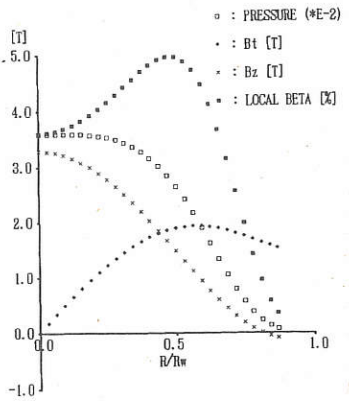

Fig.1: RFP configuration of partially relaxed state model; r_w=0.3 m, R_0=1.5 m S_0=0.4, M=5, N=2 and I_0=2 MA. Local β is defined as $2\mu_0 p(r)/B^2(r)$.

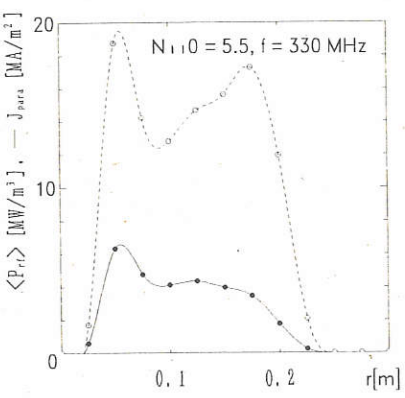

Fig.2: Radial profile of $\langle p^{rf} \rangle$ and $j_\parallel$, with $n_{\parallel 0}$=5.5 and f=330 MHz.

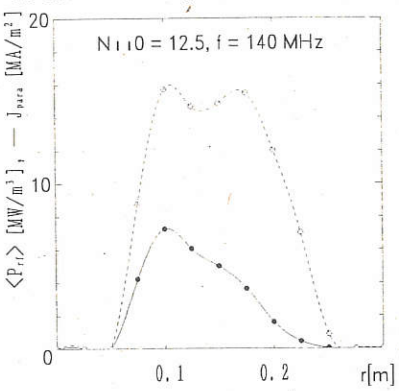

Fig.3: Radial profile of $\langle p^{rf} \rangle$ and $j_\parallel$, with $n_{\parallel 0}$=12.5 and f=140 MHz.

/1/ S.Shiina, N.Watanabe, K.Saito, Y.Kondoh, K.Hattori, Proc. Int. School of Plasma Physics,Varenna,903(1990)

/2/ Y.Kondoh, Nuclear Fusion 21, 1607(1981)

/3/ N.J.Fisch and C.F.F.Karney, Phys. Fluids 24, 27(1981)

A METHOD OF INCREASING THE ION BERNSTEIN WAVE EXCITATION EFFICIENCY IN PLASMAS

A. V. Longinov, V. A. Lukinov, S. S. Pavlov

Kharkov Institute of Physics and Technology, Kharkov, Ukraine

Introduction. The ion Bernstein wave (IBW) excitation in the plasma may be used to solve a number of problems: plasma heating, CD, two-component regime of thermonuclear burning. Low efficiency of IBW excitation is one of the main problems in using this method. The transformation of the electromagnetic flux excited by an antenna into the IBW kinetic flux is accomplished due to the plasma inhomogeneity. However, such a transformation may be efficient only for relatively weak plasma density gradients in the lower hybrid resonance (LHR) region /1/. Under real conditions the optimal gradients are often not realized and the control of edge plasma density profile is difficult.

This report suggests the method for improving the IBW excitation efficiency in the frequency range $\omega < n\omega_{ci}$, where $n=2,3,\ldots$ The method consists in introducing into the edge plasma an ion minority for which the condition $n\omega_{ci}=m\omega_c'$ is fulfilled, where $m=1,2,\ldots$ and $m<n$. Here ω_{ci} and ω_c' are the frequencies corresponding to the cyclotron resonance at the plasma boundary for bulk and minority ions, respectively. E.g. for D+T plasma H ions may be used as a minority in the regime $\omega<2\omega_{cd}$, or ^{3}He ions for $\omega<2\omega_{ct}$.

Description of the model. Consider the IBW excitation with $k_y=0$ in the inhomogeneous plasma on the numerical full-wave model /1/. The plasma density and temperature profiles characteristic for the tokamak with the divertor are shown in Fig. 1. The actual profiles have been modelled as follows. In the confinement region ($x<a$) the density and temperature change linearly, and in the divertor layer ($a<x<b$) they decay exponentially in agreement with formulas given in Fig. 1. The calculations have been performed for two characteristic density profiles n_1 and n_2, which differ essentially from the viewpoint of IBW excitation. The n_1 dependenceis characterized by the fact that $n(b)=0$ and in what follows we'll relate to this case as the plasma with the smooth boundary. For the dependence n_2 $n(b)=0$ and it describes the plasma with the sharp boundary. Illustrate the application of this method with the examples of the loop antenna /2/ as well as of the slot one /3/. The resistance R introduced by the plasma is the parameter characterizing the efficiency of the wave excitation for the loop antenna. When using the slot antenna the IBW is excited due to the coupling with the surface wave propagating along the plasma boundary. Therefore the IBW excitation efficiency is characterized by the damping length of the surface wave l' due to the IBW radiation into the plasma core. In what follows in all calculations the following parameters have been used: $\omega=1.85\omega_{ci}$, $n_a=3\cdot10^{13}\,cm^{-3}$, the density gradient in the linear region $\nabla n=4.67\cdot10^{11}\,cm^{-4}$ and

∇T=130eV/cm. For convenience we introduce the widths of the divertor layer s=b-a and of the vacuum gap d=c-b, where c is the coordinate of the screen in which the slot is made for the slot antenna or the coordinate of the loop location for the loop antenna.

The discussion of the results. Consider the IBW excitation in the D-plasma by loop antenna for the n_1 density profile with parameters close to the D111-D plasma ones in the H-mode: T_{i0}=120eV, T_{e0}=90eV, r_n=6cm, r_T=1.5cm, a=240cm, s=3cm, d=2cm and B=2T. Fig.2 shows the /Ex/ field distribution and the RF power Px flux (in relative units) for the mode with $N_{||}$=5 for two hydrogen concentrations $\alpha=n_h/n_e$=0 (curves 1) and α=0.06 (curves 2). As is seen from Fig.2 when introducing the hydrogen minority with α=0.06 the considerable ($\simeq$ 4 times) increase of the RF power flux into the plasma occurs. This is due to the fact that the LHR shifts into the denser plasma region and due to the swelling of the Ex field the IBW excitation is increased. On growing α this effect is enhanced but on exceeding some critical concentration of the minority n which is determined by the following formula:

$$n'/n_i = A'/A(Z/Z')(\omega^2 - n^2\omega_{ci}^2)/(\omega_{ci}^2 - \omega^2), \quad (1)$$

where A,Z and A',Z' are mass and charge numbers of bulk and minority ions, correspondingly, there occurs the cut-off for the IBW excitation. The small intensity fast wave will be radiated into the plasma core and the main part of RF power will be absorbed at the plasma edge due to i-i collisions.

Fig.3 shows the dependence of the resistance R vs the ion minority concentration α in the case considered. The R maximum value and, consequently, the IBW excitation efficiency is achieved in the range $\alpha\simeq$0.06 and it is approximately 6 times more than one for the α=0 case. Note that on increasing α the RF power absorption in the edge plasma increases due to i-i collisions. The dependence of the RF power P_a absorbed in the edge plasma related to the total power P_0 radiated by the antenna vs α is given in Fig.3. It is seen that this negative effect becomes essential for ion minority concentrations close to the critical one .

Consider now the IBW excitation by the slot antenna in the D+T tokamak plasma with ITER parameters: a=805cm, s=9cm, d=1cm and B=4T. Analyze first the sharp boundary plasma with T_{i0}=60eV, T_{e0}=30eV, r_n=2.3cm and r_T=13cm. Fig.4 gives the /Ex/ field distribution in the vacuum gap and in the edge plasma at α=0. In this case the surface wave with $N_{||}\simeq$1 is excited. Because of the weak coupling with IBW it has a large damping length l=125m what characterizes the low efficiency of IBW excitation. As l>1, where $l=2\pi a$ is the exciting system period along the magnetic field, the Ex field distribution has the form of a standing wave due to the interference of surface waves propagating in opposite directions from the exciting slot. In this case the antenna impedance has a resonant character /3/ that makes difficult its matching and, besides, the noticeable part of RF power ($\simeq$8%) is absorbed due to ohmic losses in the antenna elements.

Fig.5 gives the similar /Ex/ field distribution for α=0.04. It is seen that even at the relatively low α there occurs the

sharp diminishing of the surface wave damping length (l'=2.3m) and the wave becomes a travelling wave. Apart from the strong increase in the IBW excitation efficiency this case is characterized by the negligibly small ohmic losses in the antenna elements (<1%) by the mainly active input impedance of the antenna which becomes to be weakly dependent on the vacuum gap values and edge plasma parameters. Then the /Ex/ field amplitude at the plasma edge is considerably lowered (≃2 times) what diminishes the probability of appearing the unwanted nonlinear phenomena. Fig.3 gives the l' vs α dependence for this case. It is seen that the α value at which the cut-off occurs (l'→ ∞) diminishes comparing with the previous case. The considerable decrease in l' is possible for rather low α= 0.02-0.04 and the effect of RF power absorption due to i-i collisions practically does not manifest itself.

Analyze now the case of the plasma with the smooth boundary profile with the following parameters: $T_{i\alpha}$=120eV, $T_{e\alpha}$=30eV, τ_n=2.5cm, τ_T=4.5cm. Fig.6 gives the distributions of the /Ex/ field, RF power flux P_x and of the specific power D_i absorbed by ions for the surface wave mode with $N_{||}$=1.05 at α=0 (curves 1) and α=0.04 (curves 2). As is seen from the Fig.6 the IBW excitation efficiency enhancement is insignificant in this case. This is explained by the fact that due to the weak density gradient in the LHR region and the appearance of the strong Ex swelling, the coupling between the surface wave and IBW is sufficiently good even for α=0. On introducing the minority with α=0.04 the absorption due to i-i collisions is enhanced essentially. One should relate to advantageous effects connected with the minority introduction the Ex field swelling decrease in the LHR region.

The similar effect of the IBW excitation enhancement may take place in the region $\omega<n\omega_{ci}$ at n>2. In these regimes it is due to the decrease of $k_\perp^2\rho^2$ for IBW at the plasma edge with minority introduction, besides, the excitation cut-off effect at any ion minority concentration is then absent.

Conclusions. 1. The introduction of a special ion minority into the edge plasma allows one to enhance the IBW excitation efficiency when using loop antennas as well as slot ones.

2. The strongest effect is achieved in regimes with large density gradients in the edge plasma.

3. The method suggested is also suitable to control the antenna performance regime, e.g. to control the surface wave damping length when using the slot antenna.

4. In the plasma with the low ion temperature at the edge, especially for high concentrations of minority ions the part of the absorbed RF power due to i-i collisions may become noticeable.

REFERENCES

1. Longinov A.V., et al. in Contr. Fusion and Plasma Physics (Proc. 15th Europ. Conf. Venice, 1989), v.3, p.1105
2. Ono M., et al. Phys. Rev. Lett. 54 (1985) 2339
3. Longinov A.V., Lukinov V.A., in Contr. Fusion and Plasma Heating (Proc. 15th Europ. Conf. Dubrovnik, 1988), v.2, p.742

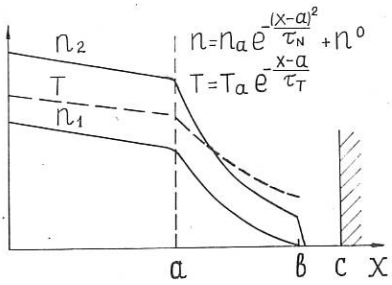

fig. 1

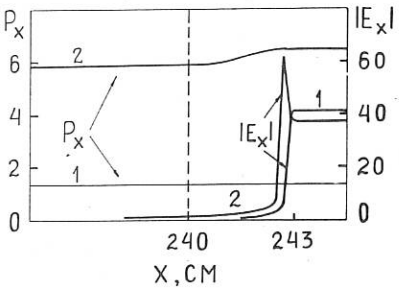

fig. 2

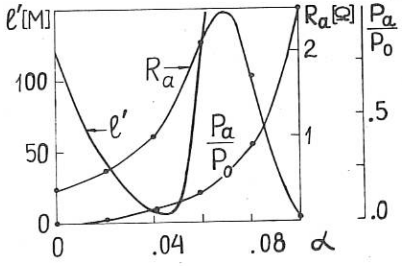

fig. 3

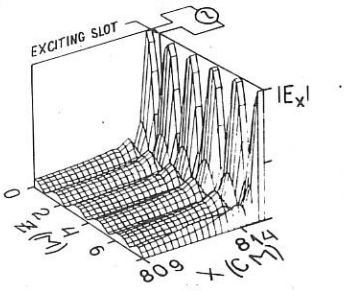

fig. 4

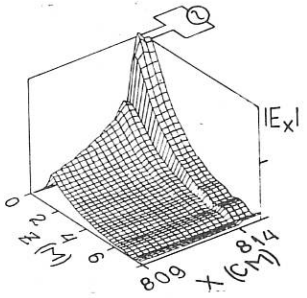

fig. 5

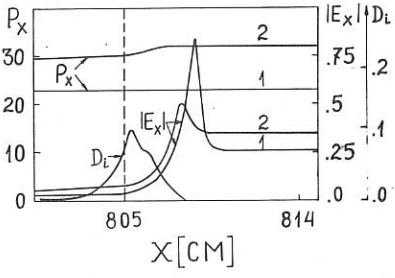

fig. 6

THE LOCAL POWER DISSIPATION OF ION BERNSTEIN WAVES IN A WEAKLY INHOMOGENEOUS PLASMA

H. WERTHMANN and M. BRAMBILLA
Max-Planck-Institut für Plasmaphysik
Boltzmannstr. 2, D-8046 Garching bei München, F.R.G.

1 Introduction

We have derived an explicit expression for the power dissipation per unit volume, P^{α}_{abs}, through particles of the species α by an Ion Bernstein wave propagating in a plane stratified plasma. The expression is also valid when the the ratio of gyroradius to wavelength cannot be assumed to be small. Under these conditions the plasma must be considered as a strongly spatially dispersive medium.

To ensure energy conservation, P^{α}_{abs} should equal the rate of change of the kinetic energy density in the plasma [1]. Starting from this fundamental principle and using the formal characteristic solution of the linear Vlasov equation, Brambilla and Krücken [2] obtained a general expression for the power dissipation

$$P^{\alpha}_{abs}(\underline{x}) = \frac{e^2 Z^2_{\alpha}}{m_{\alpha}} \lim_{\gamma \to 0+} \left\{ \gamma \int_{\mathbb{R}^3} d^3v \, \frac{F_{\alpha,M}(v, \underline{Y})}{v^{\alpha}_{th}(\underline{Y})^2} |H|^2 + (\text{drift terms}) \right\} , \qquad (1)$$

where

$$H \equiv e^{i(\omega + i\gamma)t} \int_{-\infty}^{t} dt' \underline{E}(\underline{q}, t') \cdot \underline{v} , \qquad (2)$$

with ω, the real part of the wave frequency and γ its imaginary part. Above $(\underline{q}, \underline{v})$ denotes a trajectory of the undisturbed particle motion parameterized by t', $\underline{E}(\underline{q}', \underline{v}')$ the electric field of the wave along this trajectory, $\underline{Y}$ the guiding center position and $F_{\alpha,M}(v, \underline{Y})$ a non-drifted Maxwellian without parallel gradients. $F_{\alpha,M}(v, \underline{Y})$ is the appropriate equilibrium solution of the linearized Vlasov equation valid to first order in the drift approximation. Eq.(1) holds in the limit in which the collisional mean free paths of ions and electrons are much larger than the typical wavelengths of the field.

It is easily seen, that apart from the so called drift terms proportional to density and temperature gradients, P^{α}_{abs} is a positive definite quantity. The exact form of the drift terms is not of interest in the present context, because in investigating the power deposition by h.f. waves they can be neglected.

Brambilla and Krücken [2] showed that the expression for P^{α}_{abs} given above is in agreement with the time averaged Poynting theorem, and obtained a general expression for the kinetic correction to the Poynting flux.

2 Power Dissipation in a Slab Geometry

In the following, we define a one-dimensional plasma configuration, i.e. a slab geometry, through the assumptions of a z-directed static magnetic field $\underline{B}^{stat}$ and of density,

temperature and gyrofrequency gradients pointing in the x-direction. Hence the electric field can be represented as

$$\underline{E}(\underline{x},t) = e^{-i\omega t} e^{ik_y y} \sum_{k_\parallel} e^{ik_\parallel z} \underline{E}(x;k_y,k_\parallel) \quad . \tag{3}$$

The assumption of periodicity in the z-direction restricts the $k_\parallel$-spectrum to a discrete set of values.

To derive an explicit expression for the local power deposition, valid in the slab, the trajectory and the velocity space integrations in Eq.(1) must be carried out. This requires the knowledge of the unperturbed particle trajectories. Here, we investigate only situations where the guiding-center variable $\underline{Y}_\perp$ is a constant of motion to first order in the drift approximation, i.e. the ∇B^{stat}-drift is negligible. In this case the unperturbed trajectories are known analytically and of a relatively simple form.

To perform the calculations, it is convenient to use a Fourier representation of the electric field also in the x-direction,

$$\underline{E}(x;k_y,k_\parallel) = \int_{-\infty}^{\infty} dk_x \; e^{ik_x x} \underline{\tilde{E}}(k_x,k_y,k_\parallel) \quad . \tag{4}$$

We recall that due to the plasma inhomogeinity the constitutive relation $\underline{J} = \underline{J}(\underline{E})$ for the linear h.f. plasma current can be written as an integral equation either in real x-space or in k_x-Fourier-space [3]. With Eq.(4) and the help of the expansion of $e^{iz\sin(\psi)}$ in terms of Bessel functions, we obtain the relation

$$H = e^{ik_y y} \sum_{k_\parallel} e^{ik_\parallel z} \int_{-\infty}^{\infty} dk_x \; e^{ik_x x} \sum_{n=-\infty}^{\infty} \frac{e^{in(\psi-\phi)} v_{th}^\alpha(x)}{\omega + i\gamma - k_\parallel v_\parallel - n\Omega_{C\alpha}(x)} \times \tag{5}$$

$$e^{i\frac{v_\perp}{\Omega_{C\alpha}(x)}(k_x\sin(\phi) - k_y\cos(\phi))} \underline{W}_n^\alpha(u,w;\mu) \cdot \underline{\underline{R}}^{-1}(\psi) \cdot \underline{\tilde{E}}(k_x,k_y,k_\parallel)$$

by changing the order of the k_x- and t'-integrations and integrating along the given particle orbits analytically. In this equation the angle ϕ is defined by $\phi = \mathrm{atan}(v_y/v_x) \in [0,2\pi]$. $w \equiv v_\perp/v_{th}^\alpha$ and $u \equiv v_\parallel/v_{th}^\alpha$ denote dimensionless velocities and μ is given by $\mu = k_\perp v_{th}^\alpha/\Omega_{C\alpha}$. The vector $\underline{W}_n^\alpha(u,w;\mu)$ is defined through

$$\underline{W}_n^\alpha(u,w;\mu) \equiv \frac{in}{\mu} J_n(\mu w)\underline{e}^1 - wJ_n'(\mu w)\underline{e}^2 + iuJ_n(\mu w)\underline{e}^3 \quad . \tag{6}$$

Another quantity, which enters Eq.(5), is the rotation matrix $\underline{\underline{R}}(\psi)$ describing a rotation around the z-axis by an angle $\psi = \mathrm{artan}(k_y/k_x)$.

With the help of the identity

$$\lim_{\gamma\to 0+} \frac{\gamma}{\omega - i\gamma - k_\parallel' v_\parallel - m\Omega_{C\alpha}(x)} \frac{1}{\omega + i\gamma - k_\parallel v_\parallel - n\Omega_{C\alpha}(x)} = \tag{7}$$

$$\delta_{nm}\delta_{k_\parallel k_\parallel'} \frac{\pi}{|k_\parallel|} \delta\left(v_\parallel - \frac{\omega - n\Omega_{C\alpha}(x)}{k_\parallel}\right)$$

we derive the following expression for $\lim_{\gamma\to 0+}\gamma|H|^2$, entering Eq.(1):

$$\lim_{\gamma\to 0+}\gamma|H|^2 = \sum_{k_\parallel}\frac{v_{th}^\alpha(x)\pi}{|k_\parallel|}\int_{-\infty}^{\infty}dk_x\, e^{ik_x x}\int_{-\infty}^{\infty}dk_x'\, e^{-ik_x' x}\times \tag{8}$$

$$\sum_{n=-\infty}^{\infty} e^{in(\psi-\psi')}e^{iw\varrho_\alpha(x)(k_x-k_x')\sin(\phi)}\delta\left(u-x_n^\alpha(x)\right)\times$$

$$\underline{\tilde{E}}^*(k_x',k_y,k_\parallel)\cdot\underline{\underline{R}}(\psi')\cdot\left([\underline{W}_n^\alpha(u,w;\mu')]^*\otimes\underline{W}_n^\alpha(u,w;\mu)\right)\cdot\underline{\underline{R}}^{-1}(\psi)\cdot\underline{\tilde{E}}(k_x,k_y,k_\parallel)\ .$$

Here ϱ_α denotes the thermal gyroradius and x_n^α is given by $x_n^\alpha \equiv (\omega-n\Omega_{C\alpha})/k_\parallel v_{th}^\alpha$. Eq.(7) means that only resonant particles contribute to the power dissipation.

According to Eq.(1), we still have to integrate over the velocity space. The parallel velocity integration is trivial and the ϕ integration can be carried out by expanding the Maxwellian in powers of $\mathrm{Y}_x - x$, giving to lowest order in the drift approximation the result:

$$P_{abs}^\alpha(\underline{x}) = \frac{{\omega_{P\alpha}}^2(x)}{2\sqrt{\pi}v_{th}^\alpha(x)}\times \tag{9}$$

$$\sum_{k_\parallel}\frac{1}{|k_\parallel|}\int_{-\infty}^{\infty}dk_x\, e^{ixk_x}\int_{-\infty}^{\infty}dk_x'\, e^{-ixk_x'}\sum_{n=-\infty}^{\infty}e^{in(\psi-\psi')}e^{-(x_n^\alpha)^2}\,\underline{\tilde{E}}^*(k_x',k_y,k_\parallel)\cdot\underline{\underline{R}}(\psi')\cdot$$

$$\left(\int_0^\infty dw\, we^{-w^2}\,[\underline{W}_n^\alpha(x_n^\alpha,w;\mu')]^*\otimes\underline{W}_n^\alpha(x_n^\alpha,w;\mu)\right)\cdot\underline{\underline{R}}^{-1}(\psi)\cdot\underline{\tilde{E}}(k_x,k_y,k_\parallel)\ ,$$

with $\omega_{P\alpha}$ the plasma frequency. Also perpendicular velocity integrations appearing in Eq.(9) can be evaluated analytically, so that we finally obtain:

$$\int_0^\infty dw\, we^{-w^2}\,[\underline{W}_n^\alpha(x_n^\alpha,w;\mu')]^*\otimes\underline{W}_n^\alpha(x_n^\alpha,w;\mu) = \tag{10}$$

$$\frac{1}{4}\begin{bmatrix} \frac{n^2}{\mu\mu'}S^n(\mu,\mu') & i\frac{n}{\mu'}D^n(\mu',\mu) & \frac{n}{\mu'}x_n^\alpha S^n(\mu,\mu') \\ -i\frac{n}{\mu}D^n(\mu,\mu') & T^n(\mu,\mu') & -ix_n^\alpha D^n(\mu,\mu') \\ \frac{n}{\mu}x_n^\alpha S^n(\mu,\mu') & ix_n^\alpha D^n(\mu',\mu) & (x_n^\alpha)^2 S^n(\mu,\mu') \end{bmatrix}\ ,$$

where

$$S^n(\mu,\mu') \equiv 2I_n(\tfrac{1}{2}\mu\mu')e^{-\frac{1}{4}(\mu^2+\mu'^2)}\ , \tag{11}$$

$$D^n(\mu,\mu') \equiv \left(\mu I_n'(\tfrac{1}{2}\mu\mu') - \mu' I_n(\tfrac{1}{2}\mu\mu')\right)e^{-\frac{1}{4}(\mu^2+\mu'^2)} \tag{12}$$

and

$$T^n(\mu,\mu') \equiv \left[\left(\frac{2n^2}{\mu\mu'}+\mu\mu'\right)I_n(\tfrac{1}{2}\mu\mu') - \frac{\mu^2+\mu'^2}{2}I_n'(\tfrac{1}{2}\mu\mu')\right]e^{-\frac{1}{4}(\mu^2+\mu'^2)}\ . \tag{13}$$

3 The Relation between Power Dissipation and Conductivity Kernel

The constitutive relation of the Fourier transformed current density relevant to the described slab model can be written in the form

$$\underline{\tilde{J}}(k_x,k_y,k_\parallel) = \int_{-\infty}^{\infty}dk_x'\,\underline{\underline{\tilde{\sigma}}}(k_x,k_x')\cdot\underline{\tilde{E}}(k_x',k_y,k_\parallel)\ . \tag{14}$$

The conductivity kernel $\underline{\tilde{\sigma}}(k_x, k'_x)$ in the equation above is given by the integral representation

$$\underline{\tilde{\sigma}}(k_x, k'_x) = \int_{-\infty}^{\infty} dx''\ e^{i(k'_x - k_x)x''} \underline{\sigma}(k_x, k'_x; x'') \quad , \tag{15}$$

where

$$\underline{\sigma}(k_x, k'_x; x'') = \sum_{\alpha} \frac{1}{8\pi^2} \frac{\omega_{P\alpha}^2(x'')}{k_{\|} v_{th}^{\alpha}(x'')} \sum_{n=-\infty}^{\infty} e^{in(\psi'-\psi)} \underline{\underline{T}}_{\alpha}^{n}(k_x, k'_x; k_y, k_{\|}; x'') \quad . \tag{16}$$

Here the tensor $\underline{\underline{T}}_{\alpha}^{n}(k_x, k'_x; k_y, k_{\|}; x'')$, of which the x''-dependency is due to the space variation of the plasma parameter, is given in reference [3]. We define the modified hermitian part of this tensor as

$$\left[\underline{\underline{T}}_{\alpha}^{n}(k_x, k'_x; \ldots)\right]^{\mathrm{H}} \equiv \frac{1}{2}\left(\underline{\underline{T}}_{\alpha}^{n}(k_x, k'_x; \ldots) + [\underline{\underline{T}}_{\alpha}^{n}(k'_x, k_x; \ldots)]^{\dagger}\right) \quad . \tag{17}$$

Then the expression for the dissipated power given in Eq.(9) together with Eq.(10) can be rewritten:

$$P_{abs}^{\alpha} = \frac{{\omega_{P\alpha}}^2}{8\pi v_{th}^{\alpha}} \sum_{k_{\|}} \frac{1}{|k_{\|}|} \int_{-\infty}^{\infty} dk_x\ e^{ik_x x} \int_{-\infty}^{\infty} dk'_x\ e^{-ik'_x x} \times \tag{18}$$

$$\sum_{n=-\infty}^{\infty} e^{in(\psi-\psi')} \underline{\tilde{E}}^{*}(k'_x, k_y, k_{\|}) \cdot \left[\underline{\underline{T}}_{\alpha}^{n}(k'_x, k_x; k_y, k_{\|}; x)\right]^{\mathrm{H}} \cdot \underline{\tilde{E}}(k_x, k_y, k_{\|}) \quad .$$

Finally, the summation over the different species yields the result

$$P_{abs} = \sum_{\alpha} P_{abs}^{\alpha} = \tag{19}$$

$$\pi \sum_{k_{\|}} \int_{-\infty}^{\infty} dk_x\ e^{ik_x x} \int_{-\infty}^{\infty} dk'_x\ e^{-ik'_x x} \underline{\tilde{E}}^{*}(k'_x, k_y, k_{\|}) \cdot \left[\underline{\sigma}(k'_x, k_x; x)\right]^{\mathrm{H}} \cdot \underline{\tilde{E}}(k_x, k_y, k_{\|}) \quad .$$

Moreover, this expression reduces in the limit of a homogeneous plasma to the expression of P_{abs}^{α} given by Stix [4].

The work of one of the authors (H.W.) has been financed by the Schiedel Foundation.

References

[1] B. D. McVey, R. S. Sund and J. E. Sharer, Phys. Rev. Lett. **55**, p. 507, 1985

[2] M. Brambilla, T. Krücken, Plasma Physics and Controlled Fusion **30**, p.1083, 1988

[3] M. Brambilla, Plasma Physics and Controlled Fusion **33**, p. 1029, 1991

[4] T. H. Stix, *The Theory of Plasma Waves*, McGraw-Hill, N.Y., Ch. 3.

THE SLOT-IN-RECESS ANTENNA SYSTEM FOR ION BERNSTEIN WAVE EXCITATION IN PLASMAS

V. A. Gribok, A. V. Longinov, V. A. Lukinov
Kharkov Institute of Physics and Technology, Kharkov, Ukraine

Introduction. Application of surface waves for excitation of slow waves (SW) including ion Bernstein waves (IBW) has been discussed in Ref. [1,2]. Slot antennas for excitation of surface waves are sufficiently simple, however their radiating surface may be to large. This report suggests and studies theoretically a new antenna array of a "slot in the recess" type that enables one to decrease the dimensions of the radiating surface. Fig.1 shows the sketch of such an antenna.

We assume the recesses in the first wall to be periodically positioned along the Z axis with the period L. A slot is located at the distance h from the recess center (Fig.1). Solutions of Maxwell equations for the problem considered are found by splitting the integration domain in three regions: the recess region (1), the vacuum gap (2) between the plasma and the first wall and the plasma region (3).

The driving slot is assumed to be narrow. Therefore the electric field in the slot region may be considered to be potential, the voltage Uo across the slot being fixed [1]. The electric field component along the magnetic field lines is the driving one. In this case slow waves are excited in plasma predominantly and the fast wave excitation is neglected. In region (1) one solves Maxwell equations in the form of the Fourier decomposition satisfying the condition $E_x = 0$ at the lateral walls of the slot. In the vacuum gap one puts Maxwell equations solutions in the same form. Consider the excitation of slow waves in the semi-infinite uniform plasma in the frequency range $\omega < 2\cdot\omega_{ci}$. Electromagnetic fields are taken to be a sum of the slow electromagnetic (SEW) waves and of the ion Bernstein (IBW) waves.

We use the following boundary conditions. At the plasma-vacuum boundary the E_z and H_y components are continuous and the condition $E_x|_{x=+0}=0$ [3] holds. At the vacuum-recess boundary the E_z, H_y components are continuous for $|z|<b/2$ and the E_z component vanishes for $|z|\geq b/2$ and at the recess bottom the E_z component equals U_o/δ for $|z|<\delta/2$ and E_z component vanishes for $|z|\geq\delta/2$. Using above boundary conditions one can obtain the infinite system of linear equations for solving of Maxwell equations. We employ the reduction method to solve the system obtained numerically.

On the ground of solving this system of equations we determine the RF power flux into the plasma radiated by the antenna in the form of IBW, $P = \sum_{n=-\infty}^{\infty} P_n$ where P_n are partial fluxes as well as the radiation directivity $D = (P_+ - P_-)/P$, where $P_+ = \sum_{n=1}^{\infty} P_n$, $P_- = \sum_{n=-\infty}^{-1} P_n$ together with the electromagnetic fields distributions in the recess, vacuum gap and plasma.

Besides we determine the active and reactive impedances of the antenna (slot) per unit length (in Y-direction).

As an example we give the results of numerical calculations for the IBW excitation near the second harmonic of ion cyclotron frequency $\omega = 2\cdot\omega_{cd}$ in the plasma with the following parameters: B_o = 2 T, $N_e = 10^{11}$ cm^{-3}, $T_i = T_e$ = 200 eV.

Symmetric recess. Consider the IBW excitation in plasma when the driving slot is located at the recess center. In this example the recess is 7.5 cm long, 1 cm deep and the vacuum gap value is 0.25 cm. Fig. 2 shows the distribution of the |Ex| in the recess, vacuum gap and the plasma edge region. In contrast to the antenna of the "slot in the first wall" type [4] where the field pattern in the vacuum gap corresponded to surface waves travelling in opposite directions away from the slot, now the Ex field distribution in the recess has a form of a standing wave. Such a field pattern is due to the surface wave reflection from the lateral wall of the recess. However the main portion of power is radiated from the recess section and it propagates further in the form of two cones 1,2 travelling at a small (~10°) angle to the steady magnetic field in opposite directions away from the slot.

The RF power flux spectrum is symmetric (see Fig. 3). The spectrum maximum corresponds to $N_\parallel \simeq 1.8$. Its broadening is due to the finite length of the recess. Such a slowing-down value for the surface wave is determined by the recess depth and it corresponds to the dispersion relation [2].

Long recess. Antenna arrays of the "slot in recess" type with asymmetric location of the driving slot (relative to the recess center) are of interest for application in some regimes. E. g. such arrays permit one to realize regimes of IBW excitation, the IBW travelling predominantly in one direction along magnetic field lines. They may be used to sustain steady current with IBW. As an example consider a long recess with dimensions: b = 120 m., s = 1.5 cm. in which the slot is spaced 1 m at the wall at d = 0.1 cm. The Ex field patterns are given in Fig. 4. The recess length in this example is not very large compared with the damping length of the slow wave. Therefore in the field pattern the presence of the reflected waves is essential that is manifested in the finite amplitude and oscillation of the field near the wall (standing wave effect). However even in this case with a relatively small recess length sufficiently high directivity of radiation is achieved: D = 0.8.

Fig. 5 shows the RF power flux spectrum versus $N_\parallel$ from which one sees that the spectrum possesses a strongly pronounced asymmetry with the maximum at $N_\parallel \simeq 2$.

"Slot in the resonant recess". Efficient means of considerable reduction of the "slot in the recess" type antenna array keeping the high directivity of radiation is to apply array of the "slot in the resonant recess" type. The basic design principle of such an array is as follows: a driving slot is to be located at the distance ca. $n\cdot\lambda_s/4$, where n = 1,3,5,... from the one wall of the recess and at the

distance ca. $m \cdot \lambda_s/2$, where m = 0,1,2,... from another one. Here λ_s is the wavelength of the surface wave in the plasma - recess bottom gap. Obviously, the minimum size of the antenna (recess) is equal to $\lambda_s/4$ (n = 1, m = 0).

As an example consider the calculation results of the "slot in the resonant recess" antenna for plasma parameters given previously and the vacuum gap value d = 0.25 cm. Fig.6 shows the results of calculating the radiation directivity (curves 1 - 3) versus the recess length for various recess depths. As is seen from picture the radiation directivity maximum is attained for the recess length value close to the one-fourth of the vacuum wavelength for a deeper recess and on decreasing the depth the maximum is shifted to lower values. It is due to the fact that actually the maximum of the radiation directivity is attained at the recess length that is equal approximately to the one-fourth of the surface wave length which increases on increasing the recess depth. As is seen from the Fig.6 for deeper recess when $s \gg d$ a rather high value of the radiation directivity: D = 0.91 is to achieved. As is seen from Fig.6 near the resonance the input impedance is at maximum, its real part exceeding its reactive one considerably.

The spectrum of IBW RF power flux into the plasma for the case s = 7.5 cm and the resonance length of the recess b = 0.23 m is given in Fig.7 . As is seen from this Figure the spectrum maximum corresponds to waves with $N_\parallel \simeq 5$.

Give the example of another resonant recess. Fig.8 depicts the |Ex| distribution for the antenna of the "slot in the resonant recess" type with m = 1, n = 1, at d = 0.25 cm., s = 7.5 cm. As is seen from the Fig.8 the surface waves are excited in the vacuum gap outside the recess boundary that propagate in opposite directions and are damped due to IBW radiation into plasma. At the same time, due to the resonant length of the recess and the resonant location of the slot the amplitudes of these waves are considerably different. Therefore the intensity of IBW (cones 1 and 4) excited by surface waves in plasma would differ considerably. In this case one attains the high radiation directivity D $\simeq$ 0.85.

Fig.9 shows the spectrum of IBW RF power flux into plasma for this case. The maximum of the spectrum occurs at the $N_\parallel \simeq -5$. Part of the spectrum with $N_\parallel > 0$ is determined by the presence of cones 1 and 2.

Conclusion . In conclusion we note that all cases of applying a recess for IBW excitation may be also achieved if one uses a current element for excitation instead of a slot one. Such systems may prove to be simple and especially efficient in a resonant recess case.

References

1. Longinov A.V., JTPh, v.42, 1972, p.1591.
2. Longinov A.V., Lukinov V.A. in Proc. 15th Europ. Conf., Dubrovnik, 1988, v.2, p.742.
3. Sy W.N.-Y., et. al., Nucl. Fusion, v.25, n.7, 1985, p.795.
4. Longinov A.V., Lukinov V.A., Design N4690946, 31.03.1989.

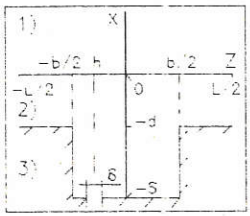

Fig. 1
1) – PLASMA REGION
2) – VACUUM GAP
3) – RECESS REGION

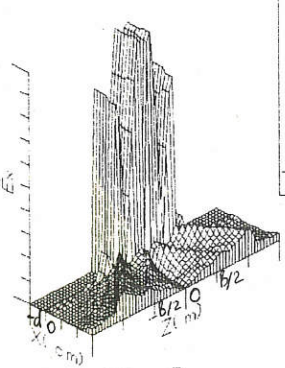

Fig. 2

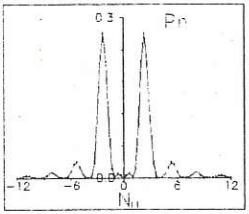

Fig. 3

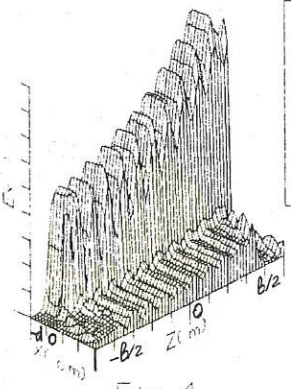

Fig. 4

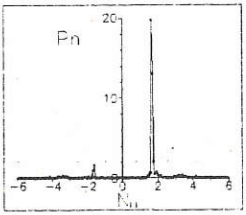

Fig. 5

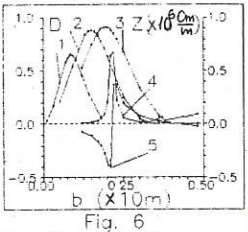

Fig. 6
1 – S = 0.75 CM
2 – S = 2.5 CM
3 – S = 7.5 CM
4 – REAL PART OF IMPEDANCE
5 – IMAGE PART OF IMPEDANCE

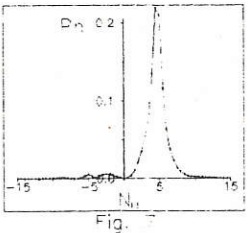

Fig. 7

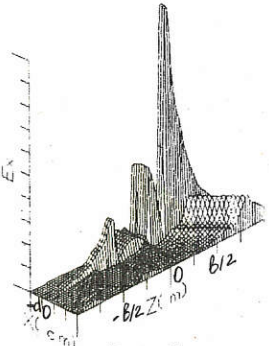

Fig. 8

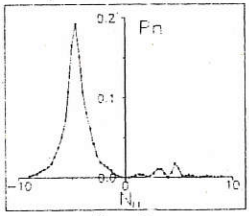

Fig. 9

RF system for plasma production and heating in TJ-I U torsatron

E. Ascasíbar, F. Castejón, L. Rodríguez R., and A. P. Navarro
(Asociación Euratom / CIEMAT. Madrid. Spain)
V. E. Dyakov, A. V. Longinov, O. S. Pavlichenko, S. S. Pavlov, and K. N. Stepanov
(KhFTI. Kharkov. Ukraine)

1. Introduction

RF techniques in the frequency range $\omega = \omega_{ci}$ allow to solve many problems in stellarators, including plasma production, ion and electron heating, non-inductive current drive in plasmas, etc. This report outlines the RF program for the TJ-IU torsatron under construction at CIEMAT [1] . The main objective of this program is to develop a technological basis (antenna arrays, RF sources, etc.) and to perform analysis of various scenarios of plasma production and heating suitable for plasma confinement and equilibrium studies in TJ-IU. Another goal is to explore convenient scenarios for the larger TJ-II heliac device, whose construction is beginning at CIEMAT [2].

2. RF scenarios

Theoretical studies, including the improvement of numerical existing models and the development of new ones, have started at CIEMAT and KhFTI. The first results from these studies have determined the basic scenarios that will be faced in the technological base as well as in the experimental program.

The main properties of the TJ-IU torsatron concerning the application of RF techniques in the range $\omega = \omega_{ci}$ (low magnetic field, small size, strong 3-D nonuniformity of the magnetic field in the radial direction and along the magnetic field lines) modify considerably the existing well studied techniques for large devices. It leads, in particular, to a strong FW-SW coupling outside the conversion zones and also to reduce the effect of opacity zones (at the plasma edge and near conversion zones) on the propagation of waves. These properties may exert favourable influences.

Preliminary studies performed with a 1-D model [3] for wave excitation in plasmas as well as with a ray tracing technique [4] have shown that the following scenarios are the most interesting for TJ-IU (some of them have been never applied before in RF experiments):

2.1. FW excitation from the low magnetic field side ($\omega \geq \omega_{ci}$)with the resonance layer inside the plasma column and the FW-SW conversion zone in the neighbourhood of the local Alfven resonance. This regime (which corresponds to one of the lowest frequencies among the listed above) is characterized by a strong slowing-down of the excited wave with longitudinal refractive index $N_{||}$=50 - 100. However, due to small plasma dimensions and strong absorption effects in the Alfven and $\omega = \omega_{ci}$ resonances, a high efficiency of the technique is predicted, in spite of FW cannot propagate in this case. Ion and electron heating are possible in this regime as well as current drive. This technique can be applied at the plasma production stage.

2.2. FW excitation in hydrogen-deuterium plasma with a high ^{3}He concentration (~ 20%). In this case FW-SW (IBW) coupling in the ion-ion hybrid resonance are important. As a result the predominant absorption by bulk ions (deuterons) and not only by ^{3}He ions, in

contrast to the minority techniques, is possible. This is an important effect because it weakens strong tail-growth of the distribution function of resonant ions inherent to the minority techniques (Fast ions are poorly confined in TJ-IU) and improves the RF heating efficiency.

2.3. FW excitation in hydrogen-deuterium plasma with ^{3}He minority Fig.1 gives the results for this regime obtained by solving Maxwell equations for a separate toroidal mode with $N_{||}$=20 and taking into account finite temperature effects. The FW is excited from the low field (external) side of TJ-IU (like LFS regime in tokamaks) with the frequency f=4.2 MHz, in a plasma with parameters: n_{He}/n_D=5%, n_H/n_D=50%, $T_{He} = T_H = T_D$ = 800 eV, T_e=400 eV. This wave is converted in the short SW in the region of D-H ion-ion hybrid resonance (see the P_k kinetic flux behaviour and the appearance of small scale oscillations of the E_R field). The SW is totally absorbed in the ion cyclotron resonance zone for He. Using SW absorption allows one to perform powerful experiments with the preferential heating of bulk ions and an improved confinement of resonant particles (cut off tail effect). Low value of the antenna quality factor, Q=13, (high value of the plasma resistance) is one of the main advantages of this scenario, therefore this method may be the most adequate for attainment of high efficiency of RF power coupling to plasma.

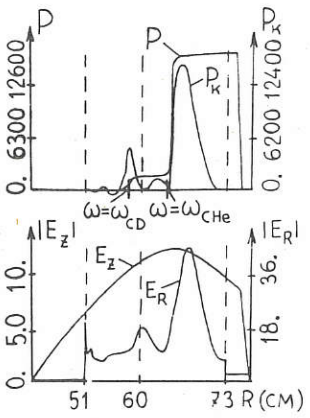

Figure 1

2.4. FW excitation in the region $\omega >> \omega_{ci}$ with electron Cherenkov absorption

Figure 2

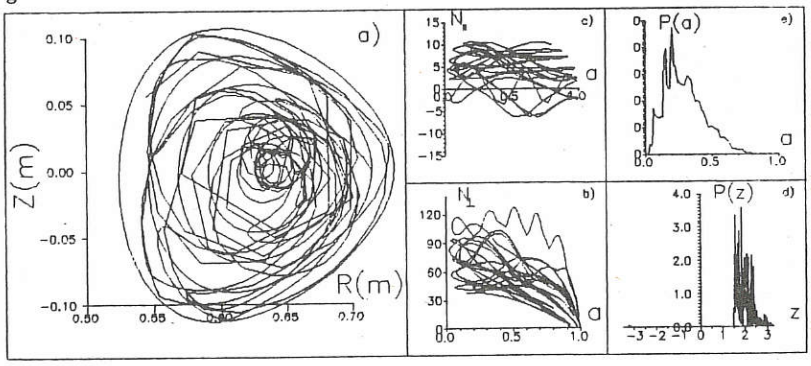

This regime will be used in TJ-IU in the range 30-150 MHz. Fig. 2 gives the calculation results obtained using a ray tracing technique for a hydrogen plasma with T(0)=1 Kev, $N_{||}$=10, f=150 MHz. As seen from the figure, after multiple reflections and refractions the ray fills the

plasma cross-section uniformly enough. Strong evolution of $N_{||}$ due to propagation under conditions of strong 3-D nonuniformity is observed. The phase velocity $v_{ph} = \omega/k_{||}$ becomes comparable with the electron thermal velocity, due to the increasing of $N_{||}$, and there occurs the absorption of the FW by thermal electrons. At the same time the power deposition profile is localized in the region with $a < 0.5$, where a is the magnetic surface coordinate. This method may be interesting for studying high-β regimes in TJ-IU and for current drive experiments

2.5. Direct SW (Ion Bernstein Wave) excitation in the range $\omega \leq 2\omega_{ci}, 3\omega_{ci}, 4\omega_{ci}$. This scenario is interesting mainly for plasma production. However other interesting regimes are possible including those with ion heating.

A number of other scenarios, which are not yet deeply studied, may prove promising under the TJ-IU conditions.

3. RF facility

To accomplish the started program of physical research a RF facility with wide range of possibilities is being developed:

The RF facility includes (Fig.3) a low frequency generator G1 with adjustable frequency in the range from 2-20 MHz having a symmetric or asymmetric output (to change the phasing of antennas). The output power of the generator is $P > 0.5$ MW with a pulse length of about 40 ms. The generator is fed by modulators M1 and M2 based on capacitive accumulators. Both modulators may be used to feed the low frequency generator in the programmed pulse regime (such a regime may be required at the plasma production stage) or one of them may feed another high frequency generator G2 (second phase). This second generator is necessary to accomplish electron heating scenarios ($\omega >> \omega_{ci}$) or scenarios with IBW excitation at $\omega > 3 - 4\omega_{ci}$. Power delivered by this generator is also $P > 0.5$ Mw. A phase rotator (PR) designed on an LC chain basis is switched into the feeder (F1, F2) to adjust smoothly the phase angle in the antennas. Supply system, feed-through insulator and the displacement system allowing to approach the plasma are the same for FW and SW antennae (A1,A2).

Figure 3

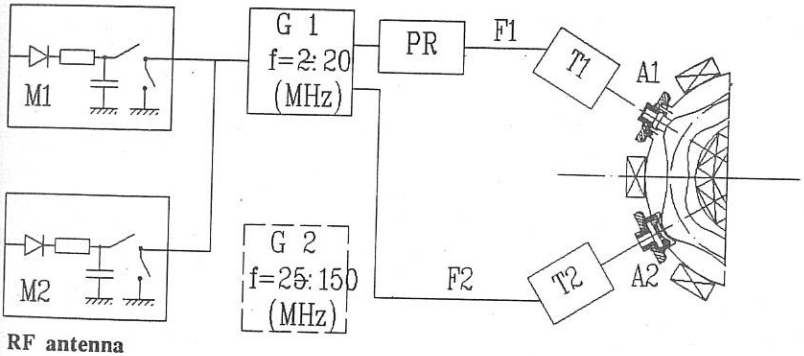

4. RF antenna

The antenna array includes 2 antennas that are installed in adjacent horizontal ports (Fig. 4), which only differ in the parts directly touching the plasma surface and determining the field

polarization.The FW antenna is constructed according to the "fir-tree" [5] pattern having low wave resistance with two current layers for a more efficient usage of the port cross-section. The surface of the electrostatic shield facing the plasma is coated with titanium nitride. Two types of current layers of the FW antenna are provided: long wavelength and short wavelength current layer. The latter can be applied only in the high frequency range f = 150 MHz.

Two types of SW antenna are also manufactured: the current one is completely similar to the FW antenna with the shield and the current layer rotated 90º, like in [5]. The relatively small radiating surface and, consequently, the limited power coupled to plasma is a disadvantage of this antenna.The potential type antenna [6] possesses ten times larger radiating surface compared with the current type as well as the possibility of some optimization of IBW coupling to plasma. Therefore the power coupled through the potential type SW antenna will be considerably higher than the one for the current-type antenna. The broad band (2-150 MHz) tuners (T1, T2) allow to syntonize antennae with the feeder for both types of antenna. It includes a set of circuit capacitors, adjustable tuning vacuum capacitors and adjustable inductance made on a coaxial resonator basis. The design and manufacture of the RF facility are planned to be finished at the end of 1992 and the program of experiments will start at the beginning of 1993.

A small device like TJ-IU has an easy access and a high versatility which allows to achieve several heating regimes. This makes this device very interesting for RF heating studies.

Figure 4

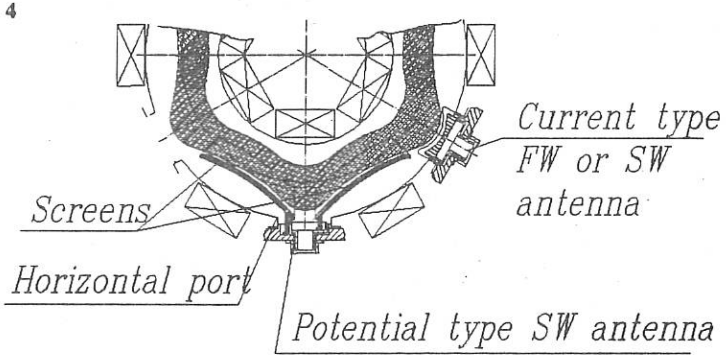

References

1. E. Ascasíbar, L. Almoguera, J. Alonso, J. Botija, J. Moreno, A. P. Navarro, M. A. Ochando, A. Perea, J. Sánchez. Fusion Technology 1990. North-Holland, vol 1, 577 (1991)
2. C. Alejaldre, J. Alonso, J. Botija, F. Castejón, J. Cepero, J. Guasp, A. L. Fraguas, L. García, V. Krivenski, R. Martin, A. P. Navarro, A. Perea, A. Rodríguez-Yunta. Fusion Technology **17**, 131 (1990).
3. Longinov A.V., Pavlov S.S., Proc. Eighth International Workshop on Stellarators. Kharkov (URSS), May 1991, p. 231.
4. Dyakov V.E., Longinov A.V., Proc. Eighth International Workshop on Stellarators. Kharkov (URSS), May 1991, p.227.
5. M. Ono et al. "Ion Bernstein wave heating experiments on PLT". 11th Proc. Kyoto-IAEA-CN-47/F-I-3.
6. A. V. Longinov. "Electromagnetic wave excitation using longitudinal electric fields". Journal of Technical Physics. Vol XLII, nº8, 1591 (1972).

The separation of Ion Bernstein waves and incoherent Ion Gyroresonant Ballistic waves in a dispersive, spatially varying medium

Tor Flå[1] , D. Cook[2] , E. Tracy[3] , and A.N. Kaufmann[2]

Abstract

Ion gyroresonant ballistic waves are studied in a spatially varying medium by a one dimensional, kinetic model equation. We solve this equation by a spectral deformation technique in Fourier space and are able to separate the coherent plasma wave modes from the incoherent gyroballistic waves. Asymptotically in a region in phase space where the coherent and incoherent modes are only weakly interacting we show that coherent plasma wave modes can be expressed in terms of the dominant discrete mode while the incoherent mode depends on the cumulated history of the coherent plasma mode.

Introduction

Our aim is to study minority fundamental and majority second harmonic ion gyroresonances and how mode conversion to ballistic modes in a spatially varying medium can lead to heating. This has already been studied in some detail in H. Ye's thesis and some other works [1,2,3,4]. The object here is to extract the collective Ion Bernstein wave (IBW) modes and the Incoherent Ion Gyroresonant Ballistic (IIGB) modes and clearify how to asymptotically solve the model equation which H. Ye derived for a one dimensional slab model for an incoming magnetosonic wave (MSW). The MSW mode frequency ω, match the gyroresonance condition at $x = 0$. If we neglect electron inertia effects, spatial variation of the resonant species background distribution,and assume a spatial variation in the magnetic field normal to the magnetic field direction, we can derive the following model equations for the first harmonic minority resonance($N = \pm 1$) and second harmonic majority resonance ($N = \pm 2$)

$$\begin{aligned}
(v - ie\frac{\partial}{\partial k})\hat{J}_{1,2} &= F_{1,2}\int dv\hat{J}_{1,2}, \\
F_{1,2}(v,k) &= g_{1,2}\beta_{1,2}(k), \\
\beta_{1,2} &= \beta_{1,20}(\frac{a_{1,2}}{(k^2-k_1^2)} + b_{1,2} + c_{1,2}(k^2-k_1^2)), \\
\int dv g_{1,2} &= 1, \\
e &= \frac{N\frac{\partial\Omega_r}{\partial x}|_{x=0}}{k_\parallel}.
\end{aligned} \tag{1}$$

Here 1 and 2 signifies first harmonic minority resonance or second harmonic majority resonance. The definition of $F_{1,2}, g_{1,2}$ and $\beta_{1,2}$ are given in [5]. The method of spectral deformation is a tool for analyzing

[1]IMR, University of Tromsø, N-9001 Tromsø,Norway
[2]LBL and Department of Physics, University of California, Berkeley, Ca 94720, USA
[3]Physics Department, College of William and Mary, Williamsburg,VA 23185, USA

phenomena associated with continous spectra and reveal the coherent plasma modes otherwise hidden in the spectrum[6]. Let us represent our equation as

$$\begin{aligned} i\frac{\partial}{\partial k}\hat{J} &= \mathcal{H}\hat{J}, \\ \mathcal{H}(v) &= \frac{1}{e}(v - F(k,v)\int_{-\infty}^{\infty} dv'), \end{aligned} \tag{2}$$

Notice that $\mathcal{H}$ is Hermitian with respect to the indefinite inner product
$< J, J >= \int_{-\infty}^{\infty} dv' g(v',k) J^* J$ where $\hat{J} = gJ$ (c.f.[7]). The operator in fact happens to be exactly the same as can be defined for a timedependent background distribution which is Fouriertransformed in space[6] and will therefore have the same structure of quadruples of discrete eigenvalues[7].The spectral deformation technique associate the operator ($\mathcal{H}$) with a one parameter family of operators $\mathcal{H}(\theta) = U(\theta)\mathcal{H}U(\theta)^{-1}$ which depend analytically on the parameter θ. Since we choose the one parameter group U to be the group of velocity space translations, it follows that we have to study the equation for the analytically continued $\hat{J}(\hat{v},k)$ where the integration contour for $\hat{v}$ is taken along a line parallell to the real axis. The following eigenfunction expansion is then obtained for eq.(2)

$$\hat{J}(\hat{v},k) = \sum_j d_j \hat{X}_j(\hat{v},k) exp(-\frac{i}{e}\int_{k_0}^{k} dk' \omega_j(k')) + \int_{\Gamma_\omega} d\omega d(\omega)\hat{X}(\hat{v},k,\omega) exp(-\frac{i}{e}\omega(k-k_0)). \tag{3}$$

Here the discrete (indexed by j) and the continuum eigenfunctions are normalized such that

$$\begin{aligned} \int_{\Gamma_\omega} d\hat{v}\hat{X}_j(\hat{v},k) &= 1, \\ \int_{\Gamma_{\hat{v}}} d\hat{v}\hat{X}(\hat{v},\omega,k) &= \phi(\omega,k). \end{aligned} \tag{4}$$

The coefficients d_j and $d(\omega)$ are given by projections of the eigenmodes on the distribution $\hat{J}(v,k_0)$ prescribed at some wavenumber k_0[5]. The discrete eigenvalues can be found by solving the following extended dispersion relation

$$\Omega(\omega_j(k),k) = 1 - exp(ie\frac{\partial^2}{\partial k \partial \omega})(\beta(k) Z_{-p}(\omega))|_{\omega=\omega_j},$$

$$\begin{aligned} Z_{-p}(\omega) &= \int_{-\infty}^{\infty} \frac{g(v,k)}{v-\omega-ip0} dv, \\ p &= sign(e). \end{aligned} \tag{6}$$

We will assume that $\omega_j(k)$ can be expanded in the following perturbation series where ϵ is a formal ordering parameter signifying the smallness of terms $\sim O(e\frac{\partial^2}{\partial k \partial \omega})$

$$\omega_j = \omega_j^{(0)} + \epsilon\omega_j^{(1)} + ... + \epsilon^n \omega_j^{(n)}. \tag{7}$$

However, only one eigenmode gives the correct asymptotic dispersion (see below) relation for large k and we henceforth index it by $j = 1$. Far from the mode conversion region we will identify $\bar{J} = \int \hat{J} dv$ by the coherent modes (MSW and IBW) and $\tilde{J} = J - \bar{J}(gJ = \hat{J})$ by the incoherent ion gyroballistic modes(IIGW). As long as the coherent IBW mode is only weakly interacting with the IIGW mode it turns out to be consistent to approximate the coherent IBW mode by

$$\begin{aligned} \bar{J}(k) &\sim \bar{J}(k_0) exp(-\frac{i}{e}\int_{k_0}^{k} \bar{\omega_1}(k')dk'), \\ \bar{\omega_1} &= \omega_1 - \epsilon\omega_1^{(1)}. \end{aligned} \tag{8}$$

From this result we can infer the absorption of the coherent wave action into incoherent wave action

$$A = 1 - exp(\frac{2}{e}\int_{k_0}^{k} Im(\bar{\omega}_1 dk') \tag{9}$$

It is interesting to transform the amplitude of the coherent mode in the asymptotic region to the x representation by the method of stationary phase for large x

$$\begin{aligned} \bar{J} &\sim \frac{\bar{J}(k_0)}{|\frac{1}{e}\frac{d\bar{\beta}}{dk}(k(x))|^{\frac{1}{2}}} exp(-\frac{i}{e}\int_{k_0}^{k(x)} \bar{\omega}_1 dk' + ik(x)x + i\sigma\frac{\pi}{4}), \\ \sigma &= sign(\frac{1}{e}\frac{d\bar{\beta}}{dk}), \\ \bar{\beta}(k) &= \beta(k) - v_0. \end{aligned} \tag{10}$$

Here $k(x) = \bar{\beta}^{-1}(ex)$ corresponds to a branch of the asymptotic dispersion relation for the coherent mode $D_j(k, x) = ex - \bar{\beta}(k) = 0$. v_0 is an averaged velocity with respect to g (index 1, 2 suppressed). Eq(10) also coincides with the usual result for wave action conservation in the x-representation.

Discussion

Since we are neglecting electron inertia effects only the part of the kinetic dispersion tensor for the non-resonant species with components perpendicular to the magnetic field need to be taken into account. In addition we only consider the Hermitian part. The perpendicular part of the dispersion tensor barring the resonant terms, is approximated by

$$\begin{aligned} \underline{\underline{D}}_\perp &= \underline{\underline{D}}^0_\perp(\mathbf{n}) + \mathbf{n}^2_\perp \underline{\underline{\delta}}(\mathbf{n}_\parallel), \\ \mathbf{n} &= \frac{c}{\omega}\mathbf{k}. \end{aligned} \tag{11}$$

Here $\underline{\underline{\delta}}(\mathbf{n}_\parallel)$ gives the temperature dependent second order FLR(finite Larmor radius) corrections to the dispersion tensor.

For the second harmonic majority resonance coupling coefficient F_2 in the gyroballistic equation it will be consistent to neglect the FLR effects in the dispersion tensor completely for $k^2_{\perp x}$ close to resonance of the magnetosonic waves and gyroballistic waves and far from IBW resonance. For the first harmonic minority resonance one has to develop the dispersion tensor to second order in FLR effects since F_1 is not a FLR correction by itself. However, only the $n^2_\perp \delta_{xx}$ correction has to be kept because the other terms in the dispersion tensor are structurally stable to small corrections. Since we do not want to study the exact nature of the IBW resonance, we expand to first order in $(k^2_{\perp x} - k^2_1)$.(In this work k is used for simplicity for $k_{\perp x}$.) Here k_1 is the wavenumber for which the coupling coefficient is singular indicating gyroresonance in phase space.

To discuss the ion cyclotron heating for the majority second harmonic gyroresonance and minority first harmonic gyroresonance, it is necessary to study the asymptotic properties of the coupling coefficient $\beta_{1,2}(k)$. We find that in both cases the coupling coefficient is singular at some $k = \pm k_1$ and approach a quadratic function for large k in our local approximation around gyroresonance in phase space. $F_{1,2}(v, k)$ determines the eigenvalue ω_1, corresponding to the dominant asymptotic mode at large $\beta_{1,2}(k)$. The asymptotic value of the discrete eigenvalue for large k and $\beta_{1,2}$ is to lowest order

$$\begin{aligned} Re(\omega^0_1) &\sim -\bar{\beta} = ex, \\ Im(\omega^0_1) &\sim -p\pi(ex)^2 g(ex). \end{aligned} \tag{12}$$

We find the normalized indefinite metric function in the coupling coefficient to be

$$g_{1,2}(v, k_\parallel) = \frac{(\frac{k_\parallel v}{N\Omega_r}\bar{\kappa}_{\parallel r1,2} + \bar{\kappa}_{\perp r1,2})}{(\frac{k_\parallel \Delta v_{\parallel r1,2}}{N\Omega_r} + \bar{\kappa}_{\perp r1,2})} g^{(0)}_r(v),$$

(14)

$$\kappa_{\|r,i} = -\frac{1}{f_r^{(0)}}\frac{\partial f_r^{(0)}}{\partial(\frac{m_r}{2}v^2)}(\Omega_r\mu)^i, i = 1,2$$

$$\kappa_{\perp r,i} = -\frac{1}{f_r^{(0)}}\frac{\partial f_r^{(0)}}{\partial(\Omega_r\mu)}(\Omega_r\mu)^i,$$

$$\Delta v_{\|r1,2} = \int dV v\kappa_{\|r1,2}f_r^{(0)},$$

$$g_r^{(0)}\bar{\kappa}_{\|,\perp ri} = 2\pi\int d\mu\mathcal{J}\kappa_{\|\perp ri}f_r^{(o)},$$

$$\bar{\kappa}_{\perp ri} = \int dV\kappa_{\perp ri}f_r^{(0)},$$

$$g_r^{(0)} = 2\pi\int d\mu\mathcal{J}f_r(o).$$

Here $f_r^{(0)}, \mathcal{J}, dV$ and μ are the resonant species background distribution function, the velocity volume element in guiding center coordinates and the magnetic moment coordinate respectively. Let us consider the mode conversion at $k = -k_1$ for high field incidence. In this case one finds the approximate relative action fluxes for transmission of the MSW mode(T), conversion to the IBW mode (C) and absorption through the the IIGW modes for $k \to -\infty$ (A)

$$T = exp(-2\pi|\eta|^2), \tag{15}$$

$$C = (1-T)exp(\frac{2}{e}\int_{-k_0}^{-\infty} Im(\bar{\omega}_1)dk'),$$

$$A = (1-T)(1-exp(\frac{2}{e}\int_{-k_0}^{-\infty} Im(\bar{\omega}_1)dk'),$$

$$T + C + A = 1.$$

Here $-k_0 < -k_1$ is some matching point just below the mode conversion point where the asymptotic theory for the discrete modes can be used. High field incidence is more complicated because it includes two mode conversion points $(k_1, -k_1)$ and it becomes necessary to use a full wave theory to include phase mixing and damping in and between the mode conversion regions. In [1,2,3,4] a free propagation model for the ballistic waves is used between the mode conversion points to account for phase mixing effects.

Acknowledgements

This research was partially supported by the U.S. Department of Energy under contract # DE-AC03-75SF00098 and NAVF.

References

[1]H. Ye, " Wave Dynamics in Phase Space and Ion Gyroresonant Absorption", Ph. D. Thesis, University of California at Berkeley(1989).
[2] H.Ye, A.N. Kaufman, Phys. Rev.L**60**, 1642 (1988).
[3] D.R. Cook, A.N. Kaufman, E.R. Tracy, T. Flå, Proceeding IX Conf. Radio Freq. Power in Plasmas, Charleston, 19-21 Aug. 1991.
[4] A.N.Kaufman, A.J.Brizard, D.R.Cook, E.R.Tracy, H.Ye, as in [3].
[5] T.Flå, D.R.Cook,E.R.Tracy,A.N.Kaufman, Ineternal report, IMR, University of Tromsø, 1991.
[6] J.D.Crawford, P.D.Hislop, Ann. Phys. **189**, 269(1989).
[7] J.Larsson, Phys. Rev.L**66**, 1466(1991).

Plasma heating and generation current drive study in the torsatron U2-M using ion Bernstein wave

Dyakov V.E., Longinov A.V.
Kharkov Institute of Physics and Technology, Kharkov, Ukraine

Experiments [1,2] have demonstrated a possibility to use slow waves (SW) in ICRF range (Alfven kinetic or ion Bernstein waves (IBW)) for plasma heating in stellarators. However up to now the processes of SW propagation and absorption in stellarators are poorly studied not only in experiment but also in theory. The main reason is difficulties in solving Maxwell equations with the account of 3-D nonuniformity of plasma inherent to stellarators. At the same time the general picture of SW propagation and absorption sufficiently well studied with 1-D models may be modified considerably for the 3-D nonuniformity case. With a number of restrictions the study of the SW propagation and absorption in ICRF range with the 3-D nonuniformity taken into account is accomplished by approximate solving Maxwell equations with the ray tracing technique. Such an approach has been used in Ref. [3] for the LH resonance region and in Ref. [4] for the IBW's. This report outlines the results of studies extending those of Ref. [4] on the investigation of IBW propagation and absorption in the U-2M torsatron. In contrast to Ref.[4] the main attention is devoted to the regimes in which ion heating is possible.

Complicated topography of the magnetic field in a stellarator (3-D nonuniformity) enables one to accomplish regimes of ion heating that have not been studied previously. Therefore below we consider the physical pattern of such regimes with a qualitative picture. Fig.1 shows the transverse refractive index $N_\perp^2$ dependence on the parameter ω/ω_{ci} for wave in plasma near the resonance $\omega = n\omega_{ci}$ zone ($n = 2,3...$) for various values of the longitudinal refractive index $N_\parallel^2$. As is seen from Fig.1 $N_\perp^2$ values for IBW's grow on increasing ω_{ci} (B growth at ω fixed) as well as on increasing $N_\parallel^2$. On increasing $N_\parallel^2$ the zone of IBW strong absorption at the resonance $\omega = n\omega_{ci}$ of bulk ions widens due to Doppler effect. Therefore at small $N_\parallel$ (for practical plasma parameters $N_\parallel \simeq 1$) the IBW propagation zone is limited by the zone of conversion into the FW and at larger $N_\parallel$ by the zone of strong cyclotron absorption. Such a pattern of IBW behaviour leads to the following effect. Let IBW be

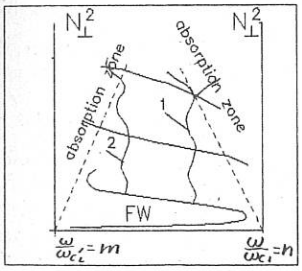

Fig.1

excited from the plasma edge near $\omega \simeq n\omega_{ci}$ with sufficiently low $N_\parallel$ (ray 1). This region is the most advantageous for efficient IBW excitation with external antennas due to small $N_\perp^2$. On propagating the wave in the plasma interior the wave enters the zone of strong cyclotron absorption at the resonance $\omega = n\omega_{ci}$ for bulk ions due to the decrease of the magnetic field modulus $|B|$ or, mainly, due to the strong increase of $N_\parallel$. As on increasing $N_\parallel$ the Cherenkov absorption by electrons enhances then, actually, the competition of two processes will take place: IBW absorption by ions and electrons. The main property of such a regime is as follows: the absorption will occur, first, by bulk ions, and, second, by particles with sufficiently high values of $v_\parallel = (\omega - n\omega_{ci})/k_\parallel$, because the quantity $(\omega - n\omega_{ci})$ is limited by a sufficiently large value in the zone for IBW propagation, third, the absorption occurs for the large $k\rho_i$ parameter ($k\rho_i \geq 1$), that switches on the efficient mechanism of tail cutting-off. These three circumstances make this scenario very attractive for powerful regimes of ion heating in stellarator-type traps because energy losses due to fast particles escape along banana trajectories may be strongly weakened. In particular, the effect of loss cones is weakened the role of which in the conventional regime of FW absorption by minority ions may be catastrophic, especially for small and medium size devices.

Similar picture occurs also for a scenario in which IBWexcitation is accomplished near the resonance $n\omega_{ci}$ for bulk ions and plasma contains ion minority of another type for which the cyclotron resonance zone ($\omega \simeq n\omega_{ci}$) is located at lesser ω/ω_{ci} values than for bulk ones. Concentration of such a minority may be sufficiently high so that as is shown in Ref.[5] the $m\omega/\omega_{ci}$ resonance zone is unattainable for IBW with small $N_\parallel$ due to the appearance of a conversion region (see Fig.1). However due to the increase of $N_\parallel$ on propagating IBW into the plasma interior a regime may be realized, in principle, when IBW approaches the region of strong cyclotron absorption by minority ions too, as it follows from the qualitative picture (ray 2, Fig.1). The above advantages are also inherent to this regime.

Illustrate the possibility of realizing such a heating scenario with two examples of heating a hydrogen plasma in the U-2M: 1) for IBW excitation near $\omega = 3\omega_{ch}$ and absorption at the resonance $\omega = 3\omega_{ch}$ by bulk ions and 2) for IBW excitation near $\omega = 2\omega_{ch}$ and absorption at the resonance $\omega = 3\omega_{cd}$ for deuterium minority ions with the following plasma parameters: $n_e = n_i = 5\cdot10^{13}\,cm^{-3}$, $T_e = T_i = 1$Kev, B = 2T.

The $\omega \leq 3\omega_{ch}$ regime (f = 85Mhz). Fig.2 shows the ray projection on the cross-section of the plasma column, $N_\parallel$ dependence on the magnetic surface mark α, ion $P_i(\alpha)$ and electron $P_e(\alpha)$ energy deposition profiles, spectral densities of energy absorption by ions $P(z_i^i)$. and electrons $P(z_o^e)$, where $z_n^i = (\omega - n\omega_{ci})/k_\parallel v_{Ti}$, $z_o^e = \omega/k_\parallel v_{Te} = v_\parallel^{res}/v_{Te}$.

As is seen from Fig.2 the ray approaches the central part of the column where it is absorbed by ions and electrons. This absorption is localized in a sufficiently narrow region ($\alpha \simeq 0.4$) due to a sharp increase of $N_\parallel$ of $N_\parallel$ in this region. As is seen from $P(z^i)$ the absorption occurs by particles with rather high $v_\parallel$ due to Doppler effect. In this case in the absorption zone the ratio ω/ω_{ci} is less than at the start point. Ions take 80% and electrons take 20% of all injected energy.

The $\omega \leq 2\omega_{ch}$ regime with absorption by deuterons at $\omega=3\omega_{cd}$ (f =43Mhz). All plasma parameters are similar to the preceding case but for the 20% minority of deuterium in a H-plasma. As is seen from Fig.3 the ray approaches the region with α =0.5 where it is totally absorbed. In this region the strong $N_\parallel$ increase also takes place. However here the absorption occurs at the resonance $\omega = 3\omega_{cd}$ for minority ions. As in the preceding case the absorption takes place by ions with high $v_\parallel$. Note that the sign changing of $N_\parallel$ (Fig.2) leads to the asymmetry of absorption by ions as well as by electrons with the symmetric spectrum of the antenna shifted with respect to the plane $\vartheta = 0^\circ$. This effect is similar to one described in Ref.[4] for tokamaks and it may lead to the steady current generation in a stellarator. In this case this current will be driven by the spectrum asymmetry effect in absorption by ions as well as by electrons and it requires a more detailed consideration of all the ray set describing the total picture of IBW excitation by a real antenna..

References

1. Byrchenko P.Ya, Volkov E.D., Kramskoj E.D., et.all P. v Zh.Exp.and Teor.Fiz.1972, v.15, p.250.
2. K.Nishimura, R.Kumazawa, T.Mutoh, et.all. Proc. 7th IAEA Workshop on Stellarators (Kharkov, 1991) p.235.
3. Grekov D.L., Dyakov V.E., Longinov A.V. Proc 12th European Conf. on Contr.Fusion and Plasma Heating (Bydapesht, 1985) V.10c., p.389
4. Dyakov V.E., Longinov A.V.Proc. 7th IAEA Workshop on Stellarators (Kharkov, 1991) p.227.
5. Longinov A.V., Pavlov S.S., Stepanov K.N. Proc. 11th Int. Conf on Plasma Physics and Contr.Fus., Kyoto, 1986, Vol.2, p.205.
6. Longinov A.V., Stepanov K.N. In: Vysokochastotnyj nagrev plasmy, Gorky, Applied Physics Institute, Ussr Academy of Sciences 1983, 105-210..

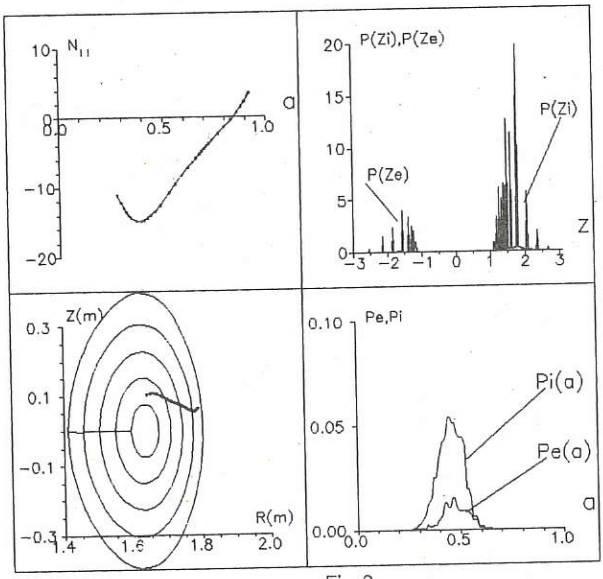
N∥
a
P(Zi),P(Ze)
P(Zi)
P(Ze)
Z
Z(m)
R(m)
Pe,Pi
Pi(a)
Pe(a)
a

Fig.2

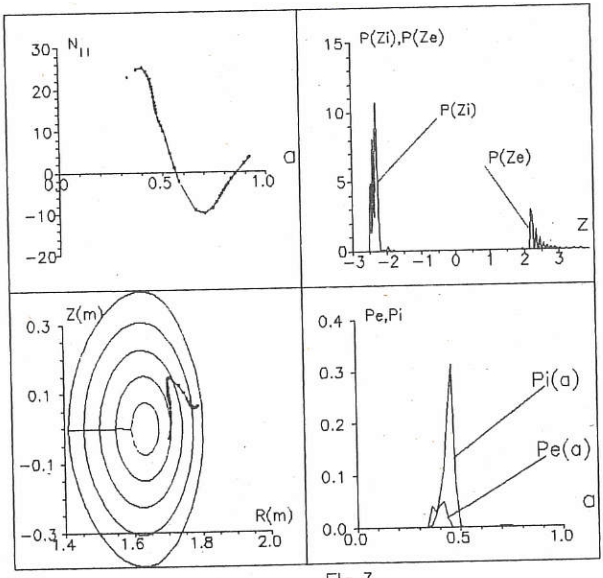
N∥
a
P(Zi),P(Ze)
P(Zi)
P(Ze)
Z
Z(m)
R(m)
Pe,Pi
Pi(a)
Pe(a)
a

Flg.3

RESISTIVE FLUX SAVING AND CURRENT PROFILE CONTROL DURING LOWER HYBRID WAVES ASSISTED CURRENT RISE IN TORE SUPRA

D. van Houtte, G.T. Hoang, E. Joffrin, P. Lecoustey, D. Moreau, F. Parlange, G. Tonon and J.C. Vallet.

Association EURATOM-CEA/DRFC CEN-CADARACHE
13108 Saint-Paul-lez-Durance (FRANCE)

1.INTRODUCTION

TORE SUPRA has been designed to study long pulse operation for times longer than the time required to reach equilibrium conditions in the plasma-wall interaction. The available flux swing is limited to 15 Wb then the plateau duration is about 12s in typical 1.3 MA ohmic discharges. This time has been extended to 35 seconds by applying Lower Hybrid (LH) waves during the flat top and the current rise. Taking into account the minimum flux consumed to rise the current, about half of the plasma surface flux is consumed in compensating the resistive losses during the current ramp [1]. So far as the current ramp is performed at low density in the presence of an electric field, LH current drive is an attractive method to reduce the flux consumption during the current rise phase. The flux saving and current profile control experiments described in this paper have been carried out with the assistance of the ohmic primary circuit at a line averaged electron density varying typically from $\bar{n}_e = 1x10^{19}\ m^{-3}$ *to* $\bar{n}_e = 2x10^{19} m^{-3}$ *at various current ramp-up rates, various LH power levels and various parallel wavenumbers. Two large multijunction launchers allow to couple up to 6 MW at a frequency of 3.7 GHz.*

2.RESISTIVE FLUX SAVING

For ohmic plasma discharges, the resistive voltage is typically V_{res}=.9 Volt and remains roughly constant during the current rise phase. With LH power this resistive voltage drops and the inductive voltage tends to increase due to a slight peaking of the current profile. Fig. 1 shows the time evolution of the plasma current, the internal inductance, the line averaged electron density, the LH power, the plasma surface flux change and the resistive component, for ohmic and LH assisted cases.The change in the surface flux consumption between the inductive (OH) and combined OH+LH current ramp-up comes mainly from the resistive flux saved and increases with the rf power level. The current increased from 0.7 to 1.4 MA at a rate of 0.4 MA/s while $\bar{n}_e$ varied from 1 to $2x10^{19}$ m^{-3}.

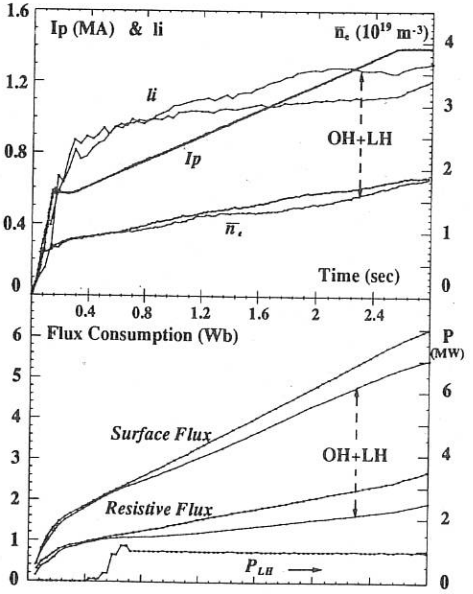

Fig. 1

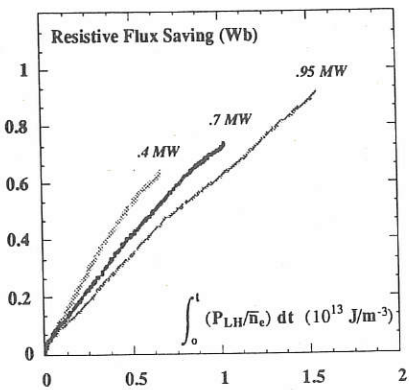

Fig. 2

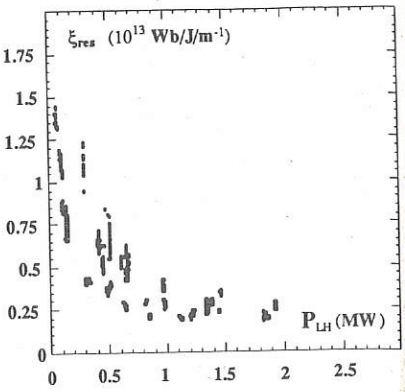

Fig. 3

Fig. 2 shows the resistive flux saving for three various LH powers as a function of the normalized rf energy input. First, we can note that the amount of resistive flux saved for the same rf energy is a function of the power level. In other hand, the resistive flux saving for a given rf power, does not increase linearly with the time integral of the LH power density. These two results are due to the electric field effect on suprathermal electrons and its dependence on the rf power and the electron density. By analogy with the definition of the global current drive efficiency given by $\eta_g \equiv (\bar{n}_e R I_p \Delta V_{res})/(P_{LH} V_{res}^{OH})$ where $\Delta V_{res} = V_{res}^{OH} - V_{res}^{OH+LH}$ represents the relative loop voltage drop, we have defined an efficiency for the resistive magnetic flux saving independent of the machine size as :

$$\xi_{res} = \Delta\Phi_{res} \Big/ \int_0^t dt \frac{P_{LH}}{\kappa\, a^2\, \bar{n}_e}$$

where κ is the plasma elongation and a its minor radius ($\kappa = 1$ and a = .8 m in TORE SUPRA) $\Delta\Phi_{res}$ is the resistive flux saving ($\Delta\Phi_{res} = \Delta\Phi^{OH} - \Delta\Phi^{OH+LH}$). Note that the plasma major radius does not enter in the definition of ξ_{res} as both the flux consumption (for a given electric field) and LH power (for given LH power and current densities) scale linearly with R. Fig. 3, where ξ_{res} is plotted as a function of the LH power, shows clearly that the resistive flux saving efficiency is enhanced at low LH powers due to the electric field effect. The resistive flux saving efficiency, ξ_{res}, varies between 0.5 and 1.5×10^{13} Wb/J/m^{-1} for power $P_{LH} \leq 0.5$ MW, and is about 0.25×10^{13} Wb/J/m^{-1} for LH powers, $P_{LH} \geq 1$ MW, for which the electric field effect is negligible. The efficiency varies little with the current ramp rates in the range dI_p/dt = .3 to .8 MA/s. These values, found during the current rise phase are similar to the flux saving efficiency obtained during the flat top phase.

This flux saving efficiency is consistent with previous experimental JT-60 results /2/ and can be used to extrapolate the potential saving of magnetic flux in ITER. Half of the minimum resistive flux consumed in the ITER ohmic ramp-up, given by $(C_{Ejima} \mu_0 R_0 I) / 2 \approx 35$ Wb (Poynting analysis method), could be saved in an operating scenario (I = 22 MA, a = 2.2 m, dI/dt =.3 MA/s, R_0 = 6 m, $\kappa_{f.t.}$ = 2) in which a LH energy $E_{LH}(GJ) \approx .7\, \kappa\, \bar{n}_e(10^{19}\ m^{-3})$, is injected during the current rise phase.

Up to date, only half of the resistive flux was saved by injection of constant LH power in the current rise because applying to high LH power can cause a MHD unstable current density profile at low plasma current level. However a judicious rf pulse shaping permits to inject higher rf energy during the current rise and save larger resistive flux.

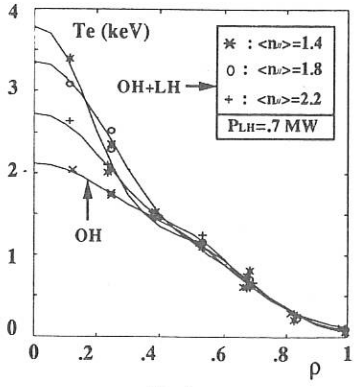

Fig. 4

3.CURRENT PROFILE CONTROL

The application of LH power during a low density current ramp-up tends to peak the thermal electron temperature profile. The peaking, defined as $T_e(0)/\langle T_e \rangle$, can reach the value of 4 which is two times higher than the ohmic one with only 1 MW. On figure 4, we have plotted the dependence of the electron temperature profile during the current rise phase in pure OH and LH assisted OH cases on three different phasings between adjacent modules, $\Delta\Phi = -90°$, 0° and +90° which correspond respectively to three different $\hat{n}_{//} \approx 1.4$, 1.8 and 2.2. Simultaneously the total current density profile, as inferred from the internal inductance l_i, peaks with respect to the ohmic one. Moreover, as indicated in figures 5 & 6, where is plotted the path of the internal inductance li as a function of the safety factor at the plasma edge $q_\psi(a)$, the current profile peaking is more pronounced as the LH power is high and the parallel wavenumber is low. The current profile broadening before the flat top phase is due to the decreasing of the I_{rf}/I_{oh} ratio when the current and the density increase during the current rise. For the highest power (P_{LH} = 0.95 MW, $\langle n_{//} \rangle$= 1.8) and the lowest wavenumber ($\langle n_{//} \rangle$= 1.4, P_{LH} = 0.7 MW), a large amplitude MHD activity is observed. This confirms that in this density range high phase velocity waves are more centrally absorbed than those with a small phase velocity. These peaked current profiles are maintained during the flat top phase to a level higher than in a pure OH discharge as indicated on Fig.7 where are plotted the steady state values of the internal inductance during the flat top phase for the seven shots shown in Fig.5 & 6.

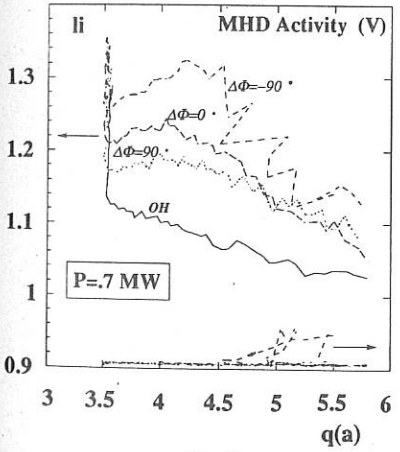

Fig. 5

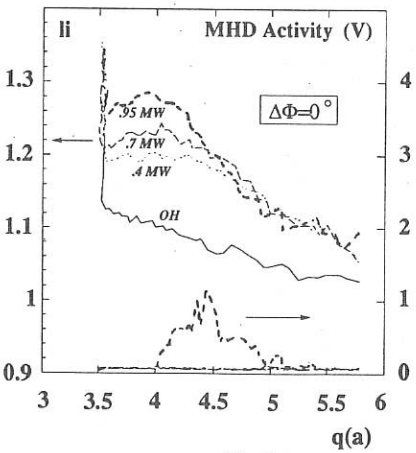

Fig. 6

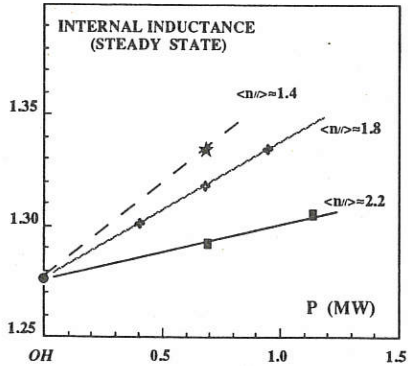

Fig. 7

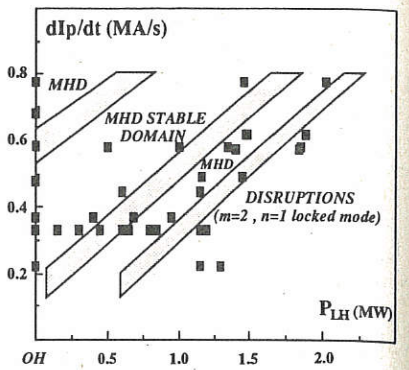

Fig. 8

A study of the energy confinement time as a function of the internal inductance l_i, shows that such peaked current profiles lead to an energy confinement time higher than the value predicted by the L-mode scaling law /3/.

In Fig. 8, we have represented the different MHD stability domains in a (dI_p/dt,P_{LH}) plane (*"MHD"* corresponds to a MHD unstable region).These domains are separated by large dotted transition zones. For a given current ramp rate $.5 \leq dI_p/dt$ (MA/s) $\leq .8$ which leads to a MHD unstable current rise in ohmic regime, the application of a low rf power ($.5 \leq P_{LH}$ (MW) ≤ 1.5) reduces the MHD Kink mode as compared to the OH cases. This leads to ramp up the current inside a MHD stable $(q_\psi(a), l_i)$ domain at a rate which is larger than the one achieved in the ohmic operation regime. Unfortunately, for a given ramp-up rate, LH power increasing (for example, $P_{LH} > 1$ MW for $dI_p/dt \approx .4$ MA/s) has a strong destabilising effect on the m=2, n=1 rotating tearing mode which increases with the power level, then locks and leads often to a major disruption or a poor flux saving efficiency. However a quiescent MHD regime can be maintained by accelerating the current ramp-up when the LH power level injected is increased. This stabilisation is interpreted as the result of a favourable equilibrium current profile obtained by combining judiciously a broad OH current density profile controlled by the current ramp-up rate and a peaked LH current profile controlled by the phasing and the LH power.

4.SUMMARY

Resistive flux saving at densities $\bar{n}_e = (1 - 2) \times 10^{19}$ m^{-3} has been studied. High flux saving efficiency ξ_{res} (0.7×10^{13} Wb/J/m^{-1}) can be achieved for a low rf power ($P_{LH} = 0.5$ MW) due to the beneficial effect of the electric field on the suprathermal electrons. However for power higher than 1 MW, the efficiency is 0.25×10^{13} Wb/J/m^{-1}. This flux saving efficiency is comparable to the one obtained during the flat top phase.

The application of the LH power during a low density current ramp-up tends to peak the electron temperature and current density profiles. The rf power level, the parallel wavenumber and the current ramp rate allow to control the trajectories of the plasma discharges during the current rise inside the MHD stable domain in the $(q_\psi(a), l_i)$ plane.

REFERENCES

/1/ D. van Houtte et al., Proc. of 18th Eur. Conf. on Controlled Fusion and Plasma Physics (Berlin, 1991), Vol. 15C, part I, p61.
/2/ O. Naito et al., Nuclear Fusion 30 (1990) 1137.
/3/ G.T. Hoang et al., Global Energy Confinement in Tore Supra, this conference.

Initial Lower Hybrid Current Drive Results and First Two-dimensional Images of Hard X-ray Emission in PBX-M

S. von Goeler, N. Asakura[1], R. Bell, S. Bernabei, M.Chance, T.K. Chu, J. Dunlap[2], A .England[2], H. Fishman, G. Gettelfinger, N.Greenough, J. Harris[2], R. Hatcher, H. Herrman, D. Ignat, R. Isler[2], S. Jardin, S. Jones[3], R. Kaita, S. Kaye, J.Kesner[3], H.Kugel, B. LeBlanc, S. Luckhardt[3], F. Levinton[4], J.Manickam, M.Okabayashi, M.Ono, S. Paul, S. Preische, P. Roney, N. Sauthoff, T.Seki[5], S. Sesnic, J.Stevens, H. Takahashi, E. Valeo, and K. Voss

Princeton Plasma Physics Laboratory, Princeton N.J., 08543 USA
[[1]JAERI(Japan), [2]ORNL(USA), [3]MIT(USA), [4]Fusion Physics & Technology(USA), [5]NIFS(Japan)]

The Princeton Beta Experiment-Modification (PBX-M) is intended to explore concepts of advanced tokamak configurations, including the development of methods for current profile control. Detailed MHD ballooning mode calculations /1/ have shown that shaping the q-profile - in particular lowering of the current density at the plasma center while increasing it near the edge - can significantly improve the MHD stability of high beta plasmas, and lead to easier access to the second stability region. In the near term the primary experimental technique on PBX-M for shaping the current profile will be Lower Hybrid Current Drive (LHCD). For this purpose a 4.6 GHz LH wave heating system has been installed on PBX-M, utilizing klystrons on loan from MIT. The final system will have a nominal power rating of 2 MW at the source. At the time of this writing, 560 kW of RF power from half of the system has been successfully launched into the plasma. A detailed description of the experimental set up is given in reference /2/.

Unique to the Lower Hybrid System on PBX-M is the use of digitally programmable phase shifters. Each of the 32 wave guides in the coupler array has a rotary-field phase shifter, analogous to the Fox/3/ mechanical phase shifter. In the PBX-M design magnetically biased ferrite substitutes for the transmission line: variable phasing results from a change in the orientation of a magnetic bias that is produced in a stator assembly. The phase shifters were successfully tested in the presence of PBX-M magnetic fields. They allow coherent variations of the $n_{\parallel}$ spectrum in a few milliseconds, as shown in Fig.1. Note the variation of the reflected power during a single plasma shot with the phase changing from 180° to 45° at 15 ms time intervals. The usual good agreement between the experimental and the theoretical value of the reflection coefficient is found.

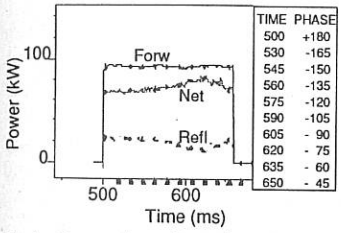

Fig.1: Forward, reflected, and net LH power vs. time for various phasings.

Lower Hybrid Waves produce a suprathermal tail of hot electrons/4/ through Landau damping of the wave spectrum, which manifests itself as a driven current. If Lower Hybrid waves are used to modify the current profile, the following critical issues have to be addressed: (a) the location of the wave damping, (b) the shape of the tail velocity

distribution, and (c) the diffusion of the suprathermal electrons in the plasma. A new diagnostic, a hard X-ray 2D tangentially-imaging camera[5] seems to be shedding some light on these questions. A schematic of the experiment is shown in Fig.2. The central element is an X-ray image intensifier tube with a 9" wide CsI scintillator screen which views the plasma through a .25" lead pinhole. Visible light is produced in the scintillator by the impinging X-rays (hv>30 keV). It releases electrons from a photo cathode which is evaporated on the CsI layer. The photoelectrons are accelerated to 25 keV and electrostatically focussed on a phosphor screen. The optical image from the phosphor screen is transferred by optical lenses onto a fiberoptic bundle. Further image intensification is achieved with a microchannel plate image intensifier, and the output detected by a 128X128 Reticon self-scanning photodiode array. The optical equipment was originally part of the PBX Soft X-ray Camera[6]. Typical output from the camera is shown in Fig.3c. It will be discussed later after we talk about the physical processes that lead to the formation of the hard X-ray images.

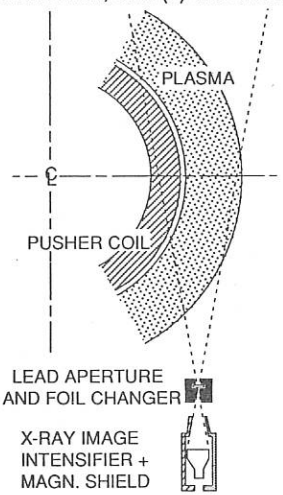

FIG.2: Schematic of the hard X-ray Camera on PBX-M

The hard X-ray emission has been modeled using a simulation code based on earlier work of Stevens[7]. This code calculates electron-ion bremsstrahlung, electron-electron bremsstrahlung, and recombination radiation for a relativistic electron velocity distribution function, which essentially is a Gaussian, characterized by three parameters: the parallel forward tail temperature $T_{\parallel f}$, the perpendicular tail temperature $T_{\perp}$, and the parallel backward temperature $T_{\parallel b}$ ('parallel' and 'perpendicular' refer to the magnetic field; 'forward' and 'backward' to the tail direction). Other distribution functions, like the Karney-Fisch distribution[8], can also be evaluated.

In Fig.3a we show a contour plot in momentum space of the distribution function ($T_{\parallel f}$ = 300 keV, and $T_{\perp} = T_{\parallel b}$ = 75 keV) that gives a reasonable fit to the experimental data. We also establish a radial profile for the suprathermal electrons in terms of magnetic flux surface Ψ (Ψ = 0 at the plasma center and Ψ=1 at the plasma edge). In the code, we can enter a magnetic surface Ψ_{se}, on which the suprathermal electrons are centered, and Gaussian spreads $\Delta\Psi_{sei}$ and $\Delta\Psi_{seo}$, which determine the density gradient of suprathermal electrons radially inwards and outwards from Ψ_{se}, respectively. The radial profile function (Ψ_{se} = .33, $\Delta\Psi_{seo}$ = .2, $\Delta\Psi_{sei}$ = .37) chosen for the comparison between experiment and theory is plotted in Fig 3b. The profile is hollow, and the density of superthermal electrons varies with the inverse major radius, i.e. it is smaller on the outside than on the inside, which we believe to be a reasonable approximation for predominantly passing particles. The location of the magnetic surfaces is obtained from the FQ code, a variation of the PEST code[9], that determines the equilibrium in PBX-M from magnetic flux loop measurements and Thomson scattering data. In order to perform the integration along a sight line, we use again the results of the MHD equilibrium code to predict the direction of the magnetic field

field vector, the angle between sight line and magnetic field, and the plasma density. The integration over sight lines is done for 12 different photon energies. Finally, an integration over all photon energies is performed for each sight line, which takes into consideration the absorption in the 3.0 mm thick aluminum window on the PBX-M tokamak and in the 1.0 mm thick aluminum window of the x-ray image intensifier, as well as the absorption efficiency of the 0.4 mm thick CsI scintillator layer in the X-ray image intensifier.

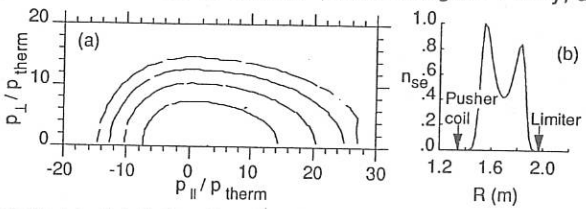

Fig.3: (a) distribution function and (b) radial profile of suprathermal electrons used in the simulation of Fig.3d.

A computed 50X50 pixel array is shown as a contour plot in Fig.3d, and compared with the 100X100 pixel experimental data, Fig.3c, utilizing common contour levels. The scale of these pictures becomes clear from a plot of the equilibrium, which is shown in Fig.3e. Shot 287677 represents a bean configuration with practically no indentation. The discharge is limited at major radius R = 1.97 m by an outside limiter. It has a plasma current of 179 kA, a peak plasma density of 2.8×10^{13} cm^{-1}, and a toroidal magnetic field on axis of 14.4 kG. 195 kW of lower hybrid power with -105° phasing was injected into the plasma at time 400 ms. The measurement was performed between time t = 440 and 480 ms. Returning now to our comparison of experimental and theoretical data, both Fig.3c and Fig.3d exhibit a steep gradient of the X-ray intensity in the midplane on the outside, which - in the computation - depends mostly on the value of $\Delta\Psi_{seo}$. The intensity reaches then a plateau, the right hand edge of which is determined by the value of Ψ_{se}. The slope in the plateau region is determined by the value of $\Delta\Psi_{sei}$. The intensity reaches then a maximum which has a characteristic sickle shape. It corresponds to the inner maximum of the radial profile function. Still further in, the intensity drops. The gradient in this region is determined mostly by the value $T_{\parallel f}$ (for a large ratio $T_{\parallel f} / T_\perp$), because the X-ray emission along a sight line is more and more perpendicular to the magnetic field. There is a very steep drop of the intensity by a factor of 2 in this region, which is due to the fact that the armor of the

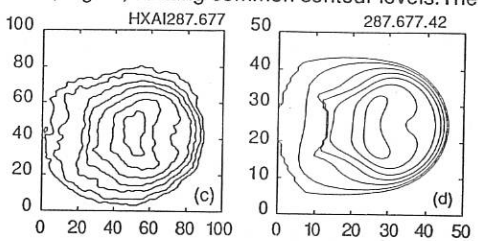

FIG.3 c + d: Contour plot of the experimental data (c) and the simulation (d). Contour levels are 0.12, 0.16, 0.23, 0.32, 0 .44, 0.62, 0.87.

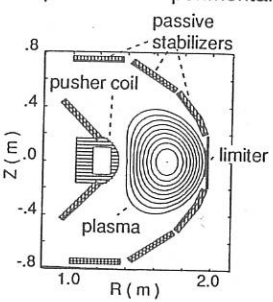

Fig.3e Equilibrium for shot 287677 at t=470 ms.

pusher coil of PBX-M occludes emission from the second path through the plasma along the sight line, as shown in Fig.2.

The agreement between the experiment and the simulation is quite good qualitatively. There is a quantitative discrepancy, however, in the height of the right hand edge of the plateau: the shoulder has a value of ≈.4 in the experimental data (Fig.3c) and, in the simulation (Fig.3d), it could not be made to decrease below ≈.55. Possible explanations include the fact that we do not allow for variations of the distribution function with radius. (This feature is included in the code but has not been checked out and implemented yet). An alternative interpretation /8/ which has been proposed for the hollow profiles on PLT assumes that that the suprathermal electrons are more energetic in the outer regions of the plasma. Furthermore, we have not yet installed absorber foils on PBX-M. A comparison of images measured with different absorber foils should allow a much better determination of the shape of the electron velocity distribution function.

At present, the exact plasma conditions for producing hollow-type profiles (more accurately the sickle shape of images) have not been identified yet. Even in shot 287677, the hollowness was reduced later in time during LHCD and may have disappeared altogether. The existence of a finite Ohmic one-turn loop voltage and the presence of electric fields that lead to runaway electron production could be an important factor to modify the behavior of energetic electrons and, consequently, the structure of the X-ray radiation pattern. During the initial PBX-M operation period, the intensity of the x-ray emission and similarly the reduction in loop voltage depended strongly on the phasing of the wave guides. The best launching angle has been near -90° corresponding to $n_{\parallel} = 2.1$ both in circular and bean-shaped plasmas. In summary, the hard X-ray imaging system is showing promise as a sensitive LH diagnostic, and further studies, including the interaction between LH and ion Bernstein waves, are in progress on PBX-M.

Acknowledgements: We are grateful to the PBX-M operations crew headed by J. Semler. We also appreciate the technical assistance of J.Gorman and R.Such. This work has been supported under DOE contract No DE-AC02-76-CHO-3073

/1/ R. Grimm, M. Chance, A. Todd, J. Manickam, M. Okabayashi, et al.: Nuclear Fusion **25**, p.805 (1985).

/2/ N. Greenough, S. Bernabei, M. Norris, S. Schweitzer, and R. Schwartz: Proc.14th IEEE Symposium on Fusion Engineering, San Diego, Vol.1, p.126 (1991).

/3/ A. Gardner Fox: Proc. I.R.E. p.1489 (1947) .

/4/ S. von Goeler, J. Stevens, C. Karney, S. Bernabei et al.: Proc. 5th Topical Conf. on Radio Frequency Plasma Heating, Madison /Wisconsin (1983).

/5/ R. Kaita, S. von Goeler, S. Sesnic et al.: Rev. Sci. Instrum. 61, p.2756 (1990).

/6/ R. Fonck, M. Reusch, K. Jaehnig, and P. Roney, SPIE Vol.691, p.111 (1986).

/7/ J. Stevens, S. von Goeler, S. Bernabei, M. Bitter, T.K. Chu, et al.: Nuclear Fusion 25, p.1528 (1985)

/8/ C. Karney and N. Fisch: Phys. Fluids 22, p.1817 (1979).

/9/ J. Johnson, H. Dalhed, J. Greene, R. Grimm, et al.: Comput. Phys 32, p.212 (1979).

PERFORMANCE OF THE LHCD IN HIGH CURRENT REGIME IN JT-60U

T. Imai, K. Ushigusa, Y. Ikeda, S. Ide, O. Naito, M. Seki,
T. Kondoh, M. Nemoto, S. Wolfe, M. Sato and H. Takeuchi

Japan Atomic Energy Research Institute,
Naka Fusion Research Establishment,
Naka-machi, Naka-gun, Ibaraki-ken, 311-01 JAPAN

1.Introduction

Powerful and efficient current drive (2MA driven current, efficiency $\eta_{CD} \equiv \bar{n}_e R_p I_{RF}/P_{LH} = 0.34 \times 10^{20} m^{-2} A/W$ and high power up to ~5 MW) was demonstrated in JT-60 LHCD /1,2/. In JT-60U, the designed plasma current is increased up to 6 MA in divertor discharge with major radius of 3.4 m and deuterium plasma operation. LHCD program in JT-60U aims further progress of LHCD to explore steady state tokamak reactor and study the profile control. The LHCD power of 2-3 MW from 24x4 multi-junction (MJ) launcher was planned from 1991 to 1992 (phase 1) and will be about 10 MW in 1993 (phase 2) by adding new 48x4 MJ launcher. At present the maximum injected power is about 1.8 MW. The emphasis of the phase 1 experiment is placed on the physics understanding of the LHCD to clarify the behavior of the fast electrons /3/ and the study of the performance of the LHCD in high current regime for the preparation of the coming high power experiment in the phase 2 experiment.

2. Experimental Results

Maximum LHCD power of ~1.8 MW at the frequency of 2 GHz has been injected into JT-60U plasma with B_t=3-4T, I_p=1-3 MA and $\bar{n}_e$ = 0.3 - 2 $\times 10^{19}$ m^{-3} in divertor discharge. The brief description of the wave launching system is given in the companion paper /4/. The peak $N_{||}$ can be varied from 1.0 to 3.0 with good directivity by changing the phasing between adjacent modules ($\Delta\phi$) composing the multi-junction launcher. The usual current drive experiment was carried out with $N_{||}^{peak}$~1.4 ($\Delta\phi$~135°) unless notified. In spite of the carbon first wall, density control was easy and very low density plasma far less than $1 \times 10^{19} m^{-3}$ was routinely possible by keeping the wall temperature 150°C after 300°C baking.

The time evolution of the 2MA LHCD discharge is shown in Fig. 1. Line averaged electron density $\bar{n}_e = 0.3 \times 10^{19} m^{-3}$ and kept constant during the LH pulse. The loop voltage dropped to almost 0 with the LH power of 1.2 MW. Current drive efficiency $\eta_{CD} \cong 0.17 \times 10^{20} m^{-2} A/W$ was obtained. The value seems to be moderate because of the very low density, but is substantially higher than that in the previous 2 MA current drive by the conventional launchers in the same density region in JT-60 /1/. The improvement of the efficiency is easily understood from better directivity and sharper spectrum than those in the previous case.

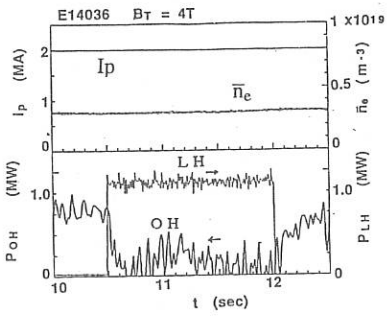

Fig. 1 The example of the 2MA LHCD discharge.

$N_{||}$ dependence of the current drive efficiency was studied by changing the phasing between the modules. Simple formulation of theoretical efficiency is given by Fisch /5/. It is applied to actual $N_{||}$ spectrum by J. Stevens /6/ and obtain the approximate theoretical efficiency which is proportional to $<N_{//}^{-2}>$. The $<N_{//}^{-2}>$ is defined as

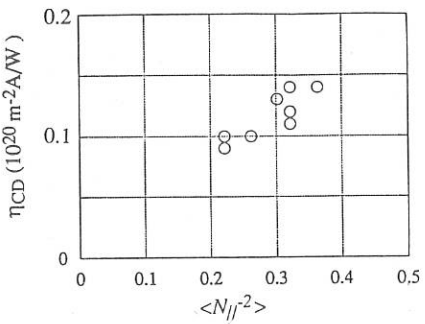

Fig. 2 Current drive efficiency vs $<N_{//}^{-2}>$.

$$<N_{//}^{-2}> \equiv \left(\int_{N_{||}^{acc}}^{\infty} N_{||}^{-2} P(N_{||}) dN_{||} \right) - \int_{-\infty}^{-N_{||}^{acc}} N_{||}^{-2} P(N_{||}) dN_{||} \Big) \Big/ \int_{-\infty}^{\infty} P(N_{||}) dN_{||},$$

where $N_{||}^{acc}$ is the accessibility limit of the $N_{||}$. It is seen the better directivity and sharper spectrum within the $N_{||}^{acc}$ limit gives the better efficiency. The experimentally obtained data of the η_{CD} are plotted as a function of $<N_{//}^{-2}>$ in Fig. 2, where the I_p=1.2MA and $\bar{n}_e \sim$

$0.5x10^{19}m^{-3}$. It is seen that the experimental values of the η_{CD} increase as the $<N_{//}^{-2}>$ increases, as expected. It is found that the design of the $N_{||}$ spectrum for the improvement of the current drive efficiency is quite important as mentioned before. The dependence of the experimental η_{CD} on $<N_{//}^{-2}>$ is slightly weaker than linear due to the $N_{||}$ upshift /7/.

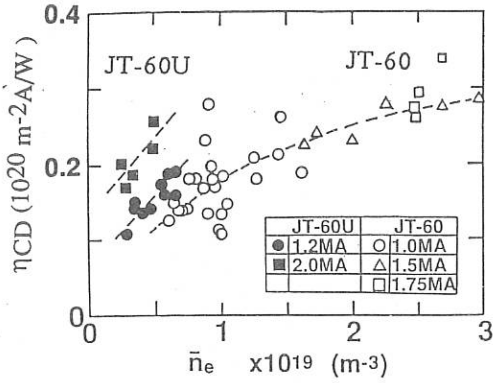

Fig. 3 Current drive efficiencies as a function of the density in JT-60U LHCD comparing with those in JT-60.

It was reported in JT-60 LHCD that the η_{CD} increases with density increase, since $\eta_{CD} \propto 1/(Z_{eff}+5)$ and the Z_{eff} decrease as density increases /8/. The efficiency η_{CD} obtained in this series of experiment are compared with the previous results in JT-60 as a function of the density. The maximum value of the η_{CD} at present is $\sim 0.25x10^{20}m^{-2}A/W$ and is still low due to low operational density. It is also seen that if we compare the η_{CD} in the same density region, the values in JT-60U is similar to those in JT-60 with the same plasma current discharge where the same type of the multi-junction launchers were used. But the values with 2MA is definitely higher than the previous ones. This is consistent with the previous T_e scaling of the η_{CD}, since higher T_e is expected in higher plasma current discharge /7/. From these results and deducing the higher η_{CD} is expected in the higher density region in JT-60U.

3. Effect of fast electron loss

It is often said that direct loss of the fast electrons to the first wall degrades the current drive efficiency and heating efficiency in LHCD experiments in small and medium size tokamaks but is predicted to be small in large tokamks with higher I_p and larger minor radius. The effect of this direct loss, actually, seemed to be small or negligible in JT-60 LHCD, since the value of the current drive efficiency agrees well with theory if $N_{||}$-upshift

is taken into account, and the confinement time of the LHCD plasma is similar to or better than NBI heating plasma /2,7/. These results indicate the slowing down process dominates the power flow of the fast electrons produced by the LHCD power in the core plasma.

Direct evidence of this fact has not been shown yet. Decay of the fast electrons and its profile measured from hard X ray signal have been studied and have shown that the diffusion loss of the fast electrons is small in JT-60U LHCD /3/. One more evidence to show this fact is obtained from the estimation of the loss power of the fast electrons hitting the divertor plate /9/. The X ray signal from the divertor plate is generated by the bremsstrahlung of the fast electrons hitting it and its intensity is approximately proportional to the loss power if the energy spectra of the fast electrons are not quite different. The X ray intensity is normalized by the IRTV camera signal and the loss power due to the direct loss of the fast electrons was estimated. The loss power is higher in lower density, high phase velocity and lower plasma current as expected. The maximum loss power is estimated to be less than 10 % of the total even in the condition of the very low density ($\sim 0.5 \times 10^{19} m^{-3}$), high phase velocity ($N_{\parallel}=1.4$) and low Ip (=1.2 MA). This is consistent with the decay of the fast electron measurement in JT-60U /3/ and previous results of the current drive efficiency and the confinement of LHCD plasma in JT-60.

4. Summary

The driven current of 2 MA has been achieved with 1.2 MW power. The current drive efficiency is substantially higher than that in 2MA discharge of JT-60, but is still moderate due to high Z_{eff} in the low density plasma at present. Effect of the direct loss of the fast electron on the current drive efficiency is small or negligible from HX measurement and X ray signal from divertor plate in JT-60U as expected. The maximum current drive efficiency is $0.25 \times 10^{20} m^{-2} A/W$ at present but is expected to increase in the coming experiment with higher density and higher power.

Acknowledgement

The authors are grateful for many useful discussions with menbers of the JT-60 Team.

References

/1/ T. Imai et al., Nuclear Fusion **28**(1988)1341-1350.
/2/ K. Ushigusa et al., Plasma Phys. and Cont. Fusion, **32** (1990)853.
/3/ T. Kondoh, et al., in this conference.
/4/ M. Seki, et al., in this conference.
/5/ N. J. Fisch, Phys. Rev. Letters **41**(1978)873.
/6/ J. Stevens, et al., Nuclear Fusion **28**(1988)217.
/7/ T. Imai et al., in Plasma Phys. and Controlled Nuclear Fusion Research 1990 (Proc. of 13 th Int. Conf., Washington) Vol. 1, IAEA, Vienna(1991) 645.
/8/ K. Ushigusa et al., Nuclear Fusion **29**(1989)1052-1055.
/9/ K. Ushigusa, private communication.

CHANGE OF INTERNAL INDUCTANCE AND ANISOTROPY DURING LOWER HYBRID CURRENT DRIVE IN ASDEX

F. Leuterer, F.X. Söldner
Max-Planck Institut für Plasmaphysik, D-8046 Garching, Germany
R. Bartiromo
ENEA, Frascati, Italy
S. Bernabei
Plasma Physics Laboratory, Princeton, USA

1) Introduction

In lower hybrid experiments we observe sawtooth stabilisation, change in the MHD-modes etc., indicating a varying current profile j(r), /1,2/. The internal inductance l_i gives an integral information about j(r) and is usually obtained from magnetic measurements, /3,4,5/, by subtracting β_{dia} from (Λ + 1), resulting in

$$D = (\Lambda + 1) - \beta_{dia} = (\beta_{par} - \beta_{perp}) + l_i/2. \qquad (1)$$

During low density current drive the anisotropy term ($\beta_{par} - \beta_{perp}$) is nonzero and positive. A change in the internal inductance is then very difficult to discriminate against the anisotropy term.

In experiments with feedback controlled constant plasma current I_p, the evaluation of the primary current rate of change, $d/dt(I_{oh})$, provides an independent method to determine changes in l_i. Any cause for a possible change of I_p, like noninductive current drive I_{rf} or release of magnetic energy due to a change in l_i, leads to a variation of $d/dt(I_{oh})$ according to the circuit equation

$$M_{oh,p}\, d/dt(I_{oh}) = (I_p - I_{rf})\, R_p + 0.5\, I_p\, d/dt L_p. \qquad (2)$$

Here $M_{oh,p}$ is the mutual inductance between transformer coil and plasma, R_p and L_p are resistance and inductance of the plasma.

The results reported here were obtained with the ASDEX 2.45 GHz lower hybrid system /6/.

2) Example

In fig.1 we show a shot (B_t=2.8 T, $\overline{n_e}$=1.35 10^{13} cm^{-3}, I_p=0.42 MA) where current drive with a low $N_{||}$ spectrum ($\Delta\phi$=75°, $N_{||}$=+1.8, $P_{75°}$ =0.695 MW) was applied from 1.0-1.8 sec, and from 1.4-1.8 sec additionally a symmetric high $N_{||}$ spectrum ($\Delta\phi$=180°, $N_{||}$=±4.4, $P_{180°}$ =0.23 MW). In the time interval 1.4-1.8 sec D is decreasing, indicating a decreasing l_i. Assuming that the high $N_{||}$ waves do not further change the anisotropy, i.e. $\Delta D = \Delta l_i$, we can calculate the related $d/dt(I_{oh})$. Its contribution to U_{loop} is $M_{oh,u}\, d/dt(I_{oh})$ and is compared in fig.1(dashed line) with the experimental result (solid line). Unfortunately I_{oh} was recorded only with a sampling rate of 5 msec, so we had to integrate over 15 msec for the calculation of $d/dt(I_{oh})$. But we still find good agreement.

The positive ΔD during 1.0-1.4 sec, however, is not due to an increasing l_i. It is caused by increasing anisotropy ($\beta_{par} - \beta_{perp}$) because of the high energy electrons resonant with the low $N_{||}$ waves. To show this, we compare the time variations of D and of $M_{oh,u}\, d/dt(I_{oh})$. In fig.1 we have $U_{loop} \approx 0$, thus a change in R_p does not contribute to equ.2. The variation of

$M_{oh,u}$ d/dt(I_{oh}) then reflects a change of l_i only. The experimental $M_{oh,u}$ d/dt(I_{oh}) indicates a small drop in l_i although ΔD is positive. If the ΔD would correspond to a positive Δl_i, then $M_{oh,u}$ d/dt(I_{oh}) should follow the dashed-dotted line in fig.1, which is not the case. This means that the positive ΔD in the first time interval is mostly due to anisotropy. Estimating the small drop in l_i from $M_{oh,u}$ d/dt(I_{oh}), $\Delta l_{i,75°} \approx -0.07$, we can calculate the anisotropy, which is about 30% larger than ΔD (dotted line in fig.1).

3) L_i-variations with combined spectra

The deposition of low $N_{||}$ current drive power is shifted radially by the additional high $N_{||}$ power,/1/. The related drop in l_i, $\Delta l_{i,180°} \approx \Delta D$, depends on the high $N_{||}$ power level $P_{180°}$ as shown in fig.2 (B_t=2.8 T, $\overline{n_e}$=1.35 10^{13} cm^{-3}, I_p=0.42 MA). Note that this $\Delta l_{i,180°}$ is additional to the small $\Delta l_{i,75°}$ occuring already during the first time interval where only low $N_{||}$ power is applied as described in fig.1.

We also get a change of Δl_i varying the high $N_{||}$ at constant high $N_{||}$ power, as shown in fig.3 (B_t=2.2 T, $\overline{n_e}$=1.35 10^{13} cm^{-3}, I_p=0.42 MA). Here high $N_{||}$ power, $P_{\Delta\phi}$ =180 kW (different $\Delta\phi$), is applied from t = 1.2-2.2 sec, while low $N_{||}$ power, $P_{90°}$ =780 kW, is applied from 1.7-2.7 sec. Initially the low $P_{\Delta\phi}$ produces only a negligable change in l_i as seen in the $M_{oh,u}$ d/dt(I_{oh}) curves. However, as soon as the 90° power is added, we see a remarkable drop in l_i, which is stronger for higher values of $N_{||}$ of the high $N_{||}$ spectrum. At t=2.2 sec $P_{\Delta\phi}$ is switched off and the strong drop in l_i, occuring at t=1.7 sec, is now reversed as seen in the $M_{oh,u}$ d/dt(I_{oh}) curves. The magnitude of ΔD, however, is quite different in the time intervals 1.7-2.2 sec and 2.2-2.7 sec, the reason being the anisotropy part of ΔD. From 2.2-2.7 sec we find $\Delta D \approx \Delta l_i$ as determined from $M_{oh,u}$ d/dt(I_{oh}), i.e. the anisotropy does not change. But from 1.7-2.2 sec, the anisotropy is changed by switching on $P_{90°}$. Calculating Δl_i from $M_{oh,u}$ d/dt(I_{oh}) and adding it to ΔD, we get the anisotropy as shown in the dotted line of the 180° curve in fig.3. We note that the time constant for establishing the anisotropy is comparable to that for l_i changes. When $P_{90°}$ is also switched off at t=2.7 sec we see no further change in l_i in the $M_{oh,u}$ d/dt(I_{oh}) curves, indicating that the l_i during 90° current drive at this power level is the same as during inductive current drive. The anisotropy part in ΔD, however, is dieing away.

4) L_i variations with narrow spectra

A single narrow spectrum can also lead to a change in l_i, depending on $N_{||}$. In fig.4 (B_t=2.2 T, $\overline{n_e}$=1.35 $10^{13}$$cm^{-3}$, I_p=0.32 MA) we show a series of shots with different $\Delta\phi$, but constant incident power P=900 kW. The D signals give positive ΔD for $\Delta\phi$=90°-120°, and only for $\Delta\phi$=135°-180° we get negative ΔD, indicating a drop of l_i. The curves $M_{oh,u}$ d/dt(I_{oh}) show that $\Delta l_i \approx 0$ for $\Delta\phi$=90°-120°, so that the positive ΔD's indicate primarily a change in anisotropy, as in the example described in fig.1. Only for the phase settings $\Delta\phi$=135°-180° we find from the $M_{oh,u}$ d/dt(I_{oh}) curves a negative Δl_i , compatible with the negative ΔD. We conclude that at this power level spectra with $\Delta\phi$>120° have a power deposition, which is shifted radially outward, the shift increasing with $N_{||}$.

The changes in anisotropy and in inductance depend also on the rf power. Two extreme cases, high $N_{||}$ ($\Delta\phi$=180°) symmetric spectrum and low $N_{||}$ ($\Delta\phi$=75°) current drive spectrum, are

shown in figs.5 and 6, where we plot $\Delta\beta_{dia}$ and $\Delta(\Lambda+1)$. In the high $N_{||}$ case we find both $\Delta\beta_{dia}$ and $\Delta(\Lambda+1)$ about proportional to P_{rf}, although with different sign. The change in l_i, estimated from $M_{oh,u}$ d/dt(I_{oh}) and shown as crosses in the figures, is found compatible with $\Delta D = \Delta(\Lambda+1- \beta_{dia}) \approx \Delta l_i$, suggesting negligable anisotropy in the high $N_{||}$ case. The low $N_{||}$ case is quite different. Contrary to $\Delta\beta_{dia}$, we find $\Delta(\Lambda+1)$ not proportional to P_{rf},/7/. Even at low power $\Delta(\Lambda+1)$ is already quite large due to the anisotropy, which is strong in the low $N_{||}$ case, and which is further enhanced at low power by the still appreciable electric field, leading eventually to runaway production /6/. In addition $M_{oh,u}$ d/dt(I_{oh}) indicates that at low power Δl_i might be slightly positive, whereas at high power it becomes negative,/8/. Thus the anisotropy is somewhat lower than ΔD at low power, but higher than ΔD at high power.

This experiment was performed in collaboration between IPP-Garching, ENEA-Frascati and PPPL-Princeton.

References

/1/ F.X. Söldner et al., 13. IAEA-Conf. on Plasma Physics and Contr. Nuclear Fusion Research, Washington 1990, Vol.1, 613, (1990)

/2/ K. McCormick et al., Phys. Rev. Lett. 58, 491, (1987)

/3/ D. Van Houtte et al., Nucl. Fusion 24, 1485, (1994)

/4/ K. Ushigusa et al., Nucl. Fusion 29, 1052, (1989)

/5/ F. Leuterer et al., 13. Europ. Conf. Contr. Fusion + Plasma Physics, Schliersee 1986, Europhys. Conf. Abstr., Vol.10C/II, 409, (1986)

/6/ F. Leuterer et al., Nucl. Fusion 31, 2315, (1991)

/7/ R. Bartiromo et al.,17. Europ. Conf. Contr. Fusion + Plasma Physics, Amsterdam1990, Europhys. Conf. Abstr., Vol.14B/III, 1092, (1990)

/8/ F.X. Söldner et al.,14. Europ. Conf. Contr. Fusion + Plasma Physics, Madrid 1987, Europhys. Conf. Abstr., Vol.11D/III, 831, (1987)

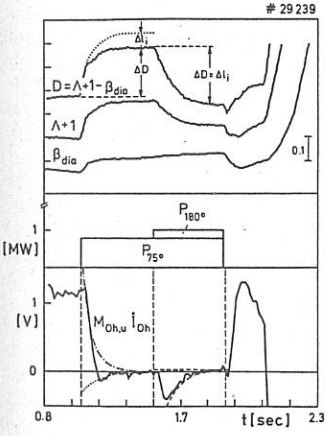

Fig.1

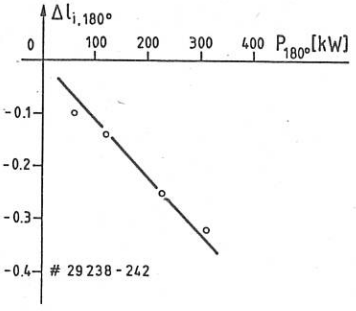

Fig.2

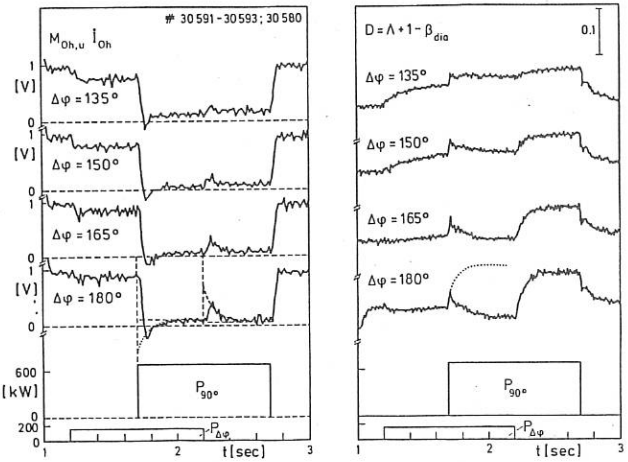

Fig.3

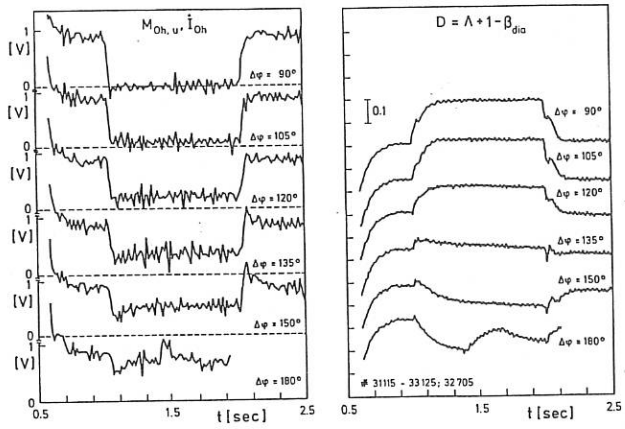

Fig.4

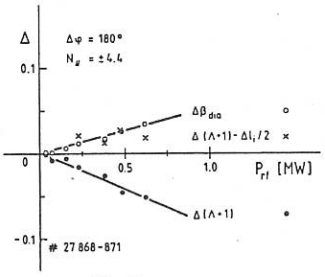

Fig.5

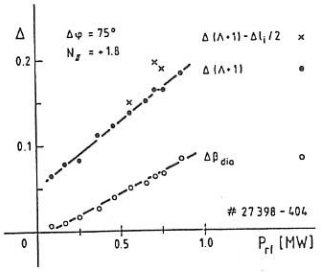

Fig.6

ELECTRON AND ION HEAT TRANSPORT WITH LH AND NBI HEATING IN ASDEX

F.X.Söldner, G.V.Pereverzev[1], R. Bartiromo[2], H.U. Fahrbach, F. Leuterer, H.D.Murmann, K.-H. Steuer and LH-team, NBI-team, ASDEX-team

Max-Planck-Institut für Plasmaphysik, D-8046 Garching, Germany, EURATOM Association

[1]I.V.Kurchatov Institute of Atomic Energy, Moscow, Russia, [2]ENEA, Frascati, Italy

Introduction

Experiments with Lower Hybrid current drive (LHCD) and heating and with neutral beam injection (NBI) were performed in ASDEX with similar plasma parameters for both and in combined operation. Higher incremental energy confinement times were found with LHCD than with NBI /1/. For the global energy confinement time a similar power dependence was obtained for both heating methods /2/. Comparison of the local transport in conditions of preferential heating of electrons by LH and of ions and electrons by NBI in conditions of weak coupling of both species should be of general interest. Recently a new code has been developed for local transport studies in LHCD plasmas /3/. Results from the analysis of discharges with LHCD and NBI combined are presented in this paper.

Transport Code Description

The 1.5D time dependent transport code ASTRA originally developed at Kurchatov Institute /4/ is based on a 2D equilibrium solver and 1D transport equations. It has been extended for modelling of LH current drive and heating. A new approach of diffusive broadening in k-space of the LH wave spectrum is taken in accordance with an analytical solution of the full wave equation. This allows filling of the so-called spectral gap between the launched wave spectrum and the initial thermal electron distribution. The subsequent solution of the kinetic and the wave energy transport equations results in smooth radial LH power deposition and current density profiles of similar shape as measured in the experiment with the Li beam diagnostics. Multiple bouncing of the wave energy between plasma interior and edge is applied until full power dissipation. The only free parameter introduced is a reflection coefficient R for back-reflection of the wave in the plasma boundary. With R=0.9-0.95 the experimentally measured total power absorption coefficient and its density dependence is reproduced.

The electron heat conductivity is described by an expression containing four terms with neoclassical, Alcator-like, MHD-enhanced and anomalous heat conductivity, the latter based on ITER scaling for global confinement. Numerical coefficients in the single terms were adjusted with modelling of one particular LHCD discharge and then kept constant for all other calculations. Good agreement between code calculations and experimental results was then obtained in a wide range of densities and powers for current drive and symmetric wave spectra /3/.

For the modelling of discharges with NBI and combined operation with LH again a validation of the numerical coefficients was carried out. Finally the same model for the electron heat conductivity was retained with the same coefficients as in the previous studies for OH target plasmas. Collisions with neutral particles are included. Also the beam driven and the bootstrap current are contained in the version of the code used here. A major task finally was the adjustement of the ion heat conductivity.

Modelling of Discharges with LH and NBI Combined

Discharges with staged injection of LH and neutral beams were modelled. An example is shown in Fig.1. Three phases of LH-current drive, combined application of LHCD+NBI and of NBI alone follow in sequence, each with 0.5 s duration long enough to reach steady-state conditions. In the upper part of Fig.1 the temporal evolution of the central electron temperature $T_e(0)$ is plotted as obtained from laser light Thomson scattering in the experiment and from the code. After begin of the LH pulse $T_e(0)$ rises strongly. During this phase sawteeth and m=1 oscillations are suppressed in the experiment /5/. In the calculation the current density profile j(r) broadens, resulting in an increase of q(0) above 1 and the disappearance of the q=1 surface and the sawtooth inversion radius r_s from the plasma. Both quantities are plotted in the lower part of Fig.1. Before q(0) rises above 1, the current profile j(r) becomes very flat in the central region and r_s disappears at finite radius nearly without shrinking.

With start of NBI the electron density rises from $\bar{n}_e=1.3 \times 10^{19}$ m^{-3} during OH and LH phase to $\bar{n}_e=2.3 \times 10^{19}$ m^{-3}. The electron temperature drops to about half value and saturates slightly above the OH level, both in experiment and calculation. The strong rise in density causes the LH-driven current to drop by about 40% in the calculation. This leads to a repeaking of the current profile, q(0) falls below 1 and the inversion radius reappears at the previous position. The subsequent increase of the electron heat conductivity through the MHD-enhanced transport results in degraded electron heating. This sequence explains consistently the drop of $T_e(0)$ in the experiment where at this time also m=1 modes reappear. During the whole duration of the NBI phase $T_e(0)$ then stays low as the higher electron density is maintained and m=1 oscillations continue.

Similar experiments at higher initial densities of $\bar{n}_e=2.7 \times 10^{19}$ m^{-3} were not affected by a strong rise in density during NBI. The m=1 modes could there be stabilized in the experiment during the whole duration of LHCD. In the code calculation a broad current profile was there maintained with q close to 1 in the central region and therefore negligible contribution of the MHD-term to heat transport. With symmetric LH wave spectra m=1 modes are not stabilized. Only moderate electron heating is obtained in this case. This is also well reproduced by the code. The current profile there is not broadened and therefore the MHD-induced transport not weakened. The models for electron heat transport and LH power and current deposition developed for LH into Ohmic target plasmas describe therefore the combined operation of LH+NBI as well without further modifications.

For the ion heat transport several models were tested. Finally a superposition of neoclassical ion heat conductivity, with a multiplier of 2, and MHD-related transport of the same form as in the electron heat conductivity was retained. The temporal evolution of central electron and ion temperatures in experiment and calculation is shown in Fig.2. During NBI ion heating prevails and $T_i(0)$ exceeds $T_e(0)$. With LHCD continuing alone after NBI, $T_i(0)$ drops nearly to the Ohmic level while the electron temperature in the center rises further to $T_e(0)$ = 2.5 keV, more than twice the Ohmic value. The large difference between electron and ion temperatures is explained by the small heat transfer from electrons to ions during preferential electron heating from the LH at high electron temperature. The temporal evolution of the central temperatures in the experiment is well reproduced by the code. For $T_e(0)$ very good quantitative agreement is obtained, while too low ion temperatures are calculated by the code for the LH phase.

Radial Energy Transport

Detailed transport studies were performed for a series of discharges with complete documentation of the temporal evolution of the ion temperature profile by active and passive neutral particle charge exchange analysis.
Central temperatures from measurements and calculations are shown in Fig.2. Radial profiles of temperatures and heat conductivities from experiment and code calculation are plotted in Fig.3 for the phase of LH+NBI combined and for LH alone. For the electrons the calculation agrees well with the experiment. In the case of the ions the charge exchange measurements in the peripheral region are affected by a systematic error due to the presence of fast particles there. The shoulder in the measured $T_i(r)$ profile during NBI is caused very likely by this effect. The evolution of the ion temperature profile could not be satisfactorily described with one single model for χ_i in all phases, as already found in the analysis of NBI-heated plasmas alone /6/. A link of χ_i to the volume integrated power like for χ_e would give a wrong radial dependence as the χ_i profile is usually flat or peaked in the center. Reasonable agreement with experimental profiles could be obtained by linking χ_i to the local power density. But then the absolute values of T_i are not reproduced for all phases. The power input to the ions during OH and LH is comparable while higher ion temperatures are obtained in the experiment during LH. This indicates that the radial ion heat transport during LHCD is reduced with comparison to the Ohmic phase. The measured ion temperature profile during LH could be reproduced by the code by using for χ_i a value between 0.5 and 1 times the neoclassical value.

Summary

Electron and ion heat transport were investigated with a 1.5D transport code for heating with LH and NBI into the same target plasmas. The model of electron heat transport developed originally for the analysis of LH heating of Ohmic target plasmas is also valid for the combined operation of LH + NBI. The high central electron temperatures after m=1 stabilization by LHCD are well reproduced by the code. The ion heat transport cannot be described by a single model for all heating scenarios. A reduction of χ_i at least to the neoclassical value has to be assumed in order to reproduce the ion temperature profiles in the experiment during LHCD.

References

/1/ Bartiromo, R., et al., 17th Europ. Conf. on Contr. Fusion and Plasma Physics, Amsterdam 1990, Vol. III, 1092.
/2/ Söldner, F.X., et al., 18th Europ. Conf. on Contr. Fusion and Plasma Physics, Berlin 1991, Vol. III, 405.
/3/ Pereverzev, G.V., et al., to be published in Nucl. Fusion (1992).
/4/ Pereverzev, G.V., et al., Internal report IPP 5/42 (1991), Max-Planck-Institut für Plasmaphysik,Garching, Germany.
/5/ Söldner, F.X, et al., 13th Int. Conf. on Plasma Physics and Controlled Nuclear Fusion Research, Washington 1990, Vol. 1, 613.
/6/ Stroth, U., et al., 18th Europ. Conf. on Contr. Fusion and Plasma Physics, Berlin 1991, Vol. I, 101.

The Lower Hybrid experiments were performed in collaboration between IPP Garching, ENEA Frascati and PPPL Princeton.

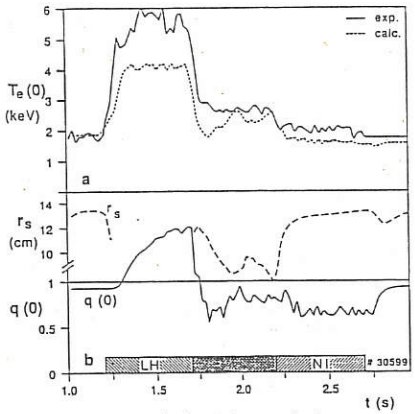

Fig. 1: Time evolution of central electron temperatures in experiment and calculation and of sawtooth inversion radius r_s and central q-value q(0) in code calculation for LH+NI. B_t=2.8 T, I_p=420 kA, P_{LH} = 0.94 MW ($\Delta\phi$=90°), P_{NI} = 1.3 MW.

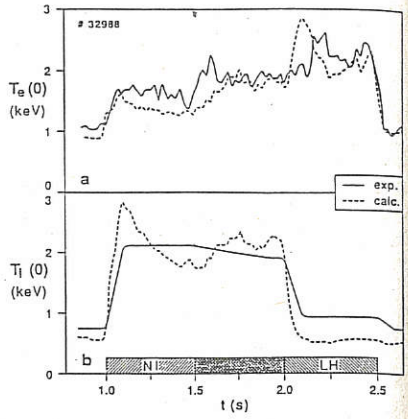

Fig. 2: Time evolution of experimental and calculated electron and ion temperatures for LH+NI. B_t=2.2 T, I_p=320 kA, P_{LH}=1.1 MW ($\Delta\phi$=90°), P_{NI}=1.8 MW.

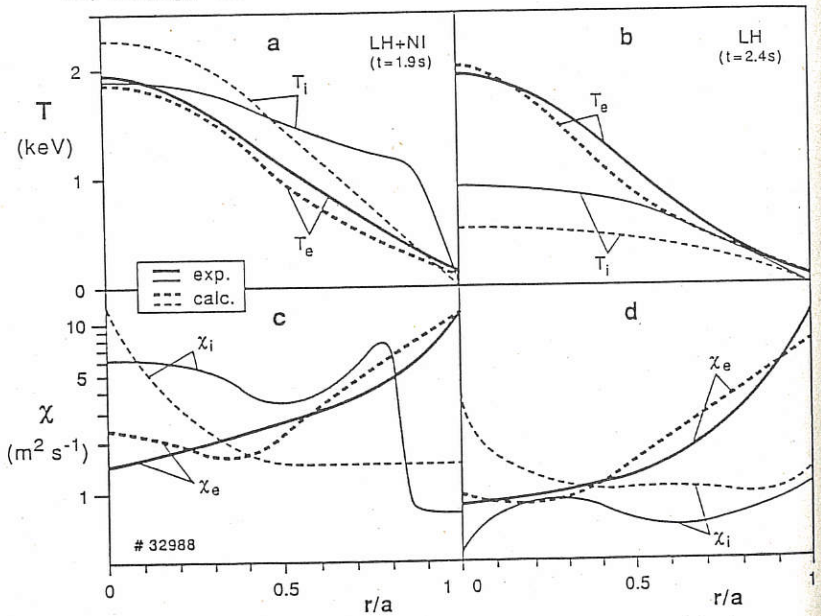

Fig. 3: Radial profiles of electron and ion temperatures and of electron and ion heat conductivities in experiment and transport code calculation for LH+NI and LH.

Experimental Studies of High Energy X-ray Emission and Bootstrap Current Generation in High βp Lower Hybrid Driven Plasmas*

J.P. Squire, M. Porkolab, P.T. Bonoli, J.A. Colborn, J. Villaseñor
Plasma Fusion Center and Research Laboratory of Electronics
MIT, Cambridge, MA 02139

Abstract

High poloidal beta ($\varepsilon\beta_p \sim 1$) plasma equilibria have been produced by injecting lower-hybrid waves with both asymmetric (current drive) and symmetric (heating) spectra in the Versator II tokamak. At high $\varepsilon\beta_p$ nearly the same plasma current was generated by the symmetric rf phasing as with the asymmetric phasing, with the loop voltage being zero in both cases. The current for symmetric injection could not be accounted for by either inductive or rf current drive, so we believe that bootstrap current generation is operative in the present experiment.

Introduction

High $\varepsilon\beta_p$ plasmas are usually produced by bulk heating with ICRH or neutral beams. A novel technique for producing high $\varepsilon\beta_p$ equilibria was pioneered at Versator by using the pressure supplied by a lower-hybrid driven energetic electron tail /1/. It has been shown that substantial poloidal beta can be achieved if the rf driven current (I_{rf}) is reduced to below the Alfvén current ($I_A \approx 17$kA), with the poloidal beta scaling as I_A/I_{rf}. The rf driven energetic tail electrons emit x-rays via bremsstrahlung, and this can be measured to gain information about the electron tail distribution /2/. In this paper we discuss x-ray measurements taken during low and high $\varepsilon\beta_p$ discharges and compare the results between current drive ($\pi/2$) and symmetric (π) injection of lower hybrid waves.

Experimental Results

Versator II is a modest sized tokamak with a circular cross section, major radius R_0=0.405m, minor radius a_L= 0.13m and $\varepsilon = a_L/R_0 = 0.32$. For plasmas discussed in this paper the toroidal field is B_0=1.0T, and the density is typically $\langle n_e \rangle \cong 7 \times 10^{18} m^{-3}$. The lower-hybrid system has a source frequency of 2.45GHz with up to 100kW of power, and the coupler is a four-waveguide grill with relative phasing set at either $\pi/2$ (asymmetric or current drive) or π (symmetric or heating). The plasma is initiated with an Ohmic heating (OH) transformer and the OH circuit is then opened. For the high $\varepsilon\beta_p$ experiments the plasma current is allowed to decay and subsequently the rf power is applied. As shown in Fig. 1, the plasma continues to decay for a short period of time then levels off typically at I_p=5kA, and the loop voltage decreases to zero. The current does not "flattop" immediately because the lower-hybrid power causes the plasma to move rapidly outward and the energetic current carrying electrons are lost on the limiter. If an attempt is made to maintain position by applying more vertical field, the plasma current flattops at higher levels, or becomes unstable. The higher current ($I_p \approx 15$kA) flattops are used as the low $\varepsilon\beta_p$ equilibria.

Plasma equilibria with both asymmetric and symmetric injection were compared for both low and high $\varepsilon\beta_p$. First the current-drive flattop equilibria were obtained, then the waveguide relative phasing was changed from $\pi/2$ to π for subsequent shots. During the low $\varepsilon\beta_p$ equilibria we observed the usual strong tangential x-ray emission indicating a substantial unidirectional electron tail, which is formed by traveling lower-hybrid waves. The profiles show that current and density peak near the center ($r\cong 0$). When attempting current drive with symmetric phasing, it was not possible to obtain a constant current phase. A small applied loop voltage (<0.3volts) was required to maintain the plasma current and a large unidirectional tail was observed again. When trying the same procedure at high $\varepsilon\beta_p$, we found that nearly the same current was generated by π phasing as with $\pi/2$, with no significant change in the loop voltage ($\Delta V_{loop} < 0.02$volts) . The x-ray and density profiles showed outward displacements consistent with a Shafranov shift. The tangential x-ray data indicate a unidirectional electron tail in both cases, but the x-ray flux for the π case was less by a factor of four (see Fig. 3).

Discussion

First we characterized the profiles of the high $\varepsilon\beta_p$ current drive discharges during the rf-driven flattop current phase. The shift of the centroid of the density and x-ray profiles were measured to be $\Delta R/a=0.27\pm0.04$. Taking this to be the Shafranov shift, theory /3/ indicates that $\beta_p=2.2\pm0.45$. We calculated $\beta_p+l_i/2=4\pm0.4$ from the measured plasma current and vertical field. In order to obtain a measurement of l_i we utilized the fact that the x-ray profile is a measure of the current profile when $J(r) = -en_{tail}(r)\langle v_{\|}\rangle$ and the x-ray flux is given by $\Gamma(y) \propto \int dz\left[Z_{eff} n_{tail}(r) n_{bulk}(r)\right]$. We fitted the energy integrated (30-200keV) x-ray profile with a Gaussian and assumed a parabolic density profile. The half width of the x-ray profile was $w_{HXR}=0.026\pm0.005$m which gave $l_i/2=1.0\pm0.2$ and $q_o=3\pm1$. Within error bars the l_i measured by the x-rays is consistent, which confirms that the emission is related to the plasma current carrying fast electrons.

We obtained quantitative information about the energetic electron velocity distribution by analysis of the tangential x-ray emission similar to that done on ALCATOR C /2/. A three-temperature Maxwellian model was used in a bremsstrahlung calculation code to fit the measured x-ray emission. The model included perpendicular ($T_\perp$), parallel backward ($T_{\|b}$) and parallel forward ($T_{\|f}$) temperatures relative to the magnetic field and rf injection direction, with a high energy cutoff in the forward direction. For simplicity we assumed that the velocity distribution was independent of the plasma radius, and we used the fitted radial profile to unfold the spatial effect on the tangential emission. We obtained a best fit of the electron distribution function by adjusting the parameters of the three temperature Maxwellian and calculated the emission by iteration until a least-squares fit was obtained. The results were $T_\perp\approx40$keV, $T_{\|b}\approx50$keV and $T_{\|f}\approx1000$keV with a cutoff at 250keV. With this model we found that for current drive phasing ($\pi/2$) at high $\varepsilon\beta_p$ all the current could be accounted for by the electron tail if $Z_{eff}=4$. We had no independent means of determining Z_{eff}, but this is not inconsistent with past estimates /4/.

At the present time the distribution function for low $\varepsilon\beta_p$ discharges has not yet been modeled, but analysis of the perpendicular profile was carried out in the same way as the above method. We found the profile width to be w_{HXR}=0.04±0.008m which is wider than that associated with the high $\varepsilon\beta_p$ equilibria. The profile difference alone can account for the difference in plasma current carried by fast electrons.

When we switched to symmetric rf injection, at high $\varepsilon\beta_p$ we found that the plasma current was almost unchanged and the loop voltage was still zero within measurement error. The x-ray flux was reduced by roughly a factor of four, but there was still an asymmetric electron tail present (see Fig. 3). These results are in contrast to those obtained with symmetric injection at low $\varepsilon\beta_p$ when an applied small loop voltage of ~0.3volts was required to maintain the plasma current. When modeling the electron tail by means of x-ray emission at high $\varepsilon\beta_p$ for symmetric phasing, we could account for only one third of the total plasma current. The results were $T_{\perp}$≈40keV, $T_{||b}$≈50keV and $T_{||f}$≈800keV with a cutoff at 300keV. This is similar to the current drive result, but the tail population was reduced by a factor of four. In these calculations we again used Z_{eff}=4.

Conclusions

We found that symmetric (π phasing) lower-hybrid injection at high values of $\varepsilon\beta_p$ generated nearly the same plasma current as an asymmetric wave injection (current drive, $\pi/2$ phasing). By means of x-ray analysis we determined that only one third of the plasma current could be accounted for with symmetric injection. This left a substantial amount of current unaccounted for, which may be the bootstrap current.

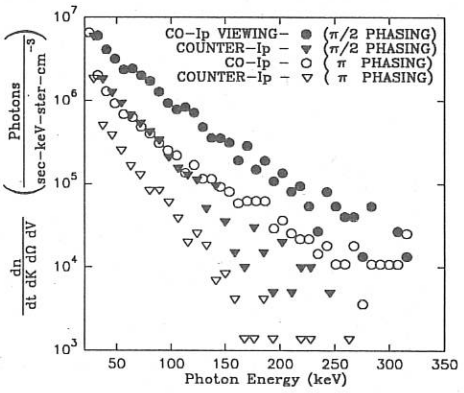

Fig. 3 A comparison of the tangential x-ray emission energy spectra for current drive (solid symbol) and symmetric (hollow symbols) rf injection at high $\varepsilon\beta_p$. The circles are viewing emissions co-current and the triangles are counter. The data are corrected for the radial emission profile.

*Supported by U.S. DOE Contract No. DE-AC02-78ET51013

References

/1/ S.C. Luckhardt, et al., Phys. Rev. Lett. **62** (1989) 1508.
/2/ S. Texter, et al., Nucl. Fusion **26** (1986) 1279.
/3/ J.P. Friedberg, *Ideal Magneto Hydrodynamics* Plenum Press, New York (1987).
/4/ M.J. Mayberry, PhD thesis, Dept. of Physics, Mass. Inst. of Tech. (1986).

The rf-created high energy electron distribution, which provides plasma current and pressure in these plasmas, was studied by a radial and tangential array of x-ray spectrometers (1x3inch NaI). The radial array consisted of 7 vertically viewing detectors that could be moved between plasma shots. The experimental layout is shown in Fig. 2a. The tangential array used the same detectors which were subsequently reconfigured to view the plasma from the side of the tokamak at a full range of angles (see Fig. 2b). A single detector was placed in the radial array and moved from shot to shot to monitor the radial x-ray profile while taking tangential data. Time integrated energy spectra and energy integrated x-ray flux data were acquired on all detectors simultaneously. By gating a multichannel analyzer (MCA) the spectra were averaged over a region where the loop voltage was zero (see Fig. 1a). X-ray energy spectra and profiles were obtained for both low $\varepsilon\beta_p$ ($\varepsilon\beta_p$~1/3) and high $\varepsilon\beta_p$ ($\varepsilon\beta_p$~1) equilibria.

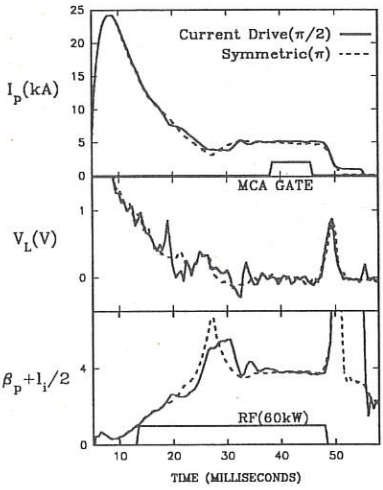

Fig. 1 This is a comparison of current drive (solid line) to symmetric (dashed line) injection at high $\varepsilon\beta_p$. (a) Plasma current with the MCA gate. (b) The loop voltage. (c) The calculated $\beta_p+l_i/2$ with the rf pulse shown.

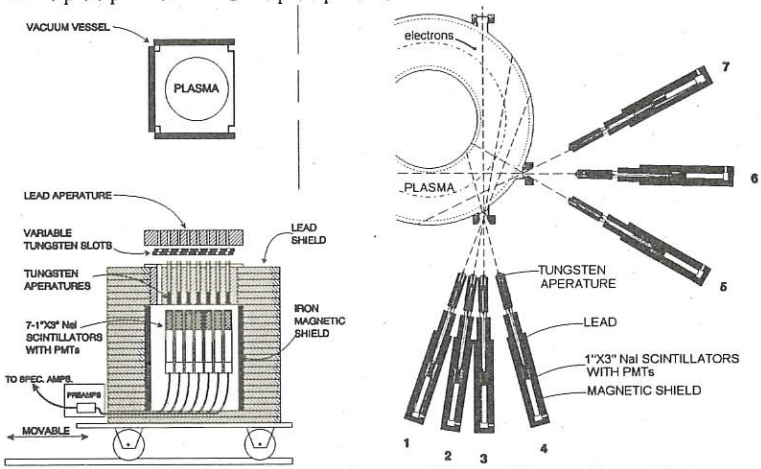

Fig 2 (a) Perpendicular radial array of x- ray detectors. (b) Tangential array of x-ray detectors.

INVESTIGATION OF HIGH ENERGY ELECTRONS PRODUCED BY LOWER HYBRID WAVES WITH MEASUREMENT OF THE HARD X-RAY IN JT-60U

T. Kondoh, S. Ide, T. Imai, K. Ushigusa, Y. Ikeda, M. Seki and H. Takeuchi
Japan Atomic Energy Research Institute, Naka Fusion Research Establishment
Naka-machi, Naka-gun, Ibaraki-ken, 311-01 Japan

Power deposition profile and confinement of fast electrons produced by lower hybrid wave (LHW) are investigated by measuring the phase shift between the hard x-ray (HX) intensity and the modulated LH power. The phase shift of HX signal is well explained by the slowing down time of the fast electrons. Accordingly, confinement of fast electron is dominated by the slowing down process. The power deposition profiles are determined by the HX intensity considering the diffusion process. We obtain the power deposition profiles that depend on the parallel refractive index of the excited wave $N_{//}$.

1. Experimental setup

Hard x-ray (HX) emission produced by the fast electrons was detected by combination of 8-channel sodium-iodide (NaI(Tl)) and scintillator-photomultiplier. Seven channels look radial profile perpendicularly to the magnetic field and the other looks tangentially (Fig. 1). NaI(Tl) detector, which 5.08 cm thick, 5.08 cm in diameter, with 2 mm aluminum vacuum window, is employed to measure the x-ray energy range of 30 keV to 1 MeV. Detectors are shielded by 23 cm of lead and 50 cm of polyethylene against the γ-rays from (n,γ) reactions and background x-rays. The photomultiplier tube is shielded against magnetic field by soft iron and μ-metal. The detected x-ray signals are processed by CAMAC and pulse-height analyzed into 256 channels every 50 msec. To measure the time response, signals are simultaneously digitized in the form of the hard x-ray count through a single channel analyzer.

2. Modeling of the time response of fast electrons

Since quasi-linear diffusion in the velocity space induced by LHW should be balanced with slowing down for ions and bulk electrons, tangential HX intensity $I_{HX//}$ can be modeled as follows if spatial diffusion process is neglected:

$$\frac{dI_{HX//}(t)}{dt} = S(t) - \frac{I_{HX//}(t)}{\tau_{SD}}, \qquad (1)$$

where $S(t)$ is source term and τ_{SD} is slowing down time of the resonant electrons with LHW.

The perpendicular HX intensity $I_{HX\perp}$ depends on perpendicular temperature rather than parallel temperature, because the emission is pointed strongly in the forward direction. Thus, $I_{HX\perp}$ is described as follows:

$$\frac{dI_{HX\perp}(t)}{dt} = b\frac{I_{HX//}(t)}{\tau_D} - \frac{I_{HX\perp}(t)}{\tau^*_{SD}}, \quad (2)$$

where τ_D is diffraction time of the resonant electrons and τ_{sd}^* is slowing down time of the fast electrons to which perpendicular HX signal is sensitive.

When source term is modulated by sinusoidal wave $S(t) = S_0\sin(\omega t)$, phase shift of $I_{HX//}$ and $I_{HX\perp}$ are $I_{HX//} \propto \sin(\omega t - \phi_{//})$ and $I_{HX\perp} \propto \sin(\omega t - \phi_\perp)$ from eq.(1) and (2), where $\phi_{//}$ and $\phi_\perp$ are phase shift given as follows,

$$\phi_{//} = \tan^{-1}(\omega\tau_{SD}) \quad (3)$$

$$\phi_\perp = \tan^{-1}(\omega\tau^*_{SD}) + \tan^{-1}(\omega\tau_{SD}) \quad (4)$$

When diffusion process is considered, these phase shift term is described as,

$$\phi = \tan^{-1}\left(\frac{\omega\tau_{SD}}{1 + 5.78\ (D\cdot\tau_{SD}/a^2)}\right) \quad (5)$$

where D is diffusion coefficient and a is plasma radius.

3. Experimental results

The power of the LHW is modulated by sinusoidal wave to investigate the diffusion and slowing down process. The modulation frequency is 5, 10 and 20 Hz and the phasing between adjacent multijunctions $\Delta\phi$ is varied with shot by shot. Two phasings of $\Delta\phi = 135°$ and $210°$ carried out, in which parallel refractive index of the excited waves $N_{//} = 1.44$ and 2.24, respectively. The LH power P_{LH} is 600 kW, power modulation rate 60 % and loop voltage is very small in this experiment. Plasma parameters are I_p = 1.2 MA, $B_T = 4$ T, $\overline{n_e} = 8\times10^{18}$ m^{-3}, and $f_{LH} = 2$ GHz. Time evolution of HX signal is fitted by $A+B\cos(\omega t+\phi)$ by least-squares fitting.

Figure 2 shows radial profiles of phase shift of HX signal and calculated value using τ_{SD} = 8 ms and 13 ms as a parameter of modulation frequency of 5, 10 and 20 Hz. While, the phase shift which taken into account the diffusion process is given by eq. (5). Because, the measured phase shift is consistent with the calculated slowing down time of the resonant electrons, the term $5.78(D\tau_{SD}/a^2)$ in eq. (5) can be neglected. Therefore, the diffusion process of the fast electron may be small compared with the slowing down process and the diffusion process is considered as $D\tau_{sd}/a^2 < 0.1$.

4. Power deposition profile

In the steady state, the fast electron density, n_f is governed by the particle balance equation,

$$S(r) = \frac{n_f(r)}{\tau_{SD}} - \nabla(D\nabla)n_f(r) \qquad (6)$$

where S(r) is source term and τ_{sd} is slowing down time of the fast electrons. The hard x-ray intensity is line integral of n_f along the line of sight L if the fast electron temperature is constant in the space.

The problem is to solve S(r) from the line integrated data, I_{HX}. Now, in order to solve the diffusion equation, we expand Fourier-Bessel method /1/ that is one of the tomographic reconstruction method. In this case we only measure 1 dimensional data, so we consider the first term of fourier series (m =0). Then we expand $n_f(r)$ in zero-th order Bessel functions, J_0:

$$n_f(r) = \sum_{k=1}^{K} c_k J_0(\lambda_k \cdot r/a) \qquad (7)$$

where λ_k is the k-th zero of $J_0(z)$ and c_k is expansion coefficient.
Assuming the diffusion coefficient D is constant in the space, S(r) is reduced to,

$$S(r) = \frac{1}{\tau_{SD}} \sum_{k=1}^{K} c_k(1 + D\lambda_k^2\tau_{SD})J_0(\lambda_k \cdot r/a) \qquad (8)$$

c_k can be solved by the least-squares fitting as minimizing the residual error E_{rr} which is defined as

$$Err = \sum_{n=1}^{Nmax} \left[I_{HX\perp}^{n} - \sum_{k=1}^{K} c_k \int_{L_n} J_0(\lambda_k \cdot r/a)\, dl \right]^2, \qquad (9)$$

where I_{HX}^{n} is the n-th signal of the HX for line of sight L_n.

Figure 3 shows the ratio of the power deposition profile for $N_{//} = 2.24$ to $N_{//} = 1.22$ deduced from equation (8) as a parameter of $D\tau_{sd}/a^2$. Deposition of $N_{//} = 1.22$ wave which has the maximum current drive efficiency, has peaked profile in the center and $N_{//} = 2.24$ has hollow profile.

5. Conclusion

It is found that the HX phase shift measured in the LH power modulation experiment is comparable with the calculated phase shift using slowing down time of the resonant fast electrons. Therefore the diffusion term can be neglected because the fast electron confinement time τ_f is larger than fast electron slowing down time.

Power deposition profiles are obtained by using the Abel inversion technique based on Bessel expansion method where the diffusion process is taken into account estimated by

the power modulation experiment. Power deposition of LHW of N// =1.22 has a peak at the center and N// =2.24 has hollow profile.

Though we used simple model of HX emission, it is necessary for a further investigation to evaluate of quantitative diffusion process using calculation code.

6. Reference

/1/ Y. Nagayama, J. Appl. Phys. **62** (1987) 2702

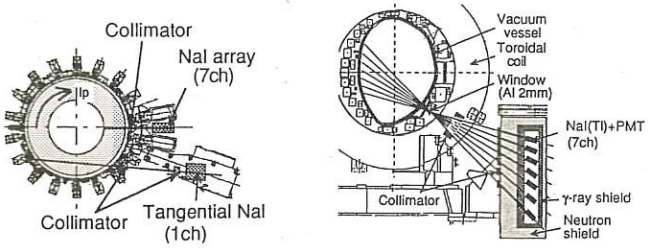

Fig. 1 Schematic diagram of the hard x-ray detectors.

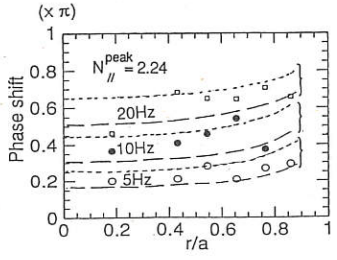

Fig. 2 Radial profile of the phase shift obtained from modulated frequency of 5 Hz (○), 10 Hz (●) and 20 Hz (□). Dashed lines and dotted lines are calculated value of phase shift τ_{sd} = 8 and 13 msec, respectively.

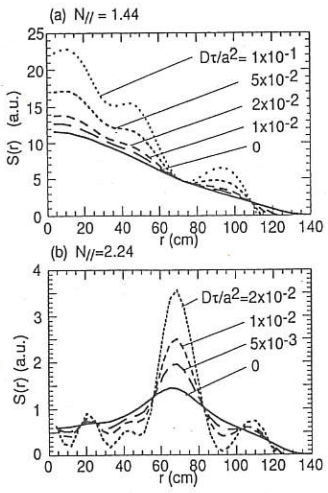

Fig. 3 Power deposition profiles at N// = 1.44 (a) and 2.24 (b), with the diffusion coefficient as a parameter.

Characterization of LH Induced Current Carrying Fast Electrons in JET

G.Ramponi, A.Airoldi
I.F.P. Associazione EURATOM/CNR/ENEA, Via Bassini, 15 - Milano (Italy)
D.Bartlett, M.Brusati, P.Froissard, C.Gormezano, F.Rimini, R.P.da Silva, C.P.Tanzi
JET JOINT UNDERTAKING, Abingdon, Oxon OX14 3EA, (UK).

1. Introduction.

Lower Hybrid Current Drive (LHCD) experiments have recently been made at JET by coupling up to 2.4 MW of RF power at 3.7 Ghz, with a power spectrum centered at $n// = 1.8 \pm 0.2$ corresponding to a resonating electron energy of about 100 keV via Electron Landau Damping /1/. The Current Drive (CD) efficiency has been observed to increase when LH and ICRH power are applied simultaneously to the plasma, suggesting that a part of the fast magnetosonic wave is absorbed on the LH-generated fast electrons/2/. An important problem of CD experiments in tokamaks is the determination of the radial distribution of the driven current and the characterization in the momentum space of the current carrying fast electrons by using appropriate diagnostic tools. For this purpose, a combined analysis of the Electron Cyclotron Emission (ECE) and of the Fast Electron Bremsstrahlung (FEB) measurements has been made, allowing the relevant parameters of the suprathermal electrons to be estimated.

2. Analysis of ECE spectra combined with FEB measurements.

In the present analysis we limit ourselves to a class of distribution functions typical of steady state regimes during the application of LH power, where the fast tail is nearly flat and is represented by a distribution function with a slowly varying dependence in the p// direction. Our aim is to estimate the perpendicular energy $E_\perp$, the position and width of the current channel, as well as the parallel energy $E_\parallel$, and the density of the suprathermal electrons. The method relies on the different and complementary sensitivity of the two diagnostics used in this analysis to the parameters we wish to estimate.

The FEB diagnostics measures the X-ray emission in the range 100 keV to 300 keV through a multichord detection system in a poloidal plane /3/. The signal is rather insensitive to $E_\perp$ (for $E_\perp << E_\parallel$), and provides an indication of the fast electrons radial profile through the emissivity profiles and of $E_\parallel$ through the the measured 'photon temperature'. This information is exploited by fitting ECE spectra through simulations where the suprathermal density is determined by the measured RF current and by iterating the intensity spectrum over $E_\perp$.

The E-mode ECE spectra, measured via an antenna viewing the plasma from the low field side near the equatorial plane, are significantly affected by non thermal emission during LH (Fig.1).

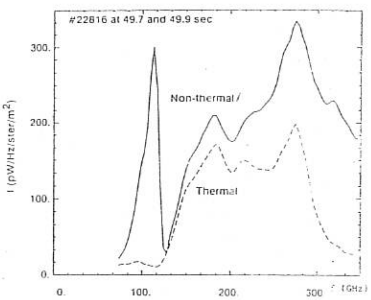

Fig.1-Thermal (full line) and non-thermal (dotted line) ECE intensity spectrum. The non-thermal emission is measured during the application of 1MW of LH power.

In particular at low frequencies, normally associated with the first thermal harmonic, fast electrons produce intense relativistically downshifted second harmonic emission, with possible contribution of third harmonic in presence of very energetic particles, as previously predicted by an ECE simulation code (ECLH code) specifically devised to calculate the emission of electron cyclotron waves for JET plasmas during LHCD /4,5/. This emission line is unaffected by reabsorption by the thermal plasma, except on the high frequency side where the second (thermal) harmonic is entering the plasma.

Moreover, the presence of the E-mode upper cutoff in this range of frequencies has two important consequencies: 1) it blocks the radiation emitted by bulk electrons as first harmonic so that very little can reach the antenna (via wall reflections); 2) it fixes an upper boundary to the energy of suprathermal electrons contributing to the observed emission intensity, by blocking the radiation emitted in the radial region where $R < R_c$, (R_c being the radial position of the cutoff layer). As a consequence, by taking into account the relativistic resonance condition for perpendicular propagation and by using the usual magnetic field profile, it is possible to identify the energy range of the electrons emitting at a frequency f in this spectral region as second and third harmonic by the relation:

$$\frac{nf_c(R_o)}{f}\frac{R_o}{R_{\max}} \le E/mc^2 + 1 \le \frac{nf_c(R_o)}{f}\frac{R_o}{R_c} \qquad (1)$$

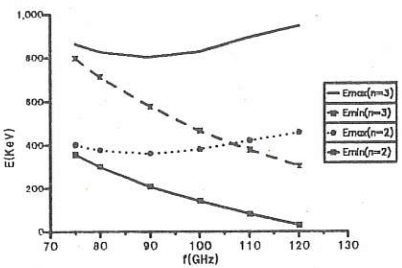

Fig.2-Maximum and minimum "allowed" energies of electrons emitting as second and third cyclotron harmonics vs frequency (pulse # 24966).

where f_c is the (thermal) cyclotron frequency at R_o (the plasma center), n is the harmonic number and $R_{\max}$ corresponds to the low field side location of suprathermal electrons. For typical plasma densities and magnetic field values of JET discharges during LH, the energy range defined by relation (1) is shown in Fig. 2 for both second and third harmonic emission.

In the ECLH code, used to simulate the ECE spectra, the emission and absorption coefficients of electron cyclotron waves are relativistically calculated along the ray path /4/. The electron distribution function, on each magnetic surface $\bar{\psi}$, is built by adding to the Maxwellian bulk, characterized by a temperature $T_b(\bar{\psi})$, a suitable number M of drifting Maxwellians of temperature T_s:

$$F(p_\perp, p_\parallel, \bar{\psi}) = w_b(\bar{\psi})\left(\frac{\mu_b}{2\pi}\right)^{3/2} e^{-\frac{\mu_b}{2}(p_\perp^2 + p_\parallel^2)} + \frac{w_s(\bar{\psi})}{M}\sum_m \left(\frac{\mu_s}{2\pi}\right)^{3/2} e^{-\frac{\mu_s}{2}p_\perp^2} e^{-\frac{\mu_s}{2}(p_\parallel - p_m)^2} \qquad (2)$$

where m is the index of a generic drifting Maxwellian, $\mu_s = m_e c^2/T_s$, $\mu_b = m_e c^2/T_b$, $p_\perp$ and $p_\parallel$ are the perpendicular and parallel components of the electron momentum in $m_e c$ units, p_m is the parallel drift of the m-th Maxwellian, and the fractional densities of bulk (w_b) and suprathermal electrons (w_s) are related by $w_b + w_s = 1$. The parallel distribution function $F(p_\parallel)$ (obtained by integrating (2) over $p_\perp$) exhibits a nearly flat tail extending from the bulk to a value p_L when : $p_m = p_{m-1} + 2\mu_s^{-1/2}$ for $1 < m \le M$, $p_1 = \mu_b^{-1/2}$, $M = 1 + \mathrm{Int}[(p_L - p_1)/2\mu_s^{-1/2}]$.

On the other hand, the interpretation of FEB emission spectra is performed by modelling the suprathermal electron distribution with a 3-temperature Maxwellian allowing their 'forward' and 'backward' parallel temperatures ($T_{\parallel F}$, $T_{\parallel B}$) to be estimated. These values are used to determine the number M of drifting Maxwellians in (2) through the relation

$$p_1 + (M-1)\mu_s^{-1/2} = \sqrt{2/\pi}\left(\sqrt{T_{\parallel F}/mc^2} - \sqrt{T_{\parallel B}/mc^2}\right) \qquad (3)$$

obtained by imposing the equality of the average parallel momentum $<p_\parallel>$ of the electrons carrying the non-inductive current.

The parameter w_s is obtained, for a given $<p_\parallel>$, from the estimated RF driven current I_{RF} through the relations:

$$I_{RF} = \iint J_{RF}(\bar{\psi})\,dA \qquad (4)$$

where dΛ is the area element, and

$$J_{RF}(\overline{\psi}) = ecn_e(\overline{\psi})\int_{-\infty}^{\infty} dp_{\parallel} f_{\parallel}(p_{\parallel}, \overline{\psi})\frac{p_{\parallel}}{\gamma} \simeq ecn_e(\overline{\psi})\frac{w_s(\overline{\psi})}{M}\sum_m p_m/\sqrt{1+p_m^2} \qquad (5)$$

by using for w_r a 'gaussian ' profile:

$$w_s(\overline{\psi}) = w_o \exp -(\overline{\psi}/\overline{\psi}_c)^2 \qquad (6)$$

where $\overline{\psi}_{min} \leq \overline{\psi} \leq 1$, and $\overline{\psi}_{min}$, $\overline{\psi}_c$ are estimated through the FEB emissivity profiles. By inserting 5) and 6) in expression 4), we get w_o from I_{RF}.
The last parameter $T_\perp = T_r$ is determined by iterating the calculated ECE radiation temperature, taking into account reflections from the walls (with a reflection coefficient R_w) and from the cutoff layer (with a reflection coefficient = 1) through the relation:

$$T_r(f) = \frac{8\pi^3 c^2}{(2\pi f)^2}\int_0^{s_a} \beta(f) e^{-\int_r^{s_a}\alpha(f)ds'} ds \,/\, (1 - R_w e^{-\int_0^{s_a}\alpha(f)ds}) \qquad (7)$$

where $T_r(f)$ is the radiation temperature observed at the antenna($s = s_a$), s is the abscissa along the ray path, α and β are the (relativistic) absorption and emission coefficients respectively. It is worth noticing that the integration along s is carried out on a full trajectory from the plasma edge (s = 0) to the cutoff layer and back to the plasma edge ($s = s_a$) after reflection. The wall reflection coefficient has been taken $R_w = 0.6$, as estimated from measured thermal spectra.

3. Results and Conclusions

We present here the results obtained in the case of three 'full current drive' JET deuterium plasmas in the limiter configuration. The relevant plasma parameters are listed in Table 1.

Table 1

#	P_{LH}(MW)	P_{ICRH}(MW)	I_{RF}(MA)	$B_T(0)$ (T)	$n_e(0)/10^{19}(m^{-3})$	$T_h(0)$ (keV)
24918	2	0	375	2.16	2	1.6
24919	0.9	1	540	3.1	1.9	6.6
24966	2	3	1030	2.94	1.5	10.7

The emissivity profiles measured by the FEB camera are shown in Fig. 3 (a,b,c).

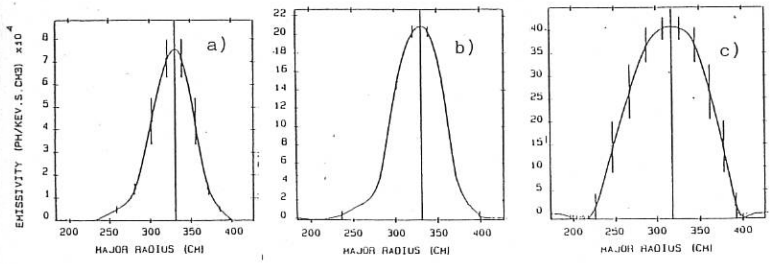

Fig.3-Abel inverted profiles of FEB emissivity for the analysed pulses: a) # 24918; b) # 24919; c) # 24966.

It may be observed that a fast electron population is established in the inner region in all these 'low density' plasmas, with the broadest profile in case of # 24966. Moreover

the 'photon temperature' increases when LH and ICRH power are applied simoultaneously to the plasma, indicating an increasing energy of fast electrons. The analysis of these data gives the results shown in Table 2:

Table 2

#	$T_{\parallel F}$(keV)	$T_{\parallel B}$(keV)	$T_{\perp}$ (keV)	$< n_z > /10^{15}\ (m^{-3})$
24918	120	2	25	2.6
24919	220	5	39	2.9
24966	800	20	80	3.5

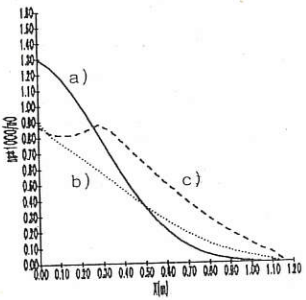

Fig.4-Fast electrons density profiles, normalized to the central plasma density : a) # 24918; b) # 24919; c) # 24966.

The suprathermal density profiles are shown in Fig.4. The $T_{\perp}$ values indicated in Table 2 have been obtained through the iteration procedure to reproduce the low frequency region of the ECE measured spectra, as shown in Fig.5(a,b,c).

In conclusion, this analysis has allowed the first identification of the relevant moments of the LH induced fast electrons in JET. It is shown that the fast electrons energy content, as well as the average parallel momentum, increases when ICRH power is added to LH power. The mechanism responsible for the observed 'synergism' is still under investigation, but it appears that the determination of the relevant parameters of fast electrons is an important step to identify the underlying physical processes.

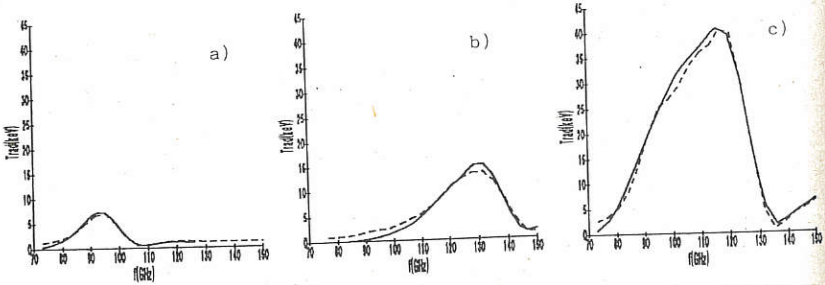

Fig.5-Measured (dashed line) and simulated (full line) non-thermal ECE spectra for a) # 24918; b) # 24919; c) # 24966.

(Work partially supported under the Euratom Mobility Contract No.131-83-7 FUSC)

References

/1/ C.Gormezano et al., *Proc. of 18th European Conf. on Contr. Fusion and Plasma Phys.*, Part III p.393, Berlin 1991
/2/ D.F.H.Start et al., *Nuclear Fusion* **30**, 2170, (1990)
/3/ Ph. Froissard et al., *Proc. of 18th European Conf. on Contr. Fusion and Plasma Phys.*, Part III p.389, Berlin 1991
/4/ A.Airoldi, A.Orefice and G.Ramponi, *Il Nuovo Cimento* **13D**, 517, (1991)
/5/ G.Ramponi et al., *Proc. of 17th European Conf. on Contr. Fusion and Plasma Phys.*, Part IV, p.1709, Amsterdam 1990

A PHENOMENOLOGICAL DESCRIPTION OF FAST ELECTRONS INDUCED BY LH WAVES IN TOKAMAKS

P. Conceição, M. Brusati*, P. Froissard*, C.A.F. Varandas

Associação EURATOM/IST, Centro de Fusão Nuclear, 1096 Lisboa CODEX, Portugal
*JET Joint Undertaking, Abingdon, Oxon, OX14 3EA, United Kingdom

1- Introduction. An important aspect of non inductive Current Drive schemes proposed for Tokamaks is the identification of the mechanisms which characterize the space and energy distribution of the current carrying particles. In the case of Lower Hybrid Current Drive (LHCD), it is relevant to identify the physical processes which contribute to the build up of an asymetric fast electron (f.e.) distribution. In this paper an aproach to this problem is presented whereupon the Fokker-Planck equation describing the phase space evolution of the f.e. distribution function is treated as a flux balance equation based on the characteristics times of the different physical mechanisms at work. This equation describes a model that considers different finite areas of phase space as different states of the f.e. population. The equation is solved analitically and the solution is coded to allow flexible handling of the experimental conditions. Transitions are allowed between neighbouring states through coupling coeficients which depend upon the physical mechanisms driving the transitions. The model treats energy diffusion of an initial f.e. population created by local local Electron Landau Damping of LH waves as a result of residual electric field and plasma slowing down effects and allows space diffusion to be assessed either numerically or a result of assuming a space diffusion model.

2- The Model. The purpose of the model is to describe the energy and space behaviour of the f.e. created by Landau Damping of the LH wave. A two dimensional grid on the phase space is considered, corresponding one dimension to the particles energy and the other to their space location. To each cell corresponds a certain number of electrons, and this number will vary due to the flows of electrons from, and to, adjacent cells.

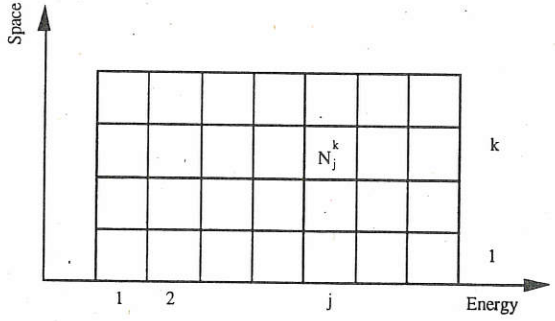

Fig-1

The physical processes responsible for this flows are: in energy, the acceleration due to the residual electric field (related to the loop voltage) and the slowing down of the f.e. due to the coulombians collisions with the plasma particles; in space, the radial diffusion of the f.e.. The equation that rules the time evolution of the number of f.e. in cell (j,k) is:

$$(1) \qquad \frac{\partial N_j^k}{\partial t} = \frac{N_{j-1}^k}{a_{j-1}^j} + \frac{N_{j+1}^k}{c_{j+1}^j} - N_j^k \cdot \left(\frac{1}{a_j^{j+1}} + \frac{1}{c_j^{j-1}} \right) + \frac{N_j^{k-1}}{d_{k-1}^k} + \frac{N_j^{k+1}}{d_{k+1}^k} - N_j^k \cdot \left(\frac{1}{d_k^{k+1}} + \frac{1}{d_k^{k-1}} \right) + s_j^k$$

The total number of electrons in all cells is given as a fraction of the plasma density. a_q^p is the time an electron takes to accelerate from the cell q to cell p; c_q^p is the time an electron takes to slow down from cell q to cell p (these correspond to electron movements in energy space, for a fixed space location); d_q^p is the time an electron takes to diffuse in space from cell q to cell p. The acceleration time is determined solving the relativistic equation of motion of an electron in an electric field; the collision time is calculated as the relativistic slowing down time of a test particle in an uniform thermalized background; the diffusion time depends on the diffusion model at stake, but no study on what diffusion model is to be considered has yet been performed. The wave power deposition on the electrons is represented, very crudely, by a source term s_j^k. This term is built with basis on the wave power spectrum. A more accurate treatment of the wave power deposition on the electrons could be performed, within the frame of the model, replacing the source by flux terms of the type N_p^q / τ_w, where the "characteristic wave deposition time" (τ_w) could be defined as $D(v)/\Delta v^2$, D being the diffusion coeficient of the quasilinear 1-D approximation of the Fokker-Planck equation /1/ and v being the parallel velocity. Since this time is much smaller than the other times at stake, it is assumed that the initial distribution of f.e. mirros a source term, that represents the wave power.

Equation (1) stands for one cell only. To describe the entire phase space, a tensorial equation is needed:

$$(2) \qquad \frac{\partial N}{\partial t} = \overline{C}\, N + s$$

In (2) N and s are matrices and $\overline{C}$ is the 3rd orther tensor containing the characteristic times. Equation (2) was solved analitically, either in the stationary, either in the time dependent situation. The solution without diffusion, therefore representing a localized spot of the plasma (no space movements of the electrons are considered) was coded.

3- **The Results.** This model has been applied to conditions simulating the JET LH experiments /2/. It was found that for a plasma density $Ne \approx 2\ 10^{19}\ m^{-3}$, and temperature $Te \approx 10$ KeV, a power spectrum centred at $N_{parallel} = 1.8 \pm 0.2$ creates a fast electron tail in the energy range 60-100 KeV. Acceleration due to a residual toroidal electric field corresponding to a loop voltage V=0.3 V is balanced by collisions with the thermal

plasma and a stationary state is aproached on a time scale of 10-100 ms (fig 2, fig 3). The role of the electric field is to couple further energy to the f.e. tail (in fig 4 no electric field is assumed; therefore electrons do not go beyond the energy corresponding to the maximum wave accessibility). This effect is counteracted by increasing the plasma density (fig 5); increasing the density the wave accessebility falls down in energy and the collisions are more important. Variation in the launched power spectrum can alter the characteristics of the f.e. population depending upon the power absortion efficiency and accessibility conditions (fig 6).

4- **Conclusions.** A phenomenological model has been described which reduces the Fokker-Planck equation to a two dimensional flux balance equation that may include the LH Electron Landau Damping (ELD) operator. This equation is solved analitically and the solution is coded to be couped to direct measurements of plasma parameters of interest in LHCD scenarios.

This method has been preliminary applied to JET like parameters in the limit where the ELD operator is treated as a source term and neglecting spatial diffusion. The main parametric dependences have been identified as the plasma collisionality and residual electric field effects. The stationary solution is achieved in few tens of miliseconds after application of LH.

This aproach is useful to undertake a sistematic analisys of the dynamics of LH induced f.e., in particular identifying the role played by spatial diffusion.

Acknowledgements. We wish to thank Dr C. Gormezano and Dr Y. Baranov for their support and useful discussions.

References

/1/ N. Fisch, Rev. Modern Physics 59 (1987) 175.

/2/ P.Froissard et al., Proc 18th EPS Conference, Berlin, June 1991.

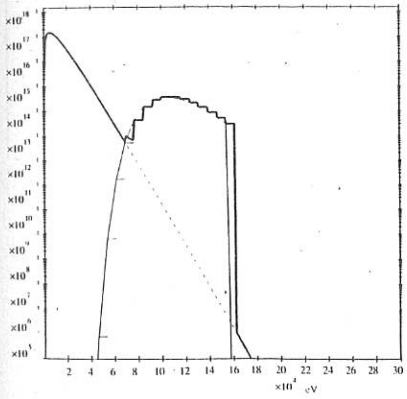

Fig 2- Density (m^{-3}); Plasma conditions: $Ne= 2.10^{19} m^{-3}$; Te= 10 KeV; V= 0.3 V; 0.1% of f.e.; Power spectrum centred at Np=1.8±0.15; 40 energy windows; initial situation (time= 0 s).

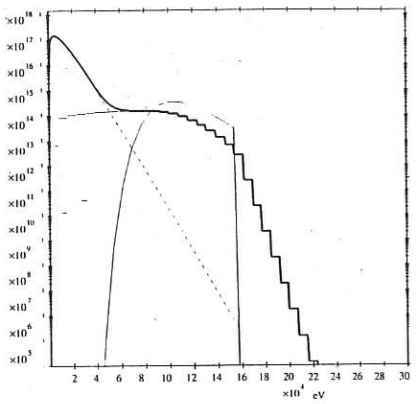

Fig 3- Same parameters as in fig 2; stationary solution.

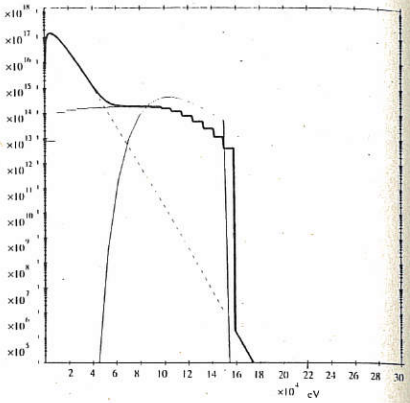

Fig 4- Same conditions as in fig 3 (a stationary solution is depicted), except that V= 0 V, no residual electric field is assumed; 35 energy windows.

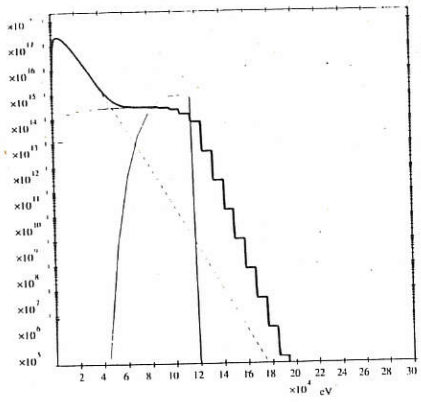

Fig 5- Ne=3.10^{19} m^{-3} ; the other conditions are as in fig 3; stationary solution; 35 energy windows.

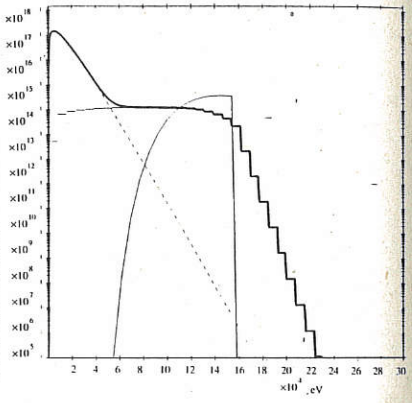

Fig 6- Power spectrum centred at Np= 1.6; the other parameters are as in fig 3; stationary solution; 40 energy windows.

Impurity Transport during RF Current Drive in WT-3 Tokamak

Masahiko NAKAMURA
Osaka Institute of Technology
Keiji SAWADA, Tetuya KAWACHI,
Hidetoshi SUEMITU, Takashi MAEKAWA,
Yasushi TERUMICHI, Shigetoshi TANAKA
Kyoto University

Introduction

It is well known that particle transport behaviour changes drastically during RF current drive. However, the physical mechanism of the change in particle transport has not been made clear. On the other hand, impurity contamination during high power RF injection is a serious problem in fusion research. Detailed study on impurity transport in RF-CD plasma is not carried out as yet.

In the present paper, we study the impurity transport in Lower Hybrid (LH) current driven plasma in the WT-3 tokamak. To trace the impurity behaviour, a small amount of Neon gas is injected into the plasma in a short pulse gas puff. After the injection, basic plasma parameters such as electron density and temperature are perturbed slightly. Spectral line intensities of Neon (Ne IV, V,.) are measured and temporal and spatial behaviours of these line are analyzed. The results show that these intensities increase gradually (typically in 20 msec). Since ionization time is much less than this time for the present plasma parameters, these time behaviours of line intensities show the ion transport in a plasma. We compare the behaviours of Neon ion in OH and LHCD plama.

Results

Experiments are carried out in the WT-3 tokamak (R=65cm, a=20cm, B_T=1.5T,). A small amount of Neon gas is injected into the plasma during the flat top phase of a discharge. Behaviours Neon ions are monitored by line intensities (Ne IV, Ne V). Each line intensity is measured along a holizontal chord. The position of the chord is changed in each shot. After an Abel inversion, we obtain a temporal and spatial behaviour I(r,t).

Typical results in OH plasma are shown in Fig.1. Here, I_P=80kA and electron density $n_e=1.2\times10^{13}cm^{-3}$ before Neon injection. Central Electron Temperature T_{e0} is estimated to be 400 eV from ECE. A short pulse (2mesc) is applied to a piezo-electric valve at t=30 msec. After some delay because of a response time of the valve, Neon is injected into the plasma at t = 40 msec. n_e increases slightly, while electron temperature Te, monitored by ECE, shows little change. Temporal behaviour of line intensity Ne V is shown at the bottem of the figure. It increases gradually and saturates at about 20 msec after the injection. Then decreases in a long time scale. A spatial profile of Ne V intensity at t=65 msec is shown in Fig.2. Because of the low ionization potential of Ne V and Ne IV relative to the bulk electron temperature of the plasma center, these line are emitted from outer region of the plasma column (typically r/a =0.5~0.6). Thus, we obtain the impurity ion behaviour in the outer region in this presentation. It is noted that line intensity is proportinal to the product of n_e, n_{Neon}, and the excitation rate coefficient $S(T_e)$; i.e. $I = A\, n_e\, n_{Neon}\, S$. $S(T_e)$ is slightly dependent on T_e in the present condition. Because n_e changes after the injection, the change of line intensity I is partly due to the change in n_e . Therefore, the value of intensity divided by n_e ,(I / n_e) , is an appropriate measure of Neon density. In Fig. 3. , we plot the

time evolutions of I/n_e for several radial positions, which show the behaviour of Neon ion. It is clearly shown that it saturates at about 20 msec after the injection of Neon (note that Neon is injected 10 msec after the gas puff trigger) and then decreases gradually. The particle confinement time of Neon ions may be possibly estimated to be 20 msec from these behaviours. These behaviours and time constant (~ 20 msec) are nearly the same for OH plasma in the range of 40 kA $\leqq I_p \leqq$ 100 kA, suggesting that impurity confinement time is slightly dependent on I_p.

The same method is applied to Lower Hybrid (LH) current driven plasma. Here, plasma current is maintained by LH power ($\leqq$ 200 kW) only. Basic plasma parameters are similar to those in OH plasma ($n_e \leqq 1\times10^{13}cm^{-3}$, T_{e0} 400 eV), thus the intensity and spatial profile of Ne IV, Ne V are essentially the same in LHCD . In Fig.4, we show the time evolutions of I / ne for LHCD plasma (I_p = 80 kA). The behaviours are quite different from those in OH plasma. After the injection, I / n_e increases gradually , but it does not saturate during the discharge. This longer duration ($\geqq$30 msec) without any saturation in LHCD means impurity confinement time is much longer than this duration. The result is consistent with the improved particle confinement in LHCD.

However, in the case of lower current IP = 48 kA in LHCD, impurity behaviours are similar to those in OH plasma. It is suggested that impurity transport property is dependent on I_p in LHCD.

Summary

Impurity transport was studied in OH and LHCD plasma in the WT-3 tokamak. , Impurity confinement time is estimated to be nearly 20 msec in OH plasma, while it is longer than 30 msec in LHCD plasma with high plasma current. Confinement time is dependent on the plasma current in LHCD.

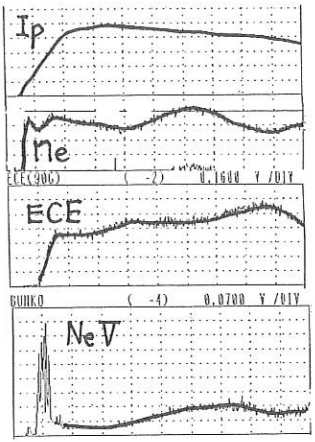

Fig. 1. Time evolution of plasma parameters after Neon injection in OH plasma

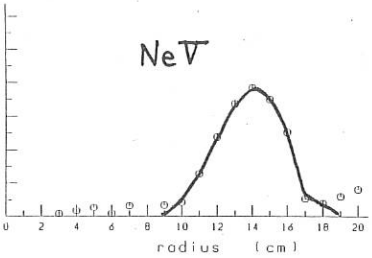

Fig. 2. Radial profile of Ne V

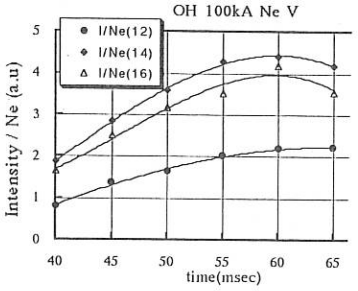

Fig. 3. Time evolution of I / n_e in OH plasma (I_p = 100 kA)

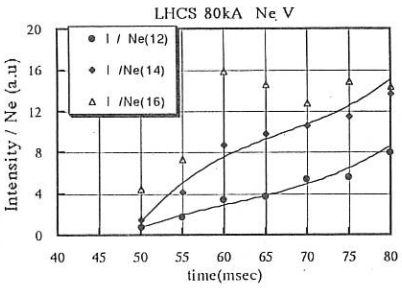

Fig. 4. Time evolution of I / n_e in LHCD plasma (I_p = 80 kA)

THE DISTANT COUPLING OF LHCD LAUNCHER IN THE JT-60U

M. Seki, Y. Ikeda, T. Imai, K. Ushigusa, O. Naitou, S. Ide, T. Kondoh, M. Nemoto, H. Takeuchi, K. Suganuma, M. Sawahata, A. Takasa, S. Takahashi, and T. Yamamoto

JAERI, NAKA FUSION RESEARCH ESTABLISHMENT
Naka-machi, Naka-gun, Ibaraki-ken, JAPAN

1. Introduction

A non-inductive current drive by using lower hybrid waves (LHCD) is one of efficient and promising schemes in a tokamak device. However it is often indicated that a precise control of plasma position is required in order to launch LH waves into the plasma efficiently. Because thin plasmas at grill mouth are needed for a good coupling, so that the distance (δ ; between a launcher head and plasma edge) is required to be small, usually, a few cm. Therefore it is important whether the LH waves can be launched at large δ.

The efficient coupling of LH waves was observed with δ more than 10 cm in the JT-60U. The experimental results suggest that the LH power might produce a tenuous plasma at a grill mouth during a good coupling. The LH waves seemed to be mainly used to drive plasma current without a degradation of the current drive efficiency. This paper presents the distant coupling in the JT-60U LHCD experiments.

2. Experimental arrangements

The present experiments were carried out by using of the newly constructed multijunction type launcher in the first campaign of JT-60 Upgrade. This launcher / 1 / is designed to launch optimized N// power spectrum for the purpose of attainment a high current drive efficiency (η_{CD}). Figure 1 shows a schematic view of the launcher. The circumferences of the grill mouth are covered with guard limiters made of c/c composite graphite for a protection from plasmas. These guard limiters are attached 3 mm beyond the grill mouth. The launcher has a double-probe in order to measure plasma density. The probe is located at right side of the mouth, and contains thermocouple in itself. The launcher position can be adjustable shot by shot in order to obtain a good coupling.

At first the LH waves were launched to the OH plasmas, a coupling property was investigated. And the LH waves were launched into NB-heated plasmas, an improvement of coupling was studied. The power of $\leq$ 1 MW was injected to plasmas in the divertor configuration with a low plasma density up to 2×10^{19} m^{-3}. The grill head was set at 1~3 cm (δ^{LH}) behind the first wall. The grill mouth was monitored by using a CCD camera during RF injection, and temperatures in various points of the grill were also measured by thermocouples.

3. Experimental results and discussions

Figure 2 shows a typical shot with a good coupling in an OH plasma. The incident power of ~500 kW was injected to the OH target plasma with Ip = 2 MA and $\overline{n_e} \sim 0.5 \times 10^{19}$ m^{-3}. Plasma position (δ^{47}; between the most outer magnetic surface and the first wall) was moved from 20 cm to 5 cm during from 3.5 to 6.5 sec.. The phase difference between main waveguides ($\Delta\Phi$(mod)) was 150 deg. in this period, and δ^{LH} was 2 cm. A reflection coefficient R gradually decreased with δ^{47}, and R rapidly dropped at 5.2 sec., and remained constant ~12 %. Emissions of visible lights around the grill were observed in a CCD camera when the plasma was coming close to the first wall. The intensity of Hα(main), which responded the interaction between the plasma and the wall, increased after the good coupling occurred. These results indicated that LH power produced thin plasmas during a good coupling, when δ^{47} was smaller than a threshold value. The edge plasma density measured by the double-probe showed that the e-holdlength λp was ~3.3 cm, the edge plasma density slowly decreased.

It was found that a certain density region was required for an attainment of a good coupling as known from fig. 3. The reflection coefficient was ~15 % when the edge density was beyond a threshold one ($\sim n_{cut\ off} \approx 5 \times 10^{16}$ m^{-3}). It was also pointed out / 2 / that the key item was to regulate neutral gas pressure at the grill mouth in order to obtain proper densities. But this reflection coefficient seems to be extremely high in spite of using a multijunction launcher. This may be the reason why that transmission lines caused the reflection coefficient to increase.

The good coupling was obtained in the case of the combination with NB, even if δ was up to 15~17 cm. The δ was larger than the case of LH alone. Figure 4 allows us to know what had happened in this phenomena. The LH power was injected to the NB-heated plasma with Ip = 2.5 MA and $\overline{n_e} = 1.9 \sim 2.3 \times 10^{19}$ m^{-3}. The δ^{47} remained nearly constant at ~14 cm, and the δ^{LH} was 3 cm. The time evolution of a probe current (Iprobe ; proportional to a plasma density) is shown. The Iprobe slightly increased with injection of NB. When LH power was launched, the density at grill mouth (n_e^{LH}) rose from 2×10^{16} m^{-3} to 8×10^{16} m^{-3} and then a good coupling was observed. The reflection coefficient was rapidly increasing as n_e^{LH} was decreasing after the stopping the NB. This experimental result indicates that thin plasmas in front of the grill were produced by LH power under the condition of the injection of NB.

After the attainment of the good coupling, LHCD experiments had been performed at large δ. Figure 5 illustrates that the η_{CD} was almost constant in the distant coupling. The η_{CD} of $\sim 2 \times 10^{19}$ A/Wm^2 at $\overline{n_e} \sim 0.5 \times 10^{19}$ m^{-3}, which was somewhat higher than that of JT-60 LHCD experiments at the same density, was obtained at R ~15 %. Tow of thermocouples inserted between a jacket and guard limiters showed a negligible small increase in temperature ($\leq$ 1 deg.). The heat flux due to edge plasmas was small and was estimated to be $\leq$ 6.6 W/cm^2. These experimental results indicated that the main part of LH wave was not absorbed at periphery, but propagated into main plasma without the degradation of η_{CD} in the distant coupling.

4. Summary

The present experiments had been carried out by using the multijunction launcher in the JT-60 Upgrade. The coupling characteristics were investigated. The reflection coefficient of 10~20 % was observed during an injection of LH power to OH plasmas, even though δ was 8~10 cm. And the good coupling was observed up to δ = 15~17 cm by the combination with NB. When the good coupling state occurred, the increase of density at the grill mouth was also observed. The degradation of the current drive efficiency was not observed in the distant coupling with R ~15 %. This experimental results indicated that the LH wave produced thin plasmas at the grill mouth, and that LH waves were mainly used to drive plasma current. The neutral gas pressure might be the key item to control the edge plasma density required for the good coupling.

The experimental results suggest the possibility of the distant coupling of LHCD launcher with low R and high η_{CD}. If we can actively control the coupling of LH waves independent of a precise control of plasma position, this procedure may be attractive for a reactor-grade tokamaks.

/1/ M.Seki, et al., Symposium on Fusion Technology (1990) 1060

/2/ Y.Ikeda, et al., to be published

Fig 1: The schematic view of the multijunction launcher in the JT-60 Upgrade.

Fig 2: Typical shot with a good coupling in an OH target plasma is shown.
The $\Delta\Phi$(mod) changed 0 ---> 360 deg. from 7.1 to 8.5 sec. for phase correction.

Fig 3: The reflection coefficient vs the edge density measured by the double-probe.

Fig 4: Time evolution of the edge density in the case of combination with NB.

Fig 5: The current drive efficiency vs the reflection coefficient.

Fig 4:

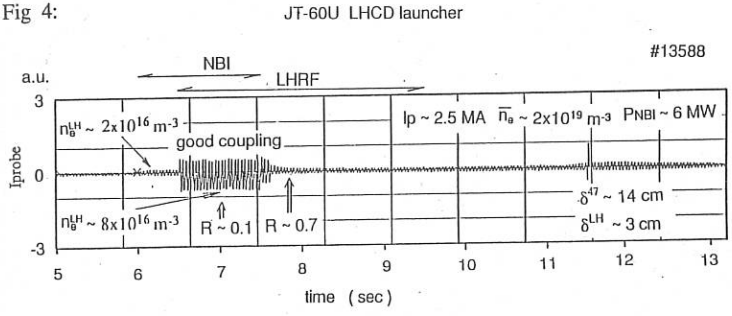

Fig 1:

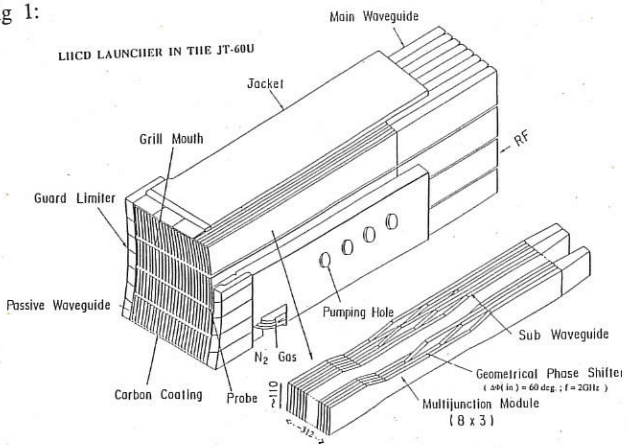

Fig 2:

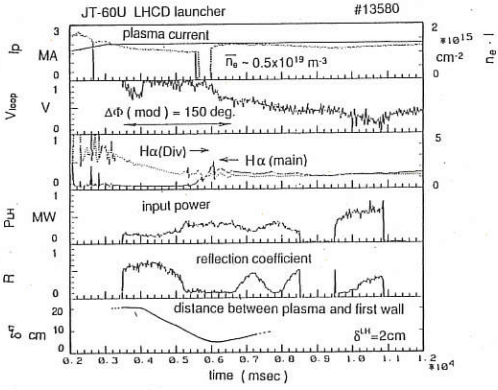

Fig 3:

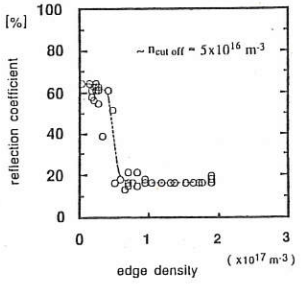

Fig 5:

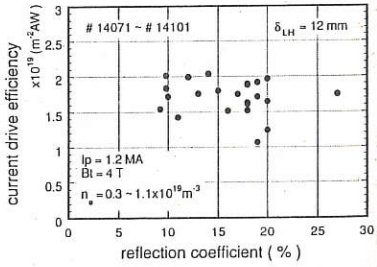

COUPLING ANALYSIS AND EXPERIMENT OF THE MUYLTIJUNCTION GRILL NEAR THE LOWER HYBRID FREQUENCY

K. Ohkubo and K. Matsumoto*

National Institute for Fusion Science, Nagoya 464-01, Japan

A generalized coupling theory of the multijunction grill has been developed by a multireflection method with the aid of scattering matrices both at the waveguide junction and the grill mouth facing a plasma. Numerical calculations have been compared in detail with experimental results for a four-junction grill designed for the JIPPTII-U tokamak.

A multijunction grill is schematically shown in Fig. 1. We denote scattering matrices at the junction plane by S_{pq} and at the grill mouth T_{pq}, incident waves propagating forward to the junction by $A_p^{(k)}$, to the mouth by $a_p^{(k)}$, scattering waves reflecting from the junction by $B_p^{(k)}$ and from the mouth by $b_p^{(k)}$ at k-th multiple reflection, where $p, q = 0, 1, \ldots n$. The global reflection coefficient in the primary waveguide Γ_0 is obtained by the ratio of total reflection wave to the incident one:

$$\Gamma_0 = \frac{\sum_{k=1}^{\infty} B_0^{(k)}}{A_0^{(1)}} \quad (1).$$ Here, $B_0^{(1)} = S_{00}A_0^{(1)}$ and $B_0^{(k)} = \sum_{p=1}^{n} S_{0p}A_p^{(k)}$ for $k \geq 2$.

It is worth while to indicate that the summation means vector addition. Similarly, the reflection coefficient in the p-th secondary waveguide at the mouth Γ_p is obtained:

$$\Gamma_p = \frac{\sum_{k=1}^{\infty} b_p^{(k)}}{\sum_{k=1}^{\infty} a_p^{(k)}}, \quad (2)$$

where $a_p^{(k)} = \Phi_{pp}B_p^{(k)}$,

$b_p^{(k)} = \sum_{q=1}^{n} T_{pq}\Phi_{qq}B_q^{(k)}$, $B_p^{(1)} = S_{p0}A_0^{(1)}$ and

$B_p^{(k)} = \sum_{q=1}^{n} S_{pq}\Phi_{qq}b_q^{(k-1)}$ for $k \geq 2$.

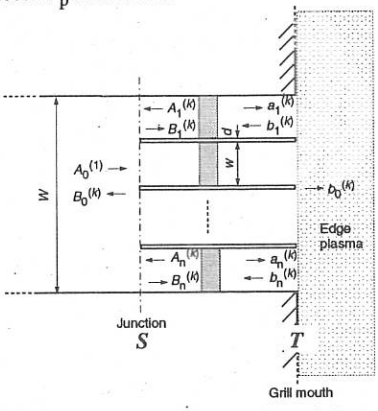

Fig. 1 Conceptual drawing of a multijunction grill.

* Present address: Department of Electronics & Informatics, Toyama Prefectural University,Toyama 939-03, Japan

Here, Φ_{qq} is the phase shift in the p-th secondary waveguide, which forms a diagonal matrix:

$$\Phi_{qq} = exp\{j[k_g L + (q-1)\Delta\phi]\},$$

where L is a length of the secondary waveguide, k_g is a wavenumber and $\Delta\phi$ is the phasing between adjacent waveguides. The elements of S_{pq} at the E-plane junction have been given by Moreau and N'guyen /1/. The scattering matrix at the mouth is calculated by a simplified conventional gill theory /2/, where the density profile in front of the mouth is modelled by the step(n_{wgd}) plus ramp(∇n_{wgd}). When an incident wave is injected only to the m-th waveguide, a scattered electric field E_{rq} at the q-th waveguide, normalized with the incident field E_{im}, is given by

$$\sum_{q=1}^{n} (w_p \delta_{pq} + U_{pq}) T_{qm} = w_p \delta_{pm} - U_{pm} , \quad (3)$$

where $T_{qm} \equiv \frac{E_{rq}}{E_{im}}$ and $\delta_{pq} = \begin{cases} 0 & (p \neq q) \\ 1 & (p = q) \end{cases}$.

Here, T_{qm} indicates a scattering coefficient which connects the q-th waveguide to the m-th one, w_p is a p-th waveguide width and U_{pq} is obtained from plasma parameters.

Numerically calculated results of coupling characteristics for the four-junction grill are shown in Fig. 2. The coupling property strongly depends on $k_g L$. It is seen that the length of the secondary waveguide is one of important parameters for grill design.

In Fig.2(b), $|E_{i2}|$ for both $k_g L$=30° and 150° are larger than unity for almost whole range of n_{wgd}/n_c. This behavior is quite distinct from the equivalent conventional grill. In Fig.2(a), $\angle E_{r2}$ has a value which is considerably different from that imposed by phasing, -270° (=360°-$\Delta\phi$): phasing is scrambling by multiple reflection between the mouth and the junction. The thick solid curve in Fig.2(f) indicates that the reflected field corresponding to the equivalent conventional grill has a large value compared with those of the multijunction grill.

Reflection coefficient in the primary waveguide

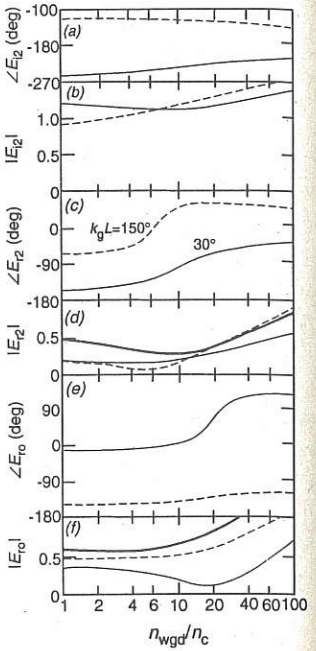

Fig. 2: RF electric fields in primary and No.2 secondary waveguides as functions of normalized density n_{wgd}/n_c for two secondary waveguide lengths of $k_g L$=30° (solid curve) and $k_g L$=150° (dashed curve). (a) phases and (b) amplitudes of forward electric fields in No.2 secondary waveguide, (c) phases and (d) amplitudes of reflected fields in the same secondary waveguide, (e) phases and (f) amplitudes of reflected fields in primary waveguide. Here, forward field in the primary waveguide $|E_{i0}|$ is set to $2\angle 0°$ and bold solid curves indicate the results for the equivalent conventional grill. Here, w=3.5cm, d=0.5cm, W=15.5cm, f=800MHz and $\nabla n_{wgd} = 1 \times 10^{11} cm^{-4}$.

and the directivity of the power spectrum radiated from the mouth are plotted as functions of $\Delta\phi$ for various k_gL in Fig.3(a) and 3(b), respectively. The value of $|\Gamma_0|$ is always small for any pair of k_gL and $\Delta\phi$ in comparison with the one in the conventional grill, which indicates the self-matching property of the multijunction grill. It is found that $|\Gamma_0|$ oscillates at a fairly regular interval with respect to $\Delta\phi$, which can be explained from phase change due to multiple reflections.

Fig.3(b) indicates that the directivity of the launched power spectrum is not always improved as compared with the one of the conventional grill, though the power launched into a plasma increases by virtue of the reduction of the reflection coefficient in the primary waveguide. The directivity becomes 0.5 for $\Delta\phi$=0° or 180° because of power-spectrum symmetry for N_z. The directivity changes remarkably with k_gL at a relatively small $\Delta\phi$, where power spectrum variations are examined as shown in Fig.4.

Power spectra of waves radiated from the multijunction grill into the plasma are shown for $\Delta\phi$=30° in Fig.4. The integral value of $P(N_z)$ over whole N_z becomes always large as compared with that of conventional grill owing to the increase of the launched power for any k_gL and $\Delta\phi$, as indicated in Fig.3(a). It is seen that as k_gL increases, $P(N_z)$ extends to a large positive N_z region, then $P(N_z)$ has parasitic peaks both in wide positive and negative N_z regions. These variation in $P(N_z)$ leads to the change in directivity, as shown in Fig.3(b). The reason why $P(N_z)$ extends to large N_z region and has parasitic peaks as the increase in k_gL is that the phasing among multi-reflected

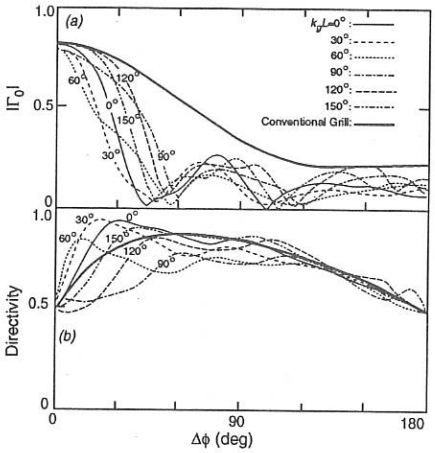

Fig.3: *(a) Electric field reflection coefficient of primary waveguide as functions of phasing $\Delta\phi$ for various normalized length k_gL of secondary waveguide. (b) Directivity of power radiated from the grill mouth into plasma as functions of $\Delta\phi$ for various k_gL, where directivity is calculated by*

$$\left(\int_1^{\infty} P(N_z)\,dN_z\right) \Big/ \left[\int_{-\infty}^{-1} P(N_z)\,dN_z + \int_1^{\infty} P(N_z)\,dN_z\right].$$

Here, n_{wgd}/n_c=10 and ∇n_{wgd}=1 $\times 10^{11} cm^{-4}$.

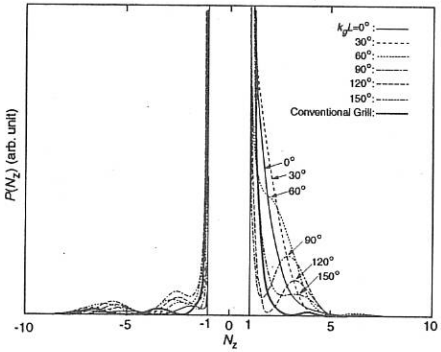

Fig.4: Power spectra of waves radiated from the grill mouth into plasma for various values of k_gL, where bold solid curves are for the equivalent conventional grill. Here, $\Delta\phi$=30°.

components at the mouth increases.

The experiments were carried out in the JIPPT-IIU tokamak by injecting the low power ($< 1W$) RF of $800MHz$ via the four-junction grill. To investigate the effect of the phasing and length on the coupling property in detail, the length of each secondary waveguide was directly changed. The every element of scattering matrices both at the junction and the mouth were directly estimated by the method of wave packet injection /3/.

The experimental and calculated results of the coupling property are shown in Fig. 5. The experimental results agree well with calculated values. Deviation of observed amplitudes from the calculated ones is considered to be resulted partly from the small disagreement between the observed scattering matrix at the grill mouth and calculated one. It is found that almost all the amplitudes vary nearly sinusoidally with k_gL, whose mechanism can be explained from phase change of multiply reflecting components. Reflection for the primary waveguide reaches a minimum when we choose the optimum length of secondary waveguide. The amplitude imbalance of forward waves in the secondary waveguides occurs and in the certain k_gL the amplitude has the value higher than 0.5 which is the value in the equivalent conventional grill.

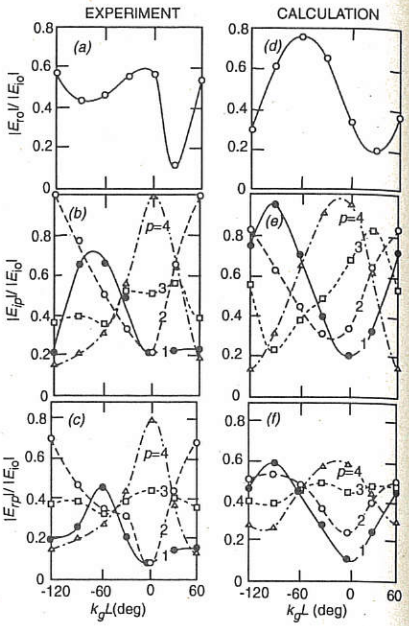

Fig. 5: Amplitude of electric fields both in primary and secondary waveguides versus normalized length k_gL of secondary waveguide, where all values are normalized to the amplitude $|E_{i0}|$ of forward wave in primary waveguide. Here, EXPERIMENT *and* CALCULATION *denote experimentally measured results and theoretically calculated ones: (a), (d) reflected wave $|E_{r0}|$ in primary waveguide. (b), (e) forward waves $|E_{ip}|$ in secondary waveguides. (c), (d) reflected waves $|E_{rp}|$ in secondary waveguides, where dots, open circles, asterisks and triangles indicate the results for 1st, 2nd, 3rd and 4th secondary waveguide, respectively. Here, $\Delta\phi=30°$, $n_{wgd}/n_c=31.6$ and $\nabla n_{wgd}=1\times10^{11}cm^{-4}$.*

The authors would like to express their thanks to Dr. T. Sato, Dr. Y. Hamada and Dr. T. Kuroda for their encouragement, and to the members of the RF group for their discussion. One of the authors (K.M.) wishes to thank Prof. M. Sato and Prof. S. Ishii for their continuous supports.

/1/ D. Moreau and T.K. N'guyen: *Couplage de l'onde lente au voisinage de la fréquence hybrid basse dans les grands tokamaks*, Association Eurtom-CEA, Centre d'études nucléaires de Fontanay-aux-Roses, Research Report EUR-CEA-FC-1246, (1983/1984).

/2/ K. Ohkubo and K. Matsumoto: Jpn. J. Appl. Phys. **26**, 142 (1987).

/3/ K. Ohkubo: Jpn. J. Appl. Phys. **30**, L1212 (1991).

MODULATIONAL INSTABILITY DEVELOPMENT AND CURRENT DRIVE

S.I.Popel, S.V.Vladimirov**, V.N.Tsytovich***
*Geosphere Dynamics Institute, Moscow, USSR
**General Physics Institute, Moscow, USSR

Recently many investigations on current driven by lower–hybrid (LH) waves in a plasma of toroidal nuclear fusion installations are carried out. Usually a theoretical approach [1] taking into account quasilinear and binary collisions effects is used to describe current drive. However a problem of comparison of the results obtained with the aid of the above theoretical approach and experimental data takes place. Namely the experimentally observed currents driven by LH waves is two–three orders of magnitude larger than those calculated using the theoretical approach adopted in [1]. The above discrepancy between theory and experiment is related with the existence of the so–called "spectral gap" (see [1], p.218), that is the gap between the parallel phase velocities of LH waves $\omega/k_{\|}$ (where $\omega, k_{\|}$ are LH wave frequency and a component of wavenumber $\vec{k}$ parallel to the external magnetic field $\vec{H}_0$) which are necessary for effective Landau damping of LH waves (i.e. velocities as high as several electron thermal velocities v_{T_e}) and the lowest parallel phase velocity in the injected LH wave spectrum (which is far above than v_{T_e} usually). Experimentally observed current drive may be explained if one accounts for filling of the "spectral gap" by LH waves. Some nonlinear effects have been drawn in current drive description to explain the "spectral gap" filling by LH waves (see, e.g. [2]). However the LH wave modulational instability (MI) effect has not been considered yet in application to current drive description. The aim of this paper is to investigate this MI influence. We shall show that for sufficiently intensive pump level of LH wave the MI can lead to "spectral gap" filling.

Let us consider the LH wave's MI for the case $(m/M)^{1/2} \lesssim \cos\theta_0 \ll 1$ (where m, M is the masses of electron and ion respectively, θ_0 is the angle between pump LH wave propagation and the external magnetic field $\vec{H}_0$ directions). This case corresponds to conditions of experiments on current drive generation by LH waves. Indeed the linear dispersion of LH waves has the form: $\omega_{\vec{k}} = (\omega_{pe}^2\cos^2\theta_0+\omega_{pi}^2)^{1/2}/(1+\omega_{pe}^2/\omega_{He}^2\sin^2\theta)^{1/2}$ (where ω_{pe}, ω_{He} are the plasma frequencies of electrons and ions respectively, ω_{He} is the

electron cyclotron frequency) while the pump LH wave frequency ω_0 obeys the conditions (see [2]) $\omega_{pe} \gg \omega_0 \gtrsim 2\omega_{LH} = 2\omega_{pi}/(1+\omega_{pe}^2/\omega_{He}^2)^{1/2}$ in the experiments on current drive. These conditions correspond to the case $(m/M)^{1/2} \lesssim \cos\theta_0 \ll 1$.

A quantitative investigation of the MI is considered by standard way [3]. Firstly the general nonlinear equation of the third order in LH wave fields is derived by using the kinetic equations for electrons and ions and Poisson equation (we use the fact that LH waves are longitudinal); perturbations of the distribution function expands in a set of terms over powers of the LH wave electric field $\vec{E}$, which up to the cubic terms are expressed through the LH wave fields and unpertubated (both electron and ion) distribution function. Further we distinguish in the obtained equation positive and negative– frequency parts of the LH wave fields: E_k^+, E_k^- (where $\vec{E}_k = \vec{k}E_k/|\vec{k}|$ is Fourier component of the LH wave electric field, $k = \{\omega,\vec{k}\}$; E_k^+, E_k^- correspond to $\omega>0$, $\omega<0$ respectively), and introduce the virtual fields E_k^χ on the low frequency $\Delta\omega \ll \omega_{LH}$. Finally we obtain the equation containing the wave fields $E_k^\pm$ only:

$$\varepsilon_{k_0} E_{k_0}^+ = 2\int \Sigma^{eff}_{k_0,k_1,k_2,k_3} E_{k_1}^+ E_{k_2}^+ E_{k_3}^- \delta(k_0-k_1-k_2-k_3)dk_1dk_2dk_3 \qquad (1)$$

where $\delta(k)=\delta(\omega)\delta(\vec{k})$, $\varepsilon_k=\varepsilon(\omega,\vec{k})$ is the linear dielectric function;

$$\Sigma^{eff}_{k_0,k_1,k_2,k_3} \approx -\frac{e^2(\Delta\vec{k})^2}{2m^2|\vec{k}_0||\vec{k}_1||\vec{k}_2||\vec{k}_3|} \cdot \frac{\varepsilon^{(i)}_{\Delta k}(\varepsilon^{(e)}_{\Delta k}-1)}{\varepsilon_{\Delta k}} \times$$

$$\left\{\frac{k_{0\parallel}k_{1\parallel}}{\omega_0^2} - \frac{i[\vec{k}_{0\perp}\vec{k}_{1\perp}]_\parallel}{\omega_{He}\omega_0}\right\} \cdot \left\{\frac{k_{2\parallel}k_{3\parallel}}{\omega_0^2} - \frac{i[\vec{k}_{2\perp}\vec{k}_{3\perp}]_\parallel}{\omega_0\,\omega_{He}}\right\}, \qquad (2)$$

here $-e$ is the electron charge, $\Delta k=k_0-k_1$; $\varepsilon^{(e,i)}_{\Delta k}$ is the electron (ion) part of the dielectric function. The expressions (1)–(2) are derived when $|\omega_0|\approx|\omega_1|\approx|\omega_2|\approx|\omega_3|\gg|\Delta\omega|$, $|\omega_0|\gg|k_{i\parallel}|v_{Te}$, $|\vec{k}_{i\perp}|v_{Te}/\omega_{He} \ll 1$, $i=0,1,2,3$.

The dispersion equation for the MI is derived from the equations obtained by such a way (as a condition for solving of a system of two equations for modulational perturbations $\delta E_k^\pm$). For the case $\Delta\vec{k}\perp\vec{k}_0$ we get

$$1 = \frac{|E_0|^2}{4\pi n m\omega_0^2}\frac{\omega_{pe}^2}{\omega_{He}^2}\frac{(\Delta\vec{k})^4}{(\vec{k}_0)^2+(\Delta\vec{k})^2}\frac{\varepsilon^{(i)}_{\Delta k}(\varepsilon^{(e)}_{\Delta k}-1)}{\varepsilon_{\Delta k}}\left[\frac{1}{\varepsilon_{\Delta k+k_0}}+\frac{1}{\varepsilon_{\Delta k-k_0}}\right], \qquad (3)$$

where n is the electron concentration; E_0, ω_0, $\vec{k}_0$ are respectively the pump field intensity, frequency and wavenumber. (We note here that when $\Delta\vec{k}\perp\vec{k}_0$ the MI effect is maximum; when $\Delta\vec{k}\parallel\vec{k}_0$ the right side of Eq.(3) is multiplied by the factor $(1+\omega_{He}^2/\omega_{pe}^2)\cos^2\theta_0$ which is far less than 1 under the conditions of experiments on current drive.)

To explain the "spectral gap" filling we should account for an appearance of LH waves with the parallel phase velocities $\omega/k_{\parallel}\ll\omega_0/k_{0\parallel}$. Since the essential change of wave number may take place as a result of the MI development (while the wave frequency cannot be changed essentially) we are interesting the case $|\Delta\vec{k}|\gg|\vec{k}_0|$. In this case for sufficiently intensive pump level

$$W/4\pi T_e \gg (|\Delta\vec{k}|v_s/\omega_0)(\omega_{pe}^2+\omega_{He}^2)\omega_{pe}^{-2}\cos^2\theta_0 \qquad (4)$$

(where $W=|E_0|^2(1+\omega_{pe}^2/\omega_{He}^2)/2\pi$, $v_s=(T_e/M)^{1/2}$, T_e is the electron temperature) the development of the MI with the maximum growth rate (for a fixed $|\Delta\vec{k}|$)

$$\Gamma^{Mod}_{|\Delta k|} \sim \omega_0\left[\frac{|\Delta\vec{k}|v_s}{\omega_0}\right]^{2/3}\left[\frac{W}{4nT_e}\frac{\omega_{pe}^2}{\omega_{pe}^2+\omega_{He}^2}\frac{1}{\cos^2\theta_0}\right]^{1/3} \qquad (5)$$

takes place.

For the moderate pump level (when an inequality opposite to the inequality (4) is fulfilled) the MI (when $\vec{k}\perp\vec{k}_0$) may be developed if the following condition takes place:

$$|\vec{k}_0|/|\Delta\vec{k}| \ll |\Delta\vec{k}|v_s/\omega_0; \qquad (6)$$

if (6) is valid and the LH wave pump level is moderate (the inequality opposite to the inequality (4) is fulfilled) then the MI growth rate is

$$\Gamma \approx \omega_0 \frac{\omega_{pe}^4}{(\omega_{pe}^2+\omega_{He}^2)(\omega_{pe}^2\cos^2\theta_0+\omega_{pi}^2)}\frac{W}{4nT_e}. \qquad (7)$$

From the view point of current drive applications it is not necessary to analyze the case of the moderate LH wave pump level when the inequality (6) is violated: the MI growth rates obtained for this case are essentially less than the growth rate (7) and also (when $T_e\sim T_i$ which corresponds to the experimental conditions on current drive) essentially less than the growth rate of induced scattering (see, e.g. [4]).

It is worth noting that the character of the LH wave MI when $|\Delta\vec{k}|\gg|\vec{k}_0|$ essentially

differs from its character when $|\vec{k}_0|=0$. The presence of the conditions like (6) points to this.

From the view point of explanation of the "spectral gap" filling it is interesting to consider an excitation of LH waves with parallel phase velocities less or approximately equal to $4.5v_{Te}$ (i.e. with $|\vec{k}| \gtrsim (\omega_0/4.5v_{Te}\cos\theta_0)$). For the pump levels $W/4nT_e \gg (\omega_{pe}^2+\omega_{He}^2)\omega_{pe}^{-2}(m/M)^{1/2}\cos\theta_0$ the relationship (4) is valid for any $|\Delta\vec{k}|_{max} \geq |\Delta\vec{k}| \gg |\vec{k}_0|$ (where $|\Delta\vec{k}|_{max}$ is determined from the condition $\Gamma^{Mod}_{|\Delta\vec{k}|}+\Gamma^{L}_{\Delta\vec{k}} = 0$; $\Gamma^{L}_{\Delta\vec{k}}$ is Landau damping rate) and consequently the development of the LH wave MI characterized by the growth rate (5) takes place. In this case LH waves with sufficiently low parallel phase velocities ($|\omega/k_{||}|_{min} \approx |\omega_0/|\Delta\vec{k}|_{max}\cos\theta_0| \lesssim 3.5v_{Te}$) can appears as a result of the MI. Hence in the discussed case of sufficiently intensive pumping the consideration of the MI is essential when describing the "spectral gap" filling by LH waves in the process of current drive generation.

If the LH wave pumping is moderate: $W/4nT_e \ll (4.5)^{-1}(\omega_{pe}^2+\omega_{He}^2)\omega_{pe}^{-2}(m/M)^{1/2}\cos\theta_0$ then for the magnitudes $|\Delta\vec{k}| \gtrsim (\omega_0/4.5v_{Te}\cos\theta_0)$ the condition (4) is not valid. Besides for $|\Delta\vec{k}| \gtrsim (\omega_0/4.5v_{Te}\cos\theta_0)$ the inequality (6) is not usually fulfilled under the conditions of experiments on current drive. Thus when the LH wave pumping is moderate ($W/4nT_e \ll (4.5)^{-1}(\omega_{pe}^2+\omega_{He}^2)\omega_{pe}^{-2}(m/M)^{1/2}\cos\theta_0$) the influence of the LH wave MI upon current drive generation is not essential as a rule.

Thus the consideration of the LH wave MI allows to account for "spectral gap" filling by LH waves when the LH wave pumping is sufficiently intensive ($W/4nT_e \gg (\omega_{pe}^2+\omega_{He}^2)\omega_{pe}^{-2}(m/M)^{1/2}\cos\theta_0$).

References

1. Fisch N.J. Rev. Mod. Phys., 59, 175 (1987).
2. Kolesnichenko Ya.I. et al. In: Voprosy teorii plazmy (Questions of Plasma Theory). M.: Energoatomizdat, 1989. Issue 17. P.3.
3. Rudakov L.I., Tsytovich V.N. Phys. Reports. 40C, 1 (1978).
4. Vladimirov S.V., Popel S.I., Tsytovich V.N. Preprint 23–A, General Physics Inst., Moscow 1991.

FAST ION GENERATION DURING RF DISCHARGE ON THE FT-2 TOKAMAK AND PARAMETRIC DECAY INSTABILITIES.

V.N.Budnikov, V.V.Djachenko, L.A.Esipov, E.R.Its, S.I.Lashkul, K.M.Novik, A.Yu.Stepanov, O.N.Shcherbinin,
A.F.Ioffe Phisical-technical Institute, St.Petersburg.

V.O. Alexandrov, I.E.Sakharov, S.V.Shatalin.
State Technical University, St.Petersburg.

A fast ion generation with energy from 0.1 up to 5.0keV has been observed unexpectedly during LHRF preionization experiment on the FT-1 tokamak [1]. The energy spectrum of the ion population was the same as in well known LHRF heating experiments on tokamaks. But the phenomenon was surprising because the ion acceleration occurs in a cold RF produced plasma without the linear conversion point for pumping wave in a contrast to hot and dense ohmic plasma.

There are different points of view on the mechanism of the fast ion generation [2,3] in a tokamak plasma. This paper is devoted to investigation of the wave power dissipation mechanism in the RF produced plasma and seems to be useful for understanding of nature of the LH wave absorption.

The RF power with f_o=918MHz is transmitted to the chamber of the FT-2 tokamak (R=55cm, a=8cm, $B_o \simeq 2.5T$, gas-hydrogen) from the low magnetic field side by the 2-waveguide grill ($\Delta\varphi=180^o$). The calculated parallel refractive index $N_\parallel$ is 2÷4; the pulse duration is up to 10ms and RF power (40÷100)kW. Basic diagnostics - CX analyzer, bolometer, two electrostatic probes and microwave enhanced scattering antennas - are located in a cross-section shifted from the grill on 90° along the torus. The microwave interferometer is arranged in the opposite cross-section.The enhanced scattering diagnostic [4] operates on probing frequency f_p=59GHz. The microwave power is provided on X-mode by a horn antenna from the high magnetic field side.

For stabilization of RF plasma start a short ohmic discharge was used 5ms before RF pulse. At the beginning of the RF pulse the density of the decay plasma was $\sim 10^{11} cm^{-3}$, which was equal to $10n_{cr}$ for the pumping power. These initial condi-

tions were suitable for exciting and propagation of electron plasma waves, which were able for ionize gas and to rise the plasma density. The RF ionization took place in a wide range of the toroidal magnetic fields (1.6÷2.4)T and at the gas pressure $\simeq 10^{-4}$mm Hg. Depending on the gas pressure and RF power applied the average plasma density was $(0.2\div1.0)10^{13}cm^{-3}$, but, as Fig.1 demonstrates, the density profile (curve 1) was found to be essentially asymmetric along the major radius. Value of n_e at r= 7.8cm was obtained by the probe. The curve 2 shows the distribution of radiation losses registered by the bolometer. Calculations permit to evaluate the ionization degree as 90% at the maximal density and $Z_{eff}\simeq1.2$. Total radiation losses at the end of discharge were equal to 30kW at 60kW input power. According to probe and optical measurements electron and ion temperatures were about 30eV and 2eV respectively.

Beginning from some threshold RF power (or plasma density) such discharge became a source of fast ions with energy (0.1÷ 3.8)keV. The power threshold was approximately 15kW and increased up to 30kW as the density was reduced. The most of experiments have been carried out at 40kW RF power and $n_e\approx8\cdot10^{12}cm^{-3}$ (Fig.1), that is far above the threshold.

Interesting results were obtained using the microwave enhance scattering diagnostics which was able to measure the frequency spectra of radiation from the vicinity of the upper hybrid resonance (UHR) location for f_p and to determine the direction of $k_\perp$ of a plasma wave. These spectra were registered in reference to f_p in frequency range of (400÷1200)MHz. One of these very complicated spectra is shown in Fig.2. There are three groups of peaks in the "red" band of the spectrum: in the vicinity of f_o; near 700MHz and then near $f_o/2\simeq450$MHz. On the contrary, only one group with $f\approx f_o/2$ exists in the "blue" side. All groups are modulated by narrow peaks separated one from another by $\Delta f\simeq31.6$MHz, what corresponds to local ion cyclotron (IC) frequency at r=6.5cm, i.e at the density maximum. The first peak at 886MHz agrees to the 28-th IC harmonic, the last one at 415 MHz to the 13-th harmonic. The spectrum was measured by analyzers with 5 and 25MHz frequency band shot by

shot.

Uncertainty in the density profile does not let to estimate correctly the position of the UHR and the region of scattering connected with it. That's why, in Fig.3 amplitudes of the scattered signal for different parts of the spectrum are presented in dependence on the toroidal magnetic field. Curves 1-3 are concerned with $n_e=8\cdot10^{12}cm^{-3}$, curve 4 - with $n_e=6\cdot10^{12}cm^{-3}$. It's seen, that oscillations with different frequencies are localized at the same place, in the density maximum (curves 1-3). As n_e is reduced the region of scattering shifts to higher magnetic field according to the UHR equation.

Several typical oscillograms are shown on Fig.4 - signal of enhanced scattering; neutral particle 1keV flux and evolution of plasma density. As it is seen, the scattered signal and the fast particle flux appear simultaneously at the moment when the density exceeds some threshold level.

The structure of observed spectrum with "red" satellites is typical for parametric decay instabilities, while scenario of decays appears to be complicated enough. A number of ways can develop simultaneously or consequently: $\omega_{LH} \Rightarrow \omega^*_{LH} + n\omega_{ci}$ or $\omega_{LH} \Rightarrow 2\omega^*_{LH}$. The last decay is characterized by "red" and "blue" satellites in accordance with the theory. But the final frequency of daughter waves in this case is not equal to f_o, rather to the frequency of the first IC harmonic peak ($28\omega_{ci}$). Probably, we have not direct decay of exited LH waves, but decay of the secondary IC wave. It is important, that the LHR condition exists for the wave with $f\simeq f_o/2$ at $n_e\simeq8\cdot10^{12}cm^{-3}$, namely, there is possibility to accelerate ions by a classical stochastic mechanism. On the other hand, we cannot exclude direct excitation of shortlength waves by the grill (perhaps, ion Berstain waves) with their decay on the next step.

Summary: the cold RF produced plasma in toroidal magnetic field is a source of the intensive fast ion flux. The mechanism of ion generation is connected with parametric decay instabilities, as in LH heating experiments on the ohmic tokamak plasma. It seems to be some universal mechanism displaying in wide range of experimental conditions.

References:

1. V.V.Djachenko, M.M.Larionov et. al. Question of Atomic Science And Technology, Nuclear Fusion Series, n4, (1989), p-19(in Russian)

2. Ch. F.F.Karney, Phys. Fluids 21 (1978) and 22 (1979).

3. Porkolab M., Bernabey S., et. al. Phys. Rev. Lett., 38 (1977), 230-234.

4. Novik K.M. Basic and Advanced Diagnostic Techniques for FusionPlasma (Proc. Course and Workshop Int. School of Plasma Physics, Varenna, (1986), vol.1.

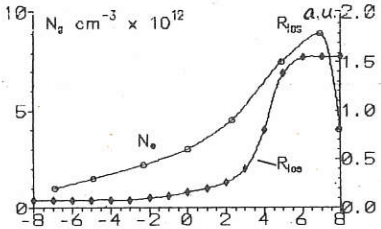

Fig. 1

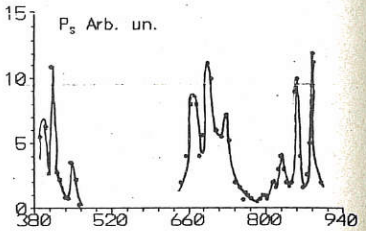

Fig 2.

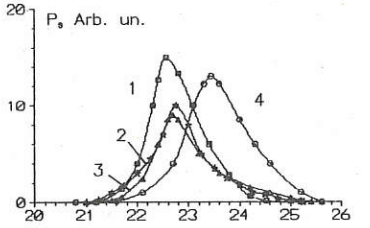

Fig 3.

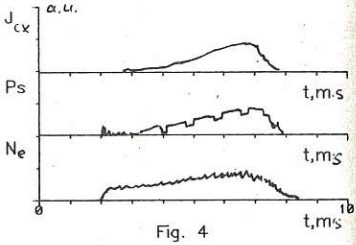

Fig. 4

MEASUREMENTS of ELECTRON CYCLOTRON EMISSION during HIGH POWER ECRH in the W7-AS STELLARATOR

U. Gasparino, H.J. Hartfuß, H. Maaßberg, V. Tribaldos*, M. Tutter
W7-AS Team#, ECRH Group**#

Max-Planck Institut für Plasmaphysik, 8046 Garching, FRG
* Asociación EURATOM-CIEMAT, 28040 Madrid, Spain
** Institut für Plasmaforschung der Universität Stuttgart, 7000 Stuttgart, FRG
# see H.J. Hartfuß , this Conference

• INTRODUCTION •

When applied to high power ECRH, the quasi-linear theory predicts the formation of a mildly suprathermal tail and a flattening in the perpendicular energy direction for the electron distribution function close to the resonance zone. In case of low field side perpendicular injection, the incident ECRH power is expected to be absorbed by "thermal electrons" and, contrary to the lower hybrid heating, no simple analytical model for the steady-state distribution function has been developed. Due to its complementarity with the absorption mechanism, the electron cyclotron emission can provide attractive tools to perform investigations on the impact of very high ECRH-power on the electron distribution function. With this aim, observation along viewing chords of "constant-B" are favourable as they permit, in principle, a detailed investigation of the high-energy part of the electron distribution function without the interference of re-absorption. Experiments of this kind have been carried out in the W7-AS Stellarator, during high power ECRH in low density plasmas ((O)-mode, perpendicular injection from low field side).

• EXPERIMENTAL CONDITIONS •

With the aim of observing the behaviour of non-thermal features driven by strong ECRH, low density plasmas have been investigated. The target plasma is created and heated up by ECRH alone (net current free operation). We discuss only results related to perpendicular injection ($k_{\|} \cdot B = 0$) of r.f. in the (O)-mode ($\nu_{ECRH} = 70$ GHz, $B_0 = 2.5$ T) from the low field side (in a toroidal plane with "tokamak-like" magnetic field structure and "elliptical" magnetic surfaces) The ECRH power was increased step by step (160, 310, 470 kW) while the density of the target plasma was kept constant during the power scan (corresponding to a central density of $n_{e,0} = 1.7 \cdot 10^{13}$ cm^{-3}). The central temperature increased from $T_{e,0} = 1.2$ keV to $T_{e,0} = 2.5$ keV. While the density profiles were typically very broad, the temperature showed peaked profiles.

The ECE was detected by receivers placed in different modules and looking along viewing chords with different properties. A "$T_e(R)$-antenna" looked from the low field side in a "tokamak-like" plane. A second one looked vertically in a toroidal plane rather close to the ECRH injection plane (similar to vertical observation in a tokamak). The third antenna looked in a plane where the magnetic field strength makes only small variations and the plasma has a "triangular" cross-section. All the three antennas looked perpendicularly into the plasma ($k_{\|} \cdot B = 0$) at the 2nd harmonic (X)-mode polarization.

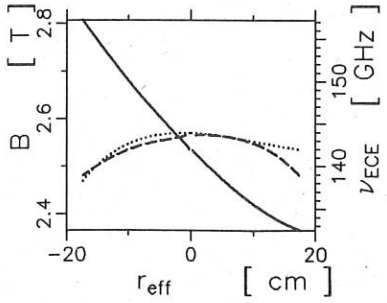

Fig. 1: magnetic field vs. corresponding effective minor radius along the three viewing chords where the ECE is measured. The full line corresponds to the "elliptical plane" low field side observation. The dashed line to the "elliptical plane" vertical observation. The dotted line to the observation in the "triangular plane". The antennas are viewing from the "positive effective radius".

• THEORETICAL DESCRIPTION •

Under the approximations of the geometrical optics, ray paths are numerically traced back from the ECE-antennas into the plasma (ray-tracing) and the energy transfer equation /1/ is then integrated at each point along the trajectory. The local relativistic emission and absorption coefficients are evaluated numerically once the electron distribution function is specified (as a function of $v_{\|}$, $v_{\perp}$ and minor radius) /2/. In case of analytical models (e.g. bi-Maxwellian, shifted Maxwellian) the parameters characterizing the test distribution function are then varied until a satisfactory (but usually not univocal) agreement with the experimental data is obtained. In a more consistent approach a Fokker-Planck equation must be solved including the (quasi-linear) heating term and the effects of collisions and radial losses (related to radial transport) /3/. Contrary to tokamak, for net current free operation the effects related to the presence of an inductive electric field are negligible. A description of trapped particles must be included. In the 3-D magnetic field topology of W7-AS this has been done only through simplified models /4/. Due to the non-axisymmetry and the existence of local B-minima, toroidally localized trapped electrons could be generated in the ECRH injection module.

• EXPERIMENTAL RESULTS •

The low field side antenna in the "elliptical" plane was generally used to determine the electron temperature profile. With the increasing of the ECRH injected power (and of the plasma temperature) a secondary peak appears on the low frequency side of the ECE-spectrum (at frequencies of typically $\nu_{ECE} \simeq 130 \div 132$ GHz). This peak has been interpreted as down-shifted emission from the central part of the plasma column (at the observed frequency the resonant electrons should have energies $E_{r\varsigma s} \simeq 30$ keV) /5/. The fact that the detected ECE-spectrum decays at even lower frequencies is an indication that the electron tail doesn't extend to much higher energies. Due to the low inverse aspect ratio of W7-AS (a [m] / R [m] =0.18/2) by allowing wall reflections (reflection coefficient $\rho \simeq 98\%$) similar secondary peaks can be reproduced even by purely Maxwellian plasmas (for $T_{e,0} \geq 2 \div 3$ keV) /5/. In this case relativistically down-shifted thermal emission from the tail of the Maxwellian distribution at the plasma axis reaches the antenna without being strongly reabsorbed and is amplified by multiple wall reflections.

An analysis of the emission related to the "vertical" and the "triangular plane" observation, gives us more sophisticated information. In these cases in fact complications introduced by re-absorption (strongly dependent on the boundary temperature and density, often known only within relatively large error bars) are minimized. If wall reflections are neglected, an overestimate for the possible amount of suprathermals is obtained. The detected emission for the case of "low power" ECRH (1 gyrotron, 160 kW, $T_{e,0} = 1.2$ keV) and "high power" ECRH (3 gyrotrons, 470 kW, $T_{e,0} = 2.5$ keV) are reported in Fig. 2.

In absence of wall reflections no emission should appear above a critical frequency ($\nu_{max} \simeq 143 \div 144$ GHz) related to the maximum B encountered along the viewing chords. For $\nu \geq \nu_{max}$ no resonant electrons exist along the viewing chord. Nevertheless the experimental results show strong emission above ν_{max}. This is believed to be a direct indication that wall reflections are not negligible (at least for $\nu \geq \nu_{max}$). At these frequencies, for the antenna in the "triangular plane" a resonant field is met in toroidal planes at least 7° degrees away from the plane of detection. As a consequence, at optically thin frequencies an emission stronger than the one related to the last single pass (as modelled in the simulation) is probably detected.

• STRUCTURE OF THE THERMAL PART OF THE SPECTRUM •

The peaked structure at a frequency just below ν_{max} is well reproduced by the simulation (see Fig. 2). The origin of this sharp maximum is explained in Fig. 3, where the radial source of the detectable emission is shown as a function of frequency. 95 % of the detected emission has its origin within the hatched region. Following the simulation, at frequencies below ν_{max} the resonant magnetic field is originally met close to the plasma center (causing the appearance of a sharp maximum just below ν_{max}). By a further decrease of ν the thermal resonance moves towards the plasma edge (see Fig. 1) causing a rapid decrease in the value of the resonant temperature (local minimum at $\nu \simeq 142$ GHz). At even lower frequencies the thermal resonance moves outside of the plasma and down-shifted emission reaches the antenna. At first the emission is still related to the optically thick boundary

region but at lower frequencies only down-shifted emission from the central plasma region (where the temperature shows its maximum) reaches the antenna. The frequency at which the sharp maximum appears gives a very precise measurement of the maximum magnetic field along the viewing chord. This structure is adequately reproduced by the simulation where the measured coil currents were used for the evaluation of the equilibrium magnetic field.

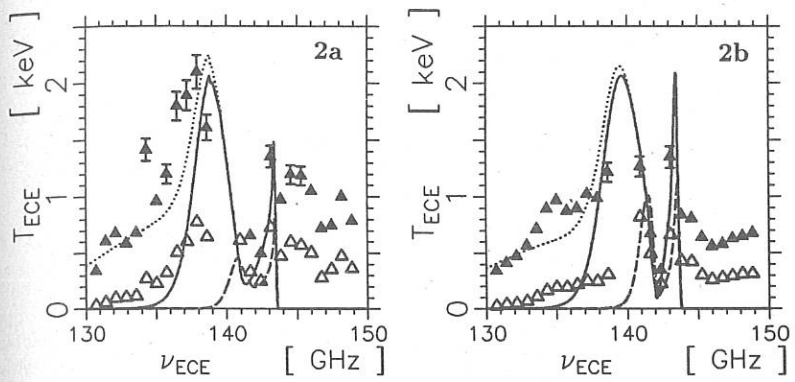

Fig. 2: measurements vs. simulation for the 1 gyrotron and the 3 gyrotrons case. Fig. 2a refers to the vertical observation. Fig. 2b to the observation in the "triangular plane". Open triangle: measurement during 1 gyr. ECRH. Full triangle: during 3 gyr. Dashed line: simulation 1 gyr. Full line: simulation 3 gyr. Dotted line: simulation for the 3 gyrotrons phase allowing for a suprathermal component (see text).

• STRUCTURE OF THE SUPRATHERMAL PART OF THE SPECTRUM •

As already noticed any quantitative conclusion can be strongly affected by the (quantitatively unknown) role played by wall reflections. Neglecting this effect an overestimation for the (eventual) deviations from the Maxwellian bulk can be obtained. The dotted line in Fig. 2 refers to a simulation where a second Maxwellian was used to model the suprathermal contribution. The parameters used correspond to suprathermal temperatures $T_{\parallel}^{s.th.} = T_{\perp}^{s.th.} = 12$ keV and a suprathermal density $n_{e,0}^{s.th.} = 0.5\%\ n_{e,0}$. This deviation from the Maxwellian bulk is introduced only close to the plasma axis ($r_{eff} \leq 2.5$ cm) where, for on-axis ECRH, the injected power is expected to be deposited. A possible broadening of the suprathermal profile as a consequence of radial diffusion is expected to play a negligible role for these plasma parameters. Taking into account that these values give an upper limit for the non-thermal components, one can conclude that low-field-side perpendicular injection of (O)-mode doesn't perturb significantly the electron distribution function even at the high power density obtained during on axis heating.

• MODULATION EXPERIMENTS •

Fig. 4 shows the reaction (amplitude and time delay) of the ECE channels to a modulation of the injected power (square wave modulation, $\nu_{mod} = 92$ Hz, $P_{mod}/P_{inj} \leq 5\%$). The signal refers to the antenna in the "triangular" plane. The amplitude behaviour agrees with the interpretation of Fig. 3, recalling that the amplitude of the heat pulse is damped during its radial propagation. The phase delay is also in agreement apart from the channels where the modulation amplitude becomes so small that the determination and the interpretation of the phase delay in terms of a propagating heat pulse is rather critical. In agreement with the interpretation of Fig. 3, the channels in the low frequency part of the spectrum show a similar time behaviour (the higher harmonics of the ECRH square wave modulation appears undamped) and phase delay as those related from the emission from the central region of the plasma.

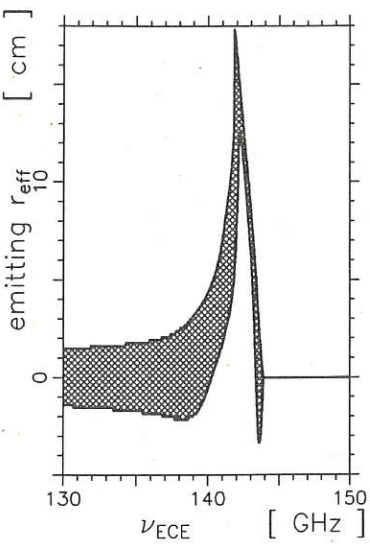

Fig. 3: radial origin of the detected ECE for the case of Fig. 2b, 3 gyrotrons, Maxwellian plasma. 95 % of the emission has its origin within the hatched region.

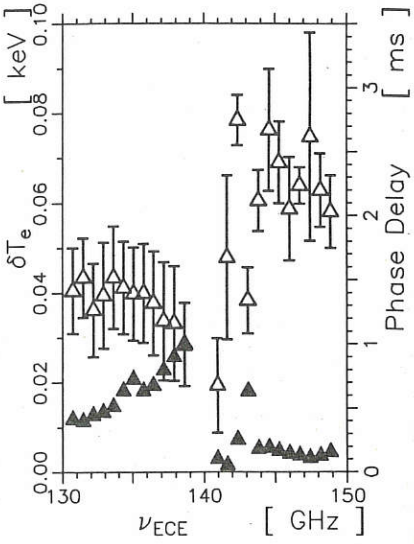

Fig. 4: Measured perturbation amplitude (full triangles) and time delay (open triangles) for the several ECE channels in case of square wave modulated ECRH.

• CONCLUSIONS •

The deformations of the electron distribution function induced by high power perpendicular injection of (O)-mode 1st-harmonic from the low field side has been estimated by an analysis of the ECE along viewing chords with different properties. For the discussed discharges, an estimation of the maximum amount of suprathermal particles leads to an energy $T_{\parallel}^{s.th.} = T_{\perp}^{s.th.} = 12$ keV and a density $n_{e,0}^{s.th.} = 0.5\%\ n_{e,0}$. These values are found in a toroidal plane far from the ECRH injection plane as well as in a rather close one. Recalling that this gives an overestimation of the deviations from the Maxwellian bulk, it results that even for relatively high perpendicularly injected ECRH power densities (the ray tracing code predicts peaked deposition profiles with maximum power densities of the order of 100 W/cm^3 and deposition widths $\simeq 1.5$ cm) the electron distribution function can be rather accurately described by its Maxwellian component. This conclusions relates only to (O)-mode injected perpendicularly from the low field side. Measurements in the current drive scenario (where, contrary to the perpendicular injection case, the injected power can be absorbed by Doppler resonant electrons of the Maxwellian tail before having to pass through the thermal bulk resonance) as well as the installation of radiation beam dumpers will permit more detailed conclusions.

• REFERENCES •

/1/ G. Bekefi, Radiation Processes in Plasmas, (Wiley & Sons, New York 1966), Chap. 1

/2/ V. Tribaldos et al., Proc. 17th EPS, Amsterdam 1990, Vol. IV, 1648

/3/ U. Gasparino et al., Proc. of the Joint Varenna-Lausanne Int. Workshop on Theory of Fusion Plasmas, Varenna 1990, 195

/4/ Yu.N. Dnestrovskij et al., Nucl. Fus. 28 (1988),267

/5/ H.J. Hartfuß et al., Int. Workshop on Collective Acceleration in Collisionless Plasmas, Cargèse 1991

SIMULATIONS OF FAST ELECTRON GENERATION BY STIMULATED RAMAN FORWARD SCATTERING IN A MAGNETIZED PLASMA

P. Bertrand[1], A. Ghizzo[1], S.J. Karttunen[2], T.J.H. Pättikangas[2], R.R.E. Salomaa[3] and M. Shoucri[4]

[1]Physique Théorique, Université de Nancy–I, France
[2]Nuclear Engineering Laboratory, Technical Research Centre of Finland, Finland
[3]Department of Technical Physics, Helsinki University of Technology, Finland
[4]Centre Canadien de Fusion Magnétique, Tokamak de Varennes, IREQ, Canada

1. Introduction

Stimulated Raman scattering (SRS) of free-electron-laser (FEL) radiation can be applied to the current drive in tokamak plasmas [1–3], because SRS generates nearly collisionless electrons with high parallel velocities. The scattered electromagnetic (EM) wave in SRS may propagate either backward (SRS-B) or forward (SRS-F). The electron plasma wave, which produces fast electrons by Landau coupling, travels in both cases in the same direction as the pump wave. The phase velocity of the plasma wave, and correspondingly the fast electron energy, in SRS-B is much lower than in SRS-F. At high temperatures and low densities, the plasma wave excited in SRS-B is heavily damped so that the Raman forward scattering prevails in long scalelength plasmas.

We present simulations performed with an Eulerian relativistic Vlasov code. Such a code renders possible a detailed examination of the low density regions of the phase-space, which are poorly described by the usual PIC codes. A second advantage is the noiseless character of the code, due to its Eulerian type [4]. SRS-F is considered in the parameter range where the phase velocity of the electrostatic plasma wave exceeds $0.9c$. The corresponding energy of the fast electrons is highly relativistic, i.e., $\gamma = (1 - v_{\rm ph}^2/c^2)^{-1/2} > 2.3$. Our simulations reveal that the plasma waves in this range are, in fact, able to produce even more energetic electrons, up to $\gamma \simeq 4 - 12$.

2. Vlasov–Maxwell simulations of SRS-F

We assume a homogeneous plasma and a simple geometry where all the waves propagate in the x-direction, parallel to the external magnetic field $\mathbf{B}_0$. Thus, circularly polarized EM waves are eigenmodes of propagation. This situation corresponds to the Raman current drive in tokamak plasmas, when the interaction region is located close to the magnetic axis and the FEL beam is aimed along the field lines [1–3]. In this geometry, the linear dispersion relation of the high frequency electromagnetic waves reduces to the familiar form $1 - k_j^2 c^2/\omega_j^2 - (\omega_p^2/\omega_j^2)(1 \mp \Omega_e/\omega_j)^{-1} = 0$, where Ω_e is the electron gyrofrequency, ω_p is the plasma frequency and $j = 0, -$. The upper sign corresponds to the right circularly polarized (RCP) waves and the lower sign to the left circularly polarized (LCP) waves. The frequency of the pump wave ω_0 is above the cut-off values. The electron plasma wave, which propagates along the magnetic field, obeys approximately

the familiar unmagnetized Bohm-Gross dispersion relation.

The conservation of the energy and momentum determine the phase matching conditions for the Stokes scattering at (k_-, ω_-): $\omega_- = \omega_0 - \omega$, $k_- = k_0 - k$ and similarly for the anti-Stokes scattering at (k_+, ω_+): $\omega_+ = \omega_0 + \omega$, $k_+ = k_0 + k$. The matching conditions of the Stokes process and the dispersion relations determine the frequencies and the wavenumbers of the waves excited in SRS.

	RCP	LCP
pump wavelength λ_0 [mm]	0.747	1.29
electron density n_e [m^{-3}]	10^{20}	10^{20}
electron temperature T_e [keV]	20	20
magnetic field B_0 [T]	4.81	4.81
plasma length L [m]	0.181	0.362
pump intensity I_0 [W/m^2]	3.58×10^{12}	2.28×10^{14}

The plasma is accurately described by the Vlasov equation for the electron distribution function $F(x, p_x, \mathbf{p}_\perp, t)$. The computational effort for a fully kinetic 1–2/2 D simulation is enormous. We have therefore considered the following class of exact solutions $F(x, p_x, \mathbf{p}_\perp, t) = \delta[\mathbf{p}_\perp - \mathbf{P}_\perp(x,t)] f(x, p_x, t)$. The reduced electron distribution function $f(x, p_x, t)$ describing the particle motion along the x-direction satisfies the one-dimensional relativistic Vlasov equation

$$\frac{\partial f}{\partial t} + \frac{p_x}{m_e \gamma} \frac{\partial f}{\partial x} + e \left[E_x + \left(\frac{\mathbf{P}_\perp}{m_e \gamma} \times \mathbf{B}_\perp \right)_x \right] \frac{\partial f}{\partial p_x} = 0 . \qquad (1)$$

In this model, the plasma is described by exact "fluid" equations in the direction normal to the external magnetic field, while its kinetic features in the direction of the magnetic field are fully preserved. The nonperiodic boundary conditions adopted are very similar to those presented in Ref. [4] for the unmagnetized case. The simulation parameters are summarized in the Table above.

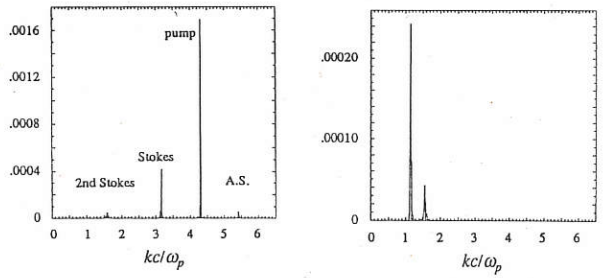

Fig. 1: *k–spectra of the electromagnetic and plasma wave at* $\omega_p t = 600$ *(RCP).*

Figure 1 shows the k-spectra of the EM field and of the plasma wave in the RCP case. The Stokes and the anti-Stokes peaks are clearly resolved in the electromagnetic spectrum. The peak positions are in good agreement with the phase matching conditions

and linear dispersion relations. Also the second Stokes wave can be seen in the EM spectrum and the corresponding plasma wave spectrum has a sideband at $kc/\omega_p \simeq 1.6$. The phase matching conditions and the linear dispersion relations predict that the wavenumbers of the second Stokes wave and of the plasma wave should be $k'_- c/\omega_p = 1.39$ and $k'c/\omega_p = 1.73$, respectively. The peaks in the electromagnetic and in the longitudinal spectra agree rather well with these values. Later, the sidebands grow further and the k-spectrum of the plasma wave broadens remarkably.

The main difference between the LCP and RCP simulations is that the Stokes cascading is possible only in the RCP case. The reason for this is that at high temperatures the second Stokes scattering of an LCP wave is possible only if $\omega_-/\omega_p > 1.60$. Because we had $\omega_-/\omega_p = 1.51$ in the LCP simulation, the second Stokes scattering could not occur. The amplitude modulations are stronger in the RCP than in the LCP case. The reason may be the presence of two plasma waves in the RCP simulation.

3. Generation of ultrafast electrons

The wave-particle interaction is strong in the RCP simulation in spite of the large phase velocity of the plasma wave, $v_{\rm ph}/v_e = 4.61$. The reason for this is that the plasma wave instantaneously reaches high local amplitudes, because it is initially weakly damped. When the lower trapping velocity approaches v_e, strong wave-particle interactions take place together with pump depletion. This leads to the plasma wave collapse and to an efficient energy transfer to the interacting electrons. This behaviour occurs especially in the RCP simulation (Fig. 2)

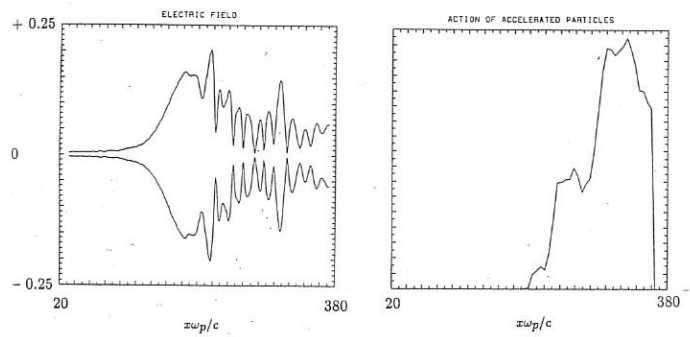

Fig. 2: *Plasma wave envelope $eE/m\omega_p c$ and the action of electrons at $\omega_p t = 730$.*

The electron acceleration was studied also with test particle calculations. The basic features of the fast electrons generation are obtained by assuming an electric field $E(x,t) = E\,\exp(-x^2/w^2)\cos(kx - \omega t + \phi)$. Because the electrons are regarded as test particles, their reaction back onto the field is neglected. The trajectory of an electron is obtained by integrating numerically the relativistic equations of motion.

Figure 3a displays the final kinetic energy $\gamma - 1$ of the electron versus the field strength eEw/mc^2. An astounding feature is the abrupt change from no-acceleration to full-acceleration at $E = E_{\rm cr}$. For $E > E_{\rm cr}$ the electron energy jumps almost stepwise

between zero and the maximum value corresponding to the upper trapping velocity $u_{up} = (v_{ph} + v_{tr})/(1 + v_{ph}v_{tr}/c^2)$ at E_{cr}, and it is thus independent of the field strength for $E > E_{cr}$. The curve has an irregular structure with windows of field strength where no acceleration occurs at all. If we fix the field amplitude E and vary its phase ϕ, which is equivalent to varying the initial position of the test electron, we obtain curves like the one in Fig. 3b. The characteristic feature is here, too, that the electron is not accelerated at all or gets almost a constant boost from the field.

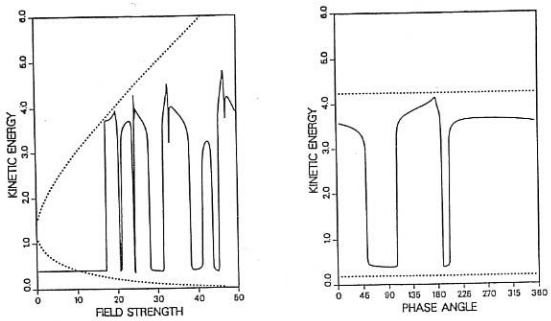

Fig. 3: *Electron energy $\gamma - 1$ vs normalized field eEw/mc and phase ϕ.*

4. Summary

We have studied the stimulated Raman forward scattering by relativistic Vlasov-Maxwell simulations in a high temperature magnetized plasma. The conditions are relevant to the Raman and to the beat wave current drive in reactor grade tokamak plasmas [1–3]. The emphasis is in relativistic wave-particle interactions. The observed electron energies clearly exceed the estimate based on the phase velocity of the plasma wave. A much better approximation for the maximum energy is obtained by using the upper trapping velocity as a characteristic velocity.

In the RCP simulation, an initially weakly damped plasma wave grows to a large amplitude and depletes the pump wave. Simultaneous strong wave-particle interaction leads to a collapse of the plasma wave and to generation of fast electrons. In the LCP run, the wave-particle interaction is more adiabatic and and also weaker. The reason for this is a higher phase velocity of the plasma wave in the LCP case.

References:

1. *B.I. Cohen et al., Fusion* **28** *(1988) 1519.*
2. *S.J. Karttunen et al., Nucl. Fusion* **31** *(1991) 1079.*
3. *A. Ghizzo et al., Nucl. Fusion* **32** *(1992) 45.*
4. *P. Bertrand et al., Phys. Fluids B* **2** *(1990) 1028.*

EFFECTS OF FLUCTUATIONS ON MAGNETOHYDRODYNAMIC WAVE HEATING AND CURRENT DRIVE

J. A. Tataronis and S. N. Antani
University of Wisconsin - Madison
Madison, WI 53706 USA

1. INTRODUCTION

In this paper, we explore the effects of particle density and magnetic field fluctuations on magnetohydrodynamic (MHD) wave propagation and current drive. Fluctuations, which are intrinsic to all plasmas, lead to scattering of coherent waves and thereby wave damping. This damping should be considered when evaluating heating and current resulting from MHD waves. We consider two important problems. The first problem is scattering in a spatially inhomogeneous plasma. We address specifically the issue of mass density fluctuation effects on the continuous spectrum of the shear Alfvén wave. In the absence of fluctuations, phase mixing resulting from the continuous spectrum is a source of Alfvén wave damping. In the presence of fluctuations, it is important to determine how this damping is modified. The second problem concerns the dependency of wave scattering on the angle of propagation and the wavelength. In this case, we assume that the fluctuations are magnetic. Previous work /1-4/ on the subject of MHD wave scattering has generally been limited to wave propagation parallel or perpendicular to the background magnetic field. We also comment on the induction of a steady plasma current as the result of the fluctuations. Our analysis assumes low level fluctuations that vary slowly in time, but are randomly distributed in space.

2. MATHEMATICAL FORMULATION OF SCATTERING PROBLEM

Our formulation of wave scattering is based on a cold, perfectly conducting, MHD fluid. The governing equations read as follows,

$$\frac{\partial \rho}{\partial t} + (\mathbf{V}\cdot\nabla)\rho = -\rho(\nabla\cdot\mathbf{V}) \tag{1}$$

$$\frac{\partial \mathbf{V}}{\partial t} + (\mathbf{V}\cdot\nabla)\mathbf{V} = \frac{1}{\mu_0\rho}(\mathbf{B}\cdot\nabla)\mathbf{B} - \frac{1}{\rho}\nabla\left(\frac{\mathbf{B}\cdot\mathbf{B}}{2\mu_0}\right) \tag{2}$$

$$\frac{\partial \mathbf{B}}{\partial t} = (\mathbf{B}\cdot\nabla)\mathbf{V} - (\mathbf{V}\cdot\nabla)\mathbf{B} - \mathbf{B}(\nabla\cdot\mathbf{V}) \tag{3}$$

where $\mathbf{B}$ and $\mathbf{V}$ are respectively the magnetic field and fluid velocity, ρ is the mass density and μ_0 is the vacuum permeability. Equations (1) and (2) express respectively mass conservation, while Eq. (3) is Faraday's law with the electric field $\mathbf{E}$ expressed in terms of $\mathbf{B}$ and $\mathbf{V}$ via Ohm's law with zero resistivity, $\mathbf{E} + \mathbf{V}\times\mathbf{B} = 0$. We explore here wave propagation in a plasma with random fluctuations in the background mass density and magnetic field. Because the background plasma is thereby a random medium, the wave fields

are random variables. Our goal in this analysis is to compute the mean, or equivalently the ensemble, averages of the random wave fields.

Our analysis is based on the mathematical technique introduced elsewhere /1-3/. The background plasma consists of a magnetic field that is the superposition of three parts: a uniform field directed parallel to the z-axis, $B_o \hat{z}$, a time-invariant random fluctuation, $\Delta\mathbf{b}(\mathbf{r})$, and a fluctuating wave field, $\tilde{\mathbf{b}}(\mathbf{r},t)$,

$$\mathbf{B} = B_o \hat{z} + \Delta\mathbf{b}(\mathbf{r}) + \tilde{\mathbf{b}}(\mathbf{r},t) \tag{4}$$

Assuming that the background plasma is stationary, the fluid velocity consists only of a fluctuating wave field, $\tilde{\mathbf{v}}(\mathbf{r},t)$,

$$\mathbf{V} = \tilde{\mathbf{v}}(\mathbf{r},t) \tag{5}$$

Finally, the mass density is a superposition of a spatially inhomogeneous background component, $\rho_o(\mathbf{r})$, a static random component, $\Delta\rho(\mathbf{r})$, and a wave field, $\tilde{\rho}(\mathbf{r},t)$,

$$\rho = \rho_o(\mathbf{r}) + \Delta\rho(\mathbf{r}) + \tilde{\rho}(\mathbf{r},t) \tag{6}$$

It is assumed that the fluctuations, $\Delta\mathbf{b}(\mathbf{r})$ and $\Delta\rho(\mathbf{r})$, have zero mean values. The problem is to find the statistical properties of the wave fields. We point out that in past studies /1-4/, the average background fields, $B_o \hat{z}$ and $\rho_o(\mathbf{r})$, are spatially invariant. Here, we explore the consequences of a spatially varying mass density. To solve for the wave fields, we proceed as follows. Equations (4) - (6) are substituted in Eqs. (1) - (3), then the resulting equations are linearized with respect to the wave fields. Retaining only terms that are linear in the fluctuations, the resulting linear equations that govern the wave fields are partial differential equations with random coefficients that can be expressed in the form,

$$(\mathbf{M} + \mathbf{V})\,\mathbf{u} = 0 \tag{7}$$

where $\mathbf{u}$ represents the wave fields, $\mathbf{M}$ denotes the differential MHD operator in the absence of fluctuations, and $\mathbf{V}$ is an operator that is determined by the background fluctuations. Although Eq. (7) cannot be solved explicitly for the random field $\mathbf{u}$, it is possible to solve for the average value $\mathbf{u}$, $\langle\mathbf{u}\rangle$, using the procedure introduced by Keller /5/. Keller's equation for $\langle\mathbf{u}\rangle$ reads,

$$\left(\mathbf{M} - \langle\mathbf{V}\mathbf{M}^{-1}\mathbf{V}\rangle\right)\langle\mathbf{u}\rangle = 0 \tag{8}$$

where $\mathbf{M}^{-1}$ represents the inverse of $\mathbf{M}$.

3. MASS DENSITY FLUCTUATIONS -- SHEAR ALFVEN CONTINUUM

In this section, we neglect magnetic field fluctuations, and consider the effects of mass density fluctuations on the Alfvén continuous spectrum. We limit our analysis to a plasma that is inhomogeneous in one spatial

dimension, namely the x-direction of an (x,y,z) Cartesian coordinate system. We also assume that the fluctuating density depends only on x and z, giving $\Delta\rho(x,z)$, and that the average wave fields also depend only on x and z. The y-component of the average velocity then satisfies the following equation

$$\left[\frac{\partial^2}{\partial z^2} + \frac{\omega^2}{v_a^2(x)}\right] \langle v_y \rangle - \frac{\omega^4}{v_a^4(x)} \left\langle \frac{\Delta\rho}{\rho_o(x)} L^{-1} \frac{\Delta\rho}{\rho_o(x)} \right\rangle = 0 \qquad (9)$$

where $v_a(x)$ is the spatially varying Alfvén speed, and L^{-1} represents the inverse of the differential operator that acts on $\langle v_y \rangle$. In addition, an harmonic time dependence, $\exp(i\omega t)$, has been assumed. If the mass density fluctuations are absent, Eq. (9) yields the familiar dispersion relation, $\omega^2 = v_a^2(x)k^2$, that characterize that Alfvén continuous spectrum. If ω is real then the wave number is also real. However, in the presence of fluctuations, the wave number is complex, which implies a complex continuum. Assuming propagation parallel to the z-axis, the following dispersion relation is readily derived from Eq. (9),

$$k^2 - \frac{\omega^2}{v_a^2(x)} - \frac{\omega^2}{v_a^2(x)} \int_{-\infty}^{\infty} \frac{dq}{2\pi} \frac{\hat{\sigma}(k-q)}{q^2 - \omega^2/v_a^2(x)} = 0 \qquad (10)$$

where $\hat{\sigma}(\alpha)$ is the Fourier transform of $\sigma(\mathbf{r}-\mathbf{r}')$, the correlation function of the density fluctuations, $\sigma(\mathbf{r}-\mathbf{r}') \equiv \langle \Delta\rho(\mathbf{r})\Delta\rho(\mathbf{r}') \rangle / \rho_o^2$. We have assumed here that the fluctuations are statistically homogenous. The Cauchy integral that appears in Eq. (10) implies that the solutions for $k(\omega,x)$ with real ω are complex. Therefore, damping is implied.

4. MAGNETIC FIELD FLUCTUATIONS -- FAST ALFVEN MODE

In this section, we comment on the scattering process resulting from magnetic field fluctuations. We neglect the mass density fluctuations, $\Delta\rho \equiv 0$, and assume that the scattering arises from $\Delta\mathbf{b}(\mathbf{r})$. We also assume that the mean mass density, $\rho_o(\mathbf{r})$, is constant in space, and we retain the spatial symmetry of the previous paragraph, namely the fluctuating background plasma and the average wave fields are independent of the y-coordinate. As a final constraint, we assume that the fluctuating magnetic field has only x and z-components. Because of the spatial symmetry, the components of $\Delta\mathbf{b}(\mathbf{r})$ can be expressed in terms of a scalar A(x,z),

$$\Delta b_x(x,z) = -\partial A(x,z)/\partial z \quad \text{and} \quad \Delta b_z(x,z) = \partial A(x,z)/\partial x \qquad (11)$$

Under the constraints assumed here, the average velocity and magnetic fields of the fast Alfvén wave have only x and y-components. The components of the random wave magnetic field satisfy two coupled equations that can be cast in matrix form,

$$\left(\nabla^2 + \frac{\omega^2}{v_a^2}\right)\boldsymbol{B} + \mathbf{Q}\cdot\boldsymbol{B} = 0 \qquad (12)$$

where $\boldsymbol{B}$ is a two element column vector containing the x and z-components of random wave field, and $\mathbf{Q}$ is a 2×2 matrix, the elements of which depend on derivatives of A(x,z). We present the elements of $\mathbf{Q}$ in a forthcoming publication. Following Keller's procedure /5/, the dispersion relation for plane waves, $\langle \boldsymbol{B}t \rangle \sim \exp(-i\mathbf{k}\cdot\mathbf{r})$, reads,

$$\left.\begin{aligned} &\det\{\mathbf{A}(\omega,\mathbf{k})\} = 0 \\ &\mathbf{A}(\omega,\mathbf{k}) = \left(k^2 - \frac{\omega^2}{v_a^2}\right)\mathbf{I} - \int_{-\infty}^{\infty} \frac{d\mathbf{q}}{(2\pi)^2} \frac{\mathbf{H}(\mathbf{q},\mathbf{k};\mathbf{k}-\mathbf{q})\,\hat{\sigma}(\mathbf{k}-\mathbf{q})}{q^2 - \omega^2/v_a^2} \end{aligned}\right\} \qquad (13)$$

In Eq. (13), $\mathbf{I}$ is the identity matrix, $\mathbf{H}(\mathbf{q},\mathbf{k};\mathbf{k}-\mathbf{q})$ is a 2×2 matrix that is derived from $\mathbf{Q}$, and $\hat{\sigma}(\mathbf{k}-\mathbf{q})$ is the Fourier transformation of the correlation function of A(x,z). Again, the Cauchy integral of Eq. (13) implies complex solutions for $\mathbf{k}(\omega)$, and therefore wave damping. The damped plane waves propagate in the direction of the wave vector $\mathbf{k}$, which is oriented oblique to the mean background magnetic field in the x-z plane.

5. THE α-EFFECT AND CURRENT DRIVE

Ohm's law of an ideal MHD fluid relates the electric field to the fluid velocity and magnetic field. Because of the random fluctuations, the electric field may have a steady average value that could, in the presence of resistivity, lead to a steady plasma current. The average electric field is derived by substituting Eqs. (4) and (5) in Ohm's law, averaging over the characteristic period of the fluctuations and finally performing an ensemble average. The resulting mean electric field reads,

$$\vec{\mathcal{E}} = -\overline{\tilde{\mathbf{v}}\times\tilde{\mathbf{b}}} - \overline{\langle \Delta\mathbf{v}\times\Delta\mathbf{b} \rangle}\,, \qquad (14)$$

where the bar ($\overline{}$) indicates time average. Equation (14) is the α-effect. It is seen that both random fluctuations and the wave fields contribute to the average electric field. We speculate that in the presence of resistivity, a steady current could appear, $\eta\mathbf{j}_o = \vec{\mathcal{E}}$, which is analogous to the current resulting from helicity waves described in Refs. /6-8/.

Work supported by U.S. DOE grant DE-FG02-88ER53264 and NSF grant PHY-8921300.

/1/ C. H. Liu, Phys. Fluids **12**, 1642 (1969).
/2/ G. C. Valley, Ap. J. **168**, 251 (1971).
/3/ G. C. Valley, Ap. J. **188**, 181 (19774).
/4/ Y. Q. Lou and R. Rosner, Ap. J. **309**, (1986).
/5/ J. B. Keller, in *Proceedings of the Symposium on Turbulence of Fluids and Plasmas*, Microwave Research Institute's Symposia Series, Vol. 18 (Wiley, New York 1969), p. 131.
/6/ R. R. Mett and J. A. Tataronis, Phys. Rev. Lett. **63**, 1380 (1989).
/7/ J. B. Taylor, Phys. Rev. Lett. **63**, 1384 (1989).
/8/ V. S. Chan, R. L. Miller, and T. Ohkawa, Phys. Fluids B **2**, 1442 (1990).

RADIAL DIFFUSION OF TOROIDALLY TRAPPED PARTICLES INDUCED BY LOWER HYBRID AND FAST WAVES

L. KRLÍN
Institute of Plasma Physics, Czech. Acad. Sci., P.O. Box 17, Prague 8, Czechoslovakia

Abstract

The interaction of RF field with toroidally trapped particles (bananas) can cause their intrinsic stochasticity diffusion both in the configuration and velocity space [1,2,3]. In RF heating and/or current drive regimes, RF field can interact with plasma particles and with thermonuclear alpha particles. The aim of this contribution is to give some analytical estimates of induced radial diffusion of alphas and of ions.

1 Canonical apparatus

For the study of RF field-banana interaction, the Hamiltonian approach is very suitable. We use the system of canonically conjugated coordinates Q_i and momenta P_i, derived and discussed in [4,5,2]. Here, Q_1 is the angle of the cyclotron rotation, and Q_2 and Q_3 are the poloidal and toroidal angles, respectively. Further, $P_1 = \frac{Mv_\perp^2}{2\omega_c}$, $P_2 = \frac{r^2 eB_T}{2}$, P_3 is determined as $1/2Mv_\parallel^2 = \frac{(P_3 - eRA_\varphi)^2}{2MR^2}$, $R = R_0 + r\cos Q_2$. R_0, a are the major and minor radii, respectively, r is the radial position of the guiding centre of a particle, A_φ is the toroidal component of the vector potential $\boldsymbol{A}$ and ω_c is the cyclotron frequency. The corresponding Hamiltonian H_0 of a particle in the toroidal system is

$$H_0 = \omega_c P_1 + \frac{(P_3 - eRA_\varphi)^2}{2MR^2} \tag{1}$$

For the case of banana trajectory, H_0 is integrable and represents the banana motion.

The effect of LHW (in its electrostatic wave representation) or of FW (as a circular left-handed polarized wave) can be described by the total Hamiltonian $H = H_0 + H_1$, where $H_{1(LHW,FW)}$ is

$$H_{1(LHW)} = e\Phi_0 \sum_n J_n(k_\perp \rho_c) \exp(in(Q_1 + Q_2) + ik_\parallel R_0 Q_3 - i\omega t) \tag{2}$$

$$H_{1(FW)} = \frac{\omega_c e E_\perp}{k_\perp \omega} \sum_n n J_n(k_\perp \rho_c) \exp(in(Q_1 + Q_2) + ik_\parallel R_0 Q_3 - i\omega t) \tag{3}$$

and where Φ_o is the amplitude of the potential of LHW, $E_\perp$ is the electric component of FW, and where ω, $k_\parallel$, $k_\perp$ are the frequency and the parallel and perpendicular components of the wave vector $\boldsymbol{k}$. The banana trajectory is given by the values r_0, $v_{\perp 0}$, $v_{\parallel 0}$, where r_0 is the largest value of the radius of the trajectory in the poloidal plane, and $v_{\perp 0}$ and $v_{\parallel 0}$ are the corresponding velocities of the particle in the same position in the equatorial plane.

2 Interaction of toroidally trapped alpha particles with LHW

For this case of this interaction, the resultant effect depends on the value of $k_\perp \rho_c$ (where ρ_c is the Larmor radius). A nonnegligible interaction can exist only for $k_\perp \rho_c > n$ (see e.g.[6]). For typical ITER parameters and for sufficiently high frequency f (in [6], $f = 5$GHz), the interaction is negligible. Nevertheless, there are still some possibilities of a stronger interaction. In [7], the proposal of the current drive, generated by intensive LHW pulses, penetrating into the plasma core, appeared. It is possible that in this case, a part of LHW spectrum can possesss a large $k_\perp$ component. Further, using the multijunction grill technique, the existence of the subsidiary part of the spectrum with e.g. three times larger $k_\parallel$ (and, therefore, also larger $k_\perp$) cannot be avoided [8]. Consequently, it is still reasonable to discuss a possible effect of LHW on alphas.

The LHW-banana interaction possesses two properties, making exact analytical discussion impossible. During one banana period, a particle can cross several resonances of the type

$$\omega - k_\parallel v_\parallel - n\omega_c = 0 \tag{4}$$

the number of which (together with their position) depends on the banana geometry. Further, LHW appears in the tokamak geometry in complicated geometrical structures (cones). To obtain some relevant analytical results, a suitable approximative approach is necessary.

The strongest LHW-banana interaction occurs in the region of the banana tip. The banana geometry (given by r_0, $v_\perp$, $v_\parallel$) in the given magnetic field and for given frequency gives the possibility to find along the banana the number of resonances ,$\triangle n$. Replacing therefore the actual resonant effect by means of $\triangle n$ resonances in the tip, we obtain for the discussed banana the upper limit of the resonance effect. The changes of the relevant coordinates by crossing of one resonance are (see also [9])

$$\triangle P_{i(i=1,2)} = -e\Phi_0 J_n(k_\perp \rho_c) nI \tag{5}$$

$$\triangle P_3 = \triangle P_1 k_\parallel R_0 \tag{6}$$

$$I = 2^{1/3}[n v_{\parallel 0} \omega_B \omega_{c0} R_0^{-2} q^{-1} r_0 (1 + r_0/R_0)^{-2}]^{-1/3} 3^{-2/3} 1/\Gamma(2/3). \tag{7}$$

Here, ω_B is the banana frequency for well trapped particles, ω_{c0} is the cyclotron frequency in the centre, q is the averaged safety factor in the banana region and Γ is the gamma function. Further, $k_\perp \Phi_0 = E_\perp$ (the perpendicular component of the electric field). Using the inverse transformation to the original coordinates we can determine the radial shift of the banana tip, $\triangle r$, and estimate the radial diffusion coefficient,D_r as

$$D_r = < (\triangle r)^2 > \omega_B / 2\pi \tag{8}$$

supposing a fully stochastic regime. For the global estimation, we shall use the averaged value of D_r

$$D_{r,av} = [\int n_{\alpha 0} dr_0]^{-1} \int\int\int dr_0 dv_{\perp 0} dv_{\parallel 0} \triangle n n_{\alpha 0} \frac{D_r}{\triangle v_{\parallel 0} \triangle v_{\perp 0} \triangle r_0} \tag{9}$$

Here, $n_\alpha(r_0)$ is the density of trapped particles, the regions $\triangle v_{\parallel 0}$, $\triangle v_{\perp 0}$ are determined by the banana geometry and $\triangle r_0$ is given by the considered region. We have evaluated approximately the value of$D_{r,av}$ for ITER parameters, for n_α as

$$n_\alpha = n_{\alpha 0}[1 - (r/a)^2]^2 \tag{10}$$

for the region $r_0(0.75a, a)$ and for $E_\perp = 10^5 V m^{-1}$. The last value corresponds approximately to ITER parameters and to 100 MW of power. We obtain

$$D_{r,av} \approx 1.3 \times 10^{-3} m^2 s^{-1}. \tag{11}$$

This rather slow diffusion declares that for LHCD (and far less for the mentioned case of the subsidiary LHW spectrum) the diffusion of alphas cannot influence the energy balance. The LHCD with the intensive pulses requires further study.

3 Interaction of toroidally trapped particles with FW

The heating of plasmas by means of FW is usually considered in the minority ions or second harmonics schemes. FW will also interact with banana ions. Here, we shall approximately estimate the effect of FW on banana particles from the minority part. This part is here supposed to be represented by protons (in the deuterium plasma). Also in this case , the resonant interaction is given by the resonant condition (4) and can be treated analogously to LHW, using for the Hamiltonian H_1 its FW representation. Contrary to the LHW case, the resonance for FW case appears approximately on one resonance surface (going e.g. through r_0). A banana trajectory can penetrate through this surface maximally four times per one banana period.

Passing the resonance region, the change Δr_0 (and, analogously, $\Delta v_{\perp 0}$, $\Delta v_{\|0}$) of the banana can be determined , using the expression for banana trajectory [3], $r = r(v_{\perp 0}, v_{\|0}, r_0, Q_2)$ and using the Hamiltonian $H_{1,FW}$,as [10]

$$\Delta r_0 = \Delta r_0(\Delta r, \Delta v_\perp, \Delta v_\|, r_0, v_{\perp 0}, v_{\|0}, Q_{2,res}), \tag{12}$$

and, analogously, for further parameters. Here, $Q_{2,res}$ is the poloidal angle Q_2 for the resonance region. The values of $\Delta v_\perp, \Delta v_\|, \Delta r$ must be determined by means of the canonical perturbation method. Analogously, only the case with the resonance in the banana tip can be treated without difficulties. Choosing further the resonance region for $r = 0$, considering $E_\perp = 10^2 V cm^{-1}$, $k_\perp = 10^2 m^{-1}$, the shifts in r_0 and in Q_{2max} are related as $\Delta r_0 \approx -r_0 \Delta Q_{2max}$. Consequently, there is a strong coupling between the change of the poloidal angle od the tip, and the radial diffusion.

Let us estimate (for a typical banana) the characteristic time, $\Delta\tau$, in which this banana changes its poloidal angle of the tip, Q_{2max}, from $Q_{2max} = \pi$ to $Q_{2max} = \pi/2$, considering changes only in the perpendicular velocity and neglecting all other changes. Choosing $r_0 = a$, $Q_{2max} = \pi$, the perpendicular energy $W_{\perp 0} = 1.6keV$, and correspondingly, $W_{\|0} = 1.8keV$, the mentioned change in Q_{2max} requires the increase $\Delta W_\perp \approx 15.4keV$. Considering further the energy diffusion coefficient, D_W as

$$D_W = < (\omega_c \Delta P_1)^2 > \omega_B/2\pi \tag{13}$$

we obtain the maximal value of D_W as $D_W \approx 2.7 \times 10^{-26} J^2 s^{-1}$. The characteristic time, $\Delta\tau$, is then given as $D_W \Delta\tau = (\Delta W_\perp)^2$, from which $\Delta\tau \approx 8 \times 10^{-4}$. Considering the lowest possible value of D_W, we obtain the following limit

$$1.3 \times 10^{-3} s < \Delta\tau < 2.5 \times 10^{-2} s. \tag{14}$$

The diffusion length, given by the neoclassical diffusion coefficient, can be for this time defined as $D_{neo} \Delta\tau = (\Delta l)^2$ and is for the weakest RF diffusion $\Delta l \doteq 0.1m < a$. Since a considerable part of the trapped minority ions will change its position to the lower magnetic part during this time, it can be assumed that trapped minority ions will predominately occupy the low magnetic field part. This effect can have interesting physical consequences (as has been mentioned by Hsu [11] and Chen [12]. (For heating on the second harmonics, the exodus of trapped plasma ions from the higher magnetic field part can be also expected. This surplus of ions can create a poloidal electric field, as mentioned in [11,12]).

4 Quasilinear lines of diffusion. Estimate of the stochasticity threshold

Having the total Hamiltonian H in the action-angle form $= H(J_i, w_i)$, and considering all frequencies ω_i independent on J_i, the energy integral, given by the integration of the canonical equations, will have the form of Kennel-Engelmann constraint (see Becoulet [9])

$$v_{\perp 0}^2(1 - \omega/\omega_{c0}) + v_{\|0}^2 = const. \tag{15}$$

(the subscripts label values on the equatorial plane). Admitting a weak nonlinearity in banana oscillations, this constraint will be modified as

$$v_{\perp 0}^2(1 - \omega/\omega_{c0} + \frac{H_2 N_2 \omega_B}{8\alpha\omega_{c0}}) + v_{\|0}^2 = const. \tag{16}$$

Here H_2 represents the energy of poloidal oscillations, α is given as $\alpha = 1/2Mr_0^2\omega_B^2$ and is substantially larger then H_2 and N_2 represents harmonics, given by banana motion. The modification can therefore bring some changes only for large N_2.

Concerning the stochasticity threshold, the more exact estimate requires - due to 3D character of banana motion - the numerical simulation. For rough estimate,the threshold can be determined, using the fact that the main changes of the phase, which appears in H_1, are given by ω_c. Then the stochasticity threshold requires (see also [13])

$$\triangle\psi = \frac{\partial\omega_c}{\partial r} \triangle r\tau_B > \pi \tag{17}$$

We have obtained for LHW and our parameter the value $\Delta\psi = 0.1$, whereas for FW the value 1.4 . We can therefore expected for LHW lower degree of the stochastization then for FW.

Acknowledgement — The author is indebted to Drs. R. Klíma, Z. Gášek, P. Pavlo and V. Petržílka for valuable discussions.

References

[1] Whang K.W., Morales G.J.(1983) Nucl.Fusion 23, 481.

[2] Krlín L. Pavlo P., Tluchoř Z., Gášek Z.(1987) Plasma Phys.Contr.Fusion 29, 1653.

[3] Gášek Z., Krlín L., Tluchoř Z. (1987) Czech.J.Phys. B 37, 571.

[4] Gášek Z., Krlín L. Tluchoř Z. (1989) Phys.Lett. A 135, 284.

[5] Krlín L.(1967) Czech.J.Phys.B 17, 112.

[6] Pavlo P., Krlín L., Tluchoř Z. (1991) Nucl.Fusion 31, 711.

[7] Cohen B.I.et al. Int. School of Plasma Physics, Chebrex 1988, 597.

[8] Hurťák O., Preinhaelter J. accepted in IEEE Transaction on Plasma Science

[9] Becoulet A., Gambier D.J., Samain A. (1991) Phys.Fluids B3, 137.

[10] Krlín L. to be published.

[11] Hsu J.Y. et al. (1984) Phys.Rew.Lett.53, 564.

[12] Chen L., Vaclavik J. Hammet G.W. (1988) Nucl.Fusion 28, 389.

[13] Helander P., Lisak M., Anderson D. (1989) IAEA,IV-101.

ICRF MINORITY PLASMA HEATING IN REALISTIC GEOMETRIES

L. Friedland and D. Cohen
Center for Plasma Physics, Racah Institute of Physics, Hebrew University Jerusalem, Israel

Conventional ICRF plasma heating theories /1/ assume variation of the cyclotron frequency at the resonance in the direction perpendicular to the background magnetic field, i.e., $\mathbf{B}\cdot\nabla|\mathbf{B}|=0$. This is not the general case in Tokamak geometries. A new conservative generalization of the Budden wave tunneling equation was suggested recently /2/ for studying the ICRF minority (H) heating problem for $\mathbf{B}\cdot\nabla|\mathbf{B}|\neq 0$ case. The generalization comprises a system of three coupled ordinary differential equations of form

$$\begin{aligned} V_a(dZ_a/dx - ik_aZ_a) &= -i\mu B \\ V_b(dZ_b/dx - ik_bZ_b) &= -i\mu B \\ VdB/dx + i\rho xB &= -i\mu^*(Z_a+Z_b) \end{aligned} \qquad (1)$$

where $k_{a,b}$, $V_{a,b}$, V and ρ are real constants, while μ is generally small, but complex. System (1) describes spatial evolution of two (electromagnetic) modes $Z_{a,b}\sim\exp(ik_{a,b}x)$ which are weakly coupled via a third (ballistic) wave-like perturbation $B\sim\exp(-i\rho x^2/2V)$. The energy flux associated with the coupled modes is conserved

$$J = V_a|Z_a|^2 + V_b|Z_b|^2 + V|B|^2 = \text{const} \qquad (2)$$

The possible mode transformations embedded in (1) can be understood by considering the local dispersion relation associated with the system

$$[V_a(k-k_a)]^{-1} + [V_b(k-k_b)]^{-1} = |\mu|^2[V(k+\rho x)]^{-1} \qquad (3)$$

The dependence k=k(x) as given by Eq.(3) is shown schematically in Fig.1.

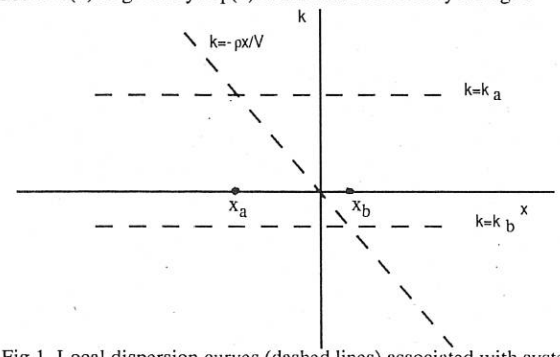

Fig.1. Local dispersion curves (dashed lines) associated with system (1).

We notice in the Figure that there exist two crossing points at $x_{a,b}=-Vk_{a,b}/\rho$ in the problem. This suggests to apply a heuristic two-step linear mode conversion approach /3/ in studying asymptotic solutions of (1) subject to given boundary conditions. For instance, if $V,V_a>0$ and $V_b<0$ and one excites only mode a at $x=-\infty$, then the transmission coefficient for this mode at x_a is $T_a^2=\exp(-2\pi\mu^2/\rho V_a)$ /4/. The conversion coefficient to the ballistic mode at x_a is $1-T_a^2$. This mode propagates to point x_b and is transmitted with the transmission coefficient $T_b^2=\exp(-2\pi\mu^2/\rho V_b)$. The fraction $C^2=T_b^2(1-T_a^2)$ of the original flux is the mode conversion coefficient in the problem. The rest of the conserved flux at point x_b, i.e., the fraction $R^2=(1-T_a^2)(1-T_b^2)$ is mode converted into the reflected electromagnetic channel b. If, in contrast, one initially excites only mode b, the transmission coefficient through the crossing x_b is T_b^2, while no energy is transferred to mode a.

The model system (1) for ICRF applications /2/ can be obtained from a modified Hermitian anisotropic pressure plasma model /5/ reduced to the lowest differential order via the congruent reduction technique /6/. The magnetic field geometry employed in Ref.2 is shown in Fig.2.

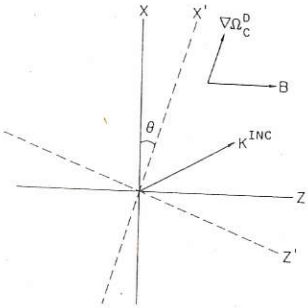

Fig.2 Magnetic field geometry and local coordinates (x,z) and (x',z').

We investigated the coupling between the incident and reflected magnetosonic wave channels at the cyclotron resonance via the minority (H) ion fluid velocity perturbation (the ballistic mode) assumed to have a small auxiliary streaming velocity V along the direction of the magnetic field. We also assumed that the efficient mode interaction takes place in the vicinity of the resonance $\omega=2\Omega_c^D=\Omega_c^H$ so that the problem is locally one-dimensional with the variation of the amplitudes of the coupled modes in the direction of $\nabla|\mathbf{B}|$ (direction x' in Fig.2). The available magnetosonic wave channels can then be found from the magnetosonic wave dispersion relation at the resonance

$$N_x^2(1+3N_z^2) - (1-3N_z^2)(1+N_z^2) = 0 \qquad (4)$$

where $\mathbf{N}=c_A\mathbf{k}/\omega$, c_A is the Alfven speed, $\mathbf{k}$ is the wave vector and ω is the wave frequency. In view of the above, we assumed that $N_{x'}$ is the same in the incident and the reflected wave channels, while $N_{z'}$ is different, as illustrated in Fig.3 showing the curve $N_x=N_x(N_z)$ defined by (4).

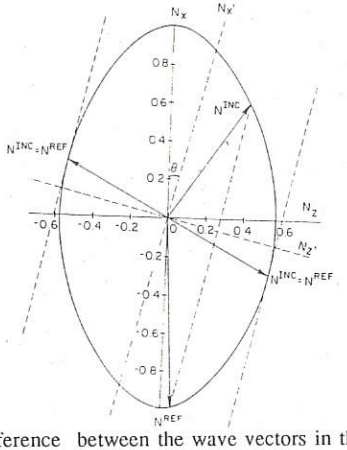

Fig.3 The dependence of N_x on N_z for the magnetosonic wave at the cyclotron resonance.

The difference between the wave vectors in the incident and reflected wave channels at the resonance in the nonzero $\mathbf{B}\bullet\nabla|\mathbf{B}|$ case makes the geometry an important factor in the problem. For instance, the magnitudes of the velocities $V_{a,b}$ in (1) and therefore also the transmission coefficients $T_{a,b}$ are different. Fig.4 presents an example of the evaluation of various mode transformation coefficients for the case when the angle between $\nabla|\mathbf{B}|$ and $\mathbf{B}$ is $\pi/3$ /2/. The case $\mathbf{B}\bullet\nabla|\mathbf{B}|=0$ is also shown in Fig.4 (the dashed line) for comparison.

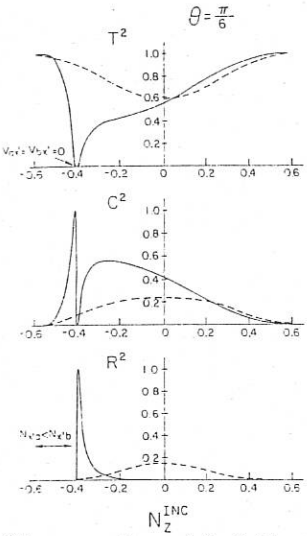

Fig.4 The dependence of the transmission, conversion and reflection coefficients on N_z component of the incident wave for the angle $\pi/3$ between $\nabla|\mathbf{B}|$ and $\mathbf{B}$ and the value $\pi\omega\omega_D n_H/2cn_D|\nabla\Omega_c^H|=0.5$.

One of the assumptions of the fluid model described above was the existence of the streaming velocity V for the minority ions. Although the mode transformation coefficients derived in Ref.2 on the basis of this model did not depend on the value of V or its direction and we could formally take the limit V-->0, the streaming velocity assumption introduces an artificial asymmetry in the problem. In order to study the validity of the approach, we included the possibility of multiple ballistic modes in the model. This generalized model allows to remove the asymmetry of the single ballistic mode approach and study the effect of the thermal spread on the mode transformations. The coupled mode system for the multiple ballistic mode case is:

$$V_a(dZ_a/dx - ik_aZ_a) = -i\sum_n \mu_n B_n$$
$$V_b(dZ_b/dx - ik_bZ_b) = -i\sum_n \mu_n B_n \qquad (5)$$
$$V_n dB_n/dx + i(\rho x+\beta_n)B_n = -i\,\mu^*_n(Z_a+Z_b)$$

The most simple situation is when we have just two ballistic modes in (5). The local dispersion diagram for this case is shown in Fig.5.

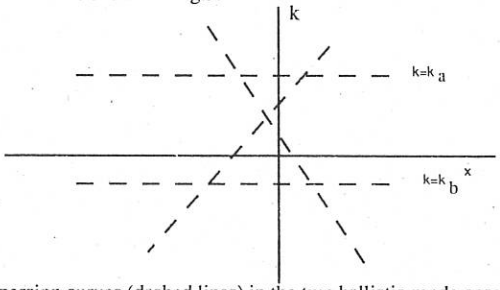

Fig.5. Dispersion curves (dashed lines) in the two ballistic mode case.

We see in Fig.5 that again the problem can be split into five simple pairwise crossings suggesting that the mode transformation coefficients can be found by successively applying the conventional pairwise mode coupling theory /4/. The results of such calculations for the reflection coefficient in the case $k_a=-k_b=k_0=3cm^{-1}$, $V_1=-V_2=6$, $V_1=-V_2=V$, $\beta_{1,2}=0$, $\rho=1cm^{-2}$ and $|\mu|^2=|\mu_1|^2+|\mu_1|^2=1cm^{-2}$ are shown in Fig.6.

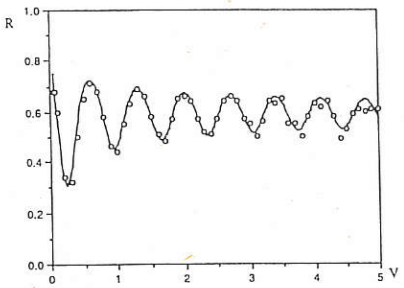

Fig.6 The reflection coefficient in the two ballistic mode case

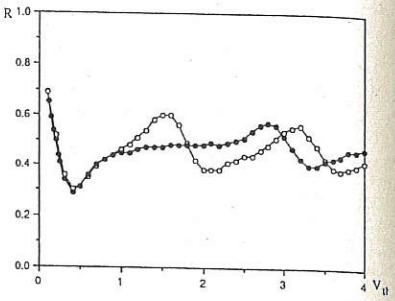

Fig.7 The reflection coefficient for four (empty circles) and eight ballistic modes.

We see in the Figure that , as expected, the reflection coefficient approaches the equivalent single ballistic mode result R=0.65 in the limit V-->0. We can also observe the presence of characteristic oscillations of the reflection coefficient as a function of V. The latter are due to the interference effect as waves originating in the incident channel ($k=k_0$) follow different paths in Fig.4 and add in the reflected ($k=-k_0$) channel. This interference effect diminishes if one adds additional ballistic modes as can be seen in Fig.7, showing the reflection coefficient for the four- and eight- ballistic mode cases with the Gaussian distribution of the values of $|\mu_n|^2$ and velocities V_n distributed symmetrically around zero with a spacing $\Delta V=2V_{th}/N$ (N+1 being an even number of the ballistic modes and V_{th} representing the thermal velocity) between the neighboring velocities V_n and V_{n+1}. Again, one reproduces the result of the single ballistic mode theory in the limit V_{th}-->0. Thus, in conclusion, the numerical results of the multiple ballistic mode model justify the analytic results for the mode transformation coefficients of Ref.2 if the thermal spread of the minority ions is sufficiently small.

This work was supported by the USDOE under contract No. DE-AC03-76SF00098 with Lawrence Berkeley Laboratory.

/1/ see, for example, R.A. Cairns, Radiofrequency Plasma Heating, (Adam Hilger, Bristol, 1991).
/2/ L. Friedland, D. Cohen, Phys. Fluids **B4**, 24 (1992).
/3/ R. Cairns and C.N. Lashmore-Davies, Phys. Fluids **26**, 1268 (1983); H. Ye and A.N. Kaufman, Phys. Rev. Lett. **60**, 1642 (1988).
/4/ L. Friedland, G. Goldner, and A. Kaufman, Phys. Rev. Lett. **58**, 1392 (1987).
/5/ L. Friedland, Phys.Fluids **B2**, 1204 (1990).
/6/ L. Friedland, A.N. Kaufman, Phys.Fluids **30**, 3050 (1987).

SIMULATION OF RUNAWAY ELECTRONS IN A TOROIDAL GEOMETRY

S.K. Sipilä*, J.A. Heikkinen* and T.J.H. Pättikangas†
*Helsinki University of Technology, Department of Technical Physics,
SF-02150 Espoo, Finland
†Technical Research Centre of Finland, Nuclear Engineering Laboratory,
P.O. Box 208, SF-02151 Espoo, Finland

1 Introduction

For accurate calculations of charged particle orbits in a toroidal geometry with complex magnetic configuration and finite plasma pressure, one is usually resorted to particle following codes /1/, in which collisions are treated by equivalent Monte Carlo scattering and friction operators. A straightforward integration of the guiding centre equation of motion is time-consuming and prone to accumulation of numerical error. Recently, hybrid integration methods /2/ utilizing the conservation of the constants of motion and various acceleration techniques have been developed, and the computing times have decreased. Most applications have dealt with energetic ions in the absence of the toroidal electric field, while no attempt to study electron dynamics in the presence of the electric field in the toroidal geometry has been published.

In Sections 2 and 3, we introduce a new code, ASCOT (Accelerated Simulation of Charged Particle Orbits in a Tokamak), for following electron and ion orbits in a three-dimensional, axisymmetric tokamak geometry. The particles are treated relativistically, and the effects of the toroidal electric field and particle collisions are included. The orbits are solved with high accuracy, and time scale acceleration is effectively utilized. The ASCOT code has been applied to a study of reverse runaway electrons during lower hybrid (LH) current ramp-up /3/. This application is described in Section 4.

2 Description of the Code

In the ASCOT code, the particle guiding centre motion including the electric force is calculated with the fourth-order Runge-Kutta method. After each time step, the location of the guiding centre is corrected by making use of the conservation of the energy $\epsilon = (\gamma - 1)m_0c^2$, the magnetic moment $\mu = \gamma^2 m_0 v_\perp^2/2B$ and the toroidal canonical angular momentum $P_\Phi = \gamma m_0 R v_\parallel B_\phi/B - q\psi$. In these equations, m_0 and q are the rest mass and charge of the particle, $v_\perp$ and $v_\parallel$ are the velocity components perpendicular and parallel to the magnetic field $\mathbf{B}$, B_Φ is the toroidal component of $\mathbf{B}$, ψ is the poloidal magnetic flux, R is the radial distance from the symmetry axis and γ is the relativistic factor. The mirror points of banana orbits are treated by diminishing the time step until a user-defined spatial error tolerance is met.

At each time step, the effects of the toroidal electric field $\mathbf{E}_\Phi$ and Coulomb collisions on the particle pitch ($\xi = v_\parallel/v$) and energy are evaluated and the constants of motion are updated for the next time step. The collisions are treated by using binomially distributed, Monte Carlo type pitch and energy scattering operators /1/ derived from the Fokker–Planck equation for a nonrelativistic, Maxwellian plasma. The changes in pitch and energy over a time step Δt are

$$\Delta\xi_{coll} = -\nu\xi\Delta t + \delta_1\left[(1-\xi^2)\nu\Delta t\right]^{1/2} \quad (1)$$

$$\Delta E_{coll} = -\sum_j 2\nu_{E,j}\Delta t\left[E - \frac{3}{2}\gamma k_B T_j - p\frac{k_B T_j}{2}\frac{d\gamma}{dp} - \frac{1}{2}\frac{\gamma k_B T_j p}{\nu_{E,j}}\frac{d\nu_{E,j}}{dp}\right] + \delta_2\left[\sum_j 4\gamma k_B T_j E\nu_{E,j}\Delta t\right]^{1/2} \quad (2)$$

$$\Delta E_{\mathbf{E}_\Phi} = q\mathbf{v}\cdot\mathbf{E}_\Phi\Delta t, \quad (3)$$

where δ_1 and δ_2 are evenly distributed random signs, ν and $\nu_{E,j}$ are the pitch and the energy scattering frequencies, E is defined as $p^2/2m_0$ for the test particle with momentum p, k_B is the Boltzmann constant and T_j is the temperature of background particle species j. The sum in Eq. (2) is taken over all background species.

3 Acceleration

The changes in the particle parameters per orbit due to the Coulomb collisions and the toroidal electric field are small at non-thermal energies. Hence, it is necessary to follow the particle for hundreds of orbits before significant changes in the particle parameters can be observed. To keep the run times reasonable, it is therefore necessary to accelerate the interaction time scales. In the ASCOT code, acceleration is achieved by multiplying the time step Δt in Eqs (1)–(3) by an acceleration factor determined from the user-defined maximal change in pitch and energy per orbit.

In Fig. 1, the pitch and energy of an electron in the toroidal electric field, in the absence of collisions, are shown as a function of time. Initially, the toroidal component of the particle velocity is in the direction of the electric field. Hence, the electron slows down in the electric field until the parallel velocity changes sign. After this, the electron is accelerated by the field to the opposite direction. Figure 1(a) shows the pitch and the energy of the electron without acceleration. The CPU time used was 680 seconds on an IBM 3090-200J system. In Fig. 1(b), the results of the same simulation with an average acceleration factor of 420 are shown. For this case, the CPU time was 1.8 seconds. In our experience, the allowed change in pitch per orbit due to the electric field has to be less than 0.5% in order to avoid significant errors. The efficiency of the

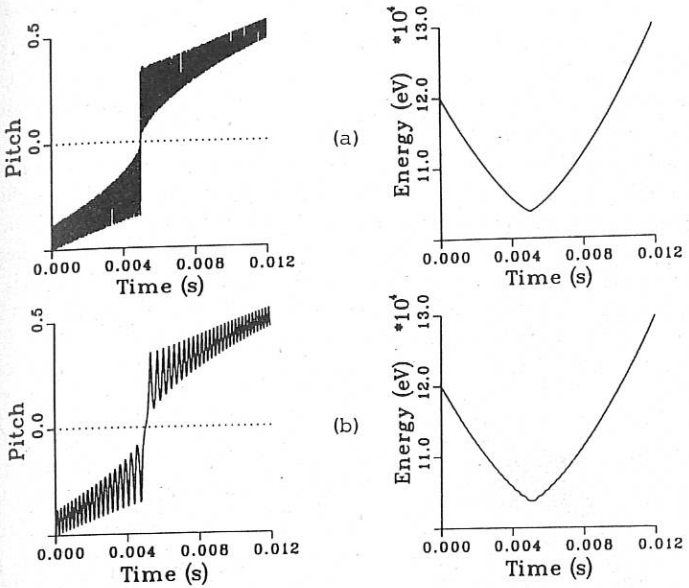

Figure 1: (a) Pitch ξ and energy of an electron with initial ξ =–0.5 and velocity 0.59c without acceleration. (b) Same as (a) with an average acceleration factor of 420. R = 3 m, a = 1.2 m, B_0 = 3.45 T, I_Φ = 4.8 MA, E_Φ = 0.06 V/m, $n_e = n_D = 5{\cdot}10^{18}$ 1/m^3.

acceleration increases with increasing particle energy. In the presence of collisions, the statistics of the code have been checked by comparing with the results of Karney and Fisch /4/ for reverse runaway electrons in lower hybrid (LH) current ramp-up.

4 Study of Reverse Runaway Electrons

The growth of the toroidal plasma current during LH current ramp-up induces an electric field in the opposite toroidal direction. Some of the current-carrying electrons may be decelerated down by this electric field and then accelerated in the opposite direction to very high energies and low collisionality, thus hampering the efficiency of the current ramp-up. These electrons are referred to as "reverse runaways". In our study, the reverse runaway probabilities are calculated for ensembles of 500 electrons at several initial points in the LH velocity diffusion region. This region is chosen to be in the vicinity of the runaway velocity v_r in order to maximize the current ramp-up efficiency /4/.

The electrons had an initial velocity component in the direction of the electric field, and the percentage of reverse runaways was recorded. The results were compared

to those obtained by Karney and Fisch /4/ by solving the Boltzmann equation in cylindrical geometry using a collision operator derived at the zero temperature limit. A good agreement of the results was found at low temperatures ($v_{th}/v_r \ll 1/6$) and for electrons near the magnetic axis. At finite temperatures ($v_{th}/v_r < 1/3$), significantly higher runaway rates were recorded for off-axis electrons (for details, see /3/). On outer magnetic surfaces, the trapped velocity cone crossed by the reverse runaway electrons is wider than near the magnetic axis (Fig. 2). This explains the higher runaway rates for off-axis electrons, because the runaway probability in the cylindrical limit /4/ is larger for negative $v_{\|}$ and increases with increasing v.

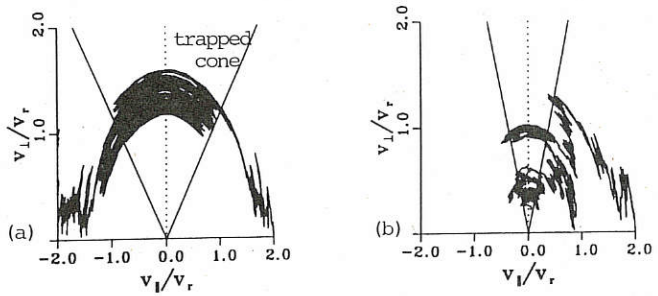

Figure 2: (a) Velocity space diffusion of a reverse runaway electron 80 cm off the magnetic axis. (b) Electron thermalization in velocity space 20 cm off the magnetic axis. The initial velocity in both cases is $(2v_r,0)$. Note the wider trapped velocity cone in (a). $R = 3$ m, $a = 1.2$ m, $B_0 = 3.45$ T, $I_\Phi = 4.8$ MA, $E_\Phi = 0.06$ V/m, $n_e = n_D = 5{\cdot}10^{18}$ 1/m^3, $T_e = T_D = 2$ keV.

Acknowledgements

This work was partly supported by the Imatran Voima Foundation.

References

/1/ A.H. Boozer and G. Kuo-Petravic, Phys. Fluids **24** (1981) 851;
C.D. Beidler *et al.*, J. Comp. Phys. **72** (1987) 220.

/2/ M.A. Kovanen and W.G.F. Core, JET Joint Undertaking report JET-P (90) 40, August 1990; for other Monte Carlo codes, see the references.

/3/ J.A. Heikkinen *et al.* in the Europhysics Topical Conference on RF heating and Current Drive of Fusion Devices, Brussels, Belgium, 7–10 July 1992 (to be published in Europhysics Conference Abstracts).

/4/ C.F.F. Karney and N.J. Fisch, Phys. Fluids **29** (1986) 180.

MODELLING OF THE FMS WAVE PROPAGATION AND TRANSFORMATION IN THE ION-CYCLOTRON FREQUENCY DOMAIN FOR THE TUMAN-3 TOKAMAK PLASMA

M.A.Irzak, I.P.Pavlov, O.N.Shcherbinin

A.F.Ioffe Physical-Technical Institute, St.Petersburg, Russia

Computational results on wave propagation and conversion in the ion cyclotron range of frequency for a multi-species plasma are described. The wave equation with non-local conductivity tensor was solved in a plane geometry for a plasma non-uniform in "radial" direction with parameters of the Tuman-3 tokamak /1/ (R_o=55 cm, a=24 cm, B_o=5.65 kG, T_{eo}=450 eV, T_{io}=150 eV, $n_o=3\cdot10^{13}cm^{-3}$, f=8 MHz, gas: D + H). The expression for induced plasma current was expanded in terms of drift parameter $\mu=(v_\perp/\Omega)/\mathrm{grad}(\log B)$ /2/. As a result, a system of diff. equations of the 6-th order was obtained, which took into account the damping on the first and second ion cyclotron harmonics, Landau and collisional damping /3/. The boundary conditions for antenna side corresponded to Fast wave Fourier harmonic excitation with N_y=0. The conditions of two types were set on the second boundary: 1- in the depth of the plasma (behind the transformation region) the forward going waves only were taken into account; 2- the full reflection of waves was assumed at the opposite wall.

The method of finite elements was used for solution of wave equation. The system of diff.equations was brought to the algebraic system by Galerkin technique. The set of amplitudes of electric fields and their derivatives for 1500 points across the plasma column was obtained as a result of solution.

Aside of transformation region where the WKB approximation was valid the solution was decomposed on six partial geometrical-optical waves. Then the Poynting fluxes were calculated both for full wave solution and for partial WKB waves. This procedure made it possible to find the one-pass coefficients of transformation, reflection and transmission in the evanescence region, as well as efficiency

of absorption in resonance regions. The cases for waves propagating both from higher and lower magnetic field side were calculated.

The Poynting fluxes for all waves are presented in Figs 1 and 2 for N_z=50 and relative hydrogen concentration C_H=15% (1 - full solution, 2 and 3 - FMS waves, 4 and 5 - Bernstein (B) waves, dashed lines - reflected waves). X axes begin at the plasma boundary, but in Fig.1 - from the lower field side (LFS excitation) and in Fig.2 - from the higher field side (HFS excitation). To get rid of the gradient effects the temperature and density profiles are taken in both cases to be uniform. The transformation region is located near the plasma axis at x≅24 cm. Behind this zone there are no reflected waves (according to boundary condition). The region of FMS wave absorption at hydrogen fundamental resonance is clearly seen at x≅20cm (Fig.1). The efficiency of this absorption is shown in Fig.3 in dependence on hydrogen concentration at N_z=50 and $n=5\cdot10^{13}cm^{-3}$ (curve 1) or $n=3\cdot10^{13}cm^{-3}$ (curve 2). In case of HFS excitation (Fig.2) the incident FMS wave converts into B wave propagating back to the plasma periphery. One can see the strong Landau damping of the B wave.

Diagrams of one-pass efficiency for transformation, transmission and reflection for LFS excitation are presented in Figs 4 and 5. All data were taken from Figures similar to Fig.1 and 2. Fig.4 shows the C_H dependence for N_z=50 and two densities: solid lines - for $5\cdot10^{13}cm^{-3}$, dashed lines - for $3\cdot10^{13}cm^{-3}$. Fig.5 shows the N_z dependence for $n=3\cdot10^{13}cm^{-3}$ and three plasma composition: solid lines - C_H=15%, dashed lines - 30%, dotted lines - 6%. It is seen that reflection goes up with the rise of plasma density and hydrogen ratio (due to broadening of evanescence zone), at the same time the optimum of transformation shifts to higher N_z. Comparison with Fig.3 shows that the mode conversion is more effective at lower densities, but ion cyclotron absorption - at higher densities.

Fig.6 shows the transmission/transformation diagram for HFS excitation. Solid line presents the case with $n=3\cdot10^{13}cm^{-3}$

and C_H=15%. As the density rises up to $5 \cdot 10^{13}$, transformation becomes more effective (dashed line). As the hydrogen ratio goes down to 6% , transmission goes up (dotted line).It should be noted that at N_z<40 the B waves form the standing wave structure (due to weak damping), and calculated values disperse strongly from monotonous solid curve. The 1% admixture of nitrogen ions (N^{+6}) resumes the B wave damping and calculated points (stars) lie nearer to solid line.

Fig.7 and 8 show the Poynting fluxes for LFS excitation at N_z=30 and C_H=6% when full reflection of all waves from the opposite wall was assumed. Density and temperature profiles were taken parabolic. In the Fig.8 case the 1% admixture of N^{+6}ions was included, what provided the strong damping of B waves in the second ion cyclotron harmonic region. The role of different absorption mechanisms is seen distinctly.

It was found that in the experimental condition of the Tuman-3 tokamak ion cyclotron one-pass absorption is not efficient enough. The effective heating can be achieved in the combined scenario only, when all mechanisms of absorption take part. The optimal range of N_z is 20-40. The fraction of hydrogen (6-15%) should be on the lower side for higher plasma density from the interval $2\text{-}4 \cdot 10^{13} cm^{-3}$.

REFERENCES

1. L.G.Askinasi,V.I.Afanas'ev et. al.,Plasma Physics and Contr. Fusion(1989),31,No.1,p.3.
2. M.Brambilla,M.Ottaviani, ibid,(1985),27,No.8,p.919.
3. M.Brambilla. Nucl.Fusion,(1988),28,No.4,p.549.

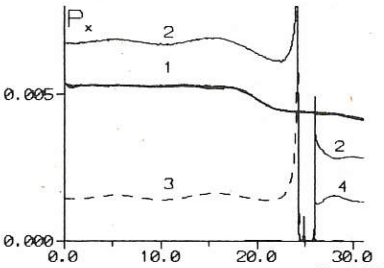

Fig.1

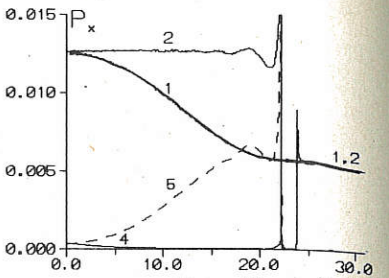

Fig.2

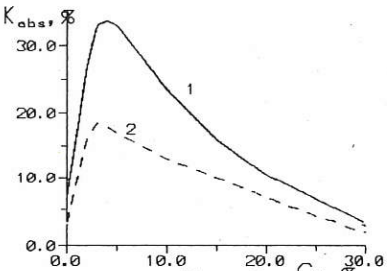

Fig.3

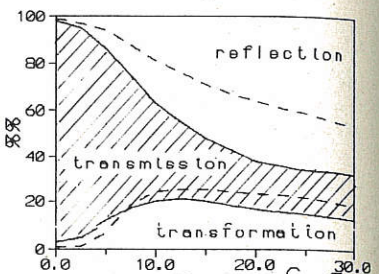

Fig.4

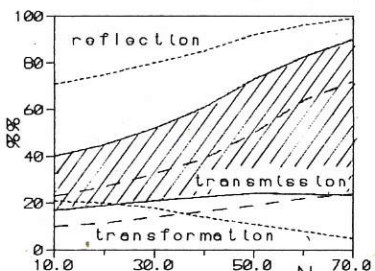

Fig.5

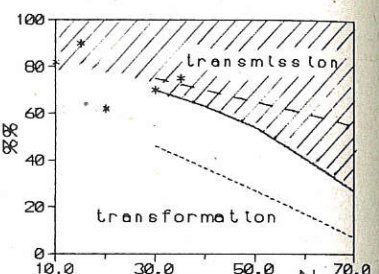

Fig.6

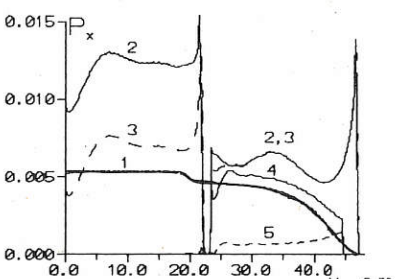

Fig.7

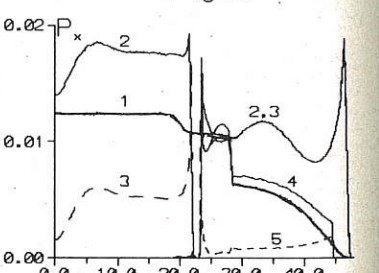

Fig.8

Topic 6:

Diagnostics

NEUTRAL PARTICLE ANALYSIS IN THE MEV RANGE IN JET

M.P.Petrov[+], V.I.Afanasyev[+], S.Corti, A.Gondhalekar,
A.V.Khudoleev[+], A.A.Korotkov[+] and A.C.Maas
JET Joint Undertaking, Abingdon, OX14 3EA, United Kingdom
[+]A.F.Ioffe Physical-Technical Institute, St.Petersburg, Russia

Time resolved measurements of density and energy spectra of ion cyclotron resonance frequency(ICRF) driven ions, α-particles and other charged fusion products in the MeV energy range are high priority objectives in JET. To this end a high energy neutral particle analyzer(NPA) GEMMA-2, developed at the Ioffe Institute[1], has been deployed on JET. In this paper the first applications of this instrument are described.

The NPA is of the E||B type, with eight energy channels having common mass selection, capable of time resolved measurement of spectra of H, D, T, ^{3}He and ^{4}He atomic flux emitted by the plasma, in the energy range $0.5 \leq E(MeV) \leq 3.5$. The NPA is equipped with a 400Å carbon foil for stripping the incident atoms, and $3cm^2$ 8μm thick (CsI+Tl) scintillator detectors optically coupled to photomultipliers for subsequent secondary ion detection, giving nearly 100% detection efficiency for the high energy ions and negligible for background neutrons and γ-rays. Measured contrast in detection efficiency between the secondary ions and neutrons is $\sim 10^5$ for the low energy and $\sim 10^8$ for the high energy channels, for 2.45MeV DD as well as 14MeV DT neutrons. Overall detection efficiency for incident H^0 and He^0 varies from 0.5 for the 0.5MeV to 0.75 for the 3.5MeV channels. The energy widths of the NPA channels vary from 7% for the low energy to 3% for high energy channels. Mass selection contrast for neighboring ions, $^3He^{++}$ and $^4He^{++}$, is ≈50.

The NPA is installed at the top of the torus at octant 4 with its vertical line-of-sight intersecting the oct.4 injected neutral beams at the plasma center, fig.1. Projection of the NPA collimator on the torus midplane is ≈8cmx7cm, and collecting solid angle is 1.26×10^{-6} sterad. In a typical heating experiment, ≅5MW of ICRF power was applied to a deuterium plasma with I_ϕ=3.5MA, B_ϕ=2.8T, and $\bar{n}_e = 1.9 \times 10^{19} m^{-3}$, fig.2. ICRF power deposition profile for the H-minority heating at 42.6MHz peaked near the plasma center and included the NPA line of sight and the injected atom beams. Into this plasma ~5MW of 120 kV $^4He^0$ beams were injected. Fig.2 shows evolution of

applied powers, $n_e(0)$, $T_e(0)$ and the count rate R_H for 0.73MeV H^0 received by the NPA, showing high count rate giving low statistical error. Notice that the H^0 flux arose soon after ICRF power was applied, and independently of the injected He^0 beam. We call this the passive flux. The active flux, arising only when the He^0 beam and ICRF were applied together, is clearly seen too. The small neutron background present during the measurements has been taken into account. The energy distribution of the H^0 flux $\Gamma_H(E)$ is shown in fig.3, for the passive flux at 6.4s and active flux at 6.6s. The spectra suggest that the fluxes arise from ion neutralization processes whose reaction rate has only a weak dependence on H^+ velocity.

The presence of the passive flux requires presence of a ion neutralization process much stronger than the initial consideration of charge-exchange reactions with injected atoms. Main candidates are (i) radiative recombination of high energy H^+ and electrons, (ii) charge-exchange between H^+ and hydrogen-like ions of beryllium and carbon, the main impurities in JET. Fig.4 shows the rate of neutralization reactions for the above processes, computed for plasma conditions prevailing in the experiment. The variation of the magnitude of $n_{DO}\cdot\langle\sigma v\rangle(s^{-1})$ with H^+ ion energy is presented. n_{DO} is the density of likely donors for electron capture by MeV H^+, $\langle\sigma v\rangle$ is the product of the reaction cross-section and relative velocity averaged over the velocity distribution. (a) curve-1 shows the rate of radiative recombination of H^+ with free electrons, (b) curve-2 shows the rate of electron capture from C^{+5} donor ions, where $n_{DO}=3\times10^{14}$ m^{-3} is used, (c) curve-3 shows the rate of electron capture from Be^{+3} ions with $n_{DO}=1\times10^{14}$ m^{-3}. The cross-sections for the last two processes were estimated using the model of two strong-coupling states[3]. The above computation was repeated for the case of the active flux where the injected He^0 beam was found to increase the density of C^{+5} and Be^{+3} ions in the plasma. Fig.5 shows the reaction rates, considering the same processes as those in fig.4, with the addition of charge-exchange reactions of H^+ with injected He^0 atoms, curve-4. It seems plausible that all these processes together could give rise to the observed fluxes when H-minority density is taken to be to 5-10% of the plasma density, which seems to be a little too high.

Fig.6 presents the energy spectrum of $^3He^0$ flux from a ^4He-plasma with ^3He-minority ICRF heating and a $^4He^0$ injected beam. The main parameters of the

plasma were $n_e(0)=3.10^{19} m^{-3}$, $T_e(0)=4.6$keV, $P_{ICRF}=1.8$MW, $P_{BEAM}=2.5$MW, $E_{BEAM}=$ 120 keV. As expected, the passive flux did not arise. Examination of the spectrum suggests that it is a result of double charge-exchange reaction with the He^0 beam, $^3He^{+2}+^4He^0 \Rightarrow {}^3He^0+^4He^{+2}$. Relative energy distribution of ^{3}He-minority, $f_{He}(E)$, derived from the measured Γ_{He}, using known charge-exchange cross-sections[4] is also shown in fig.6.

These experiments show that an NPA operating in the MeV energy range can be used for measurements of ICRF driven H-minority ions in JET, due to the fortuitous presence of a strong single electron capture processes by MeV H^+ from C^{5+} and Be^{3+} present in the plasma. In experiments using ICRF driven ^{3}He minority and ^{4}He beams, the capability for measurement of double CX MeV $^3He^0$ by an NPA was demonstrated, creating the possibility of application of such an instrument to future fusion α-particle measurements.

1. A.B.Izvozchikov et al., A.F.Ioffe Institute Report Number 1295(1988).
2. The JET Team, JET Report JET-P(91)66, December 1991.
3. L.A.Vainstein et al., "Excitation of Atoms and Broadening of Spectral Lines", Springer-Verlag, Berlin (1981)
4. D.F.Barash et al., Abstracts of ICPEC, Brisbane,Australia, 1991.

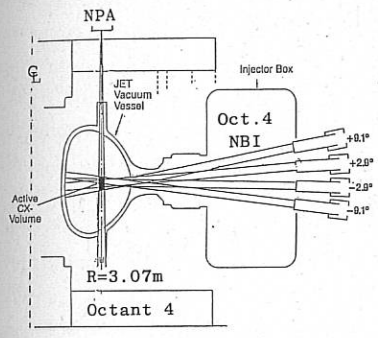

Fig.1 Experimental setup on JET.

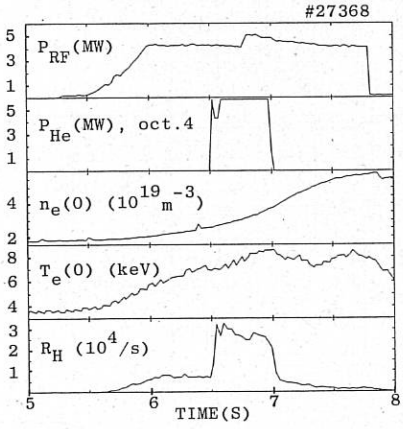

Fig.2 Evolution of plasma and heating parameters, and NPA flux.

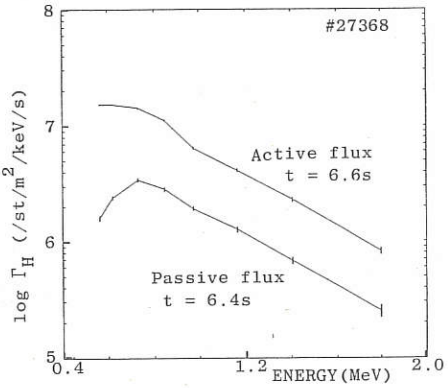

Fig.3 Energy spectrum of passive and active hydrogen flux received from the plasma.

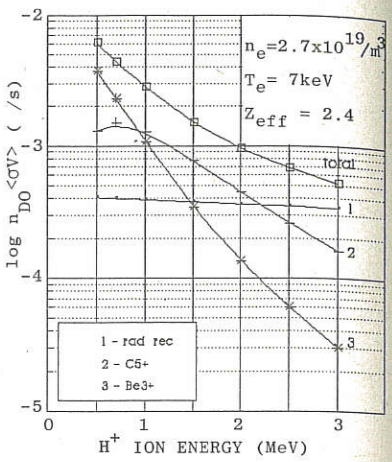

Fig.4 H^+ neutralization reaction rates for different processes for the passive flux.

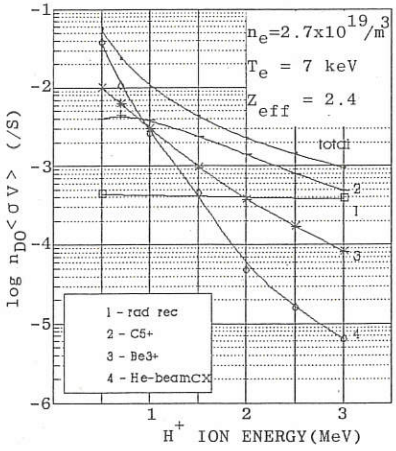

Fig.5 H^+ neutralization reaction rates for different processes for the active flux.

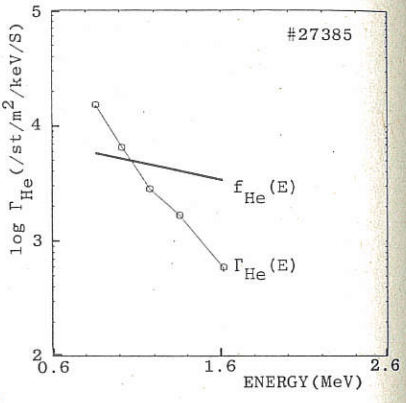

Fig.6 Energy spectrum of helium-3 flux from plasma, and deduced ion energy distribution in the plasma assuming double charge-exchange.

II-1o35

Investigation of alpha particle slowing-down features in helium neutral beam fuelling experiments at JET

M.G. von Hellermann, W.G.F. Core, J.Frieling[+], L.D. Horton
R.T.W.Koenig, W.Mandl[*], H.P.Summers, B. Wolle[#]
JET Joint Undertaking, Abingdon OX14 3EA, GB
[+]AMOLF Amsterdam, NL, [*] IPP Garching, [#]Universitaet Heidelberg, FRG

The control of alpha particle densities in the core of a burning plasma and the removal of helium ash is a central topic in the design of next-step fusion devices. This paper addresses the reliability of absolute measurements, and the detectability of slowing-down alpha particles and their velocity distribution function by charge exchange recombination spectroscopy (CXRS) . Experimental results at the JET tokamak are presented, where central helium fuelling and the slowing-down of alpha particles was simulated by injection of 140 keV $^3He^0$ beams into deuterium target plasmas during low- and high-confinement periods.

JET has recently completed an extensive atomic data base [1] required for CXRS measurements of absolute alpha particle densities and their spatial and temporal evolution. Relevant cross-sections (Fig.1) for the effective emission rate following charge are shown for the two cases of either using a neutral He-beam or a neutral D-beam as a donor for the charge exchange process.

The presence of beryllium in most of the JET plasmas requires a simultaneous treatment of Be and He CX features in the same spectral range caused by the wavelength coincidence of the BeIV (n= 8-6) and the HeII (n=4-3) transition. The problem has been solved by a coupled-parameter fit procedure, which makes use of known intensity ratios and wavelength separations both in the passive background features and active CX spectra (Fig.2). In addition to the thermal spectra of HeII, BeIV and CIII a broad pedestal with a width of $\Delta\lambda = \lambda_o v_{beam}/c = 46$ Å ($\lambda_o = 4686$ Å) is observed during injection of neutral helium beams.

The injection of high energy neutral helium beams produces a population of fast helium ions with energies from above thermal up to the injection energy. The distribution function of the fast particles is strongly anisotropic at the birth energy but subsequently isotropises in the course of the slowing-down process. The slowing-down alphas may either charge

exchange with the neutral beam in the plasma centre or escape to the plasma boundary and charge exchange with a dense layer of cold neutrals. Since the observed slowing-down intensities are found to be proportional to the product of CXRS probe beam power and the total helium fuelling beam power (JET has two independent neutral beam injection systems) we conclude that the slowing-feature indeed represents the fast alpha particles defined by the active CX volume in the plasma core. The possible presence of a high energy helium plume [2], caused by impact excited fast HeII ions moving along the field into the line-of-sight is under investigation.

We can calculate the expected CXRS spectrum produced by slowing-down alphas by evaluating by evaluating the integral:

$$f(v)_{obs} = \iiint dv'v'^2 \sin\vartheta d\vartheta d\phi \; g_{slow}(v',\vartheta,\phi)\; Q_{cx}(v_r)\; \delta(v - v'\cos\vartheta)$$

where g_{slow} is the slowing-down distribution function, $Q_{cx,eff} = \sigma(v_r)v_r$ the effective cx excitation rate (Fig.1), $v_r(v',v_b,\vartheta,\phi)$ the relative velocity between alpha and beam particle, and ϑ the angle between viewing line and v'.

As a test slowing-down function we use the anisotropic function obtained from the analytical solution of the neutral injection Fokker-Planck equation [3], where $\xi_o = \cos\phi_o$ is the initial pitch, v_b, v_c are the injection and critical velocity respectively, τ_s is the Spitzer slowing-down time, S is the beam deposition rate, $\beta = m_i Z_{eff}/2m$, where m_i, m are the plasma and beam ion mass respectively :

$$g(v,\vartheta,\phi) = S\,\tau_s\left[v^3 + v_c^3\right]^{-1} \exp\left\{-(\xi-\xi_o)^2/4\alpha\right\}/\sqrt{4\pi\alpha}$$

$$\alpha = (\beta/3)\,\log\left[(1 + (v/v_c)^3)/(1 + (v_c/v_b)^3\right]$$

A logarithmic plot both of experimental (Fig.3a) and simulated spectrum (Fig.3b) shows that, to a first approximation, the observed shape can be described by the above anisotropic function and evidence of a fast particle population within the discharge can be deduced. The fuelling power in this example is 10.5 MW injected into a target density of 2 $10^{19}m^{-3}$. In the course of the fuelling and heating phase both ion and electron temperatures increase and reach levels of 13 and 8 keV respectively . Typical thermalisation times between fast and thermal alpha particles ($t_{st} = \tau_s \ln(1 + (v_c/v_\alpha)^3)/3$) are of the order of 200 msec. For the deduction of the fast population we make use of an averaged excitation rate defined as:

$$\langle\sigma v\rangle_{eff} = \int f(v)dv \;/\; \int g(v)\; d^3v$$

For the case of a 135 keV He beam we obtain:

$$\langle\sigma v\rangle_{eff,fast} = 1.23\ 10^{-9} cm^3 s^{-1} = 0.68\ \langle\sigma v\rangle_{eff,thermal}$$

During a fuelling process the fast population density remains constant whereas the thermalised population increases almost linearly in time (Fig.4), reaching concentrations of approx. 10 to 15 % of the electron density. The total thermalised He content as monitored by the radial CX profile agrees usually quite well with the number expected from the injected beam current (Fig.5).

Typical fast particle densities observed during the He heating campaign of JET, with total powers up to 12 MW, are between 2 $10^{17} m^{-3}$ and 2 $10^{18} m^{-3}$, the lowest level corresponding to a signal/noise of 2. The detection limit has been confirmed by simulating experimental spectra superimposing calculated spectra with random noise representing photon statistical fluctuations in CX spectra and bremsstrahlung. For the future D-T phase of JET with thermo-nuclear alpha particle powers of 1 MW a detection of slowing-down alpha particles appears feasible with a significantly improved optical throughput and a fibre-less optical link in order to avoid luminescence caused by neutron bombardment.

References: [1] M von Hellermann et al., Plasma Physics **33**,1805(1991), [2] R.Fonck, Phys.Rev. **29**,3288(1984), W.G.F.Core , JET-IR(91)15.

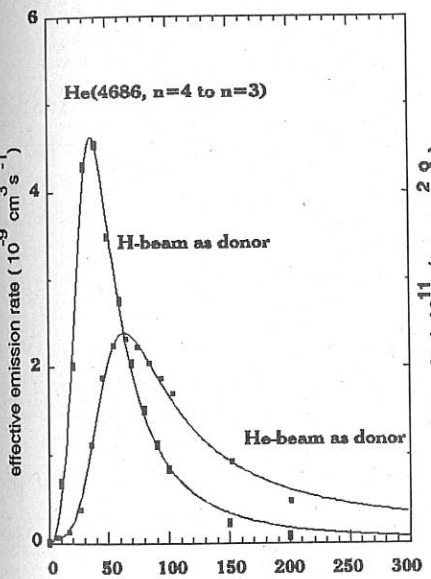

Fig.1

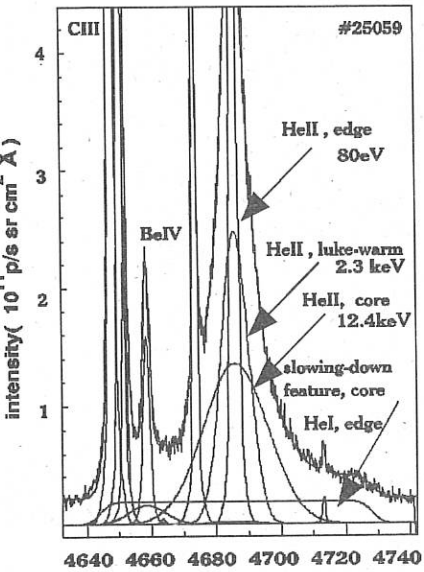

Fig.2

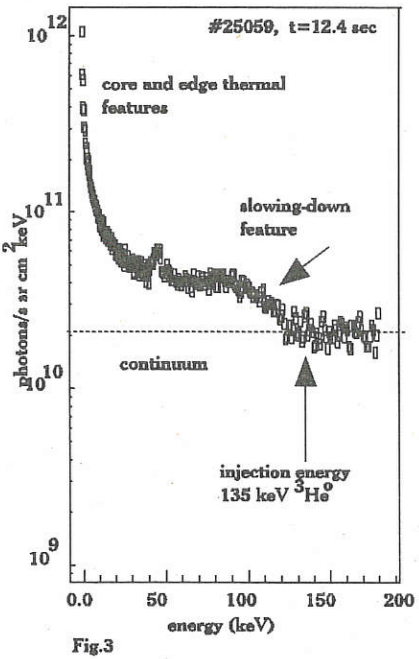

Fig.3

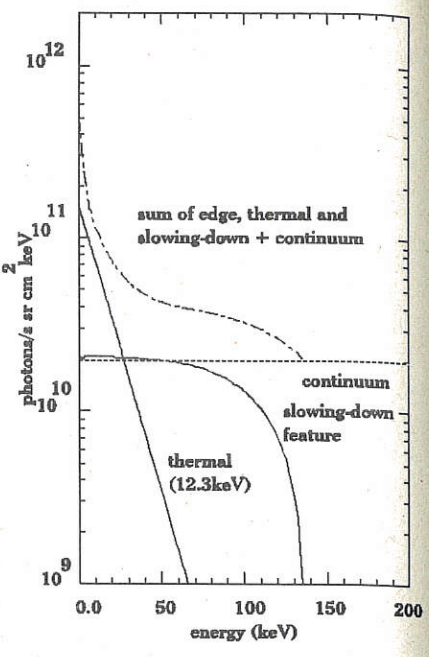

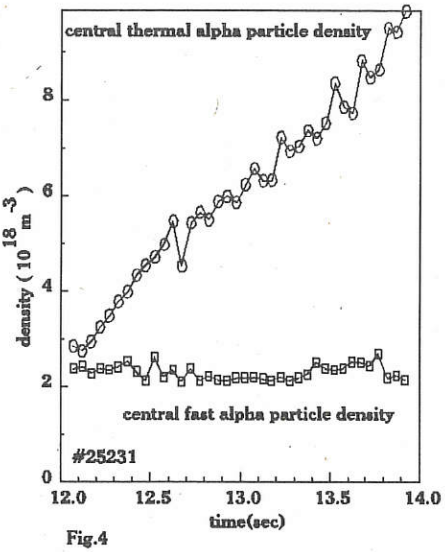

Fig.4

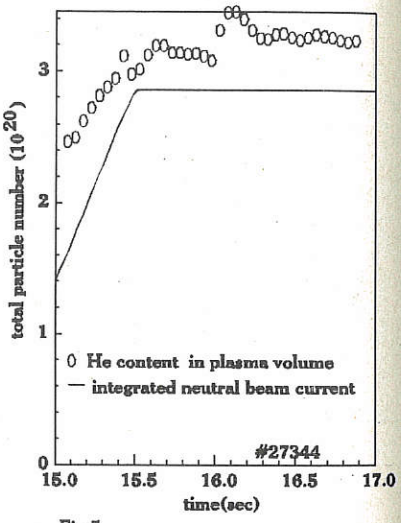

Fig.5

PROSPECTS FOR INVESTIGATION OF ALPHA PARTICLES VELOCITY DISTRIBUTION BY CHARGE EXCHANGE SPECTROSCOPY IN ITER

A.A. Korotkov, V.P. Belik, L.A. Shmaenok, Yu.Ya. Platonov*, N.N.Salashchenko*
A.F.Ioffe Physical-Technical Institute, St.Petersburg, Russia
*)Institute for Applied Physics, N.Novgorod, Russia

Abstract

A study of CHES feasibility has been carried out taking into consideration hydrogen and helium probing beams for the present choice of diagnostic ports at ITER .

It is shown that the low energy (50÷100 keV/u) helium beam is more suitable for the investigation of inner part of the ITER plasma than hydrogen one at the same initial beam density. Using HeII(304 Å) line for the diagnostics requires one order less beam power than that for HeII(4685 Å) line provided the first line is detected with efficiency close to that in the visible range. The way to solve this technical problem is discussed.

Calculations and Analysis

We consider the diagnostic scheme in which radiation is detected in the vertical plane at angle of 30° to the probing beam direction /1/. The main optics is placed away off the direct channel by means of replaceable multileyer mirror installed at the distance of 15 m from the plasma centre.

The beam atoms energy chosen is 100 keV/u for helium and 200 keV/u for hydrogen proceeding from the maximal emission intensity of the charge-exchanged alphas with energies 0.5÷1.5 Mev from plasma centre. The equivalent current of neutral particles in plasma is assumed to be 1 A at beam diameter of 10 cm which is available for the injector with one positive ion source of 4 MW and 7 MW power for helium and hydrogen beam correspondingly.

The intensity of emission of hydrogenlike helium ions

created by the charge-exchange of slowing-down alphas with beam atoms and the background radiation intensity have been calculated using new data on charge-exchange /2/ and atom beams stopping cross-sections.

Fig.1 presents the spectrum in the vicinity of resonant HeII (304 Å) line for helium beam injection on the assumption of 0.4 % of fast alphas with classical distribution function. The ratio of slowing-down time to confinement one ($g=\tau_s/\tau_c$) is varied. As a background we consider a variable part of bremsstrahlung and emission of thermal HeII ions which was estimated taking into account the density fluctuations due to drift waves. Statistics expected in the experiment allows to distinguish the variation of the distribution function which corresponds to the change of slowing-down time in the interval $0.5\ \tau_c \leq \tau_s \leq 5\ \tau_c$. The range of alphas energies available for investigation is $E_{beam} < E_\alpha < E_{\alpha max} \simeq 1.2$ MeV (if $\tau_s \ll \tau_c$). The low bound of the range is determined by the strong emission of the fast HeII ions created by the beam due to electron loss and trapped by the magnetic field (beam direction is nearly perpendicular to the magnetic field). At the same time these fast ions act as a good additional target for the charge-exchange of the fast alphas. About half intensity of the fast alphas radiation is induced by these ions.

Comparison of the diagnostic possibilities of helium and hydrogen beams is presented in Fig.2. Helium beam turns out to be much better for the investigation of the inner part of the ITER plasma especially at exposition time less than 1 sec. The reasons are a larger charge-exchange cross-section at high relative velocities for helium beam and creation of HeII target.

Fig.3 shows the spectrum in the vicinity of HeII(4685 Å) line. It is seen that for making use this line in the experiment the injector power must be about 50 times increased. Moreover influence of the collisions and strong Lorentz field on the characteristics of the visible line emission complicates interpretation of the measurements. The characteristics of the

resonant line emission is not affected by plasma environment. So we have concluded that HeII(304 Å) line is the most promising for the fast alpha particle diagnostics.

Multilayer Phase Grating

Using HeII(304 Å) line for the diagnostics of ITER plasma requires the resolution power and reflectivity of the dispersion element to be 10^3 and 5 % correspondingly. MPG is a possible candidate to solve this problem. We have begun to develop such grating and investigate its propeties. Fig.4 shows the reflectivity of the plane MPG for HeII(304 Å) line. The grating has a light concentration for the third order. High reflectivity (3.6 %) is reached because of Bragg-reflection of Mo/Si layers covering the phase structure. The reflectivity and resolution obtained are to be twice improved for the alpha particle diagnostics. Moreover the problem to produce a curve MPG with such parameters must be solved.

Conclusion

Analysis shows that 50 ÷ 100 keV/u helium injector with 4 MW ion source power could be suitable for slowing-down alphas investigation in ITER plasma provided HeII(304 Å) line is used. It means that CHES could be carried out simultaneously with neitralized alphas analysis that have undergone the double charge exchange using the same probing beam. To give a final conclusion much experimental work must be done to gain such experience in using helium beam as we have for hydrogen beam at present. Moreover the cross-sections for HeII(2s,2p, n=3,4)-states population in the charge-exchange of alphas with He and H at 0.1÷1 MeV/u energy must be measured.

References

/1/ V.I.Afanasiev, A.B.Izvozchikov, A.I.Kislyakov et.al, ITER-IL-PH-7-0-26, February 1990

/2/ D.Belkič, R.Gayet, A.Salin, IAEA Consultants' Meeting, Vienna, 1991

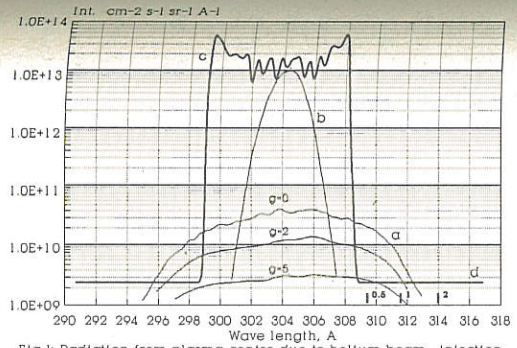

Fig 1: Radiation from plasma centre due to helium beam injection. Bold strokes point alphas energy (in MeV). (Ne=1.2E14 cm-3, Zeff=2) a-fast alphas, b-helium ash, c-fast He+, d-bremsstrahlung

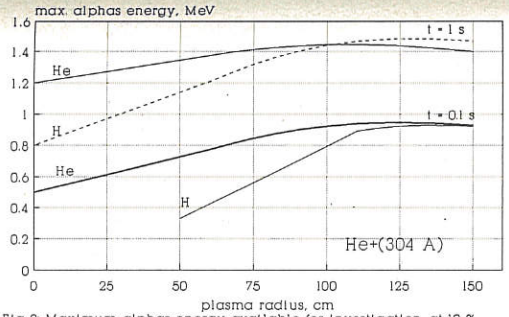

Fig 2: Maximum alphas energy available for investigation at 10 % statistic accuracy for He- and H- probing beam. t is exposition time.

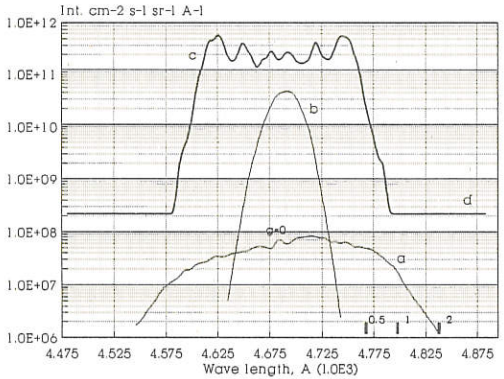

Fig 3: The same as for Fig 1 but for HeII(4685 A) line

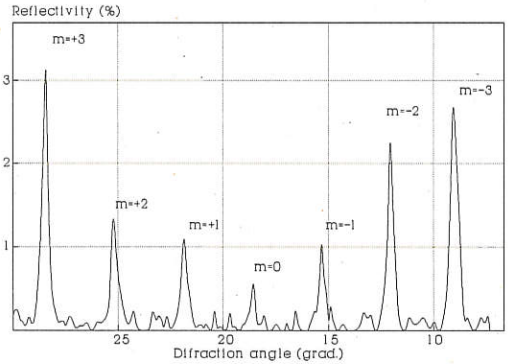

Fig 4: Reflectivity of MPG for HeII(304 A) line at incident angle of 19 grad.

II-1o43

HELIUM STOPPING CROSS-SECTION IN FUSION PLASMA TAKING INTO ACCOUNT THE MULTISTEP COLLISION PROCESSES

A.A. Korotkov

A.F.Ioffe Physical-Technical Institute, St.Petersburg, Russia

Abstract

The enhancement of the helium beam stopping cross-section due to multistep electron loss in plasma is discussed because of its importance for efficiency of plasma heating and diagnostics. The helium beam is necessary for active charge-exchange alpha-particle diagnostics /1/, where the plasma transparency for beam atoms and neutralized alphas should be taken into account. The preliminary calculations of the additional part of the stopping cross-section σ_{ad} have been carried out for a wide variety of beam and plasma parameters using atomic database available at present. The sensitivity of the results on the uncertainties of the relevant cross-sections has been studied. It has been ascertained that the phenomenon under study becomes important in plasmas with integrated line density above 10^{16} cm^{-2} expected for next-generation tokamaks (ITER,BPX) and reactor level device.

Method of Calculation

We describe the stopping cross-section as $\sigma_s = \sigma_s^o + \sigma_{ad}$, where σ_s^o applies to the electron loss from the ground state,

$$\sigma_{ad} = \Big(\sum_{k=1}^{k_m} (I_k - I_o) N_k + \sum_{k>k_m}^{k_m} K_{ok}\Big) / v_o \Big(1 + \sum_{k=1} N_k\Big),$$

I_k is the rate coefficient for electron loss from the state k due to ionisation and charge-exchange (I_o corresponds to σ_s^o), K_{ik} is the same but for excitation (deexcitation) from the state i to the state k, k_m is the maximum state number determined by the Lorentz field ionisation limit, v_o is the beam atom velocity.

The populations of singly excited states N_k are determined

from the system of coupled equations of stationary radiative-collisional model, which is valid at plasma densities $n_e \geq 10^{14}$ cm^{-3} when contribution of the metastable states to the electron loss becomes much smaller than total contribution of other excited states. Only the ground state is assumed to be initially populated (N_o=1). One-electron processes for helium interacting with electrons, hydrogen ions and impurities (He,C,O,Fe) are taken into consideration using atomic physics database described in /2/.

Eigenvalue problem is solved for the excited states with $n \leq 4$ to determine energy levels and transition probabilities for helium in Lorentz ($\vec{v}_o \times \vec{B}$) and magnetic fields. For the levels with $n \geq 5$ field-free atomic data are used and l-states are assumed to be completely mixed.

Spin System Mixing

Relativistic spin system mixing is an important mechanism of the triplet helium states population in high temperature plasma (T > 1 keV) because the rates of the spin changing transitions by electron impact become small. Taking into account this mixing we consider the basis wavefunctions as a sum of singlet and triplet parts with mixing coefficients obtained by diagonalising the energy matrix between the pure LS states in the field-free case using relativistic term in the Hamiltonian in the form suggested in /3/.

In the calculations we also take into account the additional spin system mixing taking place when occasional degeneration of singlet and triplet states occurs due to Stark effect in the Lorentz field. Fig.1 shows that spin system mixing results in several times increase of the triplet states population. The peculiarities of the triplet states population correspond to crossing energy levels of the states in $3\,^1D$ and $3\,^3D$ multiplets due to Stark effect. Collision broadening of levels promotes the spin system mixing .

Results and Discussion

The enhancement of the helium stopping cross-section due to multistep collision processes ($\delta_s = \sigma_{ad}/\sigma^o_s$) turns out to be in the range of 5% ÷ 15% for $n_e \simeq 10^{14}$ cm^{-3} (Fig.2) that is approximately four times as low as for hydrogen at the same velocity. The reasons are the lower values of the cross-sections for excitation from the ground state and larger radiative decay probabilities in the helium case.

Impurity presence in plasma reduces the excitation rate of helium at energy $E < 100\ Z$ keV/u (Z is charge of the main impurity ions) and increases this rate in the opposite case. So the behaviour of σ_{ad} versus Z_{eff} changes depending on E (Fig.3)

Despite of the small value of δ_s helium multistep electron loss is important for integrated line plasma density $n_e a > 10^{16}$ cm^{-2} expected for the next-generation tokamaks. The change of plasma trasparency for helium probing beam or for neutralized alpha-particle escaping from plasma center of ITER is presented in Fig.4. For 10% accuracy of the plasma transparency enhancement factor δ_s must be known with accuracy about 20%. To obtain such accuracy two-electron processes and inner electron loss should be considered. It is very important also to take into account the initial population of the helium metastable states in the real experiment.

Acknowledgements

The author is grateful to Dr. R.K.Janev and Dr. H.P.Summers for useful remarks. Special thanks to M.S.Samsonov for assistance with mathematical programs.

References

/1/ V.I.Afanasiev, A.B.Izvozchikov, A.I.Kislyakov et.al, "Ion Component Diagnostics on ITER by Means of Atomic Beams", ITER-IL-PH-7-0-26, February, 1990

/2/ A.A.Korotkov, Nucl. Fusion A+M Suppl., vol. 3, to be published

/3/ J.Spence, H.P.Summers, J.Phys.B **19**, 3749 (1986)

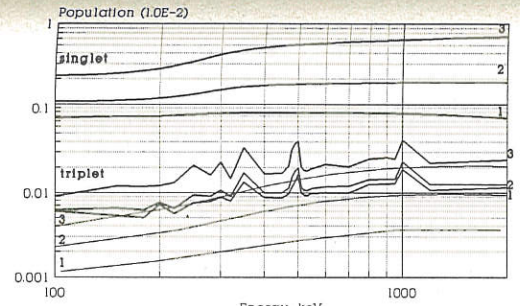

Fig 1: Total singlet and triplet states populations at various plasma density: 1- 1.0E13 cm-3, 2- 1.0E14 cm-3 , 3- 1.0E15 cm-3 (Zeff=1, T=10 keV, B=5 T) Thin curves for the case without spin system mixing

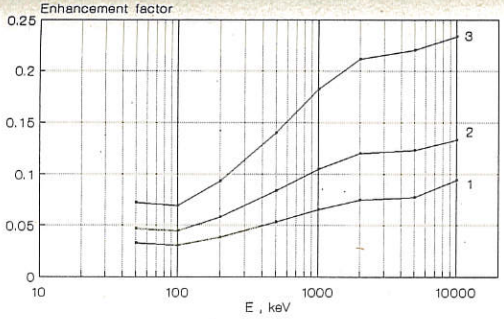

Fig 2: Energy dependence of the stopping enhancement factor for plasma parameters of Fig 1 except Zeff=2 (He:C:O:Fe=5:1.5:0.5:0.05)

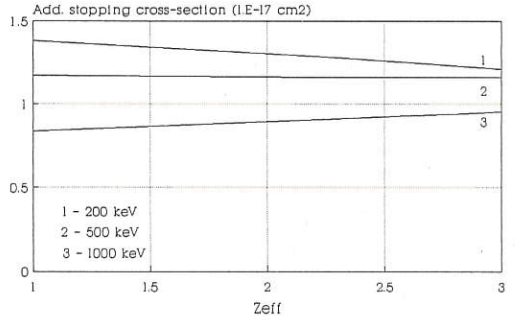

Fig 3: Dependence of the additional stopping cross-section on plasma effective charge for three values of helium energy

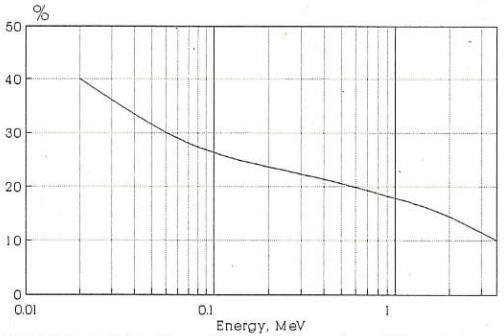

Fig 4: Change of the plasma transparency due to multistep electron loss in ITER versus helium energy (na=2.1E16 cm-2, T(0)=25 keV, Zeff=2)

NEUTRON SPECTROMETRY CONCEPTS FOR DIAGNOSING DT PLASMAS OF Q≈1

J. Källne, G Gorini*, H Condé, and PU Renberg
Department of Neutron Research, Uppsala University,
S-751 21 UPPSALA, Sweden,
*Department of Physics, University of Milan, via Celoria 16,
I-20133 MILAN, Italy

For burning DT plasmas (Q->∞) of ITER [1], we have devised the use of special HFC (high flux and count rate) neutron spectrometers (NS) [2]. These can accept very high rates (capability limit C_n^{CAP}>10-100 MHz) as limited only by the available collimated neutron flux (F_n) from the plasma; i.e., the attained count rate is $C_n=\varepsilon\cdot F_n$ with ε being the (flux) detection efficiency. C_n can be seen as the product of the statistical accuracy ($1/\sigma_N$, $\sigma_N=1/\sqrt{N_n}$) and the time resolving power ($1/\Delta t$, where Δt is the time resolution), i.e.,

$$C_n=(1/\sigma_N)^2\cdot 1/\Delta t; \qquad (1)$$

C_n is thus a figure of merit for the measurement and should be maximized [3].

The maximum ε for a HFC spectrometer (as limited by general neutron detection principles) is about 10^{-4} cm^2 for an energy resolution of $\Delta E_I/E$=2.5 % (FWHM). A conceptual design, the magnetic proton recoil (MPR) spectrometer, has been presented with $\varepsilon=2\cdot 10^{-5}$ cm^2 [4]. The MPR spectrometer would attain C_n^{MAX}=1 MHz on ITER with a rather narrow collimation providing $F_n^{MAX}\approx 5\cdot 10^{10}$ $n/cm^2\cdot s$. Minimum diagnostic requirements of σ_N=±3 % and Δt=100 ms would imply C_n^{MIN}=10 kHz and a dynamic range of $D=\varepsilon\cdot F_n^{MAX}/C_n^{MIN}$=100 on ITER; at $C_n=C_n^{MAX}$=1 MHz; the diagnostic capability reaches, for instance, Δt=1 ms at ±3%. Given these specifications, NS can be envisaged [2] to perform the essential diagnostic and control functions in burning plasma studies on reactor like tokamaks such as ITER with a planned fusion power of P_f=1 GW and a 14-MeV (d+t->α+n) neutron production rate of $Y_n=4\cdot 10^{20}$ n/s [1]. Here we shall discuss the potential role of this new type of neutron spectrometer on JET in view of the information on neutron conditions of DT plasmas now available from the preliminary tritium experiment (PTE) [5].

The results from the JET PTE discharges gave $Y_n\leq 6\cdot 10^{17}$ n/s for Q=0.15 and implying that higher values can be expected in the full parameter DT operation planned for 1996; 10^{19} n/s has been mentioned as Y_n^{MAX} for JET which is used here as a reference value to define $Y_n^{REL}=Y_n/Y_n^{MAX}$. These Q≈1 plasmas would differ in yield a factor of 40 from the ignition plasmas of ITER but the experimental conditions for neutron diagnostics will differ less since the important neutron measurements with spectrometers and cameras depend on obtainable collimated neutron flux rather than Y_n.

The F_n/Y_n-ratio will be favored at JET because it is dimensionally smaller and this ratio can also be effected by choice of collimation which controls the spatial resolution ($\Delta r/a$, where a is the plasma minor radius), i.e.,

$$F_n/Y_n=\chi_\Lambda \cdot 1/L_\Lambda^2 \cdot (\Delta r/a)^2; \quad (2)$$

here, L_Λ is the distance of observation and χ_Λ is a proportionality factor [6]. For the three main lines of sight being tangential (T) or (R) radial in the horizontal plane, and vertical (V),

$$\chi_T:\chi_R:\chi_V=1.33\cdot(A/w)^{1/2}:1:\kappa \quad (3)$$

where A is the plasma aspect ratio, κ is the elongation and $w=a_n/a$ (FWHM) is the relative neutron profile width using a standardized emissivity distribution [6]. The F_n/Y_n-value is highest for the tangential sight line ($\chi_T \approx 3.3$ for JET). A $\Delta r/a$-value of up to about 0.25 could be used without detrimental effect on a single-channel NS measurement. Finally, maximum F_n/Y_n is obtained for minimum L_Λ which we estimate to be about 10 m at JET using , for instance, a position similar to the present 2.5-MeV spectrometer with tangential sight line [7]. We thus arrive at a maximum F_n/Y_n value of $3\cdot10^{-9}$ cm^2 for JET implying $F_n^{MAX}=3\cdot10^{10}$ n/s·cm^2 at $Y_n^{MAX}=10^{19}$ n/s so that the MPR spectrometer could attain $C_n^{MAX}=600$ kHz and a dynamic range of D=60; in the recent PTE discharges [5] with $Y_n^{REL}=0.06$, C_n could have reached 36 kHz.

NS is the diagnostic that can potentially provide the most detailed information on the fusion reactivity of the plasma depending on the instrumental capabilities. The latter are illustrated here in terms of the temporal and statistical resolving power of the MPR spectrometer measurements of tarnsients in the ion temperature, $T_i(t)$, and fusion reactivity composition.

For a plasma of purely thermal fusion reactivity, the statistical error in the $T_i(t)$ determination is $\Delta T_i/T_i=\sqrt{2}\cdot\sigma_N$. For mixed thermal and supra-thermal fusion reactions [with corresponding neutron rates of $C_{n^\circ}(t)$ and $C_{n'}(t)$, and the ratio $R(t)=C_{n^\circ}/C_{n'}$], one obtains $\Delta T_i/T_i=[2(R+1)/R]^{1/2}\cdot\sigma_N$. The measurement of the fusion reactivity components have statistical errors of $\Delta C_{n^\circ}/C_{n^\circ}=[(R+1)/R]^{1/2}\cdot\sigma_N$ and $\Delta C_{n'}/C_{n'}=(R+1)^{1/2}\cdot\sigma_N$, and $\Delta R/R=(R+1)/\sqrt{R}\cdot\sigma_N$ for the ratio. The reactivity components are distinguished on the basis of the facts that C_{n° has an energy distribution of Gaussian shape with a T_i-dependent width (ΔE_i) while that of $C_{n'}$ is wider (relative to ΔE_i) and is of variable shape depending on the fast ion source and the line of observation. When these components are hard to separate even by spectral unfolding, normally based on a computed shape of $C_{n'}(E_{n'})$ for given conditions [7], the statistical errors will be larger than the basic ones quoted above; unfolding effects are not considered here.

The estimated diagnostic capability of the MPR spectrometer can be presented making use of the time traces of $Y_n(t)$, $Y_{n^\circ}(t)$ and $Y_{n'}(t)$ of the PET discharge #26148 [5]; $Y_{n'}$ was tacitly taken as the beam-plasma component of Ref. [5] ignoring the small beam-beam component. With $Y_n(t)$ and $R(t)$ of FIG. 1 as inputs, one can estimate what the statistical error of the $T_i(t)$ determination (for a set choice of Δt, normally, 100 ms) should have been for the time evolution of $T_i(t)$ as recorded. We

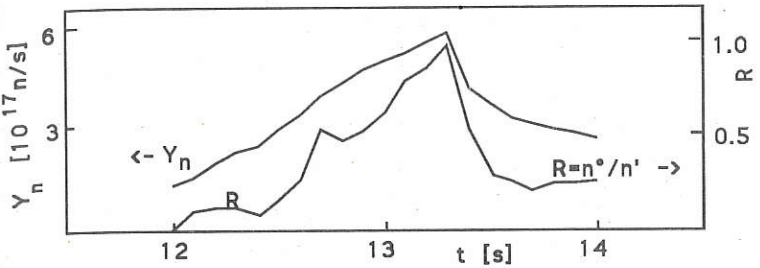

FIG. 1 Time traces on $Y_n(t)$ and $R(t)$ used for estimating statisitical errors; the data have been adapted from REF [5] as presented for shot # 26148 of JET PTE operation.

thus find (Fig. 2) that the projected $T_i(t)$-measurement with NS would have been able to detect the giant sawtooth collapsing at t=12.3 s; it would here have been an independent measurement for verification of $T_i(t)$-data and this information would pertain directly to the fusing ions themselves.

Similarly, projected statistical errors were estimated for $C_{n^\circ}(t)$ and $C_{n'}$ (t) taken as proportional to $Y_{n^\circ}(t)$ and $Y_{n'}(t)$ of the simulated data in FIG. 1 from REF [5]. The results are shown in FIG. 3. $C_{n^\circ}(t)$ is very weak in both relative and absolute terms for $t \leq 12$ s [because of low $T_i(t)$ with neutral beam injection (NBI) of low power] with a corresponding large error (≥20 %) in its determination. About 200 ms into the main NBI pulse (t≈12 s), $C_{n^\circ}(t)$ starts a steady rise to the maximum where $C_{n^\circ}(t)$ and $C_{n'}(t)$ are of equal strength. At the peak, MPR should have been able to measure these with a statistical accuracy of about ±4 % for Δt=100 ms. This suggests that NS would have been able to contribute data on the fusion reactivity composition for the plasma conditions that set off the termination of the discharge. We may also note that NS would have been able to supply simultaneously data on the fusion reactivity composition and on the relevant fusion temperature that would have provided a solid empirical base for the plasma transport calculations performed providing the simulated data shown in FIG. 1.

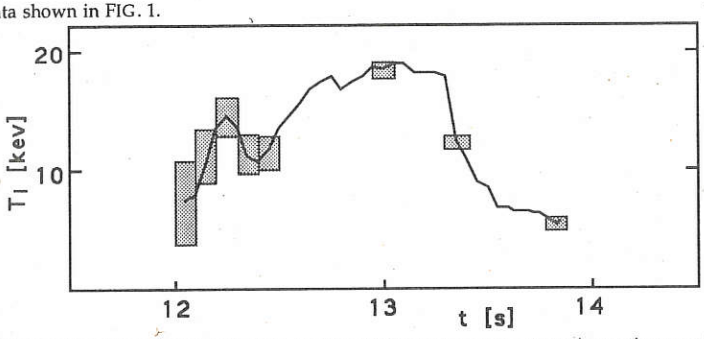

FIG. 2. Projected statistical errors in $T_i(t)$ for the MPR spectrometer assuming a time resolution of Δt=100 ms (shown as shaded areas for selected times; the $T_i(t)$-trace was adapted from REF [5]. Effects due to the finite instrumental energy resolution (ΔE_I) relative to (ΔE_i) have been neglected.

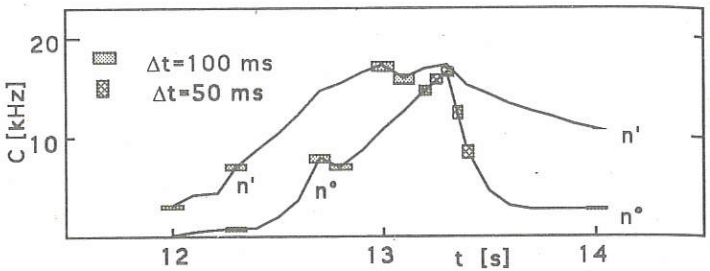

FIG. 3 Projected statistical errors (for selected times) in the thermal and supra-thermal components $C_{n°}(t)$ and $C_{n'}(t)$ from possible MPR spectromter measuremnts with Δt=100 ms and 50 ms; proportionality was assumed between $C_n(t)$ and $Y_n(t)$ taken from FIG. 1.

The above illustration refers to a JET discharge reaching Y_n^{REL}=0.06 covering a dynamic range of D=10. For 'full' power discharges reaching Y_n^{REL}=1, the statistical and temporal resolving power of measurements with the MPR spectrometer would be augmented by a factor of 4 or 16, respectively. This means that one would reach Δt=2 ms for σ_N=3 % (or 200 μs for σ_N=10 %) with capability of seeing details in the fusion reactivity transients. For instance, NS could be used to explore plasma conditions and occurence of phenomena causing the observed spontaneous discharge termination at peak fusion power; at these uncertainty levels, the statistical error should dominate over instrumental ones because of the special characteristics of the MPR-spectrometer [2]. These diagnostic capabilities far exceed those of conventional neutron spectrometers which have an intrinsic count rate ceiling of C_n^{CAP}<<100 kHz, typically, C_n^{CAP}≤5 kHz [8].

In conclusion, we note that the PTE results of JET show that HFC spectrometers could be put to good use on JET. The statistical and temporal resolving power would be comparable to other routine diagnostic systems and orders of magnitude higher than attainable with conventional neutron spectrometers. The information that could be provided on plasma reactivity parameters would be unique and not obtainable from other sources. It is also worth noting that JET would provide sufficiently high neutron fluxes for necessary prototype testing of HFC spectrometer to be required on ITER.

References.

[1] V Mukhovatov et al, Rev. Sci. Instr., 61(1990)3241 and 'ITER diagnostics', ITER Document series No. 33, IAEA, Vienna, 1990.
[2] J Källne, 'neutron diagnostics for burning plasmas of ITER/NET', Uppsala University Neutron Physics report, UU-NF #1/91 (Jan. 1992)
[3] J Källne and G Gorini, in 'Proceedings of the International Course and workshop on diagnostics for contemporary fusion experiments', (Varenna, Aug. 1991), Società Italiana di Fisica, Bologna, ISBN 88-7794-043-3, p. 1033.
[4] J. Källne and H. Enge, Nucl. Instr. Methods.**A311**(1992)595.
[5] The JET Team, Nucl. Fusion 32(1992)187.
[6] J Källne and G Gorini, UU-NF #6/91 (April 1992)
[7] ON Jarvis, in Ibid [3], p. 541.
[8] G. Grosshög, et al, and Nucl. Inst. Meth. **A249**(1986)468.

EFFECTS OF NEUTRONS ON THE JET SOFT X-RAY DETECTORS

R D Gill, B Alper and A W Edwards

JET Joint Undertaking, Abingdon, Oxon., UK

The recent preliminary tritium experiment gave an opportunity to observe the effects of high neutron fluxes on the JET soft X-ray diode arrays[1]). It is important to consider these effects to determine the future role of X-ray systems on JET and ITER and to establish that there is a reasonable understanding of both the effects during the discharge (i.e. mainly radiation induced signals and noise) and the longer term effects of radiation damage. The direct effects of neutrons fluxes have been studied with detectors in the arrays which have been blanked off to remove the flux of soft X-rays from the plasma. Typical signals are shown in fig. 1. Data was examined from three very similar shots with plasmas containing D only (26094), D plus 1% T (26095) in one PINI and the second high neutron flux D-T shot (26148). In table 1 the observed maximum radiation induced current (I_R) and the corresponding soft X-ray signal (I_x) in various detectors are shown and the detector positions are identified in fig. 2. (Channel 37 is blanked, 97 views the edge where there is no X-ray emission, 21 and 61 the centre). The maximum neutron rates for the different shots are also shown. The neutron induced signal is not significant (<2.2%) except in the DT plasma where it is 35% of the soft X-ray signal.

Table 1. Radiation and X-ray signals, and neutron rates.

Shot		I_R(nA) I_x (nA) Vertical Camera		I_R(nA) I_x (nA) Horiz. camera		D-D neutrons	D-T neutrons
		37	21	97	61	(s^{-1})	(s^{-1})
26094	D +D	80	5500	80	5100	3.25×10^{16}	
26095	D+1%T	110	6200	120	5400	4.2×10^{16}	1.06×10^{16}
26148	D+T	1400	4000	-	-	$\sim4\times10^{16}$	6.6×10^{17}

On comparing the D + D shot with the D + T shot it can be seen that the total neutron flux increases by a factor of 21.5 and that the radiation induced signal increases by a factor of 17.5. As the kerma for 14 MeV neutrons is ten times that for 2.5 MeV neutrons it would be expected that the radiation induced signal should increase in the D -T discharge by a factor of 203. This disagreement with the measurements is not understood.

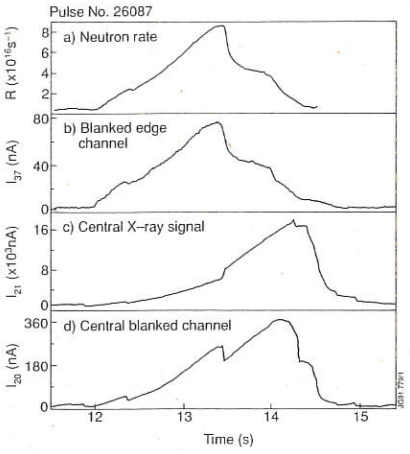

Figure 1(a) Neutron production rate (b) Edge blanked detector closely following (a). (c) Central soft X-ray signal. (d) Central blanked channel with features of (a) and (c).

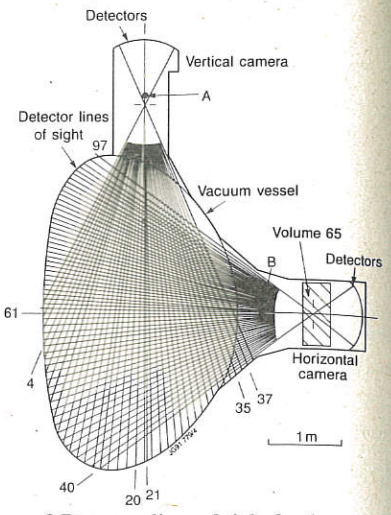

Figure 2 Detectors lines of sight for the X-ray cameras with some channels of interest marked.

Relationship of observed radiation induced signal to radiological calculations.

Extensive radiological calculations were made in the early phase of JET to establish safe operating regimes[2]). Some calculations were also done to establish radiation doses to equipment in different operational regimes[3]). Unfortunately the exact calculation for the soft X-ray systems have not been performed and in interpreting the observed data there are many uncertainties. There are two areas where comparisons have been made with experiment.

A) For the horizontal camera a comparison may be made for the D-D discharge with the calculations[3]) carried out for volume 65, just outside the main horizontal port (fig. 2).

B) A comparison may be made for both vertical and horizontal cameras with the calculations made for these port positions by Avery[2]) at points A and B of fig. 2.

Calculation A

The Avery data for volume 65 must be modified to take account of a radiation shield which has been fitted to the horizontal camera to reduce the radiation doses by up to a factor of 10. To be conservative we will reduce the Avery values by ~ 5. The calculated dose rates are 0.64 and 2.4 Rads/s from neutrons and gamma rays respectively leading to a radiation induced current of 116nA in reasonable agreement with the experimentally observed 80nA.

Calculation B

Radiological calculations have also been carried out for the vertical and horizontal ports for both D-D and D-T, but the radiological doses for standard man quoted in the report[2]) must be converted to Si doses. This can only be done in a rather approximate way without knowing the details of the calculation. Further, the detectors in both cameras are well back from the positions of the calculation (Points A and B of fig. 2) and this effect has been corrected for using the different solid angles subtended by the detectors. An allowance has also been made for the horizontal shield. This calculation gives I_R = 5 and 11nA for the horizontal and vertical cameras for the D-D shot where the experimental values are both 80nA. For the D-T shot, I_R = 780nA for the vertical camera compared with a measured value of 1400nA. Clearly, only approximate agreement is obtained. In order to get better agreement it would probably be necessary to carry out calculations which have a more accurate modelling of the regions close to the detectors.

Signal Noise The basic mechanism which produces a signal in a Si diode is that N photons or charged particles with energy E produce electron hole pairs in a time τ which contribute to the observed current I. If it takes 3.6 eV to create an e-h pair then

$$I = \frac{NEe}{3.6\tau} \quad \text{with E in eV}$$

N has a statistical variation which obeys Poisson statistics and has a root mean square deviation from average of $\pm\sqrt{N}$. Hence I has a root mean square deviation from average of

$$\frac{\delta I}{I} = \sqrt{\frac{eE}{3.6I\tau}}$$

where the reciprocal of τ should be identified with the pass band frequency (30 kHz minimum) rather than the digitization frequency (200 kHz). This equation has been found to be reasonably well satisfied for JET soft X-ray data taken in shots with few neutrons. The relationship may be written as

$$\frac{\delta I}{I} = 3.65\times10^{-8}\sqrt{E(eV)/I(A)}$$

for $1/\tau$= 30 kHz. For I_x = 3μA this gives δI_x = 4nA for the noise on I if E = 4 keV, which corresponds to the typical X-ray energy detected by the diodes.

An immediately obvious effect seen in D-T operation was that the noise was very much above the estimate of ~ 4nA for a pure X-ray source. For shot 26148 the total of the X-ray (I_x) and radiation induced current (I_R) was $I_T=I_R+I_x$ = (1+2)μA with δI = 105nA , i.e. a factor 26 more than expected for soft X-rays only. The reason for this is that for the radiation induced part of the signal, I_R, the radiation causing the current was due to α and proton interactions where the typical interaction energy per event is the order of 10 MeV. If all of the noise is ascribed to I_R then a value of E=8.3 MeV is found. This confirms the role of α's and protons, which come from reactions such as ^{28}Si (nα)^{25} Mg (Q = -2.652 MeV) or ^{28}Si(n,p)^{28} Al (Q = -3.852 MeV).

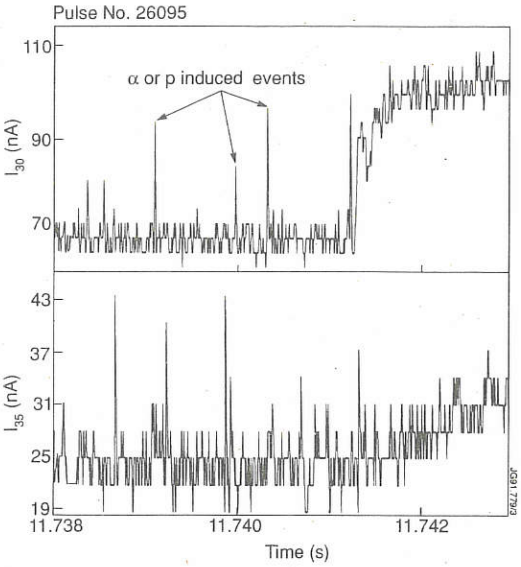

Figure 3 Clear spikes are seen due to α's or protons from reactions in the detectors.

Direct observation of heavy charged particles In the D + 1% T shot clear spikes were seen (fig. 3) on the soft X-ray signals which were conjectured to come from (nα) and other reactions in the silicon (e.g. ^{28} Si (nα)^{25} Mg). For 14 MeV incident neutrons the α's would have energies in the region of 10 MeV. Each of these would produce power over an observation time t of $P = 10^7 \times 1.6 \times 10^{-19}/t$ (W) and a current of $4.44 \times 10^{-13}/t$ (A). A total charge would be observed of 4.44×10^{-13} C. The observed charge in the spikes is 2.7×10^{-13} C in agreement and also showing that the charge from the α-events is well collected in our diodes. The frequency of these spikes is also in approximate agreement with expectations

Conclusions. The effects of neutrons in the X-ray detectors are in approximate agreement with expectations and this provides a firm basis for the design of systems to operate in much higher neutron fluxes. Preliminary studies show that soft X-ray cameras can be designed to operate satisfactorily in the full D-T phase of JET and probably the initial phases of ITER.

References

1. A W Edwards et al., Rev. Sci. Instr. 57 (1986) 2142.
2. A F Avery, AEEW-R 1615 (Reactor Division, AEE Winfrith, 1987)
3. JET Diagnostic Memo 10.

The Application of X-mode Reflectometry to the Study of Large Scale Fluctuations in TFTR

E. Mazzucato, R. Nazikian, and the TFTR-Group

Princeton Plasma Physics Laboratory
Princeton, NJ 08543 USA

Introduction

It has been suggested for some time[1-3] that microwave reflectometry has the potential for measuring the large scale structure of density fluctuations in tokamak turbulence with greatly improved spatial resolution over existing scattering techniques. The motivation for developing fluctuation diagnostics with improved spatial resolution of large scale structures is that such fluctuations may potentially account for the anomalous particle and energy transport observed in tokamaks. On TFTR we now have operational a four channel X-mode reflectometer system comprising of three fixed frequency channels at 140, 132.5, and 125 GHz and a tunable frequency channel scanning between 110-123 GHz. Each channel detects fluctuations from a region on the equatorial plane of the plasma torus with spatial resolution of ≈ 5 cm in the poloidal direction and ≈ 1 cm in the radial direction.

Properties of the plasma turbulence are inferred from the amplitude and spectral coherence of phase fluctuations impressed on the reflected wave by density irregularities at or near the cutoff. Experimental results are presented which show the existence of previously unobserved large scale ($k_\perp \rho_i << 1$) random and coherent density fluctuations in the Ohmic and Supershot[4] regimes of TFTR.

Ohmic results

Figure 1 shows a typical spectrum of measured phase fluctuations in the main core ($r/a \approx 0.4 \div 0.5$) of Ohmic and NBI plasmas. In the Ohmic case corresponding to the pre-beam phase of a TFTR supershot plasma, the relevant parameters are: R=2.45 m, a=0.8 m, B_t=4.8 T, I_p=1.4 MA, $n_e(0)=1.5\times10^{19}$ m^3, $T_e(0)$=4.0 keV, $T_i(0)$=2.0 keV. In the Ohmic case, the bandwidth of fluctuations is comparable with the drift wave frequency

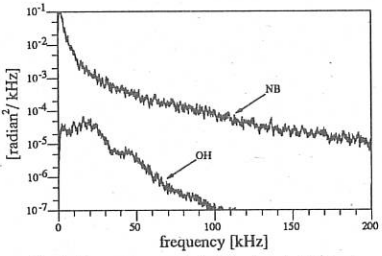

Fig. 1. Frequency spectra in Ohmic (r/a=0.4) and NBI (r/a=0.5) plasmas.

corresponding to the poloidal resolution of the diagnostic (≈1 cm^{-1}).

The radial scale length of fluctuations may be estimated by the method of correlation reflectometry[2] where the spectral coherence γ between the phase signals of two independent reflectometers is measured as a function of the radial separation δ of the cutoff layers. The spectral coherence is defined in terms of the Fourier transforms $F_{1,2}(\omega)$ of the measured phases as

$$\gamma(\omega;\delta)=\frac{\left|\langle F_1(\omega)F_2^*(\omega)\rangle\right|}{\sqrt{\langle|F_1(\omega)|^2\rangle\langle|F_2(\omega)|^2\rangle}}\ .$$

Figure 2 shows the spectral coherence for the data of Fig. 1 as a function of ω for $\delta\approx4$ cm. In Fig. 3, the spectral coherence in the range 10-20 kHz is plotted as a function of δ for the Ohmic and NBI phases where the tunable channel is stepped in frequency between successive shots. From these data it is concluded that the radial correlation length of Ohmic fluctuations at $r/a\approx0.4$ is ≈4 cm, corresponding to a coherence of ≈0.5 at the minimum separation of the cutoff layers of Fig. 2. Within the poloidal resolution of the instrument we conclude that long wavelength fluctuations in Ohmic plasmas are approximately isotropic in the region $r/a\approx0.4$. Finally, the two fixed frequency channels (140&132.5 GHz) with cutoffs near the plasma center consistently show no coherence in the Ohmic phase of the discharge (Fig. 5) for $\delta\approx15$ cm. Taking the measured correlation length of ≈4 cm as representative of fluctuations across the minor radius, then from the theory of Ref. 3 we may obtain the relative density fluctuation level $\tilde{n}_e/n_e$ as a function of major radius (Fig. 4).

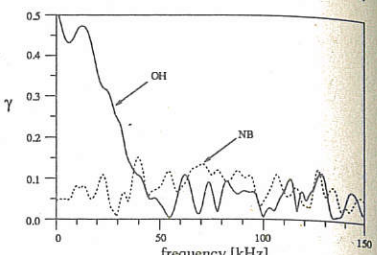

Fig. 2. Spectral coherence (δ≈4cm) of fluctuations of Fig. 1.

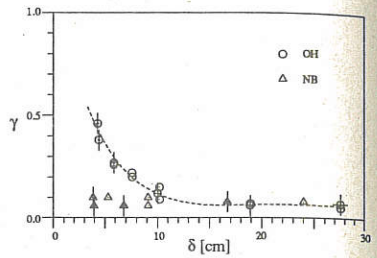

Fig. 3. Coherence @ f≈10-20 kHz vs. separation of reflecting layers

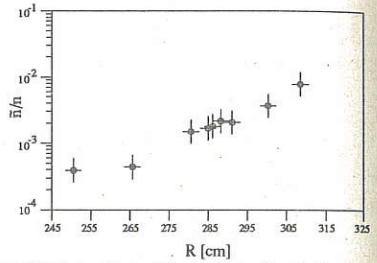

Fig. 4. Amplitude of density fluctuations in Ohmic plasmas vs. major radius.

NBI results

Fluctuation measurements similar to those made in Ohmic plasmas are shown in Figs.1-3 for NBI plasmas with a co/counter balanced beam injection power of 9 MW. These plasmas

are characterized by highly peaked density and temperature profiles with very high central ion temperatures[4]. The relevant parameters are: B_t=4.8 T, I_p=1.4 MA, $n_e(0)=3.4\times10^{19}$ m^{-3}, $T_e(0)$=8.0 keV, $T_i(0)$=22.0 keV.

The high fluctuation levels characteristic of NBI plasmas typically develops on the order of a confinement time, or ≈100 ms after beam turn on, with a frequency spectrum (Fig. 1) which extends out to ≈250 kHz. Surprisingly, for the minimum cutoff layer separation of ≈4 cm which was used in our experiment, no statistically significant level of coherence has been observed (Fig. 2). This indicates that in contrast to Ohmic plasmas, the scale length of density fluctuations is significantly less than 4 cm in the outer region of NB heated plasmas. Furthermore, unlike observations in the Ohmic phase, the spectral width of these fluctuations bears little relationship to the measured plasma rotation (<3×10^4 m s^{-1}) or drift wave frequency estimates.

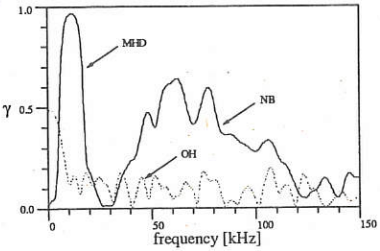

Fig. 5. Spectral coherence (δ≈15 cm) of fluctuations near the plasma center.

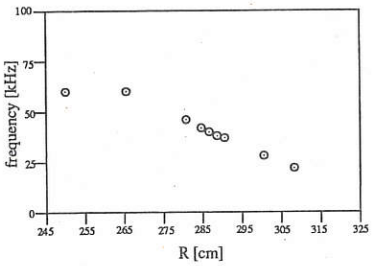

Fig. 6. Frequency of coherent oscillations vs. major radius at beginning of NBI.

In contrast to these measurements, and unlike the case of Ohmic plasmas, density fluctuations with large radial scale lengths have been observed in the central region of NBI plasmas. An example is shown in Fig. 5 where the coherence spectrum for δ≈15 cm obtained from the 140 and 132.5 GHz fixed frequency channels is displayed. These fluctuations are in the range of bounce frequencies of energetic ions in the central region of TFTR and have typically much lower amplitudes than fluctuations in the lower frequency part of the spectrum. In contrast, no significant coherence has been observed at lower frequencies except during MHD activity as in Fig. 5. These results obtained for large δ were confirmed by dropping the magnetic field to 4.2 T, thereby bringing the 125 GHz and the 110-123 GHz cutoff layers into the plasma core. For the minimum channel separation of ≈4 cm very high coherence levels (≈1) were again observed at high frequency (>50 kHz) whereas no coherence was observed at low frequency except during MHD activity.

Finally, a new coherent mode has been detected in NB plasmas with a beam power of 9 MW. This mode, not present at lower NBI powers, is observed only a few milliseconds after beam turn on with a frequency which varies with major radius as shown in Fig.6. After ≈100 ms, these coherent modes are only detectable in the central region of the plasma where they persist till the end of the beam pulse with almost unchanged frequency. The

relationship between these newly observed modes and those reported in Ref. [5] is not at all clear given that the latter are transient and have been detected only at the edge of the plasma column.

Conclusion

The newly installed X-mode reflectometer system on TFTR has already revealed entirely new information on previously unobserved large scale fluctuations in Ohmic and Supershot plasmas.

In Ohmic plasmas, fluctuations in the drift wave frequency range have been observed with long radial scale lengths (≈4 cm) and fluctuation levels varying from less than 0.1% in the plasma core to ≈1% at r/a≈0.8

In NB heated plasmas, fluctuations in the outer plasma region exhibit very broad frequency spectra which bear little resemblance to drift wave frequencies and appear uncorrelated on a scale length of ≈4 cm. On the contrary, in the central region of Supershot plasmas, low amplitude (<0.1%) fluctuations with very long (≈15 cm) correlation lengths and frequencies in range of energetic ion bounce frequencies have been observed.

Finally, a new coherent mode has been detected at the beginning of neutral beam injection which exhibits a strong radial frequency dependence.

Although these initial results are very encouraging, a great deal of further investigation is needed in order to understand the nature and distribution of these large scale structures in tokamaks and of the role they play in plasma transport.

Acknowledgments

This work was supported by U. S. Department of Energy Contract No. DE-AC02-76-CHO3073.

References

[1] E. Mazzucato (1975) *Density fluctuations in the Adiabatic Toroidal Compressor.* Princeton University Plasma Physics Laboratory Report MATT-1151.

[2] P. Cripwell, A. Costley and A. Hubbard (1989) Proc. 16th European Conf. on Controlled Fusion and Plasma Physics, Venice, Italy, Part 1, 75.

[3] E. Mazzucato and R. Nazikian (1991) Plasma Phys. Controlled Fusion **33**, 261.

[4] J. Strachan, et al. (1987) Phys. Rev. Lett. **18**, 1104.

[5] E. Fredrickson, et al. (1989) Proc. 16th European Conf. on Controlled Fusion and Plasma Physics, Venice, Italy, Part 2, 481.

A MULTI CHANNEL REFLECTOMETER FOR THE RTP TOKAMAK

S.H. Heijnen, C.A.J. Hugenholtz, M.J. van de Pol

FOM-Instituut voor Plasmafysica 'Rijnhuizen', Association EURATOM-FOM,
P.O. Box 1207, 3430 BE Nieuwegein, The Netherlands.

A multichannel reflectometer is under construction for the RTP tokamak (RTP = Rijnhuizen Tokamak Project). The system will be heterodyne and is based on the experience gathered with the JET reflectometer system.[1] However, on RTP a different approach will be used to generate and detect the multiple frequencies. The main reason for redesigning a working system is the fact that the total costs of the system are about a factor three less than that of the corresponding JET reflectometer. The system is especially suited for use on small tokamaks.

Introduction

The RTP tokamak[2] is a medium-sized tokamak, especially dedicated to the study of transport processes. It is equipped with a number of fast multichannel diagnostics,[3] two ECRH gyrotrons and a pellet injector. The electron density profile in RTP is accurately measured by a fast 19-channel interferometer and by a Thomson-scattering system. The latter diagnostic measures the density profile in a single laser shot (only once per plasma discharge). Since the density profile measurement is well covered, the reflectometer could be designed as a fixed frequency heterodyne system. The reflectometer will have eight channels, five in the Ka-band (26.5 - 40 GHz), and three in the U-band (40 - 60 GHz). It will be equipped with antennae at both the high and the low field side of the tokamak. All the channels will probe the plasma in the O-mode. The bandwidth of the system will be 100 kHz and the phase resolution 7.2°.

Design of the reflectometer

The principle of the RTP reflectometer is derived from the conventional heterodyne system. In such a system, two Gunn oscillators, locked to a frequency difference of Δf by a phase locked loop (pll), and two fundamental mixers are used for each frequency channel[1].
The microwave parts of the five-channel Ka-band system for the RTP reflectometer are presented in Fig. 1. Only the low field side system is given here. Measurements from the high field side can be performed at the expense of one additional mixer. It can be seen from Fig. 1 that although the system looks more complicated than a conventional reflectometer, one needs fewer expensive microwave components.
In this system, the principle of AM modulation is used to create upper and lower side bands according to the simple formula:

$$\sin(\alpha).\sin(\beta) = \frac{1}{2}\cos(\alpha-\beta) - \frac{1}{2}\sin(\alpha+\beta).$$

The modulation is done using an up-converter (type: Hughes 47471H-2230). This is a planar balanced mixer to which two signals are applied (IF and LO). The LO frequency is in the same band as the RF output frequency. The bandwidth of the LO is ± 5% of the central frequency. The IF frequency can be swept from 0 to 18 GHz. The maximum input power is +17 dBm for both the IF and the LO, while the maximum double side-band output power is +8 dBm integrated over all frequency components. As an example the typical output spectrum of an up-converter when it is driven by an LO of 34 GHz and an IF of 100 MHz is shown in Fig. 2.

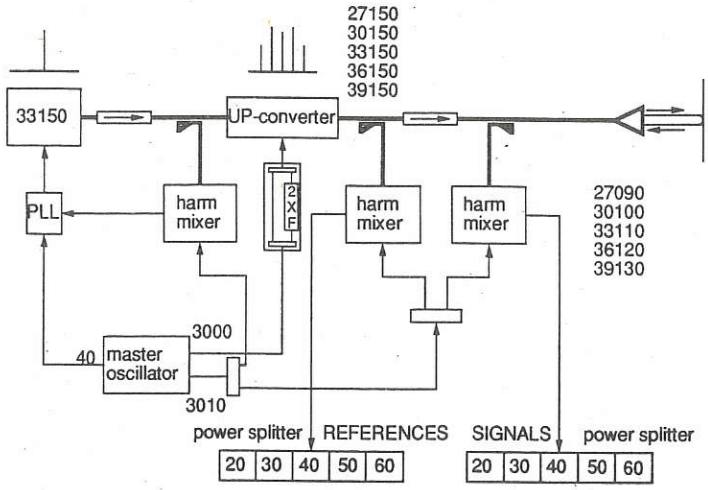

Fig. 1: Microwave components for the RTP reflectometer. This is the total five-channel system for low field-side measurements. For performing high field-side measurements as well, only one extra receiver module is needed. Frequencies are in MHz.

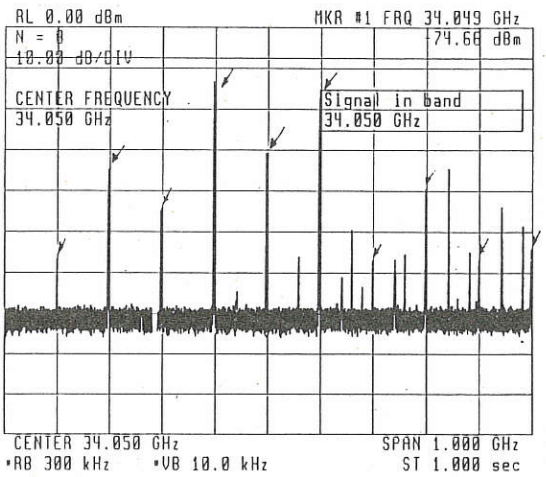

Fig. 2: Typical output spectrum of an up-converter (LO = 34 GHz, +16 dBm, IF = 100 MHz, +15 dBm). Total output power is +8 dBm. The real spectral lines are indicated with an arrow. The other lines are spurious signals generated by the spectrum analyser.

Detection is done using harmonic mixers (type: Millitech MHP-28-1) with an LO at 3010 MHz. The conversion loss and the noise figure of such a mixer is 40 dB. In Fig. 3, the IF components are shown. In a conventional reflectometer every IF-frequency is the same. For the RTP-reflectometer, however, a somewhat more complicated system has to be used to convert each IF signal to the same frequency. Since the low frequency components needed for this are relatively cheap, it will not have a large effect on the total price of the system.

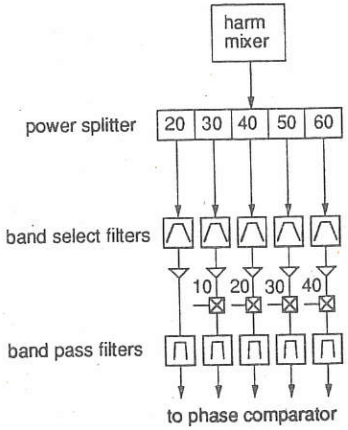

Fig. 3: The IF components of the reflectometer. To convert each channel to the same IF frequency, some extra components are needed.

Accuracy of the system

In the design of the reflectometer a minimum phase accuracy ($\Delta\phi$) of 7.2° was requested. As the phase comparator and all other IF components are designed within an accuracy of 2°, the limiting factor for the accuracy will be the signal-to-noise ratio (SNR). It can be proven that for phase measurements the minimum SNR is given by[4]:

$$\mathrm{SNR} > \frac{1}{2\pi^2}\left(\frac{360}{\Delta\phi}\right)^2.$$

For the given accuracy the minimum needed SNR is 126 (= 21 dB). The receiver noise can be calculated from the conversion loss and the noise figure, and is -82.5 dBm at the input of the mixer. A bandwitdh of 100 kHz is taken. The noise from the plasma is calculated to be ≈ -78 dBm at the input of the mixer. An average electron temperature of 1 keV is used here. This noise will be detected at every relevant harmonic, five in our case. Therefore the total noise contribution from the plasma will be -71 dBm. The total noise contribution will be the sum of the plasma noise and the receiver noise, and is -70.7 dBm. In Fig. 4, a measurement of the reflected power by the plasma is shown at a frequency of 34 GHz and a bandwidth of 200 kHz. Before the discharge starts, the losses between the two antennae, including vacuum breaks and two times one meter of fundamental waveguide, are measured to be -30 dB. During the discharge an extra loss of 7 dB is measured, so the total losses do not exceed -37 dB. In Table 1, a power balance is presented using the measurements of Fig. 4. From this table it can be concluded that the design accuracy can be met.

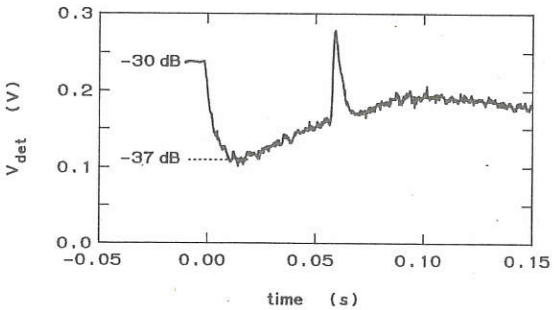

Fig. 4: Attenuation measured between the two antennae during a RTP discharge. Before the discharge the attenuation is -30 dB. During presence of the plasma the attenuation becomes maximally 7 dB larger.

noise contributions				
plasma noise	-71 dBm			
receiver noise	-82.5 dBm			
total noise		-70.7 dBm		
signal contributions				
source power per frequency component			0 dBm	
loss in plasma			-37 dB	
signal at input mixer				-37 dBm
signal-to-noise ratio				33.7 dB
maximal achievable accuracy				1.67°

Table 1: Power balance for the RTP reflectometer.

Conclusion

The advantage of the system here presented is that only a few expensive microwave components are needed, making the system relatively cheap. This makes it very attractive for groups with low budgets. The disadvantage is that the system has a low signal power and a high conversion loss, which makes it impossible to use it at large tokamaks where long waveguide runs are required.

Acknowledgement

This work was performed as part of the research programme of the association agreement of Euratom and the 'Stichting voor Fundamenteel Onderzoek der Materie' (FOM) with financial support from the 'Nederlandse Organisatie voor Wetenschappelijk Onderzoek (NWO) and Euratom.

Literature

/1/ C.A.J. Hugenholtz, Thesis Technical University Eindhoven (1990).
/2/ F.C. Schüller et al., Proc. 18th Conf. on Controlled Fusion and Plasma Phys., Berlin (1991) Vol. I, p. 121.
/3/ A.J.H. Donné et al, Rijnhuizen Report 91-207 (1991).
/4/ N. Levanon, Radar principles, John Wiley & Sons, New York (1988).

A microwave reflectometric system for tokamak ASDEX Upgrade

A. Silva, M.E. Manso, F. Serra, F. X. Söldner[1], L. Cupido, J. Pereira, J. Neves, F. Nunes, P. Varela, A. Moreira, C. Fernandes, C. Loureiro, C. Correia, J. Santos, F. Zilker[1]

[1]Max-Planck Institut für Plasmaphysik, EURATOM/IPP Association, D-8046 Garching, FRG

Centro de Fusão Nuclear, EURATOM/IST Association, 1096 Lisboa Codex, Portugal

1 - Purpose of the diagnostic

A key issue for investigation on ASDEX Upgrade with microwave reflectometry is the plasma density behavior at the edge region, aiming at contributing to the study of transport properties in the open divertor plasma configuration. A reflectometric system is beeing developed to measure density profiles and plasma fluctuations, in particular: (i) in the peripheral and scrape-off layer plasma (high and low field sides); (ii) near the magnetic X-point region; (iii) close to the ICRH antenna (to study the coupling conditions for RF waves). With the proposed reflectometric system some of the critical R & D issues for the operation of reflectometry in next step devices shall be addressed, aiming at the development of a system capable of measuring routinely density profiles with high spatial and temporal resolutions, and obtaining quantitative information about plasma density fluctuations.

Our approach is to build a robust system (with in vessel antennae), which can operate close to the tokamak by full remote control. For profile measurements it includes: microwave circuits with low level of reflections; decoupled circuits for incident and measured waves; oscillators with high phase purity signals, and fast sweep operation. In density profile evaluation sophisticated data analysis algorithms (based on previous studies performed on ASDEX), will be used. A powerful data acquisition system, with data compression facilities and high computation capability, will enable routine profile measurements.

2 - Choice of the system

The main parameters concerning the ASDEX Upgrade are: $R_0 = 1.65$ m, $a = 0.5$ m, $b = 0.8$ m, $I_p < 2$ MA, $B_t \leq 3$ T, $\bar{n}_e = 1.5 \times 10^{13}$ cm^{-3}.The frequency domains of operation are presented in Table 1. With O mode the probed densities are between $n_e \approx 0.32 \times 10^{13}$ cm^{-3} and $\approx 14.5 \times 10^{13}$ cm^{-3} corresponding to frequencies from 16 to $\approx$ 110 GHz . X mode will be used on the low field side only, as the accessibility condition on the high field side would require very high frequencies (> 120 GHz): it will enable to probe the plasma edge from densities close to zero with frequencies above 60 GHz (for $B_t \approx 3$ T). The ASDEX Upgrade reflectometry system will operate both in fixed frequency and broadband sweep, and will have the capability of performing correlation measurements. In order to minimize the influence of fluctuations during broadband operation fast frequency sweeping will be used

(< 100 μs). With O mode, spatial resolutions typically of $\approx$ 1 cm for density profiles are expected for the edge, and $\approx$ 1.5 cm for the bulk plasma (parabolic profile, $n_e(0) = 5\times10^{14}\,cm^{-3}$). In the case of X mode, for the same plasma parameters and for $B_t = 2$ T, the expected values are 0.5 cm at the edge and .1 cm at the bulk. The WKB approximation will be valid in most of the cases for the gradient and edge regions.

3 - Experimental setup

3.1 - Configuration

The typical configuration of a reflectometric channel can be seen in **Fig. 1**, where the schematic for the V-band reflectometer is shown. For profile evaluation the detection will be homodyne; for fixed frequency operation both an homodyne and an heterodyne detection will be used . For the heterodyne detection the IF will be at 1.5 GHz. The use of a PLL is foreseen and a coherent phase detector will eliminate the phase ambiguities. The system is provided with independent paths for the incident and for measured signals; such arrangement will eliminate phase errors by reflections produced in the microwave circuits, mechanical vibrations, and thermal effects .

3.2 - Microwave sources

A critical item of any reflectometric system are the microwave sources, which should provide signals with high phase purity. Our approach was to select Hyperabrupt Varactor-Tuned oscillators (HTO); these are solid state devices whose behavior is not affected by magnetic fields. They can, therefore, be placed close to the tokamak (< 5m), avoiding the use of oversized waveguides, which could lead to phase mixing due to higher mode conversion.

The HTO are only available up to 18 GHz, and to cover the required frequency bands it is necessary to use frequency multiplication. Active multipliers were chosen with output power for K and Ka bands, of the order of 15 dBm, while for the higher frequency bands is $\geq$ 5 dBm. Improved drivers were developed to allow full band sweeping in 10 μs.

3.3 - Antennae

Focused hog-horn antennae shall be used in the reflectometers probing the low and high field sides of the plasma (**Fig. 2**). The hog-horns have been optimized taking into account the results of a numerical study of its radiation characteristics in the Fresnel region. The two antennae placed inside the ICHR antennae are pyramidal horns specially designed to fit to the reduced space available. Ray-tracing studies were performed aiming to determine the focusing range and the localization of the antennae both single null and double null experiments. Numerical results indicate that the antennae: (i) should be focused beyond the probed layers, otherwise refraction occur previous to the plasma cutoff causing unwanted

divergence of the incident waves; (ii) should face the plasma at the mid-plane in both plasma geometries.

3.4 - System testing

The two K band channels were tested after installation in the tokamak. The main results are: (i) no significant resonances due to the microwave circuits are observed; (ii) the total losses are less than 2.7 dB (vacuum window $\leq$ 0.3 dB; directional coupler 0.4 dB with a isolation > 40 dB; waveguides $\approx$ 2 dB); (iii) Clear fringes can be observed when a metallic mirror is placed in front of the antenna, for different distances (see **Fig. 3**); the value of the distance can be recovered with an error of $\pm$1.5 cm.

3.5 - The control and data acquisition system

The reflectometric system shall be operated by remote control. Optical fibre links will ensure the transmission of the selected probing signals to the plasma, and of the measured signals to the data acquisition system. Considering a number of 400 fringes per sweep (maximum value foreseen for the W band) and 20 samples per fringe (error $<$ 5%), and considering a sweep time of 100 μs, the beat frequency can reach 4 MHz and a sample rate of $\approx$ 80 MHz is needed; for a minimum sweep time of 10 μs, the sample rate must therefore reach 800 MHz. The system being implemented is based on: (i) commercially available CAMAC modules (100 MHz) for the lower bands (K and Ka); (ii) the development of dedicated acquisition boards with 200 MHz and 800 MHz sampling rates, where transputers are used to allow a very fast data evaluation. These boards will be used for exploitation of the reflectometry system beyond 1992.

4. Data analysis techniques

Magnetic modes cause periodic perturbations of the density profiles; this effect can be minimized by decreasing the probing time (τ) as can be seen in the numerically simulated profiles of Figs 4(a) (τ =100 μs) and 4(b) (τ =10 μs). Broadband turbulence produces wave scattering of the incident power and phase mixing of the probing signals; this effect cannot be overcome with fast sweep operation. In profile evaluation several filtering techniques (developed for the analysis of the ASDEX data /1/), shall be implemented for routine evaluation of profiles: (i) digital bandpass filtering; (ii) filtering of the measured phase shift characteristic; (iii) nonlinear filtering, with the possibility of including a-priori phase information. Each technique has its range of applicability, that is determined by the shape of the phase shift characteristic, and by the level of the plasma fluctuations.

/1/ M.E. Manso et al, IAEA Technical Committee Meating on Microwave Reflectometry for Fusion Plasmas, JET (Culham) 1992.

Figure captions:

Fig. 1 Typical circuit configuration.

Fig. 2 Placement of the antennae inside the tokamak vessel.

Fig. 3 Fringes resulting form a full band sweep, with a mirror placed at a distance of 36 cm.

Fig. 4 Simulated density profile, showing the importance of fast sweeps to minimize the effects of density perturbations on the profile evaluation. For a perturbation with frequency of 20 KHz: (a) a 100 μs sweep; (b) a 10 μs sweep.

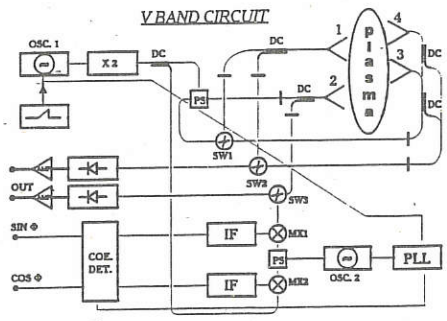

Fig. 1

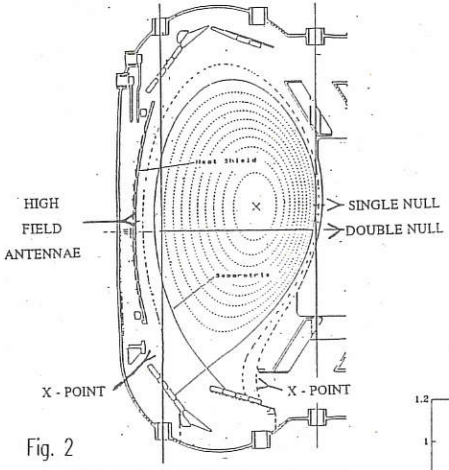

Fig. 2

Band [GHz]	Low field	High field
K (16 - 25)	O	O
Ka (25 - 36)	O	O
Q (32 - 50)	O	O
V (50 - 72)	O / X	O
W (72 - 108)	O / X	O

Table 1

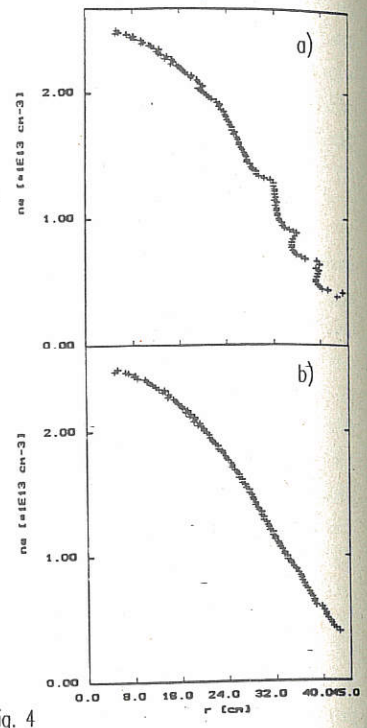

Fig. 4

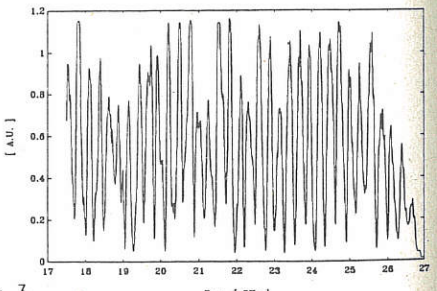

Fig. 3

SIMULATION OF CORRELATION REFLECTOMETRY

Poul Michelsen
Associtaion EURATOM-Risø National Laboratory, Risø, P.O.Box 49
DK-4000, Roskilde, Denmark
and
Hans Pécseli
Institute of Physics, The University of Oslo, P.O.Boks 1048 Blindern
N-0316 Oslo 3, Norway

Recently the principles of a new technique for diagnosing microturbulence called correlation reflectometry was presented /1/. Two microwave beams with a small difference in frequency are launched against a density profile. By measuring the phases of the reflected signals, which are functions of cut-off layer positions, it is possible by crosscorrelation technique to get information of the relative motion of plasma perturbations between two different positions.

We carry out a performance study of a model of a correlation reflectometer. A level of random plasma density fluctuations is modelled in plane geometry by superimposing moving density pulses on a given density profile. By the proper choice of the shapes of these pulses, we are in principle able to model any spectrum for disturbances propagating in the direction along the density gradient. With the speed of propagation known in the numerical experiment, we are able to determine the accuracy of the predictions of the characteristic velocity deduced from the crosscorrelation of the fluctuating phase signals of the reflectometer. Studies are carried out for statistically distributed disturbance velocities. The analysis uses a fullwave solution and results are compared with WKB-solutions /2/.

The full wave solution

We consider electromagnetic waves propagating in the x-direction in a plasma with an inhomogeneous density $n(x)$ in a constant magnetic field $B_o\hat{z}$. The wave equation can be written as:

$$\frac{d^2E}{d\xi^2} = -\varepsilon(\xi)E, \tag{1}$$

where $\xi = xk_0$ with k_0 the wavenumber in free space. We have for the O-mode that $E = E_z$ and $\varepsilon = \varepsilon_{zz}$ and for the X-mode that $E = E_y$ and $\varepsilon = \varepsilon_{xx} + \varepsilon_{xy}^2/\varepsilon_{xx}$. To solve the wave equation as a boundary value problem we assume that the range in which we seek a solution is surrounded by a medium with a constant dielectric function.

The full wave equation was solved by use of the numerical code COLSYS /3/. This code can solve boundary-value problems for mixed-order systems of ordinary differential equations. The solution method is based on spline collocation, and the code automatically finds an appropriate distribution of mesh points in order to keep the local error within certain limits specified by the user. A more general system of equations taking into account oblique propagation with respect to the magnetic field was also solved by COLSYS /4/.

A few examples of numerical solutions are shown in Fig. 1 and 2. In Fig. 1a the wave solution for an ordinary wave propagating against a steep density gradient is shown. The density is zero at the left boundary and it is equal to twice the critical density at the right boundary. In Fig. 1b corresponding curves for a wave in a density distribution with a smooth gradient are shown. A WKB solution gives in this case nearly the same solution. In order to see how a small narrow pulse will influence on the reflected wave we consider a model with a pulse moving along a smooth density gradient. In Fig. 2a the phase of the reflected wave at the left boundary is shown as a function of time, calculated by COLSYS (solid line) and by a standard WKB approximation. The pulse half-width is $5\lambda_0$ ($\lambda_0 = 2\pi/k_0$) and the amplitude

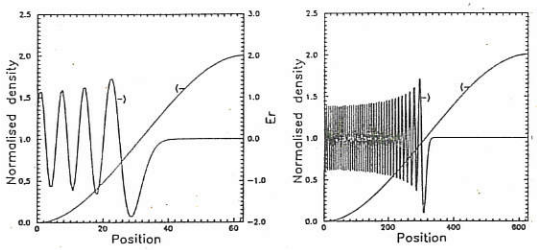

Figure 1. Wave solution for an ordinary wave reflected at the cut-off position and the density profile. a) a plasma with a steep density gradient, b) a plasma with a smooth density gradient.

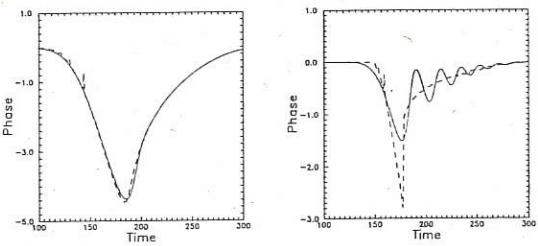

Figure 2. Phase of reflected wave versus time when a pulse moves along the density gradient. Solid line is full wave solution, dashed line is WKB solution. a) The half-width of the pulse is five wavelength, b) The half-width of the pulse is one wavelength.

is equal to 0.2 times the critical density. Similar curves are shown in Fig. 2b with a pulse half-width equal to λ_0. It is seen that large differences in the reflected wave phase appear when a narrow density pulse moves in a standing wave.

Reflectometry modelling

The fluctuations in plasma density are described as a linear superposition of pulses having constant shapes and propagating with constant velocity. The pulses may have M different shapes labelled by the index ℓ. One such pulse gives rise to a phase variation $\phi_\ell(t-t_{j,\ell})$, where $t_{j,\ell}$ denote the time where the peak value of the density pulse (with label ℓ) passes through the cut-off position in the unperturbed plasma profile. The individual pulses are assumed to be integrable and to vanish for $|t| \to \infty$ but otherwise they can be chosen arbitrarily. The autocorrelation $R(\tau)$ for the fluctuating phase signal can now be obtained /2-5/. A power spectrum $S(\omega)$ for the phase fluctuations is defined as the Fourier transform of $R(\tau)$, and it is important to note that an arbitrary prescribed spectrum can be realized by the model, actually in indefinitely many ways. The Fourier transform of the power spectrum for a two-frequency reflectometer was derived in /2/:

$$S_c(\omega) = S(\omega) \int_{-\infty}^{\infty} e^{-i\omega D/u} P(u) du, \tag{2}$$

where $P(u)$ is the probability density of velocities u, and D is the distance between two cut-off layers. For the case where all density pulses have the same velocity, i.e. $P(u) = \delta(u - u_o)$ we have the particularly simple case

$$S_c(\omega) = S(\omega) e^{-i\omega D/u_o}. \tag{3}$$

showing that all frequency components undergo a phase change proportional to ω with a coefficient D/u_o which can be used to determine u_o. In the case where the pulse velocities are statistically distributed, we have to solve (2) with the actual probability density $P(u)$.

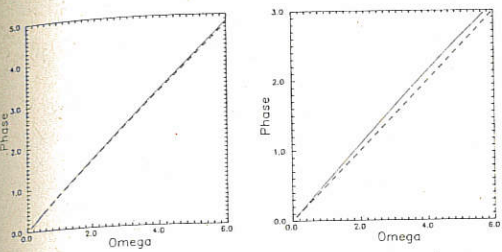

Figure 3. The function $\theta(\Omega)$ calculated for a box-like pulse velocity distribution for two values of $\alpha = a/b$. The dotted line shows the average pulse velocity. a) $\alpha =$ 0.67 and b) $\alpha = 0.33$.

We considered here a box-like distribution: $P(u) = \frac{1}{b-a}$ for $0 < a < u < b$ and 0 elsewhere The integral in (2) can then be solved analytically with the result

$$\int_a^b e^{-i\omega D/u} du = -\frac{1}{a\Omega} e^{-i(\alpha-1)\Omega} - ie^{i\Omega} E_1(a\Omega) + \frac{1}{\Omega} + ie^{i\Omega} E_1(\Omega) \qquad (4)$$

where $\alpha \equiv a/b$ and $\Omega = \omega D/a$ while $E_1(x) \equiv \int_x^\infty \frac{1}{u} e^{-iu} du$. Using (4) we can rewrite (2) in the form $F(\Omega)e^{-i\theta(\Omega)}$ with $\theta(\Omega)$ shown in Fig. for two values of α. Evidently, for $\alpha = 1$ we recover the representation (3), i.e. $\theta(\Omega) = \Omega$. For $\alpha < 1$ we find that $\theta(\Omega)$ is no longer a straight line, but has a curvature, which increases with decreasing α. Another observation is that the curve deviates from the slope corresponding to that given by the average of pulse velocities, i.e. $(a + b)/2$ in the present model for $P(u)$. This line is dotted on Fig. 3. In another model we assumed a Gaussian distribution for $P(u)$, in which case the integrals have to be evaluated numerically. However, solutions were similar to the box-case.

We may conclude that the slope of the phase function $\theta(\Omega)$ gives a quite acceptable approximation to the average pulse velocity for narrow pulse velocity distributions $P(u)$ in (2). This approximation deteriorates for increasing scatter of pulse velocities, and eventually the results can depend critically on the actual choice of $P(u)$.

Finally, we model plasma waves also by pulses of random positive or negative amplitudes, random widths, and moving with a given average velocity. The pulses each have a constant velocity which is a sum of the average velocity plus a certain random velocity specified to some limited interval. Initially the pulses are distributed randomly in space. During a run pulses disappear when they move out of the plasma, but new pulses are injected at the other boundary at random times with a given average injection rate, specified by the average number of pulses. The phase of the reflected wave is calculated for each time step. Phase curves for two different reflection points i.e. two frequencies are produced for correlation analysis.

In a real experiment the amplitude of the reflected wave will be smaller than the injected wave due to geometrical expansion of the beam, the scattering due to plasma turbulence and to plasma damping. However, these processes should not have any effect of importance on the phase of the reflected wave. Since the phase shift depends on the variation of the plasma density between the antenna and the reflection point it is not possible to know a priori which information can be extracted from the phase measurements. By considering a small perturbation moving along x we find a large contribution when the perturbation passes the cut-off point which decreases when the perturbation moves to lower densities. This decrease is monotonic when the perturbation length is larger than λ_0, but oscillating when the perturbation is short compared to λ_0 (See Fig. 2).

In Fig. 4a the correlation function is shown in a case with wave pulses propagating in a plasma without any noise. All the pulses move with the same velocity. The corresponding

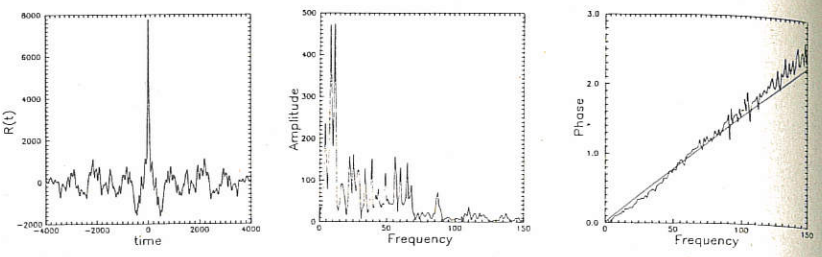

Figure 4. a) Crosscorrelation function b) crossamplitude spectrum, c) velocity of the Fourier components.

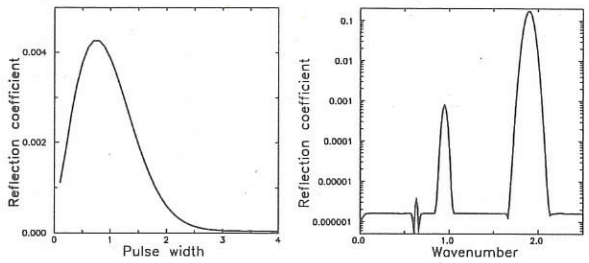

Figure 5. The reflection coefficient: a) for a single pulse, b) for a wavepacket. Pulse width and wavenumber are normalized to λ_0.

crossamplitude spectrum is shown in Fig. 4b, and in Fig. 4c the phase shift $\theta(\omega)$ of the various Fourier components is shown. The peak of the correlation function is, of course, shifted corresponding to the pulse velocity. However, the shift is of the order of 20 time steps and, therefore, not easily recognizable on Fig. 4a.

From other calculations /2/ it is evident that the estimate on $\theta(\omega)$ becomes increasingly uncertain when the velocity-spread of the structures or pulses is increased. The addition of small scale noise, has a similar effect. The estimated value of $\theta(\omega)$ becomes particularly uncertain at frequencies where the spectral amplitude is small, since the phase is here obtained as the ratio of two small quantities.

Finally we have investigated a few cases of backscattering from the turbulent plasma. When the typical wavelength of the fluctuations is comparable to λ_0, this effect may not be negligible. In Fig. 5a the reflection coefficient of a single pulse in a plasma with no cut-off (i.e. low density) is shown. The pulse amplitude is 1% of the critical density. The reflection coefficient is here quite small, but maximum when pulse width is comparable to λ_0 (the pulse width on the figure is normalized to λ_0). In Fig. 5b the reflection coefficient for a wavepacket with same amplitude as above but with a width of 50 λ_0 s shown. Reflections are seen according to the Bragg law: $2d = n/\lambda$. The three peaks are for n = 1,2 and 3. For the large peak the backscattering is seen to be $\approx$ 20%.

References

/1/ Costley, A.E. and Cripwell, P. (1989). JET–P(89) Report 82.
/2/ Michelsen, P. and Pécseli, H.L., (1991). Risø–R–592.
/3/ Ascher, U., Christiansen, J. and Russell, R.D. (1979). Math. Comp. **33**, 659.
/4/ Hansen, F.R., Lynov, J.P., Maroli, C. and Petrillo, V. (1988). J. Plasma Physics **39**, 319.
/5/ Rice, S.O. (1944). Bell System Techn. J. **23** and **24**, reprinted by N.Wax (ed.) *Selected papers on Noise and Stochastic Processes* (Dover, New York, 1954) p. 133.

Microwave Reflectometry as a Density Fluctuation Diagnostic: A Comparison Between A Controlled Laboratory Experiment and A One Dimensional Numerical Model

T.L. Rhodes, S. Baang, A.E. Chou, C.W. Domier, N.C. Luhmann, Jr., and W.A. Peebles

EE Dept. and IPFR, UCLA, Los Angeles, California 90024

Introduction. Reflectometry is currently used for the determination of density profiles and as a density fluctuation diagnostic on fusion plasma devices. Its use as a density profile diagnostic is considered to be well understood. However, a fundamental understanding of the reflectometer signal due to density fluctuations does not exist at this time. Questions include: sensitivity to fluctuation wavelength, density scale length, spatial localization, and relation of measured phase fluctuation to $\tilde{n}$. The UCLA Plasma Diagnostic Group has initiated an investigation into these basic physics questions and has reported initial results [1]. There, the reflectometer response to grid launched ion acoustic wave packets was highly localized, showing the same number of cycles and same frequency as the launched wave. In addition, a one dimensional numerical model has been developed to help elucidate the plasma-reflectometer interaction. This paper describes a comparison of laboratory results to these numerical calculations. This code is equivalent to or similar in result to codes and models used elsewhere to interpret reflectometer data. The results presented here indicate that one-dimensional and semi- two-dimensional codes do not adequately describe the physics present in the laboratory plasma-reflectometer interaction. In particular they omit 2-D effects such as refraction, diffraction, interference, and resonance absorption [2]. It is concluded that reliance on these unconfirmed models to interpret experimental data (including that from fusion plasmas) is questionable and can result in misleading conclusions.

Description of Experiment. The laboratory plasma [1] is produced in a cylindrical magnetic field free chamber 80 cm long and 60 cm in diameter (Fig. 1). Argon gas is employed, with electron and ion temperatures and densities in the range T_e=1-2 eV, T_i=0.1-0.2 eV, $n_i=n_e=1\text{-}10\times10^{11}$ cm^{-3}. A density gradient is formed with high density near the discharge filament (top of chamber), which decreases as the microwave antenna is approached (bottom of chamber). Ion acoustic waves ($\tilde{n}_{ion}/n<1\%$ and f_{ion}=15-200 kHz, $f_{ion}/f_{pi}<2\times10^{-3}$) are launched by applying a bias signal of appropriate waveform to a movable grid placed

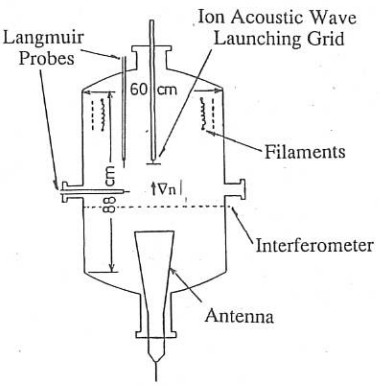

Figure 1. Experimental setup.

within the plasma. Quadrature detection of the reflected signal is used to obtain both phase and amplitude information.

Description of Numerical Model. The plasma-microwave interaction is modeled using the time independent full wave equation:

$$\frac{d^2E}{dx^2}+N^2k_o^2E=0 \qquad (1).$$

Here, $N(x)=(1-f_{pe}(x)^2/f_{rf}^2)^{1/2}$ is the plasma refractive index for the ordinary mode and contains the density profile information $n_e(x)$, $f_{pe}(x)^2=n_e(x)e^2/(4\pi^2\varepsilon_o m_e)$ is the local electron plasma frequency, $E=E(x)$ is the local value of the microwave electric field, k_o is the microwave vacuum wavenumber and f_{rf} the microwave frequency. Equation 1 represents an approximation to the laboratory plasma which neglects possibly important effects such as resonance absorption, refraction and mode conversion. An ion acoustic wave is modeled as a density perturbation superimposed upon the density profile. The code calculates the phase fluctuation that the reflectometer signal would undergo as a result of the density fluctuation.

Comparison of Model and Experiment. Figure 2 shows the code and laboratory results for ion acoustic waves with $k_{\tilde{n}}/k_o$ ranging between 0.7 and 1.4 and with $\tilde{n}/n_{crit}=0.5\%$ ($k_{\tilde{n}}$= ion acoustic wavenumber, $n_{crit}=4\pi^2f_{rf}^2\varepsilon_o m_e e^{-2}$). Both the measured and calculated responses show approximately the same frequency and number of cycles as the actual density perturbation. Note that as k_o is increased the code predicts an increase in the time delay, in agreement with the familiar Bragg law for scattering $k_{\tilde{n}}=2k_{inc}\sin(\theta/2)$ (since the wavenumber of the microwave radiation k_{inc} decreases from its vacuum value k_o, at the boundary, towards zero at the cutoff point as $k_{inc}=k_oN$, where N=local index of refraction). It was found that the dominant response predicted by code is consistent with the backscattering wavenumber matching condition $\theta=\pi \rightarrow k_{\tilde{n}}=2k_{inc}$ (although there is some indication of a smaller mirror like response at the cutoff layer). This indicates that the predicted reflectometer response is non-local since different wavenumbers interact at different positions within the plasma. A wavepacket containing many wavenumbers would appear spread out in time while in reality it is quite localized within the plasma.

From Fig. 2b one sees that there is no observable change in the experimental time delays as $k_{\tilde{n}}/k_o$ is varied. Measurements show that the reflectometer detects the ion acoustic wave near the cut-off position (i.e., $n_e=n_{e,crit}$) for a given microwave frequency f_{rf}. The lack of variation in the delay time was found to hold as the perturbation wavenumber was varied over the range $k_{\tilde{n}}/k_o=0.5\rightarrow5.0$ - a factor of 10. Thus, the experimental time delay or location of the signal does not vary substantially with the wavenumber of the density perturbation. A pulse with a wide wavenumber range would then be observed as very localized within the plasma, so that experimentally, the reflectometer signal is much more localized than predicted by the code. This is a clear, quantitative departure of experiment from the model and may indicate why

correlation reflectometers measure lengths much shorter than these models predict.

Experimentally, both amplitude ($\tilde{A}$) and phase ($\tilde{\phi}$) fluctuations are observed, both of which vary linearly with ñ: $\tilde{\phi}_{exp} \sim$ ñ and $\tilde{A}_{exp} \sim$ ñ. The code predicts that $\tilde{\phi}$ varies linearly with the density fluctuation level ñ: $\tilde{\phi}_{model} \sim$ ñ with, since the code is lossless, $\tilde{A}_{model} = 0$. The magnitude of the experimentally measured phase fluctuation is a factor of 20 or more greater than predicted by the model.

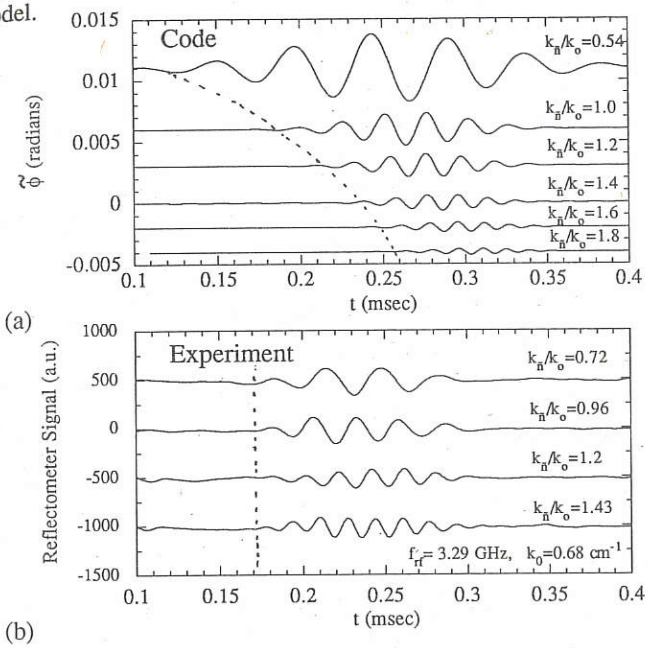

Figure 2. Time history of reflectometer response from (a) numerical model and (b) experiment for different values of ion acoustic wavenumber.

Physically, $\tilde{A}$ can be related to losses in the returned signal due to refraction, diffraction, interference, resonance absorption, etc. and is perhaps the first indication of the reason behind the observed differences between model and experiment. It should be noted that the scattered response should be present in the experiment. However, due to the magnitude of the experimentally measured values it is quite possible that it (the scattered component) is in the experimental noise level. It is planned to improve the signal-to-noise ratio and look for the wavematched signal.

The reflectometer response to perturbation wavenumber was investigated by varying $k_{ñ}$ while the density profile, microwave frequency, ñ, etc. were held constant (Fig. 3). Experimentally, it was observed that the response decreased

with increasing $k_{\tilde{n}}$, qualitatively similar to the code predictions. However, quantitatively, the reflectometer response decreases more rapidly than the model predicts for $k_{\tilde{n}}/k_o<1$, and then much less rapidly for $k_{\tilde{n}}/k_o>1$ (Fig. 3). The response extends to $k_{\tilde{n}}/k_o\approx5$, well beyond that predicted by the code.

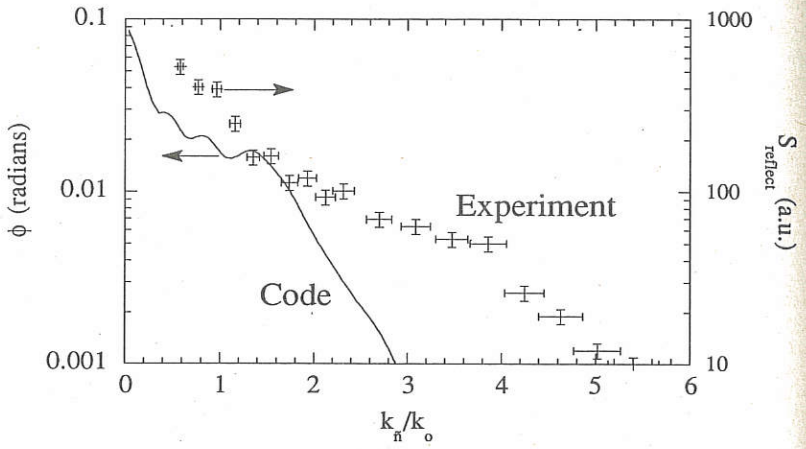

Figure 3. Calculated and measured reflectometer sensitivity to fluctuation wavenumber $k_{\tilde{n}}$.

Conclusions. From the results presented above it is clear that the numerical model does not predict the experimental measurements, so that reliance on such models could lead to erroneous results. The model predicts a one dimensional lossless reflectometer/plasma interaction. However, observations indicate the presence of some type of physical effect (2D, resonance absorption, interference, refraction) not contained in current models that is needed in order to successfully model reflectometry. A future publication will discuss these effects more fully. Future work is directed towards a fundamental understanding of reflectometry as a fluctuation diagnostic to allow the full potential of this diagnostic to be realized.

Acknowledgments. Helpful discussions with E.J. Doyle, C.L. Rettig and E. Williams are gratefully acknowledged. This work was supported by U.S. DOE Contract No. DE-FG03-86-ER53225.

[1] S. Baang, C.W. Domier, N.C. Luhmann, Jr., W.A. Peebles, and T.L. Rhodes, Rev. Sci. Instru. **61**, 3013 (1990)
[2] R.B. White and F.F. Chen, Plasma Physics,**16** 565 (1974)

AMPLITUDE MODULATION REFLECTOMETRY FOR LARGE FUSION DEVICES

J. Sánchez, V. Zhuravlev, E. de la Luna, T. Estrada, B. Brañas

ASOCIACION EURATOM/CIEMAT 28040 Madrid, Spain.

Abstract

One of the main problems which has been present in most reflectometers during the last years is the need for a coherent tracking of the phase delay: fast density fluctuations and strong modulation on the amplitude of the reflected signal usually produce 'fringe jumps' in the phase signal. In such a situation the 'history' of the phase evolution is lost and big errors can arise in the determination of the density profile. This problem will become more severe in large fusion devices, operating at high densities with high magnetic field: the cutoff wavelength becomes shorter and the phase delays involved become larger as well as the effect of the broadband fluctuations.

Amplitude modulation reflectometry (1) performs a time delay measurement by the determination of the phase delay of the modulating envelope of a millimeter wave beam reflected at the plasma. The phase delays involved are in the range $<2\pi$ and the measurement is not negatively affected by the broadband fluctuations. The phase readout can be directly obtained without complicated fringe counters: the method provides a promising possibility for real time determination of the plasma position and density profile, which will be very important for the next step devices (ITER-NET).

Introduction

The relevant information used in reflectometry for density profile determination is the differential phase shift $\delta\phi/\delta\omega$ of the beam for the different reflecting frequencies (ω). This information is usually obtained by sweeping the frequency of the launched beam, either in narrow or broad band. Due to the short vacuum wavelengths needed, most of the swept reflectometers have to deal with multiradian phase changes, induced during the sweep or by the broadband density fluctuations present in the plasma, which lead to a number of problems: the main one is the need for a continuous tracking of the phase 'history' during the sweep, to keep memory of the number of fringes. Any temporary loss of information, normally caused by fast transients or strong decreasing in the amplitude of the reflected beam, will make impossible further tracking of the phase value. In addition, spurious phase contributions can be introduced by 'phase runaway' effects during the sweep, caused by geometrical effects of the reflection on rotating structures. Finally, complicated filtering and huge data recording are needed to produce the final set of $\delta\phi/\delta\omega$ data.

A. M. reflectometry

Amplitude modulated reflectometry is to some extension an intermediate solution between the classical phase delay reflectometry, so far applied to small distances, and the time domain reflectometry, used for ionospheric studies and recently also proposed for fusion plasmas (1). Proof of principle experiments with AM reflectometer have been performed in the T-10 tokamak (2).

The differential phase shift $\delta\phi/\delta\omega$ of the reflected signal can be easily evaluated from the phase delay $\Delta\phi$ of the modulation signal. After some straightforward calculations:

$$\tau=\delta\phi/\delta\omega=\Delta\phi/\Omega$$

where Ω is the frequency of the amplitude modulation.

With a typical Ω=50 MHz the vacuum wavelength of the modulation signal is 6 m, thus moderate phase shifts ($<2\pi$) for the usual dimensions and density gradients in plasma devices (even JET-ITER) are expected. In Fig 1 the behavior of the time delay (τ=phase/Ω) for a typical exponential density profile (similar to those expected for the JET divertor plasma) is

shown. The phase delays involved are moderate (<0.8 rad). For frequencies higher than the highest cutoff frequency (63.5 GHz, $n_o=5x10^{19}m^{-3}$, O-mode) interferometer like operation is assumed.

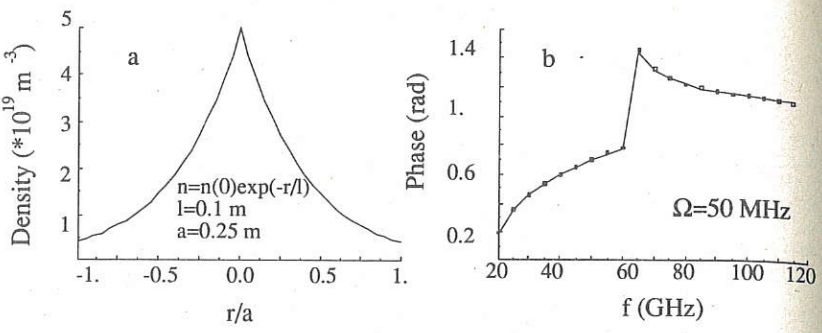

Figure 1: Typical exponential-like density profile for the JET divertor (a) and corresponding phase delay for a modulation frequency=50 MHz (b).

Experimental system

An AM reflectometer generic diagram is shown in Fig 2. The mm wave signal (O1) is modulated at frequency Ω (O2), PIN diodes can be used as modulators. The detector diodes (D1, D2) provide the modulating envelopes which are downconverted to a lower IF (1-5 MHz), amplified and phase compared at the phase meter. Heterodyne front end can be included for higher sensitivity (it will be required for large devices like JET).

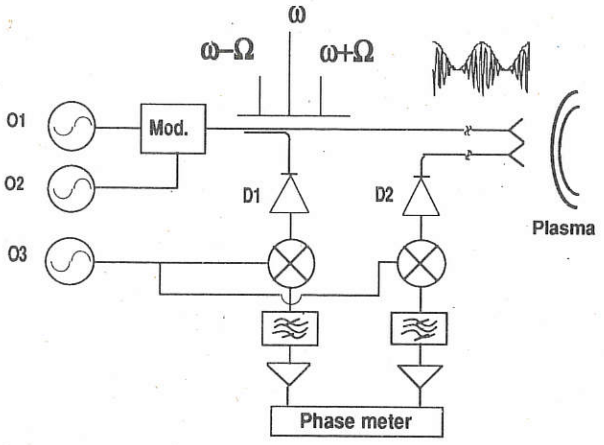

Figure 2: AM reflectometer generic diagram.

Advantages and limitations

There are some perturbations which could affect the AM measurements: density fluctuations, pulse deformation and parasitic reflections.

The density fluctuations affect the reflected beam through phase and amplitude oscillations. The phase oscillations are negligible due to the fact that the AM signal is only sensitive to differential effects. The amplitude oscillations do not affect the time delay measurements provided that their frequencies (typically 50-100 kHz) are much lower than Ω.

The main causes for pulse deformation are: higher order derivatives of the phase delay versus frequency (only the second one since the AM wave is formed by three spectral components) and spectrum deformation by dispersive effects on waveguides and plasma.

The finite second derivative appears when the phase shift between the carrier and each of the two sidebands is different and its effect is a decrease in the amplitude of the first harmonic of the modulation signal after the detector:

$$V_{out} = c1 + c2\cos\alpha\sin\Omega(t+\tau) - c3\cos 2\Omega(t+\tau)$$

with $\alpha=\Omega^2\delta^2\phi/\delta\omega^2$. Typically $\alpha<0.002$ rad for $\Omega<100$ MHz, thus the final effect is negligible.

Spectrum deformation by dispersion in the plasma and waveguides, which can affect pulse reflectometry, does not affect AM reflectometry due to the simplicity of the spectrum and the separation of the different harmonics. If the amplitudes of the carrier and both sidebands frequencies after the reflection are a, b and c, the output voltage is:

$$V_{out} = a^2 + \frac{b^2+c^2}{2} + a(b+c)\sin\Omega(t+\tau) - \frac{bc}{2}\cos 2\Omega(t+\tau)$$

The time delay of the first harmonic is not affected. The signal even survives if one of the sidebands is completely suppressed, thus higher order harmonics can be easily suppressed for recovering the time delay.

Parasitic reflections are one of the main problems for AM reflectometry: the error in the determination of the phase delay is of the order of B/A rad, for A>>B, being A and B the amplitudes of the main and parasitic signals respectively. Ideally, n parasitic references can be distinguished if we operate with n+1 harmonics of the fundamental modulation frequency, but in the experiment the situation becomes extremely complicated and parasitic references must be avoided by using separated waveguides and antennas for the launched and reflected beams.

Accuracy requirements: due to the small phase delays involved, high accuracy is required in the phase determination. This implies linear phase detectors and a good signal to noise ratio. For Ω=100 MHz, a vacuum spatial resolution of 5mm implies 1.2 degree phase accuracy, which is easily achievable with a s/n≈17dB in amplitude in front of the phase meter. For specific applications requiring higher accuracy, simultaneous operation with higher modulation frequencies can be used.

Fast monitoring of density profile

One of the simplest approaches for a simplified description of the density profile, is to use two reflectometers reflecting at symmetric positions (up and down) along the vertical axis of elongated plasmas. The difference τ_{up}-τ_{down} of the time delay signals (directly obtained as the outputs of the phase meters), can be used as a fast monitoring of the vertical shift of the density profile. Fig 3 shows the simulated time evolution of the real and measured shift of the density profile center of gravity, which oscillates while the density grows. A parabolic-like profile was used:

$$n = n_0\left[1-\left(\frac{r}{a}\right)^{\alpha}\right]^{\beta}(1+cy)$$

where α and β vary between 3 and 2 and 1.5 and 3 respectively (from t=100 to 200), and c oscillates from -1 to 1,the variation of n_0 is shown in the figure. The cutoff density is $10^{19}m^{-3}$ for both channels

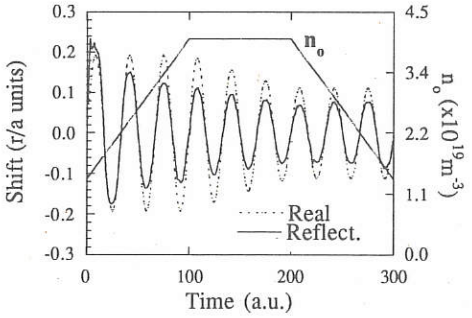

Figure 3: Simulation of density profile shift during parameter variation.

If the profile parameters α and β change, the sensitivity might change but keeping the sign of the shift and its first derivative. If the profile deformation becomes large, additional reflecting densities are needed and simple combination of the individual times delays can be used as direct monitor of the density shift.

Summary

Amplitude modulation offers the possibility of a direct readout of the differential phase delay, which is the relevant parameter for density profile studies in reflectometry. The typical filtering and fringe counting procedures are not necessary and the associated errors (fringe losses) are avoided. On the other hand pulse deformation and density fluctuations do not affect the measurement. This makes the AM reflectometry a very attractive alternative, not only for standard density profile measurements but also for fast monitoring of density profile and plasma position in large fusion devices.

References

(1) C. A. J. Hugenholtz and S. H. Heijnen. Rev. Sci. Instrum. 62 (4), 1100 (1991)
(2) V. A. Vershkov, V. A. Zhuravlev, Sov. Phys. Tech. Phys. 32 (5), 523 (1987)

Fluctuations Spectra in TORE SUPRA from Scattering Experiment

F. Gervais, D. Grésillon, P. Hennequin, A. Quéméneur, A. Truc.
PMI, Ecole Polytechnique, F-91128 Palaiseau (France)

P. Devynck, X. Garbet, J. Payan, C. Laviron, S. K. Saha.
Association Euratom-CEA, CE Cadarache, F-13108 Saint-Paul-lez-Durance (France).

Introduction

In order to measure the density fluctuations in the Tore Supra tokamak, a collective scattering CO_2 laser experiment has been installed [1]. Taking into account the pitch angle variation of the magnetic field lines in the tokamak and the perpendicularity of the fluctuation wave vectors to these field lines, some spatial resolution is obtained along the observed vertical chord. By rotating the observation wave vector $\vec{k}_s$, imposed by the geometry of the apparatus, in a horizontal plane around the measurement chord, it is possible to detect the turbulence coming mostly from the region where $\vec{k}_s$ is locally aligned with $\vec{k}$. Thus an observation zone (the top, the center or the bottom of the plasma) can be selected along the vertical chord. The power scattered signal is given by

$$S(\vec{k}_s, \alpha) = \int dy\, \delta n^2(\vec{k}_s, y) e^{-[(\alpha - \xi(y))/\delta\alpha_k]^2} \qquad (1)$$

where α is the angle between $\vec{k}_s$ and the poloidal plane, $\delta n(\vec{k}_s, y)$ is the local RMS value of the fluctuation density for the ordinate y along a vertical chord normalised by a (the plasma radius), $\delta\alpha_k = \Delta k/k_s$ is the angular apparatus resolution, with $\Delta k = 2/w$ (w is the beam waist), and $\xi(y) = B_p/B_T$ is the pitch angle of the magnetic field lines along y.

Using the foregoing, k and w spectra can be recorded for various plasma conditions.

Wave Number Spectra

To obtain the $k_\perp$ spectra of turbulence for the range of k_s values between 3 and 15 cm^{-1}, several identical ohmic shots (Ro = 2.38 m, a = 0.78 m, Ip = 1.2 MA, B_T = 3 T, $< n_e >= 2\ 10^{-19}$ m^{-3}, $q(a)$ = 3.2, He) have been realized. For all of them the fluctuations have been recorded simultaneously, along a central chord, for two different and independant wave vectors, corresponding to the center ($\alpha = 0°$) and the top ($\alpha = 5°$) of the plasma. The RMS value has been calculated and the raw results are plotted on a semi log scale versus k_s on Fig.1a. For the k_s range covered, the $k_\perp$ spectrum is found to be monotonic and therefore its maximum is located below $k_s = 3$ cm^{-1}. Both curves show a decrease of the power level with k_s and a change of the slope at $k_s = 6$ cm^{-1}. The difference between the two curves is attributed to the spatial resolution of the measurement. As k_s increases, the scattering volume observed by the diagnostic diminishes due to improvement in the spatial resolution. To correct the curves from this effect, expression (1) is calculated with an analytical form for δn, deduced from an

inversion method using scattering measurements in Tore Supra [2]; $[\delta n/n(y)]^2 = b+c|y|^p$ with $b/c = 0.004$ and $p = 7$, $n(y)$ being the local density obtained from the density profile $n/n_o = 0.1 + 0.9[1 + (r/a)^2]^{1/2}$. The form of the $k_\perp$ spectrum is assumed to be identical at each y location.

After correction (Fig.1b), both curves show the same decrease of the power level with k_s. The two curves can be taken to be identical, with a slope becoming -3.2 ± 0.2. This result is in general agreement with those found for others tokamaks [3].

Determinations of the $k_\perp$ spectrum are also performed for an internal chord ($r/a = -0.5$) and an observation angle corresponding to the bottom part of the plasma. After correction, the obtained curve (Fig. 2) is similar to the previous ones with a slope of -3.3 ± 0.3. The comparison of these results shows that the turbulence has always a wave vector aligned with the observation wave vector $\vec{k}_s$. For a central chord, $\vec{k}_s$ is in the poloidal direction and for a non central chord, $\vec{k}_s$ is a linear combination of k_r and k_θ. It seems that the $k_\perp$ spectrum is independant of the wave vector direction, which is consistent with an isotropic turbulence.

Frequency Spectra

When the diagnostic is configured to analyse the turbulence coming from the edge of the plasma (top or bottom), the measured frequency spectra often present a particular feature with two humps (Fig. 3 a, b, c). They are frequency shifted by different amounts on the positive and negative sides. The heterodyne detection allows to determine propagation direction of the density fluctuations. Looking at the lower edge of the plasma, it is possible to associate respectively the positive and negative frequency shifts to the ion and electron diamagnetic directions. It turns out that waves propagating in the ion diamagnetic direction in the laboratory frame exist at all densities. The frequency divergence between the two humps increases and the spectra grow hollow in the central part as the average density value decreases.

This shape of the spectra cannot be explained by a lack of localization. Although the possibility of ionic turbulence existing at all densities cannot be completely discarded, it is unlikely in Tore Supra ohmic discharges [4]. We propose an alternative explanation based on the existence of an inversion point of the radial electric field E_r near the plasma edge.

Indeed, if ω_0 is the electron diamagnetic frequency (electronic turbulence), in the laboratory frame the Doppler shifted drift wave frequency ω_{lab} is given by

$$\omega_{lab} = \omega_0 - k_\theta E_r / B_T$$

If E_r exhibits a change of sign at $r/a = \rho_s$, then ω_{lab} can take positive and negative values explaining the two humps observed on the spectra. We have developped a model that allows us to get the radial location of this inversion point. In expression (1), the density fluctuations at frequency ω is written as

$$[\delta n_\omega / n(y)]^2 = (b + c|y|^p) e^{-[(\omega - \omega_{lab}(y))/\Delta\omega]^2}$$

and a fitting procedure is applied to determine $\omega_{lab}(y)$ from the experimental ω spectra. When the diagnostic is set to analyse the top or the bottom part of the plasma, the

frequency spectrum can be fitted by two gaussian functions (Fig. 4) where $\omega_{lab} = 2\pi f_{max+}$ for $\omega > 0$, and $\omega_{lab} = 2\pi f_{max-}$ for $\omega < 0$. A good agreement between calculated and experimental spectra requires a very sharp signe change of E_r at $\rho_s = 0.90 \pm 0.03$ for all the considered densities.

Conclusion

The $k_\perp$ spectra decrease as k^{-3}, for $k > 6$ cm^{-1}, no maximum is found in the k range explored and it seems that the turbulence does not present a strong anisotropy. It is suspected that the two humps of the ω spectra are due to a Doppler shift linked to the inversion point of the radial electric field near the edge of the plasma, in the hypothesis of a pure electronic turbulence.

[1] A. Truc, A. Quéméneur, P. Hennequin, D. Grésillon, F. Gervais, C. Laviron, J. Olivain, S.K. Saha and P. Devynck, in *Review of Scientific Instruments*, **63**, (1992).
[2] P. Devynck, X. Garbet, C. Laviron, J. Payan, S. K. Saha, F. Gervais, P. Hennequin, A. Quéméneur, A. Truc, rapport EUR-CEA-FC 1453.
[3] P.C. Liewer, in *Nuclear Fusion*, **25**, 543 (1985).
[4] X. Garbet *et al.*, at this conference.

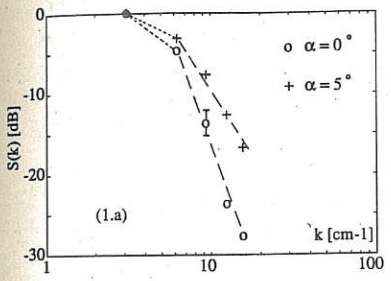

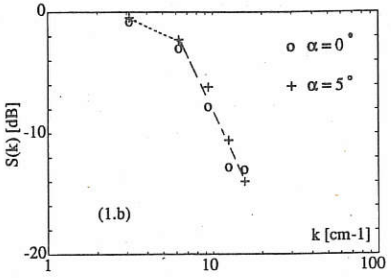

Fig. 1: Wave number spectra for a central chord a) without correction b) with correction for volume effect.

Fig. 2: Wave number spectra for an internal chord ($r/a = -0.5$) with correction for volume effect.

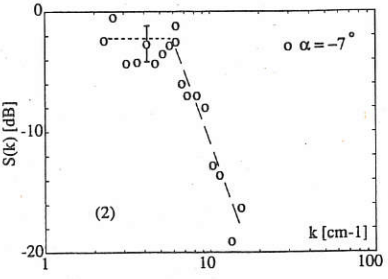

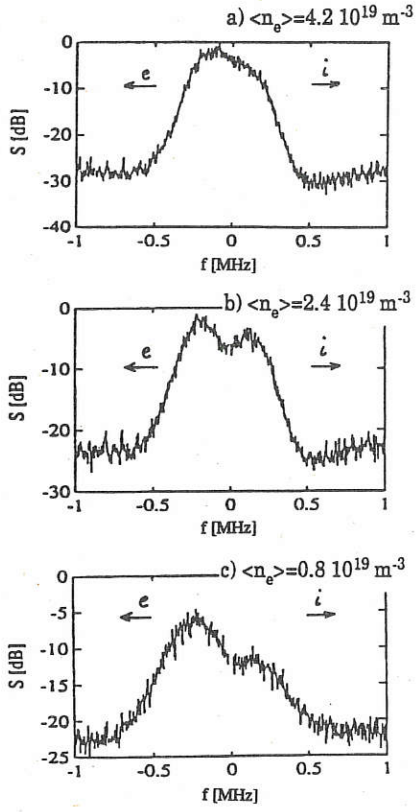

Fig. 3: Frequency spectra for a central chord ($k = 6$ cm^{-1}, $\alpha = -5°$) and $I_p = 1.65$ MA, $B_T = 4$ T, $q(a) = 3.3$.

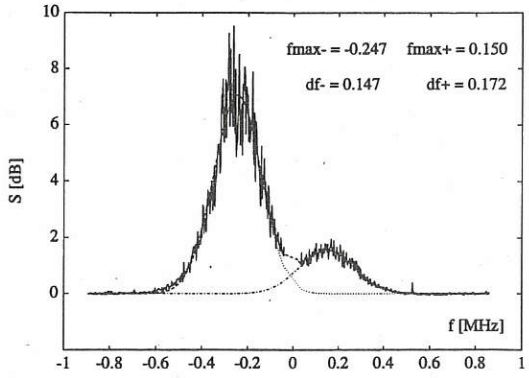

Fig. 4- Best fit of an experimental spectrum by two gaussian functions.

FROM INCOHERENT TO COLLECTIVE SCATTERING

N. Maafa, D. Grésillon, and B. Cabrit

Laboratoire de Physique des Milieux Ionisés
(Unité Propre de Recherche du C.N.R.S. N° 0287)
Ecole Polytechnique,
F - 91 128 Palaiseau (France)

Electromagnetic wave scattering is a classical diagnostic of space as well as of fusion plasmas. Two different classes of scattering mechanisms are manifested by different spectra, and receive different theoretical interpretations: Namely, the "incoherent scattering", that results from the statistical addition of independantly scattered fields from each plasma particles, and the "collective scattering", as obtained when the dielectric plasma susceptibility is macroscopicaly non-uniform.

There exist however conditions for which neither of these two models are fully appropriate, when simultaneously particle motion and macroscopic dielectric susceptiblity fluctuations must be taken into account. This could be the case of scattering experiments on magnetized, collisionless, randomly agitated, non-uniform plasmas, in conditions occuring sometimes in the magnetosphere, or in tokamaks. These conditions are met when the particle motion $\mathbf{r}(t)$, and the macroscopic motion $\mathbf{R}(t)$ result in two Doppler frequency shifts of similar order of magnitude. Specificaly, if T is a macroscopic time scale, and $\mathbf{k}$ the scattering wavevector, both motions contribute to shape the scattering spectrum when

$$\mathbf{k} \cdot \mathbf{r}(T) \approx \mathbf{k} \cdot \mathbf{R}(T)$$

In the present study, we investigate these conditions and calculate the collective scattering spectrum resulting from the motions of both a macroscopicaly non-uniform, externally agitated plasma, and of its individual particles. This effect will be illustrated by a numerical result.

1. Scattering from an elementary plasma test particle.

Any point-like electric charge in a plasma, is surrounded by a neutralyzing charged particles cloud, made of ions and electrons. In the presence of an external high frequency electromagnetic wave, the electron part of the cloud oscillates at the incident wave frequency radiating a new e.m. wave, the scattered wave. Since, in the case of long wavelength ($k\lambda_D \ll 1$, where λ_D is the Debye lentgh), plasma scattered light results prominently from dressed ions, we retain only the ion dressing electron clouds response. The elementary field radiated at an observer's position $\mathbf{r}'$ and time t, is :

$$\bar{E}_j(\bar{r}', t) = \frac{r_T}{r'} \exp\left[i (k_i \hat{n} \cdot \bar{r}' - \omega_i t) \right] \hat{n} \times (\hat{n} \times \bar{E}_{i\,\omega}) \times N_j(\bar{k}, t) \qquad (1)$$

where : k_i , ω_i , $E_{i\omega}$ are the wavenumber, angular frequency, and complex amplitude of the incident electromagnetic wave, $\mathbf{n}$ the observation direction, r_T is the Thomson radius and $N_j(\mathbf{k},t)$, is the space Fourier transform of the electron density in the Debye cloud surrounding the test ion particle, that is

$$N_j(\bar{k},t) = Z \int \frac{d\omega_1}{2\pi} dt_1 \frac{\chi_e(\bar{k},\omega_1)}{\varepsilon(\bar{k},\omega_1)} \exp\left[i\left(\omega_1 (t_1 - t) - \bar{k} \cdot \bar{r}_j(t_1) \right) \right] \tag{2}$$

where χ_e and ε are the magnetized electron fluid polarisability and dielectric constant, respectively, and r_j (t) is the ion test particle trajectory.

2.Scattering frequency spectra out of an externally agitated, nonuniform plasma.

The plasma scattered E-field is the addition of the elementary fields, $\mathbf{E}_t = \sum_j \mathbf{E}_j$.

This observation is analyzed as its (E-field) mean time correlation function,

$$\left\langle \bar{E}_t(\bar{r}',t) \cdot \bar{E}_t^*(\bar{r}',t+\tau) \right\rangle$$

The frequency spectra will later be obtained as the correlation time Fourier transform.

To perform the statistical average, we need to make a few reasonable assumptions. We chose the followings :

-The microscopic response function (χ_e/ε) at the observation scale k is stable and, to first order, independant of the plasma density.

-The process is stationnary, any statistical average over initial positions is independant of the initial time.

-The displacement is split in two independant processes: The macroscopic fluid displacement $\mathbf{R}(t)$, made of large scale, long period motion. And the microscopic displacement $\delta(t)$, made of the magnetized charged particle trajectory in the plasma frame.

- The probability particle density distribution in phase - (velocity and position) space, can be factorized, as the product of a spatial density "at the initial position", times a microscopic velocity distribution function.

-The fluid displacement Δ during a time τ is a random variable, characterized by some probability distribution $P(\Delta/\tau)$.

-We further restrict the applicability of our model to cases where "the displacement of a fluid element initially at position $\mathbf{r}$, is statistically independant of the initial density at this position, $n(\mathbf{r})$". Although not always justified, this hypothesis holds true in many usual cases, like MHD turbulence, or when the density perturbation on the one hand, and the convection motion on the other hand, occur from two different origines of different time scales.

The result of both the average and the time Fourier transform is obtained[1] as

$$S(\omega) = Z^2 \langle |n(k)|^2 \rangle \left[\sum_{n=-\infty}^{n=+\infty} A_n(k_\perp \rho_{ci}) \int \frac{d\omega_1}{k_{//}} F_i\left(\frac{\omega_1 - \omega_\Delta - n\omega_{ci}}{k_{//}} \right) S_F(\omega_1) \right] \times$$

$$\times \left| \frac{\chi_e(\bar{k}, -\omega_\Delta)}{\varepsilon(\bar{k}, -\omega_\Delta)} \right|^2 \qquad \text{where } \omega_\Delta = \omega - \omega_i \tag{3}$$

where $< |n(k)|^2 >$ is the "form factor" that measures the plasma density non-uniformity amplitude,

$F_i(\omega/k)$ the ion distribution,

$$A_n(k_\perp \rho_{ci}) = 2\pi \int_0^\infty dv_\perp v_\perp F_i(v_\perp) J_n^2\left(\frac{k_\perp v_\perp}{\omega_{ci}} \right) \text{, where } J_n \text{ is the Bessel function of first kind}$$

and $S_F(\omega)$ is the fluid motion spectrum,

$$S_F(\omega) = \int d\tau \exp(i\omega\tau) \langle \exp[i\bar{k} \cdot \bar{R}(\tau)] \rangle \tag{4}$$

3. An illustrative example.

As seen from Eq. 3, the plasma scattered spectrum is an elaborate transformation of fluid and particule motion characteristics. To pin down the effect of the individual (ion) motion on the resulting spectrum, we present a numerical solution in the following figure.

We chose a simple case of a guiding-center, isothermal plasma. The particle motion is restricted along the field lines. The thermal velocity is v_i, and the velocity distribution is shown in Fig.b. The k-vector of the scattering geometry is almost perpendicular to B: k_{par} / k_{perp} is equal to 10^{-2}. The random plasma motion is perpendicular to B. Its velocity distribution is shown in Fig.a. The mean velocity v_d is $v_d / v_i = .10^{-2}$, and the mean square deviation is $\Delta v_d / v_d = 0.1$. The velocity abscissa in Fig. a and b are labelled as Doppler frequencies normalized to $k_{perp} v_d$, and $k_{par} v_i$, respectively. Eq. 3 effects a convolution of these two functions (Fig.c), and multiply it by the response function (or screening factor) $(|\chi_e/\varepsilon|^2)$ shown in Fig.d. The resulting spectrum is shown in Fig.e.

Obviously this differs from the plain, plasma motion, Doppler spectrum that simple collective scattering theory would have calculated in that case. Particule motion here plays the dominant role. This might also happen in experiments.

Reference 1.D.Grésillon, B.Cabrit and N.Maafa, "Plasma Collective Scattering Spectra: From particle to fluid motion", submitted for publication.

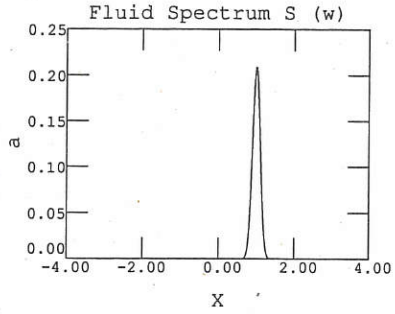
Fluid Spectrum S (w)
a
0.25
0.20
0.15
0.10
0.05
0.00
-4.00
-2.00
0.00
2.00
4.00
X

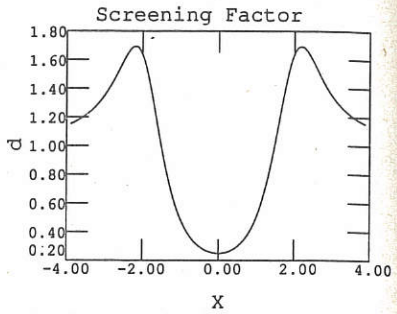
Screening Factor
d
1.80
1.60
1.40
1.20
1.00
0.80
0.60
0.40
0.20
-4.00
-2.00
0.00
2.00
4.00
X

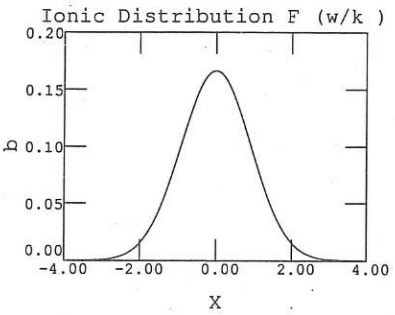
Ionic Distribution F (w/k)
b
0.20
0.15
0.10
0.05
0.00
-4.00
-2.00
0.00
2.00
4.00
X

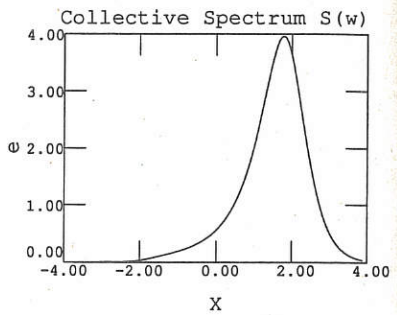
Collective Spectrum S(w)
e
4.00
3.00
2.00
1.00
0.00
-4.00
-2.00
0.00
2.00
4.00
X

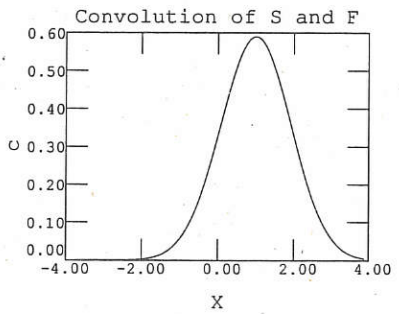
Convolution of S and F
c
0.60
0.50
0.40
0.30
0.20
0.10
0.00
-4.00
-2.00
0.00
2.00
4.00
X

$X = w/k \cdot V$

EFFECTS OF THE OHMIC PLASMA CURRENT ON COLLECTIVE SCATTERING SPECTRA

U. Tartari, S. Castiglioni, M. Lontano

Istituto di Fisica del Plasma, Associazione EURATOM/CNR/ENEA
Via Bassini, 15 - Milano (Italy)

1 - Introduction

Since the first demonstration of feasibility of a T_i measurement by collective scattering (CS) in 1988 /1/, the development of CS diagnostics aimed at the investigation of the ion distributions in tokamak plasmas has received impulse /2/ thank to the availability of high-power mm-wavelength ($f_i = 140\ GHz$) gyrotrons.

While the measurement of T_i (and eventually of fast ion tails and alpha particle distributions) is the main goal of these diagnostics, the strong sensitivity of the thermal fluctuation level, and therefore of the spectral density function $S(\underline{k}, \omega)$, to the detailed shape of the electron and ion velocity distributions, particularly near the plasma resonances, in principle can be exploited to provide additional information on specific aspects of the plasma kinetics. Recently, for example, an enhanced excitation of LH oscillations due to ion tails /3, 4/ and of the UH resonance due to a fast electron population /5/ have been predicted.

Here we present an analysis of the spectral modifications induced in the CS spectra of tokamak plasmas due to the ohmic current leading to a Spitzer-Harm distribution of the electron population. The possible role of the light impurities in hiding the dependence of $S(\underline{k}, \omega)$ on the drift parameter ξ is also investigated in some detail with reference to the FTU and JET machines. Due to the limited spectral region involved in the ion thermal CS spectrum, the ion-acoustic resonance is the natural reference frequency in this investigation.

The spectral modifications induced by a drifting electron Maxwellian population were first analyzed by Rosenbluth /6/. More recently, using the same model, a spectral asymmetry in the CS spectra of the order of 10% has been predicted for JET conditions /7/.

2 - Spectral Density function

The spectral density function $S(\underline{k}, \omega)$ has been calculated for an unmagnetized, non-isothermal, multi-component plasma. The ion species have been taken Maxwellian and the current-carrying bulk electrons have been modelled with a Spitzer-Harm distribution approximated in the Lorentz gas limit (only e-i collisions are considered) /8/, i.e.

$$f_e(v, \psi) = f_M [1 + D(v/v_{t,e}) \cos \psi] \tag{1}$$

where $D(x) = Ax^4$ and $A = -(4/\Lambda_C)(E \lambda_{D,e}/eZ_{eff})$, E being the d.c. electric field in the plasma. Here $v_{t,e} = \sqrt{2T_e/m_e}$, $\lambda_{D,e} = \sqrt{T_e/4\pi n_e e^2}$, $Z_{eff} = \Sigma_i c_i Z_i^2$; $c_i = n_i/n_e$ is the concentration of the i-th ion species, Λ_C the Coulomb logarithm, and ψ the pitch-angle in the velocity space.

$S(\underline{k}, \omega)$ can be formally written as follows:

$$S(\underline{k}, \omega) = \frac{2\pi}{k} \left| \frac{1 + H_i(\underline{k}, \omega)}{\varepsilon^M(\underline{k}, \omega) + A\eta H_e^S(\underline{k}, \omega)} \right|^2 \times \left[F_e^M\left(\frac{\omega}{k}\right) + A\eta F_e^S\left(\frac{\omega}{k}\right) \right] +$$
$$+ \frac{2\pi}{k} \sum_i Z_i^2 c_i \left| \frac{H_e^M(\underline{k}, \omega) + A\eta H_e^S(\underline{k}, \omega)}{\varepsilon^M(\underline{k}, \omega) + A\eta H_e^S(\underline{k}, \omega)} \right|^2 \times F_i^M\left(\frac{\omega}{k}\right) \tag{2}$$

where $\varepsilon^M(\underline{k}, \omega) = 1 + H_e^M(\underline{k}, \omega) + \Sigma_i H_i^M(\underline{k}, \omega)$ is the longitudinal dielectric function computed for a Maxwellian plasma and $H_e^S(\underline{k}, \omega)$, $F_e^S(\omega/k)$ are the Spitzer corrections to the electron susceptibility and unidimensional distribution, respectively. $\eta = \cos\beta = \underline{k} \cdot \underline{E}/kE$ and β is the angle between the fluctuation wavevector and the d.c. electric field. The drift parameter, $\xi = <v_\parallel> / v_{t,e} = 4A/\sqrt{\pi} \ll 1$, is the physical smallness parameter governing the expansion which leads to Eq.(1). In Eq.(2) the following definitions have been used:

$$H_e^S(\underline{k}, \omega) = \alpha^2 \left[-\pi^{-1/2} \left(-x_e e^{-x_e^2} E(x_e)(3/4 + x_e^2/2 - x_e^4) + x_e/2 + x_e^4 \right) - 3\,Y(x_e)/4 \right] \quad (3)$$

$$F_e^S(u) = -\frac{1}{\sqrt{\pi}\, v_{t,e}} \left[sign(u)(u^4 + 3u^2/2) e^{-u^2} + \frac{3\sqrt{\pi}}{4}\, u\, erfc(|u|) \right] \quad (4)$$

where

$$E(x) = -Ei(x^2) - i\pi\, sign(x)\,; \quad Y(x) = V(x) + i\pi\, erfc(|x|)\,; \quad V(x) = P \int_{-\infty}^{+\infty} dt\, \frac{erfc(|t|)}{t + x}$$

and $x_e = \omega / k v_{t,e}$. The computations have been performed by the numerical code CTS-90.

3 - Organization of the work

The asymmetry in the Spitzer-Harm electron velocity distribution leads to the appearance of an asymmetry in $S(\underline{k}, \omega)$ due to collective effects. In a pure plasma this effect is expected to be more evident at the ion acoustic (IA) peaks. Speaking of IA "peaks" instead that of resonances is more correct since for $T_e/T_i \leq 3$, while reaching a minimum, $Re\, \varepsilon_L(\underline{k}, \omega) \neq 0$ in the frequency range considered here.

The asymmetry in the spectrum has been described by the dimensionless parameter $R = (S_+ - S_-)/S_0$, where $S_{+(-)}$ is the value of $S(\underline{k}, \omega)$ at the IA peaks on the positive (negative) frequency side, and S_0 that in the absence of the d.c. electric field. The ohmic current in the plasma I_p and a model profile for the radial distribution of the current density, i.e. $j_\parallel(r) = (1 - r^2/a^2)^{\gamma_j}$, have been given as input parameters. Then, the local value of ξ has been calculated consistently with the Spitzer resistivity and accounting for Z_{eff}.

In the presence of a non negligible fraction of impurity ions, the low-frequency part of the CS spectrum can be strongly modified. This explains why the (light) impurity content of the actual plasmas must be considered for a realistic investigation on the current-induced effects.

$S(\underline{k}, \omega)$ has been evaluated for the plasma regimes typical of the FTU machine ($n_e = 10^{20}\, m^{-3}$, $T_e = 2\, keV$, $T_i = 1 \div 2\, keV$, $I_p = 1 \div 2\, MA$, $\theta_s = 90°$) and for some low-density regimes of JET ($n_e = 1.2 x 10^{19}\, m^{-3}$, $T_e = 10\, keV$, $T_i = 5 \div 10\, keV$, $I_p = 2 \div 5\, MA$, $\theta_s = 20°$). Wavevectors $\underline{k}$ are in the d.c. electric field direction, i.e. $\beta = 0°$.

Typical impurity contents have been considered for both machines. The high density FTU plasma is expected to have Z_{eff} of order one and then (by extrapolation of the available data for the early FT machine) concentrations of the dominant O-IX impurity of no more than $c = 1\%$ have been assumed. Two impurity regimes have been considered for JET: one at rather high Z_{eff}, with $c = 1\%$ of O-IX and $c = 5\%$ of C-VII, the other at low Z_{eff}, with $c = 1\%$ of O-IX and $c = 5\%$ of Be-V.

4 - Results

Fig. 1 shows the relevant peaks in a typical FTU spectrum. The small counter-asymmmetry noticeable in curve *a*), which refers to the equivalent pure and currentless plasma, is due to the inclusion of the exact (non Bragg-approximated) value of the differential k vector in the calculation. Curve *b*) shows the spectrum for the impure ($Z_{eff} \simeq 1.3$) and currentless FTU plasma. The main feature is the occurrence of a central

peak at very low frequencies. At higher impurity contents this peak can extend both in amplitude and frequency range and even embody the whole IA feature. Curve *c*) refers to the a pure, current-carrying plasma; here the asymmetry between the IA peaks is much more pronounced. The modification of this last spectrum due to the impurities is given by curve *d*), where a minor asymmetry appears also in the central impurity-induced feature.

In Fig. 2 the amount of asymmetry, as given by the ratio R, is plotted *vs.* the drift parameter ξ for a number of physical conditions. It is seen that the asymmetry can be as high as 20% in the most favourable case. A linear dependence on ξ is also clearly exhibited. The central line of the group labelled *a*) and the lines *b*) and *c*) refer to temperature ratios $T_e/T_i = 2,\ 1.5,\ 1$, respectively, with a concentration of O-VII $c = 0.5\%$. The lateral lines of the group *a*) refer to a pure hydrogen plasma (higher line) and to a plasma with $c = 1\%$ (lower line), respectively. The effect of the impurity content on the amount of asymmetry is seen to be quite small.

Fig. 3 gives the same spectral peaks for JET with reference to the low Z_{eff} (= 1.5) discharge. (The legend for the plots is the same as above). The dotted curve labelled *e*) gives an example of the spectral behaviour in the high Z_{eff} (= 3) regime. The IA peaks here are seen to fully disappear. In such cases the spectral asymmetry can still be evaluated with reference to the very low-frequency peaks produced by the impurities themselves. The reduced frequency interval, however, makes measurability more critical.

In Fig. 4 the amount of asymmetry R is plotted *vs.* ξ for the JET conditions. The lines *a*) and *c*) refer to a pure hydrogen plasma with $T_e/T_i = 2,\ 1$, respectively. Line *d*) refers to the impure plasma corresponding to the spectrum labelled *e*) in Fig. 3; here R is evaluated from the impurity-induced peaks. The lines *e*) and *f*), finally, refer to the case with $Z_{eff} = 1.5$ with R evaluated at the impurity-peaks (dashed line) and at the IA peaks (solid line), respectively. As expected, due to the lower range covered in terms of ξ, even at the highest currents in JET the deformations of the CS spectra are considerably smaller than in FTU, particularly for low T_e/T_i ratios.

5 - Conclusions

Our results indicate that in most conditions of interest the asymmetries induced by the ohmic current of a tokamak plasma should not significantly affect the CS spectra, and then the measurement of T_i.

In contrast, however, in devices characterized by a high current-density, like FTU, the above mentioned asymmetries should be quantitatively evaluable, provided that a sufficiently high S/N can be achieved in the CS measurement. The presence of not too large amounts of impurities will not substantially modify the situation.

In these last cases the spectral asymmetries could be exploited to infer the local value of the drift parameter ξ and then of the current density /9/.

References

/1/ Behn R. et al., *Phys. Rev. Lett.*, **62**, 2833 (1989).

/2/ Costley A.E. et al., *A Thomson Scattering Diagnostic to Measure Fast Ions and Alpha-particle Distributions in JET*, JET Report JET-R(88)08, 1988.

/3/ Vahala L. et al., *Nucl. Fus.*, **26**, 1595 (1986).

/4/ Galbiati S. et al., *Plasma Phys. and Contr. Fus.*, **33**, 1049 (1991).

/5/ Lontano M. and Tartari U., *Plasma Phys. and Contr. Fus.*, **31**, 1933 (1989).

/6/ Rosenbluth M.N., Rostoker N., *Phys. Fl.*, **5**, 776 (1962)

/7/ Orsitto F., *Feasibility Study of Bulk Ion Temperature Measurements on JET by means of Collective Scattering of Gyrotron Radiation*, JET Report JET-R(90)05, 1990.

/8/ Cohen R.S. et al., *Phys. Rev.*, **80**, 230 (1950); Spitzer L. et al., *Phys. Rev.*, **89**, 977 (1953).

/9/ Castiglioni S., Lontano M., *Proc. Workshop on Diagnostic for Contemporary Fusion Experiments* (Compositori, Bologna, 1992), 869 (1992).

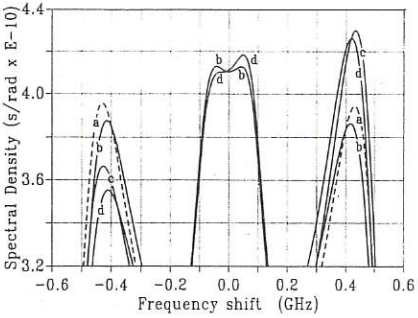

Fig. 1 - *FTU spectra ($n_e = 1x10^{20}\ m^{-3}$, $T_e = 2\ keV$, $T_i = 1\ keV$, $\theta_s = 90°$) showing ion-acoustic and impurity-induced peaks. a) Reference spectrum for the equivalent, pure, currentless plasma; b) impure ($c_{OIX} = 1\%$), currentless plasma; c) pure, current-carrying ($I_p = 2\ MA$) plasma; d) impure, current-carrying plasma.*

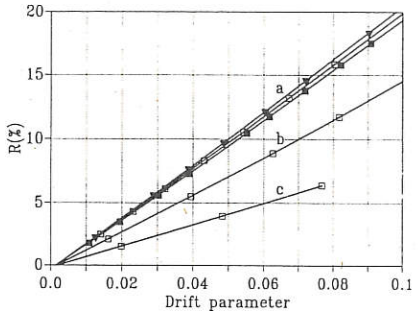

Fig. 2 - *Asymmetry ratio R vs. drift parameter ξ in FTU. Lines of group a) refer to $T_e/T_i = 2$ and show the reduction of R due to impurities (upper line: pure plasma; average line $c_{OIX} = 0.5\%$; lower line $c_{OIX} = 1\%$; b) impure plasma with $T_e/T_i = 1.5$, $c_{OIX} = 0.5\%$; c) impure plasma with $T_e/T_i = 1$, $c_{OIX} = 0.5\%$. Other plasma parameters are as in Fig. 1.*

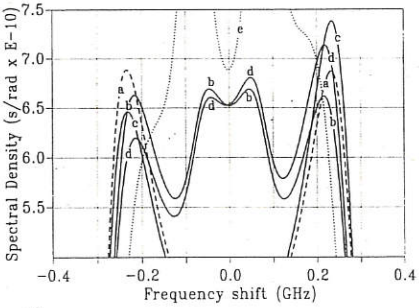

Fig. 3 - *JET spectra ($n_e = 1.2x10^{19}\ m^{-3}$, $T_e = 10\ keV$, $T_i = 5\ keV$, $\theta_s = 20°$) showing ion-acoustic and impurity-induced peaks. a) Reference spectrum for the equivalent, pure, currentless plasma; b) impure, low Z_{eff} ($c_{OIX} = 1\%$, $c_{NeV} = 3\%$), currentless plasma; c) pure, current-carrying ($I_p = 5\ MA$) plasma; d) impure, current-carrying plasma; e) impure, high Z_{eff} ($c_{OIX} = 1\%$,) $c_{CVII} = 5\%$), current-carrying plasma.*

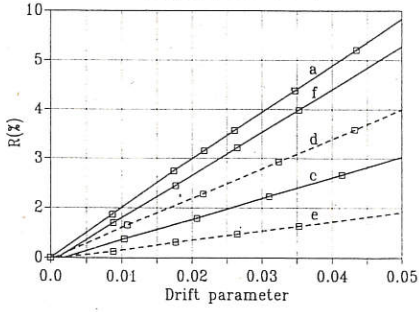

Fig. 4 - *Asymmetry ratio R vs. drift parameter ξ for JET. a) Pure plasma with $T_e/T_i = 2$ (reference to IA peaks); c) pure plasma with $T_e/T_i = 1$ (reference to IA peaks); d) impure, high Z_{eff} ($c_{OIX} = 1\%$,) $c_{CVII} = 5\%$) plasma with $T_e/T_i = 1$ (reference to impurity peaks); e) impure, high Z_{eff} plasma with $T_e/T_i = 2$ (reference to impurity peaks); f) impure, high Z_{eff} plasma with $T_e/T_i = 2$ (reference to IA peaks). Other plasma parameters are as in Fig. 3.*

ION TEMPERATURE MEASUREMENTS BY RUTHERFORD SCATTERING AT TEXTOR

H.F. Tammen, A.A.E. van Blokland [1], T. Oyevaar, F.C. Schüller and A.J.H. Donné,

FOM-Instituut voor Plasmafysica 'Rijnhuizen', Associatie Euratom-FOM, P.O.Box 1207, 3430 BE Nieuwegein, The Netherlands.

Abstract

The Rutherford scattering diagnostic at TEXTOR has been used to determine the ion temperature profile and the (relative) ion density profile on a shot-to-shot basis for a series of reproducible ohmic discharges. The profiles have been obtained for two different scattering angles and all profiles have been corrected for geometric effects that are due to the finite size of the scattering volume. First profile measurements during NBI heated discharges show up-down asymmetries.

1. Introduction

The ion temperature is an important parameter in thermonuclear research. To improve the knowledge on this parameter a Rutherford scattering diagnostic has been installed at TEXTOR, capable of performing temporal- and spatial resolved measurements /1, 2/.

A narrow beam of monoenergetic 30 keV helium atoms is injected vertically into the plasma. A small part of the beam particles is scattered, mainly in forward direction, through elastic collisions with the moving plasma ions, exchanging momentum and energy in the process. Particles that are scattered at a certain, adjustable angle (3°-8°) are energy analyzed by a time-of-flight analyser, which is equiped with coincidence techniques to suppress background events. For pure plasmas the width of the obtained spectra is directly related to the ion temperature in the scattering volume. However, it has been found that small fractions of impurities in the plasma contribute significantly to the observed spectra. Therefore function parametrization techniques are used for data analysis /3/.

2. Geometric effects

The scattered particles that are observed by the analyser originate from the scattering volume, which is defined by the intersection of the probing beam and the observational volume of the analyser (see Fig. 1). For a beam diameter B of 24 mm, a width of the analyser sight profile A of 20 mm and a scattering angle θ of 7° the total length L of the scattering volume is 351 mm. However, weighting occurs towards the centre of the scattering volume due

[1] present address: Naka Fusion Research Establishment, JAERI, Ibaraki-ken 311-01, Japan.

to the beam intensity profile and the analyser sight profile, resulting in a gaussian shaped total intensity profile. For the parameters mentioned above 75% of the particles originate from an effective length L' of 169 mm.

A second weighing factor is introduced by the ion density profile. As the scattering yield depends linearly on the local ion density more particles will be scattered from regions with higher densities, thus weighing towards the centre of the plasma. Both effects will influence the observed temperature. Simulations show that the measured central ion temperature will be slightly lower than the actual central temperature, but that temperatures obtained at positions in the outer region of the plasma will be higher than actual ones.

3. Results and discussion

The ion temperature and density profiles were obtained during a series of reproducible ohmic discharges (I_P = 350 kA, B_T = 2.25 T, $\overline{n_e} = 2.5\times10^{19}$ m^{-3}) for two scattering angles: 6° and 7°. The position of the scattering volume was adjusted on a shot-to-shot basis by shifting the analyser. The injected helium beam current was kept constant (10 mA) for all discharges. The obtained spectra were analyzed, yielding for each position the measured ion temperature and the number of particles scattered on hydrogenic ions. This number has been derived by correcting the total scattering yield for the observed presence of impurities in the scattering volume. The density and temperature profiles were derived by calculating what the measured profile would be for a certain assumed 'real' profile and comparing this with the measurements. Iteration yielded the best fit. The profiles were described by $f(r) = \alpha(1-(r^2/a^2))^\beta$, with a = 46 cm the position of the limiter.

In Fig. 2 the results for the density profile are given for both scattering angles. The lines represent the best fits, i.e. the (normalized) 'real' density profiles, and the open and closed dots the measurements for 6° and 7°, respectively. In Table 1 the fitparameters are given: the agreement is good. α is a function of scattering angle and only given for the sake of completeness. $R_{1/2}$ is the halfvalue radius. Comparison with the electron density profile, as measured by an interferometer, showed that the profiles were shaped almost identically. Fig. 3 and Table 1 show the results for the obtained ion temperature profiles. The density profile for weighting was chosen as $\beta = 1.15$ for both angles. The agreement between the two profiles is somewhat less than for the density, but still satisfactory. Comparison with the temperature profile, as deduced from neutral particle analysis, showed good agreement.

Recently profile measurements were performed for the first time during discharges where hydrogen neutral beam injection was applied to a deuterium plasma (2.2MW NBI-Co and 2.2MW NBI-Co + 1.8MW NBI-Counter, $\overline{n_e} \approx 2.0\times10^{19}$ m^{-3}). First analysis showed a number of interesting observations.

1. Spectra obtained from the centre of the plasma are dominated by the presence of a high-Z impurity peak (≈ 50% of the spectrum). Previously this was observed during NBI when deuterium was used as heating beam species, but not when hydrogen was used /3/.
2. The count rate when viewing the centre is lower than when viewing the outer region of the plasma. This is caused by an even more dominating impurity peak in the spectra from the outer region. A possible explanation is an increased presence of high-Z impurities towards the edge.
3. The observed mean and higher order moments of the time-of-flight spectrum, which are used for function parametrization, are not symmetrical around the midplane (Fig. 4). These moments are a function of bulk motion, impurity density and temperature of the ions. If both the impurity density and the temperature are assumed to be (vertically) symmetrical, only poloidal plasma rotation can cause this asymmetry. In that case there would be a stronger rotation for the NBI-Co discharge, since the slope around the centre is more pronounced. However, it is more likely that there is an up-down asymmetry in the ion temperature and the impurity density, as predicted by neo-classical theory. The subject is momentarily under study.
4. The derived central ion temperature is 2.7 ± 0.6 keV for NBI-Co and 4.5 ± 0.7 keV for NBI-Co + NBI-Counter. The error is mainly due to the large impurity peak which, together with the bulk motion, hampers an accurate interpretation of the other spectra at the moment. An other aspect which is also under study is the influence on the spectra of the non-thermal deuterium population that exists during NBI /4/. However, first estimates indicate that these effects are small.

Acknowledgement

The authors would like to thank their colleagues from TEXTOR for their assistance and interest. This work was performed under the Euratom-FOM association agreement with financial support from NWO and Euratom.

	Ion density profile			Ion temperature profile		
	(α)	β	$R_{1/2}$ (cm)	α (eV)	β	$R_{1/2}$ (cm)
6°	(7670 ± 50)	1.10 ± 0.08	31.5 ± 0.8	916 ± 40	1.17 ± 0.25	30.8 ± 2.5
7°	(3650 ± 40)	1.20 ± 0.07	30.5 ± 0.7	965 ± 30	1.52 ± 0.15	27.8 ± 1.1

Table 1 *Fitparameters for the density and temperature profile for two scattering angles.*

References

/1/ A.J.H. Donné, E.P. Barbian, H.W. van der Ven, J. Appl. Physics **62**, 3130 (1987).

/2/ A.A.E. van Blokland, E.P. Barbian, T.W.M. Grimbergen, T. Oyevaar, Rev. Sc. In. **61**, 3116 (1990).

/3/ H.F. Tammen, A.A.E. van Blokland, T. Oyevaar, F.C. Schüller, A.J.H. Donné, Rev. Sc. In., in press.

/4/ K. Tobita, Y. Kusama, M. Nemoto, H. Takeuchi, H. Yoshida et al., Nucl. Fus. **28**, 1719 (1988).

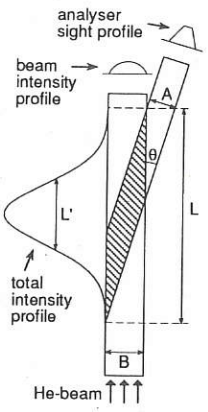

Fig. 1 *Schematic of the scattering volume with weight factors.*

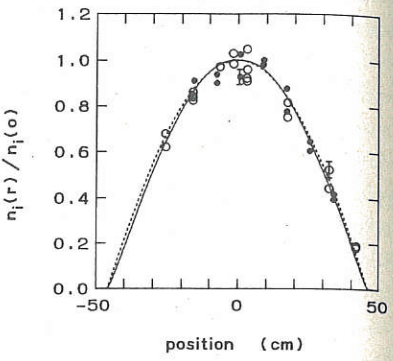

Fig. 2 *Normalized ion density profiles obtained for two scattering angles. Measurements and best fits are indicated by ∘ and --- (6°), and • and — (7°). Plasmaparameters: I_P = 350 kA, B_t = 2.25 T, $\overline{n_e} = 2.5 \times 10^{19}$ m^{-3}.*

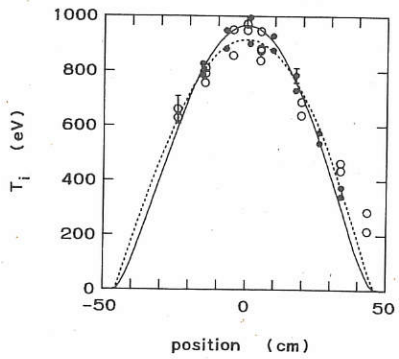

Fig. 3 *Ion temperature profiles for the the same scattering angles and plasmaparameters as Fig. 2.*

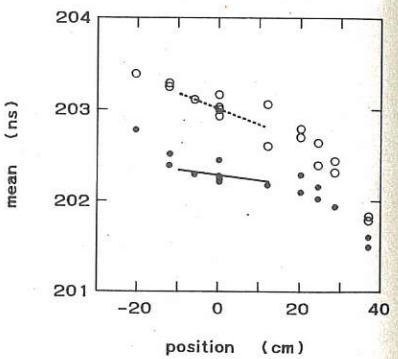

Fig. 4 *Mean of time-of-flight spectra obtained during NBI heated discharges. (∘ : NBI - Co, • : NBI - Co + Counter)*

CO_2-SCATTERING AND RF PROBE MEASUREMENTS OF LOWER-HYBRID WAVE SPECTRA IN THE PRESENCE OF LOW-FREQUENCY FLUCTUATIONS

B. Fischer and M. Krämer
Institut für Experimentalphysik II, Ruhr-Universität Bochum
D-4630 Bochum 1, Germany

Abstract
Coherent CO_2-scattering as well as rf probe diagnostics (phase-sensitive method and two-point-correlation analysis) are applied to investigate small amplitude lower-hybrid (LH) waves launched to a linear plasma column by a slow-wave antenna. It is demonstrated that low-frequency (lf) fluctuations may strongly affect the lower-hybrid (LH) wave propagation and damping.

Experiment
The investigations were performed on a linear magnetized plasma ($n_e \approx 10^{11} cm^{-3}$, $\tilde{n}_e/n_e = 0.5-1$, $T_e = 3-7eV$, $T_i = 0.5-2eV$, $B_0 = 210-220mT$, and $p = 45-180Pa$ hydrogen) produced by microwave power pulses ($f_{HF} = 6.11GHz \approx f_{ce}$, $P_{HF} = 160W$, $\tau_{pulse} \approx 10ms$) launched end-on to the discharge vessel ($L = 2.22m$, $R = 0.125m$). Cylindrical and plane Langmuir probes as well as a resonance-cone double probe were used to measure the electron temperature and density, respectively.

The LH-waves ($\omega/2\pi = 70MHz$) were launched to the plasma by a plane slow-wave antenna consisting of 6 plates driven at alternating rf potential yielding $k_\parallel = 1.05cm^{-1}$. The LH-spectra were measured by a (coherent) homodyne CO_2-laser scattering technique /1/ as well as by rf probe diagnostics /2/. By varying the scattering angle wavenumbers in the range $k_\Delta = 40 - 100cm^{-1}$ were achieved. The scattering signals were detected by a HgCdTe-detector ($f_{max} = 100MHz$, $D = 0.5mm$) and processed by a spectrum analyzer and a boxcar averager. Two probe methods were used to detect the LH waves. From *phase-sensitive* measurements, the spatial distribution of the rf potential amplitude and phase in a narrow frequency band was obtained using a network analyzer that compares the rf probe signal with a reference signal. Correlation analysis of two nearby probe signals was applied to estimate the local wavenumber and frequency spectra over a broad frequency interval in the rf range. Similarly, the low-frequency (lf) density fluctuations were diagnosed.

Results and Discussion
(a) Scattering measurements: In Fig.1, we show the results of the scattering measurements, where the detector current in the cone maximum has been plotted versus the distance z from the antenna. The observations can be summarized as follows: (i) For all pressures and scattering wavenumbers, the scattered power decreases monotonically with increasing z. (ii) The scattered signal is smaller and decreases stronger with z, if the scattering wavenumbers are larger. (iii) At lower pressures, i.e. higher lf turbulence level, the axial decrease of the current amplitude is stronger than at higher pressures. (iv) The power maximum of the wavenumber spectra is located below $40cm^{-1}$. — The observations are thus in contrast to the LH wave dispersion expected. Finally, we note that the strong drop at larger wavenumbers is associated with the limit for coherent detection, i.e. $\alpha = (k_\Delta \lambda_{De})^{-1} = 1$.
(b) Probe measurements: The rf potential profiles of the LH cone measured at different distances z from the antenna are shown in Fig.2 for the higher fluctuation level. The

amplitude in the cone maximum decreases and the phase flattens strongly with z. Relating the phase slope to the local wavenumber, i.e. $k_{LH} = \partial\varphi/\partial x$, the LH wavenumbers turn out to decrease from $k_{LH} \simeq 6cm^{-1}$ at $z = 3.5cm$ to $k_{LH} < 1cm^{-1}$ at $z = 38.5cm$. At the lower fluctuation level (not shown), the local wavenumber near the antenna corresponds roughly to the LH wavenumber expected, whereby the phase slope remains nearly constant. The experimental results were compared with numerical computations based on a model that takes into account the wavenumber spectrum at the antenna as well as the plasma inhomogeneity. Close to the antenna, the theoretical curves fit the measured traces reasonably if by nearly two orders of magnitude enhanced values for the collisional frequency (solid lines) are taken (classical coll. freq.: dashed lines).

In Fig.3, we show the results of the spectral measurements. The normalized frequency spectra, taken at different positions in the LH cone for the lower fluctuation level reveal that the rf energy is transferred from the pump peak to the sidebands when the LH waves penetrate the plasma. (For the higher fluctuation level (dashed line), the frequency spectra are strongly broadened already near the antenna.) The frequency broadening may be attributed to scattering of the LH-waves from the lf density fluctuations. The frequency spectral width of the LH waves estimated by $\Delta f \simeq \sqrt{2/3}(k_0/\zeta_0)f_{lf}\sqrt{x/l_s}$ /3/ is in good agreement with the measurements for $p = 180mPa$, where $k_0/\zeta_0 = 20$, $l_s = 8cm$, and $f_{lf} = 12kHz$ (k_0, ζ_0: LH and lf wavenumber, respectively, l_s: scattering length).

In Fig.4, the wavenumber spectra $S(k_x)$ have been plotted. In the weaker turbulent case, the mean wavenumber $\overline{k_x}$ increases with x (until $x = 0.7cm$ at $z = 18.5cm$) corresponding roughly to the LH dispersion for the main component of the antenna spectrum at the plasma edge. Simultaneously, a strong broadening was observed ($\Delta k_x \simeq \overline{k_x}$)). For the higher turbulence level (not shown), the wavenumber spectra reveal a more complicated behaviour. A peak (associated with the portion of the energy near the pump frequency) is seen to be superposed to a broad spectrum. The peak shifts to smaller wavenumbers, in agreement with the decrease of the phase slope in the phase-sensitive measurements.

In Fig.5, the radial profiles of the rf potential amplitude obtained from the two probe measurements are shown. Due to the different bandwidths the damping rates in the phase-sensitive measurements are by a factor of two larger than in the (frequency-integrated) spectral measurements. Relating the latter damping rates to damping of the total wave energy, we obtain $Im(k_\perp) = 1.2cm^{-1}$ and $Im(k_\perp) = 1.8cm^{-1}$ for $p = 180mPa$ and $p = 45mPa$, respectively. (Here, we note that the damping rates inferred from the scattering measurements are even still larger due to the strong disturbance of the wave fronts by the lf fluctuations.) The values that are nearly independent of the plasma density are by a factor 5 to 10 larger than expected from collisional and electron Landau damping. Rather, there is some correlation between the level of the lf fluctuations and the LH damping rates thus indicating an anomalous damping mechanism associated with the low-frequency turbulence.

/1/ Holzhauer E. and Massig J.H. (1978), *Plasma Physics* **20**, 867

/2/ Krämer M., Sollich N., and Dietrich J. (1988), *J. Plasma Physics* **39**, 447.

/3/ Andrews P.L., and Perkins F.W. (1983 b), *Phys. Fluids* **26**, 2546.

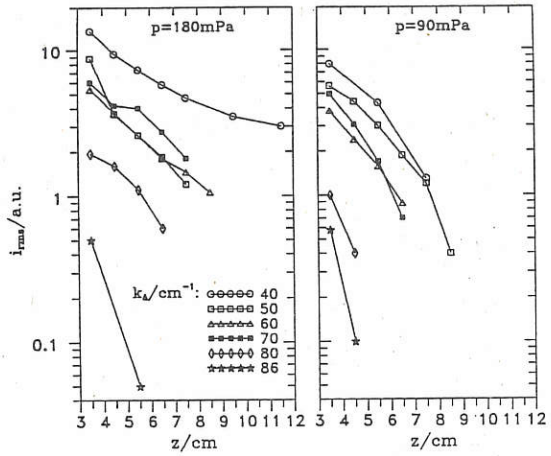

Fig.1: Detector current in LH-cone maximum vs. distance z from antenna.

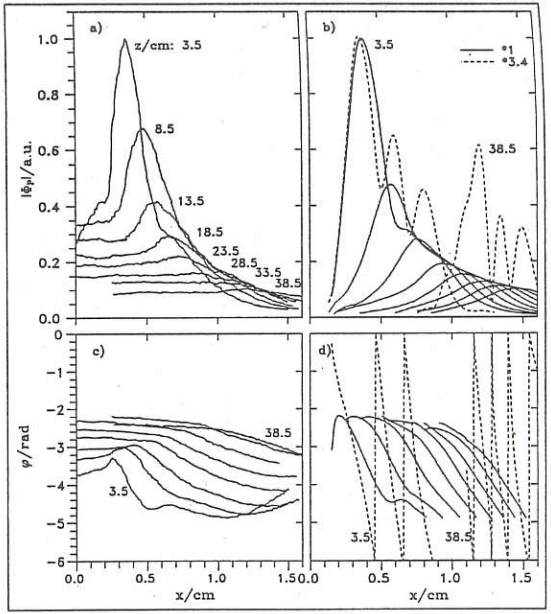

Fig.2: Potential and phase profiles (a,c: measurements, b,d: calculations). $p = 45mPa$, $T_e = 6eV$.

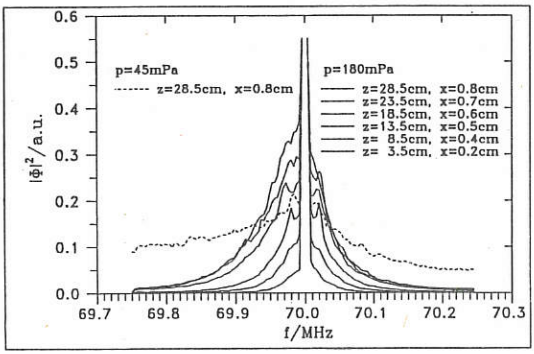

Fig.3: Frequency spectra at different positions in the LH-cone. $p = 180mPa$.

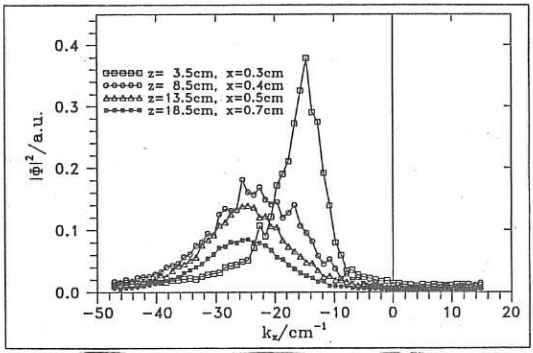

Fig.4: Radial wavenumber spectra. $p = 180mPa$.

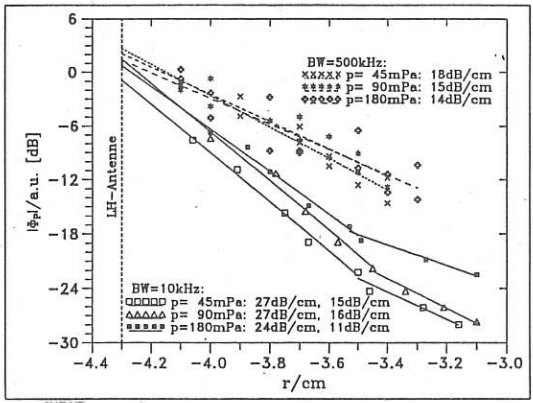

Fig.5: Spatial decrease of rf potential amplitudes from different probe measurements.

II-1o99

MEASUREMENT OF COHERENT TEMPERATURE FLUCTUATIONS ON THE STELLARATOR WENDELSTEIN 7-AS

H.J. Hartfuß, S.Sattler, W7-AS Team*, NBI-Team**, ECRH-Group***

Max-Planck-Institut für Plasmaphysik, EURATOM-Ass., 8046 Garching, FRG

Coherent modes of temperature fluctuations have been observed and radially localized with a multichannel heterodyne radiometer of the ECE diagnostics. The modes are observed during NBI discharges with edge values of the rotational transform mainly in the range between 0.32 and 0.36. The mode numbers are m=3, n=1. The oscillations in the frequency range 18 to 55 kHz are driven by the fast beam ion component. This can be concluded comparing the rapid decay (< 500 μs) of the mode after switch-off of the beams with the slowing down time and the energy confinement time. The plasma still further exists for several ten ms. Critical parameters for the occurence of the modes seem to be the density and the profile of the rotational transform. No direct impact on the confinement properties of the plasma is observed.

EXPERIMENTAL OBSERVATIONS

The ECE diagnostic allows the measurement of electron temperature fluctuations up to 100 kHz at 24 different radial positions across the temperature profile with spatial resolution in radial direction of about 1 cm for a time window of 80 ms in maximum due to restrictions of the data aquisition system used. Analysis provides radially resolved absolute and relative spectra as well as cross correlations between the different radial channels.The modes observed have relative amplitudes of a few per cent. They are simultaneously observed by other diagnostics like Mirnov coils, Soft X-ray /1/, and reflectometry. The strong correlation to the fast beam ion component was mentioned before. But similar phenomena with about ten times weaker amplitude have also been observed in purely ECR heated discharges.

---

* W7-AS Team: J. Baldzuhn, B. Bomba, R. Brakel, A. Brenner, R. Buechse, R. Burhenn, G. Cattanei, A. Dodhy, D. Dorst, A.Elsner, M. Endler, K. Engelhardt, V. Erckmann, U. Gasparino, S. Geißler, L. Giannone, P. Grigull, H. Hacker, H.J. Hartfuss, O. Heinrich, G. Herre, D. Hildebrandt, J.V. Hofmann, R. Jaenicke, F. Karger, M. Kick, H. Kroiss, G. Kuehner, A. Lazaros, H. Maassberg, C. Mahn, K. McCormick, H. Niedermeyer, W. Ohlendorf, F. Rau, H. Renner, H. Ringler, A. Rudyj, N. Ruhs, J. Saffert, F. Sardei, S. Sattler, F.Schneider, U. Schneider, G. Siller, E. Simmet, U. Stroth, G. Theimer, M. Tutter, E. Unger, F. Wagner, M. Weinlich, A. Weller, H. Wolff, E. Würsching, D. Zimmermann, M. Zippe, S. Zöpfel,

**NBI-Team: W. Ott, F.P. Penningsfeld, E. Speth, H. Teubel

***ECRH-Group: W. Kasparek, G.A. Müller, P.G. Schüller, Inst. für Plasmaforschung, Uni Stuttgart

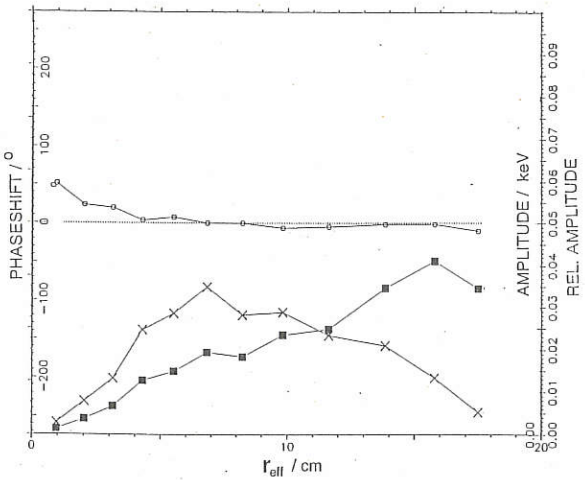

Fig. 1.: Radial behaviour of absolute (crosses) and relative (squares) amplitude and phase (open circles) of a mode of the first type. Mode frequency is 38 kHz and the phase is almost constant along the radial coordinate. The absolute maximum is 6 eV. The relative maximum is about 3.6 % and is localized at an effective radius of 15 cm. The mode was observed during balanced NBI at ι=0.358 and $n_e dl = 2.4 \cdot 10^{19}$ m $^{-2}$. The corresponding spectrum is given in Fig. 3

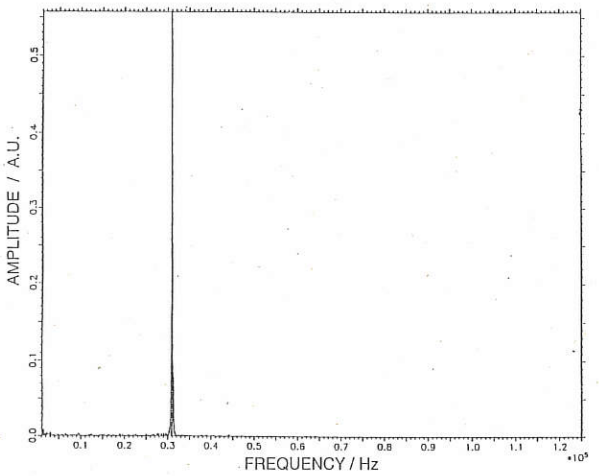

Fig. 2.: Power spectrum of a single mode of extreme amplitude observed during unbalanced NBI at ι=0.345 and $n_e dl = 2.0 \cdot 10^{19}$ m $^{-2}$. The mode frequency is 30.9 kHz, the radial behaviour is as shown in Fig. 1 with an absolute amplitude of 25 eV, a relative amplitude of 20 % localized at an effective radius of 13 cm

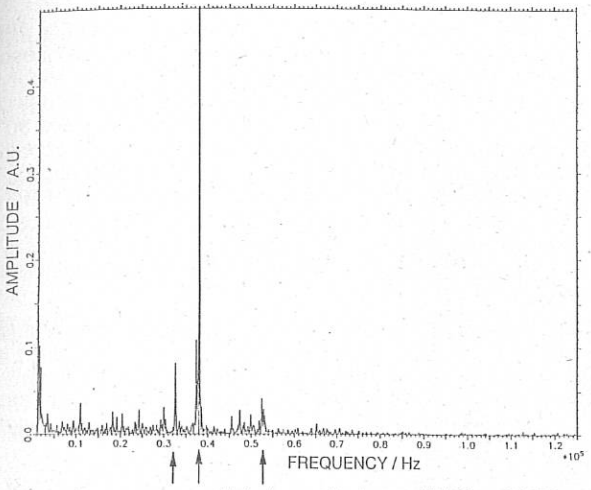

Fig. 3.: Power spectrum measured during unbalanced NBI, ι=0.358 and $n_e dl = 2.4 \cdot 10^{19}$ m $^{-2}$. Three different modes are present at the same time. The higher frequencies 38 kHz and 52.5 kHz correspond to modes of the first type (the radial behavior of the 38 kHz line is shown in Fig.1). The third frequency 32.6 kHz correponds to a mode of the second type (the radial behaviour is shown in Fig. 4).

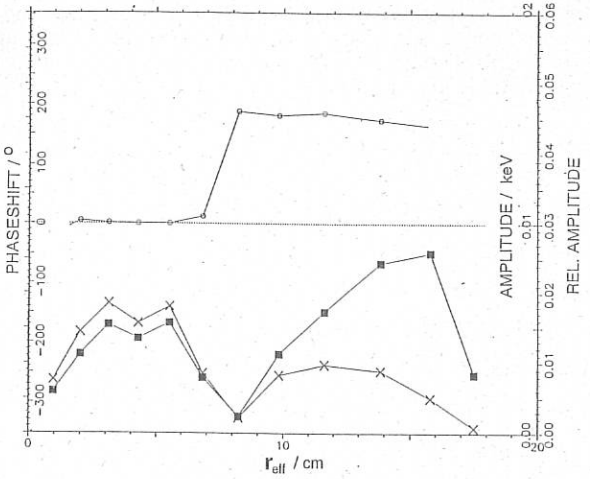

Fig. 4.: Radial behaviour of absolute (crosses) and relative (squares) amplitude and phase (open circles) of a mode of the second type. Mode frequency is 32.6 kHz and the phase shows a phase jump of π at an effective radius of 8 cm. The inner absolute maximum is 7eV. The relative maxima are 1.5% and 2.4%. The mode was observed during balanced NBI at ι=0.358 and $n_e dl = 2.4 \cdot 10^{19}$ m $^{-2}$. Its spectrum is given in Fig. 3.

Two different types of modes have been observed during NBI heated discharges: the first type shows a single maximum in both absolute and relative amplitude, radially localized between 10 and 18 cm. Minor radius of W7-AS is < 18 cm. Correlation analysis shows no phase change along the radial coordinate (Fig. 1). The frequency of this mode is between 30 KHz and 55 kHz with relative amplitudes of a few per cent. The mode appears only in the well defined range of edge rotational transform as given above. This type of mode has been observed during balanced and unbalánced NBI. A unique observation was made during unbalanced NBI: a 31 kHz mode localized at 13 cm with a relative amplitude as high as 20 % (Fig. 2). It has also been observed that two modes of this type with different frequencies can exist simultaneously (Fig. 3).

The second type of mode with frequencies typically lower than the first group, namely 18 to 35 kHz, shows two amplitude maxima which are out of phase (Fig. 4). The phase jump occurs between 6 and 12 cm. This type appears in the same configurational range as the first type. The relative amplitudes of both types are comparable. They occur simultaneously.

DISCUSSION

An interpretation of the observed features is presently under investigation and is done by the authors of reference /1/. Experimental and theoretical studies (see /2-5/ for example) have revealed that so-called global marginal stable Alfven eigenmodes (GAE) can be destabilized by alpha particles or by the fast circulating beam particles of the NBI, the latter was proven experimentally at TFTR /2/. A similar mechanism might cause the observed mode activity in Wendelstein 7-AS. If that would be the case, the different types of modes mentioned above would correspond to different radial mode numbers, since due to toroidicity effects the poloidal mode number is no longer a good mode (quantum) number /5/.

REFERENCES

/1/ A. Lazaros, R. Jaenicke, A. Weller, 18th Europ. Conf. Contr. Fus. and Plasma Phys., Berlin 1991, Vol. II, p.197,
A. Weller et al., "Mode Activity At High Plasma Pressure..." Proc 19th Europ. Conf., Innsbruck 1992, (this conference)

/2/ K.L. Wong et al., Phys. Rev. Letters, 66, 1874 (1991)

/3/ K. Appert, et al., Plasma Phys., 24, 1174 (1982)

/4/ G.Y. Fu and J.W. Van Dam, Phys. Fluids B, 1, 2404 (1989)

/5/ S. Poedts et al., JET Report, JET-P(92)03 (1992)

ELECTRON CYCLOTRON NON THERMAL SPECTRA DURING OHMIC AND RF ASSISTED DISCHARGES ON TORE SUPRA

M.TALVARD, G.GIRUZZI, W.D.LIU

Association EURATOM-CEA sur la fusion
C.E. CADARACHE F13108 St Paul lez Durance

1. Introduction

Part of the experimental program on TORE SUPRA is devoted to the study of the thermal and matter equilibria during RF assisted long discharges (> 30 s). A set of 3 Michelson interferometers viewing perpendicularly and 15° apart to the toroidal magnetic field (Doppler views) has been installed in order to investigate the properties of the non thermal electron population produced by the RF power [1]. The usual resonance condition is :

$$\omega = \frac{\omega_c}{\gamma} + k_{//} v_{//} \qquad (1)$$

where ω_c is the electron cyclotron frequency, γ the relativistic correction to the electron mass, $k_{//}$ the parallel component of the wave number and $v_{//}$ the parallel velocity of the emitting electron . Equation (1) shows that the Doppler term in the right hand side increases or decreases the resonance frequency according to the angle between the line of sight and the toroidal direction. In particular when the RF plasma current is carried by high energy electrons, the resonance takes place higher than the electron cyclotron 2nd harmonic for the Michelson view named Bs for 'Blue shifted'. Conversely, the resonance frequency is lowered for the Michelson view named Rs for 'Red shifted' (fig.1). The upshifted radiation is directly coupled to the receiving antenna while the downshifted radiation is partially absorbed by the optically thick thermal 2nd harmonic. It is then expected some anisotropy between the 3 spectral measurements.

In the next section, we report measurements obtained during Lower Hybrid Current Drive experiments for which a significant part of the plasma current is carried by non thermal electrons. The last section concerns unexpected observations obtained during the Ohmic phase. A possible explanation of both situations is proposed with the help of a 3D Fokker-Planck code coupled to an ECE calculation code.

2. RF assisted plasmas

The typical Electron Cyclotron spectra obtained on M_{Rs}, $M_{\perp}$ and M_{Bs} during LHCD experiments are reported on fig.2 for P_{RF} = 4 MW, B_T = 3.85 T, I_p = 1.3 MA, $\langle n_e \rangle = 2\ 10^{19}$ m^{-3}, V_l = .25 V at t = 6 s. Except for the 1st harmonic that has been truncated, the general shape is dominated by the downshifted 2nd harmonic emission. The main features observed over a wide range of parameters are :

. The non thermal 2nd harmonic intensity increases with the RF power coupled to the plasma but it is rather insensitive to changes in the parallel index $n_{//}$ of the launched waves related to the maximum energy of the electrons.

. The position of the non thermal peak is independent of the RF power and surprisingly also of $n_{//}$. Moreover it is independent of the Michelson view.

. The peak width is insensitive to the line of sight, the $n_{//}$ of the waves and the RF power. It is mainly determined by the plasma density. At relatively high densities ($\langle n_e \rangle > 2\ 10^{19}$ m^{-3}), the

three non thermal peaks visible on M_{Rs}, $M_{\perp}$ and M_{Bs} have a very similar shape. The peaks are asymmetric with a maximum value rather in the high frequency part of the peak. Below $\langle n_e \rangle = 2\ 10^{19}\ m^{-3}$, the latter peak is enriched with a bump in its low frequency part.

The density dependence of the suprathermal peak is essentially due to the presence of the upper cut-off between the first two harmonics, as checked by ray-tracing calculations. Thus the width of the peak is not associated with the energy extent of the electron tail.

The lack of a significant asymmetry between the two Doppler views can be understood by considering, rather than the single-particle resonance (Eq. (1)), the collective resonance velocity, i.e., the electron velocity where the emission is maximum [2]. For the 2nd harmonic down-shifted peak of fig.2, we find typically $v_{\perp} \geq v_{//}$. On the other hand, the non-thermal emission originates from the spatial region where the LH waves are absorbed, namely $r \geq a/3$ for typical Tore Supra discharges. In such regions a significant trapped electron population is present, hence for $v_{\perp} \geq v_{//}$ the distribution function is nearly symmetric in $v_{//}$. Detailed Fokker-Planck calculations confirm this simple picture, as it appears from fig. 3, where a computed distribution function is shown, together with the region in velocity space from where 80 % of the non-thermal emission originates.

3. Ohmic plasmas

The typical spectra measured during the Ohmic phase are shown in fig.4 for a stationary plasma of parameters $B_T = 3.85$ T, $I_p = 1.2$ MA, $\langle n_e \rangle = 2.\ 10^{19}\ m^{-3}$, $V_l = .85$ V at t = 6 s. The general tendencies resulting from a statistical study using more than 20 different toroidal magnetic fields between 3 and 3.9 T with plasma currents of .5 to 1.8 MA and average densities in the range 1-3 $10^{19}\ m^{-3}$ are :

. A good agreement within the error bars between the 3 intensities in the low frequency part of the 2nd cyclotron harmonic (the 3 Michelson have been absolutely calibrated separately using the same black body source installed *in situ*).

. A significative enhancement ($\Delta T_{rad}/T_e > 10$ %) for the blue shifted view in the high frequency part of the 2nd cyclotron harmonic.

. A lower intensity of the two Doppler views in the 3rd cyclotron harmonic region.

The last point can be easily interpreted. In the case of optically thin harmonics, the optical depth of the resonance layer is increased because of the wall reflectivity. For a perpendicular line of sight with walls face to face, the resulting intensity is expected closer to the black body level than for oblique views for which the total optical depth is lower.

In order to account for the two first points, it is necessary to assume a small anisotropy in the electron distribution function. From eq. (1), the curve $\omega = 2\omega_c$ corresponding to the optically thick resonance is plotted in the $(\beta_{//}, \beta_{\perp})$ plane where $\beta = v / c$ (fig.5). Non thermal electrons located above the curve, i.e in the downshifted region, are not visible from the outside since their radiation is reabsorbed by the bulk 2nd harmonic resonance. Conversely the upshifted region is directly observed by the receiving antenna. At this point, it is important to notice that the angle θ between $\vec{k}$ and the toroidal direction is a function of the major radius coordinate R because of the magnetic field lines curvature. Experimentally, we find that the Bs spectrum is significantly higher than the perpendicular spectrum for frequencies corresponding to major radius $R_0 - a_p < R < R_l = R_0 + .15$ m (R_0 and a_p are respectively the plasma major and minor radii). The resonance curves for these two limiting radii are shown in fig.5. The observed enhancement is then compatible with non thermal electrons located in the area between these two resonance curves, i.e., the grey area of fig.5. Indeed, the emission of such electrons is visible (i.e. in the upshifted region) for all radii $R_0 - a_p < R < R_l$ and reabsorbed (i.e. in the downshifted region) for all radii $R_l < R < R_0 + a_p$.

Various mechanisms able to produce such anisotropies have been investigated :

. First of all, we eliminated the natural Doppler broadening $\Delta\omega/\omega = 3$ % of the line since it would have produced the same effect on M_{Bs} as on M_{Rs}. The same remark holds for propagation or polarisation effects associated with lines of sight not perpendicular to the magnetic field. In this case, one expect slight deviations from the standard pure X and O propagation modes of the same order for the two oblique views.

. The frequency shift $\Delta\omega/\omega = .05$ % associated with the plasma current is negligible and far below the Michelson instrumental resolution (10 GHz).

. The runaway production rate has been evaluated both in the ramp-up and during the stationary phase for various experimental situations. It cannot account for more than a few eV on M_{Bs}.

. We have then considered hot electrons present in the plasma center and accelerated during sawteeth crashes /3/. Indeed, reconnection, if present, could generate current density singularities associated with very intense local electric fields. However, the expected effect would be in the opposite direction.

. It is also possible to invoke anomalous diffusion generated by magnetic fluctuations combined with the inductive electric field /4/. The diffusion coefficient proportional to $(\delta B/B)^2\, 2\pi R\, |v_{//}|$ could account for diffusion of hot electrons from the plasma core to outer regions of the plasma. However, 3D Fokker-Planck simulation including radial diffusion due to magnetic turbulence /5/ show that such electrons are not evidenced by ECE measurements and cannot account for the ΔT_{rad} observed.

. We must actually turn to mechanisms able to produce high perpendicular velocities at midly suprathermal energies. Detrapping of banana particles is indeed a good candidate to explain the anisotropy as shown on fig 5. Such electrons (10-30 keV) at the limit of the trapped-detrapped region, originates the bootstrap current by transfering their parallel momentum to the circulating particles. A recent study of the bootstrap current scaling in tokamaks leads to /6/ :

$$\frac{I_{boot}}{I_p} = \sqrt{\varepsilon}\,\beta_p\, F$$

where ε is the inverse aspect ratio, β_p the poloidal beta and F a shaping factor taking into account the peaking of both the pressure and the current density profiles. The fig. 6 represents $\Delta T_{rad} / T_e$ observed at intermediate radius on M_{Bs} as a function of β_p for a wide range of parameters. It is noticeable that high β_p values have been obtained during LHCD experiments. One has now to be sure that the observed anisotropy is not affected by non thermal electrons generated by the RF power. Although the ECE calculation code would credit the interpretation involving high perpendicular velocities, fig.6 should be completed with high β_p ICRH experiments. Another direct validation of the proposed mechanism would consist in reversing the plasma current direction which unfortunately cannot be achieved on TORE SUPRA. Quantitative estimation of ΔT_{rad} associated with electrons in the range 10-30 keV is being investigated. For a next work, we plan to introduce kinetic effects of such electrons in the Fokker-Planck equation in order to account for the observed spectral intensities.

/1/ L.RODRIGUEZ et al., Cont. Fusion and Plasma Phys. (Berlin 1991) 15c,IV,353
/2/ I. FIDONE and G. GIRUZZI, Nucl. Fus. 30 (1990) 803.
/3/ L.PORTE et al. , Cont. Fusion and Plasma Phys. (Berlin 1991) 15c,IV,357
/4/ J.E.RICE et al. , Phys. Rev. A25 (1982) 1645.
/5/ G.GIRUZZI et al. , Report EUR-CEA FC-1440 (1991) Nucl. Fus. to be published.
/6/ H.R.WILSON Nucl. Fus. 32 (1992) 257

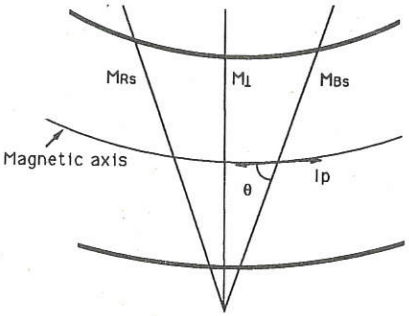

Fig.1: Michelson views in the equatorial plane (top view).

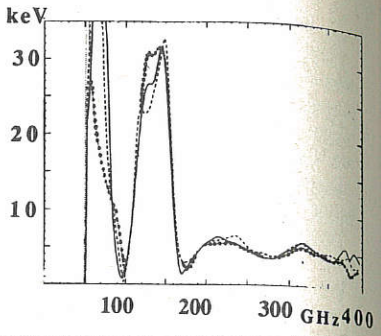

Fig.2: Michelson spectra during a LHCD assisted discharge. $M_{\perp}$: solid line. M_{Rs}: dots. M_{Bs} : dashed line.

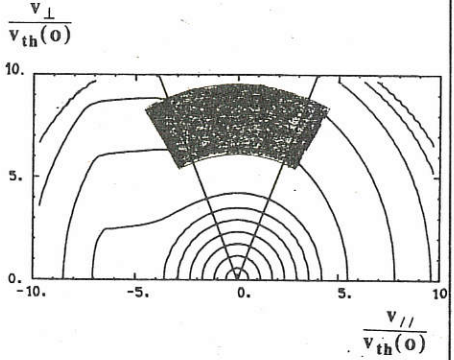

Fig.3: Fokker Planck calculation of the electron distribution function. The shaded region represents more than 80% of the measured ECE.

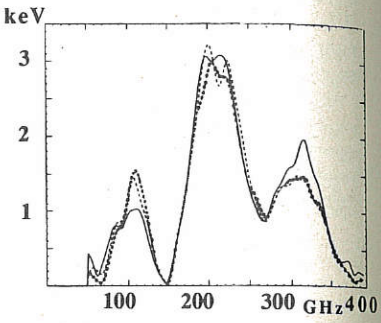

Fig.4: Michelson spectra during an Ohmic discharge. $M_{\perp}$: solid line. M_{Rs} : dots. M_{Bs}: dashed line.

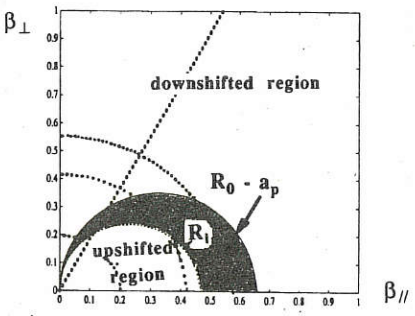

Fig.5: $\omega = 2\omega_c$ resonance in the $(\beta_{//},\beta_{\perp})$ plane. Dots correspond to energies of 10,50,100 keV. Circles : trapping limit at half plasma radius.

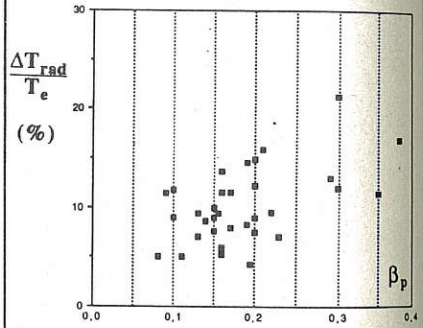

Fig.6: Anisotropy measured on M_{Bs} at half plasma radius in function of β_p.

FIRST ELECTRON CYCLOTRON EMISSION AND ELECTRON TEMPERATURE PROFILE MEASUREMENTS ON ASDEX UPGRADE

N.A. Salmon and A. Eberhagen

Max-Planck-Institut für Plasmaphysik, EURATOM Association,
D-8046 Garching, Germany

Abstract

The first results of electron cyclotron emission measurements from the ASDEX Upgrade tokamak are presented together with an overview of the diagnostic measurement capability. The measurements have been made with a Michelson interferometer and constitute the first electron temperature profile measurements of ASDEX Upgrade plasmas. A grating monochromator system and a heterodyne radiometer system are also described.

Diagnostic Overview

The cyclotron emission diagnostic system on ASDEX-Upgrade consists of a Michelson interferometer, an 8 channel grating monochromator and a 16 channel heterodyne radiometer. These instruments are located outside the tokamak biological shield. Signals are transmitted from the plasma to these instruments via an antenna system and a waveguide transmission bundle.

Antenna System and Waveguide Transmission System

The diagnostic antenna uses an imaging system to view the plasma radially in the tokamak mid-plane. It uses a TPX lens of diameter 270 mm and focal length 1000 mm to image emission from the plasma onto the entrance of a waveguide transmission bundle. The lens is mounted in a chassis which can be moved vertically enabling the diagnostics to view always through the plasma centre. Immediately prior to the entrance of the waveguide transmission bundle exists a linear polariser that is used to select either the ordinary (o) or extra-ordinary (e) mode radiation from the plasma. The waveguide transmission bundle is 25 m in length and consists of 12 circular cross-section waveguides each having a diameter of 50 mm. The antenna system excites in each of the transmission waveguides the TE_{11} mode.

The Michelson Interferometer

Using Fourier transform spectroscopy, the Michelson interferometer is used to measure the emission spectrum from the first to the fifth harmonic of the electron cyclotron frequency. These measurements can be used in the analysis of the non-maxwellien plasmas generated during electron cyclotron resonance heating or low density operation. Also, using the second harmonic portion of the e-mode emission spectrum the electron temperature profile from the ASDEX-Upgrade plasma is obtained.

The Michelson interferometer uses a roof top mirror architecture [1] and an InSb hot electron bolometer detector. In a time of 15 ms the scanning mirror can traverse a distance of 15 mm giving the instrument a frequency resolution of 10 GHz. Together

with the detector and the transmission waveguide the instrument has a spectral response from 50 to 800 GHz. On a normal aspect ratio ($R_o/a \sim 3.3$) plasma this enables measurements of the second harmonic emission from the plasma to be made from a major radius of 1.43 m out to the low field edge region. The spatial resolution of these measurements is ~12 cm.

The complete instrument, including antenna and transmission waveguide, is calibrated using large area black body thermal sources at temperatures of liquid nitrogen and room temperature. As it is not possible to place these calibration sources inside the tokamak vacuum vessel they are placed directly in front of a dummy optical imaging system which lies adjacent to the torus. In order to obtain the necessary signal to noise ratio in the calibration some 10^6 interferograms are added together coherently. The time taken to acquire such an amount of data from the Michelson interferometer is ~20 hours.

To date the Michelson interferometer has been used to measure the e-mode emission spectra on ohmically heated plasmas. Two typical spectra from an inner limiter plasma are shown in figure 1. The first spectrum is taken at the beginning of the current ramp phase and the second is taken in the flat top phase. In both cases emission into the second and third harmonics can be seen. As the optical depth in the second harmonic is larger than that in the third harmonic (~8.9 and ~0.06 respectively for the flat top case) the emission in the second harmonic is dominant. The localisation measurement capability of the instrument can be demonstrated by an experiment in which the outer boundary of the plasma was moved to smaller major radii. In this experiment the magnetic diagnostics and the function parameterisation technique [2] indicated that the centre of the plasma moved from 1.55 to 1.3 m. These measurements are in good agreement with the measured temperature profile changes during this phase as shown in figure 2.

The 8 Channel Monochromator

The 8 channel monochromator system is used for measurement of the second harmonic e-mode emission from the plasma. These measurements provide the electron temperature profiles which are used in the analysis of heat pulse propagation and the effects of MHD activity.

The 8 channel monochromator system uses the automatic blaze control architecture [3]. This is basically an architecture which enables the frequency of the diffraction mode to be changed while maintaining the system under blazed conditions. This configuration maximises the grating efficiency over a wide range of frequencies. The system has a minimum detectable temperature variation of 10 eV with a signal bandwidth of 30 kHz. The system has a spectral response from 91 to 362 GHz and a frequency resolution of 4 GHz. Measuring the second harmonic emission the system is capable of measuring temperatures from a major radius of 1.43 to 2.05 m with a spatial resolution of between 3 and 6 cm on plasmas that have central toroidal fields of 2.1 to 3.5 T. The 8 channel system consists of two separate 4 channel grating instruments. Each grating instrument has a radial coverage of ~27 cm in the plasma the radial location of which can be varied independently. Each individual channel uses a single waveguide of the waveguide transmission bundle.

The system can be calibrated independently using a standard klystron or cross-

calibrated with the Michelson interferometer using the plasma as a radiation source.

The 16 Channel Radiometer

The 16 channel radiometer is designed for measurements of temperature in the edge region of the plasma and is similar to that described in [4]. Such measurements are to be used in the analysis of H-mode and associated edge phenomena. It is also envisaged that as this instrument is capable of very localised measurements it should be suitable for studying the propagation of stimulated heat waves [5].

The radiometer uses 3 GaAs heterodyne mixers and 2 GaAs subharmonic mixers to mix down emission in a band from 43.6 to 187.1 GHz into an intermediate frequency (IF) band. At any one time only one mixer is used and radiation is directed onto this mixer by a network of waveguide switches. The IF bandwidth of the system varies from 6.5 to 17 GHz; the precise bandwidth being dependent on the mixer used. Signals in the IF band are amplified and divided into several channels by power splitters. To spectrally resolve signals in the IF band there exists in each channel a bandpass filter with a different centre frequency. Two sets of bandpass filters are used, one with passbands of 250 MHz (for plasmas with central fields of 1 to 2.5 T) and the other with passbands of 500 MHz (for 2.5 to 3.8 T plasmas). This provides the system with 16 radial viewing channels each spaced 1 cm apart and having a radial resolution of 1 to 2 cm. The signals from the bandpass filters then enter Schottky barrier diodes and are amplified and low pass filtered. The system has a time response of 10 μs and a minimum detectable temperature variation limited by statistical photon fluctuations [4] of a few electron volts.

The radiometer, including waveguide transmission and dummy imaging system is calibrated using large area low temperature thermal sources.

References

[1] Costly, A.E. et al., 'First Measurements of ECE from JET', Proc. EC-4 Fourth International Workshop on Electron Cyclotron Emission and Electron Cyclotron Resonance Heating, Rome, (1984), p1.

[2] McCarthy, P.S., Schneider, W., et al., 'Magnetic Identification on ASDEX Upgrade', this conference.

[3] Eberhagen, A. et al., 'ECE-Diagnostics of the ASDEX-Tokamak Plasmas', Proc. EC-4 Fourth International Workshop on Electron Cyclotron Emission and Electron Cyclotron Resonance Heating, Rome, (1984), p115.

[4] Salmon, N.A., Ph.D. thesis, University of London, (1990).

[5] Wilhelm, R., Max Planck Institute for Plasma Physics, Garching, Private communication, Jan. (1991).

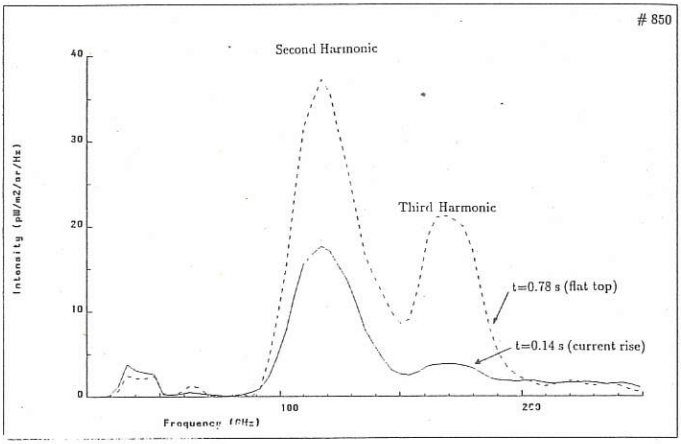

Figure 1 Extra-ordinary mode electron cyclotron emission from a typical 2.0 T central field, inner limiter, ASDEX-Upgrade plasma.

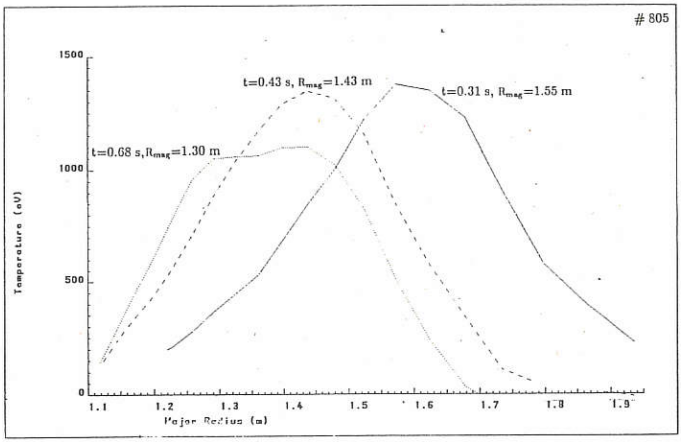

Figure 2 Electron temperature profiles during plasma movement. The magnetic centre of the plasma estimated by function parameterisation is shown for each time slice.

THE HEAVY ION BEAM DIAGNOSTIC FOR THE TOKAMAK ISTTOK

J.A.C. Cabral, A. Malaquias, A. Praxedes, W. van Toledo,
C.A.F. Varandas and J.M. Dias
Association EURATOM/IST, Centro de Fusão Nuclear
Instituto Superior Técnico, 1096 Lisboa Codex, Portugal

The heavy ion beam diagnostic (HIBD) has proven to be a powerful non-perturbing tool for studying basic plasma parameters, such as the electron density (n_e) and temperature (T_e), the poloidal magnetic field (B_p) and the plasma potential (ϕ) [1]. The method is based on time, space and energy resolved detection of secondary particles, generated by electron impact ionisation of a high-energy ion beam which is injected into the plasma. In this way information on the plasma state at the different ionisation points is obtained. The purpose of the present diagnostic is to measure in ISTTOK ($a = 0.085m, R = 0.46\ m, B_t \simeq 0.5T,\ T_e(0) \simeq 150eV, n_e(0) \simeq 5 \times 10^{18}\ m^{-3}, I_p \simeq 6kA$) the profiles of n_e, B_p and ϕ. From poloidal field measurements information on the current density profile (j) can be obtained. Furthermore, fluctuation analysis of the signals will be undertaken to obtain a better understanding of particle and heat transport mechanisms.

The HIBD is composed of the ion gun (ion source, accelerator and deflection plates) and a multiple-cell detector. The ion gun is being developed at AEA Fusion in Culham, in cooperation with CFN, while the detector and the data acquisition system are being designed at CFN. From the ion source a $1\mu A$ 20 keV Cs^+ beam will be injected into the tokamak vessel, perpendicularly to toroidal direction. By means of the deflection plates the angle by which the primary beam is injected into the plasma, can be varied over 5°. To obtain a good spatial resolution, the source will provide a very thin beam ($d < 0.5\ mm$) with a divergence of less than 5 mrad.

For a given initial ion energy and injection angle, the code calculates the ion trajectories, as shown in Fig. 1, by an iterative procedure, which is based on an analytical solution for the equation of motion in three dimensions, $(m/q)\ d\vec{v}/dt = \vec{E} + \vec{v} \times \vec{B}$. Unless otherwise stated, this code assumes parabolic profiles for n_e, T_e, j and ϕ in the core plasma inside the limiter radius, and a constant T_e and linearly decaying n_e and ϕ in the edge plasma. Furthermore, the code uses a realistic magnetic field configuration ($B_t, B_{p,int}$). The differently charged primary and secondary particles undergo separation by the magnetic field as they pass through the plasma. The points of ionisation from which the secondary beams emerge were equidistantly chosen.

In Figs 2a, 3a, 4a the secondary particle intensity along the vertical (y) axis of the detector plate, is calculated for various plasma conditions. In Figs 2b, 3b, 4b the particle distribution over the detector surface is shown. We have assumed a continuous multiple-cell detector which collects the doubly charged cesium ions created along the

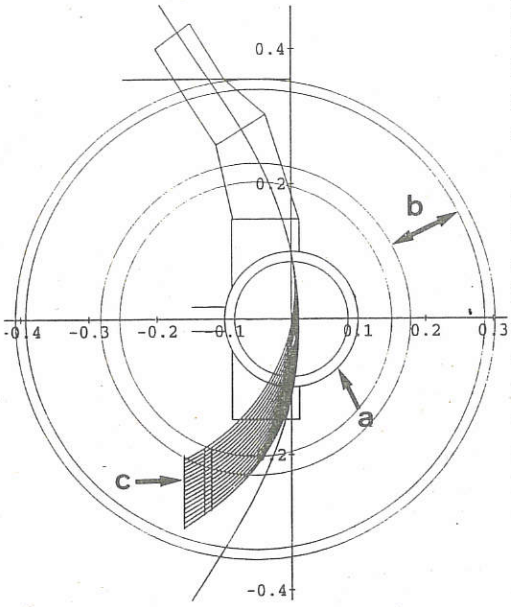

Fig. 1 - Situation and ion beam trajectories. (a) liner, (b) toroidal field coil, (c) multiple-cell detector.

entire flight path of the primary beam. The detector is mounted in the y-z plane at $x = -16$ *cm*. The toroidal axis is along z. From Figs 2b, 3b, 4b it can be seen that the detector area must be at least equal to $150 \times 10\ mm^2$.

The advantage of using a continous array is that entire profiles of n_e, ϕ and B_p can readily be measured, while, doing fluctuation analysis, a more realistic k-spectrum is obtained than with other detection techniques [2]. The size of the single detector plates determines the sample volumes, and, hence, the spatial resolution. The finite beam width has been neglected in the simulations.

For given primary beam current I_{in} the expected secondary beam intensity on the j-th detector cell can be calculated from

$$I_j = 2I_{in} \underbrace{\exp(-\int_{R_i}^{rj} n_e\,(s_1)\,\sigma_{12}\,ds_1)}_{A}\; n_e\,(r_j)\,\sigma_{12}\,dl\; \underbrace{\left(\exp(-\int_{rj}^{R_o} n_e\,(s_2)\,\sigma_{23}\,ds_2)\right)}_{B} \quad (1)$$

The points of injection, ionisation and exit from the plasma are given by R_i, r_j, and R_o, respectively. The ionisation cross sections are denoted by σ_{12} and σ_{23}. The factor A determines the attenuation of the primary beam as it passes through the plasma from the injection point R_i to the point of ionisation, r_j. The factor B determines the attenuation of the secondary beam. Since $\sigma_{23} < \sigma_{12}$, this factor was not taken into account in the calculations presented in this paper. More refined calculations, which include factor B, will be presented at the conference. The factor 2 arises from the double charge of the secondary particles. The lenght of the sample volume is dl.

In Fig. 2a the secondary beam intensity is shown for various electron densities. As is expected from Eq. (1), the detector signal is approximately proportional to the density. For large densities, an asymmetry is observed, due to the primary beam attenuation. The secondary particle distribution over the detector area, is not affected (Fig. 2b). From the intensity curve the density profile can theoretically be retrieved.

In Fig. 3a we present the beam intensity for several electron temperatures. As can be seen, this intensity does not remain constant. A change in T_e will modify the value of the ionisation cross section, especially in the temperature range expected for ISTTOK ($50 \simeq T_e \simeq 200\ eV$). From Fig. 3b it can be observed that a change in temperature (here from 100 to 300 eV) causes the spatial distribution to shift slightly into y direction, (some 2 mm) due to a change in the plasma potential, which we assumed to be given by $\phi(0) = -1.5k\ T_e$. A spatial detector resolution of 0.1 mm, corresponding to about 15 Volt, is feasible. However, poloidal field fluctuations with $\tilde{B}_p/B_p > 0.2\%$, resulting in an apparent vertical shift of the same magnitude, might hamper the interpretation of this vertical shift. Therefore direct energy analysis of the secondary particles is necessary to obtain clear potential measurements. This will require an adaptation of the detector presented here.

The influence of the plasma current on the detector signal, was also investigated. A change of the current does not affect the intensities (Fig. 4a), but gives an appreciable shift along toroidal direction (Fig. 4b). This shift is almost proportional to the plasma current. To determine the current density profile a more detailed modeling is necessary.

The HIBD can also be used to observe changes in the current profile as well as in the plasma column position. These changes are expected to occur for instance when electron cyclotron current drive will be applied in a later stage. Several current profile were chosen to simulate shifts and deformations of the normal parabolic one. It was found that a shift of the plasma column leads to a considerable change of the toroidal position of the secondary particles on the detector plate, due to the associated change in the poloidal field structure. Deformation of the parabolic current profile into a hollow profile is seen to have only a minor effect on the toroidal position. Results will be presented at the conference. More complex cases are being studied at present.

In the future, we expect to do, while covering the entire duration of a single discharge (20 ms), some 25 simultaneous profile measurements of n_e, ϕ and B_p. The signals will be sampled with a 1 MHz rate and a bandwidth of 300 kHz in order to permit the evaluation of MHD mode levels and analysis of particle transport phenomena. To make a rapid data analysis and recursion to the required plasma parameters possible, the trajectory simulation code will be used to set up an extended data base for fast profile determination, based on function parametrisation.

[1] - T.P. Crowley et al., Rev. Sci. Instrum. 61, 2989 (1990).
[2] - D.W. Ross et al., Nuclear Fusion 31, 1355 (1991).

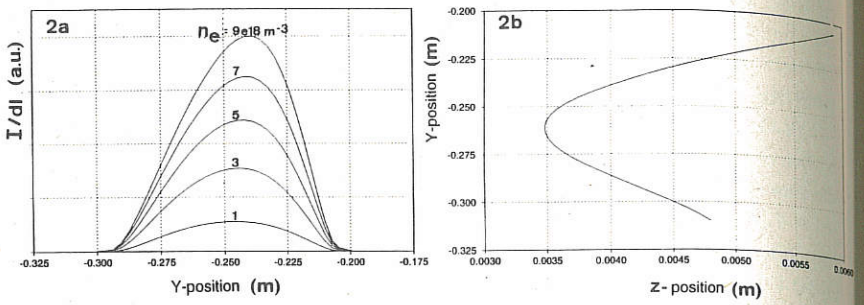

Fig. 2 - The influence of the electron density on the collector signal ($T_e = 200\ eV$; $I_p = 8kA$).

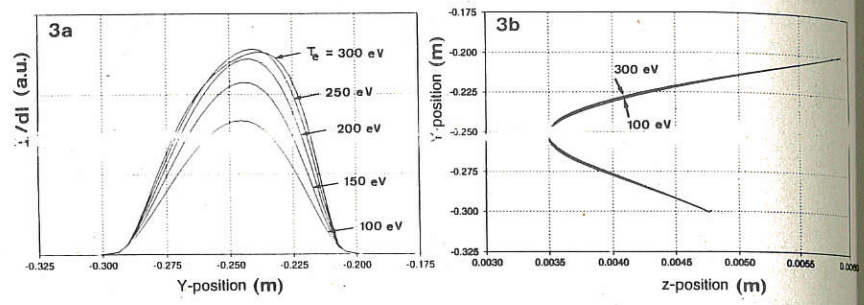

Fig. 3 - The influence of the electron temperature on the collector signal ($n_e = 5{\times}10^{18} m^{-3}$; $I_p = 8kA$).

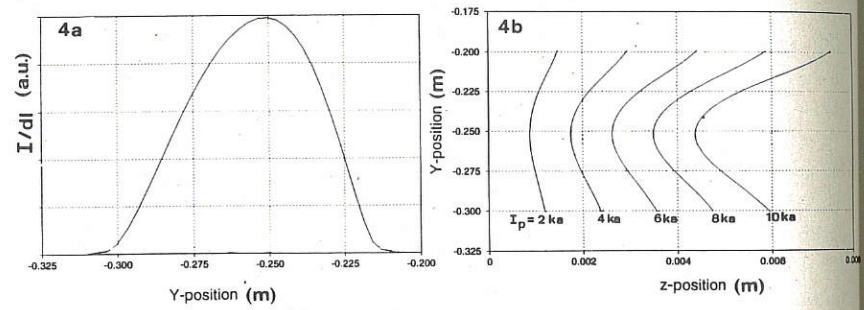

Fig. 4 - The influence of the plasma current on the collector signal ($n_e = 5 \times 10^{18} m^{-3}$; $T_e = 200\ eV$).

DEVELOPMENT OF BOXCAR IMAGING SYSTEM FOR VISUALIZING MAGNETIC FIELD STRUCTURE IN TOKAMAK PLASMA

S. Sakurai, N. Ohno and S. Takamura
Department of Electrical Engineering, Faculty of Engineering, Nagoya University,
Furo-cho, Chikusa-ku, Nagoya 464-01, Japan

INTRODUCTION : Magnetic field line structure has great effects on plasma confinement. Its imaging in tokamak confinement devices is useful to research fundamental physics of plasma transport. In a stellarator-type device, various electron beam probing methods have been generally used for mapping the magnetic surfaces, but in vacuum condition /1,2,3/. On the contrary, only the electron beam probing method by using a movable Faraday cup for beam detection was performed in the tokamak-type device /4/. We've developed an imaging system of puncture patterns of toroidally circulating electron beam on a poloidal plane so that we may know drift surfaces (≈ magnetic surfaces) and diffusion processes of test electron cloud. This instrumentation with a good spatial resolution, less than a few mm, consists of three techniques: (1) electron beam detection by scanning a fluorescent rod; (2) boxcar imaging with a high repetitive tokamak discharge /5/; (3) appropriate shuttering of fluorescent light from the rod, avoiding the strong plasma radiation. The distortion of drift orbits by an error field has been observed, which mainly comes from a toroidal magnetic field coil current. Puncture points of electron beam on the poloidal plane were found to be much diffused than might be expected from classical collisional processes.

EXPERIMENTAL ARRANGEMENT : The experimental arrangement in CSTN-III shown schematically in Fig. 1 consists of an electron gun, a fluorescent rod, an imaging system and a trigger controller. CSTN-III is a small research tokamak of major radius 40 cm, minor radius 10.3 cm, toroidal magnetic field < 0.1 T, plasma current < 1 kA. Pulse electron beam (pulse width < 100 μs) emitted by a movable electron gun is detected by a fluorescent rod located at 90° toroidally away from the gun. Fluorescent light from the rod excited by the electron impact is detected by an image-intensified CCD camera that views the poloidal cross section through a tangential port. Since the CSTN-III discharge can be reproducibly pulsed, an image of fluorescent light on the poloidal cross section can be reconstructed from pictures of fluorescent rod scanning across the poloidal cross section. The triggering of the electron gun and the camera is synchronized to the tokamak discharge. An image taken by the ICCD camera is digitized to 8 bits by the image processor. CSTN-III tokamak is operated in the high repetition rate of 10 Hz, we can integrate image data at each positions of fluorescent rod and average them over several tens of discharge to obtain puncture patterns on the poloidal cross section. The fluorescence has a decay time longer than the discharge duration (< 2 ms). To avoid a strong plasma radiation, the ICCD camera is triggered a few ms after the end of each

discharge. The fluorescent rod is excited and emits light by not only the bombardment of test electrons but also the plasma radiation. The excitation by bulk plasma electrons is negligible because the electron temperature (< 10 eV) is much lower than the minimum excitation energy of fluorescence. Therefore, to suppress the excitation by plasma radiation is crucial for successful detection of test electron beam. In order to minimize such an effect, fluorescent substance P-27 (Zn_3 $(PO_4)_2$: Mn) and Ar plasma was usually chosen. An U-shape shield plate was attached to the fluorescent rod to screen out the short wavelength photon from the plasma. Furthermore, electron beam profile with low S/N can be obtained by electron beam by subtracting the integrated image data with electron beam from those without electron beam. Thus, the instrumentation has a good spatial resolution of about 0.5 mm, and can give a puncture pattern of electron beam on the poloidal cross section in a few minutes.

RESULTS : Orbits of toroidal drift without tokamak plasma in a simple toroidal magnetic field are shown in Fig. 2 (a). The electron gun was located at X= -1,3,5,7 cm and Y= 3 cm on the poloidal cross section. The background pressure was about $1x10^{-6}$ Torr. The electron beam was drawn out through a 2-mm aperture by the bias voltage of 500 V. Electron orbits was found to be deviated from a vertical line to the outward as going downward and the deviation depends on the intensity of toroidal magnetic field. Comparing observed orbits with those calculated by an electron orbit tracing code, we concluded that the error field in horizontal direction was about 0.9 gauss in the toroidal magnetic field of 0.1 T. Drift orbits with the compensation of horizontal magnetic field coil is shown in Fig. 2 (b). The electron gun was located at X= 0,4,6,8 cm and Y= 3 cm on the poloidal cross section.

Typical puncture pattern of electron beam in the tokamak plasma is shown in Fig. 3, when the plasma current I_p = 800 A and the electron beam energy is 600 eV. A position of plasma column measured by magnetic probes was 1.5-cm outside from the center of poloidal cross section. A very clear image of electron drift surface has been observed in the present system. In order to detect the fluorescent light by electron beam excitation when the plasma current and the radiation were strong, a higher acceleration voltage will be necessary to enhance the fluorescent light emission and distinguish its light from that excited by the plasma radiation. Such a high energy acceleration makes drift surfaces of electron beam shift inside about 1 cm from the center of plasma current and therefore the magnetic surfaces.

The profiles of rotational transform of electron beam were also measured by moving the electron gun in a series of different position of minor radius to calculate the q profile. It was found to have a peeked profile when the plasma current and the toroidal magnetic field were strong.

The number of toroidal rotation of electron beam was observed about up to only 10 turns. It was very small numbers as compared to that based on the relaxation time of a classical collision. It is considered to be attributed to the electron beam scattering due to the possible magnetic fluctuation.

ACKNOWLEDGEMENT The authors would like to thank M. Mori, M. Takagi, S. Sasaki, Y. Yamakawa, K. Ohshima, E. Kimura and T. Katoh for their technical contributions. This work was supported by Ministry of Education, Science and Culture, through a grant-in-aid for scientific research (No. 03780005).

/1/ R. J. Colchin, F. S. B. Anderson et al., Rev. Sci. Instrum. **60**, 2680 (1989).
/2/ H. Yamada, K. Matsuoka, S. Okamura, K. Ida et al., Rev. Sci. Instrum. **61**, 686 (1990).
/3/ T. Y. Tou, B. D. Blackwell, L. E. Sharp, Rev. Sci. Instrum. **62**, 1149 (1991).
/4/ S. Takamura, N. Ohnishi et al., Phys. Rev. Lett. **56**, 2044 (1986)
/5/ G. J. Greene, G. Cutsogeorge and M. Ono, Rev. Sci. Instrum. **60**, 2690 (1989).

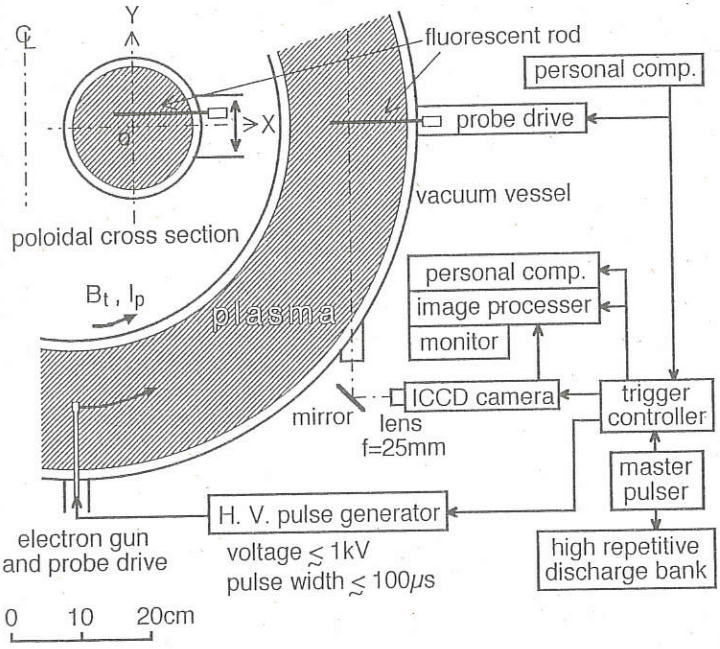

Fig 1: Schematic of experimental apparatus.

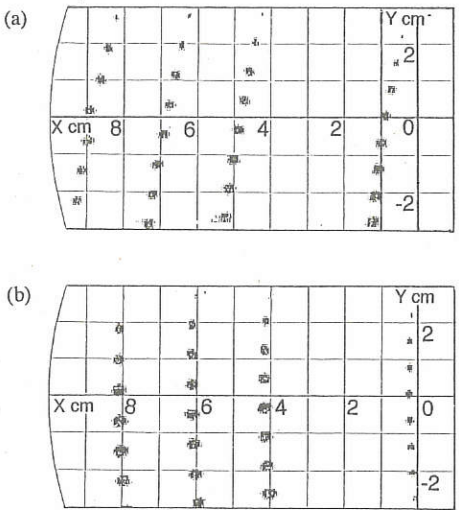

Fig. 2: Electron drift orbits in a simple toroidal magnetic field.
toroidal magnetic field Bt = 0.087 T, beam acceleration voltage Va = 500 V.
(a) before correcting the error field,
the electron gun was located at X = -1,3,5,7 cm, Y = 3 cm.
(b) with the correction of error field,
the electron gun was located at X = 0,4,6,8 cm, Y = 3 cm.

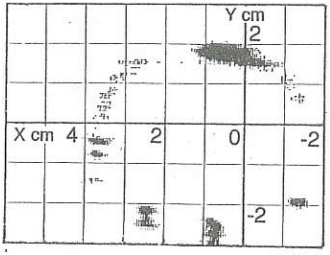

Fig. 3: Typical electron drift surface in a tokamak configuration.
plasma current Ip = 800 A, toroidal magnetic field Bt = 0.1T,
beam acceleration voltage Va = 600 V, plasma position Δ X = 1.5 cm,
the electron gun was located at X = 4 cm, Y = 0 cm.

Statistical analysis of luminescence signals observed during pellet injection.

J.Baldzuhn, W7AS - Team

Max-Planck-Institut für Plasmaphysik, EURATOM Association,
D - 8046 Garching, Fed. Rep. Germany

INTRODUCTION.

We report on a comparative study of luminescence signals measured during pellet injection into two plasma experiments, the stellarator Wendelstein W7-AS and the tokamak ASDEX. The first is characterized by low shear, while the second has shear typical for a tokamak. The luminescence signal shows strong oscillations. Two models, which could describe this phenomenon, are discussed.
The first model states that the thermal flux onto the pellet´s surface during its flight depends mainly on rational 1/q - values. On magnetic surfaces with rational 1/q, thermal flux and ablation rate are low, the luminescence signal should show a minimum.
The second model states a self-shielding of the pellet by its own ablated material, which reduces the heat flux. In this case, oscillations are mainly caused by thermodynamic effects during ablation.
Fast-Fourier-Calculations (FFT) are performed to find common frequency contributions in the luminescence signals. Additionally, several cross correlation techniques are used to investigate the role of plasma parameters as well as the value of 1/q for these oscillations.

EXPERIMENTAL AND NUMERICAL.

Deuterium pellets are injected into magnetically confined plasma discharges. Each pellet contains about $5 * 10^{19}$ atoms and has a velocity of about 600 m/s. During ablation of the pellet in the plasma, the luminescence signal is observed by means of fast photodiodes. The resulting signals are digitized and thus made available to numerical calculations /1/. We compare photographs of the ablation cloud with the registered signals. Then we try to locate rational values on the photograph and in the luminescence signals.
The luminescence signals are Fourier-transformed, and a number of transformed signals for different pellets is superposed to evaluate common frequency contributions.
Furthermore, we calculate the Cross-Correlation function for pairs of luminescence signals of different pellets. Then we evaluate the integral over a certain frequency interval in the frequency power spectrum of these Cross-Correlation function. The limits of the frequency interval are chosen such that strong common contributions from both signals lie within it.
Finally, a number of integral values is compared with mean plasma parameters for the corresponding pairs of events by means of a linear regression analysis. To test for statistical relevance of the regression, most probable limits for the linear relation are calculated by means of a 95% F-Distribution test.
Mean values of plasma parameters are taken into account as well as differences between them to find out whether two luminescence signals are ´more similar to each other´ when the corresponding difference between the plasma parameters is small.
Due to the fact that the observed parameter ranges are chosen very small, only linear dependencies need to be taken into account. No non-linear relations -as for scaling laws- have to be considered. This makes our numerical calculations extremely easy and allows for quick tests whether there exist statistical dependencies between Cross-correlation data on the one hand and certain plasma parameters on the other. To test for nonlinear relations, ansaetze for scaling laws were made by means of SAS software /2/.

We have chosen the signals of the photodiodes for these investigations, because they can easily be made accessible to numerical calculations, in contrast to photographs, which usually need image processing for evaluation. Additionally, the luminous cloud apparently follows the magnetic field lines, as already observed by the TFR-Group /3/. But this is not the information we search for.

ABLATION MODEL.

We present now a model for the ablation of a pellet as proposed by J. Neuhauser and R. Wunderlich /4/. Further descriptions of related models see /5 - 7/. This model puts emphasis on the description of the ablation as a process, which is controlled by a self-shielding of the pellet by its own, already ablated material, forming a dense and cold cloud surrounding the pellet. This cloud is responsible for a reduced heat flow along the magnetic field lines onto the surface of the pellet, and thus to a reduced ablation rate. Nethertheless, the effectivity of the self-shielding at a given moment is dominated by the ablation rate at an earlier moment, because the ablated material is magnetically captured at the instant when it is ionized, meanwhile the pellet follows its trajectory across the magnetic field lines with constant velocity.

According to this model, the ablation rate $m'(x)$ at a position x in the plasma is given by the expression

$$m'(x) = -f(x)\left(\frac{m(x)}{m_0}\right)^{2/3} \exp\left\{h(x)\int_0^{\rho_0} m'(x-\rho)g(\rho)d\rho\right\} \qquad (1)\,.$$

Here, $f(x)$ is the ablation rate of the unshielded pellet, $h(x)$ is the inverse of a mass unit per unit area which describes the attenuation of the incoming heat flux, $\rho 0$ stands for the ionization radius, $g(\rho)$ is the radial cloud profile. The term $m'(x - \rho)$ in the integral gives the retarded shielding effect on the ablation rate $m'(x)$ at position x.

Numerical and analytical analysis of the above expression lead to the striking feature that the ablation is not smooth, but is much more dominated by oscillations as a result of the non-local self-shielding.

RESULTS.

Luminescence signals are compared with photographs of the corresponding ablation cloud and q-profiles. Nethertheless, no unambiguous relations can be found between dark/bright zones on photographs, dips/peaks in the photoelectric signals and positions of rational q-values in the profiles. This holds for measurements on ASDEX as well as on Wendelstein. The only exception is given for pellet traces at ASDEX for the moment when the $q = 1$ surface is traversed. In some cases this position can be identified in our signals. At Wendelstein, in some examples the magnetic axis can be observed.

Fig. 1 shows, as an example, a photograph of the luminous cloud after pellet injection. The pellet comes from the right and moves to the left. Striations can be observed, which form a pattern of stripes parallel to the magnetic field lines.

Fig. 2 shows the result of a superposition of 31 single Fourier-transform calculations from 31 different pellets, injected into ASDEX. A common frequency contribution around 100kHz ±30kHz can be observed. Similar results with almost equal frequencies are obtained for Wendelstein. The peak at low frequencies is due to a bias on the photoelectric luminescence signals. Comparable frequencies had been observed in other plasma experiments, too /8/.

Fig. 3 shows the correlation between the integral value of the power spectrum of the Cross-correlation function for pairs of pellet injections (ordinate) and the mean q-values at the separatrix (abscissa) for the ASDEX-experiment for a total of 45 different Cross-correlation values. Linear regression as well as most probable limits for linear relation are indicated by linear / curved lines. Here, Cross-correlation data seem to be independent of q. Fig. 4

shows a similar result, but for mean peaking values of the electron density along the abscissa. Here, a linear dependency is given.

DISCUSSION.
Due to low shear at Wendelstein only a small number of rational values can appear, thus making an identification very simple. Nethertheless, it turns out that no unambiguous appointment of rational q-values to minima in the signal can be made. This holds for the photoelectric signals of the luminous cloud as well as for photographs. That shows that the q-profile cannot be determined by this method. This situation is even more complicated for the ASDEX experiment, where a large number of rational q-values is given.
Fourier analysis for a number of pellet events shows common frequency contributions around 100 kHz for both plasma experiments, despite of different q-profiles. This indicates the minor role of rational q-values for the ablation process on the one hand, but is very well consistent with the predictions made by neutral gas shielding models on the other. Taking into account the actual q-profiles and a possible influence of rational values, this frequency should be about a factor of 10 lower for Wendelstein because of the lower shear. But this effect cannot be observed.
Linear regression between Cross-Correlation values and q-values, as well as other plasma parameters like electron density or electron temperature, show that the role of the q-profiles for the luminous cloud is only of secondary importance. Much more, peaking of the electron density profile or the electron temperature seem to be the dominating factors. Nethertheless, certain extremely rational values, as q=1, can influence the luminescence signal to some extent, too.
The shearless stellarator experiment gave us the possibility the clarify the role of rational q-values for the ablation. This helps, in turn, for a better understanding of the oscillations for the ASDEX experiment in terms of the neutral shielding model, too.

ACKNOWLEDGEMENT.
The ASDEX data are provided by the ASDEX-team.

REFERENCES.
/1/ G.A. Wurden, K. Büchl, J. Hofmann, R. Lang, R. Loch, A. Rudij, W.Sandmann: *Rev. Sci. Instrum.*, **61**(11), page 3604, (1990)

/2/ W. Sandmann: Private communication.

/3/ TFR - Group, *Nuclear Fusion*, Vol. **27**, No. 12, page 1975, (1987)

/4/ J. Neuhauser, R. Wunderlich: A Model for Periodic Pellet Ablation in Toroidal Plasma Confinement Experiments, *IPP-Report* **5/30**, (1989)

/5/ L.L. Lengyel: *Phys. Fluids*, **21** , page 1945, (1978)

/6/ M. Kaufmann, K. Lackner, L.L. Lengyel, W. Schneider: *Nucl. Fusion*, **26**, page171, (1986)

/7/ W.A. Houlberg, S.L. Milora, S.E. Attenberger: ORNL / TM - 10556, (1987), Oak Ridge National Laboratory, Oak Ridge, Tennessee

/8/ R.D. Durst: *An Experimental Investigation of the Dynamics of Pellet Ablation on the Texas Experimental Tokamak,* Dissertation, The University of Texas at Austin, (1988)

Fig. 1:

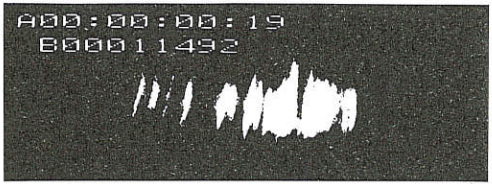

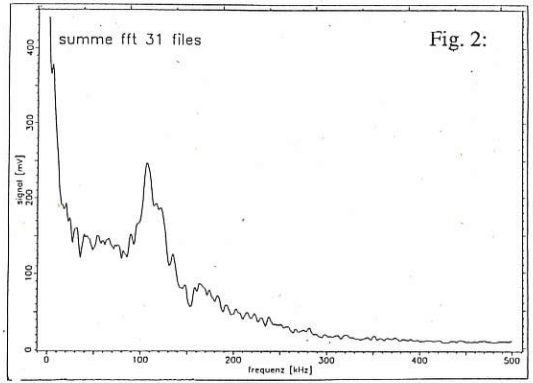

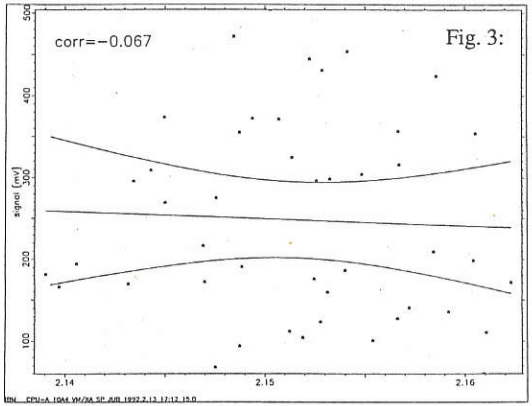

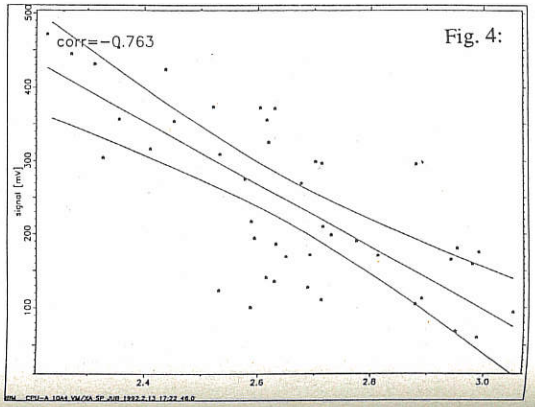

Fig. 1: Photograph of the luminous cloud.
Fig. 2: Mean power spectrum of a number of luminescence signals.
Fig. 3: Cross-correlation between pairs of pellets versus mean q-values.
Fig. 4: Cross-correlation between pairs of pellets versus peaking values of electron density.

Dispersion Interferometer for Controlled Fusion Devices

V.P.Drachev

Institute of Semiconductor Physics, Siberian Branch of the Russian Academy of Sciences, Lavrent'eva 13, 630090 Novosibirsk, Russia

Yu.I.Krasnikov and P.A.Bagryansky

Institute of Nuclear Physics, Siberian Branch of the Russian Academy of Sciences, 630090 Novosibirsk, Russia

1. INTRODUCTION

A common feature in interferometry is the presence of two independent optical channels. Since wave phase in a medium depends on the geometrical path, polarization and radiation frequency, respectively, one can distinguish three types of interferometric schemes when the channels are geometrically separated, or separation occurs in polarizations or radiation frequencies.

Traditionally, interferometers of the first type are used for plasma diagnostics in which the channels have different geometrical paths. This feature causes the basic disadvantage of such schemes - high sensitivity to vibrations. To minimize the influence of vibrations a set of forced measures are taken in traditional interferometers which complicate the diagnostic system to a large extent:

1) use of massive vibration isolation structures[1];

2) higher wavelength of probe radiation $(10.6, 118, 337\mu m)$[2];

3) use of the two-wavelength interferometers with compensation at the shorter wavelength $(0.63, 3.39\mu m)$[3].

Use of long wavelengths is constrained by the influence of refraction since in many modern plasma devices plasma gradient is large. Relatively higher line density $< n_e l >= 10^{14} \div 10^{16} cm^{-2}$ in contemporary plasma devices, in principle, makes it favorable to employ visible and near-infrared radiation where refraction is negligible and interference phase shift is sufficiently large. However, in this region interferometers are greatly subject to the influence of vibrations[2].

We have developed a measurement scheme based on a dispersion interferometer (DI), suggested independently in refs.[4,5], for plasma diagnostics in the experiments on controlled fusion. DI optical channels have the same geometrical path and are separated in radiation frequency. Use of a common optical path causes the main advantage of the DI technique – low sensitivity to vibrations of optical elements.

The use of the DI technique for diagnostics of a laser spark in air[6] and of arc discharges[7,8,9] has shown its essential advantages as compared to classical interferometers. Interest in the DI technique from the viewpoint of its application in controlled fusion devices is determined also generated by the possibility of developing a compact multichannel interferometer not requiring a vibration isolation structure.

2. THE GAS DYNAMIC TRAP

DI has been used on Gas-Dynamic Trap (GDT). The experimental GDT is a device designed to a study the physics of the idea, proposed in[11,12], plasma confinement in an

axisymmetric mirror machine with a large mirror ratio $R >> 1$ and a length exceeding the ion effective mean free path with respect to scattering into the loss cone. The detailed description of the experimental device is given in [13]. Schematic diagram of the device is shown in Fig. 1.

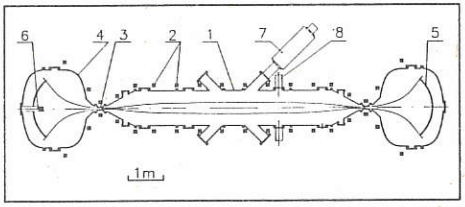

Fig. 1. Schematic diagram of Gas-Dynamic Trap device. (1) Central vacuum chamber; (2) coils of magnetic system; (3) mirror coils; (4) expander vacuum chambers; (5) plasma absorbers; (6) plasma gun; (7) atomic beam injectors; (8) optical axis of dispersion interferometer

The experiment scenario consists of the following sequence of plasma preparation, heating and decay processes. Relatively cold ($\tilde{}10eV$) preliminary plasma is injected into the device from plasma gun located in the expander (Fig.1). The time of plasma gun operation is usually $3ms$. The heating process starts after plasma gun's switching off. Atomic hydrogen beams are injected into the trap from neutral-beam injectors.

Radial density profile is close to a Gaussian one, with a characteristic radial scale length of $6.5cm$ in the midplane of the trap and a maximum on-axis density $n_{emax} = (1 \div 8) \cdot 10^{13} cm^{-2}$.

3. DI ON GAS-DYNAMIC TRAP

The DI in the simplest case consists of two optical frequency doublers between which the object under study is placed. Figure 2 clarifies the principle of its operation.

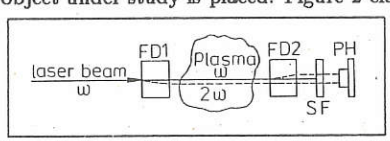

Fig. 2. Principal scheme of the DI: FD – frequency doubler; PH – photodetector; solid line – probe radiation; dashed line – second harmonics radiation.

Probe radiation with frequency ω is partially converted into the second harmonic (SH) in the first doubler, after that two waves with the frequencies ω and 2ω propagate in the medium through the same path. In the second doubler the probe radiation is again converted into SH, and the remaining portion is absorbed by the light filter. Thus, at the photodetector interference is observed between the two waves of SH. One of them is generated in the doubler before, and the other after passing the object. Interference signal from the photodetector $U(\theta)$ has the form:

$$U(\theta) \propto I_{2\omega} = I_1 + I_2 + 2\sqrt{I_1 I_2}\cos\theta \qquad 1$$

where I_1, I_2 are intensities, and θ is the difference of phases of the interacting waves. The phase difference θ is the doubled (due to conversion in the second doubler) phase of the fundamental wave minus that of the SH wave generated in the first doubler:

$$\theta = 2\varphi_1(\omega) - \varphi_2(2\omega) = (2\omega/c)\int_0^l [n(\omega) - n(2\omega)]dl \qquad 2$$

where $n(\omega)$ is refractive index of the medium under study, and integration is performed along the probe beam. Thus, the second DI feature is that the phase difference measured is determined by dispersion of the refractive index of the medium.

This is particularly useful for the DI applications to plasma diagnostics where the dispersion of refractive index is, as a rule, governed by the electrons. Using the well known expression for the plasma $n(\omega)$, it is possible to obtain the following proportion for the phase shift:

$$\Delta\theta = (3e^2/2mc^2)\lambda < n_e l >, \qquad 3$$

where λ is the probe radiation wavelength, $< n_e l >$ is line density of electrons, all the rest of the symbols are standard.

We should note that the above scheme is only weakly sensitive both to the change in the distance between doublers and to vibrations of optical elements, since the air and optical windows have low dispersion. Thus, for radiation with $\lambda = 1.06\mu m$ the quantity $[n(\omega) - n(2\omega)]$ is 5×10^{-6} for air and $\simeq 10^{-2}$ for quartz.

Evidently, DI may work in the range of wavelength where the frequency doublers exist. According to Ref.10 this range is from $0.5\mu m$ to $10.6\mu m$. To diminish the influence of refraction in our experiments we have used short-wavelength probing radiation with $\lambda = 1.06\mu m$. In this case the registration in the invisible spectral region ($\lambda = 0.53\mu m$) is an additional favourable condition.

Second-type phase-matched KTP crystals have been used as optical frequency doublers. A YAG:Nd laser ($\lambda = 1.06\mu m$) with the power of $3W$ is used as a radiation source. The quartz wedge is used for calibration and set up to linear section of curve (1). Dispersion phase difference related to plasma has been determined according to the change in photodetector signal with the plasma impulse transmission.

Note, that under the conditions of GDT experiments (and also for the majority of modern plasma devices[14]) the characteristic values of $< n_e l >$, according to expression (3), for the wavelength $\lambda = 1.06\mu m$ correspond to a phase shift $\Delta\theta < \pi$. Therefore, the sign of the phase shift can be determined by calibration.

To reduce the noise of output signal the power supply has been stabilized and a compensation of the rest noise using standardization by input SH noise has been made. It gives the relative noise level of 1.5×10^{-4} in the frequency range 100 kHz, which corresponds to $< n_e l >_{min} \simeq 10^{13} cm^{-2}$. Spatial resolution was 1 mm. Typical oscillogram of the plasma line density taken in one of the GDT working modes is shown in Fig.3. Maximum $< n_e l >$ value is $0.9 \times 10^{14} cm^{-2}$, which corresponds to $\Delta\theta = 4. \times 10^{-3}$. The time evolution of the plasma line density obtained with the help of DI is in good agreement with data observed by other diagnostic systems: Langmuir probes, diagnostic neutral beams and infrared Michaelson interferometer.

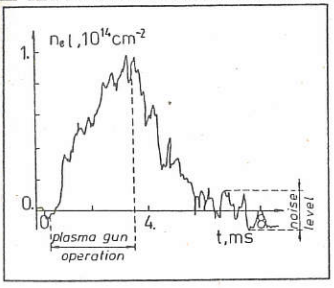

Fig. 3. The time evolution of plasma line density taken on one of the GDT working modes. The time of plasma gun operation is $3\,ms$, maximum $< n_e l >$ value is 0.9×10^{14}, the noise level $< n_e l >_{min} \approx \pm 10^{13} cm^{-2}$.

Our interferometer did not have any vibration isolation structure, all of its components were attached directly to the vessel flanges.

It is useful to make a comparison of $< n_e l >_{\min}$ values and the sensitivity of the DI system to vibration, with the Michaelson interferometer which is normally used on GDT (which uses a CO_2-laser ($\lambda = 10.6\mu m$) with compensation at $0.63\mu m$ wavelength). The DI system possesses similar sensitivity and temporal resolution for ten times shorter wavelength. The level of parasitic vibrations measured by the compensation interferometer with $\lambda = 0.63\mu m$ which was placed upon the vibration isolation structure, was $\pm 10\mu m$. It is important to stress here that in the experiments with the DI system the minimum plasma line density measured was determined exclusively by the level of uncompensated SH noise, and was in no way related to vibrations of elements. Simple estimates show that fluctuations of the length of air intervals $3\mu m$ and angular vibrations of optical elements $\simeq 2'$ will result in in parasite changes in the phase $\Delta\varphi \leq 10^{-4}$. Angular vibration estimates were made for the second frequency doubler having the length $1cm$ and dispersion 0.1.

Summing up, we note that the compactness and simplicity of the DI design allows us to consider it as a good basis for multichannel systems.

The demonstrated DI parameters demonstrated and experience of its performance on the GDT make it possible to conclude on the applicability of such measuring scheme for contemporary large tokamaks.

We are pleased to acknowledge S.G.Rautian and G.N.Alferov for helpful discussions, and L.S.Vasilenko and A.A.Ivanov for their support.

REFERENCES

[1] G.Braithwaite, A.Bulliard, J.L.Bruneau et al., The Multichannel Far Infrared Interferometer ($KG1$) on JET, Rep. JET-IR (85)08, JET, Joint Undertaking, Abindon, Oxfordshire (1985).

[2] D.Veron, in Diagnostic for Fusion Reactor Conditions (Proc. Workshop Varenna 1982), Vol.1, CEC, Brussels (1982) 283.

[3] D.R.Baker, and Shu-Tso Lee, Rev. Sci. Instrum. 49(1978)919

[4] G.V.Ostrovskaya, Kh.P.Alum, and Yu.V.Kovalchuk. Author's Certificate No.86492(USSR). Publ. in Byull, Izobret. NO.38(1981).

[5] F.A.Hopf, A.Tomita, and G.Al-Jumaily, Opt. Lett., 5, 386 (1980).

[6] Kh.P. Alum, Yu.V.Kovalchuk, and G.V.Ostrovskaya, Pisma Zh. Tekh. Fiz. 7, 1359 (1981) [So. Tech. Phys. Lett. 7, 581(1981)].

[7] G.N.Alferov, S.A.Babin, and V.P.Drachev, Zh. Tekh. Fiz. 36, 588(1986) [Sov. J. Tech. Phys. 31, 366(1986)].

[8] G.N.Alferov, S.A.Babin, and V.P.Drachev, Opt. Spectrosc.(USSR), 63, 348(1987) [Opt. spectrosk. 63, 594(1987)].

[9] Drachev V.P., Rep. ITP Siberian Br. USSR Acad., No.243-90, Novosibirsk 1990.

[10] Handbook of Lasers with Selected Data on Optical Technology Edited by R.J. Pressley, Chemical Rubber Co., Cleveland, 1971.

[11] Mirnov V.V., Ryutov D.D., Pis'ma Zh. Tekh. Fiz. 5(1979)678. [12] Mirnov V.V., Ryutov D.D., Voprosy Atomnoj Nauki i Tekhniki — Termoyadernyj Sintez, Vol. 1(1980) 57.

[13] Bagryanskij P.A., Ivanov A.A., Klesov V.V., et al, in Proc. of the XI Intern. Conf. on Plasma Physics and Controlled Nucl. Fusion Res., (Kioto 1986), Vienna, IAEA, 1987, v.3, p.467.

[14] D.V. Orlinskij and G. Magyar, Nucl. Fusion, v.28, 4(1988), p.611-697.

VISIBLE SPECTROSCOPIC MEASUREMENTS ON FTU

I. Condrea*, R. Bartiromo, G. Mazzitelli and D.H. McNeill**
Associazione EURATOM-ENEA sulla Fusione, Centro Ricerche Energia Frascati,
C.P. 65 - 00044, Frascati, Rome (Italy)

Introduction

Visible spectroscopy has been extensively used in FTU to measure the intensity of the spectral lines of hydrogen, light impurities (C,O,N) and metallic impurities (Ni, Cr, Fe). The plasma light was collected along selected tangential and radial chord views in order to observe the vacuum chamber wall and the limiter respectively.

The visible light emitted by atoms and ions was collected by a telescope and focused onto one end of a 1mm diameter fiber optics. The other end of this quartz fiber with f/3 was directly attached onto the entrance slit of a Monospec27 grating spectrometer with f/3.8 and equipped at the exit slit with an intensified linear diode array. The spectrometer can use 3 different gratings in order to have linear dispersion of 3, 6 and 24 nm/mm. We used in our experiments the second and the third gratings to cover a spectral range of 3000 Å and 700 Å respectively.

The spectrometer has been calibrated in absolute intensity using a calibrated lamp and a lambertian diffuser. The impurity influx has been derived from the absolute line intensity through the calculated value of ionization to photon emission ratio /1/.

H Plasmas

Spectra collected at the wall location show only the presence of light impurities while at the limiter metallic lines can be very prominent, see Fig. 1.

Strong lines of CIII (4651 Å) suggest a contamination of FTU with carbon. At the beginning of a long series of discharges the carbon and oxygen to hydrogen flux ratios (Γ_C/Γ_H, Γ_O/Γ_H) were 8.4% and 1.4%. After this series of shots and efficient discharge cleaning this ratio decreased to 1.2% for carbon and 0.2% for oxygen. During the same time period at the limiter Γ_C/Γ_H ratio decreased from 0.8% to 0.2%. On the contrary the analysis of the OII line at 4416 Å shows for the same shots an increase of Γ_O/Γ_H at the limiter from 0.05% to 0.15%. These observations confirmed that an accidental carbonization of the FTU vacuum vessel was produced in the previous campaign by the exposure of a plastic isolator to the plasma /2/. The absolute fluxes for the CIII and OII were generally about 6×10^{17} at/m^{2}s and 1.2×10^{17} at/m^{2}s respectively at the wall in discharges with I_p= 500 kA and n_e= 0.5×10^{20}m^{-3}. At the limiter the calculated flux is

* ENEA Fellow
** ENEA Guest

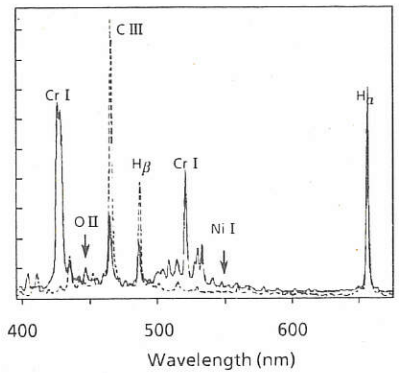

Fig 1: Spectra in H plasma at I_p= 700 kA and n_e= 0.6x10^{20} m^{-3} at the wall (dashed line) and at the limiter

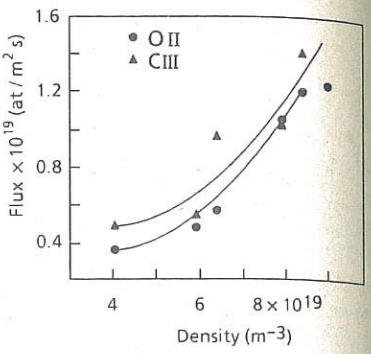

Fig 2: Dependence of the CIII and OII fluxes on the electron density, at the limiter

about 1.7x10^{19} at/m^2 s for CIII and 1.0x10^{19} at/m^2 s for OII with I_p= 700 kA and n_e= 0.9x10^{20}m^{-3}.

Usually we observe an increase of carbon and oxygen fluxes, both at the wall and limiter location, when the plasma density is increased. Figure 2 shows the OII and CIII fluxes dependence of the averaged electron density. The situation changes qualitatively for the metallic impurities. For these observations we used the CrI triplet in the 4200 Å range, the metastable terms in the 5200 Å range and the NiI doublet at 5476 Å. The ratio Γ_{CrI}/Γ_H was about 0.96% at the limiter for a plasma density of 2.5x10^{19} m^{-3}. With the increase of the averaged electron density to 8.5x10^{19} m^{-3} this ratio decreased at about 0.028%. In the same density range the ratio Γ_{NiI}/Γ_H, decreased from 0.45% to 0.018% (see Fig. 3).

Anomalously high intensities of the light impurities lines can be observed at high density but this is always related to the occurence of marfes. In FTU the marfes are characterized by a strong radial asymmetry of the H_α signals which become higher above the midplane. Figure 4 shows the CIII and H_β temporal evolution during a shot with a marfe occuring at t= 200 ms. At the beginning of the marfe, the CIII signal increases rapidly and then it remains constant until the asymmetry in the H_α profile is present. As opposite to CIII, the H_β signal shows a slow increase at the beginning and a prompt decrease at the end of the marfe. The ionisation to photon ratio for the CIII line is a strong function of the edge temperature (for our conditions, T_e= 20 keV), while the same ratio for H_β is nearly independent from the electron temperature. Accordingly, the CIII line sees the variation of the temperature during the marfe as opposite to H_β line which depends on the gas puffing and particle confinement.

In FTU shots at low plasma current can exhibit very peaked profiles of the electron density /3/. In these shots we observed that the H_α radial profile keeps its

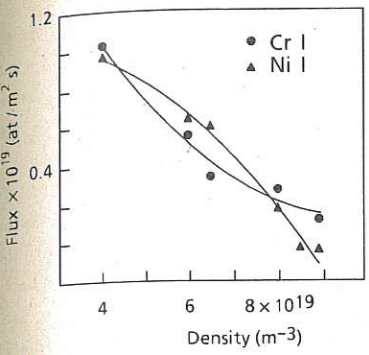

Fig 3: Dependence of the CrI and NiI fluxes on the electron density, at the limiter

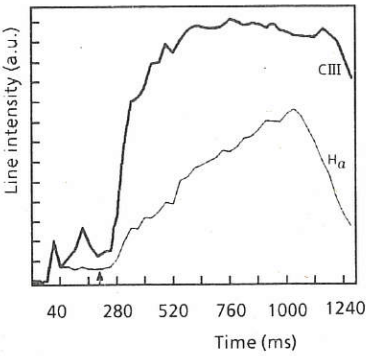

Fig 4: Temporal evolution of the CIII and H_β emission lines during a marfe

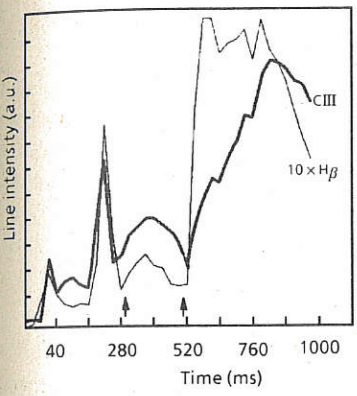

Fig. 5: Temporal evolution of the CIII and H_β emission lines during a peaked electron density profile (represented by arrows)

canonical form, but with the maximum displaced inwardly. From the temporal evolution of CIII and H_β we also observed that before the density profile peaks, these signals first increase and then decrease when peaking sets in. In this phase, the CIII intensity exceeds the H_β one as an effect of the T_e variation. At the end of this phase, when the density reaches a flat profile we observe a strong increase of the H_β and CIII (see **Fig. 5**). The light impurities have a similar behaviour at the limiter while the metallic impurities are reduced drastically to zero during the peaked phase and have a small increase after when the electron edge temperature increases and the plasma touches the limiter very near to our line of observation.

He Plasmas

In helium plasmas we observed a drop of all the impurities lines and an increase of the continuum. At the limiter, the HeII (4689 Å) to HeI (6678 Å) influx ratio ranges between 1.5 and 2.0 and the HeI (6678 Å) to HeI metastable term (5875 Å) flux ratio remains almost constant at 180. At the wall, the Γ_{HeI} to Γ_{HeI} of the metastable term ratio is not constant anymore and varies from 100 to 400 and the flux ratio

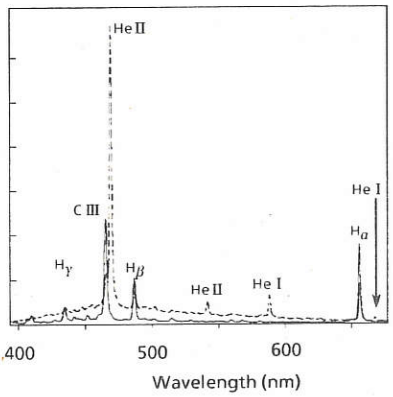

Fig 6: Spectra in He plasma (dashed line) and in H plasma, observed at I_p= 700 kA and n_e= 0.7x10^{20} m^{-3} at the wall

$\Gamma_{HeII}/\Gamma_{HeI}$ ranges from 10 to 20. At the wall this ratio becomes 10 times greater than at the limiter because we look far from the He source i.e HeI. The recycling is probably stronger at the limiter and the HeII ions are flowing through the magnetic field lines from the limiter to our viewing chord near the wall.

Calculating the carbon flux in H and He plasmas with similar parameters (700 kA and 0.7x10^{20}m^{-3}), we observed a decrease of it respectively from 1.5x10^{18} at/m^{2}s to 5.6x10^{17} at/m^{2}s at the wall and from 8.1x10^{18} at/m^{2}s to 2.7x10^{18} at/m^{2}s at the limiter. As one can observe the carbon flux is 2 times smaller in He plasmas than in H plasmas at the wall and 3 times smaller at the limiter. Figure 6 presents a comparison between a spectrum in H plasma and one in He plasma and shows this strong reduction of the impurities in the last one. The metallic impurities fluxes are also reduced about 4 times in He plasmas.

References

/1/ K. Behringer, B. Denne, M. Forrest, M. Stamp, H.P. Summers, JET- P(89) 05

/2/ D.H. McNeill et al., paper no. 1-1/185C186C190, this conference.

/3/ F. Alladio et al., paper no. 1-1/179C182C191, this conference.

Determination of O^{8+} to electron density ratio by the intensity ratio of the charge exchange recombination and the Doppler-shifted H_α emissions of the injected neutral beam

K.Kondo, F.Sano, S.Sudo[1)], H.Zushi, T.Mizuuchi, H.Okada, S.Besshou, K.Nagasaki, S.Higashijima, K.Hanatani, M.Nakasuga, M.Wakatani and T.Obiki

Plasma Physics Laboratory, Kyoto University, Uji 611 Japan

1)National Institute for Fusion Science, Chikusa, Nagoya 464-01 Japan

[1] Introduction

It has been an important issue to determine impurity density with a good spatial resolution. Recently the charge exchange recombination spectroscopy has a great attraction for ion temperature and impurity density measurements. An absolute intensity measurement of the charge exchange recombination spectra and an injected neutral beam density are necessary for determing the impurity density. In this paper, a new method for estimating the density ratio of fully ionized oxygen to the electron density is proposed, and the experimental result in Heliotron E is presented.

Two kinds of emissions due to the charge exchange recombination of fully-ionized oxygen and the Doppler-shifted H_α from the injected neutral beam are used. Their intensities are described as following;

$$I_{imp}^{cx}=GR(\lambda_{imp})\sum_{k=1}^{3} n_b(E/k)n_{imp}\langle\sigma_{cx}(E/k)V_b(E/k)\rangle \qquad (1)$$

$$I_{H\alpha}^{Dop}=GR(\lambda_{H\alpha})\sum_{k=1}^{3} n_b(E/k)n_e\langle\sigma_e v_e\rangle \qquad (2)$$

respectively. Symbol G and $R(\lambda)$ are a geometrical factor and sensitivity at the wavelengths, λ of an optical system. Beam density of the three energy components are described by $n_b(E/k)$, and $<\sigma_{cx}(E/k)V_b(E/k)>$ and $<\sigma_e v_e>$ are emission rates for charge exchange recombination and electron excitation, respectively. The intensity ratio of these emissions is related to the impurity and the electron density ratio as

$$\frac{I_{imp}^{cx}}{I_{H\alpha}^{Dop}} = \frac{R(\lambda_{imp})\, n_{imp} \sum_{k=1}^{3} \{f(E/k)\langle\sigma_{cx}(E/k)V_b(E/k)\rangle\}}{R(\lambda_{H\alpha})\, n_e \quad \langle\sigma_e v_e\rangle \sum_{k=1}^{3} f(E/k)} \qquad (3)$$

where $f(E/k)=n_b(E/k)/n_b(E)$.

This method is powerful because the density profile of the injected neutral beam is not necessary and only relative intensity ratio provides the desired impurity and the electron density ratio with a good spatial resolution, and Z_{eff} of the impurity.

[2] Experimental Results

Heliotron E is an axially asymmetric helical confinement system with l=2 and m=19 [1]. The major and averaged minor radius are 2.2 m and 0.21 m, respectively. Currentless plasmas are initiated by 53.2GHz gyrotrons and further heated by intense neutral beams. A 1.26 m visible spectrometer (SPEX 1269) with a 512-channel detector (Tracor Northern, TN6133) is employed for the measurements of the charge exchange recombination emissions of the fully ionized oxygen and H_α emissions of the hydrogen beam particles. At the center of the plasma column, the optical sightline of the spectrometer intersects the neutral beam which is injected into a plasma perpendicularly. An angle between the optical sightline and the neutral beamline is 76 degrees. The wavelengths of the H_α emissions of the injected beams shift by the Doppler effect, and these are able to distinguish from the unshifted one. Line emission at 2977 Å is observed to estimate the fully ionized oxygen density, 2977 Å which is the wavelength of O VIII originated through the charge exchange recombination by a neutral beam. The excitation rate coefficients for charge exchange recombination are discussed by Fonck [2] and Boileau [3], and the electron impact excitation rates are given by Janev [4].

Figure 1 shows the time behavior of the spectra near the H_α with and without a neutral beam. The integration time is 20 msec. The vertical scale is expanded for enhancing the Doppler-shifted H_α emissions, which appear between the unshifted H_α (6562 Å) and C II(6578, 6583 Å) emissions. The Doppler-shifted H_α emissions, which are observed during the neutral beam injection, spread due to their three energy components and the motional Stark effect. The acceleration energy (E) of the beam is 23 kV, and the typical

fractions of the three energy components of E,E/2 and E/3 are 0.33, 0.25 and 0.42 [5].

Figure 2 shows the time behavior of the electron density and the ratio of O^{8+} to electron densities in the above neutral beam heated plasma. The deuterium plasma is initiated by two 53.2 GHz gyrotrons and 1.4 MW neutral beam is injected from 30 msec to 90 msec.The density ratio of O^{8+} to electron is 2~3% and Z_{eff} by O^{8+} is computed to 1.2~1.9.

[3] Discussion and conclusion

For the intensity of the Doppler-shifted H_α emissions, equation (2), one must be careful for the contribution by the proton impact excitation. The acceleration voltage of a neutral beam increases above 40 kV, the contribution of the proton impact excitation could not be ignored [6]. The maximum acceleration voltage is 30 kV in the Heliotron E neutral beam injector, therefore, the main excitation mechanism for the Doppler-shifted H_α emissions is the electron impact collision. In this case, one more merit is provided that the excitation rates by the electron impact is insensitive to the electron temperature in the range from 100 eV to 1000 eV, and no precise electron temperature measurement is needed.

We have demonstrated the new method for estimating the fully ionized oxygen to electron density ratio by using the intensity ratio of the charge exchange recombination and the Doppler-shifted H_α emissions of the beam particles. In our experimental condition, this is considered very useful. In the case of high energy injection of the neutral beam, the intensity ratio provides the impurity to proton density ratio rather than electron.

References

[1] T.Obiki et al., Fusion Technology 17 (1990) 101
[2] R.J.Fonck et al., Phys.Rev. 29 (1984) 3288
[3] A.Boileau et al., JET-P(87) 44
[4] R.K.Janev et al., Elementary Processes in Hydrogen-Helium Plasmas (Springer-Verlag, New York, 1987)
[5] K.Kondo et al., 7th Int.Stellarator Workshop (Oak Ridge, USA 1989)
[6] V.Franco et al., Phys. Rev. A 4 (1971) 945

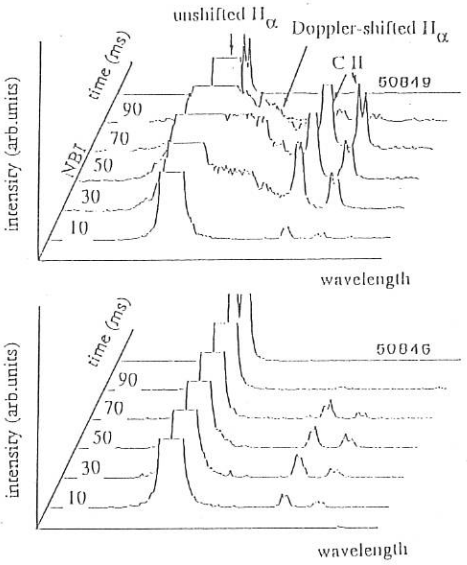

Figure 1. Time behavior of the spectra in the wavelength from 6545 Å to 6600 Å with (#50849) and without (#50846) a neutral beam. The Doppler-shifted H_α emissions appear during the neutral beam injection.

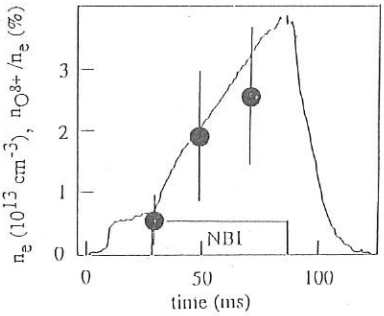

Figure 2. Time behavior of the electron density (solid line) and the density ratio of the O^{8+} to the electron (closed circles) in a beam heated plasma.

SPATIAL STRUCTURE OF NONTHERMAL FLUCTUATING ELECTRIC FIELDS IN THE TJ-I TOKAMAK

B. Zurro, F. Castejón and C. Burgos. Asociación EURATOM/CIEMAT para Fusión. E-28040 Madrid. Spain

1. Introduction. Spatial-resolved measurements of Doppler temperature of protons and impurities in the TJ-I tokamak have revealed that they cannot fit in the generally accepted frame used for line width data interpretation in tokamaks (1). Within this frame, it is assumed that due to the density and toroidal field ranges of these experiments, the line width is dominated by thermal Doppler broadening, i. e. Stark effects due to plasma microfields, Zeeman effect and the influence of plasma turbulence are negligible. The strong collisional coupling among different type of ions is used to justify that protons and impurities must have the same temperature.

By contrast, we claim in this work based on TJ-I tokamak data, that low level of stochastic electric fields, even being weak enough not to produce quasi-static Stark broadening, can induce observable effects on the ion spectral line widths. The non-thermal velocity fluctuations due to these fields produce a differential effect on the apparent temperature of proton and impurities. Experimental profiles of proton and impurity temperature, in combination with a data analysis code described in Ref. (2), have been used to deduce in the TJ-I tokamak the spatial structure of radial electric field fluctuations and their behaviour at three different plasma densities. First, we summarize the experimental and the data analysis methods and second, we present typical results obtained in this tokamak (3). The influence of magnetic fluctuations is also discussed.

2. Experimental and data analysis methods. Ion temperatures in the TJ-I tokamak are deduced from Doppler line broadening of hydrogen (line wings) and impurity lines (CV 2271 Å, OV 2781 Å,...). These measurements are performed with a 1 m monochromator having a multichannel intensified detector attached to its focal plane; spatial resolution is achieved scanning the plasma chord on a shot to shot basis. The spectral system is operated in first-third diffraction order with a resolution of 10^5-10^6.

The influence of plasma turbulence on spectral line widths has been included following the method used in astrophysics (2). If the spectral line shape is the result of the convolution of a thermal gaussian distribution and a turbulent gaussian one, the latter producing a gross mass motion, the full width at half maximum of the resulting line is given (3) by,

$\Delta\lambda = 1.665\ (\lambda/c)\ [\ (2kT/m_i) + \xi^2]^{1/2}$, where ξ is the dispersion of the gaussian microturbulence velocity distribution and the rest of parameters have the usual meaning. This value of ξ is the most probable velocity and is $\sqrt{2}$ times larger than the root-mean-square value. If this turbulent velocity is assumed to be due to E x B drifts, their components in the radial, poloidal and toroidal directions, are given by:

$$\tilde{v}_r = \frac{\tilde{E}_p}{B}, \tilde{v}_p = \frac{\tilde{E}_r}{B}, \tilde{v}_t = \frac{\tilde{E}_r B_p}{B^2} << \tilde{v}_p$$

Therefore, when observation is performed perpendicular to the toroidal field and along chords lying in a plane perpendicular to the equatorial one, v_p is important for peripheral chords and can produce ion temperature profiles that do not fall down to low values at the edge as long as non-thermal fluctuating velocities are comparable to thermal ones, whereas v_r is relevant for enhancing central ones. Radial magnetic fluctuations, rising toward the centre in tokamaks, might not have a negligible influence on the radial fluctuating velocities of the ions, and may contribute significantly when the plasma is observed along central chords. Its effect can be estimated, for root-mean-square values, by the expression:

$$\tilde{v}_r \cong \frac{v_{\|}\tilde{B}_r}{B} 2xNx\tau_p$$

where $V_{\|}$ is the ion parallel velocity. The second factor is the relative radial magnetic fluctuation, N the number of gyro-orbits per second performed by the ion, in each of which two small random perturbations occur, and τ_p the ion confinement time.

For a fixed observational geometry the data analysis code performs the average along the selected optical pixel of a set of shifted, broadened gaussians split by the local magnetic field due to the Zeeman effect. The shift takes account the projection of the local poloidal rotation velocity along the line-of-sight, and the broadening the local ion temperature and non-thermal velocity fluctuations.

3. Strength and radial decay length of fluctuating electric fields. The former method has been used to explore whether the distinct apparent temperatures of protons and impurities observed in the TJ-I tokamak (4) are or not entirely due to the influence of plasma turbulence on spectral line widths. In Fig. 1, we show how the discrepancy between the local temperature and the CV chord-averaged temperature profiles can be explained in a low density TJ-I discharge. The local temperature profile is obtained from

the H_β line wings and the charge-exchange neutral analyzer at the centre (3). The simulated profile (continuous curve) was obtained including a significant level of radial and poloidal fluctuating velocities or equivalent electric fields. E_r (rms) or v_p were described by an exponential function with its maximum at the plasma edge; and E_p (rms) or v_r (rms) were chosen with a maximum at the plasma centre. Gaussian functions could provide also a reasonable fit. Peak values (V/cm-rms-) and decay lengths (cm) of the gaussian fluctuating fields for explaining this behaviour are given in the plot for the low density case. These parameters are determined with an uncertainty of around 10 - 15 %.

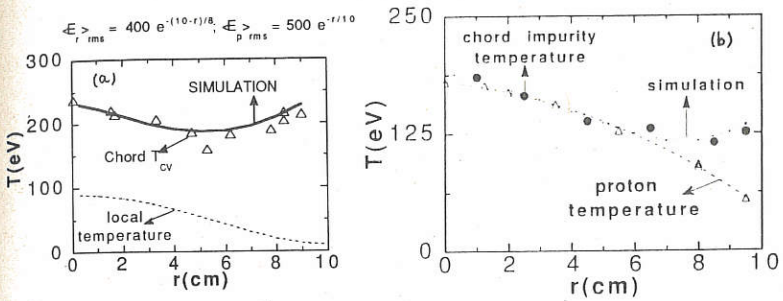

Fig. 1. (a) Comparison of experimental impurity and proton temperature profiles in a low density TJ-I discharge, $n_e = 1 \times 10^{13}$ cm^{-3}; (b) Similarly for a high density case ($n_e = 3 \times 10^{13}$ cm^{-3}). The simulations were obtained including anisotropic non-thermal velocity fluctuations, which equivalent fluctuating electric field values and radial dependence are given at the top for the low density case.

The selection of the fitting functions and parameters was guided by typical results of Langmuir probe measurements in tokamaks and the radial dependencies were chosen in order to account for the chord-averaged impurity temperature profile behaviour due to turbulence effects. The rms value and radial dependence of the radial fluctuating electric field are consistent with Langmuir probe data in tokamaks (5). By contrast, the obtained value for the poloidal fluctuating electric field (rms) is much higher than those deduced by the heavy ion beam probe (6). However, these high values cannot be ruled out from this comparison, since the present method has a bandwidth of around 1 Ghz, much higher than that of the ion beam probe method (1 Mhz). Furthermore, it is well known that in a current-carrying plasma significant turbulence can be excited in a range close to the ion cyclotron frequencies ($\geq$ 10 Mhz). An alternative explanation, to date unconsidered, of the radial fluctuating velocities could be based on the existence of radial magnetic fluctuations. Since firstly, the dependence of the deduced radial fluctuating velocities (rms) with radius,

peaking at the centre and decaying toward the edge, is the typical behaviour expected for the radial magnetic fluctuations (7) and secondly, last expression with typical values of $v_{||}$ ($1\text{-}3\times10^6$ cm/sec) and B_r/B (10^{-3}-10^{-4}) would account for the observed v_r. In this case the poloidal fluctuating velocities would be dominated by radial fluctuating electric fields and the radial fluctuating velocities by radial magnetic fluctuations.

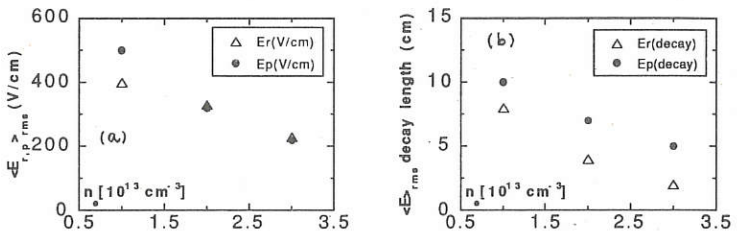

Fig. 2. (a) Plot of root mean square fluctuating electric field values (radial and poloidal) versus density; (b) Similar plot for radial decay length of these fluctuating electric fields.

In Fig. 2, the results of this type of profile analysis at three different electron plasma density are depicted. The turbulence needed to explain the impurity temperature behaviour decreases as density increases as well as its radial decay length. Since TJ-I plasma conditions are similar to those existing at the edge of large devices, a similar effect could also account for the high edge ion temperature reported in JET and for the anomalous central impurity temperatures observed in other magnetic fusion devices.

Acknowledgments. This research was partly supported by the DGCYT under project PB90-0410.

References

(1) R. Isler, Nucl. Fusion **24**, 1599 (1984).

(2) B. Zurro and C. Burgos, To be published in Rev. Sci. Instum. (1992).

(3) D. F. Gray, Lectures on Spectral-Line Analysis: F, G, and K Stars. Aylmer Express Ltd. Aylmer, Ontario. Canada (1988).

(4) B. Zurro, C. Hidalgo, B. García-Castañer and C. Pardo, Plasma Phys. Controll. Fusion **32**, 565 (1990).

(5) D. Bora, R. S. Ivanov, G. Van Oost and U. Samm, Nucl. Fusion **31**, 2383 (1991).

(6) A. J. Wootton, Private Communication.

(7) S. J. Zweben and R. J. Taylor, Nucl. Fusion **21**, 193 (1981).

Fast Analysis of Spectral Data using Neural Networks

C.M. Roach,
AEA Fusion, Culham Laboratory, Abingdon, Oxon, OX14 3DB, UK.
(Euratom/UKAEA Fusion Association)

Fast analysis techniques are highly desirable in experiments where measurements are recorded at high rates. In fusion experiments the processing required to obtain plasma parameters is usually orders of magnitude slower than the data acquisition. Spectroscopic diagnostics suffer greatly from this problem. The extraction of plasma parameters from a measured spectrum typically corresponds to a nonlinear mapping between distinct multi-dimensional spaces. Where no analytic expression for the mapping exists, conventional analysis methods (eg least squares) are usually iterative and therefore slow. With this concern in mind a fast spectral analysis method involving neural networks has been investigated.

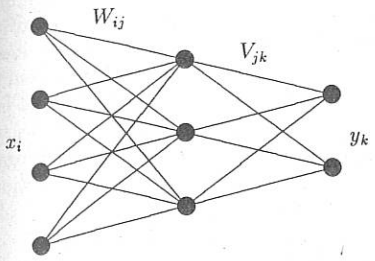

Figure 1: MLP with 1 Hidden Layer.

Neural networks are capable of performing a very wide range of nonlinear mappings using a simple structure of inter-connected nodes /1/. The strengths of the inter-connections determine the mapping, and these are called weights. The output from any node is a function of a sum of inputs coming from other nodes or from external sources. The multilayer perceptron (MLP) is a widely used neural network topology and is illustrated in Figure 1.

The MLP outputs, y_k, are calculated from the inputs, x_i, using the formula:

$$y_k = V_{0k} + V_{jk} f\left(W_{ij} x_i + W_{0j}\right) \tag{1}$$

where repeated indices are implicitly summed, and W_{ij} and V_{jk} represent the connection strengths between the hidden layer and the input and output layers respectively. V_{0k} and W_{0j} denote constant offsets to the summed inputs at each node, and f is the transfer function giving the output response from the node. A typical choice for the transfer function is the sigmoidal form:

$$f(u) = \frac{1}{1+e^{-u}} - \frac{1}{2} \tag{2}$$

and this provides nonlinearity in the network response.

Training the neural network to perform a particular mapping is straightforward though computationally intensive. It is an iterative procedure requiring a large database of examples; ie inputs and their associated target outputs, y_k^t. Starting with a random set of weights the network computes outputs, y_k^n, which are then compared with the

target values. An error function E is calculated;

$$E = \frac{1}{2} \sum_{\text{examples}} \sum_{k} \left(y_k^t - y_k^n \right)^2 \tag{3}$$

and the weights are adjusted so as to minimise E. In a MLP the derivatives of E with respect to each weight can be computed analytically using error backpropagation /2/, thereby reducing the computational effort required in the error minimisation procedure. Standard minimisation techniques like gradient descent and conjugate gradient algorithms can be exploited to minimise E efficiently.

After training, the neural network mapping is rapidly calculated using the simple operations described in equations (1) and (2), which can be implemented either in software or in hardware. Here the multilayer perceptron has been applied to the analysis of measurements from two different spectroscopic diagnostics. [1]

The simpler application, demonstrating the feasibility of the technique, concerns impurity radiation spectroscopy on the COMPASS tokamak. Three intensity measurements (R, G, B ie 'red', 'green', 'blue') bracketing the wavelength region of the radiation from a single Boron IV line, provide information on the ion rotation velocity, temperature and the impurity density. These plasma parameters are obtained from the position P, the width W, and the amplitude A of the Gaussian shaped spectral line. Given the spectral parameters A, P, W and the spectrometer response functions, the expected measurements R, G, B can readily be computed. However, we are interested in the more difficult inverse problem of mapping $R, G, B \rightarrow A, P, W$. The traditional approach to such a problem is least squares fitting, an iterative and therefore slow technique.

An MLP with one hidden layer has been trained to perform the nonlinear part of the mapping $R, G, B \rightarrow A, P, W$. If P, W are fixed, A scales linearly with $R + G + B$. This linear part of the transformation is removed by defining $\hat{B} = B/(R + G + B)$ and $\hat{R} = R/(R + G + B)$ and using the neural network to map $\hat{B}, \hat{R} \rightarrow P, W$. A may subsequently be extracted from the measurements.

The dataset to train and test the neural network was generated to fill uniformly a region of A, P, W space covering the range of experimental possibilities:

$$\begin{aligned} 0.03 < \quad & A \quad < 0.15 \\ 130.0 < \quad & P \quad < 300.0 \\ 10.0 < \quad & W \quad < 100.0 \end{aligned}$$

with rejection of the subregion of this space where $P > 230.0 + 1.5 \times W$. The rejection criterion was applied to avoid a region of space where the mapping $R, G, B \rightarrow A, P, W$ became multivalued, due to the nature of the experimental instrument functions. 1000 randomly selected A, P, W values were chosen inside the space described above, and R, G, B were calculated using the measured instrument functions.

[1] Neural networks have also been applied to other types of plasma diagnostic: eg reconstruction of the plasma boundary from coil measurements /3/ /4/, and density profile determination from infrared interferometry /5/.

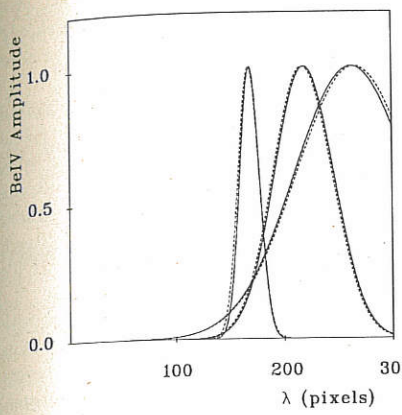

Figure 2: Three solid example test spectra with the dashed neural network fits superimposed.

MLPs with 2 inputs, a variable number N of hidden nodes, and 2 outputs were trained to map from $\hat{B}, \hat{R} \rightarrow P, W$. 900 examples were used to train the network leaving 100 examples for test purposes. With an optimum number of 50 hidden units the neural network achieved precisions of 0.9% in the Doppler shift and 2.2% in the width.

More accurate results can be obtained in this problem using function interpolation. This is a fast non-iterative method, but rapidly becomes unmanageable with the addition of further measurements or plasma parameters. Increasing the dimensionality of the mapping in this way poses no such problems for the neural network approach.

Statistical fluctuations in real measurements from the COMPASS spectrometer, operating with a time resolution of $400\mu s$, produce fit errors of 1.9% in the shift and 14.6% in the width. These errors should be borne in mind when considering the required accuracy of the reconstruction method.

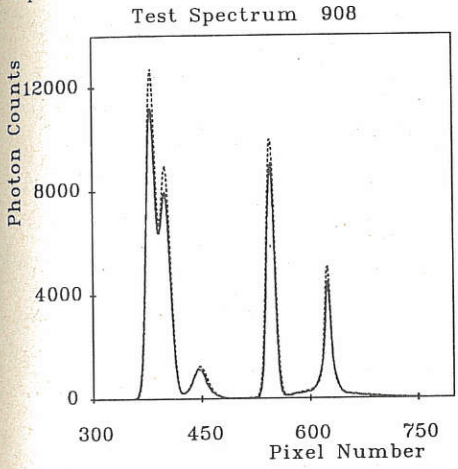

Figure 3: A simulated JET charge exchange test spectrum with the dashed neural network fit superimposed.

JET charge exchange spectra are considerably more complex, and involve eleven Gaussian spectral lines, some overlapping or collocated. The amplitudes, positions, and widths of the lines vary widely depending on the plasma conditions. Ion densities, rotation velocities and temperatures all affect the shape of the spectrum, and so charge exchange spectroscopy is a very useful diagnostic. The conventional iterative analysis procedure to extract the line parameters from the spectrum is computationally intensive, and requires human supervision to ensure that truly optimal solutions are found.

A neural network approach to the problem offers speed advantages, though would

not provide the accuracy of the iterative method. The neural network fit could supply a valuable initial guess for the conventional fit, and this in itself would reduce the need for human intervention.

The feasibility of using a neural network to analyse this data has been investigated using simulated spectra, and the results are encouraging. Figure 3 shows a typical simulated spectrum, including noise, and the neural network fit. A large MLP with 100 spectrum values as inputs, 30 hidden units and 19 spectral parameters as outputs achieved this result. The temperature of the hot component of He II is reconstructed by the network with root mean square errors of 19% and 5% with and without simulated noise respectively. These figures are to be compared with a 10% mean error from JET's standard algorithm.

A major reduction in computer time has been achieved, with the neural network results available in $\sim$ 3ms, considerably faster than the 500ms required for the iterative method. Neural networks could revolutionize the analysis of charge exchange spectra by significantly reducing the need for human supervision. Work on applying neural networks to real JET data is currently in progress.

Acknowledgements

It is a pleasure to thank Manfred von Hellermann and Paul Thomas for motivating the JET charge exchange spectroscopy work, Paddy Carolan for suggesting the COMPASS impurity radiation problem, and Chris Bishop from the Harwell Neural Networks Application Group for his valuable advice.

References

/1/ 'Multilayer Feedforward Networks are Universal Approximators', K.Hornik, M.Stinchcombe and H.White, Neural Networks, **2**, 359, (1989).

/2/ 'Parallel Distributed Processing', Volume 1 Chapter 8, D.E. Rumelhart, G.E. Hinton and R.J. Williams, MIT Press, (1986).

/3/ 'A Neural Network Approach to Tokamak Equilibrium Control' C.M.Bishop, P.M.Cox, P.S.Haynes, C.M.Roach, M.E.U.Smith, T.N.Todd and D.L.Trotman; to appear in 'NCM'91: Applications of Neural Networks', Springer-Verlag (1992).

/4/ 'Fast Non-linear Extraction of Plasma Equilibrium Parameters Using a Neural Network Mapping', J.B.Lister and H.Schnurrenberger, Nuclear Fusion **31**, 1291, (1991).

/5/ 'Neural Networks for Improved Tokamak Density Profile Reconstruction' C.M.Bishop, I.G.D.Strachan, J.O'Rourke, G.P.Maddison and P.R.Thomas; to be submitted to Reviews of Scientific Instruments, (1992)

/6/ 'Rotation Observations from the COMPASS-C Tokamak', P.G.Carolan, C.A.Bunting and R.A.Bamford, from Proceedings of IOP Plasma Physics Conference at the University of Essex, Colchester, (1991).

Tomography algorithms for visible light tomography on RTP

V.V. Pickalov*, L.C. Ingesson, A.J.H. Donné and D.C. Schram**

FOM-Instituut voor Plasmafysica 'Rijnhuizen', Association Euratom-FOM,
P.O. Box 1207, 3430 BE Nieuwegein, The Netherlands
*Permanent Address: Institute of Theoretical and Applied Mechanics, Novosibirsk, Russia
**Department of Applied Physics, Eindhoven University of Technology, The Netherlands

Introduction

A system for tomography in the wavelength range 300 - 1100 nm has been designed for the Rijnhuizen Tokamak Project (RTP). The plasma is viewed from five directions in one poloidal plane with a total of 80 *pin*-diode detectors. To obtain a sufficiently large number of photons on the detectors and to have a good spatial resolution, an optical imaging system relatively close to the emitting plasma is used to collect the light. This is in contrast with pin-hole cameras or lenses on a large distance from the plasma that are normally used in tomography. The regions of the plasma viewed by different detectors are effectively 1 cm wide (the plasma radius in RTP is 17 cm). The electrical system has a large bandwidth (200 kHz) so that fluctuations can be monitored on a microsecond timescale. Different wavelength regions can be selected by optical filtering, e.g. to study H_α- and Z_{eff}-profiles. For four of the viewing directions the imaging system consists of two spherical mirrors inside the vacuum vessel; one viewing direction has a lens system outside the vacuum instead (see Fig. 1). The system for visible light tomography has been described in more detail in Ref. 1.

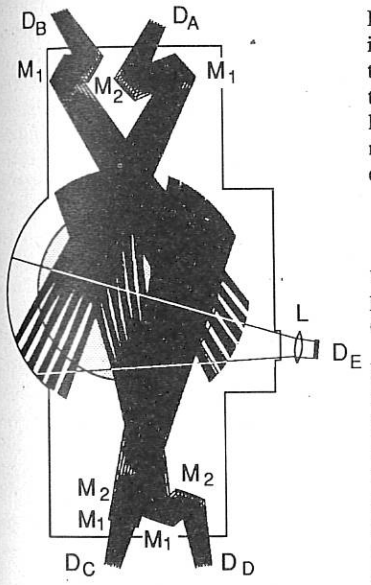

Fig. 1: The regions seen by the detector elements in the poloidal plane of the plasma (shaded) with respect to the vacuum vessel. The detectors for the different viewing directions are numbered D_A through D_E and for four viewing directions the rays that reach every third detector element are shown. M_1 and M_2 are mirrors. For the fifth viewing direction with a lens (L) only the total region viewed is shown.

Preprocessing data for tomography

Because of the complexity of the imaging, implementation of the system into common tomography codes is not straightforward. Ray-tracing is used to calculate the contribution of the local emissivities g in the plasma to the power f measured by the various detectors /1/. This can be expressed in a so-called weighting matrix W:

$$f_j = \sum_{i=1}^{N} W_{ji} g_i \quad , \qquad (1)$$

where i is the indicator of the N cells in which the poloidal cross-section is divided, and j indicates one of the M detectors. Inversion of this problem

by tomographic techniques gives an approximate emission profile.

Because of the limited number of views of the plasma, as a first approach the weighting matrix will not be used directly to obtain a reconstruction from the measurements [as for example in the Algebraic Reconstruction Technique (ART) /2/], but the number of views and the number of detectors will be "increased" by interpolation and smoothing of the measurements. The new viewing directions can best be chosen to be part of a detection system with parallel beams. The transformation from the real system to a set of parallel beams can be depicted in the so-called (p,ϕ)-plane (Fig. 2), where p is the distance of the viewing beam to the plasma centre and ϕ the angle of the line perpendicular to this beam with the horizontal. In Fig. 2 the points corresponding to the detectors of the real system and an arbitrary set of parallel beams are depicted. Interpolation and smoothing is done by fitting a surface to the measured data when the detectors are ordered in the (p,ϕ)-plane. Such an interpolation scheme for fan-beams has been developed, for the case of the current system (Fig. 2) it is under development. Two interpolation schemes have been tested: bi-linear and bi-quadratic. Computer experiments show that the bi-quadratic interpolation scheme provides a more exact reconstruction of the tomogram, albeit more time consuming.

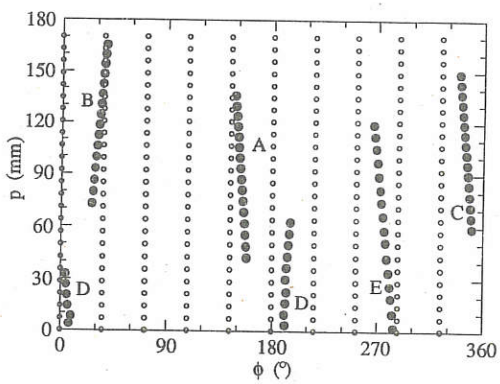

Fig. 2: The distribution of viewing beams in the real detection system (•) and a set of parallel beams (○) in the (p,ϕ)-plane (each point corresponds to one detector and the letters correspond to the viewing directions in Fig. 1).

The transformation to a set of parallel beams is not entirely straightforward because owing to the imaging system a uniformly emitting object does not result in the same measured value by the different detectors (this can be compared with the $\cos\theta$ and $\cos^4\theta$ dependences of the angle of incidence θ in the case of a lens or a pin-hole system, respectively), as is the case for parallel beams. The "scaling factor" to obtain signals for this system corresponding to parallel beams is more complicated than the simple factor in the case of lenses or pin-holes, since the contribution of the emissivity to the measured power varies along the viewing direction and perpendicular to this direction in a complicated manner /1/. An approximate scaling factor for each detector is the inverse of the line average of the weighting-matrix elements of the detector. Figure 3 shows the simulated power measured by each detector, ordered by its p-value, for three cylinder-symmetric emission phantoms before and after scaling. After the scaling the points lie on a smooth curve, while without scaling there is a large scatter of the points. The line integrals for real parallel beams of the same profiles give a slightly lower result (some per cent) for non-constant profiles, which is probably due to the fact that the approximation of the weighting matrix by a line average is not perfect (the scaling factor depends on the emission profile).

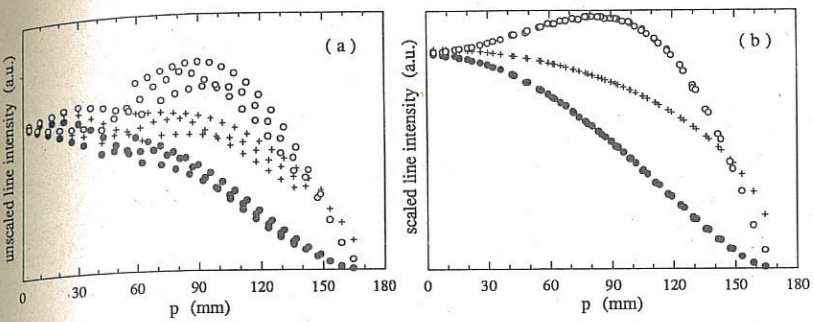

Fig. 3: Simulation of various cylinder-symmetric emission profiles with the detectors ordered according to p-value before (a) and after (b) scaling. The profiles, which are normalized so that the total emissivity is the same for all, are: + = constant, • = peaked [$p(r)$] and ∘ = hollow [$p^{1/2}(r) - 0.9\,p^2(r)$, and the maximum emissivity is at $r \approx 129$ mm]. Here $p(r) = 1 - (r/a)^2$, r is the radial coordinate and $a = 170$ mm (minor radius of tokamak).

Tomography methods

Some two-dimensional tomography algorithms have been modified for this detection system. These algorithms are: regularized schemes of the Filtration and Back Projection (FBP) /2/ algorithm and the Algebraic Reconstruction Technique (ART) /2/. The former algorithm has the form:

$$g(x,y) = \int_0^{\pi} d\phi \int_{-\infty}^{\infty} f(p,\phi) h(p + x\sin\phi - y\cos\phi)\,dp\,, \qquad (2)$$

where h is the filter function and $f(p,\phi)$ are the parallel beam projection data restored from measured signals by an interpolation scheme. Because of the finite width of the parallel beams and other properties of the imaging system that the FBP algorithm does not take into account, the resulting tomogram is convoluted by some "apparatus" or "point spread" function. It is possible to reconstruct such functions, thus obtaining an estimate of the half-width of the apparatus functions and the spatial resolution.

For the ART algorithm the following simple form was investigated:

$$g_i^{l+1} = g_i^l + \frac{f_{j(l)} - \sum_{k=1}^{N} W_{j(l)k} g_k^l}{\| W \|_{j(l)}} W_{j(l)i}\,, \qquad (3)$$

where l indicates the iteration step, $j(l) = l \bmod M$, $\| W \|_j$ is the norm of the weighting-matrix elements for detector j, and the other symbols have the same meaning as in Eq. (1). Some parts of the plasma are poorly viewed by the current system (see Fig. 1). For the ART algorithm the solution of Eq. (1) is therefore ill-conditioned. An improvement can be made by "adding signals" by interpolation, thus using *a priori* information about smoothness of the tomogram. It is also possible to take into account other *a priori* information, for example by using a smoothed tomogram obtained with the FBP algorithm.

Preliminary results

Figures 4(a) and (b) show a mathematical phantom of plasma emission (on a grid of 59 x 59). A reconstruction has been made from projections, where 5% gaussian random noise is added, by the FBP algorithm with the Erokhin-Shneiderov filter function /3/. Figure 4(c) shows the result of this reconstruction for five fan-beams with 17 detectors each (similar to the current system, but with a simpler distribution in the (p,ϕ)-plane) after interpolation to 25 sets of parallel beams with 35 detectors each. The mean error for this reconstruction is 13%, compared to 29% without interpolation. The two islands can be distinguished clearly. To examine the information content for different viewing directions of the imaging system, a scheme for calculating Kazantsev's information parameters /4/ is under development.

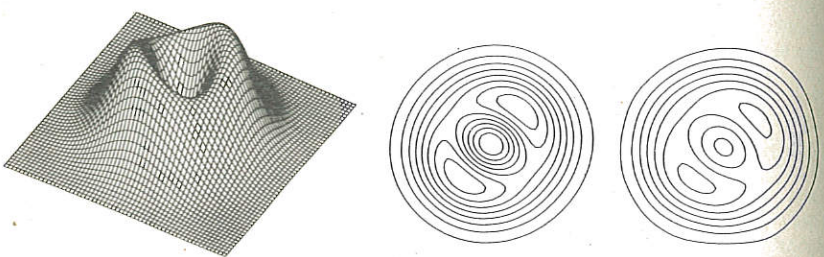

(a) (b) (c)

Fig. 4: Three-dimensional plot (a) and a contour plot (b) of a phantom of the visible light emission with $m = 2$ islands. (c) Reconstruction of the phantom, "measured" with five fan-beams and transformed to parallel beams.

Acknowledgement

This work was performed under the Euratom-FOM association agreement with financial support from NWO and Euratom.

References

/1/ L.C. Ingesson, J.J. Koning, A.J.H. Donné, D.C. Schram, "Visible light tomography using an optical imaging system", accepted for publication in Rev. Sci. Instrum. (October 1992)

/2/ G.T. Herman, ed., *Image Reconstructions from Projections* (Springer Verlag, 1979)

/3/ V.V. Pickalov, N.G. Preobrazhenskii, *Reconstructive tomography in gas dynamics and plasma physics* (Nauka, Novosibirsk, 1987) (in Russian)

/4/ I.G. Kazantsev, *Selection criteria for informative projection in computerized tomography*, preprint N 656 (Computer Center RAS, Novosibirsk, 1986) (in Russian)

INVESTIGATION OF THE SENSITIVITY OF VISIBLE CONTINUUM $Z_{eff}(0)$ TO EDGE RADIATION

G. Telesca, G. Van Oost, J. Ongena*, C. Leys, N. Schoon[1]

Laboratoire de Physique des Plasmas - Laboratorium voor Plasmafysica
Association "Euratom-Etat belge" - Associatie "Euratom-Belgische Staat"
Ecole Royale Militaire - B 1040 Brussels - Koninklijke Militaire School

[1] Laboratorium voor Natuurkunde, Faculteit Toegepaste Wetenschappen,
Universiteit Gent, Belgium

1. Introduction

The determination of Z_{eff} from visible continuum radiation is based on the assumption that the line-integrated continuum signal is mostly composed of bremsstrahlung radiation. In practice a wavelength window relatively free of spectral lines is selected, and the line-integrated continuum signal along different chords from the edge up to the central plasma is measured. The local emissivity $\varepsilon(r)$ is then calculated using an Abel inversion procedure, and the Z_{eff} profile can be obtained. Although theory and techniques are well established [1,2], in any experimental device there remains an uncertainty in the calculated value of Z_{eff} due to the non-bremsstrahlung radiation from the cooler edge plasma (e.g. emission from recombination and molecular bands). As a consequence, the local bremsstrahlung emissivity in the outer region of the plasma cannot be determined and the signal measured along every chord through the plasma contains a spurious contribution.

In this paper the error in the value of the central plasma emissivity (and Z_{eff}) due to edge radiation has been investigated. Qualitative analytical considerations have been complemented by a qualitative analysis, consisting of the comparison of test emissivity profiles with Abel-inverted profiles obtained from the integrals along central chords only.

The Z_{eff} diagnostic on TEXTOR with the data evaluation procedure is described in [3], the limiter configuration in [4].

2. Numerical analysis

For a plasma consisting of a number of concentric rings of emissivity ε_i, the line-integrated emissivity L_e along chord A crossing the center of the plasma can be written as

$$L_{eA} = \varepsilon_0 l_0 + \sum_1 \varepsilon_i \, l_{iA} \qquad (1)$$

---

* Researcher at NFSR (Belgium)

where ε_0 is the central emissivity, l_0 and l_{iA} the chord length in the central and *ith* ring for chord A. The line-integral along chord B shifted over a distance $l_0/2$ with respect to chord A is

$$L_{eB} = \sum_i \varepsilon_i \, l_{iB} \tag{2}$$

By subtracting, one obtains

$$\varepsilon_0 l_0 = (L_{eA} - L_{eB}) - \sum_i \varepsilon_i \, (l_{iA} - l_{iB}) \tag{3}$$

Thus, if the second term is small with respect to the first term on the right hand side, the central emissivity can be roughly estimated from the difference between the signals L_{eA} and L_{eB}. The error induced on the central emissivity by neglecting the second term, is reduced by taking into account additional signals from more outward lying chords, provided that the emissivity decreases towards the plasma periphery. This is normally the case for tokamak bremsstrahlung emissivity profiles. For this kind of profiles, the central emissivity, and hence $Z_{eff}(0)$, can be inferred from a set of chords crossing the plasma core.

To evaluate numerically the influence of the second term on the central emissivity determination, different test emissivity profiles have been used. Further, a poloidally symmetric non-bremsstrahlung edge contribution has been added to the test functions in order to determine the additional error on the ε_0-value.

Polynomials of the form

$$\varepsilon(r) = \varepsilon_0 \left(1 - \left(\frac{r}{a}\right)^2\right)^n \tag{4}$$

with n = 1,2,3 simulate the emissivity profile (in the present analysis hollow profiles are not considered) which is integrated along a chosen set of chords; a is the plasma radius. The line-integrals then are Abel-inverted and the resulting emissivity is compared to the test function (Fig.1,2).

It is found that, when only the most central chords, lying in the angle interval $-7 \leq \alpha \leq 7$ (Fig.2), are used for the inversion, the central value ε_c of the Abel-inverted profile matches with the central value ε_0 of the test function. In the Abel-inversion routine a zero value is imposed on the line-integrated emissivity for the chord tangential to the plasma edge.

As a further step, to simulate the non-bremsstrahlung edge contribution a ring of constant emissivity ε_b and width W_b is added to the test function (Fig.1). Following the same procedure described above, the ε_b-dependence for a (n=2)-profile of the ratio $\varepsilon_c/\varepsilon_0$ has been calculated for two different widths $W_b \approx 0.1a$ and $W_b \approx 0.25a$ (Fig.3). Even for high values of the edge contribution ($\varepsilon_b/\varepsilon_0 = 0.5$, $W_b \approx 0.25a$) the over-estimating of the central emissivity does not exceed 10%. Similar results are obtained for polynomials with n=1 and n=3. Thus, the numerical simulation demonstrates that the central emissivity can to a good approximation be obtained from a set of central chords only, even in the presence of a substantial edge signal.

3. Experimental test

On TEXTOR the limiter configuration, especially the toroidal belt limiter ALT-II, as well as the line of sight through the diagnostic port cause serious problems for a Z_{eff} evaluation. The plasma-wall interaction, which is enhanced during auxiliary heating [5] produces an important non-bremsstrahlung edge radiation at any toroidal angle. On the other hand the geometry of the optical system does generally not allow the determination of the edge contribution.

A different test has been performed using an experimental line-integrated emissivity signal from a TEXTOR discharge. In this case the magnetic surfaces are no longer concentric circles but a Shafranov shift of 5 cm (or about 0.1a) is imposed. A typical visible continuum signal as a function of the viewing angle (α=0 for a chord crossing the liner center, $\alpha \geq 0$ for LFS, $\alpha \leq 0$ for HFS) is shown in Figure 4. The strong poloidal asymmetry results from the interaction of the edge plasma with the toroidal belt limiter ALT-II. The LFS radiation is mostly composed of free-bound and molecular band radiation, which is superimposed on the bremsstrahlung signal. Therefore, sector A is not usable for Z_{eff}-evaluation.

For the interpretation of the HFS signal (sector C in Figure 4) two cases have been considered. In the first case the bremsstrahlung signal is represented by the dashed line, whereas in the second case the same signal is set to zero in region C. In both cases all chords with viewing angle $\alpha \leq \alpha_0$ are used for the inversion. The resulting Z_{eff} are represented by curves b and c in Figure 5. Although the two profiles differ substantially at the plasma edge (due to the different non-realistic assumptions concerning the edge contribution), they are nearly equal in the plasma center. This confirms that the non-bremsstrahlung edge contribution does not affect significantly the evaluation of the central Z_{eff}.

4. Conclusion

Although a data evaluation procedure in which Abel-inverted profiles are obtained from the line-integrated emissivities along central chords only, can strongly affect the reconstructed emissivity in the outer plasma, the central emissivity is rather insensitive to the edge radiation. The present analysis thus allows a reliable determination of the central value of Z_{eff}, even in cases where the edge non-bremsstrahlung radiation is significant.

References

[1] Kadota K., Otsuka M., Fujita J., Nucl.Fusion 20, 209 (1980)
[2] Vershkov V.A. et al., Sov.J.Plasma Phys. 10 (5), 515 (1984)
[3] Ongena J. et al., Fusion Technology 1990, 552 (Proc. 16 SOFT)
[4] Samm U. et al., Journal of Nucl.Mater., 24, 162 (1989)
[5] Van Oost G. et al., Fusion Eng. and Design, 12, 149 (1990)

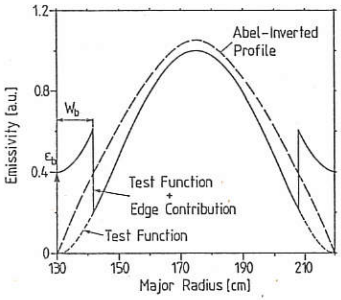

Fig.1: Test function (n=2) with added edge contribution (e_b/e_0=0.4, $W_b \approx 0.25a$), solid curve; Resulting Abel-inverted profile, dashed line.

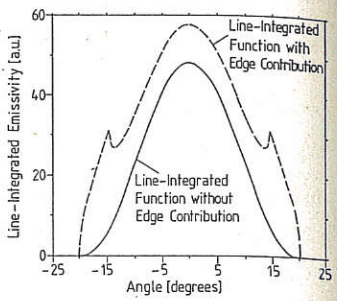

Fig.2: Line-integrated test profile (n=2) as a function of viewing angle; with (dashed curve) and without (solid curve) edge contribution (e_b/e_0=0.4, $W_b \approx 0.25a$).

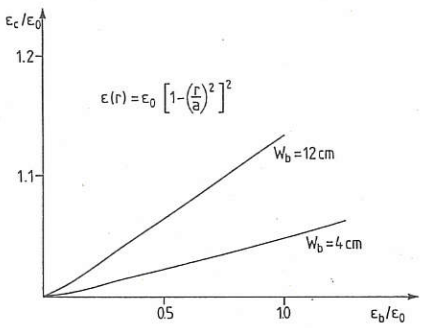

Fig.3: Central value of Abel-inverted emissivity profile as a function of the spurious edge contribution amplitude, for two different widths ($W_b \approx 0.1a$, $W_b \approx 0.25a$)

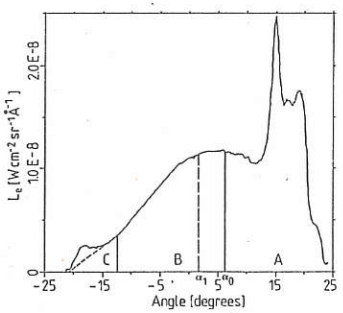

Fig.4: Experimental line-integrated signal (ohmic shot number 46403, I_p=340 kA, B_t=2.25 T, n_{e0}=3.4 10^{13}cm^{-3})

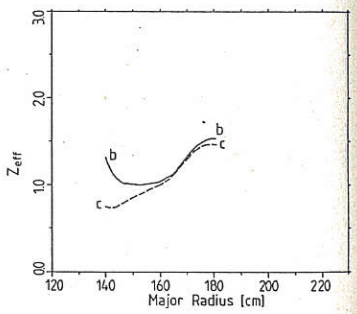

Fig.5: Calculated Z_{eff}-profiles for two different assumptions concerning the edge contribution (see text)

Spatially Resolved Diagnostics of Inhomogeneous Low Temperature Plasmas: New Techniques

T. Neger and H. Jäger
Institut für Experimentalphysik, Technische Universität Graz,
Petersgasse 16, A-8010 Graz, Austria

Most of the discharges of technical importance do not show simple distributions of the plasma parameters. In order to operate them with high efficiency, only a detailed knowledge of the plasma parameters can serve as a rational basis for an optimization of the aspired technical processes. In the case of laboratory plasmas one can often use the approximation of a plasma geometry near a homogeneous or at least rotationally symmetric one, thus enabling a straightforeward data reduction. For asymmetric plasmas a quantitative analysis of the plasma state can only be performed if more sophisticated methods are applied to the experimental procedure as well as to the data reduction. This paper outlines some recently developed methods.

Rotationally Symmetric Plasmas: New Abel-Inversion Technique

Side-on investigations of rotationally symmetric plasmas require some numerical inversion procedure in order to obtain spatially resolved distributions of the plasma parameters. An essential drawback of most of the well-known methods of Abel-inversion is their oversensitive response on discontinuities of the side-on data. Frequently problems are caused by measurement-errors and by the differentiation of too noisy data. As a consequence, the calculated radial distribution is dominated by regions of physically irrelevant oscillations.

By a new method of numerical Abel-inversion one can avoid this disadvantage /1, 2/. The unknown radial distribution is expanded in a series of cosine-functions, the amplitudes of which are calculated by least-squares-fitting of the Abel-transformed series to the measured data. The advantages of this method are: (a) The method is derivative-free, (b) neither smoothing nor any other pre-treating of the measured side-on data is necessary, (c) the actual form of the cosine-functions can be adapted to given physical conditions and (d) the method can be used as a noise-filter by choosing lower and upper frequency-limits. Experimental tests of this method versus older Abel-inversion techniques have been performed under exactly the same conditions. Additionally the reaction of the different methods on a number of computer-simulated side-on data has been analyzed. The new inversion method showed best results throughout. Therefore we would like to recommend this Fourier-method for all practical applications of Abel-inversion.

Interferometric Plasma-Diagnostics by Computerized Optical Tomography

A lack of sufficient spatial symmetry of a discharge usually prevents a serious quantitative investigation by traditional optical diagnostics. In such cases a multidirectional experimental observation has to provide the required different side-on data for the chosen tomographic reconstruction algorithm. In case of diagnostics by interferometry the investigation should be performed using holography /3,4/. This method turned out to be more convenient, as far as a simultaneous recording of the different projections is necessary.

Small steady state plasmas, which can be rotated stepwise to the required angular positions, might also be investigated using a single classical interferometer. In this case interferometry can also be performed with white light illumination, not being possible in holographic interferometry /5/. However, essential requirements on side-on projection data are both a high accuracy and a spatially continuous presentation of the profile of the wavefront phase shift which has been caused during the wave passed the plasma. Otherwise the sensitive tomographic reconstruction algorithms would yield non-reliable results. Spatial optical heterodyning turned out to be a best-suited technique for this purpose /6/. The commonly given low-frequency fringes of the plasma are superimposed by an artificially introduced high-frequency carrier fringe system. This can be easily achieved by suitable adjusting procedures. The subsequent treatment of the composed fringe pattern by fast Fourier transformation, filtering processes and back transformation provides the required resolution of the spatial phase profiles. Another increase of sensitivity can be achieved if resonance interferometry is used. It makes a selective determination of atomic particles possible.

In computerized optical tomography of plasmas - transient shock-wave plasmas might be excepted - the required number of projections can be much smaller than in tomography for medical applications. Plasmas usually do not show such high refractive index gradients as they appear comparatively as abrupt absorption changes for X-rays in medical applications /7/. The spatial information content to be resolved in plasma diagnostics frequently is relatively small. The number of necessary projections obviously depends on this given information content as well as on the size of the spatial area which should be reconstructed tomographically. However, an appropriate tomographic reconstruction algorithm has to be applied which is optimized for small numbers of projections (algebraic reconstruction technique, see ref. /7/).

If plasmas show larger gradients of the refractive index, not only the number of projections have to be increased, but also the effects of possible ray bending of the probing light beam due to refraction by the plasma has to be considered. A too large refraction would not allow to use the straight ray propagation assumption any more. Checks for this have been performed showing that usually refraction effects can be neglected. Even if small refraction effects can be already recognized, they do not affect the tomographic reconstruction remarkably. This can be generally explained because ray bending can be characterized by an effect according to the second spatial derivative of the refractive index,

whereas for the tomographic reconstruction algorithm only the first derivative of the refractive index is relevant /8/. An example of an experimental arrangement for optical tomography on the basis of holographic interferometry is given in figure 1. This arrangement is optimized to check for ray bending.

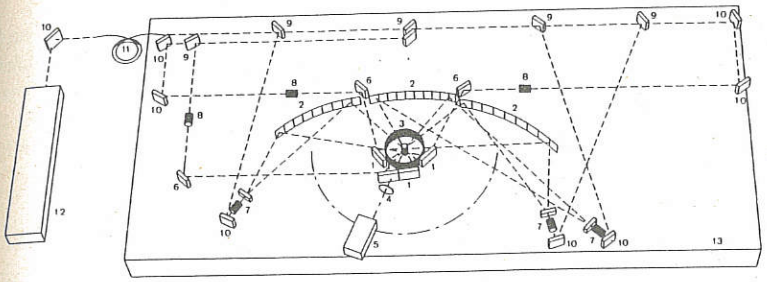

Figure1. Tomographic arrangement for simultaneous holographic recording of 28 interferograms. 1, holder for holographic plates; 2, mirror gallery; 3, zone including phase object; 4, lens for imaging the object zone on the CCD camera; 5, CCD camera; 6, two-axis-rotatable mirror; 7, beam expansion optic (cylindrical lens); 8, conventional beam expander; 9, beam splitter; 10, mirror; 11, monomode fibre; 12, tunable dye laser system; 13, optical table.

Application of Nonlinear Optics: Planar Degenerate Fourwave Mixing

A drawback of computerized optical tomography is the need for a more or less large number of side-on projections being angularly different. Disregarding the experimental problems such as adjustment, stability and complexity of the set-up in general, many plasma devices of technical interest cannot be investigated using this method because the necessary optical access from different sides is not possible due to compact constructions of the discharge vessels or due to some special type of operation.

DFWM is a non-linear optical process of third order, in which three laser beams of same frequency ω interact in a non-linear medium, emitting a fourth beam having just the same frequency ω. However, it can only be applied, if a non-linear response of the medium can be achieved yielding a finite electrical susceptibility of third order. The method of recording the phase conjugate using degenerate four-wave mixing (DFWM) is characterized by a drastic reduction of required optical beams, although it yields directly a two-dimensional signal corresponding to particle densities for the chosen cross-section in the plasma without using any computerized tomographic reconstruction algorithms.

Figure 2 presents a possible arrangement using planar DFWM. Two counter-propagating planar pumping beams (amplitudes of electrical fields being $E_1(\omega)$ and $E_2(\omega)$) select the cross-section of the plasma to be investigated (compare also ref. /9/). The probing beam ($E_3^*(\omega)$) and one of the pumping beams build up a dynamic grid (sometimes also called

dynamic hologram) in the non-linear medium. In this way the remaining pumping beam is diffracted following the Bragg-condition. In DFWM the signal wave $E_4(\omega)$ produced in this way is phase conjugated with respect to the probing beam $E_3^*(\omega)$. The observation of the intensity of this phase conjugated wave brings about the advantage that all transparent inhomogeneities are compensated by following exactly the same way back. Therefore, the quality of the obtained signal is not affected by spatial disturbances.

The spatially resolved two-dimensional intensity distribution is promptly provided by the optical process itself. It can be observed using a suitable CCD camera. No tomographic reconstruction algorithm is necessary. The mechanisms leading to non-linear optical properties in plasmas are preferably connected with saturation phenomena. However, too much absorption of the plasma might bring about optical thickness and would make it impossible to observe a phase conjugated wave or its correct intensity, respectively.

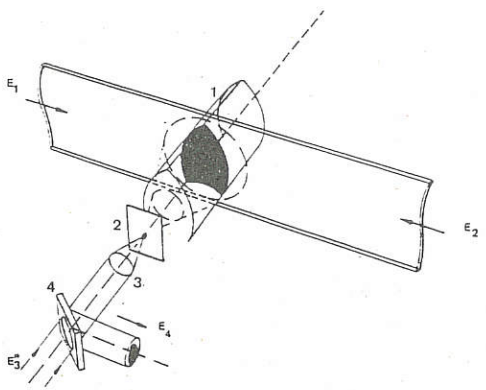

Figure 2. Sketch of experimental arrangement for spatially resolved plasma diagnostics by planar degenerate fourwave mixing. E_1, E_2, planar pumping beams; E_3^*, probing beam; E_4, phase conjugated beam (to CCD camera); 1, plasma; 2, pinhole; 3, lens; 4, beam splitter.

References

/1/ G.Pretzler, Z.Naturforsch. **46a**, 639 (1991)
/2/ G.Pretzler, H.Jäger, T.Neger, H.Philipp and J.Woisetschläger, submitted to Z.Naturforsch.
/3/ D.Vukicevic, H.Jäger, T.Neger, H.Philipp and J.Woisetschläger, Appl.Opt. **28**, 1508 (1989)
/4/ J.Woisetschläger, H.Jäger, H.Philipp, G.Pfeifer and T.Neger, Phys.Lett.A **152**, 42 (1991)
/5/ T.Neger, to be published
/6/ A.Dzubur and D.Vukicevic, Appl.Opt. **23**, 1474 (1984)
/7/ G.T.Herman, *Image Reconstruction from Projections* (Academic, New York, 1980)
/8/ H.Philipp, T.Neger, H.Jäger and J.Woisetschläger, Measurement, in press
/9/ P.Snowdon, M.Kaczmarek and P.Ewart, Proceedings of "Nato Advanced Study Institute On Combusting Flow Diagnostics", Monte Choro, Algarve, Portugal 1990

Localized Impurity Flux Measurements on Wendelstein 7-AS

J.V. Hofmann, W7-AS Team, ECRH Group, NI Group

Max-Planck-Institut für Plasmaphysik, EURATOM Ass.,
D-8046 Garching bei München, FRG

1. Introduction: In order to investigate and localize impurity influxes in the Wendelstein 7-AS stellarator a scanning mirror system has been installed which allows to measure influxes from parts of the wall, limiters and internal structures throughout the UV- and Visible spectral range 200 nm $\leq \lambda \leq$ 800 nm. The system is based on a mirror, usually positioned at the vessel wall, which can be shifted radially, rotated around this radial axis and rotated around an additional perpendicular axis, thus allowing to observe about 2/5 of the W7-AS vessel wall. The detection system comprises an intensified diode array camera coupled to an one meter Czerny-Turner spectrometer and enables to take spectra every 17 ms. The whole system is absolutely calibrated.

Our measurements concentrate on one of the bulk boronized limiters and the poloidal plane intersecting this limiter. Impurity influxes as a function of time are obtained for fix viewing directions, while spatial distributions are obtained by scanning the mirror during the discharge or by shot-to-shot variations of the line of sight, see fig. 1. All ion species within one spectrum (typically of 15 to 30 nm spectral range) are monitored simultaneously.

In the following we first concentrate on a comparison of influxes of carbon and boron from the limiter. In a next step, the poloidal distribution of BI-BIV, CII-CV and OII-OV atoms and ions is investigated. Finally, the localizations and radial extensions of the above mentioned ions are investigated in more detail and the dependence of the radial position and width of these radial emissivity profiles on plasma parameters is presented.

2. Influx from the limiter: In order to get rid of titanium influxes from a TiC-coated graphite limiter, bulk-boronized graphite (20% boron) has been installed as a limiter material in Wendelstein 7-AS. To determine the flux ratio of carbon and boron due to sputtering out of the limiter surface CI (247.856 nm) and BI (249.677 + 249.772 nm) transitions have been measured for different discharge conditions viewing the limiter, see insert of fig. 1. Since these carbon and boron transitions are separated by only a few nanometers no absolute calibration of the detection system is needed to determine the flux ratios. However, interpretation of measurements using this CI transition is complicated by the fact that its lower level is a metastable one.

Method: Fluxes of impurity species z, Γ_z, can be determined from measured intensities I_z using the well known relation

$$\Gamma_z = \frac{4\pi}{h\nu} \frac{S}{BX} I_z$$

Thus, to determine the flux ratio between carbon and boron, Γ_C/Γ_B, we need the intensity ratio, I_C/I_B, and have to determine the ratio of S / BX, the number of ionization events per photon, for both atoms. The $\left(\frac{S}{BX}\right)_C / \left(\frac{S}{BX}\right)_B$ ratios have been calculated by K. Behringer [priv.comm.] using transition probabilities from J. Kasten and from Lund. Since the actual population of the metastable CI levels is not exactly known we assumed statistical population which yields a

which yields a lower limit of the determined Γ_C/Γ_B ratio and which is the reason for the '≥' signs in the results given below.

Results: From these calculations we find a factor of 16-17 for the ratio of ionisation to excitation rate, roughly independent of electron temperature. Our measurements on W7-AS yield an intensity ratio, I_C/I_B, of 0.2 in case of He^{++} or D^+ working gas before boronization of the W7-AS vessel. After boronization the CI transition is just at or below the level of detectability and the intensity ratio is smaller than 0.2 (≈ 0.1).

Thus, we find an influx ratio of carbon and boron from the bulk-boronized graphite limiter $\Gamma_C/\Gamma_B \geq 3.5{:}1$ before and ≥ 2:1 after boronization. While the flux ratio before boronization seems to approximately reflect the carbon / boron composition of the limiter, after boronization, sputtering of carbon from the limiter surface is reduced.

3. Poloidal distribution of influxes and ions: In order to determine the origin of the impurity influxes and the poloidal distribution of the different ionization stages, we performed poloidal scans of the line of sight across the whole poloidal plane intersecting the W7-AS top limiter, as shown in fig.1. These scans have been performed during stationary phases of several series of equal discharges for all emissions within the UV and visible spectral range, 200 nm ≤ λ ≤ 800 nm.

Results: First of all, no emissions from metallic impurities like titanium, chromium or iron have been detected. All emissions found in spectral overviews and scans originate from hydrogen / deuterium, helium, boron, carbon, oxygen and calcium (part of the limiter material in 900 ppm). Our scans clearly reveal that, as shown in fig. 1, all influxes are strongly peaked at the limiter, identifying the limiter as the only prominent source for influxes within this poloidal cross section. Emission from BI, the neutral atom, is found to peak at the limiter and does show no further maximum as is expected for a strongly localized source.

While the low ionization stages clearly exhibit the strong limiter peak around S=7050, S being the scan coordinate as indicated in the insert of fig.1, and a small peak around S=6700, which corresponds to the location of the ion shells, see next section, highly ionized stages like BIV reveal a very broad poloidal distribution, extending from the limiter across the whole poloidal range of the plasma. This is seen as a result of the spread out of these ions along the magnetic field lines and is a consequence of a more uniform distribution of boron in the plasma. These signals of highly ionized species are no longer representative of local influxes but more of the ion density in the plasma.

4. Radial localization and extent of ionic shells: In addition to the local source of impurity influxes, the radial position and extension of the different ionization stages has been measured. These measurements are intended to provide information about the radial arrangement of the ionic shells, as a basis for transport calculations, and about the plasma composition across and beyond the last closed flux surface (LCFS).

Method: To measure the radial position of ionic shells one can perform radial scans across parts of the plasma cross section (during stationary phases of a discharge). During such scans, the intensity will peak when the viewing line is tangent to the flux surface where the maximum of the radial emissivity profile is located. The line-of-sight integrated intensity profile may then be converted to a radial emissivity profile by Abel inversion. The emissivity profile from Abel

inversion usually has a smaller radial extent (especially toward the plasma inside) and is located further outward.

Therefore, measurements of this kind are best done across plasma regions where the tangent on the flux surfaces is longest. However, in our case we have to avoid the dominating source of the limiter, see fig. 1. We , therefore, perform our scans across the lower part of the plasma ellipse ($6400 \leq S \leq 6950$) where the tangents to the flux surfaces are short but where no local fluxes are present. In the following we discuss the line-of-sight integrated intensity profiles.

Result: We find that the locations of the singly ionized species BII, CII and OII (already to be seen for BII in the full poloidal scans of section 3) very well coincide around a position of S=6680 for a plasma of full aperture (a=17.5 cm, limiters open). This position corresponds to the LCFS at an effective plasma radius of $r_{eff} \approx 17.5$ cm, just at the limiter position. The radial ion shells show increasing broadening and inward shift for higher ionization stages, as shown in fig. 1.

The radial extension of the singly ionized species is found to be $\Delta S_{1/2} \approx 140$, corresponding to an effective radius spread of $\Delta r_{eff,1/2} \approx 4$ cm and the profiles are found to be roughly inside / outside symmetric. However, the higher ionization stages are found to be more asymmetric towards the inside.

By limiting the plasma aperture from 17.5 cm (full aperture) over 14.4 cm finally to 12.0 cm (smallest aperture) by changing the limiter positions, we find that the ionic shells shift inward, become broader and a more and more asymmetric shoulder towards the plasma inside is building up, see fig. 2. However, we still find that a pronounced peak at the outermost position (corresponding to the full aperture) remains, indicating that the radial distribution of the ions spreads out beyond the limiter radius, as the plasma aperture is reduced (compare maxima and shoulders with the LCFS indicated by the dashed vertical lines in fig. 2).

Thus, we find that all ions of low ionization states do exist well outside the limiter radius for smallest plasma aperture, where no closed flux surfaces should exist anymore. This is a consequence of the relatively high electron temperature of $\cong$ 100 eV at the LCFS and the limiter which is much higher than the ionization potentials of these ions.

In contrast, highly ionized stages like BIV, CV and OV show a very pronounced radial shift when changing the aperture from a=17.5 cm to a=14.4 cm with no more peak remaining at the outermost position of the shell. This indicates, that the plasma outside the limiter does not comprise of these highly ionized species (with ionization potentials well above 100 eV) as a consequence of the temperature at and outside the LCFS.

5. Conclusions: We presented results of a very powerful scanning mirror diagnostic for spectroscopic impurity flux investigations in the W7-AS stellarator. Sputtering flux measurements on the bulk-boronized graphite limiter showed a clear reduction of carbon influx compared to boron, after boronization. Scans across the whole poloidal cross section of the plasma, inner wall and limiter identified the limiter as the only prominent impurity source. Important differences of the poloidal distribution between low and high ionization states were found. The radial distribution of the different ionization stages of impurity ions was measured and the results showed the existence of low ionization states well outside the limiter radius, especially for smallest plasma aperture, as well as the increasing spread of the radial distributions.

6. Pictures:

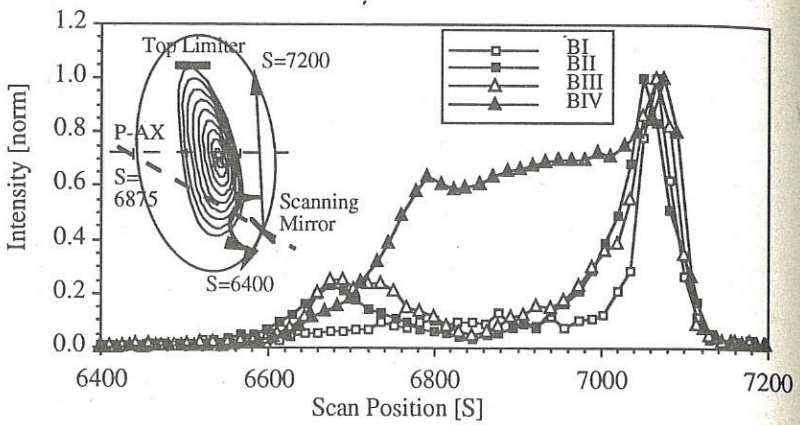

Fig.1: Intensities of boron ionisation stages as a function of the scan coordinate S (representing the poloidal position). Clearly all intensities peak at the limiter around S=7050. Note the very broad poloidal distribution of BIV!. The small peaks around S=6700 represent the radial profiles of the ionic shells. Insert: W7-AS poloidal cross section and scan range of the scanning mirror diagnostic. P-AX denotes the port axis which is located at S=6875.

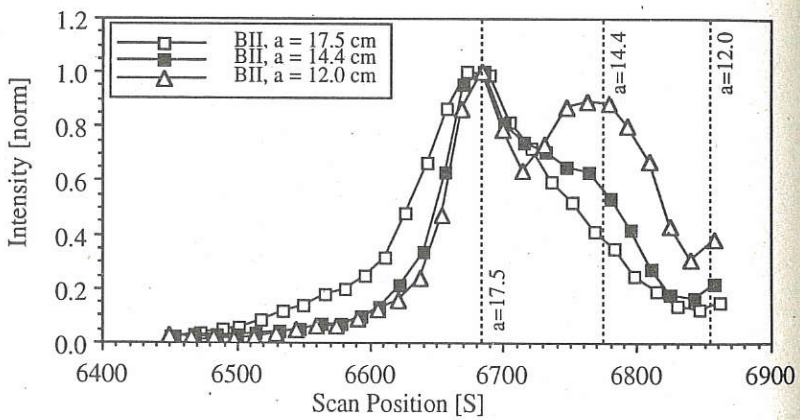

Fig.2: Dependence of the radial profiles of BII on the plasma aperture (a=17.5, 14.4 and 12.0 cm). The profiles are slightly shifted and strongly broadened (shoulder!) with decreasing aperture. The LCFS is indicated by the dashed vertical lines for the three cases.

DIAGNOSTICS FOR HYDROGEN BEHAVIOUR AT EDGE REGIONS OF HIGH TEMPERATURE PLASMAS

K. Muraoka, M. Maeda,* C. Honda, T. Okada,* K. Uchino, T. Kajiwara and H. Takenaga
Department of Energy Conversion, Kyushu University, Fukuoka 816, Japan
*Department of Electrical Engineering, Kyushu University,
Hakozaki Fukuoka 812, Japan

1. INTRODUCTION

As atomic hydrogen behaviour is divided into that around the core plasma and that around the divertor, different LIF techniques are necessary depending on the circumstances. For the former, because the hydrogen atoms supplied by NBI and pellet injection are well quantified, gas-puffed and recycled atoms have to be understood. LIF tuned to the Hα transition supplemented by emission measurements at Hα and Hβ from various toroidal and poloidal positions, yields such information. On the other hand, hydrogen atoms around the divertor region are to be diagnosed using, in addition to emissions at the Balmer series, LIF by observing fluorescence at Hα resulting from the two-photon excitation from the ground level.

In this paper, we describe the techniques, hardware, and results of experiments and feasibility studies.

2. SCHEMES

Figure 1 shows the energy level diagram of a hydrogen atom. Due to the large difference in energy between the excited levels (principal quantum number $n \geq 2$) and the ground level ($n=1$), atomic hydrogen even in a plasma is predominantly in the ground level (typically $N_2/N_1 < 10^{-3}$, where N is a population density at the suffixed level). Therefore, for maximum precision, measurements of hydrogen atoms in the ground level are desirable. Direct excitation from $n=1$ to $n=2$ requires a tunable source at the wavelength of 122

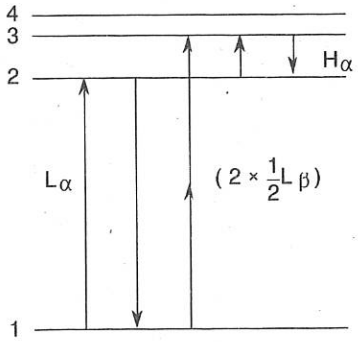

Fig.1 Energy level diagram of a hydrogen atom and transitions relevant to the present discussion.

nm. Development along this line has been pursued at several laboratories for many years, with Jülich succeeding in getting signals from the edge plasma in the TEXTOR tokamak.[1] However, handling of the tunable VUV source, combined with the necessity of reducing stray laser light, makes this approach almost impossible to apply to other large plasma machines with limited optical access.

Two alternative approaches for atomic hydrogen measurement have been proposed. In one method, the population density at n=2 is probed by exciting the Balmer series transition and observing the fluorescence at the same wavelength (Balmer series fluorescence), while in the other method, the population density at the ground level is probed by observing the Balmer alpha fluorescence caused by two-photon excitation to the n=3 level from the ground level (Lyman-beta excitation). The former technique requires sufficient electron impact excitation to populate the n=2 level, and this requires $n_e > 10^{18}$ m^{-3} and $T_e > 10$ eV. Also there has to be some means of preventing stray laser light from swamping the signal. The latter technique, on the other hand, relies on the fact that if the output of an ArF laser is passed through a Raman cell filled with D_2 gas, the first Stokes line matches the two-photon excitation of the transition (wavelength 205 nm) and, thereby, much higher laser powers are available. However, this has to be offset against the reduced cross section for the two-photon excitation. Apart from the severe requirement for high laser power, the method has some clear advantages; namely, stray laser light can be completely eliminated by a filter because the fluorescence at 656 nm is well separated from the laser wavelength and all optical components of the collection system including the fibre optics will act as rejection filters for stray laser light; interpretation of the signal is much easier than the excitation from excited states; spatial resolution is possible even with a coaxial arrangement of laser light injection and fluorescence detection; and the input wavelength is not in the VUV region so the input system can be considerably simpler.

The above arguments implicitly assume that the spectral width of the tunable lasers are wide enough to cover the Doppler width of hydrogen atoms, yielding the fluorescence proportional to atomic hydrogen density. However, if the spectral width is made narrow enough compared with the Doppler width, a portion of the hydrogen atoms resonant with the narrow laser radiation only is excited. By spectrally scanning the laser radiation and observing the resultant fluorescence, we can obtain velocity-distribution of hydrogen atoms.

3. TUNABLE LASER SOURCES

3.1 Balmer series LIF (density)

Visible laser sources tunable to the Balmer series are commercially available. Because the SN ratio for the observation is decided by the fluctuation of the background Balmer series radiation, averaging (integration) over some time interval reduces the fluctuation, yielding a

higher SN ratio. In this respect, long pulse (>1 μs) flashlamp-pumped dye lasers, rather than short pulse (~10 ns) excimer laser-pumped, are more desirable.

3.2 Balmer series LIF (velocity-distribution)

We want to measure the velocity-distribution of atoms in high temperature plasmas in a short time (≤1 ms) by reconstructing Doppler profiles. For this purpose, rapid-frequency-scan (RAFS) laser spectroscopy[2] has been developed. This technique is useful for determination of the penetration velocity of hydrogen atoms from the periphery into the core plasma.

3.3 Lyman series LIF (density)

An ArF laser with an output energy of 100 mJ in 10 ns was injected into a Raman cell of D_2 gas to yield a maximum output energy of 15 mJ in 10 ns. The tunable range of the ArF laser of 2 nm can cover the two-photon transition of the Lyman beta (205 nm). Although the measurement of velocity distribution is possible in principle, it has not yet been attempted.

4. CALIBRATION

4.1 Balmer series LIF

Saturated LIF, combined with the Rayleigh scattering calibration *in-situ* of the optical system, including the solid angle of detection, transmission through optical components and sensitivity of optical detectors, yields the absolute value of population density at n=2.[3] The total number density of atomic hydrogen is obtainable using a collisional-radiative model.

For measurements of velocity distribution of hydrogen atoms, it is only necessary to check that the measurements are performed in the linear region (fluorescence increases proportionally with laser power). Otherwise, calibration is not necessary because the relative shape of fluorescence using RAFS laser spectroscopy is directly related with the velocity distribution.

4.2 Lyman series LIF

Because a two photon process is involved, a more elaborate calibration than for the case of 4.1 is necessary here. One possibility is to use a source of known atomic hydrogen density and to perform a fluorescence experiment against it, yielding the calibration factor. The second possibility is to rely on a rate equation to interpret the saturation characteristic of fluorescence against laser power, where knowledge of hydrogen density is not necessary.[4]

5. PLASMA MEASUREMENTS

5.1 Balmer series LIF

The technique was applied both to Heliotron E[5, 6] and CHS,[6] and successfully obtained fluorescences for both density and velocity distribution. Combined with the measurements of Balmer series emission and computer simulation code DEGAS,[7] they yielded very

useful information of atomic hydrogen behaviour and particle confinement characteristics there.

5.2 Lyman series LIF

The technique was applied for the first time to measurements of atomic hydrogen density in the scrape-off layer of the Heliotron E plasma,[4] and the detection limit was found to be 1×10^{16} m^{-3}.

Based on the positive results, a feasibility study of the application of the technique to a large fusion machine, such as JET, was performed[6] and it was found to be within the reach of the available technique. Also, it was shown that the technique should yield invaluable information for understanding the pumped-divertor operation.

6. FUTURE WORK

Both LIF techniques are now at the stage of routine operation, and should yield information of particle behaviour in high temperature plasmas, which can be incorporated as input data into code analyses for particle and energy confinements.

The work described here was performed using the laser equipment at the Institute for Ionized Gases and Laser Research, Kyushu University. The authors wish to thank Heliotron E and CHS groups who made the work in Section 5 possible, Dr. M. Bowden for correcting English, and many graduate students who participated at various phases of the present studies.

REFERENCES

1) P. Bogen and Ph. Mertens, in *Proc. 4th Int. Symp. on Laser-Aided plasma Diagnostics* (Fukuoka, 1989) p. 117.
2) C. Honda, M. Maeda, K. Muraoka and M. Akazaki, Rev. Sci. Instrum. 58 (1987) 759.
3) M. Hamamoto, M. Maeda, K. Muraoka and M. Akazaki, Jpn. J. Appl. Phys. 20 (1981) 1709
4) T. Kajiwara, T. Shinkawa, K. Uchino, M. Masuda and K. Muraoka, Rev. Sci. Instrum. 62 (1991) 2345.
5) K. Muraoka, K. Uchino, M. Maeda, T. Kajiwara, K. Matsuo, T. Okada, C. Honda, Y. Suehiro, N. Yano, K. Takeda, H. Hagiwara, M. Akazaki, S. Sudo, K. Kondo, H. Matsuura, T. Mizuuchi, F. Sano, M. Sato, M. Zushi and T. Obiki, J. Nucl. Mater. 176&177 (1990)
6) K. Uchino, H. Takenaga, T. Kajiwara, T. Okada, K. Muraoka, M. Maeda, H. Iguchi, K. Ida, S. Okamura, H. Yamada, K. Matsuoka and CHS Group, J. Nucl. Mater. (submitted).
7) D. B. Heifetz, in *Physics of Plasma-Wall Interactions in Controlled Fusion,* Eds. D. E. Post and R. Behrisch (Plenum, New York, 1986) p. 695.

DETERMINATION OF PLASMA EDGE PARAMETERS WITH FAST LITHIUM BEAMS

J. Schweinzer[1], K. McCormick[1], S. Fiedler[1], F. Aumayr[2], M. Pöckl[2], and H. Winter[2]

[1] Max-Planck-Institut für Plasmaphysik, D-8046 Garching bei München, Germany F.R.
[2] Institut für Allgemeine Physik, TU Wien, Wiedner Hauptstr. 8-10, A-1040 Wien, Austria

1. INTRODUCTION

The determination of space- and time-resolved density profiles of electrons and impurity ions in the edge region of magnetically confined plasmas is of great interest for a more detailed understanding of plasma - wall interaction and scrape-off layer physics. Li beam methods are based on measuring the LiI (2s-2p) resonance line at 670.8 nm (Li-IXS) permitting evaluation of electron density profiles. In addition, characteristic light from impurity ions arising from charge exchange with Li atoms delivers information about their distribution and temperature in the plasma edge (Li-CXS).
Li injectors with keV impact energy have been installed e.g. at ASDEX (60 keV/0.5 mA, /1/, /2/) and TEXTOR (20 keV/5 to 10 mA /3/, /4/, /5/). We present an improved Li ion source based on the experimental setup /6/ used on ASDEX, which will be installed on ASDEX UPGRADE and WENDELSTEIN AS (cf. chapt. 2).
In the edge plasma the fast Li atoms interact not only with electrons, but also with hydrogen and impurity ions, and consequently become excited as well as ionized via related collisional processes (impact excitation, ionization and charge exchange). A recursive algorithm has been developed to reconstruct the plasma electron density exclusively from relative scans of the LiI 670.8 nm emission intensity along the diagnostic beam direction /7/. The influence of plasma impurities on this data evaluation procedure will be discussed (cf. chapt. 3).

2. LITHIUM ION SOURCE

The Li injector consists of a solid emitter in Pierce-type configuration, a two-tube electrostatic lens (extractor and puller, cf. fig. 1) and a charge-exchange cell using sodium.

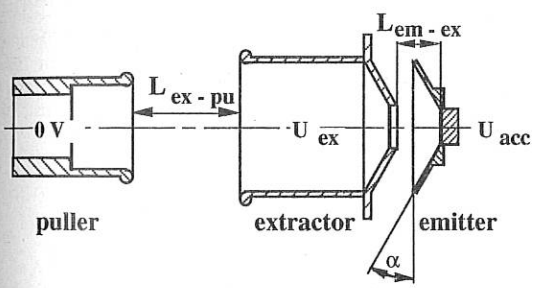

Fig. 1: Lithium ion source

The emitter is a modified 600 ion source of Spectra-Mat. Inc. coated with the lithium aluminosilicate β-Eucriptite. When heated to a temperature of about 1400 °C Li^+, currents of several mA can be extracted from the surface.
The geometric parameters L_{em-ex}, L_{ex-pu}, α and the extraction voltage U_{ex} (cf. fig. 1) have

been optimized for operation at accelerating voltages U_{acc} between 10 - 40 kV. The performance of the ion source has been investigated with a rotating-mirror beam profile monitor /6/ delivering the beam diameter d_{FWHM} and a faraday cup to measure the ion current I_{fc}. Both of them have been positioned at distances of about 2.2 m, relevant to future application on the mentioned fusion devices. Fig. 2 shows typical results for different adjustments of the ion source at U_{acc} = 35 kV which differ by slight modifications of the above mentioned parameters. The faraday cup current has been finally increased by a factor of 4 at U_{acc} = 35 kV compared with the ASDEX ion source.

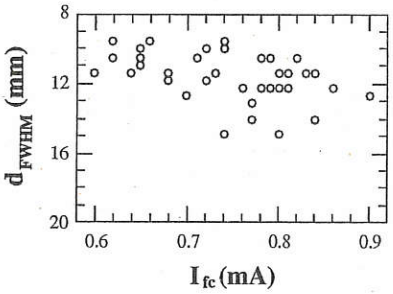

Fig. 2: Typical values of beam profile diameter and corresponding faraday cup current at U_{acc} = 35 kV

Assuming a typical Li^+ current of 0.8 mA and a neutralization rate of 80 %, the number of expected Li-IXS-photons n_γ along the beam axis per second at an injection energy of 35 keV is given by equ. 1

$$n_\gamma \; [cm^{-1}\, s^{-1}] \; = \; 1.6 \cdot 10^{14}\, N_{2p} \qquad (1)$$

N_{2p} is the radial dependent occupation number (cf. chapt. 3 and fig. 4) of the Li(2p) state and takes values between 0.01 and 0.1 for typical density profiles. This strong signal permits measurements of density profiles with high time resolution.

3. Z_{EFF} DEPENDENCE OF DENSITY RECONSTRUCTION ALGORITHM

If a local plasma coordinate z along the injected Li beam (z = 0 ... entrance of the Li beam into the plasma) is introduced as the independent variable, the rate equations for the occupation numbers $N_i(z)$ of the neutral Li states (i=1 denotes Li(2s), i=2 denotes Li(2p), and so on) and the boundary conditions are given by equs. (2a,b), respectively, using the Einstein sum convention further on.

$$\frac{dN_i(z)}{dz} = \left[n_e(z) a_{ij}^e(T(z)) + n_p(z) a_{ij}^p(T(z)) + n_q(z) a_{ij}^q(T(z)) + b_{ij} \right] N_j(z) \qquad (2a)$$

$$N_i(z=0) \; = \; \delta_{1i} \qquad (2b)$$

The coefficients a_{ij} in the rate equations cover excitation and deexcitation processes for the Li atoms from state j to state i as well as charge transfer and ionization due to collisions with electrons, protons and impurities of the plasma, respectively. These rate coefficients depend on the beam velocity and the temperature T(z) /4/. Spontaneous emission processes are described by coefficients b_{ij}. These necessary rate coefficients involving collisions of Li atoms with electrons and protons have been found by using experimental data as far as

available, and more over by a critical evaluation of various empirical cross section formulae. Cross sections for electron capture from Li into impurity ions have been derived from a scaling formula /8/. Rate coefficients for all other impurity ion - Li collision processes are derived by q^2 - scaling of the respective values for proton - Li collisions. This scaling law certainly overestimates the corresponding rate coefficients especially at lower impact energy, and must be regarded as a first step approximation.
A detailed description of the reconstruction algorithm based on equ. 2a for evaluating density profiles from Li(2s-2p) emission profiles can be found in ref. /7/.
For simplicity we assume an average q(z)-profile in combination with a model $Z_{eff}(z)$-profile ($Z_{eff}(z) = Z_{eff}$ = const. /9/) for ASDEX discharges. Taking care of quasi-neutrality, the densities n_p and n_q (equ. 2a) of, respectively, protons and impurity ions can then be expressed in terms of n_e /7/.
During the ASDEX OH-discharge #29737 the line density is raised up to the density limit. For reconstructing the electron density from measured LiI emission profiles, $Z_{eff} = 2.6$ at t = 2.1 was chosen to give good agreement with the density value from Thomson scattering at the separatrix position (cf. fig. 3). Assuming a line-density-dependence of Z_{eff} /9/ according to equ. 3

$$Z_{eff}(t) = 1 + (Z^{o}_{eff} - 1) \frac{\bar{n}_e(t_o)}{\bar{n}_e(t)} \qquad (3)$$

excellet agreement with the Thomson values is achieved for t = 0.8. Whereas a constant $Z_{eff} = 2.6$ would overestimate the density (cf. fig. 3).

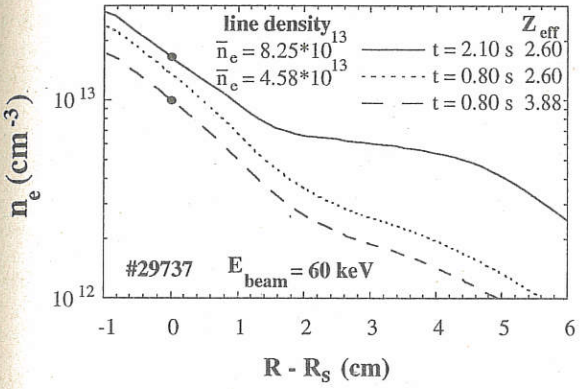

Fig. 3: Scrape-off layer density profiles for ASDEX discharge #29737 (OH mode, $B_t = 2.6$ T, $I_P = 460$ kA) evaluated with different Z_{eff} values in comparison with Thomson scattering values (symbols)

In order to investigate the sensitivity of Li-IXS on Z_{eff} at different injection energies (8 and 60 keV), LiI emission profiles have been calculated assuming an exponentially increasing electron density n_e^{in} at fixed $Z_{eff} = 2.0$. Density reconstruction from these two profiles has been performed with different Z_{eff} values (1.0, 2.5). Fig. 4 shows that the influence of Z_{eff} on the results of the diagnostic can be effectively reduced by decreasing the injection energy. Furthermore reconstruction of the plasma density is possible up to higher density values in the case of 8 keV injection energy as compared to 60 keV.

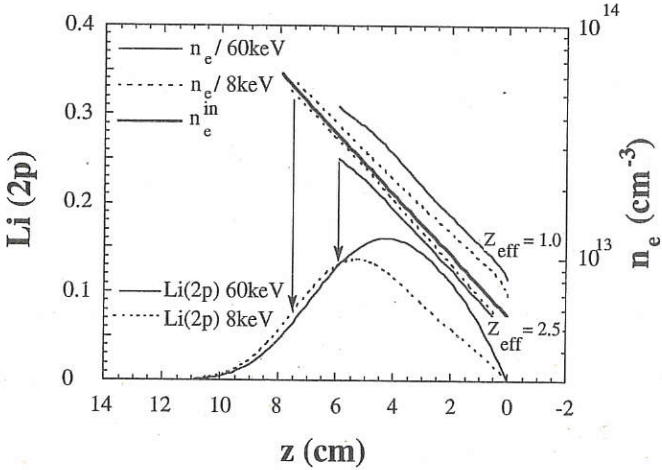

Fig. 4: Li(2p) emission profile at 8 and 60 kev injection energy, respectively, calculated from an assumed exponential increasing electron density n_e^{in}, using Z_{eff} = 2.0. The latter profiles were used to reconstruct the electron density under the assumption of different Z_{eff} values.

The Z_{eff} dependence of the plasma density reconstruction procedure in the case of 8 keV injection energy might even be weaker than shown in fig. 4, because of the for such a low impact energy inadequate q^2 scaling used for rate coefficients involving impurity ions.

CONCLUSION

Reduction of the injection energy for Li-IXS reduces the sensitivity of the method on the unknown parameter Z_{eff}, thus leading to an increased accuracy. Measuring at lower injection energies seems now feasible with the optimized ion source. Furthermore it might be considered in a future application of Li-IXS to gain at least approximate information about Z_{eff} in the plasma edge by operating the Li injector at widely different injection energies within the discussed energy range.

ACKNOWLEDGMENT

The work of one of the authors (S. F.) has been financed by the Schiedel Foundation.

REFERENCES

/1/ K. McCormick, H. Murmann, M. el Shaer, and the ASDEX and NI team *J. Nucl. Mat.* **121**, 48 (1984)
/2/ K. McCormick and the ASDEX team *Rev. Sci. Instrum.* **56**, 1063 (1985)
/3/ A. Pospieszczyk, F. Aumayr, H.L. Bay , E. Hintz, P. Leismann, Y.T. Lie, G.G. Ross, D. Rusbüldt, R.P. Schorn, B. Schweer and H. Winter *J. Nucl. Mat.* **162-164**, 574 (1989)
/4/ R.P. Schorn, E. Hintz, D. Rusbüldt, F. Aumayr, M. Schneider, E. Unterreiter and H. Winter *Appl. Phys.B* **52**, 71 (1991)
/5/ R.P. Schorn, E. Wolfrum, F. Aumayr, E. Hintz, D. Rusbüldt and H. Winter *Nucl. Fusion* **32**, 351 (1992)
/6/ K. McCormick and M. Kick, IPP Report III/82 1983
/7/ J. Schweinzer, E. Wolfrum, F. Aumayr, M. Pöckl, H. Winter, R.P. Schorn, E. Hintz and A. Unterreiter *Plasma Phys. Contr. Fusion* 1992 in print
/8/ R.K. Janev, *Phys. Let. A* **160**, 67 (1991)
/9/ K.-H. Steuer, H. Röhr and B. Kurzan, Rev. Sci. Instrum. **61** 3084 (1990)

Sniffer Probe Measurements in W7-AS

H. Wolff*, P. Grigull, W. Poschenrieder, J. Roth, P. Pech*
and the W7-AS Team

Max-Planck-Institut für Plasmaphysik, EURATOM Association,
W-8046 Garching/München, * Bereich Berlin O-Berlin, PSF 1250
Federal Republic of Germany

Introduction

Wendelstein W7-AS is a modular Advanced Stellarator with a major radius R = 2 m, effective plasma radius a ≤ 0.2 m, fivefold symmetry of the configuration and B ≤ 2.5 Tesla. The rotational transform ι can be varied between 0.25 and 0.7, the vacuum shear being low. W7-AS allows an operation free of net plasma current using ECRH and/or NBI up to 3 seconds. Typical plasma parameters obtained with ECRH are $T_e \leq 3$ keV, $T_i \leq 0.7$ keV with central densities $n_{eo} \leq 6 \times 10^{19}$ m^{-3}. The maximum electron density obtained with NBI heating was $n_{eo} = 3 \times 10^{20}$ m^{-3}, the energy confinement time ranges between 5 and 30 ms.

The edge plasma has a complex structure reflecting the 5/m symmetry of "natural" magnetic islands. A degradation of both energy and particle confinement is found at low order rational values of ι (a) at the plasma edge, whereas optimum confinement can be established in narrow ι-windows close to the resonances at ι = 1/3 and ι = 1/2. The poloidal cross-section of the plasma changes five times around the torus according to the fivefold periodicity from a vertical ellipse via a triangular shape to a vertical ellipse again. At low ι the minor plasma radius is defined by two movable limiters whereas above ι = 1/2 the edge structure becomes separatrix dominated. The complex edge structure varying with ι gives rise to inhomogeneous particle and energy flows to the wall and in-vessel installations which determine on the other hand the working gas recycling and the impurity generation affecting on their part the confinement properties of the plasma. The latter issues are essential topics of the experimental edge plasma programme of W7-AS.

Recently a sniffer probe, formerly used on the ASDEX tokamak /1/, was adapted to W7-AS with the aim to study the particle fluxes in the edge plasma and the influence of conditioning methods on various discharge regimes. The sniffer probe

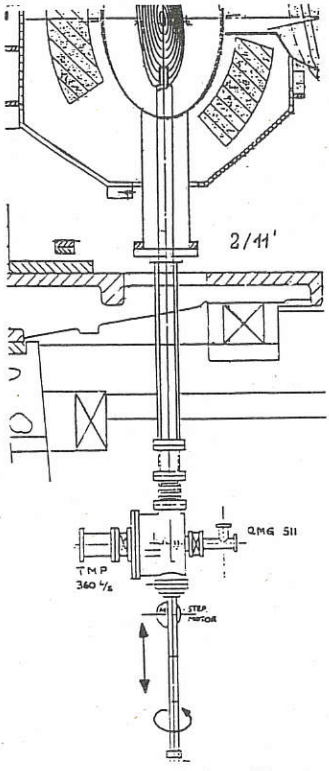

Fig. 1 Sniffer Probe position at port 2/11' of W7-AS

consists of a 2 m long tube with a graphite head near the plasma and a differentially pumped quadrupole mass spectrometer at the far end. The sniffer head with an entrance slit 5 by 20 mm^2 is equipped with Langmuir probes on both sides next to the slit. For symmetry reasons and also to allow Mach probe measurements, two more Langmuir probes are mounted on the rear side of the sniffer head.
The sniffer is mounted from the lower side near the ellipsoidal cross-section of the plasma. The entrance slit can be orientated into both toroidal directions and also moved along a chord passing near the plasma center to obtain radial flux profiles. The position of the sniffer probe is schematically shown in fig. 1. As demonstrated by the Langmuir probes next to the slit, the ion flux into the slit is inhomogeneous due to the elongated shape of the plasma and the nonsymmetric position of the sniffer.
The sniffer probe could not be calibrated for technical reasons, therefore only relative results were obtained.

Conditioning and gas retention
Initially, W7-AS was operated with metallic walls and TiC-coated graphite limiters resulting in an enhanced Ti and Fe impurity radiation limiting the accessible plasma parameter range. A considerable improvement was attained by carbonization or boronization of the inner walls.

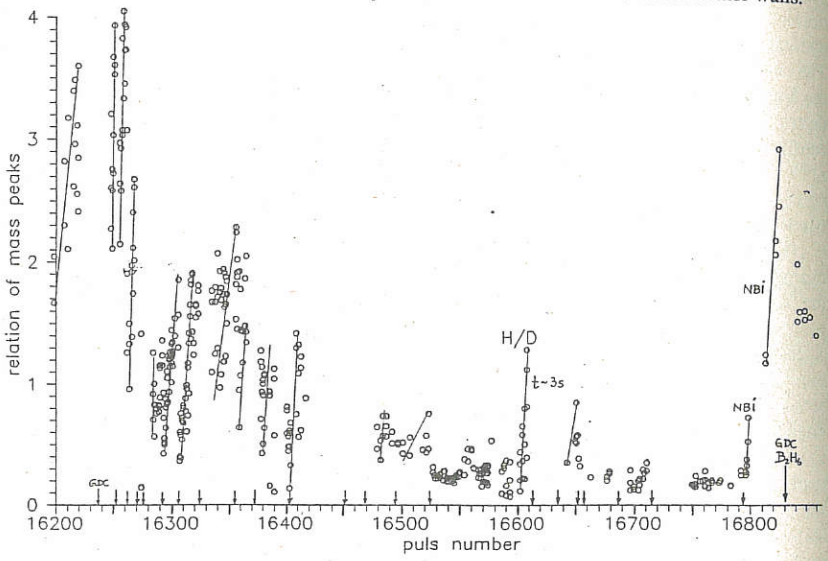

Fig. 2 Variation of the H/D ratio with the shot number

/1/ Poschenrieder W. et al Europhys. Conf. Abstract 9F (1985) p. 587
/2/ Hildebrandt, D. et al., 10. Int. Conf. Plasma Surface Interactions, Monterey, Ca. USA, March 1992

Since protective carbon or boron layers are removed from the limiter surfaces within a few pulses /2/ the TiC covered limiter tiles were subsequently replaced by tiles made of graphite with 20% boron content in the bulk. After installation of these boron-graphite limiters the W7-AS vessel was conditioned by baking at 150°C for three days and glow discharges in hydrogen for 30 hours towards the end of the baking period. After cooling down glow discharge conditioning in He was applied. Helium GDC was generally used at the beginning of every experimental day and after a varying number of plasma shots for recycling control. Initially, plasma discharges were strongly affected by uncontrolled release of hydrogen, which had probably been implanted during hydrogen GDC /3/ . Only small amounts of externally supplied He had to be used as a start-up prefill while the plasma density increased without further external fuelling during a discharge as well as from shot to shot. The newly installed limiter tiles were considered to be the main hydrogen sources therefore W7-AS was operated to attain a maximum thermal limiter load during this conditioning period. Recycling coefficients close to or below one were achieved after about 100 shots. External D-fuelling was possible beginning with shot #16087. The sniffer probe was used to study the effect of these discharge conditioning procedures. Fig. 2 shows the change of the ratio of the mass peaks H/D with the shot number. Mass peak values are taken approximately at 300 ms after pulse start. The arrows are pointing at intervals between shots with Helium glow discharge conditioning (duration of GDC 15 to 30 min.). The connecting lines show the rise of the hydrogen content during subsequent shots clearly demonstrating the degassing of H during shots. Approximately after shot #16401, no substantial H degassing took place with the exception of high power shots with increased pulse duration up to 3 seconds (eg. # 16601 - # 16610). Naturally NBI (beginning with shot #16793) using energetic H neutrals leads to an considerable increase of the H content. From the variation of the H/D ratio, it can be concluded that the primary conditioning of the hot vessel with H glow discharges produces an undesirable H charging of inner vessel components (mainly graphite components, in particular graphite limiter tiles) lasting several hundreds of shots. This result is supported by H concentration profiles obtained by nuclear reaction analysis of graphite samples taken from secondary limiters of W7-AS /4/. According to these results hydrogen is concentrated mainly

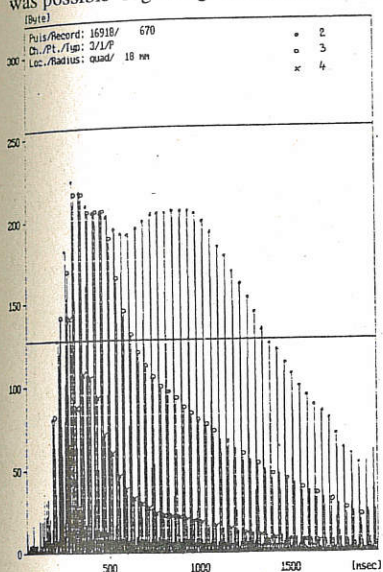

Fig. 3 Variation of H and D peaks after main pulse. Main pulse duration 400 ms (signals not corrected for transmission dependence)

/3/ R. Brakel et al., 10. Int. Conf. Plasma Surface Interactions, Monterey, CA. USA, March 92

/4/ Priv. communication from R. Behrisch; M. Laube, Institut für Kernphysik, Universität Frankfurt a. M.

in a layer of about 100 nm next to the surface. After boronization with a B_2H_6 + 90% He glow discharge hydrogen becomes again the dominating component (beginning with shot # 16830) indicating the enrichment of the boron layer with hydrogen. Suppression of the hydrogen component should be possible with the foreseen use of B_2D_6.
The presence of persisting hydrogen sources within the vessel (hardly influenced by GDC) is obvious from hydrogen emission during certain rampdown regimes presumably with runaway electron generation qualitatively shown in fig. 3. By proper timing of the different magnetic field components during rampdown these phenomena can be avoided.

Edge Plasma Structure
Besides well established diagnostics the sniffer probe should be used to study the edge plasma structure. This is of special interest, since it is intended to use the magnetic islands and the helical separatrix as a basis for the formation of natural divertors. At present, only some preliminary measurements of the edge structure with the sniffer are available. Radial scans of

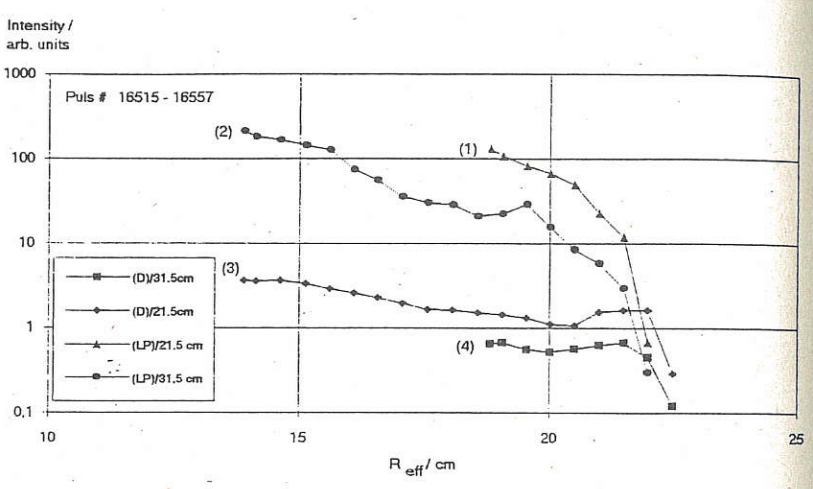

Fig. 4 Saturation current: (1) limiter position r_L = 31.5, (2) limiter position r_L = 21.5cm, Deuterium partial pressure; (3) at r_L = 21.5 cm, (4) at r_L = 31.5 cm

T_e, n_e and the saturation current were registered using the Langmuir probe mounted on the outer side (larger major radius) of the sniffer head next to the entrance slit. Fig. 4, as an example, shows the saturation current measured together with the deuterium current of the quadrupole within the same time window. Unexpectedly, there is a discrepancy between the radial decay length of both methods irrespective of the limiter position. The reason of this discrepancy is not yet clear and subject to further investigations. The hump of the deuterium signal at large radii (in immediate proximity to the wall) may be attributed to the neutral gas component.

ELECTRIC CURRENT COLLECTION BY LANGMUIR PROBE IN STRONG MAGNETIC FIELDS

M.Stanojević, M.Čerček, N.Jelić and T.Gyergyek
J.Stefan Institute, University of Ljubljana,
Jamova 39, 61111 Ljubljana, Slovenia

The central problem in plasma diagnostics with Langmuir probes in strong magnetic fields is their interaction with the plasma. The disturbance or the collection length can extend considerable distances along $\vec{B}$ into the plasma (fig.1). The results of this effect are reduction of plasma density and charged particle currents to the probe at the sheath edge and non-exponential dependence of the collected electron current on the probe bias, so non-$\vec{B}$ theory of Langmuir probe diagnostics gives incorrect information about unperturbed plasma density, n_0, and the electron temperature, T_e [1].

The diffusion model of electric current collection by a plane probe in a homogeneous magnetic field to be briefly presented considers the geometry of the probe, mutual dependence of the parallel and the cross-field charged particle transport into the collecting region of the probe and plasma density variation in the collecting region depending on both particle transport and probe geometry. Applicability of the diffusion model itself is limited by the demand that charged particle velocity distributions should be maxwellian or almost maxwellian in the characteristic time and space scale of the macroscopic transport, hence strong electric fields or large electric currents in a plasma are excluded.

In the saturation case (profiles A and D on fig.2) analytic solution for plasma density profile in the presheath ($z \in]z_s, L]$) satisfying the boundary conditions: $n(\vec{r}_\perp, L) = n(\vec{R}_\perp, z) = n_0$, can be obtained by solving the steady-state diffusion equation:

$$D_\perp^{e,i} \nabla_\perp^2 n(\vec{r}_\perp, z) + D_\parallel^{e,i} \frac{\partial^2}{\partial z^2} n(\vec{r}_\perp, z) = 0, \qquad (1)$$

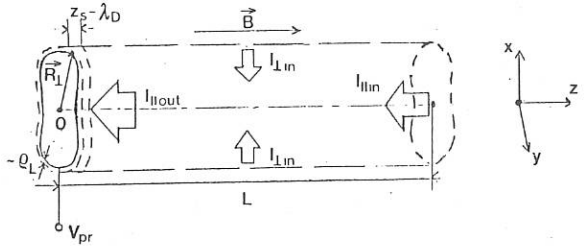

Figure 1: Electric current collection by a plane probe in a homogeneous magnetic field. Quasineutrality of the presheath ($z \in]z_s, L]$) is conserved by ambipolar current collection: $I_{\parallel out} = I_{\parallel in} + I_{\perp in}$.

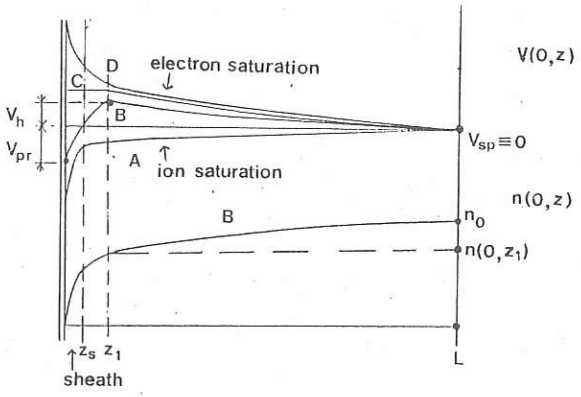

Figure 2: Axial potential and density variation at $x = y = 0$ along $\vec{B}$ in the collecting region of the probe.

where $D_{\parallel}^{e,i}$ and $D_{\perp}^{e,i}$ are some unknown ambipolar diffusion coefficients in the case of net electron and net ion collection respectively. Complicated problem of plasma-sheath transition is avoided by solving the cross-field diffusion problem for plasma density at the sheath edge, $n(\vec{r}_\perp, z_s)$:

$$D_{\perp}^{e,i} \nabla_{\perp}^2 n(\vec{r}_\perp, z_s) = S(\vec{r}_\perp), \tag{2}$$

where the sheath parameters appear only in the postulated "sink" function, S. They can be treated as known, that is measured or somehow calculated from other theories. The third equation comes from the assumption that collisionless sheath may be treated as non-interaction region for charged particles, which means that charged particle current at the sheath edge equals the collected electric current by the probe:

$$\int_S \Gamma_{\parallel}^{e,i}(\vec{r}_\perp, z_s) d^2 r_\perp = u_{e,i} \int_S n(\vec{r}_\perp, z_s) d^2 r_\perp, \tag{3}$$

where $u_e = [k_B T_e/(2\pi m_e)]^{1/2}$, $u_i = \alpha(T_i/T_e)(k_B T_e/m_i)^{1/2}$ and by assuming Einstein's relation between mobility and diffusion coefficients:

$$\Gamma_{\parallel}^{e,i} = -(1 + \tau_{e,i}) D_{\parallel}^{e,i} \frac{\partial n}{\partial z}, \tag{4}$$

where $\tau_e = T_i/T_e$ and $\tau_i = T_e/T_i$. The solution of equation (1) can be written as (for simplicity in notation indices "e,i" are omitted later on):

$$n(\vec{r}_\perp, z) = n_0 \left[1 - \sum_{j=1}^{\infty} A_j^s \mathcal{R}_j(\vec{r}_\perp) \sinh[\kappa(L^s - z)/\lambda_{\perp j}] \right], \tag{5}$$

where $\kappa = (D_\perp/D_\parallel)^{1/2}$, and $\lambda_{\perp j}$ and $\mathcal{R}_j(\vec{r}_\perp)$ should be found from the equation:

$$\nabla_\perp^2 \mathcal{R}_j + \mathcal{R}_j/\lambda_{\perp j}^2 = 0, \tag{6}$$

with the boundary conditions: $\mathcal{R}_j(\vec{R}_\perp) = \nabla_\perp \mathcal{R}_j(0) = 0$. Characteristic lengths $\lambda_{\perp j}$ depending on the geometry of the probe determine the length scale of the cross-field solutions $\mathcal{R}_j$. Unknown coefficients A_j^s and the collection length L^s can be found from equations (2) and (3). By assuming: $S(\vec{r}_\perp) \doteq n(\vec{r}_\perp, z_s)u/z_s$, saturation current collected by the probe can be written as:

$$I^s = I^{(0)}\left[1 - \sum_{j=1}^{\infty} A_j^s P_j \sinh[\kappa(L^s - z_s)/\lambda_{\perp j}]\right] \equiv I^{(0)} F^s, \tag{7}$$

where $I^{(0)} = \pm e n_0 u S$, $P_j = (1/S)\int_S \mathcal{R}_j(\vec{r}_\perp) d^2 r_\perp$, and $F^s \leq 1$ is saturation current reduction factor. Calculations for circular disc probe and plane rectangular probe show that $F^s = F^s(\Lambda_\perp^2/\lambda_{\perp j}^2)$, where $\Lambda_\perp^2 = D_\perp z_s/u$, and approximate results of various one-dimensional fluid models can be obtained as limiting cases of this model [2]. From the practical point of view , the most important results are quasi-independence of saturation ion current on the cross-field diffusion transport mechanism and weak dependence on the probe geometry ($F_i^s \leq 0.7$), so a simple determination of n_0 is possible from its measurement and after measuring n_0 and T_e, the unknown $D_\perp^e$ can be evaluated from saturation current measurement.

In the general case of current collection (profiles B and D on fig.2) electron density in the region $z \in]z_1, L]$ can be written as in equation (5), but now $A_j = A_j(V_{pr})$, $L = L(V_{pr})$ and $z_1(V_{pr}) \geq z_s$. Ions face a repulsive potential in approaching the probe, hence [1]:

$$n(\vec{r}_\perp, z_1) = n_0 \exp(-eV_h(\vec{r}_\perp)/k_B T_i). \tag{8}$$

Electrons at the top of the potential hill at $z = z_1$ face a repulsive potential $V_h(\vec{r}_\perp) - V_{pr}$ in approaching the probe, so $S(\vec{r}_\perp, V_{pr}) \doteq \exp[-e(V_h(\vec{r}_\perp) - V_{pr})/k_B T_e] n(\vec{r}_\perp, z_1) c_e/(4z_1)$, where $c_e = [8k_B T_e/(\pi m_e)]^{1/2}$ and by assuming equation (3):

$$\int_S \Gamma_\parallel^e(\vec{r}_\perp, z_1) d^2 r_\perp = \frac{c_e}{4}\int_S \exp[e(V_{pr} - V_h(\vec{r}_\perp)/k_B T_e] n(\vec{r}_\perp, z_1) d^2 r_\perp, \tag{9}$$

where $c_e = [8k_B T_e/(\pi m_e)]^{1/2}$. Final results for electron and ion current can be written as [3]:

$$I_e(\Phi_{pr}) = \begin{cases} I_e^s \mathcal{F}_e(\Phi_{pr}) \exp \Phi_{pr}, & \text{if } \Phi_{pr} < 0, \\ I_e^s, & \text{if } \Phi_{pr} \geq 0 \end{cases} \tag{10}$$

and

$$I_i(\Phi_{pr}) = \begin{cases} I_i^{th} \mathcal{F}_i(\Phi_{pr}) \exp(-\Phi_{pr}/\tau), & \text{if } \Phi_{pr} > \Phi_h, \\ I_i^s \mathcal{F}_i(\Phi_{pr}), & \text{if } \Phi_{pr} < \Phi_h, \end{cases} \tag{11}$$

where $\Phi_{pr} = eV_{pr}/k_B T_e$, $\Phi_h = eV_h/k_B T_e$, $\tau = T_i/T_e$, $I_i^{th} = e n_0 [k_B T_i/(2\pi m_i)]^{1/2} S$ and

$$\mathcal{F}_e(\Phi_{pr}) = \frac{1}{F_e^s S}\int_S d^2 r_\perp \left[1 - \sum_{j=1}^{\infty} A_j \mathcal{R}_j(\vec{r}_\perp) \sinh[\kappa_e(L - z_1)/\lambda_{\perp j}]\right]^{1+\tau} \tag{12}$$

and

$$\mathcal{F}_i(\Phi_{pr}) = 1 - \sum_{j=1}^{\infty} A_j P_j \sinh[\kappa_e(L - z_1)/\lambda_{\perp j}]. \tag{13}$$

Total current collected by the probe is obtained by adding equations (10) and (11) taking regard of the sign of the charge. Study of $\mathcal{F}_e$ and $\mathcal{F}_i$ show that $\lim_{\Phi_{pr}\to-\infty} \mathcal{F}_e = 1/F_e^s$ and $\lim_{\Phi_{pr}\to-\infty} \mathcal{F}_i = 1$, so below the floating potential, V_f, it may be assumed that:

$$I(V_{pr} < V_f) \doteq I_i^s + I_e^{th} \exp(eV_{pr}/k_B T_e), \tag{14}$$

where $I_e^{th} = -(1/4)en_0c_eS$, which means that only in that region the simple exponential low for electron collection can be used in deriving T_e. This has been already experimentally approved by some authors [4,5].

As conclusion, it should be stressed that three impotrant parameters can be derived from I-V characteristics of Langmuir probe in strong magnetic fields:

- the electron temperature, T_e, can determined by assuming the simple exponential law for electron collection for probe potentials below the floating potential;
- the unperturbed plasma density, n_0, can be almost precisely measured if the assumption of quasineutrality of saturation ion current on the cross-field diffusion mechanism is valid;
- the cross-field diffusion coefficient, $D_\perp^e$, can be evaluated from saturation electron current measurement after deriving T_e and n_0.

Presented model proves the validity of these results.

References

[1] P.C.Stangeby, J.Phys.D: Appl. Phys., **15**, 1007 (1982)

[2] M.Stanojević et al, submitted to J.Phys.D: Appl. Phys. (1991)

[3] M.Stanojević et al, submitted to Plasma Phys. Contr. Fusion (1991)

[4] J.A.Tagle, P.C.Stangeby and S.K.Erents, Plasma Phys. Contr. Fusion, **29**, 297 (1987)

[5] R.A.Pitts and P.C.Stangeby, Plasma Phys. Contr. Fusion, **32**, 1237 (1990)

A DOUBLE PROBE FOR ELECTRON FLUX MEASUREMENTS IN INHOMOGENEOUS AND TIME-VARYING PLASMAS

I. Axnäs and S. Torvén

Royal Institute of Technology, Alfvén Laboratory, Department of Plasma physics
S-10044 Stockholm, Sweden

The electron current to a Langmiur probe in a low density plasma may not in general show any clear current saturation at plasma potential. Then the full probe characteristic is needed to determine the plasma potential. On the other hand side, plasma potentials can be determined by hot, electron emitting probes, and such probes are expected to give the most reliable probe method that allows direct measurements of the plasma potential. /1, 3/

In this paper a new double probe configuration, capable of measuring electron fluxes or densities in a spatially and temporally varying plasma, is described, and data to support its utility are given. The double probe consists of a hot, electron emitting filament which is connected to a cold filament of the same size through a low impedance signal resistor. The cold probe thus tracks potential variations in the plasma and remains close to the plasma potential. The current through the signal resistor, measured with an isolation amplifier, then gives a good measure of the electron number density. The external impedance to ground is high, the electron current collected by the cold filament being re-emitted to the plasma by the hot filament. Interaction between the filaments is inhibited by placing them at right angles to the magnetic field and separating them by some electron-gyro radii.

The main advantage of this "tracking probe" is that the probe current at plasma potential is obtained by a single measurement. The probe current can then conveniantly be recorded when the probe is moved in a plasma where the potential and the density vary strongly in space. The probe also tracks time variations of the plasma potential so that a time varying density can be recorded directly as discussed further below.

The probe construction is described below and some probe tests are presented. However, first some basic features of a single emitting probe will be discussed because the operation of the double probe is based on the assumption that the hot probe floating potential U_f gives a good measure of the plasma potential U_p. The probes used here were mounted on motor-driven probe carriages in a triple plasma machine where a plasma column is confined radially by an axial magnetic field.Typical parameter values are $T_e \approx 10$ eV and $n_e \approx 10^{15}$ m^{-3}, and there is also a high energy tail in the electron energy distribution.

Theoretical models for plane electron emitting cathodes /2/ (or plane emitting probes) show that U_f may be of the order of T_e/e below U_p. Here T_e is the electron temperature in the plasma. $T_f << T_e$ is assumed where T_f is the filament temperature. This space charge effect

shows that the emitted electrons must be accelerated, and their density accordingly be reduced, before they enter the plasma. However, experimentally it has been found that U_f for a cylindrical probe approaches the plasma potential when the probe temperature is increased sufficiently /3/. This result need not be in conflict with the theoretical results because the density of the emitted electrons is reduced by a geometrical factor in the cylindrical case, and this may lead to a much smaller value of U_p-U_f. However, it should be noted that a cylindrical probe may become equivalent to a plane probe for strong magnetic fields, and then U_p-U_f may be large. In the investigations reported below, the magnetic field is such that $R_g >> R_f$, and simultaneously $R_g << d$ to avoid mutual perturbation. R_g is the electron gyro radius, R_f the filament radius and the distance d gives the separation between the probe filaments (2 mm).

Here we assume that the saturation value of U_f, obtained when the probe temperature is increased sufficiently, is a good measure of the plasma potential. The variation of U_f with increasing probe temperature is shown in Fig. 1 where a cold probe characteristic is shown together with four hot probe characteristics with different filament temperatures. The measurements were made with a single probe which could be operated cold or hot. The cold probe was also heated somewhat to avoid impurities, and a fast relay switched off the heating current during the measurements. As seen from the diagrams, U_f moves to the right and assumes a saturation value U_{fs} when the probe temperature is increased. At the saturation voltage, the emission saturation current is much larger than the electron collection current.The diagram also shows that the "separation point" between the cold and the hot probe characteristics, which sometimes is idenified as the plasma potential, is about 5 V above U_{fs}. This high value remains to be explained. If our asssumption that U_{fs} is a good measure of the plasma potential is correct, the "separation point" would be a bad measure of the plasma potential for the high emission saturation currents considered. Fig. 2 shows a hot and a cold probe characteristic measured with the same single probe as described above. It shows the measuring principle for the double probe. The floating potential of the double probe will always be somewhat lower than for a single probe, about 3 V in the case considered. Since $T_e \approx 10$ eV, the double probe may, in the case considered, be expected to give a current that is about 70% of the current at plasma potential. Such a difference is acceptable in many cases, in particular when density profiles are measured and only relative values are of interest.

Fig. 3 shows a sketch of the double probe. The hot filament consists of a 10 mm long tungsten wire (diameter 0.1 mm) which is spot welded to two molybdenum leads. Two thin alumina ceramic tubes (external diameter 1.2 mm) insulate the leads and 1.5 mm of the tungsten filament at each end, leaving 7 mm exposed length. The filament is carefully centred in the tubes so that it is not in contact with the tube walls. Using this construction the filaments maintain their high resistance to ground even if the outside of the ceramic tubes become covered with metal deposits. Besides, the relatively cold non-emitting end points of the filament are not exposed to plasma. The cold filament is similar and is mounted on a similar probe shaft. It has the same area exposed to the plasma as the hot filament. This is heated by an alternating current (50 Hz) from a transformer. This first version of the probe is made as simple as possible, and the heating current is not disconnected during the

measurements. The connection between two probe filaments through the signal resistor is alsc outside the vacuum system, at the center tap on the secondary winding of the transformer. This gives the double probe a rather high capacitance to ground. This capacitance and the probe resistance over the plasma to ground determine the upper cut-off frequency which is only about 10 kHz in the present case. For maximum time resolution, the signal resistor and the isolation amplifier should be placed on the probe carriage inside the vacuum system.

Several tests showed that the mutual perturbation of the two filaments was neglible for $R_g<d/4$. However, the double probe perturbed the plasma somewhat more than a single probe giving systematic differences which must be checked in each particular case. Fig. 4 (left) shows an axial potential profile in the plasma column when a double layer is present. Fig. 4 (right) shows that a good agreement is obtained between the axial probe current profiles mesured with the double probe and with a single probe as described in the figure caption.

References

1. Kemp R. F. and Sellen J. M., 1966, Rev. Sci. Instrum., 37 , 455; Schuss J. J. and Parker R. R., 1974, J. Appl. Phys., 45 , 4778; Makowski M. A. and Emmert G. A., 1983, Rev. Sci. Instrum., 54 , 830

2.Langmuir I., in "The collected works of Irving Langmuir", 5, 140, Ed. C. G. Suits, Pergamon Press, 1961; Crawford F. W. and Cannara A. B., 1965, J. Appl. Phys., 36 , 3135

3. Smith J. R., Hershkowitz N. and Coakley P., 1979, Rev. Sci. Instrum., 50 , 210

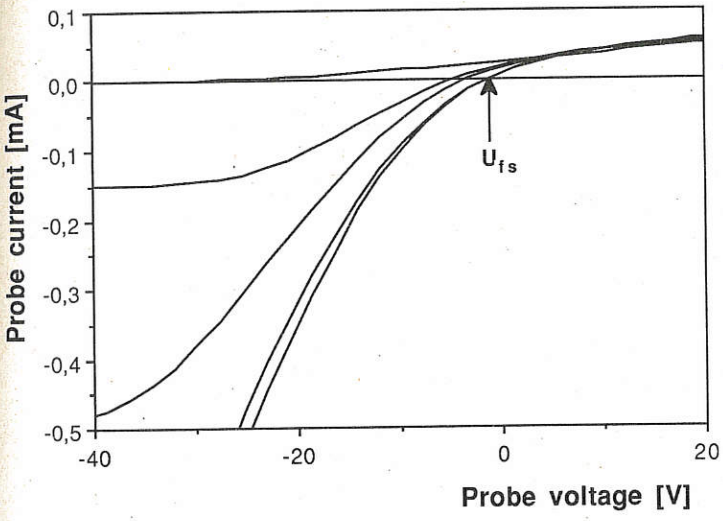

Fig.1. Single probe characteristics when the probe is cold and when it is heated to four different temperatures. The floating potential assumes a saturation value U_{fs} for sufficiently high temperatures.

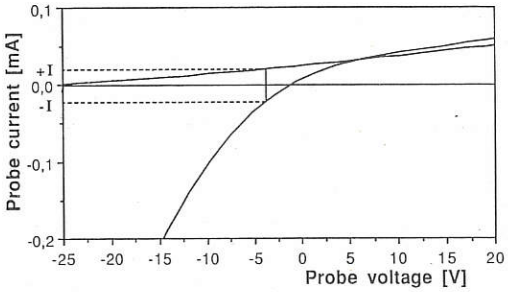

Fig.2. Single probe characteristics when the probe is cold and hot. The vertical line indicates the working point of the double probe because the potential drop over the signal resistor is negligible. The electron current I, that is collected by the cold probe, is re-emitted by the hot probe.

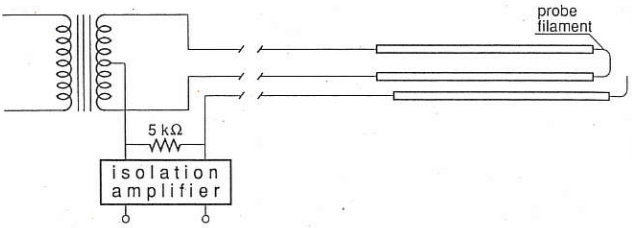

Fig.3. Schematic drawing of the double probe and the probe circuit.

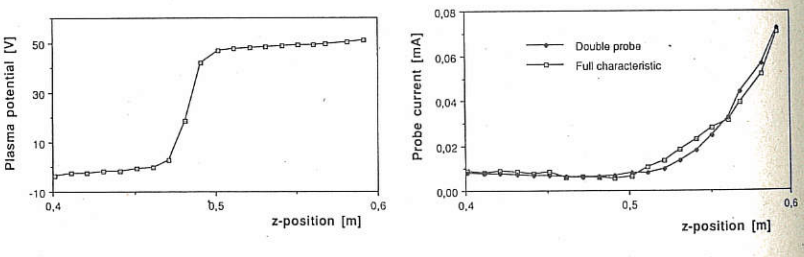

Fig. 4. (left) Variation of the plasma potential along the plasma column when a double layer is present. (right) Comparison between axial profiles of the probe current obtained with the double probe and the single probe. In the latter case, cold and hot probe characteristics were measured at each point, and the cold probe currents were taken at the floating potentials of the hot probe.

A PROCESSING METHOD OF THE PROBE CHARACTERISTIC IN A TWO ELECTRON TEMPERATURE PLASMA

D.Ruscanu, G.Popa and E.Stamate
Plasma Physics Department of "Al.I.Cuza" University
RO-6600 Iasi, Romania

The electron distribution function (EDF) has to be known in order to understand or/and to explain the phenomena which depend on velocities of the electrons. Experimentally the EDF could be measured either using on electrostatic analyzer (EA) or a Langmuir probe /1/. In the former case the EDF is proportional with the first derivative of the current-voltage characteristic of the collector, while in the latter the second derivative of the probe characteristic gives the EDF in the case that it is isotropic. Besides there are methods based on the assumption that the real EDF could be approximated by a convolution of two maxwellian distribution functions, so that the model of two electron temperature plasma is quite frequently used. The temperatures and densities of these two groups of electrons are measured by Langmuir probe and using either the method of semilogarithmic curve /2/ or a numerical method based on the best fit /3/.

In this paper we present a new method for processing of the probe characteristic based on the common Langmuir assumptions /1/ and in addition the supposition that the electron current of the Langmuir plane probe is a sum of two electron currents which correspond to two group of electrons each of each with a Maxwellian EDF. Let T_1 and T_2 be their temperatures and I_{o1} and I_{o2} their electron saturation current through the probe. Than the electron current of the probe is given by :

$$I(V) = I_{o1} \exp[a(V - V_p)] + I_{o2} \exp[b(V - V_p)] \qquad (1)$$

where

$$a = e/kT_1 \quad \text{and} \quad b = e/kT_2 \qquad (2)$$

and : V and V_p are the probe and plasma potentials measured with respect to the same reference, e the electron charge and k the Boltzmann constant.

Taking the linear combination I(V) as a solution of a differential equation, it must have the form :

$$I'' - (a + b)I' + ab\ I = 0 \qquad (3)$$

where :

$$I' = dI/dV \quad \text{and} \quad I'' = d^2I/dV^2 \qquad (4)$$

From (1) - (4) the following two functions could be set up :

$$F_1(V) = \ln[I''.I - (I')^2] = (a + b)(V - V_p) + \ln[(a - b)^2\ I_{o1}I_{o2}] \qquad (5)$$

$$F_2(V) = [(a + b)I' - I'']/I = a.b = \text{const.} \qquad (6)$$

The slope :

$$A = a + b \qquad (7)$$

of the linear dependence (5) and the constant

$$C = ab \qquad (8)$$

given by function (6) allow to determine the electron temperatures of the two groups of electrons as :

$$T_1 = (A - \sqrt{A^2 - 4C})/2C; \quad T_2 = (A + \sqrt{A^2 - 4C})/2C \qquad (9)$$

Taking the electron saturation current of the probe as the probe current at plasma potential, then :

$$I_o = I(V_p) = I_{o1} + I_{o2} \qquad (10)$$

and from (1) :

$$I'(V_p) = a.I_{o1} + b.I_{o2} \qquad (11)$$

The relations (10) and (11) allow to determine both to electron saturation currents and the densities n_{o1} and n_{o2} of the two groups of electrons as :

$$n_{o1} = I_{o1}/[2Se(8kT_1/m_e)^{1/2}]$$

$$n_{o2} = I_{o2}/[2Se(8kT_2/m_e)^{1/2}] \qquad (12)$$

where besides the known quantities S is the probe surface and m_e the electron mass.

The method was used in order to measure the plasma parameters in DP-machine of "Al.I.Cuza" University /4/. A data acquisition system and usual method of numerical procedure /5/ were used in order to apply the method. In fig.1 the experimental characteristic (curve I) is presented for an

Argon plasma at pressure of 10^{-4} mbar and using a cyclindrical probe of 5 mm length and 0.3 mm in diameter together with its first (curve I') and second (curve I") derivatives. Accordingly the functions F_1 and F_2 are presented in fig.2 having the both constants A and C also specified.

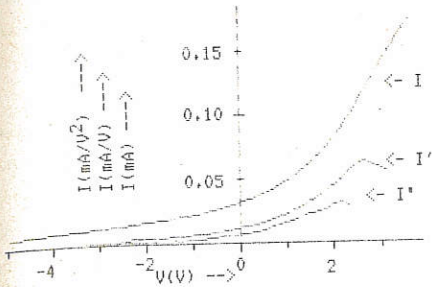

Fig.1

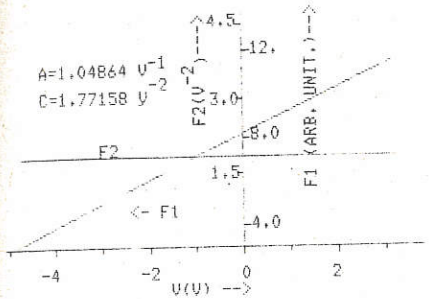

Fig.2

Using there data the temperatures and densities of both groups of electrons have computed and listed on fig.3 together with both theoretical (I_c) and experimental (I) electron current of the probe characteristic. The theoretical curve (I_c) was obtained using the above plasma parameters and function (1). In fig.4 the semilogarithmic method is used in order to obtain the plasma parameters which are listed on the same figure. A relatively large difference 50 % for electron temperature and 40 % for elec-

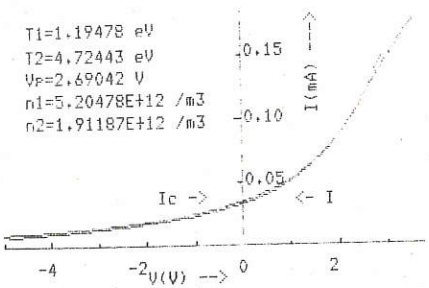

Fig.3

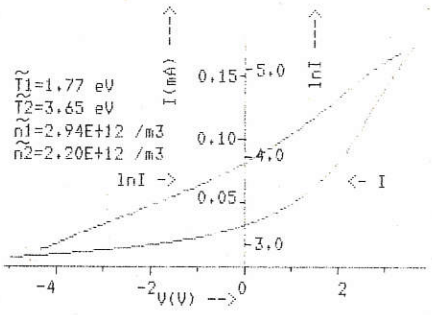

Fig.4

tron density between the values determined by these two methods caused by errors produced by classical method which could not avoid, the reciprocal influence of each group of electrons in determining the real values of the other group. As a consequence the real deconvolution semilogarithmic by method it is not possible especially than when the electron temperatures of two groups of electrons are close each other.

REFERENCES

1. J.D. Swift and M.J.R. Shwar, Electrical Probes for Plasma Diagnostics, LLIFFE Book (1970)
2. W.D. Jones, A.Lee, S.M.Gleman and H.J.Doucet, Phys.Rev. Lett. 35 (1975) 1349
3. C.J.Cellarius, L.A.Dicks and R.Turner - Z.Physik, 231 (1970) 119
4. G.Popa, Symp.on Plasma Double Layer, Riso Nat. Lab. (1982) R-472, 82
5. D.Ruscanu, G.Popa, Proc. of Nat. Conf. of Phys., Bucharest (1982) 106

COMPARISON OF THE WAVENUMBER SENSITIVITY AND THE SPATIAL RESOLUTION BETWEEN LANGMUIR PROBES AND REFLECTOMETRY IN A LONGITUDINALLY MAGNETIZED RF PLASMA WAVEGUIDE*

E. Anabitarte, J.M. Sentíes, E.G. Bustamante, M.A.G. Calderón,
M.A.G. San José, P. Monterde, J. Vila.
Departamento de Física Aplicada. Universidad de Cantabria
39005 Santander, SPAIN

Introduction

Much effort is being done to understand the connection between fluctuations and anomalous transport processes in tokamaks and stellarators /1/. Several diagnostics such as Langmuir Probes, Microwave Reflectometry, Scattering, Heavy Ion Beam Probe(HIBP)..., are used at present, to investigate fluctuations and turbulence in fusion plasmas. However, there are still many open questions in the interpretation of the experimental measurements. In particular, the spatial resolution of the Reflectometry and the wavenumber sensitivity of both Reflectometry and Langmuir Probes are important issues not well understood.

The use of Microwave Reflectometry as a diagnostic method for studying density fluctuations was suggested by the TFR Group /2/. Since then, such density fluctuations studies have been carried out on many fusion devices such as JET /3/, TJ-I /4/, ATF /5/, Doublet III-D /6/ and WVII-AS /7/. In order to get a precise explanation of these data several models have been developed. In most cases, the WKB approximation was used to calculate the phase shift modulation in the reflectometer signal due to density fluctuations at the cut-off layer. More recently, the problem of wave scattering by fluctuations close to the cut-off layer was investigated by X.L.Zou et al. /8/. A generalized wavenumber selection rule is provided for a linear density profile. The theoretical spatial resolution predicted by these models, is mainly in the 1-5 cm range. However, reflectometry correlation measurements provide much more localized signals (0.2-0.5 cm range) than expected.

The analysis and study of these problems is an important issue with impact on fusion research. Furthermore, small devices are well suited to perform this work /9/. On the basis of studying these questions, we areaddressing comparisons of spatial resolution and wavenumber sensitivity between Langmuir Probes and Reflectometry in a Plasma Linear Machine. The experimental system used for these studies and preliminary results are described in this paper.

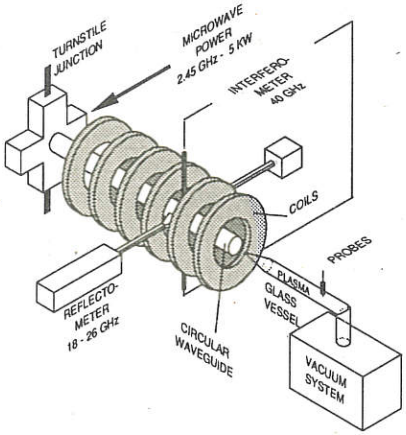

***Figure 1**. Experimental setup*

Experimental device

The experimental device is schematically shown in Fig.1. The plasma is performed in a cylindrical glass vessel with an internal diameter of 7 cm and a length of 100 cm. The vessel is located inside a circular waveguide of 8 cm in diameter. A longitudinally magnetized argon-plasma is produced by launching longitudinally (LMG) electromagnetic waves (f=2.45 GHz, 500 W<P_{LMG}<6 kW) and the system operates in a continuous regime. The source of electromagnetic oscillations is a magnetron and the microwave power is sent to a polarizer (turnstile junction) through a circulator and a directional coupler wich is used to obtain information of incident and reflected power. The stationary longitudinal magnetic field (0.05 T<B_0<0.15 T) is produced by six water-cooled coils, wich are concentric with the waveguide. The base pressure in the vacuum chamber is in the 10^{-5}-$5x10^{-6}$ torr range.

Plasma diagnosis are carried out using an array of movable Langmuir probes along the radial chord, an 8 mm interferometer and a single antenna reflectometer system working in the K -band (18-26.5 GHz). In order to get information about refraction effects on the reflectometer signal, another detection system (transmission arrangement) is placed in front of the reflectometer antenna. Electron densities are obtained with both interferometer and probes and typical measurements are n_{emax}= 10^8-10^{13} cm^{-3}. Langmuir probes give temperatures in the T_e=1-10 eV range.

Measurements

Initially our work was focused on establish, under different operating conditions, the importance of the polarization of the waves launched to produce the plasma and the plasma density behaviour as a function of the absorbed power. Figure 2 represents averaged density for the Right Hand Circularly Polarized Wave (RHCP Wave) (these measurements represent the average of a series of experimental measurements in the same conditions).

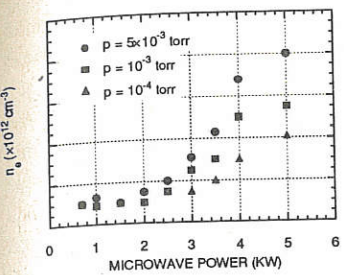

Figure 2. Averaged electron density

For high incident power(P_{LMG}>3kW), the plasma presents surface resonance and the density profile tends to be concentrated in outermost part of the plasma column with the maximum around r=2 cm (r=0 corresponds to the center of the plasma column) This fact, limits the accesibility to the reflectometer signal. Radial densities gradient length ($L_N=[(1/n_e)(dn_e/dr)]^{-1}$) are below 0.1 m that correspond theoretically to a very good spatial resolution and wavenumber sensitivity. Preliminary comparisons between reflectometer and Langmuir probes signal have been carried out for plasmas with surface resonance.

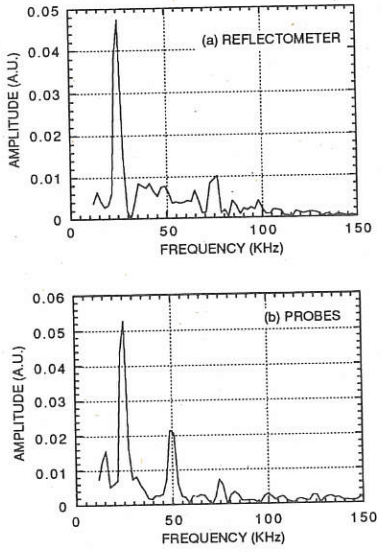

Figure 3. Power spectra of both fluctuating signals.

The emitted wave is reflected by a plasma fluctuating layer, where density value and magnetic field are such that the high cut-off frequency for the extraordinary mode (E-mode) equals the incident wave frequency. The incident frequency was 18 GHz, so the cut-off layer for a magnetic field of 0.1 T has a density of $3.4x10^{12}$ cm^{-3}. Correlation measurements were carried out between the fluctuating reflectometer signal ($V_{reflect}$) and the fluctuating saturation current (I_s) given by the probes. Fig. 3 shows fluctuation power spectra of both signals with a large peak around 25 kHz and other minor peaks.

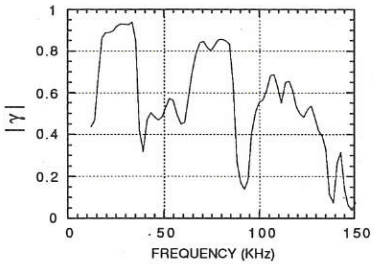

Figure 4. Probe - Reflectometer Coherency Spectrum

The fig. 4 presents the coherency between these signals with high values of γ ($\gamma>0.7$) around the frequency peaks. In this experiment, the radial position of the probes and the predicted radial position of the cut-off layer were the same ($r\approx2$ cm) However, in most cases the coherence between reflectometer and probes was very low ($\gamma<0.5$), except when large peaks appear in power spectra. This fact must be related with the longitudinal distance between radial chords scanned by the reflectometer and the Langmuir probes. In this experimental arrangement, the probes have an axial separation of 20 cm. Work is under way to move the array of probes at the same longitudinal position as the reflectometer. It is also planned, to perform the experiment under steady-state conditions in the plasma and generate low frequency waves (ion waves) in both directions, transversally and longitudinally to the magnetic field, in order to have a more controlled experiment.

Summary

The study of the spatial resolution of reflectometry and the wavenumber sensitivity of both Reflectometry and Langmuir Probes are currently being addressed in a linear plasma machine. Preliminary results, show high coherency between the probes and the reflectometer when large peaks are present in the power spectra of boths signals. It is planned to upgrade the experimental arrangement installing wire grids in order to launch low frequency waves. It is also under way to place an array of Langmuir Probes at the same longitudinal position as the reflectometer.

* This work was supported by the Dirección General de Investigación Científica y Técnica (DGYCYT) Spain under project PB90-0337

/1/ Wootton A.J. *et al.*, Phys. Fluids B **2** (12), 2879 (1990)
/2/ The TFR Group Plasma Phys. Contr. Fusion **27** (11), 1299 (1985)
/3/ Cripwell P., Costley A.E. and Hubbard A.E., Proc. 16th Europ. Conf. on Contr. Fusion and Plasma Phys., Venice, Vol. I,p 75 (1989).
/4/ Sentíes J.M. *et al*, Proc. 16th Europ. Conf. on Contr. Fusion and Plasma Phys., Venice, Vol. I, p 51 (1989).
/5/ Anabitarte E. *et al*, Proc. 17th Europ. Conf. on Contr. Fusion and Plasma Phys., Amsterdam, Vol. IV, p. 1492 (1990)
/6/ Doyle E.J. *et al*, 17th Europ. Conf. on Contr. Fusion and Plasma Phys., Amsterdam, Vol. I, p. 203 (1990)
/7/ Sánchez J. *et al*, 17th Europ. Conf. on Contr. Fusion and Plasma Phys., Amsterdam, Vol. IV, p.1572 (1990)
/8/ Zou X.L., Laurent L.and Rax J.M.,Plasma Phys. Contr. Fusion 33(8), 903 (1991)
/9/ S. Baang *et al*, Rev Sci. Instrum. **61** (10), October 1990

RF PULSE INTERACTION WITH LOW DENSITY PLASMA DIAGNOSED BY GATED LANGMUIR PROBE

G. Cicconi, P.J. Paris +), C. Rosatelli and A. Tarditi.
Dipartimento di Ingegneria Elettrica, Universita' di Genova (Italy),
+) Centre de Recherche en Physique des Plasmas, EPFL, Lausanne (Suisse).

Several experiments on interactions of centimetric microwaves with low density plasmas, in particular at low temperature and weakly ionized, have been performed in order to investigate the optimal conditions for the resonant absorption at various levels for the incident microwave power /1/2/3/. Many of these experiments were made in equilibrium afterglow plasmas /2/3/. Nevertheless experimental results concerning the temporal and spatial evolution of the plasma electron temperature, during and immediately after the interaction, do not seem available. In this paper some experimental results on this temperature evolution, obtained by using a biased Langmuir probe, are presented and commented. The probe current is gated by a boxcar amplifier in the presence of a repetitive pulsed microwave perturbation and, for a fixed delay of the gate aperture, the probe bias is slowly swept whereas the gated current is averaged over the many repeated pulses present during the time interval for scanning the whole Langmuir characteristic. For a scanning time 10^6 longer than the pulse duration time, an instantaneous I/V Langmuir characteristic may be plotted. Moreover by measuring the time-varying reflexion coefficient, during the pulse duration time, when the plasma is confined within a section of a high-Q resonator, the efficiency of the electron heating may be evaluated /4/5/. However in order to control the accuracy of this probe diagnostic, our experiment was performed with a low density diffused plasma, transparent to the microwave, so avoiding the resonance absorption and the consequent instantaneous generation of fast resonant electrons which would make the diagnostic results more difficult to interpret.

The weakly ionized argon (technical quality) plasma, produced at the pressure of 5×10^{-2} Pa (vacuum pressure 3 + 4×10^{-4}Pa) with an ionization degree of the order of 10^{-4} fills a section transversally located at one end of the tunable (variable length) cylindrical high-Q (10^3 about) copper resonator (150 lt max vol. 50 cm diam.) The diffusion plasma is extruded by 4 DC hot filament discharges generated near the resonator wall. At the

other end of the resonator, opposite to the plasma layer, is located the dipole antenna of the pump field. The Langmuir probe with a tantalum collector disk (2 mm diam) is transversally movable along the plasma radius. The conditions of the experiment are the following. The steady-state diffusion plasma (practically collisionless) is produced with a bulk density of $1.8 \times 10^9 cm^{-3}$ (electron Langmuir frequency f_p = 380 MHz) and electron and ion temperatures of 2 and 0.3 eV respectively. The microwave pump at the frequency of 423 MHz, excites the TE (111) resonator dominant mode and is pulsed modulated (PM: 25 μs pulse duration, 60 μs repetition period). The Langmuir probe bias is swept by a linear ramp of 25 sec., so the gated average is made over 10^5 pulses during the plotting of a whole Langmuir characteristic. The boxcar amplifier gate, triggered by the pump pulse, is fixed at 5 ns and the diagnostic is performed by 7 steps of the aperture delays (from 0.1 to 20 us) taken either from the initial and from the final fronts of every pump pulse in order to perform a diagnostic inside (during the pulses) and outside (between two successive pulses) the perturbation pulse.

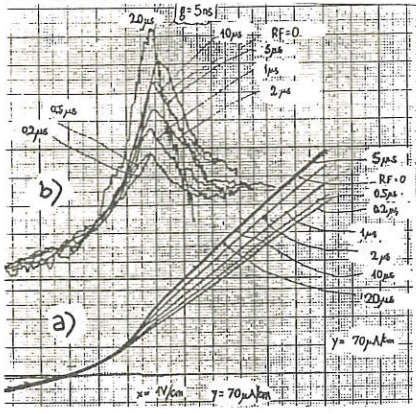

Fig. 1 (pulse outside)

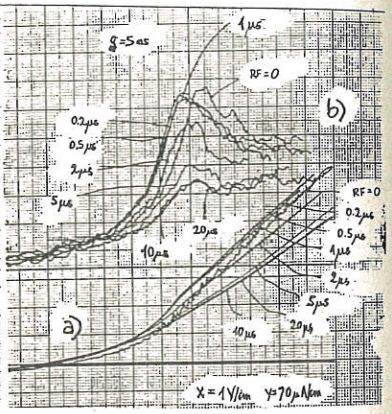

Fig. 2 (pulse inside)

Instantaneous Langmuir characteristics a) first derivatives b) for R=4cm
Transparent plasma f_p = 380 MHz, f_o = 423 MHz, P_o = 3W.

In Fig. 1 and 2 two sets of instantaneous Langmuir characteristics, detected by the probe located in a given measurement point (R = 4 cm) and plotted in a V/I (X/Y) plane, are shown along with their respective first derivatives obtained respectively outside and inside the pulse. The

instantaneous (for every gate aperture delay) electron density and temperature profiles, calculated from the locally diagnosed volumes, within a distance of 14 cm taken from the axis along the plasma radius, are reported in Fig. 3 and 4.

In order to better understand the experimental results here shown, concerning a transparent plasma, some diagnostic results, obtained by the same probe for an opaque plasma ($n = 5 \times 10^9 cm^{-3}$, $f_p = 638$ MHz $= 3/2\ f_o$), taken at discrete R outside the pulse, are shown in Figs. 7 and 8 for different times.

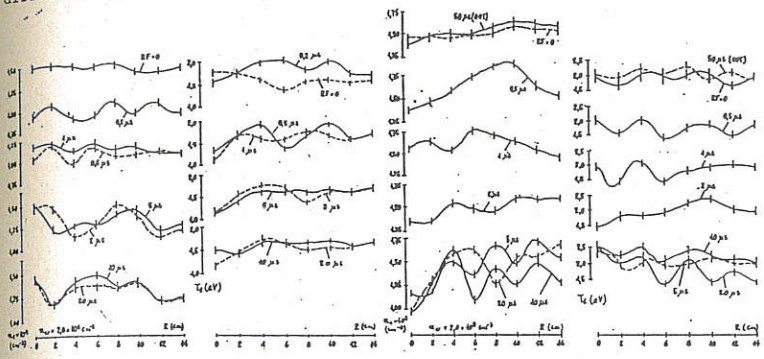

Fig. 3 (pulse outside) Fig.4 Fig. 5(pulse inside) Fig. 6
Instantaneous radial profiles of electron density and temperature.

The comments on these experimental results may be synthetised as follows.

1) The estimation of the plasma field E_p for $T_e = 2$ eV /5/ and the electric field E_o in the plasma excited by the electric energy deposited by the microwave pump ($P_o = 3W$ in 1 μs) gives respectively $E_p \cong 1$ V/cm and $E_o \cong 20$ V/cm where E_o is a strong field for nonlinear regime /5/.

2) Two important effects may be deduced: a) absorption for the pump energy within 5 μs producing a $T_e = 0.25$ eV(+25% about). In this situation a minimum pump reflected power (< 1%) may be observed; b) density (and temperature) profile seems, in a first approximation, perturbed by stationary waves of 4 cm wavelength while on the Langmuir probe current a turbulence spectrum, with enhancements in the 1 ÷ 100 kHz band, is observed. Moreover from the dispersion relation of the ion acoustic waves, for cold ions, with $Dk \ll 1$ (where the Debye radius $D = 2 \times 10^{-2}$ cm and $k = 1,5$ cm^{-1}) one estimates $f_s \cong C_s\ k \cong 6$ kHz, where $C_s \cong 2\ 10^5$ cm/s.

3) In order to interpret in a first approximation by the experimental results the absorption mechanism, considering the plasma collisionless we estimate the damping coefficient $\gamma = 10^6\ s^{-1}$. If the Landau damping might be considered as the main mechanism would have $kD \cong 3$. Because no effective plateau seems present on the distribution function evaluated by means of the first derivative of the Langmuir characteristic, we consider the trapping mechanism not important effect in this experiment.

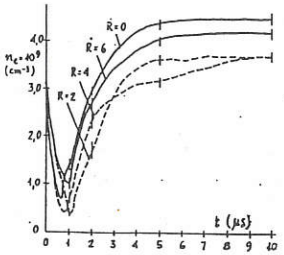

Fig. 7 Electron density.
Opaque plasma $f_g/f_o = 1,5$, $P_o = 9W$.
Pulse outside versus time.

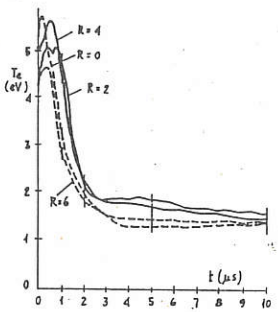

Fig. 8 Electron temperature.

4) In this context Figs. 7 and 8 may give more validity to this diagnostic method. In fact in this case strong depression of density is observed, within a time of the order of ion relaxation, which seems to travel near the thermal electron velocity.

References

/ 1/ H. Ikezi, K. Nishikawa and A. Mima. Journ. of the Physics Soc. of the Japan, 37, 766 (1974).

/ 2/ D.L. Eggleston, A.Y. Wong and G.B. Darrow. Phys. Fluids, 25(2), 257, (1982).

/ 3/ B. Cros, J. Godiot and G. Mathieussant. Phys. Fluids, B2(5), 907(1990).

/ 4/ G. Cicconi et al. Proc. of XX ICPIG, Pisa (Italy), Contr. Pap.3, 796 (1991).

/ 5/ V.L. Ginzburg. The propagation of Electromagnetic Waves in Plasmas, Pergamon Press, Oxford 1970.

DEVELOPMENT OF A DIAGNOSTIC SYSTEM FOR HIGH POWER MICROWAVE (FEL) ELECTRIC FIELDS IN THE MICROWAVE TOKAMAK EXPERIMENT

T.Oda[a)], K.Odajima, K.Takiyama[a)], J.H.Foote[b)], K.Mizuno[c)], T.Ogawa, K.Sato[d)], K.Ohasa, K.Hoshino, H.Maeda and D.G.Nilson[b)]

Japan Atomic Energy Research Institute, Tokai 319-11, Ibaraki, Japan

a) Faculty of Engineering, Hiroshima University, Higashi-Hiroshima
b) Lawrence Livermore National Laboratory, Livermore, California
c) Plasma Physics Research Institute(U.C.-Davis and LLNL), Livermore, California
d) National Institute of Fusion Science, Nagoya

1. Introduction

One of the most important diagnostics for the electron-cyclotron-frequency heating (ECH) experiments is to directly measure the spatial distribution of the microwave electric field in a plasma for understanding the absorption mechanism of the microwave in the plasma. We have developed a diagnostic system using laser-aided particle-probe spectroscopy (LAPPS) to observe the high electric field (>100 kV/cm) generated by a free electron laser (FEL) beam for the ECH study in the Microwave Tokamak Experiment (MTX) at the Lawrence Livermore National Laboratory /1/. The principle of method and an outline of the diagnostic system have been presented /2,3/. The diagnostic apparatus consists of a neutral helium beam, a dye laser exciting the neutral beam, and a spectroscopic system with originally designed collecting optics. Using the Stark effect we observe fluorescences induced by the forbidden transitions from the metastable levels of the helium atoms to obtain the electric field strength in the plasma. Similar spectroscopic measurements have been made of high frequency electric fields in plasmas, although the plasmas have quite lower densities and temperatures than the MTX plasma /4,5/.

The whole apparatus was assembled on a mock-up of the MTX torus at Japan Atomic Energy Research Institute at Tokai, and we have observed laser-induced fluorescences from the LAPPS helium beam. Measurements of beam intensity using Faraday cups and thermocouples have been also made.

2. Neutral Helium Beam

The neutral helium beam is a major component of the LAPPS diagnostic system. It consists of an ion source, neutralizer and auxiliary equipment. The basic specifications are listed below:

Beam Specifications

Ion beam current	0.8 Å
Beam energy	50 keV
Pulse width	5 ms
Repetition time	30 s
Ion species	Helium or Hydrogen
Neutralizer	Xenon or Hydrogen

3. Spectroscopic Measurements of the Neutral Beam at the Mock-Up

By using the assembled spectroscopic system, we have measured the triplet metastable atom density N_{2S} in the LAPPS helium beam. The dye laser used is excimer-laser excited, with pulse width of 25 ns and output energy of about 25 mJ at 389 nm. Figure 1 depicts a partial energy level diagram relevant to the present laser-induced fluorescences. By observing the resonant fluorescence (388.9 nm) we obtained $N_{2S} = 5.3 \times 10^{6}$ cm^{-3} for the neutral beam with energy of 46 keV.

We have also observed the cascade fluorescence (706.5 nm) as well as the resonant fluorescence. The intensity ratio obtained was 7×10^{-2} which agrees with a calculated value obtained from the branching ratio and the rate equation. Because of very limited access to the MTX plasma region, no suitable laser-beam dump can be installed. Then this cascade fluorescence, whose wavelength is far from the laser wavelength, can be observed without interference by the scattered laser light.

To obtain the divergence of beam we have observed the Doppler broadening of the resonant fluorescence (389 nm, $3^3P \leftrightarrow 2^3S$) by scanning the dye-laser with narrow width of less than 0.03 Å in wavelength. Figure 2 shows the observed wave forms of resonant fluorescence at each wavelength, where $\Delta\lambda$ indicates wavelength shift of the laser from its central wavelength. The Doppler profile obtained from this observation is shown in Fig. 3, where each intensity is obtained from integration between the indicated region with two vertical parallel broken lines in Fig. 2. The oblique angle of each beam component $\Delta\theta$ is calculated by using the Doppler effect. The e-folding divergence half angle is 0.7° at the plasma center, which agrees with a measurement by a thermocouple array.

4. Concluding Remarks

We made the absolute intensity calibration of the observed resonant fluorescence and found that the LAPPS spectroscopic system obtained 110 photoelectrons per one laser shot. Our calculations for the electric field measurement show that the measured metastable atom density is high enough to observe the forbidden fluorescence with a good S/N ratio for the FEL microwave in vacuum.

In the MTX plasma the triplet metastable atom will be rapidly attenuated due to the ionization and charge-exchange processes. In this case, the singlet metastable atom produced due to the excitation processes can be used to observe the corresponding forbidden fluorescence. Our neutral helium beam is intense enough so that the singlet metastable atoms can be produced in the plasma.

Acknowledgments

This work was performed under the DOE-JAERI Collaborative Program in the Microwave Tokamak Experiment Project (MTX). Four of us were supported in part by a Grant in Aid for International Scientific Research from the Ministry of Education, Science and Culture in Japan.

/1/ Free-Electron Laser Experiments in Alcator C, edited by K.I. Thomassen, Lawrence Livermore National Laboratory, Livermore, California, Report No.LLL PROP-00202, 1986.

/2/ K. Mizuno, T. Oda, E.B. Hooper, K. Takiyama, K. Kawasaki, and Y. Matsuda, 16th IEEE International Conference on Plasma Science, Buffalo, NY, 1989, p.140.

/3/ T. Oda, K. Odajima, K. Mizuno, K. Ohasa, M. Shiho, K. Takiyama, J.H. Foote, and D.G. Nilson, Rev. Sci. Instrum. 61, 2964 (1990).

/4/ U. Rebhan, N.J. Wiegart, and H.-J. Kunze, Phys. Lett. A85, 228(1981).

/5/ K. Takiyama, K. Kadota, T. Oda, M. Hamamoto, T. Ohgo, Y. Kamiura, K. Adati, and J. Fujita, Rev. Sci. Instrum. 59, 2351 (1988).

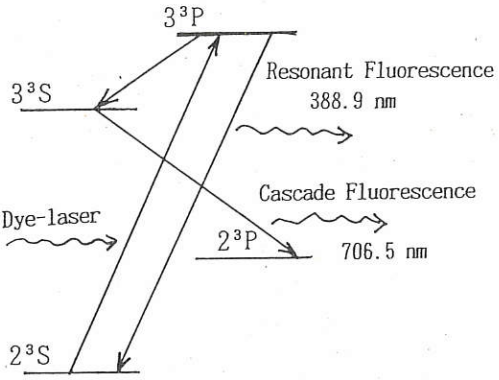

Fig. 1: Partial energy diagram of HeI relevant to the laser-induced fluorescence observations.

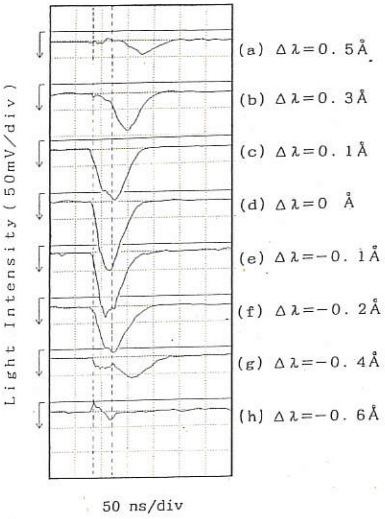

Fig. 2: Obsevation of the Doppler shift of resonant fluorescence from the neutral helium beam.

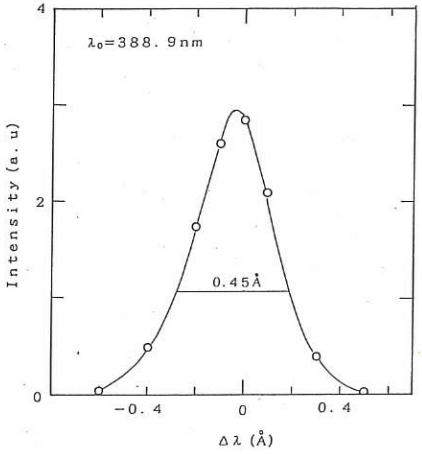

Fig. 3: The Doppler profile of resonant fluorescence.

LASER SHADOWGRAPHIC STUDY OF PLASMA SHEATH IN DENSE PLASMA FOCUS IN THE PRESENCE OF EXTERNAL AXIAL MAGNETIC FIELD

R.S. Rawat, M.P. Srivastava, and S.R. Mohanty
Department of Physics & Astrophysics, University of Delhi
Delhi - 110 007, INDIA

The Dense Plasma Focus (DPF) is a device for the production of plasma of very high density ($\simeq 10^{25-26}$ m^{-3}) and temperature in the range of 1-2 keV. This devicecan be used as a source of neutrons, X-rays, and particle beams by filling the plasma chamber with suitable gas. If we use suitable diagnostics it may be possible to study the dynamics of the plasma sheath. This is achieved with the help of laser-shadowgraphy by Lee et al. /1/. It may be further noted that the application of axial dc magnetic field (B_z) may influence the various parameters of neutrons, X-rays, and particle beams and also the dynamics of focus formation. Mather et al. /2,3/ found with the help of soft X-ray pin hole photographic analysis that B_z provided the spatial stability to the focused plasma column. Material erosion from the centre electrode and X-ray emission from the electrode face as a result of electron bombardment was also found to be reduced. Beckner and Smith /4/ investigated that the neutron yield is decreased by a factor of 40 in the presence of B_z. Bernstein and Hai /5/ also measured the energy of the neutrons and found that the average energy of the neutrons decreased. However, no study has so far been made about the influence of such B_z on plasma sheath dynamics.

We have therefore studied in the present paper the dynamics of plasma sheath in the presence of B_z with the help of N_2-laser shadowgraphic method.

We use a 3.3 kJ Mather type DPF device. DPF has a coaxial assembly of electrodes with inner hollow copper anode having a diameter of 2 cm and length of 16 cm being surrounded by six symmetrically placed copper cathodes forming a diameter of 6 cm. An external dc axial magnetic field of 1.2×10^{-2} Tesla is applied with the help of current flowing through a pair of Helmholtz coil of 115 turns each. The current to the coil is being provided by a number of batteries connected in series. The plasma chamber is maintained at the pressure of 0.6 Torr of argon and a voltage of 14 kV is applied across the electrodes. These values are taken so

as to optimize the spike in the voltage probe signal.

As shown in fig.1 the shadowgraphic system consists of (1) a TEA nitrogen laser /6/ as a UV light source of wavelength 337 nm, (2) a beam expander of quartz lenses, (3) a 30 cm focal length converging glass lens, (4) a reduction stop, and (5) a Polaroid camera. Polaroid-667 high speed B&W film is used for recording the shadowgraphs. Few plane glass slides along with RF sputtered thin film of PZT on glass are used to obtain the correct intensity of N_2-laser to be recorded on the film.

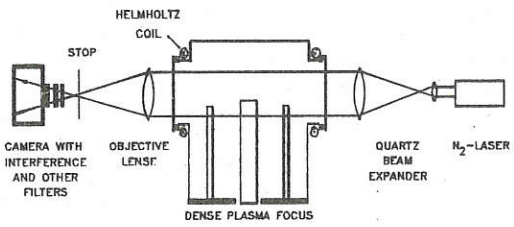

Fig.1 : Optical layout of the shadowgraphic setup.

In order to obtain the shadowgraphs it is necessary to synchronize the DPF and the laser flash by determining the focus time t_f and the laser flash time t_l and then to match these by a delay unit. The plasma focus time is defined as the time of the voltage spike on oscillogram obtained by voltage divider placed across the electrodes and was measured as t_f=5.4 μs without any B_z and t_f=5.2 μs under the influence of B_z (fig.2).

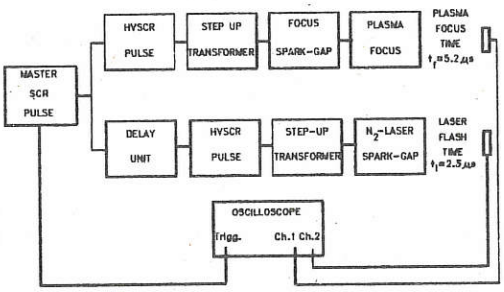

Fig.2 : Block diagram of electronic time in experimental setup

The laser flashtime as measured by photodiode BPX 65, with the delay unit bypassed, was found to be t_l=2.3 μs. Thus the required delay is $t_f - t_l$=2.9 μs, which has been obtained by introducing the delay unit in the laser line. However, because of the parallel plate swinging-cascade spark-gap jitter of the DPF, focus rundown time jitter, and laser spark-gap jitter, one requires a large number of shots to obtain the desired

shadowgraphs at different instants.

We have taken shadowgraphs with different delays to capture the different states of plasma sheath.

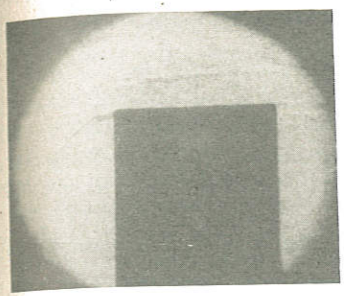

Fig.3: Shadowgraph of plasma sheath in axial rundown phase

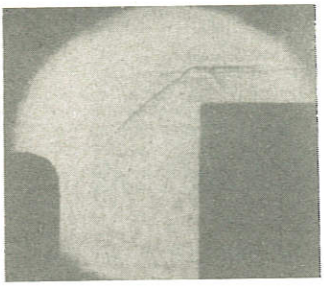

Fig.4: Shadowgraph of plasma sheath in radial phase

Fig.3 shows a shadowgraph of the axial rundown phase of the plasma sheath at the tip of the anode. This shadowgraph does not show any difference in plasma sheath structure from those which have been obtained for DPF fired without any B_z /1/. The only noticeable point in fig.3 is that at the tip of the anode the sheath is faint and diffused near the end attached to anode.

The radial collapse phase of DPF under the influence of B_z has been portrayed in the shadowgraph of fig.4. This shadowgraph shows that the diffusivity and faintness of the sheath near the anode increases as sheath collapses at the centre of the anode. Another interesting observation is that of the clearly distinct hump formation on the plasma sheath above anode. Actually, during the raidal collapse phase the magnetic field lines are frozen with plasma resulting in the compression of the B_z thus increasing the intensity of the field. This compressing magnetic field, in order to maintain equilibrium, opossess the collapsing plasma sheath in radially backward direction leading to the hump formation on the plasma sheath as can be seen on the shadowgraph. This shadowgraph also possess remarkable similarity with the shadowgraph of negative polarity focus /1/. It is also well known that for negative polarity focus too the neutron yield is considerably lower. Hence, on the basis of this one can at least say that the radial collapse phase which shows some changes

in the plasma sheath configuration is mainly responsible for neutron yield and not the axial rundown phase.

Fig.5 shows the plasma sheath in quiescent condition in which the pinch column has expanded after reaching the state of maximum compression. This shadowgraph shows the bubble formation which indicate the strong focusing event. The bubble however is not very smooth because of the trapped magnetic field.

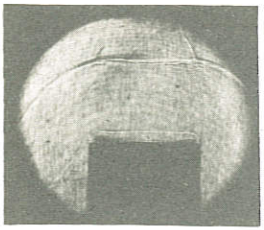

Fig.5: Shadowgraph of plasma sheath in quiescent condition.

The configuration of the plasma sheath under the influence of B_z thus shows some definite changes which can be utilized for better understanding of such DPF.

Acknowledgement

One of us (R.S.R.) is grateful to the Council of Scientific and Industrial Research, India, for providing the Senior Research Fellowship which enabled him to carry out this investigation.

/1/ S.Lee, M.A.Alabraba, A.V.Gholap, S.Kumar, K.H.Kwek, M.Nisar, R.S.Rawat, and J.Singh, J. Fiz. Malaysia **11**, 1 (1990).

/2/ J.W.Mather, P.J.Bottoms, and J.P.Carpentar, Phys. Fluids **12**, 2343 (1969).

/3/ J.W.Mather, "Methods of Experimental Phys." **9B**, 187 (1971), Academic Press, N.Y.

/4/ E.H.Beckner, and D.R.Smith, Bull. Am. Phys. Soc. **13**, 1543 (1969).

/5/ M.J.Bernstein, and F.Hai, Phys. Fluids **14**, 1010 (1971).

/6/ K.H.Kwek, T.Y.Tou, and S.Lee, IEEE Trans. Instrum. Meas., **38**, 10 (1989).

MEASUREMENT OF PLASMA DRIFTS IN SPACE AND LABORATORY PLASMAS BY THE RESONANCE CONE TECHNIQUE

V. Rohde, A. Piel
Institut für Experimentalphysik, Universität Kiel
D-2300 Kiel, Germany

1. Introduction. The radiation field of a small antenna immersed in a magnetized plasma is, for certain frequency bands, resonantly enhanced on the 'resonance cone'[1] (r.c.), which is aligned with the magnetic field, and whose apex is at the transmitting antenna. It is well known[2–4] that, in a warm plasma, electron density and -temperature can be deduced from the r.c. maximum angle and from an associated interference pattern. Because the maximum angle depends on the frequency, one expects an immediate influence of the Doppler-effect $\omega' = \omega - \vec{k} \cdot \vec{v}_d$. In the case of a field aligned electron drift, the r.c. pattern is apparently convected downstream, which leads to an upstream-downstream asymmetry of the cone-angle (Fig. 1(a)), whereas cross-field drifts bend the r.c. sidewards (Fig. 1(b)). Since this asymmetry is easily detectable, it was proposed[5–8] to use this asymmetry as a diagnostic technique for measuring the electron drift velocity. However, the cited theoretical approaches[5–8] result in different functional dependences as well as different coefficients for deducing the drift velocity from the measured asymmetry. Moreover, up to now only the case of field aligned drift has been treated rigorously. For exactly perpendicular drift, a cold-plasma approximation is available.[6] For arbitrary drift orientation, we had suggested recently[9] to use an interpolation formula, which reduces to the kinetic theory result for field-aligned drift, and uses the cold-plasma coefficients for the angular dependence. In this contribution we present experimental observations from the r.c. instrument 'COREX-1', which investigated plasma parameters and field aligned drifts in the mid-latitude ionosphere.[10] In addition, laboratory results are presented for a critical comparison of field-aligned drifts with the competing models.[5–7]

2. The COREX-1 experiments. COREX-1 was flown on the K-9M-81 rocket from Kagoshima Space Center (Japan) on Jan. 25, 1988 at 11:00 h LT. The rocket reached an apogee of 360km. The instrument used three antennas, one on a boom at the tip of the rocket, the other two on radial booms of different length (Fig. 2). Each antenna could be operated as transmitter and as receiver. The antennas consisted of 20mm dia. spheres with integrated preamplifier and mode switch. The distance of corresponding antennas is about 1m. In Fig. 2, for example, antenna I is exciting the r.c., which is then scanned by antennas II and III utilizing the rocket's spin (1.75Hz). The mode of operation is switched each $625\mu s$ according to the scheme given in the inset. In this way, we obtain four interlaced quasi-simultaneous r.c. patterns for opposing wave propagation directions. The transmitter frequency was 600 kHz, which is about half the electron cyclotron frequency.

Referring to the geometry of the r.c. in Fig. 2, we can only detect two intersections of the scanning antenna with the r.c., which are designated with R and L. For these two points we know the group velocity direction, and (according to the methods described in the next paragraph) we can construct two representative wave-vectors $\vec{k}_R$ and $\vec{k}_L$. These are the two spatial directions, on which the drift velocity vector $\vec{v}_d$ is projected in the doppler shift formula. Consequently, we can only measure a field aligned component $v_\parallel$ and a circulation component $v_\perp$.

A typical pair of r.c. curves (modes 3/4) is shown in Figure 3. There is an obvious

non-reciprocity in the positions of the main maxima. However, the non-reciprocity is not of the type expected for field-aligned drifts. In the latter case, one pair of maxima should appear inside the other, whereas here, the bold-face curve is apparently shifted to the right. This kind of symmetry breaking is typical of a contribution from perpendicular drifts. Applying the interpolation formulas derived in the subsequent paragraph, we can deduce the field aligned velocity and the circulation velocity during the flight (Fig. 4), according to the model presented in Sect. 3. Results concerning the electron density and -temperature profile in comparison with other instruments were presented elsewhere.[10]

The field-aligned drift is not significant, since the scatter is larger than the deviation of the fit-curve from zero. The circulation velocity, however, rises to unexpectedly large values (30 km/s), which by far exceeds any geophysically expected electron drift. A possible origin of such large drift velocities could be the $E \times B$ motion, which is excited by the rocket charging. Sign and direction of this drift agree with the measured rocket potential of -2V with respect to the ambient plasma. An asymmetry of the r.c. on an ionospheric rocket was also observed by Michel et al.[6], but was interpreted as an effect of Foucault currents induced in the rocket's shell that slightly alter the B-field direction. That interpretation, however, can be ruled out by our simultaneous measurements for opposing wave directions.

3. Theory. A general solution for the r.c. shape with arbitrary oblique drift direction is still lacking, because the symmetry properties of the r.c., which are utilised in calculating the r.c. potential, are only preserved for field-aligned or strictly perpendicular drift. Consequently, it is suggested here to treat the drift influence only as a first order perturbation. We start from the cold plasma dispersion relation $k_\perp^2 S + k_\parallel^2 P = 0$ and assume that the drift effects are included in the elements S and P of the dielectric tensor by using a doppler shifted wave frequency $\omega' = \omega - k_\perp v_\perp cos(\beta) + k_\parallel v_\parallel$. Expanding S and P about their values in a non-drifting plasma, we obtain the modified value of $\kappa_\perp = k_\perp r_L$:

$$\kappa_\perp = -cot(\theta_c)\kappa_\parallel + (\Omega_p^2/\Omega^3 \mid PS \mid^{1/2})(1 + (\Omega^{-2} - 1)^{-2} \mid PS \mid)2^{1/2}\kappa_\parallel(\vec{\kappa} \cdot \vec{v}_d)/v_{th} \quad (1)$$

(θ_c is the cold-plasma r.c. angle, $\beta = \angle(v_\perp, \kappa_\perp), \Omega = \omega/\omega_{ce}$.) For field-aligned drifts this is exactly Kuehl's[5] result, whereas for perpendicular drift the expression reduces to the formula of Michel et al.[6] Since thermal and drift corrections are both first order, the drift correction is also valid in the low-temperature-approximation.[5] Following Ref.[6] the potential can be evaluated by an asymptotic expansion for large R in the angular integration to obtain Kuehl's formula, except for replacing v_d by $(v_\parallel - cot(\theta_c)cos(\beta)v_\perp)$. The transition to the near field of the antenna, where the asymptotic expansion breaks down, can be obtained as follows: From numerical integrations of the potential integral in a non-drifting plasma we estimate the shift per unit frequency $\partial\theta_{max}/\partial\Omega$. The shift of the resonance angle then reads:

$$\Delta\theta_{max} = (\partial\theta_{max}/\partial\Omega)2^{1/2}\kappa_\parallel(v_\parallel - cot(\theta_c)cos(\beta)v_\perp)/v_{th} \quad (2)$$

However, we now need to know the correct vector $\vec{\kappa}$ that describes the wave packet, which is representative for the r.c. maximum. The *magnitude* of $\kappa_\parallel$ can be derived from a comparison of eq.(2) with exact kinetic calculation for field aligned drifts, yielding $\kappa_\parallel = 0.112$ at $\Omega_p = 1$, and $\kappa_\parallel = 0.116$ at $\Omega_p = 5$. The *orientaion* of $\vec{\kappa}$ is approximately perpendicular to the group velocity[2] $\vec{v}_g$, i.e., the line connecting transmitter and receiver, and $\vec{\kappa}$ is coplanar with the magnetic field $\vec{B}$. Eq. (2) quantitatively describes the 'downstream-convection' of the r.c. as depicted in Fig. 1.

4. Laboratory results. Studies of resonance cones in drifting plasmas were performed in the triple plasma device KIWI, which consists of two source chambers (90cm dia.×90cm) and a magnetized central section (30cm dia.×200cm, $B \leq 0.15T$). The electron drift is established by a small difference of the plasma potentials in the source chambers. The drift velocity is measured by evaluating the electron saturation current of a plane probe.[11] These measurements have been performed for a large range of wave frequencies and plasma densities. In addition we have compared the influence of the drift on r.c.'s in the lower and upper branch.[2] A comparison of measured r.c. angle shifts (for the lower branch) with different theories is shown in Fig. 5. There is a close agreement with our kinetic theory results. Because of the large antenna distance ($r/r_L = 180$), the low-temperature-approximation[5] gives fairly good agreement, too, whereas the cold-plasma model[7] has a completely different functional dependence, which leads to deviations by a factor of two at high drift velocities. The 'low-temperature- high-density model'[8] has been omitted from this comparison, because $\Omega_p \gg 1$ is not met, here. The absolute cone angles of the latter model deviate by 5 degrees from the other theories, even at $\Omega_p = 5$. Similar agreement with our numerical kinetic theory calculations is found throughout the parameter space. This finding justifies the use of the kinetic theory coefficients in the model of Sect. 3.

4. Conclusions. The r.c. technique is able to detect weak electron drifts ($v_d/v_{th} \leq 0.2$). In the rocket environment it helped identifying a hitherto unexpected electron motion. The quantitative diagnostics for arbitrary drift orientation can be established by a first-order perturbation model that yields two correct limiting cases. The coefficients used in this model are confirmed by laboratory experiments.

Acknowledgement. Part of the laboratory experiments were performed in a collaboration with Dr. Th. Pierre (LPMI, Nancy). Financial support by DARA under contract 01om90010 (COREX-2) is gratfully acknowledged.

References.

[1] R.K. Fisher, R.W. Gould, *Phys. Fluids* **14**, 857 (1971)
[2] H.H. Kuehl,*Phys. Fluids* **16**, 1311 (1973)
[3] L.R.O. Storey, J. Thiel, *Phys. Fluids* **21**, 2335 (1978)
[4] G. Oelerich-Hill, A. Piel, *Phys. Fluids* **B1**, 275 (1989)
[5] H.H. Kuehl, *Phys. Fluids* **17**, 1275 (1974)
[6] E. Michel, C. Beghin, A. Gonfalone, I.F. Ivanov, *Ann. Géophys. (Paris)* **31**, 463 (1975)
[7] K. Lucks, M. Krämer, *Plasma Phys.* **22**, 879 (1980)
[8] V. Fiala, V.I. Karpman, *J. Plasma Phys.* **40**, 455 (1988)
[9] A. Piel, V. Rohde, H. Thiemann, *Adv. Space Res.* **12**,(6)259 (1992)
[10] A. Piel, V. Rohde, H. Thiemann, **ESA-SP317**, p.69-74 (1991)
[11] Th. Pierre, V. Rohde, A. Piel, *Phys. Fluids* (accepted for publ.)

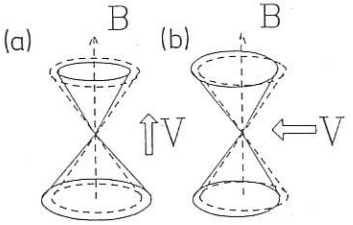

Fig. 1 Deformation of resonance cone by electron drift

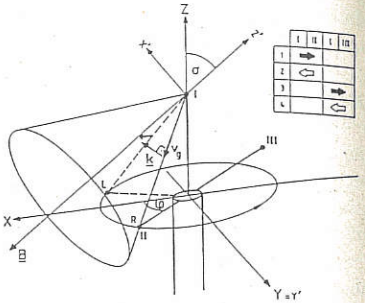

Fig. 2 Geometry of COREX-1 rocket experiment

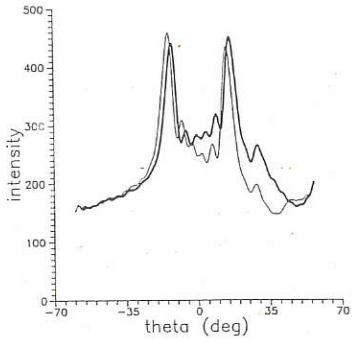

Fig. 3 Resonance cones for opposing wave propagation direction

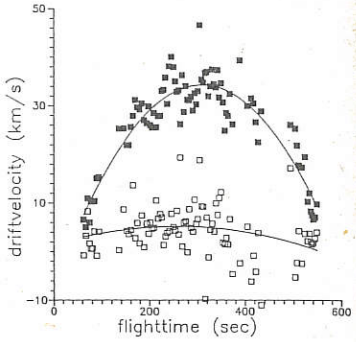

Fig. 4 Circulation velocity (full symbols) and field aligned drift (open symbols)

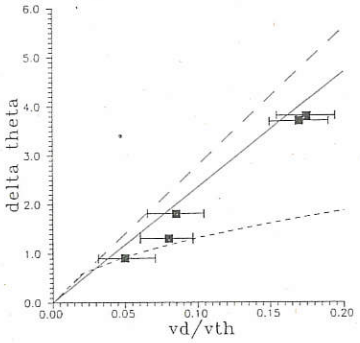

Fig. 5 Comparison of measured r.c. shift in drifting plasma with different theories: kinetic theory[4] (full line), low-temperature-approximation[5] (long dashed), cold-plasma[7] (short dashed).

THE TIME-DELAY OF A MICROWAVE SIGNAL, BACKSCATTERED AT THE HYBRID RESONANCE AND NEW POSSIBILITIES FOR THE DIAGNOSTICS OF SMALL SCALE PLASMA FLUCTUATIONS.

Arhipenko V.I., Simonchik L.V

Institute of Physics, Minsk, Belorussia

and

Budnikov V N., Gusakov E.Z., Piliya A.D., Selenin V.L.

A.F Ioffe Physical-Technical Institute, St. Petersburg

Russian Federation

Enhanced scattering (ES) is a diagnostics, based on backscattering close to a hybrid resonance layer [1,2]. Compared with conventional collective scattering, ES "sees" fluctuations with much smaller scale-lengths and produces much more strong signals. In addition, it provides automatically fairly good spatial resolution of measurements. However, the wave-vector resolution here is intrinsically poor because both incident K_I and scattered K_s wave-vectors have a rapid variation in the resonance region and the matching conditions

$$2K(x)=q \qquad (1)$$

with $K=K_I=-K_s$ can be satisfied in a wide interval of q. Here q is the fluctuation wave-vector and we suppose for simplicity that all waves propagate along the plasma inhomogeneity direction. A radar-like modification of ES using the time of flight analysis to cope with this problem is presented in this report. The method is feasible due to extremely low group velocity of the waves in the resonance vicinity. In the WKB approximation the time interval between launching a signal in the point X and its coming back is given by

$$t_d = 2\int_{X_0}^{X_s} \frac{dX}{\partial\omega/\partial K}$$

where the scattering point $X_s(q)$ is to be found from (1). Close to the resonance point X_r, $K=K(X-X_r)$ and $\frac{\partial t_d}{\partial q} = 2\frac{\partial K}{\partial \omega}\frac{\partial X_s}{\partial q} = \frac{\partial X_s}{\partial \omega} = \frac{dX_r}{d\omega}$, giving

$$t_d = -q \frac{dX_r}{d\omega} + t_0 \qquad (2)$$

with t_0 independent of q. It should be noted, that for Eq.(2) the validity of the WKB approximation is actually not necessary and it is relevant to any case of scattering close to a hybrid resonance.

Plasma probing by short pulses of microwave radiation with the frequency ω and duration τ satisfying the condition $\omega^{-1} \ll \tau \ll t_d$ is the most obvious way of employing the relation (2). A simple analysis gives for the received power in this case $P_s(t)=|I(q)|^2\langle|\delta n^2(q)\rangle|$ at $q=\frac{t-t_d}{\partial X_r/\partial\omega}$. The form-factor $I(q)$, characterizing the scattering effectiveness can be calculated for each type of a hybrid resonance, which permits to determine the fluctuation q-spectrum $\langle\delta n^2(q)\rangle$ from measured shape of the scattered pulses.

Another possible modification utilizes the probing wave with a frequency sweep. In this case the frequency shift between scattered and reference signals involves, in addition to the fluctuation frequency Ω, a term, proportional to the propagation time t_d.

The frequency spectrum of the homodyne detector output is now $P_s(\nu)=|I(q)|^2\langle|\delta n^2(q)\rangle|$ at $q=\frac{(\Omega-\nu)T}{\frac{dX_r}{d\omega}\Delta\omega}$ where $\Delta\omega$ and T are the magnitude and the period of the frequency modulation respectively. Relation between the observed frequency and the frequency of the fluctuations

$$\nu = \Omega - \frac{dX_r}{d\omega}\frac{\Delta\omega}{T} = \Omega - \frac{dX_r}{dt}q \qquad (3)$$

resembles the Doppler effect.

Feasibility of the above proposals has been tested in experiments on enhanced scattering from artificially exited ion-acoustic waves. The experiments were performed in the linear installation [3]. Radially and axially inhomogeneous argon plasma was produced at pressure $\approx 10^{-2}$ Torr in a cylinder of 2cm diameter placed in the magnetic field H=3T. The 2.4 GHz electron plasma wave at power $P_I \approx 1$mW was used for probing. The wave experienced a hybrid-type resonance in

the point where $\omega_{pe}^2(z,0)=\omega^2$. The single wave-guide antenna acted as both transmitter and receiver. The target ion-acoustic waves with different frequencies were exited parametrically by the pump of the same type with higher power 10-100 mW [3].

In the first experiment the short microwave pulses were injected into plasma and the envelop of the received signal was studied. A received pulse consisted of parts produced by reflection from the plasma edge and by scattering from the target wave. In the absence of this wave the received pulses were similar in their shape with only slight individual deviations. With the ion-acoustic wave exited in the plasma received pulses looked the same for a certain time interval Δt. Than a change of the shape was evident, indicating appearance of the signal component generated via scattering in the resonance region (Fig.1). Time delay dependence on the target frequency $f_s=\Omega/2\pi=qC_s\sqrt{\Delta T}$ ($C_s=\sqrt{T_e/m_i}$) is shown in Fig.2. In the second experiment the plasma was probed by RF pulses of both a constant frequency and a frequency varying linearly with time at the rate $\frac{df}{dt}=7.9\cdot10^{13}$ Hz/s.

The reflected signal was mixed with the reference microwave signal and resultant spectra are shown in Fig.3 for 3 different target frequencies f_s Solid lines represent the case of a constant probing frequency. The dashed lines refer to the case with the frequency sweep. Now a frequency shift f_{sw} due to the time delay of the scattered signal is clearly seen. Fig.4 compares these shifts with Eq.(3).

We can conclude now, that with the relation (2) confirmed experimentally, a very significant improvement of ES performance becomes possible.

References.

1. Novik K.M.in Basic and advanced diagnostic techniques for fusion plasmas (Proc. Course and Workshop. Int. School of Plasma Physics, Varenna, 1986, vol. 1. p.517.

2. Budnikov V.N. Nuclear Fusion, vol.31,No4(1991),p.611

3.Arhipenko V.I.,Budnikov V.N.,Gusakov E.Z, Fiz.Plasmy,vol. 13,No.6(1987),p.693

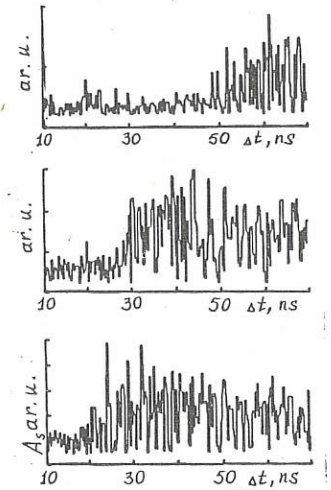

FIG. 1 PULSES SCATTERED FROM ION-ACOUSTIC WAVES WITH DIFFERENT FREQUENCIES.

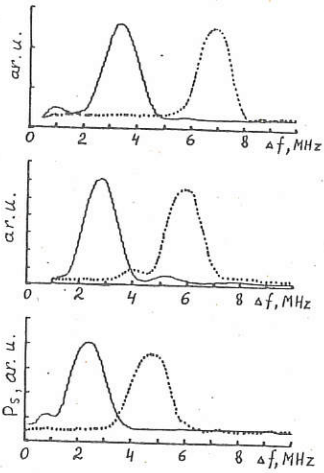

FIG. 3 SPECTRA OF DETECTED SIGNALS FOR DIFFERENT FREQUENCIES OF THE TARGET WAVE.

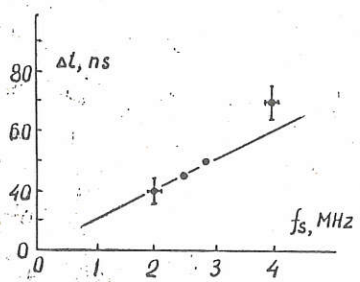

FIG. 2 PULSE TIME OF FLIGHT VERSUS THE TARGET WAVE FREQUENCY.

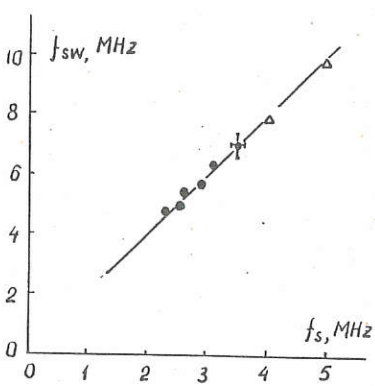

FIG. 4 FREQUENCY SHIFT BETWEEN SCATTERED AND REFERENCE SIGNALS VERSUS THE TARGET FREQUENCY.

EXCIMER LASER DRIVEN SOFT X-RAY PLASMA SOURCE: PRELIMINARY RESULTS

L.Palladino, A.Reale, G.Taglieri University of L'Aquila and INFN-LNGS, Italy
D.Batani University of Milano and INFN-LNGS, Italy
S.Bollanti, P.DiLazzaro, F.Flora, T.Letardi, G. Schina ENEA-Frascati, Roma, Italy
M.Belli, A.Scafati Physics Laboratory of ISS and INFN Sanità Roma, Italy

1. Introduction

Laser produced plasmas are very powerful laboratory-scale soft X-ray sources, already successfully applied to microscopy, microlithography, radiobiology and EXAFS. In these fields they are emerging as a complementary tool competitive with synchrotrons. The process of X-ray generation is indirect: the laser beam heats the plasma which then emits an X-ray pulse as a consequence of the high electron temperature. It has also been experimentally shown that short wavelength lasers can give a better laser-plasma coupling and hence a better X-ray conversion efficiency, which is defined as $\eta = E_X/E_L$ where E_L is the laser pulse energy and E_X the energy emitted by the plasma in the X-ray region of the electromagnetic spectrum.
A joint effort is currently taking place among different laboratories in Italy to build a small soft X-ray facility as done in other laboratories in the world. We use a laser system developed at ENEA which is a large volume (10 lt) instable cavity XeCl excimer laser (308 nm wavelength) with a 2 J, 100 nsec pulse, "useful" beam aperture 7x7 cm^2, now operating in single mode but planned for 1 Hz repetition frequency. The advantage of the unstable cavity, with respect to a stable one, is that it allows a reduced beam divergence and a 4 order of magnitude increase in laser brightness /1/. The experimental set-up was already described in /2/.

2. Experimental results

In our experiment the laser beam was focused on a copper target by using two different lens: the first one has a focal length f=239 cm; the second lens is matched doublet with a focal length f=131 cm (hence using the shortest lens we got a ≈ 4 times increase in the laser intensity in the focal spot). An accurate analysis of the focal spot in the equivalent plane showed that beam profile is not quite gaussian and only ≈ 20 % of laser energy was inside the nominal FWHM diameter. The corresponding beam divergence θ was ≈ 20 μrad. From the formula which relates the spot size d and the beam divergence $d = f\theta$ we get $d \approx 56$ μm for the longest lens and 27 μm for the shortest one. From the size of the crater produced by the laser in the target (which was analyzed on an electron microscope) we could establish an upper limit $d \leq 100$ μm for the diameter of the spot. The maximum intensity we reach is $I_L \approx 5\ 10^{11}$

W/cm^2. The diagnostic of x-ray emission was done by a PIN-XRD silicon diode (100-PIN-125 produced by Quantrad Corporation) with 0.75 μm window and thin Al filters. The vacuum in the interaction chamber was 0.1 mbar during of the measurements.

Our first experimental results show that we produce a pulse of X rays of about same duration of that of the laser pulse (Fig.1). This is already very interesting since it's been shown /3/ that sometimes excimer lasers have problems with long pulses giving in this case $t_X << t_L$ (this has been called the "pulse shortening problem").

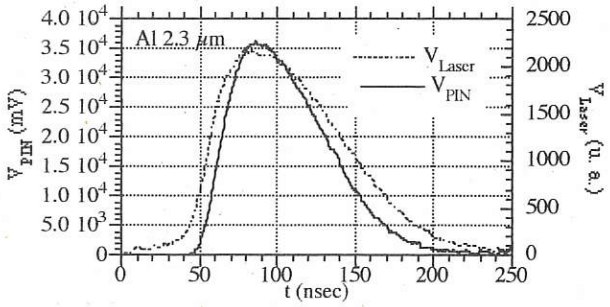

Fig.1: X-ray and laser pulses

We shows two focal scans (Fig.2), that is records of X-ray signal as a function of target position with respect to the lens best focus.

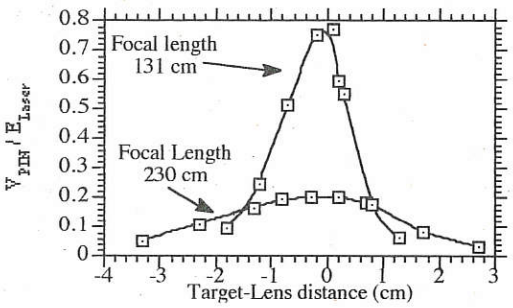

Fig.2: Focal scans

We also got images of our X-ray source with the help of a pin-hole camera fixed at one window of the interaction chamber. We shows (Fig.3) a typical densitometry pin hole image on kodak DEF film recorded with a 50 μm pin-hole filtered with 0.8 μm Al; the pin hole

camera magnification was ≈ 2. The FWHM size of the X-ray source was measured to be ≈ 80 μm in the case of the shortest lens, comparable with the laser spot size.

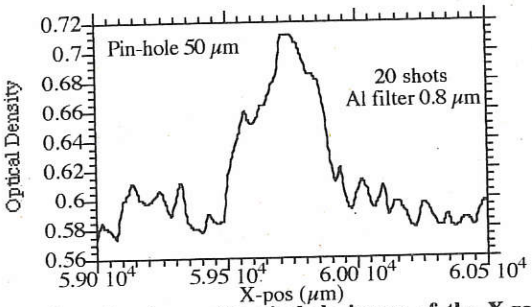

Fig.3: Densitometer trace of a pin-hole image of the X-ray source

In Fig. 4 we show the collected diode charge vs filter thickness and we conclude that the X-ray spectrum, as seen by the PIN-filters system, is centered around a 500 eV photon energy. The spectrum is the convolution of the filter transmission, the detector sensitivity (0.75 μm dead layer) and the plasma emission . We are looking at a very high energy tail of the emitted X-ray spectrum hν ≥ 400eV, indeed we reach a plasma temperature $T_e \approx 30$ eV which is not sufficient to excite bulk soft X-ray emission (the value of T_e was obtained both by energy balance considerations and by applying the formula by Colombant and Tonon /4/).

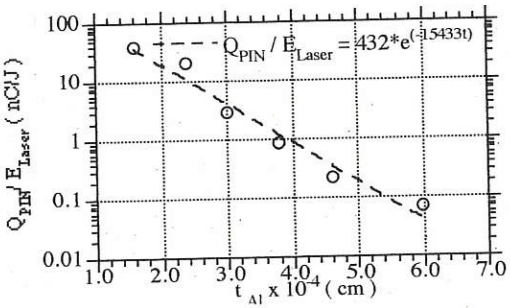

Fig.4: X-ray signal vs Al filter thickness

We have also seen by varying the energy of the laser ($5\ 10^{10}$ - $5\ 10^{11}$ W/cm^2) the X-ray signal increases quadratically with the laser intensity (Fig. 5). Since at the different intensities we still measure hν ≈ 500 eV, this means that conversion efficiency η increases linearly with laser intensity in the spectral region hν ≥ 400 eV.

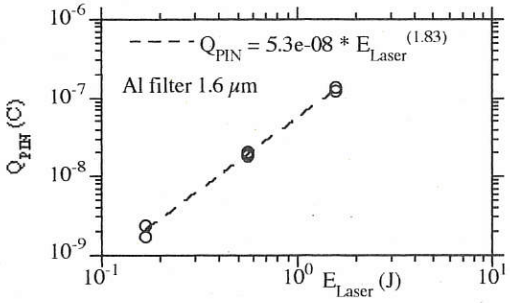

Fig.5: X-ray signal vs laser intensity

3. Conclusion

The measured X-ray signal corresponds to a conversion efficiency of about 3% for photons with energy ≥ 400 eV over the solid angle 2π, that is to 60 mJ soft X-ray energy produced per shot or 10^{12} photons/cm^2 at 10 cm from the target. The future experimental work will include a new focusing lens to obtain a greater laser intensity in the focal spot and to test different targets . The system could then be used for X-ray contact microscopy allowing single shot exposure, or for microlithography.

Acknowledgements

We thank Edmond Turcu, RAL, for the very helpful discussions. This work was fully supported by Italian INFN and ENEA.

References

/1/ S.Bollanti, P.DiLazzaro, F.Flora, T.Letardi, G.Schina, M.Pontaccio, A.Torre, C.E.Zheng "High brightness large aperture excimer laser radiation" Proc. Lasers 1991, San Diego, USA.

/2/ L.Palladino, A.Reale, D.Batani, S.Bollanti, P.DiLazzaro, F.Flora, T.Letardi, M.Belli, A.Scafati "Simple-X: an excimer laser plasma soft X-ray source for biological applications" Proc. XX ICPIG, Pisa, 1991.

/3/ I.E.Turcu, F.O'Neill, G.J.Tallents, T.Hannon, D.Batani, A.Giulietti, C.W.Wharton, R.A.Meldrum "Atmospheric Pressure operation of a repetitive KrF laser Plsma X-ray source at hν ≈ 1.1 keV" in "Excimer lasers and application II" SPIE 1990, T.Letardi ed., The Hague, Netherlands.

/4/ D.Colombant, G.F.Tonon "X-ray emission in laser-produced plasmas" J.Appl.Phys., vol.44, n.8, August 1973.

MEASUREMENTS OF INTENSE PLASMA STREAMS WITH FARADAY-TYPE COLLECTORS

J.Baranowski, M.Sadowski and E.Składnik-Sadowska
Soltan Institute for Nuclear Studies
05-400 Otwock-Świerk, Poland

High-intensity plasma-ion streams can be generated by different pulsed facilities, e.g., light-ion- beam diodes /1/, Ionotron-type devices /2/, Plasma-Focus machines /3-4/, etc. Studies of such intense plasma-ion pulses are difficult tasks, and they require the application of special diagnostic techniques /5-6/. The main aim of this paper is to report on development of Faraday-type collectors adopted for measurements of pulsed plasma-ion streams emitted from Ionotron and Plasma-Focus devices.

Experimental studies have initially been performed at the IBIS-120 device /2/ which was operated in a pulsed mode as a multi-rod plasma injector (RPI) designed for the modification of metal surfaces and the application of the pulse implantation doping (PID) technique /7/. The main questions have concerned energy deposits from an ion component of the plasma-ion stream upon the surface of investigated samples. Particular attention has also been paid to measurements of time characteristics of plasma-ion pulses in order to determine an effective exposition of the samples exposed to the ion bombardment.

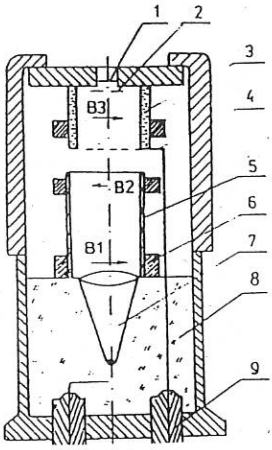

Fig. 1. Scheme of Faraday type collector: 1 - shielding screen, 2 - aperture, 3 - ceramic post, 4 - control grid, 5 - glass tube, 6 - permanent magnets, 7 - hollow inner electrode, 8 - insulating material, 9 - BNC adapter.

From the very beginning, there were applied standard Faraday cups, but because of a high plasma density it was necessary to apply the technique of bias electrostatic grids /6/. After several tests the use has been made of the Faraday-type collector of the construction very similar to that applied by G.Gerdin et al. /8/. The details of the collector have been shown in Fig.1. The Faraday cup of a conical shape has been placed within a metal casing with an entrance diaphragm equipped with a shielding grid and miniature

permanent magnets. These magnets generate a weak (~100 G) magnetic field which deflects low energy electrons. Dimensions of the mesh have been chosen taking into account the Debye length value for the investigated plasma ion streams. On the contrary to the Gerdin's design we have not used the second diaphragm but we have also applied additional permanent magnets placed in front of the Faraday cup electrode.

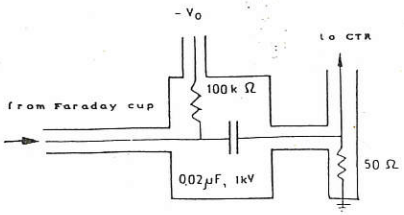

Fig. 2. Bias circuit used during measurements of plasma-ion streams.

In order to perform ion component measurements the Faraday-type collector has been connected with a simple electrical bias circuit, as shown in Fig.2. Using the collector described above and the time-of-flight (TOF) method, it has been demonstrated that one can register distinct ion pulses, as shown in Fig.3. Detailed analysis of the registered waveforms has shown that signals induced by hard X-rays and high-energy electrons can be neglected in comparison with the ion induced signals.

On the basis of detailed measurements of the plasma-ion streams emitted from the IBIS-120 device during shots with the H_2 filling, it has been found that at the distance of 48 cm the first ion pulse corresponds to protons of energy $E_H+ = 11.5$ keV, the ion current flowing through the 1-mm-dia. diaphragm reaches about 3.2 A, and the ion flux energy density amounts to 1.2 J/cm^2. At the distance of 88 cm these values amount to 10,5 keV, 1.3 A, and 0.6 J/cm^2, respectively. Analogous measurements, as performed for shots with N_2 filling, have shown that ion beam parameters depend considerably on the operational mode, which can easily be changed by variation of a gas-valve delay time. Some examples are presented in Fig.4. Changing the delay time from 180 μs (A), through 210 μs (B), up to 250 μs (C), one can obtain the nitrogen ion pulses of energy ranging from 120 keV down to 27 keV, and the ion-flux energy density varying from 0.8 to 2.6 J/cm^2. An estimate

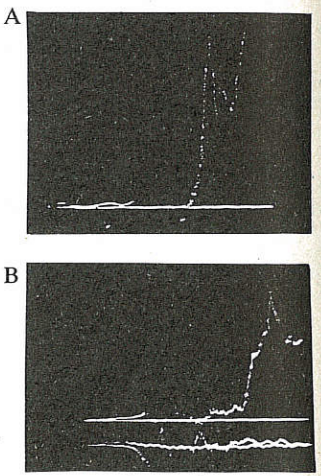

Fig. 3. Ion signals registered at the distance of 48 cm (A) and 88 cm (B). The full time base - 2 μs.

of an ion surface density shows that the IBIS-120 device can provide 10^{11}-10^{12} ions/cm^2 at the distance of about 50 cm from the electrodes.

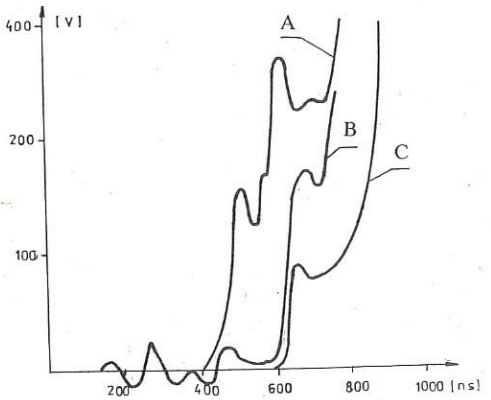

Fig. 4. Ion signals obtained from IBIS-120 device with the N_2-filling for different delay time.

Recently, using the Faraday-type collector, preliminary ion beam measurements have also been performed at the MAJA-PF facility /9/ with the D_2 filling. An example of the ion-signals has been shown in Fig.5. In that case the first ion pulse corresponds to deuterons of energy 10-15 keV. One should note that the ion beam emission reveals the multi-spike character observed in the previous PF experiments /10/.

The experimental results presented above can be summarized as follows:

1 - The Faraday-type collector developed for studies of intense plasma-ion streams can provide valuable information about ion flux parameters.

2 - Using the negative polarization ranging from 800 to 1000 V one can select the

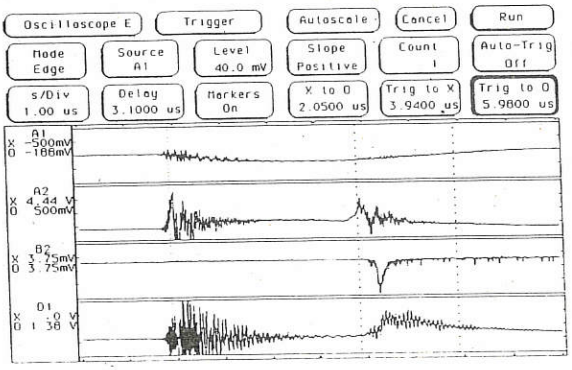

Fig. 5. Ion signals (D1) obtained from MAJA-PF facility with the D_2-filling.

positive (ion) signals only.

3 - At the IBIS-120 and MAJA-PF facilities there are observed distinct ion pulses correlated with discharge current peculiarity, and the estimated ion flux energy density remains in agreement with thermocouple measurements.

It should also be noted that more detailed ion beam studies require the application of other diagnostic techniques, e.q., nuclear truck detectors (NTDs) and/or Thomson-type analyzers.

/1/ D.L.Cook, M.P. Desjarlais, et al.: Proc. Beams'88 Conf. (Karlsruhe, July 1988), Vol.I, pp. 35-45.

/2/ M.Gryziński, J.Baranowski, et al.: ibid, pp. 319-324.

/3/ R.Gullickson, and H.Sahlin: J. Appl. Phys. 49, 1099 (1978).

/4/ M.Sadowski, H.Schmidt, and H.Herold: Phys. Lett. 83A, 435 (1981).

/5/ N,.G.Basov (Edit.): Dense Plasma Diagnostics (Izdat. Nauka, Moscow 1989) - in Russian.

/6/ St.Humphries, Jr: Charged Particle Beams (John Wiley & Sons), New York 1990.

/7/ J.Piekoszewski, M.Gryziński, J.Langner, and Z.Werner: J. Physique 43, 353 (1982).

/8/ G.Gerdin, W.Stygar, and F.Venneri: J. Appl. Phys. 52, 3269 (1981).

/9/ M.Sadowski, L.Jakubowski, and J.Żebrowski: Proc. 18th Europ. Conf. CF&PP, Berlin 1991, Part II, pp. 233-236.

/10/ M.Sadowski, J.Żebrowski et al.: Phys. Lett. 113A, 25 (1985).

NEW ČERENKOV DETECTORS FOR STUDIES OF FAST ELECTRON BEAMS FROM PLASMA DISCHARGES

L.Jakubowski, M.Sadowski, and J.Żebrowski
Soltan Institute for Nuclear Studies
05-400 Otwock-Świerk n. Warsaw, Poland

It is well known that high current plasma discharges can generate intense relativistic electron beams (REBs). If a positive electrode (anode) has an appropriate axial opening such beams can be emitted from a plasma column and used outside the main discharge region. The emission of REBs have been investigated by many authors at different experimental facilities, e.g., high-voltage pulsed diodes and high-current z-pinches. Recently, particular attention has been paid to the REBs emission from the PF-type devices [1-8].

In order to detect high-energy electrons, there have been applied various diagnostic methods, and in particular magnetic spectrometers [8,9], Faraday-type collectors [9], and Čerenkov-type detectors [7,10-11]. The magnetic spectrometers could not, however, be used for indirect measurements of primary REBs because of limitations imposed by a collimator system. The electron Faraday-cups, designed for measurements of intense REBs, required special foil filters [9], which had to be replaced after each shot and were inconvenient in the use. Better wearability and the highest time-resolution could be obtained with the Čerenkov-type detectors but their disadvantage was a relatively high energy threshold [7,10-11].

The main aim of this paper has been report on the development of new Čerenkov-type detectors, which make possible time- and space-resolved measurements of electrons of energy down to about 50 keV.

In order to improve the spatial resolution of REBs measurements, which in the previous PF experiments [10-11] was limited by large dimensions of the Čerenkov detectors, it has been proposed to use a set of miniature plastic radiators [7]. Using thin 1-mm-dia. plastic optical-cables, which were shielded from plasma visible radiation with thin metal foils, it has been shown that the Čerenkov signals can easily be observed [7].

As a next step, we have proposed to use miniature Čerenkov radiators made of different materials, as shown in Fig.1. Since for energetic electrons with velocity v, penetrating a transparent material characterized by a refractive index n, the Čerenkov radiation threshold is given by the formula

$$\beta_{th} \geq 1/n$$

where β=v/c ratio [12], using radiators with different n one can perform a rough energy analysis of incident REBs. The application of the radiators made of the optical cable plastic (characterized by n_{pl}=1.452) makes possible observations of the Čerenkov radiation from electrons of energy >194 keV. The use of glass radiators (characterized by n_{gl}=1.47) enables electrons of energy >187 keV to be detected. To perform the energy analysis by a comparison of the Čerenkov signals (see Fig.1) one has to take into account effective dimensions of the radiators and influence of VR-shielding foils.

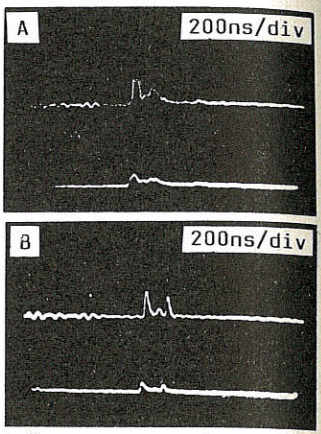

Fig.1. Čerenkov signals from plastic (upper traces) and glass radiators (lower traces) exposed to REBs in MAJA-PF facility [8] at p_o=1 torr D_2, W_0=110 kJ.

In order to lower the Čerenkov energy threshold we have been looking for a transparent material with a very high refractive index. It has been found that the miniature radiators made of diamond (n_{di}=2.42) can be applicable for measurements of electrons above β_{th}=0.413, i.e., of energy down to about 50 keV. Experimental tests have been performed at the MAJA-PF facility [8] and they have shown that the Čerenkov signals induced by numerous lower energy electrons are considerably higher, as shown in Fig.2.

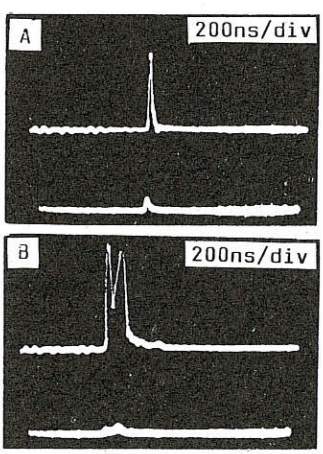

Fig.2. Čerenkov signals from diamond (upper traces) and glass radiators (lower traces) exposed to REBs in MAJA-PF-facility at p° =1 torr D_2, W_0=110 kJ.

Detailed time-resolved measurements of REBs by means of diamond and plastic Čerenkov detectors have been carried out at the PF-360-facility [8], and they have confirmed the usefulness of the diamond radiators for energy and correlation studies, as shown in Fig.3.

The analysis of REB induced Čerenkov signals obtained with the diamond radiators (upper traces in Figs.4B and 4D) with those obtained with glass detectors (lower traces in Figs. 4B and 4D),

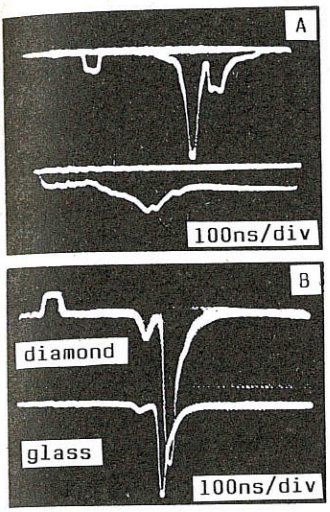

Fig.3. Correlation of neutron and r-min. signals (A) with REB induced Čerenkov pulses (B) for PF-360 facility at p_o=4 torr D_2, W_o=138 kJ, Y_n=1.1x10^{10}.

taking into account an additional 26-μm Al-filter, has shown that the population of fast electrons above 360 keV was 3-5 times smaller than that above 215 keV. Assuming that the electron energy spectrum fits to a power law $E^{-\alpha}$ one can estimate that the exponent α was equal to about 4.0 in the experiment described. Some time-shifts of the Čerenkov signals maxima (which are shown in Figs.4B and 4D) can be explained by time jitter in the emission of individual REBs, which were registered by the detectors placed in slightly different positions at the detection plane.

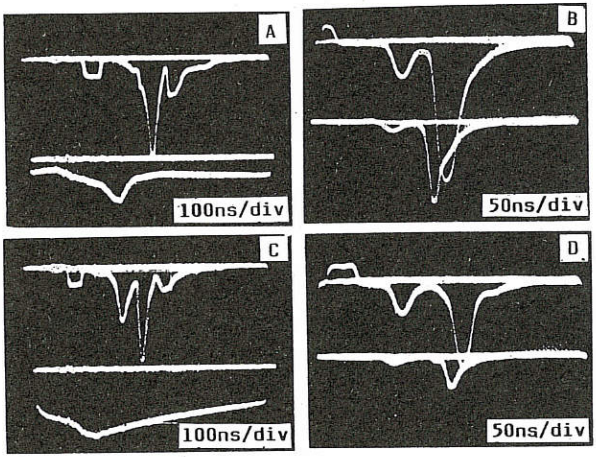

Fig.4. Comparison of neutron and r-min. signals (A&C) and REB induces Čerenkov signals (B&D) for two PF shots in PF360-facility: A&B - p_o=4 torr D_2, W_o=138 kJ, Y_n=1.1 x 10^{10}; C&D - p_o=3 torr D_2, W_o=120 kJ, Y_n=8.2 x 10^{10}.

The experimental results presented above can be summarized as follows:

1 - The application of miniature Čerenkov detector made of different materials enables time- and space-resolved measurements of REBs to be performed.

2 - The use of the diamond Čerenkov radiators makes possible to lower the Čerenkov energy threshold (down to 50 keV) and to perform simultaneous correlation and energy analysis of fast electrons emitted from plasma discharges.

1. R.L.Gullickson, R.H.Barlett: Report UCLR-75910 (Uni.California 1974).
2. K.G.Gureev, V.Imstiennik et al.: Sov. J. Plasma Phys. 1 (1975) 102.
3. V.Nardi, W.H.Bostick et al.: Proc. I LAW, Cambuguira 1982, Vol.I, p.114.
4. K.Hirano, T.Yamamoto et al.: Proc. 10th Intern. Conf. PP&CNFR, London 1984, Vol.2, p.569.
5. J.R.Smith, C.M.Luo et al.: Phys. Fluids 28 (1985) 2305.
6. P.Choi, C.Deeney et al.: Proc. Intern. Workshop PF&Z-Pinch, Toledo 1987, p.76.
7. L.Jakubowski, M.Sadowski, H.Schmidt: Proc. Workshop Phys. of Alternative Magnetic Conf. Schemes, Varenna 1970, p.
8. M.Sadowski, L.Jakubowski, J.Żebrowski: Proc. 18th Europ. Conf. CF&PP, Berlin 1991, Part II, p.233.
9. W.Stygar, G.Gerdin et al.: Nuclear Fusion 22 (1988) 1161.
10. W.Neff, H.Krompholz et al.: Phys. Lett. 79A (1980) 165.
11. H.Herold, L.Bertalot et al.: Proc. 10th Intern. Conf. PP&CFR, London 1984, Vol.2, p.591.
12. V.P.Zielov: Čerenkov radiation in high energy physics (IPST, Jerusalem 1970), Part I, p.66.

6-7o

APPLICATION OF LASER INDUCED IONIZATION TO ATOMIC HYDROGEN DENSITY MEASUREMENTS IN HIGH TEMPERATURE PLASMA

V.I.Gladuschak, V.K.Gusev, M.Yu.Kantor, Yu.V.Petrov, G.T.Razdobarin, V.V.Semenov, S.Yu.Tolstyakov

Ioffe Institute, St.-Petersburg, Russia

1. Principles of the method

The spatially resolved measurements of neutral hydrogen density in fusion plasmas now are carried out by means of laser induced fluorescence (LIF) method. To meet the requirements of high temperature plasma diagnostics the dye lasers are used generally for pumping the Balmer H_α or H_β transitions [1,2]. The hydrogen density is obtained from the measurement of laser induced the upper level population enhancement.

We have developed a new diagnostic approach based on a laser induced ionization (LII) of the upper atomic states. The ramp down of spontaneous emission from the corresponding upper levels, i.e. the burning out signal, is used to determine the current state of hydrogen atomic level populations in plasma. The LII diagnostics has much in common with LIF and has to exhibit approximately the same sensitivity ($\simeq 10^8$ cm^{-3} ground state hydrogen atoms) and spatial resolution. Nevertheless, it is more advantageous for a number of reasons. First of all the evident LIF complications connected with the laser-to-transition precise wavelength tuning has been avoided. Any conventional laser with a fixed probe frequency deals with a number of atomic levels. The large difference between the probing and spontaneous emission frequencies solves the complicated problem of stray light suppression.

The probe beam parameters are to be the following. The laser photon energy should exceed the ionization potential of the taken upper atomic level. The probe beam flux density is to be large enough to insure the utmost exhaustion of the upper level population. This is displayed by the saturation of the ramp down emission of the coupling line. The strong

saturation is useful to improve the sensitivity limit and to get rid some uncertainties in modeling assumptions accounting for the electron impact and radiative decay relaxations.

At steady state the saturation threshold is basically attained whenever the upper level ionization rate approximates the total rate including the radiative and electron impact upper level relaxations. While taking the hydrogen n=4 level ionization cross section of $0.36*10^{-17}$ cm^{-2} (at λ=694 nm) and $1.2*10^{-17}$ cm^{-2} (at λ=1055 nm) [3] the corresponding threshold saturating probe fluxes would be 2.5 MW/cm^2 and 0.5 MW/cm^2. To make these estimates the radiative decay of the fourth level was taken into account only. This may be really justified for low density plasmas. In the electron density range of 10^{13}-10^{14} cm^{-3} the saturating probe flux for the hydrogen n=4 level ionization would be a few MW/cm^2 in accordance with the electron impact relaxation rate. Such flux is relevant to Thomson scattering diagnostic experiments. From this point of view the Thomson scattering and LII diagnostics coupling appears to be possible and rather promising.

2. The testing experiment

Two types of lasers designed for Thomson scattering have been tested in experiments on FT-1 tokamak [1]. The first one was the ruby laser with 80 ns pulse duration. To clarify the infrared probing advantages the alternative Nd laser of near the same pulse duration was tested as well. To check the burning out saturation effect at H_β transition the tokamak plasma selfemission was observed alongside with the probe beam direction. The total laser illuminated chord of 30 cm-length was imaged on the multiplier photocathode.

Dependence of the burning out signal amplitude versus Nd laser beam intensity is shown in Fig.1. The solid line is just the predicted dependence when the threshold saturation flux density is taken to be 1 MW/cm^2. The strong saturation effect was observed also for the ruby laser whenever the flux density was in the range of 10 MW/cm^2. This results are in accordance with theoretical predictions.

The Nd laser operation seems to be more advantageous due to both the large ionization cross section and the more effective suppression of the infrared stray light.

3. Neutral density measurement

The LII diagnostics was used to determine the neutral hydrogen density in the FT-1 tokamak ohmic discharge. The tokamak and discharge main parameters are listed below: R=62.5 cm, a= 15 cm, $n_e(0)=2*10^{13}$ cm^{-3}, $T_e(0)=400$ eV. The measurements were performed at a distance of 12 cm from the discharge axis in the chamber section with gas puffing where the ground state hydrogen density was 10^{11} cm^{-3} according to the fluorescent measurements[4]. The plasma emission observed at the angle of 90° to the laser beam was picked up by an objective inside the solid angle of $4*10^{-3}$ sr and transmitted by the fiber optic guide line to a photomultiplier.The probe beam section of 2.5 cm height was imaged onto guide entrance slit. The total optics transmission was near of 10%.

A good coupling of the ruby laser Thomson scattering and the LII diagnostics was fulfilled using the laser multipass plasma probing developed beforehand [5]. The probe laser beam recycling inside the tokamak plasma volume allows to expand the irradiated plasma transverse section from 5*5 mm^2 up to 5*20 mm^2 which was extend along the observation axis. Due to the multipass system the total laser pulse duration was increased from 70 ns up to 200 ns [5]. The expansion of both the irradiated plasma transverse section and laser pulse duration provides the detected signal gain by about one order of magnitude at the saturation condition. The multipulse Q-switched ruby laser generating a train of 4-5 pulses of about 1 ms total length was used in this experiment. The H_β emission signal averaged over pulse train is plotted in Fig.2.

Fig.3 presents the H_β emission ramp down induced by Nd laser probing. In this case the laser beam-to-plasma matching is rather simplified due to effective stray light rejection. A wide collinear probe laser beam was restricted by the input port buffles up to 40*20 mm^2 beam cross section.

Max-Planck-Institut
8046 Garching bei München

As it follows from Figs.2,3 the signal amplitude drop by a factor of 10 is possible to pick up 10^{10} cm^{-3} of ground state hydrogen atoms. The further sensitivity improvement is apparently possible. For this purpose the upgraded Nd laser is now under design to yield atrain of a few tens of pulses at near 1 ms. The more effective detection system with higher transmission is to be used as well.

References.

1. G.T.Razdobarin,V.V.Semenov et al, Nucl. Fusion, v.19, p.1439, 1979.
2. P.Gohil, G.Kolbe, M.Forrest et al, J.Phys. D: Appl. Phys., v.16, p.333, 1983.
3. C.F.Barnet, J.A.Ray, J.C.Thompson,ORNL-3113, p.163, 1964.
4. V.S.Burakov,P.Ya.Misakov, P.A.Naumenkov et al, Phyzika Plasmi, v.13, p.575, 1987. (in Russian)
5. T.Yu. Akatova, D.G.Bulyginsky et al, Proc. 17 EPS Conf. on Contr. Fus. and Plasma Heat., Amsterdam, v.4, p.1684,1990.

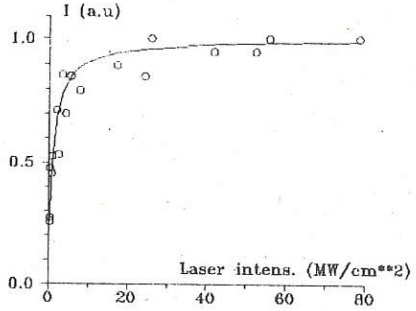

Fig. 1

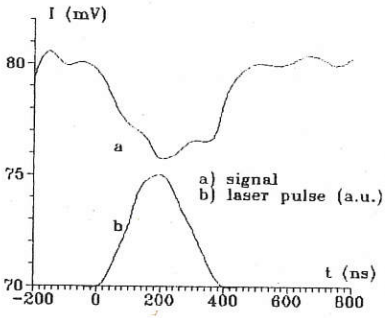

Fig. 2

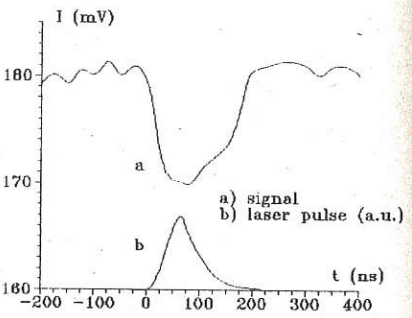

Fig. 3

Topic 7:

Inertial Confinement Fusion

Absorption of KrF Laser Pulses in Laser Produced Plasma

Isao Matsushima, Kazuyoshi Koyama, Toshihisa Tomie, Yuji Matsumoto and Yoshiro Owadano

Electrotechnical Laboratory,

1-1-4 Umezono, Tsukuba 305, Japan

The KrF laser is considered to be a promising candidate for the reactor driver of inertial confinement fusion. For reactor scale pellet compression, laser-plasma interaction with long (~20ns) UV pulse should be investigated. For this purpose, the absorption rate of KrF laser pulses incident on plane solid targets has been measured in the power density range of 10^{12} to 10^{15}W/cm^2. We varied pulse duration, bandwidth, target material and incident angle.

One beam of a six beam KrF laser system "ASHURA" /1/ was used for the experiment. The laser wavelength is 249nm. Pulse duration was 20ns, 10ns and 10ps, and multi pulse (pulse-train) irradiation of five 10ps pulses with 2ns intervals were also carried out. The laser energy of nanosecond pulses is typically 20J on target, and two bandwidths were used; a broadband of 0.2nm and a narrowband of 0.003nm. For picosecond irradiation, the typical energy on target is 10J in 5 pulses and 2J in single pulse operation. The laser beam diameter in front of the target chamber is 100mm and is focused by a spherical lens with a focal length of one meter. The incident angle of the laser beam to the targets is 10° or 22.5°. Plane aluminum and titanium targets were used. The diameter of the produced plasma is monitored by an X-ray pinhole camera which is sensitive to 1keV X-ray with a spatial resolution of 5μm. The minimum focal spot diameter is 80μm limited by spherical aberration of the focusing lens. The irradiation power density was changed by changing the lens position and the laser energy.

The reflected and scattered light energies were measured by pyroelectric calorimeters placed around the target. Temporal behaviors of specular reflected light were observed by a biplaner photo tube for some shots.

The observed scattered light was peaked at the angle for specular reflection, and the angular distribution was symmetric around the peak. Therefore the scattered energy was

obtained by integrating the reflection assuming rotational symmetry.

The measured absorption rates are plotted in Fig.1 for various irradiation conditions. For long pulse irradiation of 10 or 20ns duration, about 95% of the incident laser energy is absorbed in the power density range from 10^{12} to 5×10^{13}W/cm^2. Although the absorption with an incident angle of 10° seem to be slightly small, one should take account of ambiguity of 5% in the integration process. There are no significant differences in absorption rate by changing the target material and the laser bandwidth. An analytical model /2/ suggests that the laser energies in the long pulse shots are strongly absorbed by the inverse bremsstrahlung mechanism because of the long density scale length.

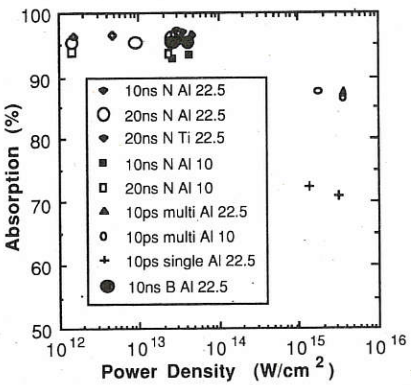

Fig.1. Absorption rate of KrF laser light as a function of incident power density for various experimental conditions: pulse duration of 10ns; 20ns or 10ps; narrow(N) or broad(B) laser bandwidth; single or multi pulse; target material of aluminum(Al) or titanium(Ti); and incident angle of 10 or 22.5 degree.

For a single 10ps pulse irradiation, the absorption rate was 72% for a power density of 4×10^{15}W/cm^2. The analytical model suggests that, with a 10ps pulse duration, the scale length of the corona region is not long enough for 100% absorption. In multi pulse irradiations, however, the absorption rate increases to near 90%. The temporal profile of the specularly reflected light has been observed in the multi pulse irradiation to clarify this difference. The oscilloscope trace is shown in Fig.2 as a dotted line. The solid line is the incident laser wave form. The ratio of the reflected light to the incident is also plotted in

arbitrary units. Although the first pulse is strongly reflected, the reflection of subsequent pulses is small. This result is normalized to fit the ratio of the summations of incident and reflected pulse height to the ratio observed in calorimeter measurement. The normalized result is shown in Fig.3 as absorption rate. The absorption rate of the first pulse agrees with the single pulse case. The absorption rate of the subsequent pulses is nearly equal to the long pulse result.

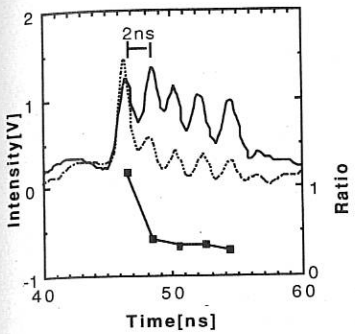

Fig.2. Oscilloscope traces of incident laser light (solid line) and specularlly reflected light (dotted line) in 10ps multi pulse irradiation. The ratio of reflected light vs incident is plotted for each pulse as a closed box.

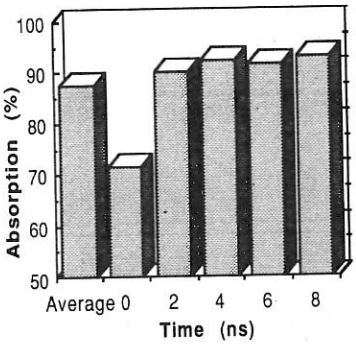

Fig.3. Absorption rate in multi pulse irradiation derived from Fig.2 by fitting the average rate to Fig.1.

The reason for the absorption improvement is considered to be that the subsequent pulses are well absorbed by the long scale length plasma produced by the previous pulses. For example, under a simple assumption of a one-dimensional adiabatic expansion, a plasma of 3μm thickness with an initial temperature of 300eV expands to 100μm in 2ns. The temperature at this time has decreased to 30eV. The subsequent pulses can be strongly absorbed in the existing plasma. As a result, even in 10^{15}W/cm^2 region, one can expect good absorption with an adequate scale length plasma which can be easily produced either by pre-pulse or ns pulse itself.

For further understanding of these results, we have started the measurements of evolution of the plasma by X-ray spectroscopy. A plasma produced on a plane target is

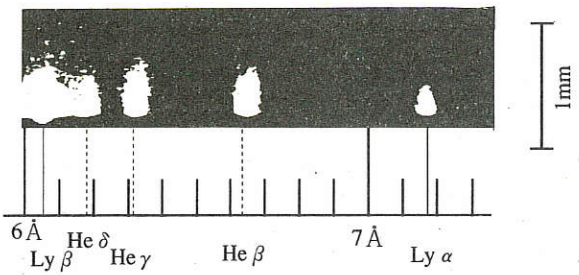

Fig.4. Observed space-resolved X-ray spectrum from a plane aluminum target. A TlAP crystal spectrometer with a beryllium window of 100μm thickness was used. The laser beam comes from upper side. The total energy of 150J in 10ns was focused into 100μmφ area.

observed from the parallel direction to the target surface by a TlAP X-ray crystal spectrometer with a slit for spatial resolution along the axis normal to the target plane. The image was detected by an X-ray CCD camera.

A preliminary result is shown in Fig.4. In this shot, five 10ns pulses were focused simultaneously in a single 100μmφ area on an aluminum target. The total laser energy was 150J and the peak power density was 2×10^{14}W/cm^2. In Fig.4, the laser beam comes from upper side and the target was placed at the bottom side. The L_y line and free-bound emissions extend for several hundred μm from the target surface, which suggest that a considerably large hot plasma is being produced by 10ns laser pulse irradiation. We are now trying to estimate the density and temperature scale length of the plasma.

/1/ Y.Owadano, I.Okuda, Y.Matsumoto, M.Tanimoto, T.Tomie, K.Koyama, and M.Yano, Laser and Particle Beams, **7**, 383 (1989).

/2/ P.Mora, Phys.Fluids, **25**, 1051 (1982).

NONSTATIONARY STIMULATED BRILLOUIN SCATTERING IN LASER PLASMA.

Rubenchik A.M., Ochirov B.D.
Institute of Automation and Electrometry, Novosibirsk, Sibirian Branch of Academy of Sciences.
Kozochkin S.M., Maluyta D.D., Strel'tsov A.P., Shirokikh A.V.
Troitsk Institute of Innovative and Thermonuclear Investigations, Troitsk, Moscow region.

Stimulated Brillouin scattering (SBS) is a known phenomenon observed in many laser plasma experiments. In spite of enormous amount of experimental and theoretical works there are some properties of SBS that have no ambiguous interpretation yet. Here we try to explain some characteristic features of SBS taking place in the high intensity laser plasma interaction.

Here we compare numerical results with experimental data obtained with use of CO_2 laser facility TIR-1 [1]. Experiments have been performed under the next parameters of the laser system: energy of up to 100 J, pulse length (FWHM) of 3 ns, contrast ratio larger than 10^7, wavelength of 10.591 mkm. The NaCl aspherical lens was used to focus the laser beam on the plane massive target. Intensity distribution in the focal plate had near Gaussian distribution with diameter (1/e) of 65 mkm, maximum intensity being $5.*10^{14}W/cm^2$. One of the most characteristic features of SBS in these experiments is its nonstationarity. It is clear from oscillograms of backscattered light presented on Fig.1. It is seen also from Fig.1 that there are essential differences in SBS temporal behavior from shot to shot for the fixed parameters of laser and plasma.

The mechanism for SBS nonstationarity in laser plasma experiments was proposed by Huller et al [2]. If the SBS growth rate g is comparable or larger than the frequency of ion sound wave w_s the wave reflected from critical surface serves as seed for SBS (strong coupling regime). In this situation the thermal noise is not important and SBS can be very strong. Hence the level of radiation reaching critical suface drops and SBS drops as well stimulating the process of nonstationarity.

An important point to notice that in the experiments SBS is suppressed near n_{cr} where steep density gradient is formed by intense laser light and occurs only from corona region. It is naturally to assume that the structure of the steepened density profile is nonstationary and the reflection coefficient from the critical surface is changed unexpectedly both during the pulse and from shot to shot affecting on the scattering process. It is important that for the stationary case of SBS there is no influence of the reflected wave on SBS

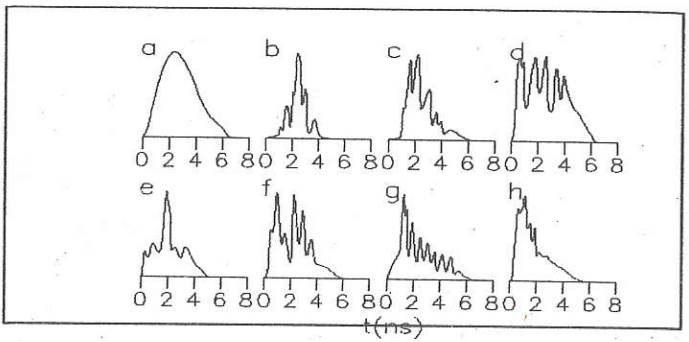

Fig.1. Experimental signals.
Parameters in experiments were: $I=5*10^{14}W/cm^2$,
plasma slab length was about 500 mkm.

properties [3,4]. The numerical simulations were carried out to check the qualitative reasoning presented above.

For the treatment of a finite size slab of length L and with a density for which the matching conditions are not exactly fulfilled and nonlinear right hand side terms to be completed by a factor taking into account the spatial mismatch. System of coupled equations describing this process in terms of slowly varying envelopes can be written as [2]:

$$\frac{\partial a_o}{\partial t} + \frac{\partial a_o}{\partial x} \quad iba_s e^{iF}$$

$$\frac{\partial a_s}{\partial t} - \frac{\partial a_s}{\partial x} = ib^* a_o e^{-iF} \qquad (1)$$

$$\frac{\partial^2 b}{\partial t^2} + \frac{Q-2iw_a}{G}\frac{\partial b}{\partial t} - i\frac{Qw_a}{G} = a_o a_s^* e^{-iF}$$

where $F = k_o - k_s - k_a$ is the relative phase which far more decisive for the mutual interactions of the three waves than any other space dependent quantity. System of equations is written in dimensionless variables a_o, a_s normalized on the incident wave amplitude, time is measured in terms of SBS growth rate G, and length is in v_a/g.

We consider strong coupling regime of interaction when envelope approximation for ion sound wave does not work properly. Term with second derivative over the time in the ion sound equation must be taken into account in this case.

$$G = (2 w_a G_o^2)^{1/3}, \qquad (2)$$

where

$$G_o = \left(\frac{W_o W_a}{8} \frac{n_o}{n_{cr}} \frac{\varepsilon_o E^2}{4\, n_{cr} T_e}\right). \qquad (3)$$

We assume that the value of Q includes Landau dumping both for electrons and ions. The ratio w_a to G was of order 0.1-0.01 and ratio of the decrement of waves Q to the instability increment G was 0.01 - 0.001.

We select the boundary conditions for pumping and reflected waves as follows:

$$a_b(0,t) = \exp(-(t/\tau)^2) \qquad 4a$$

$$a_a(L,t) = f a_b(L,t)\exp(-i w_a t) \qquad 4b$$

Here coefficient f simulates reflection from critical surface. Oscillating factor descrites frequency shift between reflected and scattered Stokes wave.

The results of numerical simulations are presented on Fig.2 and Fig.3. According to these figures, the SBS behavior is nonstationary. Specific period of modulations respects to the frequency of ion sound wave (beating between reflected and Stokes waves). More sharp modulations are the consequence of SBS nonstationarity. The temporal SBS behavior in the experiment is more smooth in comparison with simulations data. More detailed calculations reproduce also some other features of experimental data good enough, for instance wide frequency spectrum which can be explained only in terms of SBS nonstationarity.

We would like to emphasize here the essential changes in SBS behavior due to small variations of the reflection coefficient. The small changes take place also for the case of variations in plasma density and slab size. Therefore, it is naturally to explain changes in SBS behavior from shot to shot as a consequence of a small variation of these parameters.

LITERATURE

1. A.E.Akimov et al., 19 European Conference on Laser Interaction with Matter, Eds.: G.Velarde, E.Mingues, World Scientific.

2. S.Huller, P.Mulser, A.Rubenchik, Phys. Fluids B 3(12),p.3339-3352, (1991).

3. H.A.Baldis, E.M.Kampbell, W.L.Kruer, Handbook of laser plasma Physics, Vol.3, Eds.: A.Rubenchik, S.Witkowski, North Holland.
4. W.L.Kruer, The physics of laser plasma interactions, Addison Wesley, 1988.

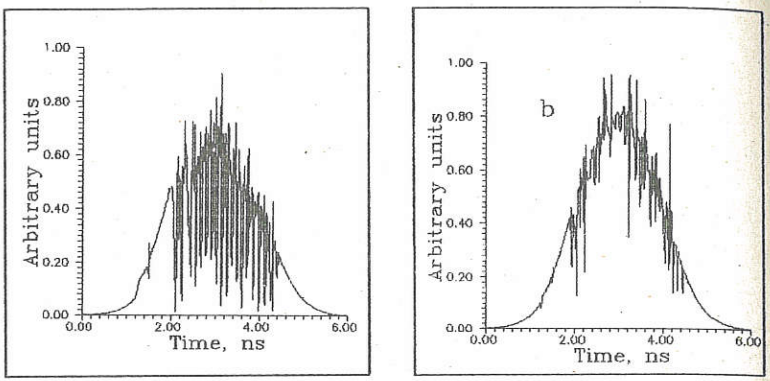

Figure 2.
Temporal dependence of scattered wave. Parameters were the same as in the experiments. a) f=0.5, b) f=0.8

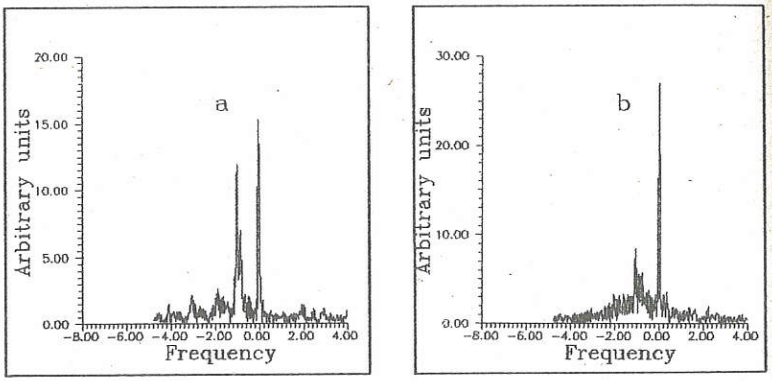

Figure 3.
Spectra corresponding to scattered waves

ABSORPTION PROCESS BY ION ACOUSTIC TURBULENCE

H. Torres-Silva[1] and P. H. Sakanaka
Instituto de Física, UNICAMP, C.P. 6165, 13081 Campinas, SP, Brazil

Abstract

We present a quantum transport theory for an interacting electron-ion-acustic mode system in the presence of a strong laser field. On the basis of the center of mass approach, the quantum-kinetic equation in their operator form directly reflect the non linear transport effects due to the laser field. When these equation is put into their macroscopic form, we obtain the absorption rate which depends on the energy loss function $Im\{-1/\varepsilon(\vec{q},\omega)\}$. We illustrate our theory, showing the proper way to calculate the collective part of the inverse Bremsstrahlung process due to ion acoustic turbulence

1 Introduction

In experiments on the interaction of intense laser field with plasmas in the critical region, where the electron temperature is much higher than the ion temperature, the presence of the ion acoustic turbulence (IAT) produces significative changes on the inverse bremsstrahlung (IB) process compared with the IB. of the Coulomb plasma. Recently, complete classical calculations was carried out on the basis of a self consistent theory for the electron distribution function and the espectrun of IAT [6], [8]. These reports show that the electron heating rate anomalously increase in the course of IB absorption of the high-frequency electromagnetic field. From the quantum-mechanical point of view, the calculations on IB. due to IAT. seem likewise inaccurate [3], [4]. Kim [5], because this theory does not show the auto-consistent saturation of IAT spectrum. In this paper, we reconsider this problem in terms of the center of mass approach [1], here we use the spatial unitary transformation (S.U.T.) of Kramer-Hennenberger [2] and the random-phase approximation (R.P.A.) for the electron-electron interaction. For a plasma ion-acoustic turbulence, we reproduce the results given by Silin et al [6], [7],[8], when the IAT spectrum, $N(q)$, is quasi-stationary.

For convenience of the theoretical description, we restrict our present study to a three-dimensional electron system. We consider N electrons scattered by n_i randomly distributed ions, and ion-acoustic turbulence (IAT), in the presence of a spatially uniform vector-potencial $\vec{A}(t) = \frac{e}{\omega_0} E_0 \cos\omega_0 t$. The time-dependent Hamiltonian can be written as in [1].

$$\hat{H} = \sum_i \frac{p_i^2}{2m} + \sum_{i,j} \frac{e^2}{|\vec{r}_i - \vec{r}_j|} + \sum_{i,\alpha} u(\vec{r}_i - \vec{R}_\alpha - \vec{a}(t)) + \sum_{i,\omega_\kappa} w(\vec{r}_i - \vec{a}(t)) \qquad (1)$$

[1]Universidade Estadual Paulista, SP, Brazil

Here $\vec{r}_i$ and $\vec{p}_i = -ih\nabla_i$ are the coordinate and momentum of the ith electron with mass m and charge e, the second term is the Coulomb interaction between electrons; $u(\vec{r} - \vec{R}_\alpha)$ denotes the potential by the ion at $\vec{R}_\alpha$, which is randomly located (R.P.A.) and $w(\vec{r})$ correspond to a equivalent potential produced by ion acoustic modes.

The electron-ion interaction is described by $\hat{H}_{ei} = \sum_{\vec{q},\alpha} U(q) e^{i\vec{q}\cdot(\vec{R}-\vec{r}_{..}-\vec{a}(t))}\hat{\rho}_q + cc$ where $\hat{\rho_q} = \sum_k c^\dagger_{k+q} c_k$ is the electron density operator and $U(q) = 4\pi Z e^2/q^2$. The ion-acustic turbulence (IAT) interactions are given by $\hat{H}_{ia} = \sum_{\vec{q},\omega_s} W(q) e^{i\vec{q}\cdot(\vec{R}-\vec{a}(t))-i\omega_s}\hat{\rho}_q + cc$ where $W(q) = (4\pi \frac{\omega_s N(q)}{q^4 v_{ti}^2})^{1/2}$ is the equivalent potential, due to IAT.

Solving the Liouville equation to the lowest order, the energy rate for the electrons is given by [1], [10]

$$\begin{aligned}
\dot{W}_e = \frac{< \dot{H}_e >}{vol} \quad = \quad & -i \sum_{k,q,n} \vec{q}\cdot\frac{i}{\hbar}(E_{k+q} - E_k) \lim_{\varepsilon\to 0^\dagger} \int_{-\infty}^{t} dt' e^{-\varepsilon(t-t')} exp\left(i\vec{q}\cdot\int_{t'}^{t}\dot{\vec{R}}(s)ds\right) \\
& n_i \mid U(\vec{q}) \mid^2 J_n^2(\vec{q}\cdot\vec{a}) e^{in\omega_0(t-t')} \hat{\Pi}(\vec{k},\vec{q},(t-t')) \\
& -i \sum_{k,q,n,\omega_s} \vec{q}\cdot\frac{i}{\hbar}(E_{k+q} - E_k) \lim_{\varepsilon\to 0^\dagger} \int_{-\infty}^{t} dt' e^{-\varepsilon(t-t')} exp\left(i\vec{q}\cdot\int_{t'}^{t}\dot{\vec{R}}(s)ds\right) \\
& \mid W(\vec{q}) \mid^2 J_n^2(\vec{q}\cdot\vec{a}) e^{i(\omega_s + n\omega_0)(t-t')} \hat{\Pi}(\vec{k},\vec{q},(t-t')) + cc \qquad (2)
\end{aligned}$$

where $\hat{\Pi}(\vec{q},\omega)$ is the Fourier transformation of the retarded Green's function $\hat{\Pi}(\vec{q},t)$, with $\dot{\vec{R}}(s) = \vec{P}(s)/M$ the drift velocity of the electron system. Here the fluctuation of the coordinates of the center-of-mass-electrons may be included. We note that this factor reflects the non linear dependence of the kinetical equations on the electron drift velocity and equation (2) is clearly consistent with the large-N approximation.

2 Plasma Transport Equation and Heating Rate

Our derivation of (2), is in microscopic form yet, from the view point of the center of mass. The energy equation is quite rigurous and general; while we are restricted our treatment to lowest-order in the electron-ion interaction and $W(q)$; our result are valid for all values of the laser electric field. Hovever the evaluation of the steady-state transport equations, including the fluctuation parts of the velocity $\dot{\vec{R}}(t)$, can be carried out only approximately. In general, we can denote the velocity $\dot{\vec{R}}$ as the sum of the drift velocity V_{CM} and its fluctuation $\delta\dot{\vec{R}}$, with $\overline{\delta\dot{\vec{R}}} = 0$, where a bar denote the ensemble average over the center of mass cooodinates, so [9] that using the cumulant approximation we have $\overline{exp\left(i\vec{q}\cdot\int_{t'}^{t}\vec{V}(s)ds\right)} = exp\left((i\vec{q}\cdot\vec{V}_{CM} - Dq^2)(t-t')\right)$ then, in the ramdom phase approximation if we take the average over the $\delta\dot{\vec{R}}$ distribution, we obtain

$$\overline{\dot{W}_e} = \sum_{q,n}\left(n\omega_0 + \vec{q}\cdot\vec{V}_{CM}\right) n_i \frac{\mid U(\vec{q}) \mid^2}{v(\vec{q})} J_n^2(\vec{q}\cdot\vec{a}) Im\left\{\frac{1}{\varepsilon(\vec{q},\delta,n\omega_0 + \vec{q}\cdot\vec{V}_{CM})}\right\} \qquad (3)$$

Equation (3) is the generalized expression of the plasma transport equation, which has included the difussion constant of the center of mass. In general D is field dependent, but in the classical limit, we can use the Einstein relation $D = \frac{k_B T}{N m \nu}$, where $\frac{1}{\nu}$, is the momentum transport time. With Dq^2, in the large-approximation, clearly for nondegenerated plasma, the correction on the energy loss function, $Im\frac{1}{\epsilon}$ can are neglected. Hovever, for degenerated plasma, specially for quase-one and two-dimensional electron gas, the correction due to the damping Dq^2 maybe significant for smaller systems and smaller densities. We remark that our theory have total validity for 1-D and 2-D electron gas, when the " volume " is redefined.

The nonlinear effects related to IAT, in the presence of a laser field, studied by Silin and colaborators, are connected with the strong absorption and scattering of radiation by ion-sound pulsations. The estimates of this anomalous absorption and scattering are functions of the angle distribution of $N(\vec{q}) = N(q)\Phi(\cos\theta_q)$, which depends on the Knudsen number, K_N. Using the quantum-mechanical approach, the authors of references [3], [4], [5], have showed that the absorption is strong when the level of ion-acoustic turbulence is high enough. However these studies were carried out under the condition of unproven isotropical wave spectrum for the ion-acoustic instability, stabilized by ion trapping, [3] without angle distribution dependence. Kim et al [5], have conjectured an equation for the heating of the electron, which is derived from a quantum-mechanical extension of Vlasov equation (Kim's equation). However the results of this theory are not convincing, because the field equations for the electron distribution function (Vlasov eq.) and the wave function $\Phi(r,t)$ (Schrödinger equation), are treated as independent variables under the condition of different gauges, i.e., length gauge and velocity gauge, respectivelly.

The proper way to obtain the heating rate, within this approach, is to follow the method proposed by Silin and Uryupin , which is based on the single-particle density matrix, where the collisional operator $\frac{\partial f(v)}{\partial t}$ is derived from the Schrödinger equation, taking into account the diagonal terms of the matrix density equation.

An alternative approach is our theory, which spite the fact that this does not give the attenuation of the radiation due to Raman scattering by the ion sound, it leads to a general expression for the ion-acoustic absorption through conversion of laser radiation into a longitudinal perturbation.

In order to compare ours results with Kim's results and also Silin's expressions we take $\omega_s \ll \omega_0$, $U(q) = 0$ and $W(q) = 4\pi e^2 \omega_s N(q) \omega_{pe}^2 / q^4 {v_t}^2$. Considering a single ion-acoustic wave, with $\omega_s \ll \omega_0$, which is proportional to $\delta(\omega_s - \omega_{IA}) + \delta(\omega_s - \omega_{IA})$, the heating rate $\dot{W}_{IA}$ is given by $\dot{W}_{IA} = \sum_q \mid A_0 \mid^2 \frac{1}{q^2} \ln qrde^{-1} \omega_0 J_1^2(x) Im\frac{1}{\epsilon}$ *where* $\mid A_0 \mid^2 = 8\pi \frac{n_e k_B T_e}{v_{te}^2} r_{de} v_s \frac{\omega_{pi}^2 \omega_{pe}}{v_{te}^2}$. In the weak-field limit, $J_n^2 = x^2/4$, from $\dot{W}_{IA}$, we can estimate the effective collision frequency, which is proportional to the factor $G(\omega_{pe}^2/\omega_0^2)$ given by Bychenkov et al. [8]. For the case sufficiently close to the critical-density region, $(\omega_0^2 - \omega_{pe}^2) \ll \omega pe^2$, we use again the approximation $Im(\frac{1}{\epsilon}) \sim \pi\delta(\epsilon_r)$, so

$$\dot{W}_{IA} = \frac{1}{(2\pi)^3} \mid A_0 \mid^2 \pi \frac{\omega_0^2}{3\omega_{pe}^2} \frac{q_D}{2zy} \int d(\phi_0 - \phi)$$

$$\int d\cos\theta_q \int dq \frac{\ln qr_{de}^{-1}}{q^3} J_1^2\left(\frac{qv_E\cos\theta_E}{\omega_0}\right)\Phi(\theta_q)\delta(q - yz^{-1}q_D) \qquad (4)$$

where $\cos\theta_E = \cos\theta_q\cos\theta + sen\theta_q sen\theta\cos(\phi_0 - \phi_q)$. Here, θ is the angle between $\vec{R}$, defined by Silin et al, and $\vec{E}$. Equation (4) contain the nonlinear effect due to the laser field and the velocity fluctuations of the center of mass. In the weak-field case, we see that the influence of the velocity fluctuations only appear in the logarithm factor, so in the vicinity of $\omega_0 = \omega_{pe}$ the effective collision frequency due to the longitudinal perturbation is proportional to $G(x = \frac{\omega_{pe}^2}{\omega_0^2}) = (\frac{\pi}{2})^{1/2}(1-x)^{-1}\ln(\frac{3z}{1-x})^{1/2}F(\theta)$. Here we are taking into account the symmetry of the turbulent noise with respect to the vector $\vec{R}$. Thus, the main contribution to the absorption at the frequency ω_0 comes from the range of plasma density in which $\omega_{pe} = \omega_0$ and electromagnetic waves transform into longitudinal plasma waves. When $z = 1$, our result agrees with the expression given by Bychenkov et al [8]. The expressions given by Kim et al, do not include the factor $F(\theta)$, which gives $\nu_\perp$ and ν_l. When $K_N \ll 1$ it also does not show the IAT distribution over the angles, which is anisotropic along the force direction $\vec{R}$. In our calculation, the geometric-optics approximation still holds, so under the condition $K_N < 1$ we have strong absorption in a plasma which is spatially non-uniform along one axis.

ACKNOWLEDGEMENT. This work was also supported by FAPESP - Fundação de Amparo à Pesquisa do Estado de São Paulo.

References

[1] H. Torres-Silva. *Interação Multifotônica em Plasmas Criados por Laser Superintenso.* PhD thesis, Univ. Estadual de Campinas, Campinas, Dec. 1990.

[2] W. C. Henneberger. *Phys. Rev. Lett.*, 21:838, (1968).

[3] S. Kim and H. Wilhelm. *Phys. Fluids*, 25:668, (1982).

[4] S. H. Kim *Il Nuovo Cimento*, 70 B:55, (1982).

[5] S. H. Kim *Phys. Fluids*, 27:675, (1984)

[6] V. P. Silin and S. A. Uryupin. *Sov. Phys. JETP*, 71:64, (1990).

[7] V. Yu. Bychenkov and V. P. Silin. *Sov. J. Plasma Phys*, 9:165, (1983)

[8] V. Yu. Bychenkov. V. P. Silin and S. A. Uryupin. *Physics Reports*, 164:119, (1988)

[9] G. Y. Hu and R. F. O'Connell. *Physica* , 149A.:1, (1988).

[10] H. Torres-Silva and P. H. Sakanaka. *Journal Phys. Soc. Japan*, 60:2985 (1991).

ABSORBED POWER INTO THE PLASMA BY LASER RADIATION AND DETERMINATION OF REFLECTION COEFFICIENT IN THE IMPLOSION OF DEUTERIUM-TRITIUM PELLETS CORRESPONDING TO THE INERTIAL CONFINEMENT FUSION.

Author: Miramar Blázquez, José Félix
Area de Ingeniería Nuclear. Escuela Técnica Superior de Ingenieros Industriales. Universidad de Zaragoza.
50015-Zaragoza (Spain)

I.-INTRODUCTION

We consider that the plasma in the crown is inhomogeneous, with collisions (BRAGINSKII, 1965), inside which there is an applied magnetic field B_0 directed along Z axis, being placed this Z axis on the normal plane to two unitary vectors that rotate in opposite directions, being $\hat{u}_i$ the left direction (from positive X axis to positive Y axis), and $\hat{u}_j$ the right direction (from positive X semiaxis to negative Y semiaxis). In relation to the polarization, the propagation vector of electromagnetic wave of the laser that is transverse electric and magnetic (TEM), is located in the direction of the Z positive axis. The electric field E_{wy} and the magnetic field H_{wx} of this electromagnetic wave are located in the direction of Y axis and X axis respectively. The permitivity tensor corresponding to the plasma aforementioned will be given by (RODRIGUEZ, 1987).

$$[\epsilon] = \begin{vmatrix} \epsilon_\perp & -i\,\epsilon_x & 0 \\ -i\,\epsilon_x & \epsilon_\perp & 0 \\ 0 & 0 & \epsilon_\parallel \end{vmatrix} \qquad (1)$$

$$\epsilon_\parallel = \epsilon_0 \left[1 - \frac{w_{pe}^2}{w\,(w - i\,\nu_{ei})} - \frac{w_{pi}^2}{w\,(w - i\,\nu_{ie})} \right] \qquad (2)$$

In the expressions (1), (2), $\epsilon_\parallel$, $\epsilon_\perp$ and ϵ_x are the components in parallel direction to the magnetic field, perpendicular direction to the magnetic field and along X axis, respectively; w is equal to the frequency (in rad/s), of the electromagnetic field ; w_{pi} and w_{pe}, the plasma frecuency of ions and electrons . The component $\epsilon_\parallel$ of the formula (2) is the only one that is not influenced by the magnetic field. (TAKASHI et al. 1987; BOL'SHOV et al., 1974). If we reject the ionic contribution ($\nu_{ie} = 0$), the terminus $\epsilon_\parallel$ of the formula (2) may be written in the following form

$$\epsilon = \frac{\epsilon_\parallel}{\epsilon_0} = 1 - \frac{w_{pe}^2}{w^2} \left(1 - i\,\frac{\nu_{ei}}{w} \right)^{-1} \qquad (3)$$

II.-ELECTROMAGNETIC FIELD EQUATIONS

If the electric field is normal to the incidence axis (mode TE), we obtain

$$\left(\nabla_{xz}^2 + k^2 \right) E_{wy} = 0 \qquad (4)$$

We suppose that the electric field are given by

$$E_{wy} = \Phi_E(z) \exp(- ik_x x) \quad (5)$$

replacing this equation in the differential equation (4), and having in mind that $k_x = k_{1x} = k_1 \sin\theta$ (6), we obtain, finally

$$\frac{d^2\Phi_E}{dz^2} + (k^2 - k_x^2)\,\Phi_E = 0 \quad (7)$$

In case of the magnetic field is normal to the incidence axis (mode TM), we will suppose that the magnetic field is given by

$$H_{wy} = k(z)\,\Phi_H(z) \exp(-iK_x x) \quad (8)$$

From here we can obtain the electromagnetic equation of the mode TM, which is similar to the equation (4), putting instead of k^2, the constant K^2 and instead of the electric field E_{wy}, the magnetic field H_{wy}. Finally, it is reached the equation

$$\frac{d^2\Phi_H}{dz^2} + (K^2 - k_x^2)\,\Phi_H = 0 \quad (9)$$

Along this paper it will be supposed a normal incidence of the laser radiation, so $k_x = 0$. We do $\epsilon_{\|} = \epsilon_z$ and we obtain

$$k^2 - k_x^2 = k^2 = w^2\mu\epsilon_z \quad (10) \; ; \qquad K^2 - k_x^2 = w^2\mu\epsilon_z \quad (11)$$

and having in mind formulae (3), (5), (7) and (10) we obtain

$$\frac{d^2E_{wy}}{dz^2} + k^2 \left[1 - \frac{w_{pe}^2}{w^2} \left(1 - i \frac{\nu_{ei}}{w} \right)^{-1} \right] E_{wy} = 0 \quad (12)$$

We will suppose that

$$\frac{w_{pe}^2}{w^2} = \frac{z}{z_0} \quad (13); \text{ where } z = \left(\frac{z_0}{k^2}\right)^{1/3} \cdot \frac{1}{a} + z_0 \quad (14)$$

being $$a = \left(1 - i \frac{\nu_{ei}}{w}\right)^{-1} \quad (15)$$

at which the expression (12) is transformed into

$$\frac{d^2E_{wy}}{d\xi^2} \left[\xi\, a^{-2} + k^{2/3} z_0^{2/3} (a^{-1} - a^{-2}) \right] E_{wy} = 0 \quad (16)$$

III.- THE ABSORPTION PROCESS OF THE LASER RADIATION

When the external part of pellet is heated by illumination of the laser light, it is ablated and expanded forming a crown of plasma, taking place into it the absorption of the laser radiation by means of a collisional mechanism that is called inverse Bremsstrahlung, before a critical density is reached which is given by (ATZENI, 1987)

$$\rho_c = m_i \frac{n_i}{n_e} \frac{m_e w_0^2}{\epsilon_0 e^2} \; Kg\; m^{-3} \quad (17)$$

where m_i and m_e are the ion and electron masses; n_i and n_e are the ion and electron densities; ϵ_0 is the dielectric constant of vacuum; e is the electron charge; finally, w_0 is the laser frequency. Above this frequency the light of the laser can not penetrate into the target, being reflected absolutely. Because of the moment conservation, the part of fuel that has not experimented the ablation is accelerated towards inside, that is to say, imploses. The irradiation intensity I, is inside the range $(I\lambda^2)_{max} \approx 10^{14}$ W cm^{-2} μm^2. Recent experiments have proved

that there are advantages using a small wavelength , $\lambda \approx \mu m$, obtaining a higher ablation pressure, a reduction of suprathermal electrons generation and a more effective absorption.

When we consider the infradense region of the crown plasma, where the absorption of the laser radiation takes place, the collision frequency is $\nu_{ei} \ll w$. So, the expression (18) results

$$\frac{d^2 E_{wy}}{d\xi^2} - \xi E_{wy} = 0 \qquad (18)$$

The solutions of the equation (18) are the known Airy functions $Ai(\xi)$ and $Bi(\xi)$. Due to the asymptotic behaviour of electromagnetic field for increasing values of independent variable and the indefinite increasing of $Bi(\xi)$ with ξ , we choose as solution the Airy function which can be expressed as a combination of Bessel modified and normal functions of order 1/3

$$Ai(\xi) = (1/3)\,(\pi \xi)^{1/2}\,[I_{-1/3}(\Phi) - I_{1/3}(\Phi)] \; ; \qquad (19)$$
$$Ai(\xi) = (1/3)\,(\pi \xi)^{1/2}\,[J_{-1/3}(\Phi) - J_{1/3}(\Phi)] \; ;$$

being $\Phi = (2/3).\,\xi^{2/3}$. When we utilize the equation (16) we obtain a new expression for Φ that is given by $\Phi = (2/3)\,\lambda\,\xi^{2/3}$ being λ a complex constant.

IV.DETERMINATION OF THE REFLECTION COEFFICIENT OF THE LASER.

The reflection coefficient of the laser radiation is calculated by the formula (RODRIGUEZ, 1987)

$$r_E(z) = \frac{Y_1^E(z) - Y_s^E(0)}{Y_1^E(z) + Y_s^E(0)} \qquad (20)$$

where $Y_1^E(z)$ is the surface impedance at z distance; $Y_1^E(0)$ is the surface impedance calculated at zero distance. Y_1^E is given by

$$Y_1^E = - \frac{\delta H_{wx}}{\delta E_{wy}} \; (21) \text{ being } \; H_{wx} = - \frac{\delta E_{wy}}{\delta z} \qquad (22)$$

Making use of the formula (14) with a = 1, we obtain

$$r_E(z) = \frac{(-\xi_1)^{1/2}\,Ai(\xi_1) - i\,Ai(\xi_1)}{(-\xi_1)^{1/2}\,Ai(\xi_1) + i\,Ai(\xi_1)} \qquad (23)$$

V.- CALCULATION OF THE ABSORBED POWER IN THE PLASMA

The absorbed power in the plasma (power crossing an arbitrary plane in z=constant), is given by

$$P = \tfrac{1}{2}\,[\,1 - r_E^2(z)\,] \iint \frac{E\,E^{*}\,dS}{\eta} \qquad (24) \; ; \text{ being } r_E(z) = \frac{E_r}{E_i} \qquad (25)$$

the reflection coefficient of the laser radiation, E is the electric field of the laser, E^{*} is its complex conjugate ,being the wave impedance of free space $\eta = (\mu_0 / \epsilon_0)^{1/2}$ (26)

If we utilize cilindrical coordinates we obtain finally

$$P = \tfrac{1}{2}\,[\,1 - r_E^2(z)\,]\,\frac{E_0^2}{\eta}\,\left(\frac{\pi\, w_0^2}{2}\right) \qquad (27)$$

being E_0 the initial value of the laser electric field and w_0 the

initial radius of spot of the laser beam (VERDEYEN, 1981).

VI.- RESULTS AND CONCLUSIONS

In this paper we utilize D-T pellets with a radius, R, with a value of 450 μm and a thickness of 40 μm. We utilize a laser irradiation intensity with a value of $I\lambda^2 = 10^{14}$ W cm^{-2} μm^2, using a wavelength of λ = 0.35 μm, corresponding to the ultraviolet range of the spectrum. The temperature of the ions is T_i = 1.5 Kev (TAKABE et al., 1989). We do the value of R_0 equal to z_0, because we consider only a dimension. We must have in mind that $n_e = Z^* n_i$, being Z^* the average charge of the ion, with a value of Z^* = 0.1 for D-T case. We consider indeed that n_e varies in function of z, in accordance with the expression $n_e(z) = n_{eo} \exp(-z/z_0)$. We take for plasma the electronic density corresponding to the crown a value of $n_{ec} = 9.1\ 10^{28}$ m^{-3}, (MULSER et al. 1989), that agrees the critical density calculated from aforementioned data. We suppose that $\nu_{ei} \ll w$. The value of the reflection coefficient is r =1.28001 10^{-1} + i 1.78667 10^{-1}, with a module value of $|r| = 2.19786\ 10^{-1}$. The last value corresponds to $(n_e)_{absorption} = 8.9\ 10^{28}$ m^{-3}, and z = 4.4 10^{-4}. The values of $|r|$ corresponding to different values of $(n_e)_{absorption}$ are around one. It may be seen that the laser light absorption takes place for values a bit smaller than n_{ec}, as it was supposed.

If we do not have in mind the condition $\nu_{ei} \ll w$, we obtain a value of r = 1.60684 10^{-1} + i 1.71958 10^{-1}, with a module of $|r| = 2.35349\ 10^{-1}$. The last value corresponds to $(n_e)_{absorption} = 8.9\ 10^{28}$ m^{-3} and z = 4.4 10^{-4}. The values of $|r|$ corresponding to different values of $(n_e)_{absorption}$ are around one.

When we take $E_0 = 7.839920563\ 10^{11}$ V/m and w_0 = 1 mm, we obtain the following values of the absorbed power in plasma

Case a) $\nu_{ei} \ll w$; P = 1.220182523 10^{15} W / m^2

Case b) not being $\nu_{ei} \ll w$; P = 1.211143690 10^{15} W / m^2

VII.- REFERENCES

ATZENI, S. (1987). "Plasma Phys. and Contr. Fus. Vol. 29, nº 11, p. 1535-1605.

BOL'SHOV, L.A., DREIZIN, Yu. A., DYKNE, A.M. (1974). J.E.T.P. Lett. Vol. 19, nº 5, p. 168-171.

BRAGINSKII, S.I. (1965). Rev. of Plasma Phys. Vol 1, p. 201-311. New York.

MULSER, P. PFALZNER, S., CORNOLTI, F. (1989). "Laser Interaction with Matter". World Scientific Publishing Co., p. 142- 145. Singapore.

RODRIGUEZ VIDAL, M. (1987)."Electromagnetismo". Tomo I. U.N.E.D., p. 209-219. Madrid.

TAKABE, H., KIHARA, Y., MIMA, K. (1989). "Laser Interaction with Matter".World Scientific Publishing Co., p.127-130. Singapore.

TAKASHI, Y., MASAKI, H., AKIO, N., and YAMANAKA, CH. (1987). 4th. Emerging Nuclear Energy Systems, p. 109-113. Ed. World Scientific Publishing Co. Singapore.

VERDEYEN, J. (1981)."Laser Electronics". Ed. Prentice Hall,Inc. Englewood Cliffs. New Jersey. USA.

EFFECT OF ELECTRON VELOCITY DISTRIBUTION ON THE HEATING OF CORE BY CORONA IN SPHERICAL PELLET

D.P. Singh, F. Giammanco*, A. Salvetti and M. Vaselli
Istituto di Fisica Atomica E Molecolare C.N.R.,
Via del Giardino 7, 56127 PISA (ITALY)
* Dipartimento di Fisica - Universita' di Pisa, PISA (ITALY)

The heating of the plasma dense core by superthermal electron cloud in spherical geometry has been investigated extensively in past years /1-3/. Consideration of the thermal flux inhibition in the plasma ablation zone and the inclusion of Z layer to reduce the mean free path of hot electrons have shown to affect the core-corona coupling in laser irradiated targets to a great extent /3,4/. The absorption of intense laser beam at the plasma critical layer in a pellet by various nonlinear processes such as resonance absorption, leads to the generation of energetic electrons that may penetrate into the internal core up to the depth of their mean free path forming a hot corona. When these hot electrons move in the inward radial direction, a counter-streaming cold electron current also flows outwardly to maintain the charge neutrality. In earlier studies this cold current was neglected and it was assumed that the hot electron density always remains equal to the plasma critical density in the core-corona overlapping region. It has also been seen in numerical simulation that the electron velocity distribution which develops in the plasma ablation region consists of a broad, nearly flat component of energetic electrons streaming from the heating region into the main body of the plasma and a cold component of counter-streaming electrons into the heating region /5/.

The aim of this paper is to study the dependence of core-corona coupling on this electron velocity distribution. Since the target dimensions are quite large as compared to the electronic mean free-path, we may follow one dimension plane flow of the electrons as far as the electron distribution is concerned. As the electron velocity distribution should be constrained by the requirements for not supporting beam plasma instabilities, and that it should represent zero net current flow to preserve charge balance, we may assume the idealized form of the electron velocity distribution function (f(v)) as /5/,

$$f(v) = n_h/v_h , \qquad 0 \le v \le v_h$$
$$= n_c/v_c , \qquad -v_c \le v \le 0 \qquad (1)$$

where v and n are velocity and density of electrons, and suffices h and c correspond to hot and cold electrons. The condition for zero net current may be written as

$$J = \int_{-\infty}^{\infty} v\ f(v)\ dv = \frac{1}{2}(n_h v_h - n_c v_c) = 0 \quad , \tag{2}$$

or $v_c = n_h v_h / n_c$

Therefore the energy flux can be given as

$$Q = \frac{1}{2}(n\ m\ v_h^3)\ (n_h / 4\ n)[1 - (n_h/n - n_h)^2] \quad , \tag{3}$$

A close look on the variation of $Q/\frac{1}{2}[n\ m\ v_h^3]$ with n_h/n shows that the former increases with the increase in the fraction of hot electron up to a maximum value corresponding to $n_h/n = 1/3$, beyond which it decreases. This is due to the fact that in the beginning the contribution of the hot electrons to $Q/\frac{1}{2}[n\ m\ v_h^3]$ is dominant, but later on the counter-streaming electrons play significant role.

The cooling rate of the corona may be given as /1/,

$$S = \frac{3}{2}\frac{k_B(T_h - T_c)}{\tau_{eq}} \int_{r_e}^{r_c} nr^2\ dr \quad ,$$

$$= \frac{3}{2}\frac{k_B(T_h - T_c)}{\tau_{eq}}\ n_{cr} r_c^3 \ln \frac{r_c}{r_e} \quad , \tag{4}$$

where k_B, T_h, T_c, r, r_e, r_c, n_{cr} and τ_{eq} are the Boltzmann constant, hot electron temperature, core temperature, radial coordinate, core radius, radius of the plasma critical layer, plasma density at r_c and the energy equipartition time between core and the coronal electrons. Here the plasma density variation in the plasma ablation has been included as indicated by computer simulation. The expression for the energy equipartition time can be given as /6/,

$$\tau_{eq} = \frac{3}{4}\sqrt{\frac{m}{\pi}}\frac{(k_B T)^{3/2}}{e^4 n_{cr} \ln \Delta} \quad , \tag{5}$$

T and ln Δ are the average electron temperature $[(T_h+T_c)/2]$ in the core corona overlapping region and coulomb logarithm. Incorporating the self - regulation condition of the corona, i.e. the width of the plasma ablation zone remains of the order of the electronic mean free path, the expression for **S** may be rewritten as,

$$S = \frac{3}{2}\frac{k_B(T_h-T_c)}{\tau_{eq}} n_{cr} r_c^3 \ln\left[1 + 2\frac{n_h}{n_{cr}}.\frac{\lambda_{hc}}{r_c}\right], \qquad (6)$$

where λ_{hc} is the hot electron mean free path given as follows,

$$\lambda_{hc} = [k_B T]^2 / [\pi e^4 (Z+1) n_{cr} r_c \ln \Delta]$$

Considering the proper plasma density variations in the whole core, the expression for core - corona coupling may be obtained from the energy balance condition between the core and the surrounding corona as,

$$\tau_c^{-1} = \frac{3}{2}\frac{\ln\left[1 + 2\frac{n_h}{n_{cr}}.\frac{\lambda_{hc}}{r_c}\right]}{\left[1 + \ln\frac{n_0}{n_{cr}}\right]}\frac{1}{\tau_{eq}}, \qquad (7)$$

n_0 is the plasma core density. The expression (7) gives the dependence of core - corona coupling on various parameters and the numerical results have been plotted for the following set of parameters:

Mass of the whole core = $(48/4\pi)\mu g$, $Q = 10^{14}\ W/cm^2$, $(n_0 / n_{cr}) = 10^4$.

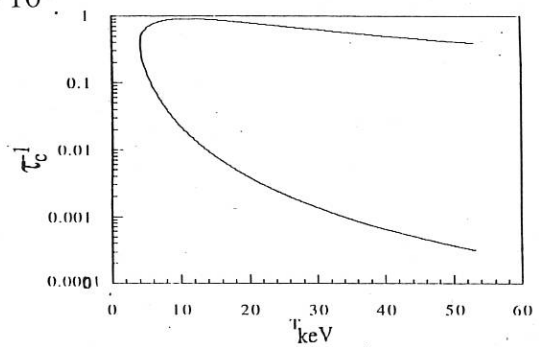

Fig. 1 : Plot of core corona-coupling (τ_c^{-1} in ns^{-1}) with mean electron temperature (T_{keV}). $\lambda_{\mu m}$ = 1.

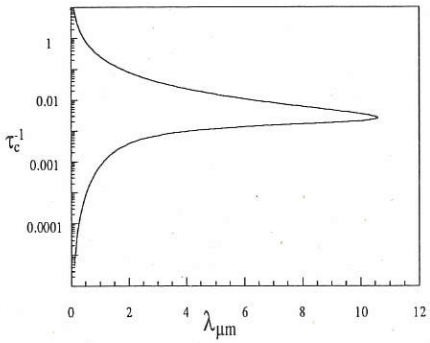

Fig. 2 : Plot of core corona - coupling (τ_c^{-1} in ns^{-1}) with laser wavelength. T_{keV} = 88.5.

Figure 1 shows the variation of τ_c^{-1} with the mean electron temperature in the overlapping region for given energy flux. It is seen that there exists a minimum value of the mean electron temperature corresponding to hot electron fraction n_h/n =1/3 and beyond which each value of temperature gives two values of n_h/n and hence two values of τ_c^{-1} . These two values of core - corona coupling correspond to two regions where hot electron and counter - streaming flux are dominant respectively. In the former case the behavior of τ_c^{-1} with mean electron temperature shows a maximum as seen in earlier studies, while it always decreases in the latter region. Figure 2 exhibits the variation of τ_c^{-1} with the laser wavelength for given energy flux. In this case too, the existence of maximum wavelength corresponding to n_h/n =1/3 and the dependence can be explained due to the above-mentioned regions.

REFERENCES

/1/ R.E. Kidder and J.W. Zink, Nuclear Fusion **12**, 325 (1972)

/2/ K.A. Brueckner and S. Jorna, Rev Mod. Physics (USA) **46**, 325 (1974)

/3/ D.P. Singh, J.J.E. Herrera and M. Vaselli, Laser And Particle Beams **7** part 1, 111 (1989)

/4/ D.P. Singh, M.A. Harith, V. Palleschi and M. Vaselli, Contrib. Plasma Physics **31**, 423 (1991)

/5/ R. L. Morse and C.W.Nielson, Physics Fluids **16**, 909 (1973)

/6/ L.Jr. Spitzer,*''Physics of Fully Ionized Gases''* Interscience, New york, 2nd Ed. (1962)

INFLUENCE OF PARTIAL CHARGE EXCHANGE ON EFFECTIVE CHARGE OF SWIFT HEAVY IONS FLOWING THROUGH DENSE HYDROGEN PLASMAS

G. Maynard, K. Katsonis, C. Deutsch
Laboratoire de Physique des Gaz et des Plasmas* et GDR 918, Bat. 212, Université Paris XI, 91405 Orsay, FRANCE.

Since 1976, extensive studies were directed toward the use of heavy ions beams as the driver for pellet implosions in connection with inertial confinement fusion (ICF) /1/. To reach high efficiency, heavy ions beams have to deposit most of their energy in a high density and high temperature plasma of low Z material. It is a well known fact that in such plasmas the energy deposition curves exhibit a Bragg peak at a projectile energy closed to 1 Mev/n. It is then crucial to have a good knowledge of the stopping power S at this energy at which the interaction between the projectiles and the plasma becomes maximum. The charge state of the projectile is an important parameter because S is nearly proportional to the square of the charge.

Experimental investigation of swift heavy ions stopping in dense hydrogen plasma produced by a Z-Pinch was initiated in France /2/ and also continued in Germany /3/. Temperatures of few eV and densities $10^{17\text{-}18}$ cm^{-3} have been obtained. New experiments are under way with densities up to $10^{20\text{-}21}$ cm^{-3}. During the life time of this high density plasma, hydrogen is often but not allways fully ionised.

To determine the ionisation state reached by the projectile, one has to determine the balance between loss and gain of electrons. Gains are due to radiative and dielectonic recombination involving free electrons and also to charge transfer from the bound electrons of the hydrogen atoms. Because charge transfer is the most effective mechanism, it plays an important role even at high ionisation stages.

We are presenting here our results from the study of the density effect on the charge transfer efficiency.

The density effect in cold solids has been extensively reviewed in the famous paper of H.D. Betz /4/ who detailed the Betz-Grodzins (BG) theory /5/. The density effect in solid arises from the very small time of flight between successive collisions, the radiative decay of excited electrons remaining inefficient. In the BG model one has to deal with all the electrons of the outer subshells. All these electrons get some excitation so their loss rate increases slightly. The average charge will be shifted by a small amount of one or two units. Due to the large number of excited electrons the total excitation energy per ion will be large enough to allow the ejection of many Auger electrons at the exit surface. Some departure from

---

* associé au CNRS

/1/ C. Deutsch, Ann. Phys. **11** (1986) 1
/2/ D. Gardès,R. Bimbot, M.F. Rivet, A. Servajean, C. Fleurier, D. Hong, C. Deutsch, G. Maynard, Particle Accelerators **38** (1992) 361
/3/ D. H. Hoffmann, K. Weyrich, H. Wahl, D. Gardès, R. Bimbot and C. Fleurier, Phys. Rev. A **42** 2313 (1990)
/4/ H.D.Betz, Rev. of Mod. Phys. **44** (1972) 465
/5/H.D. Betz and L. Grodzins, Phys. Rev. Lett. **25** (1970) 211

BG model has been examined in the case of targets with low Z /6/.

Looking at the BG model one can think that the density effect in a dense plasma is the same with the density effect in solids; we have again a lot of excitation by collisions with electrons, ions and atoms leading to many excited electrons and so to a slightly increased loss rate. It is shown here that in the case of a partially ionised hydrogen plasma, the evaluation of partial charge exchange cross section has greatly modified the BG conclusions.

To further examine the influence of the partial charge exchange we look at the particular example of 1 MeV/n I^{q+} ions passing through a hydrogen plasma which is 80% ionised. The effective charge of the iodine ion is determined for three densities : $n = n_H + n_{H+}$, $n = 10^{17}$ cm^{-3}, $n = 10^{20}$ cm^{-3} and $n = 10^{22}$ cm^{-3}. To get valuable cross sections for partial charge transfer, Classical Trajectory Monte Carlo (CTMC) calculations by K. Katsonis and G. Maynard /7/ were used. An example of the results is shown Figure 1 for I^{20+}.

In this figure one clearly see the importance of the partial recombination on excited states. The partial recombination on the ground state is nearly zero; with increasing charge the position of the maximum is shifted toward higher value of the principal quantum number n.

Cross sections for the other processes are similar to the ones used in /8/.

To analyze the average charge state of swift heavy ion we make use of an average atom model /6/,/9/ so we can take into account the excited levels of the projectile (only through the dependence on the principal quantum number n). The results of our calculations are shown in Figures 2-4 for the three densities cases. In each figure we have reported the evolution of the average charge for five initial charge states as they flow through the hydrogen plasma. For the two high densities targets we have also reported calculations where all the partial cross sections in level with principal

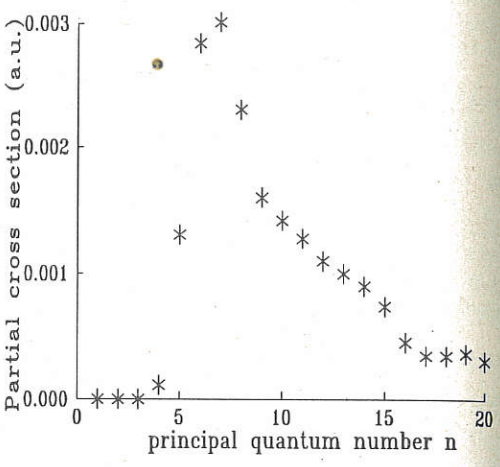

Figure 1 *Partial charge transfer cross section for 1 Mev/n I^{20+} colliding with H in πa_0^2 units.*

/6/G. Maynard, C. Deutsch, Rad. Eff. and Defects in Solids, **110** (1989) 157, see also Y. Le Beyec, S. Della-Negra, to be published

/7/K. Katsonis, G. Maynard, these proceedings; also K. Katsonis, G. Maynard and R.K. Janev, Phys. Scripta **T37** (1991) 80

/8/Th. Peter, R. Arnold, J. Meyer-ter-Vehn, Phys. Rev. Lett. **57** (1986) 1859

/9/R.M. More in : *Applied Atomic Collision Physics*, Vol. II, H. S. Massey ed. (1983)

quantum number higher than 4 have been put in the level with n = 4. This level is the first excited level above the fundamental one and corresponds to the BG prediction.

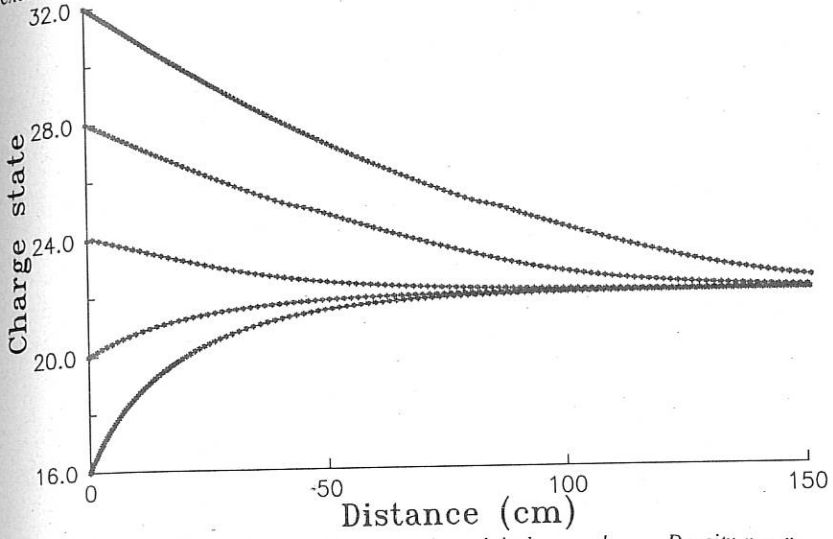

Figure 2 *Average charge state for I^{q+} flowing through hydrogen plasma. Density n = n_1*

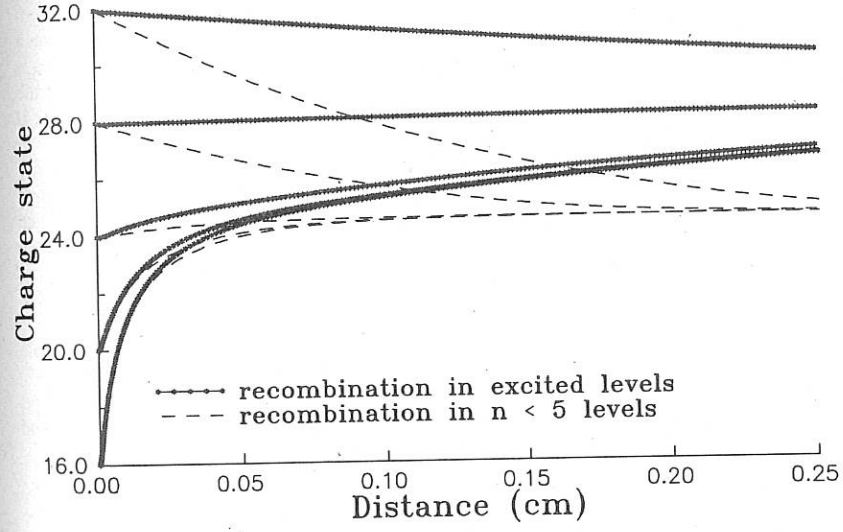

Figure 3 *Same as Figure 2 with density n = n_2*

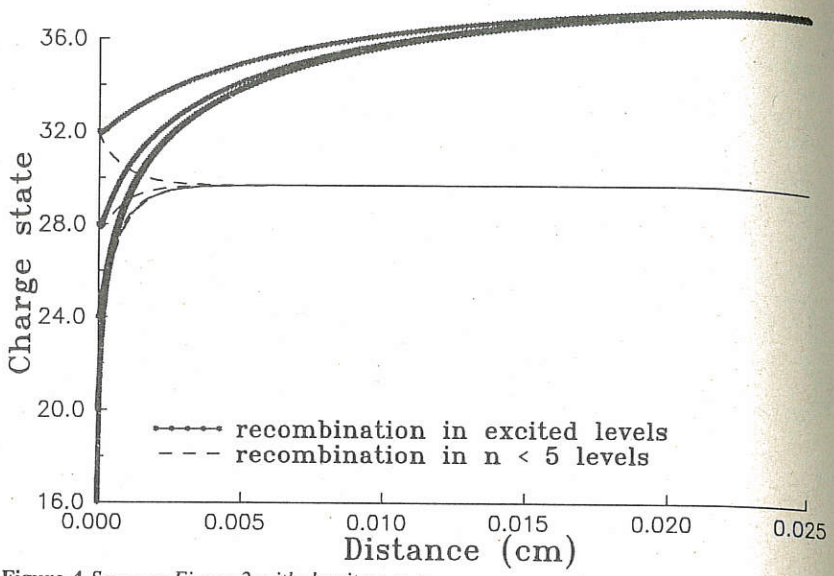

Figure 4 *Same as Figure 2 with density* $n = n_3$

When comparing Figure 2 with Figures 3 and 4 the density influence is clearly seen. For example as the density increases from $n=n_1$ to $n=n_2$ the equilibrium charge varies from 22 to 30 and the distance n.l required for reaching this equilibrium increases by more than a factor two. A very important fact on Figures 3 and 4 is the large discrepancy when there is recombination into high excited states or not. When recombinations are put in levels $n < 5$ the equilibrium charge is reduced by 6 units at $n = n_2$ and by nearly 8 units at $n = n_3$ and this is not included in the BG model.

Different initial charges have two different time scales of evolution in a high density plasma. For $n = n_3$ they change rapidly up to a distance of 5 mm in Figure 4 and then increases much slowly. This is due to the time for the fundamental $n = 3$ level to reach equilibrium. Because partial recombination in this level is very small when an electron hole is produced, it cannot be filled in again easily. So the slowly increasing of the average charge can be viewed as a hole creation and this hole population has to be added to the BG model.

It is to be noted that this process is important only for of low Z materials. For high Z plasmas the partial recombination in the ground level is not small and so there is no such hole population.

To clarify the situation, the slowing down of the projectile has not been considered here. With increasing the plasma ionisation, the dynamical effects become more important and must be also included /6/.

II-1249

Numerical simulations of X-ray diagnostics in ICF

Philippe HUMBERT
CEA - Centre d'Etudes de Limeil-Valenton, 94195 VILLENEUVE St GEORGES.

Introduction

Numerical fluid simulations of laser fusion experiments are performed using FCI2 code/1/. For direct comparison of X-ray experimental results and computed data a radiation diagnostic code has been designed /2/.

After a brief presentation of both codes we describe the diagnostic computation method and show an example of X-ray diagnostic simulation.

FCI2 and DXFCI2 codes

Laser target implosions are computed using FCI2 code. It is a two dimensional, one fluid, two temperatures (electronic and ionic) lagrangian radiation hydrodynamic code. Radiation transport equation for photons is coupled with material temperature and velocity. It is solved using multigroup diffusion or Monte-Carlo method. Atomic physics data (opacity, equation of state, ionization) are computed with or without the hypothesis of local thermodynamic equilibrium /3/.Laser absorption is treated by means of a ray tracing algorithm (geometrical optics approximation).

Imaging and X-ray spectroscopy diagnostics are computed with a radiation diagnostic code (DXFCI2) which acts as a post-processor of FCI2 code. DXFCI2 performs the numerical simulation of the following X-ray diagnostics :

- Pinhole and streak camera imaging (spatial and temporal resolution).
- Spectrometry (spectral resolution, with or without time resolution).
- X-ray radiography.

Diagnostics computation

The main task in radiation diagnostic simulation is the determination of specific intensity I_ν from which all considered diagnostics can be deduced.

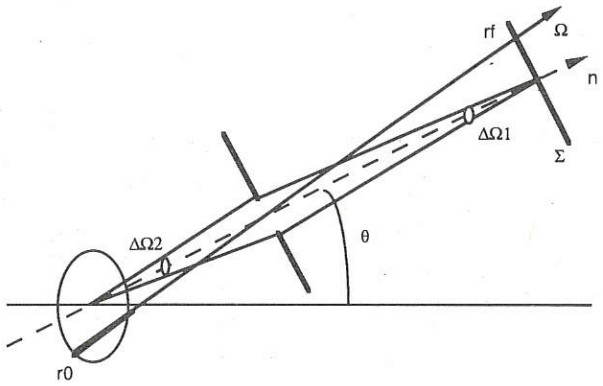

Fig. 1 : Detection geometry : An X-ray source irradiates a detector composed of a diaphragm and a film plane.

Pinhole and streak camera imaging are given by the flux F (erg/cm^2/s) :

$$F=\int_0^{\infty} F_\nu d\nu = \int_0^{\infty} d\nu \int_{\Delta\Omega_1} (\vec{n}.\vec{\Omega}) I_\nu(\vec{\Omega}) d\Omega \qquad (1)$$

Specroscopic diagnostics are computed from the spectral quantity P_ν (erg/s/eV/sr) :

$$P_\nu = \frac{1}{\Delta\Omega_2} \int_\Sigma F_\nu d\Sigma \qquad (2)$$

The specific intensity I_ν (erg/cm^{2}s/eV/sr) is the formal solution of the stationnary radiative transfer equation :

$$I_\nu(\vec{\Omega}) = I_0 e^{-\tau_0} + \int_0^{s_F} Q(s) e^{-\tau(s)} ds \qquad (3)$$

where the optical depth τ is :

$$\tau(s) = \int_s^{s_F} \sigma(s') ds' \qquad (4)$$

The target computed by FCI2 code is described by a lagrangian cylindrical 2D quadrangular mesh (R,Z) which is transfered to DXFCI2 code together with the opacity σ (cm^{-1}) and emissivity Q (erg/cm^3/s/eV).

I_ν is determined using a ray tracing algorithm. The specific intensity is computed along each ray associated with each pixel of the detector film. Equation (3) can be rewritten as :

$$I = I_0 e^{-\tau_0} + \sum_{i=1}^{M} \frac{Q_i}{\sigma_i}(1 - e^{-\sigma_i \lambda_i}) e^{-\tau_i} \qquad (5)$$

where λ_i is the distance covered by the ray whithin the torroidal zone i. These distances are determined by computing the intersections between cones generated by cylindrical mesh and lines associated with the ray tracing algorithm (Fig. 2). A vectorized implementation of the trajectography has been designed to improve computation efficiency on a Cray YMP computer.

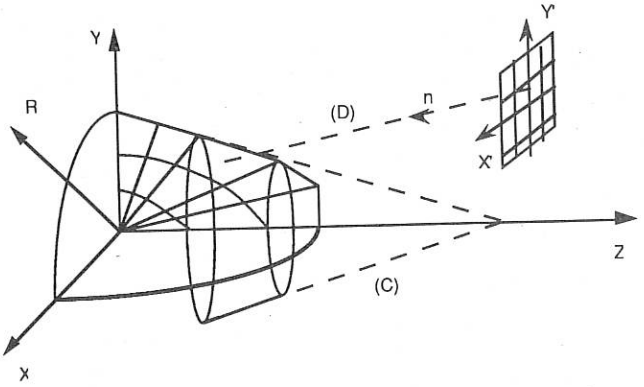

Fig. 2 : Illustration of tray tracing trajectography for radiative specific intensity computation.

Example

We consider the indirectly driven implosion of a microballoon with the two beams of Phebus laser facility /4/ The corresponding pinhole X-ray pictures of compressed parts obtained at the end of implosion are presented in figure 3. They show a good agreement between code and experimental data.

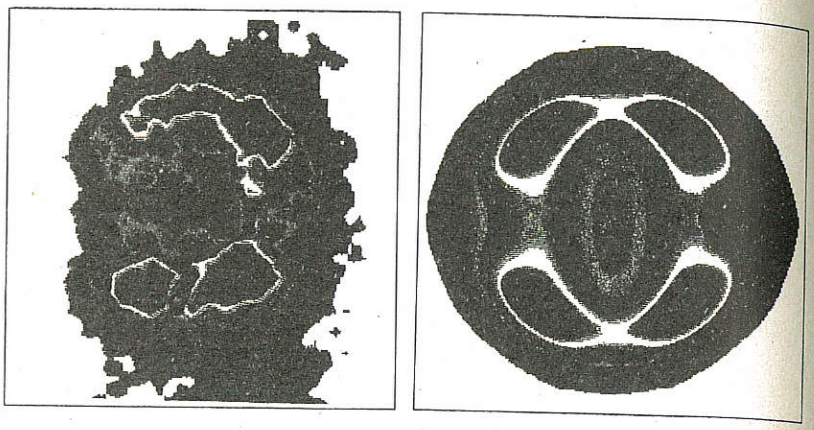

(a) (b)

Fig 3 : (a) Experimental and (b) computed X-ray pinhole picture of the indirectly driven implosion of a microballoon.

References

(1) Buresi E. et al - Laser Part. Beams 4,531 (1986)

(2) Humbert Ph - Congrés de la société française de physique - CAEN (1991)

(3) Busquet M.- Physical Review A,25,2302 (1982)

(4) Andre et al - 'ICF related experiments at CELV'
to be published in Laser Part. Beams (1992)

PLASMA-DRIVEN LINERS

H. Kilic, J.G. Linhart and A. Bortolotti
Physics Department, University of Ferrara
I-44100 Ferrara, Italy

L. Bilbao
University of Buenos Aires, Argentina

V. Nardi
Stevens Institute of Technology, Hoboken, NJ, USA

The deposition of thermal energy by laser or ion beams in an ablator is capable of producing a very large acceleration of the adjacent pusher - for power densities of 100 Terrawatts/cm^2, ablator pressure in the range of 10 Mbar is attainable.

In the case of a plasma drive such driving pressures and accelerations are not directly possible. When a snowplough (SP) is used to accelerate a thin liner, the driving pressure is that of the magnetic piston pushing the SP, i.e. at most 0.1 Mbar. However, the initial radius r_0 of the liner can be a few centimeters, instead of 1 (mm) as in the case in direct pellet implosions /1/. In order to compete with the performance of the beam-driven liners, the plasma drive must demonstrate that

a) thin liner retains a high density during the implosion (lasting a fraction of a μsec);

b) radial compression ratio r_0 / r_{min} of the order of 100 can be attained.

It is also attractive to consider the staging of two or more liners in order to get sharpening and amplifications of the pressure and/or radiation pulse /2/3/4/.

If a) and b) are verified then the final pressures produced will be comparable with those of the beam-driven implosions.

The energy source for the plasma drive can be a condenser bank or perhaps even an inductive storage. Needless to say that the cost and space occupied by these will be much smaller than those of a laser or heavy-ion beam machines and in most cases (even if staging is envisaged) the energy-transfer efficiency of the plasma drive will be superior.

/1/ L. Bilbao et al., Kerntechnik, to be published (1992).

/2/ J.G. Linhart, Laser and Particle Beams 2, 87 (1984).

/3/ J.G. Linhart, Atomenergie Kerntechnik 42, 1 (1983).

/4/ V.P. Smirnov, Plasma Phys. and Controlled Fusion 33, 1697 (1991).

We shall first discuss the theory of the plasma drive, addressing ourselves to the problems a) and b). We shall then describe the apparatus in which thin bubbles ($\delta_L < 1\,\mu m$) are imploded by an SP. In particular, the results of experiments in which the SP is produced in N_2, whereas the inside of the bubble is inflated with D_2 will be mentioned. In the conclusion some future applications of the plasma drive will be considered.

Theory

Let us consider the case of a plane liner driven by the pressure $p = (Z+1)nkT$ of a plasma cushion (equivalent to an ablator). This pressure is supposed to be maintained by an adequate magnetic pressure $B^2/8\pi$ (Fig. 1). The dense material of the liner (ρ_L) is being heated by the heat transport from the hot ablator and would, therefore, expand were it not compensated by a rising p. This is a problem similar to the Hammel-Haines analysis of the Z-pinch (see also Ref.1, App. 1).

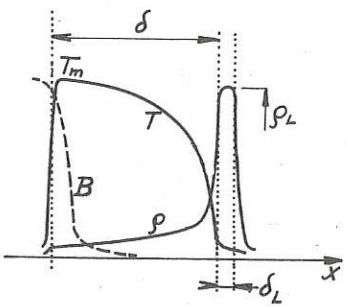

Fig. 1

Let us consider an artificially simple case in which the ρ_L does not diffuse into the ablator and $T \sim const.$, $Z = const.$ If $\delta_L = const.$, we have for the pressure rise in the liner

$$\Delta p \cong 0.5 \cdot 10^{-6} Z^{-1} \frac{T^{7/2}}{\delta} \cdot \Delta t$$

This must be compensated by the $\Delta(B^2/8\pi) = 0.02\pi\Delta(i^2)$. Therefore,

$$\frac{d(i^2)}{dt} = 0.8 \cdot 10^{-5} Z^{-1} T^{7/2} \delta^{-1} \qquad (1)$$

As we assumed that $T \sim const$, the pressure p can rise only if δ decreases. This means that $\delta = ((Z+1)NkT)/(0.02\pi i^2)$, $N = \delta \cdot n$. Substituting into Eq. (1) we get

$$\frac{d(i^2)}{dt} = 0.36 \cdot 10^{10} \frac{T^{5/2}}{(Z+1)Z \cdot N} \cdot i^2 \qquad (2a)$$

$$A$$

From which

$$i = i_0 \cdot \exp\left(\frac{A}{2}t\right) \qquad (2b)$$

The characteristic time constant is $\tau = 2/A$. Ex: $Z = 4, T = 2 \cdot 10^6 (^\circ K), N = 10^{18}$ we get $\tau \sim 2(\mu sec)$.

This, very approximate, analysis suggests that during the time of acceleration the $\Delta p/p < 1$ and consequently the thickness δ_L will not increase substantially.

We have performed numerical calculations on the radial implosion of a thin liner which confirms this conclusion /1/.
These calculations show also that the turn-around radius of our liner is less than 1 mm ($r_0 = 2\,cm$) and when the compressed medium is a D-plasma the temperature can rise to typically 1/2 (keV). Naturally one could suspect that instabilities will prevent such large radial compression ratios. Let us not forget, however, that the liner is collapsing on a dense plasma. Experiments on cylindrical SP's in Argon compressing, initially weak B_z, have shown that very large and symmetric radial compressions are possible.

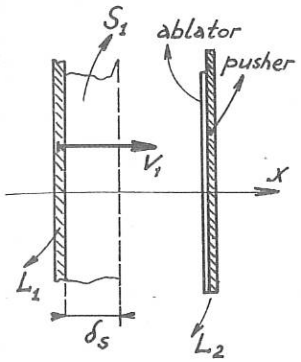

Fig. 2

Let us finally reintroduce the idea of staging, i.e. the use of two liners, to achieve accelerations and pressures comparable with the beam-driven liners. Let us suppose that the first liner L_1 snowploughs in front of itself a layer S_1 of high-Z gas (Fig. 2). Let both L_1 and S_1 impact on a second liner L_2 made of a thin ablator and a heavy pusher (e.g. Ag or Au). The S_1 will be compressed by the $\rho_1 v_1^2$ of L_1 within a time $\tau_1 = \delta_s / v_1$ and will accelerate L_2 to $v_2 \sim v_1$, within a time $\tau_2 \leq \tau_1$/5/. As δ_s can easily be of the order of 1 mm and $v_1 > 10^7$ the acceleration of L_2 will be effected within a few nsecs.

The same idea of staging can be applied to the generation of an intense and short burst of X-rays /2/. In recent experiments based on this idea /4/ X-ray pulses of 300 Terrawatts and ~2 nsecs have been generated.

Experiments

The liner in this experiment is an axisymmetric film drawn in N_2 (~Torr) between two circular lips, one on the central electrode and one on a movable cup (Fig. 3). The resulting liners are azimuthally uniform and have a thickness of $\delta = 1 \div 0.1\,\mu m$. Cylindrical and slightly convex liners were made by adjusting the inner (D_2)/outer (N_2,H_2) pressure ratio. They were imploded by a snowplough plasma driver produced in a coaxial gun discharge. The impact time of the SP on the liner is synchronized with the current maximum $I_{max} = 0.8 \div 1.3\,(MAmps)$. Early experiments and calculations /1/ have shown that the current sheet remains separated from the main body of the liner, which

/5/ J.G. Linhart, Nucl. Fusion 19, 264 (1979).

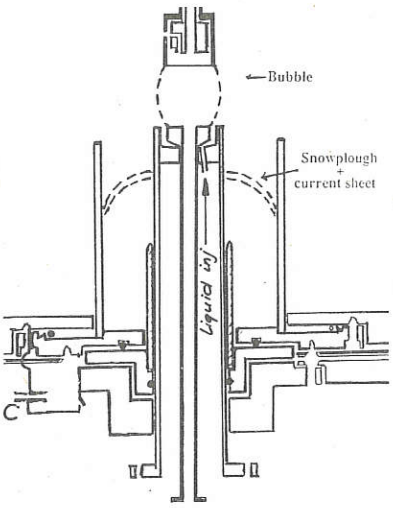

Fig. 3

retains a high density up to the moment of maximum compression. Frame pictures as well as dI/dt traces, with and without liner implosions show different times of maximum compression (pinching) time.

Some implosions were carried out by inflating the bubble with D_2 and using H_2 outside (10 Torr). In a few of theses shots neutron yields of $1 \div 2 \times 10^8$ were recorded. If these were to come from the compressed D-plasma, the turn-around radius would have to be as low as 0.4 mm!

Conclusion

Plasma drive is capable of accelerating liners without exploding them. Applications to quasi-spherical implosions are being prepared. These may be exploited in many ways. The first to be considered will be a compression of a B_ϕ field around a fibre situated on the axis of the system (see J.G. Linhart, in these proceedings). A second will be the liner staging already mentioned, particularly for the production of intense blackbody radiation inside a holhraum /3/.

Acknowledgements

This work was supported by a contract with ENEA-European Community. Thanks are due to Dr. Gnudi who participated in the early study of bubbles at low pressures.

AXIAL MAGNETIC FIELD GENERATION IN A NONUNIFORM LASER PRODUCED PLASMA

M.K.Srivastava and S.V Lawande
Theoretical Physics Division, B.A.R.C., Bombay-400085, INDIA

and

Manoranjan Khan, Chandra Das and B.Chakraborty
Faculty of Sciences, Jadhavpur University, Calcutta-700032, INDIA

Magnetic field generation in a laser produced plasma plays a vital role in inertial confinement fusion (ICF) scheme. Many transport characteristics like thermal transport inhibition, lateral plasma flow etc. which have a direct bearing over the ICF performance, are essentially determined by the self-generated magnetic field (SGMF) in the laser-produced plasma. Theoretically, a variety of mechanisms have been proposed in the last two decades that leads to generation of toroidal magnetic field. This is extensively reviewed in a recent paper by J.A.Stamper[1]. However, not much work has been done so far as the self-generated axial magnetic field (SGAMF) is concerned. An evidence of SGAMF of 0.6 MG was shown by Briand et.al.[2] in their experiment on a planar Al target irradiated by an intense pulse of short wave length laser. They also proposed that such SGAMF could grow from the small scale toroidal field through dynamo effect. However, Dragila[3] argued that this could be due to ion acoustic turbulence. Another mechanism was suggested by Chakraborty et.al.[4] which was based on the interaction between elliptically polarized standing waves. However, none of the above theories could explain the experimental results to be conducted over the wide range of parametric conditions.

In the present paper we propose that an obliquely incident spatially inhomogeneous intense and longer wavelength p-polarized laser beam could generate SGAMF in a nonuniform plasma in the range of megagauss. Moreover, for lower intensity (I) and short wavelength (λ) lasers, a field in the range of kilogauss could be produced by collsional excitation via pondermotive effect for both the s and p-polarized beam even in an uniform plasma.

The basic equations describing the motion of the plasma are

$$m_e n_e D_e(\vec{v}_e) = -\vec{\nabla}(n_e T_e) - e n_e (\vec{E}+\vec{v}_e \times \vec{B}) - m_e \nu n_e (\vec{v}_e - \vec{v}_i) \qquad (1)$$

$$M n_i D_i(\vec{v}_i) = -\vec{\nabla}(n_i T_i) + Z e n_i (\vec{E}+\vec{v}_i \times \vec{B}) + m_e \nu n_e (\vec{v}_e - \vec{v}_i) \qquad (2)$$

where notations have their usual meaning. $D_j \equiv \partial_t + (v_j.\vec{\nabla})$ (j=i,e) is the usual convective derivative. The above equations are solved along with the following Maxwell's equations in a self-consistent manner.

$$\vec{\nabla}\times\vec{E} = -\partial_t(\vec{B}), \quad \vec{\nabla}\times\vec{B} = c^{-2}\partial_t(\vec{E}) + \mu_o\vec{J}, \quad \vec{\nabla}.\vec{E} = \rho/\varepsilon_o, \quad \vec{\nabla}.\vec{B} = 0 \qquad (3)$$

$$\rho = e(Zn_i - n_e), \quad \vec{J} = e(Zn_i\vec{v}_i - n_e\vec{v}_e) \qquad (4)$$

We write the variables $f = f_o + f_1$, $f_1 = \hat{f}_1 e^{-i\omega t}$ ($\hat{f}_1 = f_R + if_I$), where f stands for n_e, $\vec{v}_e$, $\vec{E}$ and $\vec{B}$ and f_o and $\hat{f}_1$ are slowly varying function of space and time. Assuming ions to form an infinitely massive quasineutral background i.e., $n_i = n_{io}$, $\vec{v}_i = \vec{v}_o$ and $n_{io}Z = n_{eo} = n_o$ for the high frequency (ω) response, we obtain the following after separating the steady ($\omega=0$) and high frequency ($\sim e^{-i\omega t}$) components and using the approximations[5] ($n_1 \ll n_o$, $|\vec{v}_i| \sim |\vec{v}_e|$ for $I > 10^{12}$ W/cm^2, $kL_n \gg 1$, $|\omega/k| \gg |\vec{v}_e|$.

Slow Components:

$$mn_e D_e(\vec{v}_{eo}) = -\vec{\nabla}(n_e T_e) - en_e(\vec{E}_o + \vec{v}_{eo}\times\vec{B}_o) - m\nu n_e(\vec{v}_{eo} - \vec{v}_o) + \vec{\Pi} \qquad (5)$$

$$\vec{\nabla}\times\vec{E}_o = -\partial_t(\vec{B}_o), \quad \vec{\nabla}\times\vec{B}_o = \mu_o\vec{J}_o, \quad \vec{\nabla}.\vec{E}_o = 0, \quad \vec{\nabla}.\vec{B}_o = 0, \quad \vec{J}_o = en_o(\vec{v}_o - \vec{v}_{eo}) \qquad (6)$$

$$\vec{\Pi} = -mn_o[\langle\vec{\hat{v}}_i.\vec{\nabla}\vec{\hat{v}}_i\rangle + (e/m)\langle\vec{\hat{v}}_i\times\vec{\hat{B}}_i\rangle] \qquad (7)$$

Fast Components:

$$\partial_t(\vec{\hat{v}}_i) = -e\vec{\hat{E}}_i/m - T_e\vec{\nabla}n_i/mn_o - \nu\vec{\hat{v}}_i, \quad \vec{\hat{J}}_i = -en_o\vec{\hat{v}}_i \qquad (8)$$

$$\vec{\nabla}\times\vec{\hat{E}}_i = -\partial_t(\vec{\hat{B}}_i), \quad \vec{\nabla}\times\vec{\hat{B}}_i = c^{-2}\partial_t(\vec{\hat{E}}_i) + \mu_o\vec{\hat{J}}_i, \quad \vec{\nabla}.\vec{\hat{E}}_i = -en_i/\varepsilon_o, \quad \vec{\nabla}.\vec{\hat{B}}_i = 0 \qquad (9)$$

Next, neglecting the electron inertia, i.e., setting $mn_o D_e(\vec{v}_{eo}) \equiv 0$ in Eq.(5) and taking curl on both sides we get on using (6)

$$\partial_t(\vec{B}_o) = \left(\frac{\vec{\nabla}T_e\times\vec{\nabla}n_o}{en_o}\right) - \vec{\nabla}\times\left(\frac{\vec{\Pi}}{en_o}\right) + \vec{\nabla}\times(\vec{v}_o\times\vec{B}_o) + \vec{\nabla}\times\left(\frac{\vec{B}_o\times\vec{\nabla}\times\vec{B}_o}{en_o\mu_o}\right) + \left(\frac{m\nu\nabla^2\vec{B}_o}{n_o\mu_o e^2}\right) \qquad (10)$$

The first term on RHS of (10) is the usual thermoelectric term, second is the ponderomotive term, third is dynamo term, fourth is the Hall term and the last one represents diffusion of magnetic field due to collisions. For the large scale magnetic field spatial evolution of $\vec{B}_o$ can be ignored, particularly, for the short pulse laser ($v_o t_o \ll L_n$, t_o is laser pulse duration). Moreover, thermoelectric term does not contribute to axial field for the density variation along the x-direction (no lateral inhomogeneity). Thus, we expect that the pondermotive term could be important for SGAMF. Using Eqs.(7-9) for $\vec{\Pi}$ in (10), we finally obtain the following for $k\lambda_D \ll 1$ (λ_D is the Debye length), $kL_n \gg 1$, $kL_E \gg 1$ and $\Omega = \nu/\omega \ll 1$

$$\partial_t(\vec{B}_o) = -\vec{\nabla}\times\vec{\mathcal{E}}$$

$$\vec{\mathcal{E}} = (e/2m\omega^2)[\Omega(\vec{E}_R\times\vec{\nabla}\times\vec{E}_I - \vec{E}_I\times\vec{\nabla}\times\vec{E}_R) - (\vec{E}_R\times\vec{\nabla}\lambda_D^2\times\vec{D}_R + \vec{E}_I\times\vec{\nabla}\lambda_D^2\times\vec{D}_I)] \qquad (11)$$

where $\vec{\mathcal{E}}$ is an effective electric field induced due to motion of electrons by the ponderomotive force arising from the coupling of high frequency fluctuations in the plasma. The electric field $E_1=\vec{E}_R+i\vec{E}_I$ and $\hat{D}_1=\vec{\nabla}(\vec{\nabla}.\hat{E}_1)$ in Eq.(11) are obtained from the solution of

$$\vec{\nabla}\times(\vec{\nabla}\times\vec{E})=(\omega^2-\omega_p^2/c^2)\vec{E}+\beta^2\vec{D}_1. \quad \varepsilon_e=1-a\omega_p^2/\omega^2. \quad \beta^2=3S^2, \quad a=(1+i\Omega)^{-1} \qquad (12)$$

where ω_p is the plasma frequency and $S=\sqrt{(T_e/m)}$ is thermal speed of the electrons. For slowly varying functions, using the optical approximation[5], we have the following results for the axial magnetic field growth rate.

$$\Gamma_x=\partial_t(B_{0x})=\Gamma_x^c+\Gamma_x^{nc}, \qquad \Gamma_x^c=-[e\nu f_a\sin\theta_0/2mc\omega^2]\partial_z(A^2)$$

$$\Gamma_x^{nc}=[ef_a g\sin\theta_0/2m\omega^2][\sin\theta_0\{A,\partial_x(A)\}-\sqrt{(\cos^2\theta_0-N_0)}\{A,\partial_y(A)\}] \qquad (13)$$

where, A is amplitude of the laser electric field, $g=d\lambda_D^2/dx$ and $\{a.b\}=\partial_z(a)\partial_y(b)-\partial_y(a)\partial_z(b)$. It is obvious that for the normal incidence of the laser beam ($\theta_0=0$), no axial magnetic field is excited via pondermotive action. The superscripts 'c' and 'nc' represent the collisional and noncollisional contribution to the axial field respectively. For the s-polarized beam it is only the collisional part that contributes to SGAMF. Moreover, the collisional excited field may result in an uniform plasma whereas the noncollisional excitation does require the density inhomogeneity.

If for illustration we consider a Gaussian laser beam $I=I_0\exp[-(y^2+z^2)/L_E^2]$, ($I=\varepsilon_0 cA^2/2$), Eq.(13) simplifies to the following on putting values of various constants.

$$\Gamma_x^c=1.24\times10^{-10}\nu f_a\sin\theta_0(I\lambda^2/L_E) \qquad \text{(KG/100 psec)}$$

$$\Gamma_x^{nc}=18.6f_a[\sin\theta_0\sqrt{(\cos^2\theta_0-N_0)}/(1-N_0)][I\lambda^2\lambda_D^2/L_E^3L_n] \quad \text{(MG/100 psec)} \qquad (14)$$

Here all the lengths λ, λ_D, L_n, L_E are in μm, I is in units of 10^{14} W/cm^2 and ν is in sec^{-1} given by[5]

$$\nu=\nu_c N_0, \quad \nu_c=9.5\times10^{-6}n_c Z/T_e^{3/2}, \quad T_e\simeq 6.21(I_a\lambda^2)^{2/3}, \quad n_c=1.17\times10^{17}/\lambda^2 \qquad (15)$$

where, T_e is in kev, n_c is in m^{-3}. Using (15) in (14) we find that $\Gamma_x^c\sim\lambda^{-2}$, and $\Gamma_x^{nc}\sim I^{4/3}\lambda^{14/3}$.

Thus, we see that for shorter wave length lasers, the collisional contribution is large and is independent of intensity in our model. Fig.2 shows Γ_x^c versus x for the data mentioned therein. It is seen that the field is in the range of kilogauss and shows a maximum at x~23 μm. The noncollisional contribution (not shown in Fig.2) is estimated to be extremely small.

For higher intensity and longer wave length lasers, it is the noncollisional contribution that is dominant. Fig.3 shows Γ_x^c and Γ_x^{nc} vesus x for the case intense CO_2 laser. It is seen that Γ_x^{nc} increases monotonically towards the coronal region and can excite the axial field to 0.5-0.6 MG for a 100 psec pulse laser. On the other hand Γ_x^c decreases towards the coronal region and is in the range of kilogauss.

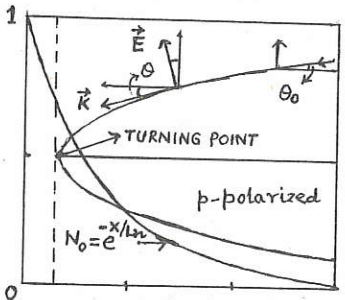

FIG.1: PROPAGATION OF EM WAVE IN A PLASMA

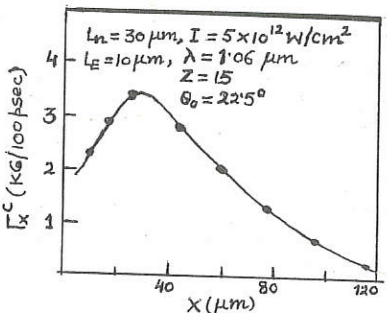

FIG.2 : Γ_x^c VERSUS X (μm) FOR LOW INTENSITY AND SHORT WAVELENGTH LASERS.

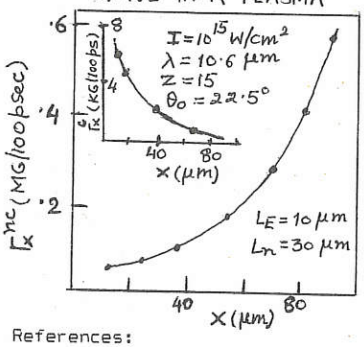

FIG 3 : Γ_x^{nc} (MG/100 psec) and Γ_x^c (KG/100 psec) VERSUS X (μm) FOR HIGH INTENSITY AND LONG WAVELENGTH LASERS

References:

1. J.A.Stamper, Laser and Particle Beams, 9,841, (1991).
2. J.Briand, V.Adrian, M El.Tamer, A.Gomes, Y.Quemener, J.P.Dinguirard and J.C.Kieffer, Phys Rev.Lett., 54,38 (1985).
3. R.Dragila, Phys.Fluids, 30,925 (1987).
4. B.Chakraborty, M.khan, B.Bhattacharya, S.Deb and H.C.Pant, Phys.Fluids, 31,1303 (1988)
5. P.Mulser, Laser-Plasma Interactions, Ed. by R.A.Cairns and J.J.Sanderson, SUSSP Publications, 1980, p-91.

Stabilization of the Rayleigh-Taylor Instability by Convection and Thermal Conduction in Smooth Density Gradient: WKB Analysis.

A.B.Bud'ko , M.A.Liberman and E.A.Bondarenko

Department of Technology, Uppsala University, Box 534, S-75121, Uppsala, Sweden

Since development of the RT modes in the ablatively accelerated plasma of laser targets imposes crucial limitations on symmetry of spherical implosions and hence on energy cumulation, it has been the subject of intensive numerical and analytical analysis in the recent years, particularly in the context of inertial confinement fusion. Recent thin-foil ablative-acceleration experiments /1,2/ as well as the results of 2D numerical simulations /1-4/ demonstrated substantial reduction of the instability growth rates compared with the classical theory predictions up to the total stabilization in the short-wavelength limit. The numerical results /4/ indicated that the main stabilization mechanism is convection.

To derive the scaling laws for the RT growth rates and cut-off wavenumbers in the wide range of flow parameters, analytical solutions attract special interest. The analytical approach based on the discontinuity model was developed to analyze the reduction of the RT growth rates by the plasma convective flow and the thermal conductivity effects /5-7/. The following major problem arises in the discontinuity approximation, which leaves the solution undetermined: the number of the boundary conditions on the perturbed ablation surface is not sufficient to derive the dispersion equation. One needs additional boundary conditions not associated with the conservation laws on the discontinuity surface to close the system of linearized equations for small perturbations. The stabilization effect of highly structured hydrodynamic profiles was studied by Mikaelian /8/ and Munro /9/ for a stationary plasma. Nevertheless, no reasonable analytical model was constructed taking into account the combined convective, thermal conductivity and density gradient reduction of the RT growth rates.

In this report we develop the analytical approach based on the WKB approximation to analyze the stabilization of the RT modes in plasma with smooth density and velocity gradients. We consider the dynamics of the RT modes in the ablatively accelerated plasma of thin foils, thus restrict our attention on the planar geometry of the unperturbed flow and assume two-dimensional perturbations $\Psi(t,x,z) = \Psi(z)\exp(ikx+\sigma t)$ in the plane XZ, the Z axis is directed along the unperturbed gradients.

The linearized equations of the ideal hydrodynamics are

$$\sigma \rho_1 + d(\rho_1 v + \rho v_{1z})/dz + ik\rho v_{1x} = 0 \quad (1)$$

$$\rho(\sigma v_{1x} + v dv_{1x}/dz) + ikP_1 = 0, \quad (2)$$

$$\rho(\sigma v_{1x} + d(v v_{1z})/dz) + dP_1/dz - \rho_1(g - v dv/dz) = 0, \quad (3)$$

$$\sigma P_1 + \gamma P_1 dv/dz + \gamma P(dv_{1z}/dz + ikv_{1x}) + v dP_1/dz + \rho g v_{1z} - \kappa_e(d^2/dz^2 - k^2)T_1 = 0 \quad (4)$$

where ρ, P, v, g, κ_e are the density, pressure, velocity, acceleration and thermal conductivity, the adiabatic index $\gamma = (\partial \ln P/\partial \ln \rho)_S$ is assumed to be constant, the subscript 1 refers to the perturbed variables. First, we shall investigate the effects of convection and hence ignore the last term in Eq.(4) corresponding to the heat conduction.

The growth rate σ is the eigenvalue of the boundary value problem for Eqs.(1)-(4). The boundary conditions as usually are assumed corresponding to the homogeneous plasma flows in the slab and in the ablation zone beyond the unstable transition region, that is all the perturbations vanish at $z \to \pm\infty$, still in the WKB model eigenfunctions are localized in the unstable region and the growth rate depends weakly on the specific form of the boundary conditions. We look for the solutions of the linearized hydrodynamic equations (1)-(4) in the WKB form:

$$\Psi(z) = \sum_j \psi_j \exp\left(k \int^z \varphi_j(z')dz'\right), \quad \Psi = v_{1z}, v_{1x}, \rho_1, P_1 \qquad (5)$$

The perturbation amplitudes $\Psi_j(z)$ as well as the phase functions $\varphi_j(z)$ are the slowly varying functions of the profile coordinate z compared with the exponential terms. Substitution of the perturbations in the form (5) into Eqs.(1)-(4) results in the four-coupled linear algebraic equations for the amplitudes. Setting the determinant of this system equal to zero we obtain the characteristic equation in the phase functions $\varphi_j(z)$

$$\Lambda_4(\varphi) \equiv \left(\Sigma+\varphi\right)^2\left(\left(\Sigma+\varphi\right)^2 + \frac{1-\varphi^2}{M^2}\right) - \frac{\alpha^2}{Frk^2}\left(\left(\Sigma+\varphi\right)\left(\Sigma+\varphi - \left(\gamma-1\right)\frac{\alpha_v}{\alpha}\right) + \frac{1}{M^2} + \frac{1}{Fr}\right) = 0 \quad (6)$$

Here the following parameters are introduced: the dimensionless growth rate $\Sigma(z) = \sigma/vk$, the velocity and inverse density profiles steepness $\alpha_v = d\ln(v)/dz$, $\alpha = -d\ln(\rho)/dz$, the Froude number $Fr(z) = v^2\alpha/g$ and the adiabatic Mach number $M(z) = v/c$. The asymptotics of the localized perturbation implies the sonic solution in the dense slab upstream flow and the coupled vorticity, entropy and sonic waves in the downstream ablation flow

$$\Psi(z) = A \exp(k\varphi_1 z), \; z \to -\infty, \quad \Psi(z) = \sum_{j=2}^{4} \psi_j \exp(k\varphi_j z), \; z \to +\infty,$$

where $\varphi_{1,2} = \dfrac{\Sigma M^2 \pm \sqrt{1 + M^2(\Sigma^2 - 1)}}{1 - M^2}$, $\varphi_{3,4} = -\Sigma$.

Location of the roots φ_j of Eq.(6) versus the profile coordinate z in the complex plane φ depends upon the parameters of the problem. Not more than two roots can be simultaneously located in the half-plane $Re(\varphi) > 0$. At certain values of z the roots can intersect and form the multiple ones. In order for the perturbation to be localized, the points on the profile must exist where the multiple root of Eq.(6) is formed by intersection of the root $\varphi_1(z)$ with some other roots $\varphi_j(z)$ in the half-plane $Re(\varphi) > 0$. The coordinates z_*, z_{**}

of these points and the corresponding values φ_*, Σ_* are obtained from the following two-coupled equations:

$$\Lambda_4(\varphi(z_*)) = 0, \qquad \partial\Lambda_4/\partial\varphi = 0. \tag{7}$$

We are looking for the maximum eigenvalue σ (for a given k) corresponding to the only roots intersection point that implies

$$\Sigma(z_*) = \Sigma_*(z_*), \quad d\Sigma(z_*)/dz = d\Sigma_*(z_*)/dz \tag{8}$$

Here Σ_* is the real and positive root of Eqs.(6),(7). Eqs.(8) yield the solution of the problem: the growth rate $\sigma = kv(z_*)\Sigma_*(z_*)$ is obtained as the implicit function of the wavenumber as well the unperturbed profiles structure. In the limit of small Mach number $M^2 << Fr << 1$ typical for a long-wavelength and sufficiently high laser irradiation Eqs.(8) can be solved explicitly. Denoting $G(z) = 4\alpha^2(1 + M^2/Fr)/(k^2Fr)$, $s = \sqrt{1 + G/27}$ the result can be written as

$$\sigma = kv(z_*)\Sigma_*(z_*) \ , \ z_* \text{ being the solution of } \frac{dG}{dz} = \frac{1-2\varphi_*^2}{1+2\varphi_*^2}\left(12\left(1-\varphi_*^2\right)^2\right)\frac{d\ln(v)}{dz},$$

$$\text{where } \varphi_* = \sqrt{1 - \frac{G^{1/3}}{(s+1)^{2/3} + (s-1)^{2/3} + G^{1/3}/3}}, \quad \Sigma_* = \frac{1-2\varphi_*^2}{\varphi_*} \ . \tag{9}$$

The necessary and sufficient condition for the positive sign of the growth rate $\sigma(k)$ is $\max(\Sigma_*(z)) > 0$. Consequently, for any given hydrodynamic profiles g(z), v(z), ρ(z), T(z) the RT growth rate vanishes if the wavenumber k reaches the value

$$k = k_0 = \sqrt{\max\left(4g(1-M^2)\,(\alpha + M^2 g/v^2)/v^2\right)} \ . \tag{10}$$

In particular, Eq.(10) yields the scalings for the cut-off wavenumber at various flow parameters. For a small Mach number (long-wavelength and high irradiation of laser beam) the stabilization of the RT instability occurs at $k_0 \sim \sqrt{g/Lv^2} \sim \alpha/\sqrt{Fr}$

Another limit: $Fr << M^2 \sim 1$, typical for short-wavelength and low irradiation of laser beam, gives rise to the scaling $k_0 \sim gM/v^2 \sim \alpha M/Fr$ in qualitative agreement with the approximation Takabe formula.

The thermal conduction effect on the RT instability stabilization is typically small compared with the convective effect. Taking into account the last term in Eq.(4) and performing the WKB analysis described above we obtain the corrections to the values of the growth rate (given by Eqs.(9)) and cut-off wavenumber (given by Eq.(10)) in the subsonic flow regime

$$\frac{\Delta k_0}{k_0} = - k_0 \frac{m\kappa_e(z_*)}{2\sqrt{2}\rho v(z_*)} , \quad \Delta\sigma = - \frac{m\kappa_e(z_*)}{4\rho v^2(z_*)} ,$$

where $m = m_i/(Z+1)$, m_i is the ion mass, Z is charge state.

In Fig.1 the growth rates σ versus wavenumber k are plotted obtained analytically (solid curve) in our model (Eqs.(8)) as well as numerically (dashed curve) by the shooting method as the eigenvalues of the boundary value problem for Eqs.(1)-(4). The unperturbed hydrodynamic profiles has been taken in the both cases corresponding to the steady - state plasma flow established after the shock and rarefaction wave propagation and a number of reflections in ablatively accelerated aluminium foil of thickness 10μm undergoing a Nd glass laser radiation (λ_0 = 1.06μm, I = 10^{13} W/cm^2).

Finally, we remark that self-consistency of the model presented implies that the local Froude number must be small Fr(z) << 1, still comparison of the analytical and numerical results reveals a satisfactory applicability of the model for ablating plasma with sharp density gradients.

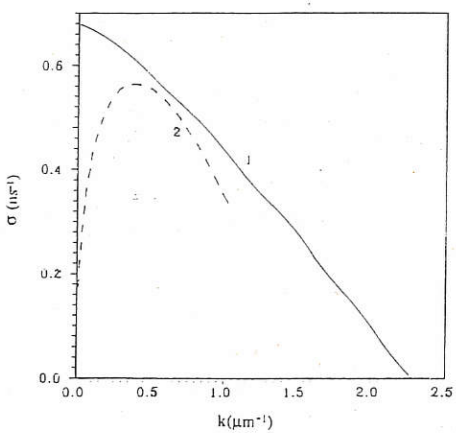

Fig.1

/1/ J.D.Kilkenny, Phys. Fluids **B2** , 1400 (1990).
/2/ J.Grun, M.H.Emery, C.K.Manka, et. al., Phys. Rev. Lett. **58**, 2672 (1987).
/3/ M.Tabak, D.H.Munro, J.P.Lindl, Phys. Fluids **B2** , 1007 (1990).
/4/ J.H.Gardner, S.E.Bodner, J.P.Dahlburg, Phys. Fluids **B3**, 1070 (1991).
/5/ S.E.Bodner, Phys. Rev. Lett. **33** , 761 (1974).
/6/ W.H.Manheimer, D.G.Colombant, Phys. Fluids **27** , 983 (1984).
/7/ H.J.Kull, S.I.Anisimov, Phys. Fluids **29** , 2067 (1986).
/8/ K.O.Mikaelian, Phys. Rev. **A 26** , 2140 (1982).
/9/ D.H.Munro, Phys. Rev. **A 38** , 1433 (1988).

FUSION-FISSION TRIGGERS FOR ADVANCED FUELS

J.G. Linhart
Physics Department, University of Ferrara
I-44100 Ferrara, Italy

The use of D-T as fuel in future fusion reactors is associated with two main drawbacks: the difficulty of providing tritium and the radioactivity and material deterioration due to large neutron fluxes. The extension of working cycles to the advanced fuels (He^3, D, Li, Be, B), which would minimize these two drawbacks, appears almost impossible in magnetically confined plasmas. Equally large obstacles appear in inertial confinement fusion (ICF) based on spherical implosions - unless one is prepared to exploit explosions approaching in magnitude those of nuclear bombs. It seems that some of these difficulties could be removed if ignition schemes based mainly on cylindrical triggers could be used.

We shall briefly describe the difference between spherical and cylindrical implosions (secs. 1 and 2), describe in some detail the mechanism of a cylindrical trigger (sec. 3) and introduce the notion of a fusion-fission trigger which appears an interesting alternative to a purely D-T detonator.

1. Ignition of an Advanced Fuel (AF) by a Spherical D-T Trigger

Let us consider a D-T plasma (density n_0, temperature $T_0 < 10^{7}$°K) in which an energy W_0 is deposited in a small spherical volume. Let us assume that W_0 is large enough so that the expansion of this volume generates a strong diverging spherical shock-wave. It can be shown /1/ that provided

$$W_0 > 4000\left(\frac{n_s}{n_0}\right)^2 b^3 \ldots (\mathrm{MJ}) \qquad (1)$$

is deposited within a radius given by

$$n_0 r_0 = 0.63 \cdot 10^{23} b^{-1} \qquad (2)$$

the fusion energy released within r_0 is larger than energy losses from the diverging shock and the shock-wave is transformed, as it progresses, into a detonation wave /2/. The optimum mean temperature T_{opt} in the r_0 – sphere should be about $1.6 \cdot 10^{8}$(°K). Here n_s is the solid state ion density and b is the fraction of nuclear output converted into heat within $3/2 \cdot r_0$. For only α – absorption $b = 1$.

The same type of analysis can be repeated for a D-plasma. We have

$$n_0' r_0' > 0.54 \cdot 10^{25} \cdot b^{-1} \quad (3) \quad \text{and} \quad W_0' > 2 \cdot 10^{6} \cdot b^{-3}\left(\frac{n_s}{n_0}\right)^2 \ldots (\mathrm{GJ}) \quad (4)$$

This is a very large energy. Let us take, e.g., $n = 10 n_s$ then $W_0' = 4 \cdot b^{-3}$ tons TNT. One way to provide such a large energy would be to use a D-T detonation (Fig.1). If one wished to use predominantly D as the main fuel, the D-detonation wave would have to proceed to a radius R several times larger than r_0'. This implies, in the above example, output energies of the order of at least 1 kton of TNT, which is not a negligible nuclear explosion.

/1/ J.G. Linhart, Nucl. Fusion 10, 24 (1970).

/2/ M.S. Chu, Phys. of Fluids 15, 413 (1972).

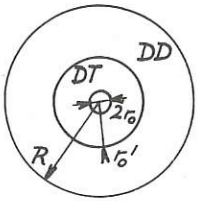

Fig. 1

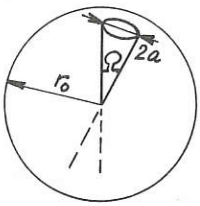

Fig. 2

Apart from this consideration, the initial compressional energy in the D sphere is beyond any driver-performance imaginable today. A somewhat more manageable situation occurs if were one to use Li, He^3, Be or Pu mixed with deuterium, but even then the energies involved are enormous.

2. Ignition of AF in a Cylindrical Geometry

It is clear that a spherical target does not promise too well for the ignition of non D-T fuels.

Let us now describe a modification of the spherical geometry, in which we consider only a conical segment of the spherical target involved in the fusion detonation /1/. We shall assume, to start with, that no heat is lost to the walls of the cone and that the walls are infinitely massive (perfect tamping). In that case the trigger energies (Eqs.(1+4)) are reduced (Fig. 2) by the factor $\Omega/4\pi = (a/2r_0)^2$. The conical trigger energy is then

$$U_0 = \frac{1}{4}\left(\frac{a}{r_0}\right)^2 W_0 \qquad (7)$$

If at $r > r_0$ the nuclear detonation propagates in a cylinder whose radius is a we can write for the input energy density u - required for the propagation of a plane detonation in D-T

$$u \geq \frac{U_0}{\pi a^2} = \frac{1}{4\pi}\frac{W_0}{r_0^2} \cong 200 b^{-1} \quad (MJ/cm^2) \qquad (8)$$

independent of the density n_0 and in good agreement with the results obtained by Chu /2/.

A similar expression can be obtained for U_0' and u'. Using Eqs. 3 and 4 we obtain

$$U_0' = \frac{1}{4}\left(\frac{a'}{r_0'}\right)^2 W_0' \quad (9) \qquad u' \cong 16 \cdot b^{-1} \qquad (GJ/cm^2) \qquad (10)$$

Let us now transform our conical sector into a cylinder. U_0 will be three times the expression given in Eq. (7), whereas U_0'' required to propagate a detonation wave in D will be

$$U_0'' = \pi a^2 u' \cong 50\frac{a^2}{b} \quad (GJ) \qquad (11)$$

It is clear that this approach promises more realistic energy outputs. If, e.g. $a = 1$ (mm), $b = 3$ then $U_0'' = 170$ (MJ) with possibly a couple of GJ as the final output. It is evident that the answer to the possible ignition of the D fuel in this configuration depends on

a) the minimum possible dimension of a;

b) the availability of sufficiently a powerful cylindrical trigger - which does not have to be a D-T spark.

Taking into account the heat loss to the walls of the tamping tube, the critical dimension a_c of the channel is

$$a_c \sim 10^3 \sqrt{< l >}\,\frac{T}{\sqrt{n_0}} \qquad (12)$$

where $< l >$ is the mean length of the detonation region.

If the D-T plane detonation wave were fully developed /3/ then $\langle l \rangle_{DT} \sim 20 n_s/n_0$ and $\langle T \rangle_{DT} \sim 10^{10}$ (°k). It is clear that the thermal loss to the walls of our cylinder and the nonlocal deposition of neutron energy will not allow such a full development of the detonation, it will lower both the $\langle l \rangle$ and $\langle T \rangle$ below $\langle l \rangle_{DT}$ and $\langle T \rangle_{DT}$. Taking $\langle l \rangle \sim 10 (n_s/n_0)$ and substituting it into Eq. (12) and choosing $\langle T \rangle = 4 \cdot 10^8$ (°k) we obtain $a_c = 6.3 (n_s/n_0)$ (12a)

It follows that the energy U_0 which must be available in order to propagate the detonation in D is (Eqs. (11) and (12))

$$U'' > \frac{2000}{b}\left(\frac{n_s}{n_0}\right)^2 \ldots (\mathrm{GJ}) \qquad (13)$$

Ex: $b = 3$, $n_0/n_s = 20$ then $U'' > 1.86$ (GJ).

This result highlights the urgent need to find a sufficiently energetic conical or cylindrical spark. We propose to solve this problem by using ideas from the domain of dense Z-pinches (DZP).

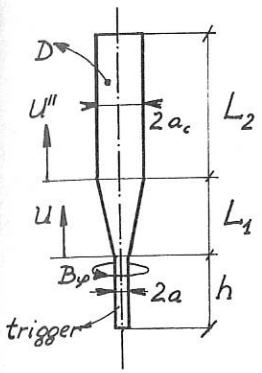

Fig. 3

3. Cylindrical Detonators

Let us consider an axial system as depicted in Fig. 3. The section h corresponds to the trigger region (spark), a transition region L_1 follows in which the energy U liberated by the trigger is transmitted as a detonation wave to the region L_2 in which D is ignited. We shall require that the energy pulse U_0 is given by Eq. (13). We shall further assume that $U \sim U''$, i.e. there is no amplification of the detonation wave in L_1. If the trigger is confined by a B_φ field the large heat loss, which limited a to values larger than a_c, does not exist and the radius a of the Z-pinch (and h) will be given by considerations of obtaining sufficiently large U whilst keeping U_0 as low as possible.

From Eqs. (7) and (2) we get

$$U_0 = 1890 \frac{a^2}{b} \ \text{(MJ)} \quad \text{and} \quad r_0 = 1.26 \cdot b^{-1} \cdot n_s/n_0. \qquad (14)$$

In order that the detonation wave develops, h must be at least equal to $\langle l \rangle_{DT}$ which is about ten times larger than r_0. In that case the thermal energy of the DZP will also be ten times U_0. The detonation within h will have the nature of a volume ignition - for which the gain G will be about 100. As $U \sim U''$ we have

$$\frac{2000}{b'}\left(\frac{n_s}{n_0'}\right)^2 \cong 2000 \frac{a^2}{b} \quad \text{giving} \quad a = \frac{n_s}{n_0'}\frac{b}{b'} \qquad (15)$$

Ex: $n_s/n_0' = \frac{1}{30}$, $\frac{b}{b'} = \frac{1}{3.3}$ then $a \approx 10^{-2}$ (cm).

/3/ R.A. Gross, Phys. of High Energy Density, Proc. School E. Fermi, Varenna 1961, p. 245 (Academic Press).

This implies (Eqs. (14) and (10)) that $U_0 \sim 1.9$ (MJ) and if $n_0/n_s = 100$ then $h \sim 1.26$ (mm). Considering that the total energy a driver must deliver includes also the energy of the B_ϕ field and other losses one sees that driver energies of the order of 10 MJ will be required if D-T is used as an axial detonator. This is not a comfortable number.

It can be shown that a fusion-fission detonator has a gain G much larger than a purely fusion one and consequently let us consider a DZP in a mixture of Pu-D-T. The compression n_0/n_s in such a pinch will have to be more than ten times that of a purely D-T target, but the temperatures required will be ten times smaller. In most cases /4/ the energies U_0 will be less than 1 (MJ), the detonation output almost 1 (GJ). The DZ pinches (in D-T and Pu-D-T) can be powered by a MVolt, nsec, coaxial line or more simply by a quasi-spherical implosion of a liner, compressing a seed B_ϕ field /4/5/. The magnetic flux serves not only as a pressure amplifier, but also as a transformer between the spherical implosion and the cylindrical compression (Fig. 4).

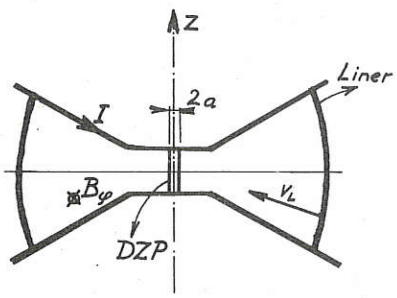

Fig. 4

Conclusion

The axial detonation wave appears to be a much more feasible trigger for advanced fuels than its spherical counterpart. It requires, however, an axial trigger, possibly of the Fu-Fi type. The output energies are in the GJoule range, which will call for a novel design of an explosion container and a repetition rate slower than 1 shot/sec.

Acknowledgement

I wish to thank several of my colleagues for useful suggestions and references, particularly so to Dr. M. Srinivasan and Prof. M. Haines.

/4/ J.G. Linhart, to be published shortly in: Czechoslovak Journal for Physics.

/5/ L. Bilbao et al., to be published in Kerntechnik, (1992).

Topic 8:

General Plasma Theory

WAVE COLLAPSE OF STRONG LOWER-HYBRID TURBULENCE

R Bingham, (Rutherford Appleton Laboratory, Chilton, Didcot, Oxfordshire, OX11 0QX, UK)
J J Su, J M Dawson (Dept. of Physics, University of California, Los Angeles CA 90024)
V D Shapiro, V Shevchenko (California Space Insitute, UCSD, San Diego, CA 92093)
V N Tsytovich, (General Physics Institute, Russian Academy of Sciences, Moscow)

Abstract
Lower-hybrid turbulence, driven by anisotropic ion distribution functions such as perpendicular velocity ring distributions or loss cone distributions, are found to be modulationally unstable. The modulational instability lead to wave collapse of the lower-hybrid wave producing elongated cavitons aligned along the magnetic field direction. We show that the modulational instability is due to the coupling of the lower-hybrid mode with both low frequency magnetic and density fluctuations producing magnetic as well as density cavities. Particle in cell simulations using a $2\frac{1}{2}$-D electromagnetic, relativistic code demonstrate that strong electron and ion acceleration takes place within the caviton like structures. The electrons are predominantly accelerated parallel to the ambient magnetic field forming high energy tails and beams with $\partial f_e/\partial v$ positive while the ions are accelerated in the perpendicular direction. Arrest of wave collapse is shown to occur through wave absorption by electrons and ions, resulting in minimum caviton dimensions of 10 Debye lengths and 100 Debye lengths perpendicular and parallel to the magnetic field respectively.

Introduction

Instabilities whose source of free energy is anisotropic ion distributions such as loss-cones, ring distributions[1] or cross field currents ie the modified two stream instability[2] are likely to produce waves around the lower-hybrid resonance frequency. Such ion distributions are found in both laboratory and space plasmas. A ring distribution for example may be formed artificially in the presence of magnetic fields by energetic particle injection, or resonant heating by electromagnetic waves. Naturally occurring ion ring distributions are found downstream of magnetized shocks[3], such as the earth's bow shock or in the solar atmosphere. The ion ring instability generates waves in the region of k space where dissipations is negligible.

In developing an analytical model for the modulational instability of large amplitude lower-hybrid waves excited by ion ring distributions we will consider the wave polarized in the plane perpendicular to the magnetic field and acts as a pump for the generation of sideband oblique ($k_\parallel \neq 0$) waves, $k_\parallel$ is the wavenumber of the sideband waves parallel to the ambient magnetic field B_z. In this case the total wave potential for lower-hybrid waves ϕ can be written in the form

$$\phi = \left[\phi_o + \phi_+ e^{i(\underline{k}_\perp \cdot \underline{r}_\perp + k_\parallel z - \omega t)} + \phi_- e^{-i(\underline{k}_\perp \cdot \underline{r}_\perp + k_\parallel z - \omega t)}\right] e^{i(\underline{k}_o \cdot \underline{r}_\perp - \omega t)} \quad (1)$$

where k_o and ω_o are the wavevector and frequency of the pump wave and $\phi_\pm$ are the Stokes and anti-Stokes sidebands with wavevectors $\underline{k}_o \pm \underline{k}$ where $\underline{k}$ is the modulation wavevector containing a component $k_\parallel$. We assume that this modulation is created by long wavelength magnetosonic waves that couple the pump wave ϕ_o to the lower-hybrid satellites $\phi_\pm$. Hence contrary to the usual treatment of the modulational instability of lower-hybrid waves in which the slow mode is associated only with density perturbations such as described by the ion-acoustic mode we will consider the case when the slowly varying low frequency mode is associated with the magnetosonic mode which will result in low frequency magnetic field modulations as well as density modulations. Due to the instability the magnetic field develops fine structure, such structure is due to the modulation of the magnetic field that has a characteristic space scale of about 10 Debye lengths perpendicular to the magnetic field direction and very prolonged along the field lines forming cigar shaped structures which contain the intense lower-hybrid waves. The equations describing the modulational instability of a high frequency lower-hybrid mode coupled with a low frequency magnetosonic mode are given by

$$-\frac{2i}{\omega_{LH}}\frac{\partial}{\partial t}\Delta\phi - R^2\Delta^2\phi + \frac{m_i}{m_e}\frac{\partial^2\phi}{\partial z^2} = i\frac{m_i}{m_e}\frac{\omega_{LH}}{\omega_{ce}}\left[\frac{\partial\phi}{\partial x}\frac{\partial\delta n}{\partial y} - n_o\frac{\partial\phi}{\partial x}\frac{\partial}{\partial x}\frac{\delta B}{B_o}\right] \tag{2}$$

for the high frequency lower-hybrid potential ϕ, and coupled to the low frequency magnetic field δB and density perturbations δn by the $\underline{\nabla}.(n_e\underline{v}_e)$ nonlinearity in the electron continuity equation and

$$\Delta\delta B - \frac{1}{v_A^2}\delta B = -\frac{4\pi e n_o c}{B_o^2\omega_{LH}^2}\frac{\partial}{\partial t}\left[\frac{\partial\phi}{\partial x}\frac{\partial}{\partial y} - \frac{\partial\phi}{\partial y}\frac{\partial}{\partial x}\right]\Delta\phi \tag{3}$$

for the low frequency magnetosonic mode coupled to the higher frequency lower-hybrid mode by the ponderomotive force due to the vector nonlinearity $[\nabla\phi \times \nabla\phi]$. The equation connecting the density and magnetic field fluctuations for magnetosonic waves is the usual one given by

$$\left(\frac{\partial^2}{\partial t^2} - c_s^2\Delta\right)\delta n = v_A^2\frac{n_o}{B_o}\Delta\delta B \tag{4}$$

In equations (2)-(4) $\Delta \approx \frac{\partial^2}{\partial x^2} + \frac{\partial^2}{\partial y^2}, \omega_{LH} = \omega_{pi}(1+\omega_{pe}^2/\omega_{ce}^2)^{\frac{1}{2}}, \omega_{pe}, \omega_{pi}, \omega_{ce}$ are the electron, ion and electron cyclotron frequencies respectively, R is the dispersion term given by $R = \left(eT_i/\omega_{LH}^2 m_i + 2T_e\omega_{pe}^2/\left(\omega_{ce}^2 m_e\left(\omega_{pe}^2+\omega_{ce}^2\right)\right)\right)^{\frac{1}{2}}$ and m_e and m_i are the electron and ion mass.

For a sufficiently strong pump wave equations (1-4) can be solved to yield the following threshold for the electric field intensity

$$\frac{k_{oy}}{k_y}\frac{c^2|E_o|^2}{B_o^2} > \frac{\omega_{LH}^2}{k^2}\frac{m_i}{m_e}\frac{k_\parallel^2}{k^2} \tag{5}$$

with the maximum growth rate being given by

$$\gamma_{MAX} = \frac{\sqrt{3}}{2^{2/3}}\left[\omega_{LH}\frac{k_{oy}}{k_y}[\underline{k}_o \times \underline{k}]_z^2\frac{c^2|\phi_o|^2}{B_o^2}\right]^{1/3} \tag{6}$$

With the development of the modulational instability a cascade to larger wavenumbers results, leading to wave collapse. As a result of wave collapse, direct wave energy transfer to the electrons and ions takes place. In order to test the wave collapse model for particle acceleration of $2\frac{1}{2}$−D particle-in-cell code was used to simulate ion-ring relaxation. An analysis of the spatial structure of the density perturbations, electric field envelope and magnetic field structure reveals the presence of wave collapse, it is within the collapsing nonlinear wavepackets that strong acceleration is found. Figure 1a,b,c represents the spatial caviton like structures produced as a result of wave collapse. Not only do we have low frequency density perturbations (Fig.1a) coupled to the high frequency electric field (Fig.1c), but we have coupling to low frequency magnetic field fluctuations (Fig.1c) which are magnetosonic modes propagating almost perpendicular to the magnetic fields. The lower-hybrid caviton structures are cigar shaped aligned with the major axis almost parallel to $\underline{B}_o$. This is in contrast to Langmuir cavitons which are pan-caked shaped with the minor axis parallel to $\underline{B}_o$.

References

1. K Akimoto, K Papadopoulos and D B Winske, *J. Plasma Physics*, 34, 445, (1985)

2. J B McBride, E Ott, P B Jay and J H Orens, *Phys. Fluids*, 157, 2367, (1972)

3. G Paschmann, N Schopke, S J Bame and J T Gosling, Geo. Res. Lett., 9, 881, (1982)

4. R Bingham, V D Shapiro, V N Tsytovich, U de Angelis, M Gilman and V I Shevchenko, *Phys. Fluids*, B3, 1728, (1991)

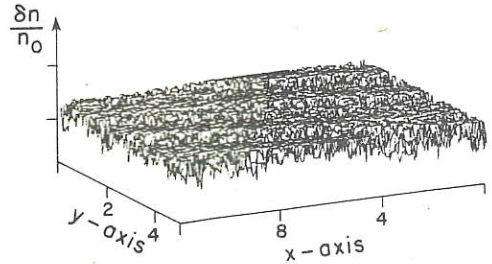
δn/n0
2
4
y-axis
8
4
x-axis

(a)

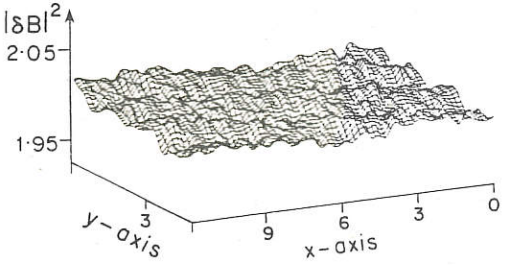
|δB|2
2·05
1·95
3
y-axis
9
6
3
0
x-axis

(b)

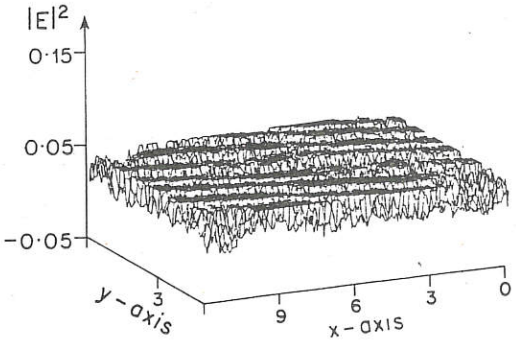
|E|2
0·15
0·05
-0·05
3
y-axis
9
6
3
0
x-axis

(c)

EMPIRICAL SPECTRAL CODES FOR TOKAMAK TURBULENCE

Gary R. Smith, Ronald H. Cohen, Eric D. Boerner, and Andris M. Dimits
Lawrence Livermore National Laboratory
Livermore, California 94550, USA

ABSTRACT

Solutions of a fluid model of tokamak turbulence are subjected to principal component analysis (PCA). The spatial structures in the fields can be described with a small number of principal components. Those principal components are used as a basis set for successful calculation of the turbulence evolution with a much smaller set of equations than used in conventional simulation.

DYNAMICAL EQUATIONS

A two-dimensional, zero-Larmor-radius, fluid model of tokamak turbulence driven by ∇T_i is described by the following equations for normalized perturbations of electrostatic potential φ, parallel flow velocity v, and ion temperature T./1/

$$\begin{aligned}
\frac{\partial \varphi}{\partial t} &= -\frac{1}{\eta_i}\frac{\partial \varphi}{\partial y} - s\frac{\partial v}{\partial y} \\
\frac{\partial v}{\partial t} &= -\left(\frac{\partial \varphi}{\partial x}\frac{\partial}{\partial y} - \frac{\partial \varphi}{\partial y}\frac{\partial}{\partial x}\right) v - s\frac{\partial T}{\partial y} - 2s\frac{\partial \varphi}{\partial y} \\
\frac{\partial T}{\partial t} &= -\left(\frac{\partial \varphi}{\partial x}\frac{\partial}{\partial y} - \frac{\partial \varphi}{\partial y}\frac{\partial}{\partial x}\right) T - \frac{\partial \varphi}{\partial y} - (\Gamma - 1)s\frac{\partial v}{\partial y}
\end{aligned} \tag{1}$$

Here, η_i is the ratio of the density gradient scale length to the ion-temperature gradient scale length, Γ is the ratio of specific heats, and the shear parameter $s = (x - 0.5)/r_s$, with r_s denoting the shear length. Throughout this paper we take $\eta_i = 4$, $\Gamma = 5/3$, and $r_s = 1/3$. These equations are solved on the domain $0 \le x \le 1$, $0 \le y \le 1$, with φ, v, and T all set to zero at the radial boundaries ($x = 0$ and $x = 1$) and with periodic boundary conditions at the poloidal boundaries ($y = 0$ and $y = 1$). Diffusion terms like

$$D_x\frac{\partial^2 \varphi}{\partial x^2} + D_y\frac{\partial^2 \varphi}{\partial y^2} - D_{4x}\frac{\partial^4 \varphi}{\partial x^4} - D_{4y}\frac{\partial^4 \varphi}{\partial y^4}$$

are added to the right-hand sides of Eqs. (1) to suppress short-wavelength modes that can cause numerical instability.

The time evolution of the variance of one of the fields is shown in Fig. 1. After initialization at low amplitude, the fields grow and enter a turbulent but transient phase. Then, transition to a higher amplitude phase occurs; the solution persists in this high phase indefinitely.

PRINCIPAL COMPONENT ANALYSIS

We represent a data set in terms of time-varying amplitudes of certain spatial patterns

$$z(x,t) = \sum_{j=1}^{m} a_j(t)\, e_j(x).$$

In contrast to other representations, PCA provides patterns and amplitudes that both satisfy orthogonality conditions:

$$\sum_{x} e_j(x)\, e_k(x) = \delta_{jk}$$

$$\sum_{t} a_j(t)\, a_k(t) = \ell_j\, \delta_{jk}.$$

The eigenvalue ℓ_j gives the variance of the projection of $z(x,t)$ onto e_j. Following Preisendorfer/2/ and Sirovich/3/, we find the ℓ_j and the $a_j(t)$ as eigenvalues and eigenvectors of the spatial covariance matrix

$$T(t,t') = \sum_{x} z(x,t)\, z(x,t').$$

The spatial pattern associated with each amplitude $a_j(t)$ is given by

$$e_j(x) = \sum_{t} z(x,t)\, a_j(t).$$

The results of PCA on 101 time samples from the high phase of the solution shown in Fig. 1 gives a 4-term representation of the fields φ, v, and T that captures almost 95% of the variance; 14 terms capture over 99%. The first two terms each capture about 44% and together represent a travelling wave with the pattern shown in Fig. 2.

EMPIRICAL SPECTRAL CODES

From the dynamical equations and the spatial patterns $e_j(x)$ found by PCA we can build an empirical spectral code (ESC)./4/ The patterns are used as a basis set for a Galerkin procedure, just as Fourier modes would be used

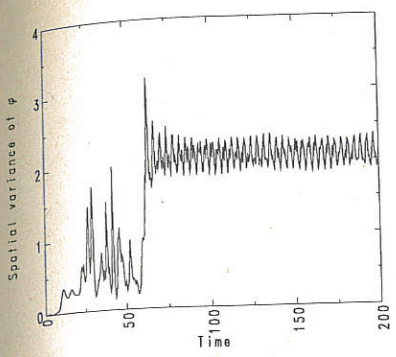

Fig. 1. Time evolution of the (arbitrarily normalized) spatial variance of the potential φ from solution of Eqs. (1).

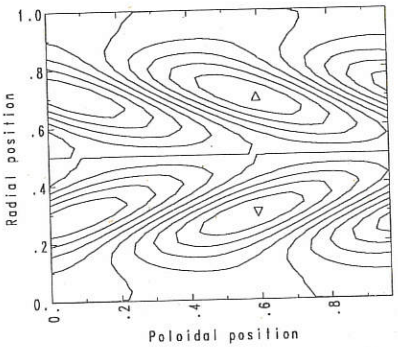

Fig. 2. Spatial pattern of the potential φ for the first principal component, computed from 101 time samples in $80 \le t \le 130$.

in building a conventional spectral code, to build an ESC that solves a set of partial differential equations by advancing time-evolution equations for the amplitudes $a_j(t)$. For a quadratically nonlinear system, like Eqs. (1), the time-evolution equations take the form

$$\dot{a}_\ell = \sum_n f_1(\ell, n)\, a_n(t) + \sum_{n,m} f_2(\ell, n, m)\, a_n(t)\, a_m(t) + f_3(\ell). \qquad (2)$$

To these equations we add damping of the form $-c_\ell\, a_\ell$. The damping rate c_ℓ depends on ℓ, the index of the N principal components (which are ordered from most to least variance captured), as follows: $c_\ell = 0$ for $\ell \le N - N_{\rm damp}$; otherwise,

$$c_\ell \propto (\ell - N + N_{\rm damp})^\gamma, \text{ with } \exp(-c_N \tau) = \epsilon.$$

A run of the empirical spectral code yields results shown in Figs. 3 and 4. With $N = 50$ and damping parameters $N_{\rm damp} = 30$, $\gamma = 2$, $\epsilon = 0.2$, and $\tau = 0.5$, the time evolution computed from the empirical spectral equations agrees in a statistical sense with the evolution obtained by conventional simulation (Fig. 3). The empirical spectral calculation generates fields with the same spectrum of principal-component amplitudes seen in the conventional-simulation data (Fig. 4).

Future investigations will perform PCA on solutions of other turbulence models and determine the utility of empirical spectral codes.

ACKNOWLEDGMENTS

Work performed for the U. S. Department of Energy by Lawrence Livermore National Laboratory under contract W-7405-ENG-48.

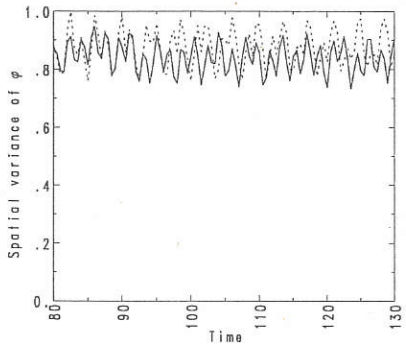

Fig. 3. Time evolution of the spatial variance of φ from conventional (dashed) and empirical-spectral (solid) integration.

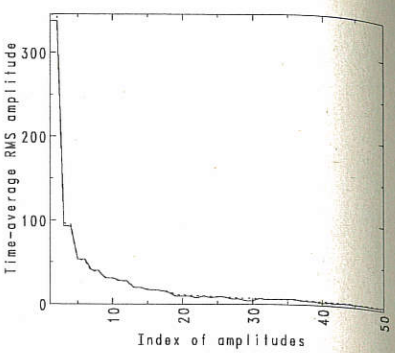

Fig. 4. Spectrum of amplitudes, averaged over $80 \leq t \leq 130$, from PCA of conventional simulation data (dashed) and from integration of the amplitude equations (2).

REFERENCES

/1/ A. M. Dimits, J. F. Drake, P. N. Guzdar, and A. B. Hassam, *Phys. Fluids B* **3**, 620 (1991).

/2/ R. W. Preisendorfer, *Principal Component Analysis in Meteorology and Oceanography* (Elsevier, Amsterdam, 1988).

/3/ L. Sirovich and H. Park, *Phys. Fluids A* **2**, 1649 (1990).

/4/ E. N. Lorenz, "Empirical orthogonal functions and statistical weather prediction," Sci. Rept. No. 1, Statistical Forecasting Project, M.I.T. Dept. of Meteorology, 1956.

FREQUENCY AND HEATER POWER DEPENDENCY OF RF GENERATED LANGMUIR TURBULENCE

A. Hanssen and E. Mjølhus
Institute of Mathematical and Physical Sciences, University of Tromsø
N-9000 Tromsø, Norway

Recently, experimental studies of Langmuir turbulence generated by a powerful radio wave transmitted from ground onto the ionospheric plasma, has been performed with remarkable simultaneous spatial, spectral, and temporal resolution /1,2/. This promises a possibility of very detailed comparison with elaborate theoretical models of electromagnetically driven Langmuir turbulence. Within this context of ionospheric experiments, the theoretical interpretation has recently become quite controversial /3,4/. The traditional view has been to expect a cascade, starting with a parametric decay instability (PDI) of the incident electromagnetic wave into a Langmuir wave and an ion acoustic wave. This scenario was developed within a weak turbulence approximation long ago /5/. Improved height resolution of the experiments /6/ showed already long ago that the radar echoes obtained at the Arecibo observatory, Puerto Rico, came from a height at which the Langmuir wave dispersion relation for the ambient plasma was not satisfied; instead, the echoes appeared to come from the reflection region $\omega = \omega_{pe}$ of the O-polarized incident radio wave. Numerical studies of a two-dimensional model (corresponding to that to be formulated below) with parameters corresponding to the reflection region /7/, leads to a "strong" (or "cavitating") Langmuir turbulence consisting of a large number of localized cycles of *nucleation* (due to cavity resonance and trapping of Langmuir wave field in density cavities), Langmuir *collapse* /8/, and *burnout*.

Here we wish to report a numerical study /9/ of the turbulence which predicts that both of these scenarios can coexist in the ionosphere, though at different heights. The model equations that were solved numerically, were one-dimensional Zakharov equations modified to include a parametric drive, and including collisional as well as Landau damping. The one-dimensional formulation represents the nucleation process well, although it does not maintain the ultimate inertial collapse. Comparisons indicate that spectral features are similar in the one- and two-dimensional models.

In non-dimensional form, the equations read

$$\begin{aligned} &[i(\partial_t + \nu_e *) + (\Delta\Omega - n) + \partial_x^2]\, E = nE_0 - \langle nE \rangle \\ &(\partial_t^2 + 2\nu_i * \partial t - \partial_x^2) n = \partial_x^2 |E + E_0|^2 \,. \end{aligned} \tag{1}$$

Since the interpretation of these equations is well-known, we only mention that E_0 represents the driving electric field, and that the operators $\nu_e *$ and $\nu_i *$ were designed to include both collisional and collisionless damping. The non-dimensional parameter

$$\Delta\Omega = \frac{3}{2\eta} \frac{M}{m} (\omega - \omega_{pe})/\omega_{pe} \tag{2}$$

($\eta = 1 + 3T_i/T_e$) represents the mismatch between the applied frequency ω and the local plasma frequency ω_{pe}. We have studied the properties of the solutions to (1) as $\Delta\Omega$ is varied. Assuming that the electron density of the ionosphere varies monotonically, $\Delta\Omega$ can be interpreted as height relative to the critical height $\omega = \omega_{pe}$, moving downwards at increasing $\Delta\Omega$. In each case, we solve (1) at constant $\Delta\Omega$, and interpret the result as a characteristic Langmuir turbulence at the corresponding height. As should be expected, we found that the turbulence is cascade dominated at large $\Delta\Omega$ and cavitation dominated at small values of $\Delta\Omega$. A good diagnosis of the nature of the turbulence is provided by calculating the ratio of the collisionless (i.e. large wave number) energy absorption to the total absorption. For the cascade dominated turbulence, the absorption is collisional, while for the cavitation dominated turbulence, the absorption is mainly collisionless. The parameter dependence shown in fig. 1 has been obtained from a large number of numerical runs.

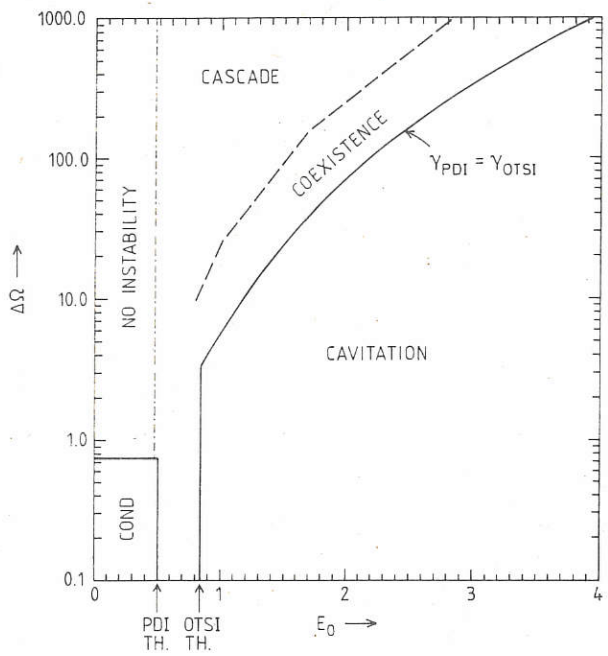

Fig. 1: Parameter plane, showing division between cascade-dominated and cavitation-dominated Langmuir turbulence. At the dashed curve, 50% of the energy dissipation is noncollisional. Above, this fraction goes rapidly to zero, while in the cavitation region below, it dominates. The region COND designates the Langmuir condensate. The thresholds for PDI and OTSI are indicated. The electron collision frequency: $\nu_e = 0.7$ (non-dimensional).

The curve dividing between the two regions shows a good fit to an analytic condition obtained by requiring that the growth rate of the OTSI equals that of the PDI; thus, the cavitating turbulence can be seen as the fully developed stage of the OTSI. In the cascade region, the details deviate substantially from the weak turbulence approximation /5/ (WTA): the number of cascades is smaller, and the development of new cascade lines as the driving parameter E_0 is increased, stops far before the Langmuir condensate is reached. This is qualitatively consistent with the experiments /3/, where no more than 3 lines are seen (similar to well-known hydrodynamic experiments /10/). When E_0 is further increased, the k (or modal) spectrum becomes continuous. When E_0 passes the threshold to cavitating turbulence, the modal spectrum extends to large k. In a transition region, coexistence of cascading and cavitating turbulence is found /11/.

In /9/, detailed predictions of radar spectra are described. In particular, in experiments performed in Tromsø using the EISCAT radar system /3/, it should be possible to observe characteristic spectra from both types of turbulence simultaneously, from separated heights, using the recent height-resolving techniques /2/.

References

/1/ F.T. Djuth, M.P. Sulzer, and J.H. Elder, Geophys. Res. Lett. **17**, 1893 (1990)
/2/ J.A. Fejer, M.P. Sulzer, and F.T. Djuth, J. Geophys. Res. **96**, 15985 (1991)
/3/ P. Stubbe, H. Kohl, and M.T. Rietveld, J. Geophys. Res., (March 1992)
/4/ D.F. DuBois, A. Hanssen, and H.A. Rose, Comment on /3/, J. Geophys. Res., (March 1992)
/5/ F.W. Perkins, C. Oberman, and E.J. Valeo, J. Geophys. Res. **79**, 1478 (1974)
/6/ D.B. Muldrew and R.L. Showen, J. Geophys. Res. **82**, 4793 (1977)
/7/ D.F. DuBois, H.A. Rose, and D. Russell, J. Geophys. Res. **95**, 21221 (1990)
/8/ V.E. Zakharov, Sov. Phys. JETP **35**, 908 (1972)
/9/ A. Hanssen, E. Mjølhus, D.F. DuBois, and H.A. Rose, J. Geophys. Res., to appear (1992)
/10/ J.P. Gollub and H.L. Swinney, Phys. Rev. Lett. **35**, 927 (1975)
/11/ D.F. DuBois, H.A. Rose, and D. Russell, Phys. Rev. Lett. **66**, 1970 (1991)

Nonlinear Modulational Instability of Whistler Waves

V.I. Karpman[1], J.P. Lynov, P. Michelsen and J. Juul Rasmussen
Association EURATOM-Risø National Laboratory,
Optics and Fluid Dynamics Dept., Risø, DK-4000 Roskilde, Denmark

The nonlinear evolution of the modulational instability (MI) of whistler waves propagating along a constant external magnetic field $\mathbf{B}_0 \parallel \hat{\mathbf{z}}$ is investigated numerically. We have considered the two most unstable branches of the modulational instability in which the whistlers are coupled to fast magnetosonic (FMS) waves and slow magnetosonic (SMS) waves, respectively /1/. For each branch our investigations are based on a numerical solution of a reduced set of equations /2,3/ in two spatial dimensions.

First we consider the interaction of whistler waves and fast magnetosound (FMS) waves which is described by the coupled equations /2,3/:

$$i(\psi_t + v\psi_z) + \tfrac{1}{2}(s_1\psi_{xx} + s_2\psi_{zz}) = C_1\nu\psi \tag{1}$$

$$\nu_{tt} - C^2\nabla^2\nu = C_2|\psi|^2_{xx}, \qquad b \approx \nu \tag{2}$$

where $\psi = (E_x - iE_y)/E_0$ is the normalized slowly varying whistler wave electric field; $\nu = (n - n_0)/n_0$, n is the slowly varying density; $b = (B_z - B_0)/B_0$, B_z is the slowly varying ambient magnetic field. The spatial coordinates are normalized with k_0, the wavenumber of the whistler wave, and time is normalized with the whistler wave frequency ω. The coefficients in (1,2) are expressed in terms of $u = \omega/\omega_c$, where ω_c is the electron cyclotron frequency: $v = v_g/v_{ph} = 2(1-u)$, $s_1 = 1 - 2u$, $s_2 = 2(1-u)(1-4u)$, $C = c_A/v_{ph} = [(m_e/m_i)/(u(1-u))]^{1/2}$, $C_1 = u$, $C_2 = uC^2/(1-u)$. Here v_{ph} and v_g are the whistler wave phase velocity and group velocity, respectively, and c_A is the Alfven velocity.

From the dispersion relation for the MI obtained by linearizing Eqs. 1-2 it is found that the growth rate of the MI is maximum for modulation wavenumbers, K, satisfying $KC - K_z v = -\frac{1}{2}(s_1K_x^2 + s_2K_z^2)$ /3,4/. The corresponding value of the modulation frequency, $\Omega = \Omega_0 + i\gamma$ is approximately given as

$$\Omega_0 \approx KC, \quad \gamma \approx [(C_1C_2)^{1/2}/(2KC)^{1/2}]K_x\psi_0. \tag{3}$$

The condition for the maximum growth rate coincides with the the resonant condition for the decay of whistler waves into a fast magnetosonic wave and another whistle wave. We define the ratio $\alpha = K_z/K_x$ and denote the value of α for which this resonance condition is satisfied by α_c. For typical parameters we have that $\Omega_0 >> \gamma$ and the modulation wave vector, $\mathbf{K}$, is almost perpendicular to the whistler wave vector, $\mathbf{k}_0$, i.e. $\alpha \ll 0$.

Equations 1–2 were solved numerically in a two-dimensional domain of size $L_x \times L_z$ with periodical boundary conditions. We employed a fully de-aliased spectral method /5/. As the initial conditions we used a modulation around the stationary solution of Eqs. 1– 2 (i.e. $\psi = \psi_0$, $\nu = 0$), which is a standing wave in the x-direction and a propagating wave in the z-direction with wavenumbers $K_{x0} = 2\pi/L_x$, $K_{z0} = 2\pi/L_z$. Furthermore, the initial modulation is chosen to coincide with the linear evolution of the modulational instability /4/.

In general we found that the long time evolution of the modulational instability proceeds in a quasi–recurrent manner at least for relatively low amplitudes. That is, we obtained a series of modulation and demodulation cycles with a slow spreading of the energy to higher

[1]Permanent address: IZMIRAN, Academic City, Moscow Region, 142092, USSR

modulation wave numbers. As the carrier wave amplitude, ψ_0, was increased the recurrence periodes become fewer associated with a faster spreading of the energy to the higher mode numbers, i.e. the randomization becomes more effective. These cases are treated in detail in Ref. 4. Subsequent calculations have revealed that the detailed evolution is strongly dependent on the exact direction of the initial modulation, i.e. of the value of α, for a given amplitude and modulation wavenumber. For $\alpha = \alpha_c$ we observed almost three recurrence periodes before a significant spreading of the energy to the higher modes (for $\psi_0 = 0.02$, $K = 0.19$). For $\alpha > \alpha_c$ the recurrence becomes significantly better and for $\alpha = 1.02\alpha_c$ more than five clear recurrence periodes are observed. For $\alpha < \alpha_c$, on the other hand the spreading to the higher modes proceed considerably faster: already for $\alpha = 0.99\alpha_c$ only one recurrence period is observed. The dependence of the other parameters for fixed α was far more weak.

An example of a persistent recurrent behavior is shown in Fig. 1, with $\alpha = 0.101 (= 1.02\alpha_c)$. A perfect recurrence is observed for the five recurrence periodes shown. During this time the energy is mainly residing in the fundamental modes as seen in Fig. 1b, where we show the evolution of the amplitude spectrum during the fourth recurrence cycle. This evolution may be described by a simplified model based on a general Hamiltonian formulation of Eqs. 1–2, which is truncated to involve only few modes /3,6/.

Secondly we consider the interaction of whistlers and slow magnetosonic (SMS) waves. The equation for the evolution of the whistler wave amplitude may still be written in the form of Eq. 1, but now $C_1 = -(1-u)$. Instead of Eq. 2 the density perturbation is governed by

$$\nu_{tt} - C_s^2 \nu_{zz} = C_2 |\psi|^2_{zz} \tag{4}$$

The evolution of the magnetic field perturbation is given by ν and ψ see Ref. 3. Here $C_s = c_s/v_{ph}$, $C_2 = -c_A^2/v_{ph}^2$, and c_s is the ion sound velocity. From the dispersion relation for the MI obtained from Eqs. 1 and 4 it is found that for the unstable branch $K_z v \approx \pm\frac{1}{2}(s_1 K_x^2 + s_2 K_z^2)$ /3/. The frequency of the unstable branch is approimately given as

$$\Omega_0 \approx \frac{1}{2}(C_1 C_2 K_z^2 \psi_0^2)^{1/3}, \quad \gamma \approx \frac{\sqrt{3}}{2}(C_1 C_2 K_z^2 \psi_0^2)^{1/3}. \tag{5}$$

Also for this case it is seen that the modulation is almost perpendicular to the wave vector, $\mathbf{k}_0$, but here $\Omega_0 \approx \gamma$.

We have solved Eqs. 1 and 4 numerically for different parameters on the unstable branch in similar way as described above for the Eqs. 1-2. We have in no case observed a recurrent behavior and the energy was constantly spreading to the higher mode numbers. An example for a low amplitude case is shown in Fig. 2. The behavior agrees well with the behavior found in Ref. 1, where a complete set of equations was used to study the SMS-branch of the MI. In the initial phase the modulation grows in accordance with the linear predictions. The modulation has a spatial structure resembling cells streched along the z-axis with the maximum of $|\psi|^2$ sligthly in front of the maximum of ν and almost no propagation along z. At the termination of the linear growth the phase shift between the maximum of $|\psi|^2$ and the maximum of ν vanishes. The subsequent oscillations in the maximum of $|\psi|^2$ (Fig. 2a) seems to be correlated with oscillations in the phase shift between the maximum of $|\psi|^2$ and the maximum of ν. In this stage we see from Fig. 2b that the energy is spreading to higher mode numbers with the tendency that the spreading proceeds mainly along the K_z-direction, i.e. the spreading proceeds along the unstable branch in the $K_z - K_x$–plane. Accordingly the cells in the spatial structure of $|\psi|^2$ tend to shrink in particular along the z-axis. Calculations with higher initial amplitude show a similar evolution with a faster spreading of the energy. We thus expect that the energy ultimately cascades to arbitrary high wave-numbers, resulting in a turbulent wave field.

The marked difference between the evolution of the SMS branch of the MI and the evolution of the FMS branch, where the energy spreads relatively slowly in a quasi-recurrent manner, is related to the linear behavior of the MI for the two branches. For the FMS branch the MI is a periodic instability with $\Omega_0 \gg \gamma$ (Eq. 3) and a significant propagation along the z-direction, while the MI of the SMS-branch is an aperiodic instability with $\Omega_0 \leq \gamma$ (Eq. 5) and almost no propagation.

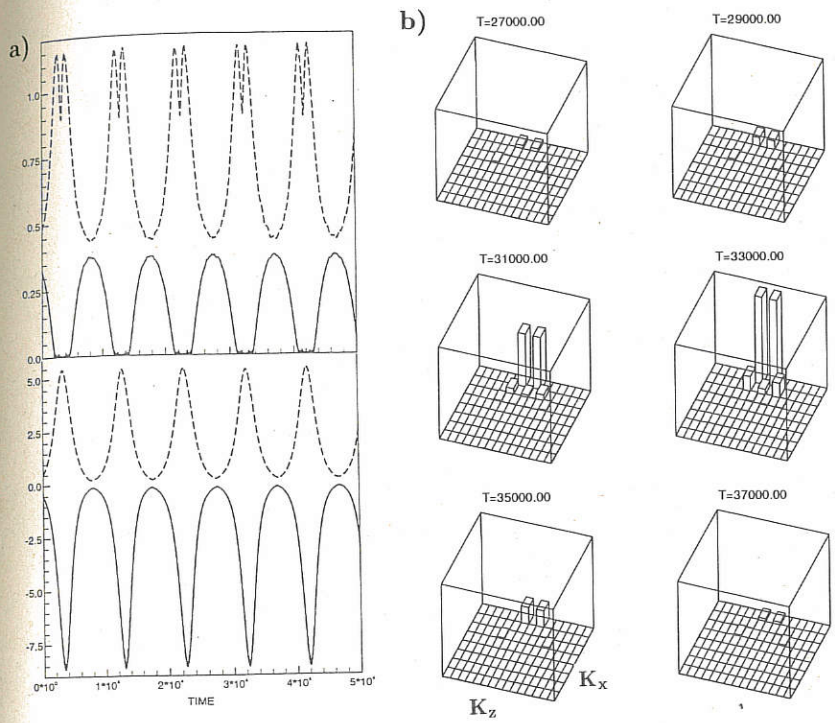

Fig. 1: Modulational instability of whistlers interacting with FMS waves. a) The temporal evolution of the maximum (dashed line) and minimum (full line) of $|\psi|^2$ (upper panel, the vertical scale is in units of 10^{-3}) and of ν (lower panel, the vertical scale is in units of 10^{-2}) b) The development of amplitude spectra of the density fluctuations ($\nu(\mathbf{K})$) during a recurrence period. 16×16 modes are used in the calculation. The parameters are $\psi_0 = 0.02$, $u = 0.4$, $K = 0.19$, and $\alpha = 0.101$.

References

/1/ V.I. Karpman and A.G. Shagalov, J. Plasma Physics **38**, 155 (1987); J. Plasma Physics **39**, 1 (1988).
/2/ V.I. Karpman and L. Stenflo, Phys. Lett. A **127**, 99 (1988).
/3/ V.I. Karpman, Phys. Lett. A **136**, 216 (1989); ibid. p. 221.
/4/ V.I. Karpman, F.R. Hansen, J.P. Lynov, H.L. Péseli and J. Juul Rasmussen Phys. Rev. Lett. **64**, 890 (1990); in: Nonlinear World, World Scientific, Singapore 1990 (eds. Bar'yakhtar et al.) Vol. 2, pp. 882- 897.
/5/ E.A. Coutsias, F.R. Hansen, T. Huld, G. Knorr and J.P. Lynov, Physica Scripta **40**, 270 (1989).
/6/ V.I. Karpman, A.G. Shagalov and J. Juul Rasmussen, Phys. Lett. A **147**, 119 (1990).

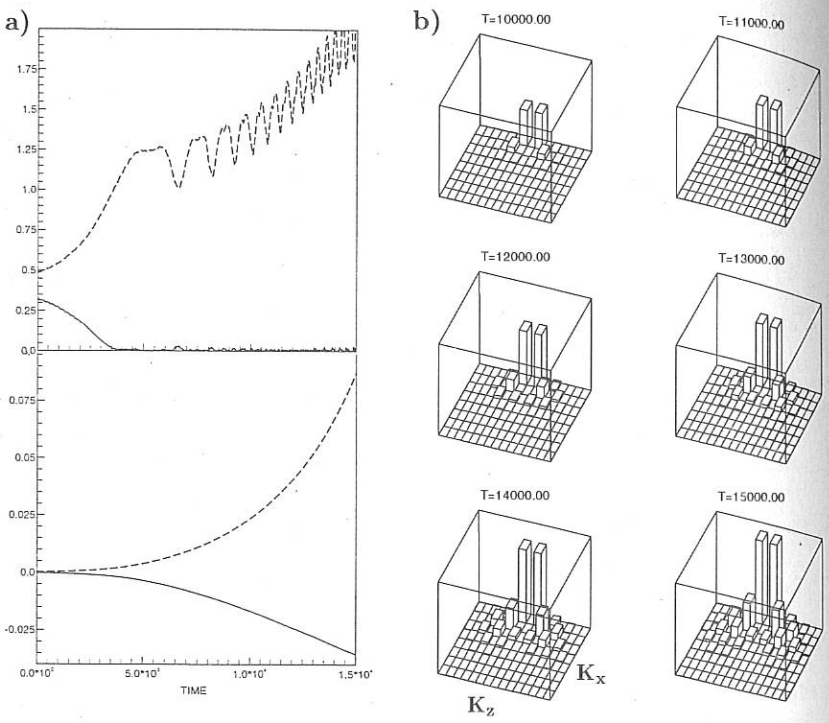

Fig. 2 Modulational instability of whistlers interacting with SMS waves. a) The temporal evolution of the maximum (dashed line) and minimum (full line) of $|\psi|^2$ (upper panel, the vertical scale is in units of 10^{-3}) and of ν (lower panel) b) The amplitude spectra of the density fluctuations ($\nu(\mathbf{K})$) during the later time of the growth $t \geq 10^4$. 16×16 modes are used in the calculation. The parameters are $\psi_0 = 0.02$, $u = 0.4$, $K = 0.364$, and $\alpha = 0.03$.

Low-Frequency Kinetic Structures in Plasma Quasiparticle Concept

O.H. Sitenko, P.P. Sosenko*

Institute for Theoretical Physics
Academy of Sciences of Ukraine, Kiev, 252130, Ukraine

1. Introduction. Considerable theoretical efforts have been undertaken to establish the existence of nonlinear localized structures in plasmas [1-3], similar to vortices in fluids and atmosphere. Vortex-like solutions have been found for various, mostly hydrodynamic, plasma models, and the conditions for their existence have been obtained in the form of dispersion relations complimentary to the dispersion relations for linear waves. These relations can be formulated as equations for zeroes of the linear dielectric permittivity. Real solutions for the wavenumber as a function of the phase velocity and plasma parameters correspond to waves, while imaginary solutions are associated with localized structures. With regard to the latter, there are several issues which seem to be not fully appreciated and explained.

The first one concerns the relevance and the significance of the linear dielectric permittivity describing strongly nonlinear plasma oscillations. Another interesting issue is the possible existence of localized structures with the size comparable to characteristic kinetic length scales, such as particle Larmor radii, and the significance of weak but finite kinetic effects for the localized structures predicted within hydrodynamic-type plasma models.

The primary goal of this report is to analyze these important issues. This requires kinetic description of the effects of strong nonlinear interaction between low-frequency oscillations within the context of renormalized plasma electrodynamics [4-6]. It is demonstrated that basic equations of the renormalized plasma electrodynamics admit solutions describing nonlinear localized structures with kinetic scale lengths. General dispersion relations are derived for such structures with regard to kinetic effects.

2. Basic Equations. Let us start from the renormalized transport equation for the nonlinear charge density ρ_{Na} of a particular plasma component [4,5]:

$$(\tilde{\partial}_t + \vec{v}_E \cdot \vec{\nabla}) \rho_{Na} = \tilde{\partial}_t \rho_a^{(2)} . \qquad (1)$$

Here the potential approximation is adopted, $\vec{v}_E \equiv (c/B_0)\vec{b} \times \vec{\nabla}\Phi$ is an electric drift velocity, Φ is the potential of an electric field, $\vec{B}_0 \equiv B_0\vec{b}$ is the induction of an external magnetic field, c is the velocity of light in the vacuum, $\rho^{(2)}$ is a formal second iteration of the charge density (calculated from the formal second iteration of the Vlasov distribution function), $\tilde{\partial}_t \equiv \partial_t + \vec{V}_g \cdot \vec{\nabla}$, $\vec{V}_g$ is the gravitational drift velocity introduced as usual to model the inhomogeneity of the external magnetic field. The electric field potential is determined self-consistently from the Poisson equation:

$$\hat{\varepsilon}\triangle\Phi = -4\pi \sum_a \rho_{Na} , \qquad (2)$$

formulated in terms of the operator $\hat{\varepsilon}$ of a linear dielectric permittivity and the nonlinear charge densities of plasma components. Equation (2) can be interpreted

also as a definition of the nonlinear charge density. The latter accounts for nonlinear contributions into a plasma charge density ρ: $\rho_N = \rho - \rho^{(0)} - \rho^{(1)}$, where $\rho^{(0)}$ is a background charge density, and $\rho^{(1)}$ is a formal first iteration of the charge density (calculated from the formal first iteration of the Vlasov distribution function). In the weak nonlinearity/turbulence theory $\rho^{(1)}$ and $\rho^{(2)}$ describe linear and quadratic plasma responses, respectively.

3. Localized Structures. In the limit of cold particles, Eqs. (1) and (2) reduce to the well-known equations (e.g., see Ref. [5]), which describe nonlinear drift (convective cell) oscillations and admit localized solutions [1,2] with the following dependence on time and coordinates:

$$\Phi(x, y, z, t) \equiv \Phi(x, y - ut - pz) \,, \tag{3}$$

where u and p are parameters, which may be related to plasma parameters. These solutions describe nonlinear structures in the plasma (vortices, etc.) with characteristic hydrodynamic scales. Therefore, let us look for the solutions of Eqs. (1) and (2) with the specified dependence (3). It can be proved that in the case of oscillations, which are small scale with regard to the inhomogeneity length scale of the background Vlasov distribution function and which are characterized by dependence (3), $\rho^{(2)} = 0$. Then, the solution of Eq. (1) is an arbitrary function P of the characteristic $\Phi - B_0 \tilde{u} x/c$ ($\tilde{u} \equiv u - V_{gy}$).

Let us consider solutions corresponding to localized and finite at infinity oscillations of the potential and the nonlinear charge density. The requirement that the solution is to be localized enables one to determine the arbitrary function after considering the limit $y \to \infty$: $P = 0$, as Φ and ρ_N tend to zero in this limit. The solution of Eq. (2) can be represented naturally as a decomposition over the eigenfunctions of the laplacian. The latter appears to be two dimensional as $\partial_z = -p\partial_y$. The relevant eigenfunctions do not satisfy the requirements to be localized and finite simultaneously. This difficulty could be circumvented if the arbitrary function could take different values in different space regions, which implies an additional dependence of the solution of the continuity equation (1) on coordinates:

$$\rho_N = \sum_{i=1}^{j} P^{(i)}(\Phi - B_0 \tilde{u} x/c)\, \theta(R^{(i)}(eta) - r) \,, \quad \theta(R) \equiv \int_{-\infty}^{R} dr\, \delta(r) \tag{4}$$

(here cylindrical coordinates are introduced as usual, $r^2 = x^2 + (y - ut - pz)^2, cos\eta = x/r$). According to Eq. (4), the plane (r, η) is divided into $j+1$ regions by the boundary curves $R^{(i)}(\eta)$: $R^{(i+1)}(\eta) > R^{(i)}(\eta)$. Clearly, Eq. (1) has a solution in the form (4) if the boundaries satisfy the following equation: $(\tilde{u}\partial_y - \vec{v}_E \cdot \vec{\nabla})\theta(R^{(i)}(\eta) - r) = 0$. This equation can be integrated to obtain the boundary conditions:

$$\Phi(R^{(i)}(\eta), \eta) = \Phi_0^{(i)} + B_0 \tilde{u} R^{(i)}(\eta)\, cos\eta/c \,, \tag{5}$$

where $\Phi_0^{(i)}$ are constants. If the nonlinear charge density is assumed to be continuous on the boundaries, then $P^{(i)}(\Phi_0^{(i)}) = 0$, however, such a requirement

seems to be unnecessary in general. Substitution of Eq. (4) into Eq. (2) yields a closed equation for the electric field potential, which is to be supplemented with the boundary conditions (5).

4. Dispersion Relation in the Outer Region. In the outer region of the plane (r,η), $r > R(\eta) \equiv max_a R_a^{(j)}(\eta)$, the potential is governed by a homogeneous equation: $\hat{\varepsilon}\triangle_\perp\Phi = 0$, where $\triangle_\perp \equiv \partial_x^2 + \partial_y^2 \approx \triangle$, when $\mid p \mid << 1$. In the case of dependence (3), one derives

$$\varepsilon(\vec{k},\omega) \;=\; \bar{\varepsilon}(k_\perp,u,p) \equiv 1 + \frac{1}{a_h^2 k_\perp^2} + \sum \frac{4\pi q^2}{m k_\perp^2} \int d\vec{v} \,\{\, [\, J_0^2(\frac{k_\perp v_\perp}{\Omega}) - 1\,] \,\frac{1}{v_\perp}\,\partial_{v_\perp} +$$

$$+\frac{1}{\Omega}\,\frac{1}{\tilde{u} - p v_\parallel}\, J_0^2(\frac{k_\perp v_\perp}{\Omega})\,[\,\partial_x - \Omega p \partial_{v_\parallel}\,]\,\}\; g_0(x, v_\parallel, v_\perp)\;. \qquad (6)$$

where the explicit expression [6] for the low-frequency dielectric permittivity is taken into account, and $\varepsilon(\vec{k},\omega)\Phi_{\vec{k}\omega}$ and $\Phi_{\vec{k}\omega}$ are the Fourier space-time representations for $\hat{\varepsilon}\Phi$ and Φ. In Eq. (6), a hot plasma component with the adiabatic distribution in the oscillation field, $\kappa_h^{(1)}(\vec{k},\omega) \equiv 1/a_h^2 k_\perp^2$ (a_h is the Debye radius for the hot component), is included explicitly, g_0 is the background Vlasov distribution (under the gyrokinetic change of variables), q and m are the charge and the mass of a particle, $\Omega \equiv qB_0/mc$, $J_n(z)$ is the Bessel function of an order n, the subscript $\parallel$ / $\perp$ is related to a vector component along/across $\vec{B}_0$, and the summation is over plasma components.

Taking into consideration the structure of the dielectric permittivity $\bar{\varepsilon}$ and the requirement that the potential is to be localized, one can look for the solution in the outer region in the form of the decomposition over eigenfunctions Φ_λ of the laplacian, with non-negative eigenvalues $1/\lambda^2$: $\triangle_\perp\Phi_\lambda = \Phi_\lambda/\lambda^2$. The representation of the Bessel function as an infinite series in powers of its argument squared and Eq. (2) yield the relation,

$$\bar{\varepsilon}(i/\lambda, u, p)/\lambda^2 \;=\; 0\;, \qquad (7)$$

between the parameters λ, u and p. Eq. (7) introduces the first dispersion relation for kinetic structures in the plasma. The second one will follow from the consideration of the inner region of the solution. The eigenfunction in the outer region can be represented as

$$\Phi_\lambda \;= \sum_n K_n\,(\frac{r}{\lambda})\,[\,A_{n\lambda}\,cos n\eta \;+\; B_{n\lambda}\,sin n\eta\,]\;, \qquad (8)$$

where $K_n(z)$ are McDonalds functions, $A_{n\lambda}$ and $B_{n\lambda}$ are constants of integration.

5. Dispersion Relation in the Inner Region. The potential in the inner region, $r < R(\eta)$, depends on the explicit form of $P_a^{(i)}$. Let us consider the simplest case of one arbitrary function. Then, the potential in the inner region satisfies the following equation: $\hat{\varepsilon}\triangle_\perp\Phi = -4\pi P(\Phi - B_0\tilde{u}x/c)$. The arbitrary function P can be expanded near the boundary, and the behavior of the potential in the inner region near the boundary can be determined from the solution of

a linear inhomogeneous equation: $\hat{\varepsilon}\triangle_\perp\Phi = -4\pi P_0 - 4\pi P_0'(\Phi - B_0\tilde{u}x/c - \Phi_0)$, where P_0 and P_0' stand for $P(\Phi_0)$ and $P'(\Phi_0)$.

It is convenient to represent the dielectric permittivity $\bar{\varepsilon}$ as an expansion in power series of $k_\perp^2$, with the first expansion term being denoted as $D_0(u,p)/k_\perp^2$, and to introduce a new function $\tilde{\Phi}$: $\Phi = \tilde{\Phi} + Yx + Z$, with coefficients Y and Z being determined from the requirement that $\tilde{\Phi}$ is to be the eigenfunction for the operator $\hat{\varepsilon}\triangle_\perp$. Thus, taking

$$Y = \frac{4\pi B_0\tilde{u}}{c}\,\frac{P_0'}{4\pi P_0' - D_0}\,, \quad Z = 4\pi\,\frac{\Phi_0 P_0' - P_0}{4\pi P_0' - D_0}\,, \tag{9}$$

one obtains: $\hat{\varepsilon}\triangle_\perp\tilde{\Phi} = -4\pi P_0'\tilde{\Phi}$. Similar to the solution for the potential in the outer region, one can represent $\tilde{\Phi}$ as a decomposition over the eigenfunctions $\tilde{\Phi}_\mu$ of the laplacian with negative eigenvalues, $-1/\mu^2$: $\triangle_\perp\tilde{\Phi}_\mu = -\tilde{\Phi}_\mu/\mu^2$, and derive a relation between the parameters μ, u and p:

$$\bar{\varepsilon}(1/\mu, u, p) = 4\pi\mu^2 P_0'\,, \tag{10}$$

which is the second dispersion relation for the low-frequency kinetic structures in the plasma. The eigenfunction in the inner region can be represented as

$$\tilde{\Phi}_\mu = \sum_n J_n\,(\frac{r}{\mu})\,[\,\tilde{A}_{n\mu}\,cosn\eta + \tilde{B}_{n\mu}\,sinn\eta\,]\,, \tag{11}$$

where $\tilde{A}_{n\mu}$ and $\tilde{B}_{n\mu}$ are integration constants.

Eqs. (7) and (10) determine the eigenvalues (and the eigenfunctions) for the outer and inner regions, while the boundary condition (5) can be used to determine the expansion coefficients in Eqs. (8) and (11) for fixed boundary. It is to be noted that the condition (5) also implies the continuity of the potential on the boundary.

6. Discussion. The kinetic theory of low-frequency localized structures in the magnetized plasma has been suggested within the context of renormalized plasma electrodynamics. The first dispersion relation for the outer region is completely determined by the linear dielectric permittivity. The significance of the latter linear feature in describing nonlinear structures can be understood within the context of the transport of nonlinear charge density. In the case of the plain wave dependence (3), the nonlinear charge density of every plasma element is conserved, and an arbitrary integration function enters the solution. The requirement that the oscillations are localized implies that the nonlinear charge density is zero in the outer region, and makes the linear dielectric permittivity the only significant property there. Meanwhile, the second dispersion relation includes features associated with nonlinear plasma polarization (the nonlinear charge density is non-zero).

* Temporary address: Dept. of Phys., UCLA, Los Angeles, CA 90024, US A.

[1] M. Makino, T. Kamimura, T. Taniuti. J. Phys. Society of Japan **50**, 980 (1981).
[2] V.P. Pavlenko, V.I. Petviashvili. Preprint IAE-3703/6. Moscow, 1982. 7p.
[3] J.D. Meiss, W. Horton. Phys. Fluids **26**, 990 (1983).

[4] A.G. Sitenko, P.P. Sosenko. In *Problems of Theoretical Physics* (Naukova Dumka, Kiev, 1986), p. 225-237.
[5] A.G. Sitenko, P.P. Sosenko. In *Proceedings 1987 International Conference on Plasma Physics: Invited Papers*, Kiev, 1987/Edited by A.G. Sitenko (World Scientific, Singapore, 1987), Vol. 1, p. 486-524.
[6] A.G. Sitenko, P.P. Sosenko. Physica Scripta **43**, 609 (1991) .

A NOVEL APPROACH TO THE INTERACTION BETWEEEN THE PLASMA WAKE FIELD AND THE DRIVING RELATIVISTIC ELECTRON BEAM

R. Fedele [1] and P.K. Shukla [2]

[1] *Istituto Nazionale di Fisica Nucleare, Sezione di Napoli, Mostra D'Oltremare Pad.20, I-80125 Napoli, Italy*

[2] *Institüt für Theoretishe Physik, Ruhr-Universität Bochum, D-4630 Bochum 1, Germany*

Recently, relativistic charged particle beams are imployed [1] for generating intense electron plasma waves or wakefields. When the phase velocity of the latter is close to the speed of light, the plasma wave can trap a nearly relativistic electron and accelerate it to extremely high energies. The idea of this novel plasma-based charged particle acceleration scheme has been verified experimentally [2].
It is well known that interaction of relativistic charged particle beams of finite extent with the background plasma can give rise to the two-stream instability, the self-bunching, the self-focusing (self-defocusing), as well as the beam filamentation and the self-pinching. In this paper, we employ the recently proposed *thermal wave model* [3] in order to study the self-consistent interaction between the plasma wakefields and the driving relativistic electron (positron) bunch in a collisionless, unmagnetized, overdense plasma. It is found that our model is capable of reproducing the main results for the beam filamentation threshold and the self-pinching equilibrium condition that are already known in the conventional theory of the beam self-interaction in collisionless plasma.

In the framework of the recently proposed *thermal wave model for relativistic charged particle beam propagation* [3], the stationary configuration of a relativistic charged-particle beam of transverse emittance ϵ, traveling along the z-axis with velocity βc ($\beta \approx 1$), under the action of a potential $u(r,\phi,z)$, is described by the Schrödinger-like equation for the so called *beam wave function* (bwf) $\Psi(r,\phi,z)$:

$$i\epsilon \frac{\partial \Psi}{\partial z} = -\frac{\epsilon^2}{2}\nabla_\perp^2 \Psi + U(r,\phi,z)\Psi \quad , \tag{1}$$

where $\nabla_\perp$ is the 2-D transverse gradient, and $U(r,z,\phi) = u(r,z,\phi)/(m_0\gamma\beta^2c^2)$. Here m_0 is the particle rest mass, c is the speed of light, and $\gamma = (1-\beta^2)^{-1/2}$ is the relativistic gamma factor. Equation (1) must be coupled with an equation for the total transverse field force ($\mathbf{F}_\perp = -m_0\gamma\beta^2c^2\nabla_\perp U$) acting on the system. In analogy with nonrelativistic quantum mechanics, z and ϵ play the role of time and Planck's constant, respectively; while in analogy with electromagnetic beam optics in the geometrical approximation, ϵ plays the role of the inverse of the wavenumber $k^{-1} = \lambda/2\pi$, and U that of the refractive index of the nonlinear medium, so that Eq.(1) corresponds to the well known Fock-Leontovich equation. The norm $\mathcal{N}$ of Ψ, viz.

$$\mathcal{N} \equiv \|\Psi\| = \left[\int_0^{2\pi} d\phi \int_0^\infty r\, dr\, |\Psi|^2\right]^{1/2} \quad , \tag{2}$$

is conserved ($d\mathcal{N}/dz = 0$) and the bwf has the following meaning: If N is the total number of the particles of the beam, then the transverse beam number density $\sigma(r,\phi,z)$ (number of particles per unit transverse section) is given by $\sigma(r,z,\phi) = (N/\mathcal{N}^2)|\Psi(r,z,\phi)|^2$. Thus, $|\Psi|^2$ gives the transverse beam density profile. Note that here Ψ is dimensionless. Let us denote with $g(\xi)$ and σ_z the longitudinal dimensionless density profile and the longitudinal beam length, respectively; where $\xi = z - \beta ct$ (t being the time). Then, it is easy to prove that the beam volumic number density $\rho_b(r,z,\phi)$ assumes the form $\rho_b(r,z,\phi) = n_b g(\xi)|\Psi(r,z,\phi)|^2$, where $n_b = N/(\mathcal{N}^2\sigma_z)$. Furthermore,

in cylindrical symmetry, the following *virial equation* and *energy-variation equation* hold (for more details see Ref.[3]:

$$\frac{d^2R^2(z)}{dz^2} = 4\mathcal{E} - 4\mathcal{V} - \frac{4\pi}{\mathcal{N}^2}\int_0^\infty \left(r\frac{\partial U}{\partial r}\right)|\Psi|^2\, r\, dr \quad , \tag{3}$$

$$\frac{d\mathcal{E}}{dz} = < \frac{\partial U}{\partial z} > = \frac{2\pi}{\mathcal{N}^2}\int_0^\infty \left(\frac{\partial U}{\partial z}\right)|\Psi|^2\, r\, dr \quad . \tag{4}$$

$(R(z) \equiv [(2\pi/\mathcal{N}^2)\int_0^\infty r\, dr\, r^2|\Psi|^2]^{1/2}$ and $\mathcal{E}(z) \equiv (2\pi/\mathcal{N}^2)\int_0^\infty r\, dr\, [(\epsilon^2/2)|\nabla_\perp\Psi|^2 + U|\Psi|^2]$ are the effective beam radius and the averaged total beam energy associated to the transverse motion, respectively).

We now consider wake field dynamics in the presence of the beam. On using the fluid theory, it can be shown that, within the linear approximation, the wakefield driven by a relativistic charged particle beam, travelling along the z-axis with velocity βc in a collisionless unmagnetized overdense plasma of density n_p ($n_p >> n_b$), obeys the following equations [4]:

$$\left(\frac{\partial^2}{\partial\xi^2} + k_p^2\right) n_1 = \mp k_p^2 \rho_b(r,z,\xi), \tag{5}$$

and

$$\left(\nabla_\perp{}^2 - k_p^2\right)\Omega = -4\pi e n_1, \tag{6}$$

where $n_1 = n_1(r,z,\xi)$ is the plasma number density perturbation, $\rho_b(r,z,\xi)$ is the beam number density, $\Omega = \Omega(r,z,\xi)$ is the plasma wakefield potential, and $k_p = \omega_p/\beta c = (4\pi n_p e^2/m_0)^{1/2}/\beta c$ is the wavenumber of the plasma wave. On the right-hand side of Eq.(5) the "-" ("+") sign is for the electron (positron) beam. In a realistic situation, the expression $\rho_b(r,z,\xi)$ in terms of $|\Psi|^2$ given by Eq.(1) with $U = u/m_0\gamma\beta^2c^2 = \pm e\Omega/m_0\gamma\beta^2c^2$ must be supplemented with Eqs.(5) and (6). In the following, we present a self-consistent description of the wakefield-beam interaction in the long beam limit (viz. $k_p\sigma_z >> 1$ or $k_p^2 >> |\partial^2/\partial\xi^2|$). Here, we get (see [4]):

$$\left(\nabla_\perp{}^2 - k_p^2\right)\Omega = \pm 4\pi e n_b g|\Psi|^2. \tag{7}$$

On the other hand, Eq.(1) takes the form

$$i\epsilon\frac{\partial}{\partial z}\Psi = -\frac{\epsilon^2}{2}\nabla_\perp^2\Psi \pm \frac{e}{m_0\gamma\beta^2c^2}\Omega\,\Psi \quad . \tag{8}$$

We observe that in the long beam limit $g = 1$ and the screening of the beam space charge is provided by Eq.(7). Equations (7) and (8) describe the self-interaction of a relativistic electron (positron) beam traveling in a collisionless unmagnetized plasma. If we solve (7) for Ω, we should find that it is a function of $|\Psi|^2$, i.e. $\Omega = \Omega(|\Psi|^2)$. Consequently, by putting the latter in (8) we get a nonlinear Schrödinger equation, which can be analyzed. In order to illustrate how the system of equations (7) and (8) self-consistently describe the beam self-focusing, we consider two limiting cases. First, we assume that the beam spot size is larger than the plasma wavelength (viz. $k_pR >> 1$ or $k_p^2 >> |\nabla_\perp|^2$). Consequently, we obtain the following cubic nonlinear Schrödinger equation :

$$i\epsilon\frac{\partial}{\partial z}\Psi = -\frac{\epsilon^2}{2}\nabla_\perp^2\Psi - \frac{n_b}{n_p\gamma}|\Psi|^2\,\Psi \tag{9}$$

Equation (9) is similar in structure to the equation which describes the self-focusing of a coherent electromagnetic beam in a nonlinear medium. We easily find that in this case the averaged total energy $\mathcal{E}$ associated with the beam is not conserved. In fact, the charged particle beam interacting with the plasma is an open system. However, by using (4) it can be proved that the quantity

$$\mathcal{A} \equiv \mathcal{E} + \frac{1}{2}\left[\frac{2\pi}{\mathcal{N}^2}\frac{n_b}{n_p\gamma}\int_0^\infty |\Psi|^4\, r\, dr\right] \tag{10}$$

is conserved, namely $d\mathcal{A}/dz = 0$, and, consequently, by using the virial equation we get $d^2R^2/dz^2 = 4\mathcal{A} = const.$, which can be immediately solved with the initial conditions $R_0 = R(z=0)$ and $(dR/dz)_{z=0} = 0$. We find $R^2(z) = R_0^2 + 2\mathcal{A}z^2$. The latter shows that $\mathcal{A}$ is negative (positive) if $(2\pi/\mathcal{N}^2)(\epsilon^2/2)\int_0^\infty |\nabla_\perp\Psi|^2\, r\, dr$ (thermal energy) is smaller (larger) than half of the self energy, $(2\pi/\mathcal{N}^2)(n_b/n_p\gamma)\int_0^\infty |\Psi|^4\, r\, dr$. Consequently, the charged particle beam would focus (defocus), as is evident from the equation for the beam caustic. A stationary solution also occurs when the thermal energy is exactly balanced by half of the self energy ($\mathcal{A} = 0$). It corresponds to a stabilization of the beam at the initial radius, which is analogous to the Bennett pinch equilibrium [5],[6]. A simple criterion for finding the threshold of the self-focusing can now be established. If we assume that the beam has a temperature T (energy units) and an initial Gaussian profile, we find

$$\mathcal{A} \approx \frac{1}{2}\left[\frac{\epsilon^2}{R_0^2} - \frac{1}{2}\frac{n_b}{n_p\gamma}\right]. \tag{11}$$

So that, by imposing $\mathcal{A} \approx 0$, we immediately obtain the threshold condition

$$\frac{\epsilon^2}{R_0^2} \approx \frac{1}{2}\frac{n_b}{n_p\gamma}, \tag{12}$$

which, since $\epsilon^2/R_0^2 = T/(m_0\gamma\beta^2c^2) \approx T/(m_0\gamma c^2)$, becomes:

$$\beta_\perp \equiv \frac{v_{th}}{c} \approx 0.7\left(\frac{n_b}{n_p\gamma}\right)^{1/2} \tag{13}$$

where $v_{th} = (T/m_0\gamma)$ is the electron (positron) thermal velocity. Equation (13) is the threshold for the Weibel (or the filamentation) instability [5]. It is interesting observing that by putting a non self-consistent aberrationless solution of (9), of Gaussian form $\Psi = exp(-r^2/R^2)$, in the virial equation (3), we find the following envelope equation :

$$\frac{d^2R}{dz^2} + \frac{2n_b/(n_p\gamma)}{R} - \frac{\epsilon^2}{R^3} = 0 \quad , \tag{14}$$

which takes into account the self-force; it is similar to the well known envelope equation which is valid for fully neutralized relativistic beam [7].

Next, we consider the limit in which the beam spot size is smaller than the plasma wavelength (viz $k_pR << 1$ or $k_p^2 << |\nabla_\perp|^2$)). For this case, the virial equation (3) becomes [4]:

$$\frac{d^2R}{dz^2} = \frac{\epsilon^2}{R^3} - \frac{2K}{R} < \int_0^r |\Psi(r',z)|^2\, r'\, dr' > \tag{15}$$

where $K \equiv 2\pi e^2 n_b/(m_0\gamma\beta^2c^2)$ is the focusing strength. By observing that $d^2R^2/dz^2 = 2[Rd^2R/dz^2 + (dR/dz)^2]$, Eq. (15) with the initial conditions $R_0 = R(z=0)$ and

$(dR/dz)_{z=0} = 0$ allows us to establish the equilibrium condition $(d^2R/dz^2 = 0)$, which, for an initial Gaussian profile gives us:

$$\frac{\epsilon^2}{R_0^2} = \frac{1}{2} K R_0^2 \quad . \tag{16}$$

This is the well known Bennett self-pinch equilibrium condition [6]. By introducing the definition of the beam current $I = eN\beta c/\sigma_z \approx eNc/\sigma_z$ and using the transverse beam emittance definition in terms of the transverse temperature T, Eq.(16) gives the well known Bennett pinch relation [6] (c.g.s. units):

$$\frac{I^2}{c^2} = N_z T \quad , \tag{17}$$

where $N_z = N/\sigma_z$ estimates the number of particles per unit longitudinal beam length. We observe that in this limiting case an aberrationless solution of (8) is also possible (we have again $\Psi = e^{-r^2/R^2}$). So, in the limit in which $\int_0^r \Psi(r', z)|^2 \; r' \; dr' \approx r^2/2$ $(r << R)$, we recover the well known envelope equation:

$$\frac{d^2R}{dz^2} + KR - \frac{\epsilon^2}{R^3} = 0 \quad , \tag{18}$$

which has been used to describe the optics of an overdense plasma lens in linear regime for the final focus in linear colliders [8].

To summarize, we have presented a novel approach for considering self-consistent interaction between the wakefield and the driving relativistic electron (positron) beam in a unmagnetized, overdense, collisionless plasma. For our purpose, we have employed the recently proposed *thermal wave model for relativistic charged particle beam propagation* [3], and in addition, the fluid equations are used to study the wakefield dynamics in the presence of the transverse profile of the beam density. We thus have a self-consistent coupling between the driving beam and the wakefields, and our treatment represents an improvement of a previous approach [1], which has completely ignored the reaction of the wakefield on the driver and did not consider the spatial evolution of the beam. It is found that the present model is capable of reproducing the main results found in the conventional theory of the beam self-interaction.

References

[1] P. Chen, J. M. Dawson, R. W. Huff, and T. Katsouleas, *Phys. Rev. Lett.* **54**, 693 (1985).

[2] J. B. Rosenzweig et al., *Phys. Rev. Lett.* **61**, 98 (1988); H. Nakanishi et al., *Phys. Rev. Lett.* **66**, 1870 (1991).

[3] R. Fedele and G. Miele, *Il Nuovo Cimento* **D13**, 1527 (1991).

[4] R. Fedele and P.K. Shukla, *Phys. Rev.* **A45**, 4045 (1992).

[5] J.J. Su, T. Katsouleas, J.M. Dawson, P. Chen, M. Jones, and R. Keinigs, *IEEE Trans. Plasma Science* **PS-15**, 192 (1987).

[6] W.H. Bennett, *Phys. Rev.* **45**, 89 (1934)

[7] J. D. Lawson, *Particle Beam and Plasmas*, CERN Rep.76-09, 13 May 1976, Lectures given in the Academic Training Programme of CERN 1973-1974, edited by A. Hofmann and E. Messerschmidt, Geneva(1976).

[8] R. Fedele and E.J.N. Wilson *Nuovo Cimento* **D12**, 1497 (1990).

SIMULTANEOUS EMISSIONS AT HARMONICS AND HALF HARMONICS OF THE ELECTRON GYROFREQUENCY

C. KRAFFT, G. MATTHIEUSSENT

Laboratoire de Physique des Gaz et des Plasmas*, Université Paris-Sud, 91405 Orsay , France

* Associated with the Centre National de la Recherche Scientifique (URA 73)

G. BELMONT

Centre de Recherches en Physique de l'Environnement, Centre National d'Etudes des Télécommunications

Centre National de la Recherche Scientifique, 92131 Issy-les-Moulineaux, France

Experiments done in space /1/ and laboratory /2/ on the interaction of an electron beam and a magnetized plasma exhibit the simultaneous excitation of waves near harmonics and half harmonics of the electron gyrofrequency ω_c. No theoretical explanation was available up to now for these double ECH series.

The dispersion equation for electrostatic modes has been solved for an anisotropic maxwellian plasma with a suprathermal population ("beam" in the text), such a distribution presenting both anisotropy and regions of $\partial f_0/\partial v_\perp > 0$. Double series of ECH can indeed be reproduced numerically by this way, for a propagation oblique to the magnetic field (angle of propagation θ).

Figure 1 shows the dispersion curves. Quasi-resonances near $(n+1/2)\omega_c$ (n=0,...) and cutoffs at $n\omega_c$ (n=2,...) can be observed on the real part (Fig.1a). Focusing on harmonic n=3, figure 1b evidences that two instabilities are generated, one near $3\omega_c$ and the other near $5/2\ \omega_c$.

A parametric study /3/ has been performed for evidencing the different destabilizing mechanisms for both kinds of emissions: the half harmonic emissions are mainly governed by the plasma and its anisotropy , while the harmonic emissions are generated by the "beam" distribution function.

The hydrodynamic / kinetic nature of the instabilities can be investigated as follows: for a wave $\omega(k_{//},k_\perp)$, the kinetic part of the growth rate is the sum of the contributions of the closest gyroresonances. Each of these contributions is mainly governed by a set of particles around a point $(v_{//n},v_{\perp n})$ where $v_{//n}$ is equal to $(\omega_r - n\omega_c)/k_{//}$ and $v_{\perp n}$ maximizes $J_n^2(k_\perp v_\perp/\omega_c)$ (n being the order of the resonance).

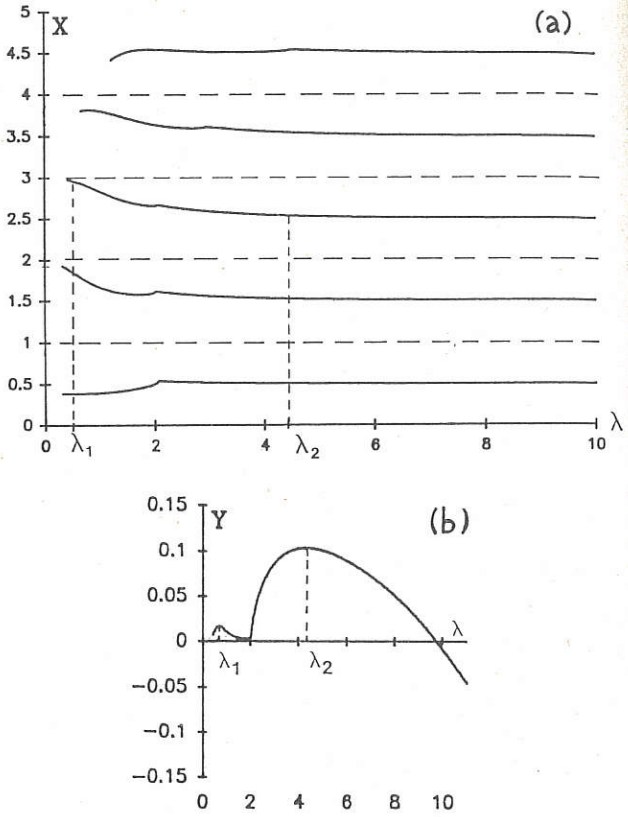

Fig 1: Dispersion curves with the following parameters :
$\omega_p^2/\omega_c^2 = 12.25$, $n_b/n_p = 0.01$, $\theta = 66.5°$, $V_{p//}/V_{p\perp} = 0.05$, $V_{b//}/V_{p\perp} = 0.5$, $V_{b\perp}/V_{b//} = 8.7$. *The labels 'b' and 'p' stand respectively for "beam" and plasma; the parallel and perpendicular thermal velocities are* $V_{//}$ *and* $V_\perp$.
(a) Real part $X = \omega_r/\omega_c$ *as a function of* $\lambda = k_\perp V_{p\perp}/\omega_c$ *for branches n=1 to n=5.*
(b) Imaginary part $Y = \omega_i/\omega_c$ *as a function of* λ, *for branch n=3.*

Figure 2 presents the loci of the points $(v_{//n}, v_{\perp n})$ when varying $k_\perp$, for the resonances n=3 and n=4 (dashed curves). A constant value of the propagation angle θ has been assumed, and each curve is parametred by $\lambda = k_\perp v_\perp/\omega_c$.

The contribution of each gyroresonance can be estimated from a particular derivative of the distribution function at the point $(v_{//n}, v_{\perp n})$:

$$\partial f_o/\partial v_{//} + \frac{n\omega_c}{k_{//} v_\perp} \partial f_o/\partial v_\perp$$

It is worth noticing that the contribution of the $\partial f_o/\partial v_\perp$ term is dominant in the usual isotropic case, while the dominant term is the $\partial f_o/\partial v_{//}$ one in the case $V_\perp >> V_{//}$ that we consider here.

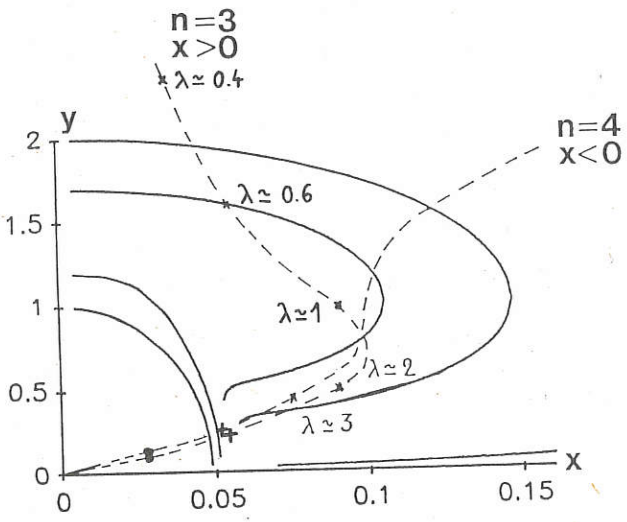

Fig 2: Kinetic contribution to the instabilities (see text).
The coordinates are $x=v_{//}/V_{b\perp}$ and $y=v_\perp/V_{b\perp}$. Parameters are the same as in Figure 1. Crosses (+) correspond to the highest value of the growth rate of half harmonic instabilities ($\lambda \simeq 5$ for n=4 and $\lambda \simeq 4$ for n=3) and dots correspond to the value of λ where stability occurs ($\lambda \simeq 10$).

From such an analysis we can conclude that:

(i) harmonic emissions are kinetic and due to the "beam" ; they are thus of the same nature as the $(n+1/2)\omega_c$ emissions studied by Kennel and Ashour-Abdalla /4/ , but with an important difference : because of the anisotropy of the "beam", the resonant particles responsible for the instability are those with $\partial f_o/\partial v_{//}>0$ (since $v_{//n}$ is negative just below the harmonics $n\omega_c$), instead of being those with $\partial f_o/\partial v_\perp>0$, which lead to maximum growth rates around $(n+1/2)\omega_c$ in the isotropic case .

(ii) half harmonic emissions are hydrodynamic and due to the core anisotropy. The kinetic effect of the "beam" that usually gives rise to instability /4/, is in our case stabilizing because of the "beam" anisotropy ($|\partial f_o/\partial v_{//}| > |\partial f_o/\partial v_\perp|$). The hydrodynamic instability of the core is of Harris type and overcomes the kinetic damping of the "beam" up to $\lambda \simeq 10$.

In order to check this mechanism, the complete dispersion relations with (Fig.3b) and without (Fig.3a) kinetic effect (i.e. with and without their resonant part) have been solved numerically, confirming the scenario.

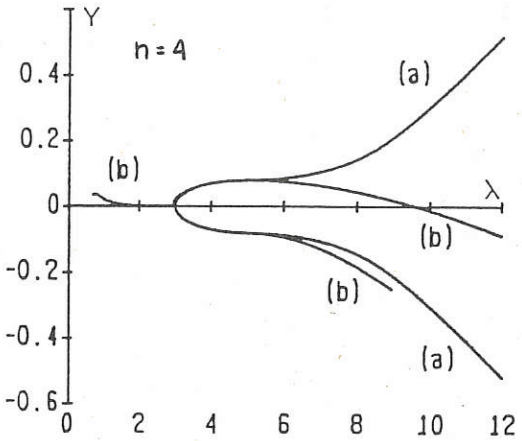

Fig 3: Variation of the growth rate with λ for the hydrodynamic approximation (curve (a)) and for the complete dispersion relation with kinetic effect (curve (b)); (a) shows the symetric imaginary parts of the hydrodynamic solutions; the hydrodynamic half harmonic instability is stabilized for $\lambda \gtrsim 10$ (b). Parameters are the same as in Figure 1.

/1/ Beghin C. et al., in Artificial Particle Beams in space plasma studies, edited by B. Grandal, Plenum Publishing Corporation, 1982.

/2/ Krafft C., G. Matthieussent, P. Thévenet, J.Godiot, J. Phys.III France, 1, 2047, 1991.

/3/ Krafft C., G. Matthieussent, P. Thévenet, G.Belmont, J. Geophys. Res., 1992, in press.

/4/ Kennel C.F., Ashour-Abdalla M., in Magnetospheric Plasma Physics, edited by A.Nishida, pp.245-344, Center for Academic Publications Tokyo, Japan, 1982.

INTENSE LASER PULSE PROPAGATION IN A PLASMA

P.K. Kaw[1], A.Sen[1] and T. Katsouleas[2]

[1]Institute for Plasma Research, Bhat, Gandhinagar 382424
[2]Deptt. of Elec. Eng. and Physics, UCLA,Ca 900024

The study of intense ($v_{osc}/c > 1$) laser pulse propagation in cold plasmas[1] is of much current interest due to recent significant advances in laser technology, such as generation of picosecond pulses with energies upto tens of joules and possible applications to particle accelerators, photon accelerators etc. One of the problems of key interest from the point of view of particle and photon acceleration is the magnitude of group velocity of such pulses since it determines the propagation speed of the associated plasma wave wakefield. Earlier attempts at investigating this problem have relied on computer simulations or exact nonlinear solutions which are infinite unmodulated waves[2-5]. The latter seem inappropriate to use for a short pulse.In this paper, we examine a class of exact one dimensional nonlinear solutions of the relativistic cold plasma equations which represent envelope solitons of light waves[6,7], in which the modulation envelope propagates as a large amplitude plasma wave in the medium. These solutions are a step beyond the well known stationary solutions in a cold plasma because the envelope and the phase propagate with different speeds so that the nonlinear relationships between the phase and group velocities can be investigated. For simplicity and clarity, we restrict our analysis to circularly polarized waves which couple to longitudinal disturbances only because the amplitude is modulated. These intense light pulses might form interesting candidates for photon accelerator schemes[8] in which the combined effect of the change in plasma density and effective electron mass (due to relativistic effect) may be used to get significant improvement in the frequency multiplication that is possible.

Our basic equations are derived from the well known relativistic set of fluid equations for a cold plasma (in one dimension)[1,3-5], by transforming to a moving frame $x - \beta t = \xi$, $t = \tau$ and assuming that the vector potential of the light wave is circularly polarised with a sinusoidal phase variation $\mathbf{A} = [\{\hat{y}a(\xi) + \hat{z}ia(\xi)\}exp(-i\lambda\tau) + c.c]$.The choice of circular polarisation allows us to avoid the generation of harmonics in all wave fields and permits integration of the fluid equations. Writing $a(\xi) = Rexp(i\theta)$, and using Poisson's equation and the wave equation the final set of coupled nonlinear equations are

$$\phi'' = \frac{u}{(\beta - u)} \tag{1}$$

with u given by

$$u = \frac{\beta(1+R^2) - (1+\phi)[(1+\phi)^2 - (1-\beta^2)(1+R^2)]^{\frac{1}{2}}}{(1+\phi)^2 + \beta^2(1+R^2)} \tag{2}$$

and

$$R'' + \frac{R}{1-\beta^2}[(\lambda^2 - \frac{M^2}{R^4})\frac{1}{1-\beta^2} - \frac{\beta}{\beta - u}\frac{1-\beta u}{1+\phi}] = 0 \tag{3}$$

where $M = R^2\{(1-\beta^2)\theta' - \lambda\beta\}$, is a constant of integration and ϕ is the normalised electrostatic potential. In our representation the amplitude $R = (A_y^2 + A_z^2)^{1/2}$ of the circularly polarised electromagnetic wave exhibits a modulation propagating at the group speed β. The question of the definition of phase speed is a little more complex. For small amplitudes R is always positive and the exponential factor contains the entire phase information. The phase speed may then be shown to be simply $1/\beta$ satisfying the conventional relation $V_p V_g = 1$. However, for arbitrary amplitudes R oscillates because of the strong $R - \phi$ coupling and the phase speed has to be defined by directly determining the z, t variation of $Rcos(\theta - \lambda\tau)$.

In the limit of weak density response,the nonlinear coupled equations can be simplified by the substitutions $\phi \approx (1+R^2)^{\frac{1}{2}} - 1$ and $n \approx (\sqrt{1+R^2})''$. Expanding in R^2 and taking $M = 0$ we get the well known envelope soliton solution

$$A_y = R_m sech[\frac{\sqrt{1-\beta^2-\lambda^2}}{1-\beta^2}(x-\beta t)]cos[\frac{\lambda\beta}{1-\beta^2}(x-\frac{t}{\beta})] \tag{4}$$

where

$$R_m = 4\sqrt{\frac{(1-\beta^2)(1-\beta^2-\lambda^2)}{4\lambda^2-(1-\beta^2)(3+\beta^2)}} \tag{5}$$

Our primary interest however is to investigate soliton solutions for arbitrary amplitudes for which we have solved equations (1-3) numerically and looked for solutions that decay exponentially as $\xi \to \pm\infty$.For λ very close to $\sqrt{1-\beta^2}$ we get small amplitude solitons which are well described by the analytic solutions (4-5). As λ is decreased the soliton amplitude increases and acceptable solutions occur only at discrete values of λ. In other words, for a fixed value of β finding soliton solutions turns out to be an eigenvalue problem in λ. The sizes and shapes of these solitons also vary as a function of λ. Typically ϕ has a characteristic bell shape whereas R has a number of nodes. Figure 1 shows a typical soliton solution for $\beta = 0.97$ and $\lambda = 0.224445$. For applications such as particle acceleration or photon acceleration, the regime of interest is $\beta \to 1$, where the group velocity is close to c. We have carried out a detailed investigation of soliton solutions in this regime. Fig. 2 is a plot of normalized group velocity V_g versus the normalized carrier frequency $\Omega(=\omega/\omega_p)$. The solid curve corresponds to soliton pulse results obtained from our numerical work. For comparison we have also plotted the linear group velocity (dashed line) $V_{gL} = \sqrt{(1-1/\Omega^2)}$ and the nonlinear group velocity for the infinite plane wave [3-5] (dotted line), $V_{g\infty} = \beta[1-(\gamma_\infty - 1)/(2\Omega^2\gamma_\infty(\gamma_\infty+1)]$. The nonlinear group velocities are closer to c than the linear group velocity. This is physically understandable because the nonlinearity makes the electrons heavier and thereby weakens the plasma dielectric effects. Finite width soliton pulses propagate slower than the infinite plane waves. Physically this is because coupling to plasma waves acts as a drag on the electromagnetic waves and slows them down. The deviations between $V_{g\infty}$ and V_{gs} can be substantial; in our numerical work, we have observed (not shown) deviations upto 25 percent of the difference between V_g and 1.

As stated earlier, the soliton pulses can only be obtained for characteristic combinations of amplitude R_0, group velocity $\beta = V_{gs}$ and frequency Ω. Figure 2. also shows the values of R_0 (the solid triangles) for which the soliton pulse solutions are obtained. Note that in the $V_{gs} - \Omega$ curves, the changing R_0 and Ω are working against each other.

Increasing Ω increases the group velocity but the simultaneously decreasing value of R_0 opposes this tendency and we see the resulting effect in our plots.

Physically these solutions correspond to a soliton in which standing light waves are set up in an 'effectively empty' cavity, because $n/\gamma \to 0$ in most of the region. Finally, the n/γ can be made to suffer a change from 1 to a large number before it drops down to zero by making the laser pulse long. In this case, all the density swept out of the pulse piles up in layers with a width of order (c/ω_p), which is the skin depth, at either edge of the pulse. Figure 3 illustrates this effect for a $p = 19$ soliton with $\beta = 0.9$ and $\lambda = 0.336$.

To conclude,we have analysed exact one dimensional solutions for modulated light pulses coupled to electron plasma waves in a cold plasma.The one-dimensional approximation is reasonable as long as transverse scale lengths are much longer than longitudinal pulse dimensions (which is a few skin depths c/ω_p). Solutions may be in the form of isolated envelope solitons or modulated periodic wave trains. Physically, the soliton pulse may be viewed as a light wave which is trapped in a plasma wave that it generates itself. The front of the pulse generates the plasma wave as a wakefield, which is then reabsorbed by the tail of the pulse. The exchange of energy between the light wave and the plasma wave also leads to a 'chirping' of the pulse (cf Fig. 1). This suggests that to experimentally create such pulses, one must not only use characteristic values of R_0 and ω but also do some appropriate chirping of the light wave. The nonlinear relationship between the group velocity and phase velocity and between the group velocity and amplitude, frequency etc. has also been discussed. Numerical results have been presented for the first time for intense pulses propagating close to the velocity of light; such pulses are of great interest from the point of view of particle and photon accelerators. We have also demonstrated the existence of light pulses where the change in n/γ inside the pulse is well above unity (Fig. 3). One can hope to get a very large frequency multiplication factor from using such pulses as photon accelerators.

References

[1]P. Sprangle, E. Esarey and A. Ting, Phys. Rev. Letts. **64**, , 2011 (1990) and references therein.

[2]W.B. Mori et al, Bull. Am. Phys. Soc. **36**, 1513 (1991);ibid 2305

[3]A.I. Akhiezer and R.V. Polovin, Zh. Eksp. Teor. Fiz. **30**, 915 (1956) [Sov. Phys. JETP **3**, 696 (1956)]

[4]P. Kaw and J. Dawson, Phys. Fluids **13**, 472 (1970)

[5]A. De Coster, Physics Reports **47**, 285 (1978)

[6]N.L. Tsintsadze and D.D. Tskhakaya,Zh. Eksp. Teor. Fiz. **72**, 480 (1977) [Sov. Phys. JETP **45**, 252 (1977)]

[7]V.A. Kozlov, A.G. Litvak and E.V. Suvorov, Zh. Eksp. Teor. Fiz. **76**, 148 (1979) [Sov. Phys. JETP **49**, 75 (1979)]

[8]S.C. Wilks, J.M. Dawson, W.B. Mori, T. Katsouleas, M.E. Jones Phys. Rev. Letts. **62**, 2600 (1989)

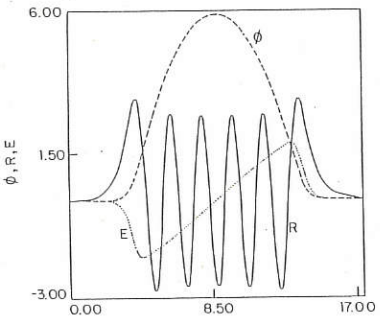

Figure 1: Electrostatic potential ϕ (dashed line), electric field E ($= -\partial\phi/\partial\xi$, dotted line) and electromagnetic wave amplitude (R) (solid line) profiles for a soliton pulse with $p = 6, \beta = 0.97$ and $\lambda = 0.224445$.

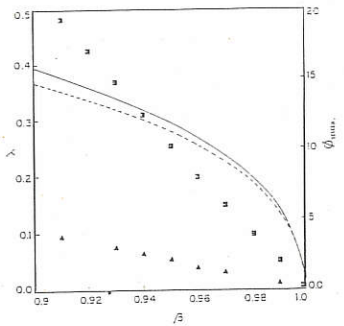

Figure 2: Normalized group velocity vs normalized frequency curves for soliton pulses (solid line), infinite pulses (dotted line) and linear pulses (dashed line). The maximum electromagnetic wave amplitude R_0 for the soliton pulse (for $p = 18$) are indicated with solid triangles.

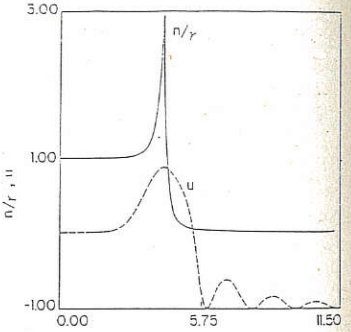

Figure 3: Variation of $\delta n/\gamma$ (solid line) and u (dashed line) for a soliton pulse with $\beta = 0.9$, $\lambda = 0.336$ and $p = 19$.

NONLINEAR DEPLETION OF SHORT AND RELATIVISTICALLY STRONG LASER PULSES IN AN UNDERDENSE PLASMA

S.V.Bulanov, I.N.Inovenkov*), V.I.Kirsanov, N.M.Naumova, A.S.Sakharov

General Physics Institute, Russian Academy of Sciences,
Vavilov Street 38, Moscow, Russia

*)Moscow State University, Moscow, Russia

The resent progress of laser technology [1] has opened a new field for investigations prompted to study the interaction of relativistically strong laser pulses of subpicosecond duration with plasmas.

We consider here the process of depletion of such strong laser pulses in an underdense plasma ($\omega_p=(4\pi e^2 n_0/m_e)^{1/2} \ll \omega_o$). We focus on short enough laser pulses for which the ion motion can be neglected, so that ions form only immobile background. Thus, our consideration is reduced to the Maxwell equations combined with the electron hydrodynamics equations. We assume the transverse size of the pulse L_{tr} to be fairly large in comparison with the characteristic plasma wavelength $L_{tr} \gg k_p^{-1} \equiv c/\omega_p$ and restrict ourselves to 1-D analysis.

To describe the fields we take as variables the dimensionless vector potential of laser field $a \equiv eA_\perp/m_e c^2$ and the electrostatic potential $\phi \equiv e\varphi/m_e c$. Further we assume the laser pulse to be relativistically strong ($|a|>1$).

It was shown in Ref.2,3 that the excitation of plasma wake-wave can provide an effective depletion of a relativistically strong electromagnetic pulse. The efficiency of excitation is maximum for fairly short pulse ($t_p < \tau_1 \equiv \omega_p^{-1}/|a|$) or for the pulse with sharp leading front ($\Delta t < \tau_1$). Or, in other words, the efficiency is maximum for the strike excitation. In the first case the characteristic time of the pulse depletion is equal to $t_{nl} = (16/3)(k_p Q)^{-1}\omega_0^2/\omega_p^3$ (where $Q = \int dx|a|^2$ at $t = 0$). In the second case for the rate of the pulse energy losses we have $dW_p/dt \simeq c(\omega_p^2/\omega_o^2)E_\perp^2/8\pi$.

Due to the relativistic growth in mass of the plasma electrons one could expect the suppression of the interaction between the main body of ultrastrong laser pulse and plasma to appear. So we would like to find out whether the depletion in underdense plasma via plasma wave excitation is,

in fact, the dominating process in the evolution of the main body of the pulse.

The interaction of a fairly long ($t_p \gg |a|^{1/2}\omega_p^{-1}$) and smooth pulse can be treated as adiabatic and there is no initial exchange of energy between the pulse and an isotropic collisionless plasma. However, as it was shown in Refs.3,4, the feature peculiar to ultrastrong pulses evolution is the formation of the region with the extremely high amplitude gradients on the pulse leading front. As the result of it the mechanism of extremely fast pulse depletion is switched on.

It appears to be that the most important among the mechanisms driving the leading front steepening is the stimulated backward Raman scattering (SBRS) which dominates on the initial stage of evolution. It manifests itself primarily for the pulses with sufficiently long rise time of amplitude. One can expect that erosion of the pulse front due to SBRS will occur first of all in the region of $|a| \simeq 1$ where the growth rate of SBRS achieves its maximum value [2]: $\gamma_{max} \simeq \omega_0(\omega_p/\omega_0)^{2/3}$.

The results of PIC simulations prove an important role of BSRS in the process of steepening of the leading front of the pulse. A typical scenario of the evolution for fairly long pulse (with $t_p = 240\pi\omega_0^{-1}$) is presented in Fig.1. Each plot in it (a,b,c,d,e) shows the profile of transverse electric field $E_\perp = (e/cm_e\omega_o)(E_y^2+E_z^2)^{1/2}$ for the different stages of evolution. The pulse is circularly polarized and has the peak amplitude $|a|_{max} = 3$. The coordinate x is normalized to c/ω_0. The plasma density is taken so that $\omega_p = \omega_o/3$. At $t=0$, the pulse is located in vacuum near the left boundary of the plasma, and then it penetrates into the plasma.

At the early stage (Fig.1a), the laser pulse does not excite the fast ($v_{ph} \simeq c$) plasma wave. But the more precise analysis of the spectrum of the plasma electron density perturbations indicates that in the region where the pulse amplitude is about 1 ($|a| \simeq 1$) there exist the density perturbations with the wave number two times greater than that of the laser radiation. Simultaneously the reflected radiation with the frequency close to the initial one appears. This fact persuades us that in this region SBRS develops.

The depletion of the pulse energy in the region of $|a| \simeq 1$ due to intense SBRS acts to produce the erosion of the leading front and formation of the jump of amplitude which could be seen in Fig.1b. Further on, the intense plasma wave excitation is switched on that results in the fast (at

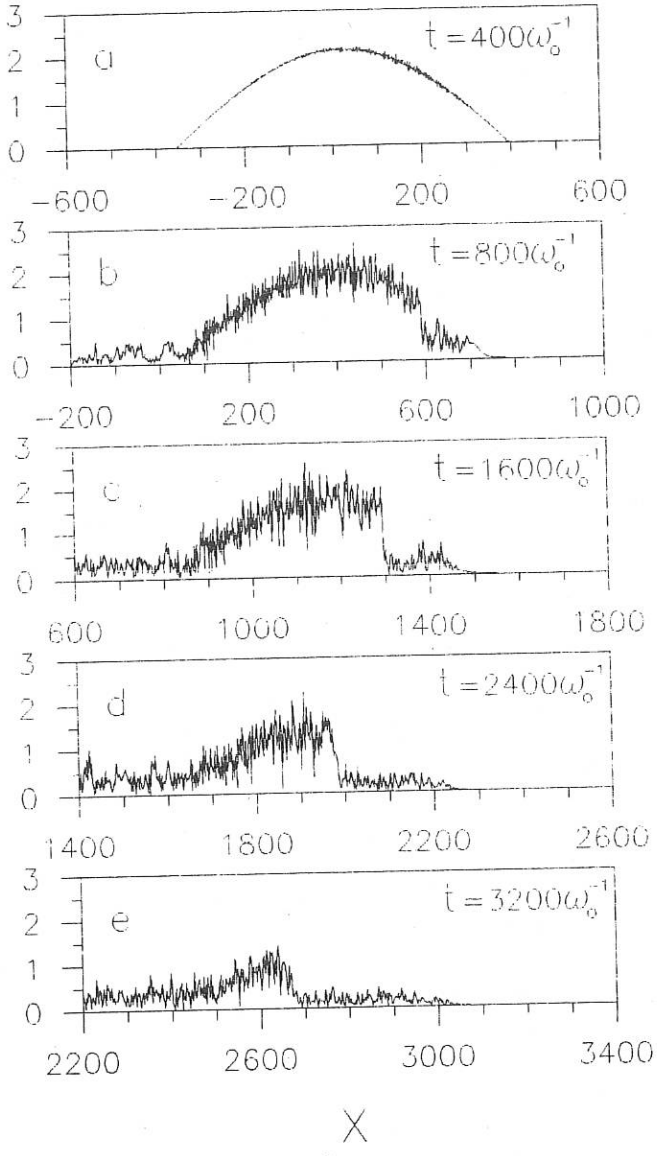

Fig. 1

the time interval $\Delta t \simeq |a|^{-1}\omega_0^2/\omega_p^3$) depletion of the part of pulse energy contained in the narrow region (with a width $\Delta x \simeq c/\omega_p|a|$) behind the jump. In the frame moving with the pulse the region of energy absorption is shifting backward into the main body of the pulse with the velocity $v \simeq -\Delta x/\Delta t \simeq -c\,\omega_p^2/\omega_o^2$ (Fig.1b,c,d,e). As a result, practically total depletion of the pulse appears (Fig.1e). For the pulse with a duration τ the time of depletion can be astimated as

$$t_{dep} \simeq \tau\,/(1-V/c) \simeq \tau\,\omega_o^2/\omega_p^2 \quad . \qquad (6)$$

More detail of this process one can find in Ref.4, where the stationary structure of the front and the characteristics of its propagation are copiously studied.

For more short pulses the steepening of the leading front can appear as the result of the variation of the group velocity along the pulse due to the relativistic electron mass growth. As the local group velocity is closer to the speed of light inside the pulse than at its leading edge, the leading front undergoes compression or steepening. The steepening is the fastest in the region with the maximum gradient of the group velocity. In fact, it occurs again in the vicinity of the point where $|a| \simeq 1$ with the characteristic time $t_{st} \simeq \omega_0^2/\omega_p^2(c\,\partial|a|/\partial x)^{-1}|_{a=1}$ and switches on the intense wakefield excitation [3].

Thus, our study shows that the most general feature of the evolution of ultrastrong laser pulses is their ultrafast depletion. It dominates even in an underdense plasma which is practically transparent for radiation of moderate intensity. It worth to mention, that the time of the total pulse deplition depends just on the pulse duration but not on its intensity.

REFERENCES

1. P.Maine,D.Stricland,P.Bado,M.Pessot,and G.Mourou, IEEE J.Quant. Electr., 24, 398 (1988); M.H.R.Hutchinson, Contemporary Phys., 30, 355 (1989)
2. S.V.Bulanov,V.I.Kirsanov,A.S.Sakharov. Sov.J.Plasma Phys., 16,543 (1990)
3. S.V.Bulanov, I.N.Inovenkov, V.I.Kirsanov, N.M.Naumova, A.S.Sakharov. Phys.Fluids B (1992) (accepted for publications)
4. S.V.Bulanov, I.N.Inovenkov, V.I.Kirsanov, N.M.Naumova, A.S.Sakharov, H.A.Shah, submitted for publication in Phys. Scripta (1992)

II-1309

Nonlinear modulated waves near marginal state of instability

Tor Flå[1] and John Wyller [2]

1 Abstract

We formulate a model equation for nonlinear modulated waves near the marginal state of instability. This equation we henceforth call the Extended Derivative Nonlinear Schrödinger equation (EDNLS). EDNLS has the same form as the Derivative Nonlinear Schrödinger (DNLS) except for a quintic nonlinear term which in special cases might be zero.

Introduction

The modulation of weakly nonlinear modulated wavetrains in dispersive media is known to be generically governed by the Nonlinear Schrödinger equation(NLS). According to Benjamin and Feir[1] the plane wave solutions of the NLS equation are modulational unstable (stable)if $pq > 0 (pq < 0)$. Here p and q are the coefficient for the dispersive and the nonlinear term respectively in the NLS equation. When $pq = 0$ for some critical wavenumber k_c, we refer to the state as as marginally stable. This state occur in different physical systems such as Stokes waves on finite depth[2], ion acoustic waves in a two electron temperature plasma[3] and ion acoustic waves in a plasma composed of electrons and positive and negative ions[4]. In all these cases the nonlinear coefficient q vanishes for a certain critical carrier wavenumber k_c, while the dispersion coefficient is strictly negative [2,4] or negative for low ion temperatures and long wavelengths[3]

In the critical regime where $q \sim k_0 - k_c \sim O(\epsilon)$, the dispersive effects and the nonlinearity of the NLS model does not balance each other. To intensify the effects of the nonlinearity, it is assumed that the perturbed fields are of order $\epsilon^{\frac{1}{2}}$. The resulting equation is a modified NLS equation[5]. This equation can be transformed to the EDNLS equation

$$r_t + |r|^2 r_x + i r_{xx} + i\sigma |r|^4 r = 0, \tag{1}$$

by means of a point- and subsequent gauge transformation[6,7]. Here σ is real and r is a complex valued function of x and t.

[1]IMR, University of Tromsø, N-9001 Tromsø, Norway
[2]Narvik Institute of Technology, P.O.Box 385, N-8501 Narvik, Norway

2 Modulational stability and discussion of cnoidal and solitary waves

The EDNLS equation has nonlinear plane wave solutions of the form

$$\begin{aligned} r &= a_0 exp[i(k_0 x - \omega_0 t)], \\ \omega_0 &= \sigma a_0^4 + a_0^2 k_0 - k_0^2, \end{aligned} \tag{2}$$

which are modulational unstable whenever $\frac{k_0}{a_0^2} > -2\sigma$.

Cnoidal and solitary waves are studied in a way analogous to Hada et al.[8] by assuming $r(x,t) = a(\zeta)exp(i\theta(\zeta) + i\alpha t)$ where α is a constant and $\zeta = x - ct$. A complete classification of the cnoidal waves for nonsingular potentials (i.e. when a integration constant called $\beta = 0$) are listed in [9] and include self modulated periodic waves, compressive and rarefactive solitary wave modulations , kink modulations and solitary wave packet modulations. The most notable features are:

- The bifurcation point at $\sigma = -\frac{3}{16}$ where the cnoidal solutions change from bounded to only bounded solutions when $\beta = 0, c > 0$.
- The solitary wave packets

$$a^2 = \frac{8|\frac{\alpha}{c^2} + \frac{1}{4}||c|}{8|\Delta|cosh(2(\frac{\alpha}{c^2} + \frac{1}{4})^{1/2}|c|(\zeta - \zeta_0)) - sign(c)}, \tag{3}$$

$$\Delta^2 = \frac{1}{12}(\frac{3}{16} - 4(\sigma + \frac{3}{16})(\frac{\alpha}{c^2} + \frac{1}{4})), \tag{4}$$

when either $c > 0, \alpha/c^2 > -\frac{1}{4}, \sigma > -\frac{3}{16}$ and $\beta = H = 0$ or $c < 0, \alpha/c^2 < -\frac{1}{4}, \sigma > -\frac{12\alpha/c^2}{16(4\alpha/c^2+1)}$ and $\beta = H = 0$. Here H is a integration constant corresponding to the invariant $H = \frac{1}{2}a'^2 + V(a)$ and V(a) is given in [9].

The boundary $\Delta = 0$ corresponds to the kink profile

$$a^2 = \frac{8|\frac{\alpha}{c^2} + \frac{1}{4}||c|}{8exp[\pm 2|\frac{\alpha}{c^2} + \frac{1}{4}|^{1/2}|c|(\zeta - \zeta_0)] + 1} \tag{5}$$

which can be interpreted as a transition state between solitary wave packets and rarefactive solitary modulations. Moreover, the $\frac{\alpha}{c^2} = -\frac{1}{4}$ limiting case for $\sigma > -\frac{3}{16}$ and $c > 0$ is represented by the "algebraic" solitary wave

$$a^2 = \frac{12c}{3c^2(\zeta - \zeta_0)^2 + 16(\sigma + \frac{3}{16})} \tag{6}$$

which represents the asymptotic limit for the solitary wave packet as $\alpha/c^2 \to -\frac{1}{4}$. In the $\sigma \to 0$ limit, we recover the Alfvén soliton[10]. We may therefore consider eq.(3) as a generalization of the normal($c < 0$) and anomalous ($c > 0$) Alfvén solitons [8] into the $\sigma \neq 0$ case.

Nonlinear behavior of the modulational instability

Thyagaraja[11] has discussed the qualitatively the dynamics of the Fourier modes of spatially periodic solutions of the NLS equation. He found that the recurrence property of the solution of a nonlinear evolution equation is connected to the existence of a finite number of effective Fourier modes (c.f.[9,11]), N_{eff}.If N_{eff} is bounded, the solution can be uniformly approximated

by a truncated Fourier series and is therefore bounded (or Lagrange stable). In addition a bound on the effective number of Fourier modes can be shown to imply that the solution is continous and therefore cannot collapse[12].(Notice we cannot give a sufficient criterion for collapse by this method.) The question we want to pose is if the quintic term in the EDNLS equation will lead to parameter regimes where no bound can be put on the effective number of Fourier modes. The three conservation laws for the EDNLS equation for energy, momentum and action are needed to find an upper bound on the effective number of Fourier modes from the EDNLS equation. We normalize the spatial period to one unit length by using the far field invariance of the EDNLS equation. Let us define the following quantities where the first two correspond to conservation of energy and momentum

$$\begin{aligned} I &= \int_0^1 |r|^2 dx, \\ Q &= \frac{1}{I}\int_0^1 -ir_x^* r dx, \\ s &= sign(Q), \\ N_{eff}^2 &= \frac{1}{4\pi^2 I}\int_0^1 |\Psi_x|^2 dx. \end{aligned} \tag{7}$$

We find the following classification:

1. $s = 1$.

The solution (N_{eff}) is always bounded and continous. This correspond to the modulational stable case if the amplitude is nearly constant.

2. $s = -1, \sigma \leq 0$.

The solution is always bounded and continous. $\sigma = 0$ corresponds to the integrable case (DNLS).

3. $s = -1, \sigma > 0$

The solution is bounded and continous for $I < I_\sigma, I_\sigma = \frac{1}{2}(3/\sigma)^{1/2}$.

If we specialize to an initially unstable, periodic, nearly constant amplitude (a_0) wave train with wavenumber k_0 and modulation wavenumber k_1, the following criterion must be satisfied to ensure noncollapsing (and possibly recurrent) solutions

$$\frac{2\pi}{I_\sigma} = Y_\sigma < Y < |Y_0| = (2(X + 2\sigma))^{1/2}, \tag{8}$$

$$\begin{aligned} X &= \frac{k_0}{a_0^2}, \\ Y &= \frac{k_1}{a_0^2}, \end{aligned} \tag{9}$$

and $X > 0, \sigma > 0$ (otherwise no criterion necessary). Notice that this criterion is impossible to fulfill when X is in the regime $0 < X < X_\sigma = Y_\sigma^2/2 - 2\sigma$ or if Y is in the long modulation regime ($Y < Y_\sigma$). This indicates that possible nonrecurrent or collapsing behavior of the solution could be searched for in the long modulation regime for $X, \sigma > 0$ or alternatively in the small positive X regime if $X_\sigma > 0$.

We have obtained numerical results on the evolution of the modulational instability into the nonlinear regime for parameter values of $\sigma \in [-1, 1]$. It is found that the EDNLS equation

for $X \approx 10 - 20$ and larger develops a recurrent pattern when$|\sigma| \leq 1$ (really $Y > Y_\sigma$) and Y somewhat less than the critical modulation wavenumber for growth. For $\sigma > 1, Y < Y_\sigma$ the unstable modulations grow and saturate in a more or less periodic wave form. Therefore, we indeed find examples of recurrent, noncollapsing solutions for $Y > Y_\sigma, \sigma > 0$ and examples of nonrecurrent solutions for $Y < Y_\sigma, \sigma > 0$. Collapsing solutions have not been found in the parameter regime we have investigated. In [13] it is argued from a discussion of renormalized solutions of the direct scattering problem for periodic modulations in the integrable case($\sigma = 0$) that the solutions will be effectively irreversible since the recurrence period will be exceedingly large in the long modulation regime $Y < Y_c = \kappa/2(1 + (1 + 2\kappa/X)^{1/2})$ where $\kappa \sim O(1)$.The reason for this is that a renormalized direct scattering solution for the modulated wave reveals an unexpected bifurcation in the nonlinear behavior of the periodic inverse scattering spectral spine structure of what linearly corresponds to the first harmonic component. In plain language, this means that the spatial first harmonic will have a complicated nonlinear behavior in time and most importantly that the period in time nonlinearly deviates from being a unit period for the spatial higher harmonic periods in time. Even if Thyagaraja criterion for recurrence is fulfilled it is expected that for modulations sufficiently large that the behavior is effectively irreversible in time. Such a behavior is confirmed from numerical simulations in [12].

Acknowledgements

This research was partially supported by the U.S. Department of Energy under contract#DE-AC03-75SF00098, NAVF and the Kempe Foundation. The authors wish to thank A. Kaufman and the MFE group at LBL for their kind hospitality and an inspiring environment.

References

[1]T.B.Benjamin, J.E.Feir, J.Fluid Mech.**27** 559(1967).
[2]T.Kakutani, K.Michihiro, J.Phys.Soc.Jpn.bf 52, 4129(1983).
[3]S.Ishiwata, S.Watanabe, H.Tanaca, J.Phys.Soc.Jpn.**58**, 519(1989).
[4]M.Saito, S.Watanabe, H.Tanaca, J.Phys.Soc.Jpn.**53**, 2304(1984).
[5]E.J.Parkes, J. Phys.A: Math. Gen. **20** ,2025(1987).
[6]A.Kundu, J. Math Phys. **25**, 3433(1984).
[7]A.Kundu, Physica **25**D, 399(1987).
[8]T.Hada, C.F.Kennel, B.Buti, JGR **94**A1, 65(1989).
[9]T.Flå; J.Wyller, preprint, accepted in Physica Scripta(1992).
[10]E.Mjølhus, J. Plasma Phys. **19**, 437(1978).
[11]A.Thyagaraja, Phys. Fluids **25**, 1973(1981).
[12]T.Flå, Phys. Scripta **40**, 206(1989).
[13]T.Flå, preprint 1991.

PLASMA OSCILLATIONS WAVE BREAKING IN INHOMOGENEOUS COLLISIONAL PLASMAS

S. De Nicola and C. Nappi, Istituto di Cibernetica del C.N.R.,
I-80072 Arco Felice, Napoli, Italy

1. Introduction

We study the free electron plasma oscillations in a collisional weakly inhomogeneous cold plasma in the hydrodynamic approximation. When the plasma is cold and inhomogeneous it can be shown/1,2/ that the ultimate fate of the non linear electron plasma oscillations, with stationary ions, is wave breaking /3/. At wave breaking the electron density diverges, the electric field becomes multivalued and the usual fluid approximation fails. Introducing a non zero temperature for the electron fluid keeps the density from taking non physical infinite values, at least when the temperature is sufficiently high or, in any case, greater than a threshold value /2/. We consider, here, the role of the collisions in preventing unphysical infinite electron density peaks from appearing during the non linear electron plasma oscillations evolution in a weakly inhomogeneous cold plasma. We find that in general the presence of damping, as could be expected, delays the wave breaking and that, less obviously, a *threshold damping* γ_c exists, beyond which the peaks in the density will remain finite /4/.

2. Weakly inhomogeneous plasma approximation

We will consider an infinitely extended plasma inhomogeneous along the x direction. To the lowest order in the electron to ion mass ratio /5/, the ion fluid can be considered immobile while the electron evolution is determined, in the presence of collisions, by the following set of equations

$$\frac{\partial n_e}{\partial t} + \frac{\partial n_e v_e}{\partial x} = 0 \qquad (1)$$

$$m_e \left(\frac{\partial v_e}{\partial t} + v_e \frac{\partial v_e}{\partial x} \right) = - eE - m_e \nu v_e \qquad (2)$$

$$\frac{\partial E}{\partial t} + v_e \frac{\partial E}{\partial x} = 4\pi e n_i(x) v_e \qquad (3)$$

We assume the following conditions

$$n_i(x,t) = n_i(x) = n_o(1+\alpha f(kx)); \quad v_i(x,t)=0; \; 0 < \alpha < 1$$
$$n_e(x,0) = n_o ; \qquad v_e(x,0) = 0$$

where n_o is the equilibrium plasma density, k^{-1} the length scale of the inhomogeneity. We note explicitly that, here, ν is the constant electron-ion collisional damping rate relative to the undisturbed plasma density n_o. In fact, the non uniformity in ν appears only through terms of order higher than α /4/, which are disregarded in this analysis. The initial electric field which drives the onset of the electron plasma oscillations is determined by Poisson's equation at t=0

$$E(x,0) = \frac{4\pi\alpha e n_o}{k} G(x),$$

Where G'(u)=f(u) and the prime denotes derivative respect to the argument. By using the dimensionless variables

$$x = kx, \quad t = \omega_{po}t, \quad n_e = \frac{n_e(x,t)}{n_o}, \quad n_i = \frac{n_i(x,t)}{n_o}, \; v_e = \frac{kv_e}{\omega_{po}}, \; E = \frac{kE}{4\pi e n_o}, \; \gamma = \frac{\nu}{\omega_{po}}$$

with $\omega_{po} = (4\pi n_o e^2/m_e)^{1/2}$, the undisturbed plasma frequency, and by introducing dimensionless Lagrangian coordinates (ξ,τ)

$$x = \xi + \phi(\xi,\tau); \qquad \tau = t; \qquad \phi(\xi,\tau) = \int_0^\tau v_e(\xi,\tau')d\tau'$$

we reduce the problem to a single equation for the electron displacement $\phi(\xi,\tau)$

$$\frac{\partial^2\phi}{\partial\tau^2} + \phi + \alpha G(\xi+\phi) + \gamma\frac{\partial\phi}{\partial\tau} = 0 ; \quad \phi(\xi,0) = 0 ; \quad \left(\frac{\partial\phi}{\partial\tau}\right)_{\tau=0} = 0 \qquad (4)$$

In the case of weakly inhomogeneous plasmas ($\alpha<<1$) the essential features of the solution of eq. (4), are still retained by a small amplitude treatment.

Then limiting ourselves only to linear terms in ϕ, /6/, we have:

$$\frac{\partial^2\phi}{\partial\tau^2} + (1+\alpha G'(\xi))\phi + \alpha G(\xi) + \gamma\frac{\partial\phi}{\partial\tau} = 0 \qquad (5)$$

whose solution, assuming γ at most to be of order α, can be approximately written as

$$\phi = \alpha G(\xi)\left(e^{-\gamma\tau/2}\cos[1 + \frac{\alpha}{2}G'(\xi)]\tau - 1\right) \qquad (6)$$

Now the density is given, in Lagrangian coordinates, by

$$n_e(\xi,\tau) = \frac{1}{1 + \frac{\partial \phi}{\partial \xi}} \approx$$

$$\approx \frac{1}{1+\alpha G'(\xi)\left(e^{-\gamma\tau/2}\cos[1+\frac{\alpha}{2}G'(\xi)]\tau - 1\right) - \frac{\alpha^2}{2}GG''\tau e^{-\gamma\tau/2}\sin[1+\frac{\alpha}{2}G'(\xi)]\tau} \qquad (7)$$

3. Results

Although a number of assumptions limit the applicability of the solution (7) it is indeed possible to learn from it the essential points we are interested in. First of all eq.(7) implies that, differently from the $\gamma=0$ case, wave breaking is not necessarily reached in every case. If γ is large enough, the exponential factor in the denominator can prevent $\partial\phi/\partial\xi$ from becoming -1 or in other words a *threshold exists* γ_c beyond which the peaks in the density will remain finite.

The envelope equation for the density is given by

$$n_e^{env}(\xi,\tau) = \frac{1}{1 - \alpha G'(\xi) - \frac{\alpha^2}{2}|G(\xi)G''(\xi)|\tau e^{-\gamma\tau/2}} \qquad (8)$$

from which we get the critical damping value,

$$\gamma_c = \frac{\alpha^2|GG''|}{e(1-\alpha G')} = \frac{\alpha^2|GG''|}{e} \qquad (9)$$

The presence of the damping delays the wave breaking and $\tau_{bc}=2/\gamma_c$ represents the upper bound for the breaking times, i.e. if a wave does not breaks within τ_{bc} it will not break any more. For values of γ above γ_c the oscillations are sufficiently damped so that only finite density peaks will appear and no wave breaking occurs. For γ values below γ_c the oscillations are not sufficiently damped to prevent electron density bursts and in this case, for $\gamma\tau << 1$ a simple analysis shows that

$$\tau_b = \frac{\tau_{bo}}{1 - \frac{\gamma}{2}\tau_{bo}} \qquad (10)$$

where

$$\tau_{bo} = \frac{2(1-\alpha G')}{\alpha^2 |GG''|} \approx \frac{2}{\alpha^2 |GG''|} \qquad (11)$$

is the breaking time in absence of damping /5/,/7/.

In Fig.1 for the sake of illustration the electron density is calculated from eq.(7) for $\gamma=0$, during the cycle 28π-30π in which the waves break. We have assumed an hyperbolic-squared ion pulse profile $f(x)=\mathrm{sech}^2(x)$ and $\alpha=0.2$,(a) is calculated for $\tau = 28.5\pi$ and b) for $\tau=29\pi$. In Fig.2 the electron density profile envelope evolution is plotted using eq.(8) as a function of normalized time (in ω_{po}^{-1} units) at $\xi = \pm 0.881$ (corresponding to the points in which wave breaking would occur earlier in absence of damping). The dimensionless damping rate is $\gamma=2 \times 10^{-3}$, greater than the threshold (9). In this case the damping is large enough to prevent electron plasma oscillations from breaking and the electron density tends asymptotically to the equilibrium value corresponding to that of the perturbed ion density background,(a) $\alpha=0.05$;(b) $\alpha=0.07$;(c) $\alpha=0.09$

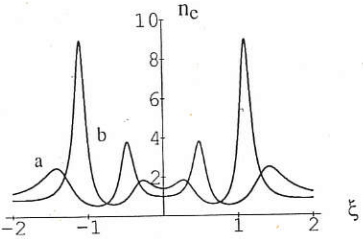

Fig.1-Electron density evolving towards wave breaking: (a)$\tau=28.5\pi$, (b)$\tau=29\pi$. The two main peaks will diverge within $\tau=30\pi$

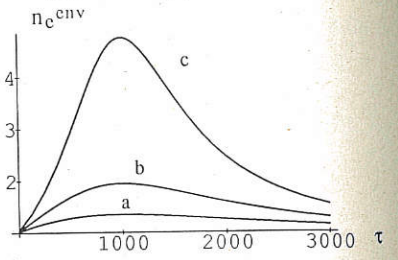

Fig.2-Evolution of the electron density envelope at $\xi=\pm 0.881$. The damping γ is large enough ($>\gamma_c$) and the amplitude saturates.

6.References

/1/ E. Infeld, G. Rowlands and S. Torvén, Phys. Rev. Lett. **62**, 2269 (1989)

/2/ E. Infeld and G. Rowlands, Phys. Rev. A. **42**, 838 (1990)

/3/ W.B. Mori and T.Katsoulcas, Phys. Scripta **T30**, 127 (1990)

/4/ S. De Nicola, C. Nappi to be published in Europhys. Lett.

/5/ C. Nappi, A. Forlani and R. Fedele, Phys. Scripta, **43**, 301 (1991)

/6/ P. Koch and J. Albritton, Phys. Rev. Lett. **32**, 1420 (1974)

/7/ S. De Nicola, R. Fedele, C. Nappi, Conference proceeding vol.29 "*Quantum Electronics and plasma physics*", G.C.Righini (Ed.), SIF, Italy 1991

II-1317

NONLINEAR ABSORPTION ON THE FRONT OF RELATIVISTICALLY STRONG ELECTROMAGNETIC PULSE IN AN UNDERDENSE PLASMA

S.V.Bulanov, I.N.Inovenkov*), V.I.Kirsanov, N.M.Naumova, A.S.Sakharov and M.A.Shah**)

General Physics Institute, Russian Academy of Sciences, Vavilov Street 38, Moscow, Russia

*)Moscow State University, Moscow, Russia

**)Permanent Address: Center for Solid State Physics, University of the Punjab, New Campus, Lahore, Pakistan.

The recent progress in producing extremely strong laser pulses [1] has made available for investigators the relativistically strong laser pulses in the field of which the energy of oscillating electron can exceed their rest energy mc^2. In the ultrarelativistic limit the matter of primary interest is to study the nonlinear interaction on the pulse edges, since inside the main body of the pulse the interaction is suppressed due to the relativistic electron mass growth. As it was shown in Ref.2 the sharp leading edge of the pulse generates an intense electron plasma wave. For the smooth pulses the leading part of the pulse can undergo steepening as a result of various nonlinear processes, for example, it can be initiated by the stimulated backward Raman scattering [3]. Once the steepening has appeared the excitation of the plasma wake is switched on and we again return to the case of a sharp leading edge.

In the present paper the propagation of a relativistically strong electromagnetic pulse in an underdense ($\omega_p^2 \ll \omega_0^2$) homogeneous plasma is considered with the focus on the possible existence of stationary structure of a pulse front. Due to the ultra fast nature of the process the ions can be regarded as an immobile neutralizing background. We shall look for the solution of the set of fully relativistic nonlinear electron fluid equations and Maxwell's equations to describe the pulse front motion. We consider one-dimensional case and the circularly polarized radiation. The low frequency electron motion is characterized by the electrostatic potential ϕ (normalized to mc^2). The high frequency field is described the normalized vector potential of the pulse field taking it in the form:

$$eA_{\perp}/mc^2 = \frac{1}{2}\left(e_o a(\xi)\exp(-i\omega t+ikx) + c.c.\right). \qquad (1)$$

Here a is the complex amplitude of the pulse field which is assumed to be stationary in the frame moving with the velocity V, $\xi = x-Vt$, vector $e_o = (y_o+iz_o)/\sqrt{2}$ is a unit vector of circular polarization, ω and k are the high frequency and wave number, respectively, which are related by the expression $k = V\omega/c^2$. The coupled equations for a and ϕ can be obtained in the form [4]

$$\frac{\partial^2 a}{\partial\xi^2} + \left\{\frac{\omega^2}{c^2} - \frac{\omega_p^2\gamma_o^2}{c^2(1+\phi)}\beta\left\{1 - \frac{1+|a|^2/2}{(1+\phi)^2\gamma_o^2}\right\}^{-1/2}\right\} a = 0. \qquad (2)$$

$$\frac{\partial^2\phi}{\partial\xi^2} - \frac{\omega_p^2\gamma_o^2}{c^2}\left\{1-\beta\left\{1 - \frac{1+|a|^2/2}{(1+\phi)^2\gamma_o^2}\right\}^{-1/2}\right\} = 0. \qquad (3)$$

where $\beta = V/c$, $\gamma_o^2 = 1/(1-\beta^2) \gg 1$, $\omega_p = (4\pi e^2 n_0/m)^{1/2}$ is the electron plasma frequency ($\omega_p \ll \omega$), and n_0 is the unperturbed electron density.

As for $\gamma_o^2 < \omega^2/\omega_p^2$ only periodical solutions exist, we restrict ourselves to the opposite case $\gamma_o^2 > \omega^2/\omega_p^2$. A typical behavior of the solution of the coupled Eqs.(2),(3) in the leading part of a relativistically strong pulse ($|a|^2 \gg 1$) is presented in Fig.1. Here $\omega/\omega_p = 100$ and $\gamma_o^2 = 1.01\omega^2/\omega_p^2$. Curve 1 and 2 correspond to the profiles of a and ϕ, respectively.

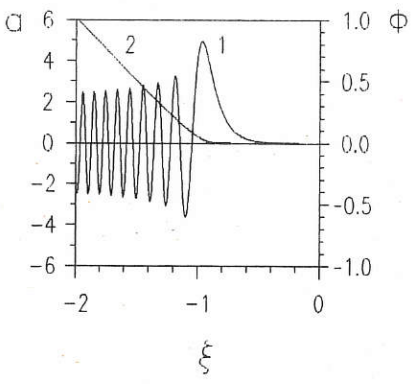

Fig.1

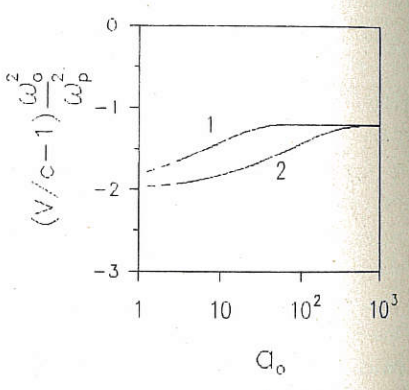

Fig.2

Ahead of the pulse (for $\xi \to +\infty$) a and ϕ go to zero. Behind the front the amplitude a oscillates. The oscillations of a can be interpreted as a superposition of two light waves with the amplitudes $a_\pm = a_m(\xi)$ and the local frequencies and wave numbers $\omega_\pm(\xi) = \omega \pm \chi(\xi)$, $k_\pm(\xi) = k \pm \varkappa(\xi)$, where

$$\varkappa(\xi) = \left\{ \frac{\omega^2}{c^2} - \frac{\omega_p^2 \gamma_o^2}{c^2(1+\phi)} \beta \left\{ 1 - \frac{1+|a|^2/2}{(1+\phi)^2 \gamma_o^2} \right\}^{-1/2} \right\}^{1/2} . \qquad (4)$$

The wave with the subscript "+" can be associated with the "fresh" radiation supplied to the front region from the bulk of the pulse. The other wave corresponds to the radiation reflected from the leading front.

Behind the front ϕ increases and for $\phi \gg 1$ Eq.(2) becomes decoupled from Eq.(3). The plus-wave propagates there as in a vacuum so that in the interior region of the pulse ω_+ and k_+ become equal to $\omega_o \equiv \omega(1+\beta) \simeq 2\omega$ and $k_o \equiv \omega(1+\beta)/c \simeq 2k$, those can be considered as the carrying frequency and the wave number of the pulse.

As the potential ϕ behind the front varies slowly in comparison with the oscillations of a, in this region the value $a_+^2 \varkappa$ is conserved. Matching the solutions in the front region with that inside the pulse, we find the value of $a_o \equiv a_+(\phi \to \infty)$ which can be associated with the amplitude of the main part of the pulse. As a_o depends on γ_o and ω_p/ω one can express V as function of ω_o and a_o. Under condition $1 \ll a_o^2 \ll \omega_o^2/\omega_p^2$ (when the Eqs.(2),(3) can be simplified considerably) we obtain

$$V/c - 1 \simeq - \frac{2\omega_p^2}{\omega_o^2} \left\{ 1 - \left(\frac{0.4 a_o^2 \omega_p^2}{\omega_o^2} \right)^{2/5} \right\} . \qquad (5)$$

For greater amplitudes ($a_o^2 \geq \omega_o^2/\omega_p^2$) the more sophisticated analysis without expanding of square root terms in Eqs.(2),(3) shows that the growth of $V/c-1$ with the increase of a_o is limited by the certain value $(V/c-1)_{max} \simeq -\omega_p^2/\omega_o^2$. This fact means that even a pulse of an infinitely large amplitude with a stationary leading front propagates at the velocity not too close to c.

The results of numerical integration which show the velocity of the stationary front as function of a_o for two values of $\omega_o/\omega_p = 10$ (curve 1) and $\omega_o/\omega_p = 100$ (curve 2) are presented in Fig.2. It can be seen that V depends rather weakly on the pulse amplitude: the value of $V/c-1$ increases from $-2\omega_p^2/\omega_o^2$ (for $1 \leq a_o \ll \omega_o/\omega_p$) up to $-1.2\omega_p^2/\omega_o^2$ (as $a_o \to \infty$).

As the group velocity of radiation inside the pulse $v_g \simeq c(1-0.5\omega_p^2/\omega_o^2(1+\phi))$ (where $\phi \gg 1$) tends to c, there is a permanent energy input into the front region, where the energy of the electromagnetic field is converted to longitudinal plasma oscillations. So, the total time of the pulse depletion with the duration τ can be estimated as

$$t_{dep} \simeq \tau /(1-V/c) \simeq \tau\ \omega_o^2/\omega_p^2 \quad . \qquad (6)$$

This is in a fairly good agreement with the results of computer simulation [5].

Stretching the exact solution of the Eqs.(2),(3) into the main body of the pulse, we can find out that in the considered model somewhere behind the leading front the potential ϕ after reaching its maximum value $\phi_{max} \gg 1$ decreases down to the values comparable with 1 , so that Eqs.(2),(3) become coupled again. In fact, even small electron temperature can lead to trapping of the plasma electrons [6] and to formation of the additional space charge inside the pulse. As a result, everywhere behind the leading front we have $\phi \gg 1$ and Eqs.(2),(3) remain decoupled. So our initial assumption that interaction is suppressed inside the pulse seems to be true. Thus, the considered above solution should be regarded primarily as the kink type solution for the pulse leading front.

REFERENCES

1. P.Maine, D.Stricland, P.Bado, M.Pessot, G.Mourou, IEEE J. Quan. Elec., 24, 398 (1988)

2. S.V.Bulanov,V.I.Kirsanov,A.S.Sakharov. Sov.J.Plasma Phys.,16,543 (1990)

3. S.V.Bulanov, I.N.Inovenkov, V.I.Kirsanov, N.M.Naumova, A.S.Sakharov. Phys.Fluids B (1992) (accepted for publications)

4. V.A.Kozlov,A.G.Litvak,E.V.Suvorov. Zh. Eksp. Teor. Fiz., 76, 148 (1979)

5. S.V.Bulanov, I.N.Inovenkov, V.I.Kirsanov, N.M.Naumova, A.S.Sakharov. Nonlinear Depletion of Short and Relativistically Strong Laser Pulse in an Underdense Plasma, *these Proceedings*

6. S.V.Bulanov,V.I.Kirsanov,A.S.Sakharov. Sov. JETP Letters, 53, 540 (1991)

"PLASMA MASER" EFFECT IN TURBULENT PLASMA WITH REGULAR AND RANDOM MAGNETIC FIELDS

J.M. Pryadko, V.N. Tsytovich
Theoretical Department, General Physics Institute,
Vavilova Street 38, Moscow, Russia

Now the investigation of possibilities of amplification of high frequency waves (Lengmuir, electromagnetic etc.) attracts the attention of many physicists. The nonlinear interaction of resonant and nonresonant waves in turbulent plasma, first considered by Tsytovich et al. /1/, is of considerable interest. The resonant waves, as a rule, are considered to be low frequency oscillations. If there is a sufficiently high extra- thermal level of the energy of the resonant oscillations, a nonlinear amplification of the high frequency nonresonant waves will take place. Such a type of interaction is called an up-conversion of the plasma oscillations energy or plasma-maser effect.

Examples of this nonlinear interaction has been observed more than once both in laboratory experiments and in astrophysics. In the latter case, the random magnetic fields, presented in many space plasmas, can play the role of low frequency resonant oscillations.

The purpose of the present paper is to point out that very high frequency electromagnetic waves can be amplified in a plasma with random magnetic fields in the presence of weak regular magnetic field H_0. Such an amplification is either due to the anisotropy of distribution of random magnetic fields $\tilde{H}_l$ or due to the anisotropy of plasma particles. It should be emphasized that the effect of electromagnetic waves amplification hasn't been discovered in the con-

/1/ V.N.Tsytovich, L. Stenflo, H. Wilhelmsson, Phys. Scr. **11**, 251 (1975)

trary case of strong magnetic fields, investigated previously /2/, under the first cyclotron resonance condition with plasma particles.

Let us consider the simplest case of weak random and weak regular magnetic fields, when the gyrofrequency ω_{He} is much less than the (electron) plasma frequency ω_{pe}: $\omega_{He}/\omega_{pe} \ll 1$, where $\omega_{He} = |e|H_0/m_e c$, $\omega_{pe} = (4\pi n_e e^2/m_e)^{1/2}$), the electron charge is $e=-|e|$, n_e and m_e are electron concentration and mass respectively, $H_0 = |\vec{H}_0|$ is the external magnetic field strength. Then these magnetic fields will alter the ground condition of plasma particles.

Let there be two kinds of oscillations in a plasma: low frequency waves with frequency and wave vector $(\Omega, \vec{q})$, for which Cherenkov resonance condition with plasma particles may be thus fulfilled: $\Omega - \vec{q}\vec{v} = 0$; and high frequency waves $(\omega, \vec{k})$, for which both Cherenkov $(\omega - \vec{k}\vec{v} \neq 0)$ and scattering (into the resonant mode) $(\omega - \Omega - (\vec{k}-\vec{q})\vec{v} \neq 0)$ resonances with particles are forbidden. We can continue to consider high frequency waves as nonresonant ones in the weak field because the probability of cyclotron resonance $\omega - k_z v_z - n\omega_{He} = 0$ under the condition of large $n \approx \omega_{pe}/\omega_{He}$ is proportional to the small factor $exp(-\omega_{pe}/\omega_{He}) \ll 1$.

Let us consider the weak random magnetic fields as the resonant waves:

$$\langle \tilde{H}_{q_i} \tilde{H}_{q'_j} \rangle = \frac{1}{2} |\tilde{H}_q|^2 \delta(q+q') \left(\delta_{ij} - \frac{q_i q'_j}{q^2}\right)$$

$$\vec{\tilde{H}}_1(t,\vec{r}) = \int dq \, \vec{\tilde{H}}_q \, exp(-i\Omega t + i(\vec{q}\vec{r})) \qquad (1)$$

A general expression for the growth rate γ of the nonresonant electromagnetic wave instability due to their non-

/2/ V.L. Ginzburg et al., Astrophisics of cosmic rays, Moscow Science Press (1990).

linear interaction with random magnetic fields can be found on the basis of the kinetic equation, extracting the regular $\Phi_E = \langle f_E \rangle$ and turbulent $\delta f_E = f_E - \Phi_E$ parts of particle distribution function (E is the energy of particles), with the aid of the technique developed in /3,4/. $\langle \ldots \rangle$ designates the statistic ensemble averaging.

This general expression, valid for any particle distribution function Φ_E, which we have found after complicated calculations, is too lengthy to include in this paper. We shall limit ourselves to the estimation of increment (decrement) γ_a in the case of even a very small anisotropy of the particle distribution function Φ_E. After some calculations, assuming isotropic random magnetic fields, we obtain:

$$\gamma_a \sim \omega_{pe} \varepsilon \frac{\omega_{pe}^3}{\omega^3} \frac{W_1}{n m_e c^2} \frac{\omega_{He}^3}{q^3 c^3} \frac{\omega_{pe}}{\omega_{He}} f(\vartheta) \qquad (2)$$

where ε ($\varepsilon \ll 1$) accounts for the degree of anisotropy, ω_{pe}, ω_{He} - (electron) plasma and cyclotron frequencies respectively, $W_1 = \langle |\tilde{H}_q|^2 / 8\pi \rangle$ - density of the energy of resonant waves, n- density of plasma particles, q- characteristic value for wave vector of random magnetic fields, $f(\theta)$ - coefficient, accounted for angular dependence γ_a in different cases of mutual orientation of vectors $\vec{k}$, $\vec{H}_0$ and $\vec{n}$, where $\vec{n}$ is a characteristic direction of anisotropy of distribution function. Only electron contribution is taken into account in (2); the analogical contribution from the ions is ($m_i / m_e \gg 1$) times less than (2) (m_e and m_i - the masses of the electron and the ion respectively) and can be omitted.

The condition under which γ_a more than analogical γ_i, which is corresponded to the isotropic function of particle

/3/ S.B. Isakov, V.S. Krivitsky, V.N. Tsytovich, Sov. Phys. JETP **63** 545 (1986)

distribution, is

$$\frac{\Omega}{qc} << \varepsilon << 1 \qquad (3)$$

The value of angular factor $f(\theta)$ depends on the kind of Φ_E distribution function.

The cosmic ray electrons and ions are indeed always slightly anisotropically distributed, due to particle diffusion in space. We can use the model distribution function for cosmic rays (for example, /2/):

$$\Phi_E = N_{c.r.}\,\Theta(E-E_0)\left(\frac{E_0}{E}\right)^{\alpha}\frac{1}{E_0}\frac{1}{(\alpha-1)}\,,\alpha>1, \qquad (4)$$

where $\Theta(E-E_0)$ - Heviside function, $N_{c.r.}$ - concentration of cosmic rays, E_0 - their threshold energy, N_0 - plasma concentration. Then

$$f(\vartheta) = \frac{1}{k\,H_0^2}\left(\frac{mc^2}{E_0}\right)^2\frac{N_{c.r.}}{N_0}\times \qquad (5)$$

$$\times\left(-8\,H_0^2(\vec{k}\vec{n})-15\,(\vec{H}_0\vec{k})(\vec{H}_0\vec{n})+120\,\frac{(\vec{H}_0\vec{k})^2}{k^2}(\vec{k}\vec{n})\right)$$

The sign of γ_a depends on the sign of $f(\theta)$. If all three vectors $\vec{H}_0$, $\vec{k}$ and $\vec{n}$ are parallel to each other then $f(\theta)\approx 1$ and the wave will propagate with amplification.

Finally, we can say that this new effect of the electromagnetic wave amplification, which hasn't yet been taken into account in the former investigations, would be able to explain the occurrence of pulses of high frequency radiation in space while other mechanisms no longer work.

/4/ V.S. Krivitsky, J.M. Pryadko, V.N. Tsytovich, Plasma Physics (rus) **16**, 801 (1990)

8-32

NONLINEAR EVOLUTION OF THE MODULATIONAL INSTABILITY AND CHAOS BY USING ID-ZAKHAROV EQUATIONS

R.P. SHARMA* and A.D. VERGA**
*Centre for Energy Studies, IIT Delhi-110016 INDIA.
**Equipe Turbulence Plasma #, Institut Mediterraneen de Technologie, Technopole de Marseille-Provence,F 13451 MARSEILLE CEDEX 13, FRANCE.

ABSTRACT

Nonlinear evolution of modulational instability by using nonlinear Schrödinger equation (NLS) in one dimension reveals a periodic recurrence of the intial conditions. Nonlinear Schrödinger equation is the adiabatic limit of Zakharov equations which couple the elestrostatic electron plasma wave and ion-acoustic wave propagation. In the present paper, we have studied the nonlinear evolution of modulational instability by using one dimensional Zakharov equations. It is seen that the effect of relaxing the condition of adiabaticity is drastic on the nonlinear evolution pattern of modulational instability. This evolution is quite sensitive to the intial conditions, recurrence is broken up and chaotic state has been observed.

1D Zakharov Model: These equations are given by[1]

$$\partial_t E + \partial_x^2 E = n E \quad , (1)$$

$$\partial_t^2 n - \partial_x^2 n = \partial_x^2 |E|^2 \quad , (2)$$

where the notations have their usual meanings[1]. These equations have been solved numerically in a periodic box for the initial condition

$$E = A_0 [1 + \beta e^{i\gamma} \cos \alpha x]$$

Pesudo spectral method was used for space integration, Leap frog method with predictor corrector was employed for the evolution in time. Figures 1 and 2 show the results obtained for the evolution of electric field. For two values of α, we see two types of patterns. To have further insight, we have plotted the mode of the maximum value of the electric field in fig. 3 for $\alpha = 1.0$ and it is seen that the recurrence as observed in NLS[2,3,4] is no longer present. The behaviour is chaotic in time. This is also obvious by looking at the Fourier components of the electric field (Figs. 4 and 5). Similarly, we have seen that the density and its Fourier components also show chaotic behaviour. For the seond pattern also (viz $\alpha = 1.2$), we have observed chaotic behaviour of electric field and density. In both the cases, the zeroth component of density is constant and its magnitude is equal to number of plasmons.

Simplified Model: Based on the results of numerical simulation, we are interested in developing a simplified model to explain the temporal behaviour (not the spatial). This model can establish atleaste the fact that, as the condition of adiabaticity is relaxed, the recurrence behaviour disappears and the existence of chaotic state can be established. Keeping this in mind, we expand the electric field and density as

$$E = \sqrt{N}\,\sin\left(\frac{a}{2}\right) e^{i\theta_0} + \sqrt{2N}\,\cos\left(\frac{a}{2}\right) e^{i\theta_1}\cos\alpha x \quad , (3)$$

$$n = N + \sqrt{2}\, n_1 \cos\alpha x \quad , (4)$$

Here N is the plasmon number. Substituting this expansion of electric field and density in Zakharov eguations, we get following system of equations

$$\dot{a} = -4 n_1 \sin\phi \quad , (5)$$

$$\dot{\phi} = \alpha^2 - 2 n_1 \cot a \cos\phi \quad , (6)$$

$$\dot{n}_1 + \alpha^2 n_1 = -\alpha^2 N \sin a \cos\phi \quad , (7)$$

$$\phi = \theta_0 - \theta_1 \quad (8)$$

When we assume the adiabaticity condition, the system of equations (5) to (8) can be written in the Hamiltonian form as

$$\dot{\phi} = \frac{\partial H}{\partial a} \quad , \quad \dot{a} = -\frac{\partial H}{\partial \phi} \quad , (9)$$

where

$$H = \frac{\alpha^2}{2} a + \frac{N}{2}\sin a + \frac{N}{2}\sin a \cos 2\phi \quad (10)$$

Obviously this system (Eqs 9,10) is integrable (as expected). One can easily find the fixed points also of this system (Eqs 9,10) and can prove that allowed range of α^2 is given by $c < \alpha^2 < 2N$. Corresponding to the unstable fixed points, the growth rate of instability γ_I is given by

$$\gamma_I = 2\left(-\alpha^4 + 2N\alpha^2\right)^{\frac{1}{2}} \equiv 2\,\gamma_{M.I} \quad (11)$$

where $\gamma_{M.I}$ is the linear growth rate of modulational instability as perdicted by NLS[2,3]. The phase space plot in this adiabatic case is plotted in fig.6 and as expected, one can see the existance of regular orbit in adiabatic case.

When adiabaticity condition is relaxed, one can find the fixed points of Eqs 5 to 8. It has been observed by us that the unstable fixed points, perdict exactly the same growth rate of modulational instability as expected by Zakharov equations in the linear stage.[5] The phase space plot in two different cases are also plotted in figs 7 and 8 in nonadiabatic case. Figure 7 if compared with Figure 6, one can observe the transition to chaotic stage when adiabaticity condition is relaxed. Figure 9 gives another phase space plot in nonadiabatic case.

Acknowledgements: This research was partially supported by EC and D.S.T. India.

REFERENCES

Equipe du laboratoire de Physique des Interactions Ioniques et Moleculaires, Universite de Provence, Unite de Recherche Associee 773 du CNRS.

1. V.E. Zakharov, Zh E.ksp. Theor. Fiz.62, 1745 (1972); Sov. Phys. JETP 35, 908 (1972).

2. H.C. Yuen and B.M. Lake Adv. Appl. Mech. 22, 67 (1982); H.C. Yuen and W. Ferguson Phys. Fluids 21, 1275 (1978).

3. P.P. Goldstein and W. Rozmus Phys. Fluids B 2, 44 (1990).

4. H.T. Moon Phy. Rev. Lett. 64, 412 (1990).

5. M.M. Shen and D.R. Nicholson Phys. Fluids 30, 1096 (1987).

Figure Capations

Fig.1 3D plot of $|E|^2$ for $\gamma=0$ and $\alpha=1.0$ when $A_c=1$, $\beta=.1$

Fig.2 3D plot of $|E|^2$ for $\gamma=c$ and $\alpha=1.2$ when $A_c=1$, $\beta=.1$

Fig.3 Plot of $|Emax|$ against time for Fig 1

Fig.4 Plot of $|E_k|$ when k=o against time for Fig 1

Fig.5 Plot of $|E_k|$ when k= α against time for Fig 1

Fig.6 Phase space plot in adiabatic case ($\alpha=1.2$, $N=1.0005$)

Fig.7 Phase space plot in nonadiabatic case ($\alpha=1.2$, $N=1.0005$)

Fig.8 3D phase space plot in nonadiabatic case ($\alpha=1.2$, $N=1.0005$)

Fig.9 Phase space plot in nonadiabatic case ($\alpha=1.2$, $N=1.0005$)

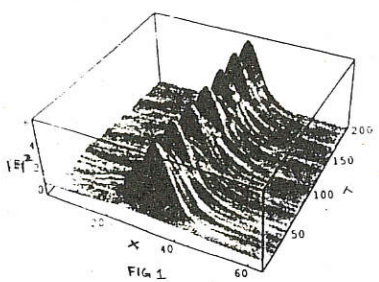

FIG 1

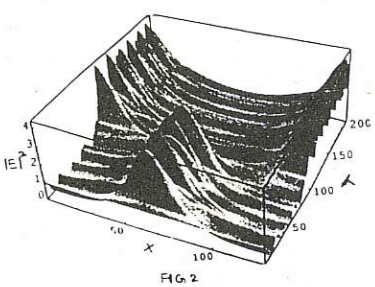

FIG 2

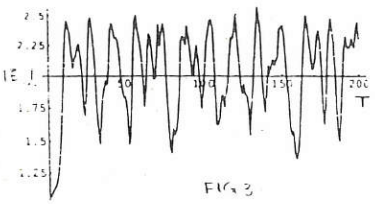

FIG 3

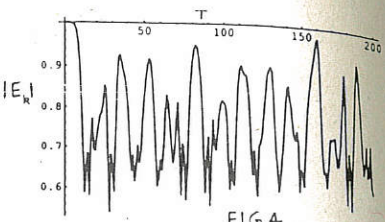

FIG 4

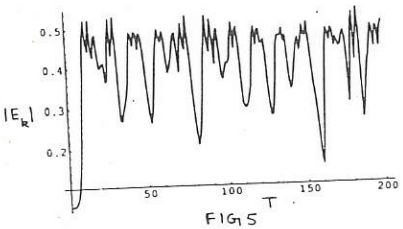

FIG 5

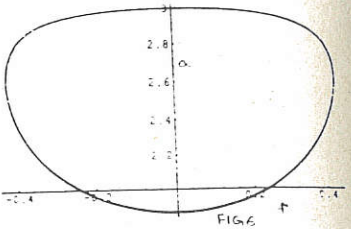

FIG 6

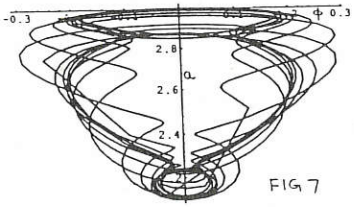

FIG 7

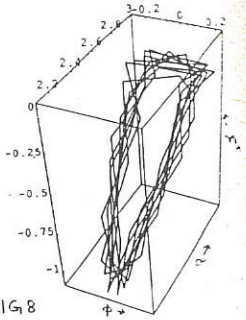

FIG 8

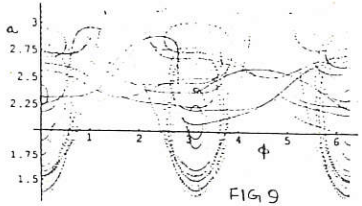

FIG 9

II-1329

Energy of Linear Quasi-neutral Electrostatic Drift Waves

Dieter Pfirsch and Darío Correa-Restrepo
Max-Planck-Institut für Plasmaphysik, EURATOM Association
D-8046 Garching, Germany

1 Introduction

Certain kinds of nonlinear instabilities are related to the existence of negative-energy perturbations. In this paper an exact energy expression for linear quasi-neutral electrostatic perturbations is derived within the framework of dissipationless multi-fluid theory, valid for any geometry. Taking the mass as a tensor with, in general, different masses parallel and perpendicular to an ambient magnetic field allows one to treat the full dynamics and also to restrict consideration to parallel dynamics or to the completely adiabatic case. Application to slab configurations yields the result that in plane geometry the adiabatic approximation does not allow negative-energy perturbations, whereas inclusion of the parallel dynamics does. This is in agreement with a numerical study of drift-wave turbulence within the framework of collisional two-fluid theory by B. Scott [1].
Unlike Scott, we consider a dissipationless theory, which is the only kind allowing unique definition of the energy of perturbations. Within such a theory the energy is a constant of the motion for any initial conditions. Whereas the nonlinear energy is just kinetic plus potential plus thermal energy, the energy of perturbations depends on constraints. In a multi-fluid quasi-neutral electrostatic theory, from which we start, such constraints are mass conservation and entropy conservation. The latter is violated if heat conduction, heat sources (e.g. Joule heating) and heat sinks play a role. Hence, the energy expressions which are obtained in this paper are, strictly speaking, valid only for situations where this is not the case or where these phenomena do not influence the entropy constraint. The latter is the case if the heat conduction is infinitely large such that the equilibrium temperature profiles $T_\nu(\mathbf{x})$ of the various particle species ν are independent of $\mathbf{x}$ and $\delta T_\nu = 0$. A vanishing temperature perturbation results in an entropy-conserving theory if one takes the adiabtic coefficients $\gamma_\nu = 1$. This is possible, however, only for the perturbations; the equilibrium energy would diverge. When we consider this case, we do it in the way that the γ's are put equal to 1 only after having obtained the perturbed energy for general γ's.
A dissipationless theory can be formulated in terms of a Lagrangian, from which the energy is immediately obtained. We start with the nonlinear theory; the linearised theory is written in terms of displacement vectors $\boldsymbol{\xi}_\nu(\mathbf{x}, t)$ such that all constraints are taken into account, as in ideal MHD theory. The procedure used is the same as that developed in a forthcoming paper by Pfirsch and Sudan [2] for ideal MHD theory, which also allows one to obtain the exact nonlinear energy with all the constraints built in (Pfirsch [3]). People working in this field [4, 1] have considered up to now only (positive semi-definite) expressions for the nonlinear energy, which do not immediatly allow to investigate the existence of negative-energy perturbations relating to nonlinear instability [5, 6, 7] .

2 Quasi-neutral electrostatic multy-fluid theory

2.1 The Lagrangian of the nonlinear theory

Quasi-neutrality means that there is no electric field energy term, and since the magnetic field is even prescribed, there is no magnetic field energy term either; instead we have to use the usual coupling terms for charged particles in electric and magnetic fields. This results in

$$L = \sum_\nu \int d^3x \left\{ \frac{1}{2} n_\nu \mathbf{v}_\nu \cdot \underline{\underline{m}}_\nu \cdot \mathbf{v}_\nu - \frac{p_\nu}{\gamma_\nu - 1} - e_\nu n_\nu \Phi + \frac{e_\nu}{c} n_\nu \mathbf{v}_\nu \cdot \mathbf{A} \right\}, \qquad (1)$$

where

$$\underline{\underline{m}}_\nu = m_{\nu\perp}\underline{\underline{I}} + (m_{\nu\parallel} - m_{\nu\perp})\mathbf{bb}\ , \qquad I_{ik} = \delta_{ik}\ , \qquad \mathbf{b} = \mathbf{B}/B\ . \tag{2}$$

In the following the index ν will be suppressed if not needed. $\mathbf{A} = \mathbf{A}(\mathbf{x})$ is the fixed equilibrium vector potential and is not to be varied but all other quantities are. As concerns n, p and $\mathbf{v}$, these variations are expressed in terms of virtual displacement vectors $\boldsymbol{\zeta}(\mathbf{x}, t)$:

$$\delta n = -\nabla\cdot(n\boldsymbol{\zeta}), \quad \delta\mathbf{v} = \dot{\boldsymbol{\zeta}} + \mathbf{v}\cdot\nabla\boldsymbol{\zeta} - \boldsymbol{\zeta}\cdot\nabla\mathbf{v}, \quad \delta p = -\boldsymbol{\zeta}\cdot\nabla p - \gamma p\nabla\cdot\boldsymbol{\zeta}\ . \tag{3}$$

The first variations, on the one hand, must yield the nonlinear equations and, on the other, will serve to yield the second-order variations, from which the linearized equations and the second-order energy follow. The kinetic energy is denoted by K and the "potential" energy by U. In the following, we write down only the integrands of the variations of these quantities. After integrations by parts, also with respect to time, as is possible in the action integral, the integrand for the first variation of the kinetic energy becomes

$$\delta^{(1)}K := -\boldsymbol{\zeta}\cdot\left(\frac{\partial}{\partial t}(n\underline{\underline{m}}\cdot\mathbf{v}) + (\nabla\cdot\mathbf{v}\underline{\underline{m}}\cdot\mathbf{v}n)\right)\ . \tag{4}$$

Again after integrations by parts and use of $\dot{n} + \nabla\cdot(n\mathbf{v}) = 0$ the integrand for the first variation of the potential energy becomes

$$\delta^{(1)}U : \boldsymbol{\zeta}\cdot\nabla p + en\boldsymbol{\zeta}\cdot\nabla\Phi + en\delta\Phi - \frac{en}{c}\boldsymbol{\zeta}\cdot(\mathbf{v}\times\mathbf{B})\ . \tag{5}$$

The requirement that the factor of $\delta\Phi$ must vanish leads to the quasi-neutrality condition

$$\sum_\nu e_\nu n_\nu = 0\ . \tag{6}$$

Vanishing of the factor of $\boldsymbol{\zeta}$ yields the correct nonlinear equations of motion

$$n\underline{\underline{m}}\cdot\left(\frac{\partial}{\partial t} + \mathbf{v}\cdot\nabla\right)\mathbf{v} = -\nabla p + en(\mathbf{E} + \frac{1}{c}\mathbf{v}\times\mathbf{B})\ . \tag{7}$$

2.2 The Lagrangian of the linearized theory

This Lagrangian is the second-order expansion in real displacements of the original Lagrangian for the exact nonlinear theory. It is obtained by varying $\delta^{(1)}K$ and $\delta^{(1)}U$ again and then replacing the virtual displacement $\boldsymbol{\zeta}$ by the real displacement $\boldsymbol{\xi}$. To the envisaged order there is no need to vary the displacement itself, since its factor vanishes because of the equilibrium equations. One finds

$$\begin{aligned}\delta^{(2)}K \ : \ & \frac{1}{2}(\nabla\cdot(\boldsymbol{\xi}\nabla\cdot(n\boldsymbol{\xi})))\mathbf{v}\cdot\underline{\underline{m}}\cdot\mathbf{v} - 2(\nabla\cdot(n\boldsymbol{\xi}))\mathbf{v}\cdot\underline{\underline{m}}\cdot(\dot{\boldsymbol{\xi}} + \mathbf{v}\cdot\nabla\boldsymbol{\xi} - \boldsymbol{\xi}\cdot\nabla\mathbf{v}) \\ & + n\mathbf{v}\cdot\underline{\underline{m}}\cdot((\dot{\boldsymbol{\xi}} + \mathbf{v}\cdot\nabla\boldsymbol{\xi} - \boldsymbol{\xi}\cdot\nabla\mathbf{v})\cdot\nabla\boldsymbol{\xi} - \boldsymbol{\xi}\cdot\nabla(\dot{\boldsymbol{\xi}} + \mathbf{v}\cdot\nabla\boldsymbol{\xi} - \boldsymbol{\xi}\cdot\nabla\mathbf{v})) \\ & + n(\dot{\boldsymbol{\xi}} + \mathbf{v}\cdot\nabla\boldsymbol{\xi} - \boldsymbol{\xi}\cdot\nabla\mathbf{v})\cdot\underline{\underline{m}}\cdot(\dot{\boldsymbol{\xi}} + \mathbf{v}\cdot\nabla\boldsymbol{\xi} - \boldsymbol{\xi}\cdot\nabla\mathbf{v})\ .\end{aligned} \tag{8}$$

The contribution to the wave energy $\mathcal{E}$ is given by the term bilinear in $\dot{\boldsymbol{\xi}}$ and the negative of the terms not containing $\dot{\boldsymbol{\xi}}$, whereas the terms linear in $\dot{\boldsymbol{\xi}}$ do not contribute:

$$\begin{aligned}2\mathcal{E}_K \ : \ & n\dot{\boldsymbol{\xi}}\cdot\underline{\underline{m}}\cdot\dot{\boldsymbol{\xi}} - n(\mathbf{v}\cdot\nabla\boldsymbol{\xi} - \boldsymbol{\xi}\cdot\nabla\mathbf{v})\cdot\underline{\underline{m}}\cdot(\mathbf{v}\cdot\nabla\boldsymbol{\xi} - \boldsymbol{\xi}\cdot\nabla\mathbf{v})^2 \\ & - \frac{1}{2}(\nabla\cdot(\boldsymbol{\xi}\nabla\cdot(n\boldsymbol{\xi})))\mathbf{v}\cdot\underline{\underline{m}}\cdot\mathbf{v} + 2(\nabla\cdot(n\boldsymbol{\xi}))\mathbf{v}\cdot\underline{\underline{m}}\cdot(\mathbf{v}\cdot\nabla\boldsymbol{\xi} - \boldsymbol{\xi}\cdot\nabla\mathbf{v}) \\ & - n\mathbf{v}\cdot\underline{\underline{m}}\cdot((\mathbf{v}\cdot\nabla\boldsymbol{\xi} - \boldsymbol{\xi}\cdot\nabla\mathbf{v})\cdot\nabla\boldsymbol{\xi} - \boldsymbol{\xi}\cdot\nabla(\mathbf{v}\cdot\nabla\boldsymbol{\xi} - \boldsymbol{\xi}\cdot\nabla\mathbf{v}))\ .\end{aligned} \tag{9}$$

For the second variation of the potential energy one obtains after some integrations by parts

$$\begin{aligned}\delta^{(2)}U \ : \ & -\boldsymbol{\xi}\cdot\nabla(\boldsymbol{\xi}\cdot\nabla p + \gamma p\nabla\cdot\boldsymbol{\xi}) - e\nabla\cdot(n\boldsymbol{\xi})\boldsymbol{\xi}\cdot\nabla\Phi \\ & + en\boldsymbol{\xi}\cdot\nabla\delta\Phi - e\nabla\cdot(n\boldsymbol{\xi})\delta\Phi \\ & + \frac{e}{c}\nabla\cdot(n\boldsymbol{\xi})(\mathbf{v}\times\mathbf{B})\cdot\boldsymbol{\xi} - \frac{e}{c}n[(\dot{\boldsymbol{\xi}} + \mathbf{v}\cdot\nabla\boldsymbol{\xi} - \boldsymbol{\xi}\cdot\nabla\mathbf{v})\times\mathbf{B}]\cdot\boldsymbol{\xi}\ .\end{aligned} \tag{10}$$

The variation of $\delta\Phi$ yields the linearized quasi-neutrality condition

$$\sum_\nu e_\nu \nabla \cdot (n_\nu \xi_\nu) = 0 \ . \tag{11}$$

The equilibrium relations

$$e(\mathbf{E} + \frac{1}{c}\mathbf{v} \times \mathbf{B}) = \frac{1}{n}\nabla p$$

and integrations by parts lead to the following contribution to $\mathcal{E}$:

$$\begin{aligned} 2\mathcal{E}_U \ : \ & (\nabla \cdot \xi)(\xi \cdot \nabla p + \gamma p \nabla \cdot \xi) + \frac{1}{n}\nabla \cdot (n\xi)\nabla p \cdot \xi \\ & -\frac{e}{c} n[(\mathbf{v} \cdot \nabla \xi - \xi \cdot \nabla \mathbf{v}) \times \mathbf{B}] \cdot \xi \ . \end{aligned} \tag{12}$$

The sum of this expression and expression (9) is twice the total wave energy.

2.3 Adiabatic approximation

This approximation means $m_e = m_i = 0$. Like Scott [1], we choose in addition $p_i = \mathbf{v}_i = 0 \Longrightarrow \mathbf{E} = 0$. Variation of the resulting second-order Lagrangian with respect to $\delta\Phi$ yields

$$\nabla \cdot (e_i n_i \xi_i) + \nabla \cdot (e_e n_e \xi_e) = 0 \tag{13}$$

and variation of ξ_i

$$0 = e_i(\delta\mathbf{E} + \frac{1}{c}\dot{\xi}_i \times \mathbf{B}) \ . \tag{14}$$

Variation with respect to ξ_e yields

$$\begin{aligned} & \frac{1}{2}\nabla(\xi_e \cdot \nabla p_e + \gamma_e p_e \nabla \cdot \xi_e) - \frac{1}{2}\nabla \cdot \xi_e \nabla p_e + \frac{1}{2}\gamma_e \nabla(p_e \nabla \cdot \xi_e) - \frac{1}{2}\frac{1}{n_e}\nabla \cdot (n_e \xi_e)\nabla p_e \\ & + \frac{1}{2} n_e \nabla(\frac{1}{n_e}\xi_e \cdot \nabla p_e) + e_e n_e(\delta\mathbf{E} + \frac{1}{c}\dot{\xi}_e \times \mathbf{B}) + \frac{1}{2}\frac{e_e}{c} n_e(\mathbf{v}_e \cdot \nabla \xi_e - \xi_e \cdot \nabla \mathbf{v}_e) \times \mathbf{B} \\ & + \frac{1}{2}\frac{e_e}{c}\nabla \cdot (\mathbf{v}_e n_e \xi_e \times \mathbf{B}) + \frac{1}{2}\frac{e_e n_e}{c}(\nabla \mathbf{v}_e) \cdot (\xi_e \times \mathbf{B}) = 0 \ . \end{aligned} \tag{15}$$

From the parallel component of this equation one derives

$$\delta\Phi = \frac{1}{e_e n_e}(\xi_e \cdot \nabla p_e + \gamma_e p_e \nabla \cdot \xi_e) = -\frac{1}{e_e n_e}\delta p_e \ . \tag{16}$$

A first expression for the wave energy is then

$$\begin{aligned} \mathcal{E} \ = \ & \int \Big\{ \frac{1}{2}(\nabla \cdot \xi_e)(\xi_e \cdot \nabla p_e + \gamma_e p_e \nabla \cdot \xi_e) + \frac{1}{2n_e}\nabla \cdot (n_e \xi_e)\xi_e \cdot \nabla p_e \\ & - \frac{e_e n_e}{2c}\xi_e \cdot ((\mathbf{v}_e \cdot \nabla \xi_e - \xi_e \cdot \nabla \mathbf{v}_e) \times \mathbf{B}) \Big\} d^3x \ . \end{aligned} \tag{17}$$

One can put this expression into a form which is similar to δW in ideal MHD. To this end we introduce $e_e n_e \mathbf{v}_e = \mathbf{j}$ and obtain the somewhat familiar looking expression

$$\mathcal{E} = \int \Big\{ \frac{1}{2}(\nabla \cdot \xi_e)(\xi_e \cdot \nabla p_e + \gamma_e p_e \nabla \cdot \xi_e) + \frac{1}{2}\xi_e \cdot \frac{1}{c}(\mathbf{j} \times \nabla \times (\xi_e \times \mathbf{B})) \Big\} d^3x \ . \tag{18}$$

Note that the last term enters the ideal MHD potential energy with the opposite sign. The reason for this difference is that there the magnetic field is not a fixed quantity but is determined self-consistently, which also leads to an additional term $(\delta\mathbf{B})^2/8\pi$.

Example

As an example, we consider a plasma slab dependent on x only; we choose $\gamma_e = 1$, $T_e = T = const.$, $\mathbf{v}_e = (0, 0, v_e) = const.$. The minimum of $\mathcal{E}$ for this configuration is zero.

2.4 Parallel dynamics in a force-free configuration

The last section has shown that the thermal energy alone does not lead to negative-energy perturbations. We therefore discuss here a one-dimensional system in which the thermal energy is altogether irrelevant, i.e. a force-free configuration, but take the parallel dynamics into account. The configuration again depends only on x. The densities and pressures are constant: n_e, $p_e = const.$, n_i, $p_i = const.$. The ion equilibrium velocity is assumed to be zero: $\mathbf{v}_i = 0$. The magnetic field follows from $\nabla \times \mathbf{B} = \lambda \mathbf{B}$, $\lambda = const.$. We choose as solutions

$$B_y = B sin\lambda x \ , \qquad B_z = B cos\lambda x \ .$$

The electron velocity $\mathbf{v}_e$ determines the current density and is therefore related to the magnetic field by

$$\frac{4\pi}{c} e_e n_e \mathbf{v}_e = \lambda \mathbf{B} \Longrightarrow \nabla \times \mathbf{v}_e = \lambda \mathbf{v}_e \Longrightarrow \nabla \cdot \mathbf{v}_e = 0 \ .$$

A consequence of this relation is that the center of mass velocity vanishes, and this means that the frame chosen is the frame of minimum equilibrium energy. Any negative-energy perturbation is therefore dynamically relevant. A simple discussion is possible in terms of initial conditions. We choose $\nabla \cdot \boldsymbol{\xi}_e = 0$, $\xi_{ex} = 0$ and obtain

$$2\mathcal{E} = \frac{1}{2} \int mn \left\{ |\dot{\xi}_{e\parallel}|^2 - (\mathbf{k} \cdot \mathbf{v}_e)^2 |\xi_{e\parallel}|^2 \right\} d^3x, \qquad \mathbf{k} = (0, k_y, k_z) \ . \tag{19}$$

In order to satisfy $\nabla \cdot \boldsymbol{\xi}_e = 0$ with $\xi_{ex} = 0$, we represent $\boldsymbol{\xi}_e$ as $\boldsymbol{\xi}_e = \boldsymbol{\eta} \times \mathbf{k}$, $\xi_{ex} = \eta_y k_z - \eta_z k_y = 0$, from which it follows that

$$\xi_{e\parallel} = (\boldsymbol{\eta} \times \mathbf{k}) \cdot \frac{\mathbf{v}_e}{v_e} = \eta_x (k_y cos\lambda x - k_z sin\lambda x) \ .$$

η_x can be chosen arbitrarily and the expression inside the parentheses vanishes only at points where $\mathbf{k} \parallel \mathbf{B}$. Since $\xi_{e\parallel}$ can initially be prescribed independently of $\xi_{e\parallel}$, one can have both postive- and negative-energy perturbations. This situation is similar to the Cherry oscillator case [5]. The configuration considered should therefore allow nonlinear instabilities. A possibly non-vanishing threshold amplitude will depend on the initial conditions, i.e. the degree of resonance present in the initial conditions.

As concerns negative-energy modes which are necessarily stable, their frequencies must obviously satisfy

$$(\frac{\omega}{k v_e})^2 < \frac{\int (\frac{k_y}{k} sin\lambda x + \frac{k_z}{k} cos\lambda x)^2 |\xi_{e\parallel}|^2 d^3x}{\int |\xi_{e\parallel}|^2 d^3x} \ .$$

References

[1] B. D. Scott, Phys. Rev. Lett. **65**, 3289 (1990)

[2] D. Pfirsch and R. N. Sudan: Ideal MHD Potential Energy to Third and Higher Orders in Displacements, to be submitted to Phys. Fluids

[3] D. Pfirsch: Non-linear MHD Instability, to be submitted to Phys. Fluids

[4] M. Wakatani and A. Hasegawa, Phys. Fluids **27**, 611 (1984)

[5] T. M. Cherry, Trans.Cambridge Philos.Soc. **23**, 199,(1925);
see E.T. Whittaker, Analytical Dynamics (Cambridge, London, 1937), Sec. 182, p. 142;
and A. Wintner, The Analytical Foundations of Celestial Mechanics, (Princeton University, Princeton, 1947), Sec. 136, p. 101

[6] D. Pfirsch, Z. Naturforsch. **45a**, 839 (1990)

[7] P. J. Morrison and M. Kotschenreuther, The Free Energy Principle, Negative Energy Modes, and Stability, Report DOE/ET-53088-280, IFSR # 280, October 1989, Institute for Fusion Studies, The University of Texas at Austin, Austin, Texas 78712

GENERAL THEORY OF MODULATIONAL INTERACTION OF TWO MODES

By Sergey V. Vladimirov and Vadim N. Tsytovich

Theoretical Department, General Physics Institute, Vavilova 38, 117942 Moscow, U.S.S.R.

The electric field in a nonlinear medium is governed by an equation:

$$\varepsilon_k E_k + \int S_{kk_1k_2} E_{k_1} E_{k_2} d^{(2)}_{12} + \int \Sigma_{kk_1k_2k_3} E_{k_1} E_{k_2} E_{k_3} d^{(3)}_{123} = 0 \ , \qquad (1)$$

where $k = (k,\omega)$, $\delta(k) \equiv \delta(k)\delta(\omega)$, $d^{(2)}_{12} \equiv dk_1 dk_2 \delta(k-k_1-k_2)$, etc., and E_k is Fourier-component of the longitudinal electric field. Further we suppose that a pump field E is a sum of wave fields with frequencies $\omega_0 \equiv \omega(k_0)$, $\omega_1 \equiv \omega(k_1)$ ($\delta\omega \equiv \omega_0 - \omega_1 \ll \omega_{0,1}$), and amplitudes $E_{0,1}$. Due to real character of the fields $E_{0,1}$ each of their spectra contains two lines - near $+\omega_{0,1}$ and near $-\omega_{0,1}$, we therefore distinguish a positive-frequency E^+_k and negative-frequency E^-_k parts for Fourier components.

In a nonlinear medium the presence of two wave fields leads to oscillations on beat and summing frequencies. In our model (1) is evident that oscillations on a near-zero frequency ($\Omega = \omega_0 - \omega_0 = \omega_1 - \omega_1$), on a beat frequency ($\pm\delta\omega$), and on double frequencies ($\pm 2\omega_0$, $\pm 2\omega_1$, $\pm(\omega_0+\omega_1)$) due to the quadratic nonlinearity, and also fields on near-pump frequencies ($\pm(\omega_0+\delta\omega)$, $\pm(\omega_1-\delta\omega)$), and triple frequencies ($\pm 3\omega_0$, $\pm 3\omega_1$, $\pm(2\omega_0+\omega_1)$, $\pm(2\omega_1+\omega_0)$) due to the cubic nonlinearity, will be present. Further we define all this fields as "virtual"; by writing virtual we assume their intensities being small in comparison with intensities of "real" pump fields. This supposition also means that the virtual frequencies are not on "mass surface" of oscillations which can propagate in the medium (including low-frequency, in comparison with the pump frequencies, oscillations).

By investigating the modulational instability of one pump mode all virtual fields due to a cubic nonlinearity are not taken into account (because of their higher order in field in comparison with virtual fields due to a quadratic nonlinearity). But in the case of two pump waves some of the "cubic" virtual fields have comparatively large intensities. These are fields on frequencies $\pm(\omega_0+\delta\omega)$ and $\pm(\omega_1-\delta\omega)$; their larger intensity in comparison with virtual fields on triple frequencies originates from small values of denominators $\varepsilon(\omega_0+\delta\omega)$, $\varepsilon(\omega_1-\delta\omega)$ near resonances $\varepsilon(\omega_{0,1})=0$ (we suppose here that near triple frequencies there are not resonances with eigenwaves of the medium).

Thus we consider the full electric field in (1) consisting of real and virtual fields by the following way:

$$E = E^-_0+E^-_0+E^+_1+E^-_1+E^V_\Delta+E^V_\delta+E^V_{-\delta}+E^V_{\delta+0}+E^V_{-\delta-0}+E^V_{-\delta+1}+E^V_{\delta-1} \quad , \qquad (2)$$

where $\delta=\delta k$, $\delta+0=\delta k+k_0$, $\delta-1=\delta k-k_1$, etc. The virtual field E^V_Δ is the field on zero frequency which is "smoothed" on a frequency $\Delta\omega$ by the modulational interaction; for the sake of simplicity we have not included in (2) all fields connected with interactions through double frequencies (usually in a plasma a contribution from these interactions is small).

By introducing (2) let us note following. We may distinguish the beat frequency $\delta\omega$ and the modulation frequency $\Delta\omega$ if

$$|\Gamma^{mod}| < |\delta\omega| . \qquad (3)$$

In the case when the opposite inequality holds with, the modulational processes fully smooth the beat frequency $\delta\omega$ and another approximation is necessary. Another restriction comes from condition of virtual character of the fields on frequencies $\pm(\omega_0+\delta\omega)$, $\pm(\omega_1-\delta\omega)$

$$\max\{|E^V_{\pm(\delta+0)}|, |E^V_{\pm(\delta-1)}|\} < |E_{0,1}| . \qquad (4)$$

Besides (4) and (5) there are another restrictions (small fields on triple frequencies, small effects from five-order in field nonlinearities, etc.), but the above conditions (4) and (5) are the most important.

In zero approximation we have

$$E^{+}_{0,1} = E_{0,1}\delta(k-k_{0,1}) \ , \quad E^{-}_{0,1} = -E^{*}_{0,1}\delta(k+k_{0,1}) \qquad (5)$$

(where "*" means complex conjugate). The pump (6) generates a virtual field on frequency

$$E_{\delta+0} = E_0^2 E_1^{*} 2\tilde{\Sigma}^{eff}_{0,0,-1}\tilde{\varepsilon}_{\delta+0}\Delta_{0,-1} \ , \qquad (6)$$

where the following notations are used

$$\tilde{\Sigma}^{eff}_{0,0,-1} \equiv \Sigma^{eff}_{0,0,-1} + 2\Sigma^{eff}_{-1,-1,0}|E_1|^2(\Sigma^{eff}_{0,1,\delta-1} + \Sigma^{eff}_{1,0,\delta-1})\tilde{\varepsilon}_{\delta-1} \ ,$$

$$\tilde{\Sigma}^{eff}_{-1,0,0} \equiv \Sigma^{eff}_{-1,0,0} + 2\Sigma^{eff}_{0,-1,-1}|E_1|^2(\Sigma^{eff}_{0,1,\delta-1} + \Sigma^{eff}_{1,0,\delta-1})\tilde{\varepsilon}_{\delta-1} \ ,$$

$$\Delta_{0,-1} \equiv 1 - 4|E_0|^2|E_1|^2(\Sigma^{eff}_{0,1,\delta-1} + \Sigma^{eff}_{-1,-0,\delta+0})\tilde{\varepsilon}_{\delta+0}\tilde{\varepsilon}_{\delta-1} \ ,$$

$$\tilde{\varepsilon}_{\delta+0} = \varepsilon_{\delta+0} + 2(\Sigma^{eff}_{\delta+0,0,-0} + \Sigma^{eff}_{0,\delta+0,-0})|E_0|^2 + 2(\Sigma^{eff}_{\delta+0,1,-1} + \Sigma^{eff}_{1,\delta+0,-1})|E_1|^2 \ . \qquad (7)$$

After replacing (0,1)⇔(-1,0) we get an analogous equation for for a virtual field on frequency $\pm(\omega_0+\delta\omega)$, etc. In equations (6),(7) we have introduced a symmetric (on the last two indices) effective third-order plasma responce:

$$\Sigma^{eff}_{j,l,m} \equiv \Sigma^{eff}(k_{j+l+m} \ , \ k_j \ , \ k_l \ , \ k_m) =$$

$$(\Sigma^{eff}_{j,l,m} + \Sigma^{eff}_{j,m,l})/2 = \Sigma_{j,l,m} - 2S_{j,l+m}S_{l,m}/\varepsilon_{l+m} \ . \qquad (8)$$

Below for the sake of simplicity we shall not write superscript "eff" in effective third-order response Σ^{eff}.

After introducing of modulational perturbations $\delta E^{\pm}$, $|\delta E^{\pm}| << |E_{0,1}|$:

$$E^{+}_{0,1} = E_{0,1}\delta(k-k_{0,1}) + \delta E^{+}_{0,1} \ , E^{-}_{0,1} = -E^{*}_{0,1}\delta(k+k_{0,1}) + \delta E^{-}_{0,1} \qquad (9)$$

one can get the following equations

$$[\varepsilon_{\Delta+0} - 4\Sigma^{S}_{\Delta+0,0,-0}|E_0|^2 - 4\Sigma^{S}_{\Delta+0,1,-1}|E_1|^2]\delta E^{+}_{\Delta+0} + [2\Sigma^{S}_{0,0,\Delta-0}E_0^2 + 4\Sigma^{S}_{\delta+0,1,\Delta-0}E^{V}_{\delta+0}E_1]\delta E^{-}_{\Delta-0} - [4\Sigma^{S}_{\Delta+1,0,-1}E_0E_1^{*} + 4\Sigma^{S}_{\Delta+1,\delta+0,-0}E^{V}_{\delta+0}E_0^{*} - 4\Sigma^{S}_{\Delta+1,1,\delta-1}E^{V}_{\delta-1}E_1]\delta E^{+}_{\Delta+1} + 4\Sigma^{S}_{0,1,\Delta-1}E_0E_1\delta E^{-}_{\Delta-1} - 4\Sigma^{S}_{\Delta+\delta+0,1,-0}E_1E_0^{*}\delta E^{V}_{\Delta+\delta+0} + 2\Sigma^{S}_{1,1,\Delta+\delta-1}E_1^2\delta E^{V}_{\Delta+\delta-1} = 0\,, \tag{10}$$

$$\varepsilon_{\Delta+\delta+0}\delta E^{V}_{\Delta+\delta+0} + 4\Sigma^{S}_{0,1,\Delta+\delta-1}E_0E_1\delta E^{V}_{\Delta+\delta-1} = [4\Sigma^{S}_{\delta+0,\Delta+0,-0}E^{V}_{\delta+0}E_0^{*} + 4\Sigma^{S}_{\Delta+0,0,-1}E_0E_1^{*} - 4\Sigma^{S}_{\Delta+0,1,\delta-1}E_1E^{V}_{\delta-1}]\delta E^{+}_{\Delta+0} + [4\Sigma^{S}_{\Delta+1,\delta+0,-1}E^{V}_{\delta+0}E_1^{*} - 4\Sigma^{S}_{\Delta+1,0,\delta-1}E_0E^{V}_{\delta-1}]\delta E^{+}_{\Delta+1} - 4\Sigma^{S}_{\delta+0,0,\Delta-0}E_0E^{V}_{\delta+0}\delta E^{-}_{\Delta-0} - [4\Sigma^{S}_{\delta+0,1,\Delta-1}E^{V}_{\delta+0}E_1 + 2\Sigma^{S}_{0,0,\Delta-1}E_0^2]\delta E^{-}_{\Delta-1}\,. \tag{11}$$

where $\Sigma^{S}_{j,l,m} \equiv (\Sigma_{j,l,m} + \Sigma_{l,j,m})/2$. Equations for another six modulational perturbations $\delta E^{-}_{\Delta-0}$, $\delta E^{\pm}_{\Delta\pm1}$, $\delta E^{V}_{\Delta-\delta-0}$, $\delta E^{V}_{\Delta\pm(\delta-1)}$ can be obtained from (10)-(11) by replacing $(0,1)\Leftrightarrow-(0,1)$, or $(0,1)\Leftrightarrow\pm(1,0)$. Let us note that because of our assumptions (we have not included into account all processes connected with interactions through virtual fields on double frequencies) it is sufficient to operate with nonlinear responses symmetrized as above (see, e.g., (8)).

REFERENCES

1. L.I. Rudakov and V.N. Tsytovich, Phys. Rep. **C40** (1978) 1.
2. C.G. Thornhill and D. ter Haar, Phys. Rep. **43** (1978) 45.
3. M.V. Goldman, Rev. Mod. Phys. **56** (1984) 709.
4. C.J. McKinstrie and P. Bingham, Phys. Fluids **B1** (1989) 230.
5. C.J. McKinstrie and G.G. Luther, Phys. Scripta **T30** (1990) 31.
6. G.G. Luther and C.J. McKinstrie, J. Opt. Soc. Am. **B7** (1990) 1125.
7. C.J. McKinstrie and M.V. Goldman, submitted to J. Opt. Soc. Am.
8. S.V. Vladimirov and V.N. Tsytovich, Sov. Phys JETP **71** (1990) 715.
9. S.V. Vladimirov and V.N. Tsytovich, Proceed. ICPIG-XX, Vol. 3 (Pisa, 1991) 637.

NONLINEAR EVOLUTION OF SOLITONS WITH OSCILLATIONS UNDER THE INFLUENCE OF RESONANT IONS

T. Honzawa, M. Arakawa and S. Singh
Department of Electric and Electronic Engineering,
Utsunomiya University, Utsunomiya 321, Japan

Effective soliton amplification is observed to occur when beam ions with an average energy around 2 eV collide with an ion acoustic soliton from behind. Further, the velocity-amplitude and the pulse width-amplitude relations of the solitons are confirmed to be almost unchanged by such strong interaction with beam ions. In addition, small oscillations behind the soliton are also observed to evolve into a large amplitude wave train under the influence of beam ions.

INTRODUCTION

Interaction of solitons with resonant particles was shown to affect their stability. Ostrovskii et al.[1] first studied theoretically the propagation of ion acoustic solitons in an ion-beam-plasma system on the assumption of a weak beam and predicted the amplification of the solitons by the beam. Okutsu et al.[2] performed an experiment on the soliton propagation in a steady-state ion-beam-plasma system and showed that the solitons could be amplified by the beam at a small rate as in the case of linear waves. Several other workers also studied the effect of resonant particles on solitons on the basis of a perturbation theory. But, in the case of strong interaction between solitons and resonant particles, the beam nonlinearity must be important. Taking account of the beam nonlinearity, Kono[3] recently studied numerically the nonlinear interaction of solitons with resonant beam ions

and the beam reflection. However, any one has not yet given experimental evidence that the beam nonlinearity plays an essential role in the soliton-beam interaction. In this paper, we give the first experimental evidence on such a strong interaction of solitons with resonant beam ions.

EXPERIMENTAL METHODS AND RESULTS

Experiments were performed using a double plasma device[4]. In the device two ion acoustic solitons were excited by applying two independent input pulses. Here, their pulse heights and widths were independently controlled and the interval between the two input pulses was externally changed. The *rear* soliton of the two, excited by the *rear* input pulse, was used for generating pulsed beam ions in the form of a precursor pulse in front of it, as shown in Fig.1a. Typical examples of the energy distributions of the beam and plasma ions, observed at a fixed position and at various times τ, are given in Fig.2, where τ is the delay time measured from the beginning of the rear input pulse. For each energy distribution of these we can calculate the average beam energy W_b as shown in crosses in Fig.3.

In this paper, an ion acoustic soliton excited by the *front* input pulse is called a *front* soliton. By externally adjusting the interval between the front and rear input pulses, we could make the front soliton interact with a group of beam ions having a desired energy distribution among the available ones, as shown in Fig.2. Examples of oscilloscope traces, showing the soliton signal under the influence of beam ions, are given in Figs.1c-1j. These indicate that the front soliton (whose peak is at time τ) and its trailing oscillations are amplified by beam ions and that the soliton amplification rate becomes larger with increasing τ (up to $\tau \simeq 80$ μsec) or with decreasing W_b. Further, we find that a soliton can be amplified by a factor of six at $W_b \simeq 2.2$-2.3 eV. (see Fig.3)

Next, we tried to clarify whether the nature of the solitary waves might be affected by the amplification or not. For the purpose we carefully studied the velocity-amplitude and the pulse width-amplitude relations of the solitary waves before and after the amplification. Observed relations between the quantities are plotted in open circles for the unperturbed waves and in solid circles for the amplified ones in Figs.4(a) and (b). Although plots in the figures are rather scattered, it is found from these that such relations as $U_s = C_s(1 + \alpha\delta N/N)$ and $(D/\lambda_D)^2(\delta N/N) = \beta$ are approximately satisfied for both the unperturbed and amplified solitons. Here, each of arrows in the figures means the corresponding relation of the same wave before and after the amplification. These results reveal that so far as the dependences of U_s and D on $\delta N/N$ are concerned, both solitary waves before and after the amplification satisfy almost the same relations.

Reaction of the soliton amplification on the energy distribution of overtaking beam ions was also studied, when effective soliton amplification was observed. As a result, we could observe a considerable change in form of the beam energy distribution induced by the soliton amplification. These data prove that the soliton amplification is caused by the help of the energy loss of the overtaking beam ions or that the beam reflection by the soliton potential hump actually occurs during the soliton-beam interaction.

Besides the phenomena described above, nonlinear evolution of trailing oscillations behind the soliton was observed under the influence of resonant beam ions. Further, the damping of the rear soliton was observed to be induced by the front soliton amplification.

REFERENCES

1. L.A.Ostrovskii et al., Sov. Phys. JETP 42, 1041 (1976).

2. E.Okutsu et al., Plasma Phys. 20, 561 (1976).

3. M.Kono, Phys. Fluids 29, 1268 (1986).

4. R.J.Taylor et al., Phys. Rev. Lett. 24, 204 (1970).

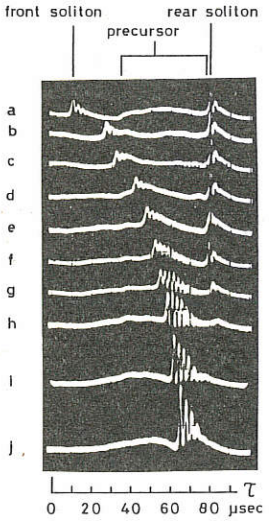

[Fig.1]

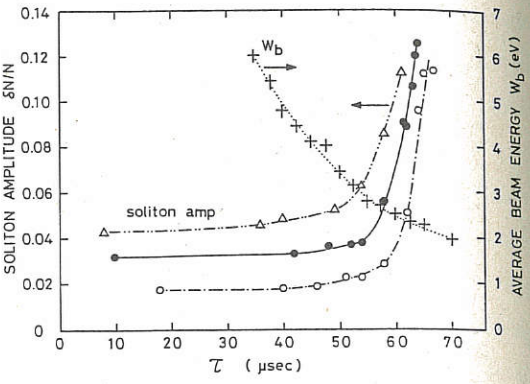

[Fig.3]

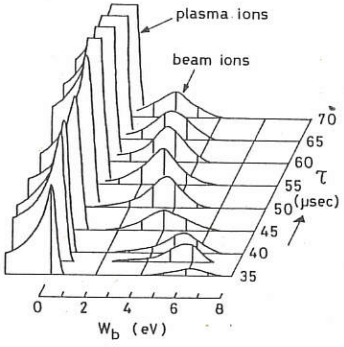

[Fig.2]

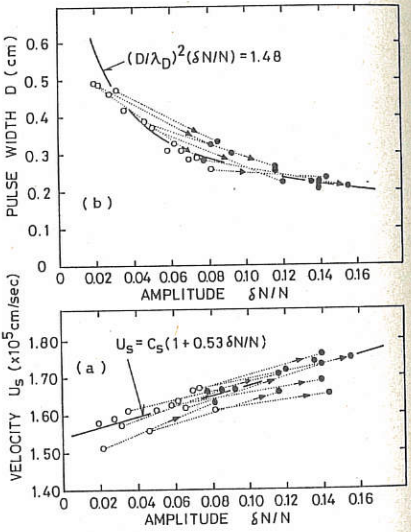

[Fig.4]

3D NON-LINEAR KINETIC EQUATION FOR THE CALCULATION OF NEOCLASSICAL EFFECTS IN TOKAMAK PLASMAS

F S Zaitsev[1], M R O'Brien[2] and M Cox[2]
[1]Moscow State University, Moscow, Russia.
[2]UKAEA/EURATOM Fusion Association, Culham Laboratory, Abingdon, UK.

Introduction Neoclassical theories of tokamak transport, e.g. /1/, have mainly been restricted to treating particle distribution functions that are close to Maxwellian and particle orbits that deviate only slightly from magnetic flux surfaces (i.e. small 'banana widths'). These approximations are not valid for many situations of interest: for example in JET non-thermal populations of fast ions with energies $\lesssim$ 10MeV and large drift orbits ($\Delta r/a \sim 0.3$) have been generated by ICRH. Also, in future large tokamaks (e.g. ITER) alpha particle distributions ($\leq$ 3.5MeV) will carry a significant fraction of the plasma pressure. To model neoclassical behaviour (radial transport, bootstrap currents, etc.) in these experiments we have derived a 3D non-linear kinetic equation for low collisionality tokamaks for which neither of these approximations is required. This advances work of other authors /2,3,4/ which while allowing non-Maxwellian distributions is less general, in particular assuming drift surfaces close to flux surfaces. In section 2 we outline the derivation of this equation and in section 3 we give a brief discussion of possible uses for the equation together with an illustration of the importance of averaging its transport coefficients over trajectories rather than flux surfaces.

Derivation of the 3D Kinetic Equation A toroidal axisymmetric plasma configuration is considered. In real space, toroidal coordinates (γ, ξ, η) are used, with γ a magnetic surface variable (e.g. its half-width in the equatorial plane), and ξ and η poloidal and toroidal angles. In velocity space, spherical coordinates (v, θ, φ) are used with v the speed, θ the pitch angle with the magnetic field and φ the gyro-angle. The system $(\gamma, \xi, \eta, v, \theta, \varphi)$ is the 'local' coordinate system and is denoted $x \equiv (x^1, x^2, x^3, x^4, x^5, x^6)$. The 3D equation is derived by averaging the full 6D kinetic equation over φ, η and ξ without the usual assumptions of small banana widths and small inverse aspect ratio. Before averaging we first transform into a coordinate system of 'constants of motion' (γ_0, v_0 and θ_0) and 'fast' variables (ξ, η and φ). The formalism given here is valid for any three independent constants of motion: a suitable choice for $(\gamma_0, v_0, \theta_0)$ used here is, respectively, the flux surface radius at the inside of the drift surface (or at the bounce point for trapped particles), a generalised speed derived from the sum of kinetic and potential energies, and the pitch angle where the particle crosses the equatorial plane at the outermost point of its trajectory (which can be on the co or counter leg for trapped particles). These values fix the trajectory and, after averaging, we obtain an equation which describes the evolution of trajectories as a whole through changes to constants of motion due to collisions. We denote the 'constants of motion' coordinate system $\bar{x} \equiv (\bar{x}^1, \bar{x}^2, \bar{x}^3, \bar{x}^4, \bar{x}^5, \bar{x}^6) \equiv (\gamma_0, \xi, \eta, v_0, \theta_0, \varphi)$.

We start from the most general kinetic equation with the Landau collision operator /5/

$$\frac{df_\alpha}{dt} = \sum_\beta \vec{\nabla} \cdot \vec{j}(f_\alpha, f_\beta) \qquad (1)$$

with f_α and f_β the distribution functions of particle species α and β, and $\vec{j}$ the flux due to collisions which in the local coordinate system is solely in the velocity space variables x^4, x^5, x^6. We rewrite eq (1) in the new coordinates $\bar{x}$ and assume low collisionality, namely that the

characteristic times for motion over the 'fast' variables $\bar{x}^2$, $\bar{x}^3$ and $\bar{x}^6$ are much less than the Coulomb relaxation time $\tau_c = (4\pi\epsilon_0^2 m_\alpha^2 v_c^3)/(n_c Z_\alpha^2 e^4 \ln\Lambda)$ (n_c, v_c and $\ln\Lambda$ are a characteristic density, speed and Coulomb logarithm and m_α and Z_α are the mass and charge number). If the largest of these times is τ then $\tau/\tau_c \ll 1$ and we search for a solution of eq (1) in the form

$$f_\alpha(t,\bar{x}) \;=\; f_\alpha^0(t,\bar{X}) + \frac{\tau}{\tau_c}\, f_\alpha^{(1)}(t,\bar{X},\bar{X}) + \left(\frac{\tau}{\tau_c}\right)^2 f_\alpha^{(2)}(t,\bar{X},\bar{X}) + \ldots$$

where $\bar{X} = (\gamma_0, v_0, \theta_0)$ and $\bar{X} = (\xi,\eta,\varphi)$. The 3D equation for f_α^0 is <u>not</u> derived by direct integration of the transformed eq (1) over fast variables since the neoclassical radial transport operator is not integrable for trapped particles. Instead, we use a different approach (details in /6/) which is now summarised. We seek an equation for $f_\alpha^0(t,\bar{X})$ with the following structure

$$A^0(\bar{X};f_\alpha^0) + \frac{\tau}{\tau_c}\, A^{(1)}(\bar{X};f_\alpha^0) + \left(\frac{\tau}{\tau_c}\right)^2 A^{(2)}(\bar{X};f_\alpha^0) + \ldots \;=\; 0$$

and choose the unknown terms $f_\alpha^{(i)}$ and $A^{(i)}$ $(i = 0,1,2...)$ to satisfy eq (1). Pairs of terms $A^{(i-1)}$ and $f_\alpha^{(i)}$ are found by splitting each term of the τ/τ_c expansion of eq (1) into two components, one of which is independent of $\bar{X}$, and equating each component to zero. We define the component of any integrable function $a(\bar{x})$ that is independent of $\bar{X}$ to be

$$\langle a\rangle \;\equiv\; \langle a\rangle_{\xi,\eta,\varphi} \;\equiv\; \frac{1}{H}\int_{\Delta\xi} d\xi \int_{\Delta\eta} d\eta \int_{\Delta\varphi} d\varphi\; a(\bar{x})\sqrt{\bar{g}}$$

where integrals are over the ranges of ξ, η and φ explored by particles described by $\bar{X}$ and $\sqrt{\bar{g}}$ is the Jacobian of the transformation from Cartesian to $\bar{x}$ coordinates. H is independent of $\bar{X}$: its value is unimportant as it does not appear in the final equation for f_α^0. If the $\langle a\rangle$ component is known then the remaining component of $a(\bar{x})$ can be defined as $\{a\} = a\sqrt{\bar{g}} - \langle a\rangle$. In the zeroth order term we have to define two unknowns $A^{(0)}$ and $f_\alpha^{(1)}$. There is no unique choice for these components: we use the definition that ensures both that f_α^0 is the distribution function in the space of constants of motion $\bar{X}$, and that the resulting equation for f_α^0 is in the form of the divergence of a flux in this space $\bar{X}$. This leads to the following equation for $f_\alpha^0(t,\bar{X})$

$$\frac{\partial f_\alpha^0}{\partial t} \;=\; \frac{v_c^3}{\tau_c} \sum_{n=1,4,5} \frac{1}{\langle 1\rangle}\, \frac{\partial}{\partial \bar{x}^n} \left[\sum_{m=1,4,5} \left(A_{nm} \frac{\partial f_\alpha^0}{\partial \bar{x}^m} \right) + B_n\, f_\alpha^0 \right] \qquad (2)$$

Note that collisions, which locally change only velocity space coordinates, change all three constants of motion: the γ_0 component of the flux is the 'radial flux'. Assuming an axisymmetric plasma and that the drift approximation for particle motion is valid gives the coefficients in eq (2) appropriate to a neoclassical description of tokamak transport. (The second assumption means that Finite Larmor Radius effects are neglected: however we emphasise that the banana width and inverse aspect ratio need not be small.) These coefficients are

$$A_{nm} \;=\; \sum_\beta \frac{Z_\beta^2 \ln\Lambda_{\alpha\beta}}{2n_c \ln\Lambda} \left\langle \frac{\partial \bar{x}^n}{\partial x^l}\, \frac{\partial \bar{x}^m}{\partial x^j} \int_0^\infty \int_0^\pi \bar{U}_{lj} f_\beta^0(t,\bar{X}') v'^2 \sin\theta' dv' d\theta' \right\rangle_{\xi,\eta}$$

$$B_n \;=\; -\sum_\beta \frac{Z_\beta^2 \ln\Lambda_{\alpha\beta}}{2n_c \ln\Lambda}\, \frac{m_\alpha}{m_\beta} \left\langle \frac{\partial \bar{x}^n}{\partial x^l} \int_0^\infty \int_0^\pi \bar{U}'_{lj} \frac{\partial f_\beta^0(t,\bar{X}')}{\partial x'^j} v'^2 \sin\theta' dv' d\theta' \right\rangle_{\xi,\eta}$$

where $\bar{X}' = \bar{X}(\gamma, \xi, \eta, v', \theta')$ and $n, m = 1,4,5$. These represent neoclassical radial diffusion (A_{11}), pitch-angle scattering (A_{55}), collisional slowing down (B_4), etc. Summation over l and j $(= 4,5)$ is assumed. Here

$$\bar{U}_{ij} = \int_0^{2\pi}\int_0^{2\pi} \frac{\partial x^l}{\partial v_i}\frac{\partial x^j}{\partial v_k} U_{ik} d\varphi d\varphi', \quad \bar{U}'_{lj} = \int_0^{2\pi}\int_0^{2\pi} \frac{\partial x^l}{\partial v_i}\frac{\partial x'^j}{\partial v'_k} U_{ik} d\varphi d\varphi', \quad i,k = X,Y,Z.$$

U_{ik} is the Landau tensor /5/ and (v_X, v_Y, v_Z) are Cartesian coordinates in velocity space. After much algebra one can show that $\bar{U}_{lj}$, $\bar{U}'_{lj}$ can be expressed in terms of complete elliptic integrals /6/. Averaged quantities are calculated for passing and trapped particles as follows

$$\langle a \rangle^p_{\xi,\eta} = 2\pi \int_{-\pi}^{\pi} a\sqrt{\bar{g}}\, d\xi, \qquad \langle a \rangle^{tr}_{\xi,\eta} = 2\pi \sum_{\sigma=-1,1} \int_{\xi_{min}(\bar{X})}^{\xi_{max}(\bar{X})} (a\sqrt{\bar{g}})_\sigma \, d\xi$$

where $\sigma = \cos\theta_0/|\cos\theta_0|$ and ξ_{min} and ξ_{max} are the poloidal angles at the reflection points, with, for 'up-down' symmetry, $\xi_{min} = -\xi_{max}$.

The averaging method is not valid for particles so near the trapped-passing boundary (TPB) that $\tau \sim \tau_c$. Thus phase space is cut by a narrow transition layer around the TPB for which special treatment is required. Proceeding from the assumption that, due to Coulomb collisions and the absence of sources at the TPB layer, the unaveraged distribution function f_α, and the normal component of the unaveraged flux $\vec{j}$, are continuous functions of $\bar{x}$ coordinates, one can derive an equation relating the fluxes entering the TPB layer /6/.

We conclude this section with a few remarks on the conditions appropriate at phase space boundaries. The coefficients A_{nm} and B_n in eq (2) vanish at the following boundaries of $\bar{x}^n$: $\gamma_0 = 0$, $v_0 = v_{0,min}$ (that is $v = 0$ for zero potential) and $\theta_0 = 0$ and π. This degeneracy means that the boundedness of f^0_α is a sufficient condition at these boundaries, at least for a numerical solution /5/. A suitable condition for $v_0 \to \infty$ is that the component of particle flux in the v_0 direction vanishes. At $\gamma_0 = \gamma_{0,max}$ a zero or Maxwellian distribution is often a convenient boundary condition. At $t = 0$, a Maxwellian distribution is usually appropriate. Solution of eq (2) with these boundary conditions would yield a distribution f^0_α from which neoclassical fluxes and currents could be obtained by calculation of suitable moments.

Discussion Analytic methods are unlikely to provide solutions to eq (2), and so computer solutions are required. A simplified version of this equation, containing only the neoclassical radial diffusion coefficient, has already been solved numerically /7/. The results were consistent with analytic results and with 2D calculations. A Fokker-Planck package FPP3D for solution of the full eq (2) has been written and is currently being tested. One use of this code will be to compare neoclassical fluxes with the coefficients A_{nm} and B_n calculated as flux surface averages and as trajectory averages. Figure 1 shows A_{11} for hydrogen ions with energies $\leq$ 10MeV in a circular JET-sized plasma with R = 3m, a = 1.2m, B_o = 2T and I_P = 1MA, conditions appropriate to minority ICRH experiments. The ions collide with electron and Deuterium Maxwellians (parabolic $n(r)$ with $n_o = 10^{20}\mathrm{m}^{-3}$ and parabolic squared $T(r)$ with T_o = 10keV). A_{11} is contoured as a function of v_0 and θ_0 for $\gamma_0 = 0.4a$ for averaging over surfaces (Fig 1(a)) and over trajectories (Fig 1(b)). Since A_{11} is the product of the radial diffusivity ($\sim 1/v_0$) and the Jacobian ($\sim v_0^2$) it increases $\sim$ linearly with speed v_0. It is almost zero for passing particles except those close to the TPB and peaks at the TPB in Fig 1(a), both properties as expected for neoclassical transport. Both the magnitude and v_0, θ_0 variation differ for the two cases showing the importance of averaging over trajectories rather than flux surfaces when calculating transport coefficients.

Derivation of operators for other effects (additional heating, magnetic ripple, other transport mechanisms, etc.) using the method described requires a choice of 'slow' and 'fast' variables that describes trajectories allowing for the relevant physics. Work in this direction is in progress.

Acknowledgments We are grateful to D.P. Kostomarov, P.N. Yushmanov, J.W. Connor and R.J. Hastie for useful discussions.

References

/1/ F.L. Hinton, R.D. Hazeltine, Reviews of Modern Physics. 48(1976)239, N.2, Part 1.
/2/ C.T. Hsu, P.J. Catto, D.J. Sigmar, Phys Fluids B 2(1990)280.
/3/ I.B. Bernstein, K.Molvig, Phys Fluids 26(6) (1983)1488.
/4/ G.S. Irisov, P.N. Yushmanov, Sov. J. Plasma Phys 12(6) June (1986) 387.
/5/ Yu.N. Dnestrovskij, D.P. Kostomarov, Numerical Simulations of Plasmas. 1986. Springer-Verlag New York Inc.
/6/ F.S. Zaitsev, M.R. O'Brien and M. Cox, submitted to Phys. Fluids B.
/7/ F.S. Zaitsev et al., 18th Conf. on Plasma Phys. and Controlled Fusion, Berlin 1991, vol IV 145.

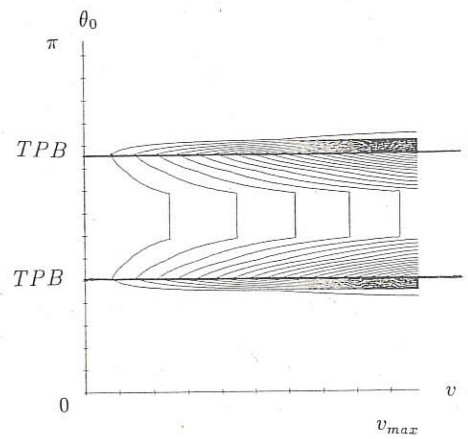

Fig 1(a) Contours of A_{11}, calculated as a flux surface integral, for hydrogen ions with $\gamma_0 = 0.4a$ in a JET-sized plasma (for conditions see text). The maximum speed corresponds to an energy of 10MeV. For a given speed, A_{11} peaks at the trapped/passing boundaries shown by the straight lines.

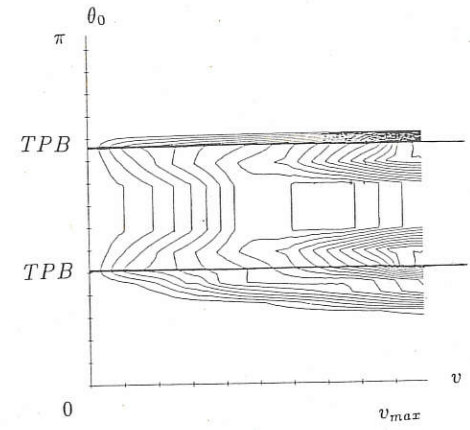

Fig 1(b) As Fig. 1(a) but with A_{11} calculated as a trajectory integral. The maximum value is only 0.37 times that in Fig 1(a). A_{11} is still symmetric, for a given v_0, in the trapped region, but asymmetric in the passing regions unlike Fig. 1(a).

NONLINEAR LENGMUR PULSES IN THE ACTIVE PLASMA.

I.V. Bachin and V.V. Prudsky.

Departament of Physics, Rostov State University,

344104, Rostov-on- Don, Russia.

In the present paper we wish to call attention to the possibility of existensce of new types solitary nonlinear Lengmur waves in the active plasma.

We consider the propagation of Lengmur wave packets in resonance with atoms, when atoms frequency Ω is equal to plasma frequency ω_L, and take in account both atoms and plasma nonlinearity / 1,2 /.

The self-consistent equations, which describe Lengmur waves in the plasma-gaseous medium, are given by

$$\left(\frac{\partial^2}{\partial t^2} - v_T^2 \frac{\partial^2}{\partial z^2}\right)(E+4\pi P) = \omega_L^2 \left(\frac{|E|^2}{E_T^2} - 1\right)E \ ,$$

$$\left(\frac{\partial^2}{\partial t^2} + \Omega^2\right) P = \frac{2d}{\hbar}\left[(NdS\Omega)^2 - \Omega^2|P|^2 - \left|\frac{\partial P}{\partial t}\right|^2\right]^{1/2} P \ , \qquad (1)$$

where $\vec{E}$ is the electric field, $\vec{P}$ is the polarization vector, $v_T=(3T/m)^{1/2}$, $\omega_L^2=4\pi e^2 n_p/m$, $E_T^2=32\pi n_p T(1 - u^2/c_S^2)$, $c_S=(2T/m)^{1/2}$ is the acoustic speed, n_p, T, m and e are the electron density, temperature, mass and charge; N, d and Ω are the atoms density, dipole moment and resonance frequency of gas.

First from the above set of equations can be derived from

equations of motion and continuity of the electron fluid and Poisson equation, second from Bloch equations.

We shall look for the solution of the nonlinear problem in the form of a circularly polarized plane waves with an slowly variated amplitude depending on $\xi = \omega_L / V_T (z - ut)$:

$$E = Nd\varepsilon(\xi)\exp i(\Phi + \varphi(\xi)) ,$$
$$P = Ndi\alpha(\xi)\exp i(\Phi + \vartheta(\xi)) , \qquad (2)$$
$$\Phi = \omega t - kz, \quad \varepsilon_1' \ll \omega\varepsilon, \quad \varepsilon_2' \ll k\varepsilon, \quad \alpha_1' \ll \omega\alpha, \quad \alpha_2' \ll k\alpha.$$

In the dimensionless parametres

$\beta = u/V_T$, $\beta_g = V_g/V_T$, $\varepsilon_T = E_T/Nd$, $\delta = (\Omega^2 - \omega^2)/2\omega_L^2$,
$q^2 = \omega_g^2/\omega_L^2$, $Q = (\omega_L^2 + k^2 V_T^2 - \omega^2)/\omega_L^2$, $\omega_g^2 = 8\pi Nd^2\Omega/\hbar$,
$V_g = kV_T^2/\omega$

the set of nonlinear equations takes the form

$$\varepsilon'' + 2i(\beta_g - \beta)\varepsilon' + \left(Q - \frac{|\varepsilon|^2}{\varepsilon^2}\right)\varepsilon = 4\pi i\alpha ,$$
$$2\beta\alpha' + i\delta\alpha = \frac{q^2}{4\pi}(1 - |\alpha|^2)^{1/2}\varepsilon . \qquad (3)$$

In the case of linear plasma Eq.(3) give equivalent well known optical self-induced transparency result soliton solution / 1 /

$$\varepsilon_1 = \varepsilon_{m1}\mathrm{ch}^{-1}(\xi/\Lambda_1) , \qquad (4)$$

$$Q_1 = \frac{q^2}{\delta}(1 + \mu^2)^{-1}, \qquad \Lambda_1 = \frac{16\pi}{q^2}\frac{\beta}{\varepsilon_{m1}} ,$$

$$\beta = \beta_g\left[1 + \frac{q^2}{\delta^2}(1 + \mu^2)^{-1}\right]^{-1}, \qquad \mu = \frac{q^2\varepsilon_{m1}}{8\pi\delta} ,$$

On other hand Eq.(3) gives famous soliton for the one-demensional nonlinear Schrodinger equation for electron plasma waves / 2 /, when atoms density vanishes

$$\varepsilon_2 = \varepsilon_{m2} ch^{-1}(\xi/\Lambda_2) , \qquad (5)$$

$$Q_2 = \varepsilon_{m2}^2/2\varepsilon_T^2 , \quad \Lambda_2 = 2^{1/2}\varepsilon_T/\varepsilon_{m2} , \quad \beta = \beta_g .$$

In the general case Eq.(3) give solitary wave type solution if

$$\varepsilon_{m1} = \varepsilon_{m2} = \varepsilon_m \qquad (6)$$

$$\Lambda_1 = \Lambda_2 = \Lambda$$

Moreover one can find soliton solution in the Eq.(3), when the dispersive effects vanish. In this case under the resonance conditions $Q = \delta = 0$ one obtains

$$\varepsilon = \left[\frac{8/q_1^2}{1+\sqrt{1+\left(\frac{1}{2\pi q_1^3 \varepsilon_T^2}\right)^2} \; ch\left(\frac{4\pi q_1}{\beta-\beta_g}\xi\right)} \right]^{1/2} . \qquad (7)$$

If the gas nonlinearity dominantes

$$\frac{1}{2\pi q_1^3 \varepsilon_T^2} \ll 1 , \qquad (8)$$

Eq.(7) transforms to Eq.(4). For "linear" gas Eq.(7) gives

$$\varepsilon = \varepsilon_m \, ch^{-1/2}\left(\frac{4\pi q_1}{\beta_g - \beta}\xi\right) , \quad \varepsilon_m = 4\sqrt{\pi q_1}\,\varepsilon_T . \qquad (9)$$

Thus, one can find differnt types of the solitary Lengmur waves in the active plasma. First of all well-knows

solitons (4) and (5) / 1,2 /. Then the combined soliton under conditions (60 / 3 / which forms in the presence both plasma dispersion and nonlinearity and active atoms nonlinearity. In the case (9) soliton existence due to nonlinear effect of getting out of phase with the wave which leads to a shift of the wave from attenuating to an amplifing phase, but at the same time full gas inversion is unreached /4,5 /. Formula (7) describes the solitary pulse existing under the conditions of the solutions both (4) and (5) / 4,5 /.

So, we establish the possibility of the existence new types of solitary Lengmur waves in the active plasma, which are essentially differ from well known soliton solutions for Schrödinger equation.

/ 1 / S.L.McColl, E.L.Hahn, Phys. Rev. Lett, 22, 908 (1967)

/ 2 / V.E.Zaharov, Soviet JETP, 62, 1745 (1972)

/ 3 / I.V.Bachin, D.V.Krasovitskiy, Soviet Plasma Physics, 13, 490,
(1987)

/ 4 / I.V.Bachin, Timurhuag Nerguy, Soviet Plasma Physics, 14, 1400, (1988)

/ 5 / I.V.Bachin, V.V.Prudsky, be published.

SOLITON FORMATION IN QUASIPARALLEL MHD WAVES

R.L. Hamilton, C.F. Kennel
Department of Physics, University of California
Los Angeles, CA 90024, USA
E. Mjølhus
Institute of Mathematical and Physical Sciences, University of Tromsø
9000 Tromsø, Norway

Satellite observations of MHD waves in the solar wind /1/ has demonstrated a wealth of characteristic wave forms in large amplitude quasiparallel MHD waves. In particular, there are many examples reminiscent of soliton train formation due to nonlinear steepening; these are the so-called shocklets, or discrete wave packets /1,2/.

From the theoretical point of view, the quasiparallel case is characterized by the confluence of the magnetosonic and Alfvénic velocities of propagation. Associated with this degeneracy, the generic models for steepening and soliton formation in weakly nonlinear and dispersive MHD waves, namely the KdV equation for the magnetosonic mode /3/ and the MKdV equation for the Alfvénic mode /4/, break down in the parallel limit. Instead, two coupled equations have to be used for unidirectional propagation in the quasiparallel case, which can be conveniently written in complex notation and normalized units as

$$\frac{\partial b}{\partial t} + \frac{\partial}{\partial x}(|b|^2 b) + i\frac{\partial^2 b}{\partial x^2} = 0\,, \tag{1}$$

for the transverse components of the magnetic field $b = b_y + ib_z$. Derivations of this equation, often called the Derivative Nonlinear Schroedinger (DNLS) equation, exist in many works; a fairly general one, including kinetic as well as multidimensional effects can be found in ref. 5. Eq. (1) is solvable by inverse scattering transform (IST); the version appropriate for the present work, allows nonvanishing although constant boundary conditions $b \to b_0 \neq 0$ as $|x| \to \infty$ /6/, where b_0 represents the deviation from strictly parallel propagation /8,9/.

The objective of this presentation is to give a brief summary of a recent study of the rich wealth of wave forms that can be derived analytically by cominations of (1) and its IST, and the extent to which such wave forms can be related to characteristic initial conditions. Details of this work is described elsewhere /7/. The main results can be described as follows:

1. The solitons of the KdV, MKdV, and NLS equations all appear as limiting forms of the solitons of the DNLS equation.

2. The DNLS allows two main classes of solitons: the one-parameter solitons (OPS) and the two-parameter solitons (TPS) /8,9/. The OPS have a definite amplitude–velocity relationship, which is shown in fig. 1. For each velocity c in the interval $c_A < c < c_M$ (c_A Alfvén and c_M magnetosonic velocities) there are two possible solitons, one rarefactive (dark) and one compressive (bright), which

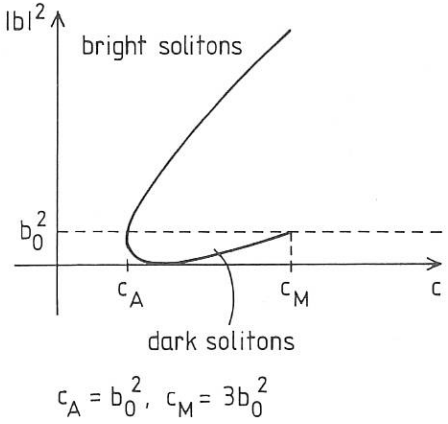

Fig. 1: Amplitude–velocity relationship of one parameter solitons.

is righthand (lefthand) polarized. The TPS are modulational solitons similar to those of the NLS equation (unstable case), and depend on two independent parameters, for example frequency and wave number. From the IST point of view, the OPS (TPS) correspond to real (complex) eigenvalues of the associated scattering problem /6/. The KdV limit appears near c_M on the lower branch of fig. 1, the MKdV limit appears near c_A (both branches), while the NLS limit corresponds to complex eigenvalues with large imaginary part.

3. In /7/, the IST scattering problem has been studied for some special initial profiles for (1), in order to extract information on under what conditions the various types of solitons are formed. In /10,11/ this problem was discussed for the parallel case. In the present work /7/, special emphasis is put on conditions for forming OPS, which requires $b_0 \neq 0$. In brief, the following mechanisms of soliton formation could be identified:

   (i) *Nonlinear steepening of wave forms.* This occurs in a pure form for a linearly polarized initial wave form. A soliton train lying on the lower branch of fig. 1, tied to the c_M end, is formed. Its extension towards c_A increases with the amplitude (depth) of the initial profile. These wave forms have a righthand polarization, just as the observed discrete wave packets /1/. It should be mentioned that the solitons on the lower branch of fig. 1 are known to be transversally unstable /12/.

   (ii) *Nonlinear steepening of modulations.* When the initial profile was circularly polarized, trains of solitons tied to the c_A end of fig. 1 were found to form. They belong to the upper (lower) branch when the initial profile is lefthand (righthand) polarized.

(iii) *Modulational instability.* When the initial profile was circularly polarized, TPS were formed whenever the criterion for modulational instability /10/ was satisfied. When the parameters of the initial wave form was varied, this could be seen as confluence of a bright and dark OPS to form a TPS.

References

/1/ M.M. Hoppe, C.T. Russell, L.A. Frank, T.E. Eastman, and E.W. Greenstadt, J. Geophys. Res. **86**, 4471 (1981)
/2/ T. Hada, C.F. Kennel, and T. Terasawa, J. Geophys. Res. **92**, 4423 (1987)
/3/ T. Kakutani, H. Ono, T. Taniuti, and C.-C. Wei, J. Phys. Soc. Japan **24**, 1159 (1968)
/4/ T. Kakutani and H. Ono, J. Phys. Soc. Japan **26**, 1305 (1969)
/5/ E. Mjølhus and J. Wyller, J. Plasma Physics **40**, 299 (1988)
/6/ T. Kawata and H. Inoue, J. Phys. Soc. Japan **44**, 1968 (1978)
/7/ R.L. Hamilton, C.F. Kennel, and E. Mjølhus, to appear in Physica Scripta (1992)
/8/ C.F. Kennel, B. Buti, T. Hada, and R. Pellat, Phys. Fluids **31**, 1949 (1988)
/9/ E. Mjølhus, Physica Scripta **40**, 227 (1989)
/10/ E. Mjølhus, J. Plasma Phys. **19**, 437 (1978)
/11/ Y.H. Ichikawa and Y. Abe, Prog. Theor. Phys. Supp. **94**, 128 (1988)
/12/ M.S. Ruderman, Fluid Dyn. **22**, 299 (1987); (Izv. Akad. Nauk. SSSR, Mekh. Ahid. i Gasa **2**, 159 (1987))

NONLINEAR WAVE BEHAVIOUR DETERMINED BY HIGH-FREQUENCY PLASMA RESPONSE

M. Georgieva, D. Khristova and A. Shivarova
Faculty of Physics, Sofia University,
BG-1126 Sofia, Bulgaria

The investigations on the self-action of the waves through the plasma nonlinearity require knowledge of the nonlinear dispersion laws (NLDLs) of the waves and the distribution of the wave field in the nonlinear case. Concerning surface waves (SWs), the nonlinear plasma mechanisms usually considered up to now are those due to the ponderomotive force action and the additional ionization /1/. The effect of the high-frequency plasma response through second harmonic generation has recently /2-5/ been introduced for describing envelope soliton formation of quasi-static SWs.

Here we present generalized consideration based on a derivation of the nonlinear plasma permittivity and the nonlinear contribution to the displacement vector which accounts for second harmonic generation. The procedure is applied for describing the nonlinear behaviour (wavenumber shift, nonlinear changes of the wave power and the transverse structure of the field) of SWs in semi-bounded plasma in the whole region of their propagation (electrodynamical study).

We consider cold collisinoless plasma imposed into high-frequency inhomogeneous electric field $\vec{E}(\vec{r},t) = (1/2)\{\vec{\mathcal{E}}(\vec{r}) \times \exp(-i\omega t) + c.c.\}$. The nonlinear plasma respose determined by the nonlinear force $\vec{F}_{NL} = -m(\vec{v}_e.\vec{\nabla})\vec{v}_e - (e/c)(\vec{v}_e \times \vec{B})$ leads to a nonlinear plasma permittivity at frequency 2ω:

$$\varepsilon_{NL} = -\gamma \vec{\nabla}.\left\{\left[\vec{\nabla}\vec{\mathcal{E}}_L^2(\vec{r})\right]\exp(-2i\omega t) + c.c.\right\} \qquad (1)$$

where $\gamma = \alpha/32\pi m\omega^2 n_0$ and $\alpha = 1 - \varepsilon_0 \equiv \omega_{p0}^2/\omega^2$; subscript "0" denotes the equilibrium quantities. Thus, the displacement vector at frequency ω is $\vec{D}(\vec{r},t) = (1/2)\left\{\vec{\mathcal{D}}(r)\exp(-i\omega t) + c.c.\right\}$ with $\vec{\mathcal{D}}(\vec{r}) = \vec{\mathcal{D}}_0(\vec{r}) + \delta\vec{\mathcal{D}}(\vec{r})$, where $\vec{\mathcal{D}}_0(\vec{r}) = \varepsilon_0\vec{\mathcal{E}}(\vec{r})$ and $\delta\vec{\mathcal{D}}(\vec{r}) =$

$-\gamma\left[\vec{\nabla}.\vec{\nabla}\vec{\mathcal{E}}_L^2(\vec{r})\right]\vec{\mathcal{E}}^*(\vec{r})$ is the nonlinear contribution.

In a wave field $\vec{\mathcal{E}}(\vec{r}) = \vec{E}(\vec{r})\exp(i\vec{k}.\vec{r})$, the nonlinear equation for the amplitude of the 'i'-electric field component is:

$$\Delta E_i(\vec{r}) + 2i\vec{k}.\vec{\nabla}E_i(\vec{r}) - (k^2 - \frac{\omega^2}{c^2}\varepsilon_0)E_i(\vec{r}) = P_i(\vec{r})e^{-2i(\vec{k}-\vec{k}_L).\vec{r}} \qquad (2)$$

where $\vec{P}(\vec{r}) = \gamma\left\{\frac{1}{\varepsilon_0}\left[if(\vec{r})(2\vec{k}_L - \vec{k}) + \vec{\nabla}f(\vec{r})\right] + \frac{\omega^2}{c^2}g(\vec{r})\vec{E}^*(\vec{r})\right\}$ is the nonlinear term obtained at weak nonlinearity and

$$g(\vec{r}) = \Delta\vec{E}_L^2(\vec{r}) + 4i\vec{k}_L.\vec{\nabla}\vec{E}_L^2(\vec{r}) - 4k_L^2\vec{E}_L^2(\vec{r}),$$

$$f(\vec{r}) = \vec{\nabla}.\left[g(\vec{r})\vec{E}^*(\vec{r})\right] + ig(\vec{r})(2\vec{k}_L - \vec{k}).\vec{E}^*(\vec{r}).$$

We apply these results to the propagation in z-direction of SWs (TM mode: $\vec{E} = (E_x(x), 0, E_z(x))$, $\vec{H} = (0, H_y(x), 0)$) along the interface ($x = 0$) between plasma and dielectric with permittivity ε_d. After linearization ($\vec{E} = \vec{E}_0 + \delta\vec{E}$, $\vec{H} = \vec{H}_0 + \delta\vec{H}$, $k = k_0 + \delta k$), eq. (2) reduces to:

$$\frac{d^2\delta E_z(x)}{dx^2} - k_{\perp 0}^2\delta E_z(x) = P_z(x) + 2k_0\delta k E_{z0}(x) \qquad (3)$$

where $k_{\perp 0}^2 = k_0^2 - (\omega^2\varepsilon_0/c^2)$, $\beta = k_0^2/k_{\perp 0}^2$, $E_{z0}(x > 0) = A \times \exp(-k_{\perp 0}x)$ and

$$P_z(x) = -(4\gamma k_{\perp 0}^4/\varepsilon_0)(1 - \beta)^2(1 + 3\beta)|A|^2 A\exp(-3k_{\perp 0}x). \qquad (4)$$

For the dielectric ($x < 0$) the replacements $P \to 0$, $\varepsilon_0 \to \varepsilon_d$ and $k_{\perp 0}^2 \to k_{\perp d0}^2 = k_0^2 - (\omega^2\varepsilon_d/c^2)$, $E_{z0}(x < 0) = B \times \exp(-k_{\perp d0}x)$ should be made in eq.(3).

The NLDL

$$\frac{\varepsilon_d}{k_{\perp d0}} + \frac{\varepsilon_0}{k_{\perp 0}}\left\{1 - \frac{\gamma k_{\perp 0}^2}{\varepsilon_0}(1-\beta)^3|A|^2 - k_0\delta k\left[\frac{1}{k_{\perp 0}^2} - \frac{1}{k_{\perp d0}^2}\right]\right\} = 0 \qquad (5)$$

is obtained from the boundary conditions at $x = 0$.

Eq.(5) results into a nonlinear contribution $\delta k = (1/8) \times (\omega_{p0}/c)$ DK $(|A|^2/E_n^2)$ to the linear wavenumber k_0 where DK given by expression:

$$DK = - \left[\varepsilon_d^{1/2} (|\varepsilon_0| - \varepsilon_d)^{3/2} / |\varepsilon_0|^{3/2} (|\varepsilon_0| + \varepsilon_d) (|\varepsilon_0| + 1)^{1/2} \right] \qquad (6)$$

is presented in Fig.1(a) for the case $\varepsilon_d = 1$. Here $E_n = m\omega^2/ek_0$ is a normalizing field amplitude. Expression (6) shows that bright solitons can be formed on the basis of this nonlinear mechanism which is in accordance with /2-5/.

The nonlinear contributions to the amplitudes of the wave field components are obtained in the form: $\delta E_z = (1/8)\, Z_x (|A|^2/E_n^2)A$, $\delta H_y = (1/8) Y (|A|^2/E_n^2) A$, $\delta E_x = (1/8) X (|A|^2/E_n^2) A$. For example, the expressions for Z ($x > 0$) and Z_d ($x < 0$) are:

$$Z = \frac{(|\varepsilon_0| - \varepsilon_d)^2}{2|\varepsilon_0|^3} e^{-k_{\perp 0} x} \left[\frac{|\varepsilon_0| + 3\varepsilon_d}{\varepsilon_d} e^{-2k_{\perp 0} x} + \varepsilon_d \frac{1 + 2k_{\perp 0} x}{|\varepsilon_0| + \varepsilon_d} \right]$$

$$Z_d = \frac{(|\varepsilon_0| - \varepsilon_d)^2}{2|\varepsilon_0|^3} e^{k_{\perp d0} x} \left[4 + \frac{|\varepsilon_0|^2 (1 - 2k_{\perp d0} x)}{\varepsilon_d (|\varepsilon_0| + \varepsilon_d)} \right] \qquad (7)$$

The variations of the quantities Z, Z_d, Y, Y_d and X, X_d in transverse direction are presented for $\varepsilon_d = 1$ in Figs.2, 3 (at different values of ω/ω_{p0}: 0.1(a); 0.2(b); 0.3(c); 0.4(d) and 0.5(e)). The relative nonlinear change of the total wave power flow $\delta S_z/S_{zL} = W (|A|^2/E_n^2)$ is given for $\varepsilon_d = 1$ in Fig. 1(b). Noteworthing is that the nonlinearity leads to an increase of the wave field amplitudes and the Poynting's vector.

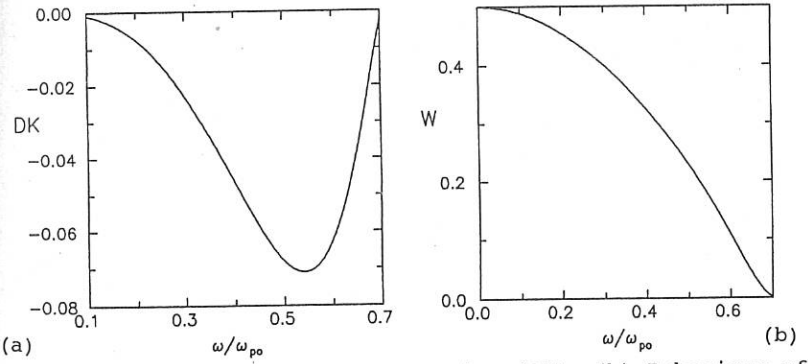

Fig 1: (a) Behaviour of DK (expression (6)); (b) Behaviour of W describing the relative change of the wave power.

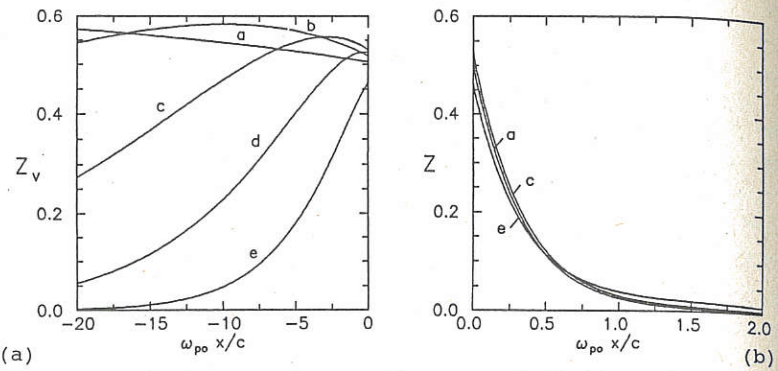

Fig 2: Variation of the nonlinear contribution to the E_z - field component away from the interface x = 0 in the vacuum (a) and the plasma (b).

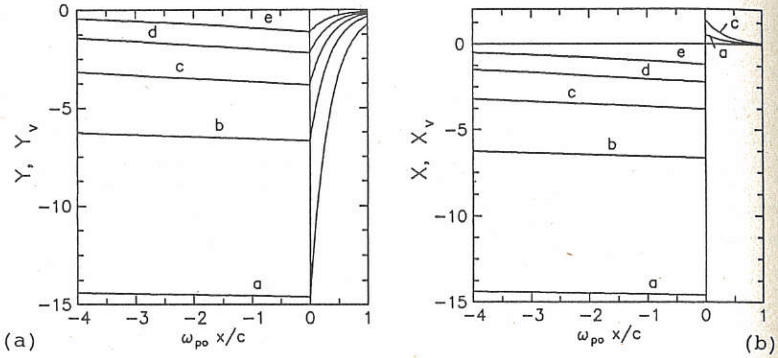

Fig 3: Variation of the nonlinear contribution to the H_y - (a) and E_x - (b) field components away from the interface x = 0.

This work was supported by the National Foundation for Scientific Research in Bulgaria (project n° F27).

/1/ A.Shivarova, in: Spatial Dispersion in Solids and Plasma, ed. P. Halevi (Elsevier, Amsterdam), ch.10 (1992), in press.

/2/ D. Grozev, A. Shivarova, J. Plasma Phys. 31, 177(1984)

/3/ L. Stenflo, O.M. Gradov, IEEE Trans. Plasma Sci. PS-14, 554(1986)

/4/ D. Grozev, A. Shivarova, A.D. Boardman, J. Plasma Phys. 38, 427(1987)

/5/ S.V. Vladimirov, V.N. Tsytovich, Fizika Plasma 14, 593 (1988)

Evolution of Electron Two-stream Instability and Generation of Nonlinear Structure

Masayoshi Tanaka

Department of High Energy Engineering Science
Kyushu University, Kasuga, Fukuoka 816, JAPAN

1 Introduction

It is well known that solitons are generated by the balancing process between dispersive effect and nonlinear steepening. We are studying to find a new route to nonlinear structure/1,2,3/. An electron two-stream instability is considered, and coupled-nonlinear equations describing the interaction of high-frequency stable mode and low-frequency unstable mode is derived. When we take the ponderomotive force of the high-frequency mode into account, a localized solution (soliton) and a periodic solution are obtained. These nonlinear structures are generated by the competitive effects between the linear instability and the nonlinear suppression; the low-frequency mode grows due to the instability, causing a density perturbation. The high frequency mode is modulated through the density perturbation, and, therefore, produces the ponderomotive force, which in turn acts on the low-frequency mode as the suppressing force against the instability. This process provides a different route to nonlinear structure and is intrinsic in unstable media.

In this paper, we present the basic equations and the fundamental solutions obtained by the Hirota's bilinear method.

2. Electron Two-Stream Instability

We consider a plasma with moving electrons and stationary ions, for which the equations of continuity and motion are given by

$$\partial_t N_e + \partial_x (N_e V_e) = 0 \tag{1}$$

$$\partial_t V_e + V_e \partial_x V_e = -(e/m)E + F/m \tag{2}$$

$$\partial_t N_i + \partial_x (N_i V_i) = 0 \tag{3}$$

$$\partial_t V_i + V_i \partial_x V_i = (e/M)E \tag{4}$$

where the subscript 'e' stands for electron, and 'i' for ions, respectively. The quantity F is introduced to include a nonlinear force. The electric field is determined by the Poisson's equation:

$$\partial_x E = 4\pi e(N_i - N_e) \quad . \tag{5}$$

Each quantity consists of low frequency perturbation and high frequency one (denoted by '~'): $N_e = n_0 + n_e + \tilde{n}_e$, $V_e = V + v_e + \tilde{v}_e$, $N_i = n_0 + n_i$, $V_i = v_i$, $E = \mathrm{E} + \tilde{E}$. We divide eqs.(1) - (4) into the high frequency part and the low frequency part, and eliminate the velocities. In the high frequency part, we extract the plane wave component which satisfy the linear dispersion relation. Introducing slowly varying function $\hat{E}(x,t)$, we rewrite

$$\tilde{E} = \hat{E}(x,t)\exp i[k_0 x - \omega_0 t], \quad (\omega_0 - k_0 V)^2 = \omega_{\mathrm{pe}}^2 \tag{6}$$

Substituting eq.(6) for $\tilde{E}$ and assuming $\partial_t \ll V\partial_x$ for the low frequency oscillation, we finally obtain the following equation:

$$-2i(\partial_x + V\partial_x)\hat{E} + V^2\partial_{xx}\hat{E} = -n_e\hat{E} \tag{7}$$

$$\left(\frac{1}{C_s^2}\partial_{tt} + 2V\partial_x\partial_t + V^2\partial_{xx} + V^4\partial_{4x}\right)n_e = -\frac{3}{2}V^2\partial_{xx}(n_e)^2 + \frac{1}{\omega_0^2}\partial_{xx}|\hat{E}|^2 \tag{8}$$

where $\mathrm{C_s}$ is the ion sound velocity, and all the quantities are normalized as usual. The ponderomotive force of the high frequency mode, the second term of eq.(8), is considered here.

3. Soliton Solution

For simplicity, we set $1/C_s^2 = 10$, $V = 1$, $\omega_0 = 1$ in the following. Introducing the dependent variable transform:

$$\hat{E} = g/f, \qquad n_e = 2(\log f)_{xx} \tag{9}$$

and the bilinear operator D_x, D_t:

$$D_x^m D_t^n g\cdot f = (\partial_x - \partial_{x'})^m(\partial_t - \partial_{t'})^n g(x,t)\cdot f(x',t')\Big|_{x'=x,t'=t}$$

we have the bilinear equations for eqs.(7) and (8):

$$[-2i(D_t + D_x) + D_x^2]g\cdot f = 0 \tag{10}$$

$$[10D_t^2 + 2D_xD_t + D_x^2 + D_x^4 + C]f\cdot f = gg^* \tag{11}$$

where C is an arbitrary constant to be determined. Using the Hirota's direct method/4/, we can construct the soliton solution with $C = 0$:

$$\hat{E} = (a/2)\sqrt{a}\,\mathrm{sech}\exp(Kx - \Omega t + \alpha)\exp i(kx - \omega t) \tag{12}$$

$$n_e = 2K^2\mathrm{sech}^2(Kx - \Omega t + \alpha) \tag{13}$$

where the soliton dispersion and the amplitude a are given by

$$\omega = k + \frac{1}{2}(K^2 - k^2), \quad \Omega = 2K(1-k) \tag{14}$$

$$a = \frac{1}{8(10\omega^2 - 2K\Omega + K^2 + 4K^4)} \tag{15}$$

4. Periodic Solution

Periodic solution is constructed with a finite C in eqs.(10) and (11). According to Nakamura/5,6/, we take the Jacobi's theta functions as g and f;

$$\hat{E} = g/f = b\frac{\theta_3(\eta|\tau)}{\theta_0(\eta|\tau)} \exp i(px + qt + \eta_0) \tag{16}$$

$$n_e = 2(logf)_{xx} = 2(log\theta_0)_{xx} \tag{17}$$

where the quantity b is an arbitrary constant to be determined, and θ_0 θ_3 are the Jacobi's elliptic θ functions. After some calculations, we have

$$\hat{E} = \frac{b}{\sqrt{k'}} dn\Big(2K(k)(Px + Qt) \,|\, k\Big) \exp i(px + qt + \eta_0) \tag{18}$$

$$n_e = 8K(k)^2P^2\left[dn^2\Big(2K(k)(Px + Qt) \,|\, k\Big) - \frac{E(k)}{K(k)}\right] \tag{19}$$

$$\tau = i\frac{K(k')}{K(k)}, \quad \hat{q} = \exp[-\pi\frac{K(k')}{K(k)}], \quad k' = \sqrt{1-k^2}$$

where $K(k)$ and $E(k)$ are the complete elliptic integral of the first kinds and the second kinds (k: generating number), respectively. The functions dn is the Jacobi's elliptic function. The amplitude b and the dispersion are given by

$$q = -p + \frac{p^2}{2} + 4\pi^2P^2\frac{A_2(\tau)}{A_0(\tau)} \qquad Q = P(p-1) \tag{20}$$

$$b^2 = 4\pi^2(10Q^2 + 2PQ + P^2)\frac{C_0(\tau)D_2(\tau) - C_2(\tau)D_0(\tau)}{2C_0(\tau)D_0(\tau)} + 16\pi^4P^4\frac{C_0(\tau)D_4(\tau) - C_4(\tau)D_0(\tau)}{2C_0(\tau)D_0(\tau)} \tag{21}$$

where $A_{1,2}(\tau)$, $C_{0,2,4}(\tau)$, and $D_{0,2,4}(\tau)$ are given by

$$A_l(\tau) = \sum_{n=-\infty}^{\infty}(-1)^n(2n)^l\hat{q}^{2n^2}, \qquad \hat{q} = \exp(i\pi\tau) \tag{22}$$

$$C_l(\tau) = \sum_{n=-\infty}^{\infty}(2n)^l\hat{q}^{2n^2}, \qquad D_l(\tau) = \sum_{n=-\infty}^{\infty}(2n-1)^l\hat{q}^{n^2+(n-1)^2} \tag{23}$$

Figure 1 shows a periodic solution given by eqs.(18) and (19).

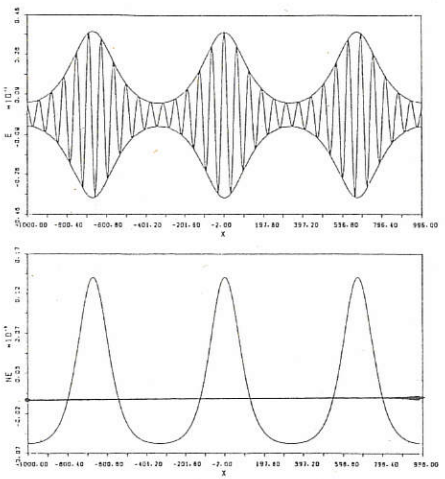

Fig. 1 Periodic solution ($k = 0.99$, Upper: $\hat{E}$; Lower: n_e)

When $k \to 1$, dn-function becomes sech-function, and $E(k)/K(k) \to 0$, In this limit, this solution is identical to the soliton solution obtained above. Noting that

$$dn^2 u - \frac{E(k)}{K(k)} = \left(\frac{\pi}{2K'}\right)^2 \sum_{n=-\infty}^{\infty} \mathrm{sech}^2 \frac{\pi K}{K'}\left(\frac{u}{2K} - n\right) - \frac{\pi}{2KK'} \tag{24}$$

we may consider the periodic solution as the sum of identical solitons separated by a equal distance, — soliton lattice/7/. It is quite interesting to examine the generation of ordered structure from the initial disturbance imposed on this system. The numerical experiments are now ongoing.

Reference

/1/ N. Yajima and M. Tanaka: Prog. Theor. Phys. Suppl. No.94 (1988) 138

/2/ M. Tanaka and T. Yajima: *Solitons in Unstable Media*, to appear in *Optical Solitons* (Springer-Verlag)

/3/ M. Kono and M. Kawakita: Phys. Fluids **B 2** (1990) 1084

/4/ R. Hirota: Direct Methods in Soliton Theory, in *Solitons, Topics in Current Physics*, ed. R. K. Bullough and P. J. Caudrey (Springer-Verlag, 1980) Vol. 17

/5/ A. Nakamura: J. Phys. Soc. Jpn. **47** (1979) 1701

/6/ A. Nakamura: J. Phys. Soc. Jpn. **48** (1980) 1365

/7/ T. Kawahara and S. Toh: Phys. Fluids **31** (1988) 2013

GYROINVARIANT SECOND ORDER DRIFTS IN ELECTRIC FIELDS OF THE SAME ORDER OF THE MAGNETIC FIELD

Pablo Martín
Depto. de Física, Universidad Simón Bolivar,Apdo 89000,Caracas 1080-A, Venezuela

Abstract
Generalizing ideas of previus papers, second order drifts are determined for charged particles moving in large electric fields, i.e. when E~0(1). The present analisis leads to compact and relatively simple forms for the perpendicular drift velocities. All the first order drifts have been determined including new ones depending of $E_{\|}$ and $E_{\|}^2$. All the drifts here present are gyroinvariant in the strict sense, no phase factors and no rotating vector appear.

Introduction:
In previuos papers a new procedure to obtain drift velocities has been developed and applied to the case of weak electric field, i.e. E~0(1), where $\epsilon = m/q$ [1,2]. Here the method is extended in order to consider the most common case, where both the electric and magnetic fields are the same order of magnitude, i.e. E~0(1).The contineous average procedure previously developed is used again. However now new operators have to be defined acording with the new scaling order. New perpendicular drift velocities have been found and the forms are very compact. In the present analysis paralled electric field is also included and consider of the the same order than the perpendicular electric field. However the analysis to second order has been limited to those terms independent of $E_{\|}$. The number of the terms $E_{\|}$ dependent is much larger than all the other drifts and they can be only included in a longer paper.

General Treatment:
The non-relativistic Lorentz equation including electric field is

$$\epsilon \, d\vec{v}/dt = \vec{E} + \vec{v} \times \vec{B}; \quad \epsilon = m/q \, , \; B \equiv B(\vec{r},t) \, \hat{b}(\vec{r},t) \, ; \quad \vec{E} = \vec{E}_{\perp} + E_{\|} \hat{b} \; ; \qquad (1)$$

The velocity $\vec{v}$ is writen as

$$\vec{v} = u \hat{b} + Q \vec{E} \times \hat{b} + \vec{w} \; ; \qquad Q = 1/B \; ; \qquad (2)$$

Here the perpendicular velocity $\vec{w}$ is defined in such a way that the electric-field drift is excluded. The operator D / Dt is also defined differently from what we did in a previuos paper[2]

$$D/Dt = \partial/\partial t + u\ \partial/\partial s + Q\vec{E} \times \hat{b} \cdot \nabla \tag{3}$$

$$d/dt = D/Dt + \vec{w} \cdot \nabla \tag{4}$$

A reference frame $\hat{e}_1, \hat{e}_2, \hat{b}$ rotating with the angular velocity $\vec{\omega}$ is also introduced

$$\vec{\omega} = \hat{b} \times (d\hat{b}/dt) = \hat{b} \times (D\hat{b}/Dt) + \hat{b} \times (\vec{w} \cdot \nabla \hat{b}) \tag{5}$$

The relative $(\delta/\delta t)$ and absolute (d/dt) derivatives are related as

$$d/dt = \delta/\delta t + \vec{\omega} \times \tag{6}$$

The parallel and perpendicular components of the Lorentz equation lead to

$$\dot{u} = E_{\parallel}/\epsilon + Q\vec{E} \times \hat{b} \cdot D\hat{b}/Dt + \vec{w} \cdot [D\hat{b}/Dt + \nabla\hat{b} \cdot \vec{E} \times \hat{b}] + \vec{w}\vec{w} : \nabla\hat{b} \tag{7}$$

$$\delta\vec{w}/\delta t + (1/\epsilon Q)\, \hat{b} \times \vec{w} = \vec{V} + \vec{w} \cdot \nabla\vec{U} \tag{8}$$

$$\vec{V} = -u\ D\hat{b}/Dt + \hat{b} \times D(Q\vec{E})/Dt \tag{9}$$

$$\vec{U} = -u\hat{b} - Q\vec{E} \times \hat{b} \tag{10}$$

Now complex variables are introduced as in previous papers [1,2], giving

$$\dot{u} = E_{\parallel}/\epsilon + \eta + \vec{w} \cdot \vec{F} + (1/2)(w^2 \hat{e}_-\hat{e}_- + w^2 \hat{e}_+\hat{e}_+) : \nabla\hat{b} \tag{11}$$

$$\dot{w} + (i/\epsilon Q)\, w = V + \vec{w} \cdot \nabla U \tag{12}$$

$$\eta = Q\vec{E} \times \hat{b} \cdot (D\hat{b}/Dt) + (1/2)\,|w|^2\ \nabla \cdot \hat{b} \tag{13}$$

$$\vec{F} = D\hat{b}/Dt + \nabla\hat{b} \cdot \vec{E} \times \hat{b} \quad ; \quad \vec{F}\ (\text{vector}) \Leftrightarrow F\ (\text{complex variable}) \tag{14}$$

The formal solution of the complex differential Eq.(12) is

$$w = w_0\, S + S \int_0^t \bar{S}\,(V + w \cdot \nabla U)\, dt \tag{15}$$

$$S = \exp\left[(-i/\epsilon)\int_0^t B\,dt\right] \qquad (16)$$

The periods T, T^+, T^-, are also definided as in previous papers , and the average $\langle\ \rangle$ is

$$\langle A \rangle = (1/2T)\int_{T^-}^{T^+} A\,dt \qquad (17)$$

The iteration formula given in the appendix has been used several times. After a lengthy algebra it is obtained

$$\langle w \rangle = -i\epsilon \langle Q V \rangle - (i\epsilon/2)|w_0|^2 \langle \nabla Q \rangle + \epsilon \langle Q^2 E_\parallel (\partial V/\partial u) \rangle$$
$$- 2i\epsilon \langle Q^2 E_\parallel^2\, \partial b/\partial s \rangle + \epsilon^2 \langle Q\, V\, DQ/Dt \rangle + (\epsilon^2/2)|w_0|^2 \langle D(Q\,\nabla Q)/Dt \rangle$$
$$+ (\epsilon^2/8)\,|w_0|^2 \langle Q\,\bar{\nabla} Q\ \nabla U \rangle + (\epsilon^2/4)|w_0|^2 \langle Q^2 (F\,\bar{\nabla} b - \bar{F} \nabla b) \rangle$$
$$+ \epsilon^2 \langle Q^2\, \eta\, (\partial V/\partial u) + \epsilon^2 \langle D(Q^2 V)/Dt \rangle + (\epsilon^2/2)|w_0|^2 \langle Q\,\nabla Q\ \nabla U \rangle$$
$$+ (1/2)\,\epsilon^2 \langle Q^2 (\bar{V}\,\nabla U - V\,\bar{\nabla} U) \rangle + (1/4)\,\epsilon^2\,|w_0|^2 \langle \bar{\nabla} (Q^2\,\nabla U) \rangle \qquad (19)$$

Several improvements have been done in the way to obtain the Eq. (19) in relation with previous papers [1,2]. In order to proceed further from Eq. (19), the guiding center has to be determined and the average procedure applied as it was done before. However we can avoid some of the rigorously of the procedure and go directly from the complex drifts to the vectorial form, obtaining

$$(\vec{w}_D)_\perp = Q\,\vec{E} \times \hat{b} + (\langle \vec{w} \rangle)_\perp = Q\,\vec{E} \times \hat{b} - \epsilon\, Q\, \hat{b} \times \vec{V} + (1/2)\,\epsilon\, w_0^2\, \hat{b} \times \nabla Q$$
$$+ \epsilon\, Q^2\, E_\parallel\, \partial \vec{V}/\partial u - 2\epsilon\, Q^3\, E_\parallel^2\, \hat{b} \times (\partial \hat{b}/\partial s) + \epsilon^2\, \vec{V}\, DQ/Dt$$
$$+ \epsilon^2\, Q^2 \eta\, \partial \vec{V}/\partial u + \epsilon^2 \hat{b} \times [\hat{b} \times D(Q^2 \vec{V})/Dt] + (1/2)\,\epsilon^2 w_0^2\, \hat{b} \times [\hat{b} \times D(Q \nabla Q)/Dt]$$
$$+ (1/2)\,\epsilon^2\, w_0^2\, Q^2\, \hat{b} \times [(\hat{b} \times \vec{F}) \cdot \nabla \hat{b}] + \epsilon^2\, Q^2\, \hat{b} \times [(\hat{b} \times \vec{V}) \cdot \nabla \vec{U}]$$
$$+ (1/2)\,\epsilon^2\, w_0^2\, Q \{ (\nabla \cdot \vec{U} - \hat{b} \cdot \partial \vec{U}/\partial s)\, \nabla Q - \hat{b} \cdot \nabla \vec{U}\, \hat{b} \times \nabla Q \}$$
$$+ (5/8)\,\epsilon^2 w_0^2 \{ \nabla Q \cdot \nabla \vec{U} - \partial Q/\partial s\, \hat{b} \cdot \partial \vec{U}/\partial s\, \hat{b} + \hat{b} \times [(\hat{b} \times \nabla Q) \cdot \nabla \vec{U}] \}$$
$$+ (1/2)\,\epsilon^2\, w_0^2\, Q^2\, (\nabla^2 \vec{U} - \partial^2 \vec{U}/\partial s^2) \qquad (20)$$

These results are to be compared with previous one [2,3,4]. First we note that there is a coincidence between the three first terms in Eq. (20) and those in Eq. (D11) of Ref.(3). It is worthy pointing out that notation here is different to that used in Ref. (3). The agreement with the results in Ref. (2) is good, once $\vec{E}$ is changed by $\epsilon\vec{E}$. The differences are mainly due to a different way of going from the complex to vectorial form. Here there are much more drifts, which do not appear previously, because they were consider of third or fourth order.

Conclusions:

Perpendicular drifts velocities up to second order have been found in the general case of E~0(1). Very compact results have been obtained which are gyroinvariant in the strict sense. No secularities appear when $E_{\|}$ is considered of the same order than $E_{\perp}$ as it was previously presented.[5] We strees that the results presented here are very compact and it seems in a convenient form to be applied.

References:

1.-P. Martín and M.G.Haines, Phys. Fluids B 2, 11(1990)
2.-P. Martín and M.G.Haines, Phys. Fluids B3, 2939(1991)
3.-R.G. Littlejohn, Phys. Fluids 24, 1730(1981)
4.-R. Balescu, "Transport Processes in Plasma" (North Holland, Amsterdam 1988), Vol I,Chapter 1.
5.-P. Martín, Bull. Am. Phys. Soc.36,2300(1991)

Appendix:

The recurrence relations that helps to understanding the steps leading to Eq. (19) is

$$\langle f(t)\, g(u)\, F(Q)\, S^n \rangle =$$

$$(i\epsilon/n)\, \langle [(\partial f/\partial t)\, g(u) + \dot{u}\, f(t)(\partial g/\partial u)]\, Q\, F(Q)\, (1-S^n) \rangle$$

$$+ (i\epsilon/n)\, \langle f(t)\, g(u)\, [(D/Dt) + \vec{w} \cdot \nabla]\, (Q\, F)\, (1-S^n) \rangle$$

CHARGE SHIELDING BY TRAPPED ION ORBITS IN DUSTY PLASMAS

J. Goree

Max-Planck-Institut für extraterrestrische Physik, D 8046 Garching, Germany

and

Dept. of Physics and Astronomy, The Univ. of Iowa, Iowa City, IA 52242 USA

Introduction

When micron-size particulates are introduced into a plasma, they acquire electric charges that can modify, or even dominate, the plasma if their density is high enough.[1,2] Theories for "dusty plasmas" have been developed for space and astrophysical applications,[2] including planetary rings, spacecraft-plasma interactions,[1,3] and interstellar clouds. Experiments in laboratory discharges reveal that micron-size dust grains can be easily introduced into a low-temperature plasma, where they may be confined for hours at a time.[4]

In this paper, a theory is developed for a subtle but worrisome effect in the charging of dust grains. Because the grain has a large negative charge, it can easily hold one or more positive ions in confined orbits, as shown in Fig. 1. Trapped ions are important because they, unlike untrapped ions, shield the grain's charge from external electromagnetic fields. This is similar to the way that electrons bound in an atom cancel the charge of the nucleus within. Electromagnetic forces on the grain are thereby reduced, and other forces, such as gravity and gas drag, will be comparatively stronger. The larger the number of trapped ions, N_{trap}, the more effective the shielding. Trapping occurs when an incoming ion suffers an inelastic collision within the grain's Debye sphere, losing energy at the same time that its orbital angular momentum is scattered into a favorable direction.

Trapping has generally been ignored in dusty plasma theories, and indeed in their antecedents in probe theory,[5,6] presumably because there is no obvious easy analytic way to quantify the effect. As a result, theorists have been unsure of the validity of their calculations that ignore the effect. To remedy this dilemma, I have developed a model for the most common case: $a \ll \lambda_D \ll \lambda_{mfp}$, where a is the grain radius, λ_D the Debye length, and λ_{mfp} the collisional mean-free-path.

The Standard Charging Model

The starting point for every theory of dusty plasmas is a charging model. The charge Q_D is related to the grain's floating potential ϕ_f by $Q_D = C\,\phi_f$, where $C = 4\,\pi\,\varepsilon_0\,a$ is the grain's capacitance. A grain collects ion and electron currents from the plasma, which add up to determine the steady-state charge, $dQ_D/dt = \Sigma\, J_\sigma\,(\phi_f) = 0$. Due to the low electron mass, ϕ_f and Q_D will always be negative, unless the grain emits electrons. A sphere in a thermalized hydrogen plasma will float to $\phi_f = -2.51\,kT/e$, where T is the ion and electron temperature. This yields a charge $Q_D = -1.7 \times 10^4\,e$, for example, if kT = 1 eV and a = 10 μm. This standard model ignores trapping.

Model of Trapped Ions

Consider a positive ion, with charge q_i, mass m_i and angular momentum M, moving toward a negatively charged grain. The ion's total energy is $E_i = m_i \dot{r}^2/2 + U_{eff}(r)$, where $U_{eff}(r) = q_i\phi(r) + M^2/2m_i r^2$. An ion is trapped if it is in a potential well, i.e., if it satisfies three requirements: its U_{eff} has a minimum, E_i is less than the maximum of U_{eff} found at nonzero r, and the orbit does not strike the grain. An untrapped ion can become trapped only if it undergoes an inelastic collision, scattering into a favorable direction and losing enough energy.

The rate of ion capture is $\dot{N}_{cap} = \Gamma_i \sigma_{cap}$, where $\Gamma_i = n_i v_i$ is the incident ion flux. Here σ_{cap} is a capture cross section

$$\sigma_{cap} = \int_0^\infty 2\pi\, p\,dp\, P_{cap}(p), \qquad (1)$$

and $P_{cap}(p)$ is the probability for an incoming ion at impact parameter p to become captured due to a collision.

What sort of collisions must be considered? Only those that result in slower ions will lead to capture. For neutral atoms and ions that are alike, charge-exchange and elastic collisions have comparable cross sections. But charge exchange yields the most ion energy loss, provided that $kT_{gas} << E_i$.

The loss process is also collisional. Eventually a collision will scatter an ion's energy and angular momentum enough that it either escapes to infinity or strikes the grain. The loss rate is $\dot{N}_{loss} = N_{trap}/\tau_{conf}$, where τ_{conf} is a confinement time.

A steady state is achieved when the capture and loss rates balance, $dN_{trap}/dt = \dot{N}_{cap} - \dot{N}_{loss} = 0$. This yields $N_{trap} = \Gamma_i \sigma_{cap} \tau_{conf}$.

Two conclusions about the physics of trapping can be made from this result. Firstly, the number N_{trap} of collisionally-trapped ions is independent of the collisional mean-free-path, because the λ_{mfp} dependances of σ_{cap} and τ_{conf} in Eq. (4) cancel. Provided that charge exchange is the dominant collision process, it does not matter how low the gas density is. Secondly, the dependence on Γ_i means that the number of trapped ions is $\propto n_i$. Consequently, more ions will be trapped by a grain in a laboratory plasma than in a less dense astrophysical plasma.

Monte Carlo Calculation

The physical model described above is implemented in a Monte Carlo calculation. It is a single-particle model, used with an ensemble of initial conditions. An ion's equation of motion, $\ddot{\underline{x}} = -(q_i/m_i)\nabla\phi$, is integrated in three dimensions with a fourth-order Runge-Kutta method. To determine if a collision took place in a time step Δt, the probability $1 - \exp(-\Delta t\,|\,\underline{v}\,|/\lambda_{mfp})$ is compared to a random number.

I make the following simplifying assumptions. Only charge-exchange collisions are included, and their cross section is constant. The incoming ions are monoenergetic. The neutral gas does not drift with respect to the grain. The grain is spherical. Finally, the electric potential is prescribed, rather than computed self-consistently:

$$\phi(r) = \frac{Q_D}{4\pi\varepsilon_0 r} \exp\left(\frac{a-r}{\lambda_D}\right), \qquad (2)$$

which neglects any trapped orbits or wake effects. This $\phi(r)$ is is valid only if: (a) the number of trapped ions is small, $N_{trap} << Q_D/e$, which may be verified from the results, (b) the Debye spheres of two grains do not overlap, (c) λ_D is much smaller than the ion gyroradius, so that any magnetic field may be ignored, and (d) there is no external potential drop $>\phi_f$ across the Debye sphere, as found for example in the electrode sheaths of a high-voltage laboratory discharge.

The simulation has two stages. First, an incoming ion with $E_i>0$ is directed toward the dust grain, at an impact parameter p. Its orbit is followed until it either undergoes a collision or escapes from the simulation volume. A new ion is born at the collision site, and its initial velocity is chosen from the gas thermal distribution. The new ion is evaluated against the three requirements to see if its orbit is trapped. This is repeated for 200 to 1000 test particles, all with the same p. The capture probability $P_{cap}(p)$ is calculated as the fraction of incoming ions that yielded a trapped ion. This first step is repeated for 40 impact parameters. The integral in Eq. (1) is then computed, yielding σ_{cap}.

Second, the new trapped ion orbits are followed one at a time until, due to collisions, they either strike the grain or escape the simulation space. A histogram of the trapped orbit lifetimes is prepared, and it is fit to a decaying exponential, $N_{trap} = N_0 \exp(-t/\tau_{conf})$ to yield the confinement time τ_{conf}.

The simulation was performed for hydrogen, with the parameters: $a = 10$ μm, $\lambda_D =$ 100 μm, $\lambda_{mfp} = 3$ mm, $E_i = 1$ eV, $T_{gas} = 406$ K ($kT_{neut} = 0.035$ eV). These parameters satisfy the requirements $a << \lambda_D << \lambda_{mfp}$ and $kT_{gas} << E_i$. Figure 2 shows the final result, N_{trap} as a function of floating potential.

Figure 2 can be used to compute N_{trap}, provided that the ion flux is low enough that $N_{trap} << Q_D/e$. For higher fluxes this will not be satisfied; N_{trap} will no longer increase linearly with Γ_i, but rather saturate at Q_D/e. A model with a self-consistent electric potential would be required to treat the saturation regime. Figure 2 also allows an evaluation of the criterion $N_{trap} < 1$, for the incoming ion flux to be small enough that ion trapping is negligible. For example, Fig. 2 shows that $N_{trap}/\Gamma_i = 10^{-15}$ m^2 s for $\phi_f = -0.5$ Volt; if ions are streaming past the grain at $v_i = 10^3$ m/s, then N_{trap} will be unity for $n_i = 10^{12}$ m^{-3}. In space plasmas $n_i << 10^{12}$ m^{-3}, while in laboratory discharges $n_i >> 10^{12}$ m^{-3}. This shows that ion trapping is negligible in space physics problems, a finding that is a confidence-builder for extant space dusty-plasma models that neglect ion trapping. But trapping in laboratory plasmas is so strong that it is often in the saturation regime.

Conclusion

Negatively charged dust grains in a plasma can trap positive ions in confined orbits, and this shields the grain from external electromagnetic fields. The number of trapped ions is determined by a balance between collisional trapping and detrapping. I find that ion trapping is very significant in laboratory plasmas, but negligible in comparatively less dense

space plasmas.

1 E.C. Whipple, Rep. Prog. Phys., 44, 1197 (1981).
2 C.K. Goertz, Rev. Geophys. 27, 271 (1989).
3 T.E. Sheridan et al., J. Geophys. Res. Space Phys. 97, 2935 (1992).
4 G.S. Selwyn, et al., J. Vac. Sci. Technol. A8, 1726 (1990).
5 J.G. Laframboise, UTIAS, Report No. 100, 1966 (unpublished).
6 Ya. L. Al'pert et al., Space Physics with Artificial Satellites, 1965, Chap. 8.

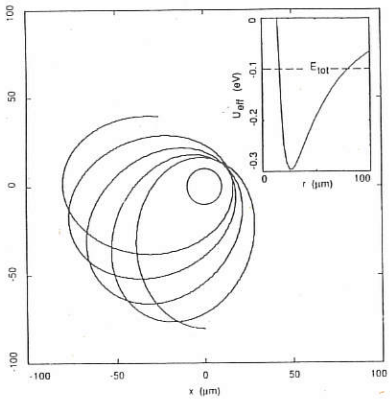

FIG. 1. Trapped hydrogen ion orbiting a negatively-charged dust grain. Parameters are E_i = -0.1 eV, ϕ_f = -2.5 V, a = 10 μm, λ_D = 100 μm, λ_{mfp} = 3 mm, E_i = 1 eV. U_{eff} (r) is shown in the inset.

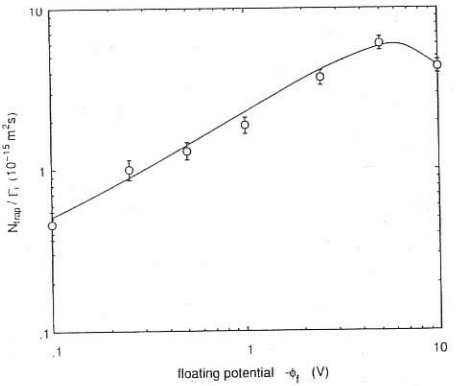

FIG. 2 Number of trapped ions N_{trap} per unit of incoming ion flux, $\Gamma_i = n_i v_i$. These results are valid if $N_{trap} << Q_D/e$.

Vlasov solution describing nonadiabatic plasma heating by magnetic compression

Hans Persson* and Olov Ågren
Group of theoretical electrotechnics, Uppsala university, Box 534, S-751 21 Sweden.
*Also with Studsvik AB.

Introduction. The aim in a nonadiabatic compression is to accelerate particles in a fast impact, where ideally the charges do not change their positions during the compression phase. An outcome of this study is a deeper understanding of how the nonadiabatic heating depends on magnetic ramping profile and initial distribution of particles. Intended applications concern heating experiments in Θ pinches and related devices, but the study can also be of interest to Migma.

The plasma from a negative ion source can form the initial state in a compression experiment. This can be beneficial for supression of space charge, in particular for toroidal configurations where line tying is not available. The negative ions gradually split, but the ionization can be triggered by external arrangements (negative ions is not useful for Migma however, as the radial focusing would be destroyed). Triggered ionization can be a mean to control the compressed plasma radius in Θ pinches and thereby improve wall stabilization.

Vlasov description. It is well known that the harmonic oscillator with a time dependent frequency describes the particle motion in a timevarying solenoidal field,

$$\ddot{\xi} + \Omega^2(t)\xi = 0 \qquad (1)$$

where $\xi = (x+iy)exp[i\int_0^t \Omega(t)\ dt]$ and $\Omega(t) = qB(t)/(2m)$ is the Larmor frequency.

Ideally, we may think of a compression heating where all particles initially are at rest. Eq. (1) shows that each ion then would reach $r = 0$ in a infinitite number of crossings. This occur at exactly the same instants for all ions, irrespektive of their initial distance from the symmetry axis, as long as their initial velocity is zero [1,2]. The magnetic field increase thus generates a strong gyrophase correlation between the particles. The resulting compressed state has a breathing oscillation at the gyro frequency. The oscillations will eventually die out when the gyrophases become decorrelated by various effects such as shielding and intrinsic stochasticity [2].

The configuration has z and θ as cyclic coordinates, and v_z and $P_\theta = m_i[rv_\theta + r^2\Omega(t)]$ are constants of motion. The equations of motion are gouverned by Eq. (1) if space charge and diamagnetic fields are ignored. There is then a third conserved quantity, i.e. the Lewis invariant,

$$I = \frac{A^2(t)}{2}\left\{ (v_r - r\frac{\dot{A}}{A})^2 + (v_\theta + r\Omega)^2 + \frac{r^2}{A^4} \right\} \qquad (2a)$$

where $A(t)$ is a solution of

$$\ddot{A} + \Omega^2(t)A = A^{-3} \qquad (2b)$$

For adiabatic changes in the magnetic field, a WKB solution of (2b) is $A(\varepsilon t) \approx |\Omega(\varepsilon t)|^{-1/2}$, and $(|q|\cdot I - qP_\theta/m_i)/2$ can then be identified as the magnetic moment.

An evolution from a stationary state with a constant magnetic field B_0 to a compressed state with the magnetic field B_1 is considered. Although B_1 is constant, the compressed state will *not* be stationary due to gyrophase correlation. The solution of (2b) at the initial and compressed state will approach the forms

$$A(t) \rightarrow \begin{cases} A_0 = |\Omega_0|^{-1/2} & , t \le 0 \\ A_1(t) = |\Omega_1|^{-1/2}[1-\kappa^2]^{-1/4}\sqrt{1+\kappa sin(\alpha+2\Omega_1 t)} & , t \ge \tau \end{cases}$$

where α is an arbitrary phase and the parameter κ is obtained by solving (2b) for a given evolution of $B(t)$. The parameter κ is zero for an adiabatic compression, while κ is close to unity if the compressed state has a strong gyrophase correlation.

We consider a time evolution of $B(t)$ with a constant "nonadiabaticity" parameter K during the whole compression cycle, i.e $B(t)$ fulfills the equation $dB/dt = K^{-1}\Omega_{gi}B = e(m_iK)^{-1}B^2(t)$, where $K < 1$ for strong ion nonadiabaticty; i.e.

$$B(t) = \begin{cases} B_0/[1-(1-\varepsilon)t/\tau] , & 0 \le t \le \tau \\ B_1 , & t \ge \tau = K\cdot(1-\varepsilon)(m_i/eB_0) \end{cases}$$

where $\varepsilon = B_0/B_1$. The equations for $A(t)$ and the parameter κ can for this profile be solved exactly. With $K < 1$, $\gamma = (1-K^2)^{1/2}$ and $x = \gamma ln(B_1/B_0)$ the result is

$$(1-\kappa^2)^{-1/2} = \frac{coshx - K^2}{1-K^2} \approx \frac{1}{2\gamma^2}\left(\frac{B_1}{B_0}\right)^\gamma$$

Rigid rotor Maxwellians, identical for the positive and negative ions, are used for the stationary initial state. The time evolution can be described by expressing the distribution functions in terms of P_θ and the conserved Lewis invariant,

$$F_\pm = \frac{n_0}{\pi v_{th,0}^2} exp[-\frac{m_i|\Omega_0|I - (\Omega_0 - u_\pm/a)P_\theta}{k_BT_0}]$$

$$= \frac{n(r,t)}{\pi\eta^2(t)v_{th,0}^2} exp[-\frac{(v_r - r\dot{A}/A)^2 + (v_\theta - \bar{v}_{\theta,\pm})^2}{\eta^2(t)\,v_{th,0}^2}]$$

where $u_+ = -u$, $u_- = u$ and the integrals over v_z are already carried out. The confinement criterion is $2a|\Omega_0| > u > 0$. The ratio $2a|\Omega_0|/u \approx \Delta r^2/r_L^2$ determines the relative size of the ion gyro radius and the density efolding length at the initial state.

The density, the mean velocities $\bar{v}_{\theta,\pm}$ and the compression function $\eta(t)$ are

$$n(r,t) = n_0\eta^2(t)\, exp[-\eta^2(t)\frac{r^2}{a^2}\frac{(2au|\Omega_0| - u^2)}{v_{th,0}^2}]$$

$$\bar{v}_{\theta,+} = -\frac{r}{a}u\cdot\{\eta^2(t) + \frac{a}{u}[|\Omega(t)| - |\Omega_0|\eta^2(t)]\} \quad ; \quad \bar{v}_{\theta,-} = -\bar{v}_{\theta,+}$$

and $\eta^2(t) = [|\Omega_0|A^2(t)]^{-1}$. The compression function is initially 1 and goes to

$$\eta^2(t) \rightarrow \eta_1^2(t) = \frac{\sqrt{1-\kappa^2}}{1+\kappa sin(\alpha+2\Omega_1 t)}\frac{B_1}{B_0}.$$

in the final state. The largest radius of the oscillating density profile occurs when $\eta_1^2(t)$ assumes its minimum. After collective phenomena have damped the oscillations, the relaxed plasma radius may be close to the maximum radius during preceeding oscillations. This seems likely if primarily symmetric $m = 0$ non-collisional processes decorrelate the gyrophases, since P_θ then is conserved. The "compression parameter" $\overline{\eta}$,

$$\overline{\eta}^2 = \frac{B_1}{B_1}\sqrt{\frac{1-\kappa}{1+\kappa}} \rightarrow \frac{1}{\gamma}\left(\frac{B_1}{B_0}\right)^{(1-\gamma)/2} \rightarrow \left(\frac{B_1}{B_0}\right)^{K^2/4}, \quad K \rightarrow 0$$

would in such a case determine the ratio of the initial plasma radius to the compressed radius. Due to higher energies, the compression in plasma radius can, for given field ratio, be *much* weaker than in adiabatic compressions. This is beneficial for wallstabilization. Ideally, a compression of order unity can be obtained.

The average particle energy at the compressed state is

$$E(\tau) = \frac{B_1}{B_0}\left\{1 + \left(\frac{1}{\sqrt{1-\kappa^2}} - 1\right)\frac{a|\Omega_0|}{u}\right\} k_B T_0$$

The first term represents the energy increment in adiabatic compressions while the last term represents the nondiabatic heating. The adiabatic heating is proportional to B, while a strongly nonadiabatic heating is proportional to B^2, as also recognized in Ref.1. This gives a possibility to obtain energies in the MeV range by compressing with large magnetic field ratios, $B_1/B_0 \approx 10^3$.

A fast compression of the plasma gives the nonadiabatic heating

$$E_{na} = \left(\frac{B_1}{B_0}\right)^{1+\gamma}\frac{(\Delta r^2/r_L^2)}{4\gamma^2} k_B T_0$$

Fig. 1 shows the dependence of compression parameter and average energy on compression time. The nonmonotonic dependencies on compression time is a consequence of gyrophase correlation. Parameters are $B_0 = 3$ mT, $B_1 = 1$ T, $k_B T_0 =$ 2 eV and $a|\Omega_0|/u = 5$. The density efolding length is 31 cm. A compression time of about 12 μs gives 10 keV energy and $\overline{\eta} \approx 4$, i.e. the relaxed compressed radius is predicted to decrease by a factor of 4 only.

For Migma an energy of 1 MeV can be obtained in a 5 μs compression by increasing B_1 to 3 T. Fig. 2 shows the dependencies of the compression ratio and the heating on compression time. A very high luminosity is obtained in this case.

Magnetic shielding. A fast compression increases the plasma β by the factor $a|\Omega_0|/u$. Allowing in the model a β up to 0.3 gives a shielding limit above which the nonadiabatic heating becomes less efficient. For the Migma parameter case this corresponds a stored particle number per unit length of $2 \cdot 10^{17}$ m^{-1}. The Migma IV experiment managed to store $3.2 \cdot 10^{11}$ particles by trapping an accelerated beam. A fast compression has the potential to exceed this particle number by orders of magnitude, but instabilities presumably give less favourable β limits.

Additional results intrinsic stochasticity will also be presented.

[1] V.P. Krivet and B.P. Peregud, Soviet Phys.-Techn. Phys. 16, 928 (1971).

[2] H. Persson, 10th European Conf. on Controlled Fusion and Plasma Physics, p. K-11 (Moscow, September 1981).and Studsvik report UDC 621.039.646.

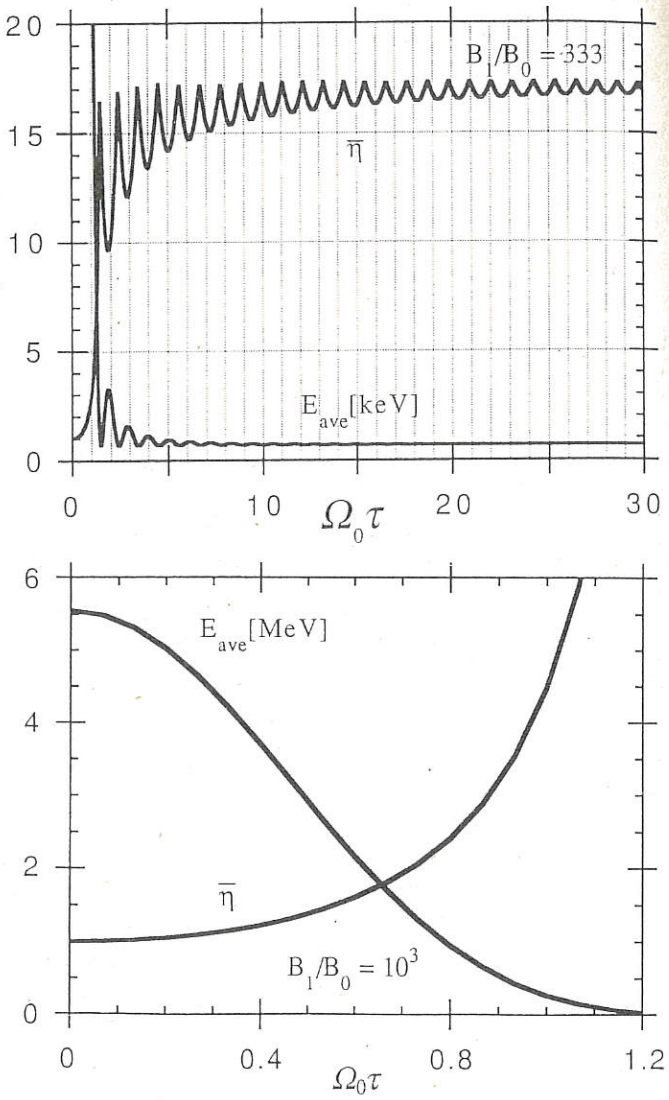

THE PADE APPROXIMATE METHOD FOR SOLVING PROBLEMS IN PLASMA KINETIC THEORY

J.R. Jasperse and B. Basu
Geophysics Directorate, Phillips Laboratory
Bedford, MA 01731, USA

The method of Pade Approximates has been a powerful tool in solving for the time dependent propagator (Green function) in model quantum field theories. We have developed a modified Pade method which we feel has promise for solving linearized collisional and weakly nonlinear problems in plasma kinetic theory. In order to illustrate the general applicability of the method, in this paper we discuss Pade solutions for the linearized collisional propagator and the collisional dielectric function for a model collisional problem.

The kinetic-Poisson equations for a collisional plasma are

$$\frac{\partial}{\partial t} + \underset{\sim}{v} \cdot \frac{\partial}{\partial \underset{\sim}{r}} + \left[\frac{q_e}{m_e} \underset{\sim}{E}(r,t) + \underset{\sim}{a}_0(v)\right] \cdot \frac{\partial}{\partial \underset{\sim}{v}} f(\underset{\sim}{r},\underset{\sim}{v},t) = \mathcal{L}(f) \quad , \tag{1}$$

$$\frac{\partial}{\partial \underset{\sim}{r}} \cdot \underset{\sim}{E}(r,t) = 4\pi \left[nq_i + nq_e \int d^3 v \, f(\underset{\sim}{r},\underset{\sim}{v},t) \right] \quad , \tag{2}$$

where f is the electron distribution function, $\mathcal{L}$ is the nonlinear collision operator which acts on the velocity-space coordinates of f, and the other quantities have their usual meanings. The procedures given in /1/ may be used to find the formal solution of the linearized initial value problem for f_1, where $f(\underset{\sim}{r},\underset{\sim}{v},t) \rightarrow f_0(\underset{\sim}{v}) + f_1(\underset{\sim}{r},\underset{\sim}{v},t)$, $\underset{\sim}{E}(r,t) \rightarrow \underset{\sim}{E}_1(r,t)$ and $\mathcal{L}(f_0 + f_1) - \mathcal{L}(f_0) = L^v f_1$. The collisional propagation operator, U^v, obeys the equation

$$\left\{\frac{\partial}{\partial t} + \underset{\sim}{v} \cdot \frac{\partial}{\partial \underset{\sim}{r}} + \underset{\sim}{a}_0(v) \cdot \frac{\partial}{\partial \underset{\sim}{v}} - L^v(v)\right\} U^v(\underset{\sim}{r},\underset{\sim}{v},t-t') = 0 \quad , \tag{3}$$

where U^v is subject to the usual causality and initial conditions. The equations in transform space $(\underset{\sim}{k},\underset{\sim}{v},\omega)$ for the collisional propagator and dielectric function in condensed notation are:

$$\tilde{U}^{v}(\omega) = \tilde{U}(\omega) + \tilde{U}(\omega) L^{v} \tilde{U}^{v}(\omega) \quad , \tag{4}$$

$$\varepsilon(\omega) = 1 - i\left(\frac{\omega_p^2}{k^2}\right) \int d^3 v \left\{ \tilde{U}^{v}(\omega) \underset{\sim}{k} \cdot \frac{\partial}{\partial \underset{\sim}{v}} f_0 \right\} \quad . \tag{5}$$

Here, $\tilde{U}(\omega)$ is the transform of U (t-t') where U obeys (3) with L^{v} set to zero.

In order to illustrate the Pade method, we choose $\underset{\sim}{a}_0(\underset{\sim}{v}) = 0$ and the simple Fokker-Planck collision operator to represent electron-ion collisions in an equilibrium plasma. In dimensionless units

$$L^{v}(\underset{\sim}{v}) = \nu \frac{\partial}{\partial \underset{\sim}{v}} \cdot \left(\underset{\sim}{v} + \frac{\partial}{\partial \underset{\sim}{v}} \right) \quad . \tag{6}$$

In this case, the exact solution for U^{v} (t-t') is given in /2/. For f_0 Maxwellian, we find that

$$\varepsilon(\omega) = 1 + \int_0^{\infty} dt \frac{1}{\nu} [1 - \exp(-\nu t)] \exp\left\{ i\omega t - \frac{k^2}{\nu^2} [\nu t - 1 + \exp(-\nu t)] \right\} \quad . \tag{7}$$

The Pade method consists of finding a modified Pade Approximate for $\tilde{U}^{v}(\omega) \underset{\sim}{k} \cdot \partial f_0 / \partial \underset{\sim}{v} \equiv \tilde{K}(\omega)$, where $\tilde{K}$ obeys the equation

$$\tilde{K}(\omega) = \tilde{U}(\omega) \underset{\sim}{k} \cdot \frac{\partial}{\partial \underset{\sim}{v}} f_0 + \tilde{U}(\omega) \nu \frac{\partial}{\partial \underset{\sim}{v}} \cdot \left(\underset{\sim}{v} + \frac{\partial}{\partial \underset{\sim}{v}} \right) \tilde{K}(\omega) \quad , \tag{8}$$

and evaluating (5) for the analytically continued ε. From the properties of (8), we seek a Pade Approximate of the form

$$\tilde{K}_P(\omega) = \frac{P_M(v_{\parallel}; \underset{\sim}{k}, \omega)}{Q_N(v_{\parallel}; \underset{\sim}{k}, \omega)} \left(\frac{1}{2\pi}\right)^{3/2} \exp\left[-\frac{v_{\parallel}^2 + v_{\perp}^2}{2} \right] \quad , \tag{9}$$

$$P_M = \sum_{m=0}^{M} p_m(\underset{\sim}{k},\omega)\, v_{\|}^m \quad ,$$

$$Q_N = \sum_{n=0}^{N} q_n(\underset{\sim}{k},\omega)\, v_{\|}^n \quad .$$

The coefficients p_m and q_n are found from (8) by a least squares optimization procedure using a sufficiently large number of $v_{\|}$ values on the interval from $-\infty$ to $+\infty$. The Pade expression for ε is

$$\varepsilon_P(\omega) = 1 - \left(\frac{i}{k^2}\right)\left\{\sum_{\ell=0}^{M-N} r_\ell(\underset{\sim}{k},\omega)\, I_\ell + \sum_{n=1}^{N} \beta_n(\underset{\sim}{k},\omega)\frac{1}{2^{1/2}} Z\left[\frac{\alpha_n(\underset{\sim}{k},\omega)}{2^{1/2}}\right]\right\} \quad , \qquad (10)$$

where the r_ℓ , β_n and α_n are found from the p_m and q_n, $I_\ell = (\ell - 1)!!$ for ℓ even and zero for ℓ odd, and Z is the Plasma Dispersion Function. The roots of the Pade and exact dispersion relations are compared below for $\nu/\omega_p = 10^{-3}$.

k/k_D = 0.1

M = N =	1	2	3	4	exact
ω_r / ω_p	1.01	1.01	1.01	1.02	1.02
$\omega_i / \omega_p \times 10^3$	-0.520	-0.520	-0.520	-0.521	-0.521

k/k_D = 0.3

M = N =	1	2	3	4	exact
ω_r / ω_p	1.16	1.16	1.16	1.16	1.16
$\omega_i / \omega_p \times 10^2$	-1.67	-1.35	-1.34	-1.34	-1.34

In conclusion, we see that a low order Pade Approximate gives a very accurate solution for the dispersion relation. We are now motivated to solve the linearized Balescu-Lenard collisional problem by the Pade method and compare to the perturbation result given in /3/.

/1/ J.R. Jasperse, Phys. Lett. 106A, 379 (1984).
/2/ S. Chandrasekhar, Rev. Mod. Phys. 15, 1 (1943).
/3/ J.R. Jasperse and B. Basu, Phys. Fluids 29, 110 (1986).

CORRELATION THEORY OF PARTICLE DISTRIBUTION NEAR THE PLASMA BOUNDARY IN THE PRESENCE OF STRONG ELECTRIC FIELD

G.M. Korchinsky, I.P. Yakimenko, A.G. Zagorodny

Institute for Theoretical Physics,
Ukrainian Academy of Sciences, 252143 Kiev, Ukraine

The purpose of the present paper is to calculate the equilibrium electron and ion distributions in bounded plasma taking into account the self-correlation effects and the presence of strong external electric field.

The basic set of equations. Consider a bounded plasma system consisting of electrons and ions. The surface S confining the volume V in which the system under consideration happens to be does not absorb incident particles. It may be shown /1-3/ that for such a system the kinetic equation has the form

$$\left\{\frac{\partial}{\partial t} + \mathbf{v}\frac{\partial}{\partial \mathbf{r}} - e_\sigma \frac{\partial \Phi(\mathbf{r},t)}{\partial \mathbf{r}} \frac{\partial}{\partial \mathbf{p}}\right\} f_\sigma(x.t) = I_\sigma \qquad (1)$$

where $X \equiv (\mathbf{r},\mathbf{p})$, $\Phi(\mathbf{r},t)$ is the self-consistent potential which satisfies the Poisson equation

$$\Delta\Phi(\mathbf{r},t) = -4\pi \sum_\sigma e_\sigma n_\sigma \int d\mathbf{p} f_\sigma(x,t) \qquad (2)$$

I_σ is the collision integral

$$I_\sigma = e_\sigma \frac{\partial}{\partial \mathbf{p}} \int d\mathbf{k} \int \mathbf{p} \sum_{\sigma'} e_{\sigma'} n_{\sigma'} \frac{\partial V(\mathbf{r},\mathbf{r}')}{\partial \mathbf{r}} \cdot$$

$$\cdot \left[G_{\sigma\sigma'}(x,x',t) + \frac{1}{n_\sigma}\delta_{\sigma\sigma'}\delta(x-x') f_\sigma(x,t)\right] \qquad (3)$$

$G_{\sigma\sigma'}(x,x',t)$ is the pair correlation function, $V(\mathbf{r},\mathbf{r}')$ is the potential of the unite charge in the system under consideration. In the equilibrium situation $G_{\sigma\sigma'}(x,x',t)$ can be represented as

$$G_{\sigma\sigma'}(x,x',t) = f_{0\sigma}(\mathbf{p}) f_{0\sigma'}(\mathbf{p}') \left[\exp\left\{-\frac{U_{\sigma\sigma'}(\mathbf{r},\mathbf{r}')}{T}\right\} - 1\right], \qquad (4)$$

where $U_{\sigma\sigma'}(r,r')$ is the effective energy of particle interaction with the influence of the plasma and external medium taken into account.

For the case of small plasma parameter

$$U_{\sigma\sigma'}(r,r') = e_\sigma e_{\sigma'} \varphi(r,r'), \tag{5}$$

where $\varphi(r,r')$ is the screened potential of the unite charge. This potential satisfies the equation

$$\Delta\varphi(r,r') - k_D^2 \varphi(r,r') = -4\pi\sigma(r,r') \tag{6}$$

with the appropriate boundary conditions. Here,

$$k_D^2 = \sum_\sigma k_{D\sigma}^2 = \sum_\sigma 4\pi e_\sigma^2 n_\sigma / T \tag{7}$$

Using Eqs. (1)-(6) one can find the following representation for the equilibrium value of collision term

$$I_\sigma = -F_\sigma(r)\frac{\partial f_\sigma(x)}{\partial p} = \frac{\partial U_\sigma(r)}{\partial r}\frac{\partial f_\sigma(x)}{\partial p} \tag{8}$$

where

$$U_\sigma(r) = \frac{e_\sigma^2}{2} \lim_{r' \to r} \left[\varphi(r,r') - \varphi_0(r,r')\right] \tag{9}$$

$\varphi_0(r,r')$ is the screened potential in the relevant unbounded system.

Thus, the Eqs. (1), (2) are reduced to the following ones

$$\left\{ v\frac{\partial}{\partial r} - \frac{\partial}{\partial r}\left[e_\sigma \Phi(k) + U_\sigma(r)\right]\right\} f_\sigma(x) = 0 \tag{10}$$

$$\Delta\Phi(r) = -4\pi \sum_\sigma e_\sigma n_\sigma \int dp f_\sigma(x) \tag{11}$$

The last equation should be supplemented with the boundary condition

$$\Phi(r) = \Phi^{ext}(r)\,|\,s \tag{12}$$

or

$$\frac{\partial\Phi(r)}{\partial r_n} = -\tilde{\varepsilon} E_n^{ext}(r)\,|\,s \tag{13}$$

Here, $\tilde{\varepsilon}$ is the dielectric constant of external medium.

Equilibrium profiles in semi-bounded plasma. Let us

consider plasma-like medium occupying the half-space $x<0$ and exposed to the electric field $\mathbf{E}=(E,00)$. In the case of the weak field $|eE/k_DT|\ll 1$ the solutions of the Eqs. (11), (12) (13) are as follows

$$f_\sigma(x) = \exp\left\{-\frac{U_\sigma(x)+e_\sigma\Phi(x)}{T}\right\} \tag{14}$$

$$\Phi(x) = -\frac{\tilde{\varepsilon}E}{k_D}e^{k_Dx} + \frac{1}{2}\sum_\sigma e_\sigma k_{D\sigma}^2\int dk\frac{k\tilde{\delta}(k)}{4k^2+3k_D^2}\cdot\left[\frac{e^{2\alpha x}}{\alpha}-2\frac{e^{k_Dx}}{k_D}\right] \tag{15}$$

where

$$U_\sigma(x) = \frac{e_\sigma^2}{2}\int dk\frac{k\tilde{\delta}(k)}{\alpha}e^{2\alpha x}$$

$$\tilde{\delta}(k) = \frac{\alpha-\tilde{\varepsilon}k}{\alpha+\tilde{\varepsilon}k}, \qquad \alpha = \sqrt{k^2+k_D^2}$$

In the opposite case $|eE/k_DT|\gtrsim 1$ it is necessary to solve nonlinear Poisson equation (11). This can be done by the iteration procedure. Let us introduce $U_\alpha(x)=\alpha U_\sigma(x)$, where $0<\alpha<1$, and consider the equation

$$\Delta\Phi(x) = -4\pi\sum_\sigma e_\sigma n_\sigma\exp\left\{-\frac{e_\sigma\Phi(x)+\alpha U_\sigma(x)}{T}\right\}|\alpha=0 \tag{16}$$

with the boundary condition

$$\Phi'(0) = -\tilde{\varepsilon}E^{(s)},$$

where $|E^{(s)}|\ll|E|$, $|e_\sigma E^{(s)}/k_DT|\ll 1$. For such boundary condition we can take the solution (15) at $\sum_\sigma e_\sigma k_{D\sigma}^2 = 0$ for the first approximation. Then we introduce the perturbation of boundary condition

$$\Phi'(0) = -\tilde{\varepsilon}(E^{(s)}+\delta E), \tag{17}$$

This leads to the perturbation of $\Phi(x)$

$$\Phi(x) = \Phi_1(x)+\delta\Phi(x). \tag{18}$$

Here $\Phi_1(x)$ is the solution of linear equation (16) at $U_\sigma=0$. Substituting Eq. (18) into Eq. (16) we obtain the equation for $\delta\Phi(x)$.

So we have the following iteration procedure

$$\Delta\delta\Phi_1(x)=\sum_\sigma k_{D\sigma}^2 \exp\left\{-\frac{e_\sigma}{T}\left[\Phi_1(x)+\sum_{j=2}^{i=1}\delta\Phi_1(x)\right]\right\}\delta\Phi_1(x)$$

$$\delta\Phi_i'(0) = -\tilde{\varepsilon}\delta E_i, \qquad i=1,2,\ldots k$$

where k is governed by the equation: $\sum_{i=2}^{k}\delta E_i + \delta E = E$.

In this manner we find the numerical solution of the Eq. (16)

$$\Phi_2(x) = \sum_{i=2}^{k}\delta\Phi_i(x)+\Phi_1(x)$$

By analogy one can construct the second cycle of the iterations

$$\Delta\delta\tilde{\Phi}_i(x) = \sum_\sigma k_{D\sigma}^2 \exp\left\{-e_\sigma\left(\Phi_2(x)+\sum_{j=1}^{i=1}\left[\delta\tilde{\Phi}_j(x)+U_\sigma(x)\delta\alpha_j\right]\right)/T\right\}\cdot$$

$$\cdot\left[\delta\tilde{\Phi}_i(x)+U_\sigma(x)\delta\alpha_i\right].$$

$$\delta\tilde{\Phi}_i(0) = 0; \qquad i=1,2,\ldots L,$$

where L is governed by $\sum_{i=2}^{L}\delta\alpha_i = 1$.

After both cycles of iterations are performed, one finds the solution of the problem

$$\Phi(x) = \Phi_2(x)+\sum_{i=2}^{L}\delta\tilde{\Phi}_i(x).$$

Detail analysis of the numerical calculations for different values of external field is presented in ref.4.

/1/ A.G. Zagorodny, A.S. Usenko, I.P. Yakimenko, Doklady Academy of Sciences of Ukr.SSR. No3, 55 (1984).

/2/ A.G. Zagorodny, A.S. Usenko, I.P. Yakimenko, Fizika Plasmy, **11**, 714 (1985) (in Russian).

/3/ A.S. Usenko, I.P. Yakimenko, A.G. Zagorodny, in: "Plasma Theory and Nonlinear and Turbulent Processes in Physics" (World Scientific, Singapore, 1989), **2**, 721.

/4/ G.M. Korchinsky, I.P. Yakimenko, A.G. Zagorodny, Phys.Scr. **45**, 380 (1992).

Possible Changes of Temperature and Density Power Law Exponents in Expressions for Plasma Transport Quantities under Many Particle Interaction Conditions

R. W. Larenz
Institute for Theoretical Physics, University of Duesseldorf
D 4000 Duesseldorf, Germany

Abstract
For plasmas with $\alpha^2 = kT/e^2 n^{\frac{1}{3}} \gg 1$ correlation effects of the ionic species and their influence on the motion of electrons are considered. It is shown that plasma transport quantities may be changed markedly if compared with results of the usually applied two body collision theory. To account for observational facts, introduction of such correlation effects seems to be necessary.

Introduction

Observations, that electron transport quantities in hot and dilute plasmas do not follow in an expected manner to theories existing up to now (see for instance remarks in /1/, /2/, /3/), reveal the need to look for mechanisms and reasons to explain this fact and to develop a better understanding by exploration of possibilities which are still given within known plasma physics fields.

The basic quantity to be considered, when dealing with transport questions, is given by the socalled "electron relaxation time τ" or a reciprocal effective electron collision frequency, where for the fully ionized plasmas considered here, collisions with ions are essential, which lead to electron orbit deflections calculated hitherto from electron orbits around individual ions. However, under conditions of plasmas with large particle numbers within a Debye-sphere, that means for the known plasma parameter $\alpha^2 = kT/e^2 n^{\frac{1}{3}} > 1$ (usual meaning of symbols), it may be questioned, whether independent electron deflections caused by individual ions alone should be considered by adding up these deflections in the known statistical manner as shown for instance by Spitzer /4/. Under conditions $\alpha > 1$ the Coulombian long range peculiarity should be taken seriously by inclusion of ionic correlation effects. Three ways to do this are proposed here with application to some important transport quantities like the electric and thermal conductivity of plasma electrons. It should be expected to arrive at a markedly changed functional dependence of these quantities on temperature T and density n, if experimental observations shall be explained.

First Method

As the ions are moving very slowly as compared to the electrons it may happen that a number N of 2 or more ions at about the same distance of a collision parameter p are acting together simultaneously on a test electron during its short transit time. To

describe this ionic correlation, the distribution $w_s(N)$ as

$$w_s(N) = (s-1)N^{-s} \quad \text{for} \quad N \geq 1, \quad s > 2 \quad \text{with} \quad \langle N \rangle = (s-1)/(s-2) \tag{1}$$

shall be introduced, which is sharply peaked at $N = 1$ to account for the still dominating case of only one individual ion being effective. Noninteger N is allowed for to represent more or less active Debye-shielding.

Now the usual procedure of adding up or integrating deflection angle ψ sine squares with respect to the collision parameter p until to the usual Debye-length limit D is performed and furthermore the averaging with $w_s(N)$ (this being open also to the interpretation that the plasma contains a series of $N = Z$-fold ionic charges). Setting the deflection sine-square sum to 1 defines the momentum relaxation time $\tau(v)$ of an electron with velocity v

$$nv \cdot \tau(v) \cdot \int_1^\infty \int_0^D \sin^2 \psi \cdot 2\pi p dp \cdot w_s(N) dN = 1, \quad \tan \psi/2 = Ne^2/mpv^2 \tag{2}$$

(m = electron mass). The N-integration may be done with help of the residue theorem. At conditions $\alpha > 1$ a little additional term, appearing at the integration, can be neglected (as it is done usually too for $N \equiv 1$). After averaging $\tau(v)$ from eq. (2) with Maxwell's v-distribution the resulting mean relaxation time τ may then be inserted into the formula for the conductivity σ by $\sigma \sim \omega_p^2 \tau$ with ω_p as plasma frequency ($\omega_p^2 = 4\pi e^2 n/m$). Neglecting numerical factors one has

$$\sigma \sim n^{(3-2x)/6} \cdot T^x \quad \text{with} \quad 2x = 3s - 6 \quad \text{or} \quad \sigma/\omega_p \sim \alpha^{3s-6} \tag{3}$$

written in a dimensionless form as a power of α and for the electron heat conductivity λ

$$\lambda \sim n^{(3-2x)/6} \cdot T^{x+1} = n^{(3-s)/2} \cdot T^{(3s-4)/2} . \tag{4}$$

For $s \geq 3$ the traditional $\sigma \sim T^{3/2}$-law appears (neglecting the Coulomb-logarithm here). Later on one will see that $x = 3/4$, $s = 5/2$ has certain preference; $s = 5/2$ corresponds to an effective together acting ion number $\langle N \rangle = 3$, a number which seems not to be high; however, the slowly decaying tail of $w_s(N)$ is of importance for this model.

Second Method

Simultaneously acting ions my be considered as an effective space charge, which naturally grows with the volume dimensions involved by the magnitude of the collision parameter. Therefore a direct relation among collision parameter p and the effective number $\langle N \rangle$ of ionic charges may be written down in the following manner involving the particle density n for dimensional reasons

$$\langle N \rangle = A \cdot (np^3)^q \tag{5}$$

with A as appropriate numerical factor and q as suitable exponent. Now one has for

the deflection angle ψ

$$\tan \psi/2 = Ae^2 n^q p^{3q-1}/mv^2 \,. \tag{6}$$

The integration of $\sin^2 \psi$ over the collision parameter p up to the Debye-length D is easily performed revealing here in an even more accentuated manner the known fact, that for $\alpha > 1$ essentially large collision parameter are contributing to the deflections. The relaxation time $\tau(v)$, established analogously to eq. (2) and averaged with the Maxwellian leads to the conductivity

$$\sigma \sim n^q \cdot T^{3(1-2q)/2} = n^{(3-2x)/6} \cdot T^x \quad \text{or} \quad \sigma/\omega_p \sim \alpha^{3(1-2q)} \tag{7}$$

written in the dimensionless form. Evidently there exists a relation for the exponents x, s and q, if an equal result shall be obtained: $2x = 3s - 6 = 3 - 6q$. Particularly for $x = 3/4$, $s = 5/2$ one has $q = 1/4$, the latter value to be explained physically in the next section.

There may some variations be applied at the first and second method, consisting for instance in a dependence of the Debye length limit on the ion number N resp. $\langle N \rangle$, which lead to certain modifications of x(s) or x(q); however, this has no essential consequence for $\sigma = f(n, T, x)$.

Third Method and Remarks

This method starts with the derivation of an ionic microfield correlation time as described at the XX ICPIG /5/. This correlation time τ_i at $\alpha > 1$ is given by the ratio of the mean particle potential ϕ at a reference point in the plasma to the mean time derivative $\dot{\phi}$

$$\tau_i = \left(\langle \phi^2 \rangle / \langle \dot{\phi}^2 \rangle \right)^{1/2} \sim n^{-1/4} \cdot T^{-3/4} \tag{8}$$

from

$$\langle \phi^2 \rangle = (2\pi e^2 n_i kT)^{1/2} \quad \text{and} \quad \langle \dot{\phi}^2 \rangle = 12\pi n_i (kT)^2/m_i \tag{9}$$

and can be obtained in the same way by the corresponding ionic fieldstrength or space charge quantities. τ_i turns out to be proportional to the reciprocal conductivity σ as plausible because more persistent ionic fields yield enhanced electron orbit deflections. As far as numerical factors are of interest, τ_i might be inserted into a Fokker-Planck-type equation to derive such factors for σ as it is suggested in /6/. Now here one has

$$\sigma \sim n^{1/4} \cdot T^{3/4} \quad \text{and} \quad \lambda \sim n^{1/4} \cdot T^{7/4} \,, \tag{10}$$

that means the exponents x, s and q of the foregoing methods have to be fixed to $x = 3/4$, $s = 5/2$, $q = 1/4$ if all three ways shall yield a common equal power law. The λ-law might be compared to the classical $T^{5/2}$-law and to a T^2-law as proposed by Minardi /8/. The value $q = 1/4$ is explained in the following way corresponding to /7/: Any effective ionic space charge in a sphere volume not transgressing a Debye-sphere will be proportional to the 1/4 power of the plasma density because fluctuations of n, proportional to $n^{1/2}$ for neutral gases, will be widely compensated by rapidly acting electron shielding of ions, so that only the fluctuation of the shielding leads to an effective ionic space charge being now proportional to $n^q = n^{1/4}$.

Generally it seems that the transport quantities at $\alpha > 1$ appear now as geometrical mean of the derivations from a pure two body problem and a collective many particle plasma problem. Particularly the temperature power-law shows tendency to lower exponents and exhibits a behaviour, which is more similar to that, what is found at conditions $\alpha \lesssim 1$ in direction to the socalled "strongly coupled plasmas" (see for instance /9/). From the dimensionless writing $\sigma/\omega_p \sim \alpha^{2x}$ it is seen, that the different power laws, whatever the value of the exponents x, s, q might be, will deliver the same result if $\alpha^2 = kT/e^2 n^{1/3}$ assumes values about $\alpha \simeq 1$. In this context it might be mentioned that σ-measurements do exist only for $\alpha \lesssim 3$. Finally, as mentioned in /5/, on calculating electron relaxation lengths from the relaxation time $\tau \sim (T/n)^{3/4}$ according to the first and second method one finds an expression already derived by D. Gabor /10/.

References

/1/ D. B. Melrose, Australian Journal of Physics 43(6), 703 (1990)

/2/ B. Balet, J.G. Cordey and P.M. Stubberfield,
Plasma Physics and Controlled Fusion 34(1), 3 (1992)

/3/ U. Stroth, G. Fussmann, K. Krieger, V. Mertens, F. Wagner,
M. Bessenrodt-Weberpals, R. Büchse, L. Giannone, W. Herrmann,
E. Simmet, K.-H. Steuer and the ASDEX Team,
Nuclear Fusion 31(12), 2291 (1991)

/4/ L. Spitzer, Jr., Physics of Fully Ionized Gases, John Wiley Sons, p. 120 ff. (1965)

/5/ R. W. Larenz, XX ICPIG, Pisa, 412 (1991)

/6/ R. W. Larenz, XIX ICPIG, Belgrade, 148 (1989)

/7/ R. W. Larenz, V ICPIG, Munich, 1650 (1961)
ICPIG = International Conference on Phenomena in Ionized Gases

/8/ E. Minardi, Plasma Physics and Controlled Fusion 30(12), 1701 (1988)

/9/ Z. Djurić, A.A. Mihajlov, V.A. Nastasyuk, M. Popović and I.M. Tkachenko,
Physics Letters A 155(6,7), 415 (1991)

/10/ D. Gabor, Physikalische Zeitschrift 34, 38 (1933)

DYNAMICAL SCREENING IN THE COULOMB RELAXATION OF ANISOTROPIC PLASMAS

U.Wolf and H. Schamel
Physikalisches Institut, Universität Bayreuth
W 8580 Bayreuth, Germany F.R.

The polarisation effect on the isotropisation of a magnetized Bi-Maxwellian plasma is investigated in the weak coupling approximation . Based on the ROSTOKER collision operator, which reduces in the magnetic field free limit to the BALESCU-LENARD operator, the equipartition frequency ν is evaluated numerically for $B \longrightarrow 0$ and analytically for $B \longrightarrow \infty$, respectively. This frequency depending nonlinearly on ϵ and B describes the approach to thermodynamic equilibrium of the anisotropy parameter $\epsilon \equiv \frac{T_\perp}{T_\parallel}$ via $\frac{d\epsilon}{dt} = (1-\epsilon)\nu(\epsilon, B)$. It is found that in both limits dynamical screening makes a negligible contribution to the relaxation process. For finite B a simplified, yet unexploited expression for $\nu(\epsilon, B)$ is presented. which invokes three new functions.

As a specific example of a dynamical system far away from thermodynamic equilibrium we consider the isotropisation of an initially anisotropic electron plasma immersed in a homogenous magnetic field. This system appears to be of interest not only because of its experimental accessibility /1,2/ but also because of its potential impact on general plasma transport in situations of weak collisionality. The equation we are starting with is essentially ROSTOKER's collision operator/3,4/ describing the Coulomb interactions in the weak coupling approximation:

$$\left(\frac{\partial f}{\partial t}\right)_C = \frac{1}{2\pi}\left(\frac{\omega_e}{2\pi}\right)^4 \frac{\partial}{\partial \vec{v}} \cdot \int\int\int_{-\infty}^{\infty}\int_{-\infty}^{\infty}\int_{-\infty}^{\infty} \exp\left\langle i\left\{[\omega - k_z v_z]s - \frac{1}{\Omega}\left[(v_y k_x - k_y v_x)(\cos(\Omega s) - 1) + (v_x k_x + v_y k_y)\sin(\Omega s)\right] + \left[\omega - k_z v_z'\right]s' - \frac{1}{\Omega}\left[\left(v_y' k_x - k_y v_x'\right)\left(\cos(\Omega s') - 1\right) + \left(v_x' k_x + v_y' k_y\right)\sin(\Omega s')\right]\right\}\right\rangle \frac{\vec{k}\vec{k}}{k^4} \cdot \left(\partial\vec{v} - \partial\vec{v}'\right) \frac{f(v_\perp, v_\parallel) f(v_\perp', v_\parallel')}{\left|\epsilon_D(B, \vec{k}, \omega)\right|^2} d^3v' ds' ds d\omega d^3k \qquad (1)$$

where ϵ_D means the dielectric function/4/. In (1) one immeadiately recognizes the undisturbed helical particle motion as well as the dynamical screening effect ($\left|\epsilon_D(B, \vec{k}, \omega)\right|^2$ in the denominator).
We assume that the distributions are described by Bi-Maxwellians/5/ and define the parallel energy

$$W_\parallel := \int \frac{m}{2} v_\parallel^2 f(\vec{v}) d^3v. \qquad (2)$$

where $\|$ refers to the direction of the magnetic field. Using the definition of the collision operator and integrating by part we get

$$\frac{dW_{\|}}{dt} = \frac{m}{2}\left(\frac{\omega_e}{2\pi}\right)^4 \int\int_{-\infty}^{\infty} \frac{k_z^2}{k^4|\epsilon_D(B,\vec{k},\omega)|^2} f_\Omega\left(T_\perp, T_{\|}, \vec{k}, \omega\right) d\omega d^3k \tag{3}$$

In (3) the function f_Ω is defined by

$$f_\Omega\left(T_\perp, T_{\|}, \vec{k}, \omega\right) :=$$
$$\frac{1}{\Omega^2}\int_{-\infty}^{\infty}\int_{-\infty}^{\infty}\left[2 - a(k_z,\Omega)\left(y^2 + 2yy'\right) - 2\frac{T_{\|}}{T_\perp} b(k_x,k_y,\Omega)\left(2y' + y\right)\cos(y')\sin(\frac{y}{2})\right]$$
$$\exp\left\{-\frac{a(k_z,\Omega)}{4}\left(4y'^2 + y^2\right) - 2b(k_x,k_y,\Omega)\left[1 - \cos(y')\cos\left(\frac{y}{2}\right)\right] + 2i\frac{\omega}{\Omega}y'\right\} dydy' \tag{4}$$

where a and b are given by $a(k_z,\Omega) = \frac{k_B T_{\|}}{m}\frac{k_z^2}{\Omega^2}$ and $b(k_x,k_y,\Omega) = \frac{k_B T_\perp}{m}\frac{k_x^2+k_y^2}{\Omega^2}$. The magnetic field is in z - direction and $\Omega = \frac{-eB}{m}$ is the the cyclotron frequency.Using the identity

$$\frac{\partial}{\partial y}\exp\left[-\frac{a}{4}\left(4y'^2 + y^2\right) + 2b\cos(y')\cos\left(\frac{y}{2}\right) + 2i\frac{\omega}{\Omega}y'\right] =$$
$$\left[-\frac{a}{2}y - b\cos(y')\sin\left(\frac{y}{2}\right)\right]\exp\left[-\frac{a}{4}\left(4y'^2 + y^2\right) + 2b\cos(y')\cos\left(\frac{y}{2}\right) + 2i\frac{\omega}{\Omega}y'\right]$$

we can integrate by part. By means of the substution

$$r' = y' - \frac{y}{2}$$
$$r = y' + \frac{y}{2}$$

we finally arrive at

$$f_\Omega(T_\perp, T_{\|}, \vec{k}, \omega) = \frac{1}{\Omega^2}\epsilon^{-2b}\left(1 - \frac{T_{\|}}{T_\perp}\right)\int_{-\infty}^{\infty}\int_{-\infty}^{\infty}\left\{\left[2 - a\left(r - r'\right)^2\right]\right.$$
$$\left.\exp\left[-\frac{a}{2}\left(r^2 + r'^2\right) + b\left(\cos r + \cos r'\right) + i\frac{\omega}{\Omega}\left(r + r'\right)\right]\right\} drdr' \tag{5}$$

The temporal evolution of the anisotropy parameter $\epsilon := \frac{T_\perp}{T_{\|}}$ is related to (3) by

$$\frac{d\epsilon}{dt} = -\frac{1}{n}\frac{(1+2\epsilon)^2}{3k_B T_0}\frac{dW_{\|}}{dt}, \tag{6}$$

which follows from energy conservation/5/. T_0 is the final isotropic temperature. Normalising time and frequency by $\frac{2\sqrt{3}}{\nu_{Spitzer}}$ and $\nu_{Spitzer}$, where $\nu_{Spitzer}$ has been defined in /6/. we arrive at our final equation

$$\frac{d\epsilon}{d\tau} = \nu(\Omega,\epsilon)(1-\epsilon) \tag{7}$$

with a corresponding equipartition frequency $\nu(\Omega,\epsilon)$ depending nonlinearly on the magnetic field strength and on the anisotropy parameter.
To extract its properties we first perform the magnetic field free limit and find

$$\nu(0,\epsilon) = \frac{4}{\sqrt{\pi}\ln\Lambda}(1+2\epsilon)^{\frac{5}{2}}\int_0^{\Lambda}\frac{1}{k}\int_0^1\frac{y^2(1-y^2)}{[\epsilon+(1-\epsilon)y^2]^{\frac{3}{2}}}\int_0^{\infty}\frac{\exp(-x^2)dxdydk}{DK(\epsilon,k,y,x)} \quad (8)$$

where the denominator representing dynamical screening is given by

$$DK(\epsilon,k,y,x):=1-\frac{1}{3}\frac{1+2\epsilon}{k^2[\epsilon+(1-\epsilon)y]}\Re\left[Z'\left(\frac{x}{\sqrt{2}}\right)\right]+\left\{\frac{1}{6}\frac{1+2\epsilon}{k^2[\epsilon+(1-\epsilon)y]}\left|Z'\left(\frac{x}{\sqrt{2}}\right)\right|\right\}^2 \quad (9)$$

Z is the plasma dispersion function/7/. Expression (8) represents the BALESCU-LENARD version of the equipartition frequency. If DK is set equal to unity, $\nu(0,\epsilon)$ is given by

$$\nu(0,\epsilon) = \frac{(1+2\epsilon)^{\frac{5}{2}}}{(1-\epsilon)^2}[g(\epsilon)(2+\epsilon)-3] \quad (10)$$

with

$$g:\mathcal{R}^+\longrightarrow\mathcal{R} \qquad g(\epsilon)=\begin{cases}\frac{1}{\sqrt{1-\epsilon}}artanh\left(\sqrt{1-\epsilon}\right) & 0<\epsilon<1\\ 1 & \epsilon=1\\ \frac{1}{\sqrt{\epsilon-1}}arctan\left(\sqrt{\epsilon-1}\right) & \epsilon>1\end{cases} \quad (11)$$

This result coincides with /5/.

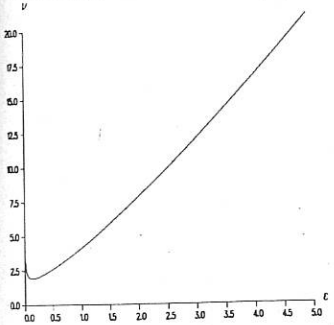

Fig.: Equipartition frequency as function of the anisotropy parameter

The numerical evaluation of (8),(9) is shown in the figure, where ν is plotted as a function of ϵ. A comparision with the corresponding expression obtained without polarisation effects ($DK \equiv 1$), found in /5/, shows that dynamical screening affects the relaxation process by less than 0.3 percent, which has been checked for $20^{-1} \leq \epsilon \leq 5$.

In the opposite limit of an infinite magnetic field ($\omega_0 \ll |\Omega|$, where ω_0 is the LANDAU frequency) we obtain $\nu(\Omega,\epsilon)\longrightarrow\sqrt{\frac{3(1+2\epsilon)}{\pi^3}}\frac{\Lambda^4}{2\Omega^4}$, where $\Lambda:=\frac{4\pi}{3}n\lambda_D^3$. Here we have used a perpendicular cut-off in k - space. This result coincides with the corresponding one of vanishing polarisation/8,9/. Thus it is shown that also in this formal limit *polarisation can be neglected.*

However the generalisation to an arbitrary finite, magnetic field remains an unsolved problem. Its solution would require the numerical solution of (6) which is related to (5) by means of (3). In the later formula f_Ω can be simplified/10/. One gets the expression

$$
\begin{aligned}
& f_\Omega(T_\perp, T_\parallel, \vec{k}, \omega) = \\
& \frac{32}{\Omega^2}\left(1-\frac{T_\parallel}{T_\perp}\right)\left\{\left[ec\left(2\frac{k_B T_\parallel}{m}\frac{k_z^2}{\Omega^2}, 2\frac{k_B T_\perp}{m}\frac{k_\perp^2}{\Omega^2}, 2\frac{\omega}{\Omega}\right)\right]^2 - \right. \\
& 4\frac{k_B T_\parallel}{m}\frac{k_z^2}{\Omega^2}\left[exxc\left(2\frac{k_B T_\parallel}{m}\frac{k_z^2}{\Omega^2}, 2\frac{k_B T_\perp}{m}\frac{k_\perp^2}{\Omega^2}, 2\frac{\omega}{\Omega}\right)\right. \\
& \left.\left. ec\left(2\frac{k_B T_\parallel}{m}\frac{k_z^2}{\Omega^2}, 2\frac{k_B T_\perp}{m}\frac{k_\perp^2}{\Omega^2}, 2\frac{\omega}{\Omega}\right) + \left(exs\left(2\frac{k_B T_\parallel}{m}\frac{k_z^2}{\Omega^2}, 2\frac{k_B T_\perp}{m}\frac{k_\perp^2}{\Omega^2}, 2\frac{\omega}{\Omega}\right)\right)^2\right]\right\} \quad (12)
\end{aligned}
$$

which invokes three new functions

$$
\begin{aligned}
ec(a,b,c) &= \int_0^\infty \exp\left(-at^2 - b\sin^2 t\right)\cos(ct)dt \\
exs(a,b,c) &= \int_0^\infty t\exp\left(-at^2 - b\sin^2 t\right)\sin(ct)dt \\
exxc(a,b,c) &= \int_0^\infty t^2\exp\left(-at^2 - b\sin^2 t\right)\cos(ct)dt
\end{aligned}
$$

Note that these functions are not independent of each other , because it holds

$$
\begin{aligned}
exs(a,b,c) &= -\frac{\partial}{\partial c}ec(a,b,c) \\
exxc(a,b,c) &= -\frac{\partial}{\partial a}ec(a,b,c)
\end{aligned}
$$

/ 1/ A.W.Hyatt, C.F. Driscoll, J.H.Malmberg, Phys.Rev.Lett. 59,2975 (1987)
/ 2/ J.H.Malmberg, Plenary Invited Lecture. this conference, ICPP1992
/ 3/ N.Rostoker,Phys.Fluids,3,922 (1960)
/ 4/ M.H.A.Hassan, C.J.H.Watson, Plasma Phys. 19,237 (1977)
/ 5/ H.Schamel, H.Hamnén, D.F.Düchs, T.E.Stringer, M.R. ÓBrien, Phys.Fluids B1,76 (1989)
/ 6/ F.L.Hinton: Handbook of Plasma Physics I, edited by M.N. Rosenbluth. North Holland Amsterdam 1989
/ 7/ B.D.Fried, S.D.Conte: The Plasma Dispersion Function, Academic Press, New York (1961)
/ 8/ G. Hübner, H.Schamel. Z.Naturforsch. 45a,1 (1990)
/ 9/ H.Schamel, G.Hübner, to be published in Z. Naturforsch. in 1992
/10/ U.Wolf, Diplomarbeit, Universität Bayreuth (1992)

WIEDEMANN-FRANZ LAW FOR MAGNETIZED PLASMAS

E. Hensler
Klinik für Strahlentherapie, Universität Innsbruck
A-6020 Innsbruck, Austria

Introduction

The electrical and the thermal conductivities of a plasma are transport coefficients of major interest in magnetic confinement fusion research. In metals the ratio of the thermal conductivity, κ, to the electrical conductivity, σ, is proportional to the temperature, T, (Wiedemann-Franz law in the form given by Lorenz: see, e.g., [1]). In this paper we investigate the so-called Lorenz number $L = \frac{\kappa}{\sigma T}$ in the case of a two-fluid plasma in a uniform magnetic field, where we have to distinguish the various directional fluxes and the electron and ion contributions. The check of the validity of the Wiedemann-Franz law for a plasma has not received much attention in the literature except in some plasma physics textbooks (see e.g. [2]), which have used simple collision terms. In the present paper we employ the full Fokker-Planck collision term.

Theory

The whole study is restricted to classical transport theory based on moments expansions of the Fokker-Planck collision term (see Balescu, [3], whose notation is used throughout this paper). Following ref. [3] we introduce dimensionless conductivities

$$\sigma_A = \frac{e^2 n_e}{m_e} \tau_e \tilde{\sigma}_A(Z, x_e) \qquad A = \|, \perp, \wedge \tag{1}$$

$$\kappa^e_A = \frac{5}{2} \frac{n_e T_e}{m_e} \tau_e \tilde{\kappa}^e_A(Z, x_e) \tag{2}$$

$$\kappa^i_A = \frac{5}{2} \frac{n_i T_i}{m_i} \tau_i \tilde{\kappa}^i_A(Z, x_i) \tag{3}$$

where τ_e and τ_i are the electron and ion collisional relaxation times, $x_e = \Omega_e \tau_e$, $x_i = \Omega_i \tau_i$, Ω_e and Ω_i denoting the electron and ion gyrofrequencies. The dimensionless conductivities $\tilde{\sigma}_A$, $\tilde{\kappa}^e_A$, $\tilde{\kappa}^i_A$ exhibit only a parametric dependence on the magnetic field, B, and the charge number Z. We define sets of Lorenz numbers for the electrons

$$L^e_A = \frac{\kappa^e_A}{\sigma_A T_e} \tag{4}$$

and for the ions

$$L^i_A = \frac{\kappa^i_A}{\sigma_A T_i} \tag{5}$$

Inserting eqs. (1)-(3) into the definitions (4) and (5) we have

$$L^e_A = \frac{5}{2} \frac{1}{e^2} \frac{\tilde{\kappa}^e_A}{\tilde{\sigma}_A} \tag{6}$$

and

$$L^i_A = \frac{5}{2} \frac{1}{e^2} \frac{m_e}{m_i} \frac{\tau_i}{\tau_e} \frac{n_i}{n_e} \frac{\tilde{\kappa}^i_A}{\tilde{\sigma}_A} \tag{7}$$

with

$$\frac{\tau_i}{\tau_e} = \sqrt{\frac{m_i}{m_e}} \left(\frac{T_i}{T_e} \right)^{\frac{3}{2}} \frac{1}{Z^2} \tag{8}$$

For the electron Lorenz numbers we observe

$$L^e_{\parallel} = L^e_{\parallel}(Z) \tag{9}$$
$$L^e_{\perp} = L^e_{\perp}(Z, x_e) \tag{10}$$
$$L^e_{\wedge} = L^e_{\wedge}(Z, x_e) \tag{11}$$

i.e. the parallel Lorenz number exhibits a parametric dependence on the charge number Z only, but no dependence on the collision frequency at all, whereas the transverse Lorenz numbers depend on Z and on the magnetic field through x_e. For the ion Lorenz numbers we deduce from eq. (7)

$$L^i_{\parallel} = L^i_{\parallel}(Z, \frac{n_i}{n_e}, \frac{T_i}{T_e}) = \frac{1}{Z^2}\frac{n_i}{n_e}\left(\frac{T_i}{T_e}\right)^{\frac{3}{2}} L^{*i}_{\parallel} \tag{12}$$

$$L^i_{\perp} = L^i_{\perp}(Z, \frac{n_i}{n_e}, \frac{T_i}{T_e}, x_i, x_e) = \frac{1}{Z^2}\frac{n_i}{n_e}\left(\frac{T_i}{T_e}\right)^{\frac{3}{2}} L^{*i}_{\perp}(Z, x_i, x_e) \tag{13}$$

$$L^i_{\wedge} = L^i_{\wedge}(Z, \frac{n_i}{n_e}, \frac{T_i}{T_e}, x_i, x_e) = \frac{1}{Z^2}\frac{n_i}{n_e}\left(\frac{T_i}{T_e}\right)^{\frac{3}{2}} L^{*i}_{\wedge}(Z, x_i, x_e) \tag{14}$$

All ion Lorenz numbers contain a factor involving the ion-electron temperature ratio. The parallel coefficient $L^{*i}_{\parallel}$ is a constant, but the transverse coefficients $L^{*i}_{\perp}$ and $L^{*i}_{\wedge}$ depend on Z and on the magnetic field. In contrast to the electron case the Z dependence comes mainly from the electrical conductivities. The above formulae, eqs. (9)-(11) and (12)-(14), are exact in the sense that they do not depend on the number of moments retained in their calculation. Using Balescu's [3] explicit results of the 13-moment expansion of the Fokker-Planck equation we arrive at the following formulae for the Lorenz numbers

$$L^e_{\parallel} = \frac{5}{2}\frac{1}{e^2}\frac{10}{13 + 4\sqrt{2}Z^{-1}} \tag{15}$$

$$L^e_{\perp} = \frac{5}{2}\frac{1}{e^2}\frac{20 + 20\sqrt{2}Z^{-1} + (65 + 20\sqrt{2}Z^{-1})x_e^2}{26 + 34\sqrt{2}Z^{-1} + 16Z^{-2} + 50x_e^2} \tag{16}$$

$$L^e_{\wedge} = \frac{5}{2}\frac{1}{e^2}\frac{190 + 100x_e^2}{259 + 104\sqrt{2}Z^{-1} + 32Z^{-2} + 100x_e^2} \tag{17}$$

$$L^i_{\parallel} = C_i\frac{10 + 10\sqrt{2}Z^{-1}}{13\sqrt{2} + 8Z^{-1}} \tag{18}$$

$$L^i_{\perp} = C_i\frac{5}{8 + 25x_i^2}\frac{16 + 32\sqrt{2}Z^{-1} + 32Z^{-2} + (449 + 104\sqrt{2}Z^{-1} + 32Z^{-2})x_e^2 + 100x_e^4}{13\sqrt{2} + 34Z^{-1} + 8\sqrt{2}Z^{-2} + 25\sqrt{2}x_e^2} \tag{19}$$

$$L^i_{\wedge} = C_i\frac{25x_i}{8 + 25x_i^2}\frac{16 + 32\sqrt{2}Z^{-1} + 32Z^{-2} + (449 + 104\sqrt{2}Z^{-1} + 32Z^{-2})x_e^2 + 100x_e^4}{(259 + 104\sqrt{2}Z^{-1} + 32Z^{-2})x_e + 100x_e^3} \tag{20}$$

with

$$C_i = \frac{5}{2}\frac{1}{e^2}\frac{1}{Z^2}\sqrt{\frac{m_e}{m_i}}\frac{n_i}{n_e}\left(\frac{T_i}{T_e}\right)^{\frac{3}{2}} \tag{21}$$

In the special case of vanishing magnetic field $B=0$ we have $L^e_\parallel = L^e_\perp$ and $L^i_\parallel = L^i_\perp$. In the limit of a very strong magnetic field $x_e \gg 1$, $x_i \gg 1$ the transverse Lorenz numbers take the following form

$$L^e_\perp = \frac{5}{2}\frac{1}{e^2}\frac{13+4\sqrt{2}Z^{-1}}{10} \tag{22}$$

$$L^e_\wedge = \frac{5}{2}\frac{1}{e^2} \tag{23}$$

$$L^i_\perp = \frac{5}{2}\frac{1}{e^2}\frac{4}{5\sqrt{2}}\sqrt{\frac{m_i}{m_e}}\frac{n_i}{n_e}\left(\frac{T_e}{T_i}\right)^{\frac{3}{2}} \tag{24}$$

$$L^i_\wedge = \frac{5}{2}\frac{1}{e^2}\frac{1}{Z}\frac{n_i}{n_e} \tag{25}$$

These limiting values of the transverse Lorenz numbers are exact universal values independent of the level of truncation of the moment expansion. This is a consequence of the universality of the respective transport coefficients in the strong magnetic field limit proven in [3]. A comparison of the Lorenz numbers calculated from the 13- and the 21-moment expansion and from Braginskii's transport coefficients [4] shows that the 13-moment expansion leads to smaller values of the Lorenz numbers due to an underestimation of the thermal conductivities, whereas the 21-moment expansion and Braginskii's method give almost identical results. Kaneko et al. [5] performed an expansion of the kinetic equation up to 50 Laguerre-Sonine polynomials for the transverse fluxes. The Lorenz numbers derived from their transport coefficients are in good agreement with those from the 21-moment expansion.

Conclusions

Wiedemann-Franz laws, i.e. constancy of the corresponding Lorenz numbers, have been found for the parallel electron fluxes, eq. (9), and the parallel ion fluxes, eq. (12). The equations for the transverse Lorenz numbers, eqs. (10), (11), (13) and (14), still contain the collisional relaxation times τ_e and τ_i . Only in the special cases of either vanishing magnetic field or very strong magnetic field, Wiedemann-Franz laws are valid for the transverse fluxes. The Wiedemann-Franz laws for magnetized plasmas constitute useful relations between the respective electrical and thermal conductivities. Within the framework of classical transport theory a generalization of the above calculations to anisotropic temperatures, partially ionized gases and to transport theory based on the Balescu-Lenard equation may be of interest. An extension to neoclassical transport theory may lead to a better understanding of the transport processes in magnetic confinement devices.

References

[1] Kittel, C., Introduction to Solid State Physics, 5th ed., J.Wiley, New York 1976.

[2] Sutton,G.W. and A. Sherman, Engineering Magnetohydrodynamics, McGraw-Hill, New York 1965.

[3] Balescu, R., Transport Processes in Plasmas, Vol.1 Classical Transport Theory, North-Holland, Amsterdam 1988.

[4] Braginskii, S.I., in: Reviews of Plasma Physics Vol.1, ed. M.A. Leontovich (Consultants Bureau, New York 1965), pp.205-311.

[5] Kaneko, S.J. and M. Taguchi, J.Phys.Soc.Jpn. **45**(1978)1380;
Kaneko, S.J. and A. Yamao, J.Phys.Soc.Jpn. **48**(1980)2098.

THE INFLUENCE OF TOROIDICITY, PRESSURE, AND LOCAL PROFILE CHANGES ON TEARING MODE STABILITY

J.W. Connor, S.C. Cowley*, R.J. Hastie and T.J. Martin
AEA Fusion, Culham Laboratory, Abingdon, Oxfordshire, OX14 3DB, UK
(Euratom/UKAEA Fusion Association)
*Princeton Plasma Physics Laboratory N.J. 08544, U.S.A.

Tearing modes appear to play a significant rôle in determining Tokamak behaviour. In high temperature plasmas realistic plasma models for the response at the resonant magnetic surfaces necessitate the use of asymptotic matching methods (the Δ' formulation) in calculations of linear stability and non-linear saturation. These calculations are complicated by toroidal and surface shape effects which cause coupling of different poloidal harmonics in a tearing mode. This leads to coupling of tearing modes centred on different resonant surfaces. However, when diamagnetic effects and sheared equilibrium flows are taken into account theory predicts /1/ that tearing will occur at only one surface (where the mode frequency $\omega_0 \simeq \omega_{*e}(1 + \frac{1}{2}\eta_e)$). At all other surfaces the plasma response is determined by the ideal inertial equations, resulting in a value of $\Delta(\omega) \simeq \omega_A/\omega_* \gg 1$. As a first approximation we treat this as infinite, and calculate the scalar $\Delta'_{m/n}$ associated with one resonant surface at a time. In general $\Delta'_{m/n}$ can be represented as an expansion about the corresponding value in a cylindrical plasma, in the form:

$$\Delta'_{m/n} = \Delta'_{\rm cyl} + \epsilon^2 a + (\beta_0/\epsilon)^2 b + \beta_0 c. \qquad (1)$$

with $\epsilon = a/R$ and $\beta_0 = 2p_0/B_0^2$ the central value of beta. Table 1 shows the dependence of $\Delta'_{\rm cyl}, a, b$, and c for the $m = 3.n = 2$ mode, obtained using the T3 stability code /2/. The equilibrium pressure profile is $p = p_0(1 - r^2/a^2)^2$, while the $q(r)$ profile is $q = q_0\left[1 + \lambda(\frac{r}{a})^{2\nu}\right]^{\frac{1}{\nu}}$ and the values $\nu = 1, 2$ and 4 correspond to the 'peaked', 'rounded' and 'flattened' profiles of Furth Rutherford and Selberg /3/.

However, when $q_0 < 1$ and coupling to the $m = 1$ harmonic is involved a much stronger effect appears due to the marginally stable nature of this harmonic. The effect is contained in the dispersion relation for $m = 2$, and $m = 1$ tearing modes obtained by Bussac et al /4/ and later by Connor et al /5/ in the form

$$\left(\frac{1}{\Delta'_{1/1}(\omega)} - \frac{\epsilon_1^2 \delta W_T}{s_1^2}\right)\left(\Delta'_{2/1}(\omega) - \Delta'^{(0)}_{2/1}\right) + \epsilon_1^2 \frac{\delta W_{12}^2}{s_1^2} = 0 \qquad (2)$$

With ideal inertial behaviour at $q = 1$ and assuming $\omega_0/\omega_A < \frac{\epsilon_1^2 \delta W_T}{s_1}$, where $\epsilon_1 = r_1/R_0, s_1 = r_1 q'(r_1)$, the effective Δ' for tearing at $q = 2$ is

$$\Delta'_{2/1} = \Delta'^{(0)}_{2/1} + \delta W_{12}^2/\delta W_T \qquad (3)$$

where $\Delta'^{(0)}_{2/1}$ has a regular expansion in ϵ and β_0 of the form (1) due to coupling of $m = 2$ to its upper, $m = 3$, sideband. However the additional toroidal term in (3) is *not*

small in ϵ or β_0. Expressions for the coupling integral δW_{12} and the ideal kink energy δW_T appear in refs (4) and (5). Table 2 records the values of $\Delta'^{(0)}_{2/1}$ and $\delta W^2_{12}/\delta W_T$ for parabolic $p(r), \epsilon = 0.1, q_0 = 0.75, q_a = 3.2$ and the same $q(r)$ profiles as in Table 1.

TABLE 1							TABLE 2			
q_o	q_a	ν	$\Delta'_{\rm cyl}$	$a/10$	$b/10$	$c/10$	ν	β_0	$\Delta'^{(0)}_{2/1}$	$\delta W^2_{12}/\delta W_T$
0.75	3.2	1	-5.10	-1.3	+15.2	-5.3	1	0.0	-1.38	0.80
0.75	3.2	2	-4.40	-1.6	+8.1	-3.1	1	0.001	-1.37	1.95
0.75	3.2	4	-5.30	-1.4	+6.8	-2.5	1	0.002	-1.33	4.60
0.75	5.2	1	-6.80	-0.96	+18.8	-4.8	2	0.0	-3.05	3.42
0.75	5.2	2	-5.20	-1.3	+14.0	-2.8	2	0.001	-3.04	8.09
0.75	5.2	4	-5.90	-1.2	+15.2	-2.2	2	0.002	-3.01	27.50
1.2	5.2	1	+0.49	-1.6	+41.5	+1.7	4	0.0	-5.05	7.51
1.2	5.2	2	+10.40	-2.2	+42.6	+2.9	4	0.001	-5.03	20.29
1.2	5.2	4	+24.30	-3.1	+39.4	-1.7	4	0.0018	-5.01	127.60

Elliptic (and triangular or higher order) shaping is responsible for analogous effects for $m \gtrsim 3$ modes. Thus, for example,

$$\Delta'_{3/1} = \Delta'^{(0)}_{3/1} + \delta W^2_{13}/\delta W_T \tag{4}$$

where

$$\delta W_{13} = \frac{1}{2}\frac{\psi_3(r_1)}{\psi_3(r_3)}\left[\frac{E'(r_1)}{\epsilon_1} - \frac{E(r_1)}{r_1\epsilon_1}\right]\left[4 + b^{(3)}\right] \tag{5}$$

with $E(r)/r = (\kappa - 1)/(\kappa + 1)(\kappa =$ elongation), ψ_3 the helical flux function for the $m = 3$ cylindrical tearing mode, $b^{(3)} = \frac{r_1}{\xi_3}\frac{d\xi_3(r_1)}{dr}(\xi_3 =$ radial displacement) and δW_T the ideal kink energy, modified to take account of shaping. Although strong elongation is frequently encountered in Tokamak plasmas, the factor $(E' - E/r)$ is typically rather small (it vanishes for an equilibrium with flat current) so that ellipticity induced coupling to $m = 1$ is less effective than toroidicity induced coupling.

Equations (3) and (4) imply that the stability of the $m = 2, n = 1$ and $m = 3, n = 1$ tearing modes cannot be calculated from cylindrical theory, even in the limit of large aspect ratio. These tearing modes are significantly more unstable in this limit than cylindrical theory would predict. However, although we have assumed $q_0 < 1$, no account has been taken of perturbations to the $q(r)$ profile which sawtoothing might generate [and which are necessary if quiescence of the $m = 1$ mode during sawtooth ramp periods is to be attributed to negative values of $\Delta'_{1/1}$ /6/].

We have calculated the effect, in a general toroidal equilibrium, of an arbitrary localised current perturbation. Defining Δ'_∞ to be the value of $\Delta'_{m/n}$ as calculated outside the zone of influence of the current perturbation and Δ'_0 to be the corresponding value at

the surface $q(r_{mn}) = m/n$ we have obtained the relation:

$$\Delta'_0 = \frac{s_0^2}{s_\infty^2}\Delta'_\infty + \mathcal{P}\frac{1}{\delta}\int_{-\infty}^{\infty} dx \left[\frac{s_0^2 q^2}{\Delta q(x)^2} - \frac{1}{x^2}\right] \tag{6}$$

with s_0 and s_∞ being the values of the shear, $s = rq'/q$, close to r_{mn} and far from it (i.e beyond the range of the localised perturbation), $\delta(\Delta q) = q(r) - m/n$ and $x = \left(\frac{r-r_{mn}}{\delta}\right)$. This formula is a generalisation of earlier ones /7,8/ to the case of perturbations which are strong enough to modify the q profile, and therefore the shear, locally. Applied to the $m = 2, n = 1$ mode it predicts modifications to $\Delta'^{cyl}_{2/1}$ similar to those found earlier /7,8/ However, at $q = 1$, it predicts that $m = 1$ stabilisation is possible. Taking, for example, $\Delta q(x) = x\left[\frac{s_0^2 + s_\infty^2 x^2}{1+x^2}\right]^{\frac{1}{2}}$ and $\Delta'_\infty = \frac{s_{\infty}^2}{\epsilon_1^2 \delta W_T}$ (eqn. (2)), equation (6) takes the form

$$\Delta'_0 = \frac{s_0^2}{\epsilon_1^2 \delta W_T} + \frac{\pi}{\delta}\left(\frac{s_0}{s_\infty} - \frac{s_\infty}{s_0}\right) \tag{7}$$

and the $m = 1$ tearing mode is stabilised for

$$s_0 < \left[\frac{\pi}{\delta} s_\infty \epsilon_1^2 \delta W_T\right]^{1/3}. \tag{8}$$

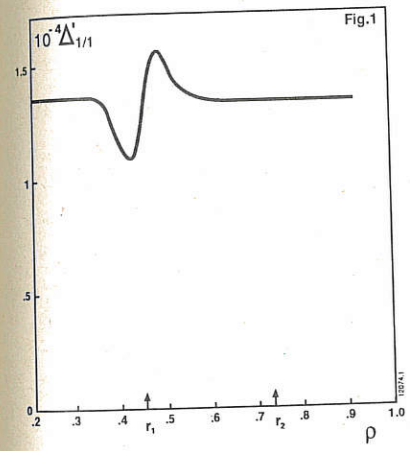

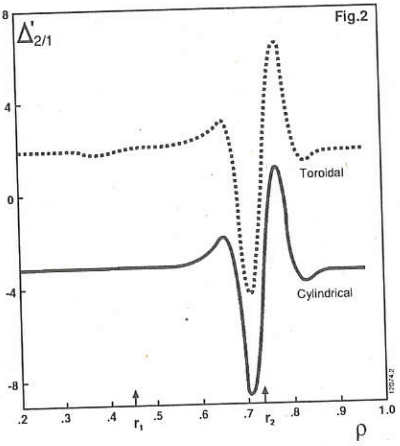

Direct computation (again using the T3 code) of $\Delta'_{1/1}$ and $\Delta'_{2/1}$ with a $q(r)$ profile of the form

$$q(r) = q_0(1 + \lambda \left(\frac{r}{a}\right)^{2\nu})^{\frac{1}{\nu}} + \Delta \left(\frac{r}{\rho}\right)^2 \exp\left[-\left(\frac{r-\rho}{\delta}\right)^2\right] \quad (9)$$

gives similar results. These are shown in Figs. 1 and 2 for $\Delta = 10^{-2}, (\delta/a)^2, = 2 \times 10^{-3}, q_0 = 0.7$, $\lambda = 25$, $\nu = 2$, $\epsilon = 0.1$, and the current location ρ varying. In Fig.1 $\Delta'_{1/1}$ shows behaviour similar to that predicted by eq.(6), but a value of $\Delta \simeq 9 \times 10^{-2}$ is necessary to obtain $\Delta'_{1/1} < 0$. In Fig.2 the values of $\Delta'_{2/1}$ (toroidal and cylindrical) are shown as ρ is varied. The toroidal value is slightly modified when the current perturbation is close to the $q = 1$ surface, and this effect becomes more pronounced at larger values of the perturbation amplitude Δ.

Conclusions

When $q_0 > 1$ (or for tearing modes with $n \gtrsim 2$) toroidal coupling increases the stability of tearing modes, while pressure driven coupling destabilises them. When $q_0 < 1$ the $m = 2, n = 1$ tearing mode is essentially toroidal in character due to its coupling to the $m = 1$ harmonic in the core. This effect renders it more unstable than in a cylindrical approximation. However due to this coupling its stability is now affected by current perturbations close to $q = 1$, in addition to the well known sensitivity to such perturbations located at the $q = 2$ surface. The rôle of sawtoothing in generating and maintaining a particular current structure around $q = 1$ must therefore be considered before the stability of the $m = 2$ tearing mode can be understood.

References

/1/ S.C. Cowley and R.J. Hastie, Phys. Fluids 31, 426 (1988)

/2/ T J Martin, J W Connor and R J Hastie, Computer Codes for Toroidal Tearing Mode Calculations, Culham Report AEA FUS 91.

/3/ H.P. Furth, P.H. Rutherford and H. Selberg, Phys. Fluids **16** 1054 (1973). .

/4/ M.N. Bussac, D. Edery, R. Pellat, J. Soulé, in Plasma Physics and Controlled Nuclear Fusion Research 1976; Proc 6th Int Conf, Berchtesgaden (IAEA, Vienna, 1977), Vol 1, p607 .

/5/ J.W. Connor et al. Phys. Fluids, 31, 577 (1988).

/6/ C.G. Gimblett et al 18th European Conf on Controlled Fusion and Plasma Physics, Vol 2, 21, Berlin 1991.

/7/ L.E. Zakharov and A.A. Subbotin, "Tearing-Mode stabilisation by generation of an additional current layer in Tokamaks", ITER-IL-Ph11-9-S-2 (1989).

/8/ E. Westerhof, Nuclear Fusion, **30**, 1143 (1990).

LINEAR AND NON-LINEAR MODELLING OF ISLAND CONTROL IN TOKAMAKS

B.M.S. Hansen*†, M.A. Hellberg*, D. Sherwell°‡, D.E. Roberts°, W.S. McLoud°
*Plasma Physics Research Institute, University of Natal, Durban, South Africa
°Fusion Studies Group, Atomic Energy Corporation, Pretoria, South Africa
†Now at Theoretical Astrophysics, California Institute of Technology, Pasadena, CA 91125, USA
‡Now at Applied Mathematics, University of Witwatersrand, Johannesburg, South Africa

1 Introduction

On a number of tokamaks (e.g. Text, Tore Supra, Tokoloshe, Tosca) auxiliary coils have been fitted which generate either ergodic field-structures at the plasma edge or relatively clean low-order Fourier modes which are resonant with the main helical tokamak field somewhere within the plasma. In this paper we present linear and non-linear calculations of magnetic islands and the control of islands in a tokamak with resonant helical fields. Some of the calculations are general, while others are associated particularly with Tokoloshe, which has R = 54cm, r_L = 24cm, I_p = 120 kA, B = 9 kG and is fitted with resonant $\ell = 1, 2, 3$ coils.

2 Newcomb equation

We assume a cylindrical model with circular cross-section equilibrium. Truncating the perturbation of the magnetic field and currents yields the Newcomb equation [1, 2, 3],

$$\Psi'' + A(r)\Psi = 0, \tag{1}$$

where

$$\Psi(r) = \frac{r^{3/2}B_{1r}}{(m^2 + k^2r^2)^{1/2}}. \tag{2}$$

The term A(r) has an integrable singularity at r=r_s, where $F(r) = \frac{mJ_{0\theta}+krJ_{0z}}{mB_{0\theta}+krB_{0z}}$ has a zero. To integrate through the singularity we follow the Laurent expansion method of Robinson and Ellis [2, 3]. However, we note that the region in which the expansion is used has to be very narrow in order to restrict the truncation error [4], a consideration not discussed by Ellis [2].

The integration procedure is thus as follows: The equation is integrated out from r=0 to r=r_s. Two integrations are then performed from r_s to r=r_L, corresponding to two different $\Delta'(0)$ matchings across the singularity at r=r_s [5]. This yields two particular solutions which allows us to specify the general solution in the form

$$B_{1r}(r) = C_1\left(B_I(r) + \alpha B_{II}(r)\right), \tag{3}$$

where the constants C_1 and α are determined by the boundary conditions and the subscripts denote the two different particular solutions.

3 Linear Solution

The above constants are determined by matching the poloidal and radial fields at the limiter radius (r_L) and coil radius (r_c). Both the field between the limiter and the coil, and that beyond the coil are assumed to be vacuum fields. We make use of the results of Hahm & Kulsrud [6], which show that a linear perturbation induced by resonant, non-homogeneous boundary conditions will evolve towards the marginally stable perturbation ($\Delta'(0) = 0$). This

will determine the constant α in (3). Once the coil current is specified, the other constants are determined from the boundary conditions. Using the marginally stable solution as $B_I(r)$, we may gauge the plasma response by comparing these results with those from the vacuum field approximation (i.e. ignoring the presence of the plasma), through the ratio

$$\frac{B_{1r}(r)}{B_{vac}(r)} = R_2 I_m(kr_L) \frac{\left[1 - \frac{K_m(kr_L) I'_m(kr_L)}{I_m(kr_L) K'_m(kr_L)}\right]}{\left[1 - \frac{K_m(kr_L)}{K'_m(kr_L)} R_2\right]} \frac{R_1(r)}{I'_m(kr)}, \tag{4}$$

with

$$R_1(r) = \frac{B_I(r)}{B_I(r_L)}; \qquad R_2 = \frac{(m^2 + k^2 r_L^2)}{kr_L} \frac{B_I(r_L)}{B_I(r_L) + r_L B'_I(r_L)}. \tag{5}$$

If the field is zero at any point inside the coil radius, then $\Delta'(0) > 0$ and hence the tearing mode is unstable. Thus, in addition to indicating the degree to which the plasma response enhances island size, (4) can be used to provide a condition for stability. Ignoring the coil, Ellis [2] used as stability criterion $B_{1r}(r_s)/B_{vac}(r_s) > 0$. We now generalize that by including the effect of a finite difference between plasma response and vacuum fields at the coil radius, yielding

$$\left(\frac{B_{1r}(r_s)}{B_{vac}(r_s)}\right)\left(\frac{B_{1r}(r_c)}{B_{vac}(r_c)}\right) > 0. \tag{6}$$

This correction is particularly significant for a machine for which the coil radius does not differ much from the limiter radius, such as Tokoloshe (r_L= 24 cm, r_c= 28 cm). See Figure 1.

4 Non-Linear Solution

To determine the island evolution we use the Rutherford equation

$$\frac{dW}{dt} = \frac{\pi}{2} \frac{\Delta'(W)}{\tau_r}, \tag{7}$$

where

$$W = 4r_s \left| \frac{B_{1r}(r_s)}{mB_{0\theta}(r_s)} \frac{q(r_s)}{r_s q'(r_s)} \right|^{1/2}, \tag{8}$$

$$\Delta'(W) = \frac{B'_{1r}(r_s + W/2) - B'_{1r}(r_s - W/2)}{B_{1r}(r_s)}. \tag{9}$$

The effect of plasma rotation on stability is also simulated by regarding the rotation as that of a solid body and using the bulk equation,

$$MR\frac{d^2\phi}{dt^2} = F_z, \tag{10}$$

where ϕ is the toroidal phase, M the total plasma mass, R the major radius, and F_z the bulk integrated $(\mathbf{J} \times \mathbf{B})_z$ force arising from the perturbed fields and currents. From (7) we have the following condition for island saturation:

$$\Delta'_I(W) + \Re e(\alpha)\Delta'_{II}(W) = 0, \tag{11}$$

where the subscripts refer to the contribution from each particular solution in (3).

4.1 Locked Modes

Island locking occurs for rotation frequency $\omega = 0$. In this limit, the boundary conditions yield

$$\Re e(\alpha) = \alpha_0 \pm \frac{I_c}{W^2}\alpha_\ell, \tag{12}$$

where α_0 and α_ℓ are constants dependent on the system parameters and where the sign is determined by whether the island locks in phase (ϕ=0) or anti-phase ($\phi = \pi$) with the coil respectively. (These are the only two phases allowed by the form of F_z obtained from (1)). Thus it is possible to determine the coil current required to produce a saturated, locked island of width W,

$$I_c = \mp\frac{W^2}{\alpha_\ell}\left(\frac{\Delta'_I(W)}{\Delta'_{II}(W)} + \alpha_0\right). \tag{13}$$

5 Results

Figure 2 shows the effect of varying q(0) and $q(r_L)$ in the linear approximation. The equilibria are classified according to their values of R_1 and R_2 [4]. Those equilibria numbered 1 and 4 are stable for all types of outer wall (i.e. ranging from superconducting to no wall at all), those numbered 2 and 5 are unstable for all walls. Type 3 consists of equilibria which are stable for a superconducting wall, but become unstable for finite wall resistivity. Although the transition from stability to instability is dependent primarily on q(0) as found by other authors [2, 3], the transition is not as sharp as reported previously [2]. For $0.6 \leq q(0) \leq 0.75$, there exist equilibria with similar q values but different stability properties. This may offer an explanation for why it has proven difficult to model Tokoloshe's 'Low MHD' operating regime ($0.7 \leq q(0) \leq 0.9, 3 \leq q(r_L) \leq 4$), since this regime falls in the transition region and hence different types of equilibria are possible for very similar boundary conditions.

Figure 3 shows the current required to produce a stationary, locked mode with mode numbers m=2, n=1. The behaviour shown here is in good qualitative agreement with experimental results on the Tokoloshe tokamak [7], where the (2,1) island has been found to be insensitive to the boundary conditions. Figure 3 is for a (3,1) perturbation and shows the solid curve $-\Delta'_I(W)/\Delta'_{II}(W)$. The dashed lines are the values of α_r (I_c=0) for the case of a superconducting wall (corresponding to a rapidly rotating plasma - lower line) and for the case of no wall (corresponding to a stationary mode - upper line). Where the solid curve intersects a dashed line, condition (11) is satisfied, and we have a saturated island. It can be seen that a rotating plasma will saturate the island, while a stationary, locked plasma will contain (3,1) islands that grow until they intersect the limiter, even for zero coil current. This is also in good qualitative agreement with experimental observations of the minor disruption in Tokoloshe [7].

References

[1] W.A.Newcomb, *Ann.Phys.*, **3**, 347 (1958)

[2] J.J.Ellis, *D.Phil thesis*, Oxford University, U.K. (1985)

[3] D.C.Robinson, *Nuc. Fus.*, **18**, 939 (1978)

[4] B.M.S.Hansen, *MSc thesis*, University of Natal, Durban, South Africa (1992)

[5] H.P.Furth, J.Killeen & M.N.Rosenbluth, *Phys. Fluids*, **6**, 459 (1963)

[6] T.S.Hahm & R.M.Kulsrud, *Report PPPL-2161*,(1984); *Phys. Fluids*, **28**, 2412 (1985)

[7] D.E. Roberts, J.D. Fletcher, G. Nothnagel, D. Sherwell, J.A.M. de Villiers & W.S. McLoud, *Phys. Rev. Lett.*, **66**, 2875 (1991)

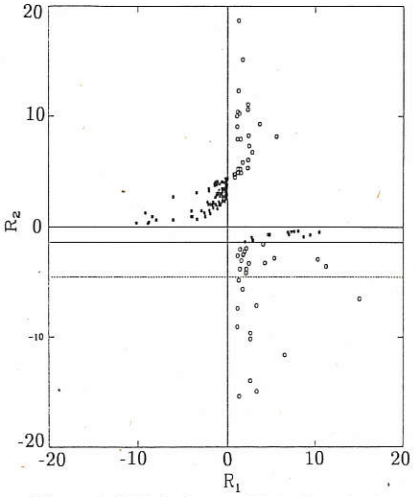

Figure 1: Tokoloshe equilibria found to be stable (o) or unstable(*) from a Δ' calculation are separated by transitions in the R_1-R_2 plane. The dashed line is the Ellis criterion.

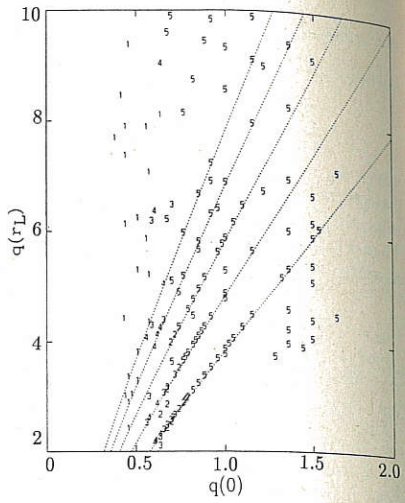

Figure 2: Classification of equilibria in q(0)-q(r_L) plane. Dashed lines represent different current density profiles, the amount of peaking increasing from the lowest to the highest line.

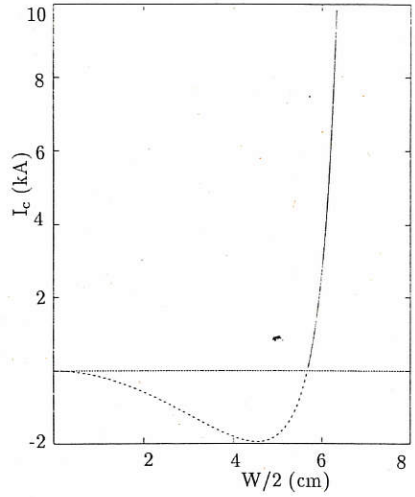

Figure 3: Current required to produce a stationary, locked (2,1) mode. The solid line indicates a stable equilibrium, the dashed part of the curve an equilibrium unstable to toroidal rotation.

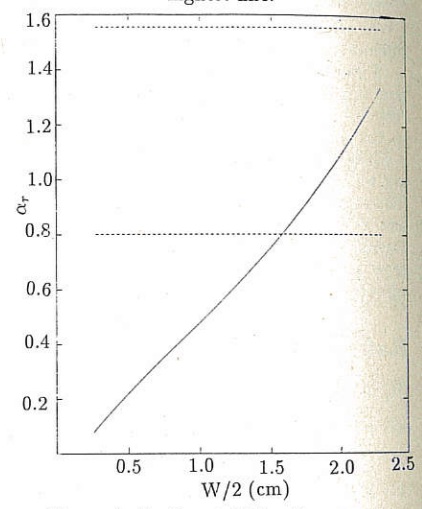

Figure 4: Similar stability diagram for a (3,1) mode. The upper line represents the no wall boundary condition, the lower line the superconducting wall boundary condition.

RESISTIVE WALL INSTABILITIES FOR AXISYMMETRIC SYSTEMS

G. Berge, Department of Applied Mathematics, University of Bergen, Norway
J.P. Freidberg, P.F.C. Massachusetts Institute of Technology, Cambridge, USA

1 Introduction

Within the framework of MHD we study a confined plasma surrounded by a vacuum region and bounded by a resistive wall. We restrict ourselves to axisymmetric systems.

To be more specific, we are interested here in the case where the configuration is stable in the presence of an infinitely conducting wall, but unstable without the wall. For physical reasons an infinitely conducting wall cannot be made. It is therefore of interest to study the effect of a resistive wall.

The results depend upon knowledge of the solution for the stability problem in the two limiting cases which we refer to as

Problem 1. The wall and the conductors in the vacuum region are not taken into account (wall and conductors at infinity).

Problem 2. The wall and the conductors in the vacuum region are taken into account as infinitely conducting elements in the proximity of the plasma.

2 A Variational Principle. The Lagrangian

We can show that a proper Lagrangian $\mathcal{L}$ for the resistive wall problem is given by

$$\mathcal{L} = \delta W_F + \delta W_i + \delta W_o + \delta W_W \,, \tag{1}$$

where: For the fluid-region

$$\delta W_F = \frac{1}{2}\int_{V_p} dV\{\frac{\mathbf{Q}^2}{\mu_0} + \gamma p(\nabla\cdot\boldsymbol{\xi})^2 - \boldsymbol{\xi}\cdot\mathbf{J}\times\mathbf{Q} + \boldsymbol{\xi}\cdot\nabla p\nabla\cdot\boldsymbol{\xi}\}dS \,, \tag{2}$$

for the inner vacuum-region, with $\nabla^2\phi_i = 0$.

$$\delta W_i \overset{def}{=} \frac{1}{2\mu_0}\int_{V_i} |\nabla\phi_i|^2 dS = \frac{1}{2\mu_0}\int_{V_i} \nabla\cdot(\phi_i\nabla\phi_i)dS \,,$$

for the outer vacuum-region, with $\nabla^2\phi_o = 0$.

$$\delta W_V^{(o)} = \frac{1}{2\mu_0}\int_{V_o} |\nabla\phi_o|^2 dS = -\frac{1}{2\mu_0}\int_{S_{wo}} \phi_o \mathbf{n}\cdot\nabla\phi_o dS \,, \tag{3}$$

and for the resistive wall region

$$\delta W_W \overset{def}{=} \frac{\sigma\gamma d}{2}\int_{S_w} |\mathbf{n}\times\mathbf{A}_{w0}|^2 dS \,.$$

Notice that in the last integration over S_w, no distinction needs to be made between inner and outer wall surfaces, since only surface quantities are involved (the "thin wall" approximation).

The governing equations of motion for the resistive wall instability may now be recovered variationally from the Lagrangian presented in eq. (1)

3 Trial Functions and Solutions

We shall now discuss functions that we shall use as a base for our trial functions. As mentioned in the introduction, we consider two associated problems :

Problem 1: There is no conducting wall present. The corresponding solutions are given by $\boldsymbol{\xi}_\infty$ and ϕ_∞.

Problem 2: The wall is infinitely conducting and makes a closed surface in the vacuum region. The corresponding solutions are given by $\boldsymbol{\xi}_b$ and ϕ_b.

Assumption: We shall assume that the two solutions $\boldsymbol{\xi}_\infty$ and $\boldsymbol{\xi}_b$ coincide in the plasma-region.

We then make the following expansion, let

$$\phi_i = c_1\phi_\infty + c_2\phi_b\,, \tag{4}$$
$$\phi_o = c_3\phi_\infty\,, \tag{5}$$

with the boundary conditions

$$\phi_\infty(\infty) = 0 \qquad \text{and} \qquad \mathbf{n}\cdot\nabla\phi_b|_{S_b} = 0\,, \tag{6}$$

and let both solutions satisfy the same boundary condition at the plasma vacuum interface ($\boldsymbol{\xi}_\infty = \boldsymbol{\xi}_b$), according to the assumption above. We shall use our Lagrangian as given in eq.(1)

$$\mathcal{L} = \delta W_F + \delta W_i + \delta W_o + \delta W_W\,. \tag{7}$$

Performing the calculation (determining an extremum), we obtain the following result, which we write in correspondence with the notations used by Haney and Freidberg /1/,

$$\bar{\gamma}\tau_D = -\frac{\delta W_\infty}{\delta W_b}\,, \tag{8}$$

with

$$\tau_D = \mu_0\sigma d\bar{b}\,, \tag{9}$$

and

$$\bar{b} = \frac{\frac{1}{2\mu_0}\int_{S_b} |\mathbf{n} \times \hat{\mathbf{A}}_{w0}|^2 dS}{\delta W_b - \delta W_\infty}, \tag{10}$$

where δW_∞ and δW_b are related to δW as defined by the Energy Principle for the two problems, 1 and 2.

One of the boundary conditions for the variational problem is a natural boundary condition. Therefore it does not have to be satisfied by the variation of the solution. This boundary condition normally is satisfied only by the exact solution, which in general is unknown. However, the error made by assuming this condition satisfied also by the variation must be small of first order. By making the assumption that the variations satisfy this boundary condition we can derive a less accurate formula that may be simpler in practical use for the purpose of evaluating $\bar{b}$,

$$\bar{b} = \frac{\frac{1}{2\mu_0}\int_{S_b} |\mathbf{n} \times \hat{\mathbf{A}}_{w0}|^2 dS}{\delta W_b - \delta W_\infty} \cong \frac{\delta W_b - \delta W_\infty}{\frac{1}{2\mu_0}\int_{S_b} |\nabla_s \phi_b|^2 dS}. \tag{11}$$

where the last step in the formula above rests on the assumptions made above. The last expression for $\bar{b}$ in eq.(11) has the virtue of being independent of $\mathbf{A}_{w0}$, it depends only on the solutions of Problem 1 and Problem 2 and the geometry of the conducting surface.

4 The Screw Pinch with Resistive Wall

According to J.P. Freidberg: Ideal Magnetohydrodynamics, /2/ (eq.(9.105)), we have

$$\gamma\tau_d = \frac{k^2b^2 + m^2}{k^2b^2 K_b' I_b' \{1 - (I_a' K_b' / I_b' K_a')\}} \frac{\delta W_\infty}{\delta W_b}, \tag{12}$$

where $\tau_d = \mu_0 \sigma d b$.

4.1 The Basic Formula

We shall first test our basic formula eq.(8). We obtain

$$\frac{\gamma}{\bar{\gamma}} = -\frac{\bar{b}}{b} \frac{k^2b^2 + m^2}{k^2b^2 K_b' I_b' \{1 - (I_a' K_b' / I_b' K_a')\}}. \tag{13}$$

We then proceed by computing $\bar{b}$. According to the formula given in eq.(10) we obtain after some algebra

$$\frac{\bar{b}}{b} = -\frac{k^2b^2}{m^2 + k^2b^2} I_b' K_b' \{1 - \frac{I_a' K_b'}{I_b' K_a'}\}. \tag{14}$$

From eq.(13) we then obtain the desired result

$$\bar{\gamma} = \gamma, \tag{15}$$

which proves that our variational formulation gives exactly the same result as obtained by standard methods.

4.2 Alternative Formula

We shall now derive the growth rate using the alternative formula given by eq.(11), from which we have

$$\frac{\bar{b}}{b} = \frac{\delta W_b - \delta W_\infty}{b\frac{1}{2\mu_0}\int_{S_b} |\nabla_s \phi_b|^2 dS} .$$

Using eq.(9.37) in /2/ we find after some algebra

$$\frac{\bar{b}}{b} = -\frac{k^2 b^2}{m^2 + k^2 b^2} I_b' K_b' \{1 - \frac{I_a' K_b'}{I_b' K_a'}\} . \tag{16}$$

This is exactly the same result as obtained in eq.(14). We then conclude that the two formulas given in eqs.(10) and (11) give exactly the same result for the case considered.

5 Key Problems

We emphasise that the present formulation relies on the solution of two classes of key problems, formulated in the introduction as Problem 1 and Problem 2. By solving these problems we obtain the information about δW_∞ and δW_b. Problem 1 has been discussed at great detail over the last 30 years or so. Problem 2 has been given less interest. This is also a much more complicated problem. It turns out, however, to be tractable in quite general terms by making extensive use of Green's function techniques.

6 Discussion

From the results obtained in Sec. 4.1 and Sec. 4.2, we notice that two apparently completely different formulas give exactly the same result. This could have the following explanation. If the base functions used for our variational problem is complete, then this result would be expected. Whether this could also be true for more general geometrises is an open question. The more general problem of incorporating an arbitrary number of resistive conductors has also been studied. Although elaborate mathematical procedures are requiered, the results turn out to be formally simple generalisations of the results presented here. A detailed account will be available /3/.

REFERENCES

/1/ S. W. Haney and J. P. Freidberg, Variational Methods for Studying Tokamak Stability in the Presence of a Thin Resistive Wall, Phys. Fluids B **1**, 1637 (1989).
/2/ J. P. Freidberg, Ideal Magnetohydrodynamics, Plenum Press 1987.
/3/ G. Berge and J.P. Freidberg. Report in print at P.F.C. Massachusetts Institute of Technology, Cambridge, USA.

STABILITY OF FORCE-FREE AXISYMMETRIC SPHERICAL PLASMA WITH FLOW

Hisaya SUGIMOTO, Hisao ASHIDA and †Takasi KURASAWA
Electrotechnical Laboratory, 1-1-4 Umezono, Tsukuba, Ibaraki 305, JAPAN
†Department of Physics, Tokyo Institute of Technology,
Ōokayama, Meguro, Tokyo 152, JAPAN

A stationary equilibrium of force-free spheromak-like plasma with a plasma flow inside and a mass flow outside is obtained. The plasma translates in a neutral gas along the axisymmetric axis with a constant velocity, when the outside mass fluid is at rest. Its stability is discussed for internal modes and free boundary modes as Rosenbluth and Bussac did for the spheromak/1/ and Sudan for the cusp-shaped plasma with plasma flow/2/. Further we use the sufficient stability condition of plasmas with flow derived by Frieman and Rotenberg/3/. Moreover we refer to the paper by Finn and Antonsen/4/ in which the comparison of the stability conditions between the use of δW for the ideal MHD state and $\delta^2 E^*$ for the Taylor state/5/ is described.

STATIONARY SOLUTION

The equations used are those of the usual ideal MHD

$$\rho\left(\frac{\partial \mathbf{v}}{\partial t} + \Omega\times\mathbf{v}\right) = -\nabla\left(p+\frac{1}{2}\rho v^2\right) + \mathbf{j}\times\mathbf{B}, \quad (\Omega = \mathrm{rot}\,\mathbf{v}),$$

$$\frac{\partial \mathbf{B}}{\partial t} = -\,\mathrm{rot}\,\mathbf{E}, \quad \mathbf{E} + \mathbf{v}\times\mathbf{B} = 0, \qquad (1)$$

where ρ= constant and $\mathbf{j}=0$, $\Omega=0$, outside the plasma. The constants of motion of eq.(1) are

$$E=\frac{1}{2}\int (\rho v^2 + B^2)\,dV, \quad K=\frac{1}{2}\int \mathbf{A}\cdot\mathbf{B}\,dV, \quad H=\int \mathbf{v}\cdot\mathbf{B}\,dV. \qquad (2)$$

We get a stationary equilibrium by minimizing E with K and H fixed i.e. with $\delta E^*=0$, and a stability condition with $\delta^2 E^*>0$, where $E^*=E-\kappa K-\mu H$, κ and μ are Lagrange multipliers for K and H, respectively. $\delta E^*=0$ yields $\mathrm{rot}\,\mathbf{B}=\lambda\mathbf{B}$, $\mathrm{rot}\,\mathbf{v}=\lambda\mathbf{v}$, $\rho\mathbf{v}=\mu\mathbf{B}$, where $\mathbf{j}\times\mathbf{B}=0$, $\Omega\times\mathbf{v}=0$, (force-free field) and $\lambda=\kappa/(1-\mu^2/\rho)$. In terms of stream functions Ψ for $\mathbf{B}$ and Φ for $\mathbf{v}$, the stationary equilibrium equations can be reduced to

$$\nabla^{*2}\Psi=-\lambda^2\Psi, \quad B_\varphi=\lambda\Psi, \quad \nabla^{*2}\Phi=-\lambda^2\Phi, \quad v_\varphi=\lambda\Phi, \quad \Phi=C_A\,\Psi, \qquad (3)$$

where $\nabla^{*2}=\frac{1}{r^2}\frac{\partial}{\partial r}\left(r^2\frac{\partial}{\partial r}\right)+\frac{1}{r^2\sin\theta}\frac{\partial}{\partial\theta}\left(\sin\theta\frac{\partial}{\partial\theta}\right)-\frac{1}{r^2\sin^2\theta}$.

We can easily get a stationary solution:

$$\Psi^{in}=\frac{1}{\lambda}j_1(\lambda r)\sin\theta, \quad \Psi^{out}=\frac{1}{2}B_0 r\left(1-\frac{a^3}{r^3}\right)\sin\theta, \quad \Phi=C_A\,\Psi,$$

$$p+\frac{1}{2}\rho v^2=const.\ \text{along the stream line}, \qquad (4)$$

where $B_0=\frac{2}{3}\frac{\sin\lambda a}{\lambda a}$ (a: the plasma radius), $C_A=\frac{\mathbf{v}}{\mathbf{B}/\sqrt{\rho}}=\frac{\mu}{\sqrt{\rho}}$, $U_0=\frac{\mu}{\rho}B_0$,

$j_n(\lambda r)$: spherical Bessel function, λa: the first zero of j_1.

$\mathbf{B}$ is given from

$$B_r=\frac{1}{r\sin\theta}\frac{\partial}{\partial\theta}(\sin\theta\Psi), \quad B_\theta=-\frac{1}{r}\frac{\partial}{\partial r}(r\Psi), \quad B_\varphi=\lambda\Psi,$$

and **v** can be obtained with replacing Ψ by Φ. Hereafter we use $\mathbf{B}_0$ and V_0 for stationary field quantity.

The characteristic feature of this stationary solution is that **B** and **v** everywhere are parallel with each other and that they make force-free field. In the stationary state E, K and H relate each other:

$$E=\frac{1}{2}\frac{1+C_A^2}{C_A}\sqrt{\rho}H=(1+C_A^2)\lambda K,$$

$$K=\frac{1}{2\lambda}\int B^2dV=const.,\quad H=\frac{\mu}{\rho}\int B^2dV=const.,\quad \lambda\mu=\frac{\rho}{2}\frac{H}{K}=const.. \tag{5}$$

As $C_A=\mu/\sqrt{\rho}$ approaches unity, E tends to minimum: $E_{min}=\sqrt{\rho}H$.

In **Fig.1** contours of $\Psi=const.$ or $\Phi=const.$ are shown and in **Fig.2** contours of $j_\varphi=-\nabla^2\Psi=const.$ or $\Omega_\varphi=-\nabla^2\Phi=const.$ are given. **B** and **v** at large r show uniform fields. We can consider that the plasma translates in a neutral gas along the axisymmetric axis with a constant velocity, when the outside mass fluid is at rest.

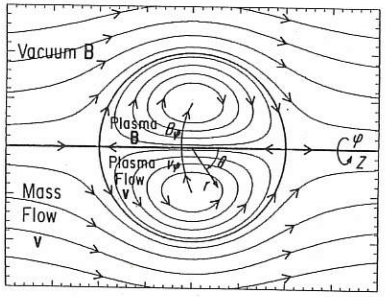

Fig.1
Surface of $\Psi=$ const. and $\Phi=$ const.. The exterior region is a vacuum magnetic field for **B** and mass flow for **v**. The inner region is a plasma magenetic field for **B** and plasma flow for **v**.

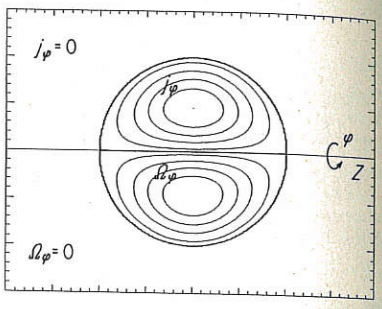

Fig.2
Surface of $j_\varphi=$ const. and $\Omega_\varphi=$ const.. The exterior region is a vacuum magnetic field and flow without vortex. The inner region is plasma current, j_φ, and flow vortex due to plasma, Ω_φ.

STABILITY CONDITION AGAINST INTERNAL MODES

We test stability for internal modes with the perturbed fields/1/ which are supposed to be in a relaxed state by minimization of E with K and H fixed. Further all perturbations of B_r and v_r vanish at the plasma surface(fixed-boundary): $j_m(\lambda_m a)=0$. Taking into account above things, we use the following perturbation which is deduced by replacing k in /1/ with λ_m:

$$\delta\mathbf{B}=\sum_{m\geq n}b_m^n e^{in\varphi}\left\{\left[m(m+1)P_m^n(x)\frac{j_m(\lambda_m r)}{\lambda_m r}\right]\mathbf{e}_r+\left[\frac{in}{\sin\theta}P_m^n j_m-\sin\theta\frac{dP_m^n}{dx}\frac{1}{\lambda_m r}\frac{drj_m}{dr}\right]\mathbf{e}_\theta\right.$$

$$+\left[\sin\theta\frac{dP_m^n}{dx}j_m+\frac{in}{\sin\theta}P_m^n\frac{1}{\lambda_m r}\frac{drj_m}{dr}\right]e_\varphi\Big\}, \tag{6}$$

where $x=\cos\theta$ in $P_m^n(x)$.

On the other hand the perturbed fields in Eulerian coordinates/3,4/ are given by

$$\delta\mathbf{v}=\frac{\partial\xi}{\partial t}+\text{rot}\,(\xi\times\mathbf{V}_0),\quad \delta\mathbf{B}=\text{rot}\,(\xi\times\mathbf{B}_0), \tag{7}$$

where we have used $\text{div}\,\xi=0$. The expression of $\delta\mathbf{v}$ is the same [rot] formula as $\delta\mathbf{B}$ except $\partial\xi/\partial t$. This makes the expression of δ^2E^* or δW symmetrical with respect to $\delta\mathbf{v}$ and $\delta\mathbf{B}$. In addition the term of $\partial\xi/\partial t$ works for gyroscopic stabilization which is important in tilting modes. Consideration over these things yields $\text{rot}\,(\xi\times\mathbf{V}_0)=(\mu_m/\rho)\mathbf{B}_m$, that is different from ideal MHD in which $\text{rot}\,(\xi\times\mathbf{V}_0)=(\mu/\rho)\mathbf{B}_m$. Thus δ^2E^* for internal modes are given:

$$\delta^2E^*=\int dV\Big[\rho(\delta\mathbf{v})^2+(\delta\mathbf{B})^2-2\mu\delta\mathbf{v}\cdot\delta\mathbf{B}-\kappa\delta\mathbf{A}\cdot\delta\mathbf{B}\Big]$$

$$=(1-C_A^2\frac{\lambda}{\lambda_m})(\lambda_m-\lambda)\int dV\mathbf{A}_m\cdot\mathbf{B}_m,\quad (\mathbf{A}_m=\frac{1}{\lambda_m}\mathbf{B}_m), \tag{8}$$

where we have used $\text{rot}\,(\xi\times\mathbf{V}_0)=(\mu_m/\rho)\mathbf{B}_m$, $\lambda=\lambda_1<\lambda_2<\lambda_3\cdot\cdot\cdot\cdot\cdot\cdot<\lambda_m$. The stability of internal modes is assured by $\delta^2E^*>0$. We find that all the modes $n>1$ and $n=1,m>1$ are stable with $C_A^2<\lambda_m/\lambda$, while $n=1,m=1$ mode, a rotation of axis, is marginally stable. For this marginal state we use the δW method/3,4/ where only the displacement of a pure rotation of axis, $\xi_0=\mathbf{r}\times\hat{y}$ is allowed.

$$L^2+T_0\delta W>0,\quad \text{with}\quad \delta W=0, \tag{9}$$

where

$$L=\int dV\xi^*(i\rho\mathbf{v}\cdot\nabla\xi)=-\mu_m\int dV\mathcal{J}_m(\xi^*\cdot\mathbf{B}_m),\quad \delta W=(1-C_A^2\frac{\lambda}{\lambda_m})(\lambda_m-\lambda)\int dV\mathbf{A}_m\cdot\mathbf{B}_m,$$

$$\mathbf{B}_m=\text{rot}\,A_m,\quad T_0=\int dV\,\rho\xi^*\cdot\xi. \tag{10}$$

The special displacement, ξ_0, yields by use of eq.(6)

$$L=-2\pi\mu\int_0^a\int_0^\pi drd\theta r^2\sin\theta\xi_0\cdot\mathcal{J}_m(\delta\mathbf{B}). \tag{11}$$

The integral, $\int_0^\pi P_m^1 d\theta\neq 0$ with $m=(\text{odd})$,

is included in eq.(11), which makes internal tilting mode stable, since $L^2>0$.

STABILITY CONDITION AGAINST SURFACE MODES

In order to study stability against surface modes we follow Rosenbluth and Bussac/1/ i.e. we test whether a pressure imbalance across the surface reinforces or opposes the displacement. The surface displacement allows the interior plasma to relax to a minimum energy state for the new surface consistent with K and H being conserved. For all $n\geq 1$ modes except $n=1,m=1$ we can use the result by Rosenbluth and Bussac, which shows that spheromak with no flow is unstable without conducting shell. As Sudan/2/ deduced from /1/, the stability condition with plasma flow against all $n\geq 1$ modes except $n=1,m=1$ is

$$\delta W_s = (1-C_A^2)\int d\mathbf{S}\cdot\xi(\mathbf{B}_0^{out}\cdot\mathbf{B}_n^{out}-\mathbf{B}_0^{in}\cdot\mathbf{B}_n^{in}) > 0. \qquad (12)$$

For tilting modes we rewrite eq.(10) to the form including surface integrals:

$$L=-\mu\int dV\,\mathcal{G}_m[(\xi\times\mathbf{B}_0)\cdot\mathrm{rot}\,\xi] + L_s, \text{where } L_s=-\mu\,\mathcal{G}_m\int d\mathbf{S}\cdot\xi(\xi\cdot\mathbf{B}_0). \qquad (13)$$

The pure rotation, $\xi_0=r\times\hat{x}$, leads to $L_s\approx 0$ by using similar θ-integral as eq.(11), $\int_0^\pi \sin^2\theta P_m^1 d\theta \approx 0$, with m=odd.

Therefore we would expect that the tilting mode is stabilized by a surface integral L_s in L^2. From eq.(12) and L^2 stabilization the stability condition for all $n\geq 1$ except $n=1, m=1$ is $1<C_A^2$ including tilting mode.

Although $n=1, m=1$ mode is marginal stable, it seems that the stability is assured. As ξ_1^1 is allowed by $\mathbf{B}_2$, its r component, δB_r, may vanish at $r=a$ ($j_2(\lambda_2 a)=0$), by taking into account the conservation of K and H. Here we can treat the problem as if the perturbation is fixed at a new surface such as fixed-boundary i.e. $\mathrm{rot}(\xi\times\mathbf{V}_0)=(\mu_2/\rho)\mathbf{B}_2$. In order to make a corresponding surface perturbation, we vary λ under the conservation of K and H. The variation on λ makes free from divergence due to $j_2(\lambda_2 a)=0$. Therefore eq.(12) is changed to

$$\delta W_s = (1-C_A^2\frac{\tilde{\lambda}}{\tilde{\lambda}_2})\frac{\tilde{\lambda}_2 a^2}{12\pi}|\xi_1^1|^2\,(j_1'(\lambda a))^2\,\frac{j_1(\tilde{\lambda}_2 a)}{j_2(\tilde{\lambda}_2 a)} > 0, \text{ with } \tilde{\lambda}_2=\lambda+\delta\lambda. \qquad (14)$$

It seems that the stability for $n=1, m=1$ is given by $C_A^2<\lambda_2/\lambda$ from eq.(14).

$n=0$ mode is special. First we consider a $n=0$ mode of fixed-boundary mode of which δB_r vanishes at the boundary: $\xi=\mathbf{B}_0\times\mathbf{A}_l/(B_0^2)$ ($\mathbf{A}_l=\mathbf{B}_l/\lambda_l$). And then we vary λ under the conservation of K and H that makes a corresponding surface perturbation. Owing to λ displacement we can use the perturbation function with new λ as if the perturbation is fixed at a new surface but is connected to the exterior region at $r=a$. We obtain due to above consideration:

$$\delta W_s = (1-C_A^2\frac{\tilde{\lambda}}{\tilde{\lambda}_l})2\pi a^2\frac{2l(l+1)}{2l+1}\frac{(b_l^0)^2}{\tilde{\lambda}_l}j_l(\tilde{\lambda}_l a)\,j_{l-1}(\tilde{\lambda}_l a) > 0. \qquad (15)$$

For mode $n=0, l=1$ which corresponds to expansion or contraction, the stability is assured with $1<C_A^2$ from eq.(15). We also find from eq.(15) that modes $n=0, l\geq 2$ are stable with $C_A^2<\tilde{\lambda}_l/\tilde{\lambda}$ ($\tilde{\lambda}=\tilde{\lambda}_1<\tilde{\lambda}_2<\cdots\cdots<\tilde{\lambda}_l$ and $\tilde{\lambda}\cong\lambda$), where $\tilde{\lambda}=\lambda+\delta\lambda$.

As a conclusion the equilibrium obtained is stable with $1<C_A<\lambda_2/\lambda$. We think that more precise examination is need for stability for modes $n=1, m=1$ and $n=0$. The existence of the invariant of the cross helicity H causes the stabilization for internal modes. Further not only the plasma flow but also the exterior mass flow play an important role for the stabilization of free boundary modes.

/1/ M.N.Rosenbluth and M.N.Bussac, Nucl.Fusion 19,489(1979).
/2/ R.N.Sudan,Pys.Rev.Lett.42,1277(1979).
/3/ E.Frieman and M.Rotenberg, Rev.Mod.Phys.32,898(1960).
/4/ J.M.Finn and T.M.Antonsen, Phys.Fluids.26,3540(1983).
/5/ J.B.Taylor, in Plasma Physics and Controlled Nuclear Fusion Research(Proc.5th Int.Conf.Tokyo, 1974)Vol.1, IAEA,Vienna(1975)161.

INTERNAL DISRUPTION = CATASTROPHIC ERGODISATION

M.A. Dubois, P. Hennequin, R. Nakach, R. Sabot.*

Association Euratom-CEA, CE Cadarache, F-13108 Saint-Paul-lez-Durance (France).

* PMI, Ecole Polytechnique, F-91128 Palaiseau (France).

Internal disruptions have been observed in tokamaks since 1973, and the best that one can say about their theoretical explanation is that there is still no consensus. Four main possibilities exist (cf the review [1] and references therein)

a) Total reconnection, as proposed by Kadomtsev.

b) Microturbulence triggered by a current singularity as proposed by Samain and Dubois.

c) Field line ergodisation due to toroidal effects on the $m = 1$ mode as proposed by Lichtenberg and Mercier.

d) Interchange as proposed by Wesson.

Theory a) is contradicted by experimental evidence (e.g. postcursors).
Theory c) needs a very low central q value ($q(0) \leq .7$).
Theory d) needs a very high central q value ($q(0) \approx 1 - \varepsilon$).
Theory d) is incomplete and qualitative.

Some recent experimental [2] and theoretical [3] results throw a new light on the problem. We will consider here only the simple sawteeth with an $m = 1$ precursor, and present a more complete interpretation.

The wide shear plateau observed around $q = 1$ by pellet injection analysis, and on some tokamaks by other methods, corroborate the theoretical result [3] that a resistive phase of the $m = 1$ precursor to the internal disruptions can exist only for non-monotonous shear profiles.

During the resistive evolution of this $m = 1$ precursor, the angle at the X–point of the separatrix decreases, and eventually would go to zero if nothing else happened. To the discontinuity of the helical field which would then appear, should correspond a singular current layer highly unstable to resistive modes. This could create a self propagating turbulence flattening profiles around $q = 1$.

In fact, an other phenomenon takes place before that: as it has been shown in the case of the two-waves problem in slab geometry [4], the shape of the separatrix strongly influences the stochasticity onset. Namely, introducing anharmonicity in the perturbation lowers the threshold and increases the diffusion coefficent. To study this in

toroidal geometry, we use a hamiltonian representation of the field lines configuration at MHD equilibrium, to which we add an $m = 1$ perturbation with an anharmonic component: we are therefore able to adjust the separatrix shape of the $m = 1$ island, and to vary continuously the angle at the X point. We compute by numerical integration of the field flow, the stochatic zone extension and the stochastic diffusion coefficient. This calculation is done for a continuously growing q-profile and also in presence of a shear plateau on $q = 1$. We use the following set of equations:

the poloidal field is taken to be

- $B_\theta = B^o_\theta(r) + B^1_\theta(r, \theta)$ (toroidal equilibrium as given by J. Blum [7], in the first order of the inverse aspect ratio $\varepsilon = a/R$)
- plus an anharmonic perturbation of the form $h_1(r, \theta) = K f(r) \cos(\theta + \phi + \alpha \sin(\theta + \phi))$ where $\alpha = 0$ gives the usual harmonic perturbation while $\alpha = 1$ gives a nul angle at the X point,

with a radial dependance (fig. 1a) $f(r) = \begin{cases} 0 & \text{for } r > 1.5\, r_1 \\ 3(r/r_1)^2 - 2(r/r_1)^3 & \text{for } r \leq 1.5\, r_1 \end{cases}$

The equilibrium is calculated for the two following profiles (fig. 1b):

monotonous current profile: $j(r) = j_o(1 - (r/a)^2)^2$

non monotonous q-profile: $\begin{cases} q(r) = q_o + (1 - q_o)\left(3(\frac{r}{r_1})^2 - 2(\frac{r}{r_1})^3\right) & \text{for } r \leq r_1 \\ q(r) = 1 + (q_a - 1)\left(\frac{(r - r_1)}{(a - r_1)}\right)^2 & \text{for } r > r_1 \end{cases}$

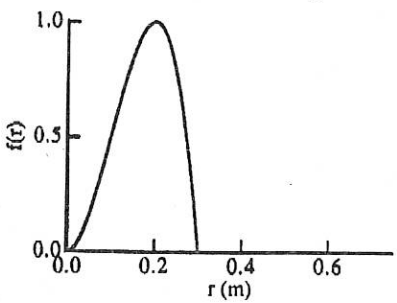

Fig 1 a: radial dependance of the $m = 1$ perturbation.

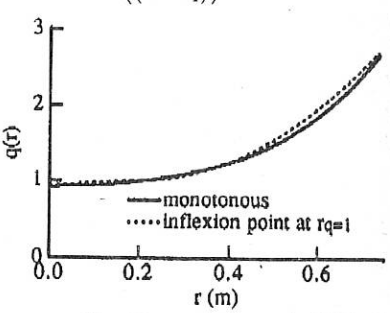

Fig 1 b: monotonous (solid line) and inflexion point (dotted) q-profiles.

On figure 2 we show the four cases: finite angle and monotonous profile, null angle and monotonous profile, finite angle and inflexion point at $q = 1$, null angle and an inflexion point at $q = 1$, with the same amplitude of the perturbation; we clearly see that both the shape of the separatrix (anharmonicity of the perturbation) and the shape of the q-profile (shear plateau at $q = 1$) have a strong effect on the stochasticity onset (fig. 2)

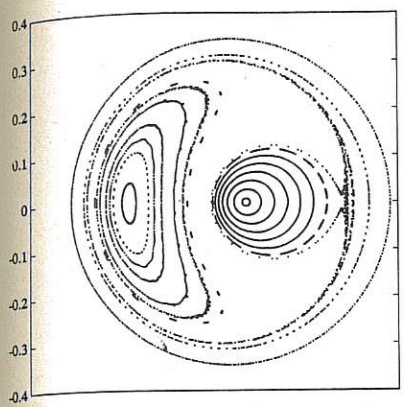

monotonous $q(r)$ and finite angle.

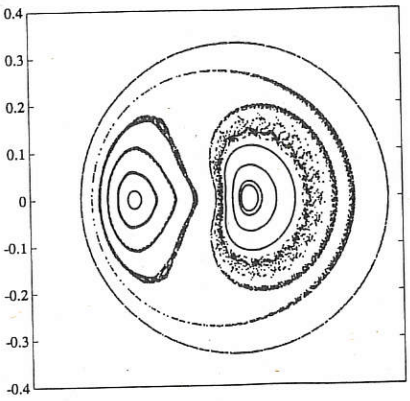

monotonous $q(r)$ and null angle.

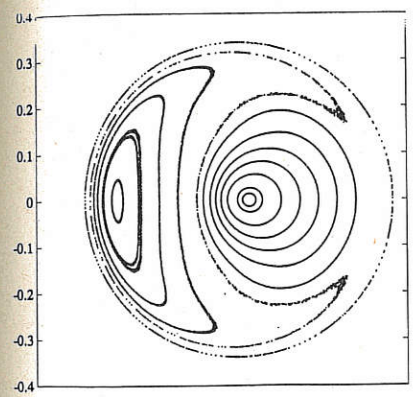

inflexion point at the $q = 1$ radius and finite angle.

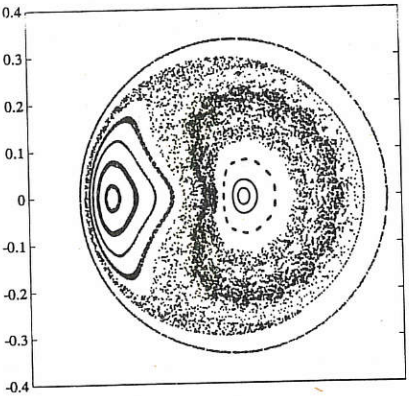

inflexion point at the $q = 1$ radius and null angle.

Fig 2: The four cases shown correspond to the same amplitude of the perturbation ($K = 6\ 10^{-3}$), in a toroidal geometry with parameters close to those of Tore Supra: $R = 2.4$ m, $a = 0.75$ m, $r_{q=1} = 0.2$ m, $q(a) = 2.8$, $q(0) = 0.93$.

We therefore suggest the following scheme for the sawtooth phenomenon (at least in the simple cases): the crash of the internal disruption is due to the sudden appearance of stochasticity in a roughly annular region, corresponding to the $q = 1$ surface. After the crash this region is completely shearless. The remain of the $m = 1$ island decreases, as it is stable in those conditions [3]. Ohmic (and possibly additionnal) heating peaks the profile, while resistive diffusion slowly erodes the shear plateau. At some point, non linear resistive growth of the $m = 1$ tearing becomes energetically favourable and the precursor starts growing again. The angle at the X–point decreases slowly, while the width of the island increases. Meanwhile, the resistive erosion of the shear plateau tends to leave an inflexion point at $q = 1$, thus accelerating the growth rate of the $m = 1$ island, and therefore the decrease of the angle at separatrix. These two effects combine to yield an extremely fast transition to stochasticity, and as the crash is due to the electron random walk in the ergodised region, it takes place in a time τ_c scaling as $RT_e^{-1/2}$, thus being practically the same for small and large tokamaks, whereas the sawtooth duration scales typically as a resistive time, i.e. with $R^2T_e^{3/2}$.

We thus retrieve a picture quite similar to the one initially suggested by A. Samain in 1976. The main difference is that the field line ergodisation which yields enhanced transport is intrinsic (hamiltonian chaos) while in the original suggestion it was caused by plasma microinstabilities. These may be present nevertheless due to the current images forming at the edge of the stochastic region, thus helping it to expand faster.

It is possible that additionnal phenomena can play a role in some cases, e.g. enhancement of the $m = 1$ perturbation growth rate [5]. Powerful numerical codes [6] could be useful to analyse the details of the crash, even if they cannot give an overall description of the complete sawtooth.

[1] J. Wesson. Review in *Theory of Fusion Plasmas, Proceedings of the 87 Varenna Workshop*, A. Bondeson *et al* editors, 253 (1987).
[2] B. Pégourié and M. A. Dubois. In *Nuclear Fusion*, **30**, 1575 (1990).
[3] M. A. Dubois, P. Hennequin. In *Nuclear Fusion*, **31**, 1409, (1991).
[4] P. Hennequin, M. A. Dubois, R. Nakach. accepted for publication in *Physics Letters*, (1992).
[5] A. J. Lichtenberg, K. Itoh, S. I. Itoh, A. Fukuyama. In *Nuclear Fusion*, **32**, 495, (1992).
[6] H. Baty, J. F. Luciani, M. N. Bussac. In *Nuclear Fusion*, **31**, 2055 (1991).
[7] J. Blum. Thèse de Doctorat d'Etat, Paris VI (1985).

Stability of Ideal Ballooning Modes Near a Magnetic Island*

C. C. Hegna and J. D. Callen
University of Wisconsin, Madison, WI 53706-1687 USA

Abstract

The stability properties of ideal ballooning modes on toroidal flux surfaces near a quasistatic magnetic island are examined. On these surfaces, magnetic field-line trajectories tend to bunch on that part of the magnetic surface closest to the X-point of the island where the effective magnetic shear is reduced. Eigenfunctions localized in helical angle near the X-point and in poloidal angle on the bad curvature side of the tokamak are more susceptible to ballooning instability than are modes in corresponding equilibria without the magnetic island. These secondary ballooning instabilities may play a part in the crash phase of sawteeth or macroscopic island dynamics.

I. Introduction

Magnetic islands can appear in toroidal plasma confinement devices from a variety of effects; inherent three-dimensionality, field errors, or nonlinearly growing resistive instabilities. The appearance of macroscopic magnetic islands causes the equilibria to three-dimensional and thus seriously complicates the issue of ideal stability analysis for these "equilibria". In this paper, we examine the stability properties of ideal ballooning modes on toroidal flux surfaces just outside the separatrix of a magnetic island. It is assumed that the island is slowly growing on ideal magnetohydrodynamic (MHD) time scales, so that the magnetic island is considered to be in MHD equilibria.

It has been suggested that secondary pressure driven instabilities may play a role in the crash phase of sawteeth [1-2]. Previously, a two-step process for internal disruptions has been put forth [1]. Initially, an m = 1 internal kink is excited and then grows nonlinearly until a neighboring, helically kinked equilibria accessible from the initial equilibrium is found [3]. This new equilibrium has an enhanced pressure gradient which triggers the onset of ideal ballooning instabilities. More recently, toroidal effects have been identified as being important in understanding the properties of m = 1 phenomena [4-6].

In this work, a general formalism is introduced to treat the effects of a magnetic island on large-n ballooning instabilities [7]. On toroidal surfaces near the island, the magnetic field-lines tend to "spend more time" on the that part of the flux surface that is nearest the X-point of the island, where the "effective magnetic shear" is smallest. Thus, an eigenfunction that is localized in helical angle near the X-point and in poloidal angle on the bad curvature side of the tokamak provides the most unstable (or least stable) perturbation. A similar calculation was carried out to examine the effect of a magnetic separatrix due to a magnetic divertor on ideal ballooning modes [8]. However, in the calculations of Ref. (8), the divertor was assumed to be axisymmetric so that the two-dimensional nature of the equilibrium was retained, whereas we examine inherently three-dimensional equilibria.

II. Equilibrium with a magnetic island

Consider the formation of an island at the surface $q = q_o = m_o/n_o$ caused by a symmetry-breaking magnetic perturbation given by $\mathbf{B}_1 = \nabla\theta \times \nabla A(\Phi,u)$, where θ is

the poloidal angle, the resonant angle is $u = \zeta - q_0\theta$, ζ is the toroidal angle angle and Φ is a radial-like variable that is a flux surface label in the limit that the magnetic island disappears. The total equilibrium field is given by $\mathbf{B} = \nabla\psi \times \nabla\theta + \nabla u \times \nabla\Phi$, where

$$\psi = \int d\Phi\, [q(\Phi) - q_0] - A \cong \frac{q_0' x^2}{2} - A \,, \tag{1}$$

in which $x = \Phi - \Phi_0$, $q(\Phi_0) = q_0$, and $q_0' = dq/d\Phi$ is evaluated at $\Phi = \Phi_0$. We will use the second form for ψ to describe the magnetic surfaces near the island. If we assume that the radial variation of A is weak and that a single harmonic approximation is sufficient, $A = \psi_{sx}\cos(n_0 u)$, where ψ_{sx} is the value of ψ on the separatrix. This form of A describes a magnetic island with half-width $w = 2\,|\psi_{sx}/q_0'|^{1/2}$.

The magnetic field in the vicinity of the rational surface satisfies $\mathbf{B}\cdot\nabla\psi = 0$. We transform from the magnetic coordinates Φ and u to a new set of coordinates given by

$$\int d\Phi^* = \int \frac{d\psi}{\Omega(\psi)} \,, \tag{2}$$

$$\int du^* = \int n_0 du\, \frac{\Omega(\psi)}{\partial_\Phi \psi(\Phi^*,u)} \,, \tag{3}$$

where $\Phi^* = \Phi^*(\psi)$ serves as a label of the magnetic surfaces modified by the magnetic island formation and u^* is an angle-like variable on the modified surfaces. The function $\Omega(\Phi^*)$ serves as the rotational transform for the magnetic surfaces near the magnetic island and is given by

$$\Omega(\Phi^*) = [\oint \frac{du}{2\pi/n_0} \frac{1}{\partial_\Phi \psi(\Phi^*,u)}]^{-1} \,. \tag{4}$$

The magnetic island width is small compared to macroscopic length scales, so $q_0' w \ll 1$. Since $\Omega \sim O(q_0' w)$ the value of Ω is small; however, $d\Omega/d\Phi^* \sim O(q_0')$ since $\Phi^* \sim O(w)$. In addition, the value of Ω goes to zero as the separatrix is approached. This describes the fact that field-lines on the separatrix stagnate near the X-point.

Using these coordinates, the equilibrium magnetic field in the presence of the magnetic island is given by

$$\mathbf{B} = \nabla u^* \times \nabla\Phi^* + \Omega(\Phi^*)\, \nabla\Phi^* \times \nabla\theta = \nabla\Phi^* \times \nabla(\Omega\theta - u^*) \,. \tag{5}$$

We will use this form of the equilibrium **B** in the stability analysis. Finally, we note that MHD equilibrium conditions require that the plasma pressure be constant on a magnetic surface; therefore $p = p(\Phi^*)$.

III. Linear Stability of Ballooning Modes

Using standard linearized ideal MHD equations and the usual eikonal representation the perturbation $\xi_1 = \tilde{\xi}\exp(inS)$ for n tending to infinity and $S = \int (\Omega\, d\theta - du^*)$, the ballooning mode δW is given by

$$\delta W = \int d\mathbf{r}\, \{|\nabla S|^2 |\nabla_\parallel \tilde{\xi}|^2 + \frac{4\pi}{|\nabla\Phi^*|}\frac{dp}{d\Phi^*}(\kappa_n^* - \kappa_g^* \frac{\nabla S\cdot\nabla\Phi^*}{B})|\tilde{\xi}|^2\} \,, \tag{6}$$

where the curvature is decomposed into its normal and geodesic contributions, $\kappa = (\kappa_n \nabla\Phi + \kappa_g \mathbf{b}\times\nabla\Phi)/|\nabla\Phi| = (\kappa_n^*\nabla\Phi^* + \kappa_g^*\mathbf{b}\times\nabla\Phi^*)/|\nabla\Phi^*|$, where $\kappa_n^* = \kappa_n$ and $\kappa_g^* = \kappa_g$

to leading order in $q_0'w$. The metric elements in δW that describe the magnetic island can be described by the factor $C = \Omega(\Phi^*)/\partial_\Phi\psi(\Phi^*,u^*) = \partial u^*(\Phi^*,u)/\partial u$. For constant-$\psi$ islands, $C = [x<x^{-1}>]^{-1}$, where the bracket is defined as an average over the modified surfaces, $<A> = \oint (du^*/2\pi)\, A(\Phi^*,u^*)$. Figure 1 plots C for different magnetic surfaces and shows that C peaks on the point of the flux surface closest to the X-point and the closer the magnetic surface is to the separatrix, the more peaked C is. In δW, the effect of the island is to change the shear parameter $s = d\ln q/d\ln r$ to $s<C^2>/C$, so that the effective shear is smallest at the point closest to the X-point of the island. Thus, by localizing the eigenfunction in helical angle near the X-point, the stabilizing effect of field-line bending can be reduced.

The pressure profile is constructed by constraining the magnitude of ∇p to be constant at the stagnation point of a magnetic surface as the island forms and evolves. By using this assumption, the factor $\alpha = -(dp/dr)(q^2R_0/B_0^2)$ of ballooning theory is modified to $C_M\alpha$, where $C_M = \Omega/\partial_\Phi\psi(\Phi^*,u_s)$ is the maximum value of C on a modified magnetic surface and u_s is the value of u^* on the magnetic surface that describes the X-point.

The ballooning mode δW is now written

$$\delta W = \int dl\ \{(C^2 + \Lambda^2)|(\partial_\theta + \Omega\partial_{u^*})\tilde{\xi}|^2 - \alpha C_M(C\cos\theta + \Lambda\sin\theta)|\tilde{\xi}|^2\}\ , \quad (7)$$

where

$$\Lambda = \frac{<C^2>}{C}\, s(\theta - \theta_0) - C_M\alpha(\sin\theta - \sin\theta_0)\ . \quad (8)$$

The last term in Eq. (8) describes the pressure modulation of the local shear that is responsible for the second stability regime. In this paper, we are considering the first stability boundary in s-α space, so we will drop this term.

To construct an analytic solution of the first stability boundary, we use a trial function for the quasimode: $\xi(\theta,u^*) = C(u^*)(1+\cos\theta)\Theta(\pi - |\theta|)$, where Θ is the Heaviside step function. The trial function is localized in helical angle near the island X-point and on the bad curvature side of the tokamak. Using this trial function, an analytic solution for the critical α for the first stability regime is derived.

$$\alpha_c = \frac{1}{C_M}\frac{0.5<C^4> + 1.39s^2<C^2>^2}{<C^3> + 0.83s<C^2><C>}\ . \quad (9)$$

Assuming constant-ψ islands, Eq. (9) is plotted in Fig. 2 for different values of the magnetic flux function. The magnetic surfaces are labeled by $k^2 = w^2/(w^2 + x_k^2)$, where x_k is the distance from the X-point to the closest point on the magnetic surface, $x_k^2 = (2q_0/q_0')(\psi - \psi_{sx})$. As shown in Fig.2, the surfaces that are closest to the island are the one's most dramatically affected by the island through the mechanism of the shear reduction described above.

IV. Discussion

Ideal ballooning stability of quasistatic MHD equilibria with a macroscopic magnetic island has is developed analytically. This special feature of the island provides a mechanism by which ballooning instabilities are more likely to occur in equilibria with an island than the associated equilibria without the island. For slowly growing magnetic islands, a growing region of flux surfaces located near the island

separatrix become more susceptible to instability, as long as the initial equilibrium is not too far from the first stability boundary.

The occurrence of secondary ballooning instabilities may be important to understanding the nonlinear properties of m = 1 resistive modes and sawteeth. A scenario reminiscent of earlier work by Bussac and Pellat [1] could be construed whereby plasma pressure is released through the appearance of ideal instabilities following a slow growth of a resistive mode. What is different between our work and that of Ref. (1) is the suggestion that the presence of a magnetic island in the equilibrium causes ballooning modes located near the X-point to be more unstable. We do not try to give a complete explanation of the sawtooth crash phase, however many of the elements of this theory are consistent with experimental observations of sawteeth on TFTR[5] and JET[6]. In addition, these secondary instabilities may also be responsible for beta collapses near magnetic islands in high-beta tokamak discharges.

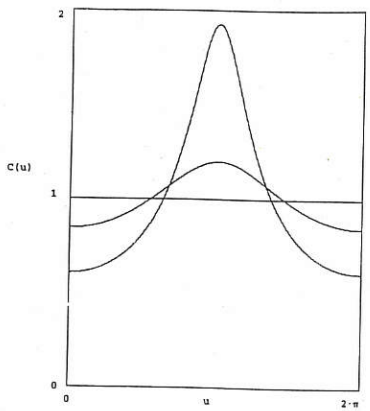

Fig. 1 – The function C vs. α for the magnetic surfaces k^2 = 0, 0.5, and 0.9. The line C =1 corresponds to k = 0 (no island). The curve peaks more prominently for larger k.

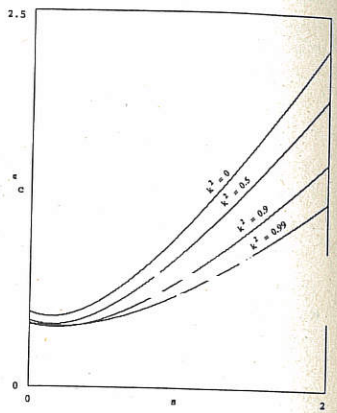

Fig. 2 – The first stability boundary for the surfaces k^2= 0, 0.5,0.9, and, 0.99. The larger the value of k, the smaller the critical α for instability.

[1] M. N. Bussac and Pellat, Phys. Rev. Lett. **59**, 2650 (1987).
[2] T. K. Chu, Nucl. Fusion **28**, 1109 (1988).
[3] M. N. Rosenbluth, P. Rutherford, and R. Y. Dagazian, Phys. Fluids **16**, 1894 (1973); Avinash, R. J. Hastie, J. B. Taylor, and S. C. Cowley, Phys. Rev. Lett. **9**, 2647 (1987).
[4] W. Park, D. A. Monticello, E. Fredrickson, and K., McGuire, Phys. Fluids B **3**, 507 (1991).
[5] Y. Nagayama, et al., Phys. Rev. Lett. **67**, 3527 (1991).
[6] P. A. Duperrex, A. Pochelon, A. Edwards, and J. Snipes, JET report JET-P(91) 43, submitted to Nucl. Fusion (1992).
[7] C. C. Hegna and J. D. Callen, UW Report UW-CPTC 92-1, submitted to Phys. Fluids B (1992).
[8] C. M. Bishop, et al., Nucl. Fusion **24**, 1579 (1984).

* Research supported by U. S. DOE grant DE-FG02-86ER53218.

SHEARED FLOW EFFECTS ON RESISTIVE PRESSURE-GRADIENT-DRIVEN TURBULENCE

L. Garcia
Universidad Complutense and Asociación Euratom-Ciemat, Madrid, Spain
B.A. Carreras and V.E. Lynch
Oak Ridge National Laboratory, Oak Ridge, USA
P.H. Diamond
University of California, San Diego, USA

The poloidal flow at the edge of a tokamak plasma plays an important role in the overall plasma confinement properties. In a turbulent plasma, poloidal flow can be generated through the Reynolds stress [1,2]. At the same time, this poloidal flow controls the level of fluctuations. Therefore, self-consistent calculations of plasma turbulence in the presence of flows are needed to identify the mechanism of confinement improvement.

Here, we study the interaction between flows and turbulence for the case of resistive pressure-gradient-driven turbulence [3]. The generation of flow trough the Reynolds stress leads to a requirement for radial propagation of the modes. One way of produce this is to have an external differential plasma rotation, which acts as "seed" flow. Another way is to include electron diamagnetic effects. In both cases, the flow is self-consistently calculated during the evolution.

POLOIDAL FLOW GENERATION

The poloidal flow generation equation is derived by taking the flux surface average of the momentum balance equation. The resulting equation gives the conservation of momentum:

$$\frac{\partial \langle V_\theta \rangle}{\partial t} = -\frac{\partial}{\partial r}\left(\langle \tilde{V}_r \tilde{V}_\theta \rangle - \frac{1}{\rho_m \mu_0} \langle \tilde{B}_r \tilde{B}_\theta \rangle \right) + \mu \frac{\partial}{\partial r}\left(\frac{1}{r}\frac{\partial}{\partial r}\left(r \langle V_\theta \rangle \right) \right),$$

where ρ_m is the mass density, μ is the viscosity, and the angular brackets, $\langle\ \rangle$, represent average over a magnetic flux surface.

When the turbulence is electrostatic, $\langle \tilde{B}_r \tilde{B}_\theta \rangle \approx 0$, and the Reynolds stress tensor is given by $\langle \tilde{V}_r \tilde{V}_\theta \rangle$. The electrostatic approximation is a good approximation for the resistive pressure-gradient-driven turbulence when neither flows nor diamagnetic effects are included. However, this is not the case when the flows and/or the real frequency are large. The most important difference is in the generated flow. Figure 1 compares the time evolution of $\langle V_\theta' \rangle$ at the resonant surface for a numerical nonlinear calculation in the single-helicity limit using the full set of equations with the time evolution using the electrostatic approximation.

We begin by studying the case of an initial poloidal flow with no diamagnetic effects included. At $t = 0$, $\langle V_\theta \rangle = V_0(r)$. In the case of a sheared poloidal flow, $V_0' \neq 0$ at the resonant surface. The linear eigenvalue problem can be solved analytically in the weak shear flow limit, $\omega_s / \gamma_0 \ll 1$. Here $\omega_s \approx k_\theta V_0' \Delta$ is the shearing rate, and γ_0 is the linear growth rate of the resistive interchange mode. The linear eigenfunction of resistive

interchange modes with no diamagnetic effects and with a weak external shear flow is

$$\tilde{\Phi}(x,\theta,\zeta,t) = \Phi_{mn} \exp\left[-i\omega t + i(m\theta + n\zeta)\right] \exp\left[-\alpha_r (x + i\delta)^2/2\right] .$$

Here, we use the shear slab approximation with $x = r - r_s$, where r_s is the singular surface of the mode considered. The dispersion relation is such that α_r and δ are real. Here, $\alpha_r = \Delta^{-2}$ and Δ is the radial width of the mode. The radial shift is proportional to the gradient of the velocity, $\delta = \Delta \omega_s / \gamma_0$.

Using the linear eigenfunction for modes with the same helicity, it is possible to calculate the contribution of such modes to the Reynolds stress tensor. From this contribution, we have the following evolution equation for the velocity shear:

$$\left.\frac{\partial \langle V_\theta' \rangle}{\partial t}\right|_{x=0} = \sum_{m,n} k_\theta \left|\frac{\Phi_{mn}}{B_0^2}\right|^2 \delta \alpha_r^2 \propto V_0' ,$$

and the evolution equation for the flow curvature $\langle V_\theta'' \rangle$ is

$$\left.\frac{\partial \langle V_\theta'' \rangle}{\partial t}\right|_{x=0} = 0 .$$

Since the shear flow is proportional to the initial shear, the effect of the turbulence is to amplify the shear flow. In the electromagnetic case, we can only make an estimate of the flow generation equation. The magnetic contribution can dominate, and the shear flow can be reduced (Fig. 1). In both cases, there is no flow curvature generation.

We have done nonlinear single- and multiple-helicity numerical calculations. Using the nonlinear three-dimensional code KITE [4], we numerically solve the set of evolution equations for the poloidal flux, stream function, and electron density [2]. The input parameters are the same as in Ref. 3, for the helicity resonant at $q = 3/2$. The nonlinear calculation was initialized with a small value of equilibrium shear flow to act as a seed.

Different values of the seed flow have been used in the nonlinear calculations. The values of V_0' at the resonant surface ranged from 0 to 5000 in units of resistive time τ_R. The largest value used causes a reduction in the linear growth rate of the ($m = 3$; $n = 2$) mode by a factor of 4, and the unstable linear spectrum is reduced to the lowest two modes. In all cases considered, the seed flow slows down the evolution of the modes, as it can be expected from the linear stability properties. However, the saturation level of fluctuations is not significantly affected by the shear flow (Fig. 2). The fluctuation spectrum at saturation is dominated by the lowest k modes in the calculation, the $m = 3$ and $m = 6$ modes. These modes are not affected by the shear flow. However, for larger values of m, there is an effect. In Fig. 2, at $t \approx 0.027\tau_R$, the case with $V_0' = 0$ has a shoulder that corresponds to the saturation of modes in the range $m = 21$ to $m = 27$. This shoulder is not visible for $V_0' = -5000$, because these higher-m modes are suppressed.

DIAMAGNETIC EFFECTS

We can make a similar analysis when electron diamagnetic effects are included, and there is no initial seed flow. In this case, the linear eigenfunction is

$$\tilde{\Phi}(x,\theta,\zeta,t) = \Phi_{mn} \exp\left[-i\omega t + i(m\theta + n\zeta)\right] \exp\left[-\alpha x^2/2\right] .$$

The coefficient $\alpha = \alpha_r + i\alpha_i$ is complex, with $\alpha_r = \Delta^{-2}$ and $\alpha_i = \alpha_r \left(\omega_e^* - \omega_c - \omega_r\right)/\gamma$.

Here $\omega_c = L_n\omega_e^*/r_c$, with r_c the radius of curvature of the field line and $\omega = \omega_r + i\gamma$. The imaginary part α_i induces the radial propagation of the mode.

Using this linear eigenfunction, it is possible to calculate the Reynolds stress tensor. From this, we obtain an evolution equation for the shear flow at the resonance surface

$$\left.\frac{\partial\langle V_\theta'\rangle}{\partial t}\right|_{x=0} = 0 ,$$

and for the flow curvature

$$\left.\frac{\partial\langle V_\theta''\rangle}{\partial t}\right|_{x=0} = 3\sum_{m,n} k_\theta \left|\frac{\Phi_{mn}}{B_0^2}\right|^2 \alpha_i\alpha_r .$$

These equations show that there is flow curvature generation by the diamagnetic effects, but no shear flow generation. Therefore, considering a seed flow and the diamagnetic terms separately allows us to separate the effect of flow shear from flow curvature in the nonlinear evolution of the resistive interchange modes.

Nonlinear single-helicity numerical calculations have been performed using the same equilibrium parameters as in the cases of an initial seed flow. The numerical results indicate that up to the deep nonlinear regime, the quasilinear calculation provides a good description of the numerical results for the flow generation. A strong flow curvatures is generated, as is apparent in the distortion of the flow patterns. In the saturation phase, the eigenfunction structure is strongly modified and the quasilinear model is no longer valid. The generated flow curvature is lower than predicted.

A small range of ω_e^* values was considered in the calculation. The electron diamagnetic velocity was varied between zero and $V_e^* = 37.7a/\tau_R$, where $\omega_e^* = k_\theta V_e^*$ and a is the minor radius. In this way, the linear growth rate is weakly affected by the electron diamagnetic effects. As a consequence, there is no slow-down in the nonlinear evolution of the instability. In spite of the small effect in the linear growth rate, as the diamagnetic effects increase, the nonlinear saturation level is substantially reduced (Fig. 3). This reduction in the fluctuation level is correlated with the generation of a significant curvature in the average poloidal flow.

CONCLUSIONS

Turbulence can generate flows through the Reynolds stress tensor. The radial structure of these flows depends on the nature of the turbulence and on the symmetry-breaking mechanism, which generates a nonzero Reynolds stress. In the case of resistive interchange turbulence with self-generated flows, the effect of shear flow on the turbulence saturation level is weak, although it can cause changes in the fluctuation spectrum. However, the effect of flow curvature on the turbulence saturation is strong, and produces a reduction of the fluctuation level.

REFERENCES

[1] P.H. Diamond and Y.B. Kim, *Phys. Fluids* **B** 3, 1626 (1991).
[2] B.A. Carreras, V.E. Lynch, and L. Garcia, *Phys. Fluids* **B** 3, 1438 (1991).
[3] B.A. Carreras, L. Garcia, and P.H. Diamond, *Phys. Fluids* **30**, 1388 (1987).
[4] L. Garcia et al., *J. Comput. Phys.* **65**, 253 (1986).

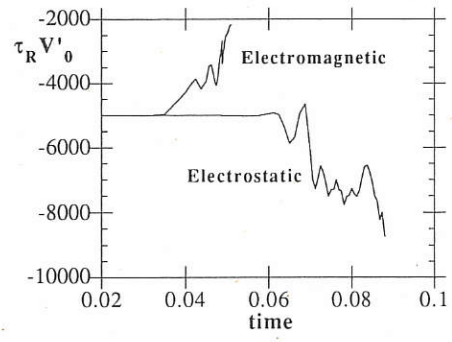

Fig. 1. Time evolution of $\langle V'_\theta \rangle$ using the full set of equations or the electrostatic approximation. The initial shear flow is -5000 and no diamagnetic effects are included in the calculation. The time is normalized to the resistive time.

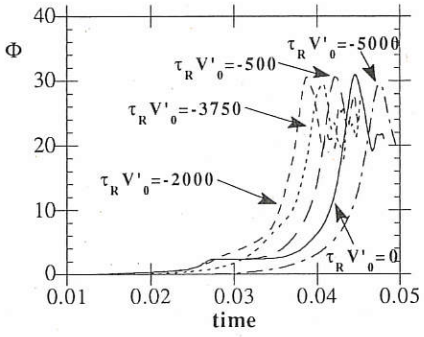

Fig. 2. Time evolution of the electrostatic potential fluctuations for different values of V'_0 at the resonant surface.

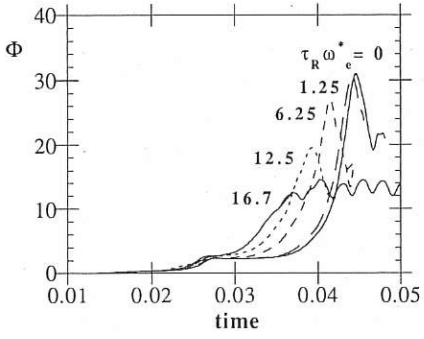

Fig. 3. Time evolution of the electrostatic potential fluctuations for different values of ω^*_e.

MECHANISM OF MHD MODES STABILIZATION BY THE ERGODIC DIVERTOR

D. EDERY, A.SAMAIN, J.C. VALLET, J.P. MORERA,
E. JOFFRIN, P. LECOUSTEY, A.L. PECQUET, M. TALVARD

Association Euratom-CEA sur la Fusion
CE/CADARACHE - F 13108 SAINT PAUL LEZ DURANCE

ABSTRACT

A new method for stabilizing MHD modes has been discovered experimentally on Tore Supra (TS) by operating the Ergodic Divertor (ED). The stochastic layer induced at the plasma boundary by the ED produces new equilibrium current density profiles, which stabilizes tearing modes at the current plateau, as well as surface kink modes during the current ramp up.

I - INTRODUCTION

It has been reported in [1;2] that the ED implemented in TS has a stabilizing influence on the MHD activity. There is a priori two main possibilities for that stabilization: a thermal effect in the islands or a Δ' effect. The first one involves the current response around the islands [3;4]. If that response corresponds to an underheating of the islands, it tends to destabilize the mode. It may be thought that the presence of the ED decreases the radiated power around q=2 surface, then reducing the underheating within the islands. Indeed, in the experiment with deuterium the ED decreases the density and thereby the radiated power around q=2 surface. However in the helium case, density, temperature and Zeff are not significantly changed while the stabilization occurs with the same characteristics. Then it may be concluded that the stabilization is not due to the decrease of underheating within the island. The other possibility to explain the stabilization is a significant variation of Δ' with the ED. The ED produces a radial magnetic field perturbation taking the form of a multihelical structure with poloidal mode numbers $15 \leq m \leq 22$ and toroidal mode number n=6 [5;6]. The created resonances are localized at the plasma edge within a thin layer of 10cm with safety factor values between $q\psi=2.5$ and 3.7. At an amplitude perturbation $\delta Br/B$ of the order of 10^{-3}, the produced magnetic islands overlap leading to a stochastic field lines topology. The resulting magnetic structure is composed of open field lines connecting the plasma to the wall. As a consequence we find that an anomalous high resistivity is produced, which leads to the vanishing of the current density j(r) in the stochastic layer and to the enhancement of the gradient dj/dr outside the q=2 surface. Moreover following the Δ' analysis we find that the new current profiles are stable against tearing modes, as it is observed on TS.

In this paper a model for the anomalous resistivity induced by the stochasticity and ergodicity of the field lines and for the mode stabilization due to the subsequent current profile shrinking is presented.

II - MODEL OF STABILIZATION BY THE ED

1) ANOMALOUS RESISTIVITY

An essential feature of the ED is that the flux lines are no longer drawn on closed magnetic surfaces but are connected to the wall. In fact two different adjacent regions are created at the plasma edge by the ED [5;7]. A first region R_W close to the wall contains field lines which connect the wall after a few number of poloidal turns. In that region the parallel current which is produced by the inductive voltage is limited by the electrostatic sheets at the junction of the field lines with the wall.This imposes a considerable reduction of the current density. Beyond the region R_W, exists a second region Rp where the field lines are still connected to the wall, but on a parallel distance which becomes larger and larger. An inductive current may now flow along the field lines by escaping the sheet junctions with the wall. Indeed field lines such as L_1, L_2, L_3...(Fig.1) originating from an unperturbed magnetic surface r=const will intersect ultimately the wall. However, before leaving this surface the lines pass very close to each other.

A parallel current may then flow along the parallel lines $L_1, L_2, L_3...$, in series with transverse currents across the thin paths from L_1 to L_2, L_2 to L_3... The parallel currents $j_{//}$ along $L_1, L_2...$, and the transverse currents $j_\perp$ beetwen L_1 and L_2, L_2 and L_3... may be derived from the reduced system of the non linear stationnary MHD equations [8;9] :

$$\begin{cases} E_{ind} \quad -\nabla_{//}U=\eta_{//}j_{//} \\ -\nabla_\perp U=\eta_\perp j_\perp \end{cases} \qquad (1)$$

$$\eta_{///}\eta_\perp(\nabla_\perp)^2U+(\nabla_{//})^2U=\nabla_{//}E_{ind} \qquad (2)$$

where E_{ind} is the inductive electric field, $\eta_{//}$ is the classical resistivity and $\eta_\perp$ the anomalous transverse resistivity corresponding to the transverse diffusion of the field lines on alfvenic time scale: $\eta_\perp \approx \mu_0 V_A{}^2 \tau_D$, where V_A is the Alfven velocity and τ_D the transverse diffusion time scale of the potential U.A dimensional analysis of (2) provides a first relation between the parallel length L of the field lines and the minimum transverse length d: $d/L \approx (\eta_{//}/\eta_\perp)^{1/2}$ (3); a second relation between d and L is obtained by expressing the exponential divergence of the field lines [10]: $L/L_0=\ln(\Delta/d)$ (4), where Δ is the radial extension of the region Rw or Rp and L_0 is the parallel scale length of the ergodic field lines ($L_0 \approx 2\pi qR$). More precisely the width Δ is the radial penetration of field lines of length L so that one may write $\Delta=(D_0L)^{1/2}$ where D_0 is the radial diffusion coefficient. From (3) and (4) one finds the expression for the parallel length L: $L=L_0\ln[\Delta(\eta_\perp/\eta_{//})^{1/2}/L_0)]$ (5).In the case of TS one has $L_0 \approx 20m$ and $D_0 \approx 10^{-4}m^2/m$. Formula (5) gives $L \approx 100m$ and $\Delta \approx 10cm$. We finally estimate that the current density is cancelled within a depth of $\sim$ 10cm from the wall (the region Rw) and then recovers over again $\sim$ 10cm its unperturbed value (region Rp).

2) STABILITY ANALYSIS

The switching on of the ED induces two phases for the current profile redistribution:

- A transient phase in which the current in region Rw is transferred instantaneously in the region Rp to maintain constant the plasma current. The transient increase of the current in the region Rp corresponds to a transient increase of the inductive voltage outside the plasma, which is effectively observed (Fig.7.b).

-A slow phase, when the displaced current in region Rp diffuses towards the plasma center. That current diffusion corresponds to an increase of the internal inductance which is also observed (Fig.7.b).

The transient increase of the current density in region Rp produces an enhancement of the gradient dj/dr in that region. To maintain constant the total current a subsequent increase of that gradient is induced just outside the q=2 surface leading to more stable profiles.The stability analysis is performed by using the "Step" profiles given in Fig.2. The current profile j(r) is a standard invariant profile inside the resonant surface $r=r_2$ where q=2. Outside that surface the current density is taken constant up to a radius r_D at a level which maintains constant the total plasma current. The action of the ED is modelized by shrinking the radius r_D from the limiter radius r=a. It may be shown that if a step profile is stable, then any other profile smoothly decreasing between r_2 and r_D is also stable (the jump dj/dr at $r=r_2$ is not accounted for in the Δ' calculation). As inside the q=2 surface the current density profile is not changed, the perturbed flux profile does not change either, thus allowing to derive the expression:

$$\Delta'=\Delta'_0+(x\Psi'/\Psi)_+-(x\Psi'_0/\Psi_0)_+ \qquad (6)$$

where $(x\Psi'/\Psi)_+$ and $(x\Psi'_0/\Psi_0)_+$ are the slopes of the magnetic flux perturbation of the tearing mode just outside the resonant position r_2, with and without ED respectively and Δ'_0 is the value

of Δ' without ED (r_D=a). The flat current profile outside the q=2 surface allows to calculate analytically these slopes.We find:

$$(x\Psi'_0/\Psi_0)_+=-2(1+x_2^4)/(1-x_2^4) \qquad (7)$$

$$(x\Psi'/\Psi)_+=-2(x_D^4+x_2^4)/(x_D^4-x_2^4) \qquad (x=r/a) \qquad (8)$$

Using (6),(7) and (8) we obtain the relation between r_D and the stabilization effect Δ'_0-Δ':

$$X_D= X_2.\left[1+\frac{1}{(\Delta'_0-\Delta')/4+X_2^4/(1-X_2^4)}\right]^{1/4} \qquad (9)$$

The line A on Fig.3 gives Δ' versus $1-x_D$ for the step profile of Fig.2. The critical value $1-x_D$=0.24 computed from (9) for which Δ' cancels gives an upper bound of the thickness of the region from which the current is expelled. This value is quite consistent with the radial extension Δ of the stochastic region calculated from (4) and (5).

III - NUMERICAL RESULTS

The proposed model has been validated by a stability computation of various current density profiles using a Δ' code. Fig.4 and Fig.5 show two such profiles, with (dotted line) and without ED (solid line) under the conditions that the current density cancels in the interval (r_D,a) and the total current is maintained constant. The case of Fig.4 corresponds to the transient phases where the deficit of current in the ergodic layer appears as a positive image just inside this layer corresponding to the observed transient voltage spike outside the plasma. The current density profile shown on Fig.5 corresponds to a steady state profile producing the observed increase of the internal inductance given in Fig.6 in terms of the ergodic width $1-x_D$=1-(r_D/a). The Δ' value for the two types of profiles are given on Fig.3. It must be stressed that the necessary stochastic width for insuring the stability (Δ'=0) is smaller than for the step profile. This necessary value falls in a range $\sim$ 15cm compatible with the actual performance of the ED.

IV - CONCLUSION

The mechanism we propose in this paper has been capable to explain the stabilization of the MHD modes by the ED. It is based on two main processes:

-An anomalous resistivity is produced at the plasma edge in an ergodic layer of 15cm width, resulting in a sudden inward evacuation of the current from the layer and a redistribution of the profile.

-The new profile first exhibits a stronger negative gradient just outside the q=2 surface, obviously favourable to stability. The profile then diffuses towards the plasma center maintaining stability.

The model allows to interpret the experimental observations on the stabilization of the MHD activity as well as on the evolution of the equilibrium parameters, i.e increase of the internal inductance and of the inductive voltage.

References:

[1]J.C.VALLET, L.POUTCHY &al. Physical Review Letters, Vol67, 1991, p2662
[2]J.C VALLET, D.EDERY &al. This conference paper n°4-1- 131
[3]P.H. REBUT & A. SAMAIN 5th Eur.Conf. Cont. Fus. & Plas. Phys, Grenoble,Vol1,p29,(1972)
[4]P.H. REBUT & M.HUGON Plasma Physics and Controlled Fusion Research 2,197 (1984)
[5]A. SAMAIN, T. BLENSKI &al. Contribution to. Plasma Physics.30, 157 (1990).
[6]A. GROSMAN, T. EVANS &al. Plasma Physics and controlled fusion 32,157 (1990)
[7]F. NGUYEN, P GHENDRIH &al. This conference paper n°4-26
[8]D.EDERY,J.L.SOULE &al. Plasma Physics and Controlled Fusion Research Vol1,269 (1980)
[9]D.EDERY,M.FREY &al. Physics of Fluids 26 (5),May 1983
[10]A.ROCHESTER,M.ROSENBLUTH Physical Review Letters, Vol 40, 1978, p38

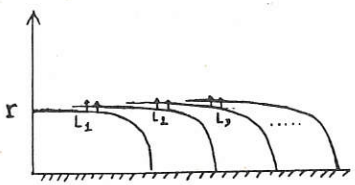

Fig.1 Wall

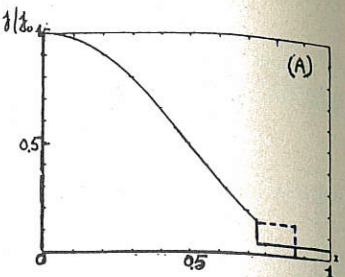

Fig.2 "STEP" current density profile (A) ED off (—); ED on (····)

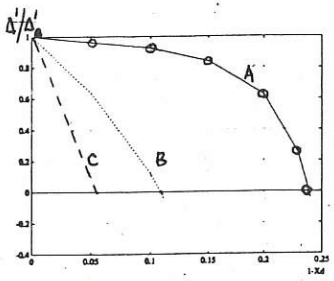

Fig.3 Stability diagram Δ'/Δ'_0 versus E.L. width for profiles (A,B,C)

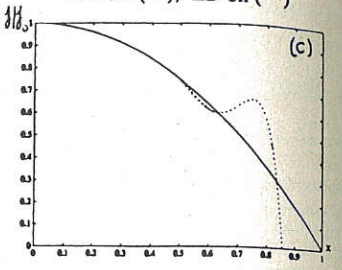

Fig.4 Transient current profile (C) ED off (—); ED on (····)

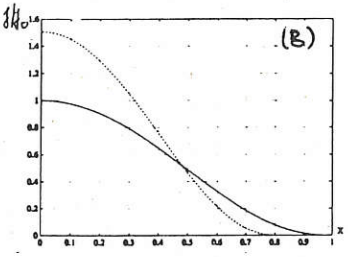

Fig.5 Stationnary current profile (B) ED off (—); ED on (····)

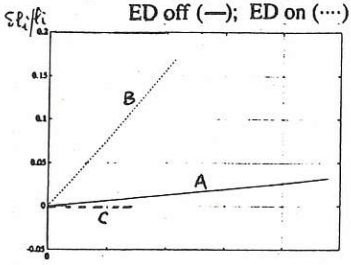

Fig.6 Relative increase of li versus EL width for current profiles (A B C)

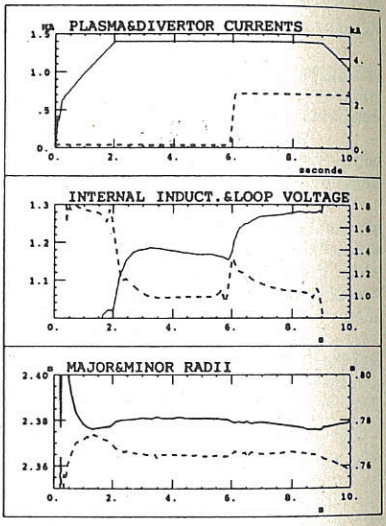

Fig.7 Experimental evolution of the inductive voltage and of the internal inductance (shot 8511).

NONLINEAR ISLAND DYNAMICS

T.J. Schep*, F.Pegoraro and J. Rem***

*FOM Instituut voor Plasmafysica Rijnhuizen, Nieuwegein, The Netherlands

**Dipartimento di Fisica Teorica, Università di Torino 10125 Torino, Italy

Coherent non linear magnetic structures, such as magnetic islands, have been widely studied in the limit of zero frequency. In this case the plasma current density distribution is constant on magnetic surfaces. In high temperature plasmas however, small amplitude magnetic perturbations, such as resistive instabilities, are found to propagate with a finite frequency when diamagnetic and/or finite gyro-radius effects are accounted for. It is thus important to investigate the dynamics of propagating nonlinear magnetic structures. Such structures are characterised by a current density distribution that is no longer constant on magnetic surfaces and tend to develop large currents at magnetic separatrices. In the highly non-collisional regimes of interest, an important effect limiting these large currents comes from the inertia of the electrons. In these regimes the conservation of the magnetic flux is replaced by the conservation of the generalized electron fluid momentum. In this paper we derive a set of non-linear two-component equations which describe single helicity perturbations and investigate the effect of electron inertia. A preliminary discussion is presented of the solutions in regimes where the amplitude of the perturbations exhibit spatial variations on a scale which is small compared to the ion gyro-radii. In the opposite limit, where the scale is large compared to the ion-gyroradii, the electric potential maintains the same functional dependence on the helical flux function ψ.

A set of equations is presented that describe the nonlinear dynamics of magnetic field structures, such as islands and current layers. We consider a periodic cylindrical configuration with periodicity length $2\pi R$. The magnetic field is

$$\vec{B} = \vec{B}_o + (\vec{h}/R) \times \nabla\psi, \tag{1}$$

where $\vec{B}_o$ is the helical field with constant rotational transform ι_o and $\psi = \psi(\chi, \lambda, t)$ is the helical flux function. Here, χ is the toroidal flux. The unit vector $\vec{h}$ is along helices $\lambda = \theta - \iota_o\phi =$ constant, θ and ϕ being the poloidal and toroidal angles, respectively. In the low-β ordering adopted in this paper the fluctuations of $\vec{B}_o$ are neglected. Close to the resonant surface, the helical flux function can be written as

$$\psi = \psi(\chi_o, t) + (\iota_o'/2)(\chi - \chi_o)^2 + \tilde{\psi}(\chi, \lambda, t), \tag{2}$$

where χ_o is the toroidal flux function at the rational surface where the rotational transform equals the rational value $\iota_o = n/m$. The second term in (2) represents the flux of the shear field, the last term represents a single helicity perturbation.

The set of dynamic equations consists of the electron momentum balance and continuity equation together with the ion response and the quasi-neutrality condition. We assume that the electron temperature remains constant along field lines. The dominant contribution to the inertia terms in the electron momentum equation comes from the

helical component v_h of the electron fluid velocity. This contribution can be combined with the Lorentz force by introducing the generalized flux function

$$\psi_e = \psi + (cm_e/e)Rv_h = \psi - d_e^2 J, \tag{3}$$

where $d_e = c/\omega_{pe}$ is the inertial skin depth, $4\pi J/cR$ is the helical current density, and

$$J = 2\iota_o B_o + \nabla^2 \psi. \tag{4}$$

The generalized magnetic field is $\vec{B}_e = \vec{B}_o + \vec{B}_e^*$ where

$$\vec{B}_e^* = R^{-1}\vec{h} \times \nabla \psi_e. \tag{5}$$

The component along $\vec{B}_e$ of the electron momentum balance is

$$\frac{1}{c}\frac{\partial \psi_e}{\partial t} = \frac{R}{B_o}\vec{B}_e^* \cdot \left(\nabla \Phi - \frac{T}{e}\frac{\nabla n}{n}\right) + \frac{c\eta}{4\pi} J, \tag{6}$$

Inserting the perpendicular component of the electron fluid velocity, as obtained from the momentum balance, into the electron continuity equation one has

$$\frac{\partial n}{\partial t} + \frac{c}{B_o}\nabla n \cdot \vec{h} \times \nabla \Phi = \frac{c}{4\pi e R B_o}\vec{B}_e^* \cdot \nabla J, \tag{7}$$

where Φ is the electrostatic potential. The nonlinearity in the helical flux is important near the rational surface where the perturbed field becomes of the order of the shear field. The perturbed density however is assumed to remain small with respect to the equilibrium density. This avoids the coupling to nonlinear electrostatic modes. The ion density has the form

$$n_i = n_o + (\chi - \chi_o)n_o' + \tilde{n}, \tag{8}$$

Omitting ion temperature gradients, the linear ion response is

$$\frac{1}{n_o}\frac{\partial \tilde{n}}{\partial t} = -\tau \frac{\partial}{\partial t}\frac{e\Phi}{T} + (\tau \frac{\partial}{\partial t} - \omega_* \frac{\partial}{\partial \lambda})P\frac{e\Phi}{T}, \tag{9}$$

where $\tau = T/T_i$ and $\omega_* = -(cT/e)n_o'/n_o$. The integral operator P represents the average of the electric potential over the gyro-orbit. We look for fast oscillatory solutions that depend on $m(-\omega t + \lambda)$ and evolve on a longer time scale $\hat{t}$ set by resistivity. After substitution of (8), (6) becomes

$$\frac{1}{c}\frac{\partial \psi_e}{\partial \hat{t}} - \frac{1}{c}(\omega - \omega_*)\frac{\partial \psi_e}{\partial \lambda} - \frac{\vec{h}}{B_o} \times \nabla \psi_e \cdot \nabla(\Phi - \frac{T\tilde{n}}{en_o}) = \frac{c\eta}{4\pi}\nabla^2 \psi, \tag{10}$$

where we have omitted the equilibrium helical current. On the fast time-scale where resistivity may be neglected, the solution of Eq. (10) is [1]

$$\Phi - \frac{T\tilde{n}}{en_o} = \frac{1}{c}(\omega - \omega_*)\left[\chi - \chi_o - (\frac{\psi_s - \psi_e}{-\iota_o'/2})^{1/2}\right]. \tag{11}$$

This solution reproduces the linearised expression of the potential for large $\chi - \chi_o$ where inertia is unimportant. The integration constant ψ_s and the sign of the square root in (11) have to be chosen such that Φ is odd and ψ is even in $\chi - \chi_o$. For perturbations with spatial variations on a scale that is large compared to the thermal ion gyro-radius ρ_i, $P \approx 1 + \rho_i^2 \nabla^2$. In this limit Eqs. (6), (7) and the linear response (9) become the nonlinear incompressible MHD equations, modified by diamagnetic effects and including parallel electron pressure effects in Ohm's law. When the scale of the perturbations is small compared to the ion gyro-radius, P is negligible and the perturbed density is the Boltzmann response, $\tilde{n}/n_o \approx -\tau e\Phi/T$. Here, we consider this latter case and combine the Boltzmann response with (8) and substitute the result into (7). Thus we obtain from (10) and (7), respectively

$$\frac{1}{c}\frac{\partial \psi_e}{\partial \hat{t}} - \frac{1}{c}(\omega - \omega_*)\frac{\partial \psi_e}{\partial \lambda} - \frac{(1+\tau)}{B_o}\vec{h} \times \nabla \psi_e \cdot \nabla \Phi = \frac{c\eta}{4\pi}\nabla^2 \psi, \tag{12}$$

and

$$\frac{\partial \Phi}{\partial \hat{t}} - (\omega + \frac{\omega_*}{\tau})\frac{\partial \Phi}{\partial \lambda} = -\frac{T_i c}{4\pi e^2 n R^2 B_o}\vec{h} \times \nabla \psi_e \cdot \nabla \nabla^2 \psi, \tag{13}$$

On the fast time-scale the solution of Eqs (12) and (13) are

$$\Phi = a_1\left[\chi - \chi_o - \left(\frac{\psi_s - \psi_e}{-\iota_o'/2}\right)^{1/2}\right], \tag{14}$$

and

$$\nabla^2 \psi = 2\chi_o B_o \iota_o' + a_1 a_2\left[1 - (\chi - \chi_o)\left(\frac{\psi_s - \psi_e}{-\iota_o'/2}\right)^{-1/2}\right], \tag{15}$$

where

$$a_1 = \frac{\omega - \omega_*}{c(1+\tau)}, \quad a_2 = c\frac{\omega + \omega_*/\tau}{-\iota_o'(T_i/m_e)(d_e^2/R^2)}. \tag{16}$$

An arbitrary function of ψ_e may be added to (15). This current would represent the currents inside the islands as well as the non uniformity of the shear current at large distances. In what follows we take $\tilde{\psi}$ in (2) to be approximately a single harmonic $\tilde{\psi} = \tilde{\psi}(\chi)\cos m\lambda$, where $\tilde{\psi}(\chi)$ is a weak function of χ near the resonant surface.

In the absence of inertia, i.e. $d_e \to 0$ so that $\psi_e = \psi$, $\psi_s = -\tilde{\psi}$ is the value of ψ on the separatrices with the x-points on the resonant surface at $\chi = \chi_o$. In this limit the current density (15) becomes singular at the separatrices. Inside islands the square roots have to be omitted in (14) and (15). The nonlinear dispersion relation of this single chain of propagating islands is obtained by matching the first harmonic of the total perturbed current outside the island $I_1 = -(8/3\pi)(a_1 a_2/r_o B_o)w$ where $w = (4\psi_s/\iota_o')^{1/2}$ is the half-width of the islands in terms of χ, to the boundary condition set by the standard cylindical Δ'. One obtains [1]

$$a_1 a_2 \approx (3\pi/16) r_o B_o \iota_o'(\Delta'/2) w. \tag{17}$$

In the derivation of (17) it has been assumed that the MHD boundary condition Δ' may be brought without change to distances of the order of the thermal ion gyro-radius. The high-m modes considered here are stable and have $\Delta' = -2m/r_o$, so that $a_1 a_2 > 0$ which

is consistent with linear theory [2]. The perturbed current has the direction of the shear current.

Since the current density is singular at the separatrices, electron inertia cannot be neglected and ψ_e-lines become different from ψ-lines. In the case $a_1 a_2 > 0$, ψ_e-lines have symmetrical x-points at

$$\chi_x - \chi_o = d_e^2 a_1 a_2 / \left[-2\iota_o'(\psi_s - \psi_{ex})\right]^{1/2}, \tag{18}$$

where ψ_{ex} is the value of ψ_e at the x-points.

We choose the value of $\left[(\psi_s - \psi_e)/(-\iota_o'/2)\right]^{1/2}$ at the x-point to be $(\chi_x - \chi_o)/\alpha$, where α is a function of d_e. Then, at the x-point, $\Phi = a_1(\chi_x - \chi_o)(1 - 1/\alpha)$ and $\nabla^2\tilde{\psi} = a_1 a_2(1-\alpha)$. In order to obtain regular ψ_e-surfaces such that $(\chi_x - \chi_o)/\alpha \to 0$ for $d_e \to 0$, we must require that $\alpha \sim O(d_e^\gamma)$, with $2/3 < \gamma < 2$. Thus we obtain $\psi_{ex} = \psi_s - d_e^2 a_1 a_2/2\ \alpha$ and $\psi_s = -\tilde{\psi}(\chi_x) + a_1 a_2 d_e^2[1/(2\alpha) - 1 + \alpha/2]$. Both Φ and $\nabla^2\tilde{\psi}$ change sign along the separatrix moving from the x-point towards the belly of the island. Since the potential Φ must be odd in $\chi - \chi_o$, ψ_e-surfaces have to be unconnected in the region between the ψ_e and ψ separatrices. The most outward ψ_e -separatrix is given by

$$\chi - \chi_o = [\alpha a_1 a_2 d_e^2/(-\iota_o')]^{1/2} + \left[2(-\tilde{\psi}(\chi_x)/\iota_o')(1 + \cos m\lambda)\right]^{1/2}. \tag{19}$$

The first term represents the shift between ψ_e and ψ separatrices. Electron inertia will redistribute the current, but the first harmonic of the total perturbed current in the layer will have approximately the same functional dependence on $a_1 a_2$ and on the island width w. Hence, disregarding the current between the separatrices,the dispersion relation (17) is reobtained.

If one assumes that the leading terms, i.e. the second and third term, in (12) remain odd functions of $m\lambda$ on the resistive time scale, then an estimate for the resistive evolution of the island width can be obtained by balancing the first term in (12) with the resistive term. As long as the shift (18) of the x-point is smaller than the width of the ψ-island, the familiar linear decay in time is obtained [3].

When $a_1 a_2 < 0$, the perturbed current has the opposite sign compared to the shear current. In this case ψ_e-islands that correspond to ψ-islands do not exist. Hence $a_1 a_2 < 0$ is not consistent with the assumed existence of "constant-ψ" islands.

[1] B.B. Kadomtsev, Nucl Fus, **31**, 1301, 1991.
[2] F. Pegoraro and T.J. Schep, Plasma Phys Contr Fus, **28**, 647, 1986
[3] P. H. Rutherford, Phys Fluids, **11**, 1903, 1973

Acknowledgements. This work was performed as part of the research programme of the association agreement of Euratom and the "Stichting voor Fundamenteel Onderzoek der Materie" (FOM) with financial support from the "Nederlandse Organisatie voor Zuiver-Wetenschappelijk Onderzoek" (ZWO) and Euratom, and with financial support from the "Consiglio Nazionale delle Ricerche" of Italy and from the "Associazione per lo Sviluppo Scientifico e Tecnologico del Piemonte" of Turin.

MAGNETIC RECONNECTION IN ELECTRON-MAGNETOHYDRODYNAMICS

S.V. BULANOV [a], F. PEGORARO [b] and A.S. SAKHAROV [a]

a) General Physics Institute Academy of Sciences USSR, Moscow, USSR.
b) Dept. of Theoretical Physics, University of Turin, Turin, Italy

The magnetic field dynamics and reconnection processes in a highly conducting plasma are investigated in regimes where Ohm's law is dominated by the Hall term using a single (electron) fluid description (Electron-magnetohydrodynamics). In these regimes, which correspond to the frequency range of the so called whistler mode, the electromagnetic field is nearly force-free: $(\boldsymbol{j} \times \boldsymbol{B})/c + en_e\boldsymbol{E} = 0$.

Small scale magnetic reconnection occurs near surfaces where $\boldsymbol{k}\cdot\boldsymbol{B} = 0$, *and tearing-type modes can be unstable due to the effect of electron inertia. The evolution of the magnetic field in the vicinity of an X- line is discussed and the propagation of whistler waves is shown to result in the steepening of their wave front and in the increase of the electric current density . A class of exact self-similar solutions is obtained which describe, within the scope of a local approximation, the magnetic collapse of three-dimensional magnetic configurations leading to the formation of flat electric current sheets. Finally, the rate of reconnection in the electron-magnetohydrodynamic frequency range is estimated in a steady state approximation.*

Electron-magnetohydrodynamics, EMHD for short, can be adopted[1] to describe the plasma behaviour in the frequency range between the ion and the electron cyclotron frequencies, corresponding to the range of propagation of the whistler mode. In this description the ions are assumed to remain at rest, and the plasma is quasi-neutral. An important similarity between ordinary MHD and EMHD arises from the fact that both theories lead to the conservation of the magnetic flux when resistive dissipation and/or electron inertia effects are neglected. In MHD the magnetic field is frozen in the plasma flow, whereas in EMHD it is frozen in the flow of the electrons. The EMHD equations are obtained from the two-fluid system of equations by considering the limit of small scale lengths L, $L \ll d_i$, where $d_i = c/\omega_{pi}$ is the ion inertial skin depth, and of frequencies $\omega \gg \Omega_i$, the ion cyclotron frequency. In this limit $v_i \ll v_e$, so that the ions can be treated as an immobile neutralising

background, and the current density **J** can be expressed in terms of the electron velocity through the relationship

$$\mathbf{v}_e = -(\mathbf{J}/ne) = -\alpha \nabla \times \mathbf{B}, \tag{1}$$

where $\alpha = c/(4\pi ne)$. If the plasma density is uniform, the electron flow is incompressible ($\nabla \cdot \mathbf{v}_e = 0$) so as to maintain quasi-neutrality. Neglecting resistivity, we have

$$\partial(\mathbf{B} - d_e^2 \Delta \mathbf{B})/\partial t = -\alpha \nabla \times [(\nabla \times \mathbf{B}) \times (\mathbf{B} - d_e^2 \Delta \mathbf{B})], \tag{2}$$

where $d_e = c/\omega_{pe}$ is the electron inertial skin depth. The field $\mathbf{B} - d_e^2 \Delta \mathbf{B}$, which reduces to **B** for scale lengths much larger than d_e, is frozen in the electron flow. Linearising Eq.(2) in a uniform magnetic configuration gives the dispersion relation of small amplitude whistler modes $\omega = \alpha B_o k k_\parallel / (1 + k^2 d_e^2)$.

First we investigate the onset of tearing modes with frequency in the range of the whistler waves [tearing modes in this range were first derived in Ref.2]. We refer to the one-dimensional equilibrium configuration $\mathbf{B}_o = B_{oz}\mathbf{e}_z + B_{oy}(x/L)\,\mathbf{e}_y$, with $L \gg d_e$, current density $J_o = (c/4\pi L)\, B'_{oy}$, and constant particle density. We consider two-dimensional perturbations $\mathbf{B} = \mathbf{b}(x) \exp(\gamma t + iky)$, linearise Eq. (2) and obtain

$$\gamma \left[1 + d_e^2 \left(k^2 - \frac{d^2}{dx^2}\right)\right] b_z = -\alpha B_{oy} \left(k^2 - \frac{d^2}{dx^2}\right) b_x - \alpha \left(\frac{d^2 B_{oy}}{dx^2}\right) b_x, \tag{3}$$

$$\gamma \left[1 + d_e^2 \left(k^2 - \frac{d^2}{dx^2}\right)\right] b_x = \alpha k^2 B_{oy} b_z . \tag{4}$$

We look for modes such that $\gamma \tau_W \ll 1$ with $\tau_W = L^2/(a B'_{oy})$ the whistler time. Then, a quasi-static approximation holds in an external region, $|x| \gg \delta$, $\delta \ll L$. In this region Eqs. (3,4) reduce to the well-known equation

$$\left(k^2 - \frac{d^2}{dx^2}\right) b_x + \left(B_{oy}^{-1} \frac{d^2 B_{oy}}{dx^2}\right) b_x = 0, \tag{5}$$

with $b_z/\gamma = b_x/(\alpha k^2 B_{oy})$ playing the role of the x-component of the displacement in the MHD equations. As in the MHD case, Eq.(5) defines a logarithmic jump parameter Δ'. In the internal region $k^2 \ll d^2/dx^2$, and Eqs. (3,4) reduce, in the appropriate dimensionless variables, to

$$\gamma \left[1 - d_e^2 \frac{d^2}{dx^2}\right] b_z = x \frac{d^2}{dx^2} b_x , \qquad \gamma \left[1 - d_e^2 \frac{d^2}{dx^2}\right] b_x = x k^2 b_z . \tag{6}$$

Assuming $k^2 \sim O(\delta^o)$, we obtain the "constant -ψ" ordering $d^2 b_x/dx^2 \sim b_x/\delta$, $d^2 b_z/dx^2 \sim b_z/\delta^2$ which, in the case of the EMHD tearing modes, gives $\delta \sim \gamma \sim d_e^2$. Thus the first of Eqs. (6) becomes $-\gamma d_e^2 d^2 b_z/dx^2 = x d^2 b_x/dx^2$ and Eqs. (6) are formally equivalent to the MHD layer equations. An alternative formulation can be obtained[3,4] in terms of a Fourier representation.

This latter procedure can be conveniently extended to large values of Δ' where the "constant - ψ" ordering breaks. The resulting dispersion relation[3] for $\Delta' > 0$ is

$$\gamma = (\Delta')^2 \frac{\alpha B'_{0y}}{L^2} \left[\frac{k d_e^2}{L}\right] \left[\frac{\Gamma(1/4)}{2\pi\Gamma(3/4)}\right]^2 . \qquad (7)$$

The magnetic islands thus produced differ from those found in resistive MHD and are twisted (non rigidly) due to the freezing of the magnetic field in the electron motion along the z-axis.

The properties of the wave propagation in the neighbourhood of an X-line can illustrate the type of phenomena that occur in non-uniform fields. In the case of small MHD perturbations it was found[5] that singularities in the perturbed current density form either at the X-line or at the magnetic separatrices. These singularities are related to the formation of non-linear current sheets and to magnetic field line reconnection. In the case of small amplitude whistler waves, the singularities form in the neighbourhood of the separatrices. We refer to a uniform plasma in a (current free) magnetic configuration of the form $\mathbf{B}_0 = B_{0z}\,\mathbf{e}_z + \mathbf{B}_{0\perp}(x,y)$, where $\mathbf{B}_{0\perp} = h(x\mathbf{e}_x - y\mathbf{e}_y)$, and consider two-dimensional perturbations $\tilde{\mathbf{B}}(x,y,t)$. Then

$$\frac{\partial(\tilde{B}_z - d_e^2 \Delta \tilde{B}_z)}{\partial t} = -\frac{4\pi\alpha}{c}(\mathbf{B}_{0\perp}\cdot\nabla)\tilde{J}_z\,, \quad \frac{\partial(\tilde{J}_z - d_e^2 v \tilde{J}_z)}{\partial t} = \frac{c\alpha}{4\pi}\Delta(\mathbf{B}_{0\perp}\cdot\nabla)\tilde{B}_z. \qquad (8)$$

In terms of a Fourier representation, with $\zeta = k_x k_y$ and $r = |k_x/k_y|^{1/2}$, we obtain

$$\frac{\partial^2 [1+d_e^2\,\zeta(r^2+1/r^2)]\,\hat{J}_z}{\partial t^2} = \zeta(r^2+1/r^2)\, r \frac{\partial}{\partial r}[1+d_e^2\,\zeta\,(r^2+1/r^2)]^{-1} r \frac{\partial}{\partial r}\hat{J}_z. \qquad (9)$$

The behaviour of $\hat{J}_z(k,q,t)$ for $k_x, k_y \to \infty$ determines the form of $\tilde{J}_z$ in the neighbourhood of the separatrices. If electron inertia is neglected, a steepening of the mode amplitude occurs[3] similar to that found[5] for MHD modes. However, when the effect of electron inertia is included, the perturbed current density distribution remains singular. This behaviour differs from that of a finite electron conductivity which is sufficient to regularize MHD perturbations.

The phenomenon of magnetic collapse of three-dimensional configurations in EMHD can be illustrated by considering self-similar solutions[3,6,7]. The electron flow is assumed to consist of a uniform deformation and the magnetic field to be of the type

$$x_i(t) = M_{ij}(t)\, x_j^0 + m_i(t), \qquad B_i(\mathbf{x},t) = C_i(t) + B_{ij}(t)\, x_j + A_{ijk}(t)\, x_j\, x_k. \qquad (10)$$

while the time evolution of the coefficients $A_{ijk}(t)$, $B_{ij}(t)$, $C_i(t)$, $M_{ij}(t)$, and $m_i(t)$ is given by

$$A_{ik\ell}(t) = M_{ij}\, A_{jmn}(0)\, M^{-1}_{mk}\, M^{-1}_{n\ell}, \quad B_{ik}(t) = (M_{ij}(B_{jm}(0)M^{-1}_{mk} - 2A_{jmn}(0)\, M^{-1}_{nk}\, M^{-1}_{m\ell}\, m_\ell),$$

$$C_i(t) = M_{ij}(C_j(0) - d_e 2A_{j\ell\ell}(0)B_{jm}(0)M^{-1}_{mn}m_n + A_{jmn}(0)M^{-1}_{m\ell}M^{-1}_{nk}m_\ell m_k) + d_e 2A_{i\ell\ell}(t),$$

$$\dot{M}_{ij} = -2\alpha\,\varepsilon_{ik\ell}\, M_{\ell m}\, M^{-1}_{nk}\, A_{mnj}(0), \qquad \dot{m}_i = -\alpha\,\varepsilon_{ik\ell}\, M_{\ell m}\, B_{mn}(0)\, M^{-1}_{nk}. \qquad (11)$$

For illustration we consider the two-dimensional configuration given by $A_{123}(0) = A_{132}(0) = f_1$, $A_{213}(0) = A_{231}(0) = f_2$, with all other coefficients of $A_{ijk}(0)$ equal to zero. If $f_1 f_2 > 0$, the field lines are hyperbolae, and we find that the angle between the separatrices tends to zero i.e., the configuration becomes one-dimensional. If $f_1 f_2 < 0$ the field lines are ellipses, but become circles in a finite time while $|B| \to \infty$, and the configuration becomes axially symmetric.

Singular distributions of the electric current occur naturally within the framework of EMHD in the neighbourhood of a hyperbolic magnetic structure with a zero line. Magnetic field line reconnection occurs inside a thin current sheet, with thickness a and width $b \gg a$. The electrons flow towards the current sheet with velocity v_{in} along the y-axis, together with the frozen-in magnetic field. Due to the tension of the field lines the electrons are ejected from the sheet with a velocity v_{out} along the x-axis. Inside the current sheet, electrons move also in the z-direction with velocity v_z, producing a current density along z, displacing the field lines and creating a z-component of **B**. The velocities v_{in} and v_{out} are connected by the particle conservation condition $b\, v_{in} = a\, v_{out}$. From Maxwell's equations we obtain $B_x/a \equiv (4\pi en/c)v_z$, and $B_z/a \equiv (4\pi en/c)v_x$. Imposing the condition that the reconnection process is stationary we have $E_y = 0$, i.e. $B_z\, v_{out} = B_x\, v_z$ and finally $B_z = B_x$, and $v_{out} = v_z$. In agreement with the conservation of the canonical electron momentum we have $v_z = eA_z/(m_e c) \sim a\, eB_x/(m_e c)$, where A_z is the z-component of the vector potential. Then it follows that

$$a \sim d_e = c/\omega_{pe}\,, \qquad (12)$$

i.e., the thickness of the current layer in EMHD is determined by electron inertia. The strength of the magnetic field in the vicinity of the hyperbolic zero-line is proportional to the distance r from this line, $|\mathbf{B}| \propto hr$, thus we obtain

$$v_{in} = v_{out}\,(a/b) \sim hc/(4\pi en) = \alpha h. \qquad (13)$$

The width b of the sheet is determined by the condition that the strength $(2I/bc)$ of the magnetic field generated by the total current I flowing in the sheet be of the order of the background field hb, which leads to $b \sim (2I/hc)^{1/2}$.

References

[1] A.S.Kingsep, K.V.Chukbar and V.V.Yan'kov, in "Reviews of Plasma Physics ", edited by B.Kadomtsev (Consultants Bureau, New York, 1990) vol.**16**, p 243. [2] S.V.Basova, S.A.Varentsova, A.V.Gordeev, A.V Gulin, V.Yu.Shuvaev, Sov. J. Plasma Phys. **17**, 362, (1991). [3] S.V.Bulanov, F.Pegoraro and A.S.Sakharov, Phys of Fluids **B**, in press. [4] F.Pegoraro and T.J.Schep, Plasma Phys. and Contr. Fus. **28**, 647, (1986). [5] S.V.Bulanov, F.Pegoraro and S.G.Shasharina, Plasma Phys. and Contr. Fus. **32**, 377, (1990). [6] S.V.Bulanov and M.A.Ol'shanetskij, Phys. Lett. **100A**, 36, (1984). [7] S.V.Bulanov and M.A.Ol'shanetskij, Sov. J. Plasma Phys. **11**, 425 ,(1985).

II-1433

Radial propagation of microturbulence in tokamaks

X.Garbet, L.Laurent, J.P. Roubin, A.Samain

Association Euratom CEA DRFC/ SPPF
CEN Cadarache F-13108 St Paul lez Durance France

I Introduction

Energy confinement time in tokamaks exhibits a clear dependence on global plasma parameters. This is not the case for transport coefficients of which dependence on local plasma parameters cannot be precisely established. The aim of the present paper is to give a possible explanation of this behaviour: turbulence propagates radially because of departure from cylindrical geometry. This implies that the turbulence level at a given point and hence transport coefficients are not only functions of local plasma parameters. A quantitative estimate of the propagation velocity is given derived from a Lagrangian formalism. Two cases are considered: the effect of toroidicity (section 2) as already qualitatively discussed in [1] and the effect of non linear mode-mode coupling (section 3). In the last section, the consequences of this model are discussed. This process does not depend on the type of instability. For the sake of simplicity only electrostatic perturbations will be considered in the present paper.

II Toroidal coupling

In cylindrical approximation, an electrostatic perturbation U(x,t) can be expressed as:

$$U(x,t) = U_0(r-r_m)\, e^{-i\omega t+im\theta-in\phi} \qquad (1)$$

In (1), θ (ϕ) is the poloidal (toroidal) angle, r is the minor radius and r_m its value at the resonant surface where the safety factor q is equal to m/n. The radial eigenfunction function U_0 is assumed to be even. In toroidal geometry U(x) is described by a sum of modes:

$$U(x,t) = \sum_m U_m(r-r_m)\, e^{-i\omega t+im\theta-in\phi} \quad \text{with} \quad U_m(r-r_m) = f(r_m)\, e^{im\delta}\, U_0(r-r_m) \qquad (2)$$

The modes are assumed to have the same shape U_0 and a phase mismatch δ between modes is allowed. Their amplitude is a slowly varying function f(r). If f is a constant, expression (2) is equivalent to the ballooning representation. Lets $\rho(U)$ be the plasma charge response to U. The self consistency (i.e. plasma quasineutrality) can be expressed by stating that the functional $\mathbb{L}(\omega,U,U^*) = \int dr\, \rho(U)\, U^*$ is extremum in U^*. Note that at the extremum $\mathbb{L}$ must be equal to zero. It can be shown that the energy balance of a mode is obtained developing $\mathbb{L}(\omega,U,U^*)$ around a zero growth rate state ($\gamma=\mathrm{Im}\omega \ll \omega$) and multiplying by ω the imaginary part:

$$\mathbb{L}(\omega+i\gamma,U,U^*)=0 \quad \text{then} \quad \gamma\,\omega\,\frac{\partial}{\partial\omega}\,\mathrm{Re}\mathbb{L}(\omega,U,U^*) + \omega\,\mathrm{Im}\mathbb{L} = 0 \qquad (3)$$

The first term represents the growth of the energy content of the mode , $W = \omega \frac{\partial}{\partial \omega} \mathrm{Re}\, \mathbb{L}$ and the second one, $P = \omega \mathrm{Im} \mathbb{L}$, is the power exchanged between the mode and the particles. The functional is a sum over mode numbers m and particle species s (temperature T_s, density n_s, and diamagnetic frequency $m\omega_s^*$):

$$\mathbb{L}(\omega,U,U^*) = \sum_m \sum_s \left(\mathbb{L}^{m,s}_{cyl}(\omega,U,U^*) + \mathbb{L}^{m,s}_{coupling}(\omega,U,U^*) \right) \quad (4)$$

We consider that part of the functional corresponding to a mode m characterized by its resonant surface r_m. In the following $\rho = r - r_m$, and $d = r/ms$ is the distance between two adjacent resonant surfaces, R the major radius and s the shear parameter. The "cylindrical" part reads:

$$\mathbb{L}^{m,s}_{cyl} = \frac{n_s e^2}{T_s} f^2(md)\, 4\pi^2 Rr \int d\rho \left(U_o^2 - \left\langle \left(\frac{\omega - m\omega_s^*}{\omega - \rho d^{-1} v_{//}/qR} \right) |J_o U_o|^2 \right\rangle \right) \quad (5)$$

The first term represents the adiabatic response, the second one the non adiabatic response where the denominator is the standard Landau damping term, and J_o accounts for the cyclotron motion. For the sake of simplicity trapped particle response is not expressed. The part related to toroidal coupling is only significant for ions:

$$\mathbb{L}^{m,i}_{coupling}(\omega,U,U^*) = - \sum_{\varepsilon=-1,+1} \frac{ne^2}{T_i} f((m+\varepsilon)d)\, f(md) e^{i\varepsilon\delta}\, \mathbb{I}_\varepsilon \quad (6)$$

$$\text{with} \quad \mathbb{I}_\varepsilon = 4\pi^2 Rr \int d\rho \left\langle \frac{\omega - m\omega_i^*}{\omega - \rho d^{-1} v_{//}/qR} \Delta(v_{//}) \left[r\frac{\partial}{\partial \rho} - \varepsilon m \right] J_o U_o(\rho - \varepsilon d)\, J_o U_o^*(\rho) \right\rangle \quad (7)$$

The coupling contains two terms $\varepsilon = +/-1$ corresponding to the interaction of the mode m with its two neighbours. The toroidal coupling strength is determined by the parameter $\Delta(v_{//})$, the horizontal shift of the trajectory normalized to the minor radius ($\Delta \approx q\rho_{thi} V_{//}/2rV_{thi}$). Since $U(\rho)$ is even and $\Delta(v_{//})$ is odd the two integrals $\mathbb{I}_\varepsilon$ in $\mathbb{L}^m_{coupling}$ are equal. Hence:

$$\mathrm{Im}\, \mathbb{L}^m_{coupling}(\omega,U,U^*) = \frac{ne^2}{T_i} \left(2\cos\delta f^2(md)\, \mathrm{Im}\, \mathbb{I}_1 + d\sin\delta \frac{df^2(x)}{dx} \mathrm{Re}\, \mathbb{I}_1 \right) \quad (8)$$

The mode is driven by a power source from the particles which exists in cylindrical geometry $P = \mathrm{Im}\, \mathbb{L}^m_{cyl}$ and an additional term proportional to $\cos\delta\, \mathrm{Im}\, \mathbb{I}_1$ due to toroidicity. When $\delta \neq 0$ a new term appears which can be expressed as the divergence of an energy flux:

$$\phi(x) = \frac{n_i e^2}{T_i} d \sin\delta\, \omega \mathrm{Re}\mathbb{I}\, f^2(x) \quad (9)$$

Dividing Φ by the energy density W, a group velocity can be obtained, $V_{group} = \Phi/W$. It should be noted that one has also $V_{group} = d\frac{\partial}{\partial\delta}\mathbb{L}^m \Big/ \frac{\partial}{\partial\omega}\mathbb{L}^m$ as already found in [1]. Using

expressions (5- 7), a simplified expression of V_g can be found neglecting Larmor radius effects and velocity dependance of $\Delta(v_{//})$ and of diamagnetic frequency.

$$V_{group} = \frac{V^* k_\theta \rho_{thi}}{s} \sin\delta \left(\int d\rho \ Re \ (1+\frac{1}{k_\theta \partial r}) \ U_o(\rho-\varepsilon d) U_o^*(\rho) \right) \left(\int d\rho \ |J_o U_o|^2 \right)^{-1} \qquad (10)$$

This velocity is a fraction of the diamagnetic one. It can be noted that modes with $\delta=0(\pi)$, i.e. ballooned on the equatorial plane do not propagate, and that the direction of propagation depends on the sign of δ i.e. whether the mode is ballooned at the top or the bottom of the plasma. This can be understood arguing that energy is taken to the mode by particle escaping from the larger amplitude zone by curvature drift.

III Non linear coupling

The turbulence can be described as a superposition of modes localized around resonant surfaces r. Each mode is characterized by the triple index $L_\alpha=(m_\alpha,n_\alpha,v_\alpha)$ giving poloidal, toroidal wavenumber and frequency. By analogy with first case, a "standard shape" is assumed, $U_o(r-r_\alpha)$, multiplied by a complex amplitude u_α the time average of which does not depend on space. The gradient of the turbulence level is represented by the function $f(r_\alpha)$:

$$U(x,t)=\sum_{L_\alpha} U_\alpha(r-r_\alpha) \, e^{i(m_\alpha\theta(t)+n_\alpha\phi(t)-v_\alpha\omega t)} \qquad U_\alpha(r-r_\alpha) = f(r_\alpha) \, u_\alpha U_o(r-r_\alpha) \qquad (11)$$

For a given mode L_α, the cylindrical part is given by (5) and the non linear part reads :

$$\mathbb{L}^{\alpha}_{coupling} = -\sum_{\beta} \frac{ne^2}{2T_i} f(r_\alpha) \, f(r_\beta) \, f(r_{\alpha-\beta}) \, u_\alpha^* u_\beta \, u_{\alpha-\beta} \, \mathbb{I}_{\alpha,\beta} \qquad (12)$$

$$\mathbb{I}_{\alpha,\beta} =$$

$$4\pi^2 R r \, PP \int \frac{dK_\alpha dK_\beta}{4\pi^2} \left\langle \frac{i\Gamma_{\alpha,\beta}(m_\beta(K_\alpha-K_\beta)-(m_\alpha-m_\beta)K_\beta)}{v_\alpha \omega r} U_o^*(K_\alpha) U_o(K_\alpha-K_\beta) U_o(K_\beta) \right\rangle e^{-i\Lambda(K\alpha,K\beta)}$$

and $\Lambda(K\alpha,K\beta) = K\beta(r\beta-r\alpha)-(K\alpha-K\beta)(r\alpha-\beta-r\alpha)$ and $\Gamma_{\alpha,\beta} = \frac{\omega_i^*}{\omega B}\left(\frac{m\beta}{v\beta} - \frac{m_\alpha-m\beta}{v\alpha-v\beta}\right)$

Using an expansion of f around r_α in (12) one obtains a first term proportional to $f^3(r_\alpha)$ which gives the average power lost by the mode α by coupling with is neighbours and a second one which can be expressed as:

$$-\frac{ne^2}{2T_i}\frac{df^3}{dr}(r_\alpha)\sum_\beta \frac{(r_\beta+r_{\alpha-\beta}-2r_\alpha)}{3}\,\mathrm{Im}\left(\mathbb{I}_{\alpha,\beta}\,u^*_\alpha u_\beta u_{\alpha-\beta}\right) \qquad (13)$$

This equation is similar to equation (8) except that there is a sum over many modes. The main difference is the phase between interacting modes is not so well defined as in toroidal case where it was +/- δ. The integral $\mathbb{I}_{\alpha,\beta}$ is slowly varying with modes and in a first approximation can be taken constant. The term $(r_\beta+r_{\alpha-\beta}-2r_\alpha)(u^*_\alpha u_\beta u_{\alpha-\beta})$ is the analog of dδ in section 2. If it is constant in space, (13) is the divergence of an energy flux. Using the mixing length rule to estimate the turbulence amplitude, a group velocity which is a fraction of the diamagnetic velocity is found. Nevertheless the constant phase matching has not been proven in the present paper and one can also envisage that the "average phase" in (13) is random. In this case the energy flux propagates by jumps of order of the turbulence scale i.e. a few times the ion Larmor radius at εv* where ε lies between -1 and +1. It is found that turbulence amplitude has a diffusive behaviour with $D \approx 1 m^2 s^{-1}$.

IV Discussion:

The profile of turbulence level in tokamaks appears to be controlled by two processes:
- The energy source which is approximatively given by its expression in cylindrical geometry.
- A radial propagation of energy contained in fluctuations at velocities scaling like the diamagnetic velocity. It may be due to the toroidal coupling as well as non linear coupling of modes localized on neighbouring magnetic surfaces. Toroidal coupling convects energy while non linear coupling may create a convection or a diffusion since phase matching between adjacent modes makes both behaviours possible. It should be noted that, as this is the case for standard waves, propagation can be hampered by impedance mismatch due for example to diamagnetic velocity shear.

Some practical consequences are expected. The heat conductivity may not depend on local parameter but rather on a weighted stability of the whole profile. For instance the turbulence level at the plasma edge could be dominated by the influence of turbulence propagating from the SOL rather than local stability. As already discussed in [1] this model explains some features of the turbulent front observed during pellet injection.

References

[1] X. Garbet, L.Laurent, F.Mourgues, A.Samain, J.P. Roubin Proc. 16th European Conference. Venice 1989, edited by S.Segre, H.Knœpfel, E.Sindoni (Vol I p 299)

ON THE THRESHOLD OF THE ION TEMPERATURE GRADIENT DRIVEN MODE

S.C. Guo[+], F. Romanelli, G. Rewoldt[++], W.M. Tang[++]
Associazione EURATOM-ENEA sulla Fusione, Centro Ricerche Energia Frascati,
C.P. 65 - 00044, Frascati, Rome (Italy)

The ion temperature gradient driven mode (η_i-mode η_i=dln T_i/dln n) is believed to play a major role in affecting the energy transport in Tokamak devices. The η_i-mode dynamics near threshold is affected by several kinetic effects. In this paper an unified picture of the η_i-mode dynamics is provided by using a model differential equations and general explicit expressions for the threshold valid in all the parameter range of interest for a tokamak are given. It is found that this result is in very good agreement with that of the numerical solutions of the full kinetic integral equation /1/.

The stability analysis is separated into two parts, short and long wavelength limits. The assumptions of a pure plasma with circular shape and low-β equilibrium are used here and the electrostatic approximation is employed. Nevertheless the range of validity of our results cover all the collisionality domain of interest, long and short wavelengths, and moderately low and finite shear, peaked and flat density profiles. In addition we fully account for the effects related to toroidal geometry.

In the short wavelength limit ($k_\theta \rho_i \approx \varepsilon_T^{1/4}$), the mode has a moderate or strong ballooning structure, hence the strong coupling approximation can be applied /2/. Within this approximation the magnetic drift resonance can be replaced with the value at θ=0, and the ion responses can be conveniently obtained by solving the gyrokinetic equation in the real space, rather than in ballooning space. The quasineutrality equation is then given by

$$\frac{b_s}{\tau} s^2 \frac{d}{dz} B(z) \frac{d\phi}{dz} - [1 + \frac{1+\delta_T}{\tau} - A(z) + \frac{b_s}{\tau} B(z) - \frac{b_s}{2\tau} s^2 \frac{d^2}{dz^2} B(z)] \phi = 0 \qquad (1)$$

with

$$A(z) = \int d^3 v_\parallel F_M \frac{\omega - \omega_{*Ti}}{\omega - \omega_{Doi} - (v_\parallel/qR) z}, \qquad B(z) = \int d^3 v F_M v_\parallel^2 \frac{\omega - \omega_{*Ti}}{\omega - \omega_{Doi} - (v_\parallel/qR) z} \qquad (2)$$

and

$$\delta_T(\omega) = -\frac{2}{\sqrt{\pi}} (2\varepsilon)^{1/2} \int_0^\infty dE E^{1/2} \frac{\omega - \omega_{Te}}{\omega - \overline{\omega_{De}} + i\nu_{eeff} E^{-3/2}} e^{-E} \qquad (3)$$

+ Permanent address: Institute of Physics, Chinese Academy of Sciences, P.O. Box 603, 100080, Beijing, P.R. China
++ Princeton Plasma Laboratory, Princeton University, P.O. Box 451, Princeton, N.J. 08544

where ϕ is the electrostatic potential, $\omega_{*Tj}=\omega_{*j}[1+\eta_j(E-3/2)]$, $\omega_{Doj}=-2ck_\theta T_j/(e_jBR)$ $(v_\perp^2/2+v_\parallel^2)$, $\omega_{*j}=-ck_\theta T_j/(e_jBL_{nj})$, the velocity is normalized to the thermal velocity $v_{tj}=(2T_j/m_j)^{1/2}$, $E=v^2$ is the energy, δ_T is related to the trapped electron response, ω_{De} is the bounce averaged electron magnetic drift frequency. The term proportional to B(z) is associated to the finite Larmor radius correction. Note that in Eq. (1), the parallel ion dynamics, the magnetic drift resonance and the finite Larmor radius corrections are all taken into account. The trapped ion contribution is neglected here because from the ordering scheme we have $\omega\approx\omega_{ti}\,\varepsilon_T^{-1/4}>\omega_{bi}$, and $k_\perp\rho_{bi}\approx k_\perp\rho_i\varepsilon^{-1/2}\approx\varepsilon_T^{1/4}\,\varepsilon^{-1/2}\gg 1$. So the trapped ions are expected to have a very weak effect on the mode.

It is convenient to neglect at first the effect of trapped electrons. The numerical solutions of Eq. (1) is shown in Fig. 1 in the η_i vs. ε_n plane for $b_s=0.1$, $\tau=1$, s=q=1 (curve c). We can see that for $\varepsilon_n\to 0$, the threshold approaches an almost constant value $\eta_{ic}\approx 1.2$, while in the flat density limit a convenient representation for the threshold is

$$\varepsilon_{Tc}=[\frac{4}{3}(1+\frac{1}{\tau})(1+\alpha_T\frac{s}{q})]^{-1} \tag{4}$$

with $\alpha_T\approx 2$. For $q\to\infty$ Eq. (4) can readily recover the result from the local theory given by Ref. 2 (curve a) and it is also qualitatively similar to that of Ref. 3 in the sheared slab limit ($s/q\gg 1$) shown in curve b. Moreover, this result is, within 10% in agreement with the result of the full numerical solution presented in Ref. 2 ($\eta_{ic}\approx 4$ for $\tau=1$, s=0.5 and q=1.5 instead of $\eta_{ic}\approx 4.4$ from Eq. (4)) where the effect of the modulation of the parallel velocity along the magnetic field line was neglected. The result is also in broad agreement with analysis of the full equation in Ref. 4 which found $\varepsilon_{Tc}=\varepsilon_n/\eta_{ic}=0.2$ for $\tau=1$, s=0.5 and q=1.5, while Eq. (4) predicts $\varepsilon_{Tc}=0.225$. In order to understand the physical origin of the threshold, the full kinetic integral equation /1/ has been solved in the flat density limit obtaining the threshold value $\varepsilon_{Tc}=0.165$ for adiabatic electrons and full (trapped and circulating) ion responses. The value of the threshold is insensitive to trapped ion dynamics, as expected in the short wave length limit. The numerical solution using only the circulating ion response yields $\varepsilon_{Tc}=0.178$ for $b_s=0.1$, $\tau=1$, s=1 and q=1.5, while for the same parameters, according to our expression Eq. (4), we have $\varepsilon_{Tc}=0.16$. In Fig. 2 we compare the mode frequencies and

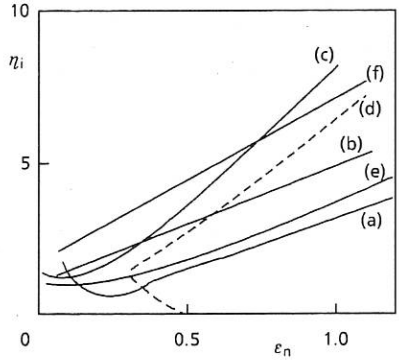

Fig. 1

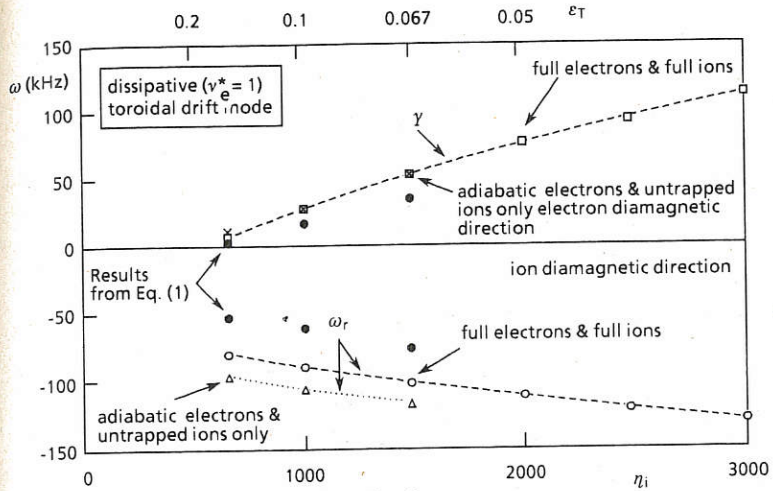

Fig. 2

growth rates between the two approaches where the solid points are the results from Eq. (1), others are from the integral equation (1). The above results indicate that trapped ion effects are negligible in the determining the threshold in the short wavelength region. Meanwhile, the good agreement between the threshold obtained from Eq. (1) and that obtained from the full kinetic equation shows that the strong coupling approximation used in our analysis is well valid.

We now consider the effect of the trapped electron dynamics on the stability of the mode. We can expect very little effect in the flat density limit because the strongly stabilizing mechanism associated to the ion resonances cannot be overcome by the destabilizing effect of the trapped electron dynamics /5/. This is indeed shown in Fig. 1 where the results for ε=0.15, b_s=0.1, s=q=τ=1 and ν_e^*=0 are plotted (curve d). This conclusion is also consistent with that from integral equation in the flat density limit which yield ε_{Tc}=0.169 and ε_{Tc}=0.165 for ν_e^*=0 and ν_e^*=1 respectively. For low ε_n values the mode propagates in the electron diamagnetic direction and it is not affected by the ion magnetic drift resonance. However the ion Landau resonance still provides a strong stabilizing mechanism and we can expect that, unless the trapped electron response is large, the mode is stable. From Fig. 1 it is possible to see that for electron collisionality sufficiently low the mode can be unstable below $\eta_{ic} \simeq 1.2$. For high values of collisionality the trapped electron response is small and the mode is strongly stable.

In the long wavelength limit ($k_\theta \rho_i \ll \varepsilon_T^{1/4}$), the eigenfunction becomes broad and the strong coupling approximation can no longer be applied. In this case, two branches exist, a toroidal and slablike branch /6/. In present paper attention is focused on the

slab like branch, which has the mode structure along the equilibrium magnetic field dominated by the secular scale, with superimposed small oscillations on the connection length scale. It is convenient to employ two scale analysis to solve the gyrokinetic equation for the ion responses. Upon introducing as a smallness parameter $\delta=k_\theta\rho_i$, but ordering $\varepsilon_T=O(1)$, the following ordering is obtained: $\omega\approx(\omega_{pi}*k_\theta\rho_i \quad \omega_{ti})^{1/2}\approx\delta\omega_{ti}$ and $\theta\approx[\varepsilon_T{}^{1/2}/(k_\theta\rho_i)^2]^{1/2}\approx\delta^{-1}$. In this case the effect of parallel compressibility is important on the secular scale, and the stability of the mode is determined by the Landau resonance $\omega\approx k_\parallel v_{ti}$. The quasineutrality equation is solved both numerically and analytically /7/.

For collisionless ion dynamic we obtain the threshold expression in the flat density limit

$$\varepsilon_{Tc}=[(1+1/\tau)\,(2\varepsilon)^{-1/2}]^{-1} \tag{5}$$

This expression is very similar to that obtained in the short wavelength regime when parallel dynamics is neglected /2/. Below this thresholds the mode is destabilized by the trapped ion effect.

For larger values of collisionality ($\nu_{ieff}>\omega_{di}\varepsilon^{-1/2}$) the trapped ion response can be neglected everywhere. This limit is equivalent to the sheared slab case studied in Ref. 3 except that the finite Larmor radius correction are enhanced by a Pfirsch-Schluter factor ($1+2q^2\beta_2$), which accounts for the finite radial excursion of a particle due to the drift motion. The explicit expression for the threshold is

$$\varepsilon_{Tc}=[\alpha_s(b_s)(1+1/\tau)\,(s/q)\,(1+2q^2\beta_2)^{1/2}]^{-1} \tag{6}$$

where the value of α_s depends on b_s, for $b_s=0.02$ $\alpha_s\approx1.7$, and β_2 is a constant with the value around 1.5. In Fig. 1, curves e and f show the numerical solutions in the long wave length limit for $\nu_i^*=0$ and $\nu_i^*=\infty$ respectively, where the trapped electron response is neglected. Other parameters are $b_s=0.01$ $s=q=\tau=1$, $\varepsilon=0.15$.

REFERENCES

/1/ G. Rewoldt, W.M. Tang, and E.A. Frieman, Phys. Fluids 21, 1513 (1978)

/2/ F. Romanelli, Phys. Fluids **B1**, 1080 (1989)

/3/ T.S. Hahm and W.M. Tang, Phys. Fluids **B1**, 1185 (1989)

/4/ X. Garbet, L. Laurent, F. Morgues-Millot, J.P. Roubin, A. Samain, X.L. Zou, J. Chinardet in Controll. Fusion and Plasma Phys, 18th Proc. Europ. Conf., Berlin (1991), Vol. 15C, Part. IV, 21

/5/ F. Romanelli and S. Briguglio, Phys. Fluids **B2**, 754 (1990)

/6/ Liu Chen, S. Briguglio and F. Romanelli, Phys. Fluids **B3**, 611 (1991)

/7/ S.C. Guo and F. Romanelli submitted to Phys. Fluids

STABILITY AND TRANSPORT DUE TO ITG MODES IN A TOROIDAL PLASMA WITH IMPURITIES, TRAPPED ELECTRONS AND VORTEX FORMATION EFFECTS

Anders Jarmén, Mats Fröjdh, Vladimir Pavlenko* and Jan Weiland
Institute for Electromagnetic Field Theory , EURATOM-NFR Association
Chalmers University of Technology
S-412 96 Göteborg, Sweden

* Permanent address: Institute for Nuclear Research, Ukrainian Academy of Sciences, Prospekt Nauki 47, 252 028 Kiev, Ukraine

Energy losses due to the presence of impurities in fusion plasmas is well known. Also, the presence of ITG (ion temperature gradient) and trapped electron modes in Tokamaks are probably important for the transport and confinement properties /1,2/. These modes have been studied at our institute using both a toroidal fluid model and kinetic descriptions /3,4/. Stability properties have been mapped and energy and particle transport coefficients have been derived using quasi-linear theory and numerical turbulence simulations.

In this work a plasma with two ion species, background and impurities, is treated. Both species are described by a toroidal fluid model. The trapped electrons are described kinetically by the Vlasov equation with an energy dependent Krook collison term and an effective collision frequency $\nu_{ef} = \nu_{ei}/\varepsilon$ (ε = inverse aspect ratio). The untrapped electrons are assumed to follow a Maxwellian distribution at the perturbation potential ϕ. Assuming a plasma in the dissipative regime the total electron density response to ϕ will be a Boltzmann function with a non-adiabatic modification due to the dissipative trapped electron effect: $\delta n_e / n_e = (1 - i\alpha)\, e\phi / T_e$.

The trapped electron effect is,in general, destabilizing. Trapped electron instabilities and an electron particle and heat transport are set up. It turns out that a simple analytical condition for marginal stability may be derived. It can be written as

$$\eta_j = \frac{2}{3} - \frac{10}{9} b_j \pm (1 - \varepsilon_{nj}) \left(1 - \frac{5}{3} b_j \right) \frac{\sqrt{10}}{3} \qquad (1)$$

where index j refers to either the background (j=i) or the impurity (j=I) ion species. Here $\eta = L_n / L_T$, $\varepsilon_n = 2L_n / L_B$ and $b = k^2 \rho^2$ where L_n, L_T and L_E are the characteristic scale lengths ($L_n^{-1} = -(1/n)(dn/dr)$ etc.) for density,

temperature and magnetic field, k is the wave number and ρ is the Larmor radius. The stability boundaries, as given by (1), are illustrated in Fig. 1.

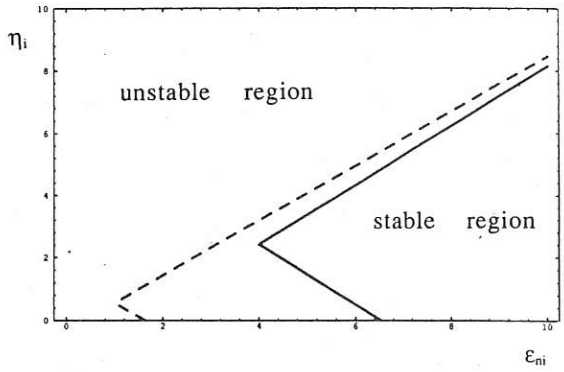

Fig. 1. Marginal stability diagram for $\varepsilon_{ni}/\varepsilon_{ni} = \eta_i/\eta_i = 0.25$, $Z_I = 4$, $b_i = 0.1$, $b_I = (9/16)\, b_i$. Dashed line ↔ background mode, full line ↔ impurity mode.

For the modes studied here we may assume a weak turbulence situation ($\omega = \omega_r + i\gamma$; $\gamma < \omega_r$). Then the quasi-linear approximation may be used to derive the diffusion coefficients. For the electrons we obtain

$$D_e = \frac{1}{2} L_{ne} \alpha \frac{k_y ce}{BT_e} |\phi|^2 \qquad (2)$$

$$\chi_e = \frac{1}{2} L_{Te} \frac{7}{3} \alpha \frac{k_y ce}{BT_e} |\phi|^2 \qquad (3)$$

and for the ions we obtain

$$D_j = \frac{1}{2} L_{nj} F_j \frac{k_y ce}{BT_e} |\phi|^2 \qquad (4)$$

$$\chi_j = \frac{1}{2} L_{Tj} G_j \frac{k_y ce}{BT_e} |\phi|^2 \qquad (5)$$

where F_j and G_j are functions of $\omega, Z_I, \varepsilon_n, \eta, \tau$ and other parameters of the two ion species. An estimation of the saturation level of the potential may be obtained by balancing the linear growth against the dominant convective non-linearity in the continuity equation. This gives $\phi = B\gamma/(ck_x)$. It turns out that inward ion particle and heat transport may exist in certain parameter regimes. The electron transport, however, is always outward. We also note that $D_e/\chi_e = 3\eta_e/7$. We consider now the transport phenomena in η_i -mode turbulence assuming that this turbulence is an ensemble of dipolar vortices. Analytical properties of these vortices were described earlier /5/. It is known, that the frequency

spectrum of the fluctuations depends on the velocity of the vortices which is coupled to the amplitude. Accordingly larger amplitude vortices give a broader spectrum in ω. It may become considerably broader than in the weakly nonlinear regime and therefore in better agreement with experiment. Let us construct a L*L 2 dimensional model in which we have N vortices randomly distributed similar to gas molecules. Each vortex then represents a separate degree of freedom of the system. We now introduce the ordering $\varepsilon = \omega / \Omega_{ci} = \upsilon / c_s \ll 1$. Then with distance between vortices $r_{in}^2 = L^2 / N$ and the radius R of the vortex we can form the dimensionless parameter (packing parameter) $\mu = R^2 / r_{in}^2 = N / N_{max}$ where $N_{max} = L^2 / R^2$ is the maximum number of vortices. We will assume that the energy density W of the perturbation is constant in the time scale of interest and that we have equipartition of energy between the degrees of freedom (vortices). Denoting the energy of each vortex by E_v we have $WL^2 = NE_v = NI\phi^2$, where I is a constant. Introducing now the characteristic wave number k = 1/R and the packing parameter μ we obtain

$$\phi = I^{-1/2} W^{1/2} \mu^{-1/2} k^{-1} \tag{6}$$

We now introduce the probability A(N) for the system to be in the N vortex state and furthermore assume these vortices to have random phases and positions. We consider a simple model of turbulence dynamics. The vortices are spontaneously excited with a rate ν_{ex} determined by the linear instability of the η_i-mode and decay due to mutual collisions after a time τ_D. In the stationary case these processes have to be in balance, leading to the formation of an inertial range with a stationary spectrum. We will now derive the approximate power dependence of the spectrum of the turbulence mentioned above. According to our previous ordering we have $\nu_{ex} \approx \varepsilon k \rho_s \Omega_{ci}$. The decay time τ_D is given by $\tau_D = L^2 / \upsilon N \sigma$ where σ is the cross section for vortex collisions which we can estimate to be of order R. Then we have $\nu_D \approx \tau_D^{-1} \approx \varepsilon \mu^{1/2} N^{1/2} c_s L^{-1}$. In the equilibrium state we then have $\nu_{ex} = A(N)\, \nu_D$ and the probability of the state is given by $A(N) = \nu_{ex} \nu_D^{-1} \approx \mu^{-1/2} N^{-1/2}$. In order to obtain the k spectrum of the turbulence we have to know the spectrum of the vortex solution and to take an ensemble average. Taking into account that the localization of the vortices in real space corresponds to a finite width in k space we can approximate the Fourier component of the potential as $\phi_k \approx \phi\, k^{-s}$ where s is positive and of order 1 and k>1/R. We will

keep s unspecified for the time being. We may now calculate the k spectrum as an ensemble average. Taking into account (6) and making the ensemble averaging we obtain

$$<|\phi_k|^2> = \int |\phi_k|^2 A(N)\, dN \approx \text{const}\ \mu^{-1} k^{-(2s+1)} \tag{7}$$

The energy is thus transferred from the region in k space where the vortices are created to the large k where the dissipative processes become important. We will now use the spectrum (7) to calculate the ion thermal conductivity. We assume that due to collisions between vortices the stream lines are reconnected and particles can move in a random walk process from one vortex to another and thereby cause anomalous transport. This assumption has been verified by numerical simulations of drift vortices. We will here consider a simple test particle diffusion picture to evaluate the thermal conductivity. We note that this gives the same result as a calculation using a fluid model in the incompressible limit. For the thermal conductivity we have

$$\chi_i = (2\pi)^{-2} \int < v_k^2 > k^{-2} D^{-1}\, dk \tag{8}$$

where < > denote ensemble average and k is the Fourier component of the particle drift velocity. Assuming now that the main drift of the particles is E x B drift we finally obtain

$$\chi_i = (2\pi)^{-1} c B_0^{-1} \left(\int |\phi_k|^2\, dk \right)^{1/2} \approx \mu^{1/2(s-1/2)}\, \phi^{s-1/2} \tag{9}$$

We now have to consider what is the most realistic value of s. This value may be different under different circumstances. One possible way of obtaining s is by comparison with experimental or numerical spectra. As an example we may take the spectrum shown in Fig.7 of Ref.6. This corresponds to $\phi\ k^{-1,5}$. A comparison with (7) then gives s=1. This corresponds to the thermal conductivity that is proportional to the square root of the potential of the perturbation. Such a dependence was first obtained in numerical simulations by Kleva and Drake. This result was confirmed by an estimate of the diffusion coefficient in the plasma with vortex flow /7/.

References.

1. R.Paccagnella, F.Romanelli, S.Briguglio, Nucl. Fus. 30, 545 (1990).
2. S.Migliuolo, Impurities and Ion Temperature Gradient Modes, JET Report 34 (1991).
3. A.Jarmén, Phys. Script. 43 , 89 (1991).
4. M.Fröjdh, M.Liljeström, H.Nordman, Nucl. Fus. 32, 419 (1992).
5. P.K.Shukla and J.Weiland, Phys.Lett. A136 , 59 (1989).
6. H.Nordman and J.Weiland, Nucl. Fus. 29, 262 (1989).
7. M.N.Rosenbluth, H.L.Berk, I.Doxas, W.Horton, Phys.Fluids 30 , 2636 (1987).

DISSIPATIVE-DRIFT WAVE INSTABILITY IN THE PRESENCE OF IMPURITY RADIATION

R. Bharuthram [a] and P. K. Shukla

Institut für Theoretische Physik, Ruhr-Universität Bochum,
D-4630 Bochum 1, Germany

[a] Permanent address: Department of Physics, University of Durban-Westville, Durban 4000, and Plasma Physics Research Institute, University of Natal, Durban 4001, South Africa.

It is believed that electrostatic fluctuations in edge plasmas are usually triggered by micro and macroscopic plasma instabilities /1/. The latter involve dissipative-drift waves as well as tearing and rippling modes in nonuniform plasmas. However, if the plasma edge contains impurity radiation, then the radiative condensation instability /2-5/ could be the cause of nonthermal fluctuations. The radiative condensation instabilities have been extensively investigated in a homogeneous plasma by many authors /2-4/. The effect of equilibrium density and electron temperature inhomogeneites in the study of radiative condensation instabilities has been examined by Shukla and Yu /5/. They found new drift-like modes driven by the combined effect of impurity radiation losss and the equilibrium density and temperature gradients. The analyses of Shukla and Yu /5/ is, however, limited to low-freuency, long wavelength collisionless drift waves. Since the edge plasma of toroidal devices is highly collisional /6/, the results of collisionless theories cannot be directly applied to explain the origin of nonthermal fluctuations.

In this paper, we study the influence of impurity radiation on the dissipative- drift wave instability in a collision-dominated nonuniform plasma embedded in a homogeneous magnetic field.

We consider a nonuniform collisional electron-ion plasma in the presence of impurity radiation and a homogeneous magnetic field $\mathbf{B}_o = B_o\hat{\mathbf{z}}$. The density and electron temperature gradients are maintained by some external sources. In the presence of low-frequency ($|\partial_t|, \nu_{ei} << \omega_{ci} << \omega_{ce}$, where $\omega_{cj} = eB_o/m_jc$ is the gyrofrequency of the j-th species (j = e(i) for the electrons(ions)) electrostatic fluctuations, the electron and ion fluid velocities are given by

$$\mathbf{v}_e \approx \mathbf{v}_{EB} - \frac{c}{eB_on_e}\hat{\mathbf{z}}\times\nabla(n_eT_e) + v_{ez}\hat{\mathbf{z}}\,, \tag{1}$$

and

$$\mathbf{v}_i \approx \mathbf{v}_{EB} + \frac{c}{eB_on_i}\hat{\mathbf{z}}\times\nabla(n_iT_i) - \frac{c}{B_o\omega_{ci}}(\partial_t + \mathbf{v}_i\cdot\nabla)\nabla_\perp\phi + \mathbf{v}_\Pi\,, \tag{2}$$

where $\mathbf{v}_{EB} = (c/B_o)\hat{\mathbf{z}}\times\nabla\phi$ is the $\mathbf{E}\times\mathbf{B}$ drift, the second term in (1) and (2) are the respective diamagnetic drifts, the third term in (2) is the ion polarization drift, $\mathbf{v}_\Pi$ is the drift associated with the collisionless viscosity tensor, ϕ is the electrostatic potential, $n_j(T_j)$ is the number density (temperature) of the j-th species, m_j is the mass, e is the magnitude of the electron charge, and c is the speed of light. For simplicity, we have ignored the ion motion parallel to the external magnetic field.

The parallel component of the electron fluid velocity v_{ez} is determined by

$$(d_t + \nu_e)v_{ez} = \frac{e}{m_e}\partial_z\left[\phi - \frac{T_{eo}}{e}\frac{n_{e1}}{n_o} - \frac{(1+\alpha)T_{e1}}{e}\right]\,, \tag{3}$$

where $d_t = \partial_t + \mathrm{v}_{EB}\cdot\nabla + v_{ez}\partial_z$, ν_e is the electron-ion collision frequency, $\alpha = 1.33\nu_e/(\nu_n + 1.87\nu_e)$, ν_n is the electron-neutral collision frequency, and the particle number density n_j and the electron temperature T_e have been expressed in terms of an equilibrium and a perturbed part as: $n_j = n_{jo}(x) + n_{j1}$ and $T_e = T_{eo}(x) + T_{e1}$ The evolution of the electron temperature perturbation is governed by the energy equation

$$\left(\frac{3}{2}d_t + \frac{1}{\tau} - D_\perp\nabla_\perp^2 - D_\parallel\partial_z^2\right)T_{e1} - \frac{3c}{2B_o}\hat{\mathbf{z}}\times\nabla T_{eo}\cdot\nabla\phi$$
$$-T_{eo}\left(d_t\frac{n_{e1}}{n_o} - \frac{c}{B_o}\hat{\mathbf{z}}\times\nabla ln\, n_o\cdot\nabla\phi\right) + \alpha T_{eo}\partial_z v_{ez} = -n_{zo}\frac{dI_z(T_{eo})}{dT_{eo}}T_{e1} - \frac{n_{zo}}{n_o}I_z(T_{eo})n_{e1}\,, \quad (4)$$

where τ is the electron energy relaxation rate, and the perpendicular ($D_\perp$) and parallel ($D_\parallel$) diffusion coefficients for $\nu_e << \omega_{ce}$ are given by $3.2T_{eo}/m_e\nu_e$ and $4.7T_{eo}\nu_e/m_e\omega_{ce}^2$, respectively. The radiation cooling rate is modelled as $n_e n_{zo} I_z(T_e)/n_o$, where n_{zo} is the average impurity density. The radiation cooling rate terms are shown on the right-hand side of (4), where the electron temperature and the number density perturbations are considered.

Inserting (1) into the electron continuity equation we obtain

$$d_t n_{e1} - \frac{c}{B_o}\hat{\mathbf{z}}\times\nabla n_o\cdot\nabla\phi + n_o\partial_z v_{ez} = 0\,. \quad (5)$$

On the other hand, substitution of (2) into the ion continuity equation yields

$$(\partial_t + \mathrm{v}_{EB}\cdot\nabla)(n_{i1} - n_o\rho_s^2\nabla_\perp^2\phi) - \frac{c}{B_o}\hat{\mathbf{z}}\times\nabla n_o\cdot\nabla\phi = 0\,, \quad (6)$$

where $\rho_i^2 \mid \nabla_\perp^2 \mid << 1$ has been assumed and the nonlinear ion diamagnetic drift contribution in the polarization drift has been neglected. Here ρ_i is the ion Larmor radius, $\rho_s = c_s/\omega_{ci}$, and $c_s = (T_{eo}/m_i)^{1/2}$ is the ion sound velocity.

The system of equations (3), (4), (5) and (6) is closed with help of the quasineutrality condition $n_{e1} = n_{i1}$, which is a good approximation for a dense plasma in which the ion plasma frequency is much larger than the ion gyrofrequency.

The local linear dispersion is now derived by assuming that the scale lengths of the density and electron temperature inhomogeneities are much larger than the wavelength of fluctuations which vary as $exp\{i(\mathrm{k}\cdot\mathbf{r} - \omega t)\}$, where k is the wave number and ω the frequency. Fourier transforming (3) and (5) and combining them, we obtain for the electron number density perturbation

$$\frac{n_{e1}}{n_o} = \left[\frac{c}{B_o}(\kappa_n k_y + k_z^2\frac{\omega_{ce}}{\nu_e})\phi + \frac{(1+\alpha)k_z^2 T_{e1}}{m_e\nu_e}\right]\left(\omega + \frac{ik_z^2 v_{te}^2}{\nu_e}\right)^{-1}\,, \quad (7)$$

where $v_{te} = (T_{eo}/m_e)^{1/2}$ is the electron thermal velocity, $\kappa_n = -dln\, n_o/dx$, and $\nu_e << \mid \omega \mid$ has been assumed. In a similar manner, from the energy equation (4) one obtains

$$(\omega + i\omega_\chi + i\gamma_T)\frac{T_{e1}}{T_{eo}} = \left[\frac{2}{3}(1+\alpha)\omega - i\gamma_n\right]\frac{n_{e1}}{n_o} - \left[\frac{2}{3}(1+\alpha)\omega_e^* - \omega_T^*\right]\frac{e\phi}{T_{eo}}\,, \quad (8)$$

where $\omega_e^* = k_y\kappa_n cT_{eo}/eB_o$,$\omega_T^* = k_y\kappa_T cT_{eo}/eB_o$ with $\kappa_T = -d\, ln\, T_{eo}(x)/dx$, $\omega_\chi = (2/3)[k_\perp^2 D_\perp + k_\parallel^2 D_\parallel + \frac{1}{\tau}]$, $\gamma_T = -\frac{2}{3}n_{zo}dI_z/dT_{eo}$ and $\gamma_n = \frac{2}{3}n_{zo}I_z(T_{eo})/T_{eo}$.

Eliminating the electron temperature perturbation from (7) and (8), we have

$$\left[(\omega+i\gamma_T)(\omega+i\frac{k_z^2v_{te}^2}{\nu_e})+\frac{(1+\alpha)k_z^2v_{te}^2}{\nu_e}\left(\frac{2}{3}(1+\alpha)\omega-i\gamma_n\right)\right]\frac{n_{e1}}{n_o}$$
$$=\left[(\omega+i\gamma_T)(\omega_e*+\frac{\omega_{ce}k_z^2c_s^2}{\omega_{ci}\nu_e})-\frac{(1+\alpha)k_z^2v_{te}^2}{\nu_e}\left(\frac{2}{3}(1+\alpha)\omega_e^*-\omega_T^*\right)\right]\frac{e\phi}{T_{eo}}. \quad (9)$$

For the ions, we obtain from (6)

$$\frac{n_{i1}}{n_o}=\left(\frac{\omega_e^*}{\omega}-k_\perp^2\rho_s^2\right)\frac{e\phi}{T_{eo}}. \quad (10)$$

We now combine (9) and (10) assuming $n_{e1}=n_{i1}$. The resultant dispersion relation reads

$$(\omega_e^*-\omega k_\perp^2\rho_s^2)\left[(\omega+i\gamma_T)(\omega+i\frac{k_z^2v_{te}^2}{\nu}-\frac{(1+\alpha)k_z2v_{te}^2}{\nu_e}[\frac{2}{3}(1+\alpha)\omega-i\gamma_n]\right]$$
$$=\omega\left[(\omega+i\gamma_T)(\omega_e^*+\frac{\omega_{ce}k_z^2c_s^2}{\omega_{ci}\nu_e}-\frac{(1+\alpha)k_z^2v_{te}^2}{\nu_e}[\frac{2}{3}(1+\alpha)\omega_e*-\omega_T*]\right]. \quad (11)$$

Equation (11) is our local general dispersion relation for dissipative drift wave instability including the impurity radiation loss and arbitrary values of $k_z^2v_{te}^2/\nu_e$. When the latter is much larger than $\mid\omega\mid$, then (11) takes the form

$$(1+\frac{i}{\gamma_T'}[\frac{2}{3}(1+\alpha)\omega-i\gamma_n])(\frac{\omega_e^*}{\omega}-k_\perp^2\rho_s^2)$$
$$=(1-i\frac{\nu_e\omega_e*}{k_z^2v_{te}^2}+\frac{i}{\gamma_T'}[\omega_T^*+\frac{2}{3}(1+\alpha)\omega_e^*]), \quad (12)$$

where $\gamma_T'=\omega_\chi+\gamma_T$. For $k_\perp^2\rho_s^2>>\mid\omega_e^*/\omega\mid$, (12) gives $\omega=(1+\gamma_n/\gamma_T')\omega_e^*(1+iX)/(1+X^2)$, where $X=(\nu_e\omega_e^*/k_z^2v_{te}^2)-(\omega_T^*/\gamma_T')$If we express the frequency as $\omega=\omega_r+i\gamma$, with $\mid\gamma\mid<<\omega_r$, then in the limit $\mid\omega\mid,\gamma_n<<\gamma_T$, we obtain $\omega_r=\omega_e^*/(1+k_\perp^2\rho_s^2)$, and

$$\gamma/\omega_r=\left[\frac{1}{\gamma_T}(1+\alpha)\{\frac{2}{3}(1+\alpha)\omega_e^*-\omega_T^*\}+\frac{\nu_e\omega_e^*}{k_\parallel^2v_{te}^2}\right]/(1+k_\perp^2\rho_s^2). \quad (13)$$

Clearly, the growth rate of the dissipative drift wave instability is modified due to the presence of impurity radiation.

We now present an estimate for fluctuation driven cross-field particle and electron energy transports. From the quasilinear particle flux $\Gamma_n=\sum_k n_{e1k}v_{kx}^*+c.c.=-D_n\frac{dn_o}{dx}$, where the asterics and c.c stand for the complex conjugate, we find

$$D_n=\frac{2v_{te}^2}{\omega_{ce}}\sum_k\frac{k_y}{\kappa_n}\frac{\gamma_k\omega_e^*}{\omega_r^2}\mid\frac{e\phi_k}{T_{eo}}\mid^2. \quad (14)$$

On the other hand, from the quasilinear heat flux $\Gamma_{Tx}=\frac{3}{2}\sum_k T_{e1k}v_{kx}^*+c.c.=-D_T\frac{dT_{eo}}{dx}$, we obtain

$$D_T=\frac{3v_{te}^2}{\omega_{ce}}\sum_k\frac{k_y}{(1+\alpha)\kappa_T}\left[\frac{\nu_e\omega_e^*}{k_\parallel^2v_{te}^2}-\frac{\gamma}{\omega_e^*}\right]$$

$$\times \left[\frac{\frac{2}{3}(1+\alpha)\omega_r + \frac{\nu_e \omega_e^*}{k_\parallel^2 v_{te}^2}(\gamma - \gamma_n)}{\frac{2}{3}(1+\alpha)\omega_e^* - \omega_T^*} - 1 \right] \mid \frac{e\phi_k}{T_{eo}} \mid^2 . \qquad (15)$$

The level of nonthermal potential fluctuation in (14) and (15) is estimated by means of the mixing length hypothesis, together with (8). We find that $\mid e\phi_k/T_{eo} \mid \approx \pi\kappa_n/k_\perp[1 + (\frac{\nu_e\omega_e^*}{k_\parallel^2 v_{te}^2})^2]^{1/2}$.

The dispersion relation (11) is solved for the following TEXT tokamak parameters : $B_o = 2\,T$, $T_{eo} = 15\,eV$, $n_o = 5{\times}10^{12}\,cm^{-3}$, $n_{Zo}/n_o = 0.02$, $L_T = \kappa_T^{-1} = 7.0\,cm$, $L_n = \kappa_n^{-1} = L_T$, $I_Z \approx 1{\times}10^{-24} J\,cm^3/s$, and $I_Z/T_{eo} \approx dT_Z/dT_{eo}$. We have taken $\nu_e = 1.0{\times}10^6 s^{-1}$, and neglected electron-neutral collisions ($\nu_n = 0$). We have studied the variation of the normalized growth rate γ/ω_{ci} as a function of the propagation angle k_z/k for three different wave numbers. It is seen that γ attains a maximum for an intermediate k value. Furthermore, we observe that the maximum growth rate shifts to lower k values as the propagation angle (measured with respect to $\mathbf{B}_o$) decreases. For $k_z/k = 0.0001$ and $k = 40\,cm^{-1}$, we use the growth rate and real frequency values to estimate D_n and D_T. One finds $D_n \approx 1.6{\times}10^3\,cm^2/s = 0.35\,D_B$, and $D_T \approx 6.9{\times}10^3\,cm^2/s = 1.5\,D_B$, where D_B is the Bohm-diffusion coefficient.

To summarize, we have studied the influence of the impurity radiation on the dissipative-drift wave instability taking into account the electron temperature perturbation. For parameters typical of the TEXT tokamak, the instability is found to grow for wave numbers in the range $10 - 100\,cm^{-1}$, with maximum growth shifting to lower k-values as the propagation angle (with respect to $\mathbf{B}_o$) decreases. For illustrative purposes, we have also presented estimates for the quasilinear particle (D_n) and electron heat (D_T) transports. It emerges that suprathermal low-frequency electrostatic fluctuations in collsional plasmas can give rise to significant cross-field particle and electron energy diffusions. Thus, the present results provide a clue to the understanding of electrostatic fluctuations and anomalous particle and heat transports that are observed in tokamak edge plasmas, which are dominated by charged particle collisions and the impurity radiation.

One of us (RB) acknowledges the support of the Alexander von Humboldt Foundation (Germany) and the FRD (South Africa). This research was supported by the European Economic Community through an operation grant.

/1/ J. C. Callen, B. A. Carreras, and R. D. Stambaugh, Phys. Today, January 1992, p. 34.
/2/ T. E. Stringer, *in Proccedings of the Twelfth European Conference on Controlled Fusion and Plasma Physics*, Budapest (European Physical Society, Budapest, 1985), part I, p. 86 (1985).
/3/ J. Neuhauser, W. Schneider, and R. O. Wunderlich, Nucl. Fusion **26**, 1679 (1986).
/4/ J. F. Drake, L. Sparks, and G. Van Hoven, Phys. Fluids **31**, 813 (1988).
/5/ P. K. Shukla and M. Y. Yu, Nucl. Fusion **29**, 1047 (1989).
/6/ Y. Z. Zhang and S. M. Mahajan, Phys. Fluids B **4**, 207 (1992).

Nonadiabaticity and toroidal mode coupling in collisional drift waves

M. Schlüter and B. D. Scott
Max-Planck-Institut für Plasmaphysik
W8046 Garching bei München, Germany

Based on Braginskii's fluid equations, nonadiabatic collisional drift wave equations in a sheared toroidal magnetic field are derived. The linearized equations are solved for both the linear and the nonlinear regime, i.e., for linear and nonlinear slab mode widths. Thus recent results of nonlinear drift wave theory in slab geometry are taken into account which indicate a radical change of the mode structure by nonlinear processes. On the other side, the model overcomes restrictions of present day computers, which do not allow a fully self-consistent nonlinear treatment of nonadiabaticity and toroidicity.

Introduction

With regard to the universal appearence of anomalous transport in tokamaks, drift wave instabilities in sheared magnetic fields have been studied intensively [1, 2, 3]. Conventional models have failed to reproduce the observed levels, of turbulence as well as of transport. Nevertheless, recent nonlinear numerical simulations of drift wave turbulence [4], self-consistently treating nonadiabaticity and shear, showed qualitative agreement with observed edge fluctuations. The geometry in these studies was sheared slab. Consequently the question arises how the results are modified by the toroidal geometry of the magnetic field in the tokamak. Unfortunately, a consistent nonlinear treatment of nonadiabaticity and toroidicity is still beyond the capability of present day computers [5]. In order to overcome this problem, the nonlinear toroidal situation is modelled by linear equations, but with adjusted parameters. With toroidal terms absent, the coefficients are varied to match linear mode widths to their nonlinear counterparts. The effects of toroidicity are studied by then introducing the toroidal terms.

Model equations

In order to focus on nonadiabatic collisional electron dynamics, Braginskii's fluid equations [6] are taken for cold ions, with a parallel viscosity to take the place of ion Landau damping. For simplicity, the isothermal case is considered, but the complete dynamics are briefly considered for the fluctuation energetics. A standard large aspect ratio expansion is taken for the toroidal (ρ, θ, ζ) equilibrium. In an axisymmetric configuration the poloidal variation of B couples a mode m to its neighbours $m \pm 1$ at the same toroidal mode number n. With $\Delta m/m \ll 1$, and mode widths small compared

to equilibrium scale lengths by $\Delta/L \ll 1$, the following two-dimensional (2D) set of equations for the overall mode is generated:

$$\frac{\partial}{\partial t}\left(\frac{\partial^2}{\partial x^2} - K^2\right)\phi_m = -C^{-1}x^2 h_m - i\epsilon_n\left(n_{m-1} + n_{m+1} - K^{-1}\frac{\partial}{\partial x}\left(n_{m-1} - n_{m+1}\right)\right)$$

$$\frac{\partial n_m}{\partial t} = iLxu_m - C^{-1}x^2 h_m + (\gamma - i)\,\phi_m - i\epsilon_n\left(h_{m-1} + h_{m+1} - K^{-1}\frac{\partial}{\partial x}\left(h_{m-1} - h_{m+1}\right)\right)$$

$$\frac{\partial u_m}{\partial t} = iLxn_m - \mu x^2 u_m$$

The normalizations are $n_m = \widetilde{n}_m/n_0$, $\phi_m = e\widetilde{\phi}_m/T_e$, $u_m = \widetilde{v}_{i\|m}/c_s$, $c_s = \rho_s/\Omega_i$, $h_m = n_m - \phi_m$, $K = k_y\rho_s$, $k_y = m/\rho$, $\rho_s = (T_e/M_i)^{1/2}\,c/eB_0$, $t = t\omega_{*e}$, $L = L_n\hat{s}/qR_0$, and $\hat{s} = \rho(\partial q/\partial\rho)$ is the shear parameter. The normalized distance from the m'th rational surface is $x = (\rho - \rho_m)/\rho_s$, the γ is an external drive, and the parameter $C = 0.51\,(\nu_{ei}/\omega_{*e})\,(L_s/L_n)^2\,(m_e/M_i)$ controls the width of the nonadiabatic layer, Δ_D, as $C \equiv (\Delta_D^2/\rho_s^2)$.

Fluctuation energetics

The fluctuation 'energy' E is calculated from the 2D set of equations [4], with

$$E \equiv \frac{1}{2}\left\langle |\nabla_\perp\phi|^2 + n^2 + u^2 + [(3/2)T^2]\right\rangle$$

$$\left\langle(\cdots)\right\rangle = \int_{-\infty}^{+\infty} dx \int_{-\pi}^{+\pi}\frac{d\theta}{2\pi}\int_{-\pi}^{+\pi}\frac{d\zeta}{2\pi}(\cdots)$$

Toroidal terms disappear in the mode growth rate Γ up to $O(\Delta/L)$:

$$\Gamma = \frac{1}{2E}\sum_m \frac{\partial E_m}{\partial t} = \Gamma_n + [\Gamma_t] + \Gamma_\gamma - \Gamma_c - \Gamma_s + O\left(\frac{\Delta}{L}\right)$$

where Γ_n and Γ_T are the sources from ∇n and ∇T, respectively, Γ_c is collisional dissipation, Γ_s is parallel ion damping, and Γ_γ is external driving. This suggests that instability is not directly driven by toroidicity, but by changes in the mode structure. Accordingly, localization by toroidal effects causes a reduction in the nonadiabatic radial mode widths. This in turn reduces the rms $k_\|$, weakening the sinks (which are proportional to $k_\|^2$), and leaving the mode relatively more strongly driven by the sources.

One dimensional (1D) model

The above 2D drift wave equations can be simplified to a 1D set by assuming like mode structure on neighboring (i.e., all) rational surfaces: $\phi_{m\pm j}(x) = \phi_m(x \mp j\Delta_{rs})$, where $\Delta_{rs} = 1/\hat{s}K$ is the inter-surface spacing. (This is the first part of the standard

ballooning treatments – a radial Fourier transform would be the second [7]. Note that the phases must also be chosen – they are usually as here taken to be equal.) Omitting the subscript m, there is

$$\frac{\partial}{\partial t}\left(\frac{\partial^2}{\partial x^2} - K^2\right)\phi = -C^{-1}x^2 h - i\epsilon_n\left(n_- + n_+ - K^{-1}\frac{\partial}{\partial x}(n_- - n_+)\right)$$

$$\frac{\partial n}{\partial t} = iLxu - C^{-1}x^2 h + (\gamma - i)\,\phi - i\epsilon_n\left(h_- + h_+ - K^{-1}\frac{\partial}{\partial x}(h_- - h_+)\right)$$

$$\frac{\partial u}{\partial t} = iLxn - \mu x^2 u$$

where, e.g., $n = n(x)$, and $n_\pm = n(x \mp \Delta_{rs})$. The overall mode is obtained by adding a certain number Δm of modes with a small spectral width, i.e., $\Delta m/m \ll 1$. The equations are solved numerically by a scheme which is explicit for all terms except the nonadiabatic ones $\propto C^{-1}$, for which an implicit scheme is used [5]. For typical ASDEX OH edge parameters and for a poloidal mode number $m = 100$, an unstable eigenmode is found, with $\Delta_h < \Delta_\phi \sim \Delta_{rs}$. (The Δ's refer to the respective $1/e$-widths of the fluctuations.) The destabilization is due to the narrow, but steep, profile of the nonadiabatic layer. This gives rise to a sharp compression in the electrons' perpendicular velocity, which contributes appreciatively to the density fluctuation. The overall poloidal structure, with a bulk formation on the outside of the torus (ballooning), nevertheless shows antiballooning for the averaged amplitude (the radially integrated squared of ϕ): maximum near the *inside* of the torus, in contrast to conventional expectation and illustrating the lack of direct effect of toroidicity on the energetics.

Implications for the nonlinear regime

To address the possible consequences in the nonlinear regime, the parameters in the equations are artificially chosen to reflect typical nonlinear (slab) mode widths by the linear equations. The toroidal terms are first switched off by setting $\epsilon_n = 0$. The coefficients in the obtained linear slab equations then are adjusted such that $\Delta_h \propto k_y^{-1/2}$, Δ_ϕ independent of k_y, with $\Delta_h \ll \Delta_\phi$, as per results from turbulence computations [8]. Following experimental indications of peak activity near $k_y\rho_s = 0.3$, the absolute values of Δ_h are determined by setting $\Delta_h = \Delta_{rs}/2$, i.e., marginal overlap at the driven scales, for $\hat{s} = 1.3$ at that $k_y\rho_s$. Then the toroidal terms are switched on. A simple expectation of the result might have been unchanged Δ_h for $k_y\rho_s < 0.3$ (slab widths) and for higher $k_y\rho_s$ a reduction to $\Delta_h \propto k_y^{-1}$ – space filling by neighbours. What actually takes place is that the toroidal localization is stronger, due to a double effect. The toroidal localization directly affects both h and ϕ, but then the changed ϕ in turn affects h (the latter effect is that active for the strict linear modes, as above). Thus toroidicity has a strong nonlocal influence on the mode shape of h.

Conclusions and outlook

Study of the energetics in the toroidal collisional drift wave equations suggests the absence of a so-called 'curvature drive', since the toroidal terms disappear up to $O(\Delta/L)$ – for arbitrary mode structure in the general, 2D case. This suggests that 'toroidicity induced' instability is not the result of a new free energy source, but of changes in the mode structure. A direct consequence of this result is that in the isothermal case, the 1D model gives rise to antiballooning in the ϕ-amplitude, in contrast to conventional expectation. The h, on the other hand, is not in overlap and hence exhibits no ballooning effects. When h is brought into overlap by considering mode widths commensurate with nonlinear calculations, a severe localization of the modes occurs, which removes the nonlinear slab overlap. This suggests an enhanced instability also in the nonlinear situation, caused by preferential reduction of the dissipation terms relative to the sources. However, this effect has been presently obtained only for a linear situation, not only with like mode structure on the different rational surfaces but also with vanishing relative phases. In the nonlinear, turbulent situation neither of these are tenable, and the actual results could become rather complicated. As a first step towards resolving this question, a slow, random de-phasing is being incorporated into the 1D computations. Further, a 2D extension of this work, allowing for general mode structure, is planned.

Acknowledgments

This work was supported by the Max-Planck-Gesellschaft.

References

[1] TANG, W. M., Nucl. Fusion **18** (1978) 1089.

[2] LIEWER, P. C., Nucl. Fusion **25** (1985) 543.

[3] WOOTON, A. J., CARRERAS, B.A, MATSUMOTO, H., et al., Phys. Fluids B **2** (1990) 2879.

[4] SCOTT, B., D., Phys. Rev. Lett. **65** (1990) 3289.

[5] SCOTT, B. D., J. Comput. Phys. **78** (1988) 114.

[6] BRAGINSKII, S. I., in Reviews of Plasma Physics, Vol. 1, (LEONTOVICH, M. A., Ed.) Consultants Bureau, New York (1965) 205.

[7] CHEN, L., CHENG, C. Z., Phys. Fluids, **23** (1980) 2242

[8] SCOTT, B. D., BIGLARI, H., TERRY, P. W., DIAMOND, P. H., Phys. Fluids B **3** (1991) 51.

ON THE "CAPTURED" ENERGY IN FREELY DECAYING TWO-DIMENSIONAL HYDRODYNAMIC AND DRIFT-WAVE PLASMA TURBULENCE.

S.V.Bazdenkov, N.N.Kukharkin
I.V.Kurchatov Institute of Atomic Energy, Moscow 123182, Russia.

1. INTRODUCTION.

The intriguing question of the features of freely decaying turbulence has been studied for a long time /1,2/. "Selective decay" mechanisms have been proposed to describe these processes in 2-D turbulence in fluids and plasmas /3,4/. In 2-D turbulence large scale motions treated as self-organized structures are known to appear because of the inverse cascade of energy and direct cascade of enstrophy (mean-square vorticity) /5/. Due to differences in decay rates of various inviscid invariants, self-organization in turbulent flows can be considered as a process with "survival" of structures with minimal values of fast-decaying invariants and constancy of long-lived ones. The central point of this approach is the choice of invariants. The choice of energy as a long-lived invariant and enstrophy as fast-decaying one has already become classical. However, the question arises: why is it enstrophy, and not some other invariants connected with the vorticity of a flow, that determines the self-organized state? While the choice of long-lived invariant is more or less evident because it is always possible to choose the most conserved invariant, at the same time it is very hard to justify the choice of the fast-decaying invariant. Meanwhile the kind of self-organized state is crucially dependent on this choice. What choice takes place in real decaying turbulence? The present paper is devoted to the analysis of these questions.

2. BASIC EQUATIONS.

We consider 2-D incompressible turbulent flow with boundary conditions 2π-periodic in the (x,y) plane, described by the Navier-Stokes (NS) equation

$$\frac{\partial}{\partial t}(\nabla^2\psi) - ([\nabla\psi,\vec{e}_z]\cdot\nabla)\nabla^2\psi - \nu\nabla^4\psi = 0, \qquad (1)$$

where ψ is a stream function: $\vec{V}=[\vec{e}_z,\nabla\psi]$. The drift-wave turbulence in magnetized plasma is described by the Hasegawa-Mima (HM)

equation for electrostatic potential ϕ, which is similar to (1).

$$\frac{\partial}{\partial t}(\nabla^2\phi-\phi) - ([\nabla\phi,\vec{e}_z]\cdot\nabla)\nabla^2\phi - \nu\nabla^4\phi = 0. \qquad (2)$$

We present here expressions for NS equation and only pictures for both equations. Details for HM equation will be published elsewhere. In the absence of viscosity (ν=0) the equation (1) has the following invariants: energy $E=1/2\int(\nabla\psi)^2 dxdy$, and any functional of vorticity $J(\omega)$ ($\omega = \Delta\psi = (\mathrm{rot}\vec{V})_z$), $J=1/2\int F(\Delta\psi)dxdy$, where F is an arbitrary function. In particular, integrals S_n of the form $S_n=1/2\int(\Delta\psi)^n dxdy$ (S_2 is the enstrophy) are conserved.

In the viscid case ($\nu\neq0$) the decay rates of ideal invariants are given by the expressions

$$\frac{d}{dt}E = -2\nu S_2$$

$$\frac{d}{dt}S_n = -\nu n(n-1)\int(\Delta\psi)^{n-2}(\nabla\Delta\psi)^2 dx\,dy \equiv -2\nu n(n-1)R_n . \qquad (3)$$

The functional R_2 is called palinstrophy.

One can see from (3) that the rate of decay of S_n increases with growth of n. However, functions E(t) and $S_n(t)$ can give poor information on the structure of the decaying turbulence. Suggested here "phase portraits" of the system in the form of functions of normed rates of the decay of the ideal invariants versus normed values of these invariants are more illustrative and allow to discover new features of decaying turbulence. Let us introduce the following variables:

$$\alpha_n = S_n(t)/S_n(0); \quad \beta_n = \dot{S}_n(t)/\dot{S}_n(0) = R_n(t)/R_n(0), \qquad (4)$$

$$\xi = E(t)/E(0); \quad \eta = \dot{E}(t)/\dot{E}(0) = S_2(t)/S_2(0). \qquad (5)$$

The functions $\beta_n = \beta_n(\alpha_n)$ and $\eta = \eta(\xi)$ are parametric (time t is the parameter) curves, which begin at the point (1,1) and come to the point (0,0) at $t = \infty$. In general it is hard to predict a priori and to justify the form of these curves. However, from numerical calculations, the form of these curves appears to be universal. This result allows us to speak about the universal character of turbulence decay.

3. "CAPTURE" OF ENERGY IN FREELY DECAYING TURBULENCE.

Equations (1) and (2) were solved numerically by fully dealiased 128x128 spectral code /6/ for various initial conditions.

Figures 1a and 2a show the typical phase portraits of turbulence in the form of the function "invariant vs invariant decay rate" for the following initial conditions: ν=0.00075, the microscale Reynolds number $Re_\lambda = E/(\nu S_2^{1/2}) \simeq 74$, and (for NS equation) E=0.12, $S_2 \simeq 5$, $S_4 \simeq 117$, $S_6 \simeq 3.7\times10^3$, $S_8 \simeq 1.3\times10^5$. Markers are put at every 1000th time step (Δt=3.9). Figures 1b and 2b show modal spectra E(k) and $S_2(k)$ and isovorticity lines at t=0, t=11.7, t=23.4.

All numerical experiments point to the existence of a certain non-zero value of "captured" energy to which the system evolves. The curve $\eta(\xi)$ consists of two parts. The first part, with roughly constant slope, clearly points to a definite separated value of energy, the "captured" energy, given by intersection of the mean tangent slope of this curve with the abscissae axis; the second part occurs after quantitative changes in the system when the size of vortices become comparable to the characteristic scale of the system. Increase of viscosity leads to decrease of the slope of the first part of $\eta(\xi)$ toward the abscissae axis and to decrease of the value of the "captured" energy. This behaviour may be treated in the following way. Due to the energy cascade toward smaller wavenumbers and the enstrophy cascade toward larger wavenumbers the initially localized spectrum spreads through all wavenumbers because the dissipation is essentially at large k. It leads to the "capture" of part of the initial energy. The other, "non-captured" part of the energy is transferred together with enstrophy due to the relation $S(k)=k^2E(k)$ and is dissipated because of the viscosity at shorter wavelengths. The enstrophy cascade to small scales leads to amplification of the vorticity gradients, i.e palinstrophy R_2 and other quantities R_n. The increase of the curves $\beta_n(\alpha_n)$ from (1,1) in Fig. 1a and 2a corresponds to this process. Later when most of the enstrophy is concentrated at small scales, viscosity begins to play an essential role. It leads to dissipation of small vortices and compensates for the rise of palinstrophy. As a result, the rate of increase of R_n is reduced and then R_n begin to decrease. More detailed analytical and numerical results will be presented in the near future.

/1/ S.Goldstein, Proc.Camb.Phil.Soc., **47**, 554 (1951).
/2/ A.S.Monin, A.M.Yaglom, Mechanics of Fluids, Cambridge, (1975).
/3/ W.H.Matthaeus, D.Montgomery, Ann.NY Acad. Sci., **357**, 203 (1980)
/4/ A.Hasegawa, Adv. Phys., **34**, 1 (1985).
/5/ R.H.Kraichnan, Phys. Fluids, **10**, 1417 (1967).
/6/ S.A.Orszag, Stud. Appl. Math., **50**, 293 (1971).

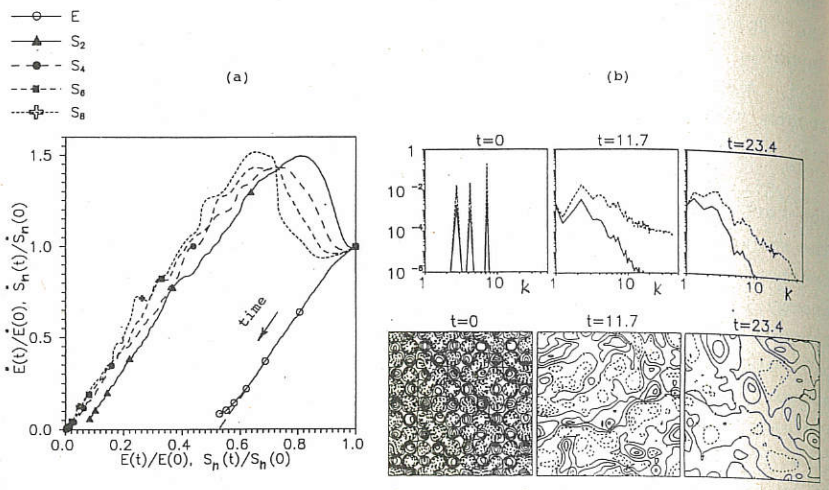

Fig.1 Navier-Stokes equation: (a) phase portraits of turbulence, curves begin at the point (1,1) at t=0 and come to (0,0) at t=∞ ; (b) modal spectra of energy (solid) and enstrophy (dashed), and isovorticity lines.

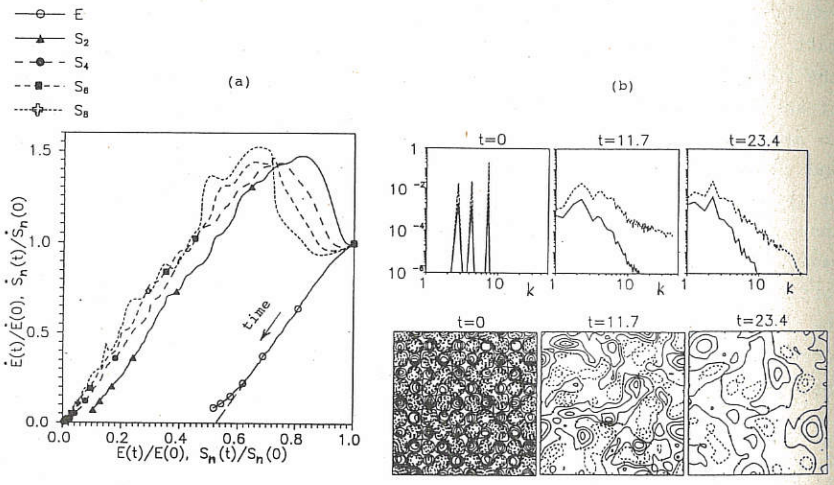

Fig.2 Hasegava-Mima equation: (a) phase portraits of turbulence, curves begin at the point (1,1) at t=0 and come to (0,0) at t=∞ ; (b) modal spectra of energy (solid) and enstrophy (dashed), and isovorticity lines.

Effect of parallel heat flows on electron heat conduction losses due to electrostatic turbulence

G. Becker

Max-Planck-Institut für Plasmaphysik,
Euratom-IPP Association, Garching bei München,
Federal Republic of Germany

ABSTRACT. The contribution of fluctuating electric fields to the anomalous electron thermal transport in hot plasmas is investigated. It is shown that in the long mean free path limit the electron heat conduction $\|\vec{B}$ and the associated dissipation are too small to severely reduce the temperature fluctuations driven by electrostatic turbulence, $\widetilde{T}_e$, and the conductive electron heat loss q_e^E. Parallel heat flows which are orders of magnitude higher and cause a strong reduction of $\widetilde{T}_e$ and q_e^E are only obtained when the collisional conductivity ($n_e X_{e\|}^c \propto T_e^{5/2}$) is applied beyond its range of validity. Electrostatic turbulence continues to be the likely cause of the anomalous particle and electron energy fluxes in hot tokamaks. This result is supported by empirical transport properties in various confinement regimes.

The important question of whether electrostatic or magnetic turbulence is responsible for the anomalous electron heat conduction in tokamaks is still not resolved. One objection to an electrostatic contribution often advanced is that in hot plasmas very high electron heat flows $\|\vec{B}$ occur. The associated strong dissipation is supposed to suppress marked temperature fluctuations and radial electron heat conduction. In estimates of the parallel heat flux, the Spitzer-Härm conductivity |1, 2| is usually applied. Owing to $n_e \chi_{e\|}^c \propto T_e^{5/2}$, it can reach extremely high values in the inner plasma.
This Letter studies the contribution of the electrostatic turbulence to the anomalous electron energy transport in hot plasmas. It deals with the dissipative effect of parallel electron heat conduction on the temperature fluctuations $\widetilde{T}_e$ and on the radial conductive electron heat loss. The radial fluxes induced by fluctuating electrostatic ($\widetilde{E}_\theta$) and magnetic ($\widetilde{B}_r$) fields are

$$\Gamma = \frac{1}{B_t} < \widetilde{E}_\theta \widetilde{n}_e > \tag{1}$$

$$q_e = \frac{3}{2} n_e \frac{1}{B_t} < \widetilde{E}_\theta \widetilde{T}_e > -n_e \chi_e \Big(\frac{\widetilde{B}_r}{B_t}\Big) \nabla T_e \tag{2}$$

$$Q_e^{conv} \approx \frac{3}{2} T_e \Gamma \tag{3}$$

where Γ is the particle flux of electrons and ions; q_e and Q_e^{conv} are the fluxes due to electron heat conduction and convection, respectively. The angular brackets denote averages over space and time. The particle flux Γ is due to electrostatic turbulence because the $\widetilde{B}_r$ contribution is negligibly small. Results from heavy ion beam probe measurements in the interior of TEXT |3| show that the particle flux induced by $\widetilde{E}_\theta$ can essentially account for the experimental flux. By contrast, the magnitudes of the two terms in Eq.(2) cannot be experimentally determined since, at present, neither $\widetilde{T}_e$

nor $\widetilde{B}_r$ is a measurable quantity in hot plasmas. A rough estimate of the $\widetilde{B}_r/B_t$ level can only be obtained from the confinement of runaway electrons.
Electrostatic turbulence due to low-frequency modes ($\omega \ll \omega_{ci}$) such as drift instabilities excites $\widetilde{T}_e$ at a rate of about $\omega_{*e} \simeq 1.3 \times 10^6 s^{-1}$ with ω_{*e} being the electron diamagnetic drift frequency. This excitation competes with the dissipation by parallel electron heat conduction, which is approximated by

$$\frac{1}{\tau_{dis}} \frac{3}{2} n_e T_{emn} \approx -\nabla_{\|} \vec{q}_{e\|} \tag{4}$$

where

$$T_{emn} = T_{emn}(0) sin\ k_{\|} l \tag{5}$$

Here, m and n denote the poloidal and toroidal mode numbers, respectively, and $k_{\|}$ is the parallel wave number. In the collision-dominated case |2|, the heat flow is local and can be written as

$$q^c_{e\|} \approx n_{ex} \chi^c_{e\|} k_{\|} T_{emn} \tag{6}$$

yielding

$$\frac{1}{\tau_{dis}} \approx \frac{2}{3} k^2_{\|} \chi^c_{e\|} \tag{7}$$

with

$$\chi^c_{e\|}(cm^2 s^{-1}) = 5.6 \times 10^{15} T_e(eV) \tau_e(s) \tag{8}$$

Typical parameters in H-mode plasmas of ASDEX (major radius $R_0 = 165cm$, minor radius $a = 40cm$) taken in the middle of the confinement zone at $r = 2a/3$ are $T_e = 1.2keV, n_e = 3 \times 10^{13} cm^{-3}, Z_{eff} = 2, q = 1.5, R_0 q = 247.5cm$, dimensionless shear $s = (r/q)\partial q/\partial r = 0.95$ and electron-electron collision time $\tau_e = 1.8 \times 10^{-5} s$. The temperature and density values in L-mode plasmas are somewhat smaller. Setting the parallel wave number of electrostatic modes $k_{\|} = (R_o q)^{-1} = 4.04 \times 10^{-3} cm^{-1}$, we obtain $\chi^c_{e\|} = 1.2 \times 10^{14} cm^2 s^{-1}$ and $\tau^{-1}_{dis} \approx 1.35 \times 10^9 s^{-1}$, which exceeds ω_{*e} by three orders of magnitude.

The impact of such high parallel heat diffusivity and dissipation on T_{emn} and $\widetilde{T}_e$ will be discussed in more detail. For given mode numbers m and n, the resonant surface at $r = r_s$ is defined by $m = nq(r_s)$. The value of $k_{\|}$ depends on the distance $x = r - r_s$ and is expressed by

$$k_{\|} = \frac{m - nq}{R_0 q} = -\frac{m}{r} \frac{x}{R_0 q} s \tag{9}$$

At the resonant surface, it follows that $k_{\|} = 0$ and $\lambda_{\|} \to \infty$. The $k_{\|} = (R_0 q)^{-1}$ used above corresponds to $m - nq(r_0) = 1$ and $|x_0| = |r_0 - r_s| = 0.9cm$ with $m = 30$ and

$n = 20$. Approaching the resonant surface results in smaller values of $k_\parallel$ and τ_{dis}^{-1}. At $m - nq = 3.1 \times 10^{-2}$ and a correspondingly reduced $k_\parallel$ value $\tau_{dis}^{-1} \approx \omega_{*e}$ is reached with $\chi_{e\parallel}^c = 1.2 \times 10^{14} cm^2 s^{-1}$. The distance from r_s thus declines to $3.1 \times 10^{-2} |x_0|$. Marked T_{emn} amplitudes are only possible in a narrow range around the resonant surface, where, since $k_\parallel$ is small, the dissipation rate is below the excitation rate of the temperature fluctuations. This shrinkage of the radial mode width takes place at all mode numbers and thus causes a strong reduction of the $\widetilde{T}_e$ level. The electrostatic component of the radial electron heat conduction (see Eq.(2)) can be written as

$$q_e^E \simeq \frac{3}{2} n_e \frac{1}{B_t} \widetilde{\phi}_{rms} \bar{k}_\theta \widetilde{T}_{erms} |\bar{\gamma}_{T\phi}| sin\bar{\alpha}_{T\phi} \tag{10}$$

where $\bar{\gamma}_{T\phi}$ and $\bar{\alpha}_{T\phi}$ are the coherence and phase angle between the temperature and potential fluctuations, respectively. Reducing the radial mode width of T_{emn} means increasing k_r^T. Isotropic turbulence in the plane $\perp \vec{B}$ implies that k_θ^T rises together with k_r^T. This cannot, however, compensate the decrease of $\widetilde{T}_{erms}$, since k_θ^T does not enter into Eq.(10). The $\bar{k}_\theta$ value there results from $\widetilde{E}_\theta$ and is thus connected with the potential fluctuations. It is concluded that the very high parallel heat flux resulting from $\chi_{e\parallel}^c$ would keep $\widetilde{T}_{erms}$ at a low level and prevent a significant conductive electron heat loss due to electrostatic turbulence.

The electron mean free path $\parallel \vec{B}$ is defined by

$$\lambda_e = v_e \tau_e \tag{11}$$

with the mean velocity $v_e = (2T_e/m_e)^{\frac{1}{2}}$. The temperature gradient length $\parallel \vec{B}$ is

$$L_\parallel = \frac{T_{emn}}{|\nabla_\parallel T_{emn}|} = \frac{1}{k_\parallel} \tag{12}$$

It is not generally known that application of the collisional electron heat diffusivity $\chi_{e\parallel}^c$ |1, 2| is restricted to very small $\lambda_e/L_\parallel$ ratios ($\lambda_e/L_\parallel \lesssim 2 \times 10^{-3}$)|4, 5|. The reason for this is the energetic electrons in the tail of the distribution, which carry most of the heat conduction flux and exhibit relatively large mean free paths. Using $\chi_{e\parallel}^c$ beyond its range of validity always yields parallel heat flows and dissipation rates which are too high |4|. Overestimation already occurs at the plasma edge and can become huge in the interior.

Evaluating the mean free path at the above plasma parameters yields $\lambda_e = 3.76 \times 10^4 cm$. For $k_\parallel = (R_0 q)^{-1}$, one obtains $\lambda_e/L_\parallel = 152$, i.e. the local heat flow model is not applicable. It is necessary to determine the parallel thermal flux in the long mean free path limit. Kinetic Fokker-Planck calculations |4| have shown that for $\lambda_e/L_\parallel \gg 1$ the electron thermal conduction comes very close to the collisionless asymptotic limit. It should be mentioned that in the simulations the velocity distributions of the electrons injected at each boundary are Maxwellian. For long mean free paths, however, non-Maxwellian distributions might be present, which can give rise to different heat conduction. Thus, the following expression represents an estimate of the conductive heat flux in the collisionless case:

$$q_{e\|}^{nl} \simeq \frac{4}{\pi^{\frac{3}{2}}} n_e v_e T_{emn}(0) cos\ k_\| l \tag{13}$$

Thermal conduction here is a non-local process, with $q_{e\|}^{nl}$ only amounting to 0.3% of $q_{e\|}^{c}$ evaluated from Eq.(6) with $k_\| = (R_0 q)^{-1}$. Substitution of Eq.(13) into Eq.(4) yields

$$\frac{1}{\tau_{dis}} \approx \frac{8}{3\pi^{\frac{3}{2}}} k_\| v_e \tag{14}$$

which comes close to the parallel collisionless dissipation rate $\omega_t = k_\| v_e$ with ω_t being the transit frequency. For $k_\| = (R_0 q)^{-1}$, one obtains $\tau_{dis}^{-1} \approx 4.0 \times 10^6 s^{-1}$, which exceeds ω_{*e} by only a factor of three. This means that non-local parallel heat conduction does not markedly affect the radial mode structure of T_{emn} and the temperature fluctuation level. We conclude that a substantial conductive electron heat loss due to electrostatic turbulence is possible in hot plasmas. Parallel heat fluxes which are orders of magnitude higher and result in a severe reduction of $\widetilde{T}_e$ and q_e^E are only predicted when $\chi_{e\|}^{c}$ is incorrectly used in the case of long mean free paths.

The picture of both particle and energy fluxes being induced by electrostatic turbulence agrees with empirical transport properties, e.g. with the coupling between particle and electron energy transport found in all confinement regimes and with $\chi_e/D \approx 3.3$ |6|. By contrast, stochastic magnetic fields are expected to cause high electron heat conduction but small mass transport, resulting in χ_e/D ratios considerably above three. Recently, transport in ergodic magnetic fields has become questionable in the interior plasma. It is supposed to yield positive radial electric fields, whereas negative fields are measured.

Acknowledgement

The author appreciates useful discussions with B.D. Scott.

References

|1| Spitzer, L., Härm, R., Phys. Rev. 89 (1953) 977.

|2| Braginskii, S.J., "Transport Processes in a Plasma", in Reviews of Plasma Physics 1, Consultants Bureau (1965) 205.

|3| Wootton, A.J., Carreras, B.A., Matsumoto, H., et al., Phys. Fluids B 2 (1990) 2879.

|4| Khan, S.A., Rognlien, T.D., Phys. Fluids 24 (1981) 1442.

|5| Luciani, J.F., Mora, P., Virmont, J., Phys. Rev. Lett. 51 (1983) 1664.

|6| Becker, G., Nucl. Fusion 30 (1990) 1610.

AN ENERGY BALANCE APPROACH TO L-H TRANSITION AT THE EDGE

Julio J. Martinell and Guadalupe Ramos
Instituto de Ciencias Nucleares, U.N.A.M.
A. Postal 70-543, 04510 México D.F., MEXICO

The transition to the H-mode is a phenomenom that is not well understood and its study provides a good opportunity for elucidating the characteristics of the transport processes at play in tokamaks, especially near de edge region. It is quite clear now that the L-H transition takes place at the plasma edge and that it is associated to a sheared poloidal rotation in this region. Even though the H-mode is a regime that appears in relation to auxiliary heated discharges, it has been possible to produce an improved confinement regime in Ohmic discharges, similar to the H-mode, when a poloidal edge rotation is induced by means of electrodes that give rise to a radial current /1/. This indicates that radial transport is strongly influenced by shear of the poloidal flow. It is not yet clear whether this transport reduction is due to modification of particle orbits or to a decrement in the fluctuation level due to velocity shear. Some models have been proposed in relation to the latter explanation /2/.

The L-H transition is basically initiated at the edge but once the H-mode is established it influences the confinement properties all over the plasma column, improving core confinement by a factor of two. Experiments have found a number of features that are characteristic of the H-mode, common to all the different machines where it is observed. Edge conditioning is determinant for the appearance of the H-mode, which is reflected in the fact that it is usually observed in diverted configurations; for limiter plasmas a careful wall treatment has to be performed for this mode to be present. An important feature commonly observed is the pedestal shape of the temperature profiles, with a large edge temperature gradient. This is normally associated to a thermal barrier formed near the border of the column. According to this view, the increased edge temperature is just the result of accumulation of energy flowing from the center. Here we show that the pedestal temperature profiles can also be obtained as the result of a transition to a different equilibrium state, which would take place at the time of the L-H transition. Although this is similar to state bifurcation theories commonly used to explain the transition, it is rather a situation with double equilibria. The existance of these states depends upon the type of energy transport produced by the turbulence; only for some kind of models can we have a transition of the sort described.

We shall be concerned with the energy balance in the edge region and look for thermal equilibrium states. This region is modeled by an annulus formed by the outer part of the plasma column, which we approximate by a cylinder. A radial electric field or current may be established across the annulus by a certain mechanism which could be due to ion orbit losses /3/ or non-ambipolar electron diffusion /4/. As a result, the annular region experiences a poloidal rotation wheras the central part stays without motion. Then, there is a slippage layer between

the two regions that we assume to be very thin, where there is a large velocity shear. This has two effects on the energy balance: on the one hand viscous dissipation becomes important, increasing the energy content of the annulus, while on the other hand the diffusive energy flux comming from the core region is quenched, producing a reduction of energy input to the edge. We will not deal with the mechanisms that inhibit the transport at the boundary layer, and assume only that the anomalous diffusivity is reduced by an amount that implicitly depends on the shear. An important point is the kind of radial transport that dominates in this region. Since there in no consensus about the dominant mechanism for edge transport, we try several models and choose those that give rise to a transition of the edge temperature within our treatment. In this way we can incline the balance for a particular type of models.

The energy balance equation in steady state for the present case can be written as,

$$\boldsymbol{E}\cdot\boldsymbol{J}+P_s+(-\mathrm{P}:\nabla\boldsymbol{V})-\nabla\cdot\boldsymbol{q}=0 \qquad (1)$$

where $\boldsymbol{E}\cdot\boldsymbol{J}$ is the Ohmic heating power, P_s represents all the other power sources, in particular, the one coming from any type of auxiliary heating, P is the stress tensor which involves viscous stress when the fluid velocity $\boldsymbol{V}$ has a shear, and $\boldsymbol{q}$ is the total (ion plus electron) heat flux. Since the transport is asumed to be primarily diffusive, the heat flux for each species is expressed in terms of the corresponding thermal diffusivity χ_j as $\boldsymbol{q}_j=\chi_j\nabla(n_jT_j)$. Impurity radiation can also be included in the term P_s as a negative source, but we ingore it in first approximation since it is difficult to know its form theoretically. Now, we use Eq.(1) for the edge region and integrate over the annular volume assuming its width Δr is much smaller than the radius of the column a, obtaining,

$$\boldsymbol{q}_N\equiv\boldsymbol{q}_{out}-\boldsymbol{q}_{in}\left(1-\frac{\Delta r}{a}\right)=[\boldsymbol{E}\cdot\boldsymbol{J}+P_s-\mathrm{P}:\nabla V]\left(1-\left(1-\frac{\Delta r}{a}\right)^2\right)\frac{a}{2} \qquad (2)$$

where the subscripts *in* and *out* refer to fluxes that enter and leave the annulus through the inner and outer borders, respectively. Solutions to this equation give the thermal equilibria. We are actually interested in the temperatures of these equilibria, and thus we regard Eq.(2) as an equation for T. Therefore we have to specify the temperature scaling of all terms in order to study the properties of the solutions.

The Ohmic heating may scale differently with temperatue depending on how the edge processes determine the variation of J and E with T. If the electric field is weakly dependent on the temperature then, in terms of the conductivity σ, one has $\sigma E^2 \sim T^{3/2}$, but for a situation where the current density does not change with T the scaling would be inverse, $J^2/\sigma \sim T^{-3/2}$. We will first analyze the former case. For the auxilary heating we may assume that the temperature dependence is not relevant and so we

regard it as a constant. For the viscous dissipation, since the only relevant component of the velocity gradient is dV_θ/dr, only the term $P_{f\theta} = \eta\ dV_\theta/dr$ is important, where the viscosity scales as $\eta \sim T^{-1/2}$. The velocity shear also depends on the temperature since the boundary layer, where it peaks, must have a width of the order of the ion gyroradius, which scales as $\rho_i \sim T^{1/2}$. Therefore, using $dV_\theta/dr \sim V_\theta/\rho_i$ we get that the viscous term scales as $T^{-3/2}$.

The scaling of the diffusivities is more delicate since it depends strongly on the process that produces the transport. There is a great variety of models that produce different scalings. An anlysis of the various possibilities shows that the scaling that produces multiple equilibria within the present context is $\chi_e \sim T^{1/2}$, which is obtained, for instance from models based on magnetic fluctuations /5/. Ion transprt should also be included, but this is usually smaller; it is of the order of the neoclassical value which scales as $\chi_i \sim T^{-1/2}$, so only for very low temperatures can it dominate. In order to simulate the inhibition in the transport produced by the rotation, we divide the electron flux coming from the center by a parameter α that we vary externally as the rotation speed is changed. With all this scalings Eq.(2) can be represented graphically as in Fig. 1, where the two sides of the equation, representing losses and gains, are shown as functions of temperature. The parameters used are typical of a large tokamak such as JET or D-III. The intersection points correspond to equilibrium states, and in this case there are two of them. The curves without symbols are for a case where rotation is weak or zero, while those with the symbols are obtained when rotation is important.

In the absence of rotation the two equilibrium points have very different temperatures and consequently it is highly unlikely to have a transition from the low to the high temperature state. Since the high temperature in this case is too large for the values normally attained at the edge, what one observes in the experiment is the low temperature, which we identify with the L-mode. As rotation is initiated the two points come closer, aided too by the increment in injected power, so that it will eventually be a transition to the state with high temperature, for a certain value of the rotation and the auxiliary heating. If rotation is now slowed down a little the two points may again separate but the edge is now in the high temperature state. This is identified with the H-mode, producing pedestal-type profiles. In this way, the characteristic temperature profiles of the H-mode will be the result of a transition in the energy balance.

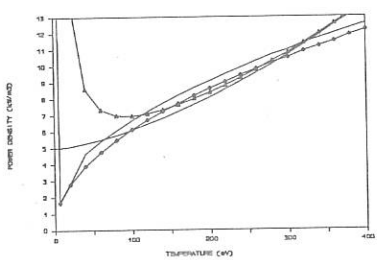

Fig.1: Edge power balance in terms of temperature.

Let us now turn to the case in which the current density is not dependent on temperature, so that the Ohmic heating is

proportional to $T^{-3/2}$. The scalings of the other terms will not change, so this term adds directly to the viscous friction because the scaling is the same. The right hand side of Eq.(2) is then of the form *const1 + const2* $T^{-3/2}$. For the heat fluxes we have a different situation, since for obtaining double solutions the appropriate scaling is found to be $\chi_e \sim T^{-1/2}$. This is characteristic, for instance, of collisional drift modes with circulating electrons /6/. Plotting again the losses and gains in function of temperature we have the situation depicted in Fig.2. Here the same process can be applied for the two equilibria, so that a transition to the state with high edge temperature can result as rotation and injected power increase.

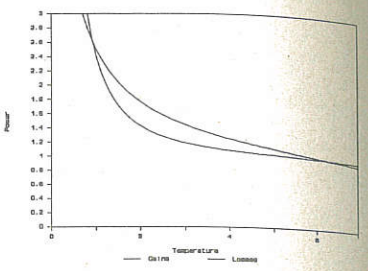

Fig.2: Power balance for $P_{OH} \sim T^{-3/2}$

The effect of impurity radiation has been investigated with a crude model for the line radiation. Since the dependence with temperature is of the form $T^{-1/2}$ it is important only in the side of lower temperatures, and, analogously to the ion heat fluxes, does not alter the results significantly. However, the L-H transition is a phenomenom that takes place essentially at the edge, and all processes that take place there should be of relevance. We have to include these effects in order to have more reliable results, in particular, the recycling processes ought to be important and have to be quantified in hte present model. A possibility of this approach is that it allows a correlation of transport models with the transition properties, and thus can be a way of discriminating among the different existing models. A similar effort on deciding for a certain class of transport models has been taken /7/ using a variational principle that minimizes the entropy production, and the results in favor of a scaling of the type $T^{1/2}$ agree with those reached here in the first analysis.

/1/ R.J. Taylor *el al.*, Phys. Rev. Lett. **63**, 2365 (1989)
/2/ e.g. Y.B. Kim *el al.*, Phys. Fluids B **2**, 2143 (1990)
/3/ K.C. Shaing *et al.*, Phys. Fluids B **2**, 1492 (1990)
/4/ S.I. Itoh and K. Itoh, Nucl. Fusion **29**, 1031 (1989)
/5/ e.g. P.N. Guzdar *et al.*, Phys. Rev. Lett. **57**, 2818 (1986)
/6/ R.R. Dominguez and R.E. Waltz, Nucl. Fusion **27**, 65 (1987)
/7/ J.J. Martinell *et al.*, Plasma Phys. Cont. Fusion **34** in press (1992)

PEDESTAL SUSTENANCE AND HEAT TRANSPORT AT THE EDGE IN THE H-TRANSITION

E. Minardi

Istituto di Fisica del Plasma, Assoc. EUR-ENEA-CNR
VIa Bassini 15, 20133 Milano, Italy

Above a critical value of the current and temperature pedestals a neighbouring bifurcating state of the tokamak configuration in the confinement zone exists (associated with a broader, more convex current density profile) which can be reached with a magnetic flux-conserving transition accompanied by an increase of the magnetic entropy of the collective configuration /1/. The figure shows the current pedestal formation when the resistive axial electric field E decreases at constant current and constant magnetic entropy. The decrease of E could be due to a local heating associated with a sawtooth crash. The values of the pedestal corresponding to the existence of a bifurcated state with higher entropy and same magnetic flux correspond to the positive value of the parameter H shown in the figure. Thus contrary to recent attempts /2,3,4/ the bifurcation concerns the bulk of the plasma rather than the edge. In the following we give arguments showing that the pedestal sustenance necessary for the formation of the bifurcated state, could be explained entirely in the framework of the neoclassical behaviour of the ions.

We shall apply the results of Hirshman and Sigmar /5/ and use the same notations. Our basic equations are the steady-state parallel momentum equations for ions

$$\langle \vec{B} \cdot (\nabla \cdot \overleftrightarrow{\Pi}_i) \rangle = 0 \qquad (1)$$

and the neoclassical expression for the ion heat flux

$$\frac{q_i^{\psi}}{T_i} = - \left\langle \frac{\vec{n} \times \nabla\psi}{M_i \, \Omega_i} \cdot (\nabla \cdot \overleftrightarrow{\Theta}_i + \frac{5}{2} n \, \nabla T_i) \right\rangle \qquad (2)$$

where (we shall drop henceforth the subscript i referring to the ions)

$$\langle \vec{B} \cdot \nabla \cdot \overleftrightarrow{\Pi} \rangle = 3 \langle (\vec{n} \cdot \nabla B)^2 \rangle \left[\mu_1 u_\theta + \frac{5}{2} \mu_2 \frac{q_\theta}{p} \right] \qquad (3)$$

$$\langle \vec{B}\cdot\nabla\cdot\overleftrightarrow{\theta} \rangle = 3 \langle (\vec{n}\cdot\nabla B)^2 \rangle \left[\mu_2 u_\theta + \frac{2}{5} \mu_3 \frac{q_\theta}{p} \right] \tag{4}$$

$$u_\theta = \frac{\vec{u}^1\cdot\nabla\theta}{\vec{B}\cdot\nabla\theta} \quad , \qquad q_\theta = \frac{\vec{q}^1\cdot\nabla\theta}{B\vec{\cdot}\nabla\theta} \quad , \tag{5}$$

$$\vec{u}^1 = \vec{u}_\perp + \vec{u}_\parallel \quad , \qquad \vec{q}^1 = \vec{q}_\perp + \vec{q}_\parallel \tag{6}$$

$$\vec{u}_\perp = \frac{c\,\vec{B}\times\nabla p}{Zen\,B^2} + \frac{c\,\vec{E}\times\vec{B}}{B^2} \quad , \qquad \vec{q}_\perp = \frac{5}{2} p \frac{c\,\vec{B}\times\nabla T}{Z\,e\,B^2} \tag{7}$$

All effects related to the ohmic axial electric field will be neglected considering that the energy balance is dominated by high density auxiliary power. Also we shall take $T=T(\psi)$ and neglect terms of order $(B_{pol}/B_{tor})^2$. Under these approximations one can verify that $\nabla\cdot n\vec{u}_\perp = 0$, $\nabla\cdot\vec{q}_\perp = 0$, so that the parallel parts $\vec{u}_\parallel$, $\vec{q}_\parallel$ are not needed for a vanishing divergence of the particle and heat flows. In accordance with neoclassical theory one has the equality

$$\left\langle \frac{R\,\vec{B}\cdot\nabla\cdot\overleftrightarrow{\theta}}{B} \right\rangle = \frac{1}{2\pi} \left\langle \frac{\vec{B}\times\nabla\psi\cdot\nabla\cdot\overleftrightarrow{\theta}}{B^2} \right\rangle \tag{8}$$

Thus the following expression for the radial heat flux is obtained from (2):

$$\frac{q^\psi}{T} = -2\pi \left\langle \frac{c\,R\,\vec{B}\cdot\nabla\cdot\overleftrightarrow{\theta}}{Z\,e\,B} \right\rangle \tag{9}$$

From the parallel momentum equation (1) and from (3), neglecting $\vec{u}$, $\vec{q}$ (consistently with a vanishing divergence of the flows, as noted above) and using the relation (7) for $\vec{q}_\perp$, one arrives at the expression

$$(\vec{u}_\perp)_\theta = -\frac{\mu_2}{\mu_1} \frac{c}{Z\,e\,B} \frac{dT}{dr} \tag{10}$$

where we specialized to the case of flux surfaces with circular cross section. Finally insertion of (10) into the first relation (7) gives

$$\frac{E_r}{B} = \frac{1}{Z\,e\,B} \left[\frac{dT}{dr} \left(\frac{\mu_2}{\mu_1} + 1 \right) + \frac{T}{n} \frac{dn}{dr} \right] \tag{11}$$

The coefficients μ_1 and μ_2 depend on the regime of collisionality at the edge, which, in a space average across the layer, can be reasonably supposed to be in the region of the plateau. Thus $\mu_1 > 0$, $\mu_2 > 0$ and the negative gradients give rise to a positive poloidal rotation (10) and a

negative radial electric field (11).

We consider a narrow layer with thickness Δ in the outer neighbourhood $s \leq r \leq s+\Delta$ of the surface $q_s \sim 2$ across which the temperature drops to zero. Neglecting the radial dependance of all quantities except T(r) and noting that $\langle(\vec{n}\cdot\nabla B)^2\rangle \sim (B_\theta/R)^2$, the radial heat flux can be written in the form

$$q_r = -G\,(T(r)/T_s)^{3/2}\,\frac{dT}{dr} \qquad (12)$$

where $T_s=T(s)$ is a value of the temperature pedestal (related to the current density pedestal by Spitzer resistivity) which corresponds to a positive H, so that the system is susceptible of an entropy increasing transition. In the plateau regime G is given by the expression

$$G = \frac{11}{2}\left(\frac{\pi M}{2}\right)^{1/2}\left(\frac{c}{Z e B}\right)^2 \frac{q_s n_s}{R} T_s^{3/2} \qquad (13)$$

where n_s is the density at r=s.

We write the equation for the energy balance in the layer simply in the form

$$\frac{1}{r}\frac{d}{dr}(rQ(r)) = p_A \qquad (s\leq r\leq s+\Delta) \qquad (14)$$

where

$$Q(r) = \frac{C}{r} + q_r = \frac{C}{r} - G\left(\frac{T(r)}{T_s}\right)^{3/2}\frac{dT}{dr} \quad (s \leq r \leq s+\Delta) \qquad (15)$$

The constant C is determined by a boundary condition on the surface r=s. The heat flow per unit surface Q(s) impinging from the plasma upon the layer across the surface r=s is $Q(s)=p_A s/2$ (neglecting the ohmic contribution). This flow is essentially due to the anomalous thermal conductivity of the electrons in the plasma bulk. Let us suppose that the electron conductivity κ_e becomes very large when r tends to s on the inner side, while κ_e dT/dr remains finite. In the limit of κ_e tending to infinity, dT/dr tends to zero and $-\kappa_e$ dT/dr tends to Q(s). Thus, the continuity of Q(r) at r=s requires C=sQ(s) and $(dT/dr)_s=0$. Then the only divergent contribution to the heat flow in the layer is given by $q_r(r-s)$ and describes a modification of the flow which builds up across the layer and is entirely originated by the viscous neoclassical effects of the ions outlined above. THe flow Q(r) is continuous across the layer, as well as the temperature and the (vanishing) temperature gradient.

The integration of (14) gives up to second order in r-s

$$\left[\frac{T(r)}{T_s} \right]^{5/2} = 1 - \frac{5}{4} \frac{p_A}{GT_s} (r-s)^2 \qquad (16)$$

The boundary condition $T(s+\Delta)=0$ fixes the thickness of the boundary layer as follows

$$\Delta = \frac{c}{ZeB} T_s^{5/4} \left[\frac{\pi M}{2} \right]^{1/4} \left[\frac{24}{5} \frac{q_s n_s}{p_A R} \right]^{1/2} \qquad (17)$$

Thus, according to the description above, the temperature profile exhibits a shoulder near r=s, corresponding to a vanishing of the temperature gradient. For r>s, the temperature drops rapidly across a narrow layer whose thickness Δ is typically of few centimeters.

The temperature gradient tends to minus infinity for $r \to s + \Delta$, while the heat flow remains finite.

It follows that the poloidal velocity (10) should also tend to infinity, but a natural limit to the present theory is represented by the sonic velocity, whose related compressional effects are not taken into account in our treatment.

/1/ Minardi, E. (1992) Plasma Phys. Contr. Fusion 34, 301.
/2/ Shaing, K.C., Crume, Jr. (1989) Phys. Rev. Lett. 63, 2369.
/3/ Hassan, A.N., Antonsen T.M. Jr., Drake, J.F. and Liu, C.S. (1991) Phys. Rev. Lett. 66, 309.
/4/ Hinton, F.L. (1991) Phys. Fluids B3 (3), 696.
/5/ Hirshman, S.P. and Sigmar D.J. (1981) Nucl. Fusion 21, 1079.

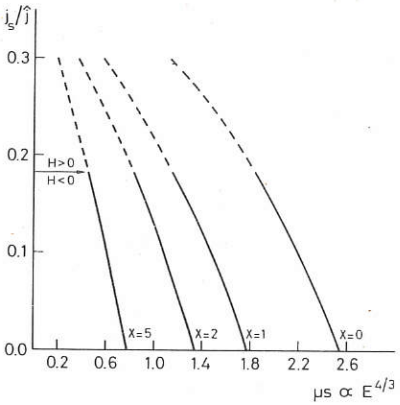

Current pedestal as function of the electric field in a isoentropic transformation. Bifurcating states exist for H>0.

NON-STANDARD HIGH ENERGY ION ORBITS

L.-G. Eriksson, H. Berk*, F. Porcelli and R. Stankiewicz

JET Joint Undertaking, Abingdon, Oxon OX14 3EA, UK
*Institute for Fusion Studies, University of Texas at Austin, USA

Introduction. During intense ICRF-heating in JET, the resonating minority ions are often accelerated up to energies in the MeV range. For such ions, the standard "banana" orbits are distorted near the magnetic axis into "potato shaped" orbits, with a characteristic width $\delta_p = (2qv_\perp/\Omega R)^{2/3}R$. For a 1 MeV hydrogen ion in a JET-like environment, $\delta_p \sim$ 30cm. Since, in JET, the width of the ICRF absorption region is typically of the order of or less than 30cm, most minority ions acquire non-standard potato orbits during on-axis high power ICRF-heating.

We present an analytic solution of the Fokker-Planck equation for perpendicular neutral injection of very energetic ions. Ions accelerated by ICRF can be expected to behave in a similar manner. The fast ions pressure profiles and a non standard fast ion current are discussed here. Furthermore, the stabilising influence of fast ions with large orbit widths on internal kink modes is also investigated. It is found that the maximum stabilising effect can be obtained by focusing the ICRF field as much as possible on the magnetic axis.

Orbit Analysis. The orbit followed by a particle in a tokamak can be derived from the three invariants of the motion, $E = mv^2/2$ (energy), $\mu = mv_\perp^2/2B$ (magnetic momentum), and $P_\phi = \Psi + RBv\phi/\Omega_c$ (toroidal angular momentum), where Ψ is the poloidal flux function. In this work we consider only trapped particles. We can therefore use the radius at the turning point of an orbit, r_1, defined such that $P\phi = \Psi(r_1)$, as an invariant instead of $P\phi$. For the sake of analytic simplicity we consider an equilibrium where the departure from concentric magnetic surfaces is $0(\varepsilon)$ and the safety factor q is constant. To leading order in ε, the orbits are then described by [1]

$$\pm(1-\Lambda+\varepsilon\cos\theta)^{1/2} = \Delta^{-1}\left(\varepsilon^2-\varepsilon_1^2\right) \qquad (1)$$

where, $\Lambda = \mu B_o/E$, $\varepsilon = r/R$, $B = B_o(1-\varepsilon\cos\theta)$ and $\Delta = 2qv/(\Omega_c R)$.

Bounce averages can be expressed as $\langle A\rangle = \tau_b^{-1}\oint(d\tau/d\varepsilon)Ad\varepsilon$, with τ_b the orbit bounce time. The time along the orbit is $d\tau = Rd\varepsilon/v_{Dr}$ where the radial component of the magnetic drift velocity is given by $v_{Dr} = v_{Do}\sin\theta$, $v_{Do} = \mu B/(\Omega_c R)$. Eq. (1) can be used to obtain $\sin\theta$ as a function of ε and an analytic expression for $d\tau/d\varepsilon$ can be found.

Fokker-Planck Equation for Neutral Beam Injection of Energetic Ions. Here we consider perpendicular injection of energetic ions with $v>>v_c$, where v_c is the critical velocity for which ion and electron collisions become equally important. A simplified bounce-averaged Fokker-Planck equation for such ions can be written, in the variables v, Λ, r, τ, as (cf. [2]),

$$\frac{\partial F}{\partial t} = \left\langle\frac{1}{\tau_s}\right\rangle\frac{1}{v^2}\frac{\partial}{\partial v}\left(v^3F\right) + \left\langle\frac{r^2-r_1^2}{\tau_s}\right\rangle\frac{\partial F}{\partial r_1^2} + \langle S\rangle \qquad (2)$$

The first two terms on the r.h.s. of eq. (3) represents electron drag. Since the drag changes the velocity of an ion, including the parallel velocity, P_ϕ is also changed. This leads to a vertical drift of the turning point position, which is described by the second term on the r.h.s. of eq. (3).

We consider injection in the poloidal plane and ionisation in a layer symmetric around the magnetic axis. The bounce averaged source is then given by,

$$\langle S\rangle = C\,\delta(v-v_o)S_o(r_1)\left[\tau_b^{-1}\,\delta(\Lambda-1-\varepsilon_1) + \tau_b^{-1}\,\delta(\Lambda-1+\varepsilon_1)\right] \qquad (3)$$

where $C = 2q^2/(\pi\Omega_c\Delta_o v_o 2)$, v_o is the injection velocity Δ_o is Δ for $v = v_o$ and S_o gives the number of particles injected per unit volume and unit time.

We introduce the following normalisations: $\tau = t/\tau_s$, $x \equiv v/v_o$, $z \equiv r_t^2 \bar{\delta}_{po}^{-2} x^{-4/3}$, $\left\langle r^2 - r_t^2 \right\rangle = \bar{\delta}_{po}^2 x^{4/3} g\ (z, x)$ with the orbit averaged potato width given by: $\bar{\delta}_{po} = \sqrt{\pi}\Gamma(2/3)\Delta_0^{4/3}R^2/\Gamma(1/6)$. If we assume τ_s to be independent of r the solution to Eq. (3) with the source term Eq. (4) can be written as

$$x^3 v_o^3 F = H(1-x)\, H\left(1-e^{-\tau}\right) S_o\left(\bar{\delta}_{po}\sqrt{z_*}\right)\left[\tau_b^{-1}\delta\left(\Lambda - 1 + \sqrt{z_*}\,\bar{\delta}_{po}\, R^{-1}\right) + \tau_b^{-1}\,\delta\left(\Lambda - 1 - \sqrt{z_*}\,\bar{\delta}_{po}R^{-1}\right)\right] \quad (4)$$

where H is the unit step function $z_* = z_*(z, \tau)$ is the initial value which gives z when the equation below is integrated from $\tau' = 0$ to $\tau' = \tau$,

$$dz/d\tau' = g\left(z, x(\tau')\right) + 4z/3, \quad x(t) = e^{-\tau'} \quad (5)$$

We have used this solution to analyse injection in the MeV range into a JET-like plasma. The following test case has been used: $E_{inj} = 1/2 m v_o^2 = 1$MeV, $P_{NBI} = 10$MW, $Te = 10$KeV, $n_e = 3.10^{19} m^{-3}$ and a constant source between r = 0 and $\left(r/\bar{\delta}_{po}\right)^2 = 0.15$. Fig. 1 shows the steady state distribution for different velocities. In Fig. 2 the evolution of the orbit of an ion injected at the low field side of the magnetic axis is shown. Figs. 3 and 4 show the steady state pressure and toroidal current profiles, respectively. The toroidal fast ion current is a consequence of the finite orbit width. In the zero banana width limit the pressure profile would be constant for $\left(r/\bar{\delta}_{po}\right)^2 = 0$ to 0.15 and zero for $\left(r/\bar{\delta}_{po}\right)^2 > 0.15$. As can be seen in Fig. 1 the zero banana width limit would give a very poor representation of the actual profile. The toroidal current scales as $j_{\parallel}\left(r/\bar{\delta}_{po}\right) = 0.5 e n_h v_o\, \bar{\delta}_{po}^{1/2} R^{-1/2}\, f\left(r/\bar{\delta}_{po}\right)$ where n_h is the fast ion density and f is a form factor of order unity, see Fig. 4. It is interesting to note that the total fast ion current is about 0.3MA and that it is concentrated to a narrow central region. Thus, it should play an important role for the current profile in the centre of the plasma for cases where the electron back current cannot compensate it.

Internal Kink Stabilization. We consider low frequency ($\omega/\langle\omega_D\rangle \to 0$) m = n = 1 perturbations, where $\langle\omega_D\rangle$ is the bounce averaged magnetic drift frequency. With the ordering ($\delta_p \sim r$), the solution to the drift-kinetic equation reads [3]

$$\delta f = -\left[\vec{\xi}_\perp \cdot \nabla\Psi - \frac{\mu B}{\Omega}\sum_{-\infty p}^{\infty} Y_p\left(P_\phi, E, \mu\right)\frac{\exp\left(ip\omega_b\tau\right)}{\langle\omega_D\rangle + p\omega_b}\right]\frac{\partial F}{\partial P_\phi}, \quad (6)$$

where $Y_p\left(P_\phi, E, \mu\right) = \oint \frac{d\tau}{\tau_b}\left(\vec{\xi}_\perp \cdot \nabla B\right)\exp\left[-i\left(\langle\omega_D\rangle + p\omega_b\right)\tau\right]$, $\omega_b = 2\pi/\tau_b$ and the perpendicular displacement is related to the perturbed magnetic field through $\delta\vec{B} = \nabla \times \left(\vec{\xi}_\perp \times \vec{B}\right)$. The perturbed fast particle energy is [3]

$$\delta W_{hot} = \frac{1}{2}\int d^3x \vec{\xi}_\perp^* \cdot \left(\nabla \cdot \delta\overleftrightarrow{P}_h\right) = 2\pi^2 m_h \int dP_\phi dE d\Lambda \tau_b \frac{\partial F}{\partial P_\phi}\frac{E^3\Lambda^2}{R^2\Omega\langle\omega_D\rangle}(A - S), \quad (7)$$

where $A = \left[R^2\Omega\langle\omega_D\rangle / E\Lambda\right]\langle|\xi_r|^2(\varepsilon/q)\cos\theta\rangle$ and $S = \sum_{-\infty}^{\infty} p\left[\langle\omega_D\rangle / \left(\langle\omega_D\rangle + p\omega_B\right)\right] |RY_p/B|^2$.

Eq. (7) is valid for arbitary F and it includes circulating orbits (provided one interprets $<\omega_D>$ as $<\dot{\phi}>$). For potato orbits, $\langle\omega_D\rangle \sim \omega_b$. so that enough terms of the series S have to be retained to obtain convergence. Note that A-S vanishes for a constant q = 1.

Analytic progress in the evaluation of δW_{hot} is possible if we assume the simplified distribution function , being a function of E, Λ and $P_\phi = \Psi(r_1)$,

$$F(r_1, E, \Lambda) = CH(r_1)\, H(r_* - r_1)\delta(E - E_h)\ \delta(\Lambda - 1), \tag{8}$$

with C = const, which represents trapped particles with orbits tangent to a vertical layer going through the magnetic axis up to a distance r_*. This choice mocks up the case of on-axis ICRF heating, with r_* is the width of the RF absorption layer. In figure 3 we present a graph of δW_{hot} vs r_*/δ_p for a model q profile such that (r/q) (dq/dr) << 1 for $r \le r_{max} = \max\{\delta_p, r_*\}$, and $q_o = 0.7$. From this result it may be concluded that the thin banana approximation yields roughly the correct numerical value of δW_{hot} provided one does not allow the radial width of the fast ion distribution to become smaller than the average orbit width. The situation, however, becomes more complex if the q profile varies significantly along the particle orbit. Results for a parabolic q profile are shown in figure 4. Realistic JET parameters for on-axis, high power ($P_{RF} \ge 10$MW) ICRF discharges are r_s~30-50cm, δ_p~20-30cm, r_*~15-20cm, q_o ~ 0.7 with r_s the q=1 radius. In this case, when δ_p becomes a sizeable fraction of r_s, there is a significant quantitative difference between the predictions of the thin banana theory and those of the full orbit theory, the latter being more pessimistic. One interesting consequence that may be checked experimentally is the existence of an optimum ICRF heating power to produce maximum stabilisation. Exceedingly large values of P_{RF} may result in orbits whose size is too large to produce effective stabilization.

References:

[1] T. Stringer, Plasma Physics **16** (1974) 651.
[2] V.Ya. Goloborod'ko et al. Nucl. Fusion **23** (1983) 399.
[3] F. Porcelli et al. submitted to Phys. Fluids B (1992).

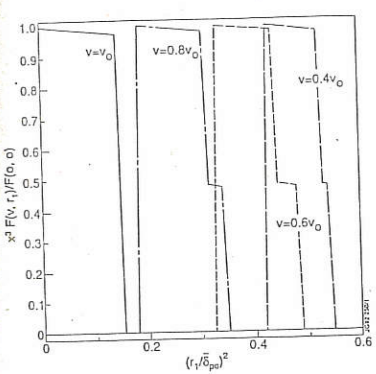

Fig. 1 Distribution function.

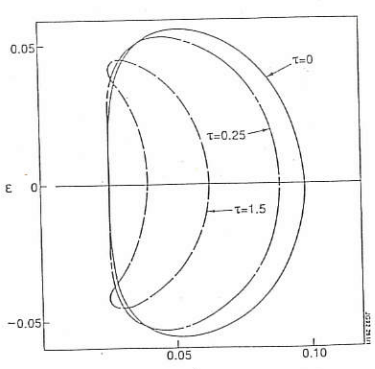

Fig. 2 Evolution of an ion orbit.

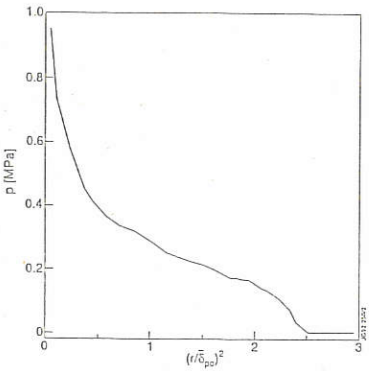

Fig. 3 Pressure profile.

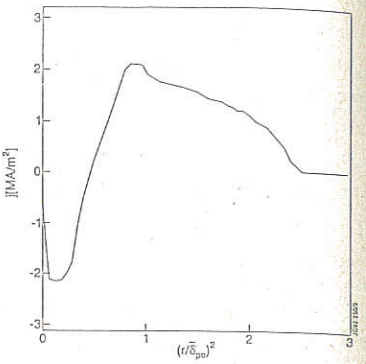

Fig. 4 Current density profile.

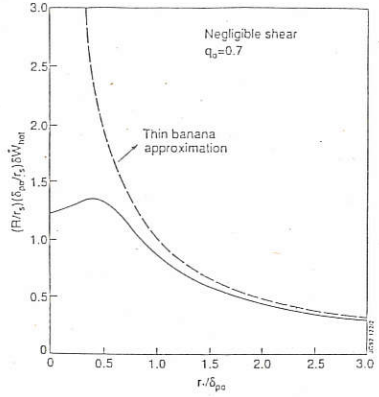

Fig. 5 Perturbed fast particle energy versus r_*/δ_{p0}.

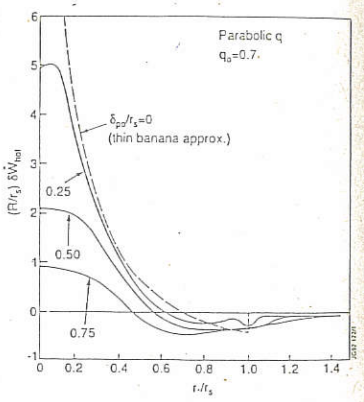

Fig. 6 Perturbed fast particle energy versus r_*/r_s.

Plasma transport as a dissipative structure

Kazuya Uehara

Experimental Plasma Physics Laboratory, Tokai Branch, Naka Fusion Research Establishment, Japan Atomic Energy Research Institute, Tokai, Ibaraki, Japan

The physical basis for transport analysis of magnetized plasma has for a long time been based on two body collisional diffusion theory, including neo-classical and quasi-linear theory. In the former, it is mainly considered that charged particles which wind themselves around the magnetic field lines can deviate from their orbits only through collisions. Fluctuational fields are neglected although the plasma has many modes of fluctuation. In the latter, a system of conservative equations is used for describing transport processes, even though transport is a typical dissipative process /1/. Fluid models do not serve to elucidate the mechanisms of diffusion since a Maxwellian is a priori assumed for the distribution function. It is believed in non-equilibrium statistical mechanics that the fluctuation-dissipation theorem would rule such a dissipation process when the deviation from thermal equilibrium is not so large /2/. The Einstein relation, $D=v^2/\nu$, is one typical of the fluctuation-dissipation theorem, where D is the diffusion coefficient, v is the thermal velocity, ν is the collision frequency. Since ν decreases with T, D must increase with T in usual. It is just a Bohm-like diffusion to keep this picture. Since the advent of the stellarator, Bohm-like diffusion coefficient has been said to satisfy experiments. However, the derivation of the Bohm-like diffusion coefficient has not been satisfactory for the following reasons. First, wherefore is the diffusion coefficient to be 1/16 ? Second, the kinetic meaning of this diffusion is unknown since the Bohm diffusion coefficient does not include the collision frequency. Third, when magnetic field is zero, D becomes infinite even though D must coincide with the Einstein relation in that limit.

In this paper, we survey plasma transport theory from the standpoint of zero order non-equilibrium statistical mechanics, and we develop the general theory of diffusion in a magnetized plasma using an asymmetric distribution function. This will provide a more detailed physical basis for previous experimental reports /3/ and will clarify how diffusion can be suppressed in magnetic fusion traps.

Particle flux Γ, is given by $\Gamma=\int_{-\infty}^{\infty} vf dv$. When the distribution function f is an even function, $\Gamma=0$. Therefore no flow exists. When f is asymmetric, $\Gamma \neq 0$. Therefore a flow is formed. For the existence of a flow, the distribution function must be deformed by some constraints which disturb the thermal equilibrium. The Maxwellian distribution function f_0 for electrons is deformed f by applying an electric field E, a magnetic field B, and a density gradient. The deformed distribution f must relax to f_0 on a time scale τ, which is the most simple dissipative model to exhibit irreversibility. The Boltzmann equation, which describes this process is

$$\frac{\partial f}{\partial t} + v \cdot \frac{\partial f}{\partial r} + \frac{e}{m} (E + v \times B) \cdot \frac{\partial f}{\partial v} = - \frac{f - f_0}{\tau} \qquad (1)$$

were τ is the inverse of the collision frequency $\nu(=\tau^{-1})$. We can estimate the deformed distribution function assuming the solution as the form $f=f_0 - v\cdot c\partial f_0/\partial\varepsilon$, where $\varepsilon=mv^2/2 + \Phi(r)$ and $\Phi(r)$ is the potential energy. The value of c can be estimated using vector analysis, which is often used in the derivation of the electric conductivity in solid state physics /4/. So we obtain the asymmetric distribution function

$$f = f_0 - \frac{\tau'}{1+\omega^2\tau'^2}\{ v + \tau'^2(\omega\cdot v)\omega - \tau'\omega \times v\}\cdot\frac{\partial f_0}{\partial r}$$

$$+ \frac{e\tau'}{1+\omega^2\tau'^2}\{ v + \tau'^2(\omega\cdot v)\omega - \tau'\omega \times v\}\cdot E\frac{\partial f_0}{\partial\varepsilon} \qquad (2)$$

where $\tau'= (\tau^{-1} - i\omega_0)^{-1}$, ω is the cyclotron frequency and ω_0 is the frequency of density fluctuation. We can obtain transport coefficient using above f

$$\Gamma_1 = \int_{-\infty}^{\infty} v\, fdv = - D\frac{\partial n}{\partial r} + \frac{\sigma}{e}E = \sum_j L_{ij}X_j \qquad (3)$$

The R.H.S. of eq.(3) express the Onsager relation in which X_j is a generalized force and L_{ij} is the resistance of flow.

First, we consider a simple configuration, i.e., we define the magnetic field direction as the z direction and the density gradient direction as the x direction, so that $B=B(0,0,B_z)$, $\tilde{E}=\tilde{E}(\tilde{E}_x,\tilde{E}_y,\tilde{E}_z)$ and $\partial f_0/\partial r=\partial f_0/\partial r(\partial f_0/\partial x,0,0)$, where $\tilde{E}$ is the fluctuational electric field caused by plasma waves satisfying the dispersion relations. We obtain the radial flux in the x direction as $\Gamma_x= \int_{-\infty}^{\infty} v_x f dv_x dv_y dv_z$, where we consider the diffusion of electrons since electrons with slow speed are dragged by ion with fast speed (ambipolar diffusion). The fluctuational electric field is derived from the potential fluctuation $\tilde{\Phi}$, which is $\tilde{E}= - \partial\tilde{\Phi}/\partial r$, where $\tilde{\Phi}$ is caused by the density fluctuation $\tilde{n}=\tilde{n}_0\exp i(k\cdot r - \omega_0 t)$. When the density fluctuation is growing in time, there exists a phase difference δ between $\tilde{\Phi}$ and $\tilde{n}$, such that $\tilde{\Phi} = \frac{kT_e}{e}\frac{\tilde{n}}{n}(1 - i\delta)$ The real flux is obtained by the time average and we can obtain this by taking the real part of the complex conjugate. The value of $Re\langle\tilde{E}_x\tilde{n}^*\rangle = \frac{kT_e}{e}\frac{k_x}{n}\langle\tilde{n}^2\rangle\delta$ and $Re\langle\tilde{E}_y\tilde{n}^*\rangle= \frac{kT_e}{e}\frac{k_y}{n}\langle\tilde{n}^2\rangle\delta$. Thus, we obtain the diffusion coefficient for low frequency fluctuations ($\nu >> \omega_0$) by setting $\Gamma_x= -D_{eff}n/L'$

$$D_{eff} = \frac{kT_e}{m\nu} \frac{\frac{L'}{L} + (\frac{\tilde{n}_0}{n})^2 k_x L'\delta + (\frac{\tilde{n}_0}{n})^2 \frac{\omega}{\nu} k_y L'\delta}{1 + (\frac{\omega}{\nu})^2} \quad (4)$$

where we have used the relation $\partial n/\partial x = n/L$ and the value of L' is a quantity so that D_{eff}/L' is the flow velocity of the flux Γ_x. When the first term in the numerator of eq.(4) is dominant, the value of D becomes the well-known classical diffusion coefficient when L'=L. However, the third term in the numerator of eq.(4) is typically much larger than the first and second term since it is typically observed experimentally /5/ that $(n_0/n)^2 = 10^{-3}$ and $\omega/\nu \approx 10^9$. So, we obtain the cross field radial diffusion coefficient for the normal plasma state as, $D_{eff} = D_B \approx \frac{1}{\gamma}\frac{kT_e}{eB}$ since $(\omega/\nu)^2 >> 1$, where $\gamma = ((\tilde{n}/n)^2 k_y L'(\gamma/\omega_0))^{-1}$ and $\delta = \gamma_w/\omega_0$, where γ_w is the growth rate of the fluctuation. This is just the Bohm-like diffusion coefficient when the growth rate γ_w does not depend on plasma temperature.

Next, we consider the tokamak configuration as $E = E(\tilde{E}_x, \tilde{E}_y, E_z + \tilde{E}_z)$ and $B = B(0, B_y, B_z)$, where B_z is the toroidal magnetic field and E_z is due to the loop voltage. The oscillation term including $\tilde{E}_z$ can be neglected because E_z is much larger than the fluctuation term ($E_z >> \tilde{E}_z$). Thus, the diffusion coefficient becomes $D \approx D_B - B_y E_z L'/B^2$ since $1 >> (\omega/\nu)^2$. Thus, in tokamaks the DC electric field can suppress the radial flux, which is useful for improving plasma confinement. The following remarks are listed.

(1) Equation (4) can be regarded as the form of a fluctuation-dissipation theorem in the presence of a magnetic field, $D_{eff} = v^{*2}/\nu$, where $v^{*2} = (kT_e/[m(1+(\omega/\nu)^2)])(L'/L + (\tilde{n}_0/n)^2 k_x L'\delta + (\tilde{n}_0/n)^2 (\omega/\nu) k_x L'\delta)$ is square of the effective thermal velocity. (2) When there exists a magnetic fluctuation, this must contribute to the deformation of the distribution function since the flux term $\tilde{n}\tilde{v} \propto \tilde{\omega}\tilde{E}_y\tilde{n}$ is important, as can be seen in eq.(4). (3) The value of γ in D_B must include the sum of many waves as $\gamma^{-1} = \Sigma_k (\tilde{n}_{k0}/n_k)^2 k_{ky} L'(\gamma_k/\omega_{0k})$ since many species of instability are candidates to cause the transport. (4) We can resolve the deformation of distribution function to bring the suppression of transport by external force such as electric field and the density gradient.

When $B=0(\omega=0)$, D becomes well-known Einstein relation$(=kT_e/m\nu)$ since $1 >> (\tilde{n}_0/n)^2 k_x L'\delta$. When $B \neq 0$ and $(\tilde{n}_0/n)^2 = 0$, which is the case of classical diffusion, D decreases since v^* decreases due to the increase of effective

mass by the factor $((1+(\omega/\nu)^2))$. A similar idea of heavy electron mass is seen in solid state physics. When $B\neq 0, (\tilde{n}_0/n)^2 \neq 0$, which is the usual plasma case, D increases more than $(\tilde{n}_0/n)^2 = 0$ case since v^* increases due to $\tilde{E} \times B$ drift. The important point is that all drift velocities are determined by the balance with collisions, in which ν is in the denominator of eq.(4) and that flux is composed of a linear superposition of the term including the density gradient and the $\tilde{E} \times B$ drift term as seen in R.H.S. of eq.(3).

The effective force can resolve the deformation of distribution function to suppress the transport. The value of E_z in the tokamak configuration performs this. Usually the fluctuational electric field becomes zero when time averaged. However, when the fluctuation is growing in time and/or the wave is traveling, the fluctuation does not cancel after time averaging. The former case yields Bohm-like diffusion and the latter is the case of Landau damping for resonant electrons. Non-linear coupling between electric field and magnetic field is essential for magnetized plasma. The effective electric field is produced by the thermal potential Φ ($E= -\nabla\Phi$) as the case of mirror machine. Recent study of the H mode in tokamaks indicates that the electric field is effective in this case as well.

In random walk theory, density gradient to cause the non-equilibrium state is not necessary, whereas the Einstein relation is defined stretching over both equilibrium and non-equilibrium states. A Bohm-like diffusion coefficient is often derived from the scheme of drift wave turbulence /6/. The growth rate of the drift wave is indeed a function of the density gradient, however, the fluctuations causing the transport are not limited to the drift wave in general. It is not an original observation that the Bohm-like diffusion coefficient can be derived when the growth rate of the turbulence wave has no dependence on the temperature. The original point in this paper is the use of deformation of the distribution function to determine the cross-field diffusion coefficient, whereas classical diffusion and Bohm-like diffusion have previously been treated separately /6/. The physical picture developed here explained why Bohm-like diffusion is dominant in a typical plasma, since the spontaneous fluctuation level $(\tilde{n}_0/n)^2$ is greater than 10^{-6}. Experimental knowledge of the kind of fluctuation involved will allow further refinement of the theory.

In conclusion, plasma transport in a magnetic field has been formulated from the standpoint of a dissipative structure. A form of the fluctuation-dissipation theorem has been derived for the case of transport in a magnetized plasma, based on the deviation from the thermal equilibrium state and the non-linear coupling between fluctuational electric and magnetic fields in the plasma.

/1/ P.Glansdorff and I.Prigigine, Thermodynamic Theory of Structure, Stability and Fluctuations, Wiley Interscience, London 1971
/2/ R.Kubo, J.Phys. Soc. Jpn. 12, 570.(1957)
/3/ K.Uehara, O.Naito,M.Seki and K.Hoshino, Phys.Rev. Lett. 64,757 (1990)
/4/ J.M.Ziman, Principles of the Theory of Solids, Cambridge University Press, 1964
/5/ A.J. Wootton et al., Plasma Phys. & Contr. Fusion 30, 1409 (1988)
/6/ K.Miyamoto, Plasma Physics for Nuclear Fusion, MIT press, New York 1985

AMBIPOLAR TRANSPORT IN A MAGNETICALLY PERTURBED TOKAMAK EDGE-REGION

R.W. Wittenberg, M. A. Hellberg, W. Feneberg*
Plasma Physics Research Institute, Department of Physics, University of Natal, 4001 Durban, South Africa
*MPI für Plasmaphysik, EURATOM Association, D-8046 Garching, Germany

1 Introduction

Magnetic perturbation of the plasma edge-region of a tokamak may be caused by a number of different sources. Some tokamaks (e.g. Tore Supra, Text) are fitted with ancillary coils yielding magnetic fields which may give rise to ergodicity or may be resonant with the main helical tokamak field somewhere within the plasma. Engineering flaws and tearing instabilities may similarly perturb the magnetic configuration.

In this paper we examine collisional effects on particle and energy fluxes in a weakly stochastic magnetic field in a tokamak edge-region. As before[1], we use the drift-kinetic equation with self-consistent BGK collision term and apply a Chapman-Enskog expansion. Cylindrical flux surfaces are perturbed by a stochastic field having a radial component, and radial transport is dominated by the parallel contribution.

We now extend the earlier studies[1] by allowing for an ambipolar electric field, including perturbations in potential on the flux surface and carrying out a parameter survey.

2 Collisional Transport Equations

We consider a weak stochastic magnetic field, whose radial component b_r may be expanded as

$$b_r = \sum\sum\sum b_{\omega,m,n}(r)\exp(i(\omega t + m\theta - n\phi)). \tag{1}$$

In principle the frequency ω could be due to instabilities, but in our applications we shall normally consider only the diamagnetic drift frequency ω_D superimposed on static fields due to the rotation of the plasma relative to auxiliary coils.

The particle flux perpendicular to the unperturbed cylindrical flux surfaces is dominated by diffusion along the inclined field lines, given by

$$\Gamma_r = < b_r \int f v_\parallel d^3v >, \tag{2}$$

where $< .. >$ represents a time-average over the magnetic surfaces, i.e. over θ, ϕ and t, and f is the total velocity distribution function. A similar relation describes the radial thermal flux Q_r.

We find f_j for the two species by solving the linearized drift kinetic equations with BGK (or Krook)[2] collision terms, using a Chapman-Enskög expansion. The electron equation is

$$\frac{\partial f_e}{\partial t} + (v_\parallel \hat{\mathbf{B}} + \mathbf{v_E}).\nabla f_e - \frac{q}{m}(\hat{\mathbf{B}}.\nabla\phi)\frac{\partial f_e}{\partial v_\parallel} = \nu_{e,e}(f^M_{e,e} - f_e) + \nu_{e,i}(f^M_{e,i} - f_e). \tag{3}$$

Here the Maxwellian $f^M_{e,e}$ describing the electron-electron collisions is chosen to have self-consistent values of density n_e, drift $\mathbf{u}_e$ and temperature T_e of the total (perturbed) distribution, i.e. particle number, momentum and energy are conserved in the collisions. The term describing electron-ion collisions ($f^M_{e,i}$) conserves particles and energy, but momentum

transfer is allowed, representing electron-ion friction. In the ion equation ion-ion collisions only are considered, using a fully self-consistent BGK term. The perturbed distribution function f_1 is represented by a series similar to that for b_r. Having found the perturbations f_1 to the two distribution functions, one may calculate the particle and heat fluxes.

Previously, in considering each species separately and assuming that the potential varied radially only (i.e. ϕ is constant on a magnetic surface), we found[1] that both particle and heat flux for a given species may be expressed in terms of two contributions, viz. one $\propto \{(n'/n) \pm (e\phi'/T)\}$ and one $\propto \{T'/T\}$, where the radial density and temperature gradients are those for the particular species under consideration. We also evaluated the form factors (coefficients of these different terms) near the resonance, i.e. for the parallel wavenumber $k_\parallel = (m - nq)/Rq = 0$, where m and n are the usual poloidal and toroidal mode numbers, R the major radius and q the safety factor. The form factors are functions of $k_\parallel$ and ω.

In this paper we now include the effect of an ambipolar electric field, and also allow the potential to vary on the magnetic surface, i.e. it has both a radially varying ϕ_o and a Fourier component $\phi_{m,n}$. The ambipolarity condition provides an equation for $\phi_{m,n}$. In evaluating the fluxes, we find the following relations for their Fourier modes (subscript $x = \omega, m, n$):

$$\Gamma^e_{r,x} = \Gamma^i_{r,x} = -n_{eo} \mid b_x \mid^2 \{D_1[T_{eo}\frac{n'_{eo}}{n_{eo}} + T_{io}\frac{n'_{io}}{n_{io}}] + D_2 T'_{eo} + D_3 T'_{io}\}, \tag{4}$$

$$Q^i_{r,x} = -n_{io}T_{io} \mid b_x \mid^2 \{A^i_1[T_{eo}\frac{n'_{eo}}{n_{eo}} + T_{io}\frac{n'_{io}}{n_{io}}] + A^i_2 T'_{io} + A^i_3 T'_{eo}\}, \tag{5}$$

$$Q^e_{r,x} = -n_{eo}T_{eo} \mid b_x \mid^2 \{A^e_1[T_{eo}\frac{n'_{eo}}{n_{eo}} + T_{io}\frac{n'_{io}}{n_{io}}] + A^e_2 T'_{eo} + A^e_3 T'_{io}\}. \tag{6}$$

We note that in principle all four gradients now affect all the fluxes evaluated and that the terms involving density gradients in each case have a coupled form, linking the density gradients of the two species.

The coefficients D_α, A^i_α and A^e_α are all complicated functions of the four dimensionless parameters $\beta_j = k_\parallel v_{th,j}/\nu_j$ and $\gamma_j = (\omega + m\omega_D)/\nu_j$, where $j = i, e$, and ν_j is the collision frequency.

3 Results

We have explored how the fluxes vary in the vicinity of the resonant surfaces by carrying out numerical evaluations of the coefficients as a function of β. We assume deuterons with $T_i \simeq T_e$ and thus use $\gamma_i = 60\gamma_e$ and $\beta_i = \beta_e = \beta$. In addition to considering typical parameters for the Tore Supra edge-region, we also consider a range of values so as to study scaling with γ. We present graphs for $\gamma_i = 18$, $\gamma_e = 0.3$.

3.1 Particle Flux

In Figure 1 we present the coefficients for the common particle flux. As expected, ambipolar losses are dominated by the ion behaviour and the behaviour is reminiscent of that found earlier for the ions in dealing with the separate species[1].

Coefficients D_1 and D_3 have similar magnitudes, i.e. not only the density gradients, but also the ion temperature gradient plays a significant role in the particle flux. Both these coefficients vanish at the magnetic resonance ($k_\parallel = 0$) and peak at about $\beta \sim 0.6\gamma_i$. We note that $\beta = \gamma_i$ is equivalent to the wave-particle resonance $(\omega + m\omega_D) = k_\parallel v_{th,i}$. By varying γ we find that the width of the peak in D_1 scales as $\Delta\beta \sim 0.45\gamma_i$, while that of D_3 varies as $\Delta\beta \sim 0.3\gamma_i$. The height of both peaks varies as $\propto \gamma_i^{-1}$, i.e. $\propto \nu_i$. Thus the ion collision frequency drives the ambipolar radial particle loss rate due to flux along the inclined field-lines.

3.2 Thermal Flux

The ion thermal flux is similar to that found in the absence of the ambipolar field[1]. Clearly the largest term is A_2^i, i.e. the contribution proportional to the ion temperature gradient. It has a non-zero minimum at $k_\parallel = 0$, with a peak at $\beta \sim 0.5\gamma_i$. This peak has a width $\Delta\beta \sim 0.3\gamma_i$, and it is followed by a minimum at about $\beta \sim 0.8\gamma_i$. In addition to A_2^i, A_1^i also plays a significant role, but it changes sign for $\beta \geq 0.7\gamma_i$, i.e. further from the magnetic resonance ($k_\parallel = 0$), the ion energy flows up the density gradient. Both the depth and the width of the minimum in the curve are found to be $\propto \gamma_i$. The electron temperature gradient plays a negligible role in the ion heat flow.

The coefficient A_2^e of the electron thermal flux, which is associated with the electron temperature gradient, exceeds all other heat flow coefficients by a factor of order $\sim 10^2$. It peaks strongly at the magnetic resonance $k_\parallel = 0$[1,3], the peak height being virtually independent of γ_e over a wide range, but falling off slowly for larger values (~ 1). Collisions cause broadening of the δ-function resonance[3], with halfwidth $\Delta\beta \propto \gamma^{0.5}$. For larger values of γ_e we note that the peak value of the coefficient is shifted slightly from $\beta = 0$. For small β the other two terms make a negligible contribution by comparison with the electron temperature gradient term, but they might play a role when considering the spatial variation because of their greater width in β and thus spatially.

3.3 Spatial Variation

We have further carried out a preliminary evaluation of the spatial (r-)dependence of the coefficients, so as to investigate the resultant radial flows in a device. Using typical values for Tore Supra (m = 18...24, n = 6), we find that the dominant heat flow, due to the electrons, is confined to a very narrow resonant region about the resonant surfaces, whose spacing is considerably greater than the typical width $\Delta\beta \sim \gamma_e^{0.5}$, and thus we would not expect this collisional broadening to play a significant role for electron heat flow. On the other hand, both the particle flux and the ion heat flow contributions peak away from $k_\parallel = 0$, with peak positions and widths of order $\gamma_i/2$, and this leads to overlap between the contributions from adjacent resonances, leading to an escape channel to the boundary.

4 Conclusion

The scaling we have found shows that the particle flux and ion heat flow are dominated by wave-particle type interactions with the ions, satisfying $(\omega + m\omega_D) \propto k_\parallel v_{th,i}$, while the electron thermal flux is largely associated with the magnetic resonance $k_\parallel = 0$. In all cases collisions cause broadening of the peaks.

5 References

1. W. Feneberg and M.A. Hellberg, *Proc XV Eur Conf on Contr Fusion & Plasma Phys, Dubrovnik*, 1081 (1988); W. Feneberg and M.A. Hellberg, *Contrib to Plasma Phys*, **28**, 329 (1988); M.A. Hellberg, et al., *Proc Int Conf Plasma Phys, New Delhi*, 885 (1989).
2. P.L. Bhatnagar, E.P. Gross and M. Krook, *Phys Rev*, **94**, 511 (1954).
3. A.B. Rechester and M.N. Rosenbluth, *Phys Rev Letts*, **40**, 38 (1978).

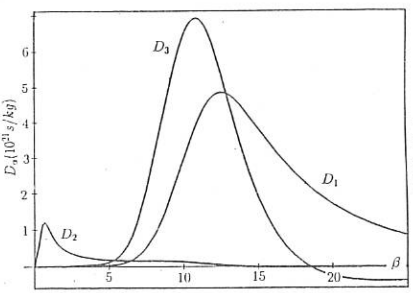

Figure 1: Particle flux coefficients, D_α.

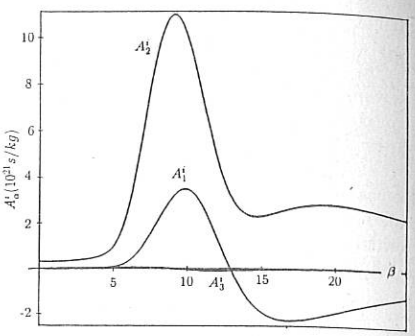

Figure 2: Ion heat flow coefficients, A_α^i.

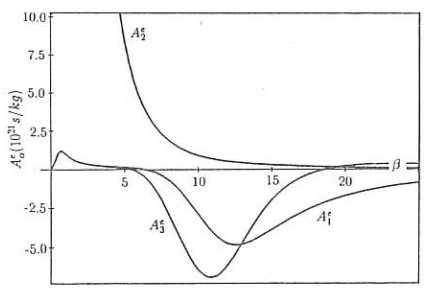

Figure 3: Electron heat flow coefficients, A_α^e.

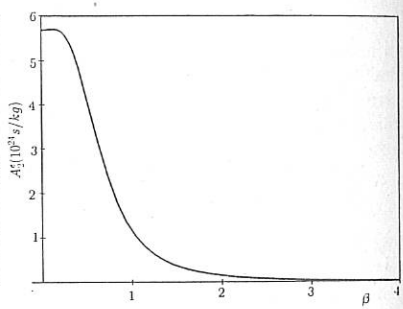

Figure 4: Dominant heat flow coefficient, A_2^e.

NEOCLASSICAL TRANSPORT WITH SURFACE VARIATION OF THE MACROSCOPIC QUANTITIES

W. Feneberg Max-Planck-Institut für Plasmaphysik,
EURATOM-IPP Ass., 8046 Garching, Germany

INTRODUCTION:

The inclusion of poloidal variations of temperature, flow velocity and density into the neoclassical theory is possible, if one investigates solutions of a linearized kinetic equation obtained from the Fokker-Planck equation by gyroradius ordering. Complementary to the usual drift kinetic theory where radial transport is described by the gyro center motion only, here the losses are also based on the drift terms arising from the fast gyromotion in conjunction with surface variations of the macroscopic quantities. While the effects of the gyrocenter motion are completely present within this theory, the radial transport due to the drift terms also included here exists even if the gyrocenter is in a fixed position. From this calculation one finds the poloidal variation of the parallel viscous forces and the parallel heat fluxes in the banana collisionality regime. This approach provides a bridge between the two usual extreme plasma descriptions, namely the collisional fluid Braginskii equations and collisionless kinetic descriptions by including the collisions directly via momentum approach. Such moment expansions using an orthonormal sequence of functions should work for all collisionalities, but the number of terms necessary for an accurate answer is large in the long mean free path regime as it is shown below.

A. THE TREATMENT OF THE COMPLETE KINETIC EQUATION:

Starting from the Fokker-Planck equation for the distribution function the ansatz $f = f_M + f_l$ is appropriate, where f_M is a local Maxwellian with two temperatures T_{II} and $T_\perp$. f_l is chosen to satisfy the conditions $\int f_l \delta^3 w = \int w_{II} f_l \delta^3 w = \int w_{II}^2 f_l \delta^3 w = \int w_\perp^2 f_l \delta^3\, w = 0$, therefore it does not contribute to the moments of density, flow and temperature, defined already by the Maxwellian. ($\vec{w}$ is the particle random velocity.) f_l is separated in $f_l = f_M(\varphi_l + \varphi_2)$, with φ_1 describing that part of the distribution function which is independent from the gyrophase. The equation for φ_l is correct to first oder in δ, the usual gyroradius parameter. All phase dependent parts of f_l are contained within φ_2. It is that quantity from which the radial transport can be computed in second order δ^2 being composed by a lot of pieces coming from the solution for φ_1 which enters the equation for φ_2. In first order δ the solution for φ_2 describes the well known poloidal heat flow $\nabla T \times \vec{B}$, with ∇T here the radial gradient of the temperature.
The equation for $\varphi_1 = \varphi_1(w_{II}, w_\perp^2, \vec{x})$ reads (for the electrons):

$$L_l\varphi_1 + L_2\varphi_2 + L_3 f_M = I_e(f) - \frac{m_e}{n_e T_{II}} f_M w_{II} \int w_{II} I_e \delta^3 w + 0(\delta^2) \qquad (1)$$

The left hand side consists of 3 parts:

a) The homogeneous part:

$$L_I\varphi_1 = w_{II}\vec{b}\nabla'(f_M\varphi_I) + \frac{w_\perp^2}{2}\nabla\cdot\vec{b}(\partial(f_M\varphi_I)/\partial w_{II} - 2w_{II}\partial(f_M\varphi_I)/\partial w_\perp^2)$$

(∇' means the derivation at fixed $w_{II}, w_\perp^2$)
This expression is consistent with that given by the work of Hinton and Wong |1|. It contains the curvature of the magnetic field ($\vec{b}$ = unit vektor of $\vec{B}$) which becomes comparable with the collision term $I_e(f)$ on the right side at the transition from plateau to the banana region. In the paper published last year |2| this term was omitted. Therefore these results are only valid in the plateau region. In addition one finds two driving terms:

b) $L_2\varphi_2 = f_M\left(\frac{m_e w^2}{2T_o} - \frac{5}{2}\right)\frac{w^2}{\Omega_e T_o}\nabla T_o\left(\frac{\nabla B}{B}\times\vec{b}\right)$. It contais with ∇T_o the radial gradient of the zero order temperature T_o, which is a flux function. (Ω_e is the electron gyro frequency.) This term stands for the divergence of the poloidal heat flow determinig the surface variation of the temperature.

c) All surface varying quantities coming from the local Maxwellian are part of $L_3 f_M$:

$$\begin{aligned} L_3 f_M = {} & f_M\frac{w_{II}}{T_{II}}\vec{b}\nabla T_{II}\left(\frac{m_e w_{II}^2}{2T_{II}} - \frac{3}{2}\right) + \frac{f_M}{T_\perp}w_{II}\vec{b}\nabla T_\perp\left(\frac{m_e w_\perp^2}{2T_\perp} - 1\right) \\ & - f_M w_{II}\frac{w_\perp^2}{2}\nabla\vec{b}\left(\frac{m_e}{T_{II}} - \frac{m_e}{T_\perp}\right) - f_M\frac{w_{II}}{T_{II}}(T_{II} - T_\perp)\nabla\vec{b} + f_M\nabla\cdot\vec{V}\left(\frac{m_e w_\perp^2}{2T_\perp} - 1\right) \\ & + f_M\vec{b}(\vec{b}\nabla)\vec{V}\left(w_{II}^2\frac{m_e}{T_{II}} - w_\perp^2\frac{m_e}{2T_\perp}\right) \end{aligned}$$

Here $T_{II}, T_\perp, \vec{V}$ are the parallel- and perpendicular temperature, $\vec{V}$ the mean velocity. (The same equation for φ_1 exists by the way for the ions, replacing m_e with m_i and Ω_e with - Ω_i.) All quantities in the equation above are considered to be of first order in δ. Therefore one is restricted here to small mean velocities $\vec{V}/v_{th} \approx \delta, v_{th}$ being the thermal velocity.

Beside this equation for φ_I there exist the two moment equations for particle- and momemtum conservation which had been used to eleminate the density variation and the parallel electric field from the Fokker-Planck equation:

$$\nabla(n_e\vec{V}) = 0 \tag{2}$$

$$(p_{II} - p_\perp)\nabla\vec{b} + \vec{b}\nabla p_{II} + en_e\vec{b}\vec{E} = \int m_e w_{II} I_e \delta^3 w \tag{3}$$

Here the equation for φ_1 (equ. 1) is much simpler than the recast kinetic equation given by Wang |3|, but the physical content is the same.

B. MOMENT EXPANSIONS FOR A 1-d KINETIC EQUATION.

Using the model collision operator of Clemmow and Dougherty $I_e(f) = \nu\frac{\partial}{\partial w_{II}}(w_{II}f + \frac{T_{II}}{m_e}\frac{\partial f}{\partial w_{II}})$ which preserves particles, momentum and energy, one can study a solution

for φ_1 which depends only from the parallel velocity $x = w_{II}/v_{th}$ making the ansatz $\varphi_l = \sum_{n=3}^{N} a_n(\Theta)H_n(x)$. (Here $v_{th} = (T_{II}/m_e)^{1/2}$ is the thermal velocity, ν the collision frequency and H_n is the $n-th$ Hermite polynomial.)
Multiplying the kin. equ. with $H_n(x)$ one gets by integration a system of linear moment equations for the coefficients a_n. This model is very similar to the work of Stevens and Weitzner |4| dealing with the same problem of moment approximation methods. One has to look for solutions of the system which are periodic with respect to the poloidal angle Θ. This condition of periodicity was studied extensively by Stevens and Weitzner. Here the simple ansatz is made $a_n = a_{n,o} + a_{n,s}sin\Theta + a_{n,c}cos\Theta$, neglecting higher Fourier components.
This ansatz is consistent with an expansion in $\epsilon = r/R$. We are using here and in the following chapter circular magnetic surfaces with $\nabla \cdot \vec{b} = \epsilon sin\Theta/Rq$ and $\nabla T_o(\frac{\nabla B}{B} \times \vec{b}) = -T_o' sin\Theta/R$. ($T_o'$ is the derivation to r.)
In analogy to a_n for the parallel temperature T_{II} also the ansatz is made $T_{II} = T_{II,o}(1 + \tilde{T}_{II,s}sin\Theta + \tilde{T}_{II,c}cos\Theta)$. For the special case of $Rq/\epsilon^2\lambda = 0.1$, which is a realistic value for JET, one obtains for $\tilde{T}_{II,s}$ the following results using N Hermite polynomials within the expansion:(λ being the mean free path, Rq the poloidal rotation connection legth, $\tilde{V}_{\Theta,o} = V_{\Theta,o}/v_{th}$, with $V_{\Theta,o}$ the poloidal rotation velocity of the electrons, ϱ_g the electron gyroradius)

$$N = 20 : \tilde{T}_{II,s} = 0.79Rq/\epsilon^2\lambda(-q\tilde{V}_{\Theta,o} + \varrho_g T_o' q/T_o)$$
$$N = 30 : \tilde{T}_{II,s} = 0.68Rq/\epsilon^2\lambda(-q\tilde{V}_{\Theta,o} + \varrho_g T_o' q/T_o)$$

Low order approximations give the following analytic results in the limit $Rq/\lambda >> 1$:

$$N = 3 : \tilde{T}_{II,s} = 2Rq/\lambda(-q\tilde{V}_{\Theta,o} + 5/2\varrho_o T_o' q/T_o) \quad (\text{Grad's } 13-\text{moment method})$$
$$N = 4 : \tilde{T}_{II,s} = 8Rq/\epsilon^2\lambda(-q\tilde{V}_{\Theta,o} + \varrho_g T_o' q/T_o)$$
$$N = 5 : \tilde{T}_{II,s} = Rq/\lambda(-14/3\tilde{V}_{\Theta,o} + 23/3\varrho_g T_o' q/T_o)$$

The pure convergence observed does not depend from the existence of the magnetic curvature respectively the trapped particles. In the calculation last year |2| omitting the curvature term $\nabla \cdot \vec{b}$ from the kinetic equation the same number N was needed.

C. THE LORENTZ GAS MODEL:

This model is considered to give the neoclassical transport coefficients for the electrons correct up to a factor of 2. It is more appropriate here to work with the pitch angle variable η defined with $w_{II} = \eta w$ and w the amount of the particle velocity, such that $\varphi_l = \varphi_l(\eta_l w_l \vec{x})$. Following Braginskii the $e-i$ collision operator for a pure plasma with $Z = 1$ is:

$$I_e(f) = \frac{2\pi\ell n\Lambda e^4 n_e}{m_e^2}\left(\frac{1}{w^3}\frac{\partial}{\partial\eta}\left((1-\eta^2)\frac{\partial f_e}{\partial\eta}\right) - 2f_{e,M}d_{II}\frac{\eta}{w^2}\frac{m_e}{T_\perp}\right) + 0(m_e/m_i)$$

(d_{II} is here the $e-i$ drift velocity parallel to the magnetic field.)
The homogeneous part $L_l\varphi_l$ of equ. (1) now reads:

$$L_l\varphi_l = \eta w\vec{b}\nabla(f_M\varphi_l) + \frac{w}{2}\nabla\vec{b}(1-\eta^2)\partial(f_M\varphi_l)/\partial\eta$$

Expanding ϕ_l in a series of Legendre polynomials $\phi_l = \sum_{n=0}^{N} a_n P_n(\eta)$ one obtains for $a_n = a_n(w_l\Theta)$ a system of linear equations which can easily be solved with the Fourier ansatz of chapter B. The conditions on φ_l (see p. 1) must be fulfilled for each Fourier component of the moments of a_o, a_l, a_2. Together with the moment equations (2,3) for particles and momentum one arrives at the end at 5 conditions from which the surface variation of the temperature is completely determined as function of the poloidal rotation velocity, the radial temp. gradient and the drift velocity. The parallel viscosity now reads:

$$\tilde{T}_{II,s} - \tilde{T}_{\perp,s} = N_l \tilde{V}^{(e)}_{\Theta,o} + N_2 \varrho_g T_e'/T_e + N_3 \tilde{d}_{II,o} = (P_{II,s} - P_{\perp,s})/n_e$$
$$\tilde{T}_{II,c} - \tilde{T}_{\perp,c} = M_l \tilde{V}^{(e)}_{\Theta,o} + M_2 \varrho_g T_e'/T_e + M_3 \tilde{d}_{II,0} = (P_{II,c} - P_{\perp,c})/n_e$$

The quantities $N_l, N_2, N_3, M_l, M_2, M_3$ are integrals over the velocity w. This work is still in progress.

|1| F.L. Hinton, S.K. Wong, Phys. Fluids 28 (10), 1985

|2| W. Feneberg, W. Kerner, EPS Berlin

|3| J.P. Wang, Report University of Wisconsin, UW-CPTC 91-1

|4| D.C. Stevens, H. Weitzner and D. Pfirsch, New York University, PACS Nos.: 51.10 +y, 52.25 Dg, 52.25 Fi

I would like to acknowledge the numerical calculations made by G. Fußmann and helpful discussions with H. Weitzner.

Time-dependent Neutron Rate Interpretation for Deuterium Injection into Deuterium Plasmas

B. Wolle, L.-G. Eriksson+, K. Hübner, P.D. Morgan+, G. Sadler+,
L.N. Tsintsadze* and M.G. von Hellermann+
Institut für Angewandte Physik, Universität Heidelberg, D-6900 Heidelberg.
+JET Joint Undertaking, Abingdon Oxon. OX14 3EA, UK.
*Institute of Physics, Georgian Academy of Science, Tbilisi 77, Georgia.

ABSTRACT

We present a comparatively fast, time-dependent code for neutron rate interpretation of neutral beam heated tokamak plasmas which is based on a Fokker-Planck model for injected ions. Results from the code for test cases illustrate the time scales involved in neutron production. Finally, first results of time-dependent interpretation calculations for JET hot-ion mode discharges are presented.

INTRODUCTION

Neutron diagnostics offer one of the most direct ways to obtain information about the deuteron characteristics in fusion plasmas such as densities and temperatures. Thus, neutron diagnostics are of increasing importance for future fusion devices and efforts are being made to improve the present methods for interpreting neutron signals. Using the measured fusion reaction rate, e.g. measured neutron rates, it is possible to carry out interpretation calculations by modelling of the ion velocity distribution and extract plasma parameters such as densities and temperatures. For Maxwellian plasmas this is a straightforward procedure. However, during neutral beam injection the velocity distribution of the injected ions becomes non-Maxwellian, leading to a strong enhancement of the fusion reaction rate above the thermal level. Thus, it is important to use models which describe the non-Maxwellian velocity distributions in neutral beam heated plasmas with sufficient accuracy. Sophisticated but time-consuming codes, such as TRANSP, are commonly used to obtain information about the plasma deuterons. However, these codes are not practicable for routine analysis, i.e. for more than a very small sample of experimental conditions.

INTERPRETATION CODE

The input data to our interpretation code NR-FPS (Neutron-Rate Fokker-Planck Solver) are whenever possible, measured plasma data. The neutral beam deposition profile is calculated through deposition codes which are using the measured data as well. For our reactivity calculations, we use newly available cross-section data /2/. The code includes tail-tail fusion reaction rates, which are important but

often had to be neglected since they are difficult to calculate. The value of the plasma parameters of interest, for example n_D, is obtained by using an iteration technique. There, the evolution of the distribution function and the fusion reactivity from the previous time-point is calculated by varying the plasma parameter of interest in such a way that the measured and calculated neutron rates finally agree. This agreement is after 3-4 iterations typically better than 1%. The output of an interpretation calculation comprises the composition of the measured neutron rate with respect to thermal, beam-thermal and beam-beam components of origin and the iterated value of the plasma parameter. Of course, our code also allows prediction of neutron rates and neutron emission profiles. Here the average uncertainty can be less than 20%, provided the input data are measured with sufficient accuracy /1/.

The code is based on the time-dependent Fokker-Planck equation including relevant source and loss terms. In order to make the computation time sufficiently short for routine analysis, the 2D Fokker-Planck equation is solved by expanding the distribution in the eigenfunctions of the pitch angle scattering operator. Thus the problem is reduced to a set of 1D parabolic differential equations. Usually, only the first few orders (typically 4-6) need to be calculated to obtain a reasonable accuracy. We solve the 1D equations with a finite element method. Further details about our code and the numerical schemes are given in /1/.

NUMERICAL RESULTS

As an example, we considered a plasma with $T_e = T_i = 5$ keV, $n_e = n_D = 2 \cdot 10^{13}\text{cm}^{-3}$ and 80 keV D^0-injection with a source rate of $S_0 = 2 \cdot 10^{13}\text{cm}^{-3}\text{s}^{-1}$. The injection angle was set to 45° and source and loss term have been balanced. In this example, the slowing-down time for the ions on electrons is $\tau_s \approx 1.25$ s. Spitzer's critical energy E_α, below which collisions on ions are more important than collisions on electrons, is about 93 keV. The time needed to establish the velocity distribution below the injection velocity, t_{st}, i.e. the time it takes for a particle to slow down from the injection velocity to the thermal region, can be estimated from the time-dependent Fokker-Planck equation. Using the high energy approximation neglecting

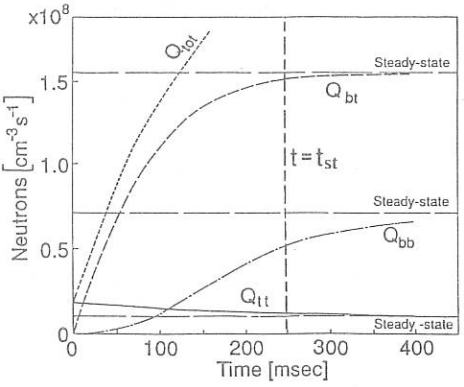

FIG. 1: *Thermal (Q_{tt}), Beam-thermal(Q_{bt}) and beam-beam (Q_{bb}) neutron rates for the test case data as functions of time.*

diffusive terms, we obtain:

$$t_{st} = \frac{\tau_s}{3} \ln\left(1 + \left(\frac{E_o}{E_\alpha}\right)^{3/2}\right) \quad (1)$$

where E_o is the injection energy. With the values given above, t_{st} is approximately 0.25 s. In Fig. 1, the neutron rates due to thermal, beam-thermal and beam-beam neutron production are plotted vs. time. Since the beam-thermal neutron production is mostly affected by slowing-down processes, more than 90% of the steady-state level is reached after this time. For the beam-beam neutron production however, the much slower diffusive time scale is relevant and thus quasi steady-state conditions are reached much later in this example. The expression for t_{st}, Eq. (1), gives a criterion for deciding when steady-state calculations are valid. In order to resolve the evolution of the neutron rate on time scales shorter than the one given by t_{st}, time-dependent calculations are necessary.

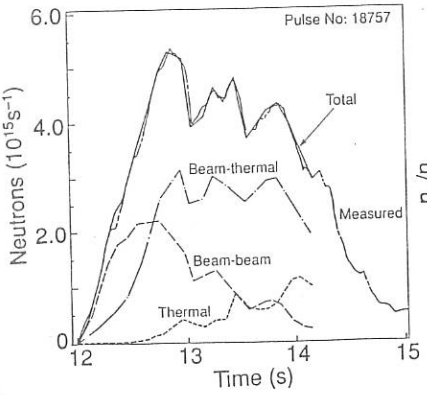

FIG. 2: *Measured neutron rate together with the results (total, thermal, beam-thermal and beam-beam neutron rates) of the interpertation calculation after 3 iterations.*

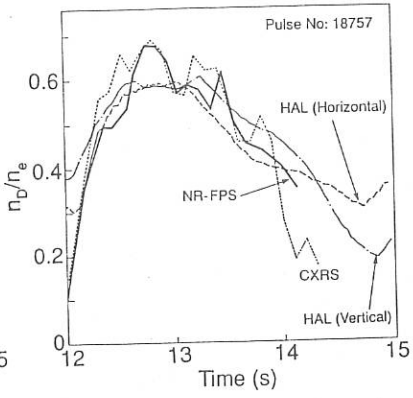

FIG. 3: *Calculated dilution ratio n_D/n_e as a function of time after 3 iterations together with measured data from the CX-diagnostic (CXRS) and the visible bremsstrahlung Z_{eff} (HAL).*

NEUTRON RATE INTERPRETATION

To demonstrate the applicability of our method, we present calculations for JET discharges with intense 80 keV deuterium injection into a plasma with rather low electron density. The neutron rate thus is very sensitive to small changes of the deuteron density and interpretation calculations to determine n_D/n_e-ratios can be carried out with good accuracy /3/. We follow the deuteron velocity distribution in time for 11 flux surfaces and iteratively calculate the dilution ratio n_D/n_e from the measured neutron rates for typically 10-20 time points of interest during the

neutral beam injection phase. For a single time and radius point, the calculation of the deuteron distribution and the reactivity calculation takes approximately 0.15 s CPU time on the IBM 3090.

In the cases discussed here, the calculated neutron rate using the obtained dilution ratio is matching the measured neutron rates after 3 iterations rather accurately. This is shown in Fig. 2, where the calculated total neutron rate corresponding to the 3rd iteration step to obtain the dilution ratio for the discharge #18757 is plotted in time together with the measurement. Clearly, the agreement between calculation and measurement is sufficient to end the iteration process. The calculated composition of the total neutron rate with respect to thermal, beam-thermal and beam-beam production is plotted in Fig. 2 as well. Fig. 3 shows the obtained n_D/n_e-values for discharge #18757 as a function of time together with the measured data from the CXRS-diagnostics and the values obtained from the visible bremsstrahlung Z_{eff} assuming carbon as impurity ion species. The different n_D/n_e-traces agree well which demonstrates the potential of our methods for future plasma diagnostics.

Due to the low density at the beginning of the injection phase, the slowing-down time scale is relatively long, which leads to a comparatively large fraction of fast ions, typically more than 40% of the total deuteron density. Thus the non-thermal neutron production and in particular the beam-beam neutron production dominates. For slightly later times, with increasing thermal density, the beam-thermal neutron production starts to contribute significantly to the total neutron production, while the beam-beam production however still remains dominating. Then, with rising electron density, the slowing-down times become shorter which leads to a decrease of the fast particle density to values of 20-40% of the deuteron density. The beam-beam neutron production is therefore decreasing and most of the neutrons originate from beam-thermal production, in these cases between 60 and 70%.

ACKNOWLEDGEMENTS – The authors acknowledge the contribution of the JET team in the production of the data used in this paper. Furthermore, one of the authors, B. Wolle, would like to thank JET Theory Division for its hospitality and Prof. D. Düchs for his encouraging interest in this work.

REFERENCES

/1/ Wolle B. and Eriksson L.-G. (1992), Rep. JET-R(92)02, JET Joint Undertaking, Abingdon, Oxfordshire.

/2/ Bosch H.-S., and Hale G. M. (1990), *Proc. 17th Eur. Conf. on Controlled Fusion and Plasma Heating*, Amsterdam, 1990, Vol. 14B, Part II, p. 873 and to be published in *Nucl. Fusion*.

/3/ Wolle B. et. al. (1991). *Plasma Phys. Contr. Fusion* **33**, 1863.

MULTIDIMENSIONAL WKB SOLUTION OF A WAVE EQUATION

G.V. Pereverzev[1]

I.V. Kurchatov Institute of Atomic Energy, Moscow, Russia

An asymptotic method of solving the wave equation for electrostatic waves in inhomogeneous anisotropic plasmas is developed. This method is an extension of the WKB method to a multidimensional case [1,2]. It reduces the general wave equation to a set of ordinary differential equations similar to that of the eikonal approach and includes the latter as a particular case. However, the WKB method makes use of another kind of asymptotic expansion and unlike the eikonal approach describes the wave properties, i.e. diffraction and interference. Recently the WKB method was used to show that diffraction plays a considerable role in lower hybrid wave spectrum broadening and filling of the spectral gap [3,4].

We consider the equation for electrostatic waves in plasmas:

$$\frac{\partial}{\partial x^j}\varepsilon^{jk}\frac{\partial \Phi}{\partial x^k} = 0. \tag{1}$$

Summation from one to three is implied for the repeating indexes. An asymptotic solution of Eq.(1) is sought in the form

$$\Phi(\vec{r}) = A\varphi_\nu(\sqrt{k_0}v)\varphi_\mu(\sqrt{k_0}u)\exp(ik_0S). \tag{2}$$

Here $A(\vec{r})$, $S(\vec{r})$, $v(\vec{r})$, $u(\vec{r})$ are unknown functions to be determined. $\varphi_\nu(\xi)$ is the function of the parabolic cylinder.

The solution (2) makes use of the asymptotic expansion with respect to the large parameter

$$k_0 = L/\lambda \gg 1,$$

where $L = \min|\nabla \ln|\varepsilon^{jk}||^{-1}$ is a characteristic medium inhomogeneity scale and λ is the wave length. All unknown functions are assumed to have the same characteristic size of spatial variation as the medium inhomogeneity length L:

$$L \approx \min|\nabla \ln|A||^{-1} \approx \min|\nabla \ln|S||^{-1} \approx \min|\nabla \ln|v||^{-1} \approx \min|\nabla \ln|u||^{-1}. \tag{3}$$

Substitution of Eq.(2) in the wave equation (1) results in

$$\begin{aligned}
&-k_0^2 A\varphi_\nu\varphi_\mu\varepsilon^{jk}\left[S_jS_k - v^2v_jv_k - u^2u_ju_k\right] \\
&\quad +ik_0^{3/2}A\left[\varphi'_\nu\varphi_\nu(\varepsilon^{jk}+\varepsilon^{kj})S_jv_k + \varphi_\nu\varphi'_\mu(\varepsilon^{jk}+\varepsilon^{kj})S_ju_k\right] \\
&\quad +ik_0\varphi_\nu\varphi_\mu\left\{(\varepsilon^{jk}+\varepsilon^{kj})A_jS_k + A(\varepsilon^{jk}S_k)_j + iA\varepsilon^{jk}\left[(2\nu+1)v_jv_k + (2\mu+1)u_ju_k\right]\right\} \\
&\quad +ik_0A\varphi'_\nu\varphi'_\mu(\varepsilon^{jk}+\varepsilon^{kj})v_ju_k + O(k_0^{1/2}) = 0.
\end{aligned} \tag{4}$$

Here the Roman subscripts denote partial derivatives with respect to the correspondent spatial coordinates, i.e. $f_j = \partial f/\partial x^j$. The next property of the function of the parabolic cylinder $\varphi_\nu(\xi)$ was used in the derivation of Eq.(4):

$$\varphi''_\nu(\xi) + (2\nu+1)\varphi_\nu(\xi) - \xi^2\varphi_\nu(\xi) = 0.$$

This also shows that φ''_ν is of the same order as φ_ν with respect to the large parameter k_0. So all dependences on the large parameter of expansion k_0 in Eq.(4) are shown explicitly. To

[1]Presently at Max-Planck-Institut für Plasmaphysik, Garching, Germany

satisfy Eq.(4), it is sufficient to satisfy the following set of equations

$$H = 0, \tag{5}$$

$$v_j V^j = 0, \qquad u_j V^j = 0, \tag{6}$$

$$(\varepsilon^{jk} + \varepsilon^{kj}) v_j u_k = 0, \tag{7}$$

$$iA_j V^j + iA(\varepsilon^{jk} S_k)_j - A(2\nu + 1)\varepsilon^{jk} v_j v_k - A(2\mu + 1)\varepsilon^{jk} u_j u_k = 0, \tag{8}$$

where the notations

$$H \stackrel{\text{def}}{=} \varepsilon^{jk} S_j S_k - v^2 \varepsilon^{jk} v_j v_k - u^2 \varepsilon^{jk} u_j u_k, \qquad V^j \stackrel{\text{def}}{=} (\varepsilon^{jk} + \varepsilon^{kj}) S_k = \partial H / \partial S_j$$

are used. We now have the set of equations (5)-(8) for the 4 unknown functions $S = S(\vec{r})$, $v = v(\vec{r})$, $u = u(\vec{r})$ and $A = A(\vec{r})$. The wave amplitude A is included in Eq.(8) solely. It will be found afterwards. Therefore consider the set of equations (5)-(7).

First of all note that it has a solution

$$x^i = q^i(\tau), \qquad S_i = p_i(\tau), \qquad v(\vec{r}) \equiv u(\vec{r}) \equiv 0, \tag{9}$$

where the functions $q^i(\tau)$ and $p_i(\tau)$ are determined by the Hamiltonian equations

$$\frac{dq^i}{d\tau} = \frac{\partial H_0}{\partial S_i}, \qquad \frac{dp_i}{d\tau} = -\frac{\partial H_0}{\partial x^i}, \tag{10}$$

H_0 being the Hamiltonian of the eikonal approximation for the wave equation (1)

$$H_0 \stackrel{\text{def}}{=} \varepsilon^{jk} S_j S_k. \tag{11}$$

Consequently, the solution (10) coincides with the solution of Eq.(1) in the eikonal approximation. In the general case, $v(\vec{r}) \not\equiv 0$ and $u(\vec{r}) \not\equiv 0$ and Eqs.(9) do not give a solution of system (5)-(7) any longer. However, the first two of Eqs.(9) still represent an approximate solution of Eqs.(5)-(7) in the vicinity of the spatial curve $v(\vec{r}) = u(\vec{r}) = 0$. It is clear that this curve is a trajectory (ray) of Eq.(1). So each ray generates a family of solutions such that $v = u = 0$ on the ray, but $v \neq 0$ and $u \neq 0$ outside this ray. Such solutions with nonzero v and u will be sought. The expression

$$\nabla|\Phi| = \nabla\left[|A|\varphi_\nu(\sqrt{k_0}v)|\varphi_\mu(\sqrt{k_0}u)\right] = \sqrt{k_0}|A|\left[\varphi'_\nu \nabla v + \varphi'_\mu \nabla u\right] + o(k_0^{1/2})$$

shows that ∇v and ∇u are the directions of the fastest decay of the wave amplitude $|\Phi|$. As follows from Eqs.(6), both vectors are orthogonal to the direction of the group velocity $\vec{V}$. Thus, as expected, the wave solution is located in the vicinity of the ray $v(\vec{r}) = 0$, $u(\vec{r}) = 0$ and the wave energy propagates along this ray. We call this ray *the reference ray* and denote it as R.

The functions of the parabolic cylinder can be expressed in terms of the Hermite polynomials $H_\nu(\xi)$: $\varphi_\nu(\xi) = e^{-\xi^2/2} H_\nu(\xi)/\sqrt{\pi^{1/2} 2^\nu \nu!}$. This shows that an exponential factor is present in all terms of Eq.(4) and allows one to seek an approximate solution of this equation in the vicinity of the reference ray $v(\vec{r}) = u(\vec{r}) = 0$ in the form of power series involving the powers of v and u. The estimation

$$\left(\sqrt{v^2 + u^2}\right)^l \exp\left(-k_0(v^2 + u^2)/2\right) \leq (ek_0/l)^{-l/2}$$

shows that increasing the power of v by unity is equivalent to transition to the next approximation with respect to $k_0^{1/2}$. This means that in Eq.(4) in leading order, we need to retain terms including $v^0, u^0, v^1, u^1, v^2, u^2$, and vu, and in the next $(k_0^{3/2})$ order, those including v^0, v^1, u^0 and u^1. Finally, in the second approximation of the expansion with respect to $k_0^{1/2}$ it is sufficient

to retain zero order terms of the expansion with respect to powers of v and u only. Consequently, it is sufficient to satisfy Eq.(5) with an accuracy of $v^0, u^0, v^1, u^1, v^2, u^2, vu$, Eq.(6) with an accuracy of v^0, u^0, v^1, u^1 and Eqs.(7)-(8) with an accuracy v^0, u^0, i.e. when all functions are evaluated at the reference ray R. The first two requirements can be written in the following form:

$$H|_R = D_v H|_R = D_u H|_R = 0, \tag{12}$$

$$(v_j V^j)|_R = (u_j V^j)|_R = 0, \tag{13}$$

$$D_v(v_j V^j)|_R = D_u(v_j V^j)|_R = D_v(u_j V^j)|_R = D_u(u_j V^j)|_R = 0, \tag{14}$$

$$D^2_{vv} H|_R = D^2_{uu} H|_R = D^2_{vu} H|_R = 0. \tag{15}$$

The operators D_v and D_u used above denote the derivatives which are calculated with allowance for both explicit and implicit dependences of $H[v, u, x^i(\tau, v, u), S_i(\tau, v, u), v_i(\tau, v, u), u_i(\tau, v, u)]$ and other functions of v and u, respectively. We shall define the unknown functions $x^i = x^i(\tau, v, u)$, $S_i = S_i(\tau, v, u)$ as solutions of the set of equations

$$\left.\frac{\partial x^i}{\partial \tau}\right|_R = \left.\frac{\partial H}{\partial S_i}\right|_R, \qquad \left.\frac{\partial S_i}{\partial \tau}\right|_R = -\left.\frac{\partial H}{\partial x^i}\right|_R, \tag{16}$$

similar to Eqs.(10). As far as $\partial H/\partial S_i = \partial H_0/\partial S_i$ and $\partial H/\partial x^i|_R = \partial H_0/\partial x^i|_R$ are valid, the only difference between Eqs.(10) and Eqs.(16) is that the former define a variety of characteristics of Eq.(1), while the latter determine a single ray, namely the ray passing through the point $v(\vec{r})|_\Sigma = u(\vec{r})|_\Sigma = 0$ on the surface Σ, at which the initial conditions for Eq.(1) are given. The satisfaction of Eqs.(12) follows from the relations $H|_R = H_0|_R = 0$, $D_v H|_R = D_v H_0|_R = 0$, $D_u H|_R = D_u H_0|_R = 0$ and the statement that the reference ray is the solution of Eqs.(10) as well as Eqs.(16). This ray can now be defined either as the cros-section of the two surfaces $v(\vec{r}) = u(\vec{r}) = 0$ or by the parametric equations $x^i = q^i(\tau)$.

In the following all equations will be considered along the reference ray solely, and so the subscript R will be omitted. Consider a new coordinate system $\{\tau(\vec{r}), v(\vec{r}), u(\vec{r})\}$ related to the reference ray. For such a coordinate system the vector $\vec{e}_\tau = \partial x^i/\partial\tau$ is a basis vector. It coincides with the vector $\vec{V}$ of the group velocity and shows the direction along the ray. The vectors ∇v and ∇u are reciprocal vectors perpendicular to $\vec{e}_\tau$. The satisfaction of Eqs.(13) is ensured by the relations $\nabla v \cdot \vec{e}_\tau = 0$ and $\nabla u \cdot \vec{e}_\tau = 0$, which are valid for any coordinate system. The condition that the functions $\{\tau, v, u\}$ produce a coordinate system is the only condition imposed on the functions $v = v(\vec{r})$, $u = u(\vec{r})$ so far. At the beginning of the reference ray, i.e. on the surface Σ, these functions may be given arbitrarily. Then their evolution along the ray is determined by Eqs.(14),(15). In order to define these functions, note that Eqs.(14) are valid for any τ. It follows that $D_\tau(u_j V^j) = 0$. Together with Eqs.(14) this means that $D_{x^i}(u_j V^j) = 0$. The latter reads

$$\frac{\partial}{\partial\tau} u_i = -\left[\frac{\partial^2 H_0}{\partial x^i \partial S_j} + \frac{\partial^2 H_0}{\partial S_j \partial S_k} S_{ik}\right] u_j. \tag{17}$$

The same operations on Eqs.(15) give

$$\begin{aligned}\frac{\partial S_{ij}}{\partial\tau} \;=\; & -\frac{\partial^2 H_0}{\partial x^i \partial x^j} - \frac{\partial^2 H_0}{\partial x^i \partial S_k} S_{jk} - \frac{\partial^2 H_0}{\partial x^j \partial S_k} S_{ik} - \frac{\partial^2 H_0}{\partial S_l \partial S_k} S_{il} S_{jk} \\ & + 2\varepsilon^{kl} v_k v_l v_i v_j + 2\varepsilon^{kl} u_k u_l u_i u_j.\end{aligned} \tag{18}$$

An equation for v_i similar to Eq.(17) for u_i can easily be obtained, but the particular case of the electrostatic wave equation (1) enables considerable simplification. As follows from the dispersion relation for this case,

$$\frac{\partial S}{\partial\tau} = S_i V^i = \frac{1}{2} H_0 = 0,$$

the phase S does not change along the R: $S(\tau) = S|_\Sigma = S_0$. So the vector of the phase velocity ∇S is orthogonal to the vector of the group velocity $\vec{V}$, and the coordinate vector ∇v may be chosen as collinear to the vector ∇S: $\nabla v = \gamma \nabla S$. It is not difficult to show that under this condition Eqs.(14) are satisfied identically for arbitrary $\gamma = \gamma(v,u)$. The relation $\nabla v = \gamma(v,u)\nabla S$ as well as Eq.(7) may now be considered as initial conditions and, being satisfied once on the surface Σ, they will be satisfied all along the reference ray R. Moreover, $\varepsilon^{jk} v_j v_k = \gamma^2 H_0 = 0$ and the correspondent terms drop out of Eqs.(8) and (18). For the sake of simplicity we assume $\gamma = \gamma_0 \equiv$ Const and $S_0 = 0$, yielding $v = \gamma_0 S$.

By taking Eqs.(10) and (13) into account the first term of Eq.(8) may be written as $i\partial A/\partial\tau$. The amplitude A is then obtained by integration along the reference ray. Finally, a solution of the equation (1) reads

$$\Phi(\tau, S, u) = \sum_{\nu\mu} C_{\nu\mu} H_\nu(\sqrt{k_0}\gamma_0 S) H_\mu(\sqrt{k_0}u) \exp\left\{-\tfrac{1}{2}k_0(\gamma_0^2 S^2 + u^2) + ik_0 S + i\varphi(\tau)\right\}. \quad (19)$$

Here a small correction to the phase $\varphi(\tau) = \int_0^\tau \left[i(\varepsilon^{jk}S_k)_j - (2\mu+1)(\varepsilon^{jk}u_j u_k)\right] d\tau$ describes the plasma gyrotropy (the first term) and the fraction of waves having wave vectors different from the carrier wave vector of the wave envelope $\vec{k} = k_0 \nabla S|_R = \{k_0 p_i(\tau)\}$. Equation (19) gives a general solution of the wave equation (1). Actually, the functions of the parabolic cylinder form a complete set of basis functions, and so with the appropriate choice of the constants $C_{\nu\mu}$ it is possible to match any field distribution on the boundary surface Σ. The solution (19) should be completed with the relation between the two coordinate systems used above. Within the required accuracy this relation reads $x^i = q^i(\tau) + u\partial x^i/\partial u + (S - S_0)\partial x^i/\partial S + \frac{1}{2}(S - S_0)^2 \partial^2 x^i/\partial S^2$. The transition from the quantities $q_i(\tau)$, $p_i(\tau)$, $u_i(\tau)$, $S_{ij}(\tau)$, which are determined by Eqs.(10), (17) and (18), to the unknown quantities $\partial x^i/\partial u$, $\partial x^i/\partial S$ and $\partial^2 x^i/\partial S^2$ is realized by the general rules.

The main characteristic feature of the approach developed above is the appearance of the new intermediate space scale Λ such that $\lambda \ll \Lambda \ll L$. Λ is the length of the exponential decay of the wave amplitude across the direction of the group velocity $\vec{V}$. As distinct from the conventional theory of geometric optics, our approach retains the wave description across the direction of the reference ray. Along the ray the usual eikonal approach is used. The method developed therefore includes the conventional theory of geometric optics as a particular case. The wave properties are described by the second string in Eq.(18) and by the last two terms in Eq.(7). These terms become significant when the beam width, which is inversely proportional to $\sqrt{(\nabla u)^2 + (\nabla v)^2}$, decreases. This takes place, for example, in the vicinity of a caustic or focus. Physically it is clear that the behaviour of the wave beam width is coupled with the curvature of the wave front. In agreement with this, the second derivatives S_{ij} representing the curvature and the beam width term appear in the same Eq.(18). A close description of the Gaussian wave beam propagation is provided by the method of geometric optics with complex phase [5]. The latter method was used in [6] for the case of EC wave propagation.

In conclusion, note that the approach developed, in spite of its broader applicability, is simpler for numerical treatment than the eikonal approach because the number of equations to be solved in the WKB method is less than that in the eikonal approximation. The method developed may be used for calculating wave fields in problems of RF heating, current drive and plasma diagnostics with microwave beams.

References

1. V.P. Maslov, Complex WKB Method in Nonlinear Equations, Nauka, Moscow, 1977 (in Russian).
2. V.M. Babitch and V.S. Boldyrev, Asymptotic methods in Problems of Short Wave Diffraction, Nauka, Moscow, 1972 (in Russian).
3. G.V. Pereverzev, JETP Letters, **44** (1986) 549.
4. G.V. Pereverzev, Nucl. Fusion (1992) (to be published).
5. S. Choudhary and L.B. Felsen, Proceedings of the IEEE **62** (1974) 1530.
6. E. Mazzucato, Phys. Fluids **B1** (1989) 1855.

ELECTRON CYCLOTRON EMISSION AND ABSORPTION FOR A TWO-DIMENSIONAL MOMENTUM DISTRIBUTION

M.Bornatici

Physics Department, University of Ferrara, Ferrara, Italy, and Physics Department "A.Volta" ,University of Pavia, Pavia, Italy

Abstract. Analytic expressions for the electron cyclotron emissivity of a two-dimensional (2-D) momentum distribution, i.e. for a $\delta(\mu)$-distribution in the cosine of the pitch angle μ, are obtained for both low and high frequencies.For the high-frequency range for which the Carlini approximation to the Bessel function is used, the 2-D emissivity of the perpendicular extraordinary mode is a factor $\left(\frac{2}{\sqrt{\pi}}\right)\left(\frac{\omega}{\omega_c}\right)^{1/2}$ (>1) larger than the corresponding emissivity averaged with respect to an isotropic pitch angle distribution, such a result being consistent with a Gaussian shape in μ of width $(\omega_c/\omega)^{1/2}$. The emission coefficient, i.e. the emissivity integrated over the energy distribution, and the absorption coefficient are evaluated for the case of a 2-D relativistic Maxwellian. In particular, for frequencies such that $\chi_\perp \equiv (9/2)(\omega/\omega_c)(T_\perp/mc^2) >> 1$, the 2-D absorption coefficient is a factor $\chi_\perp^{1/6}$ larger than the corrresponding 3-D result.

Introduction. For an electron momentum distribution F (p, μ) which is a separable function of momentum p and the cosine of the pitch angle $\mu = p_\parallel/p$, i.e. $F(p,\mu)=f(p)\varphi(\mu)$, the coefficient of electron cyclotron (spontaneous) emission is (1,2)

$$\eta^{(i)}(\omega,\theta)=4\pi(mc)^3 n_0 \int_1^\infty d\gamma\gamma(\gamma^2-1)^{1/2} f(p)\eta^{(i)}(\omega,\theta,\gamma) \qquad (1)$$

where $\eta^{(i)}(\omega,\theta,\gamma)$ is the emissivity from the single electron, referred to the ith mode and averaged over the pitch angle distribution $\varphi(\mu)$,

$$\eta^{(i)}(\omega,\theta,\gamma) = \left(\frac{N_r}{N}\right)^2 \cos\beta \, \frac{e^2\omega}{4\pi c\gamma} \, \frac{1}{N\sin^2\theta} \, \frac{\rho \pm \sin^2\theta}{2\rho} \sum_{n=1}^{\infty} \left(\frac{n\omega_c}{\omega}\right)^{-2}$$

$$\int_{-1}^{1} d\mu\varphi(\mu) \left| \left(\frac{E_x - iE_y}{E_y} + \frac{\omega}{n\omega_c} N_\perp \frac{p}{mc} \mu \frac{E_z}{E_y} \right) J_n + i\frac{b}{n} J_{n+1} \right|^2 \delta\left(\gamma - N_\parallel \frac{p}{mc}\mu - \frac{n\omega_c}{\omega}\right) \qquad (2)$$

where $N=N^{(i)}$ and $N_r=N_r^{(i)}$, i=X;O, are, respectively, the (cold) refractive and ray refractive index of the extraordinary (X) and ordinary (0) mode, with $N_\perp = N\sin\theta$ and $N_\parallel = N\cos\theta$, θ being the angle between the equilibrium magnetic field $\underline{B}_0 = B_0 \hat{\underline{z}}$ and the wave vector $\underline{k} = k_\perp \hat{\underline{x}} + k_\parallel \hat{\underline{z}}$; the angle β is such that $\beta = \sphericalangle(\underline{k}, \underline{S})$, with $\underline{S}$ the electromagnetic power flux density, which, in the cold plasma limit, reduces to the Poynting vector so that $4\pi |\underline{S}|/c |E_y|^2 = (N/\cos\beta)\,(2\rho/(\rho \pm \sin^2\theta))$, the plus (minus)

sign referring to the X-mode (O-mode), with

$\mathfrak{p}\equiv(\sin^4\theta+4(\omega/\omega_c)^2[1-(\omega_p/\omega)^2]^2\cos^2\theta)^{1/2}$. Furthermore, $J_\nu\equiv J_\nu(b)$ is the Bessel function of order ν and argument $b\equiv(\omega/\omega_c)\,N_\perp(p/mc)(1-\mu^2)^{1/2}$, and $\gamma=[1+(p/mc)^2]^{1/2}$, is the relativistic energy factor. The effect of the mode polarization in (2) is evaluated in the cold-plasma limit (1,2), which is, in general, accurate for all the harmonics except the first harmonic of the X-mode near the resonance $\omega=\omega_c$ [1] .

The absorption coefficient $\alpha^{(i)}(\omega,\theta)$ is obtained from (1) along with (2) with the replacement (1,3)

$$f(p)\,\varphi(\mu)\rightarrow -\frac{8\pi^3c^2}{N_r^2\omega^2}\,\frac{m\gamma}{p}\left[\varphi(\mu)\,\frac{df}{dp}-\left(\frac{\mu}{p}-\frac{N_{||}}{mc\gamma}\right)f(p)\,\frac{d\varphi}{d\mu}\right] \qquad (3)$$

Emission and absorption in two dimensions. For a two -dimensioal (2-D) distribution, i.e. $\varphi(\mu)=2\delta(\mu)$, the integration in (2) is straigtforward, with the result

$$\eta^{(i)}(\omega,\theta)=N_r^2\frac{\omega^2(mc^2)}{8\pi^3c^2}\sum_n\left[-\frac{p^2}{(mc)^2\gamma}\,\frac{d\ln p}{d\ln(pf)}\right]_{\gamma=n\omega_{c/\omega}}\alpha_n^{(i)}(\omega,\theta) \qquad (4)$$

with the absorption coefficient at the n th harmonic given by

$$\alpha^{(i)}n(\omega,\theta)=\pi\,\frac{\omega_p^2}{\omega c}\,\frac{\cos\beta}{N}\,\frac{\rho\pm\sin^2\theta}{2\rho}\left[\left(\frac{n\omega_c}{\omega}\right)^2-1\right]\left[J_n'(b_n)+\frac{nA^{(i)}(\omega,\theta)}{b_n}J_n(b_n)\right]^2$$

$$\left[-4\pi(mc)^4\,\frac{\gamma}{p}\,\frac{d(p\,f)}{d\,p}\right]_{\gamma=n\omega_{c/\omega}} \qquad (5)$$

where $A^{(i)}(\omega,\theta)\equiv iE_x/E_y$ and $b_n\equiv nN_\perp[1-(\omega/n\omega_c)^2]^{1/2}$, $\omega\le n\omega_c$
For the specific case of a 2-D relativistic Maxwellian distribution, the quantity within the square brackets in (4) is $(T_\perp/mc^2)$, whereas the last factor on the r.h.s. of (5) equals $a_2\mu_\perp^2e^{-\mu_\perp\left(\frac{n\omega_c}{\omega}-1\right)}$, with $a_2\equiv\mu_\perp/(\mu_\perp+1)$ and $\mu_\perp\equiv mc^2/T_\perp$.
By making use of the series representation of the Bessel functions, one can write (5) as

$$\alpha^{(i)}(\omega,\theta)=a_2\frac{\omega_p^2}{\omega_c c}\,d^{(i)}(\omega,\theta)\sum_{n=2}^{\infty}\frac{n^{2n-1}}{2^n n!}[N_\perp^{(i)}]^{2n-3}\left(\frac{T_\perp}{mc^2}\right)^{n-2}$$

$$\sum_{k=0}^{\infty}c_{n,k}\,f_{n,k}^{(i)}(\omega)\left[(nN_\perp^{(i)})^2\,\frac{T_\perp}{mc^2}\right]^k G_{n+k} \qquad (6)$$

where $d^{(i)}(\omega,\theta)\equiv\sin\theta(\cos\beta/N)[(\mathfrak{p}\pm\sin^2\theta)/2\mathfrak{p}]\,[1+A^{(i)}\omega,\theta)]^2$ and

$$G_{q\equiv}\frac{\pi}{q!}\left(\frac{\omega}{n\omega_c}\right)^{2q-3}\left[\frac{\mu_\perp}{2}\left(\left(\frac{n\omega_c}{\omega}\right)^2-1\right)\right]^q e^{-\mu_\perp\left(\frac{n\omega_c}{\omega}-1\right)},\ \omega<n\omega_c \qquad (7)$$

$c_{n,k}$ and $f^{(i)}{}_{n,k}$ are connected with the series representation of the Bessel functions and are both equal to 1 for k=0 (2). Note that with

$T_\perp\rightarrow T$, $G_{n+k}\rightarrow G_{n+k+1/2}$ and $a_2\rightarrow a_3\equiv(\pi/2\mu)^{1/2}\,e^{-\mu}/K_2(\mu)$,(6) and (7) reduce to the result for a 3-D relativistic Maxwellian (2).

Expression (6) is particularly convenient when the individual adjacent lines do not overlap significantly, i.e. for $\Delta\omega_n(\approx\sqrt{2\pi}\, n^{3/2}(T_\perp/mc^2)\omega_c)<\omega_c$.For $\Delta\omega_n>\omega_c$, i.e. for values of the harmonic number much greater than unity, such that the absorption (emission) profile tends to a continuum, it is more appropriate to make use of asymptotic approximations to the Bessel functions whic are valid for large argument and order; One such approximation is the Carlini approximation, which yields for the X-mode (in the tenuous plasma limit)

$$\alpha^{(x)}(\omega,\theta)=a_2\frac{\omega_p^2}{\omega_c c}\sum_{n>\omega/\omega_c}\left(\frac{T_\perp}{mc^2}\right)^{n-2} g_n\left(\frac{n\omega_c}{\omega},\mu_\perp\right)e^{-\frac{n}{\gamma}\cos^2\theta} \qquad (8a)$$

with the profile function

$$g_q\left(\frac{n\omega_c}{\omega},\mu_\perp\right)\equiv\frac{1}{2}\left(\frac{\omega_c}{\omega}\right)^2 e^{2\frac{\omega}{\omega_c}}\left[\mu_\perp\frac{\left(\frac{n\omega_c}{\omega}-1\right)}{\left(\frac{n\omega_c}{\omega}+1\right)}\right]^q e^{-\mu_\perp\left(\frac{n\omega_c}{\omega}-1\right)} \qquad (9a)$$

It is instructive to note that for $\omega\approx n\omega_c$ and $n>>1$, result (8a) is the same as (6) to lowest order in both $\cos^2\theta$ and the finite Larmor radius corrections (only the k=0-term in (6)), since

$$g_n=\frac{n^{2n-1}}{2^n n!}G_n \qquad (10)$$

as it follows from the comparison of (7) and (9a) along with Stirling's formula

$n!=\sqrt{2\pi n}\,(n/e)^n$.

For the continuous part of the spectrum, it is appropriate to replace the summation over n in (8a) by an integration over $\gamma\left(n=(\omega/\omega_c)\gamma, \text{ so that } \sum_n\rightarrow\frac{\omega}{\omega_c}\int d\gamma\right)$, with the result that

$$\alpha^{(x)}(\omega,\theta)=a_2\frac{\omega_p^2}{\omega_c c}\mu_\perp^{1/2}e^{\mu_\perp}G(\varpi,\theta,\mu_\perp) \qquad (8b)$$

with the profile function.

$$G(\varpi,\theta,\mu_\perp)\equiv\frac{\mu_\perp^{3/2}}{2}\frac{e^{\varpi(2-\cos^2\theta)}}{\varpi}\int_1^\infty d\gamma\left(\frac{\gamma-1}{\gamma+1}\right)^{\varpi\gamma}e^{-\mu_\perp\gamma},\quad \varpi\equiv\frac{\omega}{\omega_c} \qquad (9b)$$

In terms of the single-particle emissivity $\eta^{(x)}(\omega,\theta,\gamma)$, cf (2) , result (8b) and (9b) amounts to

$$\eta^{(x)}(\omega,\theta,\gamma)=\frac{e^2\omega}{4\pi^2 c\gamma}\left(\frac{\gamma-1}{\gamma+1}\right)^{\varpi\gamma}e^{\varpi(2-\cos^2\theta)}\equiv\eta_\perp^{(x)}(\omega,\gamma)\,e^{-\varpi\cos^2\theta},\ \varpi>>\gamma^2 \qquad (10a)$$

i.e., the angular distribution is a Gaussian centered at $\theta=\pi/2$ and of width $(\omega_c/\omega)^{1/2}$. As a consequence, for perpendicular propagation the absorption coefficient (8b) is larger by a factor $\left(\frac{2}{\sqrt{\pi}}\right)\left(\frac{\omega}{\omega_c}\right)^{1/2}(>1)$ than the corresponding quantity averaged over θ (3). On the other hand, referring to perpendicular propagation, the emissivity (10a) is also larger than the corresponding quantity averaged over the isotropic pitch angle distribution (1) by the

same factor $\left(\frac{2}{\sqrt{\pi}}\right)\left(\frac{\omega}{\omega_c}\right)^{1/2}$ (>1) . The latter result follows from the fact that, for $\omega>>\omega_c$, the relevant pitch-angle-dependence of the emissivity is also a Gaussian of width $(\omega_c/\omega)^{1/2}$,(4), i.e.,

$$\eta_\perp^{(x)}(\omega,\gamma,\mu)= \eta_\perp^{(x)}(\omega,\gamma)\, e^{-\frac{\omega}{\omega_c}\mu^2}\left(\rightarrow\sqrt{\pi}\left(\frac{\omega_c}{\omega}\right)^{1/2}\eta_\perp^{(x)}(\omega,\gamma)\delta(\mu),\ \text{for}\ \frac{\omega_c}{\omega}\rightarrow 0\right) \qquad (11)$$

In the limit of highly-relativistic energies, i.e. for $\gamma>>1$, (10a) yields

$$\eta_\perp^{(x)}(\omega,\gamma>>1)\approx \frac{e^2\omega}{4\pi^2 c\gamma}\, e^{-\frac{2}{3}\frac{\omega}{\omega_c\gamma^2}\left(1+\frac{3}{5\gamma^2}\right)} \qquad (10c)$$

and, consequently, from (9b) one gets,

$$G_\perp(\varpi,\mu_\perp)= \frac{3\sqrt{\pi}}{2}\,\chi_\perp^{-5/6}\, e^{-\mu_\perp(\chi_\perp^{1/3}+\frac{9}{20\chi_\perp^{1/3}})}, \quad \chi_\perp\equiv\frac{9}{2}\frac{\varpi}{\mu_\perp}>>1 \qquad (12)$$

obtained by carrying out the relevant γ-integration in (9b) by the method of steepest descent. With respect to the absorption coefficient of the X-mode for a 3-D relativistic Maxwellian, result (8b), (12), with $T_\perp\rightarrow T$, is larger by a factor $(a_3/a_2)\,\chi^{1/6}$ (>1). Instead of using (1) - (3), the absorption coefficient can be obtained in terms of the anti-Hermitian part of the dielectric tensor (1). In particular, for perpendicular propagation one gets (8b) with the profile function $G_\perp(\varpi,\mu_\perp)$ given by

$$G_\perp(\varpi,\mu_\perp)=\sqrt{\frac{2}{\pi}}\,\mu_\perp^{3/2}\ \mathrm{Re}\left\{\int_0^\infty d\tau\left[\cos\tau K\left(\frac{3}{2},\sqrt{R(\tau)}\right)+\varpi^2(1-\cos\tau)^2\,K\left(\frac{5}{2},\sqrt{R(\tau)}\right)\right]\right\}$$

with $K(\nu,z)\equiv z^{-\nu}K_\nu(z)$, and $K_\nu(z)$ denoting the modified Bessel function of the second kind,

$R(\tau)\equiv(\mu_\perp - i\varpi\tau)^2+2\varpi^2(1-\cos\tau)$

One can now proceed to an asymptotic evaluation of the integral in $G_\perp$ by the method of steepest descent, along the same line as for the 3-D Maxwellian distribution (1), and one obtains exactly the result (12).

Acknowledgement. This work was supported by the Ministero della Pubblica Istruzione of Italy.

References

(1) M.Bornatici, R.Cano, O.DeBarbieri and F.Engelmann, Nucl.Fusion 23,1153 (1983), and references herein.
(2) M.Bornatici and U.Ruffina, in Controlled Fusion and Plasma Heating (Proc. 13th Eur.Conf. Schliersee, 1986), Vol.10C, Part II, pag.254.
(3) J.M.Dawson, in Fusion, Vol.1, Part B, p.453 (Teller Ed.Academic, New York, 1981).
(4) P.A.Robinson, Plasma Phys.Contr.Fusion 27, 1037 (1985).

OBLIQUE PROPAGATION OF ELECTRON-CYCLOTRON-WAVES IN NON-MAXWELLIAN, WEAKLY RELATIVISTIC VLASOV-PLASMAS

F. MOSER
Institut für Plasmaforschung der Universität Stuttgart
D-7000 Stuttgart-80, Pfaffenwaldring 31, Fed. Republic of Germany

ABSTRACT:
Electron distribution functions and drift motions of the electrons parallel to a constant magnetic field determine the propagation of electromagnetic and electrostatic waves oblique to the magnetic field especially in the frequency range of the electron-cyclotron resonances. The dielectric tensor due to Orefice (1), Shkarofsky (2), Krivenski et al. (3) and Moser et al. (4) is used to investigate the dispersion and absorption of electrostatic and electromagnetic waves propagating obliquely to the constant magnetic field in a weakly relativistic Vlasov-Plasma. In calculating the dielectric tensor elements isotropic distribution functions (Maxwellian-, drifting Maxwellian-and loss-cone-distribution functions) and Finite-Larmor-Radius development to arbitrary order are considered.

THE DIELECTRIC TENSOR:

The plasma is assumed to be homogeneous in a constant external magnetic field $\vec{B}_0$. Due to Orefice (1), Shkarofsky (2), Krivenski et al. (3) and Moser et al. (4) the dielectric tensor for a weakly relativistic plasma is given by:

a) for a Maxwellian distribution function f_1 with an electron drift $\vec{v}_0 \parallel \vec{B}_0$:

$$f_1(p_\perp, p_\parallel) = \left(\frac{\mu_1}{2\pi}\right)^{\frac{3}{2}} \exp\left[-\frac{1}{2}\mu_1\left(p_\perp^2 + (p_\parallel - p_0)^2\right)\right] \qquad (1)$$

is:

$$\varepsilon_{ij} = \delta_{ij} + \left(\frac{\omega_{pe}}{\omega}\right)^2 \cdot \left\{-2\mu_1 \sum_{s=-\infty}^{+\infty} \sum_{k=0}^{+\infty} c_{i,j}(s,k) \left(\frac{2}{\mu_1}\right)^{|s|+k-1} \gamma_0^{h+1} \cdot (|s|+k)!\, \hat{Q}(h) + \mu_1 p_0^2 \Gamma_{i,j}\right\} \qquad (2)$$

b) for a loss-cone distribution function f_2 with a loss-cone index $m_\perp$

$$f_2(p_\perp, p_\parallel) = n_0\, p_\perp^{2m_\perp} \exp\left[-\frac{1}{2}\mu_2\left(p_\perp^2 + p_\parallel^2\right)\right] \qquad (3)$$

with

$$n_0 = \frac{1}{m_\perp!}\left(\frac{\mu_2}{2\pi}\right)^{\frac{3}{2}}\left(\frac{\mu_2}{2}\right)^{m_\perp}$$

there is:

$$\varepsilon_{ij} = \delta_{ij} + \left(\frac{\omega_{pe}}{\omega}\right)^2 \cdot \left\{-\frac{2\mu_2}{m_\perp} \sum_{s=-\infty}^{+\infty} \sum_{k=0}^{+\infty} c_{i,j}(s,k) \left(\frac{2}{\mu_2}\right)^{|s|+k-1} \cdot (|s|+k+m_\perp)!\, \hat{Q}(h) - \Gamma_{i,j}\right\}. \qquad (4)$$

$\vec{p} = p_{\parallel}\hat{e}_{\parallel} + p_{\perp}\hat{e}_{\perp}$ is the electron momentum in units of $m_{eo}c$, m_{eo} is the electron rest mass, c is the speed of light in vacuum, ω_{pe}, ω_{ce} and ω are the electron plasma frequency, the electron cyclotron frequency and the frequency of the electromagnetic wave field. The indices $\perp$ and $\parallel$ refer to the direction perpendicular and parallel to the magnetic field $\vec{B}_o$, $\Gamma_{ij} = \delta_{i3}\delta_{3j}$ and $\gamma_o = \sqrt{1+p_o^2}$. The relativistic parameters $\mu_{1,2}$ are defined to: $\mu_{1,2} = c^2/v_{th\,1,2}^2$ with $v_{th\,1,2}^2 = k\,T_{e\,1,2}/m_{eo}$ the electron thermal velocities for the isotropic electron temperatures $T_{e\,1}$ and $T_{e\,2}$.
The coefficients $c_{ij}(s,k)$ and the functions $\hat{Q}(h)$ and $\hat{Q}(h)$ are described and discussed in (1) and (3).

The WAVE-EQUATION and the DISPERSION-RELATION:
If the dielectric tensor $\varepsilon(\omega, \vec{k})$ is known, the wave equation for the electric wave field $\delta\vec{E}$ is given by:

$$\vec{k} \times \vec{k} \times \delta\vec{E} + \left(\frac{\omega}{c}\right)^2 \varepsilon(\omega,\vec{k})\,\delta\vec{E} = 0 \qquad (5)$$

With $\vec{n} = \frac{c}{\omega}\vec{k}$ ($\vec{n}$: komplex index of refraction, $\vec{k}$: wave vector) and $\bar{k}_i = \frac{k_i}{|\vec{k}|}$

there results from (5) the dispersion equation:

$$\mathrm{Det}\,|\Lambda_{ij}| = 0. \qquad (6a)$$

with $$\Lambda_{ij} = n^2(\bar{k}_i\bar{k}_j - \delta_{ij}) + \varepsilon_{ij}(\omega,\vec{k}). \qquad (6b)$$

NUMERICAL SOLUTION and RESULTS:
The dispersion equation (6a) and the wave equation (5) are solved numerically using the method of complex residual calculation in the root finding code. In the numerical calculation of the tensor elements the recursion formulae for the generalized relativistic dispersion functions due to Shkarofsky (2) and Robinson (5) are used.
Two characteristic examples are shown in the figures 1) and 2). In Fig.1) the anomalous dispersion and damping rate for the fast O.W. is shown for a propagation oblique to the magnetic field in an isotropic, weakly relativistic, Maxwellian plasma without electron drift in the frequency range around ω_{ce}. In Fig.2) the influence of the loss-cone index $m_{e\perp}$ on the dispersion and absorption for the fast O.W. is shown propagating perpendicularly to the magnetic field in a weakly relativistic plasma with an electron loss-cone distribution function without drift in the frequency range around ω_{ce}.

REFERENCES:

(1) A. Orefice, J. Plasma Physics 39, (1988) 61.
(2) I. P. Shkarofsky, J. Plasma Physics 35, (1986) 319.
(3) V. Krivenski et al., J. Plasma Physics 30, (1983) 125.
(4) F. Moser et al., Proc. 18th Europ. Conf. on Controlled Fusion and Plasma Physics, Berlin, 1991, Vol. IV. 121.
(5) P. A. Robinson, J. Plasma Physics 37, (1987) 435.

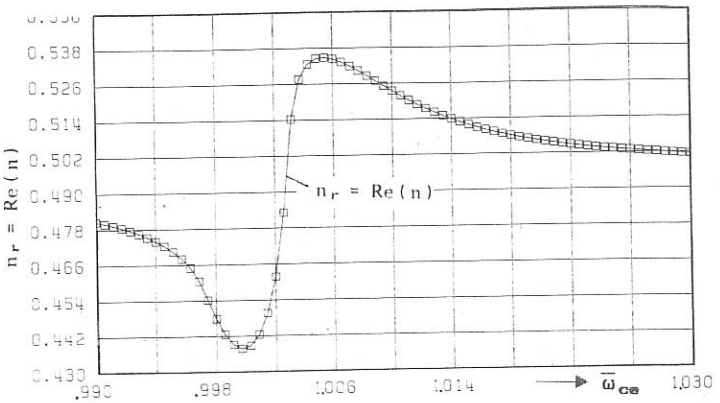

Fig. 1 a) Anomalous dispersion of the fast ordinary wave in the frequency range $\omega \approx \omega_{ce}$. Real part of the index of refraction, $n_r = Re(n)$, versus the normalized frequency $\bar{\omega}_{ce} = \omega_{ce}/\omega$ for a propagation with $\Theta = 80^o$ to the constant magnetic field $\vec{B}_o$.
(plasma parameters: $\bar{\omega}^2_{pe} = 0.8$, $T_e = 1$ keV, Maxwellian with $\rho_o = 0$)

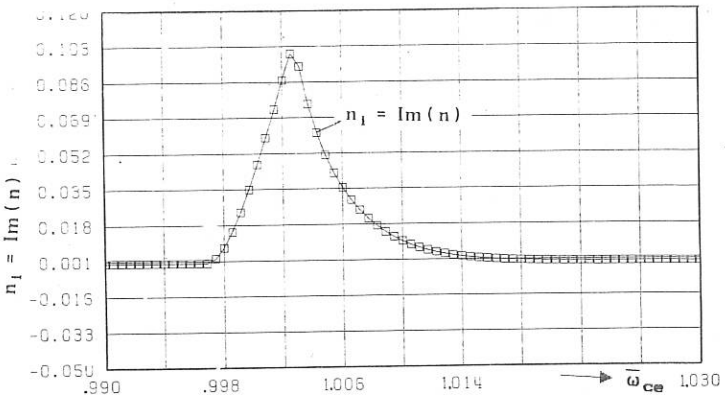

Fig. 1 b) Damping rate $n_i = Im(n)$ for the fast ordinary wave in the frequency range $\omega \approx \omega_{ce}$ propagating obliquely to the constant magnetic field $\vec{B}_o$ with $\Theta = 80^o$ to the magnetic field versus the normalized frequency $\bar{\omega}_{ce}$.
(plasma parameters as in Fig.1a)

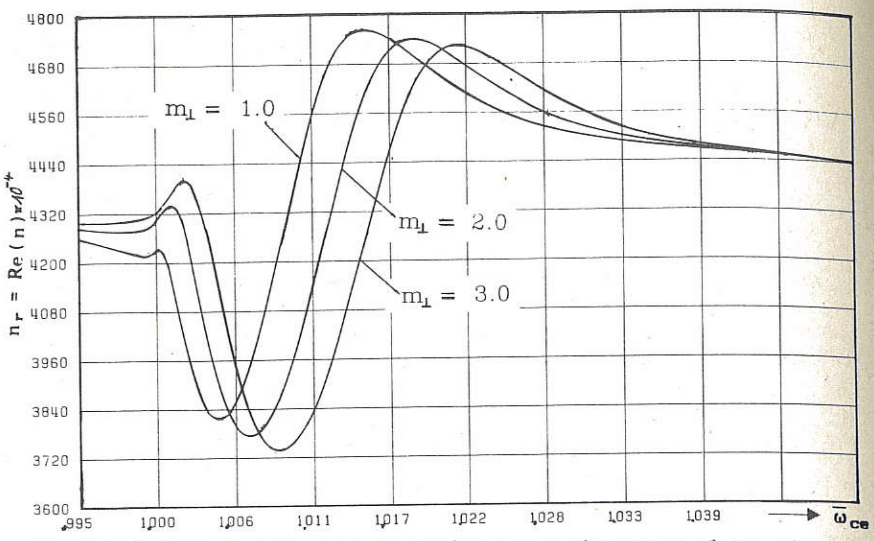

Fig. 2a) Influence of the loss-cone-index $m_\perp$ on the curves of anomalous dispersion of the fast ordinary wave in the frequency range $\omega \approx \omega_{ce}$. Real part of the index of refraction, $n_r = Re(n)$, versus the normalized frequency $\bar{\omega}_{ce}$ for perpendicular propagation to the magnetic field.
(plasma parameters : $\bar{\omega}_{pe}^2 = 1$, $\Theta = 90^0$, $T_e = 1$ keV, loss-cone-distribution)

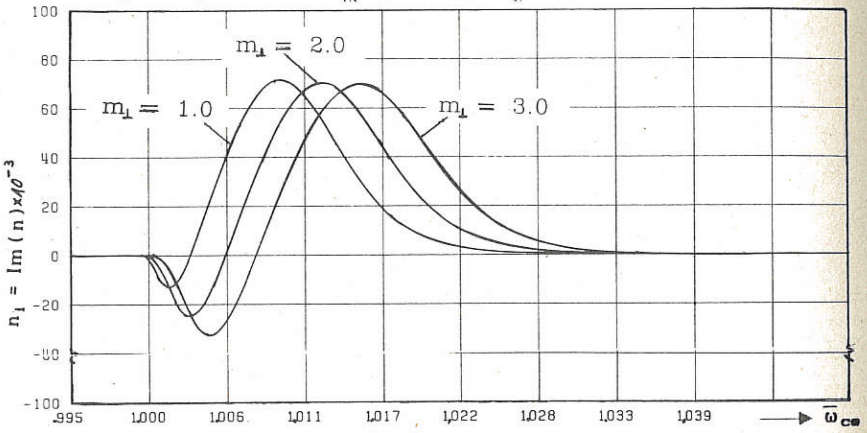

Fig. 2b) Influence of the loss-cone-index $m_\perp$ on the damping constant of the fast ordinary wave in the frequency range $\omega \approx \omega_{ce}$ propagating perpendicularly to the magnetic field. Imaginary part of the index of refraction, $n_i = Im(n)$, versus the normalized frequency $\bar{\omega}_{ce}$.
(plasma parameters as in Fig. 2a)

PARTIALLY TRANSIENT PLASMA RESPONSE NEAR AN ATTAINABLE HARMONIC STATE

Lim Chee-Seng* and Kurt Suchy
Institut für Theoretische Physik II der Universität Düsseldorf,
W-4000 Düsseldorf 1, Federal Republic of Germany

A warm collisionless plasma with slowly varying space-time dependent inhomogeneities is responding to the unsteady and partially time-harmonic source current

$$\underset{\sim}{J}(\underset{\sim}{X}) = \underset{\sim}{I}(\underset{\sim}{X})\exp(-i\omega t)$$

which, after being switched-on at zero instant, acts from a time-independent bounded region $\mathcal{R}$ about the origin and eventually becomes fully time-harmonic at the real frequency ω:

$$\underset{\sim}{I}(\underset{\sim}{X}) \equiv \underset{\sim}{0} \text{ when } t < 0,$$

$$\underset{\sim}{I}(\underset{\sim}{X}) \equiv \underset{\sim}{0} \text{ beyond } \mathcal{R} \ (t > 0),$$

$$\underset{\sim}{I}(\underset{\sim}{X}) \longrightarrow \underset{\sim}{\mathcal{I}}(\underset{\sim}{x}) \not\equiv \underset{\sim}{0} \text{ over } \mathcal{R} \text{ as } t \longrightarrow \infty.$$

$\underset{\sim}{X} = (\underset{\sim}{x},t)$ denotes the space-time 4-vector. The response to a spatially anisotropic source function of this kind has been investigated for a general homogeneous isotropic medium [1]. It differs significantly from transient response, which has been studied for the 'multiple water-bag' plasma [2].

The plasma response is governed by

$$\frac{\partial}{\partial t}\underset{\sim}{j} - \underset{\sim}{\omega}_c \times \underset{\sim}{j} + qm^{-1}\frac{\partial}{\partial \underset{\sim}{x}}p = qm^{-1}\rho\underset{\sim}{E},$$

$$qm^{-1}\frac{\partial}{\partial t}p = -c^2\frac{\partial}{\partial \underset{\sim}{x}}\cdot\underset{\sim}{j},$$

$$\frac{\partial}{\partial \underset{\sim}{x}} \times \underset{\sim}{H} = \underset{\sim}{j} + \underset{\sim}{J} + \epsilon\frac{\partial}{\partial t}\underset{\sim}{E},$$

$$\mu\frac{\partial}{\partial t}\underset{\sim}{H} = -\frac{\partial}{\partial x} \times \underset{\sim}{E},$$

*Permanent Address:
Department of Mathematics
National University of Singapore
Singapore 0511, Republic of Singapore

m and q being particle mass and particle charge. The charge density $\rho = \rho(;\underset{\sim}{X})$, electron cyclotron frequency $\underset{\sim}{\omega}_c = \underset{\sim}{\omega}_c(;\underset{\sim}{X})$, adiabatic sound speed $c = c(;\underset{\sim}{X})$ are slowly varying unlike the electric and magnetic fields $\underset{\sim}{E}$ and $\underset{\sim}{H}$, induced electrical current of density $\underset{\sim}{j}$ and electron pressure p which are fast-and-slow varying with $\underset{\sim}{X}$. The electron plasma frequency $\omega_p(;\underset{\sim}{X})$ is given by $\epsilon\omega_p^2(;\underset{\sim}{X}) = qm^{-1}\rho(;\underset{\sim}{X})$.

The problem is treated by a technique [3] - [6] of geometric optics. An asymptotic resolution yields the long-range and large-time response tensor

$$(\underset{\sim}{E}|\underset{\sim}{H}) \sim \sum_{n=1,2} \underset{\sim}{U}_n^{tr} + \underset{\sim}{U}_n^{pp}$$

which, provided $|\underset{\sim}{x}| < tc(;\underset{\sim}{X})$ and $|\underset{\sim}{x}| < t(\epsilon\mu)^{-1/2}$, involves the transient wavefunctions

$$\underset{\sim}{U}_n^{tr} = (\underset{\sim}{i}_n\omega_{nn} - i\omega\underset{\sim}{j}_n)\underset{\sim}{p}_n C_n + (\underset{\sim}{j}_n\omega_{nn} + i\omega\underset{\sim}{i}_n)\underset{\sim}{p}_n S_n,$$

where

$$C_n \\ S_n = \frac{k_{nn}\overset{\cos}{\sin}(|\underset{\sim}{x}|k_{nn} - t\omega_{nn} - \pi/4)}{(2\pi)^{3/2}|\underset{\sim}{x}|(t|\omega_{n\,kk}(k_{nn};\underset{\sim}{X})|)^{1/2}(\omega^2 - \omega_{nn}^2)},$$

$$\underset{\sim}{i}_n \\ \underset{\sim}{j}_n = \iiint_{\mathcal{R}} d^3\underset{\sim}{y}\ \underset{\sim}{I}(\underset{\sim}{y},0)\overset{\cos}{\sin}(\hat{\underset{\sim}{x}}\cdot\underset{\sim}{y}k_{nn}) + \iiint_{\mathcal{R}} d^3\underset{\sim}{y}\int_0^\infty ds\ e^{-i\omega s}\partial\underset{\sim}{I}(\underset{\sim}{y},s)/\partial s\ \overset{\cos}{\sin}(\hat{\underset{\sim}{x}}\cdot\underset{\sim}{y}k_{nn} - s\omega_{nn})$$

for n = 1,2 and

$$\underset{\sim}{p}_1 = \epsilon^{-1}(\hat{\underset{\sim}{x}}^T\hat{\underset{\sim}{x}}|\underset{\sim}{0}_3)\omega_p^2(;\underset{\sim}{X})\omega_{11}^{-2},$$

$$\underset{\sim}{p}_2 = \epsilon^{-1}(\underset{\sim}{I}_3 - \hat{\underset{\sim}{x}}^T\hat{\underset{\sim}{x}}|\epsilon t^{-1}\underset{\sim}{x}\times\underset{\sim}{I}_3),$$

$$\omega_{11} = \omega_{11}(|\underset{\sim}{x}|/t;\underset{\sim}{X}) = t\omega_p(;\underset{\sim}{X})c(;\underset{\sim}{X})[t^2c^2(;\underset{\sim}{X}) - |\underset{\sim}{x}|^2]^{-1/2},$$

$$\omega_{22} = \omega_{22}(|\underset{\sim}{x}|/t;\underset{\sim}{X}) = t\omega_p(;\underset{\sim}{X})(\epsilon\mu)^{-1/2}[t^2(\epsilon\mu)^{-1} - |\underset{\sim}{x}|^2]^{-1/2},$$

with $k_{11} = k_{11}(|\underset{\sim}{x}|/t;\underset{\sim}{X}) = |\underset{\sim}{x}|\omega_p(;\underset{\sim}{X})c^{-1}(;\underset{\sim}{X})[t^2c^2(;\underset{\sim}{X}) - |\underset{\sim}{x}|^2]^{-1/2}$,

$$k_{22} = k_{22}(|\underset{\sim}{x}|/t;\underset{\sim}{X}) = |\underset{\sim}{x}|\omega_p(;\underset{\sim}{X})(\epsilon\mu)^{1/2}[t^2(\epsilon\mu)^{-1} - |\underset{\sim}{x}|^2]^{-1/2}.$$

$$\omega_1(k;\underset{\sim}{X}) = [\omega_p^2(;\underset{\sim}{X}) + k^2c^2(;\underset{\sim}{X})]^{1/2},$$

$$\omega_2(k;\underset{\sim}{X}) = [\omega_p^2(;\underset{\sim}{X}) + k^2(\epsilon\mu)^{-1}]^{1/2}.$$

Here, $\hat{\underset{\sim}{x}} = \underset{\sim}{x}|\underset{\sim}{x}|^{-1}$ while $\underset{\sim}{I}_3$ and $\underset{\sim}{0}_3$ denote the 3 × 3 identity and zero

tensors. The response also includes, when $|\omega| > \omega_p(;\underset{\sim}{X})$, the partially time-harmonic wavefunctions

$$\underset{\sim}{U}_1^{pp} = \frac{\omega_p^2(;\underset{\sim}{X})\overset{*}{\underset{\sim}{I}}(k_1\hat{\underset{\sim}{x}},t)}{4\pi|\underset{\sim}{x}|\epsilon\omega c^2(;\underset{\sim}{X})}(\hat{\underset{\sim}{x}}^{T\wedge}\hat{\underset{\sim}{x}}|\underset{\sim}{0}_3)\exp[i(k_1|\underset{\sim}{x}|-\omega t+\tfrac{1}{2}\pi)]$$

provided $$|\underset{\sim}{x}| < tc(;\underset{\sim}{X})[1-\omega_p^2(;\underset{\sim}{X})/\omega^2]^{1/2},$$

$$\underset{\sim}{U}_2^{pp} = \frac{\overset{*}{\underset{\sim}{I}}(k_2\hat{\underset{\sim}{x}},t)}{4\pi|\underset{\sim}{x}|}(\underset{\sim}{I}_3-\hat{\underset{\sim}{x}}^{T\wedge}\hat{\underset{\sim}{x}})(\underset{\sim}{I}_3\omega\mu|k_2\hat{\underset{\sim}{x}}\times\underset{\sim}{I}_3)\exp[i(k_2|\underset{\sim}{x}|-\omega t+\tfrac{1}{2}\pi)]$$

provided $$|\underset{\sim}{x}| < t(\epsilon\mu)^{-1/2}[1-\omega_p^2(;\underset{\sim}{X})/\omega^2]^{1/2},$$

and where $$k_1 = c^{-1}(;\underset{\sim}{X})[\omega^2-\omega_p^2(;\underset{\sim}{X})]^{1/2}\mathrm{sgn}\omega,$$

$$k_2 = (\epsilon\mu)^{1/2}[\omega^2-\omega_p^2(;\underset{\sim}{X})]^{1/2}\mathrm{sgn}\omega.$$

$$\overset{*}{\underset{\sim}{I}}(\underset{\sim}{k},t) = \iiint_{\mathcal{R}} d^3\underset{\sim}{y}\ \underset{\sim}{I}(\underset{\sim}{y},t)\exp(-i\underset{\sim}{k}\cdot\underset{\sim}{y}).$$

The wavefunction $\underset{\sim}{U}_n^{tr}$ represents transient plasma-acoustic (n=1) and plasma-optic (n=2) waves propagating behind, respectively, an almost spherical acoustic slower-front and a completely spherical optic faster-front. Those waves suffer fast spherical-and-temporal attenuations. Their spectrum is fast varying with $|\underset{\sim}{x}|/t$ and slow varying with $\underset{\sim}{X}$. They are superposed upon partially time-harmonic waves represented by $\underset{\sim}{U}_n^{pp}$, viz., partially time-harmonic plasma-acoustic (n=1) and plasma-optic (n=2) waves. These progagate behind, respectively, an almost spherical plasma-acoustic slower-front (preceded by the acoustic front enclosing the transient plasma-acoustic wave $\underset{\sim}{U}_1^{tr}$) and an almost spherical plasma-optic faster-front (preceded by the optic front enclosing the transient plasma-optic wave $\underset{\sim}{U}_2^{tr}$). Amplitudes of $\underset{\sim}{U}_n^{pp}$ are spatially fast attenuated and execute source current induced fast variations with direction and time as well as plasma imparted slow variations in space-time.

Actually, the asymptotic magnetic field response $\underset{\sim}{H}$ exhibits neither transient nor partially time-harmonic plasma-acoustic behaviours. It is a purely plasma-optic field.

Let us finally consider the response development at some fixed

long-range location when $t \gg |\underset{\sim}{x}|$, assuming $|\omega| > \omega_p(;\underset{\sim}{X})$. First, all four fronts are far remote to an observer. With regard to the transient modes, each wave frequency $\omega_{nn} \sim \omega_p(;\underset{\sim}{X})$ and wavenumber $k_{nn} \sim 0$. In particular, each transient wavefunction $\underset{\sim}{U}^{tr}_n \sim \underset{\sim}{0}$. The response is therefore almost time-harmonic:

$$(\underset{\sim}{E}|\underset{\sim}{H}) \sim \sum_{n=1,2} \underset{\sim}{U}^{pp}_n,$$

and may ultimately attain a time-harmonic state wherein $\overset{*}{\underset{\sim}{I}}(k \underset{n\sim}{\hat{x}},t)$ becomes

$$\overset{*}{\underset{\sim}{I}}(k \underset{n\sim}{\hat{x}},\infty) = \iiint_{\mathcal{R}} d^3\underset{\sim}{y}\ \underset{\sim}{\mathcal{J}}(\underset{\sim}{y}) \exp(-ik\underset{\sim}{\cdot}\underset{\sim}{y}).$$

This report is based on part of an investigation initiated at the Institute for Theoretical Physics II, University of Düsseldorf. We are grateful to the Deutsche Forschungsgemeinschaft for full funding of the visiting research appointment of L. C.-S. as Guest Professor in that institute. L. C.-S. thanks its members as well as Frau Dr. Barbara Suchy and Frau Theresia Bernstein for the very warm hospitality and kindness received.

[1] L. Chee-Seng, Proc. Roy. Soc. London Ser. A364, 181-209 (1978).

[2] L. Chee-Seng, Proc. Roy. Soc. London Ser. A421, 109-152 (1989).

[3] K. Suchy, J. Plasma Phys. 28, 185-192 (1982).

[4] K. Suchy, Kleinheubacher Berichte 25, 245-268 (1982).

[5] K. Suchy, in Proceedings of the Workshop on Mathematical Aspects of Fluid and Plasma Dynamics, Trieste, pp. 537-554 (Universita Degli Studi di Trieste, Facolta di Scienze, Istituto di Meccanica, 1984).

[6] I. B. Bernstein and L. Friedland, in Handbook of Plasma Physics Vol. I, Editors: A. A. Galeev and R. N. Sudan, pp. 367-418 (North Holland: Amsterdam, 1983).

Mode Coupling Of The Ordinary And Extraordinary Waves In A Cylindrical Plasma

D.Ramsay

E.W.Laing

ABSTRACT

We use the cold plasma, two fluid model to study waves in a non-uniform, cylindrical magnetic equilibrium. Firstly, a condition for a self-consistent helical equilibrium is derived and used to identify some useful special cases. The method of finding full wave equations, in the approximation of linear waves, is outlined, followed by a simplified set of equations for the coupled modes in the plasma.

1. The Cold Plasma Model

We use the following model:

$$\frac{\partial n_s}{\partial t} + \nabla\cdot(n_s \mathbf{v}_s) = 0 \,, \tag{1}$$

$$m_s \frac{D\mathbf{v}_s}{Dt} = q_s(\mathbf{E} + \mathbf{v}_s \times \mathbf{B}) \,, \tag{2}$$

$$\nabla\times\mathbf{E} = -\frac{\partial \mathbf{B}}{\partial t} \,, \tag{3}$$

$$\nabla\times\mathbf{B} = \mu_0\mathbf{J} + (\frac{1}{c^2})\frac{\partial \mathbf{E}}{\partial t} \,, \tag{4}$$

$$\mathbf{J} = \sum_s n_s q_s \mathbf{v}_s \,, \tag{5}$$

where, s, $s = i, e$, denotes particle species and $\frac{D}{Dt}$ is the convective derivative $\frac{\partial}{\partial t} + (\mathbf{v}_s\cdot\nabla)$.

2. Helical Equilibria

We wish to study the consequences of imposing a helical equilibrium magnetic field on a plasma. It is convenient to use cylindrical polar coordinates, and to put

$$\mathbf{B}_0 = B_0(0, f, g) \,, \tag{6}$$

We also assume that all quantities in (1)-(6), can only be functions of r. This ensures that a system of odes, rather than pdes is obtained. To specify the form of $\mathbf{B}_0$ further, we must solve (1)-(5) with $\frac{\partial}{\partial t} = 0$. For simplicity, set $n_0 = constant$, $\mathbf{E}_0 = 0$, and,

$$\mathbf{v}_{oi} = -\frac{m_e}{m_i}\mathbf{v}_{oe} \,. \tag{7}$$

This last condition ensures zero net momentum in the plasma. Overall neutrality is obtained by putting $n_{oi} = n_{oe} = n_0$, and $q_i = e$, $q_e = -e$. These assumptions allow (1)-(6) to be re-expressed in terms of a condition on $\mathbf{B}_0$, viz:

$$\left[g'\right]^2 = \frac{1}{L^2}\left[rgg' + f(rf)'\right], \tag{8}$$

where, $\frac{1}{L^2} = \frac{\omega_p^2}{c^2}\left[1 + \frac{m_e}{m_i}\right]$, and $\omega_p^2 = \frac{n_0 e^2}{\varepsilon_0 m_e}$ defines the electron plasma frequency.

It can be shown that the more common "force-free field" assumption often used in constructing equilibria is equivalent to the rhs of (10) being zero.

By prescribing the additional condition

$$f = -\kappa g', \tag{9}$$

the field components can be found explicitly in terms of the two scale lengths L and κ, which are, at present, arbitrary:

$$g = Ar^{\nu} J_{\nu}\left(\frac{r}{\kappa}\right) + Br^{\nu} Y_{\nu}\left(\frac{r}{\kappa}\right), \tag{10}$$

$$f = -Ar^{\nu} J_{\nu-1}\left(\frac{r}{\kappa}\right) - Br^{\nu} Y_{\nu-1}\left(\frac{r}{\kappa}\right), \tag{11}$$

where J_ν denotes the Bessel function of order ν , $\nu = \frac{L^2}{2\kappa^2}$.

This analytic solution includes as special cases,

$$g = A\left[\frac{2}{\pi}\right]^{\frac{1}{2}} \cos\left(\frac{r}{\kappa}\right), \tag{12}$$

$$f = -A\left[\frac{2}{\pi}\right]^{\frac{1}{2}} \sin\left(\frac{r}{\kappa}\right),$$

for $\nu = \frac{1}{2}$,

$$g = constant \quad , \quad f = 0, \tag{13}$$

for $\kappa \to \infty$, with L remaining arbitrary, and

$$g = A J_0\left(\frac{r}{\kappa}\right), \; f = A J_1\left(\frac{r}{\kappa}\right), \tag{14}$$

for $L \to 0$, with κ remaining arbitrary.

3. Wave Solutions: Fourth Order Differential System

We now look for wave solutions, using the standard technique of assuming small perturbations to an equilibrium situation. Assuming harmonic time dependence, taking the motion of the ions to be negligible, and considering only waves with radial wave vector, we find:

$$-i\omega n + n_o \nabla\cdot\mathbf{v} + \nabla n\cdot\mathbf{v}_o = 0, \tag{15}$$

$$m_e\left[-i\omega\mathbf{v} + (\mathbf{v}_o\cdot\nabla)\mathbf{v} + (\mathbf{v}\cdot\nabla)\mathbf{v}_o\right] = -e\left[\mathbf{E} + \mathbf{v}_o\times\mathbf{B} + \mathbf{v}\times\mathbf{B}_0\right], \tag{16}$$

$$\nabla\times\mathbf{E} = i\omega\mathbf{B}, \tag{17}$$

$$\nabla\times\mathbf{B} = \mu_0\mathbf{J} - \frac{i\omega}{c^2}\mathbf{E}\,, \tag{18}$$

$$\mathbf{J} = -e(n_o\mathbf{v} + n\mathbf{v}_o)\,, \tag{19}$$

where the subscript o denotes an equilibrium quantity.

The procedure now followed is to obtain all quantities in terms of E. Although straightforward, the complexity of the resulting algebra can be formidable and dealing with these equations by hand is a daunting task. The use of computer algebra makes this process much less tedious and error-prone. In this case REDUCE 3.3 was used to obtain the final formulation of the problem. The equations obtained have the form:

$$\begin{aligned} a_1E_\theta'' + a_2E_\theta' + a_3E_\theta + a_4E_z'' + a_5E_z' + a_6E_z = 0\,, \\ b_1E_\theta'' + b_2E_\theta' + b_3E_\theta + b_4E_z'' + b_5E_z' + b_6E_z = 0\,, \end{aligned} \tag{20}$$

where $' = \frac{d}{dr}$, and $a_i\,, b_i$ depend on equilibrium velocities and magnetic fields and their gradients (the full expressions are very complex and we do not reproduce them here).

The fourth order differential system seems to be a common theme in all problems of non-uniform wave propagation where dependence on only one coordinate is assumed. Diver, Laing and Sellar (1989) obtain an exactly analogous system, this time for E_x and E_y with z as independent variable. This structure corresponds physically to two independent wave solutions to the problem.

4. A Uniform Equilibrium

It is instructive to consider the special case of field (13), corresponding to a uniform magnetic spine. The waves admissible in such a medium are well known (Stix 1962), but are usually calculated in Cartesian coordinates. In cylindrical polar coordinates, the normal modes of the plasma separate more naturally into equivalents of the ordinary and extraordinary waves. The spatial part of the electric field then becomes, for standing waves, in the notation of Stix:

$$E_\theta = A\,J_1(pr)\,, \tag{21}$$

$$E_z = A\,J_0(qr)\,, \tag{22}$$

$$\left[\frac{cp}{\omega}\right]^2 = \frac{RL}{S}\,,\quad \left[\frac{cq}{\omega}\right]^2 = P\,.$$

5. An Approximate Approach

In order to obtain a more tractable system of equations, suppose that the terms involving equilibrium velocities are negligible, then:

$$\left[\frac{1}{\rho}(\rho E_\theta)'\right]' + \frac{\kappa^2}{L^2}(\alpha + \beta g^2 + \gamma f^2)E_\theta = \frac{\kappa^2}{L^2}\delta f g E_z\,, \tag{23}$$

$$\frac{1}{\rho}\left[\rho E_z'\right]' + \frac{\kappa^2}{L^2}(\alpha + \beta f^2 + \gamma g^2)E_z = \frac{\kappa^2}{L^2}\delta f g E_\theta\,, \tag{24}$$

where,

$$\alpha = \frac{\omega^2(\omega^2 - \Omega^2 - \omega_p^2)}{\omega_p^2(\omega^2 - \Omega^2)}\,,\quad \beta = \frac{-\omega_p^2\,\Omega_0^2}{(\omega^2 - \Omega^2)(\omega^2 - \Omega^2 - \omega_p^2)}\,,$$

$$\gamma = \frac{\Omega_0^2}{(\omega^2 - \Omega^2)}\,,\quad \delta = \frac{-\Omega_0^2}{(\omega^2 - \Omega^2 - \omega_p^2)}\,,$$

$$\Omega^2 = \Omega_0^2(f^2 + g^2), \quad \mathbf{B} = B_0(0, f(\frac{r}{\kappa}), g(\frac{r}{\kappa})), \quad \rho = \frac{r}{\kappa}, \quad ' = \frac{d}{d\rho},$$

and $\Omega_0 = \frac{eB_0}{m_e}$. Note that the electron cyclotron frequency here is Ω, rather than Ω_0, so that, for a given choice of ω, there may be a value of r for which the coefficients in (23) and (24) are resonant, unless $\Omega(r)$ is bounded. In contrast to the uniform case, where resonances affect the whole plasma, or none of it, we have a situation where, unless special choices of $\mathbf{B}_0$ are made, the effects of resonances have to be included in all attempts to solve (23) and (24).

We consider first one such special choice, the field (12). This avoids the resonance problem, and corresponds to choosing $\kappa = L$. We then have:

$$\left[\frac{1}{\rho}(\rho E_\theta)'\right]' + (a + b\cos^2\rho)E_\theta = b\sin\rho\cos\rho E_z, \tag{25}$$

$$\frac{1}{\rho}\left[\rho E_z'\right]' + (a + b\sin^2\rho)E_z = b\sin\rho\cos\rho E_z, \tag{26}$$

where $a = \alpha - \gamma$, and $b = \delta = \beta - \gamma$.

6. Boundary Conditions

To be consistent with the choice of coordinate system, we must have $E_\theta(0) = 0$, while the choice of only r dependence means that $E_z'(0) = 0$. To produce the two further conditions necessary for a complete solution of (25) and (26), we can either set values of E_θ and E_z at the origin for an initial value problem, or at some non-zero value of r, giving a boundary value problem. The later approach can be used to join our helical field onto a uniform one at some appropriate point. (Compare this with the procedure in Diver et al (1989), where a uniform field is joined onto a spatially rotating field).

Numerical solutions of (25) and (26) are currently being sought.

7. References

DIVER, D., LAING, E.W., SELLAR, C.C. 1989 *Journal Of Plasma Physics* ,**42**, 153

REDUCE 3.3 Users Manual , High Level Hardware Ltd, Oxford,U.K.

STIX, T., 1962 *The Theory Of Plasma Waves.* McGraw-Hill

HIGH FREQUENCY ELECTROSTATIC PLASMA INSTABILITIES AND TURBULENCE IN THE LOWER IONOSPHERE

B. Basu, J.R. Jasperse and J.M. Retterer
Geophysics Directorate, Phillips Laboratory
Hanscom AFB, MA, USA

D.T. Decker
Institute for Space Research, Boston College
Chestnut Hill, MA, USA

T. Chang
Center for Space Research, MIT
Cambridge, MA, USA

It has been known for some time that calculations of the collisional electron distribution function in the 2 to 4 eV energy range which neglect wave-particle interactions disagree with rocket measurements in both the auroral and sunlit, midlatitude lower ionospheres. The latter show a filling-in of the 2 to 5 eV valley in the isotropic distribution function predicted by the zero-order calculations. Recently, a rocket experiment in the auroral zone recorded intense plasma waves near upper hybrid frequency in the altitude range of 130-170 km; separate incoherent scatter radar experiments at Sondrestrom also showed strong backscattered signals from plasma waves with wavelengths ~ 11 cm. We can tie all these observations together by invoking the existence of electron cyclotron and upper hybrid plasma instabilities driven by the suprathermal bump in the electron energy distribution around 5 eV /1/. In this paper, we review the solutions for the electron distribution function including collisions but neglecting wave-particle effects, the observations, and the linear stability analysis. We also present quasilinear calculations and particle simulations which we have carried out in our study of this problem.

The basic equations are

$$\left[\frac{\partial}{\partial t} + \underline{v}\cdot\frac{\partial}{\partial \underline{r}} + \frac{q_e}{m_e}(\underline{E} + \underline{v}\times\underline{B}_o/c)\cdot\frac{\partial}{\partial \underline{v}}\right] f = S + L(f) + J(f) \quad , \qquad (1)$$

$$\frac{\partial}{\partial \underline{r}} \cdot \underline{E} = 4\pi \left(nq_i + nq_e \int d\underline{v} f \right) \quad . \tag{2}$$

Here S is a known source function, L represents the linear Boltzmann integrals for elastic and inelastic electron-neutral collisions as well as the electron-ion recombination collisions, and J is the nonlinear Fokker-Planck electron-charged particle collision integral /2/. The other quantities have their usual meanings. The steady state, isotropic solutions of Eq. (1) have been obtained numerically for $\underline{E} = 0$ and for the photoelectron source at midlatitudes and the precipitating electron source at auroral latitudes. The results for vf_0 (v) from 1 to 10 eV in the case of a photoelectron source are shown in the left panel of Fig. 1.

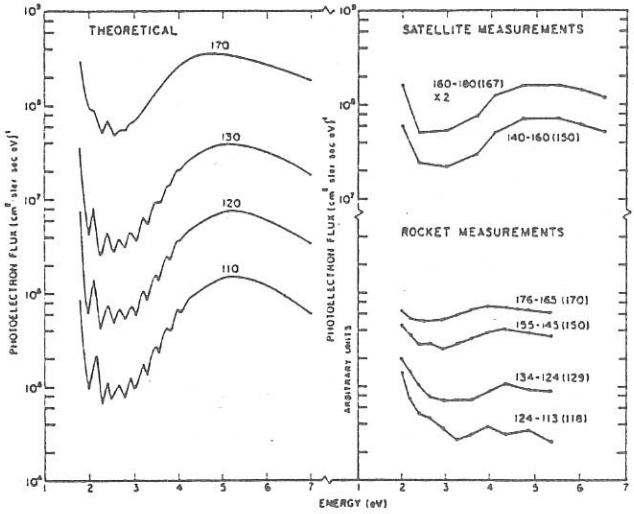

Fig. 1. Measured and calculated photoelectron energy spectra at various altitudes in km.

The dip in the calculated electron distribution function near 2 eV is caused by a peak in the e-N_2 vibrational excitation cross section. In the right panel, experimental data show flatter distributions than that predicted by the calculations. Similar disagreements between

calculations and observations are also found at auroral latitudes with the precipitating electron source.

In order to study the stability of (1) and (2) to small amplitude, high frequency electrostatic perturbations, we may neglect the ion dynamics and seek a solution of the form $f = f_0(v) + f_1(\underline{r},\underline{v},t)$. In the linearized equation for f_1, we may show that below about 170 km electron-electron collisions may be neglected in favor of electron-neutral collisions and that elastic electron-neutral collisions dominate the inelastic ones with regard to the damping of the waves. The Boltzmann electron-neutral elastic collision integral in the limit as the electron-to-neutral mass ratio is zero is /2/:

$$L f_1 = -\nu_o(v) f_1 + \frac{\nu_o(v)}{4\pi} \int d\underline{v}' \frac{\delta(v-v')}{(v')^2} f_1(\underline{r},\underline{v}',t) \quad . \tag{3}$$

Here $\nu_o(v)$ is the elastic electron-neutral collision frequency for a nearly isotropic differential cross section. Using standard methods, we obtain the dispersion relation in the presence of electron-neutral elastic collisions as:

$$0 = \varepsilon(\underline{k},\omega) = 1 + \frac{\omega_p^2}{k^2} \int d\underline{v} \left(1 - \frac{i\nu_o}{2} \sum_n I_n(v)\right)^{-1}$$

$$\times \sum_n \frac{J_n^2(k_\perp v_\perp / \omega_c)}{\omega + i\nu_o - n\omega_c - k_\parallel v_\parallel} \left(\frac{n\omega_c}{v_\perp} \frac{\partial}{\partial v_\perp} + k_\parallel \frac{\partial}{\partial v_\parallel}\right) f_0(v) \quad , \tag{4}$$

where the I_n functions are

$$I_n(v) = \int_0^\pi d\theta \sin\theta \frac{J_n^2(k_\perp v \sin\theta / \omega_c)}{\omega + i\nu_o - n\omega_c - k_\parallel v \cos\theta} \quad . \tag{5}$$

Here, $\omega_c = |q_e B_0 / m_e c|$ and other quantities have their usual meanings. It can be shown that (4) is approximately equivalent to the BGK result obtained in /1/.

The dispersion relation has been studied for a Maxwellian thermal population and a suprathermal bump near 5 eV for the following three situations: the daytime midlatitude ionosphere; the diffuse aurora; and a stable auroral arc. In each case, two types of unstable plasma modes have been identified: the resonant upper hybrid mode from about 125 to 170 km, and the non-resonant electron cyclotron modes from about 100 to 130 km. In the latter case, the instabilities occur in several narrow layers a few kilometers thick.

Using standard procedures, we find that the self-consistent quasilinear equation for $f_0(v_\parallel, v_\perp, t)$ is

$$\left[\frac{\partial}{\partial t} + \frac{q_e}{m_e c}(\underline{v} \times \underline{B}_o) \cdot \frac{\partial}{\partial \underline{v}}\right] f_0 = S_0 + L(f_0) + J(f_0)$$

$$+ \frac{\partial}{\partial \underline{v}} \cdot \underline{D}(\underline{v}) \cdot \frac{\partial}{\partial \underline{v}} f_0(v_\parallel, v_\perp, t) + \frac{\partial}{\partial \underline{v}} \cdot \underline{K}(\underline{v}, \underline{v}') \cdot \frac{\partial}{\partial \underline{v}'} f_0(v'_\parallel, v'_\perp, t) \quad . \tag{6}$$

In (6) $\underline{D}$ is a second order tensor operator which produces a diffusion-like term and $\underline{K}$ is a second order tensor integral operator which produces a nondiffusion-like term and both depend on $\nu_0(v)$. From an H-theorem that may be demonstrated from (6), it is possible to show that the effect of the $\underline{D}$ and $\underline{K}$ terms is to produce a flattening in f_0 from 2 to 6 eV. Numerical simulations show such flattening as well as the heating of the Maxwellian electrons.

/1/ B. Basu, T. Chang, and J.R. Jasperse, Geophys. Res. Lett. 9, 68 (1982).

/2/ J.R. Jasperse, in Physics of Space Plasmas, Ed. by T.S. Chang, B. Coppi and J.R. Jasperse, SPI Conference Proceedings and Reprint Series (Scientific Publishers, Cambridge, MA, 1981), vol. 4.

Numerical Calculation Based on Multipole Expansions was used to study The Linear Instability in a DP Machine.

C. Cereceda, J. Ruiz, J. Puerta
Universidad Simón Bolivar
Depto de Física, Apdo.89000, Caracas-Venezuela

ABSTRACT

Experiments to excite ion acustic instability in ion beam plasma system have been carried out during the last years. Numerical studies to characterize this phenomena based on the wavelenghts and growth rates of the linear instability are in good agreement with the observations. In this paper we report the effect produced by addition of impurities in the system and analyzing this via the solution of the dispersion relation of the electrostatic mode with the impurity term. To solve the resulting equation we use the multipole expansion for the dispersion relation of Martin and Gonsalez[1] to get an expresion easier to work numerically. In order to follow the evolution of this region versus the concentration of the impurity as parameter and observing the change of the growth rate ($Im(\Omega)$) of the most unstable mode. In the case of no impurity we compare our results with those obtained by G. Bonhomme et al.[2].

I.- INTRODUCTION

The characteristic modes of propagation of ion acustic waves in multiespecies plasmas [3],[4] and the instability in ion beam-plasma systems are in accordance with the prediction of solutions of the linear dispertion relation[5]. For the ion acustic shock wave generated through the injection of a transient ion beam in the plasma target of a double plasma (DP) machine, G. Bonhome et al.[2], have shown the relation between the potential dip observed behind the shock front and the nonlinear solitary wave. They explain the occurrence of instability at velocities lower than the usual beam plasma instability[6] by the local aceleration of the ion beam in the potential well.

In this paper we introduce a new method for the calculation of the unstable mode growth rate as a funtion of beam velocity and wave length, by the use of the two-pole approximation for the Z dispertion function[1] which is very accurate in the whole range. The expresion that we obtained for the dispersion relation is easy to solve with this method as well in the case of no impurity as in the multispecies case. In this way we can follow the evolution of the instability with very high accuracy.

II.- LINEAR THEORY OF INSTABILITIES IN ION ACOUSTIC PLASMA WAVES

For an ion beam in a two species system, it is well known that the adimensional dispesion relation of the electrostatic mode can be written as :

$$(1)\quad 1 + [1 + \xi_e . Z(\xi_e)]/K^2 + [1 + \xi_{i1} . Z(\xi_{i1})][T_e . \mu_{i1}/T_{i1} . K^2] + [1 + \xi_{b1} . Z(\xi_{b1})][T_e . \alpha_1/T_{b1} . K^2] + [1 + \xi_{i2} . Z(\xi_{i2})][T_e . \mu_{i2}/T_{i2} . K^2] + [1 + \xi_{b2} . Z(\xi_{b2})][T_e . \alpha_2/T_{b2} . K^2] = 0$$

Where $K = k/k_{De}$, $\Omega = \omega/\omega_{pi}$, $\alpha_j = n_{bj}/n_0$, $\mu_{ij} = n_{ij}/n_0$, and j define a subindex for each species.

The plasma dispersion function can be written in the standard form:

$$(2) \quad Z(\xi_j) = (1/\sqrt{\pi}) \int_{-\infty}^{+\infty} [\exp(-s^2)/(s - \xi_j)]\, ds \ ,$$

where the arguments of this function are given by :

$$(3) \quad \xi_e = (1/\sqrt{2}).(\omega_{pi}/\omega_{pe}).(\Omega/K) \ , \quad \xi_i = (1/\sqrt{2})\sqrt{T_e/T_i}\,.(\Omega/K)$$

$$\xi_b = \sqrt{T_e/2T_b}\ [\Omega/K - U_b] \quad , \quad \xi_{b2} = \sqrt{T_e/2T_{b2}}\,[\sqrt{m_{i2}/m_{i1}}\ (\Omega/K - U_b)]$$

$$\xi_{i2} = \sqrt{m_{i1}.T_e/2m_{i1}T_{i2}}\ (\Omega/K)$$

since $U_{b2} = \sqrt{m_{i1}/m_{i2}}\ U_b$ and $U_b = V_b/c_s$ are the beam velocities normalized by the ion acoustic velocity c_s.

The two-pole approximation for the plasma dispersion function $Z(\xi)$ obtained by P., Martin and A., Gonzales [1], by modifying the Padè method including in addition to the power series, one term of the asymptotic expansion. This approximation for the Z function is better than that of Fried and Comte [3], and leads to a polynomial equation for the dispersion relation. This approximation is:

$$(4) \quad \tilde{Z}(\xi) \approx b/(a - \xi) - b^*/(a^* - \xi)$$

with $a \approx 0.5138 - 1.0324i$
$b \approx 0.5000 + 1.2891i$

Using this approximant, the dispersion relation becomes simply a quotient of two polynomes of ten degree in Ω:

$$(5) \quad \frac{A_0 + A_1\Omega + \ldots\ldots\ldots + A_{10}\Omega^{10}}{B_0 + B_1\Omega + \ldots\ldots\ldots + B_{10}\Omega^{10}} = 0$$

with complex coefficients which are functions of the beam velocity U_b, the wave number K and the impurity concentration μ_{i2}.

Numerical calculation[7] of the numerator polynom roots gives the frequency values (Ω), provided that this roots are different to those of the denominator polynom.

For the ion beam plasma system without impurities the last two terms of the dispersion relation (eq.1) do not appear and its rational expresion obtained with the dipole approximation is one of sixth degree in Ω.

$$(6) \quad \frac{C_0 + C_1\Omega + \ldots\ldots + C_6\Omega^6}{D_0 + D_1\Omega + \ldots\ldots + D_6\Omega^6} = 0 \ .$$

Since in the linear theory the electrostatic waves are assumed to have the form $E(x,t)=E_0.\exp[i(Kx-\omega t)]$,for real K, those complex values for ω with $Im(\omega)>0$ lead to the unstable mode of growing waves.
When a transient step of potential is applied between the source and target chambers of the DP-machine, the ion beam plasma system is perturbed. It has been reported [2] the existence of a potential well behind the shock front where the ion beam can induce a local ion acustic instability.

III.- RESULTS AND CONCLUSIONS

The dispersion relation(Eq.1) has been first solved for an Argon plasma with zero impurity concentration, and beam-plasma parameters: $T_e/T_i=30$, $\alpha_i=0.1$ and $T_i/T_b=20$. The branch of the roots with the largest $Im(\Omega)>0$ and $Re(\Omega)>0$ (i.e. right propagating waves) represents the most unstable mode. The values of the normalized wavelength λ/λ_{Di} for a given beam velocity are shown in Fig.1.

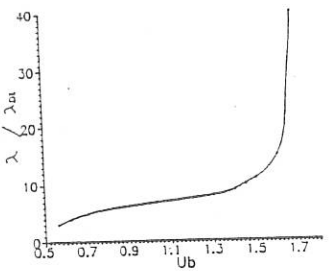

Fig. 1. WAVELENGTH OF THE MOST UNSTABLE MODE VERSUS BEAM VELOCITY.

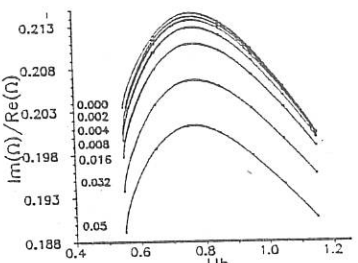

Fig.2. GROWTH RATE VS. BEAM VELOCITY FOR SEVERAL VALUES OF IMPURITY CONCENTRATION. Ti/Tb=20. WAVELENGTH= 7.5 λ_{Di}.

The unstable range stands for values of beam velocity between 0.5 and $1.7c_s$. The shape of this curve is in agreement with that previously reported [2], both curves diverge for beam velocities larger than $V_b \approx 1.75c_s$.
Figure.2 shows the growth rate of the slow beam mode versus the beam velocity for $\lambda=7.5\lambda_{Di}$ and for several values of impurity concentration of Helium ions.The largest growth rate is achieved at $V_b=0.70c_s$.The effect of impurity concentration on the instability is shown in Fig.3.
This figure shows a linear decreasing in the growth rate with the concentration of the light ion impurities. It is observed that the largest growth rate is always achieved for $V_b \approx 0.7c_s$, still for high concentrations as 0.05.

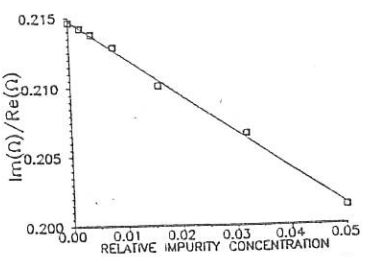

Fig.3. MAXIMUM GROWTH RATE $Im(\Omega)/Re(\Omega)$ AS A FUNCTION OF IMPURITY CONCENTRATION.

IV.- REFERENCES

1.- P. Martin and M. Gonzales
Phys.Fluids, 22, 1413 (1979).

2.- G. Bonhomme et al. ,
Preprint, L.P.M.I., U.R.A. 835 du CNRS,Universitè de Nancy I,
BP 239, F-54506 Vandoeuvre Cedex, France.

3.- B. Fried et al.,
Phys. Fluids, 14 , 2388 (1971)

4.- Y. Nakamura, M. Nakamura and T. Itoh
Phys. Rev. Lett, 37 , 209 (1976)

5.- E. Stella
Interaccion Onda-Particula en ondas iónico acústicas en un plasma de argón y helio.
Tesis. (1979)
Universidad Simón Bolivar, Caracas-Venezuela

6.- T. Pierre et. al.,
Plasma Phys., 27 , 1497 (1985)

7.- S. Wolfram
Mathematica, A System for Doing Mathematics by Computer,
p.606,Addison-Wesley Publishing, N.Y.(1991)

DISPERSION CHARACTERISTICS OF ELECTROMAGNETIC WAVES IN DIPOLAR (m = ±1) MODES TRAVELLING ALONG A MAGNETIZED PLASMA COLUMN

E. Benova, I. Ghanashev* and I. Zhelyazkov*

Department of Physics, Institute for Foreign Students,
BG-1111 Sofia, Bulgaria

* Faculty of Physics, Sofia University, BG-1126 Sofia, Bulgaria

The modelling of isotropic plasma columns sustained by travelling electromagnetic waves in the dipolar mode (angular dependence $exp\ im\varphi$, $m = \pm 1$) shows that the $m = \pm 1$ modes have identical dispersion characteristics /1/. In the presence of an external static magnetic field, however, the modes behave rather differently. This observation arose in studying the axial structures of magnetized plasma columns surrounded by vacuum and produced by travelling electromagnetic waves in the dipolar modes /2/.

We examine the propagation of electromagnetic waves along a homogeneous cold plasma column of radius R and electron number density n immersed in an axial constant magnetic field $\mathbf{B}_0 = B_0\hat{z}$. The time dependence is assumed to be $\propto exp(-i\omega t)$ and the axial wave number is k. Starting from Maxwell's equations and following the method used in Ref. 3, a dispersion relation of the kind

$$\mathcal{D}_m(\omega, k, n, R, B_0) = 0 \qquad (1)$$

has been obtained /2/. In studying the axial distributions of plasma and wave characteristics in the case when the plasma is produced by the wave itself, (1) is considered as a phase diagram (n as a function of k at ω, R and B_0 being constant). Introducing the variable $x = kR$ and parameters $\sigma = \omega R/c$, $\Omega = \omega_c/\omega$ the phase diagrams can be plotted in dimensionless form (ω/ω_p versus x at σ and Ω being constants). Here $\omega_c = eB_0/m_e c$ and $\omega_p = (4\pi ne^2/m_e)^{1/2}$ are the electron cyclotron and plasma frequencies. An example of such diagrams for $\sigma = 0.5$ and different magnetic fields is shown in Fig. 1 for both $m = +1$ and $m = -1$ modes. The behavior of the $m = +1$ mode is regular -- the corresponding phase curves change their form continuously from the $\Omega = 0$ to the $\Omega \to \infty$ curve as increasing the magnetic field. This is not the case for the $m = -1$ mode. For strong magnetic fields ($\Omega > 1$) the phase curves continuously approach the $\Omega \to \infty$ curve remaining below it. A peculiarity of these curves is the appearance of a "turning point", where

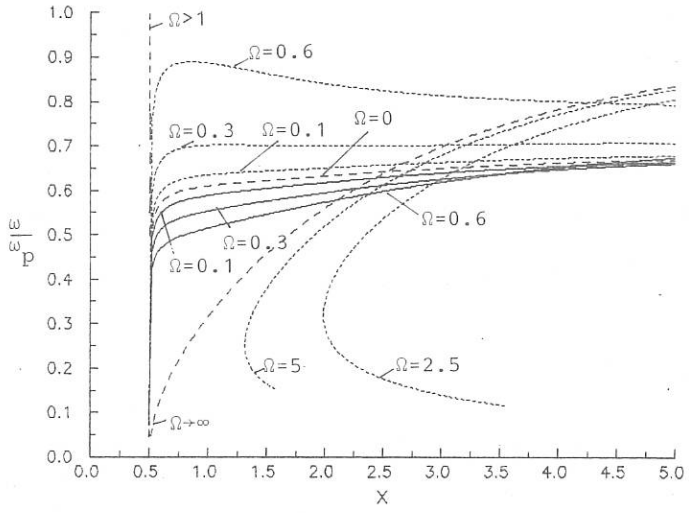

Fig. 1. Phase diagrams for the m=+1 mode (———) at σ=0.5 and Ω=0.1,0.3 and 0.6. The phase curves for the m=-1 mode (----) are calculated at Ω =0.1,0.3,0.6,2.5 and 5. The large-dashed curves correspond to the case of an isotropic plasma (Ω=0) and an infinite magnetic field ($\Omega\to\infty$).

the slope changes its sign. Another peculiarity of the $\Omega > 1$ case is the existence of a second solution to (1) plotted as an almost vertical line at $x \approx \sigma = 0.5$. We note that in this case the solutions for all $\Omega > 1$ are so close to the $x = \sigma$ line that they are scarcely distinguishable from it and from each other. For weak magnetic fields ($\Omega < 1$) the phase diagrams lie entirely above the $\Omega = 0$ curve and there is no continuous transition from the $\Omega > 1$ to the $\Omega < 1$ case. It is the purpose of this communication, to find the source of this strange behavior in the phase diagrams of the m = -1 waves.

In order to do this we compute the pure dispersion curves instead of phase diagrams. This means that now we assume that there exists a homogeneous magnetized plasma column with electron number density n (normalized through $s = \omega_p R/c$), along which a dipolar wave travels. The dispersion curves are obtained from (1) as dependencies x versus ω/ω_p assuming s and B_0 constants. A family of dispersion curves for $s = 0.188$ ($n = 10^{10}$ cm^{-3},

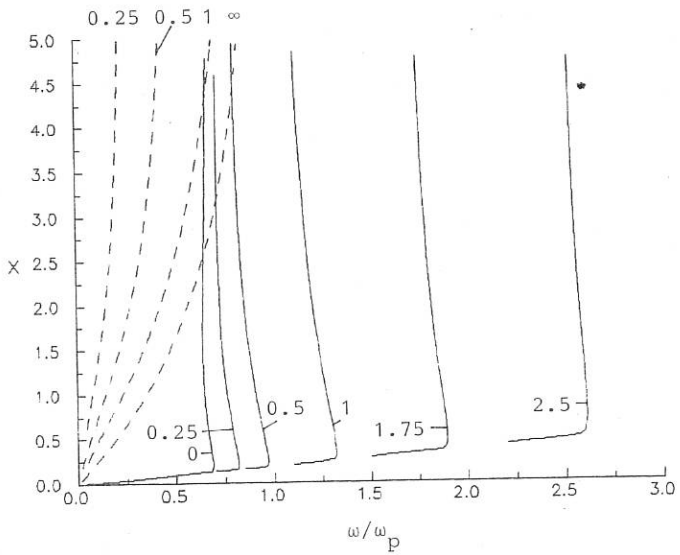

Fig. 2. Dispersion relation of the m=-1 mode at s=0.188 and $\bar{\Omega} \equiv \omega_c/\omega_p = 0, 0.25, 0.5, 1, 1.75, 2.5$ and ∞.

R = 1 cm) for different magnetic fields are presented in Fig. 2. One can see two sets of curves with rather different courses, which explain all observed peculiarities in the corresponding phase diagrams. The first set of curves (continuous lines) correspond to the $\Omega < 1$ solutions and to the vertical lines at $\Omega > 1$. For small normalized frequencies ω/ω_p the dimensionless wave numbers x follow the straight line $x \approx s \times (\omega/\omega_p)$, which corresponds to the vertical lines $x \approx \sigma$ in the phase diagrams. With increasing x ω tends to ω_c at strong magnetic fields ($\omega_c/\omega_p \gg 1$) and to a frequency slightly exceeding $\omega_p/\sqrt{2}$ at weak magnetic fields ($\omega_c/\omega_p \ll 1$). These solutions are not interesting for practical purposes since they correspond to either backward waves or loosely bound to the plasma waves. The other set of solutions (dashed lines in Fig. 2) describe forward waves and might be of interest for experiments. They exist in the frequency domain from zero to ω_c at weak magnetic fields and from zero to ω_p at strong magnetic fields. They are well localized for all frequencies in that domain. These solutions correspond to the "turning-point" curves in the

phase diagrams for $\Omega > 1$. Figure 3 shows how such a turning point curve can be obtained from a set of dispersion curves with different normalized densi-

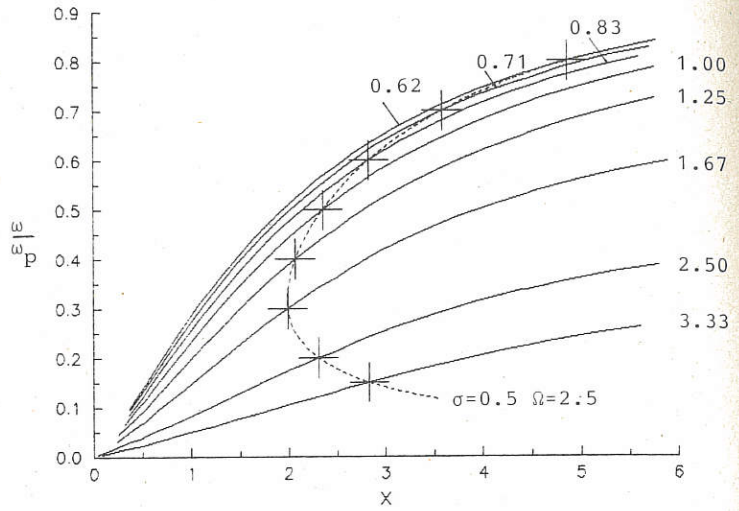

Fig. 3. Dispersion curves of the m=-1 mode at different values of the parameter s and a fixed magnetic field $\omega_c R/c=1.25$.

densities s at the same magnetic field. It is worth noting that the negative-slope-part of the phase curve *does not correspond to a backward wave* and we must be cautious in the interpretation of the phase diagrams.

Acknowledgments: This work was supported by the Ministry of Education and Science under Grant F-42/91.

References

/1/ E. Benova, I. Ghanashev, I. Zhelyazkov, J. Plasma Phys. **45**, 137 (1991)

/2/ E. Benova, P. Staikov, I. Zhelyazkov, J. Plasma Phys. -- in press

/3/ E. Benova, I. Zhelyazkov, P. Staikov, F. Cap, Phys. Rev. A **44**, 2625 (1991)

CYCLOTRON AUTORESONANCE CURRENT DRIVE IN TOKAMAKS

A.Yu.Kuyanov, A.A.Skovoroda, A.V.Timofeev, A.V.Zvonkov

I.V.Kurchatov Institute, Moscow, Russian Federation

The possibility of current drive (CD) in a tokamak by electromagnetic waves under electron cyclotron autoresonance (CAR) conditions is analyzed.

CAR effect consists in almost unlimited acceleration of electrons by a monochromatic electromagnetic wave with the parallel (along the magnetic field) refraction index $N_\parallel=1$. During the heating in CAR regime the parallel momentum of electrons grows substantially along with the energy. These circumstances make the use of CAR for current drive very attractive.

The possibility of continuous acceleration of electrons by the wave with $N_\parallel \geq 1$ in inhomogeneous magnetic field was noted in [1,2]. For $N_\parallel > 1$ the relativistic decrease of cyclotron frequency as a result of heating is compensated by the shift of the resonance point to the higher magnetic field region. By the action of this mechanism the appearance of a flow of electrons with energies 0.1-0.4 MeV, escaped through one end of OGRA-4 mirror machine during the gyrotron pulse, was explained [3]. In these experiments ECR waves were launched into the trap along the magnetic field and the flow of energetic electrons had the same direction as the wave.

In a tokamak the compensation of the relativistic decrease of cyclotron frequency is more difficult because of smaller magnetic field variation along the electron trajectory. But requirements to the magnetic field inhomogeneity become weaker near CAR regime ($N_\parallel \to 1$). One can hope that with the aid of waves with $N_\parallel=1$ it will be possible to generate the directed flow of high energy electrons in a tokamak, that is to drive an electric current with high efficiency.

ECR condition

$$\gamma = N_\parallel q_\parallel + \frac{n\omega}{\omega} eO \qquad (1)$$

for $N_\parallel$=1 coincides with the equation of lines of quasilinear ECR diffusion in the momentum space

$$\gamma = \frac{q_\parallel}{N_\parallel} + \text{const}, \qquad (2)$$

here q = p/mc, γ - relativistic factor, n - harmonic number, ω_{e0} - cold electron cyclotron frequency. From (2) one can see, that for q ~ 1 electrons gain substantial parallel momentum from the wave. Thus, CD under CAR condition has much in common with low hybrid CD.

Cold plasma dispersion function allows us to define parameters for which the inequality $N_\parallel \geq 1$ is possible. On Fig.1 the dependence of the angle θ ($N_\parallel$=1, $N_\perp$=tanθ) on $(\omega_p/\omega)^2$ at $(\omega_{e0}/\omega)^2$=1.05 for extraordinary wave is shown. It is seen that in a tokamak CAR condition can be fulfilled on the fundamental harmonic of cyclotron frequency for launching of the extraordinary wave from the high field side at small angles to the magnetic axis.

For launching of such waves there are some obstacles, but they can be overcome. At first, small launching angle does not prevent the wave from penetration into the plasma core, because group velocity of the wave is inclined steeper to the magnetic axis then phase velocity. This fact is illustrated by the Fig.2, where the dependence of the value

$$C = (V_{g\parallel}/V_{g\perp}) \; / \; (V_{ph\parallel}/V_{ph\perp})$$

on $(\omega_p/\omega)^2$ at $(\omega_{e0}/\omega)^2$=1.05 for the extraordinary wave with $N_\parallel$=1 is shown.

Another obstacle results from the conservation of the product $N_t R$ along the ray due to toroidal symmetry, here N_t is a toroidal projection of the refraction index, R is the distance from the torus axis. If CAR condition is fulfilled on the magnetic axis R_0, then at the plasma-vacuum boundary for launching from the high field side ($R_1 < R_0$) the inequality $N_t = R_0/R_1 > 1$ must be valid. But such waves in vacuum are impossible. Hence, the only possibility is vertical launching from the top (or bottom) of a tokamak. An example of ray

tracing and absorption calculations for T-10 tokamak (R_0=150cm, a=28cm, quadratic profile of density $n_{e0}=10^{13}cm^{-3}((\omega_p/\omega)^2=0.2)$ and temperature T_{e0}=1KeV, launching angles 20° to the horizontal plane and 0°,10°,20° inside the tokamak, $(\omega_{e0}/\omega)^2$=1.2) is shown. Note, that for preferential absorption of the wave in the plasma core (not the periphery) it is necessary to displace the ECR zone outside the launching radius [4].

For estimation of the efficiency of CAR CD model calculations were made with the aid of high energy relativistic Fokker-Plank equation

$$\frac{df}{dt} = q_t^3 \left\{ \frac{2}{q^2} \frac{d}{dq} \left[\gamma^2 (f + \frac{q_t^2 \gamma}{q} \frac{df}{dq}) \right] + \frac{\gamma(1+Z)}{q^3} \frac{d}{d\mu}(1-\mu^2) \frac{df}{d\mu} \right\} +$$

$$+ \frac{1}{q^2} \left[q \frac{d}{dq} - (\mu - \frac{N_\parallel q}{\gamma}) \frac{d}{d\mu} \right] D(1-\mu^2) \left[q \frac{d}{dq} - (\mu - \frac{N_\parallel q}{\gamma}) \frac{d}{d\mu} \right] f ,$$

here $q_t^2=T_e/mc^2$, Z- effective charge, $\mu=q_\parallel/q$, D - normalized ECR diffusion coefficient. Assuming q_t=0.1 and nonzero value D=0.1 in a narrow zone near the resonance curve (1) $(\omega_{e0}/\omega = 1.07\pm\Delta)$, the distribution function with the account of trapped particles (μ_c=0.26) was calculated for two variants: 1 - $N_\parallel$=0.34, Δ=0.02; 2 - $N_\parallel$=1, Δ=0.04. Results of calculations shown on Fig.4 display the effective acceleration of electrons under CAR conditions. In the second variant CD appears to be substantially more effective for large enough values of D. Note, that the obvious shortcoming of this scheme is the existence of countercurrent that can reduce total CD efficiency.

References

[1] Hafizi B., Aamodt R.E., Phys.Fluids, 30, 3059, 1987.
[2] Zhil'tsov V.A., Skovoroda A.A., Timofeev A.V. et al. Fizika plasmy, 17, 771, 1991.
[3] Zhil'tsov V.A., Skovoroda A.A., Timofeev A.V. et al. 18th Eur.Conf.Contr.Fus. and Pl.Phys., Berlin, 1991, v.15C,II-265
[4] Dendy R.O., Harvey R.W., O'Brien M.R., Pl.Phys. and Contr.Fus. 29, 769, 1987.

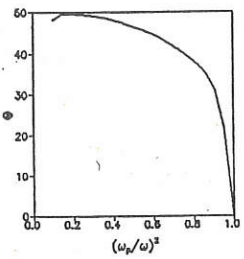

Figure 1

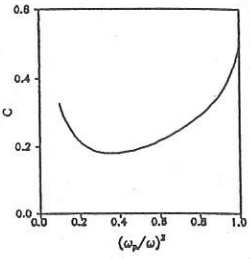

Figure 2

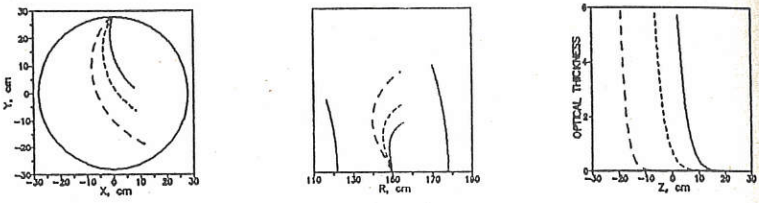

Figure 3

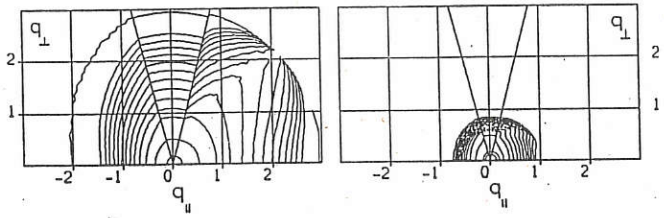

Figure 4

Application of a reconstructive MHD code based on the formalism of the toroidal multipoles to the ITER Tokamak

F. Alladio, P. Lalousis *, P. Micozzi
ENEA, CRE Frascati, via E.Fermi 27, C.P. 65 -00044 Frascati, Rome, Italy

1 - Introduction

One of the most important diagnostics both for the present tokamak experiments as well as for the future devices, aimed at achieving ignited plasmas, is the MHD equilibrium reconstruction. The reconstruction of the MHD equilibrium is obtained from the data of magnetic probes which measure magnetic fields and fluxes on a contour that encloses the plasma column.

The aim of this work is to generalize the reconstructive equilibrium code ODIN /1/ to fulfill the following requirements:

i) the capability to treat any possible magnetic probe set;

ii) a fast identification of plasma boundary characteristics (such as elongation and shape of the outermost magnetic surface, X-point positions, limiter contact point, etc.);

iii) the possibility to provide global plasma quantities such as the poloidal beta β_p, the internal self-inductance l_i, the diamagnetism μ_i and the total plasma current I_p, in addition with some local plasma quantities such as the shape of the magnetic surfaces and the position of the magnetic axis;

iv) the ability to obtain quantitative information about local equilibrium quantities such as the safety factor and toroidal current density profiles.

In order to simulate the ITER equilibria, the reconstructive code ODIN has been interfaced with the Finite Element predictive equilibrium code PROTEUS /4/ that provides the values of the fluxes and of the magnetic fields at the probe positions for the current ITER reference scenarios.

2 - Characteristics of the Code

The method of solution of the Grad-Shafranov equation used in the ODIN code is based on a particular coordinate system (the full toroidal (Θ, ω, Φ) /2/) that is the most natural for a toroidal device. It allows to reduce the full two-dimensional problem of the magnetostatic plasma equilibrium to a one-dimensional one, and greatly shortens the computer time needed for the solution.
In fact, by adopting this coordinate system the scalar, magnetic flux, function Ψ can

* The NET Team, c/o Max-Planck IPP, Boltzmannstr. 2, 8046 Garching, Germany

be expanded in the following multipolar form:

$$\Psi = \frac{1}{\sqrt{ch\Theta - \cos\omega}} \sum_{m=0}^{m_{max}} [M_m^{l,c}(\Theta) g_m(ch\Theta) + M_m^{i,c} f_m(ch\Theta)] \cos(m\omega) + [sinus\ part] \qquad (1)$$

where $f_m(ch\Theta)$ and $g_m(ch\Theta)$ are special functions (Fock functions /2/), and M_m are the toroidal multipolar moments. Such an expression is truncated /1/ at $m_{max} = 3$.
The flux function expressed in such a form is fully analytical in the poloidal coordinate (ω), so that all the physical informations about the current density distribution inside the plasma are included in the radial (Θ) behaviour of the multipolar moments $M_m(\Theta)$, that are constant outside the plasma region.

The values of the multipolar moments on a circle (at constant Θ) that does not cross the last magnetic surface of the plasma are the boundary conditions of the problem. If the spectrum of the multipolar moments is known (fitting the experimental data measured by the magnetic probe set) then it is possible to reconstruct the MHD equilibrium.

3 - The Problem of the Best Fit of the Magnetic Data

The main difficulty that has been solved in order to generalize the ODIN code to treat very elongated plasmas (such as in the ITER case) is the choice of the method of best fitting the magnetic probes data. This difficulty arises because the magnetic probes are not placed on a Θ = constant surface but spread in a range $[\Theta_{min}, \Theta_{max}]$ (fig.(1)). In fact the chosen toroidal coordinate system on which the integration mesh is built has to fulfil two main requirements:

a) the minimum Θ spanned from the magnetic probes must not cross the poloidal field coils;
b) the maximum Θ must not cross a significant amount of the plasma current distribution.

The necessity for these two requirements is discussed in reference /1/. The first constraint can be relaxed by subtracting the Ψ produced by the coils internal to the mesh during the equilibrium iterations, but the second one is absolutely compulsory. As one can see in fig.1 (ITER case), a realistic pick-up coil set (surface 1 fig.(1)) for an elongated machine cannot agree with requirement (b).

The solution that has been adopted is to transfer the boundary conditions (the values of the multipolar moments) coming from the magnetic measurements to a contour that fulfills the requirement (b).
Therefore the fluxes and fields have to be propagated in the vacuum region enclosed between the two contours (surface 1 and surface 2 fig.(1)).
The solution to the mathematical problem of calculating fluxes and fields on surface 2 from measurements on surface 1 is based on the application of the vector Green's theorem /3/.

4 - Reconstruction of ITER Equilibria

The reconstructive ODIN code has been applied to ITER equilibria calculated by the predictive code PROTEUS for the current ITER magnetic configurations and operating scenarios. Both limiter and double null configurations, with up-down symmetry, have been successfully reproduced.

Two representative examples of comparisons between configurations calculated by PROTEUS and the reconstructed ones by ODIN are shown in Table 1.
The relative precision on the estimate of the global plasma parameters as β_p and l_i is of the order of 5% (for non-circular plasmas), also for low values of $\beta_p + l_i/2$; the precision on the total plasma current is better than 1%; that of magnetic axis and X-point positions, elongation and triangularity spans from 1 to 3%. Correct information is also obtained about the safety factor and toroidal current profiles.

	Results calculated by PROTEUS	Results calculated by ODIN
(a) Double null configuration		
Plasma Current	22.00 MA	22.02 MA
Flux at the Magnetic axis	55.03 Wb	54.13 Wb
Flux at the boundary	-40.95 Wb	- 41.74 Wb
β_p , $l_i/2$	0.454, 0.340	0.472, 0.330
Position of Magnetic axis	6.26 m	6.36 m
Position of the X-Point(r,z)	(4.72,-4.78)	(4.76,-4.70)
Plasma Position		
minimum r	3.844 m	3.893 m
maximum r	8.176 m	8.074 m
minimum z	-4.78 m	-4.70 m
maximum z	4.78 m	4.70 m
(b) Limiter configuration		
Plasma Current	10.00 MA	10.03 MA
Flux at the Magnetic axis	126.47 Wb	127.67 Wb
Flux at the boundary	79.75 Wb	79.63 Wb
β_p , $l_i/2$	0.061, 0.369	0.062, 0.391
Position of Magnetic axis	5.97 m	5.96 m
Plasma Position		
minimum r	3.714 m	3.712 m
maximum r	7.984 m	7.912 m
minimum z	-3.002 m	-2.947 m
maximum z	3.001 m	2.947 m

Table 1

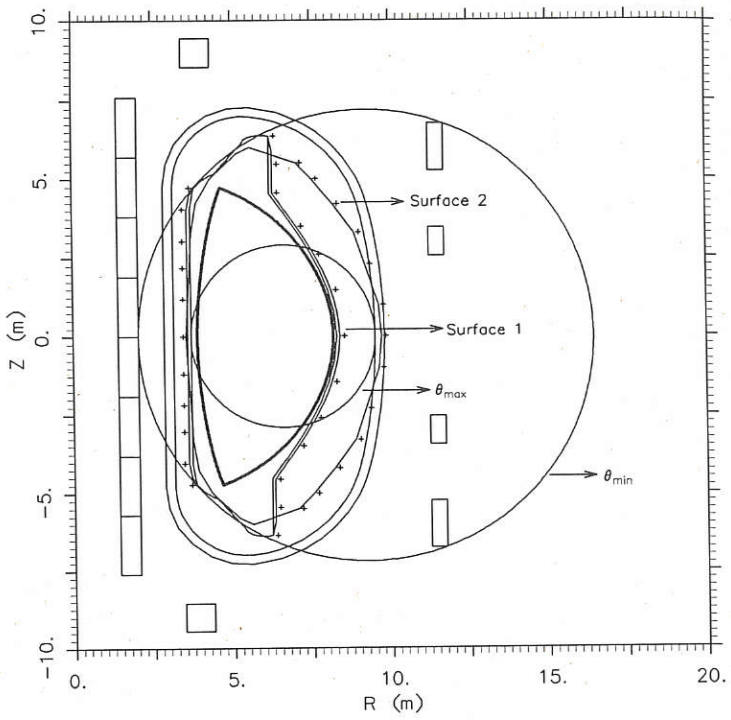

Fig. 1

Schematic representation of the ITER poloidal field system and a tentative set of magnetic measurements located behind the first wall of the machine. Surface 1 is the probe measurement contour, surface 2 is the contour upon which the toroidal multipole moments are constant. The $[\theta_{min}, \theta_{max}]$ spanned by surface 2 fulfills the requirement (b) of Chapt.3.

Acknowledgments

It is a pleasure to thank Dr. O.DeBarbieri for help on the PROTEUS code.

References

/1/ Alladio F., Crisanti F., Nucl. Fusion 26 (1986) 1143
/2/ Morse P.M., Feshbach H., Methods of Theoretical Physics, McGraw - Hill (1953)
/3/ Hakkarainen S.P., Freidberg J.P., MIT Report PFC/RR-87-22 (1987)
/4/ R. Albanese, J. Blum, O. DeBarbieri, The 12th Conference on the Numerical Simulation of Plasmas, California, Sept. 1987.

MHD THEORY WITH INDUCED SURFACE CURRENT EFFECTS

B. Lehnert
Alfvén Laboratory, Royal Institute of Technology
S 10044 Stockholm, Sweden

Introduction

This paper reconsiders the dynamics of a plasma body of finite size, immersed in a magnetic field $\underline{B}_{co}$ generated by steady currents in fixed external conductors. In equilibrium the plasma is confined by the magnetic field $\underline{B}_o = \underline{B}_{jo} + \underline{B}_{co}$ where $\underline{B}_{jo}$ is due to a current density $\underline{j}_o = \mathrm{curl}\underline{B}_{jo}/\mu_o$. The equilibrium is perturbed by a plasma displacement $\underline{\xi}(\underline{r},t)$ where $\underline{r} = (x,y,z)$. Free-boundary modes in an inhomogeneous external field $\underline{B}_{co}$ have earlier been shown to generate electromagnetically induced surface current effects which influence the dynamics of the plasma /1/. These effects will be further investigated here, in particular their impact on the energy principle /2/ and on ideal MHD theory in general.

The Induced Surface Current Effects

The analysis is restricted to equilibria where no surface currents are driven by a pressure jump at the boundary, even if such currents could in principle be included. For an observer following the local boundary motion of an ideal ("superconducting") plasma, the inhomogeneity of the external field $\underline{B}_{co}$ is experienced as a time variation of $\underline{B}_{co}$ at the vacuum side of the plasma boundary, whereas the frozen-in part of $\underline{B}_{co}$ on the plasma side remains unaffected in first order. The corresponding field jump generates an induced surface current.

For a small displacement $\tilde{\underline{\xi}}$ the induced surface current density thus becomes /1/

$$\tilde{\underline{K}}_B = (1/\mu_o)\,\hat{\underline{n}} \times [\,(\tilde{\underline{\xi}}\cdot\underline{\nabla})\underline{B}_{co}] \tag{1}$$

where $\hat{\underline{n}}$ is the outward directed normal of the surface. The work of the force $\tilde{\underline{K}}_B \times \underline{B}_o$ results in a contribution to the potential energy which can be cast into the forms

$$\delta W_B = (1/2)\iint_S \tilde{\underline{K}}_B \cdot \tilde{\underline{A}}\,dS = (1/2\mu_o)\iint_S w_B\,dS = (1/2\mu_o)\iiint_V w_B\,dS \tag{2}$$

where S and V are the surface and volume of the plasma body, $\tilde{\underline{A}} = \tilde{\underline{\xi}} \times \underline{B}_o$ and

$$W_B = \tilde{\underline{\xi}}\cdot\hat{\underline{n}}\{\,\underline{B}_o\cdot[(\tilde{\underline{\xi}}\cdot\underline{\nabla})\underline{B}_{co}]\} = -(\hat{\underline{n}}\cdot\tilde{\underline{\xi}})(\tilde{\underline{B}}_c\cdot\underline{B}_o) \tag{3}$$

$$w_B = \mathrm{div}(\tilde{\underline{A}}\times\tilde{\underline{B}}_c)\ ; \qquad \tilde{\underline{B}}_c = -[(\tilde{\underline{\xi}}\cdot\underline{\nabla})]\underline{B}_{co} \tag{4}$$

The transition from the second to the third member of eq. (3) has been performed by means of the vector identity

$$\underline{a}\cdot(\underline{b}\cdot\underline{\nabla})\underline{c} = \underline{b}\cdot(\underline{a}\cdot\underline{\nabla})\underline{c} + \underline{b}\cdot(\underline{a}\times \mathrm{curl}\underline{c}) \qquad (5)$$

combined with the conditions $\mathrm{curl}\underline{B}_{co} = 0$ and $\hat{\underline{n}}\cdot\underline{B}_o = 0$. Here Q_o and $\tilde{Q}$ denote unperturbed and small perturbed parts of any quantity Q. As shown elsewhere /1/, δW_B of eq. (2) sometimes yields an important stabilizing contribution.

The question now arises how a finite force $\tilde{\underline{K}}_B \times \underline{B}_o$ on an infinitely thin boundary layer becomes reconcilable with the pressure balance. The answer is that the displacement should be considered to grow slowly from zero at time $t = 0$ to its final value, i.e. on a long time scale as compared to the time for MHD signals to traverse the plasma body. The surface force is then transferred into a volume force, as for any physical system where a body is pushed at its surface by a surface force, and is kept together by internal binding forces. The equivalent volume force effect is here given by w_B in eqs. (2) and (4). The pressure boundary condition of conventional theory /2/ thereby becomes preserved /1/.

If, on the other hand, the plasma body is "pushed" violently by a rapidly growing displacement, strong induced surface currents arise which produce large inertial forces on the utmost layers, thereby leading to shock-like signals propagating into the plasma interior.

The non-linear case of large displacements yields an expression for the induced surface current being analogous to eq. (1), and to a plasma behaviour which becomes similar to that just described for small displacements.

The Conventional Plasma Volume Force

Conventional theory is based on the equilibrium condition and the momentum balance equation, i.e.

$$\underline{j}_o \times \underline{B}_o = \underline{\nabla} p_o \qquad (6)$$

$$\rho_o(\partial^2\tilde{\underline{\xi}}/\partial t^2) = \tilde{\underline{F}}_V \equiv \tilde{\underline{j}}\times\underline{B}_o + \underline{j}_o\times\tilde{\underline{B}} + \underline{\nabla}(\gamma p_o \mathrm{div}\tilde{\underline{\xi}} + \tilde{\underline{\xi}}\cdot\underline{\nabla}p_o) \qquad (7)$$

where $\tilde{\underline{B}} = \mathrm{curl}\tilde{\underline{A}}$, $\tilde{\underline{j}} = \mathrm{curl}\tilde{\underline{B}}/\mu_o$, ρ_o is the mass density, and γ stands for the ratio between the specific heats. The change in potential energy due to the plasma volume force $\tilde{\underline{F}}_V$ becomes

$$\delta W_V = -(1/2)\iiint_V \tilde{\underline{\xi}}\cdot\tilde{\underline{F}}_V dV \equiv (1/2\mu_o)\iiint_V w_V dV \qquad (8)$$

This contribution and eq. (7) form the basis of the conventional theory /2/. All reformulations of the integral (8) into surface integrals and volume integrals in vacuo are due to deductions containing no additional assumptions or constraints,

except the imposed boundary conditions. Eqs. (7) and (8) also represent the real forces acting on the plasma.

Any arbitrary displacement can be written as

$$\tilde{\underline{\xi}}(\underline{r},t) = \tilde{\underline{\xi}}_c(t) + \tilde{\underline{\eta}}(\underline{r},t) \tag{9}$$

where $\tilde{\underline{\xi}}_c$ is a constant (rigid) part and $\tilde{\underline{\eta}}$ is the remaining inhomogeneous part. Introducing the operator

$$\tilde{\underline{D}} = [(\partial\tilde{\underline{\eta}}/\partial x)\cdot\underline{\nabla},\ (\partial\tilde{\underline{\eta}}/\partial y)\cdot\underline{\nabla},\ (\partial\tilde{\underline{\eta}}/\partial z)\cdot\underline{\nabla}] \tag{10}$$

the volume force $\tilde{\underline{F}}_V$ of eq. (7) can be written as

$$\begin{aligned}\tilde{\underline{F}}_V = {} & [(\tilde{\underline{\xi}}_c + \tilde{\underline{\eta}})\cdot\underline{\nabla}](\underline{\nabla}p_o - \underline{j}_o\times\underline{B}_o) + \\ & + \{\mathrm{curl}[(\underline{B}_o\cdot\underline{\nabla})\tilde{\underline{\eta}} - \underline{B}_o\,\mathrm{div}\tilde{\underline{\eta}}] - \tilde{\underline{D}}\times\underline{B}_o\}\times\underline{B}_o/\mu_o + \\ & + \underline{j}_o\times[(\underline{B}_o\cdot\underline{\nabla})\tilde{\underline{\eta}} - \underline{B}_o\,\mathrm{div}\tilde{\underline{\eta}}] + \underline{\nabla}(\gamma p_o\,\mathrm{div}\tilde{\underline{\eta}}) + \tilde{\underline{D}}p_o\end{aligned} \tag{11}$$

where the first term of the right-hand member vanishes according to the equilibrium condition (6).

A Test Case of Conventional Theory

We are now free to consider a special case where $\tilde{\underline{\eta}} \equiv 0$ and $\tilde{\underline{\xi}} = \tilde{\underline{\xi}}_c$, i.e. rigid body displacement of a plasma confined in closed field line geometry. Such a displacement obviously causes induced surface currents and forces on the plasma. This is easily seen in a frame where the plasma is at rest. In this frame all field quantities are time-independent, except the inhomogeneous field $\underline{B}_{co}$ which is then experienced as the result of a translatory motion of the current-carrying external conductors. In this case eqs. (8)-(11) yield $\tilde{\underline{F}}_V = 0$ and $\delta W_V = 0$, as expected when a rigid displacement moves the entire plasma such as to produce no internal work by its volume force $\tilde{\underline{F}}_V$. The remaining work is then due to the induced surface current effects.

When neglecting these effects and using relations (6)-(8) of the conventional theory, the rigid displacement would leave the plasma unaffected by the motion. This is an incorrect result.

Extended Theory including Induced Surface Current Effects

From expressions (2)-(5), the total change in potential energy can now be written in the extended form

$$\delta W = \delta W_V + \delta W_B = (1/2\mu_o)\iiint_V (w_V + w_B)\,dV =$$

$$= -(1/2)\iiint_V \tilde{\underline{\xi}}\cdot(\tilde{\underline{F}}_V + \tilde{\underline{F}}_B)\,dV$$

$$\tilde{\underline{F}}_B = \{\mathrm{curl}[(\tilde{\underline{\xi}}\cdot\underline{\nabla})\underline{B}_{co}]\}\times\underline{B}_o/\mu_o + \{[\mathrm{curl}(\tilde{\underline{\xi}}\times\underline{B}_o)]\cdot\underline{\nabla}\}\ \underline{B}_{co}/\mu_o \quad (13)$$

Here $\tilde{\underline{F}}_B$ is an equivalent volume force due to the induced surface current effects.

For slow global modes the dynamics could be approximated by an equation equivalent to eq. (7) in which $\tilde{\underline{F}}_V$ is replaced by $\underline{F}_V + \tilde{\underline{F}}_B$ and integrated over the plasma volume. For arbitrary time scales, however, the dynamic behaviour of the plasma and its eigenmodes should become more complicated.

According to expressions (11) and (13) the induced surface current effects can become as important to free-boundary modes as any other effect of the plasma forces. For an external field $\underline{B}_{co}$ which is comparable to $\underline{B}_{jo}$ or stronger, this applies when $L_{Bc} = |\underline{B}_{co}|/|\underline{\nabla}B_{co}| \lesssim L_{Bj} = |\underline{B}_{jo}|/|\underline{\nabla}B_{jo}|$.

The importance of induced surface current effects to various confinement schemes can be estimated in terms of the ratio $|\tilde{\underline{F}}_B|/|\tilde{\underline{F}}_V|$ and the lengths L_{Bc} and L_{Bj}. For tokamaks and similar schemes the weak radial (horizontal) inhomogeneity of $\underline{B}_{co}$ results in comparatively weak induced surface current effects, and axial (vertical) displacements become uninfluenced by such effects. In contrast to this, the strongly inhomogeneous field $\underline{B}_{co}$ of Extrap /1/ gives rise to substantial induced surface current effects on free-boundary modes, for displacements in most spatial directions.

Conclusions

For free-boundary modes conventional MHD theory holds true in a strict sense only in a homogeneous externally imposed magnetic field. Modifications due to induced surface current effects become necessary, in particular in a strongly inhomogeneous external field.

/1/ B. Lehnert, Plasma Phys.Contr.Fusion 33, 1757(1991).

/2/ I.B. Bernstein, E.A. Frieman, M.D. Kruskal, R.M. Kulsrud, Proc.Roy.Soc.A 244, 17(1958).

EXACT SURFACE WAVES ON SPHERES AND CYLINDERS

M.Y. Yu[a] and L. Stenflo
Department of Plasma Physics
Umeå University
S-90187 Umeå, Sweden

Low-temperature (less than 10 to 20 eV) plasmas are of importance in space physics as well as in many technological applications of plasma physics, such as high-power beam and microwave generation, surface processing of materials, cutting and welding of various metals, etc. In contrast to the con-fining magnetic fields of hot plasmas, the geometries of cold plasmas are fixed and do not depend on its properties, except in the presence of chemical reactions such as sputtering, etc. It is thus of interest to study the effect of the configuration on the behavior of the plasma inside and at the interface. Here, such effects on electrostatic electron plasma waves is investigated using the cold-fluid theory. We first determine the appropriate spatial structures of the waves, such that the governing equations can be reduced to a set of nonlinear ordinary differential equations, with only the time coordinate as the variable. The latter are then integrated numerically to yield periodic solutions. The method is similar to that used by Lorenz/1/ for studying deterministic chaos, except that here no truncation or approximation of any kind is made, so that the method is mathematically exact. In special cases, exact analytical solutions can also be obtained.

The cold-fluid equations for the electron dynamics are

$$\dot{n} + \nabla\cdot(n\mathbf{v}) = 0 , \tag{1}$$

$$\dot{\mathbf{v}} + \mathbf{v}\cdot\nabla\mathbf{v} = -\frac{q}{m}\nabla\phi , \tag{2}$$

and the Poisson's equation is

$$\epsilon_0\nabla^2\phi = -q(n - n_0) , \tag{3}$$

where n_0 is the constant density of the stationary ions, the dot denotes ∂_t, and the other notations are standard. The boundary condition is the continuity of the perpendicular component of the current density across the interaface, namely

$$J_r = qnv_r - \epsilon_0\partial_r\dot{\phi} . \tag{4}$$

Let us first consider the case of a cold plasma confined by a spherical linear dielectric (with dielectric constant ϵ) container of radius R /2/. We shall show that for $r < R$ the physical quantities can behave like

$$n = n(t) , \tag{5}$$

$$\mathbf{v} = (x\hat{\mathbf{x}} + y\hat{\mathbf{y}})v_m(t)/R + z\hat{\mathbf{z}}v_c(t)/R ,$$

$$\phi = \frac{r^2}{R^2}(1-3\cos^2\theta)\phi_m(t) + \left[\frac{r^2}{R^2}-1\right]\phi_c(t). \tag{7}$$

For $r > R$, one has from the Poisson's equation (3) the linear vacuum solution

$$\phi = \frac{R^3}{r^3}(1-3\cos^2\theta)\phi_m(t). \tag{8}$$

It is easily verified that when (5) - (7) are substituted into (1) - (3), and the boundary condition (4) is applied, one obtains the following ordinary differential equations in t:

$$\dot{\Phi} = \tfrac{1}{15}N(W-V), \tag{9}$$

$$\dot{N} = -N(2W+V), \tag{10}$$

$$\dot{W} = -W^2 - 2\Phi + \tfrac{1}{3}(N-1), \tag{11}$$

$$\dot{V} = -V^2 + 4\Phi + \tfrac{1}{3}(N-1), \tag{12}$$

where we have normalized t by ω_p^{-1} and defined $N = n/n_0$, $W = v_m/\omega_p R$, $\Phi = q\phi_m/m\omega_p^2 R^2$, $V = v_c/\omega_p R$, respectively. Note that no approximation has been made in deriving (9) - (12).

Typical results of numerical integration of (9) - (12) are shown in Figs. (1) and (2). That is, nonlinear waves, or periodic solutions with the spatial structures given by (5) - (7), exist. In fact, Fig. 2 represents a special, yet still exact, case in which $\Phi = 0$ and $V = W$, so that the equations can be reduced to

$$3\ddot{f} + f = f^{-2}, \tag{13}$$

where $f = N^{-1/3}$. (13) corresponds to $v_\theta = 0$, and admits analytic solutions in terms of elliptic integrals.

Now we consider the case of a plasma confined by an infinitely long cylindrical dielectric /3/ with radius R. In this case, we make the Ansätze

$$v = \left\{[v_2 + v_1\cos(2\theta)]\hat{r} - v_1\sin(2\theta)\hat{\theta}\right\} r/R, \tag{14}$$

$$n = n(t), \tag{15}$$

$$(q\varphi/m)_{r<R} = [\varphi_m\cos(2\theta) + \varphi_c]r^2/R^2 - \varphi_c, \tag{16}$$

The governing equations then reduce to

$$\dot{n} + 2nv_2/R = 0\,, \tag{17}$$

$$\dot{v}_2 + \left(v_1^2 + v_2^2\right)/R = -2\varphi_c/R\,, \tag{18}$$

$$\dot{v}_1 + 2v_1v_2/R = -2\varphi_m/R, \tag{19}$$

$$4\varphi_c/R^2 = -w_p^2(n - n_i)/n_0. \tag{20}$$

The solution of the Poisson's equation in the dielectric container is

$$(q\varphi/m)_{r>R} = \varphi_m(R/r)^2\cos(2\theta). \tag{21}$$

From the boundary condition, one then obtains the nonlinear ordinary differential equations

$$\ddot{N}/N - \frac{3}{2}\left(\dot{N}/N\right)^2 - \left(\dot{\Phi}/N\right)^2 = 1 - N, \tag{22}$$

$$\ddot{\Phi} + N\Phi/\gamma = 2\dot{\Phi}\dot{N}/N, \qquad \gamma = 1 + \epsilon, \tag{23}$$

where $\Phi = 2^{3/2}(1+\epsilon)\varphi_m/R^2w_p^2$ Typical numerical solutions are shown in Figs. 3 and 4. The latter corresponds to the case $\epsilon \to \infty$, which is of interest to energy-storage and high-power pulse research. One can also obtain analytical solutions here.

Our approach can be extended to include multi-species as well as warm plasmas. For example, in the cylindrical case for a multi-component plasma, one can make the same Ansätze (14) and (15) for each species, together with the Ansatz

$$\phi = [\,\phi_m(t)\cos(2\theta) + \phi_c(t)]\,r^2/R^2 - \phi_c(t), \tag{24}$$

for the potential. For a warm single-component plasma governed by the warm adiabatic fluid equations, one can again make the Ansätze (14) - (16), together with the Ansatz

$$T = [\,T_m(t)\cos(2\theta) + T_c(t)]\,r^2/R^2 - T_c(t), \tag{25}$$

for the temperature T. In fact, a multi-component warm plasma can also be treated in the same manner. One can also include the effects of dissipation by means of simple transport models. In all these cases, nonlinear ordinary differential equations describing the time behavior of the physical quantities can be derived and solved numerically for physical solutions. Due to the

mathematical exactness of the resulting equations, our problems are especially valuable in testing analytical as well as numerical approximation procedures.

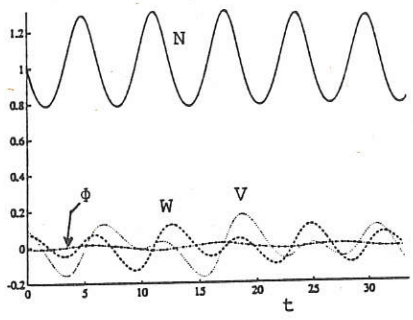

Fig. 1

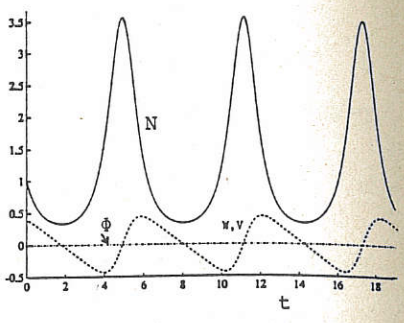

Fig. 2

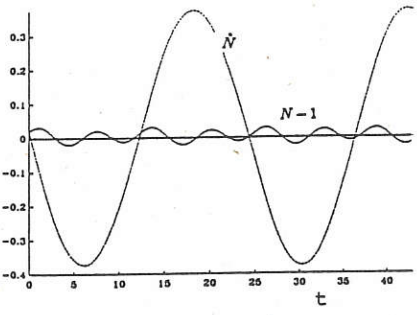

Fig. 3

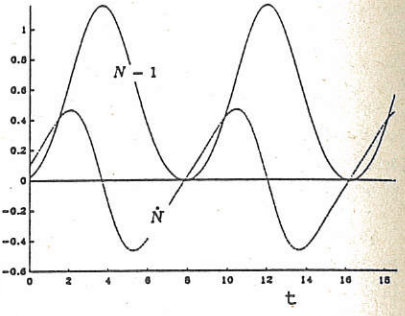

Fig. 4

This work was partially supported by the Sonderforschungs-bereich 191 Niedertemperaturplasmen.

[a] Permanent address: Institut für Theoretische Physik, Ruhr Universität, D-4630 Bochum, Germany.

/1/ E.N. Lorenz, J. Atmos. Sci. **20**, 130 (1963)
/2/ L. Stenflo and M.Y. Yu, Phys. Rev. A**42**, 4894 (1990)
/3/ M.Y. Yu and L. Stenflo, IEEE Plasma Sci. **19**, 641 (1991)

Ist AND IInd ELLIPTIC SOLUTIONS TO THE EXTENDED GRAD-SHAFRANOV-SCHLUTER EQUATION FOR ASYMMETRIC TOKAMAK PLASMA WITH STATIONARY FLOWS

R. Żelazny, R. Stankiewicz, A. Gałkowski, and S. Potempski

RCC CYFRONET of the Institute of Atomic Energy
05-400 OTWOCK-ŚWIERK, POLAND

1. Introduction

The existence of poloidal flow transforms the elliptic Grad-Shafranov-Schluter equation into a system of mixed type partial differential equation (EGSS equation) and an algebraic Bernoulli' equation. The computer program for solving EGSS equations using inverse method and Fourier decomposition has been prepared. The specific test solutions in the first and second ellipticity regions have been found.

2. Physical problem

Assuming axisymmetric, toroidal geometry, the MHD equations (in the cylindrical coordinate system R, Z, ϕ) can be written in the form [1]:

$$(2.1)\qquad \nabla \cdot \left[\left(1 - \frac{(\psi_M')^2}{\rho}\right)\frac{\nabla\psi}{R^2}\right] + \frac{JJ_M'}{R^2} + \rho H_M' - \frac{C'\rho^\gamma}{\gamma - 1} + \frac{1}{\rho R^2}\left[\psi_M' |\nabla\psi|^2 + JL\right]\psi_M'' - L\Phi'' = 0 ,$$

$$(2.2)\qquad H_M - \frac{1}{2}\left(|\nabla\psi|^2 + J^2\right)\frac{(\psi_M')^2}{R^2\rho^2} + \frac{1}{2}R^2(\Phi')^2 - \frac{\gamma C\rho^{\gamma-1}}{\gamma-1} = 0.$$

where ψ_M, Φ, C, H_M and J_M depend only on ψ. Symbols ψ and ψ_M denote the poloidal fluxes of the magnetic induction $\underline{B}$ and of the flow field momentum $\rho\underline{v}$ respectively, Φ is the electric potential and C denotes the entropy of the fluid. The prime denotes the differentiation with respect to ψ.

Denoting by $A \equiv |\psi_M'|\rho^{-1/2}$ the Alfven Mach number of the poloidal flow, by $\beta \equiv \frac{\gamma p}{\gamma p + B^2}$ the speed of the trailing cusp of the slow wave and by A_s and A_f the speeds of the slow and fast compressive, magneto-accoustic waves in MHD, we find that the EGSS equation becomes of the elliptic type over intervals: $0 \le A^2 < \beta$ (Ist elliptic region), $A_s^2 < A^2 < 1$ (IInd elliptic region) and $1 < A^2 < A_f^2$ (IIIrd elliptic region); elsewhere the equation is hyperbolic.

3. Method of solving the EGSS equation

The method we have used to solve (2.1-2.2) is based on the inverse method and the Fourier decomposition. The coordinates R,Z are expanded in a truncated Fourier series in θ namely:

$$R(\delta,\theta) = R_0 - R_1\cos\theta + \sum_{i=2}^{N_R}(R_i^c\cos i\theta - R_i^s\sin i\theta),$$

$$Z(\delta,\theta) = Z_0 + ER_1\sin\theta + EZ_1\cos\theta + E\sum_{i=2}^{N_R}(R_i^s\cos i\theta + R_i^c\sin i\theta). \quad (3.1)$$

This form does not assume any symmetry.

At outer boundary $\delta = 1$: we have fixed $2(N_R+1)+1$ conditions:

$$R_0=R_{0b},\ R_1=R_{1b},\ R_i^c=R_{ib}^c,\ E=E_b,\ Z_0=Z_{0b},\ Z_1=Z_{1b},\ R_i^s=R_{ib}^s,\ i=2,..,N_R.$$

The shooting method applied for solving resulting nonlinear ODE should allow to find possible multiple solutions for different characteristic profiles.

4. Results of numerical calculations

In our test calculations we have used the following profiles:

$$p = p_o(1-1.604\delta^2+0.211\delta^4+0.393\delta^6),$$

$$J = J_o(1+0.008\delta^2 - 0.004\delta^4),$$

$$\rho = \rho_o(1-0.2\delta^2-0.7\delta^4).$$

Flow and other profiles have been selected in the following way:

$$\Phi' = \lambda\,\Phi_o'\,(1-\delta^2),\quad \psi_M' = \lambda\,\psi_{Mo}'\,(1-\delta^2),$$

$$J_M = \left[1-\frac{(\psi_M')^2}{\rho}\right]J + \lambda^2R_o^2\psi_{Mo}'\Phi_o'(1-\delta^2),$$

$$H_M = \frac{\gamma C\rho^{\gamma-1}}{\gamma-1},\quad C = p\rho^{-\gamma}.$$

The λ parameter has been used for scaling the magnitude of flows.

The test case N° I (symmetric) is characterized by (cf(3.1)):

$$R_o = 1.43,\ R_1 = 0.42,\ E = 1.2,\ R_i^c = R_i^s = Z_o = Z_1 = 0.$$

The test case N° II (asymmetric) is characterized by:

$$R_o = 1.43,\ R_1 = 0.42,\ E = 1.2,\ R_2^c = 0.03,\ Z_o = 0.3,\ Z_1 = 0.03$$

$$R_2^s = 0.01,\ R_1^c = R_1^s = 0.0,\ \text{for } i \geq 3.$$

Numerical calculations have been performed for the 1st and 2nd

ellipticity regions. Figures 1 to 8 show results for the symmetric case while Figs.9 to 16 show results for the asymmetric case. In both cases magnitude of the flow was chosen to be $\lambda = 0.1$.

Comparing the 1st (Figs.1-4 and 9-12) and 2nd (Figs.5-8 and 13-16) ellipticity solutions one can see that the magnetic configurations, characterized roughly by ψ_{max} and ΔR_m, are different: the value of ψ_{max} is higher in case of the 1st ellipticity solution. Plasma configurations, characterized by the position of density axis and by density itself, are completely different in both cases: plasma column is markedly shifted inward in case of the 2nd ellipticity solution, while it is only slightly shifted outward (with respect to the geometrical axis) in case of the 1st ellipticity solution. The density maximum ρ_{max} is smaller (more than one order of magnitude) for the 2nd ellipticity solution. The 2nd ellipticity solution is much more sensitive to the magnitude of flow: E_m, ψ_{max}, ρ_{max}, $|\Delta R_\rho|$ increase markedly with the magnitude of flow increasing, opposite to the 1st ellipticity solution. Note that the 2nd ellipticity solutions correspond to the more elongated plasma cross-sections (elongation increases with λ increasing).

5. Conclusion

Numerical results obtained as yet show that multiple solutions corresponding to different Bernoulli branches of solutions exist with distinct physical properties. This fact gives possibility to explore an idea of sudden jumps from one branch to another one as a mechanism responsible for some relaxation phenomena like L/H transition. Radial electric field does change at the 1st/2nd eliptic transition, this obserwation being in line with the theories by Itoh & Itoh [2] and by Shaing *et al* [3], exploiting the idea of electric field influence on edge plasma transport and thereby, on the improvement of energy and particle confinement. Some refinement of the code should allow us to study bifurcation processes corresponding to the nonlinearity of the EGSS equation connected with characteristic profiles.

This work has been partly supported by the Grant No 20193 91 01 from KBN in Poland and JET Contract No JA8/00516.

[1] R.Żelazny *et al*, JET Report JET-R(91)05; and references cited herein

[2] S.I.Itoh and K.Itoh, Nuclear Fusion 29,6(1989)1031

[3] K.C.Shaing, W.A.Houlberg,and E.C.Crume, IAEA Conference, Nice, 1988

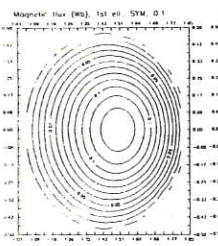

Fig.1

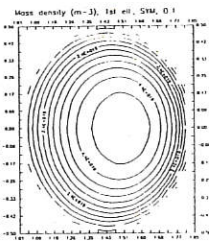

Fig.2

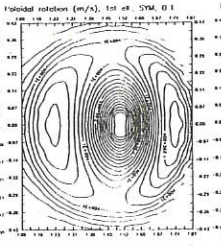

Fig.3

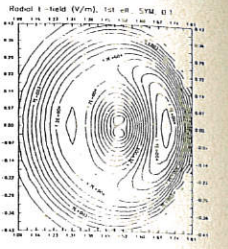

Fig.4

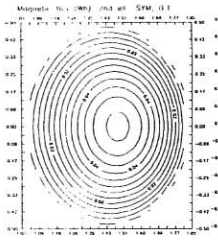

Fig.5

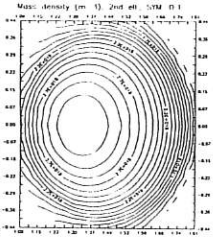

Fig.6

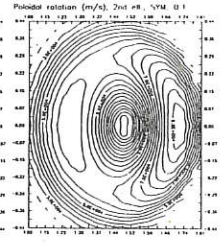

Fig.7

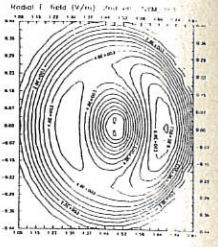

Fig.8

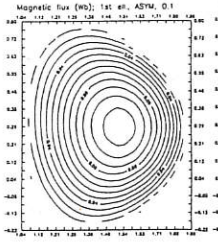

Fig.9

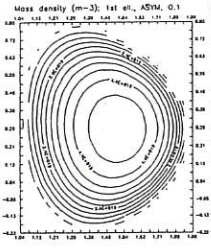

Fig.10

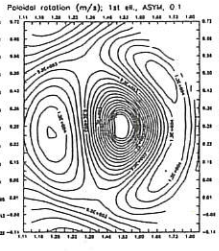

Fig.11

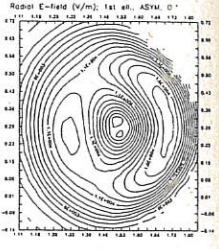

Fig.12

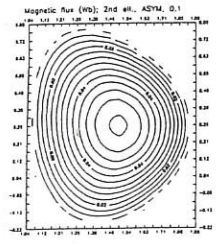

Fig.13

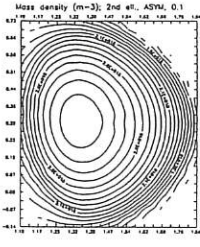

Fig.14

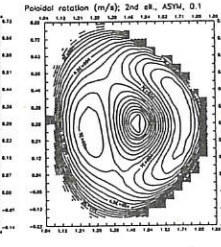

Fig.15

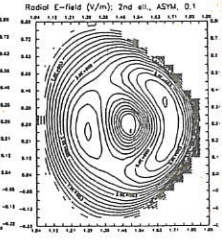

Fig.16

A New Fast 2-d MHD-Equilibrium Solver

G. Hübner, Physikalisches Institut, Universität Bayreuth, W-8580 Bayreuth, Germany

1. Introduction

Nowadays, the tokamak device is regarded as a first candidate for a fusion reactor. In this device, as is well known, the toroidal magnetic field is by an order of magnitude larger than the poloidal field. In addition, the radial component of the poloidal field is usually small compared with the azimuthal component. This is also true for small aspect ratio (fat) tokamaks.

Therefore, it seems natural to make an expansion of the governing equations of plasma dynamics in these small quantities, an expansion that should be valid for arbitrary aspect ratio.

To be concrete, we shall use the following description of the magnetic field vector

$$\vec{B} = B(\sin\beta\,\hat{e}_r + \sin\alpha\cos\beta\,\hat{e}_\theta + \cos\alpha\cos\beta\,\hat{e}_\zeta)$$

$\hat{e}_r, \hat{e}_\theta, \hat{e}_\zeta$ being orthogonal unit vectors of the standard toroidal coordinate system.

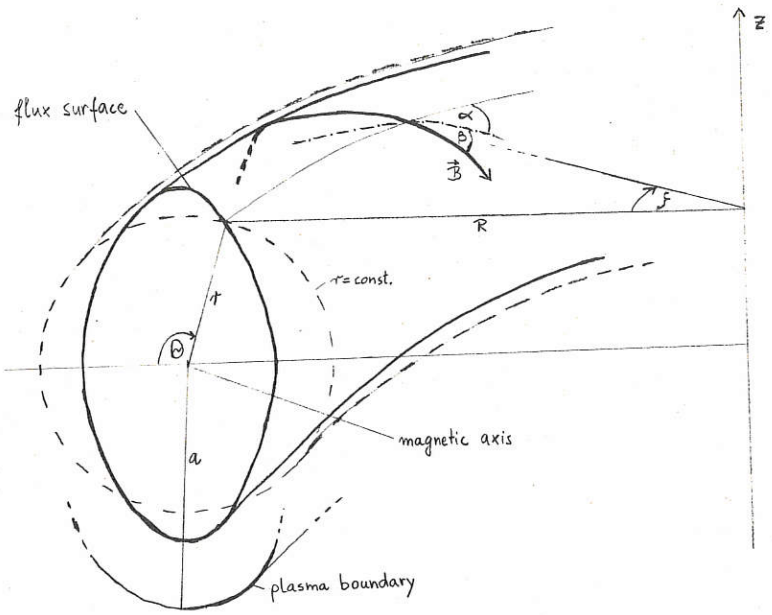

Fig 1: Magnetic field description via B, α, β

The magnetic field is, thus, characterized through three quantities B, α, β, which are functions of r and θ for the axisymmetric static case, considered here.

α and β are regarded as small being of order $\delta = \epsilon/q(\vec{r}_b)$ where ϵ is the inverse aspect ratio and $q(\vec{r}_b)$ is the safety factor at the plasma boundary

$$q = (2\pi)^{-1} \int_0^{2\pi} d\theta \, r/(R \tan\alpha)$$

(the integral has to be performed over a flux surface boundary $r = r_b(\theta)$).

2. MHD-Model

A widely accepted model for calculating plasma equilibria in tokamaks is the ideal MHD-Model [1]. Here, the governing equations are used in the following form

$$\begin{aligned}
\nabla \cdot \vec{B} &= 0 && (1)\\
(\nabla \times \vec{B})_\perp &= \mu_0 B^{-2} \vec{B} \times \nabla p && (2),(3)\\
\nabla \cdot \vec{j}_\perp = \nabla \cdot (B^{-2}\vec{B} \times \nabla p) &= -\mu_0^{-1} \nabla \cdot (\nabla \times \vec{B})_\parallel = -\nabla \cdot \vec{j}_\parallel && (4)\\
\vec{B} \cdot \nabla p &= 0 && (5)
\end{aligned}$$

$\perp$ ($\parallel$) means the components perpendicular (parallel) to $\vec{B}$.

3. Perturbation expansion

The magnetic field is expanded in the smallness parameter δ and, furthermore, the low-beta-case is assumed ($2\mu_0 p/(B_0^e)^2 = \mathcal{O}(\delta^2)$), where B_0^e is the external magnetic field at $r = 0$.

$$\begin{aligned}
\alpha &= \alpha_1 + \mathcal{O}(\delta^3)\\
\beta &= \beta_1 + \mathcal{O}(\delta^3)\\
B &= B_0 + B_2 + \mathcal{O}(\delta^4)\\
p &= p_2 + \mathcal{O}(\delta^4)
\end{aligned} \qquad (6)$$

Substitution into (1)-(5) yields to lowest order in δ

$$(1) \rightsquigarrow \mathcal{O}(\delta): \quad \partial_r(r\beta_1) + \partial_\theta \alpha_1 = 0 \qquad (7)$$

$$(2),(3) \rightsquigarrow \mathcal{O}(\delta^2): \quad B_0 = B_0^e R_0/R \qquad (8)$$

$$\mathcal{O}(\delta^3): \quad r\partial_r[RB_2/(R_0 B_0^e) - (\alpha_1^2 + \beta_1^2)/2] = -R\alpha_1[\partial_r(r\alpha_1/R) - \partial_\theta(\beta_1/R)] - \\ -\mu_0 R^2/(R_0 B_0^e)^2 r\partial_r p_2 \qquad (9)$$

$$(4) \rightsquigarrow \mathcal{O}(\delta^2): \quad [\beta_1 r\partial_r + \alpha_1\partial_\theta - \beta_1 R_0/R - \alpha_1 r\sin\theta/R][\partial_r(r\alpha_1/R) - \partial_\theta(\beta_1/R)] = \\ 2\mu_0 r/(R_0 B_0^e)^2 (r\sin\theta\partial_r + \cos\theta\partial_\theta) p_2 \qquad (10)$$

$$(5) \rightsquigarrow \mathcal{O}(\delta^3): \quad (\beta_1 r\partial_r + \alpha_1\partial_\theta) p_2 = 0 \qquad (11)$$

From (7),(10) and (11) α_1, β_1 and p_2 are calculated with the following ansatz with up-down symmetry of the flux surfaces

$$\begin{aligned}
\alpha_1(r,\theta) &= \epsilon R/r \textstyle\sum_{n=0}^{n_{max}} \sum_{k=2}^{k_{max}} a_n^k \cos n\theta (r/a)^k\\
\beta_1(r,\theta) &= \epsilon R/r \textstyle\sum_{n=1}^{n_{max}} \sum_{k=2}^{k_{max}} b_n^k \sin n\theta (r/a)^k\\
p_2(r,\theta) &= (B_0^e)^2/(2\mu_0) \textstyle\sum_{n=0}^{n_{max}} \sum_{k=0}^{k_{max}} p_n^k \cos n\theta (r/a)^k
\end{aligned} \qquad (12)$$

The coefficients a_0^k ($k = 2, 3, \ldots$) and p_0^k ($k = 0, 2, 3, \ldots$) can be specified arbitrarily conform with zeroth order pressure and q-profiles $p_0(r), a_0(r)$. The remaining coefficients are now calculated as

$b_n^k \overset{(7)}{\rightsquigarrow} a_n^k \overset{(11)}{\rightsquigarrow} p_n^k$ (for $n = 1, \ldots, n_{max}$ and $k = 2, \ldots, k_{max}$)

It turns out that the coefficients $a_s^s = b_s^s$ $(s = 2, 3, \ldots)$ can be chosen arbitrarily. They are chosen here to match a prescribed plasma boundary as good as possible (least-squares-fit).

Having calculated α_1, β_1, p_2, $I_2 = (RB_\zeta)_2 = RB_2 - R_0 B_0^s(\alpha_1^2 + \beta_1^2)/2$ is calculated from (9) up to a constant which is determined from the requirement $I_2(\vec{r}_b) = 0$.

The poloidal flux ψ_p is calculated from α_1

$$\psi_p(r,\theta) = 2\pi R_0 B_0^s \int_0^r dr'\, \alpha_1(r',\theta) \quad + \mathcal{O}(\delta^3)$$

4. The relation between B, α, β and the conventional magnetic field description

The conventional magnetic field description of the axisymmetric tokamak field is (e.g., [2])

$$\vec{B} = (2\pi)^{-1} \nabla\zeta \times \nabla\psi_p + I(\psi_p)\nabla\zeta = \vec{B}_p + \vec{B}_t$$

where $\nabla\zeta = R^{-1}\hat{e}_\zeta$, $\vec{B}_p(\vec{B}_t)$ is the poloidal (toroidal) component of $\vec{B}$.

$\vec{B}$ is characterized through *two* scalar functions $\psi_p = \psi_p(r,\theta)$ and $I = I(\psi_p)$. This description of a 3d-vector field $\vec{B}$ via two scalar functions is guaranteed because of the incompressibility of $\vec{B}$: $\nabla \cdot \vec{B} = 0$ [2].

Within the new, alternative description *three* scalar functions $B(r,\theta), \alpha(r,\theta)$ and $\beta(r,\theta)$ characterize $\vec{B}$. They are subjected to the nonholonomic constraint

$$\nabla \cdot \vec{B} = 0 \leftrightarrow \partial_r(rRB\sin\beta) + \partial_\theta(RB\sin\alpha\cos\beta) = 0$$

note that this constraint is used to calculate α (to lowest order) from β $(b_n^k \overset{(7)}{\rightsquigarrow} a_n^k)$.

Nevertheless, there is a unique relation between ψ_p, I and B, α, β

$$\left.\begin{array}{rcl} \psi_p(r,\theta) & = & 2\pi \int_0^r dr\; RB\sin\alpha\cos\beta \\ I(r,\theta) & = & RB\cos\alpha\cos\beta \end{array}\right\} \left\{\begin{array}{rcl} B & = & (2\pi R)^{-1}\sqrt{4\pi^2 I^2 + (\nabla\psi_p)^2} \\ \tan\alpha & = & (2\pi I)^{-1}\partial_r\psi_p \\ \sin\beta & = & -r^{-1}(4\pi^2 I^2 + (\nabla\psi_p)^2)^{-1/2}\partial_\theta\psi_p \end{array}\right.$$

where $(\nabla\psi_p)^2 = (\partial_r\psi_p)^2 + r^{-2}(\partial_\theta\psi_p)^2$.

5. Comparison with Grad-Schlüter-Shafranov-equation

As is well known, for the function $\psi \doteq (2\pi)^{-1}(\psi_p - \psi_p(\vec{r}_b))$ the GSS-equation can be derived [1]

$$\Delta^*\psi = -I\partial_\psi I - \mu_0 R^2 \partial_\psi p \qquad (13)$$

The flux functions $I(\psi) = RB_t$ and the pressure $p(\psi)$ have to be specified a priori rather than $a_0(r)$ and $p_0(r)$ from above. The advantage of the new approach is, of course, that $a_0(r)$ and $p_0(r)$ can be taken directly from experiment and/or stability considerations, whereas $I(\psi)$ and $p(\psi)$ are usually taken as simple algebraic functions of ψ. Note also that the lowest order $I(\psi)$ is calculated *a posteriori* with the new method. Furthermore, the solution of the GSS-equation requires a more elaborate and sophisticated treatment than the numerical calculations based on the above approach.

6. Test of the new method with analytic Solov'ev equilibria

A famous solution of (13) is (see [3])

$$\frac{\psi(z,R)}{a^2 B_0^e} = c_1 (z/a)^2 [(R/R_0)^2 + c_2] + c_3 [(R/R_0)^2 - 1]^2 + \frac{\psi_0}{a^2 B_0^e}$$

with $z = r\sin\theta$ and $R = R_0 + r\cos\theta$.
For this solution $p(\psi)$ and $I(\psi)$ are given by

$$\frac{2\mu_0 p(\psi)}{(B_0^e)^2} = -4(c_1 + 4\epsilon^2 c_3)\frac{\psi}{R_0^2 B_0^e}$$

$$\frac{I(\psi)}{R_0 B_0^e} = \pm\sqrt{1 - 4c_1 c_2 \frac{\psi}{R_0^2 B_0^e}}$$

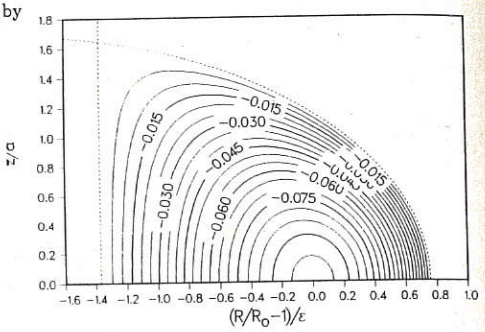

Fig 2: Solov'ev separatrix equilibrium
$\epsilon = 0.5, c_1 = 0.08, c_2 = -0.1, c_3 = 0.12$

In (12) $n_{max} = 4$ and $k_{max} = 4$ is chosen and a_2^2, a_3^3 are fitted to the prescribed boundary condition $\psi(r_b(\theta), \theta) = 0$, where $r_b(\theta)$ is the plasma surface.

Several values have been chosen for the parameters c_1, c_2 and c_3, the residuum $(\psi_{exact} - \psi_{num})/\psi(r = 0))$ is always found to be smaller than 0.1 % at the boundary and even smaller in the interior plasma. This corresponds to an accuracy of the order of 1mm for the plasma boundary when the plasma radius is about 1m. 10 iterations were chosen for the equilibrium solver yielding good convergence. Even elongated- and separatrix equilibria can be calculated with the same accuracy.

During the test runs it was noticed that the numerical solution converges to the analytical one for a certain set of parameters, namely, if $I(\psi)$ =const. was chosen (i.e., purely toroidal plasma current). Indeed, it can be shown that the perturbation equations (7)-(11) are equivalent to the exact MHD-equations in the case I =const., if one makes the following identifications

$$\alpha \rightarrow RB/(R_0 B_0^e)\sin\alpha\cos\beta \qquad \beta \rightarrow RB/(R_0 B_0^e)\sin\beta$$

7. Further possible applications and extensions of the method

One can think of using the new method also for profile shape optimization, MHD stability calculations, transport codes or on line feedback control of plasma discharges.

Further extensions could be the calculation of 3-d (Stellarator) equilibria, equilibria with flow and/or anisotropic pressure, or non up-down symmetric equilibria.

[1] Freidberg J.P., Rev. of Mod. Phys. **54**, 801 (1982).

[2] Hirschman S.P. and Sigmar D.J., Nucl. Fusion **21**, 1079 (1981).

[3] Solov'ev L.S., Sov. Phys. JETP **26**, 400 (1968).

A CIVIL ENGINEERING APPROACH TO IDEAL MHD

V.O. Jensen
Association Euratom-Risø National Laboratory
Optics and Fluid Dynamics Department, Risø National Laboratory
DK-4000 Roskilde, Denmark

Introduction

It is well known that a magnetic field can be conceived as a medium where an isotropic compressive stress, $B^2/2\mu_o$, is superimposed on a tensile stress, B^2/μ_o, parallel to the lines of force. When a stationary ideal MHD plasma is present in the magnetic field, the particle pressure adds to the magnetic stresses to form a combined stress tensor. Calculations of plasma equilibria based on this concept are very similar to calculations in civil engineering of static structures based on compressive, tensile, and shear stresses. Therefore the very simple physical pictures known from civil engineering when used in plasma physics provide simple physical understanding and facilitate the physical interpretation of the results.

In an earlier paper[1] the concept was used to derive and discuss the equilibrium equations for θ-, Z-, and screw pinches and the Grad-Shafranov shift in a tokamak plasma with circular cross sections of the flux surfaces. Here the concept is used to discuss the virial theorem and to obtain a simple physical interpretation of this theorem. We also reconsider the Grad-Shafranov shift in a tokamak plasma and show that a situation where all flux surfaces have circular cross sections cannot be an exact solution to the ideal MHD equations.

The concept of magnetic stresses

Combining the time independent equations of ideal MHD

$$\mathbf{j} \times \mathbf{B} = \nabla p, \quad \nabla \times \mathbf{B} = \mu_o \mathbf{j}, \quad \text{and} \quad \nabla \cdot \mathbf{B} = 0$$

leads to the well known expression

$$\nabla p = -\nabla \frac{B^2}{2\mu_o} + \nabla \cdot \frac{\mathbf{BB}}{\mu_o} \equiv \nabla \cdot T_m \quad . \tag{1}$$

The physical interpretation of Eq. (1) is that any differential volumen element, dV, in a region with plasma and/or magnetic field is acted upon by a resulting force $d\mathbf{K} = (\nabla \cdot T_m - \nabla p)dV$. Equilibrium requires $d\mathbf{K} = 0$.

The form of the magnetic stress tensor, T_m, in (1) also shows that a magnetic field can be conceived as a medium acting with an isotropic magnetic pressure, $B^2/2\mu_o$, superimposed by a tensile stress, B^2/μ_o, acting along the field lines. Thus the stresses acting on a volumen through a surface element crossed by magnetic field lines (see Fig. 1) are:

- an isotropic magnetic pressure, $B^2/2\mu_o$, acting perpendicularly to the element,
- a tensile magnetic stress, $B^2{}_\perp/\mu_o$, acting perpendicularly to the element,
- a magnetic shear stress, $B_\parallel B_\perp/\mu_o$, acting parallel to the surface element in the $B_\parallel$-direction,
- a particle pressure (if present) acting perpendicularly to the element.

Equilibrium requires that the sum of all the corresponding forces acting on all surface elements of the volumen should be zero.

In practical use it often pays to consider volumen elements shaped as flux tubes with plane end plates cut perpendicularly to the field lines. For such shapes all surface forces caused by shear stresses disappear.

The virial theorem

By using this concept it is easy to show the virial theorem for an axisymmetric toroidal plasma. The virial theorem states that a plasma cannot be confined by magnetic fields generated solely by currents running in the plasma.

Let us consider an axisymmetric toroidal plasma as shown in Fig. 2. Because of the particle pressure the plasma tends to expand in the $\hat{R}$- as well as in the $\hat{r}$-direction. To obtain equilibrium the plasma pressure must be balanced by magnetic stresses. Currents in an axisymmetric plasma can generate toroidal and poloidal magnetic fields. The toroidal field is confined to the plasma, while the poloidal field can occupy the plasma as well as the vacuum outside where it takes the well-known shape of the magnetic field around a single turn coil.

Let us consider a flux tube segment of the plasma expanding 180° in the ϕ-direction as shown shaded in Fig. 2. The tendency to expand in the $\hat{r}$-direction can be balanced only by a poloidal magnetic field, which is therefore needed. Being stronger at the inner side of the torus for $90^\circ < \theta < 270^\circ$ than at the outer side for $-90^\circ < \theta < 90^\circ$, the poloidal field will act upon the plasma with a resulting force tending to expand it in the $\hat{R}$-direction. As a result the segment will be acted upon by a magnetic force in the y-direction which adds to the particle pressure force acting at the plane end plates.

The segment can only be kept in balance by introducing a toroidal magnetic field in the plasma. This field will act on the end plates with tensile forces in the -y-direction. Such a toroidal field in the plasma will in turn add to the particle pressure and thereby increase the tendency to expansion in the $\hat{r}$-direction. To compensate for this a still stronger poloidal field is needed. This increased poloidal field will in turn give rise to an increased force on the segment in the y-direction which again can only be compensated by an increased toroidal field, and so forth.

Simple calculations based on conservative approximations show that it is not possible to obtain balance between the forces on the plasma segment. It is clear that a poloidal field inside the plasma will only give rise to a force in the y-

direction as it will act on the two end plates with a magnetic pressure. We therefore assume that the poloidal field is present only outside the plasma. Further we will assume that the poloidal field has an R^{-1}-dependence and will neglect that it is further weakened at the outer side of the plasma as is known from fields around single coils. It is clear that the toroidal field is more efficient in providing a strong force in the -y-direction if it takes the same high strength over the whole plasma. We therefore assume the toroidal field to be constant over the entire plasma cross section except for the R^{-1}-dependence.

Based on these simplifying assumptions it is easy to show that the sum of the y-components of all magnetic forces acting on the segment can just cancel. There is no way to compensate for the forces in the y-direction caused by the particle pressures at the end plates. Therefore the segment cannot be in equilibrium. As a relaxation of any of the simplifying assumptions into a more realistic physical situation only leads to an increased resulting force in the y-direction, it is clear that the virial theorem holds good for an axisymmetric toroidal plasma.

The nonexistence of only circular cross sections

The concept of magnetic stresses was used to derive the external Grad-Shafranov shift in a axisymmetric tokamak where all flux tube cross sections were assumed to be circular[1]. Fig. 3 shows the geometry and defines the shift as $\Delta(r) = R(o)-R(r)$.

Using $\nabla\cdot\mathbf{B} = 0$ leads to

$$B_t(r,\theta) = B_t(r)\,\frac{R(r)}{R(r)+r\cos\theta} \quad \text{and} \quad B_p(r,\theta) = B_p(r)\,\frac{R(r)}{\left[R(r)+r\cos\theta\right]\left[1-\frac{d\Delta(r)}{dr}\cos\theta\right]},$$

where $B_t(r)$ and $B_p(r)$ are the values of toroidal and poloidal fields, respectively, for $\theta = \pm\,\pi/2$. Straightforward calculations based on force balance on the flux tube segments as a whole lead to the well-known expression for the external shift[2,3].

$$\Delta_{ext} = \frac{b^2}{2R(0)}\left\{\left(\beta_p + \frac{l_i - 1}{2}\right)\left(1-\frac{a^2}{b^2}\right) + \ln\frac{b}{a}\right\}$$

indicating that the same approximations are used in the two kinds of derivations.

By inspecting the magnetic forces it is easy to show that although the segments as a whole are in equilibrium when acted upon by the fields mentioned above, small differential volumen of the segments are not in equilibrium. This shows that the assumption of circular cross sections of all segments is not a physical possibility. In mathematical terms the reason is that the poloidal field $B_p(r,\theta)$ given above violates the Maxwell equation $\nabla\times B_p = 0$.

Conclusion

The virial theorem for a axisymmetric toroidal plasma has been demonstrated by means of the concept of magnetic stresses. The same concept was used to demonstrate that flux tubes around a toroidal plasma cannot all have circular cross sections.

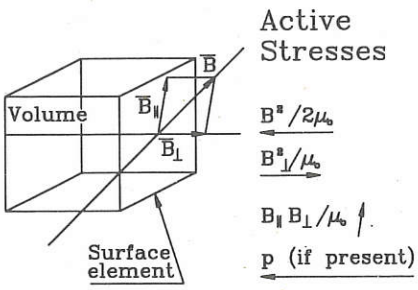

Fig.11 Magnetic stresses active on a surface element

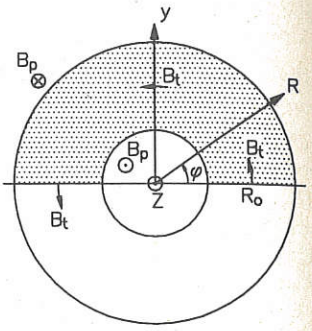

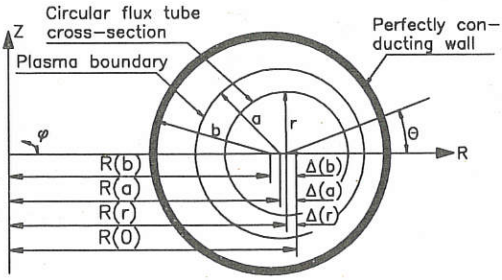

Fig. 3. Tokamak flux tubes cannot all have circular crossections

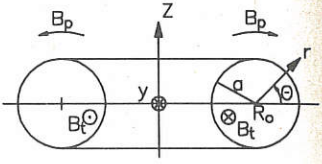

Fig. 2. The virial theorem for an axisymmetric toroidal plasma

References

1) V.O. Jensen, Contr. 18th European Conf. on Cont. Fusion and Plasma Physics. Berlin, 3-7 June 1991. Proceedings Vol. 15C, Part IV, p. 181-184.

2) J.P. Freidberg, Ideal Magnetohydrodynamics. Plenum Press 1987.

3) V.D. Shafranov, In Reviews of Plasma Physics, Vol. II, edited by M.A. Leontovich, Consultants Bureau, New York 1966.

A GENERAL FORMULATION OF NONLINEAR PLASMA THEORIES

S. Kuhn and A.S. de Assis*

Plasma and Energy Physics Group, Institute for Theoretical Physics
University of Innsbruck, A-6020 Innsbruck, Austria

**Permanent address: Instituto de Matemática, Universidade Federal Fluminense, 24020 Niterói, RJ, Brazil*

1. Introduction and summary. The dynamics of any plasma system are generally governed by (i) evolution equations (fluid or kinetic) with related boundary conditions for the plasma, (ii) Maxwell's equations with related boundary conditions for the electromagnetic fields, and (iii) "external–circuit equations" for the external–circuit currents. These "complete" systems are usually very complex, and experience shows that it is extremely difficult to obtain detailed solutions for any but the very simplest cases.

On the other hand, the systems in question share a common nonlinear structure, and in the present paper we propose a general formalism exhibiting and making use of just this basic structure. The usefulness of this formalism, whose general features are outlined in Sec. 2, lies in the fact that it permits one to study dynamic problems in all generality, having to specialize the results to a particular system only as the last step. In Sec. 3, our formalism is specialized to the case of periodic nonlinear oscillations, and a general formula connecting the nonlinear frequency shift and the saturation amplitude of small–amplitude steady–state oscillations about a given time–independent state is derived. In Sec. 4, this formula is evaluated for 1d collisionless electron plasma waves in a thermal plasma.

2. Basic equations in operator notation. To reduce the general plasma problem to its basic structure, we first introduce the acronyms ξ for the independent variables (except time) and $\eta(\xi,t)$ for the dependent ones. In a fluid theory we have $\xi \equiv \mathbf{x}$ and (e.g.) $\eta(\xi,t) = \{n_1(\mathbf{x},t), p_1(\mathbf{x},t), n_2(\mathbf{x},t), \ldots, \mathbf{E}(\mathbf{x},t), \mathbf{B}(\mathbf{x},t), \ldots.\}$, while in a kinetic theory $\xi \equiv \{\mathbf{x},\mathbf{v}\}$ and (e.g.) $\eta(\xi,t) \equiv \{f_1(\mathbf{x},\mathbf{v},t), f_2(\mathbf{x},\mathbf{v},t) \ldots, \mathbf{E}(\mathbf{x},t), \mathbf{B}(\mathbf{x},t), \ldots.\}$. Then, for kinetic theories (and some restricted classes of fluid theories) the closed system of evolution equations and related boundary conditions of the plasma system in question can be symbolically written in the form

$$A\partial_t\eta + B\eta + C\eta\eta = r\,, \tag{2.1}$$

where $\partial_t \equiv \partial/\partial t$, A, B and C are given operators with (A and B linear and C bilinear) acting only on ξ, and $r(\xi,t)$ represents the "driving" terms. (Extensions to systems with other kinds of nonlinearities are easily possible.) In the present paper these operators will be assumed to be time–independent. In general, Eq. (2.1) must be solved with the initial condition $\eta(\xi,t=0) = \eta_0$, with $\eta_0(\xi)$ given.

3. Dc–ac decomposition. To conveniently study deviations from a given time–independent (dc) state, we decompose η and r in the form $\eta(\xi,t) = \bar{\eta}(\xi) + \tilde{\eta}(\xi,t)$ and $r(\xi,t) = \bar{r}(\xi) + \tilde{r}(\xi,t)$, where $\bar{\eta}(\xi)$ and $\bar{r}(\xi)$ are the respective d.c. components and $\tilde{\eta}(\xi,t)$ and $\tilde{r}(\xi,t)$ are some time–dependent deviations therefrom. Assuming $\bar{r}$ and $\tilde{r}$ to be known, the equations for $\bar{\eta}$ and $\tilde{\eta}$ read

$$B\bar{\eta} + C\bar{\eta}\bar{\eta} = \bar{r}\,, \tag{3.1}$$

$$A\partial_t\tilde{\eta} + [B + 2C^s\bar{\eta}]\tilde{\eta} = \tilde{r} - C\tilde{\eta}\tilde{\eta}\,, \tag{3.2}$$

where C^s is the symmetrical part of C.

4. Linearized evolution equation and linear eigenmodes. For sufficiently small perturbations $\tilde{\eta}$, Eq. (3.2) can be linearized by neglecting the term $C\tilde{\eta}\tilde{\eta}$. In what follows we will need to consider real linear eigenmodes of the form

$$\tilde{\eta}^{lin}(\xi,t) = \hat{\eta}^{lin}\exp(-i\omega^{lin}t) + [\hat{\eta}^{lin}]^*\exp(i[\omega^{lin}]^*t) \tag{4.1}$$

where $\hat{\eta}^{lin}(\xi)$ is the (unnormalized) linear eigenmode profile and $\omega^{lin} = \omega_r^{lin} + i\omega_i^{lin}$ is the linear eigenfrequency. Inserting (4.2) into the *linearized* version of Eq. (3.2) we readily find that $\hat{\eta}^{lin}(\xi)$ satisfies the equation

$$\mathcal{L}(\omega^{lin})\,\hat{\eta}^{lin} = 0\,, \tag{4.2}$$

where $\mathcal{L}(\Omega) \equiv -i\Omega A + (B + 2C^s\bar{\eta})$, and that the eigenfrequency is given by setting the determinant of $\mathcal{L}$ equal to zero. For convenience, we also define a "normalized" linear eigenmode profile $\check{\eta}$ by

$$\hat{\eta}^{lin}(\xi;a,\omega_r^{lin},\omega_i^{lin}) \equiv a\,\check{\eta}(\xi,\omega_r^{lin},\omega_i^{lin})\,, \tag{4.3}$$

where we have explicitly indicated the dependencies on the parameters a (real amplitude constant), ω_r^{lin} and ω_i^{lin}. Both a and $\check{\eta}$ can be specified by some appropriate initial conditions and the decomposition (4.2) is by no means unique.

5. Periodic nonlinear oscillations. Looking now for a nonlinear final state with periodic time dependence and a well–defined spectrum of harmonics, we expand any perturbation $\tilde{\eta}$ in a Fourier series with respect to time:

$$\tilde{\eta}(\xi,t) = \hat{\eta}_0(\xi) + \sum_{n=1}^{\infty}\{\hat{\eta}_n(\xi)\exp(-in\omega t) + [\hat{\eta}_n(\xi)]^*\exp(in\omega t)\} \tag{5.1}$$

where $\hat{\eta}_0$ and ω are real and $\hat{\eta}_n$ is the complex spatial profile of the n*th* harmonic. Since we agree to consider only real perturbations, we have $\hat{\eta}_{-n} = \hat{\eta}_n{}^*$ so that we can write the Fourier expansions as

$$\tilde{\eta}(\xi,t) = \sum_{n=-\infty}^{\infty}\hat{\eta}_n(\xi)\exp(-in\omega t) \quad \text{and} \quad \tilde{r}(\xi,t) = \sum_{n=-\infty}^{\infty}\hat{r}_n(\xi)\exp(-in\omega t)\,. \tag{5.2,3}$$

Inserting these expansions into (3.2) and collecting terms belonging to each harmonic order n, the fully nonlinear n–*th* order equation is obtained in the form

$$\mathscr{L}(n\omega)\hat{\eta}_n + C \sum_{m=-\infty}^{\infty} \hat{\eta}_m \hat{\eta}_{n-m} = \hat{r}_n . \qquad (5.4)$$

In general, this symbolic equation represents a complicated nonlinear system of coupled integro–differential equations, and solving it in practice requires truncation of the series at some value $|n| = N$ ("N–harmonic approximation") which must be chosen so as to still recover the physical phenomena one is interested in. In particular, oscillations of this kind occurring in the Pierce diode[1,2] have been treated in a 3–harmonic approximation[3] and a 1–harmonic approximation,[4] cf. below.

6. The 2–harmonic approximation. As a first step, we assume the perturbation to be so small that it can reasonably well be described in the 2–harmonic approximation ($N = 2$), so that in (5.2) only the terms with $n = -2, -1, 0, +1, +2$ must be kept formally. Also, from now on we consider only undriven systems, i.e., we assume $\hat{r}_0$, $\hat{r}_1$ and $\hat{r}_2$ to vanish identically. Then, neglecting fourth–order terms, the full system (5.4) reduces to the following set of equations for the unknowns $\hat{\eta}_0$, $\hat{\eta}_1$, $\hat{\eta}_2$ and ω:

$$\mathscr{L}(0)\hat{\eta}_0 + 2C^s\{\hat{\eta}_1\hat{\eta}_{-1}\} = 0 , \qquad (n = 0) \quad (6.1)$$

$$\mathscr{L}(\omega)\hat{\eta}_1 + 2C^s\{\hat{\eta}_0\hat{\eta}_1 + \hat{\eta}_2\hat{\eta}_{-1}\} = 0 , \qquad (n = 1) \quad (6.2)$$

$$\mathscr{L}(2\omega)\hat{\eta}_2 + C\{\hat{\eta}_1\hat{\eta}_1\} = 0 . \qquad (n = 2) \quad (6.3)$$

The situation described by the 2–harmonic approximation is that of a single linear eigenmode with $\omega_i^{lin} \geq 0$ having saturated at a small–amplitude steady state. Hence, it is appropriate to assume that the profile $\hat{\eta}_1$ and the fundamental frequency ω are close to the corresponding linear quantities:

$$\hat{\eta}_1(\xi;\omega) = a\,\check{\eta}(\xi;\omega) + \delta\hat{\eta}(\xi) \quad \text{and} \quad \omega = \omega^{lin} + \delta\omega , \qquad (6.4,5)$$

where $\delta\hat{\eta}$ and $\delta\omega$ are the "profile shift" and the "frequency shift", respectively, and $\delta\omega_i$ must be equal to $-\omega_i^{lin}$. Inserting (6.4) and (6.5) into Eqs. (6.1) to (6.3), keeping only the leading terms and combining the ensuing equations, we find that in this approximation $\delta\hat{\eta}$ equals zero while $\delta\omega_r$ and a are related through the formula

$$\left[\left[\delta\omega_r\frac{\partial}{\partial\omega_r} + \delta\omega_i\frac{\partial}{\partial\omega_i}\right]\left[\mathscr{L}\check{\eta}\right]\right]_{\omega^{lin}} + 2C^s\left[\hat{\eta}_0\check{\eta} + \hat{\eta}_2\check{\eta}^*\right] = 0 , \qquad (6.6)$$

where

$$\hat{\eta}_0 = -2a^2[\mathscr{L}(0)]^{-1}\{C^s\check{\eta}\check{\eta}^*\} \quad \text{and} \quad \hat{\eta}_2 = -2a^2[\mathscr{L}(2\omega^{lin})]^{-1}\{C\check{\eta}\check{\eta}\} . \qquad (6.7,8)$$

7. Example of application: 1d collisionless electron plasma wave in a warm plasma. The basic equations are[2-5]

$$\frac{\partial n}{\partial t} + \frac{\partial}{\partial x}(nv) = 0 , \qquad \frac{\partial v}{\partial t} + v\frac{\partial v}{\partial x} + \frac{e}{m}E + \frac{3}{m}Cn\frac{\partial n}{\partial x} = 0 , \qquad (7.1,2)$$

$$\frac{\partial E}{\partial x} + \frac{e}{\epsilon_0}n = \frac{e}{\epsilon_0}n_0 , \qquad (7.3)$$

where we have assumed the adiabatic law $pn^{-3} = C$, and in vectorial form

$$\begin{bmatrix} 1 & 0 & 0 \\ 0 & 1 & 0 \\ 0 & 0 & 0 \end{bmatrix} \frac{\partial}{\partial t} \begin{bmatrix} n \\ v \\ E \end{bmatrix} + \begin{bmatrix} 0 & 0 & 0 \\ 0 & 0 & e/m \\ e/\epsilon_0 & 0 & \partial_x \end{bmatrix} \begin{bmatrix} n \\ v \\ E \end{bmatrix} + \begin{bmatrix} \partial_x(nv) \\ v\partial_x v + (3C/m)n\partial_x n \\ 0 \end{bmatrix} = 0 . \qquad (7.4)$$

This means that $\eta(\xi,t) \equiv [n(x,t), v(x,t), E(x,t)]^t$, and comparing this with our general vector equation (2.1) readily yields the explicit forms of the operators A, B, and C for the special case under consideration.

Before being able to use Eq. (6.6), we have to determine the dc solution $\bar{\eta}$, the operator $\mathscr{L}$, the linear eigenfrequency ω^{lin}, and the normalized eigenmode profile $\check{\eta}$. For the dc state we choose $\bar{\eta} = [\bar{n},\bar{v},0]^t$, and the linear eigenfrequency is given by $\omega^{lin} = (1+3k^2\lambda_D^2)^{\frac{1}{2}} + k\bar{v}$. Choosing a single traveling wave with initial condition $\tilde{E}(x,t=0) = a$ and $\partial_t\tilde{E}(x,t=0) = 0$ we find the normalized eigenmode profile in the form

$$\check{\eta} = \begin{bmatrix} k\epsilon_0/2ie \\ e(1 + 3k^2\lambda_D^2)/[2im(\omega^{lin}-k\bar{v})] \\ 1/2 \end{bmatrix} \exp(ikx) . \qquad (7.5)$$

While the first–order profile is given by $\hat{\eta}_1 = a\check{\eta}$, the zero– and second–order profiles are obtained as $\hat{\eta}_0 = 0$ and $\hat{\eta}_2 = a^2[h_1, h_2, h_3]^t$, with $h_1 = -(2ik\epsilon_0/e)h_3$, $h_2 = (k\epsilon_0/4i\bar{n}e)\alpha_2(1 + \beta_2\kappa^2)$, and $h_3 = (k\epsilon_0/4m\bar{n}\omega_p)\alpha_3(1 + \beta_3\kappa^2)$. Here $\kappa \equiv k\lambda_D$, $\bar{\kappa} \equiv k\bar{v}/\omega_p$, and the α's and β's are fairly simple rational functions, such as $\alpha_3 = 1/(5 + 4\bar{\kappa} - 4\bar{\kappa}^2)$ and $\beta_3 = (-19 - 2\bar{\kappa} - 4\bar{\kappa}^2)/(5 + 4\bar{\kappa} - 4\bar{\kappa}^2)$. Inserting these results into (6.6) and taking the long–wavelength limit ($\kappa \ll 1$, $\bar{\kappa} \ll 1$) we find, after lengthy but straightforward calculations, the frequency shift

$$\delta\omega = -\frac{e^2 a^2 k^2}{10m^2\omega_p^3}\left[1 + \frac{57}{10}\kappa^2 - \frac{4}{5}\bar{\kappa}\right] \qquad (7.6)$$

Note that even in the cold–plasma case ($\kappa \to 0$) $\delta\omega$ does not vanish if $\bar{v} \neq 0$. Also, the k–scaling of (7.6) is different from that given in Ref. 5, which might be related to the multiple–time–scale formalism used there. In any case, further study is necessary to locate the source of this discrepancy.

Acknowledgments. This work was supported by the Austrian Science Foundation (Contracts P7005 and P8405), the Austrian Academic Exchange Service (ÖAD), and the Brazilian Conselho Nacional de Desenvolvimento Científico e Tecnológico (CNPq).

References

[1]J.R. Pierce, J. Appl. Phys. **15**, 721 (1944).
[2]B.B. Godfrey, Phys. Fluids **30**, 1553 (1987).
[3]M. Hörhager and S. Kuhn, Phys. Fluids B **11**, 2743 (1990).
[4]W. Pfendt, Diploma thesis, Institute for Theoretical Physics, University of Innsbruck, Austria (1991).
[5]G. Auer, Plasma Physics **21**, 895 (1979) and references therein.

Uniqueness of solution to a stationary boundary kinetic problem.

Zhykharsky A.V.
Scientific-technical Centre "Kinetika",
P.O.Box 36, 630078, Novosibirsk, Russia

The paper treats the question of uniqueness of solution to the boundary kinetic problem. This analysis is based on the accurate solutions to the stationary one-dimensional boundary kinetic problem obtained in /1/ for the limited plasma system. In the paper a simplified problem statement is used (no account is taken of the external magnetic field, a simpliest form of boundary conditions is accepted) which, however, covers all features of the problem considered. Omitting the details of the conclusion (they can be found in the work /1/) we'll write a set of Vlasov stationary kinetic equations for the cases of plane, cylindrical and spherical geometry of the problem

$$V_r \frac{\partial f_k}{\partial r} - \frac{\partial U_k}{\partial r} \frac{\partial f_k}{\partial V_r} = 0 , \qquad (1)$$

where $U_k = \left(\frac{e}{m}\right)_k \Phi$ - is a plane case;

$U_k = \frac{M^2}{2r^2} + \left(\frac{e}{m}\right)_k \Phi$ - is a cylindrical case;

$U_k = \frac{S}{2r^2} + \left(\frac{e}{m}\right)_k \Phi$ - is a spherical case;

Φ is electric potential; M and S are independent variables (angular moments of particles). Index "k" denotes k-component of the plasma.

The boundary conditions for the system (1) will be written as

$$f_k(R_1)\,|_{V_r>0} = g_{1k}\left(\frac{|V|^2}{2}\right), \qquad f_k(R_2)\,|_{V_r<0} = g_{2k}\left(\frac{|V|^2}{2}\right) \qquad (2)$$

Index "1" relates to the boundary surface (plane, cylinder or sphere) with the coordinate $r = R_1$, index "2" relates to the boundary surface with the coordinate $r = R_2$, with $R_2 > R_1$.

The solution to the stationary boundary kinetic problem (1),(2), obtained in /1/ has the form

$$f_k = H(\lambda_k) \cdot g_{1k}\left(\frac{|V|^2}{2} + \left(\frac{e}{m}\right)_k \cdot [\Phi - \Phi_1]\right) + H(-\lambda_k) \cdot g_{2k}\left(\frac{|V|^2}{2} + \left(\frac{e}{m}\right)_k \cdot [\Phi - \Phi_2]\right)$$

where $\lambda_k = V_r - \mathrm{sign}(r - \tilde{r}_k)\sqrt{[2\,(\tilde{U}_k - U_k)]}$, (3)

$\tilde{U}_k = \max_{R_1 \le r \le R_2} (U_k)$, $U_k(\tilde{r}_k) = \tilde{U}_k$.

For analysis of the uniqueness of solution (3) to the boundary kinetic problem (1), (2) we'll consider the functions as

$$f_k^* = H(\lambda_k) \cdot g_{1k}(E_{1k}) \cdot F_{1k}(E_{1k}) + H(-\lambda_k) \cdot g_{2k}(E_{2k}) \cdot F_{2k}(E_{2k}) \ , \tag{4}$$

where $E_{1,2k} = \frac{|V|^2}{2} + \left(\frac{e}{m}\right)_k \cdot [\Phi - \Phi_{1,2}]$, $F_k(E_k) = \begin{cases} 1 \text{ with } E_k \geq 0 \\ \text{arbitrary} \\ \text{function} \quad \text{with } E_k < 0 \end{cases}$

We can show that the functions (4) are a solution to the boundary kinetic problem (1), (2) since the equations of the system (1) are linear and the functions E_k are the particular solutions to the equations of this system (see theorems 1 and 2 in work /1/). Thus there has been found a class of the functions which are the solutions to the boundary kinetic problem (1), (2). Thereby it is proved that the solution (3) is not unique.

There arises a question: what is the cause of absence of the uniqueness of a solution to the boundary kinetic problem (1), (2) and is it possible to formulate a boundary problem so as to exclude arbitrariness from determining the functions F_k in the expressions (4)?

To provide an answer to this question we'll calculate the values of the functions f_k^* at the system boundary. From determination of the functions λ_k (see expression (3)) it follows that

$$\lambda_k(R_1) = V_r + \sqrt{[2\,(\tilde{U}_k - U_k(R_1))]} = V_r + a_k \ , \tag{5}$$

$$\lambda_k(R_2) = V_r - \sqrt{[2\,(\tilde{U}_k - U_k(R_2))]} = V_r - b_k \ , \quad \text{where } a_k, b_k > 0$$

Consequetly, taking account of the expression (4)

$$f_k^*(R_1) = \begin{cases} g_{1k}\left(\frac{|V|^2}{2}\right) & \text{with } V_r > -a_k \\ g_{2k}\left(\frac{|V|^2}{2} + \left(\frac{e}{m}\right)_k \cdot [\Phi_1 - \Phi_2]\right) \cdot F_{2k}\left(\frac{|V|^2}{2} + \left(\frac{e}{m}\right)_k \cdot [\Phi_1 - \Phi_2]\right) & , V_r < -a_k \end{cases}$$

$$f_k^*(R_2) = \begin{cases} g_{1k}\left(\frac{|V|^2}{2} + \left(\frac{e}{m}\right)_k \cdot [\Phi_2 - \Phi_1]\right) \cdot F_{1k}\left(\frac{|V|^2}{2} + \left(\frac{e}{m}\right)_k \cdot [\Phi_2 - \Phi_1]\right) & , V_r > b_k \\ g_{2k}\left(\frac{|V|^2}{2}\right) & \text{with } V_r < b_k \end{cases} \tag{6}$$

According to definition the function F_k are different from unity when $E_k < 0$. Let's estimate E_k taking account of the restrictions imposed on V_r. Let's consider the case of spherical geometry (plane and cylindrical geometry are treated similarly). Here we have

$$\frac{|V|^2}{2} = \frac{V_r^2}{2} + \frac{S}{2r^2} \ , \qquad U_k = \frac{S}{2r^2} + \left(\frac{e}{m}\right)_k \cdot \Phi \ .$$

Consequetly, taking account of the definitions a_k (see (5)) we'll obtain

$$E_{2k}(R_1) > \left(\frac{a_k^2}{2} + \frac{S^2}{2R_1} + \left(\frac{e}{m}\right)_k [\Phi_1 - \Phi_2]\right) = \widetilde{U}_k - \left(\frac{e}{m}\right)_k \Phi_2 \geq$$

$$\left(\frac{S^2}{2R_2} + \left(\frac{e}{m}\right)_k \cdot \Phi_2 - \left(\frac{e}{m}\right)_k \cdot \Phi_2\right) > 0 ,$$

since according to definition $\widetilde{U}_k \geq U_k(r_0)$, where r_0 - is any point of the interval $[R_1, R_2]$.

Likewise we can show that $E_{1k}(R_2) > 0$ with $V_r > b_k$. Thus it is established that at the system boundary the function F_k are always equal to unity and, consequently, we can draw the conclusion that it is impossible to formulate the boundary conditions for the stationary kinetic problem so as to exclude arbitrariness when determing the functions F_k in the expressions (4). At first sight it may seem that the result obtained is the consequence of the kinetic problem statement accepted.

Indeed the statement (1), (2) implies dependence of the distribution functions (DF) of particles on the potential Φ. However, the potential Φ also in its turn depends on the distribution functions of particles (it is a self-matched problem). The appropriate relation is established through the Poisson equation

$$\varepsilon_0 \Delta\Phi = -\sum_k c_k \int_{(\infty)} f_k^* \cdot dV . \qquad (7)$$

However a closer examination makes it clear that the equation (7) cannot serve to indentify the functions f_k^* . Moreover, it is impossible to do even with the predetermined potential Φ since the right side of the equation (7) contains not the functions f_k^* but only their first moments. In the case where the potential Φ is not determined one should bear in mind that the equation acquires physical sense only after calculating (or if such calculation is feasible in principle) the integral on the right side of the equation. Thus we come to the conclusion that uncertainty when determining the functions (4), i.e. the absence of uniqueness of the solution to the boundary kinetic problem (1), (2) is a fundamental property inherent in the stationary boundary kinetic problem.

The results obtained for the trapped particles to be available in the system necessitate revaluating the role and the plase of the stationary kinetic problem in a general kinetic approach.

The point of the problem is that, on the one hand, one of the fundamental postulates of statistical physics is an assertion that between the system state and the DF of particles forming this system there exists a rigorous one-to-one correspondence. That is the DF of particles describes fully and uniquely the system state. On the other hand, the results obtained permit drawing the conclusion that there exist physical situations where the solutions to the stationary kinetic problem can be represented by quite a set of DF with different DF of trapped particles which, nevertheless, produce at the area boundaries cosiderred equal flows of substance, energy etc. It is evident that the very fact of equality of the flows produced by different DF implies that

there exists no experimental way of discriminating these states of the physical system, i.e., establishing a one-to-one correspondence between the state and the DF of particles forming this system.

Consequently, one has either to abandon the existing formulation postulating a one-to-one correspondens between the DF of particles and the sysytem state or to seriously revise the notion "stationary kinetic problem".

The results obtained in the work serve as evidence for drawing the conclusion that the cause of the absence of solution uniqueness for the boundary problem (1), (2) is the accepted formulation of the stationary problem.

Indeed when formulating the stationary boundary kinetic problem in the work /1/ the condition of stationarity ($\frac{\partial}{\partial t} = 0$) was accepted as an initial condition of stating the problem. Yet such an approach implicitly implies that the DF of particles of the system obtained as a result of solving this problem must be invariable on the infinite time interval $t \in [-\infty, \infty]$. It is evident that such a situation is not physically feasible. Thus, we come to the conclusion that the basic feature of the accepted statement of the stationary problem is completely ignoring the prehistory of transition of the system from some initial state to a final stationary state. Consequently, one can advance the following hypothesis:

a one-to-one correspondens between a stationary state of the system and the DF of particles forming this system can be obtained only as a result of treating a trasition process of the system from a pre-set initial state to a final stationary state.It is evident that a rigorous verification of this hypothesis is possible only if based on an accurate solution to the non-stationary boundary kinetic problem.

However if the hypothesis is assumed to be true one can formulate two significant consequences:

(a) since a stationary state of the system should be considered as some final state arising as a result of limiting transition ($t \to \infty$) from the pre-set initial state then also the formulation of the stationary kinetic problem must correspond to this conception;

(b) if the analysis of the non-stationary kinetic problem indicates that a stationary state of the system depends on the transition method of the system to this state one should conclude that the concept "non-reversibility" arises implicitly just in determining the notion "Distribution Function".

Consequently there will arise prerequisites for asserting that "non-reversibility" is one of the fundamental concepts of statistical physics.

/1/. Zhykharsky A.V. Physica Scripta, 44, p. 606.

Solution to the Boundary Kinetic Problem Presenting the Interaction of the Plasma Flows with a Solid

Zhykharsky A.V., Shmykov V.N.
Scientific-technical Centre "Kinetika",
P.O.Box 36, 630078, Novosibirsk, Russia

The paper treats the stationary one-dimensional statement of the boundary kinetic problem presenting the interaction of the plasma flows with a solid. The cases of planer, cylindrical and spherical geometry have been investigated for which all physical situations confined to the one-dimensional problem have been considered. The diagrams of statements are presented in the Table. When formulating the boundary kinetic problem statement we assume that plane, cylinder or sphere with the coordinate R_1 denotes the solid surface and the R_2 - coordinate surface denotes the plasma boundary. The notion "plasma boundary" implies that outside this boundary (i.e. with $r > R_2$) the plasma is in a equlibrium state, the distribution functions for plasma components with $r > R_2$ being described by the Maxwell distribution functions with a space velocity shift by the quantity "V_{ok}" (here and further index "k" denotes k-component of the plasma). It is evident that inside the plasma there exist no surfaces to be identified with the plasma boundary. Yet in case of obtaining an accurate analytical solution to the boundary kinetic problem statement considered and effecting a limit-transition $R_2 \to \infty$ of the distribution functions obtained for the plasma components we will have a description of plasma flow-solid interaction when the "equilibrium" plasma flow is preset at infinity. A plasma motion as a whole with respect to the solid surface is simulated by a special type of boundary conditions for the distribution functions of the plasma components. It is implied that all particles of the plasma k-component entering the area considered in addition to the thermal velocity have the velocity "V_{ok}". The external magnetic field is assumed to be equal to zero. However one should bear in mind that in the cases where the plasma flow moves along the solid boundary (see in the Table the relative cases for planer and cylindrical geometry), in the system there may be available an inherent, different from zero, magnetic field of currents. This factor should be taken into account when solving the boundary kinetic problem.

We'll formulate the boundary problem statement taking account of the assumptions made. Omitting the details of the conclusion (they can be found in the work /1/) we'll write a set of kinetic equations for the plasma components as

$$V_r \cdot \frac{\partial f_k}{\partial r} - \frac{\partial U_k}{\partial r} \cdot \frac{\partial f_k}{\partial V_r} = 0 \; ; \qquad (1)$$

The boundary conditions for distribution functions will be written as

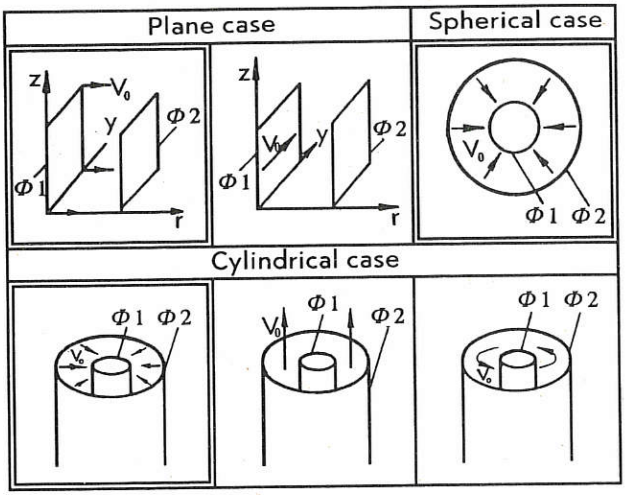

Table. The diagrams of stationary one — dimensional statements of the boundary kinetic problem.

$$f_k(R_1)\ |v_r > 0 = g_{1k}\left(\frac{|V|^2}{2}\right), \qquad f_k(R_2)|\ v_r < 0 = g_{2k}\left(\frac{|V-V_0|^2}{2}\right) \tag{2}$$

where g_{1k} and g_{2k} are arbitrary functions. The expression for the generalized potential U_k depending on the direction of the vector "V_{0k}" (see Table) have the following for

- planar case

a) $V_0 \parallel V_r$: $\quad U_k = \left(\frac{e}{m}\right)_k \Phi$,

b) $V_0 \parallel V_z$: $\quad U_k = \frac{1}{2}\left[S - \left(\frac{e}{m}\right)_k A_z(r)\right]^2 + \left(\frac{e}{m}\right)_k \Phi$;

- cylindrical case

a) $V_0 \parallel V_r$: $\quad U_k = \frac{M^2}{2r^2} + \left(\frac{e}{m}\right)_k \Phi$,

b) $V_0 \parallel V_z$: $\quad U_k = \frac{M^2}{2r^2} + \frac{1}{2}\left[S - \left(\frac{e}{m}\right)_k A_z(r)\right]^2 + \left(\frac{e}{m}\right)_k \Phi$; (3)

c) $V_0 \parallel V_\varphi$: $\quad U_k = \frac{1}{2}\left[\frac{M}{r} - \left(\frac{e}{m}\right)_k A_\varphi(r)\right]^2 + \left(\frac{e}{m}\right)_k \Phi$;

- spherical case

$$V_0 \parallel V_r: \qquad U_k = \frac{S}{2r^2} + \left(\frac{e}{m}\right)_k \Phi \ .$$

In these expressions the quantities M and S are independent variables (see /1/). The electric field is presented through the potential "Φ" and the magbetic field through the appropriate components of the vector potential "A".

The solution to the boundary kinetic problem (1), (2) is the functions of the form /1/

$$f_k = H(\lambda_k) \cdot g_{1k}(E_{1k}) + H(-\lambda_k) \cdot g_{2k}(E_{2k}) \ ,$$

$$\text{where} \quad \lambda_k = V_r - \text{sign}(r - \tilde{r}_k)\sqrt{[2\,(\tilde{U}_k - U_k)]} \ , \tag{4}$$

$$\tilde{U}_k = \max_{R_1 \le r \le R_2} (U_k) \ , \qquad U_k(\tilde{r}_k) = \tilde{U}_k \ .$$

and H is the Heaviside function. The functions E_{1k}, E_{2k} must be expressed through the motion integrals (i.e. through solutions of kinetic equations). Herewith these expressions must satisfy the conditions (2).

We'll write expressions for E_{2k} satifying these equations. The variables M and S, the expressions (3) have been used in writing

- planar case

a) $V_0 \parallel V_r$: $$E_{2k} = \frac{1}{2}\left\{\sqrt{[V_r^2 + 2[U_k - U_k(R_2)]} - V_{ok}\right\}^2 + \frac{V_y^2}{2} + \frac{V_z^2}{2} \ ,$$

b) $V_0 \parallel V_z$: $$E_{2k} = \frac{V_r^2}{2} + U_k - U_k(R_2) + \frac{V_y^2}{2} + \frac{1}{2}[S - \left(\frac{e}{m}\right)_k A_z(R_2) - V_{ok}]^2 \ ;$$

- cylindrical case

a) $V_0 \parallel V_r$: $$E_{2k} = \frac{1}{2}\left\{\sqrt{[V_r^2 + 2[U_k - U_k(R_2)]} - V_{ok}\right\}^2 + \frac{M^2}{2R_2^2} + \frac{V_z^2}{2} \ ,$$

b) $V_0 \parallel V_z$: $$E_{2k} = \frac{V_r^2}{2} + U_k - U_k(R_2) + \frac{M^2}{2R_2^2} + \frac{1}{2}[S - \left(\frac{e}{m}\right)_k A_z(R_2) - V_{ok}]^2 \ ;$$

c) $V_0 \parallel V_\varphi$: $$E_{2k} = \frac{V_r^2}{2} + U_k - U_k(R_2) + \frac{1}{2}[\frac{M}{R_2} - \left(\frac{e}{m}\right)_k A_\varphi(R_2) - V_{ok}]^2 + \frac{V_z^2}{2} \ ;$$

- spherical case

$$V_0 \parallel V_r: \qquad E_{2k} = \frac{1}{2}\left\{\sqrt{[V_r^2 + 2[U_k - U_k(R_2)]} - V_{ok}\right\}^2 + \frac{S}{2R_2^2} \ ;$$

The expressions for E_{1k} can be obtained from the expression for E_{2k}, assuming $V_{ok}= 0$ and making a substitution: $R_2 \to R_1$.

By making a substitution in the equations it is easy to make sure that the functions (4) with the expressions obtained above for E_{1k} and E_{2k} are the solutions to the boundary kinetic problem (1), (2). It should be noted that the expressions for the function E_{2k} are the generalized solution obtained by H.Schamel in the work /2/. However, unlike the results of the work /2/ in our case the boundary conditions /2/ are satisfied by the functions (4) not only through pre-setting a special kind of functions E_{2k} but also through employing the function $H(\pm\lambda_k)$. The latter is significant in principle since it is this factor that permits obtaining a mathematically rigorous solution to the boundary kinetic problem (1), (2). When solving specific applied problems on the basis of the distribution functions obtained (4) one should mind the following. When treating plasma motion along the solid surface one is required to numerically solve a set of self-matched equations. It is equations for determining the electric potential of the system and the appropriate component of the inherent magnetic field.

For example, for the problem of a two-component plasma flow (plasma consists of electrons and one kind ions) along the axis of an infinite cylindrical solid the system of field equations takes the form

$$\frac{1}{r}\frac{\partial}{\partial r}\left(r\frac{\partial \Phi}{\partial r}\right) = -\frac{e}{\varepsilon_0}(n_i - n_e) ,$$

$$\frac{1}{r}\frac{\partial}{\partial r}\left(r\frac{\partial A_z}{\partial r}\right) = -e\mu_0(j_{z,i} - j_{z,e}) ,$$

$$n_{e,i}= \int_{(\infty)} f_{e,i}\, dV ; \qquad j_{z(e,i)}= \left\{ \int_{(\infty)} V f_{e,i}\, dV \right\}_z ,$$

where $n_{e,i}$ is density of electrons and ions; $j_{z(e,i)}$ is components of the density of the electrons and ions flows.

Φ, A_z is the scalar and vectorial potentials accordingly. It is evident that this system of equations can be solved only on pre-setting a specific kind of the functions $g_{1e,i}(E_{1e,i})$ and $g_{2e,i}(E_{2e,i})$ in the expressions (4).

The results presented in the paper complete the consideration of the one-dimensional stationary boundary kinetic problem since the paper together with the work /1/ present all the physical statements investigated which are reducible to a one-dimensional problem due to geometric symmetry. Yet the question of uniqueness of the solutions obtained to the boundary kinetic problem remains still open.

/1/. Zhykharsky A.V. Physica Scripta, v.44:6, p.606.

/2/. Schamel H., Physics Reports (review section of Phys. Lett) 140, 161 (1986).

A THEORETICAL MODEL FOR TRANSIENT CATAPHORETIC SEGREGATION

Nicoleta Dumitrascu, D.Berbece, Gh.Popa
Faculty of Physics, "Al.I.Cuza" University
R-6600 Iasi, Romania

Cataphoresis is the term used to describe the establishment of differences in the partial pressures of the gas constituents in a positive plasma column between the anode and the cathode ends of the discharge. A systematic experimental study means measurements of the axial density distributions for different ion species and the efficiency of cataphoretic segregation (its dependence on composition of the mixture, discharge parameters and discharge tube configuration) /1,2/. A theoretical model on this phenomenon has to take into account both the mechanism by which the various gas particles are converted into ions and the transport phenomena due to selective momentum transfer to the neutrals of electrons and ions.

Till now the former mechanism was partially neglected and Shair /3/ and Sanctorum /4,5/ have proposed a model for time-dependent cataphoresis governed by a diffusion equation with a supplementary term for the transport of ions in the axial electric field. Sanctorum et al. /4,5/ give an analytical and numerical solution using appropriate initial and boundary conditions at the electrodes and at the ends of the device. On obtain the admixture density $n(x,t)$ as a function of place x and time t following the ignition of the discharge.

A comparison between experimental results concerning transient cataphoretic separation and theoretical data shows considerable discrepancies at the cathode side of the discharge tube and at the first moments of the ignition of the discharge /4/.

We propose a more general equation using thermodynamic considerations. The conservation equation for the size Y is:

$$(\partial Y/\partial t) = -\nabla\vec{J} + S \qquad (1)$$

where S is the source term and $\vec{J} = \vec{J}(n_1, \ldots n_p, \nabla n_1 \ldots \nabla n_p, \vec{E}, t)$.

For irreversible processes near equilibrium (like cataphoretic segregation), the flux depends linear with thermodynamic forces:

$$\vec{J_i} = \sum_{k=0}^{p} L_{ik}\,\vec{F_k} \qquad i = 0,\ldots,p \qquad (2)$$

where L_{ik} are phenomenological coefficients.

If Y is the density of particles, then their transport is due to both the drift in axial electric field and the density gradients, eq.(2) give in the matrix form

$$\vec{J} = D\nabla n + \mu\, n\, U\, \vec{E} \qquad (3)$$

where

$$\vec{J} = \begin{vmatrix} \vec{J_0} \\ \vdots \\ \vec{J_p} \end{vmatrix} \quad ; \quad n = \begin{vmatrix} n_0 \\ \vdots \\ n_p \end{vmatrix} \quad ; \quad \mu = \begin{vmatrix} \alpha_0\mu_0 & \ldots & 0 \\ \vdots & & \vdots \\ 0 & \ldots & \alpha_p\mu_p \end{vmatrix}$$

It is reasonable to assume that ions are produced and disappear in regions near electrodes and the transport processes (superposed on the dynamical equilibrium which is established in the ignition moments of the discharge) prevail in the positive plasma column (the source-terms are zero).

Now the eq. (1) and (3) can be written for several gas mixtures. With the known assumptions on obtain the equation used by Sanctorum /4,5/. If several types of ions (or even neutrals) are present in the discharge plasma then they should be taken into account to the cataphoretic segregation. There are experimental proves that cluster molecules are present in a rather large number in the discharge /6,7/ and a theoretical model have to consider them.

Consequently, if we have another species important in the transfer momentum process, from (1) and (3) on obtain the following system of equations :

$$\begin{cases} (\partial n_0/\partial t) = D_0(\partial^2 n_0/\partial x^2) + D(\partial^2 n_1/\partial x^2) + e_0(\partial n_0/\partial x) \\ (\partial n_1/\partial t) = D(\partial^2 n_0/\partial x^2) + D_1(\partial^2 n_1/\partial x^2) + e_1(\partial n_1/\partial x) \end{cases} \qquad (4)$$

It describes time dependence of axial distribution of the two species n_o and n_1, which we have considered important in the process of momentum transfer.From (4) on obtain:

$$\frac{\partial^2 n_o}{\partial t^2} - (D_o+D_1)\frac{\partial^3 n_o}{\partial x^2 \partial t} + (e_o+e_1)\frac{\partial^2 n_o}{\partial x \partial t} = (D^2-D_oD_1)\frac{\partial^4 n_o}{\partial x^4} +$$

$$+ (D_oe_1 + D_1e_o)\frac{\partial^3 n_o}{\partial x^3} - e_oe_1\frac{\partial^2 n_o}{\partial x^2}$$

which describes time dependence for axial distribution of n_o.

We are searching the solution for (4) in the form :

$$\begin{vmatrix} n_o(x,t) \\ n_1(x,t) \end{vmatrix} = \begin{vmatrix} n_o(x,\infty) \\ n_1(x,\infty) \end{vmatrix} + \sum_{n=-\infty}^{\infty} \begin{vmatrix} P_n(t) \\ Q_n(t) \end{vmatrix} \exp[(i(2\pi n/L)x)] \qquad (5)$$

where only the real part of the expression having physical meaning ; L is the length of discharge tube; $n_{o,1}(x,\infty)$ axial density distribution in the steady-state:

$$n_o(x,\infty) = A_1 \exp(r_1x) + A_2 \exp(r_2x) \quad \text{and}$$

$$n_1(x,\infty) = B_1 \exp(r_1x) + + B_2 \exp(r_2x) \quad \text{with}$$

$$r_{1,2} = 1/2\,\frac{D_oe_1+D_1e_o}{D^2 - D_oD_1} \pm \sqrt{(1/2\,\frac{D_oe_1+D_1e_o}{D^2 - D_oD_1})^2 + \frac{e_o\,e_1}{D^2 - D_oD_1}} < 0 \qquad (6)$$

The coefficients A_1, A_2, B_1, B_2 can be obtain (we suppose that the flow of matter is zero at the ends of discharge tube) from the system of equations.

$$\begin{vmatrix} \frac{\exp(r_1L)-1}{r_1L} & \frac{\exp(r_2L)-1}{r_2L} & 0 & 0 \\ 0 & 0 & \frac{\exp(r_1L)-1}{r_1L} & \frac{\exp(r_2L)-1}{r_2L} \\ D_or_1 + e_o & D_or_2 + e_o & Dr_1 & Dr_2 \\ Dr_1 & Dr_2 & D_1r_1 + e_1 & D_1r_2 + e_1 \end{vmatrix} \begin{vmatrix} A_1 \\ A_2 \\ B_1 \\ B_2 \end{vmatrix} = \begin{vmatrix} n_o(0) \\ n_1(0) \\ 0 \\ 0 \end{vmatrix}$$

$n_{o,1}(0)$ are initial concentrations of the two species considering an uniform initial distribution in the discharge

tube. The functions $P_n(t)$ and $Q_n(t)$ are given by

$$\begin{vmatrix} P_n(t) \\ Q_n(t) \end{vmatrix} = \begin{vmatrix} a_n \\ c_n \end{vmatrix} \exp(p_1 t) + \begin{vmatrix} b_n \\ d_n \end{vmatrix} \exp(p_2 t)$$

where

$$p_{1,2} = -1/2\ (2\pi n/L)[(2\pi n/L)(D_o + D_1) - i(e_o + e_1)] *$$

$$\left[1 \pm \sqrt{1 - 4\, \frac{(D_o \frac{2\pi n}{L} - i.e_o)(D_1 \frac{2\pi n}{L} - i.e_1) - (\frac{2\pi n}{L})^2 D^2}{\left| \frac{2\pi n}{L} (D_o + D_1) - i(e_o + e_1) \right|^2}} \right]$$

The coefficients a_n and b_n are :

$$a_n = [p_2 P_n(0) - \dot{P}_n(0)]/(p_2 - p_1)$$

and

$$b_n = [p_1 P_n(0) - \dot{P}_n(0)]/(p_1 - p_2)$$

where

$$\dot{P}_n(0) = -\frac{2\pi n}{L}(D_o \frac{2\pi n}{L} - i.e_o) P_n(0) - (\frac{2\pi n}{L})^2 D.Q_n(0)$$

$$\begin{vmatrix} P_n(0) \\ Q_n(0) \end{vmatrix} = \begin{vmatrix} A_1 \\ B_1 \end{vmatrix} \frac{1 - \exp(r_1 L)}{r_1 L - i.2\pi n} + \begin{vmatrix} A_2 \\ B_2 \end{vmatrix} \frac{1 - \exp(r_2 L)}{r_2 L - i.2\pi n}$$

These preliminary results allow to :

- a more general equation for description of axial cataphoresis and who gives supplementary diffusion modes;
- the presence of the cluster molecules in the theoretical model might give an explanation for the discrepancy between theoretical and experimental data /4/.

REFERENCES

1. J.Freudenthal, Physica 36 , 365 (1967)
2. J.Freudenthal, J.Appl.Phys., 38 , 4818 (1967)
3. F.H.Shair, D.S.Remer, J.Appl.Phys., 39 , 5762 (1968)
4. C.Sanctorum, L.Bonte, L.Jacques, Physica 104C, 457 (1981)
5. J.Ongena, C.Sanctorum, W.Wieme, Physica 125C , 321 (1984)
6. J.P.Gaur, L.M.Chanin, J.Appl.Phys., 41 , 106 (1970)
7. R.B.Tombers, L.M.Chanin, J.Appl.Phys., 42 , 5204 (1971)

AUTHOR INDEX

Aceto S. I-525,I-529
Adams J.M. I-67,I-251
Afanasyev V.I. I-151,II-1031
Agarici G. II-885
Ågren O. II-1369
Airoldi A. II-973
Akiyama H. I-403
Akiyama R. I-517
Al-Karkhy A. I-639
Al-Mashhadany E.M. I-691
Alava M.J. III-1923
Alejaldre C. I-565
Aleksandrov V.O. I-111
Alexandroaei D. III-1957
Alexandrov V.O. II-997
Ali-Arshad S. I-227,I-335,I-339
Alladio F. I-23,I-545,II-1525
Allen J.E. III-1973,III-1977,III-2033
Alper B. I-331,I-335,I-339,II-1051
Alport M.J. III-1895
Amatucci W.E. III-1895
Anabitarte E. II-1183
Anderson D. I-391
Anderson D.V. I-557
Annaratone B.M. III-1977
Antani S.N. II-1009
Antoni V. I-631
Antsiferov P. I-683
Aoyama K. III-1765
Apostol I. III-2049
Appala N.P. III-1943
Appel L.C. I-31
Apruzzese G. I-463
Aragon F. I-299
Arakawa M. II-1337
Aramaki E.A. I-675
Araujo M.S.T. I-419
Arhipenko V.I. II-1203
Arimoto H. I-513,I-517
Asakura N. II-949
Ascasibar E. I-565,II-933
Ashida H. II-1405
Ashkenazy J. III-2117
Assis A.S. II-1549
Assis A.S. I-679,III-1619,III-1667,III-1785
Atanasiu C.V. I-367
Aumayr F. II-1163
Austin M.E. I-115
Avakian M. I-479
Axnäs I. II-1175,III-1875
Azevedo C.A. I-679,III-1619
Azizov E.A. I-47
Baang S. II-1071
Baba T. I-489
Baboolal S. III-1819
Bachin I.V. II-1345
Bachmann P. II-747
Badalec J. I-219
Baelmans T. II-747
Bagatin M. I-631
Bagdasarov A. I-371
Bagryansky P.A. II-1123
Bahrim B. III-2049
Bahrim C. III-2049
Baity F.W. II-893
Baker K.B. III-1591
Bakos J.S. I-303
Balbin R. II-783,II-791
Baldzuhn J. II-1119
Balet B. I-3,I-19,I-59,I-63,I-263,II-881
Barabaschi P. I-167
Baranowski J. II-1211
Barnsley R. I-291
Barrett P.J. III-1803
Bartiromo R. II-957,II-961,II-1127
Bartlett D.V. I-119,I-147,I-163, I-255,I-407,II-973
Basiuk V. I-175
Basu B. II-1373,II-1509
Batani D. II-1207,III-2017
Batchelor D.B. II-913
Batistoni P. I-545
Baumgärtel K. III-1571
Baylor L.R. I-255,I-521,I-525
Bazdenkov S.V. II-1453
Beaumont B. II-885
Becker G. II-1457
Becoulet A. I-175,II-885,II-905
Behrisch R. II-843
Beidler C.D. I-533,I-569,I-581
Belik V.P. II-1039
Bell J.D. I-525,I-529
Bell M.G. I-39
Bell R. I-39,II-949
Belli M. II-1207
Belmont G. II-1297
Belyakov V.A. I-471
Bender S.E. I-471
Bengtson R.D. I-91
Benova E. II-1517,III-2041
Berbece D. II-1561
Berge G. II-1401
Berger By G. II-885
Bergsåker H. I-607
Berk H. II-1469
Bernabei S. II-949,II-957
Berni L.A. I-675
Bertolini E. I-167
Berton F. I-23
Bertrand P. II-807,II-1005,III-1737,III-1741
Besedin N.T. I-569
Besshou S. I-489,II-1131
Bharuthram R. II-1445
Bhatnagar V.P. I-327,II-897,II-901
Bibet P. I-159,II-885
Biborosch L. III-2029
Bickley A. I-379
Bigelow T.S. I-521,I-525
Bilbao L. II-1253
Bingham R. II-1271,III-1627
Birdsall C.K. III-1993
Bizarro J.P. I-27,II-885
Blazquez J.F.M. II-1237
Blumenfeld L. III-2055
Boedo J. I-155
Boerner E.D. II-1275
Bohm M. III-1875
Boileau A. I-215
Bollanti S. II-1207
Bond D.S. I-251
Bondarenko E.A. II-1261
Bondeson A. I-343,I-399
Bonhomme G. III-1737,III-1879
Bonitz M. III-2091
Bonoli P.T. II-965
Boozer A.H. II-863,III-1713
Bora D. III-1575,III-1583,III-2021
Borba D. I-439

Borisov N.D. III-1587
Bornath Th. III-2091
Bornatici M. II-1493
Borrass K. II-735
Bortolotti A. I-695,II-1253
Bosch H.-S. II-747
Bosia G. II-897
Bosia P. II-901
Boucher C. I-215
Boucher D. I-59
Boucher I. III-1883
Bowles J. III-1935
Braams B. II-747
Bracco G. I-23,I-127,I-295
Braithwaite N.St.J. III-1973
Brambilla M. II-925
Branas B. I-99,II-1075
Brasilio Z.A. II-803
Bravanec R.V. I-115
Bravo E. III-1607
Bretz N. I-203
Breun R. II-839
Brouchous D. II-839
Brower D.L. I-115,I-363
Browning P.K. I-639
Brusati M. I-3,I-119,I-307,II-897,II-973,II-977
Bruschi A. I-23
Bryant D.A. III-1627
Brzosko J.S. I-695
Brzozowski B.P. I-595
Brzozowski J. I-291,I-611
Büchl K. I-459,II-743
Büchse R. I-375,I-379
Bud'ko A. I-635,I-671,II-1261
Budnikov V.N. II-997,II-1203
Budny R.V. I-39,I-43,I-203
Buffa A. I-619
Bulanin V.V. I-111
Bulanov S.V. I-541,II-1305,II-1317,II-1429
Buneman O. III-1579
Buratti P. I-23,I-127,I-463
Bures M. I-3,I-19,I-255,I-307,II-881,II-897
Bürger G. I-303
Burgos C. I-299,II-1135
Burrell K.H. I-11,I-179,I-183,I-243,I-275
Bush C.E. I-203
Bustamante E.G. II-1183
Buzhinskij O.I. I-47
Cabral J.A.C. II-1111
Cabral-Prieto A. III-1947
Cabrit B. II-1083,III-1591
Caldas I.L. I-419,II-803
Calderon M.A.G. II-1183
Callen J.D. II-1413
Calvin M. I-211
Campbell D.J. I-227,I-239,I-375,
II-735,II-881,II-897
Caner M. III-2117
Capes H. I-107
Capitain J.J. II-885
Carlson A. II-783,II-787
Carlstrom T.N. I-235
Carolan P.G. I-411
Carrasco J. I-175,II-885
Carreras B.A. I-521,I-525,I-565,I-569,II-1417
Carroll III J.J. III-1895
Carter M.D. II-913
Castejon F. II-933,II-1135
Castiglioni S. II-1087
Castro R.M. II-803
Catto P.J. I-91
Cercek M. II-1171,III-1761
Cereceda C. II-1513
Cermak I. III-1989
Cha S.S. I-451
Chakraborty B. II-1257
Challis C.D. I-15,I-311,I-335,I-379
Chance M.S. I-435,II-949
Chang C.S. I-315
Chang T. II-1509
Chankin A.V. II-779
Chao J.K. III-1615
Chatelier M. I-159
Chavez-Alarcon E. I-483,III-1947
Chekroud D. III-1729
Chen F.F. III-1701,III-1789
Chen H.H. III-2059
Chen J.Y. I-363
Chen X.P. I-107
Cherkhani R. III-1737
Chernobaj A.P. I-47
Cherubini A. II-901
Chevlaier G. III-1701
Chittenden J.P. I-655
Chiu C.Y. III-1615
Chiu S.C. II-893
Chiueh T.H. III-1615
Cho S. III-2133
Chodura R. II-871
Choi E.H. III-2133
Chou A.E. II-1071
Chou C.K. III-2059
Christensen M. I-279
Christiansen J.P. I-15
Chu M.S. I-243,I-435
Chu R. III-1811
Chu T.K. II-949
Chudin N.V. I-367
Cicconi G. II-1187,III-2037
Ciubotariu-Jassy C.I. III-1681
Claaßen H.A. II-771
Clement S. I-307,II-723,II-727,II-735,II-823
Clupek M. I-713
Coffey I.H. I-291
Cohen D. II-1017
Cohen R.H. II-1275
Colborn J.A. II-965
Colchin R.J. I-525
Colton A. I-227
Colunga-Sanchez S. I-483,III-1947
Compant La Fontaine A. III-2113,III-2125
Conceicao P. II-977
Condé H. II-1047
Condrea I. I-295,II-1127
Connor J.W. II-1393
Connor K.A. I-529
Conrads H. II-775
Conroy S. I-67,I-167,I-251
Cook D. II-937
Cooper W.A. I-557,I-589
Coppi B. I-139
Coppins M. I-663
Cordey J.G. I-15,I-191-59,I-63,I-263
Core W.G.F. II-1035
Correa-Restrepo D. II-1329,III-1753
Correia C. II-1063
Corti S. I-151,II-1031
Costa S. I-619
Costley A.E. I-163,I-199,I-407
Cottrell G.A. I-327,II-881,II-897
Coulon J.P. I-107
Couture P. I-215
Cowley S.C. II-1393
Cox M. II-897,II-1341
Cripwell P. I-199,I-227,I-407,I-439
Crisanti F. I-463
Cross R.C. II-815
Cruz-Jimenez S. III-1947
Cunningham G. I-639
Cuperman S. III-2117

Cupido L. II-1063
D'haeseleer W.D. I-533,II-755
da Costa O. I-327
da Cruz Jr. D.F. I-267
da Silva R.P. II-803,II-973
Darrow D.S. I-203,I-431
Das A.C. II-1257,III-1611
Dawson J.M. II-1271,III-1627
De Angelis R. I-279,I-295
de Blank H.J. I-247,I-339
de Esch B. I-167
de Esch H.P.L. I-339
de Gentile B. I-27
De Haas J.C.M. I-83,I-87
De Kock L. I-227,II-723
De la Luna E. II-1075
De Luca F. I-23,I-75
De Nicola S. II-1313
De Villiers J.A.M. I-387,I-415,II-795
DeBlank H.J. I-335
DeBoo J.C. I-11
DeChiara P. I-695
Decker D.T. II-1509
Decoste R. I-215
Decyk V.K. III-1839
DeEsch H. II-897
DeGrassie J.S. II-893
Deksnis E. I-167
DeMichelis C. II-847
Dempers C.A. III-1773
Dendy R.O. I-327
Deng C.B. I-347
Deng H.C. I-223
Deng Z.C. I-223
Deutsch C. II-1245
Deutsch H. III-2095
Devynck P. I-107,II-1079
Di Lazzaro P. II-1207
Diamond P.H. II-1417
Dias J.M. II-1111
Diaz-Pinto A. III-1607
Diebold D. II-839
Dietz J. I-167
Dimits A.M. II-1275
Ding W.X. III-1765
DiPeso G. III-1993
Dippel K.H. I-403
Dmitriev V.I. I-47
Dodel G. I-191
Domier C.W. II-1071
Domier D.W. III-1939
Dominguez N. I-525,I-561,I-565,I-569
Donaldson N. I-647
Dong J.F. I-223,I-395
Donné A.J.H. II-1091,II-1143
Donoso G. III-1795
Dory R.A. I-521
Doyle E.J. I-179,I-243
Drachev V.P. II-1123
Drake J.F. I-351
Drake J.R. I-595,I-599
Drawin H.W. I-159
Dubois M.A. I-103,II-1409
Duck R. I-31,I-399
Dudnikova G.I. III-1639
Dumitrascu N. II-1561
Duncan P.J. III-1729
Dunlap J.L. I-525,II-949
Duong H. I-435
Durst R. I-203
Dwivedi C.B. III-1611
Dyabilin K.S. I-493
Dyachenko V.V. II-997
Dyakov V.E. II-933,II-941
Dyer G.R. I-521,I-525
Eberhagen A. II-1107
Edery D. II-855,II-1421
Edlinger J. III-2149
Edwards A.W. I-255,I-327,I-331,I-339,I-355, I-375,I-379,II-897,II-1051
Ehrenberg J. I-307
Ekiel-Jezewska M. III-1951
Elevant T. II-881
Elfimov A.G. I-319
Elliott J.A. III-1725
Emmoth B. I-607
Endler M. II-783,II-787
Engelhardt W. II-743
England A.C. I-521,I-525,II-949
Erba M. I-623
Erckmann V. I-497
Erdweg M. II-827
Erents S.K. II-723
Eriksson L.-G. I-343,II-881,II-897, II-1469,II-1485
Esipov L.A. II-997
Estrada T. I-99,II-1075
Euringer H. II-775
Fahrbach H.U. II-961
Fajans J. III-1811,III-1899
Fang S. I-615
Farynski A. I-717
Fasoli A. III-1863
Fedele R. II-1293
Fedorov O.V. I-471
Feix G. III-1643
Feix M. III-1741
Feneberg W. II-1477,II-1481
Fernandes C. II-1063
Ferron J.R. I-55
Fiedler S. II-1163
Fiedorowicz H. I-717
Fielding S.J. I-31
Fijalkow E. III-1741
Finken K.H. I-155,I-403
Finkenthal D. I-275
Fischer B. II-1095
Fishman H. II-949
Fitzpatrick R. I-411,I-423
Flå T. II-937,II-1309,III-1951
Fletcher J.D. I-387,I-415,II-795
Flora F. II-1207
Foltin M. III-2067,III-2075
Fonck R. I-203,II-839
Fontanesi M. III-2017
Foote J.H. II-1191
Foster C.A. I-159
Fowler T.K. I-711
Franz D. I-683
Fredrickson E.D. I-39,I-203,I-351,I-431
Freidberg J.P. II-1401
Freysinger W. III-2079,III-2083,III-2087
Friaca A.C.S. III-1647
Friedland L. II-1017
Frieling J. II-1035
Frigione D. I-463
Froissard P. I-119,II-973,II-977
Fröjdh M. II-1441
Fu B.Z. I-395
Fuchs C. I-403,II-835
Fujiwara M. I-513
Fukuda T. I-87,I-199
Fussmann G. II-831,II-835
Gabris R. III-2129
Gadeberg M. I-255
Galassi A. III-2017
Galkowski A. II-1537
Gandy R. I-115
Gangadhara R.T. III-1671
Ganguli A. III-1943

Garbet X. I-107,II-1079,II-1433
Garcia D. III-1607
Garcia L. I-565,II-1417
Garcia-Cortes I. II-791
Gasparino U. I-493,I-497,I-505,I-581,II-1001
Gavrilescu C. III-1969
Gaytan-Gallardo E. I-483,III-1947
Gee S.J. I-639
Gentle K.W. I-115
Georgieva M. II-1353
Géraud A. I-159
Gernhardt J. I-455,I-459
Gervais F. I-107,II-1079
Gettelfinger G. II-949
Ghanashev I. II-1517
Ghanem E.-S. I-131
Ghendrih Ph. II-851
Ghizzo A. II-807,II-1005,III-1737,III-1741
Ghorannevisse M. I-479
Giammanco F. II-1241
Giannella R. I-279,I-283,I-287
Giannone L. I-497,II-783,II-787
Gibson K.J. I-31
Gil C. I-107
Gill R.D. I-331,I-355,I-375,II-1051
Gimblett C. I-335
Giruzzi G. II-905,II-1103
Gladuschak V.I. II-1219
Glagolev V.M. I-703
Glosik J. III-1989,III-2083
Glowienka J.C. I-529
Goedbloed J.P. I-247
Gohil P. I-183,I-243,I-275
Golant V.E. I-471
Goldfinger R.C. II-913
Golubyatnikov G.Yu. III-1831
Gondhalekar A. I-151,I-239,II-1031
Gonella C. III-2055
Gong D.F. I-395
Gonhhalekar A. I-147
Goniche M. II-885
Goree J. II-1365
Gorini G. I-75,II-1047
Gormezano C. I-15,I-119,II-897,II-973
Goruppa A.A. III-1977
Gottardi N. I-255,I-279,II-723,II-727
Goulding R.H. II-893
Gowers C. I-15
Graffmann E. II-771
Green B. I-167
Greene J.M. I-435
Greenfield C.M. I-11
Greenough N. II-949
Greenwald R.A. III-1591
Gregory B. I-215
Grek B. I-39
Grekov D.L. I-569
Grésillon D. II-1079,II-1083,III-1591
Gribok V.A. II-929
Grigull P. II-1167
Grill V. III-2075,III-2095
Grisham L. I-43
Groebner R.J. I-179,I-183,I-187,I-275
Grosman A. II-847,II-851
Grozev D. III-2041
Gruber O. I-451,I-455,I-459,II-743
Gruber R. I-557,I-589
Gryaznevich M. I-399
Gudowska I. I-607
Günther K. II-875
Guo D.Q. I-347
Guo G.C. I-223,I-395
Guo S.C. II-1437
Gusakov E.Z. II-1203
Gusev V.K. II-1219
Gyergyek T. II-1171,III-1761
Hadjoudj Y. III-1915
Hahnheuser R. I-647
Haines M.G. I-655
Hakr J. I-667
Hall D.S. III-1627
Hamilton R.L. II-1349
Han J. I-335
Hanada K. I-79
Hanatani K. I-489,II-1131
Hansel A. III-2079
Hansen B.M.S. II-1397
Hanson G.R. I-525
Hanssen A. II-1279
Hanuise C. III-1591
Harbour P.J. II-723
Harmeyer E. I-581
Harris G. I-107
Harris J.H. I-525,II-949
Hartfuß H.J. I-497,II-1001,II-1099
Harvey R.W. II-893
Hasegawa A. I-711
Hastie R.J. II-1393
Hatakeyama R. III-1705,III-1709,III-1765,III-1919
Hatcher R. II-949
Hazeltine R. I-211
Hegna C.C. II-1413
Heidbrink W.W. I-435
Heijnen S.H. II-1059
Heikkinen J.A. II-1021,III-1923
Hellberg M.A. I-387,II-1397,II-1477,III-1819
Hellblom G. I-595
Heller M.V.A.P. II-803
Hender T.C. I-335,I-339,I-399,I-411,I-423
Hennequin P. I-107,II-1079,II-1409
Hensler E. II-1389
Herrmann H. II-949
Hershkowitz N. II-839,II-909
Hess W. II-847
Hesthaven J.S. III-1903
Heuraux S. III-1915
Hidalgo C. II-783,II-791
Higashijma S. II-1131
Hill D.N. I-243,II-751
Hill K.W. I-39
Hillis D.L. I-275
Hirano Y. II-917
Hirayama S. I-699
Hirshman S.P. I-589
Hoang G.T. I-27,I-103,II-885,II-945
Hoenen F. I-155
Hoffman D.J. II-893
Hofmann F. I-343,I-467
Hofmann J.V. II-1155
Hogan J.T. I-275
Hogeweij G.M.D. I-71,I-75
Holzhauer E. I-191
Honda C. II-1159
Honda R.Y. I-675
Hong J.S. III-2033
Honzawa T. II-1337,III-1603,III-1911
Hörhager M. III-1685
Hori M. III-1965
Hörling P. I-611
Horton L.D. I-307,II-1035
Hoshino K. II-1191
Hosokawa M. I-513,I-517
Howarth P.J.A. I-251
Huang K.Q. I-223
Huang R. I-347
Huart M. I-167
Hübner G. II-1541
Hübner K. II-1485
Hugenholtz C.A.J. II-1059

Hugill J. I-31
Hugon M. I-3,I-119
Huguet M. I-167
Humbert P. II-1249
Hutchinson D.P. I-521
Hutter T. I-27,I-107
Huysmans G.T.A. I-247
Hyatt A.W. I-187
Ianopol B. III-1957
Ida K. I-513,I-517
Ide S. II-953,II-969,II-985
Idei H. I-513,I-517
Ignacz P.N. I-303
Ignat D. II-949
Iguchi H. I-513,I-517
Iima M. I-489
Ijiri Y. I-489
Ikeda Y. II-953,II-969,II-985
Ikegawa M. III-2109
Ikehata T. III-1891,III-1985
Imai T. II-953,II-969,II-985
Ingesson L.C. II-1143
Inoue M. III-1651
Inovenkov I.N. II-1305,II-1317
Intrator T. II-839
Irie M. I-643
Irzak M.A. II-1025
Ishii H. II-917
Ishii S. III-1961
Isler R.C. I-521,I-525,I-529,II-949
Its E.R. II-997
Iwama N. III-1961
Jacchia A. I-23,I-75
Jäckel H.J. II-723,II-823
Jackson G.L. I-11
Jacquinot J. I-167,I-311,I-327,I-335, II-881,II-897,II-901
Jadoul M. I-359
Jaeger E.F. II-913
Jaenicke R. I-549
Jafelice L.C. III-1647
Jäger H. II-1151
Jakovenko V.P. I-47
Jakubka K. I-219
Jakubowski L. II-1215
James R.A. II-893
Janeschitz G. II-723,II-727
Janicki C. I-215
Jardin S. II-949
Jarmen A. II-1441
Jarvis N. II-881
Jarvis O.N. I-67,I-167,I-251
Jaspers R. I-155
Jasperse J.R. II-1373,II-1509
Jassby D.L. I-39,I-43
Jelic N. II-1171,III-1761
Jenichen F. II-835
Jensen V.O. II-1545
Jernigan T.C. I-521,I-525
Ji H. I-521
Jiang Y. I-363
Jiang Y.X. I-223
Jiang Z.X. I-603
Jimenez J.A. I-561
Jimenez-Dominguez H. I-483,III-1947
Jobes F. I-39
Joffrin E. II-855,II-945,II-1421
Johnson D.W. I-39
Johnson J.L. I-577
Johnson L.C. I-39
Jones I.R. I-647
Jones S.E. I-163,I-407,II-949
Jones T. I-255,II-881
Jones T.C.C. I-19
Jones T.T.C. I-3,I-263,I-307
Jong R.A. II-751
Jülich A. I-455
Junker J. I-509
Junker W. II-743
Kahlbaum T. III-2009
Kaita R. II-949
Kajiwara T. II-1159
Kakehi Y. III-2109
Kakoulidis E. II-767
Kallenbach A. I-231,I-459,II-835
Källne E. I-611
Källne J. II-1047
Kalvin S. I-303
Kamp L.P.J. III-1745
Kanaev A.I. I-47
Kaneko O. I-517
Kantor M.Yu. II-1219
Kaplan Z. III-2117
Kardaun O.J.W.F. I-7,I-35
Kardon B. I-303
Karlson E.T. I-635,I-671
Karlsson P. I-595
Karpman V.I. II-1283
Karttunen S.J. II-1005
Katsonis K. II-1245,III-2063
Katsouleas T. II-1301
Kaufmann A.N. II-937,III-1951
Kaufmann M. II-743,II-747
Kauschke U. III-1981
KavinA.A. I-471
Kaw P.K. II-1301
Kawabe T. I-699,III-2155
Kawachi T. II-981
Kawaguchi N. III-1651
Kawai Y. III-1733,III-1807,III-1855,III-1887
Kawashima H. II-893
Kaye S. II-949
Kennel C.F. II-1349
Kerner W. I-247,I-335,I-439
Kesner J. I-407,II-949
Khan M. II-1257
Kholin N.N. III-2137
Khristova D. II-1353
Khudoleev A.V. I-151,I-167,II-1031
Kick M. I-505,I-509
Kilic H. I-695,II-1253
Kim J. I-183
Kim S.K. III-2133
Kinsey J. I-131
Kirsanov V.I. II-1305,II-1317
Kishino T. I-79
Kisigami Y. I-79
Kislov D.A. I-207,I-371
Kiss`ovski Zh. III-2013
Kißlinger J. I-501,I-549,I-585,I-569,I-581
Kitajima M. III-2155
Kiyama H. II-799
Kiyama S. II-799,III-1781
Klepper C.C. I-275
Kletecka P. I-219
Kleva R.G. I-351
Klinger T. III-1677,III-1843
Knorr G. II-807,III-1721
Kobayashi J. III-2109
Kobayashi S. I-489
Kocsis G. I-303
Koepke M.E. III-1895
Kogoshi S. I-403
Kohmoto T. I-517
Kolesnichenko Y.I. I-391
Komori A. III-1733,III-1807,III-1851, III-1855,III-1887
Kondo K. I-489,II-1131
Kondoh T. II-953,II-969,II-985
Kondoh Y. II-917

König R. I-167,I-263,I-339,I-379, II-881,II-1035
Konings J.A. I-71
Kono M. III-1851,III-1855,III-1887
Köppendörfer W. I-451
Korchinsky G.M. II-1377
Korn J. III-1717
Korneev D.O. I-111
Korolev A. III-1599
Korotkov A.A. II-1031,II-1039,II-1043
Kortshagen U. III-2145
Koslovski H.R. I-383,I-403
Kostsov Y.A. I-471
Kovan I.A. I-47
Kovrizhnykh L.M. I-525
Koyama K. II-1225
Kozochkin S.M. II-1229
Krafft C. II-1297
Kramer G.J. I-15,I-227,I-259,I-335,I-339
Krämer M. II-1095
Krämer-Flecken A. I-95,I-383
Krasilnikov A.V. I-47
Krasnikov Yu.I. II-1123
Krause A. I-451
Kravarik J. I-667
Kremp D. III-2091
Krieger K. II-831
Krishan V. III-1671
Krlin L. II-1013
Kroegler H. I-463
Krumm P. III-1773
Kryska L. I-219
Kuang G. I-359
Kubarev Y.V. III-2137
Kubes P. I-667
Kubo H. III-1631
Kubo S. I-513,I-517
Kugel H. II-949
Kuhn S. II-1549,III-1685,III-1777, III-1785,III-2001
Kühner G. I-501,I-581
Kukharkin N.N. II-1453
Kulhanek P. I-667
Kupfer K. II-885,II-905
Kupschus P. I-255
Kurasawa T. II-1405
Kurdel M. III-2095
Kuroki H. III-2155
Kus A. I-7,I-35
Kusaka S. III-1931
Kusano K. III-1631
Kuus H. II-885
Kuvshinov B.N. I-703
Kuyanov A.Yu. II-1521
Kwak J.K. III-2133
Kyriakakis G. II-767
La Haye R.J. I-179,I-187
Lachambre J.-L. I-215
Lackner K. I-455,I-459
Lafrance D. I-215
Laing E.W. II-1505
Lakhina G.S. III-1623
Lalousis P. II-1525
Lao L.L. I-11,I-55,I-243,I-435
Larenz R.W. II-1381
Larsson J. III-1749
Lashkul S.I. II-997
Last J. I-167
Laurent L. I-27,II-1433
Lauro-Taroni L. I-279,I-283,I-287
Laviron C. I-107,II-1079
Lawande S.V. II-1257
Lawson K.D. I-3,I-19,I-291,I-307
Lazaros A. I-549
Lazzaro E. I-443
Le Clair G. I-215
Le Gourrierec P. III-2125
LeBlanc B. II-949
Leboeuf J.N. I-525
Leclert G. III-1883,III-1915
Lecoustey P. II-855,II-945,II-1421
Lee D.K. I-525
Lehnert B. II-1529
Lengyel L.L. I-323
Lesourd M. II-727,II-823
Letardi T. II-1207
Leubner C. III-1667
Leuterer F. II-957,II-961
Levinton F. II-949
Levitsky A.N. I-471
Leys C. II-1147
Lezius M. III-2071,III-2075
Li G.X. I-347
Li H.Z. I-223
Li J. I-31,I-615
Li K.H. I-223
Li L.H I-347
Li Q. I-615
Li W.L. I-115
Liang W.X. I-395
Liberman M.A. I-635,I-671,II-1261,III-1599
Lieder G. I-459
Likin K.M. I-525
Lim C.S. II-1501
Lin H. I-363
Lindinger W. III-2079,III-2083,III-2087
Lingertat J. II-727,II-823
Linhart J.G. II-1253,II-1265
Liniers M. II-791
Lisak M. I-391
Litaudon X. I-27,II-885
Liu W.D. II-1103
Liu-Hinz C. I-215
Loarte A. II-723
Lohr J.L.T.C. II-893
Lok J. I-267
Lomas P.J. I-3,I-19,I-147,I-255,I-307, II-881,II-897
Longinov A.V. II-921,II-929,II-933,II-941
Lontano M. II-1087
Lopes Cardozo N.J. I-71,I-75,I-123,I-155
Lopez-Callejas R. I-483,III-1947
Lopez-Fraguas A. I-565,I-577
Loughlin M.J. I-167,I-251
Loureiro C. II-1063
Louvet P. III-2113,III-2125
Lovisetto L. I-463
Lowry C.J. I-239,II-723,II-727
Lozneanu E. III-1769
Luckhardt S.C. I-407,II-949
Luhmann Jr. N.C. I-363,I-179,II-1071,III-1939
Lukac P. III-2067,III-2129
Lukinov V.A. II-921,II-929
Luo C. I-615
Lyadina E. I-371
Lynch V.E. I-569,II-1417
Lynov J.-P. II-811,II-1283,III-1903,III-1907
Lyon J.F. I-525
Ma C.H. I-521,I-525
Maafa N. II-1083
Maas A.C. I-151,I-167,II-1031
Maaßberg H. I-493,I-497,I-505,I-509, I-549,I-569,I-581
Mace R.L. III-1819
Machida M. I-675
Maciel H.S. III-1835
MacLatchy C. I-215
Maeda H. II-1191
Maeda M. I-517,II-1159
Maehara T. I-79

Maekawa T. I-79,II-981
Maggi C.F. II-823
Magula P. I-219
Magyar G. I-283
Maier H. III-2001
Majeski R. II-839
Makino K. I-79
Malaquias A. II-1111
Maluyta D.D. II-1229
Mancuso A. I-545
Mandl W. II-1035
Manhood S.J. I-31
Manickam J. I-43,I-351,II-949
Mank G. I-155
Mansfield D.K. I-39
Manso M.E. I-231,II-1063
Mantica P. I-23,I-75
Marcus F.B. I-67,I-251,I-263,I-339,I-379, II-881,II-897
Margreiter D. III-2095
Märk T.D. III-2067,III-2071,III-2075,III-2095
Martin F. I-215
Martin G. I-175
Martin P. I-623,II-1361,III-1795
Martin R. I-639
Martin T.J. II-1393
Martin-Solis R. I-147
Martinell J.J. II-1461
Martines E. I-631
Mase H. III-1891,III-1985
Mast K.F. II-835
Matias J. I-231
Matsui T. III-2121
Matsukawa M. I-447
Matsumoto K. II-989,III-1961
Matsumoto Y. II-1225
Matsuoka K. I-513,I-517
Matsuoka M. I-171
Matsushima I. II-1225
Matsuura H. I-489
Matsuura O.T. III-1619
Matthews G.F. II-823
Matthieussent G. II-1297
Mattioli M. I-279,I-283,II-847
Mauel M.E. I-711
Mayberry M.J. II-893
Mayer H.-M. II-835
Maynard G. II-1245,III-2063
Mazur S. I-595,I-599
Mazzitelli G. I-295,I-463,II-1127
Mazzucato E. I-203,II-1055
McCarthy P.J. I-451,I-455,I-459
McCormick K. II-763,II-767,II-1163
McCracken G.M. II-779
McCune D.C. I-39,I-43
McGuire K.M. I-43,I-203,I-351
McKee G. II-839
McLoud W.S. II-1397
McNeill D.H. I-295,II-1127
McWilliams R. III-1935
Medley S.S. I-203
Medvedev S.Yu. I-319
Meigs A. I-211
Meis C. III-2113
Meister C.-V. III-2159
Melendez-Lugo L. I-483,III-1947
Melnick I.M. I-291
Merazzi S. I-557,I-589
Merkel P. I-585
Mertens V. I-451,II-743
Meyer R.L. III-2113
Mezzetti F. I-695
Michaud D. I-215
Michelsen P. II-1067,II-1283
Micozzi P. II-1525
Mieno T. III-1859,III-1919
Miklaszewski R. I-717
Mikoshiba H. III-1651
Miljak D.G. II-815
Minami T. I-79
Minardi E. II-1465
Minyaev O.A. I-471
Mioduszewski P.K. I-275
Mirnov S.V. I-47
Mirrashidi P. III-1993
Miura S. I-171
Miyakuni S. III-1709
Miyamoto T. I-659
Mizuno K. II-1191
Mizuno N. I-699
Mizuuchi T. I-489,II-1131
Mjølhus E. II-1279,II-1349
Mlynar J. I-219
Mohamed-Benkadda M.S. II-855
Mohanty S.R. II-1195
Moiseev S.S. I-707
Molinari V. III-2037
Monakhov I.A. I-47
Monier-Garbet P. II-847
Monterde P. II-1183
Monticello D.A. I-351,I-577
Moradshahi M. I-479
Morales G.J. I-135,III-1839
Moreau D. I-27,I-159,I-175,II-885, II-905,II-945
Moreira A. II-1063
Morera J.P. II-1421
Morgan P.D. I-3,I-119,I-255,I-307,II-1485
Morimoto S. I-521
Morin M. III-2055
Morita S. I-513,I-517
Moroz P.E. II-909
Morris A.W. I-31,I-411,I-423
Morsi H. I-3,I-255
Morsi H.W. I-19
Moser F. II-1497
Motojima O. I-521
Mroczkowski M. I-717
Muir D. I-59
Murakami M. I-521,I-525,I-529
Muraoka K. I-517,II-1159
Murawski K. III-1635
Murmann H.D. II-961
Mynick H.E. I-431
Myra J.R. I-91
Nagao K. III-1733
Nagasaki K. I-489,II-1131
Nagasawa T. III-1815
Nagashima K. I-83,I-87
Nagayama Y. I-351
Naito O. II-953
Naitou O. II-985
Nakach R. II-1409
Nakamura M. I-79,II-981
Nakamura Y. I-489,I-557
Nakasuga M. I-489,II-1131
Nambu M. III-1693
Nappi C. II-1313
Nardi V. I-695,II-1253
Naujoks D. II-843
Naumova N.M. II-1305,II-1317
Navarro A.P. II-933
Nave M.F.F. I-227,I-247,I-327,I-335, I-339,I-439
Nazikian R. I-203,I-431,II-1055
Neger T. II-1151
Neill G.F. I-227
Nejoh Y. III-1655,III-1799
Nemoto M. II-953,II-985
Nenovski P. III-1635

Neubert T. . . . III-1579
Neudatchin S.V. . . . I-59
Neuhauser J. . . . II-743,II-747,II-767
Neves J. . . . II-1063
Neyatani Y. . . . I-171,I-447
Nguyen F. . . . II-851
Niedermeyer H. . . . II-783,II-787
Nielsen A.H. . . . II-811
Nielsen P. . . . I-3,I-19,I-255,I-307
Nilson D.G. . . . II-1191
Ninomiya H. . . . I-447
Nishida Y. . . . III-1815,III-1927,III-1931
Nishikawa K.-I. . . . III-1579
Nishimura K. . . . I-513,I-517
Nishio R. . . . III-2121
Nishitani T. . . . I-171
Noda N. . . . I-403,I-513,I-517
Nonaka S. . . . III-2045
Nordlund P. . . . I-595,I-599
Norimine T. . . . III-1855
Nothnagel G. . . . I-415,II-795
Notte J. . . . III-1811
Novik K.M. . . . II-997
Nührenberg J. . . . I-553
Nunes F. . . . II-1063
Nycander J. . . . III-1903,III-1907
O'Brien D.P. . . . I-63,I-311,I-335,I-339
O'Brien M.R. . . . I-147,I-423,II-897,II-1341
O'Rourke J. . . . I-15,I-255,I-259,I-311, I-335,I-339,I-379
Obiki T. . . . I-489,II-1131
Ochando M.A. . . . I-99,II-791
Ochirov B.D. . . . II-1229
Oda T. . . . II-1191
Oda Y. . . . II-859
Odajima K. . . . II-1191
Ogawa T. . . . II-1191
Ohasa K. . . . II-1191
Ohkubo K. . . . II-989
Ohno N. . . . II-1115,III-1807
Øien A.H. . . . III-1997
Okabayashi M. . . . II-949
Okada H. . . . I-489,II-1131
Okada T. . . . II-1159,III-2099
Okamura S. . . . I-513,I-517
Ongena J. . . . II-1147
Ono M. . . . II-949
Oomens A.A.M. . . . I-71,I-267
Orishich A.M. . . . III-1689
Orsitto F. . . . I-295
Ortolani S. . . . I-623
Osborne T.H. . . . I-11,I-235
Osborne T.O. . . . I-243
Owadano Y. . . . II-1225
Oyevaar Th. . . . II-1091
Ozaki T. . . . I-517
Paccagnella R. . . . I-627
Pacher G.W. . . . I-475,II-755
Pacher H.D. . . . I-475,II-755
Pacios L. . . . I-299
Pakter R. . . . III-1697
Palladino L. . . . II-1207
Panaccione L. . . . I-295
Pantis G. . . . I-143
Parail V.V. . . . I-207
Pardo C. . . . I-99,I-299
Paris P.J. . . . II-1187,III-1863
Park C.W. . . . III-2133
Park H.K. . . . I-39
Park J.K. . . . III-2133
Park W. . . . I-351
Parker R.D. . . . I-427
Parlange F. . . . II-885,II-945
Parys P. . . . I-717
Pasini D. . . . I-279,I-283,I-331
Patel A. . . . I-291
Patel T.K. . . . I-291
Pättikangas T.J.H. . . . II-1005,II-1021
Paul S. . . . I-203,II-949
Pavlenko V. . . . II-1441
Pavlichenko O.S. . . . I-569,II-933
Pavlov I.P. . . . II-1025
Pavlov S.S. . . . II-921,II-933
Payan J. . . . I-107,II-1079
Peacock N.J. . . . I-291
Pech P. . . . II-1167
Pecquet A.L. . . . I-107,II-855,II-1421
Pécseli H.L. . . . II-811,II-1067
Pedit H. . . . III-1777
Pedrosa M.A. . . . II-791
Peebles W.A. . . . I-363,I-179,II-1071,III-1939
Pegoraro F. . . . I-139,II-1425,II-1429
Pégourié B. . . . I-103,I-159
Penningsfeld F.-P. . . . I-537
Pereira J. . . . II-1063
Pereverzev G.V. . . . II-961,II-1489
Persson H. . . . II-1369
Pestryakova G.A. . . . I-319
Peters M. . . . I-75
Petrov A.A. . . . I-47
Petrov M.P. . . . I-151,I-167,II-1031
Petrov V.G. . . . I-47
Petrov Y.V. . . . II-1219
Petrzilka V. . . . I-271
Petty C.C. . . . II-893
Peurrung A.J. . . . III-1899
Peysson Y. . . . I-27,I-159,II-885
Pfau R. . . . I-683
Pfirsch D. . . . II-1329,III-1753
Philipona R. . . . I-179
Philipps V. . . . II-827
Phillips P.E. . . . I-115
Pichal J. . . . I-667
Pickalov V.V. . . . II-1143
Piel A. . . . II-1199,III-1677,III-1843
Pierre T. . . . III-1879,III-1883,III-1915
Pietrzyk Z.A. . . . II-763
Piffl V. . . . I-713
Piliya A.D. . . . II-1203
Pinsker R.I. . . . II-893
Pironkova A. . . . III-2013
Pisarczyk T. . . . I-717
Plapp B.B. . . . III-1659
Platonov Yu.Ya. . . . II-1039
Pöckl M. . . . II-1163
Podda S. . . . I-463
Poll H.U. . . . III-2095
Ponomarenko A.G. . . . III-1689
Popa G. . . . II-1179,II-1561,III-1757,III-1969
Popel S.I. . . . II-993
Popov G.H. . . . III-1803
Porcelli F. . . . I-439,II-897,II-901,II-1469
Porkolab M. . . . II-893,II-965
Porte L. . . . I-119,I-163,I-407
Porter G.D. . . . II-751
Portnov D.V. . . . I-47
Poschenrieder W. . . . II-1167
Potempski S. . . . II-1537
Poutchy L. . . . II-847
Powell C. . . . I-695
Prasad G. . . . III-1575,III-1583,III-2021
Prater R. . . . II-893
Praxedes A. . . . II-1111
Praxmarer C. . . . III-2079,III-2083
Preische S. . . . II-949
Probert P. . . . II-839
Proshin M.A. . . . I-703
Prudsky V.V. . . . II-1345
Pryadko J.M. . . . II-1321
Puerta J. . . . II-1513

Pulker H.K. III-2149
Punithavelu A.M. III-2025
Punjabi A. II-863
Putvinskii S. I-167
Qin Y.W. I-223
Quallis A.L. I-525
Quéméneur A. I-107,II-1079
Radford G. II-727
Ramachandran H. I-135,III-1839
Ramos G. II-1461
Ramos J.J. I-407
Ramponi G. II-973
Ramsay D. II-1505
Ramsey A.T. I-39,I-203
Ran L.B. I-223
Rao N.N. III-1643
Rasmussen D.A. I-521,I-525
Rasmussen J.J. II-811,II-1283,III-1907
Rau F. I-569,I-581
Raus J. I-713
Rauth T. III-2075
Rawat R.S. II-1195,III-2141
Razdobarin G.T. II-1219
Razumova K.A. I-207,I-371
Reale A. II-1207
Rebut P.-H. II-731
Reiman A.H. I-577
Reiter D. II-739,II-747
Rem J. II-1425
Renberg P.U. II-1047
Renner H. I-493,I-501,I-505
Rensink M.E. II-751
Retterer J.M. II-1509
Rettig C.L. I-11,I-179
Rewoldt G. II-1437
Rey G. II-885
Reyna L.G. III-2103
Rhee C. III-2133
Rhodes T.L. I-179,II-1071
Riccardi C. III-2017
Rice W.K.M. III-1819
Richards B. I-115
Righi E. II-881
Rille E. III-2149
Rimini F. I-119,II-897,II-973
Ringler H. I-493,I-501,I-505,I-581
Rizzato F.B. III-1697
Roach C.M. II-1139
Roberts D.E. I-387,I-415,II-795,II-1397
Robinson D.C. I-31,I-399
Rodriguez L. II-933
Rodriguez-Yunta A. I-99
Roe G. I-639
Rognlien T.D. II-751
Rohde V. II-1199
Röhr H. II-743
Romanelli F. I-463,II-1437
Romannikov A.N. I-47
Rommers J.H. I-267
Roney P. II-949
Rosatelli C. II-1187
Ross D.W. I-115
Ross G.G. I-215
Rossi A. I-623
Roth J. II-831,II-1167
Roubin J.-P. I-175,II-1433
Rousculp C. III-1827,III-1831
Rowan W.L. I-115,I-211
Rubenchik A.M. II-1229
Rudyj A. II-783,II-787
Ruiz J. II-1513
Rupasov A. I-683
Rusbridge M.G. I-639,III-1725,III-1729
Rusbüldt D. I-155,II-775
Ruscanu D. II-1179
Rynn N. III-1935
Ryter F. I-7,I-195,II-889
Sabbagh S.A. I-43
Sabot R. I-103,II-1409
Sadler G. I-3,I-67,I-167,I-251,I-255, I-263,I-439,II-881,II-1485
Sadowski M. I-691,II-1211,II-1215
Safronov V.P. III-2137
Sagar R. III-2141
Sagara A. I-513,I-517
Saha S.K. I-107,II-1079
Saibene G. II-723,II-727
Saito K. II-917
Sakakibara S. I-517
Sakamoto K. I-489
Sakamoto M. I-403
Sakanaka P.H. I-675,I-679,II-1233,III-1619
Sakasai A. I-87
Sakawa Y. III-1965
Sakharov A.S. II-1305,II-1317,II-1429
Sakharov I.E. II-997
Sakharov N.V. I-471
Sakurai S. II-859,II-1115
Salas A. I-577
Salashchenko N.N. II-1039
Salat A. I-573
Salmon N.A. II-1107
Salomaa R.R.E. II-1005
Salvetti A. II-1241
Samain A. II-851,II-855,II-1421,II-1433
Samm U. II-759
San Jose M.A.G. II-1183
Sanchez J. II-1075
Sandeman J. III-1725
Sanduloviciu M. III-1769,III-1957,III-2029
Sano F. I-489,II-1131
Santiago M.A.M. I-675,III-1785
Santos J. II-1063
Sanuki H. I-513,I-517
Saoutic B. I-175,II-885,II-905
Sardei F. I-505,I-509,I-549
Sarksyan K.A. I-525
Sartori R. I-3,I-307
Sasao M. I-67
Sato K.N. I-403,II-1191
Sato M. I-489,I-521,II-953
Sato N. III-1705,III-1709,III-1765,III-1919
Sato N.Y. III-1705,III-1709,III-1985
Sato T. III-1631,III-1965
Sattler S. II-1099
Sauer K. III-1571
Sauthoff N. II-949
Savrukhin P. I-371
Sawada K. II-981
Sawahata M. II-985
Saxena Y.C. III-1575,III-1583,III-1847, III-1867,III-2021
Sayal V.K. III-1823
Sborchia C. I-167
Scafati A. II-1207
Schamel H. II-1385,III-1717
Scheffel J. I-663
Scheier P. III-2071,III-2095
Schep T.J. II-1425
Schiavi A. I-619
Schina G. II-1207
Schissel D.P. I-11,I-235
Schivell J. I-203
Schlanges M. III-2091
Schlüter H. III-1981,III-2145
Schlüter M. II-1449
Schmid M. I-327
Schmidt G.L. I-59,I-255,I-307
Schmidt H. I-683
Schneidenbach H. III-2009

Schneider R.S. II-747,III-1697
Schneider W. I-459
Schoch P.M. I-115
Schoon N. II-1147
Schram D.C. II-1143
Schrittwieser R. III-1757,III-1773
Schüller F.C. I-71,I-123,I-155,II-1091
Schulz D. I-683
Schumacher U. II-835
Schupfer N. III-1785
Schwab C. I-549
Schweinzer J. II-763,II-1163
Schwelberger J.G. I-529
Schwenn U. I-557
Scott B.D. II-1449
Scott S.D. I-39,I-43,I-203
Scoville J.T. I-187
Segre S.E. I-127,I-295
Seidel U. I-451,I-455
Seki M. II-953,II-969,II-985
Seki S. II-949
Selenin V.L. II-1203
Semenov I.B. I-47
Semenov V.V. II-1219
Sen A. II-1301
Senju T. I-489
Senties J.M. II-1183
Seraydarian R.P. I-183,I-275
Sergeyev A.A. I-111
Serichol N. III-1607
Serra F. I-231,II-1063
Sesnic S. II-949
Sethia G.C. III-2021
Shah H.A. II-1317
Shakhovets K.G. I-471
Shapiro V.D. II-1271
Sharapov V.M. I-47
Sharma R.P. II-1325
Sharma S.K. III-1567,III-1595
Sharma S.R. III-1823
Shasharina S.G. I-541
Shatalin S.V. II-997
Shats M.G. I-525
Shcherbinin O.N. II-997,II-1025
Sheridan T.E. III-1895
Sherwell D. II-795,II-1397
Shevchenko V. II-1271
Shi M.L. I-395
Shigueoka H. I-679,III-1619
Shiina S. II-917
Shimada T. II-917
Shinno H. III-2155
Shirai H. I-83
Shirokikh A.V. II-1229
Shishkin A.A. I-569
Shivarova A. II-1353,III-2013
Shmaenok L.A. II-1039
Shmykov V. II-1557
Shoji T. III-1965,III-2121
Shoucri M. II-807,II-1005,III-1721,III-1741
Shoyama H. III-1733
Shukla P.K. II-1293,II-1445,III-1587, III-1611,III-1643
Sibley A. I-327
Sicha M. III-1989
Silva A. I-231,II-1063
Simonchik L.V. II-1203
Simonetto A. I-443
Simonini R. I-259
Sindoni E. III-2017
Sing D.C. I-115
Singer C. I-131
Singh A.K. III-1847,III-1867
Singh D.P. II-1241
Singh S. II-1337,III-1603,III-1911
Sinman A. I-651
Sinman S. I-651
Sipilö S.K. II-1021
Sips A.C.C. I-259
Sitenko A.G. II-1287
Skalny J.D. III-2129
Skiff F. III-1863
Skladnik-Sadowska E. II-1211
Skorik M.A. III-1973,III-1977
Skovoroda A.A. II-1521
Sluijter F.W. III-1745
Smeulders P. I-251,I-327,I-331, I-335,I-339,I-439
Smith D. III-2083
Smith G.R. II-1275
Smith R. I-163
Smith R.J. I-407
Snipes J.A. I-39
Snytnikov V.N. III-1689
Sobehart J. III-2103
Solano E. I-211
Söldner F.X. II-957,II-961,II-1063
Soltwisch H. I-403
Sørensen J. II-839
Sosenko P.P. II-1287
Sotnikov S.M. I-47
Spangler S.R. III-1659
Spathis P.N. I-323
Squire J.P. II-965
Srivastava M.K. II-1257
Srivastava M.P. II-1195,III-2141
St.-Onge M. I-215
Stäbler A. II-743
Staikov P. III-2041
Staines G.W. I-647
Stallings D.C. II-913
Stamate E. II-1179
Stamp M.F. I-119,I-307,I-311,I-335, I-339,II-727,II-819
Stankiewicz R. II-1469,II-1537
Stanojevic M. II-1171,III-1761
Stansfield B. I-215
Start D.F.H. I-3,I-19,I-255,I-327, II-881,II-897,II-901
Stenflo L. II-1533,III-1587
Stenzel R.L. III-1827,III-1831,III-1871
Stepanov A.Yu. II-997
Stepanov K.N. II-933
Stephan K. III-2095
Steuer K.-H. II-743,II-961
Stevens J. II-949
Stöckel J. I-219
Stork D. I-167,I-311,I-339,I-379,II-897
Stotler D. I-43
Strait E.J. I-435
Stratton B.C. I-203
Stratton B.E. I-39
Strel'tsov A.P. II-1229
Stroth U. I-7,I-35,I-195I-509,
Stubberfield P.M. I-15,I-63,I-255,I-263,I-311
Su J.J. II-1271,III-1627
Subbotin A.A. I-367
Suchy K. II-1501
Sudarshan A. III-1567,III-1595
Sudo S. I-489,II-1131
Suemitu H. II-981
Suganuma K. II-985
Sugawara M. III-2099
Sugimoto H. II-1405
Sugimoto M. III-1887
Sumini M. III-2037
Summers D.D.R. I-3,I-307,I-335,II-723, II-727,II-779,II-823
Summers H.P. II-823,II-1035
Sun S.Q. I-223

Sunka P. I-713
Surendra M. III-1993
Sutcliffe M. III-1725
Suyazov N.V. I-707
Suzuki K. III-2121
Sykes A. I-31,I-399
Synakowski E.J. I-39,I-203
Szczurek M. I-717
Szigeti J. I-303
Szydlowski A. I-691
Tabares F.L. I-99
Tagle J.A. II-723
Taglieri G. II-1207
Takahashi C. I-513,I-517
Takahashi H. II-949
Takahashi S. II-985
Takamura S. II-859,II-1115,III-1807
Takasa A. II-985
Takeiri Y. I-517
Takenaga H. I-517,II-1159
Takeuchi H. I-171,II-953,II-969,II-985
Takita Y. I-513,I-517
Takiyama K. II-1191
Takizuka T. I-51
Talasman S.J. III-1957
Talvard M. II-855,II-1103,II-1421
Tamano T. III-1631
Tamaoki M. III-1733
Tammen H.F. II-1091
Tanabe T. III-1985
Tanaka M. II-1357,III-1733,III-1855,
III-1859,III-1887
Tanaka S. I-79,II-981
Tanaka T. II-839
Tang W.M. II-1437
Tanga A. I-3,I-19,I-255,I-443,II-881,II-897
Tani K. I-171
Tanizuka N. III-1651
Tanzi C. II-973
Tarditi A. II-1187
Taroni A. I-3,I-15,I-19,II-727,II-901
Tartari U. II-1087
Tashaev Y.N. III-2137
Tataronis J.A. II-909,II-1009
Tavares-Azevedo M. I-675
Taylor G. I-39,I-203,I-351
Taylor T.S. I-11,I-55,I-243,I-435
Telesca G. II-771,II-1147
Tennfors E. I-607
Terreault B. I-215
Terumichi Y. I-79,II-981
Teubel A. I-537
Theimer G. II-783,II-787
Thomas C.E. I-525
Thomas P.R. I-239,II-727,II-819
Thomsen K. I-19
Thomsen K. I-3,I-63
Throumoulopoulos G.N. I-143
Tibone F. I-15,I-19,I-311,I-335,I-339
Tichy M. III-1989
Tielemans A.J.H. I-267
Timm R. III-1677
Timofeev A.V. I-703,II-1521
Tobita K. I-171
Todoroki J. I-513
Toi K. I-513
Tokar M.Z. I-95,II-739,II-759
Tolstyakov S.Yu. II-1219
Toma M. III-2029
Tomie T. II-1225
Tonon G. I-27,II-885,II-945
Torres-Silva H. II-1233
Torvén S. II-1175,III-1875
Toshi K. I-489
Towner H.H. I-39
Tracy E. II-937
Tran M.Q. III-1863
Tribaldos V. II-1001
Truc A. I-107,II-1079
Tsintsadze L.N. II-1485
Tsois N. II-767
Tsui K.-H. I-675
Tsytovich V.N. II-993,II-1271,II-1321,II-1333
Tubbing B.J.D. I-15,I-167,I-311,I-335,
I-339,II-897
Tuchida K. III-2121
Tudisco O. I-23,I-463
Tugarinov S.N. I-47
Turnbull A.D. I-243,I-435
Turner M.F. I-31
Tuszewski M. I-431
Tutter M. I-497,II-1001
Uberoi C. III-1663
Uchino K. I-517,II-1159
Uckan T. I-525,I-529
Ueda M. I-513,I-517
Uehara K. II-1473
Uehara M. III-1835
Umesh G. III-1943
Urrutia J.M. III-1827,III-1831
Ushigusa K. I-447,II-953,II-969,II-985
Vahedi V. III-1993
Valanju P.M. I-115,I-211
Valencia-Alvarado R. I-483,III-1947
Valeo E. II-949
Vallet J.C. II-847,II-855,II-945,II-1421
Valovic M. I-31
Van Belle P. I-67,I-167,I-251,II-881
Van Blokland A.A.E. II-1091
Van Bruggen-Kerkhof M.J. III-1745
Van de Pol M.J. II-1059
Van Dijk G. I-267
Van Gelder J.F.M. I-267
Van Houtte D. I-27,II-885,II-945
Van Lammeren A.C.A.P. I-123
Van Milligen B.Ph. I-123
Van Oost G. II-771,II-1147
Van Toledo W. II-1111
Van Vurren G.W. I-387,I-415
Vannucci A. I-419
Varandas C.A.F. II-977,II-1111
Varela P. I-231,II-1063
Varias A. I-561,I-565
Varma R.K. III-2025
Vaselli M. II-1241
Vasilescu C. III-2049
Vasiliev V.I. I-471
Vega J. I-99,I-299
Veres G. I-303
Verga A.D. II-1325
Verheest F. III-1623
Verma A. II-863
Verreck M. I-123
Vietzke E. II-827
Vila J. II-1183
Villain J.P. III-1591
Villard L. I-343
Villasenor J. II-965
Vladimirov S.V. II-993,II-1333
Vlases G. II-723,II-727,II-735
Vogl G. III-2149
Voitsekhovich I.A. I-207
Volkov V. I-371
Vollmer O. I-7
Von Goeler S. II-949
Von Hellermann M.G. I-63,I-263,I-439,
II-881,II-1035,II-1485
Voss K. II-949
Vshivkov V.A. III-1639
Wade M.R. I-275

Wagner F. I-7,I-195,I-231
Wahlberg C. I-603
Waidmann G. I-95,I-359
Wakatani M. I-489,I-557,II-1131
Walder G. III-2095
Walsh M.J. I-31
Walters P.E. II-795
Wang E.Y. I-223
Wang J. I-695
Wang Z.H. I-215,I-223
Ward D.J. I-3,I-19,I-255,I-343,I-467
Warrick C.D. II-897
Watkins M.L. II-731
Watkins N. I-251
Weiland J. II-1441
Weinlich M. II-787
Welander A. I-595
Weller A. I-549
Werthmann H. II-925
Wesson J. II-897
West W.P. I-275
White R.B. I-431
Wieland R.M. I-43,I-203
Wilgen J.B. I-521,I-525
Wing W.R. I-521
Winkler C. III-2095
Winter H. II-1163
Winter J. I-11
Wising F. I-391
Wittenberg R.W. II-1477
Wobig H. I-569,I-581,II-867
Wolf G.H. I-95
Wolf U. II-1385
Wolfe S. II-953
Wolff H. II-1167
Wolle B. II-1035,II-1485
Wong K.-L. I-431
Wootton A.J. I-91,I-115
Woskov P.P. I-407
Woyke W. I-451,I-455
Wunderlich R. I-459
Wurtele J.S. III-1811
Wyller J. II-1309
Xie J.K. I-347
Xu S. I-647
Xu Y. I-615
Yadav L.L. III-1823
Yaguchi K. I-489
Yakimenko I.P. I-707,II-1377
Yakovenko Yu.V. I-391
Yamada H. I-513,I-517,I-521
Yamada I. I-513,I-517
Yamagiwa K. III-1859
Yamaguchi H. I-699
Yamamoto T. II-985
Yang H.R. I-223
Yang J.W. I-223,I-395
Yang Q.W. I-223
Yang S.K. I-223
Yang X.Z. I-363
Yao L.H. I-223
Yao Q. III-1713
Yi P. I-615
Yu C.X. I-363
Yu M.Y. II-1533
Yuan C.J. I-223
Yugami N. III-1927,III-1931
Zacek F. I-219
Zagorodny A.G. II-1377
Zaitsev F.S. II-1341
Zakharov A.P. I-47
Zakharov L.E. I-367
Zakharov Yu.P. III-1689
Zakouril P. III-1989
Zambreanu V. I-687
Zanza V. I-127,I-295
Zaporowski B. III-2005
Zarnstorff M.C. I-39,I-43
Zastrow K.-D. I-595,I-611
Zebrowski J. I-691,II-1215
Zehrfeld H.P. I-459
Zelazny R. II-1537
Zenevich V.A. III-2087
Zerbini M. I-127,I-463
Zhang G.Y. I-395
Zhang P. I-615
Zhang S. I-615
Zhang S.X. I-223
Zhao S.J. I-363
Zhelyazkov I. II-1517,III-1635,III-2041
Zheng L.-J. I-553
Zheng Y.Z. I-223
Zhong Y.Z. I-395
Zhuravlev V. II-1075
Zhykharsky A. II-1553,II-1557
Zielinski J.J. I-525,I-529
Zilker F. II-1063
Zohm H. I-231,I-235,I-243,II-743
Zoita V. I-687
Zoler D. III-2117
Zoletnik S. I-303
Zolfaghari A. I-163,I-335,I-339,I-407
Zolotukhin A.V. I-569
Zöpfel S. I-509
Zuo H.N. I-223
Zurro B. I-99,I-299,II-1135
Zushi H. I-489,II-1131
Zvonkov A.V. II-1521
Zweben S.J. I-43,I-203,I-431
Zwingmann P.W. I-311,I-335,I-339